Scuola Normale Superiore

Classe di Scienze

Theory and simulations of free and supported metal nanoclusters and nanoalloys

---

by Alessandro Fortunelli

e-mail: alessandro.fortunelli@cnr.it

Pisa, December 2011

To my father

Contents

Introduction

Metal nanoclusters and nanoalloys (i.e., pure or mixed metallic aggregates of dimensions ranging between 1 and 100 nanometers) are a subject of great interest in basic science as well as in current technology where they find many applications (and many more promising ones have been prospected in the literature) for their unique properties: from chemical sensing (artificial noses) to heterogeneous catalysis [LewisCR1993; HandbookHetCat2008], from magnetic recording to opto-electronic devices, thermal treatment of cancer, and "cell imaging", i.e. colorimetric probes for DNA detection [KreibigBook1995; BurdaCR2005; HalasCR2011; MortonCR2011]. In a wide historical perspective, all this may be thought to stem as an outspring of metallurgy thousands of years ago, when humanity unknowingly discovered how to produce metal nanoparticles and to exploit their surface plasmonic resonance, i.e., the coherent and collective oscillation of electrons involved in metallic bond in confined systems subjected to electromagnetic radiation of proper wave length, for esthetic purposes (stained glass and fine glassware, with coloring durable till today) [DanielCR2004]. Materials containing metal nanoparticles were later also proposed for curative use [DanielCR2004]. A more conscious step forward was achieved in mid-XIX century by Michael Faraday, with the preparation of colloidal suspensions via chemical reduction of metal salts in the presence of stabilizing agents in solution [FaradayPTRSL1857]. The physics of nanoscale metal clusters then strongly developed in the XX century with the advent of nanocatalysis and dramatically in recent years, following the continuous advances in synthetic and characterization tools that allow one to manipulate matter at the nanometer scale by preparing and measuring the properties of nanostructured systems with increasing precision [MaACSN2010; DelFattiGB2008; NetzerSS2010; PileniNM2003; JudaiJACS2004; GambardellaS2003] and the developments of theoretical methods able to rationalize and predict experimental behavior and properties [EbertRPP1996; CaroBook2008; ChenJPCC2010; ZhuMP2011].

The reasons of the interest in metallic nanosystems and their fascinating applications lie in the peculiar features of the confined metallic bond [McWeenyBook1980]. The presence of conduction band electrons whose mobility enhances transport and response properties [TimpNanotechnology1999] combined in transition metals with localized electrons in incomplete d-shells, assuring both easy formation and breaking of chemical bonds (and thus a rich and varied chemistry) and large magnetic moments, and the sensitivity of these properties to coupling with size, shape, composition and external fields make of metal nanoparticles and nanoalloys really unique materials, an ideal topic of research and investigation in many fields of science and technology.

Theory and simulations currently play an increasingly important role in the study of these materials, rationalizing the observed behavior and sometimes anticipating and triggering promising applications. As in other fields of chemistry and physics, first-principles theoretical approaches (i.e., approaches based on an explicit description of the many-electron wave function) have proved able to describe with fair accuracy the complexities of the chemical bond in such systems. However, their application is limited by the involved computational effort, rapidly increasing as a function of the size of the system. Among first-principles approaches, density-functional theory (DFT) is most often employed, as it currently represents the best compromise between accuracy and computational effort. Despite the inherent demands of DFT calculations, contemporary advances both in methods and hardware are continuously extending the range of systems to which they can be successfully applied, and nowadays electronic structure simulations are routinely conducted using one of the several black-box packages available. This is the realm of the present Thesis.

Much of the work here described thus concerns aggregates of size between a few and few fifty atoms (say – below 150 atoms), a size interval of particular interest for two reasons: (1) it represents the link (both conceptually and in the reality of a growth process) between molecule-like systems on the one side and bulk-like systems on the other, and (2) first-principles approaches are here both applicable and probably indispensable. It is found in fact that finite-size effects, especially those from quantum origins, are particularly relevant in the size range below 1-2 hundreds atoms, and give rise to a behavior fundamentally different from that of systems only slightly larger. For example, the interaction with surface defects in the case of supported systems, the mobility, or the fact that electronic effects such as those connected with electronic shell closure have been experimentally proven to be determining only for clusters smaller than about 50-150 atoms [deHeerRMP1993], etc. To use a celebrated expression, we are still in the strongly non-scalable régime where “each atom counts”. The possibility offered by recent software and hardware advances to realize a fully first-principles investigation of these systems thus perfectly matches their scientific relevance and offers the chance to study in a realistic way effects of quantum origin and the associated peculiar properties in a size range in which they are crucial. Our strategic choice of devoting effort on this size range has hence paid off, see below the list of main results.

Particles few nanometers in size are also very interesting but still basically outside the scope of purely first-principles approaches. A significant portion of the work here described was therefore aimed at developing methods that allow one to extend the scope of computational simulations and achieve reliable predictions on these systems via a hybrid combination of first-principles and empirical approaches or via exclusively empirical methods. A thorough comparison with more rigorous approaches in the 1-2 nm size range has also shown that current empirical models are sometimes inadequate or at least have limitations to describe the interesting physics of these systems and new models have been developed or suggested.

In the work reported in the present thesis much attention has been focused on the study of the structural properties of metal nanoclusters. The importance of structure-property relationships is well known in general. It is particularly crucial in this field, in which the incremental and scarcely directional character of the metallic bond makes that metal nanoparticles can assume and are found in a huge variety of different configurations and morphologies, so diverse as to substantially influence the corresponding properties. A link can be made here to the general field of "rugged energy landscapes" [WalesBook2003], i.e., the study of complex systems whose potential energy surface presents a great number of close local minima interconnected by small energy barriers. For such systems, the prediction of the low-energy structures and the mechanisms of their inter-conversion is essential to achieve a predictive computational science. Only through a deeper understanding and orientation of the factors that govern the spatial arrangement of atoms it is possible to control the synthesis and growth processes and then ultimately the system properties. Moreover, structural phenomena present an intrinsic interest in themselves for the new physics they involve and originate [LordBook2006]. Focus on the structural properties was also paralleled by the recent advances at the experimental level in the structural characterization especially of supported clusters [LibudaSSR2005; RenaudS2003; YacamanTC2002; PauwelsPRB2000]. Only very recently and for the first time it has in fact been possible to monitor the interaction of single atomic species with an oxide surface [YulikovPRL2006], the supported cluster morphology [BarthNT2006], and the characteristics of oxide surfaces both regular [BarthPRL2003; SterrerACIE2006] and defected [LeroyPRL2005; HammPRL2006]. On the one hand, this experimental information has allowed us to cross-check and validate theoretical models and predictions. On the other hand, experimental data often required theoretical modeling as a natural complement for their correct interpretation and to provide missing information. The synergy between theory and experiment is thus particularly beneficial and productive in this field, as proven also by the results to be described in the following.

In-depth knowledge on properties other than structural ones is anyway essential in applications and thus the ultimate target of any theoretical effort. Preliminary but very promising results on optical, magnetic and catalytic properties will be presented in the last chapter of this Thesis, and are one main focus of our current research.

The classes of systems here investigated will deal nearly exclusively with particles either free or supported on various oxide surfaces. Ligand-protected particles, such as those originally investigated by Faraday or their more recent counterparts embedded in polymer matrices or bio-compatible coatings which have important bio-medical applications, will not be considered. It should be underlined however that the methods here described can apply equally well to these other classes of materials, and we believe that such an extension is desirable, and indeed we present a preliminary example in the last section of this Thesis.

These investigations (and those pursued by other research groups) have brought about a wealth of basic knowledge on metal nanoclusters and nanoalloys, furnishing a deeper – sometimes novel – interpretation of experiments and significantly increasing our understanding of these systems. Many specific features of the metallic bond at the nanoscale have been highlighted, especially in the range of sub-nanometer to few-nanometer particles. Exotic morphologies and unusual structural arrangements have been rationalized and their links to peculiar properties of metal particles have been proposed. Among the most interesting results to be described in the following chapters, we mention:

- the development of original methods for structural prediction: density-functional/global-optimization (DF-GO) [ApraPRB2006; BarcaroCEJ2007], density-functional/empirical-potential [BarcaroJPCB2006b;BorbonPCCP2007; FerrandoPCCP2008] (DF-EP), large-size extrapolation [BalettoJCP2002], symmetry orbits & chemical ordering [FortunelliJMS1999b; BarcaroNL2011a] and reactive global-optimization (RGO) algorithms [NegreirosNS2012]: methodological advances have been fundamental to derive new results and discover novel phenomena;
- the derivation of general concepts for gas-phase and supported metal nanoclusters and nanoalloys [ApraJMS2000; BarcaroJTCT2005; FerrandoPRB2005];
- for gas-phase metal nanoclusters and nanoalloys the discovery of novel structural motifs: amorphous [ApraPRL2004], hybrid five-fold/close-packed [BorbonJPCC2007; BorbonJCP2008], poly-icosahedral [RossiPRL2004], and chemical ordering patterns: patchy multi-shell [BarcaroNL2011a];
- for oxide-supported metal nanoclusters and nanoalloys the discovery of novel structural motifs, surface magic clusters and interface-stabilized phases [BarcaroJPCC2007; BarcaroPRB2007; BarcaroPRL2007; FerrandoPRL2009; FerrandoACSN2008; BarcaroJPCL2010];
- the mobility of small clusters and its importance for growth [BarcaroPRL2005];
- the topic of surface nanopatterning and template-assisted growth [GavioliPSS2011];
- the understanding of cooperative phase transformations in metal-on-ultrathin-oxide metal-supported systems [BarcaroJPCC2009; CavalierePCCP2011].

In the following, after an introductory chapter to the basic theoretical and computational approaches used in the study of free and supported metal nanoclusters and nanoalloys, examples of predictive computational science in the field of the structure and properties of metal nanoclusters and nanoalloys either free or supported on oxide surfaces will be presented with the aim of providing the basic concepts and ideas of this research, its present capabilities and limitations. A chapter on dynamical phenomena and properties will conclude the Thesis.

Chapter 2

Methods

The recent years have witnessed an explosive surge in the development and applications of computational science. The availability of increasingly more powerful, faster and cheaper computers and of an increasing number of computational packages (many of which freely accessible) that are more and more reliable, efficient and user-friendly has stimulated this surge, and a large community of computationally-oriented people is now active in practically all fields of science, ranging from both experimental and theoretical researchers to undergraduate and graduate students. The field of metal nanoclusters and nanoalloys is no exception to this general trend. Paralleling the impressive recent advances in the experimental characterization techniques, see e.g. Refs. [LibudaSSR2005; RenaudS2003; YacamanTC2002; PauwelsPRB2000], in the latest years an increasing number of theoretical and computational studies have appeared on this topic, especially dealing with the prediction of the structural properties of these systems, but also extending to magnetic, optical and catalytic response. This explosive behavior is not without its drawbacks. A risk of indiscriminate use is always present, also considering the fact that a bit of empiricism is required in the choice of the numerical parameters of the simulations, i.e., the numerical details of the algorithms used in solving the corresponding equations. This risk can be avoided if the basic concepts on which theoretical approaches, ranging from first-principles approaches to quasicontinuum methods, rely are kept in mind. The aim of the present chapter is to provide an introductory description of these basic concepts and theoretical tools commonly employed in the study of metal nanoclusters and nanoalloys.

The chapter is organized as follows. We first present a brief introduction to first-principles approaches, focusing special attention on advantages and limitations of density-functional theory (DFT). We then review empirical approaches and briefly mention effective Hamiltonians. The problem of how to achieve accurate structural predictions in the field of metal nanoparticles and nanoalloys is then dealt with, and a hierarchical multi-scale computational protocol is discussed. The use of electronically and/or structurally “magic” clusters is successively described together with the associated advantages and assured simplifications. A section dealing with issues specific to multi-component metal clusters (or nanoalloys) concludes the chapter.

2.1 First-principles approaches to the description of metal nanoclusters and nanoalloys

Let us start by defining a general framework for our analysis: the considerations that follow can be found in standard textbooks [MahanBook2008; CohenBook2006] and are here summarized for convenience of the reader. The phenomena we are interested in involve energies typically in the range from a few cm^{-1} to a few tens of electron-Volts (eV). In this energy range, which includes much of chemistry, molecular and solid state physics, and materials science, the behavior of the system is well described by one variant of Quantum Mechanics (QM). Specifically, for systems constituted of light elements a full solution of the Schrödinger equation [SchrodingerPR1926] would provide an accurate description of the system, whereas for systems containing heavy elements relativistic corrections, described for a single electron by the Dirac equation [DiracPRS1928], come into play. Even though, in fact, the typical energies and thus the physics of the valence electrons (those determining the chemistry of the system) are non-relativistic, the interaction of the valence electrons with the core ones, i.e., the electrons closer to and strongly affected by the proximity to the nuclei and whose speed can approach that of light, appreciably modifies the field in which valence electrons move and thus ultimately their chemical behavior, with gold being the prototypical example in this context [PyykkoACIE2004]. Metal nanoclusters and nanoalloys, both bare and in various environments, perfectly fit in this framework, in the sense that bonding in these systems can be accurately described by Quantum Mechanics. The problem, however, is that it is impossible with the present computational resources to obtain accurate solutions even of the non-relativistic Schrödinger equation for systems exceeding few particles (nuclei and electrons). One is therefore necessarily led to some sort of approximate theoretical treatments, which are traditionally distinguished into first-principles and (semi-)empirical ones. Theoretical approaches are named ‘first-principles’ when they do not rely on input sources other than basic physical constants, such as the Planck’s constant, the speed of light in vacuum, etc. In these approaches one aims at an explicit (though approximate) description of the electronic wave function of the system. There is a debate in the literature on whether density-functional approaches (for whose description see below) can be considered as ‘first-principles’ or not. On the one hand, their validity relies on rigorous mathematical theorems [HohenbergPR1964; KohnPR1965]. On the other hand, in their practical implementation they use functional forms which may sometimes contain parameters fitted onto experimental data or other sources, so that their standing as ‘first-principles’ in some cases is dubious. Nevertheless, as they are based on an explicit description of the electronic wave function (at least of the electronic wave function of a model non-interacting system) and in key cases do not make use of empirical fitting of the in principle exact density functional, it is common practice by many to include them into ‘first-principles’ approaches. We adopt this practice here, and we include density-functional approaches into the ‘first-principles’ ones. With respect to empirical

approaches, in which the bonding interactions are expressed in terms of analytic functions of the system coordinates containing atomic or molecular parameters fitted on experimental or theoretical data, first-principles methods are more accurate but much more demanding in terms of computational resources, and thus applicable to a more restricted set of material systems. To study more complex systems, a multi-scale approach is usually invoked. This approach, which will be described in a next section, is based on the idea that systems containing a limited number of atoms are best described by rigorous first-principles approaches which are also used to single out the basic interactions and phenomena occurring in these systems, while by increasing the number of atoms the same physics of the system simplifies and some details of the Quantum Mechanical description become progressively less important whereas those still surviving as essential can be described in terms of a limited set of effective parameters (Renormalization Group ideas, see Fig. 10 below). For definitiveness, we assume to work from the start in the so-called Born-Oppenheimer approximation [BornAnnP1927], i.e., we take advantage of the much larger mass of the nuclei with respect to electrons and thus of their lesser mobility to solve the electronic problem at fixed nuclear coordinates, then providing the nuclei with a Potential Energy Surface (PES) for their movement, and considering residual effects such as electron-phonon coupling as perturbations.

The main problem in solving the Schrödinger equation for the electrons in the Born-Oppenheimer approximation is that the electronic wave function has a strong many-body character. In other words, the behavior of an electron in any region of space in principle depends on the relative position of all the other electrons. The first decisive simplification (or approximation) therefore consists in disentangling the behavior of a single particle (electron) from that of the rest of the system, and thus to formulate the many-body problem in terms of uncoupled or independent sets of single-particle equations. In the simplest instance, this is realized in the Hartree-Fock approximation, whose equations are the following:

$$\left(-\frac{\hbar^2}{2m}\nabla^2 + V(\boldsymbol{r}) + \int \frac{\sum_{j=1}^{N}\left[\varphi_j^*(\boldsymbol{r}')\varphi_j(\boldsymbol{r}')\right]}{|\boldsymbol{r}-\boldsymbol{r}'|}d\boldsymbol{r}'\right)\varphi_i(\boldsymbol{r}) - \sum_{j=1}^{N}\left(\int \frac{\varphi_j^*(\boldsymbol{r}')\varphi_i(\boldsymbol{r}')}{|\boldsymbol{r}-\boldsymbol{r}'|}d\boldsymbol{r}'\right)\varphi_j(\boldsymbol{r}) = \lambda_i\,\varphi_i(\boldsymbol{r}) \qquad (1)$$

In Eq. (1) the $\left(-\frac{\hbar^2}{2m}\nabla^2\right)$ term is the kinetic energy operator, the $V(\boldsymbol{r})$ term is the external electrostatic potential due to the nuclei, $\int \frac{\sum_{j=1}^{N}\left[\varphi_j^*(\boldsymbol{r}')\varphi_j(\boldsymbol{r}')\right]}{|\boldsymbol{r}-\boldsymbol{r}'|}d\boldsymbol{r}' = \int \frac{\rho(\boldsymbol{r}')}{|\boldsymbol{r}-\boldsymbol{r}'|}d\boldsymbol{r}'$ and $\sum_{j=1}^{N}\left(\int \frac{\varphi_j^*(\boldsymbol{r}')\varphi_i(\boldsymbol{r}')}{|\boldsymbol{r}-\boldsymbol{r}'|}d\boldsymbol{r}'\right)$ are the Coulomb and exchange operators, respectively, describing the average field generated by all the electrons, and λ_i is the one-electron or orbital energy of the $\varphi_i(\boldsymbol{r})$ orbital, while $\rho(\boldsymbol{r})$ is the total electron density. The Hartree-Fock equations are obtained by assuming that the electronic wave function can be written as a (properly anti-symmetrized) product of wave functions for each

single electron (i.e., a so-called Slater determinant) and minimizing the total energy as a function of the $\varphi_i(\boldsymbol{r})$ orbitals (the wave functions for the single electrons). As can be seen from Eq. (1), according to the Hartree-Fock approximation one has to solve a single-particle (or one-electron) Hamiltonian and to derive the single-particle (or one-electron) wave functions (or orbitals) and energies, from which the total energy of the system can be obtained. As the Coulomb and exchange operators in turn depend on the one-electron orbitals $\varphi_i(\boldsymbol{r})$, the Hartree-Fock equations are usually solved in a self-consistent fashion, in which trial orbitals are used to construct the Coulomb and exchange operators and thus the Hartree-Fock Hamiltonian, from whose solution one derives new orbitals that are again used as input to build a new Hartree-Fock Hamiltonian and so on until convergence is achieved. It should be noted that – due to the non-linear character of the Hartree-Fock equations – the total energy does not coincide with the sum of the single-particle or orbital energies: this is necessary to avoid double-counting of the Coulomb and exchange contributions and is a typical feature of single-particle approaches, at variance with the original Schrödinger equation which is many-body but linear. The advantages of the Hartree-Fock approximation are apparent: the complexity of the complete solution of the Schrödinger equation reduces to finding an average description of the electron cloud which produces an effective field in which the electrons themselves move. This originates the self-consistent character of the problem: the average or effective field generated by the one-electron orbitals must be consistent with the motion predicted for electrons moving in this same field. The switch from linear to non-linear mathematics entails well-known issues (e.g., convergence problems, that in some cases can be severe). These issues should always be kept in mind when applying black-box electronic structure codes, but this drawback is more than compensated by the enlargement of the set of systems that can now be treated. Presently, self-consistent calculations can indeed be conducted on systems composed of several thousand electrons, and further progress (both in terms of the size of affordable systems and in terms of speed of computations) are expected to come about in the future following the continuous advances in hardware and software. An important feature in this respect is that, even though the interaction between the single particle (electron) and the effective field in which the particles are moving needs to be described, it is possible to devise techniques which exploit the local character of this particle/field interaction and achieve so-called "linear scaling", i.e., a simple proportionality between the size of the system (typically the total number of atoms, N) and the cost of the simulation [StrainS1996, GoedeckerRMP1999]. It should be noted that linear scaling is far from being automatically achieved: a naively implemented Hartree-Fock method scales as N^{3-4}, while an advanced and very accurate post-Hartree-Fock method such as coupled-cluster perturbation expansion including single and double excitations and a perturbative treatment of triple excitation (CCSD-T) in principle scales as N^{7-8} if the simplifications due to locality of interactions are not exploited. This means that doubling the size of the system entails a computational cost at least 8 times higher for an untamed Hartree-Fock calculation (and up to 256 times higher for an untamed CCSD-T calculation). A proper and

efficient numerical solution of the single-particle equations is therefore mandatory to extend the scope of simulations to realistic systems.

Apart from technical issues of efficient implementation, what is lacking in the Hartree-Fock approximation from the in-principle point of view is the treatment of correlation effects, i.e., the phenomena and the energy contributions due to the fact that electrons in reality do not move in an average or effective field generated by the other electrons, but interact among each other in a many-body fashion, so that their motion is "correlated". This aspect becomes crucial when electrons get close in real space: the associated effects are grouped under the term of short-range correlation. For example, one speaks of the Coulomb hole, i.e., the depletion in the pair electron density with respect to the Hartree-Fock predictions due to the Coulombic repulsion when two electrons approach each other. Still relying on an explicit description of the electronic wave function, one can improve upon the Hartree-Fock approximation by using so-called post-Hartree-Fock or 'ab initio' first-principles approaches. In these approaches variational or perturbative methods are applied to expand the electronic wave function in terms of excitations with respect to the Hartree-Fock wave function (the Slater determinant): by moving one electron from an orbital which is occupied in the ground-state Slater determinant to an unoccupied (or virtual) orbital, one obtains a single excitation, by moving two electrons from occupied to virtual orbitals one obtains a double excitation, etc. Configuration Interaction (CI) or multi-configuration self-consistent-field (MC-SCF) are the most popular among the post-Hartree-Fock variational methods, while Moeller-Plesset (MP) or Coupled Cluster (CC) methods are eminent among the perturbative methods [SzaboBook1996]. In principle, these approaches can reach a high accuracy. However, one main difficulty lies in the inefficient description of short-range correlation or the Coulomb hole, associated with the slow convergence of the expansion of the two-body electronic wave function for small values of the relative electron distance in terms of product functions of the coordinates of the two electrons. Furthermore, for systems such as those composed of metal atoms in which electronic states of different character are very close in energy (say – nd^{10}, $nd^{9}(n+1)s^{1}$ and $nd^{8}(n+1)s^{2}$ in a end-of-row transition metal) it is difficult at the ab initio level to find the correct balance in the description of differential correlation effects. For metal clusters, other problems also come from so-called long-range correlation effects. Metallic systems in fact as a rule present a very small band or HOMO-LUMO gap, i.e., a very small energy difference between their Highest Occupied Molecular Orbital (HOMO) and Lowest Unoccupied Molecular Orbital (LUMO). This makes them quite different from insulating systems in terms of localization properties of the electronic wave function [MarchRPP1968] and convergence of post-Hartree-Fock methods, as it entails the presence of a wealth of low-energy electronic excitations and the need of a delicate balance in the description of their interaction to achieve an accurate assessment of the system energetics. It can be recalled in this connection that the Hartree-Fock approximation is known to describe very poorly a system which is usually taken as a model of the metallic bond, i.e., the electron gas or "jellium" (an idealized system composed of electrons moving

in a constant external potential). In detail, it is known that the band width and the density of electronic states at the Fermi level (i.e., the energy threshold between occupied and unoccupied orbitals) are severely exaggerated at the Hartree-Fock level [KittelBook1996]. Remnants of this behavior can be observed also for metal clusters, undermining the use of the Hartree-Fock exchange in standard hybrid DFT approaches for these systems (see below) [ApraJMS2000; NavaPCCP2003]. In short, quasi-degeneracies and vanishing gaps cause issues to ab initio first-principles approaches, and the net result is that they are not much used in the field of metal nanoclusters, so that they will not be discussed in detail here.

The problems associated with short-range and some long-range correlation effects can be overcome by density-functional theory (DFT). DFT in its Kohn-Sham version is a single-particle (or one-electron) method. The Kohn-Sham equations are therefore formally equivalent to the Hartree-Fock ones, and read:

$$\left(-\frac{\hbar^2}{2m}\nabla^2 + V(\boldsymbol{r}) + \int \frac{\rho(\boldsymbol{r}')}{|\boldsymbol{r}-\boldsymbol{r}'|}d\boldsymbol{r}' + V_{xc}[\rho(\boldsymbol{r})](\boldsymbol{r})\right)\varphi_i(\boldsymbol{r}) = \lambda_i\,\varphi_i(\boldsymbol{r}) \qquad (2)$$

where the exchange operator in the Hartree-Fock equations is now replaced by an exchange-correlation (or xc-) operator, $V_{xc}[\rho(\boldsymbol{r})]$, which is a functional of the electron density, thus an xc-functional. Two theorems from the ’60 [HohenbergPR1964; KohnPR1965] assure that the method is in principle exact, i.e., that it exists an exact xc-functional of the electron density such that the total energy constructed on the basis of the one-electron orbitals derived from the solutions of Eq. (2) provides the exact energy of the system. It should be noted in passing that, as in the Hartree-Fock case, the non-linear character of the Kohn-Sham equations makes that the total energy is not the sum of one-electron energies. The basic problem of DFT is that the exact xc-functional is unknown. Even worse, in the few exactly soluble model cases in which it has been possible to derive the correct expression for the xc-functional, this has proved to be extremely complicated. It is thus generally thought that knowledge of the exact xc-functional is tantamount to the exact solution of the Schrödinger equation and is thus practically out of question. The goal of present research is to derive increasingly accurate approximations to the exact xc-functional. This goal is often framed within the so-called Jacob’s ladder [PerdewJCP2005], which allows one to rank the various approximations to the exact xc-functional according to a well defined hierarchy. The xc-functionals most commonly employed at present for metal nanoclusters are the first two rungs of the ladder: the Local Density Approximation (LDA), in which the xc-functional is composed of the Slater exchange (simply proportional to the third root of the electron density) [DiracPCPS1930; SlaterBook1972] plus a correlation functional parametrized on accurate results derived for the homogeneous electron gas, and the Generalized Gradient Approximation (GGA), in which LDA is corrected via terms depending on

the gradient of the electron density [PerdewPRL1985; PerdewPRB1986; PerdewPRL1996]. LDA and GGA are called local or semi-local xc-functionals.

The third rung in the Jacob's ladder corresponds to the so-called meta-GGA xc-functionals, which make use not only of the local value of the electron density and its gradients, but also of the kinetic energy density for the occupied Kohn-Sham orbitals:

$$\tau_\sigma(\mathbf{r}) = \sum_i^{occup} (1/2) \left| \nabla \varphi_{i\sigma}(\mathbf{r}) \right|^2 \quad (3)$$

where σ is the spin. One non-empirical example of meta-GGA approaches is given in Ref. [TaoPRL2003]. The third rung of DFT somewhat improves upon the second (GGA) one, providing usually better values of atomization energies and also of structural parameters [StaroverovPRB2004].

Other very common xc-functionals correspond to the fourth rung of the Jacob's ladder, are named hybrid xc-functionals, and consist in a mixture of a GGA exchange and Hartree-Fock exchange [BeckeJCP1993; AdamoJCP1999; BeckeJCP2005]. The related formula for the exchange and correlation energy reads:

$$E_{xc}^{hybrid} = a\, E_x^{HF} + (1\text{-}a)\, E_x^{GGA} + E_c^{GGA} \quad (4)$$

where E_{xc}^{hybrid} is the xc-functional for the hybrid approach, E_x^{HF} is the Hartree-Fock exchange, E_x^{GGA} is a GGA exchange functional, E_c^{GGA} is a GGA correlation functional, and a is a parameter ranging between 0 and 1 (an analogous equation holds for the xc-potential). It should be noted that the admixture of a fraction of Hartree-Fock exchange is not an ad hoc trick, but is formally justified by adiabatic connection arguments, i.e., a rigorous formal connection between the non-interacting Kohn-Sham system and the physical one [YangJCP1998]. Actually, it is worthwhile recalling here that from a historical and genetic point of view the first DFT approach which went beyond LDA was developed by Salvetti and coworkers in the mid-'70 [ColleTCA1975]. This pioneering (even visionary) approach was basically an exact exchange plus an orbital-dependent correlation functional whose basic ingredient was the kinetic energy density for the occupied Kohn-Sham orbitals reported in Eq. (3), and was extremely influential for the successive developments of DFT. It should also be noted that the Hartree-Fock exchange is a functional not of the one-electron density but of the one-electron density matrix [McWeenyBook1969]:

$$\rho(\boldsymbol{x},\boldsymbol{x}') = N \int \Psi(\boldsymbol{x},\boldsymbol{x}_2,\ldots,\boldsymbol{x}_N) \times \int \Psi^*(\boldsymbol{x}',\boldsymbol{x}_2,\ldots,\boldsymbol{x}_N)\, d\boldsymbol{x}_2 \ldots d\boldsymbol{x}_N \quad (5)$$

where $\Psi(\boldsymbol{x},\boldsymbol{x}_2,\ldots,\boldsymbol{x}_N)$ is the many-electron wave function and $\boldsymbol{x}$ is a compound coordinate representing space $(\boldsymbol{r})$ and spin variables. The electron density is the diagonal part of $\rho(\boldsymbol{x},\boldsymbol{x}')$: $\rho(\boldsymbol{x}) = \rho(\boldsymbol{x},\boldsymbol{x})$. The kinetic energy density of the non-interacting electron system can also be expressed in terms of its one-electron density matrix, so that the xc-functional of Ref. [ColleTCA1975] is really a matrix-density

functional rather than a density functional. The fact that the Hartree-Fock exchange implies the use of the one-electron density matrix rather than the one-electron density has consequences from both in-principle and practical points of view. From an in-principle point of view this opens the way to xc-functionals explicitly depending on one-electron orbitals. This is advantageous in some respects. In particular, local or semi-local xc-functionals inherently suffer from the self-interaction correction (SIC) error, i.e., an erroneous attribution of a correlation energy to single-electron systems [PerdewPRB1981]. The use of the density matrix instead of the density allows hybrid xc-functionals to correct for this error, which should be negligible for spin-compensated metals, but can be substantial for systems with unpaired/localized electrons. From a practical viewpoint, however, the evaluation of the Hartree-Fock exchange is numerically harder than that of a functional of the electron density. To make an example without entering into technical details, while Hartree-Fock and later hybrid xc-functionals have been implemented in periodic codes using localized basis functions since a long time [Dovesi2006], their implementation in periodic codes using extended or delocalized (plane waves) basis sets is recent and computationally demanding [SchimkaJCP2011]. Moreover, auxiliary basis sets for expanding the electron density can be utilized to achieve linear scaling [FortunelliJCC1991; FortunelliCPL1991; ScuseriaJPCA1999; DunlapMP2010], but the extension to the density matrix is more complicated [FortunelliJCC1991; WeigendJCP2009]. In this connection, hybrid xc-functionals have been recently proposed that take advantage of so-called range-separation [HeydJCP2003]. In these approaches the $1/r_{12}$ term in the Hartree-Fock exchange is partitioned into a short-range and a long-range component and the latter (long-range) component in the exchange is screened, i.e., they consider only its short-range part, thus allowing a much more efficient numerical evaluation even for metallic systems [FortunelliCPL1991; Dovesi2006]. The corresponding exchange and correlation energy thus become [HeydJCP2003]:

$$E_{xc}^{\omega hybrid} = a\, E_x^{HF,SR}(\omega) + (1\text{-}a)\, E_x^{GGA,SR}(\omega) + E_x^{GGA,LR}(\omega) + E_c^{GGA} \qquad (6)$$

where ω is the screening parameter, $E_x^{HF,SR}(\omega)$ is the short-range part of the Hartree-Fock exchange, $E_x^{GGA,SR}(\omega)$ is the short-range part of the GGA exchange, is the long-range part of the GGA exchange, and is the GGA correlation functional.

The advantage of using hybrid xc-functionals is recognized when treating insulators or in general systems with a substantial HOMO-LUMO gap, such as oxides, but also organic molecules, for whose energetics the introduction of a Hartree-Fock term is often beneficial [BeckeJCP1993; AdamoJCP1999; BeckeJCP2005]. Due to the reduced SIC error, also the description of the magnetic properties of transition metal complexes is often improved by the use of hybrid DFT approaches [BaroneJACS1998], as well as systems with unpaired [AdamoJCP1995; ImprotaCR2004] or localized electrons. As mentioned above, these advantages can be undermined in the case of metal clusters (or in general gap-less systems) by an erroneous treatment of the electron-gas bonding [ApraJMS2000], so that standard

hybrid xc-functionals are in general little used when studying metal clusters. However, it should be pointed out that range-separated hybrid xc-functionals could be helpful also in this respect (apart from being computationally cheaper) as screening the long-range component of the exchange operator allows one to include exact exchange over a distance of few chemical bonds but reduces the issues connected with Hartree-Fock exchange in metallic systems, which are mostly due to its long-range component. Another promising recent approach is represented by the so-called local hybrid xc-functionals, in which the Hartree-Fock component is modulated by a space-dependent factor, see e.g. Refs. [TranPRL2009; HaunschildJCP2010] and references therein, in such a way that different parts of the systems are described by a different combination of Hartree-Fock and GGA exchanges, as pioneered to the best of our knowledge for the first time long ago in Ref. [CausaPS1988]. Also local hybrid approaches could in principle be advantageous and accurate for metal nanoclusters. Despite these favorable and promising features, however, more advanced hybrid xc-functionals (screened or local) have not been used extensively in the field of metal nanoclusters, probably because of a long-standing bias against the use of the Hartree-Fock exchange in metals, so that there is not yet enough evidence of their performance and accuracy. It is easy to foresee that this lack of knowledge will be filled in a near future.

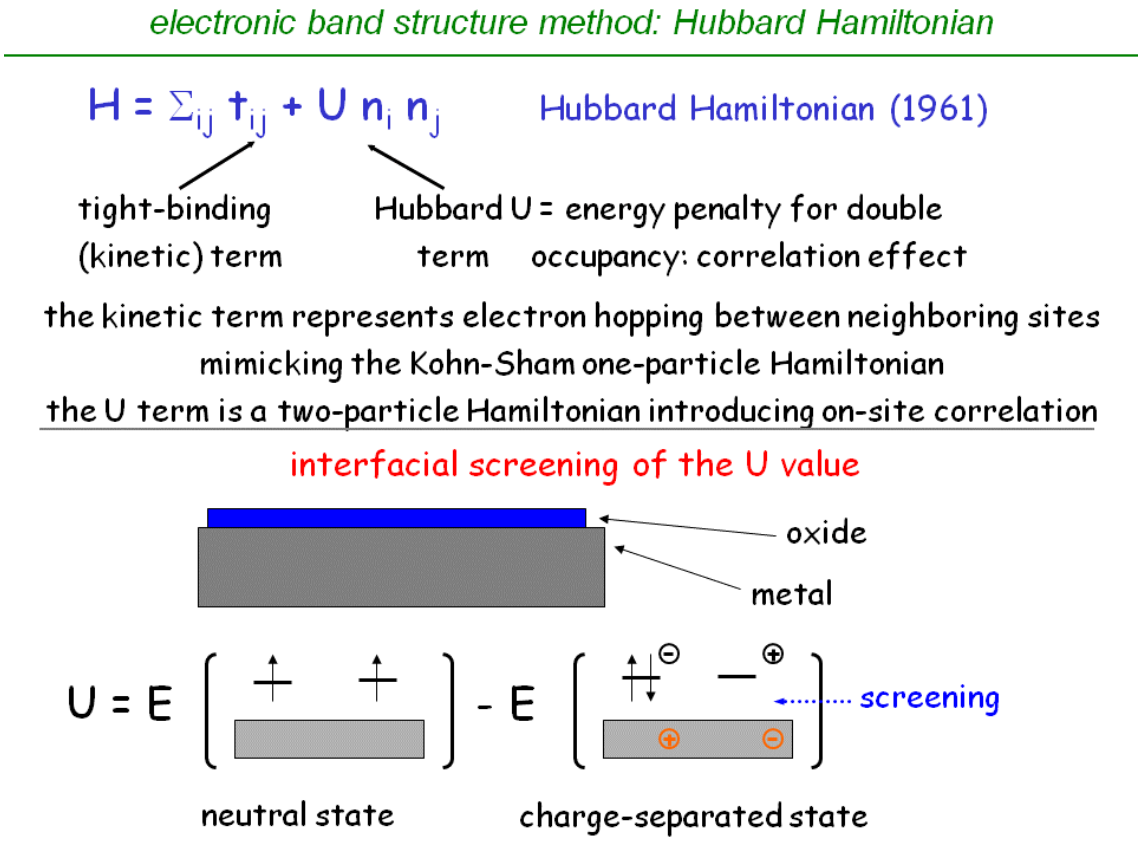

Fig. 1: Definition of the Hubbard Hamiltonian.

An extension of DFT is the so-called DFT+U method [AnisimovPRB1991]. This approach was developed to correct for the deficiencies of LDA and GGA xc-functionals in describing localized (or strongly correlated) electron systems. In these systems electron-electron scattering is not weak as in ideal metals where electrons spend most of their time in the internuclear regions: rather, electrons are here confined in localized inner-shell orbitals, as it happens with incomplete d- or f-shells. Therefore, electron-electron repulsion (giving rise to correlated motion) is here non-negligible with respect to the kinetic energy of electrons, and it can be so strong as to destroy the metallic character of the system and produce insulators (the Mott-Hubbard Metal-Insulator Transition [AustinS1970]). For obvious reasons, such systems are awkward to describe within a one-electron formalism, but their physics is conveniently modellized by effective Hamiltonian such as the Hubbard one:

$$\hat{H}^{Hubbard} = \sum_{ij}^{nn\text{-}sites} t_{ij} + \sum_{ij}^{sites} U\, n_j\, n_i \qquad (7)$$

where the Hubbard Hamiltonian $\hat{H}^{Hubbard}$ [HubbardRMP1961] is composed of a kinetic energy term t_{ij}, i.e., an electron hopping between nearest-neighbor sites, which models the band structure of the system, plus an electronic repulsion term, usually limited to the on-site component $U\, n_i\, n_i$. The idea of the DFT+U method is to combine the versatility of the DFT approach with a mean-field Hubbard-like correction due to electron-electron interactions, i.e., an energy penalty for the double occupation of specific orbitals, see Fig. 1. In detail, the DFT+U energy expression reads:

$$E_{DFT+U} = E_{DFT} + E_{Hubbard}[\{n_i\}] - E_{dc}[\{n_i\}] \qquad (8)$$

where E_{DFT} is the usual DFT total energy, $E_{Hubbard}[\{n_i\}]$ is the on-site Hubbard correlation functional, depending on the set of $\{n_i\}$, the generalized atomic occupations for the "Hubbard" atoms, i.e., the atoms with strongly correlated electrons, and $E_{dc}[\{n_i\}]$ is the mean-field approximation to the on-site correlation functional, which has to be subtracted to avoid double counting. The generalized atomic occupations $\{n_i\}$ are evaluated e.g. by Lowdin projecting the Kohn-Sham orbitals onto atomic-like basis functions, or via similar procedures. As these can be cheaply evaluated as a one-electron operators, the cost of a DFT+U calculation is only slightly (say – 10%-40%) larger than a standard DFT one (ignoring possible issues of convergence of the iterative self-consistent procedure). However, one has the bonus that the spectrum of one-electron eigenvalues is modified by a term: $U\,(1/2 - n_i)$ which opens a gap between occupied ($n_i \approx 1$) and unoccupied ($n_i \approx 0$) orbitals, and the DFT band gap problem is often effectively cured. This addition thus improves upon the description of localized electronic states via DFT and is widely used e.g. to treat magnetic insulators [CococcioniPRB2005]. The U value can in principle be evaluated a priori [FortunelliJCP1997; FortunelliPRB1997; PickettPRB1998], but it is common practice to derive it empirically by comparison with experiment, see e.g. Ref. [BarcaroJCP2010]. One of the advantages of the DFT+U approach is that it is

possible to add the U term selectively on certain atoms. In this way, one can describe composite systems such as metal/oxide ones by simultaneously retaining a satisfactory treatment of the metal component (described via a GGA DFT method) together with a fair description of the oxide component (via the DFT+*U* approach). In this connection, it can be added that the U value for the oxide layer at the interface with a metal support should be reduced with respect to the value appropriate to the bulk because of screening effects [BarcaroJCP2010; AltieriPRB2009], as depicted in Fig. 1. The DFT+*U* approach is thus especially advantageous when dealing with metal nanoclusters supported on ultra-thin oxides, as discussed below.

Another source of inaccuracy in the standard DFT approach is represented by long-range correlation effects connected with dispersion effects. Their origin lies in the dynamical polarization of the electron cloud induced by the presence of electrons belonging to nearby species. These are typically quantitatively smaller than typical bonding contributions, but originate terms in the PES decaying as inverse powers of atom-atom distances, and are thus awkward to describe in standard DFT using a functional of the electron density whose tails decay exponentially outside the atoms [MarchRPP1968]. Furthermore, dispersion effects are sometimes important especially for clusters of heavier metals [OlsonJACS2005]. The most common and rather effective way to account for these effects is to add semi-empirical terms to the total energy in the form of $C_6[n]/r^6$ tail corrections [FortunelliCPL1994; FortunelliJMS1995; GrimmeJCC2006], where r is an interatomic distance and $C_6[n]$ is a numerical coefficient, and the open debate is on how to choose the $C_6[n]$ coefficients in the physically most consistent way [TkatchenkoPRL2009].

Apart from so-called ab initio or post-Hartree-Fock approaches, first-principles methods that go beyond DFT also exist. Among these post-DFT methods we mention the Random Phase Approximation (RPA) and the so-called GW approach [OnidaRMP2002], see e.g. Ref. [BorbonPRB2012]. A different path to the solution of the Schrödinger equation passes through methods of statistical integration such as the Quantum Monte Carlo one [BoothJCP2010]. Note that all these methods can describe long-range correlation energy terms such as those involved in dispersion interactions. Despite the intrinsically high computational demands of these methods, orders of magnitude higher than standard DFT, their use is constantly increasing and it can be foreseen that it will become more widespread in the next future, especially for those systems and properties for which DFT presents limitations.

For supported clusters, from a technical point of view one has the additional problem of how to deal with extended (formally infinite) systems. To deal with this issue, both periodic and cluster models have been used with equal success in the description of supported metal nanoclusters. Periodic models make use of a supercell which is replicated in 2D or 3D and separation of individual supported particles is achieved by considering large enough cells, while cluster models truncate the infinite system (the support) at some point and account for boundary effects for example via external

potentials or other embedding techniques [FortunelliBook1992; HuangJCP2011] (see also Sec. 5.1 for embedding techniques in general). The two approaches are in principle equivalent, and indeed it has been shown in several cases that they produce comparable results once technical issues are properly taken care of, see e.g. Refs. [NasluzovJCP2001; BarcaroCEJ2007]. It should be noted in this connection that, when dealing with charged systems within the usual supercell approximation, the electrostatic interaction between the defect and its images is divergent and needs to be corrected [MakovPRB1995], so that periodic cell methods are usually considered as being less appropriate for charged systems. Moreover, in studying phases that present a net dipole moment perpendicular to the surface and periodic 3D modeling it is advisable to include a dipole correction into the Hamiltonian [BengtssonPRB1999] as it effectively cancels spurious interactions due to the periodic boundary conditions in planar polar slabs [RanjanPRB2008]. In the following description of research work and results, details of the numerical techniques used to solve the Kohn-Sham equations will not be explicitly given, and we refer to the original publications for their precise discussion. In general, care has been taken that the numerical parameters of the calculations, i.e., the numerical details of the algorithms used to solve the Kohn-Sham equations (such as basis sets, energy and density thresholds, etc.) were converged. However, it should be recalled that – especially for third-row transition or noble metals, such as Pt and Au – DF predictions actually depend on fine details of the calculations, including the basis set and even the choice of the pseudo-potential, in addition to the xc-functional.

Despite these limitations and the on-going research of improved and more versatile xc-functionals and on post-DFT approaches, DFT is the first-principles method most often employed in calculations on metal nanoclusters and nanoalloys, as it currently represents the best compromise between accuracy and computational effort. Being a single-particle (or one-electron) method it can scale linearly with the size of the system, i.e., it presents the lowest computational cost among first-principles approaches. Moreover, it is thought to efficiently describe short-range correlation effects and long-range effects associated with electron-gas bonding, which are both difficult to deal with by using post-Hartree-Fock ab initio first-principles approaches (see the discussion above).

Its current status in the field of metal nanoclusters can be summarized as follows. The most commonly utilized approaches are based on GGA xc-functionals. For bare metal clusters GGA approaches are often accurate enough, even though meta-GGA sometimes improve in terms of the prediction of energetics and structural parameters [StaroverovPRB2004]. Dispersion effects are important in some cases [OlsonJACS2005] and can be easily included via empirical corrections as mentioned above. Standard hybrid xc-functionals are usually avoided [ApraJMS2000; NavaPCCP2003], but there is a lack of knowledge on the performance and accuracy of screened and local hybrid methods. For supported clusters, the situation is similar, if not worse, in the sense that there is an even more severe lack of rigorous

knowledge. As an exception, an interesting recent study has shown by comparison with accurate post-DFT results that adhesion of very small Au clusters on a simple ionic support is well described by GGA functionals plus empirical dispersion corrections, although for a spin-uncompensated cluster such as the single Au atom the SIC error can be appreciable, whereas hybrid approaches (even screened ones) tend to underestimate the metal/surface interaction [BorbonPRB2012].

Many black-box packages are nowadays available to perform a wide range of electronic structure simulations within DFT, from total energy calculations, to structure optimizations, to the search for saddle points, to response properties, etc. Some of them are open-source codes that can be freely downloaded from the Web, and an increasing number of them has graphical interfaces that allow users to build up the system of their interest with a modest effort (for one example among the many possible ones, see e.g. Refs. [GiannozziJPCM2009; KokaljCMS2003]). A risk of indiscriminate use is of course present, especially considering the fact that a bit of empiricism or at least consolidated experience is strongly required in the crucial choice of the numerical parameters of the calculations, i.e., the numerical details of the algorithms used in solving the Kohn-Sham equations (such as basis sets, energy and density thresholds, pseudo-potentials, etc.) such as to produce results that are numerically robust and make physical sense. This risk is reduced if the basic principles discussed above behind such simulations are kept in mind. In any case the availability of such packages (cumulating decades of experience in applied mathematics and being continuously developed and improved) has significantly widened the scope and enhanced the impact of computational disciplines on both basic and applied research and even on industrial applications.

2.2 Empirical potentials

Several empirical potentials (EP) have been proposed and are often successfully used to describe the physics of the metal-metal interaction. Among these, the most popular are the embedded-atom-model [DawPRB1984] and glue-model [ErcolessiPRL1986] potentials, those based on the second-moment-approximation to the tight-binding (TB) energy (SMATB) [CyrotPRB1971; GuptaPRB1981; RosatoPMA1989], and their variants. To avoid confusion, note that the SMATB potentials, even though formally derived from a tight-binding formalism, are completely equivalent to the other EP, see Eqs. (9-11) below and the brief discussion of the TB approach at the end of this subsection. In general, in all these empirical schemes it is assumed that the total energy of the system can be expressed as the sum of atomic site energies with a many-body character, i.e., depending in an analytically compact form upon the number, distance, and orientation of the neighbours of each given metal atom. The fundamentally many-body character of the metal-metal interaction should be strongly stressed as a specific feature without which the interesting physics is completely lost. In other words, metal-metal interaction is not simply additive [CyrotPRB1971], and

the strength of a metal-metal bond substantially depends on its environment, i.e., on the number and distance of neighboring metal atoms, see the discussion for the SMATB EP below. This feature for example explains the bond-order/bond-length correlation [SolerSSC2001], i.e., the fact that the strength and the optimal metal-metal distance depend on the coordination number. Clearly from a computational point of view evaluating a simple analytic formula is extremely cheaper than solving some form of Schrödinger equation, and if one is concerned simply with the energy of the ground state of the system one can be fully satisfied with an empirical expression, if this is sufficiently accurate. Once one has this expression, it can be used to search for the low-energy minima of the PES, or in Molecular Dynamics (MD) simulations of the time evolution of the system, or in any other total energy calculation. In such a way one can easily treat systems containing millions of atoms, orders of magnitude larger than those accessible to first-principles approaches. However, EP also have intrinsic limitations that will be analysed in detail in Sec. 3.2.

In the work here presented, SMATB empirical potentials have always been used, in which the energy of a pure metal aggregate (E_i^{mm}) is expressed as [RosatoPMA1989]:

$$E_i^{mm} = E_i^r + E_i^a \tag{9}$$

with

$$E_i^r = \sum_{j<i, r_{ij}<r_c} A \exp\left[-p\left(\frac{r_{ij}}{r_o} - 1\right)\right] \tag{10}$$

$$E_i^a = -\left\{\sum_{j<i, r_{ij}<r_c} \xi^2 \exp\left[-2q\left(\frac{r_{ij}}{r_o} - 1\right)\right]\right\}^{\frac{1}{2}} \tag{11}$$

where r_{ij} is the distance between atoms i and j, r_c is a cut-off radius, and r_0 is the nearest-neighbour distance in the bulk. In Eq. (9) E_i^r is the repulsive component and E_i^a is the attractive one. Note the square root in Eq. (11) which gives the EP its non-additive (many-body) character. The potential is smoothly linked to zero by a polynomial function, e.g. between second- and third-neighbour distances (the cut-off radius r_c), but it should be noted that the zeroing of the potential can also be treated as a parameter to add further flexibility to the SMATB potential, for example to fit the difference between the fcc and hcp bulk phases, that is very sensitive to this quantity, as done e.g. in Ref. [FerrandoACSN2008]. The parameter set (A, ξ , p, q, r_0) (we recall that only four of these parameters are independent, as one of them is fixed by the equilibrium condition) is fitted to experimental bulk quantities, such as the binding energy, the equilibrium geometry, the elastic modulus, and usually one elastic constant [RosatoPMA1989]. We stress however that this is not necessarily the optimal choice. In fact, whereas the binding energy, the equilibrium geometry and the

elastic modulus (which is connected with the "stickiness" [DoyeJCP1995; BalettoJCP2002] of the metal-metal interaction) are fundamental quantities, the absolute values and the anisotropy of the surface energies are equally important to determine the shape of a nanocluster via the Wulff construction [WulffZK1901]. These latter quantities are not accurately measured at the experimental level, whereas they can be reasonably estimated from first-principles calculations. This is particularly true for the anisotropy of the surface energies, that is usually pretty robust to changes in the details of the theoretical approach (such as the choice of the xc-functional) and is thus believed to be reliably predicted at the theoretical level, so that it can be profitably used in fitting EP parameters [FerrandoACSN2008; NegreirosJCP2010].

Apart from these technical details, the SMATB EP lend themselves to illustrate in a particularly clear and analytic way the specific feature of the metallic bond. For example, it can be easily shown that the optimal energy $E_{min}(N)$ of an ideal system composed of only N-coordinated atoms is given by: $E_{min}(N) = E_{min}(12) \cdot (N/12)^{\alpha}$, where the exponent α is $\alpha = (p - 2q)/(p - q)$, while the corresponding equilibrium distance $R_{min}(N)$ is $R_{min}(N) = r_0[1 - \ln(12/N)/(p - q)]$. This illustrates how the strength and the equilibrium distance of a metal-metal bond depend upon coordination (i.e., the bond-order/bond-length correlation phenomenon mentioned above), and shows how this is controlled by the difference $(p - q)$ [or $(p - 2q)$]. Qualitative analysis can thus be easily made using analytic tools, which represents a significant advantage of SMATB EP (in addition to computational cheapness) with respect to sophisticated wave function approaches. In this respect, a crucial quantity is the "stickiness" of the metal-metal interaction [DoyeJCP1995], i.e. the ratio between the bulk modulus and the cohesive energy per atom for the given species. This determines for example the cross-over size among different structural motifs (see the discussion in Sec. 3.1). As shown in Ref. [BalettoJCP2002], the stickiness has a particularly simple expression for SMATB potentials, being essentially proportional to the product $p \cdot q$.

For mixed or multi-component systems, such as nanoalloys [JellinekCPL1996; FortunelliJMS1999b; FerrandoCR2008] (treated in Sec. 2.6), it is not difficult to generalize the definition given in Eqs. (9-11): one can simply use parameter sets (A_{KL}, ξ_{KL}, p_{KL}, q_{KL}, $r_{0,KL}$) which depend on the given (KL) pair of atoms. However, the problem of arriving at an accurate parametrization is here more complicated, as the *match* among the energy scales of the different elements composing the alloy becomes crucial. For bulk alloy systems, reasonably accurate empirical potentials have been developed [PunPM2009]. For nanoparticles the situation is still not completely clear, and more validation and development studies are strongly needed.

For supported metal particles, the total energy is usually written as the sum of the metal-metal energy contribution (E_i^{mm}), evaluated as described above, and the metal-surface interaction (E_i^{mo}) introduced as an separate additive contribution. The total

binding energy E_{bnd} of a cluster of N atoms is then written as the sum of atomic contributions E^i:

$$E_{bnd} = \sum_{i=1}^{N} E_i \tag{12}$$

with

$$E_i = E_i^{mm} + E_i^{mo} \tag{13}$$

where E_i^{mm} and E_i^{mo} model the metal-metal and metal-oxide interactions, respectively. A rather restricted set of choices is available in the literature for the metal-oxide interaction term. In the work here described, only those analytic forms of E_i^{mo} were considered that originated from the empirical potential proposed in Ref. [VervischPRB2002] for the square-symmetry MgO(100) surface. In this framework, a rigid metal-oxide potential energy surface is assumed, and the interaction energy between the metal cluster and the MgO(001) surface is modelled as a sum of interactions of each metal atom with the substrate. As a key-feature, this interaction presents a many-body character, i.e., it depends on the metal coverage, so that a metal atom surrounded by other metal atoms has a weaker interaction with the substrate than an isolated adatom. Again, the many-body character of the metallic bond has fundamental effects on the structural properties of metal nanoparticles, see e.g. the discussion in Ref. [BarcaroJPCL2010]. The dependence of this interaction on the distance from the substrate (z) is described via a Morse-like function, whereas a periodic cosine function is used to model the dependence of the interaction energy on x and y coordinates. The functional form of E_i^{mo} is [VervischPRB2002]:

$$\begin{aligned} E_i^{mo}(x_i,y_i,z_i,Z_i) &= a_1(x_i,y_i,Z_i)\left\{e^{-2a_2(x_i,y_i,Z_i)[z_i-a_3(x_i,y_i,Z_i)]} - 2e^{-a_2(x_i,y_i,Z_i)[z_i-a_3(x_i,y_i,Z_i)]}\right\} \\ a_j(x_i,y_i,Z_i) &= b_{j1}(x_i,y_i) + b_{j2}(x_i,y_i)e^{-Z_i/b_{j3}(x_i,y_i)} \\ b_{jk}(x_i,y_i) &= c_{jk1} + c_{jk2}\{\cos(\chi x_i) + \cos(\chi y_i)\} + c_{jk3}\{\cos[\chi(x_i+y_i)] + \cos[\chi(x_i-y_i)]\} \end{aligned} \tag{14}$$

In Eq. (14) Z_i is the number of metal nearest-neighbors of atom i, and $\chi = 2\pi/a$, with a the oxygen-oxygen distance in the substrate. The x and y coordinates are parallel to the <110> directions. Z_i is usually calculated including all neighbours within 1.25 r_0, with r_0 the nearest neighbour distance in the bulk metal, but the cut-off distance can also be used as a further parameter of the model. In the absence of accurate experimental data, the parameters contained in the model are fitted against first-principles DF calculations in order to take into account the main energetic characteristic of the metal-oxide interaction in the case of non-reactive interfaces. Note that it is assumed that the metal-oxide interaction is weak, with no interdiffusion and small interfacial charge transfer, and is principally due to polarization effects and van der Waals interactions, with only a small contribution from covalent metal-

oxygen bond. Eq. (14) contains 27 parameters c_{jkl}. The procedure so far used for fitting the c_{jkl} parameters is system-dependent. It is based on: (i) the choice of three ideal fitting systems (selected among the single atom, the (001) epitaxial pseudomorphic monolayer, the (001) epitaxial multilayer, and small clusters) and three surface sites (on top of oxygen and magnesium ions and in the hollow site positioned halfway between two oxygen ions), (ii) the derivation of the interaction energy curves in the corresponding nine cases, and (iii) their analysis to extract the values of interaction energy, distance, and curvature at equilibrium, which are directly related to the c_{jkl}. For example, in the case of Pd the fitting systems can be chosen as the single atom, the (001)epitaxial monolayer, and the (001) epitaxial bilayer as in the original work [VervischPRB2002]. The EP derived through such an approach for Pd produces results in some agreement with DF calculations [BarcaroPRL2007] for clusters of sizes up to 30 atoms. However, a drawback of such a model is that it does not take into proper account the "metal-on-top" effect [BarcaroJCTC2005], i.e., the enhancement in the adhesion energy due to the stabilizing contribution of metal atoms above the one directly interacting with the substrate. Such an effect, already present in the Pd/MgO and Pt/MgO systems, becomes dominant for noble metals such as Cu, Ag and Au, to such a degree that the behaviour of the adhesion energy as a function of coordination is not monotonic any more: the adhesion energy of the (001) monolayer is smaller in absolute value than that of the (001) bilayer (for analogous reasons, for example Pd or Pt dimers on MgO(001) lie horizontally on the substrate, whereas Ag and Au dimers are vertical [BarcaroJCTC2005]). To circumvent this problem without abandoning the simplicity of the original model, a possibility exemplified in Ref. [FerrandoJCP2009] is to select in the fitting procedure ideal systems in which the metal-on-top effect is implicitly included. For example, in the Ag and Au cases we found that replacing the (001) monolayer with the five-atom square pyramid is sufficient to obtain a smooth behaviour of the adhesion energy with coordination. It should be added that the choice of three ideal fitting systems and three surface sites drastically simplifies the derivation of the EP parameters and is usually a good starting point for the derivation of an accurate EP, but of course can be replaced (and has actually been replaced in various difficult cases, see e.g. Refs. [FerrandoACSN2008; RossiPCCP2010; BarcaroJPCL2010]) by more general fitting schemes in which the results of available DF calculations on any supported metal particles are used as input data in a self-consistent fashion (see Figs. 9,10 later). This is fundumental when the lattice mismatch between the metal and the support is so large as to make epitaxial pseudomorphic systems unphysical or at least unrealistic as fitting systems, such as for Co, Ni, Cu on MgO(100). We note in passing that the metal-substrate interaction from both the first-principles DF calculations and the analytic form of the EP in Eqs. (14) does not include van der Waals terms explicitly. The size of these terms is not usually accurately evaluated. This should not be a major drawback, as they can be easily added a posteriori, but it is important to assess their size, and investigations are being conducted in this direction [BorbonPRB2012]. The parameters c_{jkl} in Eqs. (14) for several metals can be found on the Web [WebParam]. It can be finally noted that

the relaxation of the constraint of a rigid metal-oxide potential energy surface is expected to be important in some cases, and is currently under study.

We mentioned at the beginning of this subsection an entirely different class of theoretical methods: that of empirical Hamiltonians, such as the tight-binding, TB, one. As these methods have not been intensively used in the field of metal nanoclusters and nanoalloys, we will not discuss them. However, we mention that the possibility but also the possible obstacles in deriving TB parameters on the basis of DFT calculations were explored in Refs. [FortunelliIJQC2004; ApraIJQC2004] with promising results. This topic (the use of empirical Hamiltonians as intermediate approaches between first-principles methods and empirical potentials) could become of interest in the theoretical community. For example, we are currently testing alternative ways to derive DFT-based TB parameters, also in view of studying the optical response of metal nanoparticles in a size range in which first-principles simulations are not yet feasible and the validity of electrodynamical models is questionable.

2.3 Effective Hamiltonians and continuum methods

For large suspended particles (say - containing more than 1-2 thousand atoms), use has often been made in the literature of effective Hamiltonians. The idea behind these approaches is that – once a metal particle reaches a given size – fluctuations and peculiarities due to the details of local atomic relaxations are suppressed, so that these subtleties do not need to be described by empirical potentials any more, and one can use atomic site energies [YangJCP1996] depending only on the number (possibly also the orientation) of neighboring atoms. A considerable speed-up in the total energy calculations (with the associated in principle limitations) is thus assured by the simplification of the many-body component of the energy expression and by the fact that geometry optimisations are not performed (i.e., forces are not calculated). This is particularly useful in the context of alloy nanoparticles, where it is in practice heavy, even using empirical potentials, to calculate the energy of a large particle as a function of the degrees of freedom associated with chemical ordering at the rate required by statistical thermodynamics simulations in the same way that it is done for the phase diagram of bulk systems [LopassoPRB2003]. In this context, Ising-type Hamiltonians with so-called effective cluster interactions are often introduced to simplify energy evaluation [PolakSSR2000; AbrikosovRPP2008]. It should be noted that – even though they are called ‘Hamiltonians’ – effective Hamiltonians are very different from the Hamiltonians used in first-principles approaches, as no equations need to be solved and the total energy of the system is simply evaluated by summing the atomic-site energies. The difficulty with these Hamiltonians is that one is required to have already solved the structural problem, i.e., to have a stable motif for which the atomic-site energetics can be defined. This difficulty is even keener for particles deposited on a substrate, as dislocations, distortions, etc. are created at the interface

due to the particle/substrate lattice mismatch. A different avenue to further reduce the number of degrees of freedom in nanoparticle systems is represented by the use of multi-scale methods combining atomistic and continuum simulations, as in the so-called quasicontinuum approach [TadmorPM1996]. This approach can be useful for example to overcome the limitations of rigid models of the oxide surface and to include reaction elastic fields that may be important in some cases in determining the energetics of adhesion and epitaxial relationships. To the best of our knowledge, effective Hamiltonians and quasicontinuum methods have not yet been applied to the study of supported metal clusters, but it is possible that this gap will be filled in the future.

2.4 Tools for structure prediction: a hierarchical multi-scale approach

Among the peculiar features of the metallic bond, the two ones that are probably the most important in the study of the structural properties of metal nanoclusters and nanoalloys are its "greedy" and non-directional (or, better, scarcely directional) character [PaulingBook1960; McWeenyBook1980]. As greedy character it is meant that the coordination number of a metal atom can reach high values, spanning from one to 12 or more (coordination numbers of 13, 14 are also observed [FrankAC1958; FrankAC1959]) with a relatively slow saturation in terms of bond energies, i.e., the average bond strength is only slowly decreasing with increasing the coordination number. Secondly, the metal-metal interaction is scarcely directional: even though in some transition metals such as Au the hybridization of s and d orbitals entails some bonding directionality [OlivierPRB2008; PyykkoACIE2004; HakkinenCSR2008], especially for simple metals one encounters a nearly isotropic dependence of the bond energy on the bond angular variables. These two features makes that metal nanoclusters present a highly "fluxional" character, i.e., they can be found in structurally rather different configurations which however all lie in a narrow energy range. This effect is particularly apparent in small clusters. To make an example, the energy differences between the global minimum and the lowest-energy isomers of small Ag clusters in the gas-phase or adsorbed on defected oxide surface – namely, the F_s-defected MgO(100) surface (see the next sections for more details on this surface) – are reported in Fig. 2 [BarcaroCEJ2007]. It can be seen that the lower values for such differences amount to at most 0.1-0.2 eV, and that the effect of the interaction with the surface in this case is to further increase this fluxional character, i.e., to reduce these energy differences.

Ag_N clusters on the F_s-defected MgO(100) terrace

fluxional character

ΔE	Ag_4	Ag_6	Ag_8	Ag_{10}
gas-phase	-	0.2-0.6	0.1-0.2	0.1-0.3
absorbed	0.01-0.03	0.03-0.20	0.03-0.30	0.11-0.98

Fig. 2: Energy differences between the global minimum and the lowest-energy isomers of small Ag clusters in the gas-phase or adsorbed on the F_s-defected MgO(100) surface

issue in structure prediction: variety of cluster structures

"greedy" and "fluxional" character of metal-metal interaction

⇩

a variety of possible structural motifs

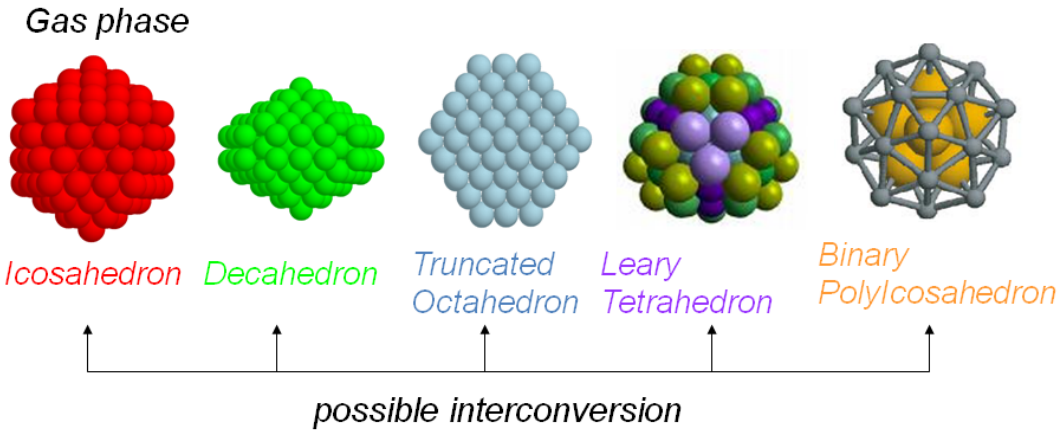

⇒ how to predict the cluster structure(s) ?

Fig. 3: Examples of structural motifs which are observed in metal nanoclusters and nanoalloys

It is thus an experimental observation with a sound theoretical basis that metal nanoparticles and nanoalloys can exhibit an impressive variety of different structures and morphologies: some representative examples are shown in Fig. 3. The fact that the PES of a metal cluster system is characterized by a large number of local minima with relatively small energy differences represents a challenge at the theoretical/computational level if accurate quantitative predictions are sought for. A convenient connection can be made here with the general topic and the theory of rough energy landscapes [WalesBook2003]. This feature is in fact shared by many different materials, such as biological macromolecules, amorphous polymers, etc. so that general tools have been developed to tackle this problem.

In the field of metal nanoclusters, the most successful computational algorithms that have been developed in recent years to perform a systematic sampling of their PES [FerrandoPCCP2008] are based on a hierarchy of length scales, i.e., in these approaches the choice of the theoretical modeling to be employed in performing simulations on a specific system is tuned according to its size, as illustrated in Fig. 4. The idea behind these hierarchical approaches is to use for systems of different size the approach which is most efficient and also makes physical sense for each one of them. They will be briefly reviewed here.

theoretical tools for structure determination and growth

- ***"small" systems (N ≤ 40):***

density-functional basin-hopping (DF-BH) algorithm

- ***"intermediate" systems (40 ≤ N ≤ 200):***

density-functional empirical-potential (DF-EP) algorithm

- ***"large" systems (200 ≤ N ≤ 1000):***

empirical-potential global optimization (EP-GO) algorithm

- ***"very large" systems (1000 ≤ N ≤ 10000):***

extrapolation based on structural motifs

Fig. 4: Hierarchy of computational methods for structure prediction as a function of the size of the particle.

All the methods aimed at a systematic sampling of the PES are based on global optimization techniques [SahimiCSE2010], i.e., those computational techniques aimed at finding the absolute minimum (or global minimum) of a mathematical

function which can be very complex and exhibit very many minima differing by small energy amounts (as in the case of metal clusters due to their fluxional character). This is the problem of sampling in the most efficient and at the same time thorough way a very complex and rough PES. One of the simplest and most efficient techniques among global optimization ones is the so-called Monte-Carlo-with-minimization or basin-hopping (BH) algorithm. This approach has been proposed more than 20 years ago [LiPNAS1987] and used in pioneering investigations in the field of gas-phase metal nanoclusters (described within empirical potentials) conducted by Doye and Wales [WalesJPCA1997; WalesS1999]. When coupled with a DFT evaluation of energy and forces one speaks of the DF-BH approach: one of its first implementations to free metal clusters, in particular to Au_{20}, can be found in Ref. [ApraPRB2006], while its first application to supported metal clusters was to Ag clusters adsorbed on a Fs-defected MgO(100) surface in Ref. [BarcaroCEJ2007]. The BH algorithm is pictorially described in Fig. 5.

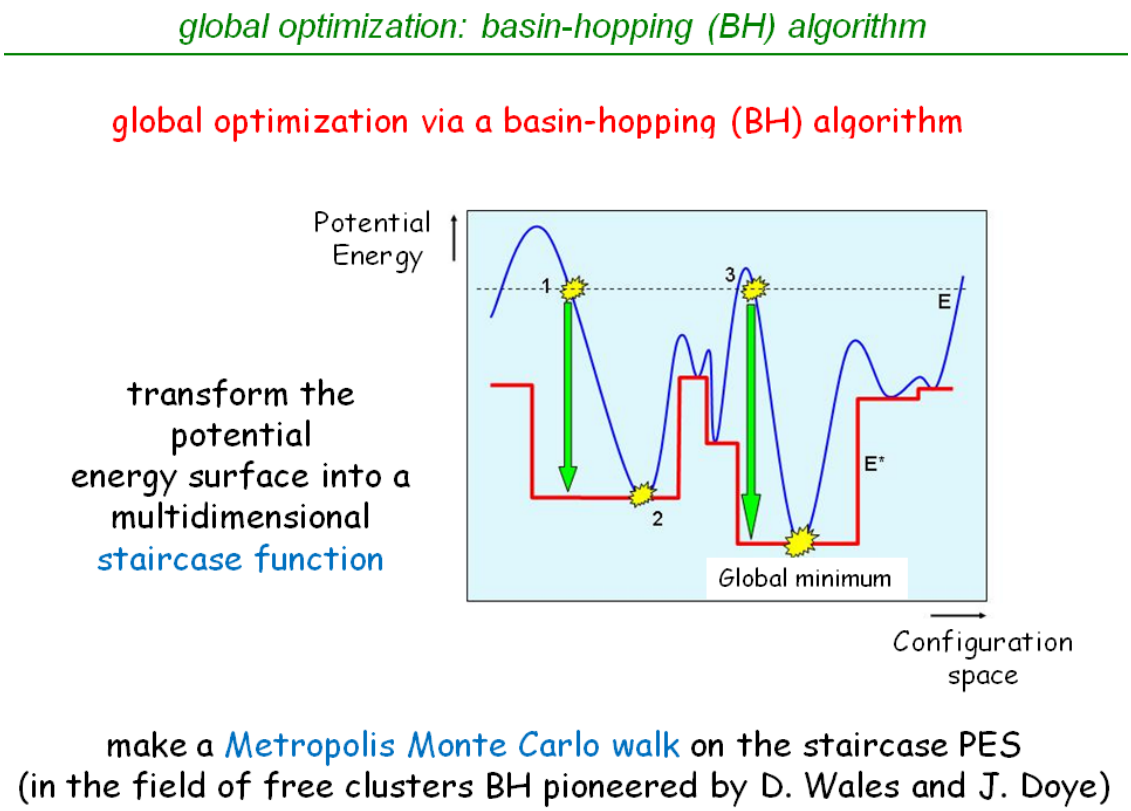

Fig. 5: Schematic (one-dimensional) depiction of the Basin Hopping (BH) or Monte Carlo with minimization approach.

In this approach, Metropolis Monte Carlo walks are performed on a modified potential energy surface, which is obtained by associating to each point of the configuration space the energy of its closest local minimum. In practice, the BH algorithm consists of the following steps:

(1) an initial random configuration of the metal cluster is chosen, a local geometry optimization is performed, and the final energy (the fitness parameter) is registered as E_1;
(2) starting from the relaxed configuration, the atoms of the metal cluster are subjected to a random move, a new local geometry optimization is performed, and the final energy is registered as E_2;
(3) a random number (rndm) between 0 and 1 is generated and the movement of step 2 is accepted only if $\exp[(E_1 - E_2)/(k_B T)] > \text{rndm}$ (Metropolis criterion);
(4) steps 2 and 3 – the Monte Carlo steps – are repeated a given number of times.

Depending on the $k_B T$ parameter, which plays the role of a fictitious temperature, some high-energy configurations are accepted and the search is able to explore different structural motifs (belonging to different funnels of the PES) of the metal cluster. A crucial point in the implementation of the BH search is choice of the random move. Two kinds of elementary displacement moves are usually employed in the Monte Carlo simulations. The *shake* move is simply a spatial "kick" in which each atom is randomly displaced within a sphere of a given radius centred on its position or - equivalently - through movements of up to ±(a given quantity) in each Cartesian directions. This move is very efficient when the number of atoms does not exceed – say – 100. In the *dynamics* move, a short run of unstable Molecular Dynamics at high temperature (in the range 2000-3000 K) is performed, which is especially effective for larger clusters [RossiJPCM2009]. In the case of multi-component systems such as alloyed nanoclusters or nanoalloys an important random move is an exchange of the coordinates of two species, as realized in the BH exchange-only algorithm [BorbonPCCP2007]. The thoroughness of the BH search is much increased when the BH protocol is coupled with *structural recognition* algorithms, i.e., algorithms which classify geometrical configurations as belonging to a given structural motif (or structural family). For example, this can be a fcc motif, or a icosahedral, or decahedral one, or more exotic ones, as depicted in Fig. 3. Structural recognition is achieved by defining one or several order parameters, i.e., analytic many-body functions of the systems coordinates such as those derived from a Common Neighbor Analysis [HoneycuttJPC1987; FakenCMS1994], or – in the case of supported clusters – the number of atoms that are in contact with the substrate, or many other possibilities depending on the specific system and the ingenuity of researchers. The coupling between the BH algorithm and structural recognition can be realized in many ways. In the simplest case, one can group a posteriori the low-energy configurations obtained by the BH search into structural families, as in the DF-EP approach (see below). In more sophisticated protocols, one can use structural recognition to orient the BH search, i.e., to avoid parts of the PES that have been already explored or belong to a structural funnel which is not of interest. For example, in the work here reviewed the parallel excitable walkers (PEW) algorithm [RossiCPL2006] has often been used, which is based on the concept of excitable walkers, performing parallel Monte Carlo walks on the locally minimized potential energy surface and effectively repelling each other in an appropriate order parameter

space. A further enhancement of the thoroughness of the BH search is obtained by performing both unseeded BH searches and (usually shorter) seeded searches starting from properly chosen initial configurations, for example from structures belonging to motifs found at nearby sizes or from structures found at the same size for other metals (system comparison from databases), see Ref. [FerrandoPCCP2008] for an overview of the many possibilities. Local atomic defects are then eliminated by runs in which the elementary move displaces single atoms on the cluster surface. Other popular global optimization tools comprise genetic algorithms (see e.g. Ref. [JohnstonDT2003]), see Ref. [FerrandoPCCP2008] for a review of global optimisation methods applied to metal nanoclusters and nanoalloys.

The hierarchy described in Fig. 4 is implemented in the following way.

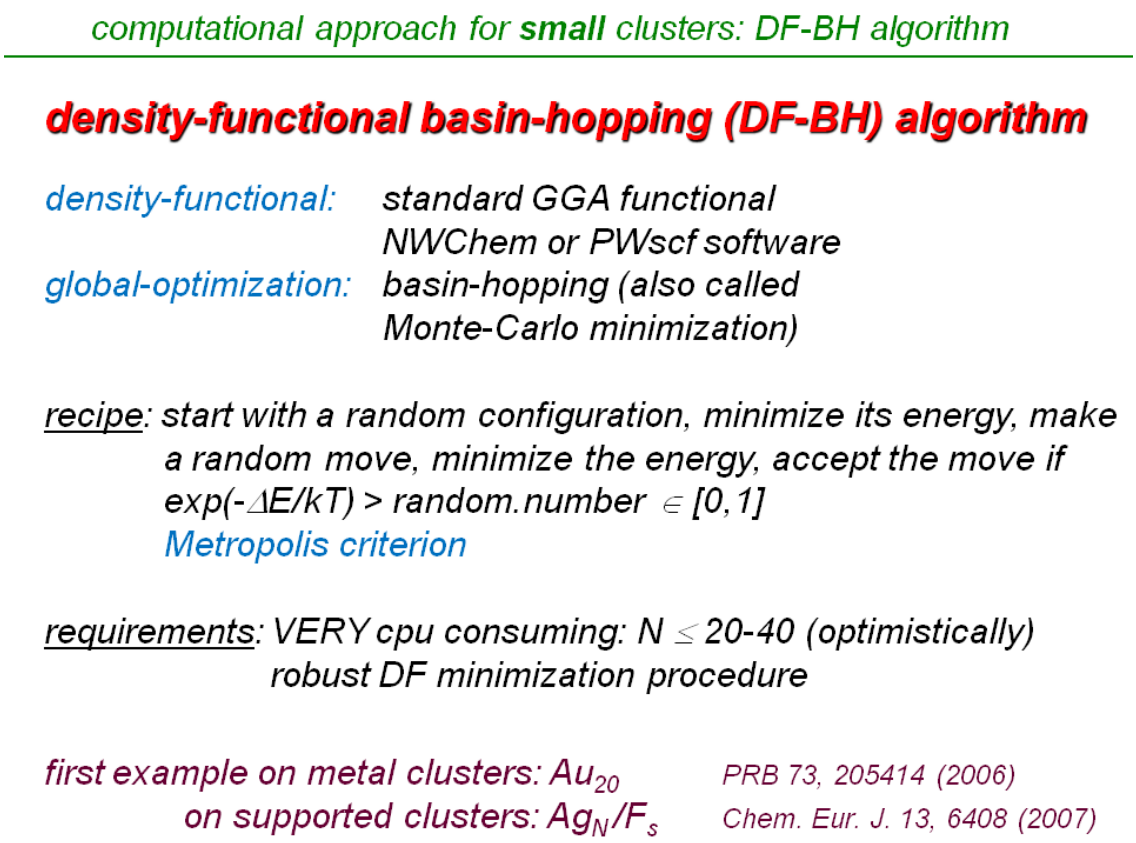

Fig. 6: Schematics of the DF-BH method

For small clusters (with a number of atoms, N, less than a few tens, presently N ≤ 40), it is computationally feasible to conduct a global optimization (in the form of the BH algorithm) using energy and forces derived from a first-principles (usually DFT) method in the so-called DF-BH method, see e.g. Ref. [ApraPRB2006] for one of the first implementations for gas-phase metal nanoclusters (or e.g. Ref. [GhaziJPCA2009] for a recent application), Ref. [BarcaroCEJ2007] for the first implementation for supported metal nanoclusters, and Refs. [BarcaroJPCC2007; BarcaroFD2008] for the first implementations to (supported) alloy nanoclusters. A

pictorial view of the DF-BH scheme is shown in Fig. 6. It makes sense to use a DFT approach for such small clusters since in this size range the metallic bond is not yet (or not fully) developed, the systems have a pronounced molecular character, and the transferability of empirical potentials (EP) is extremely limited. In short, for small clusters the finite character of the system is best described at the first-principles level.

Clearly, the maximum number of atoms which can be feasibly treated using this approach is limited by the available computational resources. For supported particles, it can be noted that some atoms of the oxide substrate are explicitly described at the quantum mechanical level (either using a cluster model or a periodic approach), even though in the case of non-reactive interfaces they can be frozen in the Monte Carlo random move [BarcaroCEJ2007]. The presence of the surface makes calculations appreciably heavier than for suspended systems, and justifies a present limit estimate somewhat lower than in the gas-phase: $N \leq 20$ (this limit will obviously be increased in the future along with the advances in computational devices). Given the small size of the clusters, a standard BH algorithm has so far been utilized, in which structural recognition techniques were used a posteriori only to classify structural motifs, but it is easy to foresee that more sophisticated approaches will be soon implemented in an effort to increase the size of the investigated systems. As an aside remark, we underline that a DF-BH approach can be useful in the investigation of catalysis by very small metal clusters, as implied in preliminary investigation [BarcaroTCA2009], and that this is likely to become one of the main avenues of future developments, as discussed in Chapter 5. This falls within the general topic of the influence of ligand species on the structural properties of metal clusters, a topic still to be fully explored at the theoretical level, see again the discussion in Chapter 5.

Aggregates with a total number of atoms between 40 and 200 are very interesting as they are still in the non-scalable régime in terms of electronic, magnetic, etc. properties [YudanovJCP2002] and at the same time novel structures are continuously being discovered in this size range, exhibiting e.g. polytetrahedral character, hybrid combinations of close-packed and five-fold-symmetry motifs, or other exotic forms. For these aggregates it is still feasible to perform numerous DF calculations at various sizes using common computational resources (even though around the upper size limit heavy parallelism is needed to bring throughput to manageable levels). A full DF-BH approach however becomes progressively less and less feasible in practice, not only because the computational effort associated with a single DF relaxation becomes sizeable, but above all because the number of Monte Carlo BH steps required for an exhaustive exploration of the potential energy surface of these systems rapidly increases with the size of the system. More approximate methods such as empirical potentials must be employed. An efficient possibility is to replace the DF-BH approach with a combination of DFT and EP simulations, in the DF-EP method, see Fig. 7.

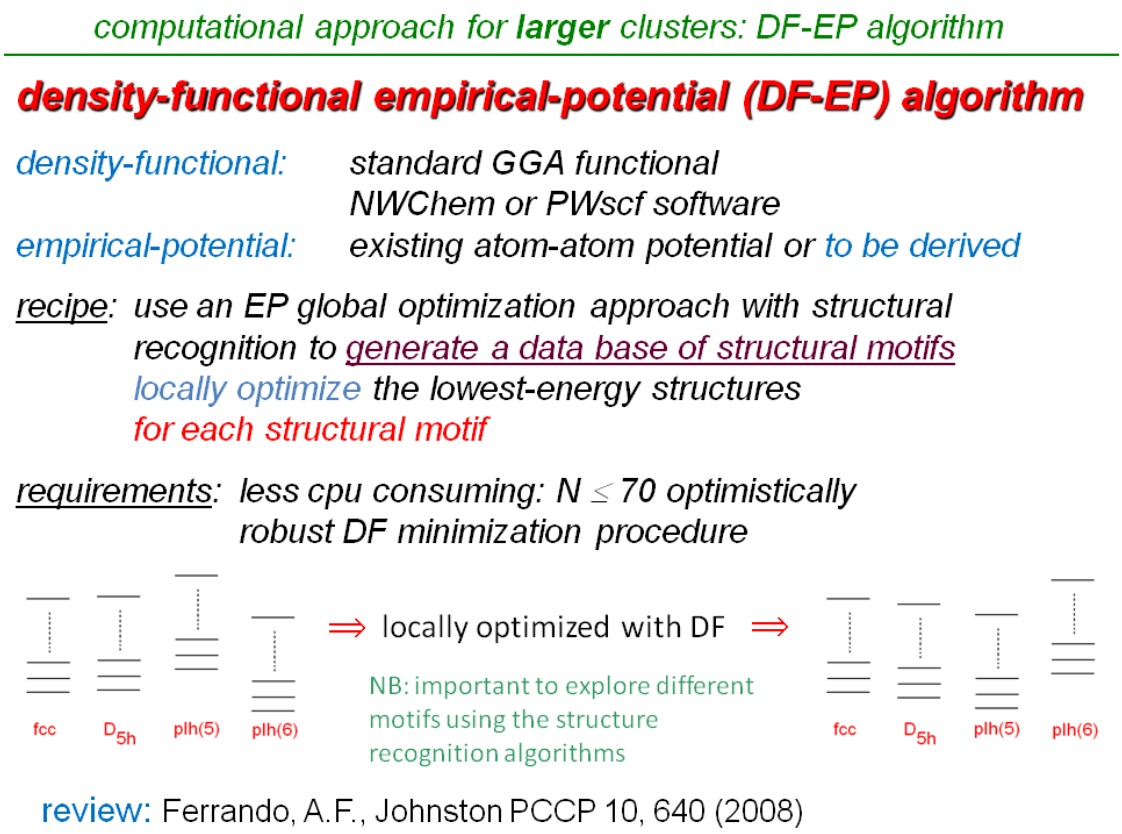

Fig. 7: Schematics of the DF-EP method

In this approach, first proposed in Refs. [BarcaroJPCB2006b; BorbonPCCP2007] and reviewed in Ref. [FerrandoPCCP2008], an EP for the given system is first selected (or developed). Second, a thorough global optimization search using e.g. the BH technique with structural recognition algorithms is conducted using this EP. Third, one or more order parameters are defined and are used to group the low-energy configurations produced by the BH search into structural families or basins. Note that this step is an automatic outcome of the BH search if algorithms based on structural recognition [RossiCPL2006] are utilized. Fourth, a few of the low-energy configurations belonging to each structural basin are subjected to local geometry relaxation using a DF method, and the changes in the relative energy ordering of the structural basins are analysed. Finally, if these changes highlight inconsistencies or inaccuracies in the EP, the DF results are used to refine the EP in a self-consistent process, see Fig. 9. The idea behind this approach is that in this size range the system progressively tends toward bulk metallic behavior, which is however not yet fully developed: for such systems, the limitations of EPs (either intrinsic or due to an incorrect parameterisation, see section 2.2) can hinder them from predicting the relative energy ordering of the various structural families, but they should be more accurate and able to single out the lowest-energy configurations belonging to a given structural family, see Figs. 7 and 9 for a schematic description of the DF-EP approach. In this respect, it is very important that the EP and the BH search are able to produce as much structural diversity as possible [FerrandoPCCP2008]. Moreover, as suggested above, a self-consistent re-parameterisation of the EP is often a

necessary option, see Fig. 9. It can finally be noted that massive adsorption of ligands can appreciably alterate the structural landscape of metal particles, see e.g. Refs. [NeymanCT2005; BorbonEPJD2009] and references therein. For exploring this issue, metal-ligand EPs would be very convenient, a topic on which research is presently very active.

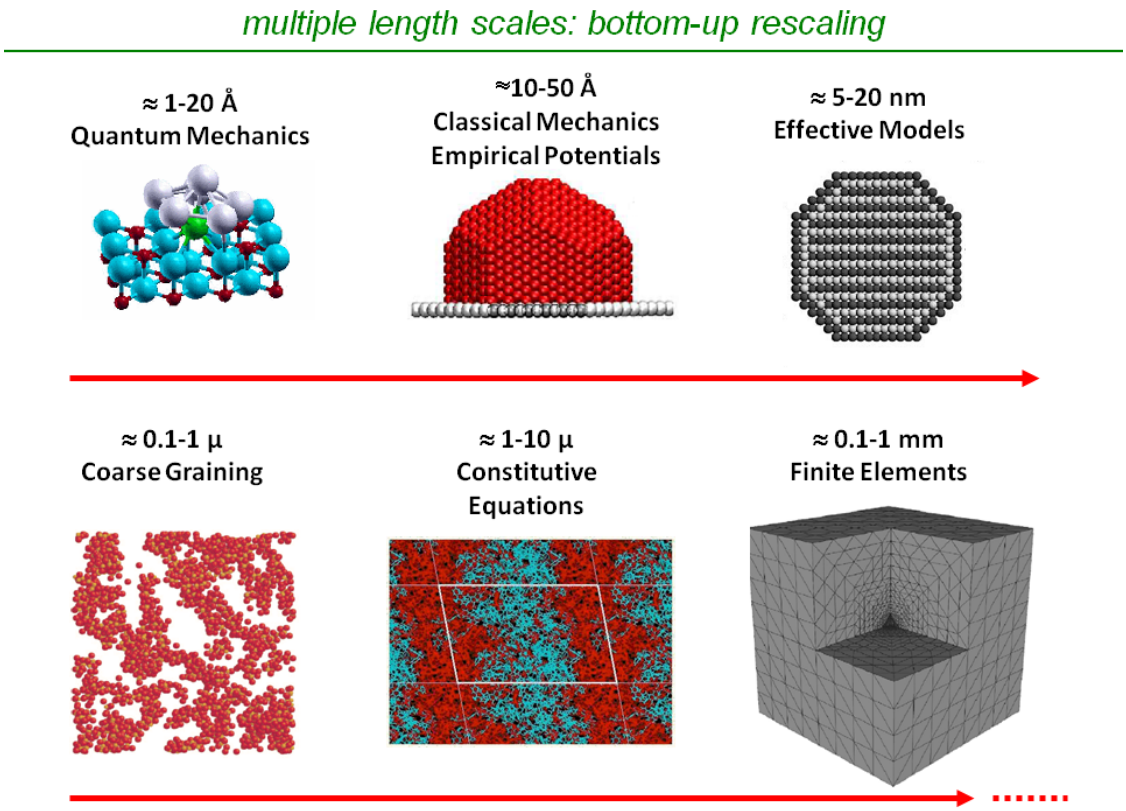

Fig. 8: Multi-scale framework for structure prediction.

For yet larger clusters (presently $200 \leq N \leq 2000$), even performing DFT calculations becomes progressively unfeasible, at least to conduct them in large numbers, and one has to rely entirely on global optimization searches based on EP approaches. This makes sense also from a theoretical point of view, as these larger particles start to exhibit a clear metallic character (see e.g. Ref. [FortunelliJMS1999b]) and a lesser amount of low-coordinated atoms, so that an average description of the metallic bond should be reasonable and EP predictions are expected and usually found to become more and more accurate [NegreirosJCP2010]. BH searches based on EPs are computationally feasible and can be performed usually with success up to 500-2000 atoms for pure particles, and 200-500 for binary particles. In this connection, it must be kept in mind that the success of global optimisation searches is highly system-dependent. For example, nickel and copper nanoparticles are easier to optimise than gold nanoparticles of the same size, because the energy landscape of gold is more rugged due to the higher stickiness of gold-gold interactions [BalettoJCP2002]. All the techniques relying on structural recognition can obviously be employed to enhance the success rate, and the research on the development of more efficient

algorithms is very active. It can be noted in passing that the constraint given by the presence of the support does not necessarily make the search for the global minimum more difficult, on the contrary it sometimes reduces the fluxional character of the metal particle.

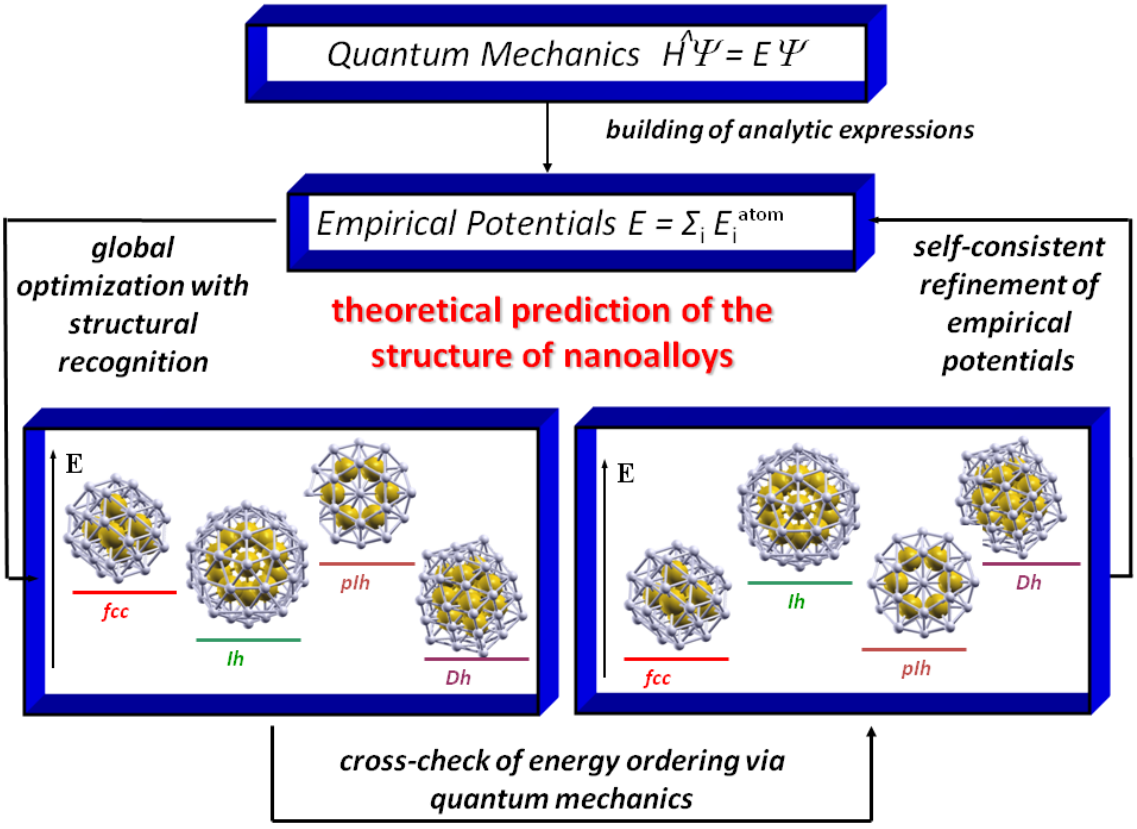

Fig. 9: Flow diagram of the DF-EP approach

When a particle has more than 1000-2000 atoms, global optimisation using EPs becomes extremely difficult or even computationally unaffordable. Moreover, it is often over-informative. The same size of the system (with hundreds of atoms in the interior of the particle whose energetics progressively dominates over that of surface atoms) in fact usually quenches structural diversity and simplifies the problem, orienting the system into few low-energy competing motifs. It is thus meaningful and efficient to focus on these motifs and study their crossover as a function of the number of atoms. The idea/strategy is that for these large particles the competing low-energy structural motifs have been singled out at smaller sizes and are known. Large clusters belonging to these motifs can then be constructed, their geometry can be locally optimized and their energy can be extrapolated and compared to predict energetic crossover and phase transformations among structural families, as done e.g. in Ref. [BalettoJCP2002] for suspended particles and in Ref. [FerrandoACSN2008] for supported particles. As discussed in the next section, “magic” configurations (i.e., exhibiting structural shell closure) are very helpful in defining a convex envelope of the energetics of structural families as functions of the size of the cluster. Moreover,

in this size range some details of the structural relaxation which are reasonably well described by EP become less and less important. One can thus use even more simplified effective models or effective Hamiltonians methods based on atomic site energetics [PolakSSR2000; AbrikosovRPP2008] to evaluate the energetics of the system, as discussed in the previous subsection, as these methods are expected to become more and more accurate. Once a metal/ligand empirical potential is available, this strategy can be employed to investigate phenomena such as morphological transformations due to ligand adsorption [JohanekS2004]. In the absence of such potentials, an even more simplified possibility is to assume a given morphology and use information on surface energies and the Wulff-Kaishev construction [WulffZK1901; KaishewPhDTh1952; HenryPSS2005] to predict the optimal-shape configurations, as implemented in [MolinaCT2011].

Such a hierarchical approach to structure prediction can thus be rephrased or recast in terms of a multi-scale framework, see Fig. 8. Starting from few-atom systems in which DFT can be routinely applied, the first and from the point of view of the topic of this chapter the most crucial step of such a multi-scale approach is depicted in Figs. 8 and 9, and connect first-principles or QM calculations, e.g., DFT ones, with EP modeling. From an analysis of QM calculations one singles out the basic physics of the system and which are the basic physical ingredients that an empirical force field must contain. An analytic EP is then built and used in a thorough search combined with structure recognition. The energy ordering among the competing structural families predicted by the EP is then tested and cross-checked at the DFT level. If this test suggests that an improvement of the EP is necessary, a new fit of the EP parameters is conducted, a new EP is generated and a thorough search is performed again using the newly derived parameters. This search may (and often will) produce a different set of structural motifs, whose low-energy configurations are then tested and cross-checked again at the DFT level. This procedure is repeated as many times as needed until self-consistency is achieved.

From our experience, the achievement of self-consistency between DFT and EP is often important, and its lack points to an intrinsic deficiency in the physical principles upon which the EP has been built. Development of an EP, apart from being considered an art in itself [PettiforMSEA2004], is therefore also important in stimulating a deeper analysis of the DFT results from which a sounder knowledge of the physics of the system usually derives. It so happens in fact that the first version of the EP predicts an energy landscape which is rather different from the DFT one, and self-consistent refinement is needed. This is realized by an enlargement of the fitting set, i.e., the set of configurations which are included in the fit of the EP parameters, which corresponds to an increase of information on the physics of the system. In this respect, the ‘overlap’ regions of the length scale framework in which both approaches (DFT and EP in the present case) can simultaneously be applied assume a crucial importance, see Fig. 10. These are the regions in which it is important to achieve as great a structural diversity as possible [FerrandoPCCP2008].

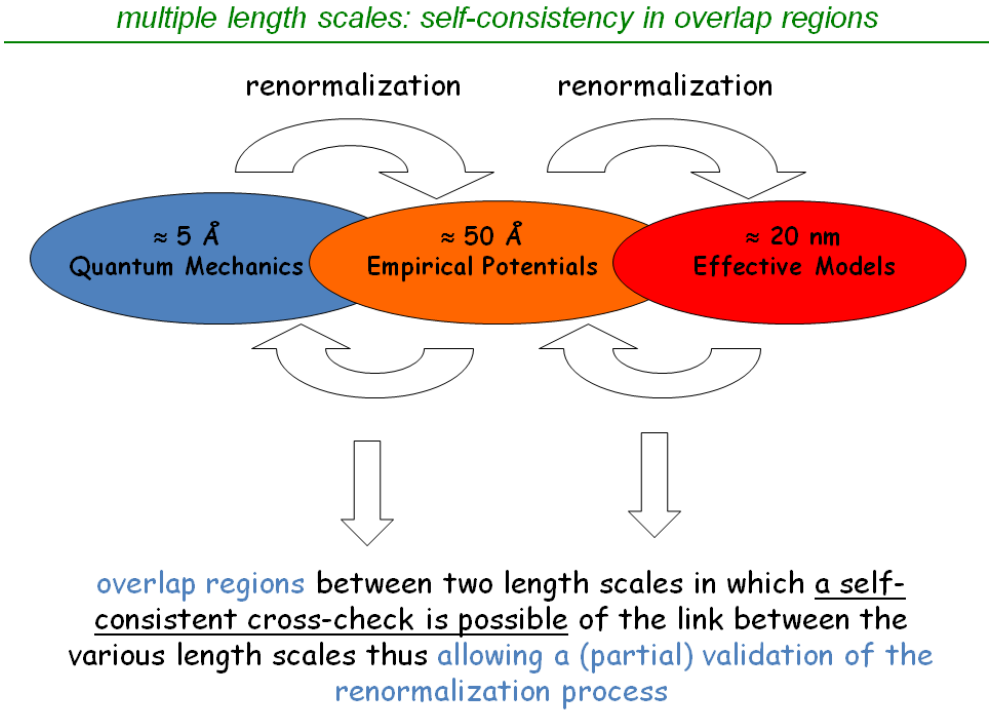

Fig. 10: Schematic depiction of the intersection of computational methods for different length scales and their overlap regions.

2.5 Magic clusters

Magic metal clusters are aggregates of metal atoms which present electronic and/or structural shell closure, often associated with a peculiar energetic stability. Structural shell closure is achieved when the number of atoms is such that a high-symmetry structural motif is completed, such as icosahedral, decahedral, octahedral, etc., see Fig. 3. When the electrons of the cluster complete a valence shell, and a substantial energy gap (of the order of 1-2 eV) exists between the HOMO and LUMO levels, an electronic shell closure is also achieved. The jellium model or one of its variants [deHeerRMP1993], i.e., models in which nearly free valence electrons are assumed to move in a homogeneous ionic background, can be used to rationalize electronic shell closure effects, with the predicted magic numbers of valence electrons for example for the spherical homogeneous jellium model at N = 2, 8, 20, … Due to enhanced stability, structural or electronic shell closures are often associated with a "spike" in the binding energy curve as a function of the number of metal atoms, with the incremental formation energy of a magic cluster of size N typically appreciably larger than that of the (N + 1) cluster.

Magic clusters are useful from a number of viewpoints. First of all, the great interest in them from an experimental point of view lies in the expectation that their high stability favours the synthesis of fully monodisperse systems, while structural and

electronic shell closures should entail peculiar electron transport [WangSM2001], chemical [GracianiJPCB2006], optical [KreibigBook1995], etc., properties, which may lend themselves to technological applications. Structure-property relationships are particularly transparent for magic clusters.

After their theoretical prediction [EkardtPRB1984] and experimental discovery as peaks of unusual abundance in the mass spectra of gas-aggregated alkali metal vapours [KnightPRL1984; PedersenN1991; MartinJCP1994], many examples of gas-phase magic clusters have been experimentally observed (see, e.g., Refs. [LiS2003; BaePRB2005]) or theoretically predicted (see, e.g., Refs. [PyykkoACIE2002; RossiPRL2004; GaoJACS2005; KarttunenCC2008]). Prolonging the lifetime of gas-phase species by, e.g., adsorption onto a surface is a prerequisite for the exploitation of their properties in technological applications, and many efforts have been devoted in the search of surface magic clusters [WangJPCM2001]. Many of the currently known examples concern metal-on-semiconductor [VitaliPRL1999; LiPRL2002; ChiuPRL2006] or metal-on-ionic-salt [HakkinenPRL1996] systems, while metal-on-metal systems [NayakPRB1997; ZhuangPRB2004; FichthornPRB2003] are expected to be stable only at low temperatures due to a weaker strength of electronic and structural shell closures on metal surfaces [WangJPCM2001]. Despite their possible relevance in applications, surface magic clusters on oxide substrates have been much less investigated, essentially because of the difficulties associated with their experimental characterization, so that for example – to the best of our knowledge – there are only three predicted or observed cases of electronic surface magic clusters on oxide substrates [BarcaroJPCC2007; BarcaroPRB2007; LinPRL1999].

Small magic clusters are interesting in terms of electronic shell closure, and thus of electronic properties. To make one example, in Fig. 11 the first example of a surface magic (binary) metal cluster is presented, which is also helpful to exemplify what can typically be expected in this field. Small $PdAg_N$ clusters in the gas phase, studied via a DF-BH algorithm in Ref. [BarcaroJPCC2007], present a transition from planar to 3D global minimum structures between $PdAg_4$, which is still planar, and $PdAg_5$, which is 3D. $PdAg_6$ however represents an exception to this rule, and is still planar due to an electronic shell-closure effect. Assuming in fact that Pd has a d^{10} configuration as in the single atom (and thus formally no valence electrons) and counting 1 valence electron per Ag atom, one finds for $PdAg_6$ a total of 6 valence electrons, thus achieving shell closure in the 2D jellium model. This stabilizes the planar configuration with respect to the compact one despite the fact that compact configurations are more stable than planar ones already for $PdAg_5$. The HOMO-LUMO gap of the planar global minimum of $PdAg_6$ is indeed significant: 1.5 eV, to be compared with the 1.1 eV gap of $PdAg_8$. $PdAg_6$ has also a 3D isomer which is only slightly higher in energy than the planar global minimum (energy difference of 0.15 eV, see Fig. 11). This isomer has a HOMO-LUMO gap reduced due to breaking of the planar symmetry: 1.1 eV. When these small Pd-Ag clusters are deposited on an F_s-defected MgO(100) surface (see Chapter 4 for more details on this surface) the

interaction with the surface favors a configuration in which the Pd atom is bound directly to the defect (Pd interacts with the surface more strongly than Ag) and the geometry is distorted to 3D to allow a better adhesion of the crown of Ag atoms to the surface. Furthermore, the F_s defect now contributes with 2 electrons to the valence electron count (see the next section), for a total of 8 valence electrons, thus achieving shell closure for the 3D spherical homogeneous jellium model. The HOMO-LUMO gap for the supported cluster is indeed higher than its 3D analogue in the gas phase, being restored to about 1.5 eV.

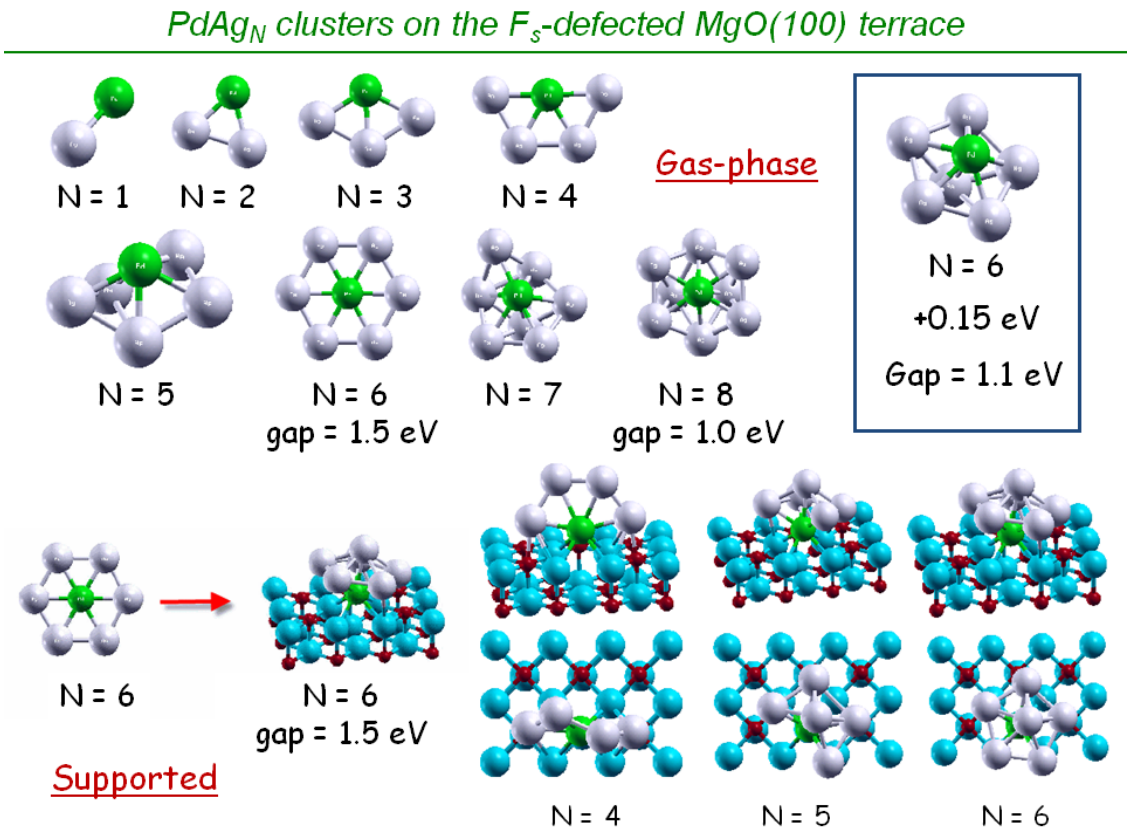

Fig. 11: Small $PdAg_N$ clusters studied via a DF-BH algorithm both in the gas-phase and supported on the F_s-defected MgO(100) surface (see text for details).

For larger clusters, electronic shells get closer in energy and electronic shell closure effects become progressively less important (see however a nice example in [AkolaJACS2008]). On the contrary, structural shell closure can still play a relevant role in assuring an extra stability to magic structures [deHeerRMP1993].

Apart from the extra stability associated with shell closure, structurally magic clusters are also very helpful in other respects in the theoretical analysis. Magic clusters in fact as a rule exhibit high symmetry, which can be exploited in several ways.

For example, from a computational point of view structural magic clusters are useful as a tool in structural predictions.

First, some first-principles codes (especially those utilizing localized basis sets) can efficiently exploit the point group symmetry to reduce the computational effort [HaberlenJCP1997; AhlrichsPCCP1999]. This reduction can reach up to the order of the symmetry group in some parts of the code (for example, the calculation of the Coulomb two-electron integrals in codes using finite basis sets) or even up to a power of the order of the symmetry group higher than 1 in some other parts (e.g., the dimension of the matrices to be diagonalized can be reduced by a factor roughly equal to the order of the symmetry group, so that the computational effort to diagonalize them is reduced by a power of the symmetry group of at least 2).

Second, structurally magic clusters can be useful in structure prediction to extrapolate the energy as a function of size to large clusters, as mentioned in the previous section, see Fig. 4. It is known in fact that the energy of metal clusters belonging to a given structural family often present an irregular behaviour with cluster size among non-magic structures [GhaziJPCA2009; BaoPRB2009], due to the different site energies of atoms belonging to incomplete shells. For magic structures, instead, it is possible to construct large clusters belonging to a given structural motif, locally optimize their structure, and obtain the behavior of the binding energy as a function of size for the given structural motif [BalettoJCP2002]. The envelope of the excess energy as a function of size for these magic (optimal-shape) configurations provides a convenient way of defining the minimum of the excess energy for that particular motif, and thus allows one to study the ideal energetic crossover and phase transformations among different motifs among different motifs [BalettoJCP2002; FerrandoACSN2008]. Note however that this procedure can hide more subtle phenomena such as re-entrant thermodynamic phase transitions e.g. due to the irregular behaviour of the energy of a structural family with cluster size [BalettoRMP2005].

Third, the full point group symmetry can be used to partition the atoms into atomic shells of symmetry-equivalent atoms, also known as symmetry “shells” or symmetry “orbits” of the point group [FortunelliJMS1999b; FortunelliJMS2000; WalesBook2003; BorbonPCCP2007; BarcaroNL2011a], i.e., groups of symmetry-equivalent species which are converted into one another by the operations of the symmetry group. Just to make a very simple example, let us consider a 38-atom truncated octahedral cluster, as shown in Fig. 12. It is made of an inner (core) shell of 6 octahedral atoms and an outer shell of 32 atoms. The number of orbits is three: orbit-1 is formed by the 6 atoms of the inner shell; orbit-2 by the 8 atoms at the center of the (111) facets, and orbit-3 by the 24 atoms on the (100) facets. One can thus describe a 38-atom cluster by defining the coordinates of only three atoms. In passing we note that, in general, a given truncated octahedral cluster is characterized by two indexes: the length of the edge of the complete octahedron and the number of layers cut at each vertex. A similar analysis can be done for the other structural motifs that are commonly encountered in the study of metal nanoclusters and nanoalloys, some of them shown in Fig. 3. They range from simple pieces of a crystal lattice, such as variously truncated octahedral (from regular octahedra to cubes) for the fcc lattice, to

non-crystalline arrangements, such as all those containing 5-fold symmetry axes: icosahedra and (possibly Marks-truncated) decahedra [MarksPMA1984]. More recently also poly-icosahedra [RossiPRL2004] or in general poly-tetrahedra, and hybrid arrangements combining in various ways crystalline and non-crystalline motifs have been shown to be competitive for medium-sized (especially alloyed) clusters.

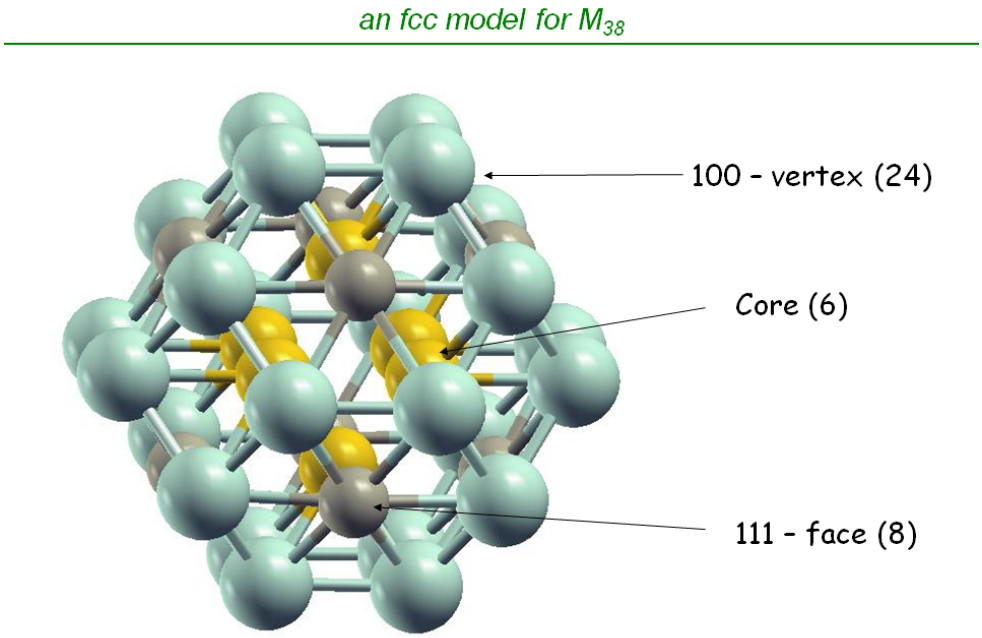

Fig. 12: Shell structure in the 38-atom truncated octahedral cluster.

As described in more detail in the next section, the use of highly symmetrical (magic) configurations as a convenient way to reduce the number of structural degrees of freedom in global optimizations is very effective in the field of alloy nanoparticles, in which the degrees of freedom associated with chemical ordering and composition increase in a combinatorial way with the size of the system and make systematic searches very difficult. In this case, the definition of symmetry "orbits", allows one to restrict the global optimisation search by typically a factor 6-24 in the number of species for given highly-symmetrical structures, with a corresponding exponential reduction in the complexity of the problem. It can finally be noted that high-symmetry configurations can also be used to study the effect of ligand adsorption, see e.g. Refs. [NeymanCT2005; BorbonEPJD2009] and references therein.

2.6 Nanoalloys

As mentioned above, magic structures are also important in the study of nanoalloys. Combining nanostructured metal systems or metal nanodots with alloying results in a class of systems of great interest in terms of both basic and applied science: alloyed metal nanoparticles or nanoalloys [JellinekCPL1996; FortunelliJMS1999b; FerrandoCR2008], see Fig. 13. These systems have many applications ranging from catalysis, to optics and magnetism. The reasons of their importance lie in the fact that additional structural motifs with respect to pure systems can be created, and the chemical and physical properties of the particles can be tuned by varying the composition and the degree of atomic mixing (chemical ordering or compositional structure).

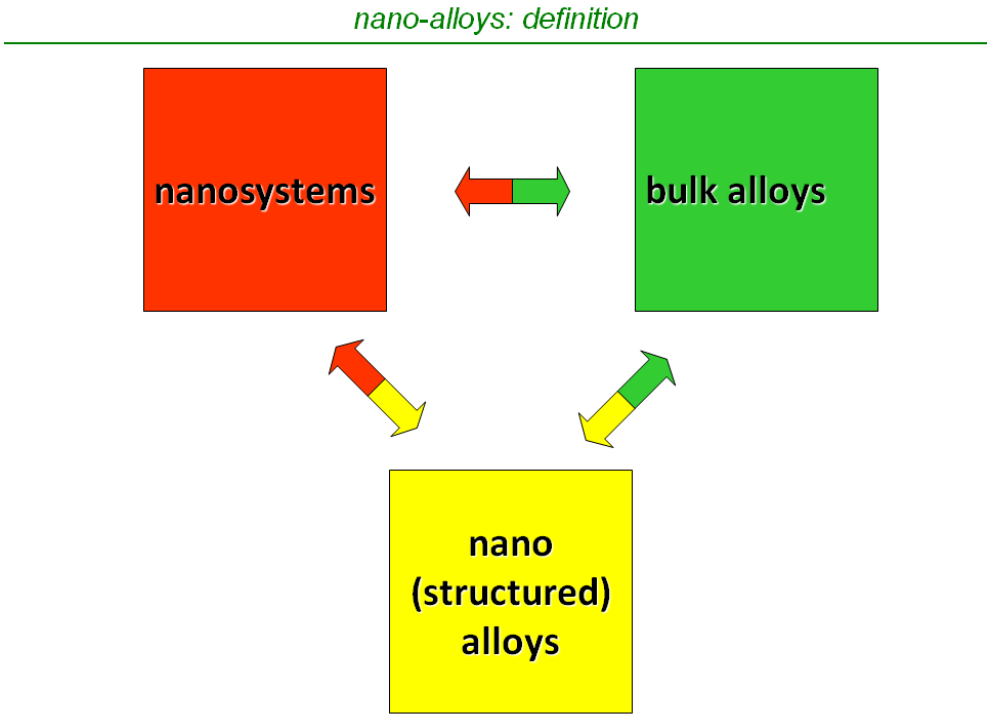

Fig. 13: Definition of nanoalloys.

Concerning composition, a very useful concept to compare the stability of nanoalloys of different chemical composition is that of mixing energy. Its definition represents the natural generalization of the corresponding concept used for bulk alloys and was proposed in Ref. [FortunelliJMS1999b] in the context of empirical methods and applied to DFT energetics in Ref. [FerrandoPRB2005], and reads:

$$\Delta[N_A, N_B] = E_{alloy}[N_A, N_B] - N_A\, E_A\,[N] / N - N_B\, E_B\,[N] / N \qquad (15)$$

where $E_{alloy}[N_A, N_B]$ is the global minimum energy of a nanoalloy cluster composed of N_A atoms of the species A and N_B atoms of the species B, $N = N_A + N_B$ is the total number of atoms in the cluster, $E_A\,[N]$ is the global minimum energy of a pure cluster

of N atoms and E_B [N] is the corresponding quantity for the B species. $\Delta[N_A, N_B]$ is the mixing energy of the given nanoalloy at a specific composition, i.e., the energy released by mixing N_A A-type clusters and N_B B-type clusters all of size N to produce N alloyed clusters of size N with composition (N_A, N_B), with all clusters in their global minimum configuration, divided by N. The quantity $\Delta[N_A, N_B]$ provides a measure of how thermodynamically favorable is alloying at the given size and composition.

The crux of theoretical and experimental research on nanoalloys is connected with the degree of atomic mixing or chemical ordering or compositional structure of the particles (i.e., the distribution of the different atomic species in the structural framework). This property is often crucial in determining the system properties. Ag-Au particles, for example, may exhibit a different optical response depending on whether they are core-shell or random solutions [BroyerFD2007]. Mechanical properties are equally known to be strongly affected by surface segregation [BiswasPRL2010]. The precise arrangement of the species in the particle is also important in catalysis, dominated by processes occurring at surface or subsurface shells, and changes in the segregation pattern under operating conditions have been observed [TaoS2008]. Several mixing patterns have been described in the literature [FerrandoCR2008], such as core-shell or in general multishell ordering (in which concentric shells of different elements alternate), random solutions, ordered arrangements (more or less related to the known ordered phases of bulk alloys), and Janus-like segregation typical of immiscible components. Order parameters associated with chemical order have also been defined to distinguish the various ordered phases of bulk alloys [AtanasovEPJD2009], even though seldom used so far in the nanoalloy structural search [AtanasovSS2009]. The problem at the experimental level is that, while composition can be easily controlled, it is difficult to precisely control the chemical ordering of a nanoparticle. In this context theoretical methods can provide relevant information which nicely complements and sometimes prefigures experiment, but the prediction of the correct chemical ordering is not an easy task, especially at the first-principles level, due to the combinatorial increase in the number of possible “homotops” (isomers sharing the same skeletal structure and composition but differing in the mixing pattern) [JellinekCPL1996]. In detail, for a cluster with a given structure and N atoms of which N_A of species A and N_B of species B, one has $(N)!/((N_A)!(N_B)!)$ possible different homotops, neglecting the simplifications due to the point symmetry group.

A viable procedure for example in the context of the BH approach is to consider random moves based on an exchange of the coordinates of two atomic species, as realized in the exchange-only BH algorithm [BorbonPCCP2007].

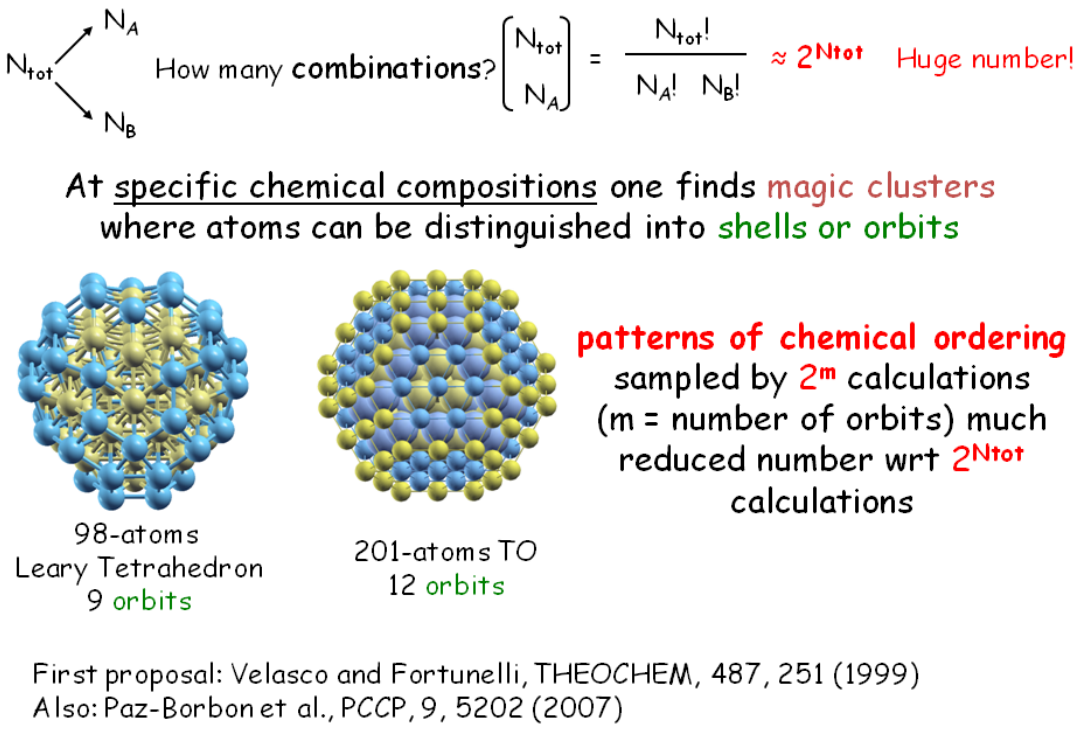

Fig. 14: Basic ideas behind the symmetry shell or orbit approach and the associated simplifications in the computational sampling of the chemical ordering phase space, with two examples of magic structures and their subdivision into symmetry orbits.

An alternative and more effective solution is to consider structurally magic clusters. In this approach, proposed in Ref. [FortunelliJMS1999b], the point group symmetry is exploited to partition the atoms into symmetry orbits: the degrees of freedom of the system are thus reduced from N to the number of symmetry-inequivalent orbits, N_{orb}, and correspondingly the number of distinct homotops is exponentially decreased, making first-principles simulations feasible even for medium-sized particles. For example, the segregation patterns of face-centered-cubic-like (fcc-like) PdPt nanoparticles in the size range between 38 and 201 atoms and over a broad range of compositions was recently studied [BarcaroNL2011a], finding that the interplay of metal-metal homo- and hetero-interactions produces an unusual Pt surface segregation in Pd-rich particles (in spite of the larger Pt bulk energy) and a novel patchy multishell pattern around equimolar composition in which each shell is decorated by “patches” of like atoms, see Fig. 14.

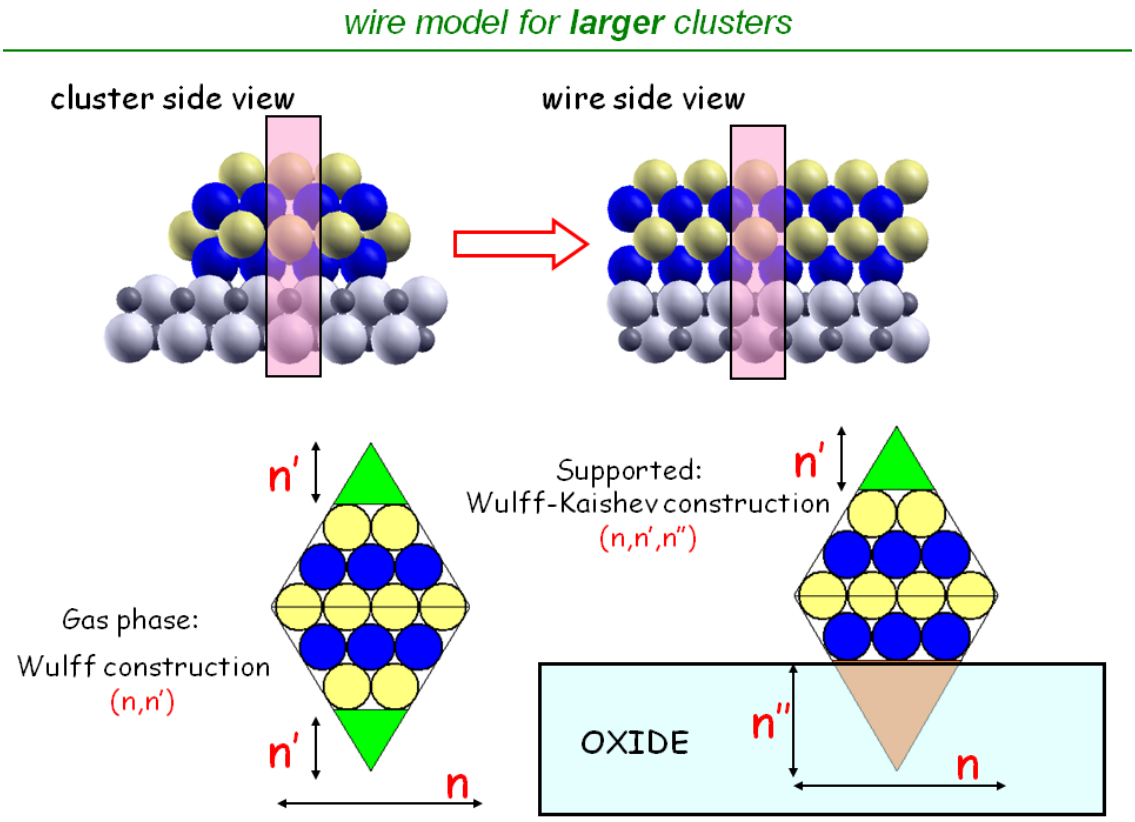

Fig. 15: Study of supported binary particles via a 1D wire approach.

In this connection it can be added that another very efficient tool to drastically reduce the computational effort and to enlarge the scope of systems amenable to first-principles simulations is based on the use of periodic models, see e.g. Ref. [MolinaPRB2004]. Instead of studying a 0D nanodot, in fact, one can consider a 1D or "wire" model, as depicted in Fig. 15. In this figure, the correspondence between a truncated octahedral 0D cluster, supported on a square-symmetry oxide surface to a 1D wire in which the section of the cluster is replicated ad infinitum, is shown. As in the case of magic clusters, in this approach one exploits symmetry (in this case, periodic symmetry) to strongly reduce the number of non-equivalent atoms (in this case, those contained in the unit cell). In Fig. 15 the indexes defining the level of truncation of the wire corners are shown. These often correspond to the Wulff (for free particles) or Wulff-Kaishev (for supported particles) construction, i.e., the optimal shape of the wire predicted by proportioning the truncations to the surface and interfacial energies, see Refs. [HenrySSR2005; GoniakowskiJCP2009] for more details. The simplifications assured by the use of wire models in terms of reduction of the number of atoms in the unit cell and also of the degrees of freedom of the system are apparent. Through the use of such models, 1D system with a unit cell of 110-120 atoms can be constructed resembling or mimicking 0D particles with 7-8 times this number of atoms, which would be otherwise extremely expensive or hardly affordable with the present computational facilities.

Structurally magic clusters can finally be very useful in the prediction of the properties of metal nanoclusters and nanoalloys, see also Chapter 5.

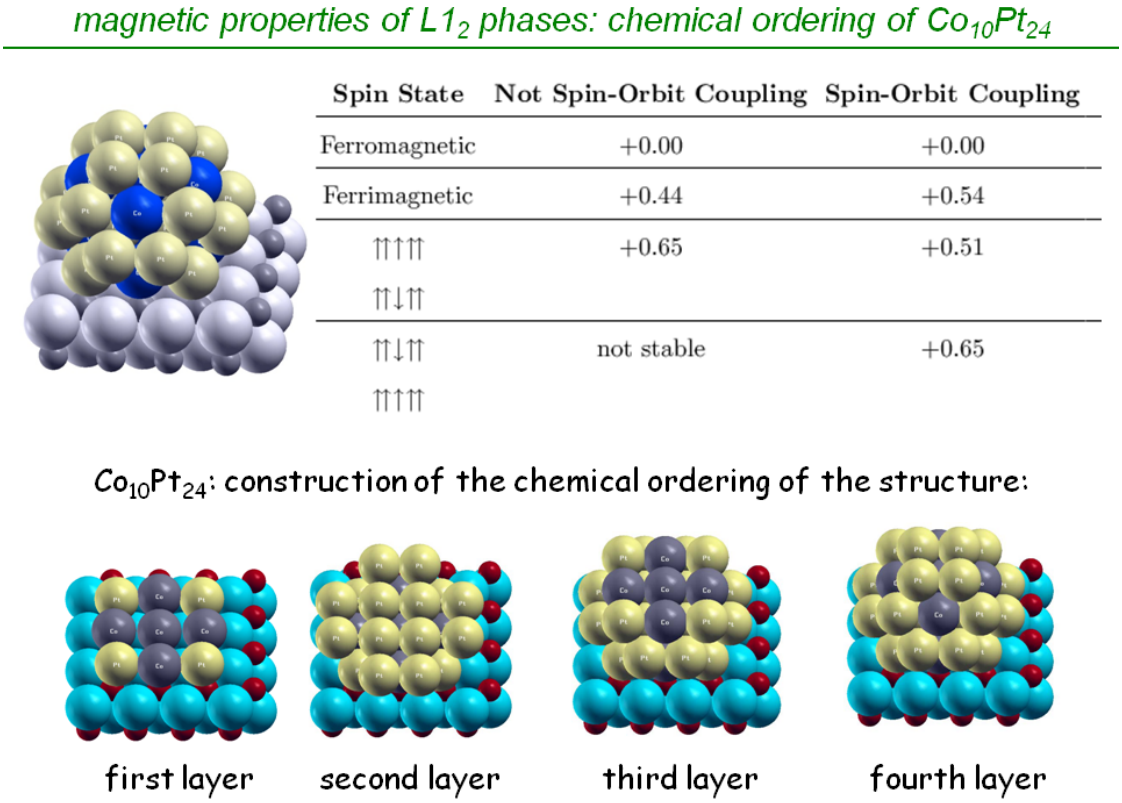

Fig. 16: Magnetic ordering in PtCo nanoparticles supported on MgO(100).

For example, an approach based on the study of magic clusters has recently been applied to investigate the optical properties of Au clusters in the size range of 150-170 atoms with various shapes [DuranteJPCC2011]. In this case the use of symmetry can reduce by orders of magnitude the computational effort, as the electronic excitations which make up the optical response can be catalogued into appropriate irreducible representations of the symmetry group, and the interactions among excitations belonging to irreducible representations not coupled by the proper perturbation operator are automatically null by symmetry. The size range around 150-200 atoms is about the maximum that can be confidently treated when studying optical response using current computational resources even with a full exploitation of point group symmetry, but future developments can probably double this size limit in the next future. The approach employed in Ref. [DuranteJPCC2011] is currently being extended from pure metal nanoclusters to the study of the optical properties of nanoalloys, i.e., Ag-Au and other alloyed nanoclusters [BarcaroJPCC2011], and coupled with 1D (wire) models [SementaPrep2012].

As another example, magic clusters can be used in the study of magnetic properties of metal nanoclusters and nanoalloys. In Fig. 16 a 34-atom Co-Pt cluster with $L1_2$ chemical ordering is shown supported on the MgO(100) surface. Partitioning the

atoms of the cluster into layers and shells allows one to investigate the spin-spin coupling constants in this cluster. The results (also shown in Fig. 16) indicate that significant spin-spin coupling constants are found in the cluster. Other magnetic properties such as the Magnetic Anisotropy Energy (MAE), i.e., the energy difference between different orientations of the magnetization axis of a nanoparticle, can in general be also calculated. An approach similar in spirit to this one has been developed in which a wire model is applied to investigate interface effects on the magnetism of CoPt particles supported on MgO(100) [BarcaroNL2011b].

Chapter 3

Gas-phase clusters

A lively line of research dating back to more than 30 years ago is involved in the study of metal nanoclusters in free beams [deHeerRMP1993; MilaniBook1999; BinnsSSR2001; BalettoRMP2005]. This research is very interesting, as it allows one to study bonding in metal nanoclusters without interference by environmental effects. The first investigations concerned clusters of gas-rare elements [RaoultRSI1973], but they were soon extended to pure metal clusters [SattlerPRL1980; DietzJCP1981] and later to mixed ones [RoussetSRL1996; CottancinPRB2000]. Several experimental techniques are now available to produce and characterize clusters in the gas-phase [BornholmZPD1991; ReinhardPRL1997; YacamanJVSTB2001]. Given the affordability of computational simulations for these systems, this has allowed a close cross-check of theory and experiment for prototypical aggregates, and is still a source of important information (see e.g. Refs. [GrueneS2008; SocaciuJACS2003]). However, it is not easy to obtain detailed experimental information on the structure of free clusters, which in practice often puts the burden and the honor of structural characterization onto theoretical approaches, or at least a combined experimental/theoretical analyses [HakkinenJPCA2003; GrueneS2008].

In the present chapter, we will focus on the novel structural motifs appearing in metal nanoclusters, the proper theoretical methods for predicting them, and the problem posed by the huge increase in the number of degrees of freedom in mixed or multi-component nanoclusters (or nanoalloys).

3.1 Novel structural motifs

Due to the "greedy" and "fluxional" character of the metal-metal interaction [McWeenyBook1980; PaulingBook1960], i.e., the fact that metal atoms can sustain a wide range of coordination numbers (up to 12-14) and that the energy barriers between various structures are not too high so that particles may transition among them in working conditions, metal nanoparticles and nanoalloys exhibit an impressive variety of different morphologies. The structure of metal particles is thus a topic which has fascinated scientists since a long time [MarksRPP1994; BalettoRMP2005], and is still at the forefront of current research, due to both unsolved fundamental challenges and its close links with particle functions and properties, and thus its relevance in several technological applications [LibudaSSR2005]. The explosive surge of activity of recent years, see e.g. the collection of data in Ref. [CCDB], has

enriched the set of classical structural motifs [MarksRPP94] (i.e., decahedral, icosahedral and crystalline, such as fcc, hcp or bcc, configurations) with new additions. Among these a notable class is that of polyicosahedra (pIh) [RossiPRL2004; DoyePRL2005]. pIh structures are built by packing elementary icosahedra (Ih) of 13 atoms in such a way that core (interior) atoms in the structure are surrounded by a complete Ih_{13} shell [RossiPRL2004]. They have been predicted to be kinetically favoured due to coalescence or rapid growth, but also to be thermodynamically stable for given isolated particles [GhaziJPCA2009], especially for binary metal nanoclusters (or nanoalloys) in proper combinations of the constituent metals [RapalloJCP2005; RossiJCP2005]. pIh motifs are important also as they can be seen as the finite-size analogues of Frank-Kasper bulk phases [FrankAC1958] and thus, ultimately, quasi-crystals [ShechtmanPRL1984; DubostN1986]. Another important novel family is represented by hybrid motifs, such as hybrid decahedral/close-packed structures, in which a close-packed core in the form of a trigonal pyramid or bipyramid is surrounded by atoms growing on the core faces in hcp(111) stacking plus further atoms arranged along edges between two faces thus creating a local decahedral arrangement, see e.g. Refs. [LearyPRE1999; BorbonPCCP2007; BorbonJCP2008]. A renowned examples are also the planar or cage structures of Au clusters in the size range between a few and few tens of atoms [HakkinenPRL2002]. In passing we also note that in the context of supported particles (which is the topic of the next chapter), the exploration of novel and exotic morphologies and their stabilization on a substrate via unusual epitaxial relations also represent an exciting route in determining specific properties and developing advanced devices [LordBook2006; XiongACIE2007], especially for oxide substrates, that are of special importance for their multifunctional flexibility ranging from insulators to semi- and super-conductors. Information on these novel families for suspended particles is presently scattered over several references and still awaits to be framed in a comprehensive picture. This is a fortiori true for supported metal particles, for which research is at a very initial stage, and more and more novel morphologies and epitaxial relationships are expected to be produced in a near future (for example by considering non-square-symmetry oxides) in addition to those reviewed in the following for the MgO(100) surface. In this chapter we will present a brief survey of recent developments stemming from our work.

For pure clusters, the traditional scenario is that of a crossover between crystalline and non-crystalline structural motifs [MarksRPP1994]. For example, for noble or quasi-noble metals such as those considered in Ref. [BalettoJCP2002] three structural motifs are in competition: icosahedra (Ih) and decahedra (Dh), as representative of non-crystalline arrangements, and truncated octahedra (Oh) as pieces of the fcc bulk crystal. Icosahedra have a quasispherical shape and a close-packed surface with 20 distorted (111)-like facets. The Ih structure is obtained by packing together twenty tetrahedra sharing a common vertex. This packing is only possible if the tetrahedra are distorted, and this causes the structure to have a high internal strain. Icosahedra are thus expected to be favorable at small sizes, where the efficient minimization of

the surface energy prevails over the strain contribution, which is proportional to the cluster volume. The decahedral structure is obtained by packing five tetrahedra so that they have a common edge. In this way, the surface is again close-packed, being formed by 10 (111)-like facets, but the resulting cluster shape is quite far form a spherical one. Better Dh structures can be obtained, however, by truncating the clusters. The Ino truncation exposes five rectangular (100)-like facets. The latter facets are not close-packed, but the resulting shape is closer to a sphere. However, this is not usually the best decahedral shape, since the energetically costly (100) facets are rather large in the Ino Dh. A better solution was given by Marks, who proposed further truncations, which are done in such a way to create (111)-like re-entrant facets. In this way, the cluster shape remains still close to a sphere, but smaller open (100)-like facets are exposed in favor of (111) facets. From the point of view of the surface energy, icosahedra are still better for small clusters, but decahedra have less internal strain, and become more favorable than icosahedra at increasing sizes. fcc clusters are expected to be the most favorable in the macroscopic limit, because this is the bulk lattice symmetry for the metals considered in Ref. [BalettoJCP2002]. fcc octahedra present only (111) facets, but are very far from the spherical shape. Truncated octahedra have a better surface/volume ratio, but expose large (100) facets. Therefore, fcc structures present a large surface energy, but they lack internal strain, and are thus expected to dominate at large sizes. This was indeed found from simulations based on an empirical potential [BalettoJCP2002], in which it was also shown that it is possible to rationalize the behavior of clusters of different elements in terms of crossover size by introducing a simple quantity: the stickiness of the interatomic potential [DoyeJCP1995], i.e. the ratio between the bulk modulus and the cohesive energy per atom for the given species. Since non-crystalline structures are distorted even in the unrelaxed structure, i.e., nearest-neighbor atoms are placed at distances which are different from the nearest-neighbor distance in the bulk solid, in a metal which increases strongly its energy for a change in interatomic distances (i.e., which has a “sticky” interatomic potential), non-crystalline structures will be strongly disfavored and this metal will present small crossover sizes. On the contrary, elements with less sticky interactions present larger crossover sizes.

In the last years this traditional scenario turned out to be oversimplified, and many unusual or exotic morphologies were discovered as low-energy structures of metal nanoclusters [CCDB]. Despite these latest enrichments, it is our belief that even for nanoclusters of pure elements the database of possible low-energy structural motifs is presently not yet completed. Two simple examples will be considered here for pure nanoclusters, concerning small to medium-sized Pt nanoclusters.

Let us consider for example a simple Pt_{13} cluster. N=13 is a magic number for truncated octahedral arrangements, as well as icosahedral and decahedral ones, and one can focus on the energy ordering of these three motifs. From DF calculations [ApraJPCA2003] it turns out that the situation is more complex than one might naively expect. First, at this small size the electronic ground state of even a non-

magnetic metal such as platinum can be high-spin [deHeerRMP1993]: in Ih Pt_{13}, for example, the high-spin state S=4 is lower in energy than the S=1 state even though by only a few hundredth of an eV. Second, geometry relaxation and Jahn-Teller symmetry breaking appreciably alter the energy ordering among structural motifs by stabilizing the symmetry-broken Oh→D4h structure by more than 2 eV. Oh→D4h (i.e., the cuboctahedral structure Jahn-Teller distorted to D4h symmetry) thus become the lowest-energy among the three structural motifs, contrary to "traditional" expectations. Third, and very interestingly, a more accurate inspection shows that the D4h lowest-energy structure actually represents something in between a bcc and a fcc arrangement, which differs substantially from both of them. Moreover, one finds a different high-spin D4h local minimum (denoted D4h' in Ref. [ApraJPCA2003]) which resembles more the bcc idealized one, and is only at 0.25 eV above the D4h lowest-energy configuration. The presence of low-lying local minima corresponding to structural isomers (even exhibiting the same symmetry!) can have an influence on the mechanical properties of the Pt13 nanocluster.

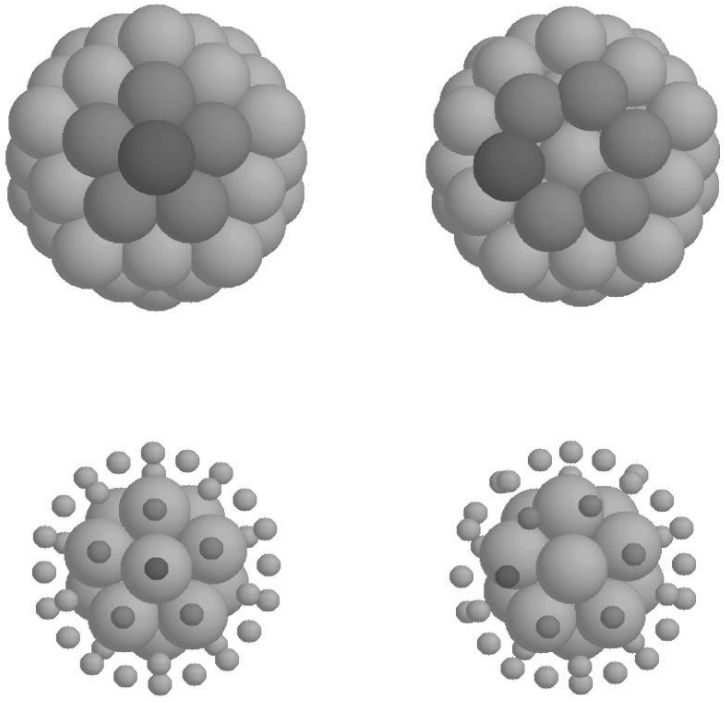

Fig. 17: Ih55 (left column) and rosette (right column) structures, as obtained within an empirical potential description. In the bottom row, the atoms of the external shell are represented with small spheres to show the 13 atoms forming the cluster core. The rosette is obtained from the Ih55 by displacing a vertex atom (dark gray) to form a hexagonal ring together with its five neighbors of the Ih55 surface.

Increasing the size of the cluster to Pt_{55} brings about further novel structural phenomena. First, the order of the three motifs is now that expected on the basis of general strain considerations: Ih < D5h < Oh, confirming the exceptional character of Pt13. Second, an *expansion* of the atoms at the center of the (100) facets is observed

[ApraJMS2000], giving the optimized structures a typical swelled appearance [ApraJPCA2003; DuranteJPCC2011], to be contrasted with the usual bond-length *contraction* in finite systems due to bond-order/bond-length correlation which is a typical many-body feature of the metallic bond [RosatoPMA1989]. This effect, which is observed not only for platinum but also for gold, is connected with bonding directionality effects typical of third-row transition metals [OlivierPRB2008]. Third, the icosahedral arrangement undergo an amorphization process which lowers significantly the particle energy and which is of general significance (the same mechanism underlies the formation of amorphous structures in e.g. Au nanoclusters). This process, schematically depicted in Fig. 17 (taken from Ref. [ApraPRL2004]), involves a rosette-like structural transformations at fivefold vertices, which transforms a fivefold vertex into a hexagonal ring. Its physical origin lies again in the peculiar interplay between the bond order–bond length correlation in metallic systems. Inner highly-coordinated atoms would in fact prefer to have neighbors at the ideal distance of the bulk fcc crystal, while surface atoms would better have contracted bonds. This is contrary of what happens in an Ih structure, where inner bonds are more compressed than surface bonds. In the rosette structure the surface is rearranged in such a way that there are fewer bonds than in the Ih55, but these bonds are shorter on average. Moreover, the inner core is expanded, and its atoms are less compressed than in the Ih_{55}. The final result is that inner atoms lower their energy at the expense of surface atoms.

Despite these interesting results on pure species, the great enrichment in the database of structural motifs for gas-phase clusters realized in latest years has been mostly due to multi-component nanoclusters or nanoalloys. Four cases will be here discussed: poly-icosahedral arrangements, two examples of five-fold/crystalline hybrids, and a novel chemical ordering pattern.

The starting point is again the frustrated character of icosahedral arrangements which are in principle favored at small/medium sizes because of bond counting reasons but at the price of a substantial internal stress. By mixing two metals with a different atomic size and by adopting a core-shell chemical ordering, one can achieve a great stabilization of an Ih-type structure if the smaller elements segregates into the core and if the size mismatch is of the proper amount. This simple prescription is realized in practice in a slightly more complicated way, in the sense that the preferred structures turn out to be not traditional Mackay icosahedra (Ih), but rather poly-icosahedra or pIh [RossiPRL2004]. These are clusters belonging to the poly-tetrahedral family [DoyePRL2001] and are built by packing elementary Ih of 13 atoms, as shown in Fig. 18 (taken from Ref. [RossiPRL2004]). In general, a pIh of size N made of N_1 and N_2 atoms of two different species and comprising m interpenetrating Ih_{13} is denoted as (N_1,N_2) pIh^m. Further investigations showed the ubiquitous character of pIh structures, connected not only with the core-shell stabilization of size-mismatched systems in five-fold pIh [RapalloJCP2005], but also because six-fold pIh can exhibit a large number of mixed bonds [RossiJCP2005] and

can thus be favored for binary nanoalloys whose phase diagram in the bulk is characterized by ordered phases driven by the strength of mixed bonds [BarcaroJPCL2010], and even for pure clusters with long-range interaction potentials [GhaziJPCA2009; AguadoJCP2010].

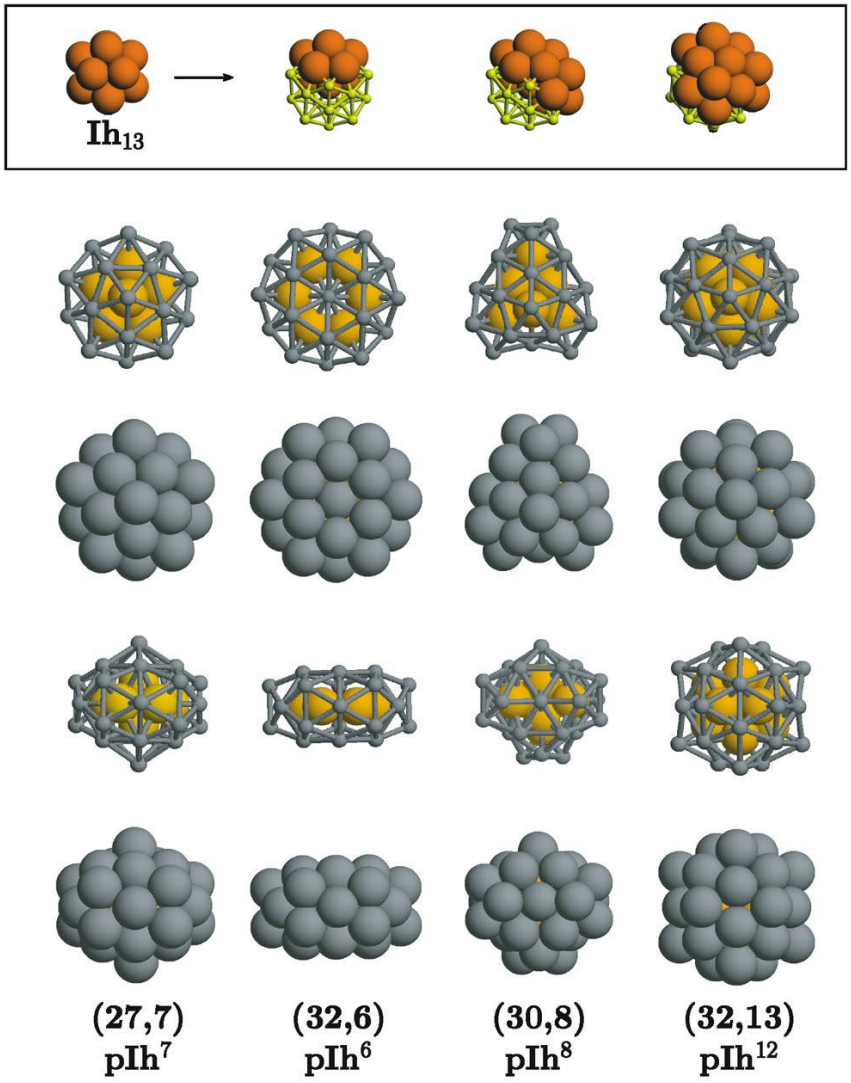

Fig. 18: Examples of pIh clusters. pIh clusters are built by packing elementary Ih13 clusters, as shown in the top row, where three different fragments of the pIh7 structure are given. From left to right, the fragments comprise one, two, and four interpenetrating Ih13. Below, a selection of core-shell pIh is given. Each pIh is shown in four views; in two of them the element with larger size (gray color) is represented by small points to show the arrangement of the core atoms of the element with smaller size (orange color). The (27;7) pIh7 has a decahedral core of 7 atoms, and the 27 surface atoms are placed in an anti-Mackay overlayer. The (32;6) pIh6 is a pancake structure, with the six inner atoms placed on a regular hexagonal ring. The (30;8) pIh8 is the perfect core-shell structure including the maximum number of core atoms at size 38. The (32;13) pIh12 is the complete anti-Mackay icosahedron of size 45, including a perfect Ih13 core.

Other novel morphologies involve hybridization of five-fold-symmetry and crystalline structural motifs. Suppose to mix two species with a very different

cohesion in the bulk, and suppose also that the size mismatch between the two species is small or such that the more cohesive element also presents the smaller size. In these conditions, it is not unreasonable to expect a core-shell arrangement with a core segregation of the latter species. Moreover, once this species achieves full coordination in the core (i.e., coordination number = 12), it will tend to arrange in a close-packed (cp) configuration. The less cohesive species, instead, being surface-segregated and thus low-coordinated, will tend to adopt a non-crystalline, five-fold arrangement. These are hybrid structures which combine a close-packed core with a decahedral or icosahedral surface.

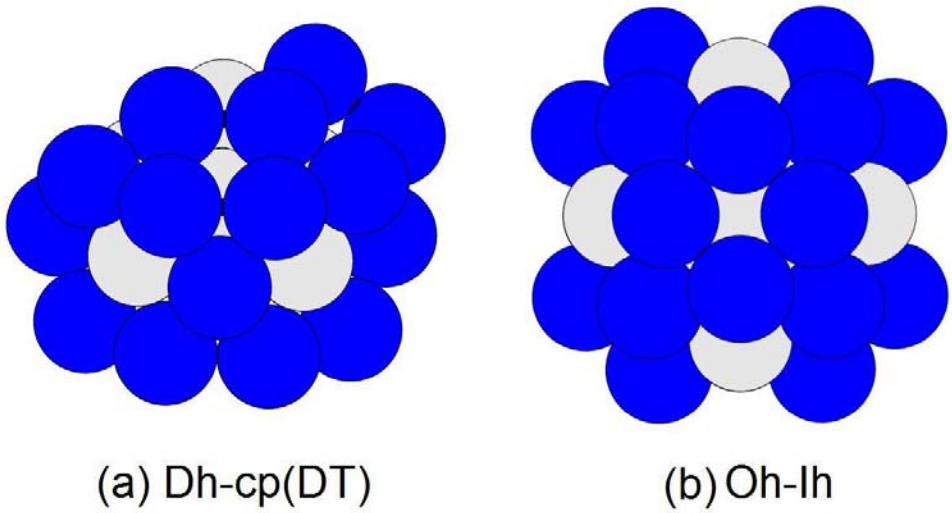

Fig. 19: Two hybrid five-fold-symmetry/close-packed structures: (a) Dh-cp(DT) at size N = 34, and (b) OhIh at size N=38. See text for more details.

One such example is the Dh-cp (DT) structure described in Ref. [BorbonJPCC2007] for $(Pd\text{-}Pt)_{34}$, see Fig. 19(a). At $Pd_{14}Pt_{20}$ composition, the internal core made of Pt atoms is a double tetrahedron or trigonal bipyramid (i.e., two tetrahedra sharing a face). Pd atoms can grow on the (111) faces of these two tetrahedra in a regular hcp (111) stacking. On each of the 6 faces of the Pt double tetrahedron (each one formed by 6 Pt atoms), three Pd atoms can grow, giving a total of 18 surface Pd atoms. The two remaining Pd atoms lie on an edge between two faces belonging to the same Pt tetrahedron, thus creating what it is locally a decahedron with its 5-fold axis coinciding with the shared edge. Simultaneously, there is a deformation of the 12 Pd atoms located next to the three edges shared by the two tetrahedra; these Pd atoms minimize their local energy by getting closer to each other and forming three other local decahedral motifs whose axes coincide with the three edges shared by the two tetrahedra. The growth mechanism of the Pd atoms on top of the Pt double tetrahedron is similar to that responsible for the interconversion between 5-fold structural families [BalettoPRB2001; RodriguezPRL2004]. The Dh-cp (DT) structure can be thought of belonging to the family of so-called Leary tetrahedra [LearyPRE1999; BorbonPCCP2007]. Note however that at these small sizes the

interplay of bond count and bond strength is subtle, and it turns out that the Leary tetrahedron is not favored at its own magic number (N = 44) but in the size range right below it (around 34 atoms).

Another example of a hybrid structural motif is the Oh-Ih structure described in Ref. [BorbonJCP2008] for $(Ag\text{-}Pt)_{38}$, see Fig. 19(b). This structure is similar to the TO_{38} structure as it has an internal octahedral core. However, the surface atoms do not grow exactly on top of the (111) faces of the internal octahedron (as would happen in a TO_{38} arrangement) but are placed according to a distorted arrangement, in such a way that only two square faces (instead of six as in the TO38) and no hexagonal faces are created. From an internal perspective, it resembles two double icosahedra joined by the central atoms, and in this sense it can be considered as an example of a mixed five-fold-symmetric/closed-packed arrangement.

Finally, novel chemical ordering patterns have also been described. An example of this is shown for a $(Pd\text{-}Pt)_{201}$ nanoparticle in Fig. 20 taken from Ref. [BarcaroNL2011a]. For this system DFT results for a few Pt impurities within a Pd-rich cluster unexpectedly show a marked tendency of Pt to populate the (111) surface, in agreement with coordination-dependent bond-energy variations (CBEV) predictions [RubinovichPRB2009], but opposite to what is found in extended systems (this is thus a feature peculiar to the nanoscale). This tendency is latent at smaller sizes but strongly increases with cluster size and is only clearly realized when the (111) facets are of the right size. Furthermore a new picture emerges around composition 1:1. The lowest-energy chemical ordering pattern, e.g., at composition 110-91 is reported in Fig. 20, and it is clearly a multi-shell arrangement, but of a different kind. As can be drawn from an inspection of this figure, the structure of the fourth shell is such that Pt atoms occupy the center of surface (111) facets, whereas Pd atoms occupy the (100) facets and the edges of the surface shell. However, for the subsurface shell the chemical order is reversed with respect to that of the surface shell: Pd atoms occupy the three central positions of the (111) facets, whereas Pt occupies the (100) facets and the edges. In other words, in correspondence with segregation of Pt at the center of surface facets, we find a segregation of Pd at the center of the underlying facets, and so on. In this segregation pattern each shell is a "patchwork" of islands of atoms of the two elements, but the order of the patchwork is reversed in the alternating shells. This is realized in a clear way starting at a sufficiently large size (1.7-1.9 nm) and around composition ≈50-50%. Note that this arrangement is not bound to a precise number of atoms but is stable in a range of compositions around the equimolar one between at least 45-55% and 58-42% compositions. It can also be recalled in this context that the minimum in the mixing energy for PdPt clusters at the DFT level is realized at compositions between 30% and 50% in Pt, i.e., in the range in which patchy multi-shell arrangements are favored. The origins of this unique chemical ordering can be rationalized in terms of the different behavior of site-energetics of the two elements as a function of the coordination number, i.e., the preferential strengthening of Pt-Pt (and Pt-Pd) intra-

surface and Pd-Pd (and Pt-Pd) surface-subsurface bonds. Furthermore, the multi-shell patchy arrangements allow the system to minimize the number of weak Pd-Pd bonds with respect to the stronger Pt-Pt and heterobonds between the two elements, which is energetically advantageous as Pd-Pt mixing is exothermic: in a way, the subsurface order is driven by the chemical order of the outer shell.

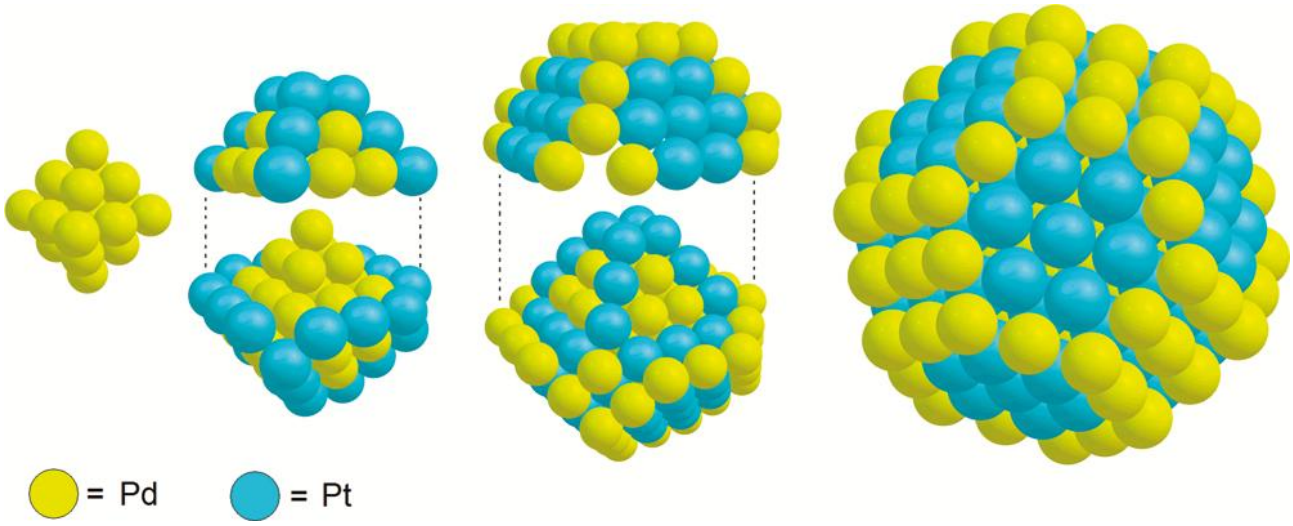

Fig. 20: Schematic depiction of the patchy multi-shell arrangement: on an octahedral 6-atom Pd core (right-most image), two patchy Pd-Pt shells are successively superimposed until the full 201-atom truncated ocahedron is formed (left-most image).

3.2 Methodology: empirical potentials vs. first-principles

The reliability of empirical potentials based on the second-moment approximation of the tight-binding approach (SMATB) [RosatoPMA1989] for gas-phase clusters has been checked against experimental data and DF results in several cases, usually finding results in not too bad agreement with experiment [BarcaroPRL2007; RossiNT2007; BalettoPRL2000; OlanderPRB2007]. It should be reminded however that this kind of empirical potentials has some intrinsic limitations. Indeed, apart from the fact that it obviously cannot account for the structure of very small clusters, as the behaviour of the binding energy with the coordination number at very low coordination is more complicated than the simple form implied by the SMATB potential, four main sources of discrepancies between empirical potentials and first-principles predictions were found through a detailed comparison of DF and SMATB results [FerrandoPRB2005]:

(i) band structure effects, connected with the inhomogeneous distribution of the one-electron energy levels, particularly apparent in the case of:
(ii) electronic shell closure effects, where the completion of the electronic shell is associated with an extra stability that could only be caught by including very-

high-order TB terms (see the discussion of magic clusters in the previous chapter);

(iii) magnetic interference effects, where the interaction among magnetic moments is not intrinsically described by SMATB potentials and should be added separately, again for example using explicit TB approaches [XiePRB2001];

(iv) charge transfer effects, important in the case of multi-component systems composed of elements with diverse electron affinities;

(v) chemical bonding or in general directionality effects.

To provide concrete examples, let us focus on three effects of quantum origin not described by usual empirical potentials: electronic shell closure, directionality and charge transfer effects.

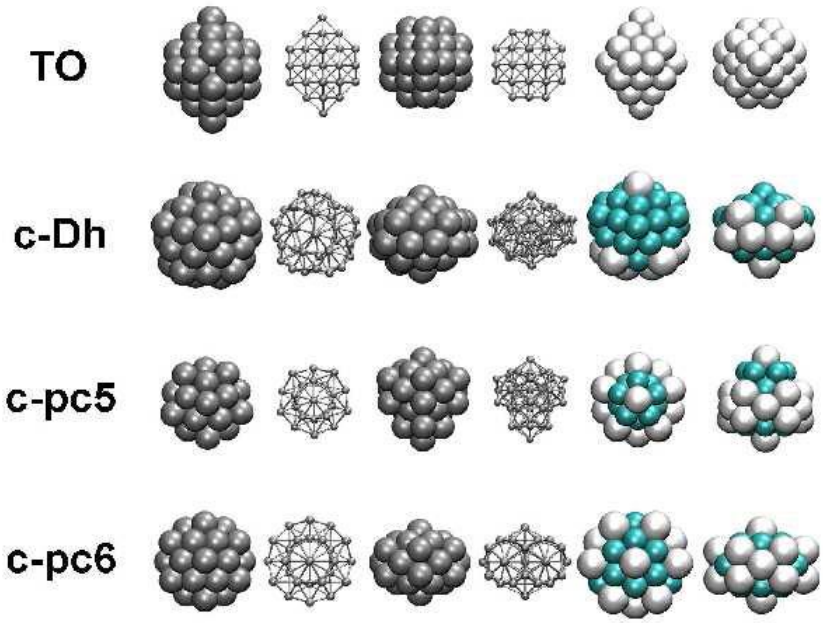

Fig. 21: Structural motifs of (Ag-Cu)40 clusters (see text for an explanation).

Electronic shell closure effects. The binary Ag-Cu system is of interest under several viewpoints. It has already been observed that the size mismatch between the two species, the difference in surface energies and the low miscibility of the two elements in the bulk favor e.g. at size N=34 the magic poly-icosahedral structures described in the previous section [RossiPRL2004]. Interesting results are obtained also at size N=40. This size is interesting as it is a magic number for the spherical jellium model both with an harmonic potential and and infinite-well potential, and also because a competition between crystalline and non-crystalline motifs is expected at this size which is between N=38 (structural magic number for the truncated octahedron) and N=44 (structural magic number for the regular octahedron). Note that for Ag and Cu, which are mono-valent metals, the number of valence electrons coincide with the number of atoms. A DF-EP approach applied to Ag-Cu nanoclusters for size around 40 atoms [BarcaroJPCB2006b] singled out the structural motifs depicted in Fig. 21.

These can be distinguished into: crystal-like (such as the truncated octahedron, TO, with two additional atoms on the square facets), distorted or capped decahedral (c-Dh), capped five-fold poly-icosahedral (or capped five-fold pancake, c-pc5, obtained from the perfect 34-atom pIh[7] by adding 5 atoms around and an additional atom on the symmetry axis), capped six-fold poly-icosahedral (or capped six-fold pancake, c-pc6, obtained from the 38-atom pIh[6] by adding 2 atoms on the symmetry axis). A comparison of the energetics predicted by the empirical potential and DFT is illuminating in terms of electronic shell closure effects. First, for the pure Ag_{40} cluster the empirical potential predicts c-pc6 to be much lower in energy than c-pc5, which is reasonable, as c-pc6 is much less strained than c-pc5 and Ag is a "sticky" metal. On the contrary, DFT completely reverses this energy ordering and predicts c-pc5 to be lower in energy than c-pc6 by 0.5 eV. The origin of this discrepancy for a simple metal such as Ag cannot be other than electronic. c-pc5 in fact presents a large HOMO-LUMO gap of 0.73 eV, whereas c-pc6 is a Jahn-Teller system with a vanishing energy gap. This is due to the different interplay between structure and electronic structure for the two clusters: as shown in Fig. 22, c-pc5 presents energy gaps at both 34 and 40 electrons, whereas c-pc6 only at 34 electrons. In the nomenclature of the jellium model, the order of one-electron energy levels is: 1s1p1d2s1f2p1g. It so happens that, for c-pc6, the 2p orbital is destabilized and get mixed with the 1g level, thus loosing the N=40 shell closure.

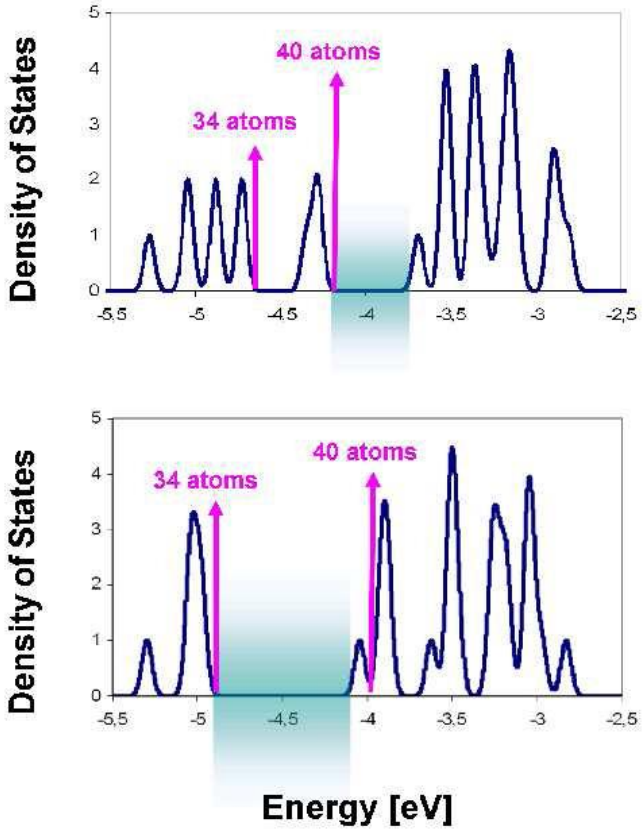

Fig. 22: Density-Of-States (DOS) for c-pc5 and c-pc6 clusters obtained from a tight-binding calculation.

This electronic shell closure effect becomes dramatic in the case of binary Ag-Cu clusters. In the whole composition range from Ag_6Cu_{34} to $Ag_{34}Cu_6$ the c-pc5 structure invariably present HOMO-LUMO gaps of the order of 0.7-0.8 eV and this, added to the stability assured by core-shell pIh arrangements with Cu atoms in the core, results in its always being predicted as the global minimum.

A last observation before leaving the topic of electronic shell closure effects. The most famous case in this respect is represented by the high-symmetry tetrahedral structure of the Au_{20} cluster in the gas-phase [LiS2003]. Concernig this species, in Ref. [ApraPRB2006] it was shown that the extra stability associated with electronic shell closure is crucial to give the tetrahedral structure a lead over its competitors. Indeed, independently of the choice of the DFT xc-functional, the global minimum was always found to be the perfect T_d. This however was not the case for the higher-lying isomers. Depending on the choice of the xc-functional, the first isomer could vary from a compact arrangement at the LDA level via a cage configuration at the PBE level to a planar structure at the BLYP level [ApraPRB2006]. In passing, this confirms the already mentioned extreme sensitivity of Au-Au bonding to the choice of the theoretical approach: in addition to the xc-functional, also the fine details of the calculations, including the basis set and even the choice of the pseudo-potential.

Directionality effects. In general, pure EAM or SMATB empirical potentials lack directionality terms. Baskes [BaskesPRL1987; BaskesPRB1992] was the first to call for the introduction of angular terms into embedded-atom-model empirical potentials, i.e., terms depending on the angular distribution of neighbours around a given atom. The form he proposed is based on the theory of the multipolar expansion of the density defined as a set of points, whose lowest-order terms are the dipole, the quadrupole and the octupole, and is sometimes included in current empirical potentials, see e.g. Ref. [PunPM2009]. These terms have been shown to be especially important for third-row transition metals such as Au or Pt, in which the relativistic destabilization of the d-orbitals brings them to play an active role in the metal-metal interaction [FortunelliJMS1999a; ApraJPCA2003], giving rise to strong directionality effects. For example, only a proper inclusion of these terms allows one to predict planar or cages structures of small Au clusters [OlivierPRB2008]. In particular in Ref. [OlivierPRB2008] a detailed analysis of density-functional calculations on gold model clusters and surfaces was conducted, and an empirical potential for gold, including angular corrections, was derived. In this analysis it was found it necessary to introduce higher-order non-linear terms (specifically, the product dipole-quadrupole) to describe directionality effects in the gold-gold interaction, terms that do not seem to have been previously used. Preliminary tests showed that the proposed empirical potential possesses novel features with respect to the existing ones, such as for the first time for empirical potentials a strong tendency of small Au clusters toward cage configurations, and represents a good starting point for future investigations. An alternative (and computationally more expensive) path is to resort

to methods dealing directly or indirectly with the full TB Hamiltonian [GoringeRPP1997; FortunelliJMS2000; FortunelliIJQC2004, AokiPMS2007].

Charge transfer effects. These effects can be important in selected cases. For example, in Ref. [BorbonJCP2008] it was shown probably for the first time that bond polarization in mixed Ag-Au medium-sized clusters reverses chemical ordering. In other words, all previous simulations conducted using empirical potentials on Ag-Au nanoparticles had predicted silver segregation at the surface and gold segregation in the core of the particles, following the order of surface energies and the cohesive strength of the two metals. At variance with these predictions, DFT calculations found that Au preferentially segregates at the surface of the cluster. The reason behind this counter-intuitive behavior is simply that Au acquires electronic charge from Ag in the cluster. Being then negatively charged, it prefers to occupy low-coordinated sites in which its electron cloud is not compressed by neighboring species. This was confirmed by an analysis of the energies of semi-core levels (i.e., 5s for Au and 4s for Ag) in Ag–Au and pure Ag and Au clusters. These levels correspond to states which are not heavily involved in chemical bonding and their shift indicates the direction and the size of the charge transfer because an increase in the electronic density on one atom (negative charge) causes a destabilization of its core levels (on the opposite, increased positive charge leads to core level stabilization). To disentangle electronic and structural effects (which is possible as structural relaxation following Ag–Au exchange is a minor one), the values of the semi-core levels for the mixed clusters were compared with those of the pure silver and gold clusters at a frozen geometry. It was found that in all cases gold atoms acquire negative charge (i.e., the energies of their 5*s* levels rise), while the silver atoms acquire a corresponding positive charge (i.e., their 4*s* levels drop in energy). Both energy shifts are of the order of 0.5 eV in absolute value and are opposite in sign. To separate the effects of the two main factors that contribute to the optimal chemical ordering in Ag-Au nanoclusters: the number of mixed versus pure bonds (i.e., the number of Ag–Au versus Au–Au and Ag–Ag bonds) and charge transfer effects, and to quantify them independently, several structures characterized by a different chemical ordering were generated and classified on the basis of the number of pure and mixed bonds. In all the structures, the total number of bonds was kept fixed (two atoms were considered to form a bond when their separation was less than 3.0 Å). The results of these calculations are reported in Fig. 23 (taken from Ref. [BorbonJCP2008]), where the clusters are classified according to the number of mixed bonds (note that the structures were chosen in such a way that if two clusters have the same number of mixed bonds, the numbers of pure Ag–Ag and Au–Au bonds were also the same). As can be seen from an inspection of Fig. 23, the best chemical ordering (lowest energy) is obtained in correspondence with the maximum number of mixed bonds in the cluster; the total energy roughly increases when the number of mixed bonds decreases. However, charge transfer effects are also important: An estimate of their size can be made on the basis of the energy spread of clusters characterized by the same number of mixed bonds. From such an analysis, it

was found that the maximum variations associated with charge transfer effects were of the order of 0.5–0.7 eV (these values being by chance very similar to the core level shifts of the two species). It thus seems necessary for a realistic description of the Ag–Au system to consider additional terms in the empirical potential that take into account electrostatic contributions.

Such a development was undertaken in Ref. [CerbelaudPCCP2011], where charge transfer between atoms was modeled by a modification of a previously proposed charge equilibration method [RappeJPC1991]. In particular, In Ref. [CerbelaudPCCP2011] it was found it necessary for a correct reproduction of charge transfer effects in Ag-Au nanoclusters to introduce coordination-dependent electronegativity and hardness. It was then shown that the inclusion of charge transfer effects is important for improving the agreement of the atomistic model with density-functional calculations, leading to the determination of lower-energy chemical ordering patterns.

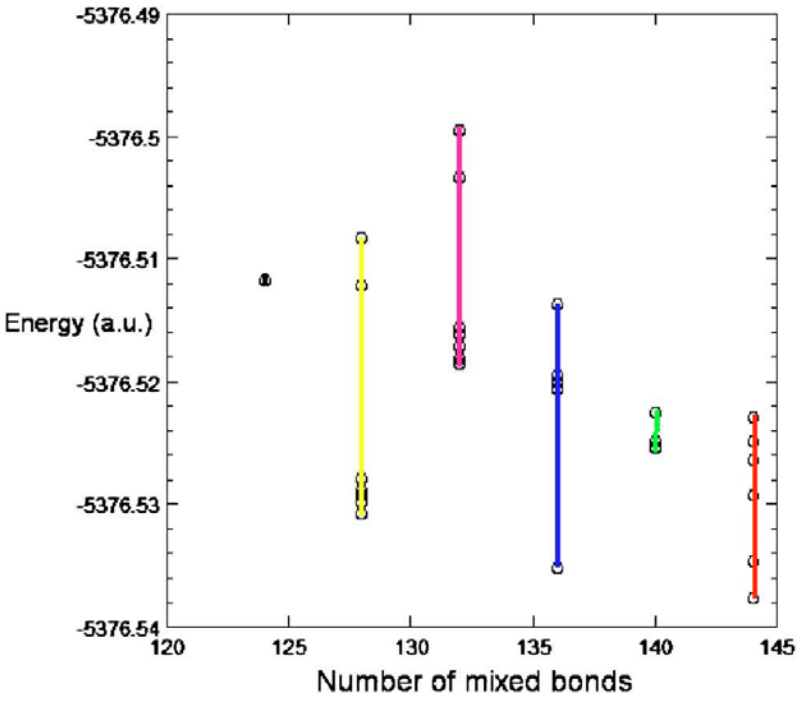

Fig. 23: Total energy as a function of the number of mixed bonds for several Au19Ag19 truncated octahedral structures. Clusters presenting a variable number of mixed bonds are obtained by permuting the positions of the surface gold and silver atoms in the square _100_ facets. The energy spread at a fixed number of mixed bonds gives an estimate of the charge transfer effects.

We recall other investigated gas-phase clusters: PdPt and AuPd [BorbonJPCC2007; BorbonJCP2008; PittawayJPCC2009], Ag-Pd [NegreirosJCP2010], AuCu [BarcaroJPCB2006b].

Chapter 4

Supported Clusters

Metal clusters supported on oxide substrates have traditionally attracted considerable attention due to their scientific interest and technological applications in several fields, ranging from heterogeneous catalysis to optoelectronic and magnetic devices [FreundSS2002]. In the field of in surface chemistry and catalysis, for example, one important issue is to clearly identify the effect of dimensionality on the chemical reactivity of heterogeneous systems, and this has produced the new field of nanocatalysis, i.e., catalysis by pure and alloyed metal particles with dimensions in the nanometer range [HeizBook2007].

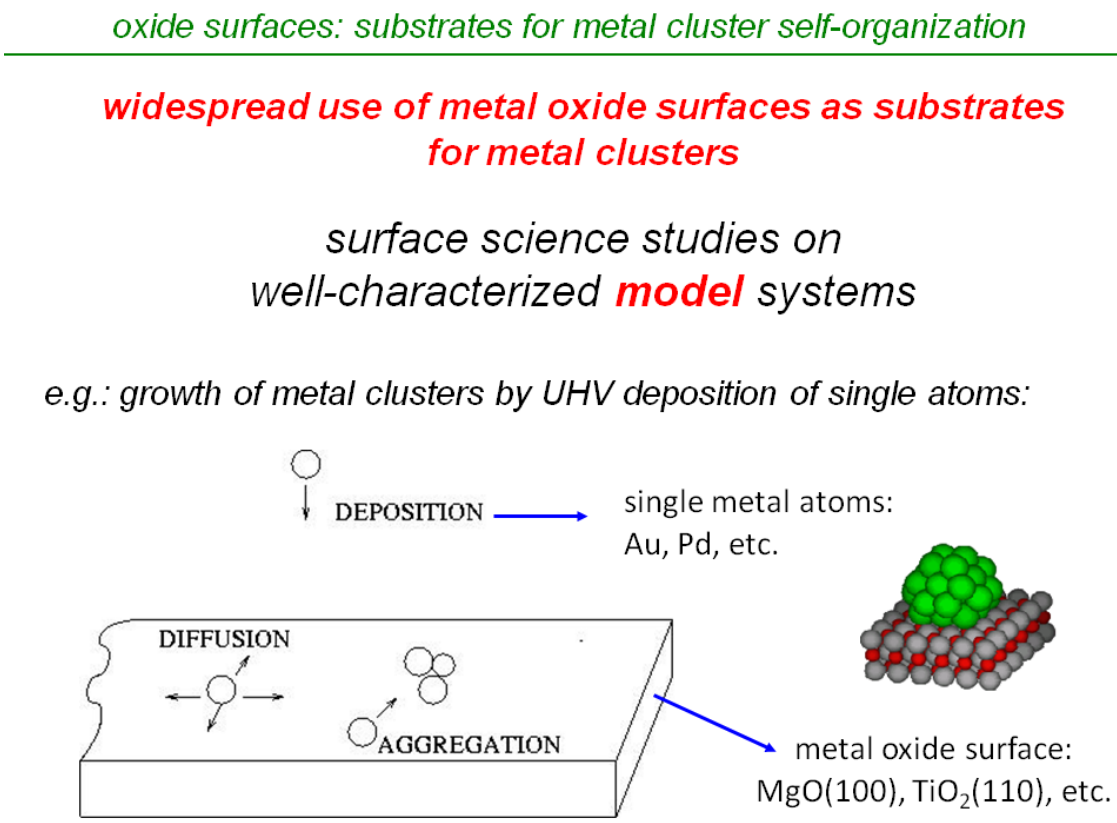

Fig. 24: Processes of adsorption, diffusion and self-organization of metal atoms deposited on an oxide surface.

However, a major general problem that needs to be overcome in the applications of metal nanoparticles and nanoalloys is related to the intrinsic instability of the nanoparticles: due to their high surface/volume ratio, nanoparticles tend to decrease their energy by coalescing into larger particles (Ostwald ripening and sintering

processes). This makes their characterization difficult and the exploitation of their innovative properties on a long time scale or under realistic reaction conditions non-trivial. Being intrinsically unstable, nanoparticles can only survive in the presence of kinetic barriers which avoid mass transfer and agglomeration processes, due e.g. to the presence of surfactants or when stabilized by specific nanoparticle/substrate interactions. In this context, metal oxide substrates are often used as supports for the growth of metal particles, as defects in oxides have been demonstrated to be effective in stabilizing metal nanoparticles [FreundSS2002]. This attention has prompted a wealth of fundamental surface science studies in which the complicated real world systems are replaced by metal-on-oxide systems created by depositing gas-phase atoms or preformed clusters onto a single-crystal oxide surface under UHV conditions, and then the processes of adsorption, diffusion and self-organization are characterized in great detail, see Fig. 24 [ErtlPT1999; HenrySSR1998]. The aim of these studies is to derive accurate knowledge on model systems in ideal conditions that can then help in clarifying the complex phenomena occurring in real world systems, with the final goal of achieving (at least qualitative) understanding of structure-property relationships. Characterizing, predicting, and controlling the structure of metal particles and their epitaxial relationship to the underlying substrate represent key steps in this perspective. Mere knowledge of the global minimum structure is obviously not sufficient to predict the behaviour of metal particles in complex environments and/or under kinetic conditions. For example, it has been shown that metal particles can undergo structure fluctuations and bistabilities during experiments reproducing typical catalytic conditions [JohanekS2004]. However, structure determination is a necessary step of great importance as a preliminary check for validation purposes in the study of more complicated processes and also in view of "static" phenomena such as optical and magnetic properties – but even chemical ones under mild conditions. On the experimental side, advances have been recently realized that allow one to characterize with a good degree of certainty the structure and morphology of supported metal particles [RenaudS2003; BarthNT2006; StierleMRSB2007; YacamanTC2002; SilvestreJC2006; HenryPSS2005; PauwelsPRB2000; LiN2008; MolenbroekTC2009]. On the theoretical side, computational approaches play an important role because, if sufficient accuracy is achieved, they can provide structural information which nicely complements that derived via experiments. Effective tools are nowadays available to explore and predict the structural properties of metal nanoparticles, ranging from combined empirical-potential/first-principles global optimisation algorithms to statistical mechanics techniques with improved sampling [BalettoJCP2002; FerrandoPCCP2008; BarcaroPRL2007; GoniakowskiJCG2005; FerrandoACSN2008; FerrandoJCP2009; GoniakowskiJCP2009; BarcaroJPCL2010]. This chapter is concerned with the theoretical description of the structure of supported metal nanoparticles and nanoalloys. Its aim is to provide an introductory description of the basic concepts, issues and tools developed in the field of computational methods and to review our contribution to recent advances in this field, presenting examples of applications which can give a flavor of what is the current state of research. Attention

will be limited to oxide substrates and open problems and challenges will be highlighted that still need to be addressed to make the perspective of a computer-aided synthetic laboratory of metal clusters come true. The discussion will be focused on the prediction of structural features of metal nanoparticles and nanoalloys supported on the MgO(100) surface taken as a prototypical model substrate. It can be noted in passing that a very important topic but one which has not been much investigated from the theoretical point of view is the thermal stability of the supported particles. This is a central issue especially in heterogeneous catalysis when the reactions to be catalyzed are strongly exothermic (as in the case of CO and NO oxidation catalyzed by gold particles [HutchingsACA2005]), as the evolved heat can induce particle detachment from the substrate, Ostwald ripening and sintering [ParkerTC2007] leading to larger particles and/or to the loss of beneficial particle/substrate interactions [ChenTC2007; MattheyS2007], and thus to deactivation of the catalyst. In this respect, an interesting experiment but one which to the best of our knowledge has not yet been realized in practice (despite having been suggested since the Faraday Discussion 138) is irradiation heating of nanoparticles of plasmonic metals deposited on a substrate kept at low-temperature. Surface heating via excitation of plasmonic resonance (see Sec. 5.3) and dissipation coupled with interface cooling should produce interesting frustration effects, including preferential reactivity of surface-adsorbed (at variance with interface-adsorbed) chemical species. A partial nanoparticle size selection due to the shift of the plasmon peak is an interesting side point of the proposed experiment.

Concerning the investigated systems in more detail, attention has been mainly limited so far to noble (Cu, Ag, Au) and quasi-noble (Ni, Pd, Pt) metals on the MgO(100) surface with the (nearly exclusive) addition of Fe and Co. These metal/oxide pairs are interesting in themselves. MgO(001) is one of the most studied models of single crystal oxide surfaces, [FreundSS2002; HenrySSR1998] due to the relevance of MgO to a wide range of applications in surface science, electronics and catalysis [VinkAPL2002; ParkinNM2004; ChoAP2007]. In addition, MgO is also a useful model system, due to its simple crystal structure and high stability, and can be fabricated in a range of morphologies, including thin films, single crystals and nanoparticles with well defined size and shape [BeckerBBGPC1995; KnozingerJMCA2000]. It should be recalled here that – in addition to the extensive studies of metal nanoparticles deposited on the MgO(100) support – investigations have also dealt with small metal clusters on aluminum oxides [HinnemannJPCC2007; ValeroJC2007; VajdaNM2009; LeeACIE2009], titanium oxides [MattheyS2007; ZhangPCCP2008], and others. It is easy to foresee that more systematic investigations along the lines already explored for MgO(100) will be conducted on these oxides in the near future. Supported Ni, Pd and Pt particles (in pure form or as alloys) play an important role in many catalytic applications [BondBook1987], and so does Au (and to a more limited extent Cu and Ag) in the nanoscopic régime [BondBook2006], while Cu, Ag and Au particles are also of interest for their optical (plasmonic) response [KreibigBook1995]. In addition, in the context of the structural

prediction of supported metal particles these systems have general significance as they are representative of metal/oxide pairs where the oxide is of square symmetry and which span a range of adhesion from weak to moderate while exhibiting a small (about 3 % for Ag and Au), medium (about 7-8 % for Pd and Pt) or large (about 16-19 % for Ni and Cu) mismatch between the oxide and bulk metal lattice parameters.

The chapter is organized as follows. In the first section, structural motifs and concepts needed to understand the structure of supported metal nanoclusters discussed in the following sections will be briefly recalled. Examples of applications especially focusing on the possibility of creating interface-stabilized phases will then be given for small to medium-sized and larger aggregates following the philosophy expounded in Sec. 2.4. A section devoted to "exotic" substrates in the form of oxide ultrathin films grown on single-crystal metal surfaces and some remarks on future perspectives will conclude the chapter.

4.1 Concepts in metal/surface interaction

As thoroughly discussed in Chapter 2, to which we refer for the following brief resumè, given the size and the complexity of the systems that are typically encountered and the difficulty in describing correlation effects in metal-metal and metal-surface bonding, among first-principles approaches DFT methods [KohnRMP1999] currently represent the best compromise between accuracy and computational effort in the study of oxide-supported metal nanoparticles. The choice of the specific approximation to the exchange-correlation (xc-) functional is however non-trivial: either functionals based on the generalised gradient approximation (GGA) [PerdewPRL1996; BurkeJCP1998] or hybrid functionals [BeckeJCP1993; AdamoJCP1999; BeckeJCP2005] are usually employed. The problem with these interfacial systems is that the xc-functional that best describes the oxide component is often not well suited for the metallic one, and vice versa, while very little is known about the validation of the xc-functional for the description of the oxide/metal interaction. Standard hybrid xc-functionals, that contain a Hartree-Fock exchange component, for example, are often able to better describe the energetics of bulk oxides with respect to GGA xc-functionals, but their Hartree-Fock exchange component gives problems in the description of metallic particles [ApraJMS2000]. For inert oxide surfaces (non-reactive metal-oxide interfaces) one can think that the substrate acts as a rigid source of electrostatic or dispersion interactions for the metal particles, so that a proper description of metal-metal bonding alone is crucial to the accuracy of the theoretical predictions, and GGA xc-functionals are in fact normally employed in the calculations described in the next sections. However, one should also recall that a chemical bonding component is always present in the metal-surface interaction, and this is true a fortiori in more complex situations. This problem is particularly keen for transition metal oxides and/or when metallic elements in low oxidation states are present within the oxide layer, possibly as a consequence of the

interaction itself with the metal clusters. In these cases, care should be taken to make sure that electron localisation in these species is correctly dealt with, and that the xc-functional is able to grasp the physics involved. As mentioned in Sec. 2.4, an interesting possibility in this respect is to augment the DF xc-functional with a Hubbard *U*-term in the so-called DF+*U* approach [AnisimovPRB1991; AnisimovPRB1993; LiechtensteinPRB1995], which has been shown to provide more accurate predictions of the electronic structure of transition metals in bulk oxides than local or semilocal approaches. A feature that is not usually underlined (but see e.g. Ref. [BarcaroJCP2010]) is that the DF+*U* approach is also attractive because it allows one to assign a different value of *U* to each atom, even of the same element but experiencing different bonding situations. In the case of oxide ultrathin films, for example, one can use a pure DF approach for the metal particles (which is usually thought to be appropriate), and a DF+*U* approach with variable *U* values for the transition metal atoms in the oxide support.

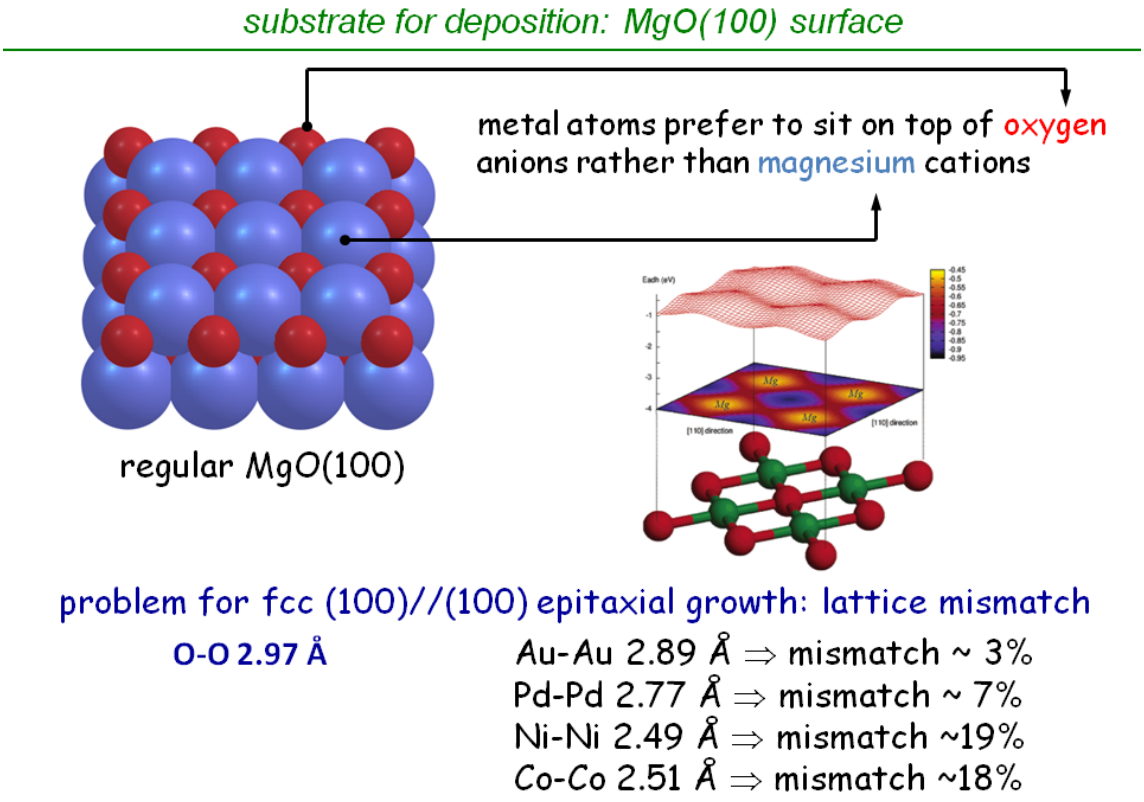

Fig. 25: Schematic structure of the regular MgO(100) surface (left), potential energy surface of a metal atom deposited on this surface (right), and comparison of lattice parameters for MgO and selected metals (bottom).

The first issue to be faced when studying the structure of supported metal nanoparticles concerns the epitaxial relationships between the substrate and the particles. The general features of the interaction of single metal atoms with the regular MgO(100) surface have been amply discussed in the literature

[YudanovCPL1997; NeymanNC1997; SousaJCP2001; MoriPRB2002; MatveevSS1999; BarcaroTCA2007]. In the case of oxides made of simple metals, such as MgO, the tendency of absorbing atop the O^{2-} site rather than the Mg^{2+} or hollow sites (representing respectively a maximum or a saddle point in the potential energy surface of a single metal atoms over the MgO surface) is a common trend among transition metal atoms [MusolinoSS1998; YudanovCPL1997; NeymanNC1997; MatveevSS1999; YulikovPRL2006], see Fig. 25, a phenomenon which can be rationalized. The metal/substrate interaction can in fact be partitioned into several contributions. The stabilizing contributions are of three types: (1) chemical bonding, (2) electrostatic stabilization, and (3) dispersion interactions. The Pauli repulsion between the metal cloud and the electronic density of the surface represents, instead, the main destabilizing contribution. This repulsion is certainly stronger for the coinage metal atoms that are characterized by a diffuse unpaired *s* electron, and this gives a rough explanation of the smaller adhesion energies of Cu, Ag, and Au with respect to transition metal atoms such as Pd or Ni. The Coulomb potential (point 2) generated by the ionic surface induces electrostatic effects: the metal system polarizes under the influence of the oxide electrostatic field. The induced polarization can in turn polarize the charge cloud of the oxide atoms: in the case of e.g. MgO, this effect will of course be much larger for the diffuse and "soft" oxygen anions than for the compact and "hard" magnesium cations. Another effect (which however is not taken into account in standard DFT calculations) is due to the dispersion interactions (point 3) originating in the dynamical polarization of electron clouds by the presence of nearby electrons (see Sec. 2.1). This effect will again be larger for metal positions on-top of oxygen rather than magnesium. Finally, a chemical (covalent) bonding component (point 1) can also be present even in simple oxides, in which case it will as a rule be larger for the oxygen anions than for the magnesium cations. Several effects thus conjure to make oxygen anions more favorable adsorption sites than metal cations in simple oxide supports such as MgO(100). It can be noted in passing that a full analysis of the metal/surface interaction in prototypical cases has not yet been developed due to the computational burden of performing accurate ab initio or post-DFT calculations on relatively large systems [LopezJCP1999], thus free from SIC errors and including dispersion interactions, but it would be very interesting to ascertain the weight of the various contributions, and investigations are being conducted in this direction as recalled above [BorbonPRB2012].

A subtle peculiar effect which often plays an important role in determining the structure of small (especially coinage) metal clusters is the so-called "metal-on-top" stabilization effect [BarcaroJCTC2005]. This is an enhancement in the metal-surface adhesion energy due to the presence of metal atoms above the one directly in contact with the oxide substrate, and is connected with the fact that the electron density of metal atoms sitting on top of the negatively charged oxygen anions is repelled and polarized away from the surface: the presence of other metal atoms on top of those directly in contact with the oxide that can receive and delocalise this excess of

electron charge repelled by the O^{2-} anions thus decreases the energy (a correspondent mechanism is operative on top of the Mg^{2+} cations). This effect explains for example the fact that coinage metal dimers and trimers adopt an upright configuration perpendicular rather than parallel to the regular MgO(100) surface, and concurs for example to stabilize supported Au cages up to N = 40 (see below). Such an effect is already present in the Pd/MgO and Pt/MgO systems, but it becomes so dominant for coinage metals such as Cu, Ag and Au that – as discussed in Sec. 2.2 – the behaviour of the adhesion energy as a function of coordination is not monotonic any more: the adhesion energy of the (001) monolayer is smaller in absolute value than that of the (001) bilayer. In Sec. 2.2 it was shown how to circumvent this problem in deriving an empirical potential for the interaction of Ag and Au with MgO(100) without abandoning the simplicity of the original model, i.e. by selecting in the fitting procedure ideal systems in which the metal-on-top effect is implicitly included. For Cu there is the additional problem that the choice of three ideal fitting systems and three surface sites makes epitaxial pseudomorphic multilayers unphysical or at least unrealistic as fitting systems and must be replaced by more general fitting schemes in which the results of available DF calculations on any supported metal particles are used as input data in a self-consistent fashion [FerrandoACSN2008; RossiPCCP2010; BarcaroJPCL2010].

Other effects are connected with epitaxial relationships, see Fig. 25. Since metal atoms prefer to stay on top of oxygen atoms and the O-O first-neighbor distance for example in MgO(100) is 2.97 Å, if the optimal metal-metal distance in the bulk is smaller than this value (as is usually the case), the lattice mismatch between the substrate and the growing particle will produce frustration and strain that need to be alleviated. For nanoparticles, this mismatch will be even more pronounced than for extended systems as a consequence of the shrinking of metal-metal distances due to the reduced coordination (bond-order/bond-length correlation, see Sec. 2.2). This strain can be reduced by the creation of interfacial dislocations [FreundBook2003], i.e., defect lines at the interface by which the nanoparticles achieve a better match to the substrate. Another possibility is to develop exotic morphologies which are not favored in the bulk but become favored because of a better adhesion and interfacial energy, a possibility which is particularly likely if the lattice mismatch between metal and oxide is large [FerrandoACSN2008]. Of course, these interface-stabilized phases must eventually produce a crossover to the thermodynamically stable bulk phase, depending on the growth conditions and on the associated kinetic energy barriers, as indeed found [FerrandoACSN2008].

So far we have considered regular, undefected oxide surfaces. It has been shown however that metal cluster can easily diffuse on regular, undefected surface [MusolinoPRL1999; XuPRL2005; BarcaroPRL2005] (see also Sec. 5.1). This implies that a perfect surface can be unable to stabilize metal nanoparticles and avoid sintering. It is therefore believed that surface defects play a crucial role as trapping and nucleation centers. Defects can be distinguished into local and extended. Two

examples of prototypical local defects that have been studied in great detail are the oxygen vacancy (or F_s-center) and the double vacancy (DV) on the MgO (100) surface. The F_s defect is obtained by removing a neutral oxygen atom from the surface, thus leaving behind a cavity filled with 2 electrons trapped by the Madelung potential created by the surface. It is usually chosen as an example of a neutral local defect, but charged Fs-centers obtained by removing one or both trapped electrons have also been studied [NeymanJACS2005]. The DV defect on the MgO (100) surface is instead obtained by removing a MgO neutral pair from the surface, thus leaving behind a larger cavity with no trapped electrons. Extended as opposed to local defects are for example step edges. Other possibilities include combinations of local defects with extended ones such as Fs-centers at steps, corners, kinks, etc. [ChiesaACR2006]. The importance of such defects on the properties of oxide surfaces as supports for the growth of metal clusters has been widely debated. Clearly, the way of preparing the surface plays a crucial role in determining the relative abundance of the various types of defects, and this may have a bearing on the adsorption properties of the oxide surface, and hence on the catalytic activity of metal nanoparticles supported on it, which might help explaining why heterogeneous catalysis is often considered as a kind of "black magic". What can be certainly said at the theoretical level is the fact that the presence of a defect appreciably modifies the PES of metal atoms around the defect center [MoselerPRL2002; BarcaroJPCB2006a]. Let us consider for example the absorption of a single Au atom on the regular and defected MgO (100) surface. We fix the Au position in the plane parallel to the oxide surface and optimize its distance from the surface.

defects on the MgO(100) surface: the F_s center

The oxygen vacancy: a prototype defect

Au-F_s topography

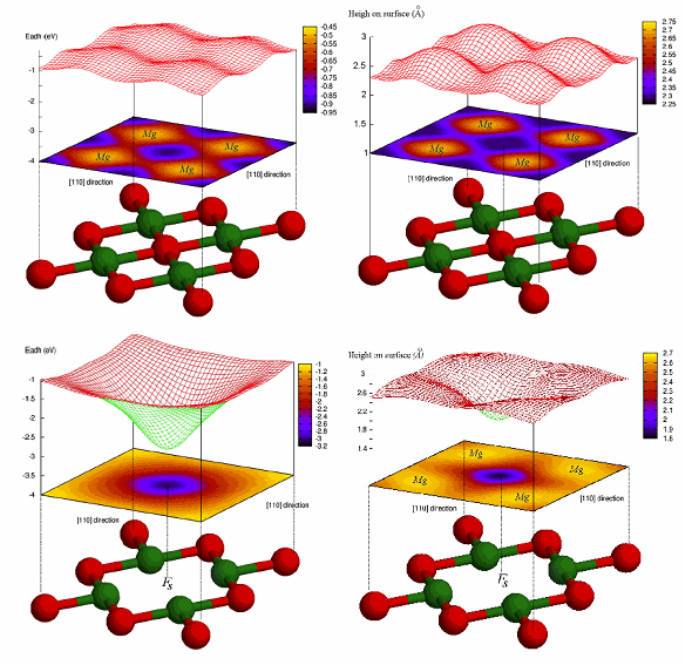

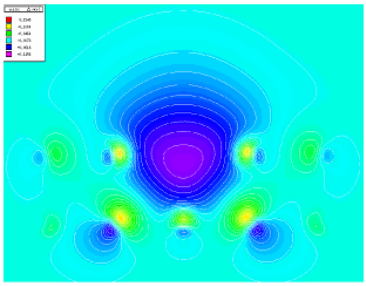

General features of the metal/defect interaction:

1. *Increase of the interaction energy*
2. *Rotational Invariance*
3. *Double Frustration*

Verified in the case of Ag and Au interaction

Fig. 26: Potential energy surface (left panel) and equilibrium height (middle panel) for adsorption of a single Au atom on the regular (upper left and middle images) and F_s-defected (lower left and middle images) MgO(100) surface. Plot of electron density at a F_s defect (upper right image).

Fig. 26 shows the resulting absorption topography, that is, the equilibrium distance and absorption energy as a function of the in-plane position, for both the regular (top panels) and the defected (bottom panels) surfaces [BarcaroJPCB2006a]. A completely different energy and equilibrium distance landscape is immediately apparent in the two cases. On the regular surface, one finds a rather flat potential energy surface, exhibiting minima in correspondence of the oxygen atoms, maxima on the magnesium atoms, and saddle points on the hollow sites, with a maximum adhesion energy of 0.91 eV and energy barriers of about 0.2 eV for the diffusion between neighboring oxygen sites. Correspondingly, the equilibrium height exhibits minima at 2.30 Å on the oxygen sites, maxima at 2.71 Å on the magnesium sites, and saddle points at 2.40 Å on the hollow sites. The in-plane distance between the energy minima corresponds to the MgO lattice parameter of about 2.97 Å: this value is larger than the typical Au-Au distances (the Au-Au distance in the bulk is 2.885 Å, smaller distances are normally found in Au nanoclusters), thus inducing a frustration (mismatch) in the metal growth on the MgO (100) surface. The presence of the Fs defect completely alters this situation, with the resulting potential energy and equilibrium height surfaces exhibiting three major features:

(a) the energy minimum in correspondence of the defect site is much deeper, with an adhesion energy of 3.07 eV;
(b) a large basin of attraction is produced around the defect, with an adhesion energy of 1.62 eV on the magnesium atoms first-neighbors to the vacancy (to be compared to a value of 0.5 eV for the regular surface), extending its influence up to third neighbors, and exhibiting an approximate cylindrical symmetry: this is due to a strong perturbation of the electrostatic potential outside the surface with respect to the regular, undefected system, which affects the polarization and thus the adhesion characteristics of the metal atom;
(c) there is a large difference between the equilibrium distance atop the defect (about 1.8 Å), strongly reduced with respect to the absorption onto the regular surface, and that atop the neighboring sites (2.65 Å on the magnesium and 2.59 Å on the oxygen sites first-neighbors to the vacancy, respectively), for which an increase in the absorption energy unexpectedly corresponds to an almost general increase in the equilibrium distance. The equilibrium distance then slowly relaxes to the values typical of the adsorption on the regular surface as the Au atom gets farther from the defect. The topography of the equilibrium distance as a function of the in-plane coordinates thus corresponds to a "crater" around the F_s center.

These three features determine the characteristics of the metal growth around the F_s defect:

- due to the strong interaction of gold with the oxygen vacancy, this defect can act as an efficient trapping center for the nucleation of metal clusters;
- the approximate cylindrical symmetry of the adhesion energy around the defect site ensures the metal clusters a considerable rotational freedom, by which the clusters can rotate on the surface keeping the atom atop the defect fixed, as the adhesion energy to the surface is essentially determined by the distance of the site with which the metal atom is interacting from the defect, rather than by its chemical identity;
- the strong variation of the equilibrium distance around the defect site finally entails that the growth of metal clusters is frustrated not only horizontally with respect to the surface, due to the mismatch between MgO and Au lattice parameters, but also vertically, due to the appreciable difference in the equilibrium height for the atom interacting directly with the F_s center and the neighboring atoms interacting with the surrounding sites, a feature which can be described as a "double frustration".

In the right-hand-side of Fig. 26, the electron density contour of the HOMO orbital of the F_s-defected MgO(100) surface is shown, taken from Ref. [BarcaroTCA2007]. The shape of this orbital, which lies in the band gap of the insulator oxide and presents a strong *s*-character, shows how the two electrons trapped in the cavity are not fully confined by the Madelung potential of the solid; their density, on the contrary, protrudes out of the cavity and extends also above the sites around the vacancy. This partially explains the strong perturbation to the metal/surface interaction associated with the presence of the defect.

Still concerning the metal/surface interaction, an issue which has long been debated in the theoretical literature is that of the charge transfer between the metal and the oxide. For a single Au atom on the regular MgO(100) surface as a model of an ionic and inert oxide surface, it has been proved both experimentally and theoretically that no much charge transfer exists, but rather a significant polarization of the Au electron cloud [YulikovPRL2006]. However, other systems may be different. Some useful information in this regard can be drawn from an analysis of extended model systems such as oxide ultra-thin films on metal surfaces [FreundCSR2008]. These are composite systems formed by a very thin (ultra-thin) film, i.e., few-monolayer-thick, of an oxide grown on a single-crystal metal surface, see Fig. 27 (see also Sec. 4.3 and Fig. 64 in Sec. 5.4.2), and are interesting in a variety of ways, e.g. in this context to study the basics of metal/surface interaction. The availability of extended metal/oxide interfaces is interesting from an experimental point of view as it allows one to use space-averaged characterization techniques rather than local probes. In some cases a charge transfer between the metal and oxide components has then been clearly demonstrated. For example, as already mentioned it has been shown that MgO(100)

yields electronic charge to Mo(100) [PacchioniPRL2005]. This charge transfer strongly reduces the surface dipole moment of the Mo(100) surface, and thus its work function, i.e., the amount of energy necessary to take one electron from the interior of the system and bring it to the vacuum. It can thus be expected that sufficiently large Ag nanoparticles deposited on MgO(100) will acquire electronic charge from the substrate. The opposite effect, i.e., a transfer of electronic charge from the metal support to the oxide, can be found in other metal/oxide combinations. For example, it is found for a monolayer of NiO on the same Ag(100) substrate, see Fig. 27 for a pictorial view.

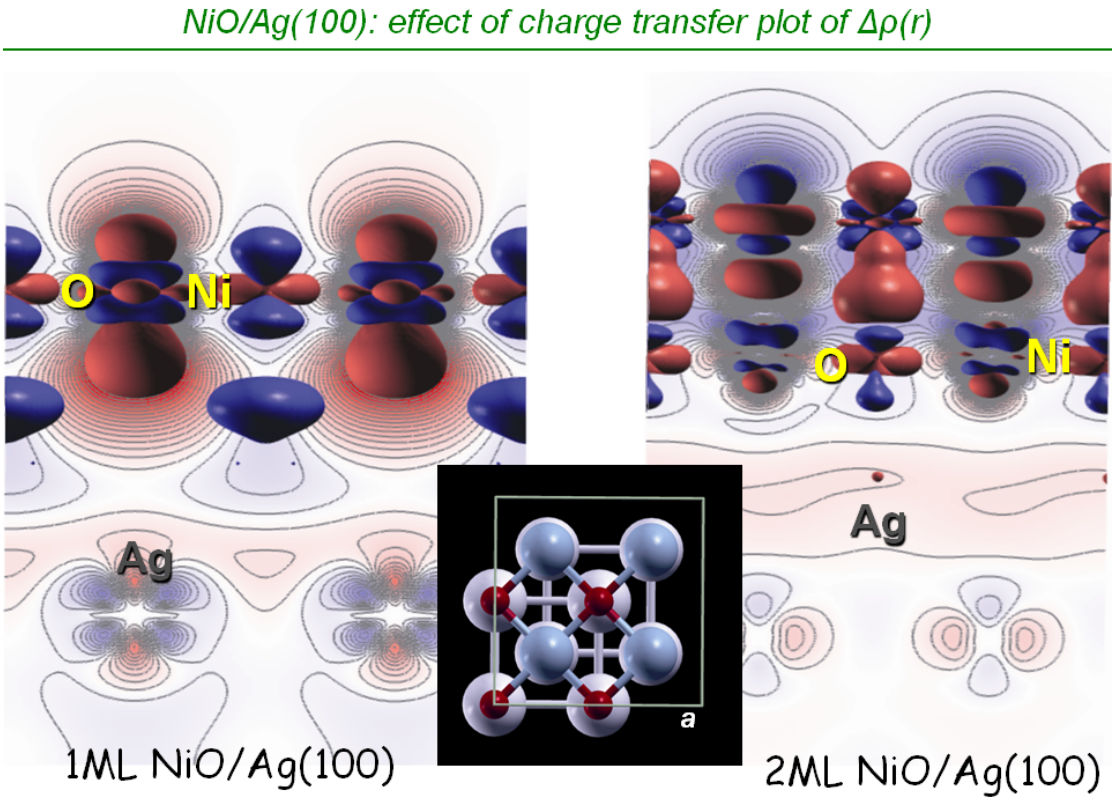

Fig. 27: Electron density difference plots are shown between the composite oxide-on-metal systems and the separated fragments. Red regions represent an increase in the electronic density, whereas blue regions represent a depletion.

In this picture it can also be appreciated that the charge transfer is much reduced in passing from an NiO monolayer to a NiO bilayer, a subtle effect proving that charge exchange between interacting systems depend sensitively on dimensionality and geometrical parameters. In the present case the fact that thickening of the oxide layer is accompanied by a partial reversal of the charge flow, or a decrease in the charge transfer dipole moment, is due to electrostatic repulsion, as the extra electrons on the Ni atoms of the first layer are pushed back into the silver substrate by the influence of the O ions on the second layer. The work function of a system is an important quantity, as it determines its redox properties. Charge transfer effects modulating the work function are thus relevant as they can appreciably modify properties such as

adsorption or interaction with deposited species. For example, it has been shown (see also Sec. 4.3) that the work function of the system composed of a MgO(100) ultra-thin film grown on Ag(100) is so low, due to the transfer of electronic charge from the oxide to the metal, that it becomes smaller than the electron affinity of small Au clusters deposited on top so that the Au clusters can acquire a sizable charge from the metal support, get negatively charged and thus exhibit very unusual morphologies, being planar and parallel (fully adhering) to the surface instead of perpendicular to it or compact [RicciPRL2006; LinPRL2009].

4.2 Interface-stabilized phases

In the context of supported particles, the exploration of novel and exotic morphologies and their stabilization on a substrate via unusual epitaxial relations represent an exciting route in determining specific properties and developing advanced devices [LordBook2006; XiongACIE2007], especially for oxide substrates, that are of special importance for their multifunctional flexibility ranging from insulators to semi- and super-conductors. This section is thus mainly devoted to this fascinating topic. The results will be presented ordered according to the size of the metal aggregate following the lines of the hierarchical multi-scale approach to structure prediction expounded in Sec. 2.4.

4.2.1. Small clusters

When dealing with small clusters ($N \leq 40$), one is confronted with the issue of the presence of defects in the substrate. It has been shown in fact that for several systems in a range of substrate preparation and metal deposition conditions cluster nucleation occurs preferentially at defect sites rather than on regular terraces, see, e.g., Ref. [HaasPRB2000]. This has been rationalized by accurate studies of the diffusion of single atoms and small clusters on the regular MgO(100) surface, showing that small clusters are very mobile on regular surfaces [BarcaroJCTC2005; XuPRL2005; BarcaroPRL2005; BarcaroNJP2007; FerrandoJPCM2009], so that they are able to reach defect sites in the usual deposition conditions (see Sec. 5.1). An interesting problem is thus represented by the influence of the underlying defect on the structure of the very small particles.

The first task is to single out the right defect for a given oxide surface. This is not an obvious task, as the type and abundance of defect sites e.g. on MgO(100) surfaces has been shown to depend appreciably on the preparation method. The most abundant defects are usually thought to be oxygen vacancies (possibly bearing a positive charge) and double vacancies as point defects, and (100) step edges as extended defects. Point defects in general seem to be rare when thin MgO(100) films are grown by Mg reactive deposition on metal surfaces in an oxygen background and then

annealed at high temperatures [WendtPSS2003], but both neutral and charged F_s-centres can be easily generated by post-processing these films [KolmakovJCP2000; KimJPCB2002; ArenzCPC2006]. In particular, recent work has shown that F_s-defects (both neutral and charged) are common when thin MgO(100) films are subjected to electron bombardment and subsequent annealing [SterrerPRL2005]. Probably due to the kinetics of the defect diffusion during annealing, F_s-centres are mostly found on kinks or steps rather than on regular terraces under such experimental conditions [SterrerPRL2005]. However, theoretical analysis has always focused on metal atoms and clusters adsorbed on F_s-centres on regular terraces. This is due to technical reasons and should not change qualitative predictions with respect to more precise modelling of the defected site. Moreover, such a limit can be easily overcome in the future if a more accurate experimental/theoretical comparison will be pursued.

The oxygen vacancy (also called F_s or color centre due to its optical absorption properties) is obtained by removing a neutral oxygen atom from the MgO lattice [MarkovitsPRB2003; DelVittoJPCB2005; YangPRB2002; NeymanJACS2005; MatveevSS1999; BarcaroJCTC2005; SanchezJPCA1999; GiordanoSS2005; MolinaACA2005; MolinaJCP2005; MoselerPRL2002; SousaJCP2001; MoriPRB2002; WendtPSS2003; BogicevicSS2002]. It is one of the most studied defects of the MgO(100) surface [KantorovichSS1995; PacchioniSS1998; MatveevSS1999; BogicevicSS2002; KramerSS2002; SousaJCP2001; MoriPRB2002; WendtPSS2003; PacchioniCPC2003; CarrascoPRL2004; WorzCPL2004; NeymanJACS2005; MolinaACA2005; YoonS2005; YanJACS2005; WalterPRB2005; DelVittoJPCB2005; CoquetJMC2006; CarrascoJCP2006; SterrerACIE2006; InntamAPA2006; NeymanCEJ2006; ArenzCPC2006]. Both static and dynamic properties have been studied: electron density maps and density-of-states plots [MoriPRB2002; PacchioniCPC2003], formation energy and diffusion energy barriers [BogicevicSS2002; KantorovichSS1995; PacchioniSS1998; CarrascoPRL2004; CarrascoJCP2006], and optical properties [SousaJCP2001; WendtPSS2003]. An intense study has been conducted on metal clusters adsorbed on the F_s-defect [BogicevicSS2002; MatveevSS1999; WendtPSS2003; WorzCPL2004; NeymanJACS2005; MolinaACA2005; YoonS2005; WalterPRB2005; DelVittoJPCB2005; CoquetJMC2006; SterrerACIE2006; InntamAPA2006; NeymanCEJ2006; ArenzCPC2006]. It has also been suggested that this type of defect can have an important effect on the catalytic activity of extremely small supported clusters [ArenzCPC2006; ChiesaACR2006].

An overview of the interaction of small (N = 1-3) coinage metal clusters, intermediate (Au_{20}) gold clusters and extended (pseudomorphic epitaxial monolayer and bilayer) depositions with the neutral F_s-centre has been presented in Refs. [BarcaroJCTC2005; BarcaroJPCB2006a]. As discussed in the previous section, the main finding that can be drawn from this investigation specifically in the case of gold (but this behaviour can be generalized to other metals) is that the presence of a neutral oxygen vacancy appreciably modifies the potential energy landscape of a

single atom moving in its surrounding, as depicted in Fig. 26, and that this has important consequences on the growth of small gold clusters atop the defect site, since not only the interaction of the gold atom directly atop on the defect is strongly increased and its equilibrium distance from the surface decreased, but the absorption over a larger region extending up to third- and fourth-neighbour sites is appreciably altered. All of this produces a rotational and structural fluxional character of gold clusters absorbed on the F_s-defect, by which the clusters can almost freely rotate around an axis perpendicular to the surface, leaving the atom directly interacting with the defect site fixed; and one finds a competition between metal cluster configurations with a reduced absorption energy, but a small distortion with respect to the gas-phase structure and thus a stronger metallic bond, and configurations in which the metal-metal distances between the atom atop the defect and its nearest neighbours are elongated (double frustration), but the overall configuration is stabilized by larger adhesion energies. This was explicitly shown for the Au_3 and Au_4 lowest-energy structures, and for the tetrahedral Au_{20} and a gold monolayer absorbed on an oxygen vacancy [BarcaroJPCB2006a].

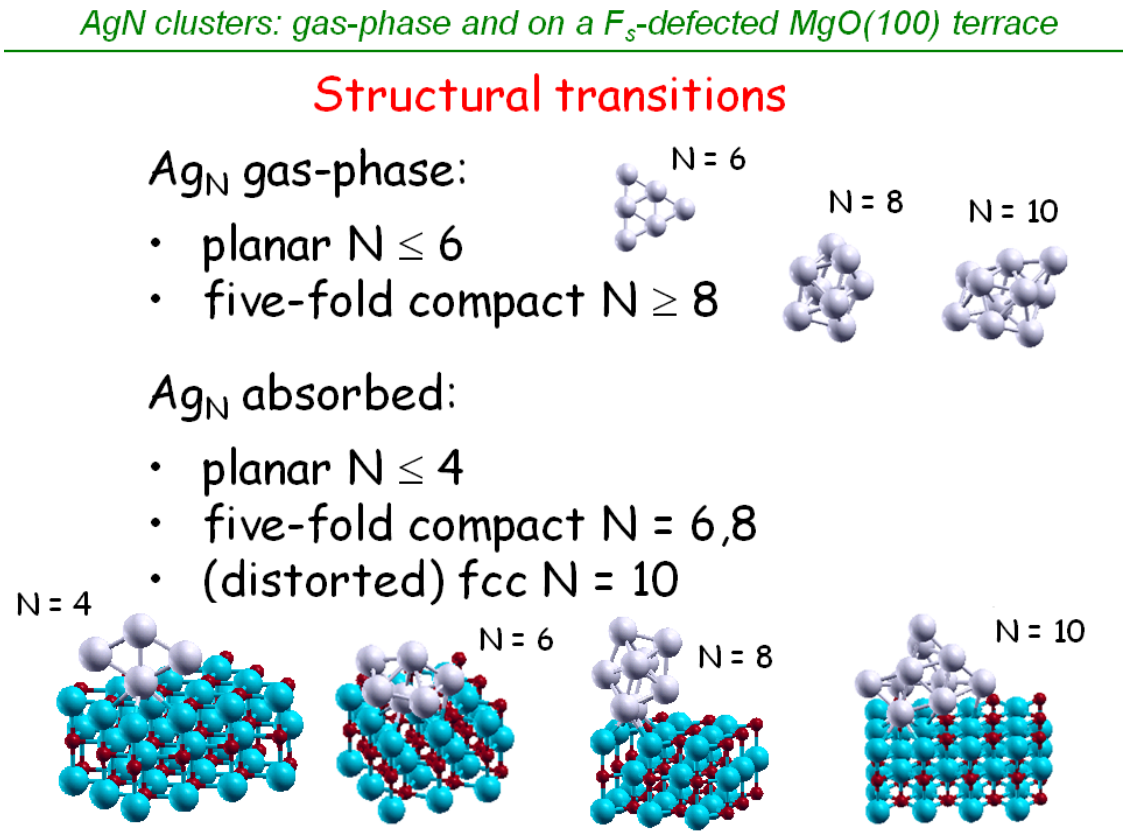

Fig. 28: Global minima of silver clusters both in the gas-phase and supported on an F_s-defected MgO(100) surface.

The implications of these findings on the structure of clusters larger than trimers and tetramers were investigated. For example, in Ref. [BarcaroCEJ2007] the structure of Ag_N clusters (N = 1-10), both in the gas phase and grown on a MgO(100) terrace containing F_s-defects, was investigated by a DF-BH approach. In analogy with what

observed in the case of gold, it was found that the presence of the defect implies a double frustration and a cylindrical invariance of the metal-surface interaction, causing small Ag clusters growing around the F_s-defect to exhibit a highly fluxional character, with energy differences between the putative global minima and the low-lying isomers amounting to few hundredths of an eV. Nevertheless, two different structural crossovers were found to be induced by the metal-defect interaction for the adsorbed clusters (see Fig. 28, taken from Ref. [BarcaroCEJ2007]) in such a way that: (1) planar structures prevail for $N \leq 4$ (as in the gas phase); (2) noncrystalline (fivefold-symmetric) structures, which are the lowest-energy ones in the gas phase for medium-sized Ag_N clusters ($N \geq 7$), prevail for N= 6-8; (3) distorted face-centred cubic (fcc) structures grown pseudomorphically on the defected surface prevail for N = 10. The interaction with the F_s-defect thus substantially modifies the structural scenario. The transition from five-fold to fcc motifs and the fact that it is anticipated by more than an order of magnitude in size with respect to the gas-phase is rationalized in terms of the double frustration effect, which increases the bond strain of the non-crystalline structures. Detrapping energies from the defect were also calculated; the lowest-energy pathway corresponds to the detachment of a dimer (a general feature for coinage metal clusters). Despite the fluxionality inherent in such small clusters, this tendency towards crystalline structures (possibly combined with kinetic trapping) could help explain why experimentally [RevenantNIMB2006] only truncated octahedra are observed in molecular beam epitaxy experiments of Ag deposition on the MgO(100) surface, even at very small sizes (height ~1 nm, lateral width ~1-2 nm), despite the fact that fivefold symmetric structures are the ground state for Ag clusters in the gas phase in this size range [BalettoPRL2000], see also the discussion in Sec. 4.2.3.

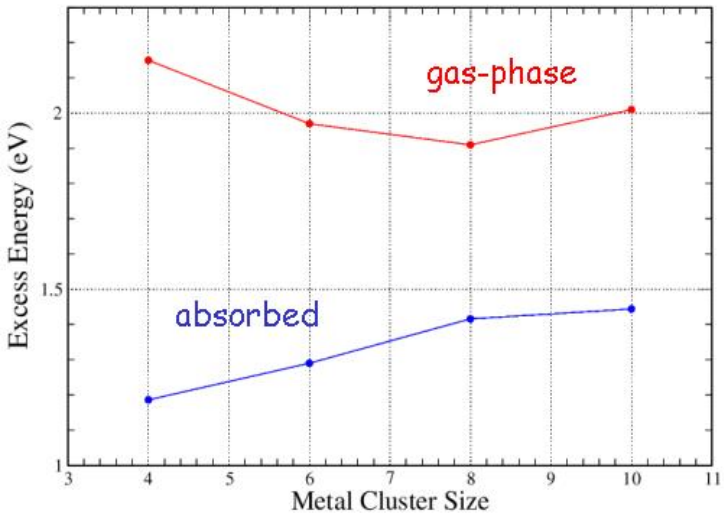

FIG. 29: Excess energy as a function of cluster size for gas-phase Ag structures (upper red line), and adsorbed on an F_s-defect (lower blue line).

It is interesting to consider the question whether surface magic metal clusters can exist adsorbed on oxide surfaces. For example, it is well known that N = 8 corresponds to an electronic magic number of the spherical jellium model. One could thus expect a particular stability associated to Ag_8, at least in the gas phase. Fig. 29 shows the behaviour of the excess energy for Ag_N clusters in the size range N = 4-10 both in the gas phase and when adsorbed on the F_s -defected surface. The excess energy $E_{exc}(N)$ is defined in Eq. (16), in which $E_{bnd}(N)$ is the metallic binding energy of the clusters in the gas phase, or the total binding energy (metallic energy plus adhesion energy) for the adsorbed clusters, and ε_{coh} is the bulk fcc cohesive energy of the metal calculated within the DF approach (2.50 eV):

$$E_{exc}(N) = \frac{E_{bnd}(N) - N\varepsilon_{coh}}{N^{2/3}} \qquad (16)$$

From Fig. 29, we see that in the gas phase Ag_8 does not present an exceptional stability (somewhat at variance with the predictions of the jellium model), being only modestly favoured with respect to sizes six and ten, even though a minimum in the excess energy is found at size 8. This is due to the fact that the valence *5s* orbital of the silver atom is too expanded to fit the Ag-Ag interatomic distances, and the energy stabilization associated with the jellium shell closure is frustrated by a destructive interference of the electronic wavelength [FerrandoPRB2005]. When the cluster is adsorbed on the defect, the situation is further worsened by the weak adhesion of this cluster with respect to the neighbouring sizes. In order not to distort excessively with respect to the gas-phase structure, in fact, Ag_8 adsorbs with only two atoms directly interacting with the surface. The final result is that the excess energy for the adsorbed clusters in this size range is a monotonously increasing function of the cluster size.

Alloying can however change this situation. In particular, Pd_1Ag_N (N = 1-8) clusters adsorbed on the F_s-defected MgO(100) terrace have been studied in Ref. [BarcaroJPCC2007], as discussed in detail in Sec. 2.5. There, it has been shown that Pd_1Ag_6 possesses the typical features of a magic cluster, i.e., a differential formation energy remarkably larger than that of neighbouring clusters and a large HOMO-LUMO gap, signatures of both structural and electronic peculiar stability, simultaneously exhibiting a clear fluxional character. This is the first example of an electronic magic cluster on an oxide surface. The magic character of Pd_1Ag_6 can be rationalized in terms of an electronic shell-closure with 8 valence electrons, involving also the electrons trapped in the oxygen vacancy, coupled with a good adhesion to the defected surface. A structural transition from planar to non-crystalline 5-fold symmetric configurations is also found for both free and adsorbed Pd_1Ag_N clusters in

this size range. In analogy with the gold and silver pure cases, the presence of the F_s-centre causes the Pd-Ag clusters to exhibit a fluxional character with the lowest-energy isomers lying at 0.1-0.3 eV above the global minimum. An explicit synthetic route to the Pd_1Ag_6 cluster was also proposed in Ref. [BarcaroJPCC2007], passing through the sequential deposition of Pd and Ag atoms (exploiting the unfavourable dimerization of Pd on the F_s-centre) or the deposition of mass selected binary clusters (the latter is the more viable as the Pd_1Ag_6 cluster is magic in the gas phase, too). To the best of our knowledge these routes have not been explored so far.

The double vacancy (DV) [LunsfordJPC1966; OjamaeJCP1998; BogicevicSS1999; RicciJCP2002; BarthPRL2003; GiordanoPRL2004; BarcaroJCTC2005; DelVittoJPCB2005] is a neutral defect and corresponds to the removal of an MgO dimer in the [100] direction of the regular oxide terrace, see Fig. 30.

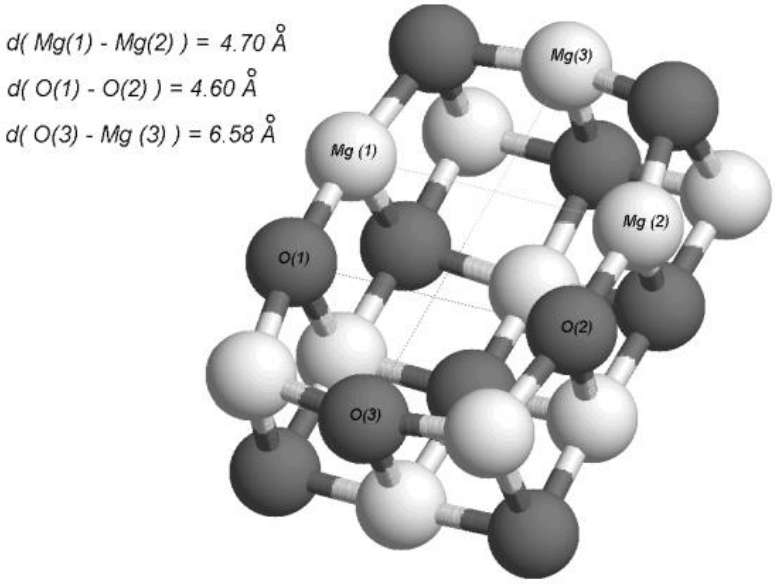

FIG. 30: Relaxed geometry of the MgO(100) surface around a double-vacancy (DV) defect.

It is believed that DV are the most abundant point defects when MgO(100) surfaces are prepared via cleaving MgO crystals under Ultra-High Vacuum (UHV) [BarthPRL2003], even though wide regular terraces prevail in this case and the surface concentration of DV defects remains low (about 10^{13} cm^{-2}). Furthermore, it has been shown, see e.g. Ref. [GiordanoPRL2004; BarcaroJCTC2005], that the DV can act as a strong trapping centre for metal species. The fact that the DV is the most likely candidate as a nucleation centre for the growth of metal clusters on UHV-

cleaved MgO(100) surfaces together with its low concentration make that this surface represents an ideal substrate for studying isolated supported metal clusters, and hence their single-particle properties in the absence of cluster-cluster interactions. It is therefore of interest to study the structure of small metal aggregates adsorbed on a DV-defected MgO(100) terrace and the influence of the metal/surface interaction on it as a function of the metal cluster size. Such studies have been conducted in Refs. [BarcaroJCTC2005; BarcaroPRB2007; BarcaroFD2008; BarcaroCPL2008].

First, it was found that – at variance with the neutral oxygen vacancy – the presence of the double vacancy induces a strong structural and energetic modification in the surrounding oxide lattice [MatveevSS1999], see Fig. 30; moreover, this structural relaxation changes according to the extent of the metal deposition on the surface, i.e., it is strongest for the single atom and levels off reaching a stable configuration (both in terms of geometry and distortion energy) when larger clusters are considered [BarcaroJCTC2005; BarcaroPRB2007; BarcaroFD2008; BarcaroCPL2008]. Small (N = 1-3) coinage metal clusters and extended (pseudomorphic epitaxial monolayer and bilayer) depositions were considered in Ref. [BarcaroJCTC2005], slightly larger (N = 4-10) Ag and Au aggregates were treated in Refs. [BarcaroPRB2007] and [BarcaroCPL2008], respectively, while Ag_N clusters (N = 6-8) alloyed with 1-2 Cu, Au or Pd atoms were studied in Ref. [BarcaroFD2008]. A general feature of metal adsorption on the DV defect is that the first metal atom adsorb close to the site left empty by the removal of the Mg atom and penetrates deeply into the cavity reaching almost the same height as the Mg and O atoms of the surface oxide layer. This is more evident for example in the case of Cu, that has a small size, than for Ag or Au, whose larger size is more difficult to accommodate within the cavity. The second atom then places itself on top of the neighbouring empty site of the vacancy, giving rise to a structurally frustrated cluster growth analogous to the "double frustration" effect observed on the F_s-defect [BarcaroJPCB2006a] (i.e., the metal growth around the local defect is frustrated not only horizontally by the mismatch of the lattice constant of the metal and of the oxide but also vertically by the difference in equilibrium lengths of the atoms adsorbed on the neighbouring sites). When translated into extended depositions (pseudomorphic epitaxial monolayers and bilayers), this in fact implies a corrugation of the metal slab in correspondence with the empty O site of the DV, more pronounced for Au and especially Cu than for Ag. In particular, in the Cu case the formation of clear dislocation patterns in the (3X3) cell can be observed, with the so-formed islands placing themselves in a lateral position with respect to the defect, which suggests a peripheral growth of larger clusters with respect to the DV [BarcaroJCTC2005].

The results of DF-BH studies on Ag_N [BarcaroPRB2007] and Au_N [BarcaroCPL2008] clusters (N = 4-10) confirm the differences between these two coinage metals. For Au clusters one finds a highly fluxional character in this size range, with energy differences between the putative global minima and the lowest-lying isomer amounting to few hundredths of an eV. Concurrently, no Au magic

clusters are found. Au_6 itself, that exhibits a planar configuration and is energetically favoured in the gas-phase with respect to the other even sizes thanks to an electronic shell-closure effect, presents a much reduced HOMO-LUMO gap once adsorbed on the DV, and its dimer incremental formation energy is similar to that of the neighbouring sizes, actually even smaller than that of Au_{10}, which presents a comparable HOMO-LUMO gap. This is due to the fact that the tendency of Au_N clusters with $N \leq 12$ to planarity conflicts with the demands of compact structures to maximize the adhesion to the oxide surface. These requirements are general, and could only be overcome in the case of positively charged Au clusters, which in the gas phase attain 3D arrangements at $N = 8$ instead of N ~ 13 [GilbJCP2002]. This structural frustration should translate into a very low melting temperature [BalettoRMP2005] and peculiar catalytic activity of such systems [MeersonEPJD2005; HakkinenACIE2003]. Another consequence is that small energy differences are found between different structural motifs, in particular fcc-like and five-fold-symmetry ones. This supports the possibility that the co-existence of different epitaxies observed in molecular beam epitaxy experiments [MeersonEPJD2005] is due to fluxional behaviour and/or kinetic trapping into local structural funnels (see also the discussion in Sec. 4.2.3).

Ag_N clusters (N = 4-10) lend themselves to a more clear-cut structural analysis [BarcaroPRB2007]. First of all, a single structural transition can be observed for gas-phase clusters: from planar to compact configurations at size 8 [MoselerPRL2002]. At variance, two different structural transitions can be observed for the supported clusters: from planar to compact at size 6 and from compact structures exhibiting five-fold symmetry axes to compact structures that are distorted pieces of an fcc lattice at size 10. The presence of the defected surface thus makes an appreciable difference on the structural properties of these small Ag clusters. Moreover, the fluxional character of metal clusters in this size range is only partly confirmed for Ag, because Ag_8 is found to exhibit a magic character, much more pronounced than in the gas-phase, with the highest incremental formation energy and the lowest incremental formation energy for the (N+1) cluster (Ag_9) in the considered size range, in close analogy with the surface magic cluster $PdAg_6$ (see the inset in Fig. 11), and a HOMO-LUMO gap of 1.7 eV. The shell closure at N = 8 in fact combines with a very compact atomic arrangement, as shown in Fig. 31. In other words, the cluster/defected-surface interaction strongly reinforces the magic character of Ag_8, thus producing a system with peculiar chemical and electronic properties: a substantially greater stability and a larger HOMO-LUMO gap than neighboring sizes. Additionally, Ag_8 exhibits a more compact structure with respect to the neighboring sizes, with no Ag atoms hanging over the MgO surface, and this has consequences on its chemical properties. The magic character of Ag_8 suggests the possibility of selectively producing it via a properly devised synthetic method, a possibility so far unfortunately unexplored.

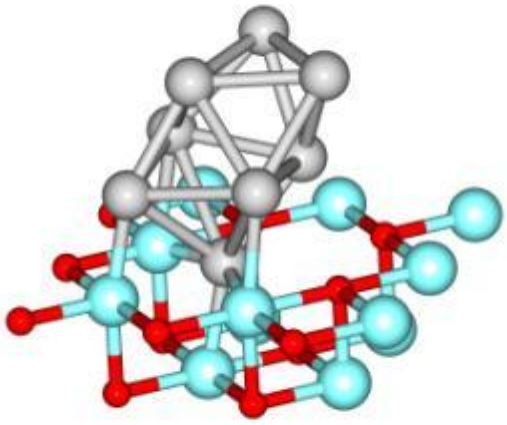

FIG. 31: Schematic picture of the Ag_8 global minimum adsorbed on the DV-defected MgO(100) surface. Silver atoms are depicted as grey light spheres, magnesium atoms as red small spheres, and oxygen atoms as light blue big spheres.

Concerning the effect of the magic character of Ag_8 onto its chemical properties, it can be noted that its electron affinity is smaller by ~ 0.3 eV with respect to Ag_6 and Ag_{10}, its ionization potential is larger than that of Ag_6 (that - being planar - also presents electronic and structural shell closure), and its interaction with the O_2 molecule is only 0.49 eV vs. 1.0 and 1.2 eV for Ag_6 and Ag_{10}, respectively [BarcaroPRB2007] (all this will be also discussed in Sec. 5.4.1). The last feature is particularly noteworthy, in the sense that Ag_8 appears to be less reactive with respect to Ag_N clusters of neighbouring sizes. This can contribute to its selective synthesis: once a mixture of Ag_N species of different sizes is experimentally produced, reaction with O_2 in properly selected conditions can destroy the more reactive species and leave Ag_8 as the only intact survivor. A similar strategy has been recently employed to produce medium-sized ligand-protected Au clusters [ChakiJACS2008]. Moreover, smaller interaction energies with incoming species can be useful when a fine tuning of the cluster catalytic activity is sought for. The reasons of this weaker Ag_8-O_2 interaction are at the same time electronic and structural. The electronic shell closure contributes by roughly 0.25 eV to decrease the O_2 interaction energy, while a further decrease by ~ 0.35 eV is given by its more compact structure with respect to neighbouring sizes, with no Ag atoms hanging over the MgO surface, thus disfavouring the interaction of the O atom not directly bound to the metal cluster with the MgO(100) surface, that would produce a further stabilizing contribution.

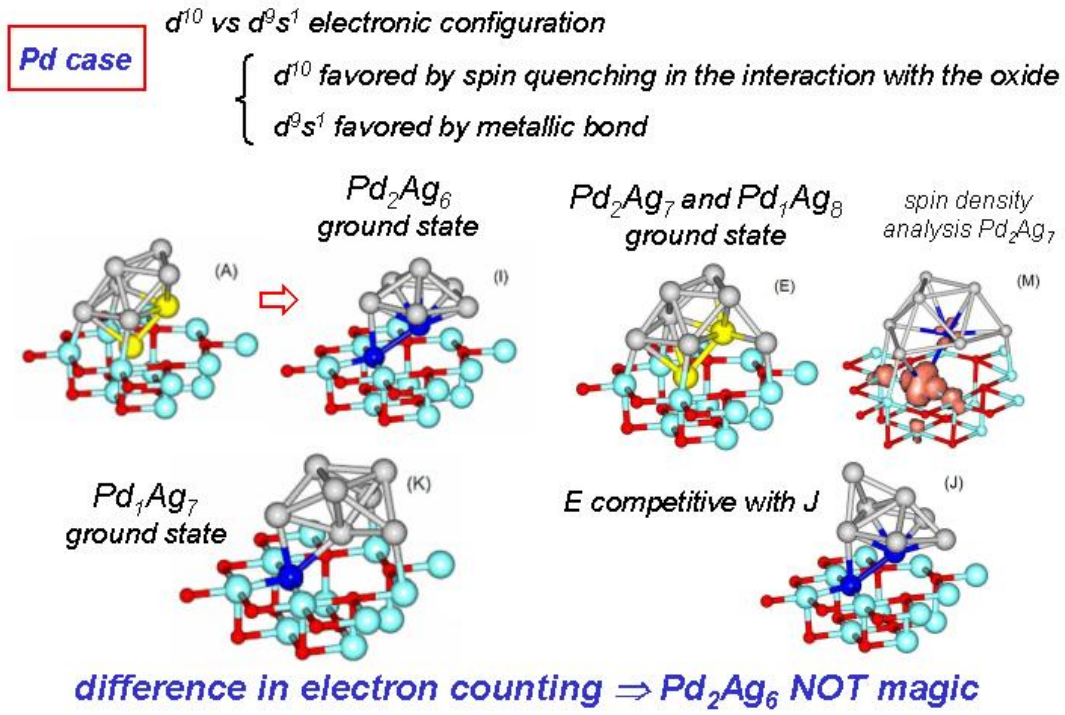

FIG. 32: Schematic drawing of Pd_2Ag_6 (I), Pd_2Ag_7 (J) and Pd_1Ag_7 (K) structures. (A) and (E) structures from Fig. 33. (M) shows the electron spin density plot for structure (E) of Pd_2Ag_7. In the metal clusters, grey metal atoms represent Ag, yellow metal atoms represent M; in the oxide support, lighter light blue atoms represent O and darker red atoms Mg.

The effect of alloying on the Ag_8 magic cluster was studied in Ref. [BarcaroFD2008], where Ag_N clusters (N = 6-8) alloyed with 1-2 Cu, Au or Pd atoms were investigated. Figs. 32 and 33 show some of the low-energy structures found for M_LAg_N (M = Au, Cu, Pd; L = 1, 2; N = 6-8) clusters adsorbed on the DV defect. Alloying with Au_2 was found not to change significantly the situation: the Au atoms, with a stronger interaction with the MgO surface, are directly adsorbed on the DV, whereas the silver atoms form a shell covering them (this structural ordering is also favoured by the lower surface energy of silver with respect to gold). Apart from this, alloying with gold does not change the energetic ordering of the considered configurations with respect to pure silver clusters, and also the HOMO-LUMO gaps are very similar. Also in the case of the Cu-Ag bimetallic system, the larger interaction of the copper atom and dimer with the DV with respect to silver atoms determines the formation of a core-shell structure with a Cu core. With respect to the gold atom, the copper atom has a reduced size, and replacing one or two Ag atoms with Cu atoms implies a relaxation consisting in a shrinking of the silver-copper distances. This is however counteracted by the "double frustration" characterizing the interaction with the surface [BarcaroPRB2007; BarcaroJPCB2006b], which hence plays a destabilizing role for Ag-Cu clusters. The consequences of this destabilization are the reduction of

the HOMO-LUMO gaps at the Fermi level and of the energy differences between global minimum and higher-energy configurations with respect to pure silver clusters, thus corresponding to an increased fluxional character of the clusters. It can be noted that in the gas phase alloying with Cu has an opposite effect on Ag clusters, producing core-shell configurations exhibiting great stability [RossiPRL2004].

Finally, at variance with the Cu and Au cases, alloying with Pd is found to make a qualitative difference on both the geometry and the electronic structure of the clusters. Considering the Pd_2Ag_N case (N = 6-8) as an example, it was found first of all that the two Pd atoms fill up the vacancy sites as in the case of Cu and Au (Fig. 33-E). By then analysing the electron spin density of Pd_2Ag_7 (Fig. 32-M), it was found that the electron spin is localized on a d electron of the Pd atom inside the DV cage. This Pd atom is thus promoted to a $4d^9 5s^1$ configuration and the *5s* electron takes part in the metallic bond, whereas the Pd atom outside the defect keeps its $4d^{10}$ gas-phase configuration. This electronic situation is forced by the requirements of the metallic bond - which tends to complete an 8-electron shell - but is disfavoured by the metal-surface interaction which would tend to quench the spin of the Pd atoms interacting with the surface [MarkovitsPRB2003]. It is interesting to note that, in a way, the situation now resembles that found for the single oxygen vacancy: after one of the Pd atoms has filled the Mg site of the DV, the oxygen site is left available for the interaction with metal clusters, in a similar way to what happens for the single oxygen vacancy [BarcaroJPCB2006a]. The major difference with respect to the single oxygen vacancy case is that the electron count is different here, because the Pd atom inside the defect contributes with only one electron, whereas in the neutral F_s case the defect contributes with two electrons. This implies a mismatch between structural and electronic shell closure which, together with the destabilization of high-spin configuration for the atoms interacting with the surface, hinders the formation of binary Pd-Ag magic clusters adsorbed on the DV, at variance with the F_s-defected surface [BarcaroJPCC2007]. The requirements of the metallic bond are thus in conflict with the optimal metal-surface interaction. For the Pd_2Ag_6 cluster, which is a spin-restricted system, both Pd atoms are now approximately in a $4d^{10}$ electronic configuration, which however implies an electron count of 6 (a non-magic number) and a weakening of the metallic bond. The structural properties of the system are also strongly affected by the presence of Pd atoms, with the creation of a pronounced basin of attraction towards a pentagonal bipyramid motif, with the 6 Ag atoms in Pd_2Ag_6 forming a pentagonal bipyramid on top of the Pd atom above the empty O site of the vacancy - see structure (I) of Fig. 32]. Most other competitive structures of Ag_8 undergo a remarkable rearrangement towards the pentagonal bipyramid motif when alloyed with Pd_2. Structure (I), which completes the bipyramid, results in the global minimum. Structure (D) in Fig. 33, an incomplete tetrahedron, is the most competitive motif not based on the pentagonal bipyramid, being only 0.22 eV above the ground-state. In passing, we observe that predictions about the spin properties of these clusters could be experimentally verified by EPR measurements [SterrerPRL2005], and that the reduced magic character of the Pd-Ag

(and also Cu-Ag) DV-supported clusters translate in an enhanced fluxional character which could be important for their catalytic activity [HakkinenACIE2003].

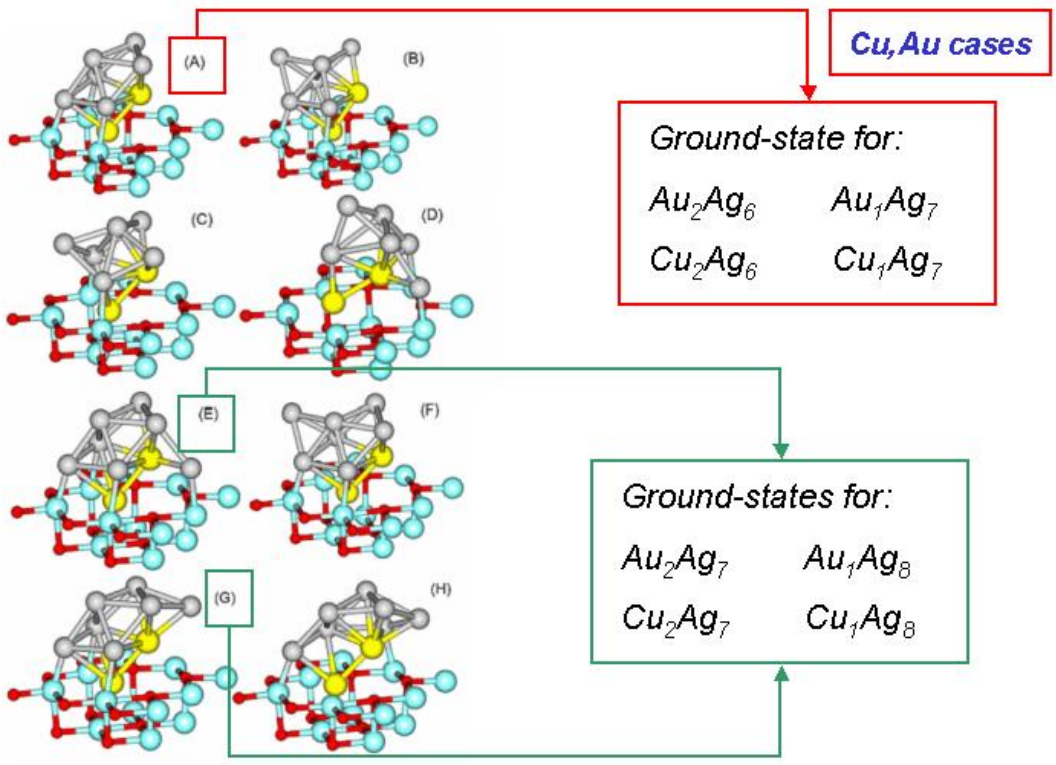

FIG. 33: Schematic drawing of the structures of M_2Ag_6 (A)–(D) and M_2Ag_7 (E)–(H) clusters (M = Au, Cu). Colour coding as in Fig. 32.

A very limited number of calculations have dealt with (100) steps as extended defects, see e.g. Ref. [DiValentinSS2006] and references quoted in Ref. [FerrandoJPCM2009]. This is unfortunate, as these are thought to be the most common extended defects on a MgO(100) surface, and their influence on the growth of metal particles can be clearly seen at the experimental level [HenryPSS2005]. Moreover, theoretical modelling of such defects is not particularly cumbersome at the theoretical level, and it is to be expected that more studies will be performed on this topic in a near future.

4.2.2. Intermediate-size clusters

All the systems discussed in the previous section were simulated via a DF-GO approach [BarcaroCEJ2007]. Somewhat larger clusters can be investigated via a DF-EP approach, as discussed in Sec. 2.4. Clusters containing few tens of atoms can present nanofacets of different symmetries and orientations, edges between nanofacets, corners (in some cases truncated corners), and overhangs at the interface

with the support, see Fig. 34 for the case of Pd clusters. These nanoscale features give a variety of adsorption sites, with different symmetries and properties, confined in a very small region of space, which can be very important for applications. For example, this may originate low-energy pathways for chemical reactions, as in the case of the CO + NO reaction on Pd clusters adsorbed on MgO, in which a low-temperature reaction mechanism is observed in small nanoclusters (below 30 atoms) but not in larger clusters or bulk surfaces [WorzJACS2003]. It can be noted that overhangs in Au/MgO(001) clusters have been suggested to be very favorable sites for CO oxidation [MolinaACA2005].

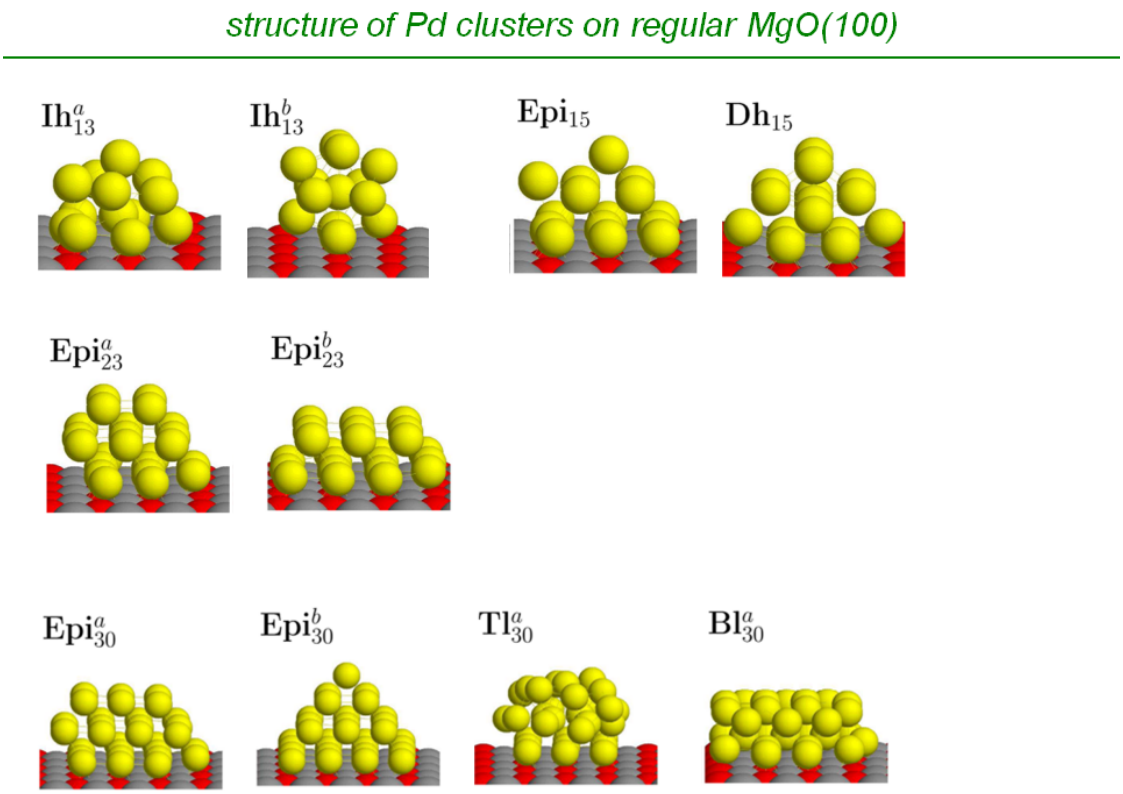

Fig. 34: Some structural motifs of palladium clusters adsorbed on MgO(100) surface.

When considering larger clusters, the issue of the presence of defects in the substrate becomes progressively less important. It is to be expected in fact that the influence of, e.g., an underlying local defect (which has acted as a nucleation centre) is negligible (or at least progressively less crucial) on medium-sized clusters or larger metal particles, unless kinetic trapping into structural funnels takes place, as hypothesized for specific systems [BarcaroCEJ2007; BarcaroCPL2008; BarcaroPRB2007] and mentioned in the previous section. It can also be recalled that deposition at sufficiently low temperatures or high fluxes may cause the nucleation of metal clusters on regular terrace sites. It is therefore sensible to focus on clusters adsorbed on the regular MgO(100) surface, with the only remark that extended defects such as

steps should in principle be also considered, as these defects can act as nucleation centres (even though less effectively than single or double vacancies), and – being extended – can have an influence on a growing large cluster (see also Sec. 4.2.3). A few medium-sized systems have been thoroughly investigated using the combined DF-EP algorithm [BarcaroJPCB2006b; BorbonJPCC2007; FerrandoPCCP2008] outlined in Sec. 2.4 and will be discussed in the following: Pd [BarcaroPRL2007], Au [FerrandoPRL2009], Ni [FerrandoACSN2008], and CoPt [BarcaroJPCL2010] clusters.

Pd clusters on MgO(001) represent one of the most studied model catalysts, and it is therefore important as a proof-of-principle test to be able to reliably predict their structures. The starting point of the investigation pursued in Ref. [BarcaroPRL2007] consisted the fact that experimental evidence [HenrySSR1998; GiorgioPMB1993; HenryPSS2005] showed Pd clusters of size N ~100 or more with fcc structures in (100) epitaxy with the substrate, while several DF calculations, see e.g. Refs. [FerrariPCCP1999; XuPRL2005; BarcaroPRL2005], predicted that very small clusters (i.e., below N = 10) present a very different epitaxy, e.g. having triangular facets in contact with the square-symmetry MgO(100) surface (Pd_4 is a tetrahedron, Pd_5 is a square pyramid, Pd_6 is an octahedron lying on the surface with one of their facets, etc.). If DFT is a reliable approach, it is then to be expected that a transition to configurations with (100) epitaxy should occur somewhere in between 10 and 100 atoms, but the actual size is experimentally unknown. Empirical potentials are not fully informative, as they give different answers depending on the model, so that accurate DFT results are needed. This expectation was supported by the results of Ref. [BarcaroPRL2007] in which a systematic search for the lowest-energy structures of Pd clusters adsorbed on the regular MgO(001) surface was performed via a DF-EP approach [BarcaroJPCB2006b; BorbonJPCC2007; FerrandoPCCP2008]. Clusters were adsorbed on the flat regular oxide surface and not on surface defects. In the spirit of the DF-EP approach, the database of candidate structures to be re-optimized at the DFT level was constructed to include clusters belonging to several different structural families, and not simply the lowest-energy isomers of the prevailing family. The DF-EP search was conducted in a very thorough way, especially at sizes N = 11-15 and 30, where a large database of structures was generated using two different EPs [VervischPRB2002; RossiJPCB2006], and several low-energy structures belonging to all the structural families were locally optimised at the DF level. From this study it derived that the transition to configurations with (100) epitaxy occurs at very small sizes, between 10 and 15 atoms. Even more importantly, it was shown that fcc structures form truncations and overhangs also at rather small sizes, below N = 30. Several competing configurations are given in Figs. 35 and 36, where low-energy structures of Pd clusters on the regular MgO(100) surface are shown for sizes N = 11-15 and N = 18-30, respectively, with the corresponding total binding energy (E_{bnd}) and energy separation with respect to the lowest-energy isomer at a given size (ΔE) reported in Table I.

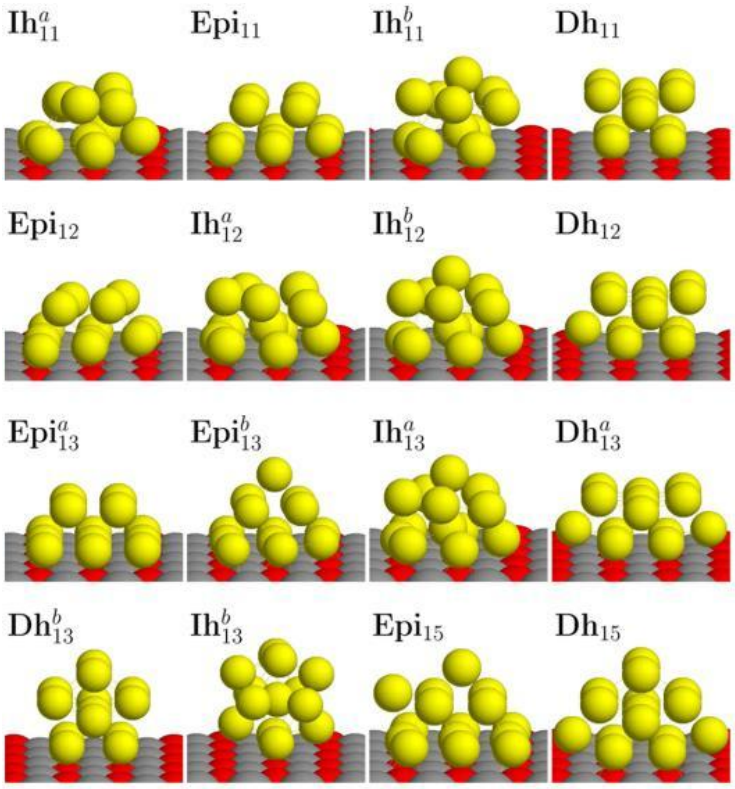

FIG. 35: Pd clusters on MgO(001) at sizes $11 \leq 15$. Energies are reported in Table I.

Between 10 and 15 atoms, a competition among three main structural motifs was found: epitaxial (Epi), icosahedral (Ih), and decahedral (Dh) clusters, see Fig. 35. Epi clusters are epitaxial clusters obtained from the perfect square-basis pyramid of 14 atoms: an atom is added on a triangular facet of the pyramid to produce the cluster Epi_{15}. The Ih family comprises the perfect Mackay icosahedron of 13 atoms (Ih^b_{13}), and a distorted icosahedron (Ih^a_{13}), which presents a better matching with the substrate and a much lower energy. The Dh family is made of fragments of a decahedron presenting a fivefold axis which runs parallel to the MgO(001) surface, such as Dh_{15}, see Fig. 35. It was found that Epi structures clearly prevail for $N \geq 12$. The metal-oxide interaction is not strong enough to cause a 2D cluster growth: the most stable cluster shapes are 3D. However, the metal-substrate interaction is crucial in determining the best cluster structures. In the gas phase, I_h and D_h clusters are much more stable than fcc truncated pyramids. However, this is not sufficient to counterbalance the better adhesion to the substrate of Epi clusters for $N \geq 12$. For example, at size $N = 13$, neither the undistorted icosahedron, nor a buckled biplanar structure, which are favored in gas phase, can compete with the (001) epitaxy truncated pyramids. For Epi clusters truncations of the vertex atom of the fcc square pyramid or of its basal corner atoms is already favoured.

At larger sizes the motifs competing with Epi ones can be classified as bilayers (Bl) and trilayers (Tl) as shown in Fig. 36.

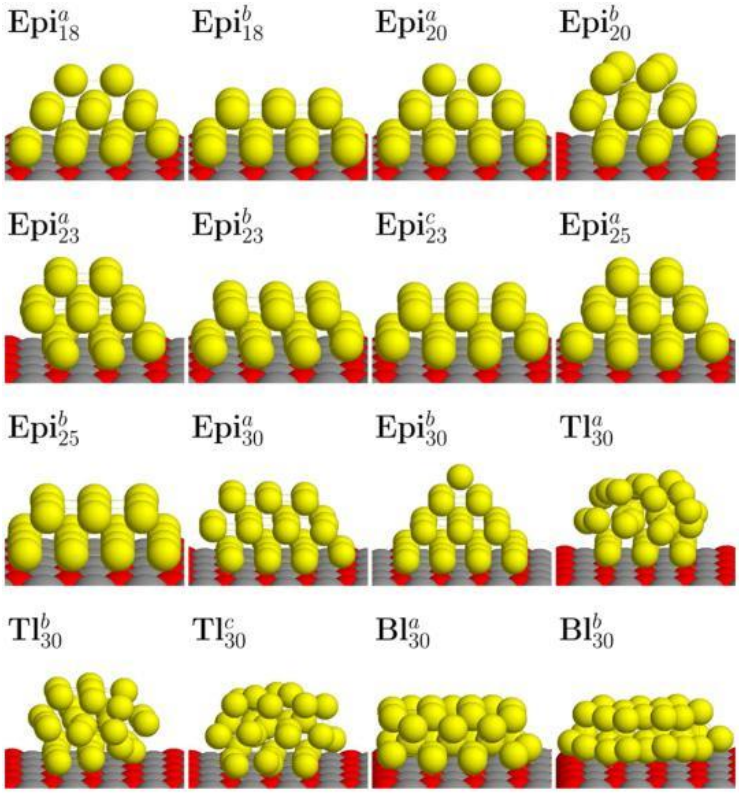

FIG. 36: Pd clusters on MgO(001) at sizes 18 ≤ 30. Energies are reported in Table I.

At N = 30, the most favorable Epi clusters are the perfect pyramid (Epi^{b}_{30}) and a structure presenting truncations and overhangs (Epi^{a}_{30}). The best Tl structure (Tl^{a}_{30}) has its bottom layer in good (001) epitaxy with the substrate, but the second and third layers do not continue this arrangement. Both Bl structures present (111) facets in contact with the substrate. It can be noted that Epi structures are lower in energy at N=30, with larger differences than for N < 15: (001) epitaxy is more and more favored as size increases. Moreover, overhangs are found to be already present for clusters in the size range 15 ≤ N ≤ 30. A single overhanging atom is found in Epi_{15}. More significantly, well-developed overhanging atomic rows are present in Epi^{a}_{23}, which is clearly lower in energy than the structures without overhangs, and even in Epi^{a}_{30}, which is slightly better than the complete pyramid Epi^{b}_{30}, see Fig. 36, a particularly significant fact as Epi^{b}_{30} is a magic structure for the pyramidal motif. Structures with overhangs optimize metal-metal interactions at the expense of the adhesion with the substrate, since metallic bonding is improved by a more compact cluster shape, while adhesion suffers from the decrease of the number of atoms in the cluster basis. However, the metal-on-top effect partially compensates this decrease by an improvement of the adhesion energy per basal atom: basal atoms on an edge below an overhang better adhere to the substrate than other basal edge atoms. In summary, in Ref. [BarcaroPRL2007] it was demonstrated that the transition towards fcc clusters in (001) epitaxy with the MgO substrate is taking place between sizes 11

and 13. At variance with the behavior of smaller clusters, from these sizes on, the metal-substrate interaction becomes crucial, so that the best Pd/MgO(001) clusters are not only different from the best gas-phase Pd clusters, but also grow in very good fcc (001) epitaxy with the underlying MgO lattice. The results for N around 30 show that the energy difference between epitaxial and non-epitaxial clusters becomes larger with increasing size, which supports the transition from nonepitaxial to epitaxial configurations. In epitaxial clusters, overhanging atomic rows are developed already at quite small sizes. Standard empirical potentials are unable to quantitatively predict the actual structures of the most stable clusters around N = 13 and the details of the shapes of larger clusters, such as preferential truncations and overhangs, due to the neglect of energy contributions such as the metal-on-top one effect.

Cluster	E_{bnd}	ΔE	Cluster	E_{bnd}	ΔE	Cluster	E_{bnd}	ΔE
Ih^{a}_{11}	-28.57	0.00	Dh^{a}_{13}	-34.20	0.41	Epi^{c}_{23}	-64.48	0.36
Epi_{11}	-28.42	0.15	Dh^{b}_{13}	-33.69	0.92	Epi^{a}_{25}	-71.19	0.00
Ih^{b}_{11}	-28.03	0.54	Ih^{b}_{13}	-32.90	1.71	Epi^{b}_{25}	-70.48	0.71
Dh_{11}	-27.92	0.65	Epi_{15}	-40.55	0.00	Epi^{a}_{30}	-86.77	0.00
Epi_{12}	-31.69	0.00	Dh_{15}	-40.29	0.26	Epi^{b}_{30}	-86.69	0.08
Ih^{a}_{12}	-31.32	0.37	Epi^{a}_{18}	-49.42	0.00	Tl^{a}_{30}	-86.29	0.48
Ih^{b}_{12}	-31.29	0.40	Epi^{b}_{18}	-49.38	0.04	Tl^{b}_{30}	-85.97	0.80
Dh_{12}	-30.98	0.71	Epi^{a}_{20}	-55.80	0.00	Tl^{c}_{30}	-85.60	1.17
Epi^{a}_{13}	-34.61	0.00	Epi^{b}_{20}	-55.25	0.55	Bl^{a}_{30}	-85.48	1.29
Epi^{b}_{13}	-34.47	0.14	Epi^{a}_{23}	-64.84	0.00	Bl^{b}_{30}	-84.94	1.83
Ih^{a}_{13}	-34.41	0.20	Epi^{b}_{23}	-64.61	0.23			

TABLE I: Energies (in eV) of the clusters shown in Figs. 35 and 36: E_{bnd} is the total binding energy, ΔE is the energy separation from the lowest-energy isomer at a given size.

The case of Au is different [FerrandoPRL2009], as it often happens due to gold's unique structural behaviour [DanielCR2004; PyykkoACIE2004; PyykkoICA2005; PyykkoCSR2008]. In the same size range between 25 and 40 atoms in which Pd clusters develop fcc epitaxial configurations, a similar DF/GGA approach predict that hollow gold cages are the most favourable structures on the MgO(001) surface. In particular, the interaction with the substrate stabilizes a novel class of hollow cage nanoparticles, the open pyramidal hollow cages, which have no counterpart in free-space clusters. The key to the formation is in the structure of Fig. 37(a).

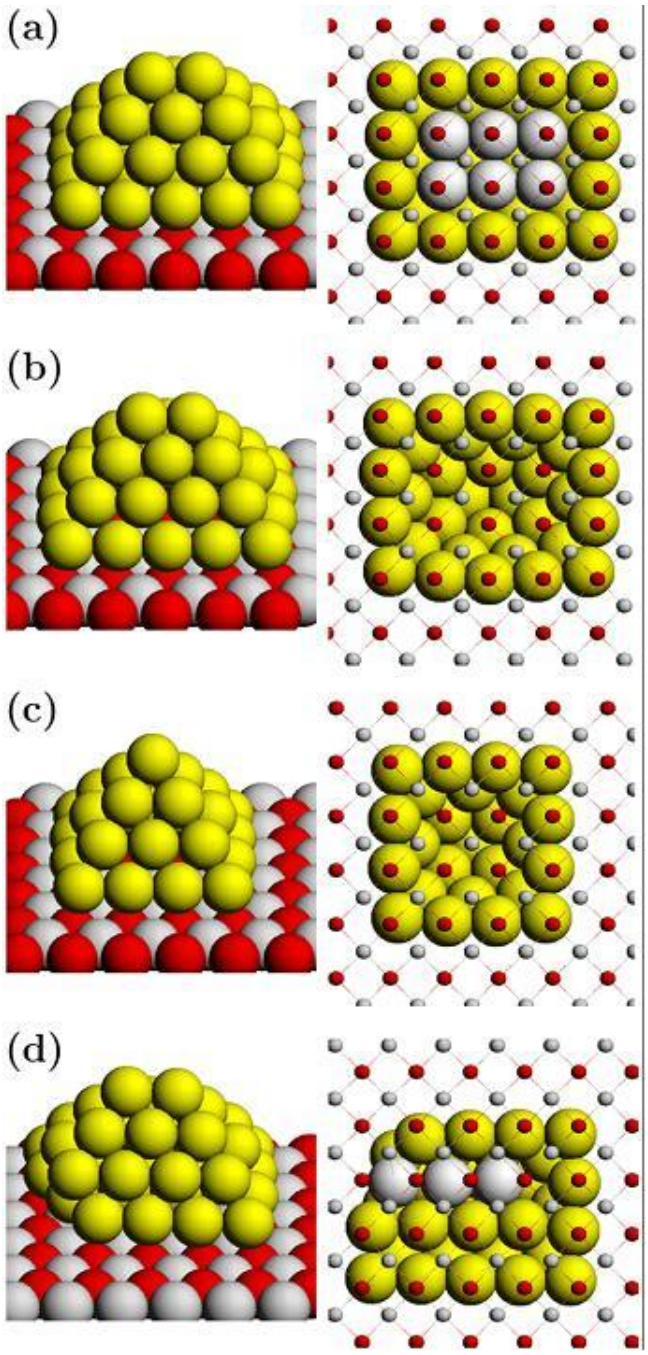

FIG. 37: Substrate-stabilized cages. (a) Rectangular pyramidal cage of 38 atoms. In the right column, bottom view of this cluster, where O and Mg atoms are small spheres, to show the basal layer of the cage. This plane consists of 20 atoms, of which 14 belongs to its perimeter, and 6 (in white) belong to its inner part. (b) Rectangular open cage of 32 atoms obtained by removing six basal atoms from (a). (c) Square open cage of 25 atoms. (d) Rectangular cage with distorted basal plane – in the right column, the three atoms in white are in bridge positions between neighbouring oxygens.

This is a 38-atom rectangular cage pyramid obtained by removing the two inner atoms from the compact pyramid at $N = 40$. This structure matches the substrate with 20 atoms and is in close competition with the best compact structures. However, it can be observed that its basal layer presents a substantial reconstruction, as shown in the right panel of Fig. 37(a). In fact, while the atoms of the perimeter of the basal layer are in close contact with MgO, the six central atoms (in white in the figure) are pushed up, with their z coordinates in average higher by almost 0.3 Å, as if they were repelled by the substrate. This observation suggested the possibility of building up a new cage motif by simply removing the atoms in the interior of the basal layer. This led to the open pyramidal hollow cages of Figs. 37(b) and 37(c), whose basis is reduced to atoms along the perimeter only. The rectangular cage of Fig. 37(b) has size 32; complete square open cages are at $N = 25$, see Fig. 37(c), and 41; a rectangular open cage with 6X4 basis is at $N = 39$. The range 23-42 can be covered by cutting basal corners or adding adatoms on the lateral close-packed facets. The pyramidal hollow cage motif is the most stable in the size range $N = 25$-40 according to the DF/GGA calculations [FerrandoPRL2009]. $N = 32$ is particularly interesting, as this is an electronic magic number for the jellium model on a spherical shell [PyykkoNN2007], and a geometrical magic size for high-symmetry cage structures, in particular, for an icosahedral cage, corresponding to the external shell of the 45-atom anti-Mackay icosahedron [RossiPRL2004]. When deposited on MgO(001) this cage matches the substrate reasonably well, with four gold atoms on oxygen sites, and is lower in energy than compact structures. However, the open cage of Fig. 37(b) is lower than the icosahedral cage by 0.53 eV, and thus more stable than compact structures by almost 1.2 eV. It is interesting to note that this is also true for anionic Au_{32} species: the pyramidal open cage in this case is found to be still lower in energy than the icosahedral hollow cage and the compact pyramid. Thus, at variance with the gas phase, where negatively charging the Au_{32} cluster induces a transition from the icosahedral cage to compact low-symmetry structures [JohanssonJPCC2008; JalboutJPCA2008; JiACIE2005], supported pyramidal open cages resist negative charging. This is explained by the fact that their stabilization mechanism is not connected to electronic shell closure, but to the general physics of the Au-Au and Au-surface interaction, and is thus more robust than in gas phase. Two reasons (specific to the physics of Au bonding) in fact concur to determine the special stability of pyramidal open cages. First, gold has a ubiquitous tendency to form close-packed monolayers in undercoordinated systems [OlivierPRB2008]. This is due to that fact that this metal looses only 8 % of its binding energy in passing from the bulk 12-coordinated situation to close-packed 6-coordinated monolayers, a fact that reverberates in the planarity of small clusters [GilbJCP2002; FurcheJCP2002; HakkinenPRL2002], the reconstruction of low-index Au surfaces [OlivierPRB2008], and stabilizes the compact facets of supported pyramidal cages. Second, the Au/surface interactions also present peculiar features with a directional and strongly many-body character. In fact, a single Au atom interacts appreciably with the oxygen

ions of MgO also via a chemical bond component. However, the strength of this interaction drops rapidly with Au coordination, as a result of the competition with metal-metal bonds. This shifts the interaction mechanism of higher coordinated clusters to a largely prevailing polarization component with a strong metal-on-top effect [BarcaroJCTC2005]. The net result is that highly coordinated Au atoms dislike being in contact with the oxide surface, whereas the interaction of low-coordinated atoms is much more favourable, especially if enhanced by the metal-on-top effect. The open pyramidal cages perfectly meet these features, presenting low-coordinated basal atoms with a proper set of on-top neighbours. The substrate thus plays a key role in inducing the formation of cages, which become favourable even for sizes and charge states for which gas-phase clusters are expected to be compact. It can be finally noted that extended defects such as steps should further stabilize pyramidal cage arrangements and their simple (001) epitaxy with respect to non-crystalline configurations or more complex epitaxial relationships.

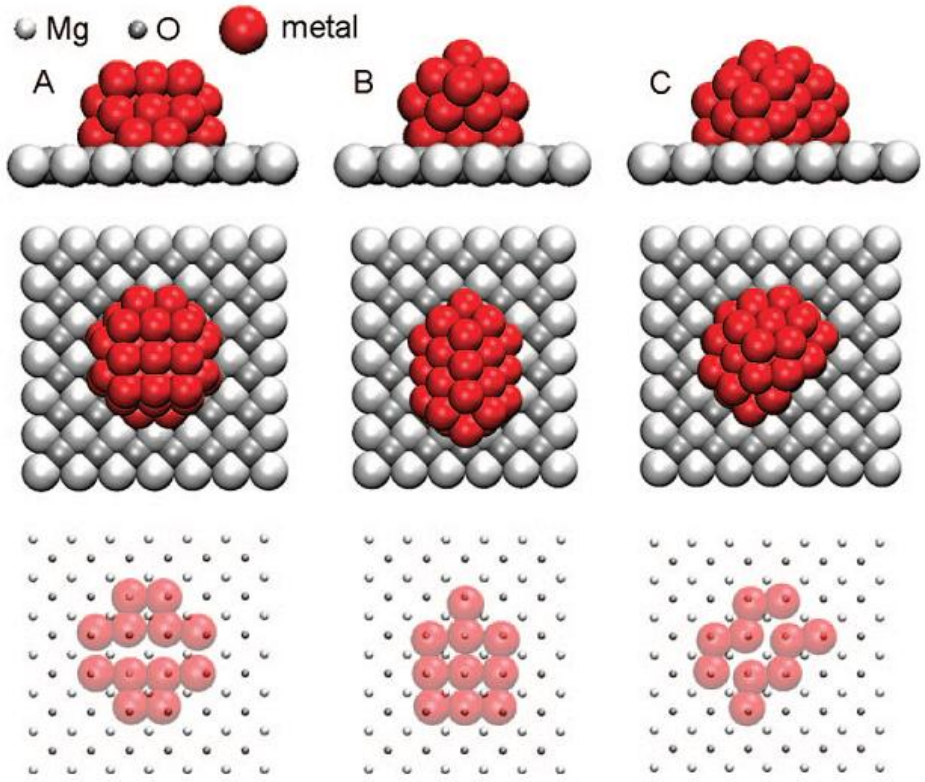

FIG. 38: Representative structures of the three significant structural motifs of 40-atom Ni nanodots on MgO: (A) fcc(001) motif, (B) 5-fold motif, and (C) hcp motif. From top to bottom, side, top, and bottom views of the dots. The bottom view shows only the atoms that are in contact with the substrate. The energies of the nanoparticles are reported in Table II.

Gold and palladium are elements for which the mismatch between the lattice parameter of the bulk metal and the oxygen-oxygen distance in the MgO(100) substrate is not large: 2.75 Å and 2.89 Å are the metal-metal distances in bulk fcc Pd

and Au, respectively, while 2.97 Å is the O-O first neighbour distance in magnesium oxide, whence a size mismatch around 7 % and 3 %, respectively. It is interesting to ask oneself what happens in the presence of a more substantial size mismatch, as for example in the case of Ni, Co or Cu, which are all fcc in the bulk and whose lattice parameters are 2.51, 2.49, 2.56 Å, thus with a size mismatch around 14-16% with respect to (100) epitaxy.

The case of Ni has been treated in great detail [FerrandoACSN2008; RossiPCCP2010]. For $N \leq 50$, three main structural motifs were singled out by a thorough DF-EP search and are shown in Fig. 38 at $N = 40$. The first motif recalls the structure of bulk Ni: nanoclusters belonging to this motif are fcc nanocrystals which grow in (001) epitaxy with the oxide substrate, and will thus be referred to as fcc(001) motif. However, due to the large size mismatch between the nearest-neighbour distance in bulk Ni and the O-O distance in the MgO substrate, these nanoclusters are often strongly distorted and/or dislocations between close-packed planes are observed. These dislocations appear already for very small sizes and help the structure in decreasing its strong internal strain. The second motif (referred to as 5-fold motif) is non-crystalline. Nanoclusters belonging to this motif present at least one local 5-fold symmetry. Finally, the third motif is made of hcp nanocrystals, whose close-packed planes, alternating in ... ABAB ... stacking, are *perpendicular* to the oxide substrate and oriented along the [100] (or equivalently the [010]) direction of the substrate. DF-EP thorough searches show that, as the size of the clusters increases above N = 40, the lowest-energy structures are hcp for almost all sizes.

Size	Structure	E_{bnd}	ΔE_{bnd}	E_{adh}	E_{met}
Ni_{30}	5-fold	-114.60	0.00	-7.46	-107.14
	hcp	-114.11	0.45	-7.15	-106.96
	fcc(100)	-113.91	0.49	-7.59	-106.32
Ni_{40}	hcp	-155.78	0.00	-8.71	-147.07
	5-fold	-155.42	0.35	-7.90	-147.52
	fcc(100)	-154.40	1.38	-8.68	-145.72
Ni_{50}	hcp	-197.70	0.00	-10.61	-187.09
	5-fold	-197.13	0.57	-9.51	-187.62
	fcc(100)	-196.64	1.06	-10.25	-186.39

Table II. DFT results on the energetics of Ni/MgO(001) nanodots. Ebnd is the binding energy of the nanoparticle, ΔE_{bnd} is the energy difference from the lowest isomer, Eadh is the adhesion energy between the nanoparticle and the substrate, and Emet is the metallic atomization energy. All energies are in eV.

Table II clearly shows the increasing preference toward hcp configurations as size increases and, by decomposing the total binding energy into its adhesion and purely metallic components, helps one in understanding this trend. The metallic energy is calculated by separating the nanocluster from the surface and calculating its metallic binding energy without any further relaxation, while the adhesion energy is the difference between the total binding energy and the metallic energy. 5-fold structures

have favourable metallic energy, but a bad matching with the substrate, so that their adhesion is weak. On the contrary, fcc(001) structures can have strong adhesion with the substrate if a large number of metal atoms is in contact with it. This is possible only if the shape of the nanodot is not compact. Finally, hcp structures better match the substrate, so that their adhesion is as strong with fewer atoms in contact. Shapes of hcp structures are thus more compact than those of fcc(001) structures, with a better metallic energy.

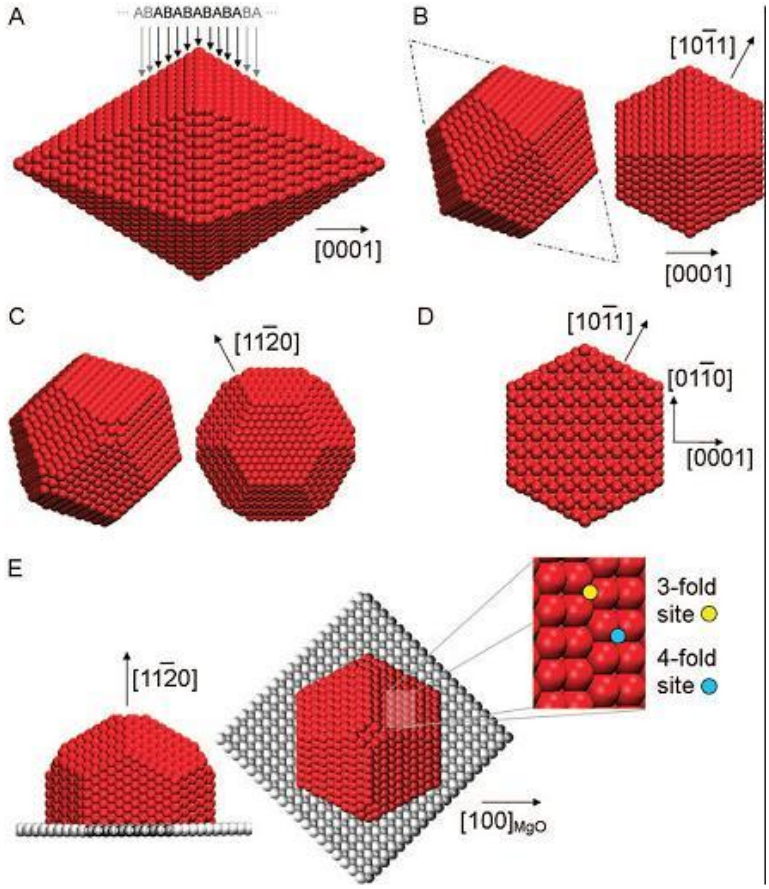

FIG. 39: Morphology of the hcp motif. The hcp motif is obtained by truncating hexagonal bi-pyramids (A), whose axis is parallel to the c-axis of the hcp lattice of the metal. The first cut (B) eliminates top and bottom vertices of the pyramids, thus generating hexagonal (0001) faces. The second cut (C) eliminates lateral vertices, creating small (1120) facets, with their typical zig-zag atomic arrangement. The final cut (D) is due to the contact with the substrate, and generates a large (1120) face. Close-packed planes are perpendicular to the substrate. The nanodot is finally oriented in such a way that the [0001] direction of the hcp metal lattice is aligned with the [100] direction of the oxide substrate (E). The nanodot exposes also large (1011) facets, whose atomic arrangement is shown in the inset. These facets present a large number of 3-fold and 4-fold adsorption sites which are in close contact with each other.

The morphology of the hcp nanodots is easily understood from an analysis of Fig. 39. The hcp nanodots are truncated hexagonal bipyramids, whose axis coincides with the c axis of the hcp lattice. These bipyramids are cut to expose (0001), (1011), and small (1120) surfaces (we note in passing that these surfaces offer a variety of adsorption sites of unusual geometry, in particular, the (1011) facets present both 3-fold and 4-fold sites in close contact). A larger (1120) face is in contact with the substrate, where Ni atoms assume a typical configuration in zig-zag rows. The driving forces leading to the stabilization of the hcp nanodots can be summarized as follows. First of all, in these interface-stabilized phases, the hcp epitaxy is adopted to realize a good matching with the substrate. This geometric criterion is shown in Fig. 40.

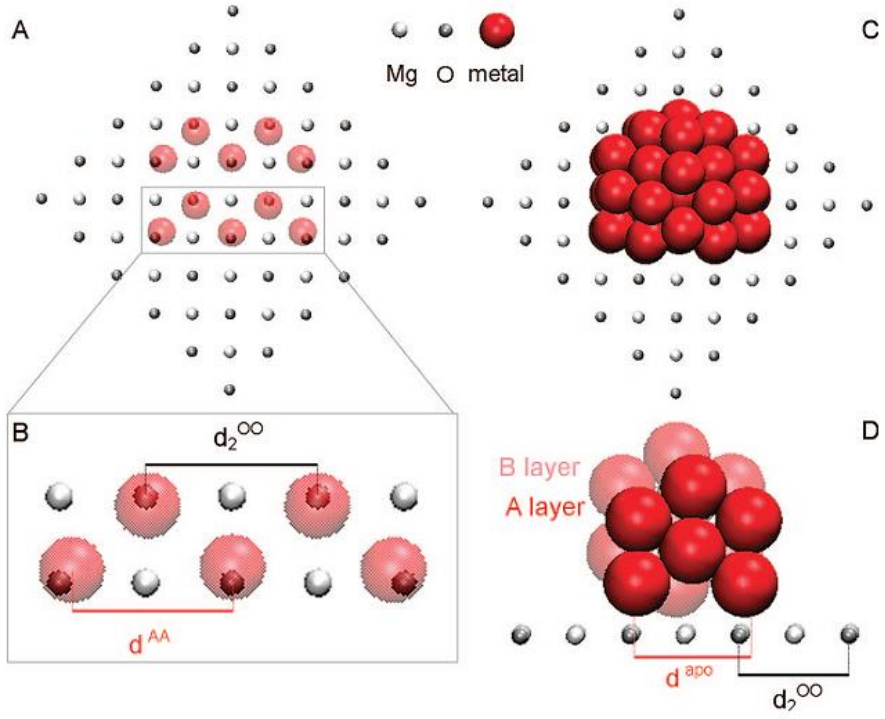

FIG. 40: Matching of the hcp nanodots with the oxide surface. The criterion of good matching is that the distance between A planes in the hcp lattice (d^{AA}) and the apothema of 7-atom hexagons in the close packed faces (d^{apo}) are both close to the distance between second-neighbor oxygens in the substrate ($d^{OO}{}_2$).

Let $d^{OO}{}_1$ and $d^{OO}{}_2=\sqrt{2}\ d^{OO}{}_1$ be the distances between first and second oxygen neighbours in the substrate, respectively. Let d^{MM} be the first neighbour distance in the bulk metal, $d^{apo}=\sqrt{3}\ d^{MM}$ the double of the apothema of 7-atom hexagons, and d^{AA} the distance between A planes in the hcp bulk. In an ideal hcp lattice, $d^{AA}=\sqrt{8/3}\ d^{MM}$. A good matching of the hcp phase is possible when both d^{apo} / $d^{OO}{}_2$ and d^{AA} / $d^{OO}{}_2$ are close to 1. For an ideal hcp lattice this implies that d^{MM} / $d^{OO}{}_1 \sim 0.8$. This condition

warrants a bad matching of the fcc(001) epitaxy, for which $d^{MM} / d^{OO}{}_1 \sim 1$ should hold. Therefore, the fcc(001) epitaxy is automatically disfavoured when the hcp (1120) epitaxy is favoured. This makes it possible to stabilize hcp nanodots also for metals that are fcc in the bulk, provided that the interaction with the substrate is sufficiently strong to overcome the energetic cost of building up the hcp phase. The second requirement to be fulfilled is that the hcp-fcc energy difference should not be too large. In this connection, we note that the above substrate-matching criterion is similar to that of the body-centred-cubic (bcc) (001) epitaxy. In fact, in the bcc(001) epitaxy, the metal atoms that are in contact with the substrate are at second neighbour distance $d^{MM}{}_2 = 2\, d^{MM} /\sqrt{3}$. When $d^{apo} / d^{OO}{}_2 \sim 1$ and $d^{AA} / d^{OO}{}_2 \sim 1$, also $d^{MM}{}_2 / d^{OO}{}_1 \sim 1$, so that a good hcp (1120) matching implies a good bcc(001) matching. However, bcc(001) epitaxy is strongly disfavoured as a norm for metals which are not bcc in the bulk because of the much larger bcc-fcc energy difference with respect to the hcp-fcc one [DinsdaleCALPHAD1991]. Finally, the (1011) faces should not be too energetically disfavoured with respect to (0001) faces, because the total area of the (1011) faces is large in the hcp nanodots. Following these criteria, a general class of hcp structures has been predicted in Ref. [FerrandoACSN2008], to which several metal/substrate combinations should belong, such as Ni/MgO, Pd/CaO, Pt/CaO, Ni/CoO, and Co/MgO. It is to be noted that Ni, Pd and Pt are fcc, not hcp in the bulk, so that a transition to fcc configurations is expected to occur with increasing size of the particles, as discussed in the next section. It can also be underlined as an aside observation that these hcp nanoparticles exhibit unconventional features under a number of viewpoints in terms of adsorption or catalytic sites: the (1011) facets have peculiar adsorption sites with unusual or strained coordination, they make unusual angles with the other, mostly close-packed, facets, and both the(1011) and the close-packed facets present sharp interfaces with the oxide substrates, very different from the acute or obtuse angles of fcc pyramids or overhangs. The effect of all this on catalysis is promising [OsterlundBook2007] but has still to be investigated. Finally, we underline that, when the size mismatch is appreciably larger than ~ 19%, as in the case of Ni, Co or Cu on CaO(100) or BaO(100), hcp structures will not be favoured, and still different epitaxial relationships have been hypothesized [NunezPRB2006].

Other “exotic” epitaxial relationships can be conceived, and have been actually found in more complex cases, such as in particular binary metal clusters. Great attention has traditionally been focused and is increasingly focusing on nanoalloy particles, i.e., metallic systems composed of two or more elements whose dimensions lie in the nanometre size range. As a first explorative study in this direction the case of CoPt particles adsorbed on MgO(100) has been considered in Ref. [BarcaroJPCL2010]. This system presents several reasons of interest. First of all, CoPt is potentially useful for applications in magnetism [FavrePRB2006] and catalysis [GauthierPRL2001] and is thus being widely studied at the nanoscale [GrunerPRL2008; PenuelasPRL2008]. Second, it is a good test of the effect of adhesion on the structure of metal clusters. Pt clusters with $N \leq 100$ are thought in fact to exhibit amorphous-like (or, better, reconstructed icosahedral) configurations [ApraPRL2004], and become fcc-like when

adsorbed on the MgO(100) surface in analogy to what happens with Pd clusters [BarcaroPRL2007]. Co clusters in the same size range are believed to be decahedral, and become hcp when adsorbed on the same surface [FerrandoACSN2008]. For free CoPt medium-sized clusters, polyicosahedral (pIh) structures [RossiPRL2004; RossiFD2008] are expected. It should be noted however that the type of pIh structures here involved are different from those found in other cases [RossiPRL2004]. A typical example is a cluster of 38 atoms, Co_6Pt_{32}, shown in Fig. 41.

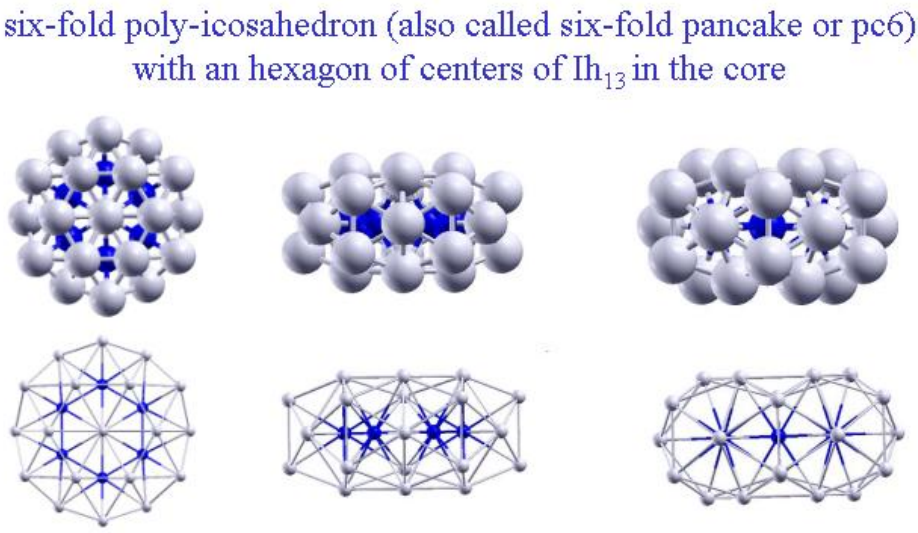

FIG. 41: Schematic pictures of a free polyicosahedral (pIh6) structures at a composition of Co_6Pt_{32}. Top view on the left side, side views on the middle and right sides, respectively. Cobalt atoms are in blue, and platinum atoms are in grey.

This is a Frank-Kasper polyhedron [FrankAC1958] with a disclination line running along its symmetry axis and can be identified with the “six-fold pancake” (a pIh structure exhibiting a six- fold symmetry axis, hereafter pIh6). While pIh free clusters with five-fold symmetry have been shown to be of special energetic stability in binary systems, such as Ag-Cu and Ag-Ni, with atomic size mismatch and sizeable difference in surface energies among the two elements, both favouring core-shell chemical ordering [RossiPRL2004], the origin of the stability of other classes of pIh structures was still unclear, and no theoretical predictions of surface-supported pIh structures had been reported before Ref. [BarcaroJPCL2010]. The effect that

adsorption on the MgO(100) surface has on six-fold-symmetry pIh clusters is thus of interest also from the point of view of basic science.

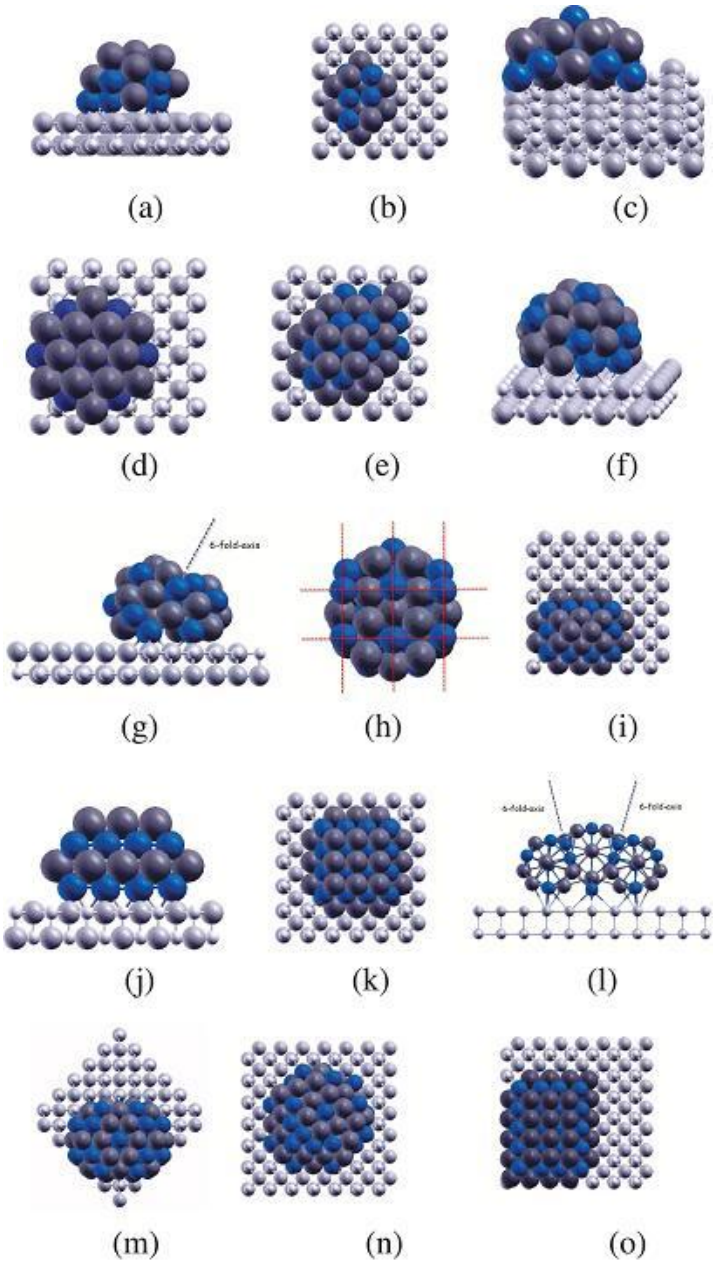

FIG. 42: Schematic pictures of various supported CoPt clusters: (a) $Co_{10}Pt_{10}$ double icosahedron (N=19) plus a lateral Co atom lying on the surface; (b) $Co_{10}Pt_{10}$ $L1_0$-type structure; (c) $Co_{10}Pt_{10}$ incomplete pIh; (d) $Co_{20}Pt_{20}$ pIh6-based structure; (e) $Co_{20}Pt_{20}$ $L1_0$-type structure; (f) $Co_{20}Pt_{20}$ incomplete pIh; (g) $Co_{24}Pt_{24}$ pIh6-based structure with its disclination axis indicated; (h) bottom view of 2g to better show its epitaxial relationship to the substrate; (i) $Co_{20}Pt_{20}$ $L1_0$-type structure; (j) side view of a $Co_{32}Pt_{30}$ $L1_0$-type structure; (k) top view of 2j; (l) side view of a $Co_{32}Pt_{32}$ double-pIh6-based structure with its two disclination axes indicated; (m) top view of 2l; (n) $Co_{40}Pt_{40}$

structure based on the double-pIh6 plus an fcc-type surface growth; (o) $Co_{40}Pt_{40}$ $L1_0$-type truncated pyramid. Color coding: O in light grey, Mg in white, Pt in dark grey and Co in blue.

The starting point is the bulk lattice: at 50-50 % composition, bulk solid CoPt presents an ordered phase of $L1_0$ structure, with tetragonal crystal lattice, alternating homogeneous Pt and Co planes along a (001) axis. The lattice parameter of such a phase is not too distant from that of pure Pt, and one could expect that the square-symmetry MgO(001) substrate should favour the $L1_0$ phase in the same way that it favours fcc-like arrangements for pure medium-sized supported Pt clusters. On the contrary, as a counterintuitive result it was found [BarcaroJPCL2010] that adhesion on MgO(100) enhances the stability of Frank-Kasper cluster structures, via a novel mechanism of matching the surface. The reason of this phenomenon is basically related once more to the many-body character of the metal-oxide interaction and its consequence that the lowest-energy structures are dominated by one-layer Co segregation at the interface with the substrate (a phenomenon of possible general significance for supported nanoalloys with a sufficiently strong adhesion to the substrate). The adhesion strength of a metal atom to the surface in fact depends appreciably on its coordination number (the number of first-neighbour metal atoms surrounding the interacting one). Such a many-body character is much more pronounced for Pt than for Co; the strong Pt/Pt bonds compete with and quickly weaken the Pt/MgO interaction, quenching it from values appreciably higher than the Co/MgO interaction in the case of a single atom (~ 2.5 eV for the Pt atom versus ~ 1 eV for the Co atom on the O-site) to definitely smaller values already for coordination number = 4 (~ 0.45 eV for Pt versus ~ 0.75 eV for Co on the O-site). This entails that, once a cluster reaches a critical size such that the adhesion energy favours the formation of an interface involving a substantial number of atoms thus exhibiting non-negligible coordination numbers, there will be a strong tendency for Co to form a segregated layer at the interface. For fcc-like particles, one concurrently finds that Pt has a strong tendency to form a segregated layer at the topmost (100) facet, in agreement with experimental observations [FavrePRB2006; ShapiroPRB1999]. For these particles, then, one-layer Co surface segregation at the interface together with one-layer Pt surface segregation at the topmost facet translates into $L1_0$ chemical ordering and entails that even numbers of layers possess a magic character. The presence of a pure Co first layer in fact favours the formation of a pure Pt second layer, and so on, thus strongly reinforcing the tendency already present in suspended particles [GrunerPRL2008]. However, this also implies that bulk-like gas-phase clusters must be cut to be accommodated on the substrate, as shown for example in Fig. 42(j). On the contrary, pIh clusters can be satisfactorily accommodated on the substrate while preserving their gas-phase shape, simply segregating cobalt at the interface. Some examples of supported CoPt clusters are shown in Fig. 42. From these examples, it can be seen that pIh structures can accommodate on the surface either adding lateral Co atoms at the interface as in Fig. 42(d), or by tilting their six-fold symmetry axis and by inserting further Co atoms to

fill up the void so created as in Fig. 42(g,h,l,m). In the latter case (which is more interesting as it allows pIh structures to be competitive also at sizes different from magic ones) the added Co atoms produce a (100) pseudomorphic epitaxy with the substrate to realize the best match with the oxide surface, see a detailed view in Fig. 42(h). Moreover, a tilted pIh6 can match with another one tilted in the opposite way creating a structure, shown in Fig. 42(l,m),which achieves shell closure at $N = 64$. The driving force to pIh structures was also analysed in Ref. [BarcaroJPCL2010], and found to possess some general significance. Certain classes of pIh structures, in fact, particularly those exhibiting six-fold symmetry axes such as pIh6, maximize the number of mixed bonds [RossiJCP2005]. This implies that pIh configurations will be favourable also for those binary alloys, such as, for example, CoPt, whose phase diagram [AMSHandbook1992] is characterized by ordered phases essentially driven by the strength of the mixed bonds and thus be expected to be of common occurrence in the field of nanoalloys. The possibility of stabilizing other types of pIh structures on appropriate substrates is currently under consideration in our labs.

4.2.3. Large and very large clusters

When considering even larger clusters, the presence of defects in the substrate becomes definitively of little importance. The EP-GO approach can be routinely conducted for sizes around 100-500 atoms for supported clusters, but afterwards it sensibly gives way to extrapolations based on structural motifs. In fact as nanoparticle size increases few competing structural motifs become dominant. The significant motifs can be singled out by global optimisation searches in the size range below 500 atoms [FerrandoACSN2008; FerrandoJCP2009; GoniakowskiJCP2009; NegreirosSS2011] (actually up to 1000 atoms in Ref. [FerrandoACSN2008]), and then compared for larger sizes (up to several thousand atoms) by local minimization of perfect structures at geometrical magic numbers [BalettoJCP2002]. For even larger sizes, in which the contribution of nanoparticle edges and vertices becomes negligible, but dislocations do not yet appear, the Wulff-Kaishew construction [WulffZK1901; KaishewPhDTh1952; HenryPSS2005] can be of help in comparing different crystalline motifs, especially if modified as detailed below. In the following we will concentrate on five pure metal systems (Au, Ag, Pd, Pt, Ni) and one bimetallic system (Ag-Pd) on the same substrate: MgO(001). As in the case of smaller sizes, the behaviour will be different depending on the lattice mismatch between metal and oxide, which varies from small (Ag and Au), to medium (Pd and Pt) and large (Ni).

For Ag, Au, Pd and Pt, global optimisation searches for large particles, up to 200-300 atoms [FerrandoJCP2009; GoniakowskiJCP2009] singled out three dominant motifs: fcc clusters in (001) epitaxy, fcc clusters in (111) epitaxy, and decahedral clusters which adhere to the substrate with a pseudo-(001) facet [FerrandoACSN2008]. Icosahedral clusters cannot achieve a good matching with the substrate, and are

therefore never favourable. Concerning fcc clusters, the competition between the (001) and the (111) epitaxy is due to the following reason. The (001) epitaxy has a stronger adhesion energy per unit contact area, due to its better matching with the square-symmetry substrate, especially when the lattice mismatch between metal and oxide is small. However, in the (111) epitaxy this can be compensated by a larger contact area, so that the total adhesion energy may become even larger than in the (001) epitaxy. In Ag/MgO(001), extensive calculations [FerrandoJCP2009] predict that the fcc(001) motif is dominant in the size range up to 3000 atoms at least, followed by the decahedral and by the fcc(111) motifs. This compares well with the experimental data on this system [RobachPRB1998; RevenantNIMB2006], which find the fcc(001) epitaxy dominant for all sizes. Also the calculated aspect ratio of the nanoparticles is in good agreement with the experimental data. On the contrary, calculations on the Au/MgO(001) system [FerrandoJCP2009] reveal a close competition between the fcc epitaxies, with decahedral clusters being higher in energy. For sizes below around 1000 atoms, the fcc(001) epitaxy prevails. Then a crossover range follows, in which both fcc epitaxies are very close in energy, and finally, for sizes above 1500 atoms, the fcc(111) epitaxy prevails. These results are again in agreement with the available experimental data. In fact, for sizes below 1000 atoms, only fcc(001)structures are observed [PauwelsPRB2000], while for larger nanoparticles both epitaxies are produced [HenryPSS2005].

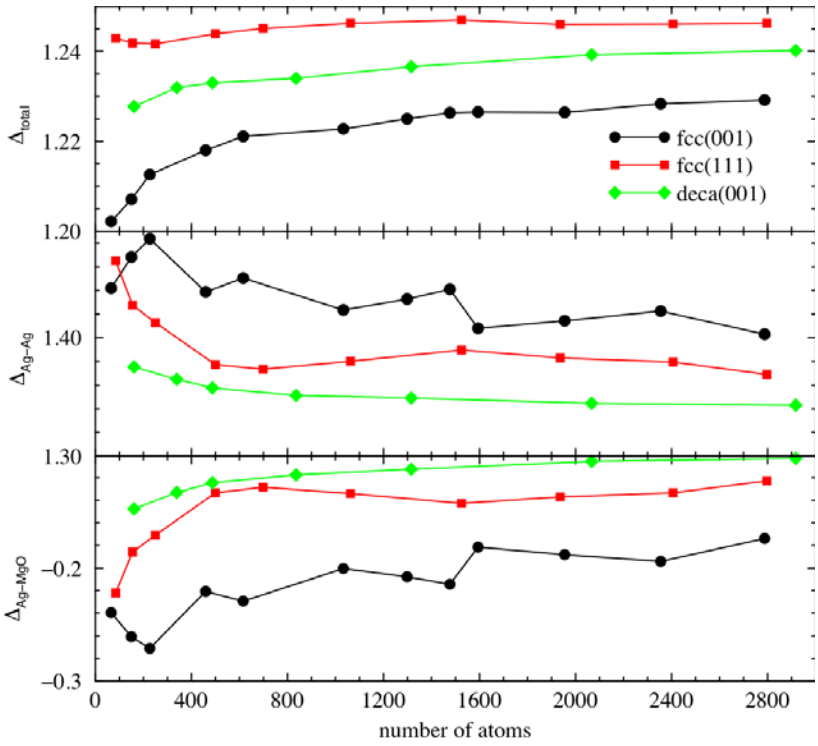

Fig. 43: Δ_{total}, Δ_{Ag-Ag}, and Δ_{Ag-MgO} (in eV) for fcc(001), fcc(111), and Dh Ag nanoparticles.

An interesting observation in this context is that – if one plots separately adhesion and metallic energies as function of the cluster size as done in Refs. [FerrandoJCP2009; GoniakowskiJCP2009] – one finds that they exhibit an antiphase

behaviour: when the former increases, the latter drops down and vice versa, so that they compensate to a good extent, for the case of Ag nanoparticles see Fig. 43 taken from Ref. [FerrandoJCP2009]. This is a clear sign that the shape of the clusters is the result of the competition between metallic bond and metal-substrate interaction. Typically, within each structural motif, the clusters tend to grow according to a given shape which optimizes for example the metal substrate interaction energy, until this requires too high an energetic prize at which point the competing quantity (the metal-metal interaction energy) sets in, overcoming the corresponding energy penalty and the structure "collapses" or better realizes a transition into a different shape.

Pd and Pt are the most controversial cases. The calculations [GoniakowskiJCP2009] predict a crossover between (001) and (111) epitaxies at rather small sizes, well below 1000 atoms. This size-dependent crossover has not been observed experimentally. However, the experiments observe a temperature-dependent change of epitaxy in Pt/MgO(001) [OlanderPRB2007], which is still to be investigated theoretically. To solve this apory, it has been hypothesized in Ref. [GoniakowskiJCP2009] that the mobility of large clusters [FerrandoJPCM2009] and the influence of extended defects such as steps [HenryPSS2005] (as discussed in previous sections) might play a role in reconciling theory and experiment. In other words, the mobility of single atoms and small clusters (see Sec. 5.1) and the scarcity of point defects on the UHV-cleaved MgO(100) surface make that extended step edges relatively abundant on MgO(100) act as heterogeneous nucleation centers. On these defects, however, the (001) epitaxy is favored with respect to the (111) one. Such an hypothesis is in tune with available information and allows one to set up a consistent picture reconciling theory and experiment on these systems [HenrySSR1998; RenaudS2003; NoltePRB2008].

It should be noted that for all these metals the Wulff-Kaishew construction predicts that the (111) epitaxy should prevail in the large size limit [GoniakowskiJCP2009], in a clear way for Au, Pt and Pt, and marginally for Ag. A crossover to the (001) epitaxy with decreasing size can be recovered if a size-dependent adhesion energy per unit contact area is taken into account in the construction [GoniakowskiJCP2009]. In fact, the adhesion energy per unit contact area of the fcc(001) epitaxy increases appreciably as the nanoparticle adheres with a smaller facet, because the contact atoms can more easily accommodate the lattice mismatch with the substrate. This is especially evident for Pd and Pt. On the contrary, the adhesion energy per unit contact area of the fcc(111) epitaxy is almost constant with size. According to this size-dependent Wulff-Kaishew construction [GoniakowskiJCP2009], a crossover to the fcc(001) epitaxy is predicted when the cluster size becomes sufficiently small.

It can also be noted in passing that a convenient way to explore the optimal shape of a crystalline particle (size of overhangs, etc.) is to consider wires, see e.g. Refs. [MolinaPRB2004; BarcaroJPCL2010]. This is extremely useful to keep the computational effort to a reasonable level, which is crucial at the DF level.

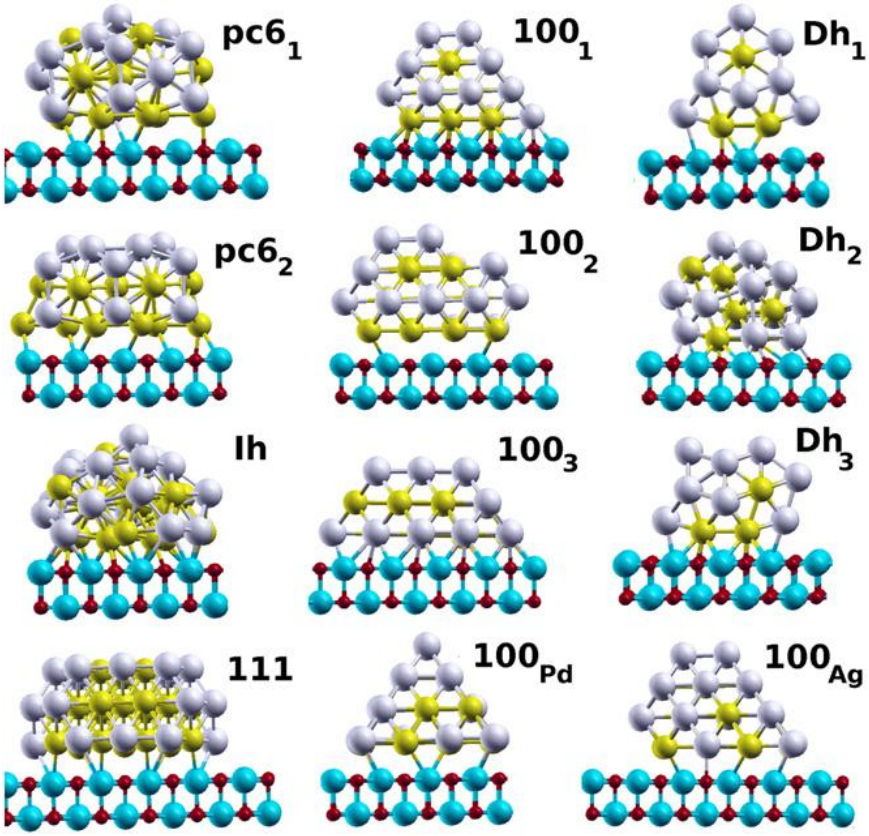

Fig. 44: The main structural motifs of Ag-Pd 40-atom clusters at composition 50% are shown. Ag, Pd, Mg and O atoms are in grey, yellow, blue and red, respectively.

An interesting possibility is offered by mixing two metals with a different behavior, such as Ag and Pd. This possibility was explored in Ref. [NegreirosSS2011]. Although the analysis was conducted up to size 400, let us focus on the results at size 40 which have been validated by DFT calculations. The structural motifs in competition at size N = 40 are shown in Fig. 44 taken from Ref. [NegreirosSS2011]. Dh structures, such as Dh_1, Dh_2 and Dh_3, correspond to different (incomplete) decahedra, while Ih represent icosahedra. Among poly-icosahedral (pIh) structures, the six-fold pIh (or "pancake", pc6) occurs most frequently. It achieves shell closure at size 38 atoms: $pc6_1$ and $pc6_2$ correspond to two different ways of arranging two additional atoms on the perfect 38-atom pc6. $fcc(100)_1$, $fcc(100)_2$ and $fcc(100)_3$ are fcc(100) stackings that expose different number of 5-fold and 6-fold faces. Finally, $fcc(100)_{Ag}$ and $fcc(100)_{Pd}$ corresponds to the best fcc(100) structure for pure Ag and Pd, respectively, while fcc(111) adheres to the substrate with a (111) facet. The most notable result that can be derived from an analysis of the results of Ref. [NegreirosSS2011] is that at composition 50% the most stable structure at both the EP and DF levels is the pc6. Given that this motif is not competitive for the pure counterparts and that it is not the most stable for gas-phase Ag-Pd clusters at composition 50% [NegreirosJCP2010], its low energy can only be understood by a stabilization due to the combined effects of alloying and (once again) the interface. In other words, Ag-Pd mixing on MgO(100) creates a pocket of stability in the Ag-Pd

supported nanoalloys phase diagram. This structure is very stable at the EP and DF level at 40-atom size, competing with fcc(100) and Dh motifs. The square-symmetry MgO(100) substrate has once more the surprising effect of stabilizing a six-fold-symmetry poly-icosahedral structure.

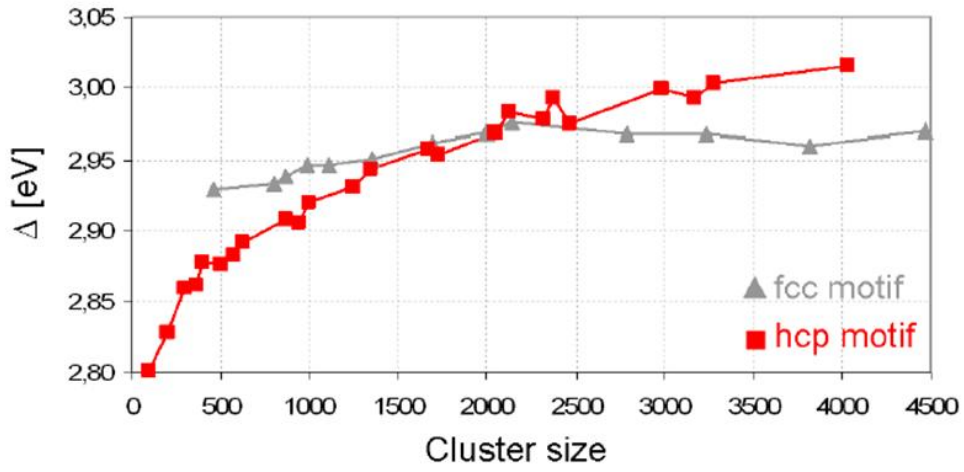

FIG. 45: Crossover between structural motifs of nanodots. The excess energy $\Delta = (E_{bnd} - N\varepsilon_{Ni}) / N^{2/3}$ is plotted for the fcc(001) (A) and the hcp (B) motifs. A crossover from the hcp to the fcc(001) motif takes place for sizes between 2000 and 2500 atoms, corresponding to nanoparticle thickness of ~2.5 nm and width of ~ 4.5 nm.

The case of Ni on MgO(100) is quite different, as anticipated in the previous section. Global optimisation searches have been performed for all sizes below 100 atoms within an EP model [FerrandoACSN2008], and for selected sizes in the range between 100 and 1000 atoms. All the searches have singled out hcp structures as the lowest in energy. In more detail it can be observed that, as size increases, stacking faults in the hcp appear. These faults create local fcc arrangements, which are however not oriented in the same way as the fcc(001) or fcc(111) epitaxies that we discussed for Au, Ag, Pd and Pt, as it should be noted that the close-packed planes are still perpendicular to the substrate. This is in very good agreement with experiment, in which stacking faults have been experimentally observed in the hcp clusters as size increases [TianAPL2005]. In the limit of large sizes a transition to bulk-like fcc structure is expected for Ni particles, as discussed in the previous section. Experiment [TianAPL2005] finds a transition to the usual fcc(001) structures for diameters larger than about 5 nm. At the EP level, the comparison of hcp and fcc(001) motifs as a function of size locates this transition between 2000 and 2500 atoms, as shown in Fig. 45, corresponding to cluster diameters of about 4.5 nm, in excellent agreement with experimental data. We underline in passing that in order to predict accurately the structural phase transition from hcp to fcc configurations, it is crucial to develop an EP which correctly reproduces both the surface energies of Ni and the energy difference between hcp and fcc bulk phases

[DinsdaleCALPHAD1991]. Finally, we stress that the actual mechanism by which a growing hcp cluster transform into an fcc(001) structure as size increases is still to be investigated. This remark can be generalized to the observation that there is a severe lack of information on dynamical phenomena occurring in supported metal particles, with the exception of diffusion, see e.g. Refs. [BarcaroJCTC2005; XuPRL2005; BarcaroPRL2005, BarcaroNJP2007; FerrandoJPCM2009]. It is easy to predict that the study of dynamical phenomena such as growth, melting, and morphology transformations will be the subject of great interest in a near future.

4.3 Metal nanoclusters supported on exotic (ultra-thin oxide) substrates

Ultrathin oxide films grown on single-crystal metal supports (i.e., films with thickness up to a few monolayers, ML, or = 1-2 nm) have attracted increasing attention in the field of surface science since the first, pioneering studies dating about 20 years ago, see, e.g., Refs. [JaegerSS1991; BardiSS1992]. Among the many reasons for interest in these systems is their conductive nature and thus the possibility of characterising them via scanning tunnelling microscopy, photoemission and electron excitation techniques, etc. This has allowed researchers to fully clarify their atomistic structures in many cases, and to discover that sometimes these do not have a counterpart in the bulk, but are specific to the nanoscale régime. Several recent reviews have summarised the considerable amount of experimental and theoretical work so far accumulated [SurnevPSS2003; ChenJPCM2008; FreundCSR2008; WuIRPC2009; FinazziSSR2009]. These systems have then been also studied at the experimental level as substrates for the growth of metal nanoparticle and nanoalloys [FreundCT2005; FreundSS2007]. The replacement of oxide single crystal surfaces with ultrathin films grown on metal supports has brought basic research one step further away from the materials used in standard technology, simultaneously producing a wealth of fundamental knowledge and posing novel issues and challenges. Latest research, in fact, has found that the underlying metal support is not neutral and can actively participate in the adsorption process, to such an extent that these systems should better be described as metal-on-oxide-on-metal materials [FreysoldtPRL2007]. Among the novel phenomena arising as a consequence of the nanoscale thickness of the oxide and the proximity of the metal support, one of the most studied is the possibility of a charge transfer between the metal surface and the deposited metal clusters, as recently theoretically predicted [ReppS2004; PacchioniPRL2005; RicciPRL2006] and experimentally confirmed [ReppS2004; SterrerPRL2007a; SterrerPRL2007b] (see also further theoretical analysis in Ref. [WalterPRL2007]). This phenomenon was discovered for Au atoms adsorbed on ionic non-polar films grown on low-index metal single crystal surfaces, such as NaCl or MgO on Ag(100) or Mo(100) [ReppS2004; PacchioniPRL2005; RicciPRL2006; SterrerPRL2007a; SterrerPRL2007b; FrondeliusNJP2007; AgnoliJPCB2005]

(species other than metals have also been investigated, see e.g. Ref. [GronbeckJPCB2006]). For some of these non-polar oxide films, it so happens that the oxide layer yields electron charge to the metal and this, combined with charge compression effects, reduces its work function to such an extent that metal atoms or aggregates with large electron affinity can acquire negative charge, see the discussion in Sec. 4.1. This is however not the only emergent effect in oxide nanostructures. For example, a rich variety of oxide *polar* nanophases [GoniakowskiRPP2008] grown on compact metal surfaces has been discovered in latest years, and new additions are continuously enriching the field, see e.g. Ref. [BarcaroPCCP2008] for an extensive list of references. These new phases possess some common features: (a) the oxide film is few (one or two) monolayers thick; (b) the metal of the oxide is at the oxide-support interface while oxygen forms a topmost overlayer (this arrangement repeats itself in the subsequent layers); (c) as a consequence, these systems are polar, i.e. they present a finite dipole moment perpendicular to the surface; (d) the oxide phase is often modulated into regular nanostructured patterns; (e) these patterns sometimes open up into point defects, i.e. holes which expose the bare metal support. These features make these systems extremely promising as templates for the growth of ordered arrays of metal nanoclusters, and indeed their potentialities in this respect have already been convincingly demonstrated in selected examples, see e.g. Refs. [BeckerTCC2009; WuCNS2009] for recent reviews and Ref. [GavioliPSS2011] for a general review on this topic. It can be noted that the polar character of these phase makes that the system work function is often not decreased but sometimes even increased with respect to the pure metal support, see Sec. 4.1. Computational approaches are expected to play an important role in the study of these phenomena, both because they can help resolving the atomistic structure of the oxide ultrathin films and because they can provide invaluable information on the basic metal-oxide-metal interactions, which can hardly be derived via even the most advanced experiments. However, due to the size of the typical unit cells and other (both technical and in-principle) problems, the theoretical study of metal clusters on ultrathin oxide substrates is only at its beginning, and – with few exceptions – only the adsorption of single atom species has been considered. Given the perspective importance of this field, we provide in this section some information on the topic of metal adsorption on exotic (ultrathin) oxide substrates.

For the sake of brevity, we will limit our attention to a specific TiO_x/Pt(111) ultrathin film (hereafter referred to as z'-TiO_x), which has been shown to represent a suitable template model system, and briefly review the main recent findings. In this template, the zig-zag-like structure observed by scanning tunnelling microscopy (STM) has been described as an ordered array of rows (troughs), spaced 1.44 nm apart, separating compact TiO_x stripes [SedonaPRB2008]. In particular, the presence of picoholes within the troughs, consisting of Ti vacancies exposing the bare substrate surface, has been proved. These picoholes are effective as nucleation sites for e.g. Au nanoparticle growth [SedonaJPCC2007; RizziPCCP2009]. As an important technical

point, the dimension of the unit cell in this system is not excessive, allowing one to limit the computational effort and develop systematic investigations.

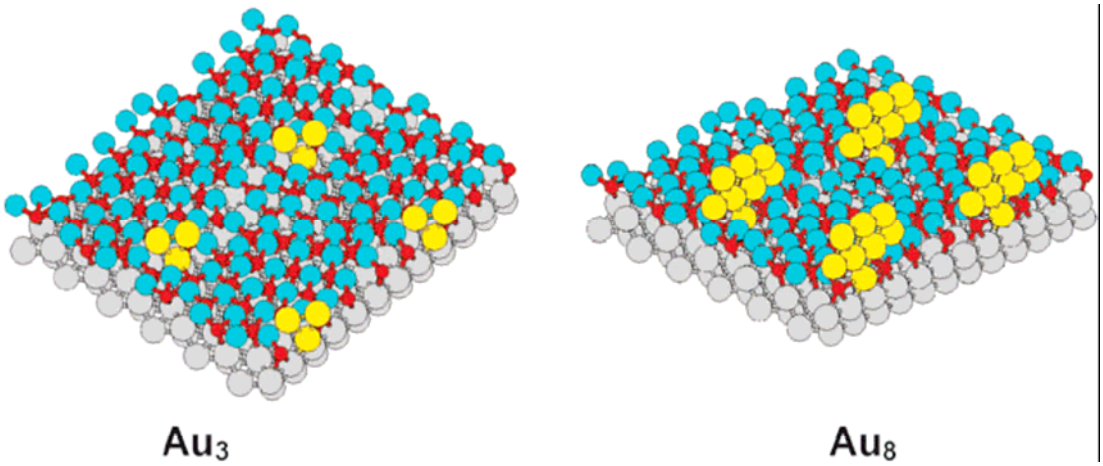

Fig. 46: DF-optimized structures for the adsorption of Au_N clusters on a TiOx/Pt(111) phase: platinum atoms are grey, oxygen atoms are light blue, titanium atoms are red, gold atoms are yellow

In Ref. [BarcaroPCCP2008], Au and Pd single atoms have been used to probe the energy landscape of metal adsorption on the z'- TiO_x /Pt(111) phase (and an analogous nanostructured ultrathin TiO_x template). It was found that Pd atoms are adsorbed according to a very flat potential energy landscape on the compact TiO_x stripes, and are thus expected to diffuse rapidly in these regions, whereas they are strongly adsorbed on the defective holes where they penetrate into the oxide layer and get in contact with underlying metal. This confirms that these defective holes can act as strong trapping and nucleation centres for the growth of Pd clusters. On the contrary, a Au atom interacts with the TiO_x stripes according to two different régimes: (1) a weak interaction régime on top of overlayer oxygens, in which the Au atom remains essentially neutral and exhibits a rather low adsorption energy (less than 0.3 eV); (2) a strongly interacting régime on top of the Ti atoms, in which Au acquires negative charge from the metal support and extracts a titanium atom from the interface, with a correspondingly much larger (around 1 eV) adsorption energy. It was argued that the driving force for the latter régime lies in the strength of the Au-Ti electrostatic interaction or covalent bond, rather than in an image-charge stabilization, which explains the differences of this phenomenon with respect to analogous charge transfer effects occurring in non-polar ultrathin films [ReppS2004; PacchioniPRL2005]. Also due to the large polaronic reconstruction of the oxide layer accompanying the strongly interacting régime, it was also argued that it is not observed at sufficiently high temperatures, when the Au atoms diffuse rapidly on the stripes and finally get trapped by the defective holes, in agreement with experimental findings: the diffusion energy barriers are in fact predicted by DFT simulations to be about 0.4 eV. It is important to underline that the adsorption on the defective holes is weaker than in the Pd case and presents a double-minimum energy profile, with a first energy minimum at a longer distance from the Pt(111) surface (2.9 Å) and with a smaller adhesion energy (1.4 eV), and an inner minimum at a smaller distance (2.2 Å)

and with a larger adhesion energy (1.7 eV). These features are closely analogous to those exhibited by metal adsorption on other oxide polar ultrathin phases, such as $AlO_x/Ni_3Al(111)$ and suggest a general framework shared by metal adsorption phenomena on these phases, very different from what is known for the adsorption on single-crystal oxide surfaces reviewed in the previous section.

The growth of larger Au clusters on the z'-TiO_x /Pt(111) phase has also been considered in Refs. [RizziPCCP2009; BarcaroJPCC2009]. A DF-BH algorithm was applied for Au_N clusters with $N \leq 8$ adsorbed on the defective hole and seeded searches were conducted up to N = 11. The main outcome of these studies is that the Au clusters are anchored with a single atom to the defective hole. They are in electronic contact with the underlying Pt(111) surface, with which in principle they can exchange charge, even though their static charge is essentially neutral. Being so small, they interact mainly with the part of the oxide substrate closer to the defective troughs, this interaction is rather weak and they grow according to structures similar to the global minima in the gas phase. They are thus planar in the investigated size range, with the cluster plane nearly perpendicular to the oxide surface, see Fig. 46. A comparison with experimental results of STM, high-resolution core and valence level photoemission and angle-scanned and energy-scanned photoelectron diffraction was reported in Ref. [RizziPCCP2009], finding an overall fair agreement.

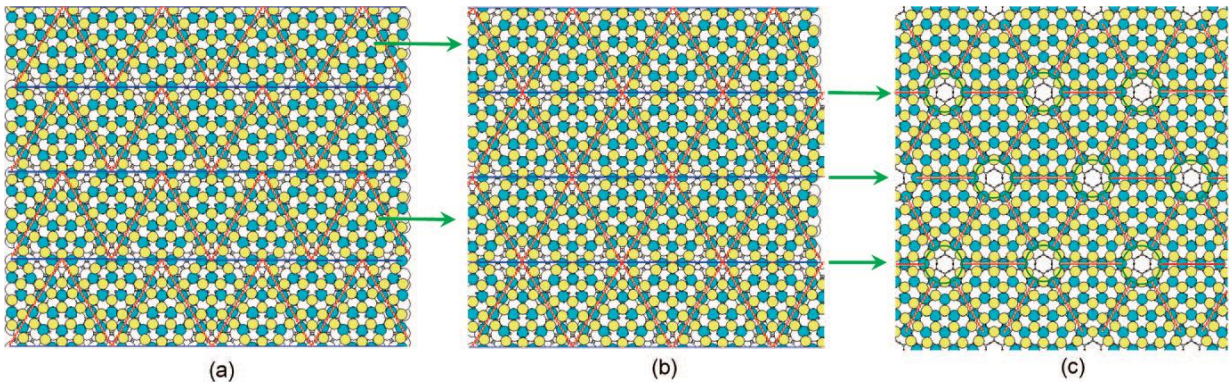

Fig. 47: Schematic representation of the transformation from (a) the rectangular z'-TiO*x* /Pt(111) phase to (b) an intermediate (hexagonal) z'-phase with still two holes per cell, to (c) an hexagonal z'-phase with only one hole per cell and full *p6m* symmetry. Pt, Ti, and O, atoms are represented as gray, yellow, light blue colors, respectively.

As a very interesting phenomenon, the interaction of the metal clusters with the substrate was found to change the energetic landscape of the oxide film itself, in particular favouring hexagonal rather than rectangular arrangements, due to the fact that the hole in this way can enlarge and better accommodate Au species in its interior. A cooperative thermal phase transformation from the rectangular to the hexagonal phase can thus be expected for this metal-on-oxide-on-metal composite system, by which Au clusters self-organized and trapped on the defective holes do not coalesce with increasing temperature, but rearrange their shape and positions together with the more mobile regions of the oxide, transforming from a rectangular

to an hexagonal configuration, as depicted in Fig. 47, taken from Ref. [BarcaroJPCL2009]. This expectation is fully in tune with and allows rationalization of experimental observations [SedonaJPCC2007].

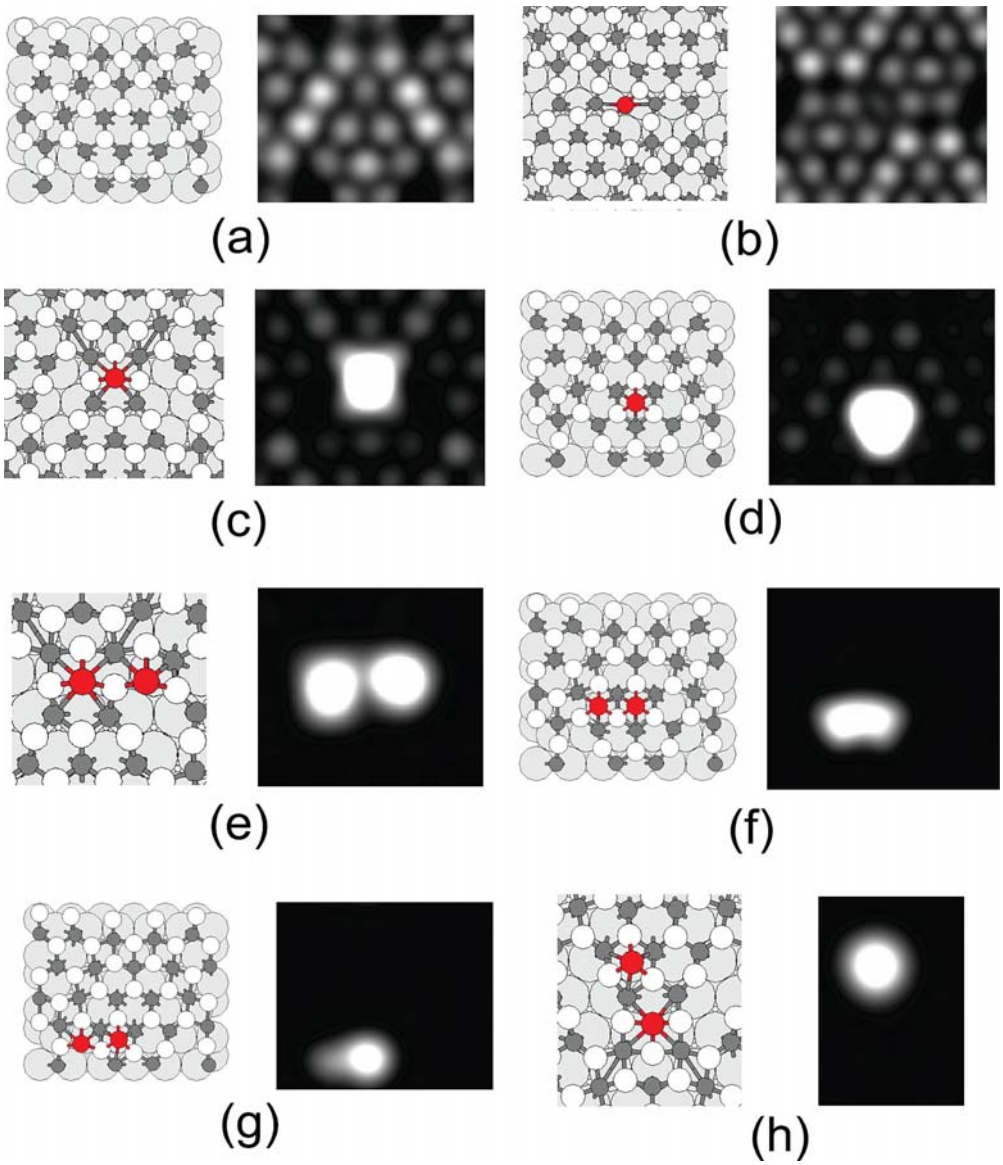

Fig. 48: Structure and simulated STM images of the *z'*-TiO*x* substrate (a) and of Fe adatoms (b-d) and addimers (e-h) adsorbed on it. The bias for the STM images is 1.55 eV for the bare substrate and the Fe adatoms, 0.89 eV for the Fe addimers. Fe atoms in red, O in dark grey, Ti in white and Pt in light grey.

All this concerns Pd and Au as prototypical examples. Other species can however behave in a very different way. The role of the specific nanoparticle-template interactions and the way they are important to modulate mobility and thus to drive nanoparticle ordering has been addressed in Refs. [BarcaroJPCA2009; CavalierePCCP2009], see also Ref. [GavioliPSS2011] for a general review on this topic and Sec. 5.2. In this work, the different features of the adsorption of Au and Fe on the z'-TiO_x/Pt(111) phase have been compared, and it has been shown that the oxygen affinity of the metal species, in addition to the interplay of thermodynamic

and kinetic effects in the growth process, is a key parameter for modelling metal/oxide interactions and has a profound influence on the structure and morphology of the growing nanoclusters.

We show as an example in Fig. 48 (taken from Ref. [BarcaroJPCA2009]) some results of simulations of the adsorption of Fe atoms and dimers on the z'-TiO_x/Pt(111) phase. The appearance of this figure is completely different from the Au case. The source of this difference is basically that the Fe atoms are positively charged by the interaction with the surface. This explains the bright spots associated with them in STM images at positive bias seen in the figure, and produces an increase in the slab dipole moment after Fe adsorption, and a slight repulsion among Fe adatoms adsorbed in adjacent sites on the stripe regions, see Sec. 5.2 for further discussion.

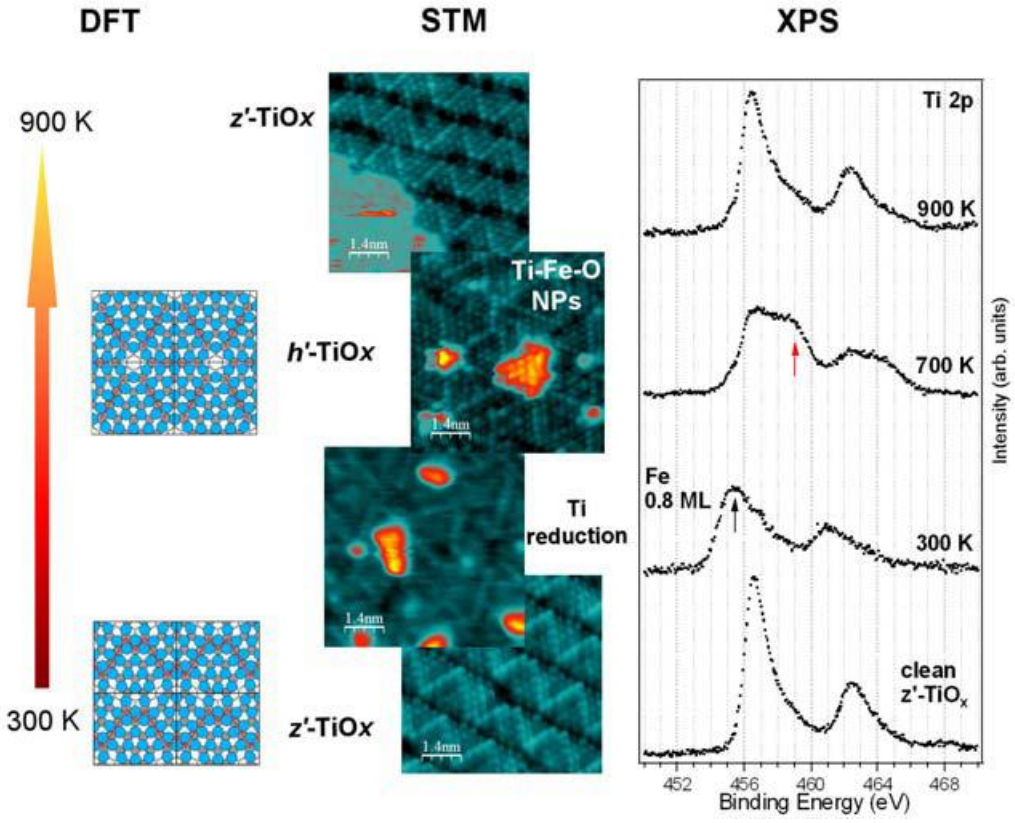

Fig. 49: sequential redox processes and structural transformations occurring by increasing temperature in the Fe/TiOx/Pt(111) system.

As a consequence of this strikingly different behavior, a phase transformation induced by thermal treatment has been observed also in the case of Fe clusters on the z'-TiO_x/Pt(111) ultra-thin titania film [CavalierePCCP2011], somewhat analogous even though technically very different to that discussed above for Au clusters. In this case, the progressive increase in temperature induces a series of sequential redox processes and structural transformations by which the initial reduction of the underlying titania phase by deposited Fe at room temperature is followed by Fe diffusion and partial penetration into the substrate at intermediate temperatures. This

triggers the formation of a bi-component material in which mixed FeO/TiO_2 nanoislands coexist on a structurally different ultrathin film, notably restructured (from rectangular to hexagonal) and reduced (from Ti:O = 1:1.25 to 1:1.14) with respect to the original phase. Further heating recovers the pristine titania phase while Fe dissolves into the substrate, see Fig. 49 taken from Ref. [CavalierePCCP2011] for a pictorial view of these phenomena.

It should be clear from this very synthetic overview that much work needs to be done in this field, and surprises could be expected, so that it will likely represent an important direction of development in a near future. For example, the possibility of investigating the *electronic* properties of supported clusters (thanks to the metal proximity effect but also possibly strongly influenced by it) represents an exciting chance which is being explored in our lab in collaboration with experimental groups.

4.4 Concluding remarks

The aim of the present chapter was to review recent advances in the theoretical prediction of the structural properties of metal nanoclusters and nanoalloys supported on oxide substrates. Attention has been limited to model surface science systems, for which a detailed comparison with available experimental information can be made, but the methods so validated are in principle applicable with equal confidence to "real world" materials. The main message that we would like to be drawn from this overview is that theoretical tools have reached a level in which they can give a very significant contribution to the understanding and a priori prediction of such a complex subject as the structure and morphology of supported metal nanoparticles. Clearly, much work still remains to be done, as remarked in the previous sections along with the presentation of the results. Basically, three main scientific issues need to be dealt with to extend the scope of the approaches so far developed: (i) both first-principles and empirical methods should be further refined (especially for multicomponent systems); (ii) more complex oxides than MgO(100) should be systematically investigated, such as non-square-symmetry and transition metal oxides or exotic substrates in the form of ultrathin films; (iii) dynamical phenomena such as growth and melting in addition to simple diffusion should be investigated in greater depth (see the next chapter). Moreover, the presence of ligands and in general realistic working conditions should be included in the theoretical analysis. Despite this, we believe that the results presented above show that the avenue of a predictive computational science of structure-property relationships in supported metal nanodots is open for both model and real materials, with the most difficult and also perhaps most fascinating applications being in the field of nanocatalysis (for which see again the next chapter).

Chapter 5

Dynamics and properties

The aim of the present chapter is to provide an introductory description of the basic concepts and tools utilized in the study of beyond-static phenomena, and to present examples of recent applications which can give a flavor of what is the current status of research in this field. Two sections on dynamic processes such as growth on regular (5.1) or nanostructured (5.2) substrates and how they can be dealt with at the first-principles level begin the chapter, followed by two sections on optical (5.3) and catalytic (5.4) properties. Brief perspective remarks (5.5) will conclude the Thesis.

5.1 Atom-atom exchange, diffusion and growth

In the previous chapters we have focused on static processes and structure prediction, and we have described length-rescaling ideas. Kinetic processes such as diffusion, growth and reaction, and the corresponding time-rescaling approaches [VoterARMR2002], have been simply mentioned. However, it is known that length and time scales are intimately associated, in the sense that – very roughly – the interesting dynamics of larger systems become progressively slower. In this section we will briefly touch upon this subject on which a huge literature is present.

At the lowest end, i.e., the fastest, of the time scales it is possible to conduct first-principles Molecular Dynamics (MD) simulations. In these simulations, both the electronic and the nuclear degrees of freedom are simultaneously described. This implies a time step of the order of hundredths of femtoseconds (i.e., $10^{-17}/10^{-16}$ sec). Considering that current simulations typically run for at most 10^6 steps, it derives that these simulations can cover a time span of tens of picoseconds. One of the most popular among these approaches is the Car-Parrinello method [CarPRL1985]. An important possibility is realized when the process of interest requires a description at the Quantum Mechanical level and occurs on a fast time scale but involves only a limited part of the system, with this part being coupled to a possibly complex environment (such as a solvent) whose evolution can be described classically. In such a case it is reasonable to describe the interesting part of the system at the Quantum Mechanical first-principles level, and the environment at the Classical or Molecular Mechanics level, giving rise to so-called QM/MM hybrid approaches [ShoemakerJPCA1999]. These approaches fall within the general problem of embedding [FortunelliBook1992; HuangJCP2011], i.e., the problem of setting up appropriate boundary conditions when attention is focused on a subset of a larger

system whose behavior is supposed to be known and one aims at taking advantage of this to simplify and reduce the computational effort. Embedding techniques can be used both at the dynamical and at the static level: one popular embedding approach is the ONIOM protocol [FortunelliSS1991; FortunelliBook1992; SvenssonJPC1996].

A crucial issue using first-principles approaches in dynamical studies is whether it is possible to simulate time scales longer than few picoseconds. The answer can be affirmative if the process under study is an activated one. An activated process is one in which the system oscillates most of the time in the neighborhood of a given local minimum or inherent structure [StillingerS1984; StillingerS1995], which is left by overcoming an energy barrier to jump into another local minimum, and so on. Several strategies can be devised to deal with this problem [VoterARMR2002]. One strategy is to first single out and enumerate all (or as many as possible) local minima in the PES, and then establish how they are connected via saddle points. Such information is often graphically summarized in terms of disconnectivity diagram (or tree or graph) [WalesBook2003]. A complete knowledge of the topology and connectivity of the inherent structures would allow one to predict the system behavior as a function of temperature (both thermodynamics and kinetics: phase diagram and evolution), via e.g. kinetic Monte Carlo simulations [ReuterPRB2006]. In these simulations one starts from a given local minimum, enumerates the possible paths leaving this minimum, and realizes the transition to one of them selected according to a Metropolis criterion. From a technical point of view, an exhaustive search of all the low-energy local minima at the first-principles level can be conducted via the global optimization algorithms discussed in previous sections. Saddle points and energy barriers can also be found using first-principles approaches. One can distinguish two cases, according to whether one has a knowledge of the initial and final configurations of the local minima to be connected or not. In the former case, the Nudged Elastic Band (NEB) method [MillsPRL1994] is one of the most popular to find the reaction path between the two configurations and is implemented in many electronic structure codes, even though other methods have been proposed as numerically more robust [delCampoJCP2008]. If knowledge on the final configuration is lacking, then the search for the local minima connected to the starting structure can be conducted via several methods, see e.g. Ref. [OlsenJCP2004]. To make a simple example, the process of diffusion of a vacancy (i.e., a vacancy-atom exchange) in the core of a truncated octahedral Ag_{37} cluster is graphically shown in Fig. 50.

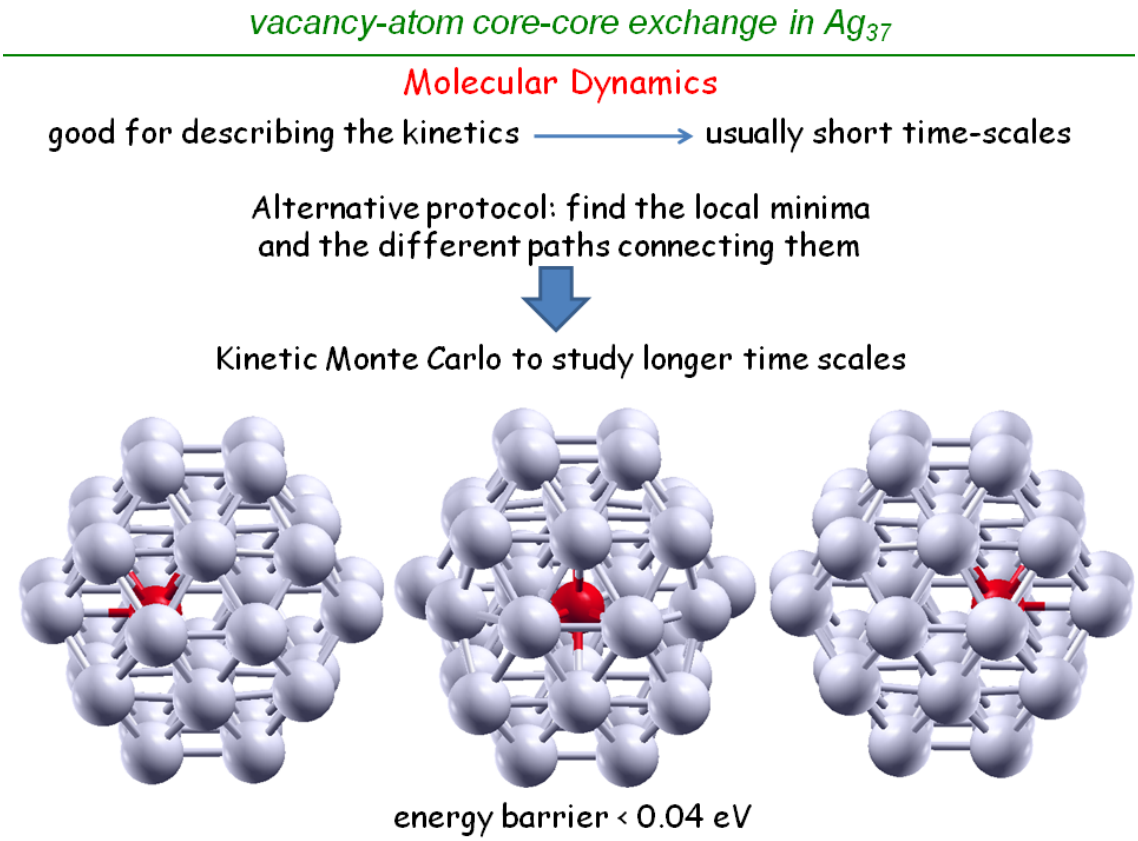

Fig. 50: Vacancy diffusion within the core of a Ag_{37} truncated octahedral cluster.

The formation and diffusion of a vacancy within a silver nanocluster was studied employing this combination of first-principles and statistical mechanics simulations in Ref. [TaherkhaniCPL2010]. A 38-atom truncated-octahedral (TO) arrangement and its homologue with 37 Ag atoms and one vacancy were considered, and density-functional calculations were performed to derive the energies of the local minima and the energy barriers connecting them. These data were then used as an input for a study of the system dynamics via a kinetic Monte Carlo algorithm, evaluating site occupancies, diffusion coefficient and equilibration time. It was found that vacancy formation and diffusion represents a viable path for atom-atom exchange in this system. This finding is intriguing in view of the generalization of this approach to nanoalloys. To date, in fact a thorough study at the first-principles level of the dynamics of chemical ordering in alloy nanoparticles is still lacking. Attention has so far been focused on the chemical ordering thermodynamic phase transitions. These are very interesting but it is not clear whether they are also relevant to realistic conditions. Studies of atom/atom exchange dynamics have been conducted so far only at the empirical potential level. The accuracy of empirical methods in predicting delicate quantities such as diffusion energy barriers is however a question of debate. Indeed, preliminary simulations conducted in our laboratory on mixed Ag-Pt nanoparticles have shown that a first-principles approach following the lines of Ref. [TaherkhaniCPL2010] can indeed be fruitful and provide enlightening indications on the kinetics of chemical ordering in nanoalloys [NegreirosPrep2012].

Another phenomenon in the field of supported metal clusters that can be typically studied via this type of approaches is self-organization and growth by deposition of metal atoms from the gas-phase. The adsorption configurations that are the local minima of the system and the diffusion mechanisms connecting them can be singled out, and the corresponding energetics evaluated in detail. An interesting fact, already mentioned in the previous sections, which has been discovered via first-principles simulations [MusolinoPRL1999; BarcaroJCTC2005; XuPRL2005; BarcaroPRL2005; BarcaroNJP2007; FerrandoJPCM2009] is that small metal clusters can diffuse on a regular oxide surface such as MgO(100) even faster than adatoms, see Fig. 51.

diffusion of Pd, Ag, Au clusters on the regular MgO(100) surface

results of DF-NEB* diffusion energy barriers

(values in eV)	*Pd*	*Au*	*Ag*
Monomer	*0.39*	*0.22*	*0.10*
Dimer	*0.39*	*0.62*	*0.22*
Trimer	*0.30*	*0.19*	*0.12*
Tetramer	*0.38*	*0.42*	*0.21*
DFT ⇨	*~ 0.38*	*~ 0.20*	*~ 0.10*

interesting to note in passing: M_2 and M_4 for Ag and Au diffuse more slowly than M_1 and M_3

**DF-NEB (Density-Functional Nudged Elastic Band)*

Fig. 51: Diffusion energy barriers of small palladium, gold and silver clusters diffusing on the regular MgO(100) surface.

As the surface on which deposition occurs is usually composed of regular terraces and various kinds of defects, with the latter usually acting as trapping centers, the mobility of metal species is crucial in determining whether nucleation occurs (preferentially) at defects or on the flat surface. Fast diffusion causes nucleation at defects only, whereas slow diffusion allows nucleation also on flat terraces. Due to the difficulty of directly measuring diffusion coefficients and of imaging diffusion processes in experiments, most of the available results in this field have been obtained in the domain of theory and simulations. However, information about the mobility of adatoms and small clusters can be inferred from the effects that such mobility has on quantities that can be more easily measured at the experimental level, such as the defect density as a function of the growth conditions. Epitaxial

relationships are important in this field as they are often the determining factors of cluster mobility. For metals on MgO(100), e.g., already dimers and trimers may not stay flat on the surface in their lowest-energy configuration due to the metal-on-top effect [BarcaroJCTC2005] mentioned in a previous section. For example, see Fig. 52, neutral copper, silver and gold dimers prefer to stay vertical on regular MgO(001) terraces, even though the situation can be different on ultrathin films, where gold clusters can be charged. Palladium dimers stay horizontal, but palladium trimers adopt a vertical configuration. Due to these subtle epitaxial effects, small clusters on the MgO(100) surface can present a variety of interesting diffusion mechanisms. In addition to simple hopping between favorable adsorption sites, rotation, sliding, leapfrog, walking, concertina, flipping, twisting, rolling and rocking mechanisms have been shown to take place, depending on the type of metal (i.e. the features of its interaction with the surface) and the size of the cluster [FerrandoJPCM2009], see Fig. 52.

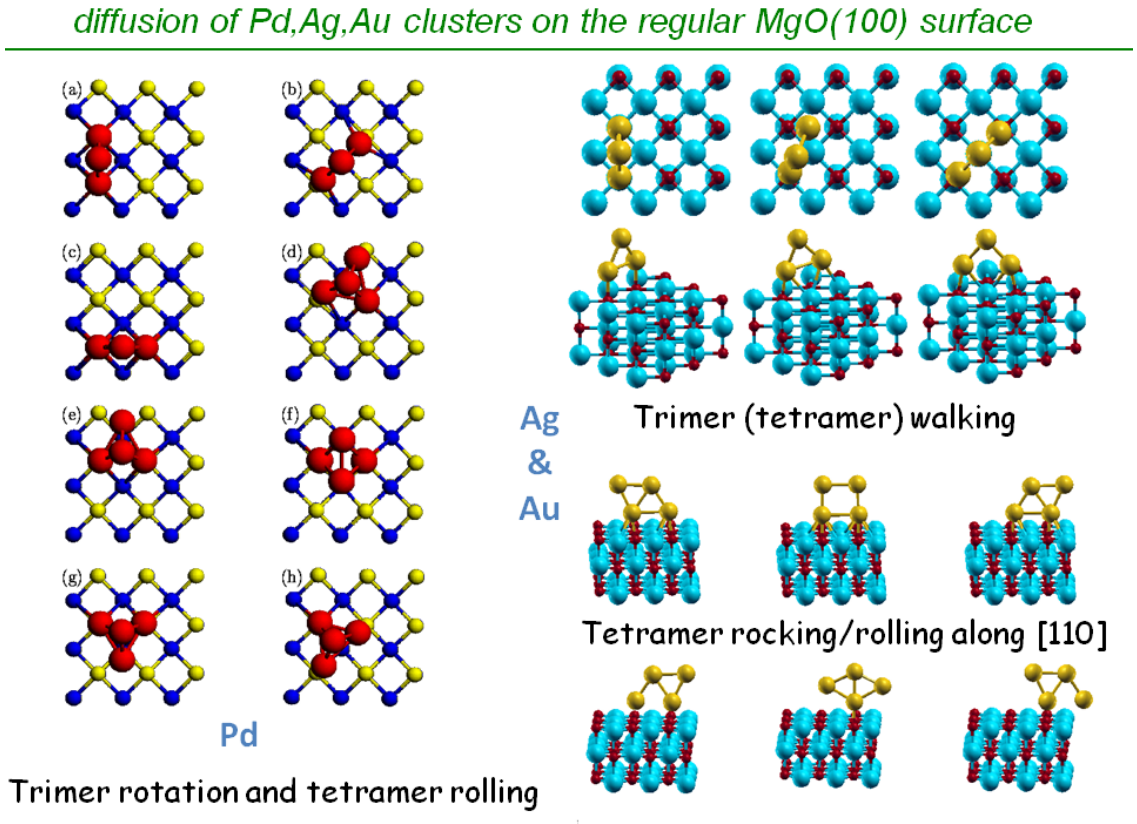

Fig. 52: Diffusion mechanisms of trimer and tetramer clusters on the regular MgO(100) surface.

Apart from the basic interest of these phenomena, it was found that diffusion of small clusters and not only adatoms is crucial to reconcile theoretical predictions and experimental data, see Fig. 53. In an experiment that has stimulated much theoretical work [HaasPRB2000], Pd adatoms were deposited on MgO(001) in a wide range of temperatures, from 200 to 800 K, and the temperature-dependent island density was measured. This density was found to be constant from 200 to about 600 K, and to

drop suddenly down above this temperature. The constant island density until low temperature was an indication of nucleation at defects down to low temperatures, with a negligible proportion of nucleation on terraces. The experimental estimate of the diffusion energy barrier was less than 0.3 eV, at variance with DFT calculations, predicting it to be at least 0.34-0.41 eV. The discrepancy between the experimental estimate and the calculations was solved [BarcaroPRL2005] by noting that small clusters, up to the tetramer, also strongly contribute to the mobility of palladium down to 200 K, as trimers or tetramers are in fact even more mobile than monomers. Therefore, in determining whether nucleation occurs either on terrace sites or at defects, the mobility of monomers and of small clusters must be taken into account.

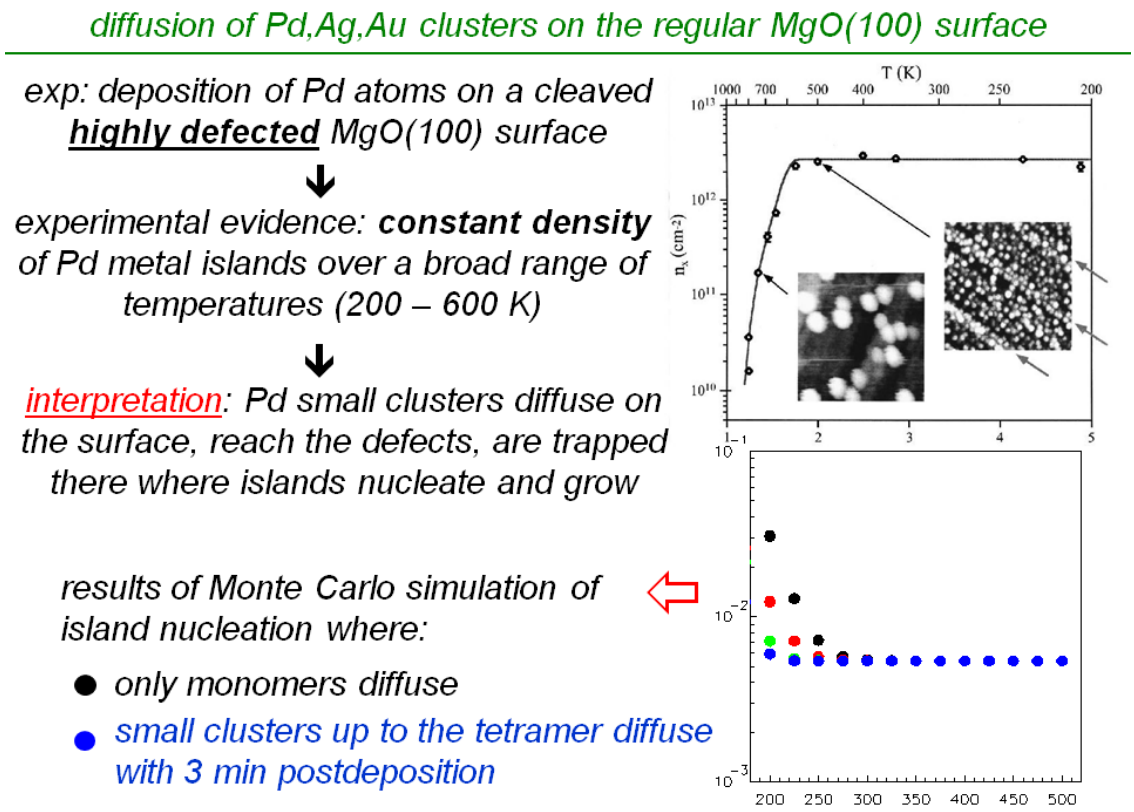

Fig. 53: Experiment-theory comparison in the case of small palladium clusters diffusing and growing on the MgO(100) surface.

This type of approaches can be employed not only for studying growth, but also other interesting dynamical phenomena, with heterogeneous catalysis being the most prominent (see the next sections), and is expected to become commonplace in a near future.

5.2 Diffusion on ultrathin oxides and surface nanopatterning

In analogy with what done for thick oxide supports, the mobility of atomic or cluster species on more exotic substrates such as ultra-thin oxide films can be and has actually been studied. As already mentioned in a previous chapter, the diffusion of Au and Fe atoms on various ultra-thin films of titanium oxide grown on the Pt(111) surface was investigated [BarcaroPCCP2008; BarcaroJPCA2009; CavalierePCCP2009], finding and rationalizing substantial differences between the two metal species on the same substrate. Mobility issues were also the topic of Ref. [SedonaJPCL2008], where a combined experimental/theoretical study of the growth of Au nanoparticles on two titania phases with very different stoichiometry and defect concentration was presented.

The study of diffusion and growth on ultra-thin oxide naturally leads to the topic of template assisted assembly and surface nanopatterning. As the catalytic activity and in general all the properties of metal nanoparticles are strongly size-dependent, reducing size dispersion is obviously an important goal. Furthermore, particle-particle distances are also important in determining the collective properties of ensembles of metal nanoparticles. A lively line of the current research is thus concerned with metal oxide substrates used as templates for the growth of size-selected and ordered nanoparticle arrays [GavioliPSS2011]. In this connection and in relation with surface defects, this is tantamount to know whether the defects are randomly distributed over the surface or are organized in regular patterns, i.e., the topic of surface nanopatterning [BruneN1998], see Fig. 54. The possibility of having a surface regularly nanopatterned with arrays of trapping centers is very intriguing as it has the advantage of automatically reducing the size dispersion [LeeAPL1998] and allowing one to study cluster-cluster interaction [GavioliPSS2011]. It has been shown in fact both theoretically and experimentally that an ordered array of defect trapping centers can narrow the size distribution of metal particles growing on a support down to 5-10% with respect to 30-40% expected for random nucleation [LeeAPL1998]. Furthermore, new properties can arise when regular arrays of metal nanoparticles are created. In this case, a hierarchical material is obtained where the primary building blocks are organized to create a long-range-ordered secondary structure, a super-lattice of the primary building blocks. In such a hierarchical material, nanoscale forces between the building blocks are active, which can generate new collective functionalities originated by the ensemble behavior of the metal particles [ClaridgeACSN2009; VelevAM2009]. As an example, regular arrays of metal NPs allow to control the resonance frequency of the localized surface plasmon [ChanNL2007] and they are good candidates for sensors and extremely high-density data storage devices [WangJACS2007].

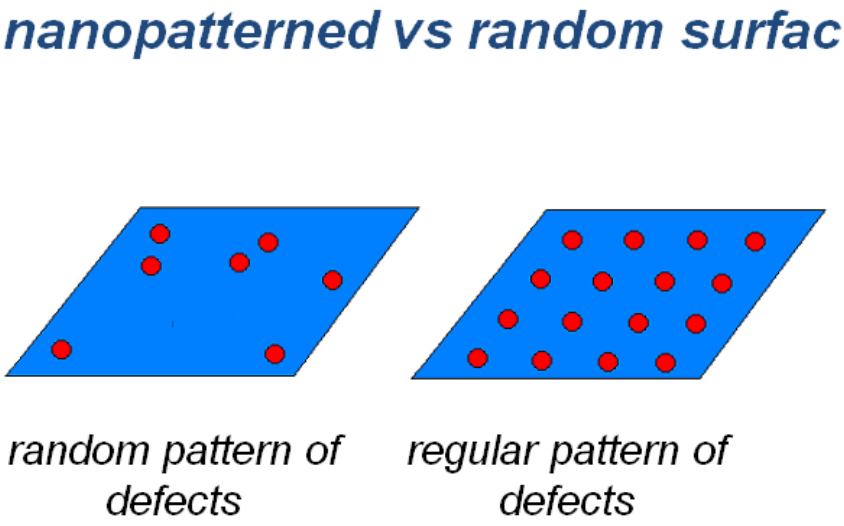

Fig. 54: Defects randomly distributed or organized according to a regular nanopattern on a surface.

From the analysis conducted in Refs. [BarcaroPCCP2008; SedonaJPCL2008; BarcaroJPCA2009; CavalierePCCP2009; GavioliPSS2011] it resulted that a good templating substrate should indeed posses nucleation sites that are geometrical in nature, but also that these sites are effective in templating metal nanoparticles if the energy landscape for surface diffusion of metal, in part determined by the oxygen affinity, allows the diffusing species to actually reach the most energetically favorable adsorption sites and if these are able to effectively trap the metal NPs. Moreover, the layer stiffness with respect to modifications induced by the metal wave functions to allow accommodation of adatoms in the geometrical defects should also be taken into account to explain and predict the behavior of these systems. What can happen in fact is: (1) if the metal/oxide interaction outside the trapping centers is too strong and/or the temperature is not high enough, the defects will not be accessible via diffusion of metal adatoms on the surface and random, off-defect nucleation can occur; (2) if the defect requires a reconstruction to adapt to the incoming metal species, this can also dramatically reduce its efficiency as a nucleation center or can lead to cooperative phase transformations of the complex metal-particles/ultra-thin-film/metal-surface system e.g. in post-growth heating processes [BarcaroJPCC2009; CavalierePCCP2011]; (3) in the absence of geometrical defects, adatom charging effects can hinder aggregation and lead to self-organization in proper experimental conditions [GavioliPSS2011].

5.3 Optical (and magnetic) properties

Metal nanoclusters are very attractive for optical applications [KreibigBook1995] because their electronic structure and consequently their optical response are sensitive to structural parameters such as size, shape and – for multi-component systems – composition and chemical ordering. For simple or noble metal nanoclusters, the main feature of the optical response to excitation by light is an absorption band in the UV-visible range related to the surface plasmonic resonance (SPR), i.e., a coherent and collective oscillations of the electrons involved in the metallic bond subjected to electromagnetic radiation of proper wave length. Although this effect has been employed by humanity since thousands of years and despite numerous studies [HalasCR2011; MortonCR2011], rigorous data on this topic are partly lacking and are thus strongly needed, especially for the smaller and the alloyed particles. Mie theory [KreibigBook1995], which is appropriate for bulk systems, can be extended to nanoparticles via mesoscopic empirical models such as the DDA (Discrete Dipole Approximation) or electrodynamical models, but the validity of these models is questioned for metal nanoparticles of few nm in size and especially for more complicated cases such as multi-component metallic nanoparticles – or nanoalloys. In addition to structural morphology and chemical composition, in fact, chemical ordering is expected to play a fundamental role in determining the optical properties of nanoalloys, being one of the reasons why they display distinctive properties as compared to their constituents, but the exact extent of the interplay between local and collective electronic states in inter-atomic metallic bonding as a function of the distribution of the atomic species within the particle is still scarcely known, despite the substantial amount of experimental work devoted to the optical properties of bimetallic particles, especially on the Ag-Au system. To answer this need of rigorous information and respond to some of the basic questions still existing in this field (e.g., the exact dependence of the shape and peak of SPR upon nanoparticle size, shape, composition, chemical ordering and environmental effects) first-principles approaches, in particular those based on Time-Dependent Density-Functional-Theory (TDDFT) [CasidaBook1995], can give a decisive contribution. The computational effort of TDDFT however increases so rapidly with the size of the system that one needs to push this approach to its present limits to produce results on clusters of experimentally and physically interesting size. As mentioned in a previous chapter, an effective tool to enlarge as much as possible the size of computationally affordable systems is to consider high-symmetry magic clusters. The exploitation of symmetry (with high-order point groups such as Oh or Ih) can reduce by orders of magnitude the computational effort, as the electronic excitations which make up the optical response can be catalogued into appropriate irreducible representations of the symmetry group, and the interactions among excitations belonging to irreducible representations not coupled by the proper perturbation operator are automatically null by symmetry. The size range around 150-200 atoms is about the maximum that can be confidently treated when studying linear optical response using current computational resources even with a full exploitation of point group symmetry, but

future developments can probably double this size limit in the next future. Anyway clusters of 150-200 atoms are large enough to start observing a resonance peak that will lead to the SPR.

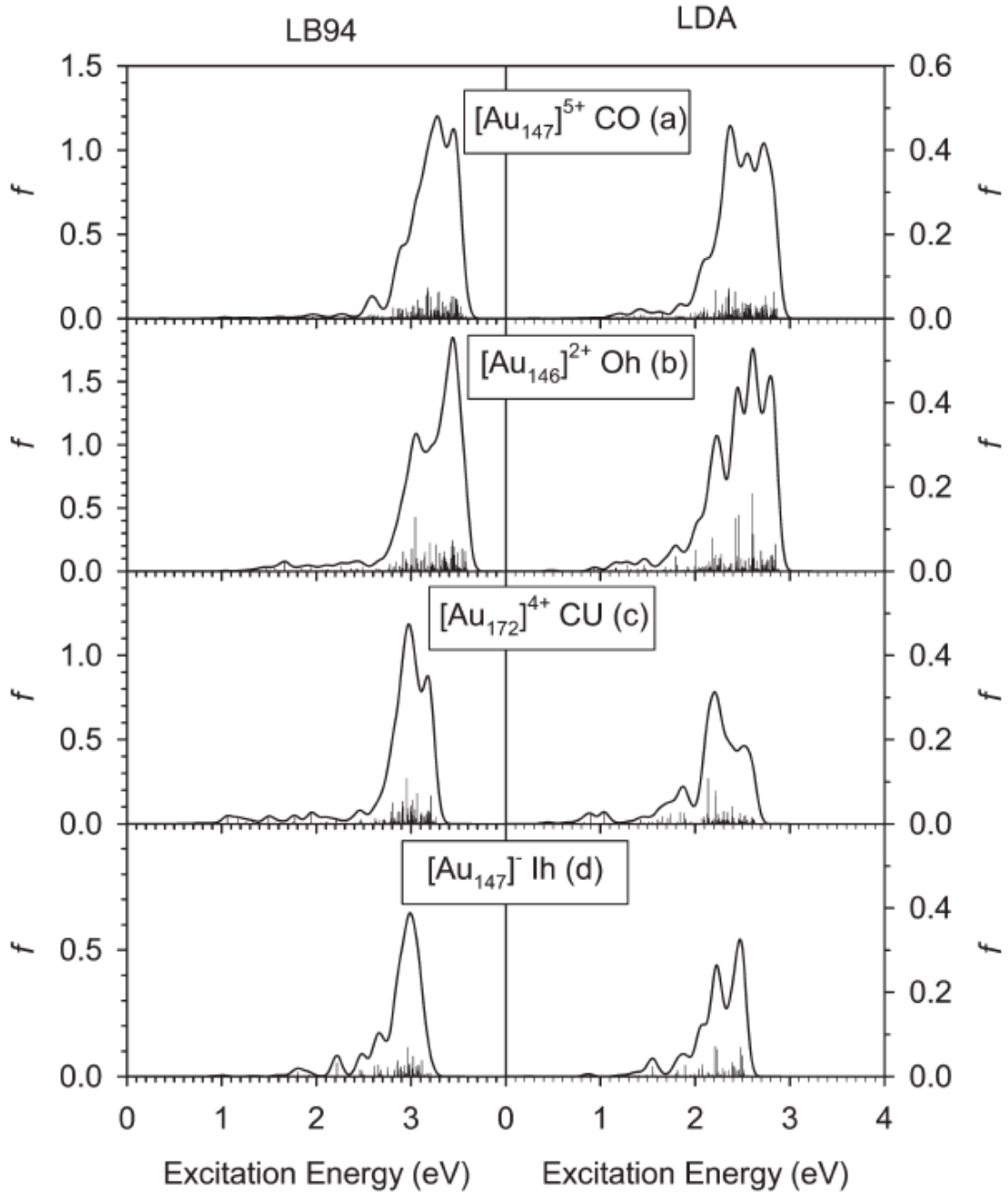

Fig. 55: Photoabsorption spectra simulated via a TDDFT approach at the LB94 and LDA level for Au nanoclusters at LDA-relaxed geometries: CO = cuboctahedron, Oh = octahedron, CU = cube, Ih = icosahedron.

Using this approach, the optical properties of Au nanoclusters in the size range around 150-170 atoms were studied as a function of the approximation used for the DFT exchange-correlation (xc-) functional and the shape or morphology of the

nanocluster [DuranteJPCC2011]. From this study, it resulted that the position of the peak in the absorption spectrum was weakly dependent on the shape of the Au cluster but was essentially related to its size and to the DFT methodology (xc-functional) used in the calculations, and that the predictions of the van Leeuwen-Baerends (LB94) xc-functional compared better with the available experimental data with respect to those of the local density approximation (LDA) xc-functional. The main results of this work are shown in Fig. 55, taken from Ref. [DuranteJPCC2011].

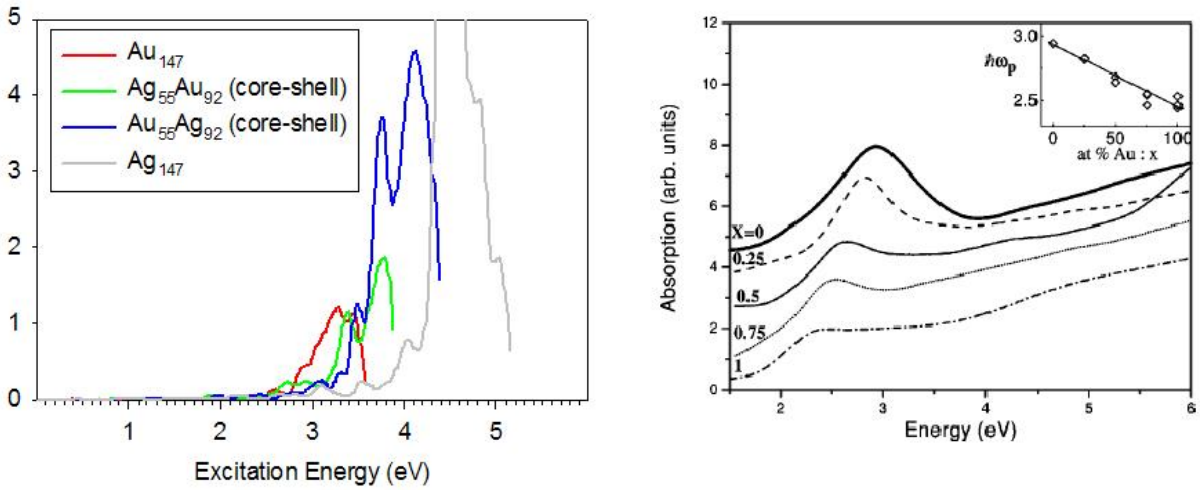

Fig. 56: Photoabsorption spectra of cube-octahedral bimetallic clusters with increasing silver concentration. Left box: calculated TDDFT LB94 spectra, right box: experimental spectra.

As mentioned above, the high symmetry assured by magic structures is particularly convenient for nanoalloys, as it can be exploited not only to reduce the computational effort but also to partition the atoms into symmetry shells or orbits, i.e., groups of symmetry-equivalent species (which are converted into one another by the operations of the symmetry group). This exponentially reduces the configurational degrees of freedom of the system, making sampling of the nanoalloys configurational phase space feasible via first-principles simulations even for medium-sized particles [FortunelliJMS1999b]. This magic-cluster approach was applied in recent work to pure Ag and mixed Ag-Au nanoclusters of size around 150 atom, focusing on the effect of alloying on the optical response of these systems [BarcaroJPCC2011]. It was found that the absorption spectrum of Ag clusters is slightly more sensitive to the particle shape than that of Au clusters, that configurations with rather different chemical ordering (such as core-shell vs. intermixed ones) present spectra with similar position and intensity but different shape, and that the plasmonic peak shifts to higher energies, gets relatively narrower and gains in intensity by increasing the Ag concentration in the cluster. All these data are in excellent agreement with and allow one to rationalize available experimental information. An example of the kind of agreement between theory and experiment that can be obtained is shown in Fig. 56 (taken from Ref. [BarcaroJPCC2011]), where it should be taken into account for a

proper comparison that experimental spectra are shifted at lower energy with respect to gas-phase systems due to environmental (matrix) effects. This good agreement opens promising perspectives for applications also in view of the possibility of investigating more complicated systems such as those presenting chiral and magneto-optical effects [EbertRPP1996] and "plasmonics", i.e. interaction among plamonic resonances and between these and molecular absorption (surface-enhanced spectroscopies). Note in passing that the metal nanoparticles can be described in a simplified way as a polarizable continuum model, as pioneered to the best of our knowledge for the first time in Ref. [FortunelliCPL1996; FortunelliJMS1998].

The approach employed in Ref. [DuranteJPCC2011] is currently being extended to other pure and alloyed metal nanoclusters, and coupled with 1D (wire) models. Magnetic properties are also currently under investigation. An approach similar in spirit to this one has in fact been developed in which a wire model was applied to investigate interface effects on the magnetism of CoPt particles supported on MgO(100) [BarcaroNL2011b], rationalizing the effect of a simple oxide substrate on the magnetic properties of the supported nanoparticles.

5.4 Catalytic properties

Understanding, controlling, and ultimately designing catalytic systems with the desired activity and selectivity is a major challenge of contemporary chemistry [LewisCR1993]. The scope of this challenge is extremely wide, being relevant to battery technology, ultra-capacitors, fuel cells, environmental chemistry, and catalytic processes for sustainable energy production, with heterogeneous catalysis by metal nanoclusters, i.e., metallic particles in the 1-100 nm diameter range, representing one of the major avenues [HandbookHetCat2008]. Improved catalysts can increase efficiency leading to reduced energy requirements, while increasing product selectivity and concomitantly decreasing wastes and emissions. Theory and simulations are expected to play an important role in this challenge. If a molecular-level understanding of the detailed steps of chemical reaction mechanisms is to be achieved, in fact, and despite the limitations of current approaches, the often sufficiently accurate prediction of the topology of local minima and saddle points in the energy hyper-surface renders theoretical simulations an invaluable tool. In addition, the possibility of performing computational 'gedanken experiment' and thus to disentangle, via in-depth analyses, the origin of the basic interactions in complex multifunctional systems such as those involved in catalytic chemistry is also unique to the theoretical level.

5.4.1. Chemisorption

As a first and introductory step in a theoretical study of catalysis, the adsorption of ligand molecules on supported metal clusters was studied via DFT methods by

several groups [NeymanPCCP2007]. We present in this section a few such examples taken from our own work, before tackling the problem of simulating real catalytic processes.

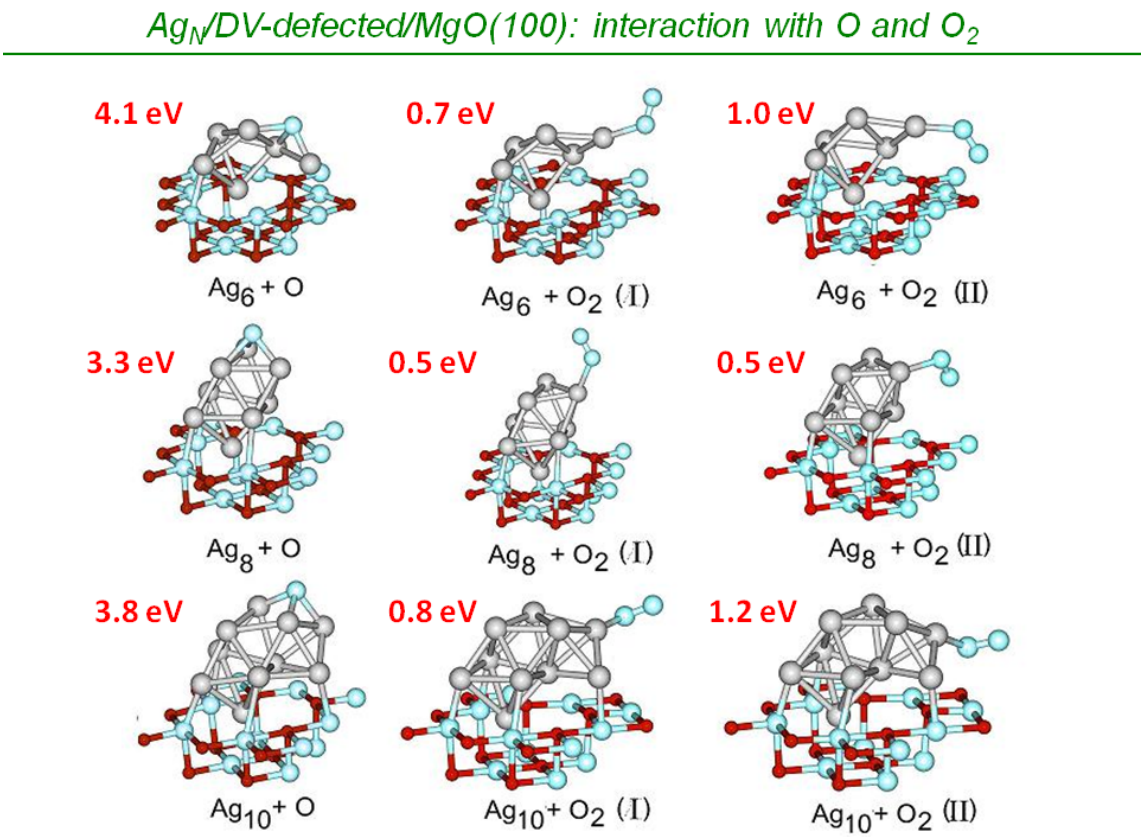

Fig. 57: Adsorption of atomic and molecular oxygen (in two different interaction modes: I and II) on DV-MgO(100) supported silver clusters. Adsorption energies (in red) in eV. Oxygen, magnesium and silver atoms are represented by light blue, red and grey spheres, respectively.

In Fig. 57 the optimal adsorption modes of an undissociated O_2 molecule or an O atom on small Ag clusters supported on a DV-defected MgO(100) surface are shown (taken from Ref. [BarcaroPRB2007]). This system, which has been discussed in more detail in a previous section, is interesting to test whether being a surface magic cluster – Ag_8 on the DV-defected MgO(100) surface is one such clusters – can make a difference in the chemical properties of metal particles. From the results shown in Fig. 57 the answer comes out to be positive. It can first be noted from Fig. 57 that O binds preferentially to a triangular facet of the metal clusters, in agreement with the known behavior on crystal surfaces. Moreover, the peculiarity of Ag_8 as compared to Ag_6 or Ag_{10} is apparent, as its reaction energy with O is more than 0.5 eV smaller than that of the other clusters, due to both structural (shape of the cluster and exposed facets) and electronic effects. The results for the interaction with O_2 are in line with these findings and present an additional interesting structural effect. O_2, in fact, can adsorb on Ag clusters interacting through a single O atom, with the second O atom pointing away from the MgO surface (mode I) or with the second O atom pointing toward the surface and interacting with a Mg ion (mode II). Both interaction modes

are possible for Ag_6, Ag_8, and Ag_{10}, but it can be observed that in the case of Ag_6 and Ag_{10} the interaction energy with O_2 is larger by roughly 0.3–0.4 eV in interaction mode II with respect to interaction mode I, whereas in the case of Ag_8 modes I and II have practically the same interaction energy. This is due to the more compact structural arrangement of Ag_8, which does not present overhangs of metal atoms on the MgO(100) surface and thus does not favor the interaction of the O atom not directly bound to the metal cluster with the surface. This is interesting, as it has been hypothesized that an interaction mode II connected with the presence of overhangs affects the catalytic activity of Au clusters [MolinaPRB2004]. Smaller interaction energies with incoming species, which seem to be typical of electronically and/or structurally magic clusters, could be useful when a fine tuning of the cluster catalytic activity is sought for.

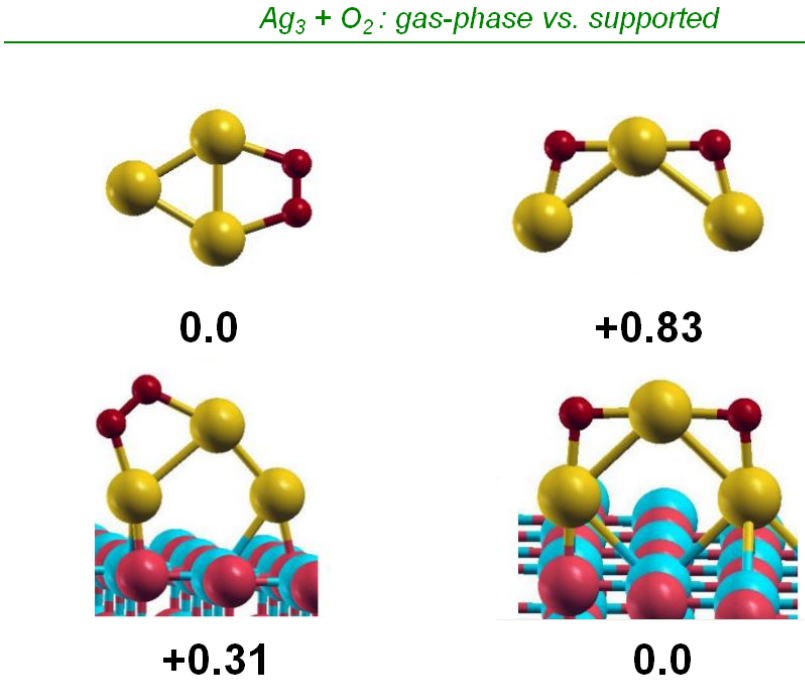

Fig. 58: Adsorption of an oxygen molecule on gas-phase and MgO(100)-supported silver trimers. Relative energies in eV.

A clear and (to the best of our knowledge) so far unnoticed example of the fact that the presence of the oxide surface can make a big difference on the chemical properties of supported metal clusters not only in terms of geometrical and electronic structures as just discussed but also in terms of direct influence of the surface on the metal/ligand interaction is presented in Fig. 58. In this figure it is shown that according to DFT predictions the dissociation of an O_2 molecule is energetically unfavorable on a gas-phase Ag_3 cluster but becomes thermodynamically favored when Ag_3 is supported even on the regular undefected MgO(100) surface which is the classical example of an inert support. This is due to the fact that the dissociated configurations have a much larger dipole moment which can favorably interact with the electrostatic field generated by the ionic, charge-separated oxide surface and has crucial consequences on the chemical properties of oxide-supported Ag_3, as this can

thus become an active oxidation catalyst [LeiS2010]. A similar phenomenon occurs for Au_3 clusters, and is of particular interest as it is associated with the unexpected catalytic activity of Au nanoclusters. In other words, interfacial metal atoms can exhibit an entirely different chemistry.

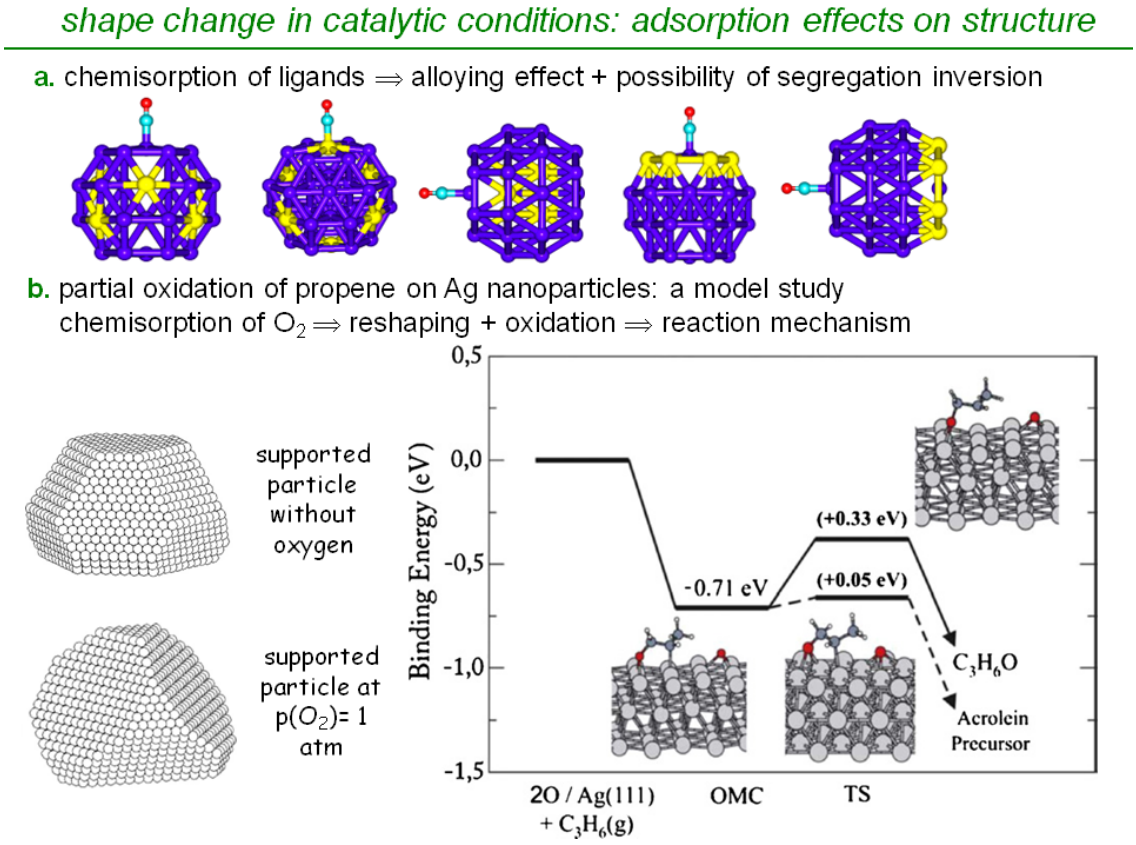

Fig. 59: Change in shape and chemical ordering in nanoparticles as a consequence of adsorption processes. (a) A fcc 38-atom model for studying adsorption of a CO molecule at the center of (111) facets of binary nanoalloys with different chemical environments, leading to tuning of adsorption energies by alloying and possible segregation inversion. (b) Left: reshaping of supported Ag nanoparticles as a consequence of oxygen adsorption at two O_2 pressures; right: reaction mechanism of propene on an oxidized Ag surface.

Larger clusters can also be treated, see Fig. 59. For example, the adsorption of ligands on metal nanoparticles and nanoalloys can be studied via DFT methods and how this modifies the structure of the particles [BorbonEPJD2009] or the chemical ordering (segregation) within an alloyed nanoparticle [WestJPCC2010]. Ligands can in fact reshape and reorganize segregation in metal nanoparticles in reaction conditions, a phenomenon more and more often observed as the detail of experimental characterization improves [JohanekS2004; HerzingS2008] and which can be predicted at the theoretical level, see e.g. Ref. [MolinaCT2011] and Fig. 59(b).

To start with the simplest example, in Ref. [MolinaCT2011] the energetics of Ag compact surfaces – namely the (111), (100) and (110) surfaces – was studied via DFT calculations in the absence and in the presence of adsorbed oxygen species, and this

was used to predict the nanoparticle equilibrium shape via the Wulff-Kaishev construction. It was found that adsorbed oxygen significantly stabilizes the more open (100) facets, thus entailing a substantial reshaping of the nanoparticles as a function of the oxygen pressure, as shown in the right-hand-most part of Fig. 59(b). These predictions were in fair agreement with experimental results. The actual activity of these Ag nanoparticles in the partial oxidation of propene to acrolein and propylene oxide was also modeled in Ref. [MolinaCT2011] – see left-most part of Fig. 59(b).

These considerations apply when the size of the nanoparticles is large enough that a crystalline morphology can be assumed, so that only the particle shape needs to be determined. For smaller particles the situation can be quite different. For example, in Ref. [BorbonEPJD2009] the following problem was posed: consider a cluster of size around 38-39 atoms. For such a case, the possible low-energy high-symmetry configurations can be taken from the database of structural motifs accumulated in previous work, and are shown in Fig. 60.

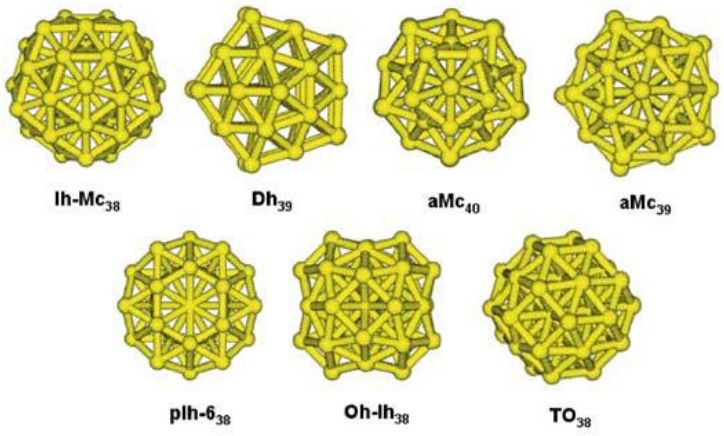

Fig. 60: High-symmetry structural motifs in competition around size N=38-39.

They consist of: an incomplete Mackay icosahedron (Ih-Mc_{38}), a Ino decahedron (Dh_{39}), an anti-Mackay pIh (aMc_{40}) and the corresponding structure obtained by local optimization of aMc_{40} for a Au cluster and removal of a single atom protruding out of the cluster tip (aMc_{39}), a pIh^6 pancake (pIh-6_{38}), a hybrid five-fold-symmetry/close-packed structure (Oh-Ih_{38}), and a truncated octahedron (TO_{38}). If we consider pure Pd, Pt and Au clusters, DFT will predict a given energy ordering among these configurations. The question now is: does absorption of ligands (such as CO and H) modify this structural energy ordering ? and how ? The answer to these questions is provided in Fig. 61, where the changes in the energy ordering among the structural motifs discussed above upon chemicorption of CO or H is reported, and can be summarized in two main observations: (1) the interaction of Pd and Pt clusters with H

increases the coordination of surface atoms and thus reduces the stress of strained structures (such as Ih or pIh) for these "sticky" metals, with the exception of the pIh-6_{38} structure which does not present internal stress, whereas for Au clusters the net result is a strong stabilization of more open arrangements which presents low-coordinated and thus more reactive sites of an otherwise inert element; (2) the interaction with CO appreciably changes the cluster potential energy landscape, with distortion energies more than doubled with respect to the H case, so that massive CO coordination brings about a partial disruption of metal-metal bonds and a flattening of the PES with much reduced energy differences among the different structural motifs.

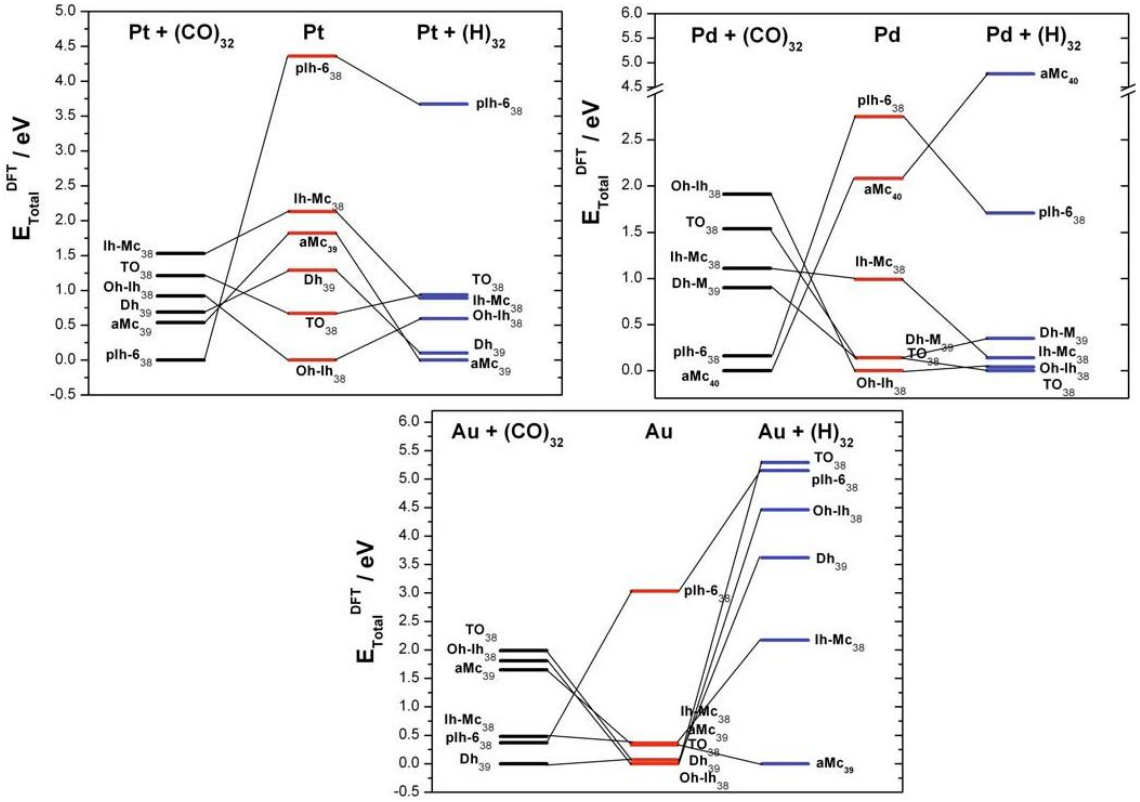

Fig. 61: Comparison of relative energies of structural motifs for Pd, Pt and Au clusters before and after a-top chemisorption of 32 CO molecules or H atoms. The DFT total energy is rescaled when necessary for 38-atom metal clusters by using the binding energy per atom.

It can be noted in passing that previous studies at the tight-binding (empirical) level of the electronic and chemisorption properties of metal nanoclusters (see e.g. pure Pt and Fe and mixed Fe-Pt nanoclusters in Refs. [FortunelliJMS1999b; FortunelliJMS2000; FortunelliJMS2002]) and on the *relationships* between them are no more fashionable in this field, now that such studies can be conducted at the first-principles level with reasonable computational resources [FortunelliJMS2002]. However, we believe that the analysis of Fukui functions performed in older work could still be useful (or could be even more needed) to understand the results of more sophisticated approaches. It can also be noted that the study of Ref. [FortunelliJMS2002] on the interaction of Pt_{13} and $FePt_{12}$ with benzene, ethylene and

formaldehyde was to the best of our knowledge one of the first on the chemisorption properties of nanoalloys conducted at the first-principles level.

Switching from pure metal nanoclusters to nanoalloys introduces the interesting issue of the coupling between ligand chemisorption and chemical ordering. This issue was investigated in detail in Ref. [WestJPCC2010], where a model setup was considered, shown in Fig. 59(a), in which high-symmetry 38-atom truncated-octahedral (TO) clusters with compositions A_6B_{32} and B_6A_{32} were used as substrates to bind a single CO molecule or a H atom in centroid sites for the following (A,B) pairs: (Au,Pd), (Pd,Pt), and (Cu,Pt), and the relative changes in the energetics of the systems upon ligand coordination were analyzed. Qualitative similarities but quantitative differences were found between CO and H cases (as examples of reducing agents), and a wide variety of behavior for the three (A,B) pairs. In summary, the main results of this study were that, in AuPd, Pd-CO bonding is not strongly affected by neighboring Au atoms but the $Pd_{core}Au_{surface}$ segregation pattern (favored for bare particles) is expected to be *inverted* in the presence of CO coordinating species. At the other extreme, in CuPt, both Pt-CO and Pt-H bonding are strongly enhanced by neighboring Cu atoms, but the predicted segregation pattern differs from that expected on the basis of results for extended systems due to finite-size effects. These findings are of great momentum in our opinion, as we believe that: (1) the results in terms of nanoalloys chemical ordering of many experiments and many synthetic procedures cannot be understood without taking into account the status of the nanoparticle surface, i.e., the coating of the nanoparticles; (2) the preferential strengthening or weakening of metal/ligand bonds due to the presence of co-adsorbed species (i.e., non-linear or cooperative or many-body or synergic interactions) play a crucial role in nanocatalysis, as shown in exploratory DFT simulations [NegreirosNS2012].

As a last example we will consider metal clusters in a different environment: surfactant coating of metal nanoparticles in the homogeneous phase producing colloidal suspensions originally investigated by Michael Faraday. These suspensions are formed by metal nanoparticles which are stabilized by protective shells/layers to prevent coalescence phenomena [PileniCRC2003]. The possibility of effectively stabilizing nanometric metallic particles with a high surface/volume ratio in solution allows for a quickly growing number of technological applications of such colloidal suspensions [BonnemannEJIC2001]. Bottom-up methods to produce these systems are based on the synthesis of metallic particles starting from elementary constituents, i.e., single atoms, ions, or small clusters. These methods primarily consist on the reduction of metal salts via chemical processes, the use of electrochemical techniques, the controlled decomposition of organometallic metastable compounds or the aggregation of metallic species in low oxidation states. A large number of stabilizing species, donor ligands, polymers and surfactants are used to control the growth of the freshly formed metallic particles and to protect the growing units from coalescence into the thermodynamic equilibrium phase (the bulk crystal). In this

context, the use of olefinic complexes of metals in a low oxidation states proves to be a clean route for obtaining colloidal suspensions of mono- and bi-metallic particles. Experimental evidence has in fact shown that in the presence of only the solvent molecules the stability of these suspensions at room temperature is limited to a few days, while with the use of surfactants the stability of metal aggregates is extended to a few months. The effective mechanisms by which growth eventually takes place, however, are not known, and are difficult to investigate experimentally, due to the lack of proper characterization tools able to furnish information on reactive processes in situ and in real time. Computational approaches can provide a very useful support in this sense. In Ref. [BarcaroTCA2009], such an enterprise was undertaken in the specific case of neutral small Pt clusters interacting with surfactants in which the ligand is based on unsaturated organic groups.

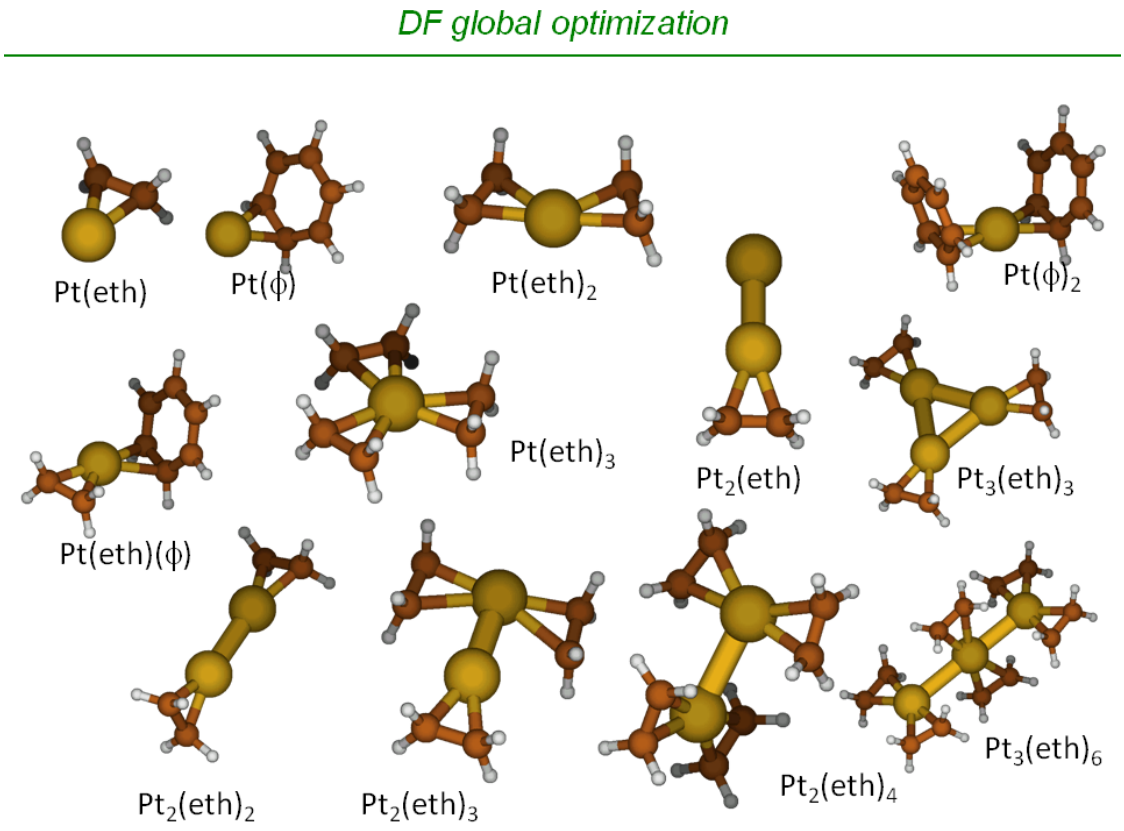

Fig. 62: Structures of $Pt_n(ligand)_m$ (n = 1, 3) metallorganic complexes in the case of vinylic (eth = ethylene) and arylic (Φ =benzene) ligands.

In detail, a theoretical first-principles study of the $Pt_n(ligand)_m$ (n = 1-3) metallorganic complexes was performed, by varying the number of metal atoms and the nature and number of organic coordinate ligands (specifically, vinylic and arylic ligands), see Fig. 62. Several conclusions were drawn from such a study. First, the fact that the Pt/C=C interaction has a many-body character, i.e., the binding energy appreciably decreases with the number of interacting C=C units. Second, the weaker binding of aromatic species with respect to vinylic species, due to the need of disrupting π-electron conjugation, which makes that a third aromatic molecule does

not bind to a doubly-coordinated Pt center, thus leaving it free for further aggregation. Third, the relatively low values of the ligand detachment energy barriers from a fully coordinated Pt center that can be overcome at room or slightly higher temperatures. Fourth, the fact that two binding mechanisms are possible between a small Pt cluster and a C=C bond: one involving the formation of σ bonds between Pt and C atoms (σ-interaction mode) and one in which the metal/ligand interaction takes place through a donation/back-donation mechanism (π -interaction mode). Additionally, two régimes could be distinguished in the growth of coated Pt clusters: a "coordinatively saturated" régime, in which the ratio among the number of ligands and the number of metal atoms is high and the ligand/organic π-interaction mode is preferred, and a "coordinatively unsaturated" régime, in which this ratio is low and the ligand/organic σ-interaction mode is preferred. The coordinative unsaturation typical of the latter régime favors more complicated, reactive processes, such as oxidative insertion of Pt atoms into a C–H bond. These conclusions were in tune with available experimental data, and suggested a positive role of theoretical simulations in the study of the nucleation and growth of metal clusters in the homogeneous phase in terms of accurate prediction of the energetics and of the kinetic growth parameters.

5.4.2. Theoretical nanocatalysis

The observation that the coordinatively unsaturated régime in $Pt_n(ligand)_m$ complexes favors reactive processes, such as oxidative insertion of a Pt atom into a C–H bond, see Fig. 63, introduces us into the field of theoretical nanocatalysis.

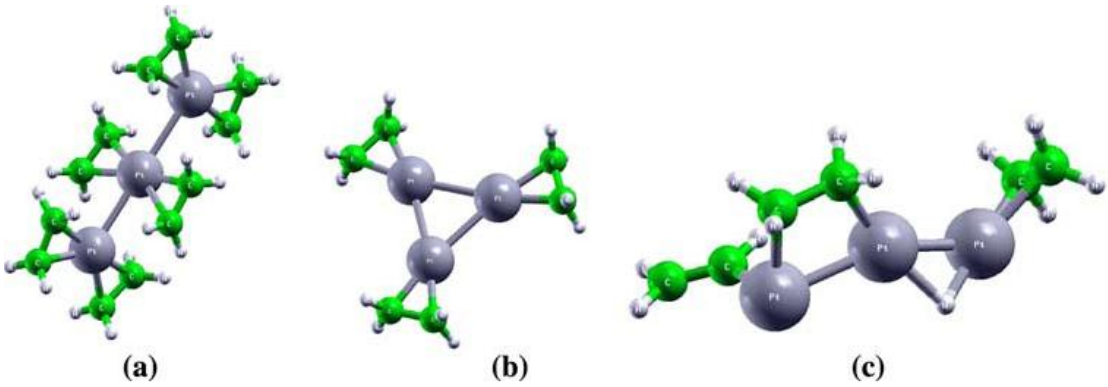

Fig. 63: (a) Putative global minimum of the $Pt_3(C_2H_4)_6$ complex; (b) π-adsorption configuration of the $Pt_3(C_2H_4)_3$ complex; (c) insertion of a Pt in a C–H bond in the $Pt_3(C_2H_4)_3$ complex to give an hydride complex. (c) is lower in energy by 0.33 eV at the DFT level with respect to (b). The total spin is S = 0 for all the configurations shown. Carbons in green, hydrogens in white and platinums in dark grey.

This observation in fact stemmed in the work of Ref. [BarcaroTCA2009] simply as an unintentional by-product of a global optimization (DF-BH) structural search. In other words, while performing a DF-BH search on a $Pt_3(C_2H_4)_3$ complex (thus, in the

coordinatively unsaturated régime), even freezing in the shake moves the geometry of ethylene molecules, the search automatically produced a reactive step in which Pt attacked a C-H bond. The spontaneous question one can answer is thus: is it possible and fruitful to exploit global optimization algorithms in theoretical (nano)catalysis ? After all, structural searches are about energies and geometries, i.e., … catalysis!

Before trying to answer this question, let us spend a few words on the present scientific context. In recent years a particularly intriguing research field in heterogeneous nanocatalysis has been offered by the discovery of the importance of sub-nanometer metal clusters, i.e., the experimental proof that extremely small (1-20 atoms) metal nanoparticles (pure or alloyed) can in many cases be the true actors of catalysis or at least actors with rather different and sometimes more interesting behavior with respect to larger nanoparticles [WorzJACS2003; HerzingS2008; LeiS2010]. From sophisticated surface science experiments it has first been shown that size-selected clusters deposited on model surfaces in UHV exhibit peculiar adsorption and chemical properties [WorzJACS2003]. The same has then been proven true on realistic surfaces and non-UHV conditions, e.g., in the oxidation of CO [HerzingS2008] or the partial oxidation of propylene by Ag_3 [LeiS2010]. Actually, even in real-world catalysis indications of the relevance of sub-nanometer species in specific catalytic reactions had already been drawn from in-situ synchrotron X-ray measurements [BazinACA2000]. In the size range from a few to few tens of atoms, metal clusters exhibit a molecule-like character, the metallic bond is only partially developed, and finite-size effects are in the extremely non-scalable regime in which “each atom counts”. This represents a complication but also a great opportunity for predictive computational science. By a noteworthy coincidence, in fact, the evolving picture of catalysis by sub-nanometer clusters at the experimental level perfectly matches recent developments in theoretical tools, in which both software and hardware advances make that systematic searches on very small nanometric particles are now accessible to first-principles computational protocols.

Two main issues are however faced when investigating at the theoretical level heterogeneous catalysis by sub-nanometer metal clusters. First, with respect to catalysis on extended metal surfaces there is no bulk system to constrain the catalytic component into a limited number of competing configurations. This entails a greater structural freedom and a fluxional character of the composite metal-nanocluster-plus-ligands system, whence the need of efficient computational algorithms for structural exploration and sampling. A second issue lies in the fact that at this size range empirical potentials for the metal-metal and metal-ligand interactions are often not accurate enough to produce reliable results, also because of the strong many-body (cooperative) effects taking place in these systems. First-principles calculations must therefore be used, which are computationally much more demanding. We assume that any realistic simulation of heterogeneous nanocatalysis should be based on some kind of systematic search employing first-principles calculations.

In a simple way, a theoretical/computational approach to nanocatalysis can be envisaged along the lines of the previous discussion in section 5.1 or on the Pt insertion into a C–H bond as consisting of the following steps [BarcaroCEJ2007]: (1) exploring the PES of the combined substrate/metal-cluster/adsorbants system and deriving the set of local minima via first-principles global optimization calculations; (2) determining the energy barriers and the Arrhenius prefactors for transformation among these local minima; (3) simulating the catalytic dynamics at a finite temperature via e.g. kinetic Monte Carlo simulations [ReuterPRB2006]. After all, first-principles global optimization techniques are well established in the computational context, and in recent years a density-functional/basin-hopping (DF-BH) approach was actually applied in our laboratory to metal clusters both in the gas-phase [ApraPRB2006] and supported on an oxide surface [BarcaroCEJ2007; BarcaroJPCC2007; BarcaroPRB2007], including oxygen ligands [BarcaroPRB2007]. Moreover, dynamical processes such as the growth of supported metal clusters were successfully simulated using an approach similar in spirit to that suggested above [XuPRL2005; BarcaroPRL2005]. We indeed tested this approach in the field of nanocatalysis (unpublished work) but found it not fully satisfactory. There are two main drawbacks. The first one is connected with the fact that catalysis is often a kinetics-driven rather than a thermodynamics-driven process. For example, in the partial oxidation of propylene the desired product is propylene oxide or acrolein, not CO_2 and H_2O. The attraction basin in the phase space associated with partial oxidation is much thinner than that related to full combustion. Unless one devises ad-hoc tricks and constraints of limited validity, a global optimization search will thus spend most of the time sampling the basin of undesired thermodynamically favored products. The reason why these products are not achieved is of course connected with energy barriers: those leading to CO_2 and H_2O are larger than those for partial oxidation, and it seems sensible to use this information in the global search. The second drawback is that the number of local minima generated by the global optimization search, even in simple system such as catalysis by subnanometer clusters and limiting the energy interval to – say – few eV from the global minimum, is of the order of a few hundreds. The number of pairs of local minima for which a kinetic constant should in principle be calculated is therefore of the order of several tens of thousands, somewhat impractical with the present computational resources and certainly very inefficient as the vast majority of these energy barriers are larger than 1-2 eV. One can select a posteriori a subset of the local minima on the basis of ad-hoc criteria, but again this procedure lacks generality and is liable to overlooking important reaction pathways.

An alternative and very promising possibility has been recently proposed in Ref. [NegreirosNS2012], where a rigorous computational approach to heterogeneous nanocatalysis by subnanometer metal clusters (pure and alloyed) was presented and discussed in depth. This approach is based on a computational sampling of the reaction paths in nanocatalysis via a global search in the phase space of structures and stoichiometry combined with filtering which takes into account the given

experimental conditions (catalytically relevant temperature and reactant pressure), i.e. in which – at variance with global optimization algorithms [WalesS1999] – reaction rates are evaluated in real time and are used to orient the system evolution according to the given experimental conditions, thus realistically mimicking the reaction paths occurring at a specific site during the catalytic process. The approach is thus named Reactive Global Optimization (RGO). It relies on the idea that the preferred reaction path should be automatically selected on the basis of energy barriers (or, better, kinetic constants), and corresponds to an incremental exploration of the disconnectivity diagram (or tree or graph) of the system [WalesBook2003]. Starting from any node in the tree, the algorithm explores its immediate neighborhood and proceeds from one vertex to the next according to simple rules based on the set of reaction rates. In this sense the algorithm is fully realistic, as it mimics the way a real system actually behaves, following low-energy-barrier (high-reaction-rate) paths and pruning low-reaction-rate branches. The RGO algorithm is also ideally adapted to massively parallel computers, as exploring a graph is a disconnected sequential task (which is less true for global optimization algorithms). In this regard, it is important to underline that the proposed protocol can efficiently exploit the cumulative and non-overlapping character character of the knowledge so generated. This is achieved by simply requiring that all the virtual actors running in parallel store their results into a common area so that unexplored branches can be picked up by a parallel process and unnecessary duplications can be avoided (which represent a great burden for global optimization algorithms). Finally, the proposed approach produces results of general significance in a two-fold respect: (1) it is possible to define databases of local minima and saddle points as a reference for future studies, and (2) these databases can be analyzed in terms of topological classes thus allowing one to derive general trends, rationalize experimental findings and predict grand phenomena. In Ref. [NegreirosNS2012], the approach was tested in the specific case of oxidation reactions catalyzed by Ag_3 supported on a model oxide substrate, the MgO(100) surface, via first-principles density-functional theory (DFT) calculations, focusing in particular on propylene partial oxidation and CO oxidation. From this study several general conclusions were derived: the crucial effect of the ionic substrate on the catalytic activity of small metal clusters, the role of reaction energy barriers in the interplay between thermodynamics and kinetics in the outcome of the catalytic process, and the analogy between the results obtained on the MgO(100) surface and on a rather different support in the literature pointing to the MgO(100) surface as a good model of a simple ionic substrate. Finally, we note as an interesting development that one can elaborate upon this protocol by combining it with previous proposals, e.g., one can bias the structural moves of a single actor: (1) by using an order parameter [BarcaroJPCB2006b; BorbonJPCC2007; FerrandoPCCP2008] or a metadynamics routine [IannuzziPRL2003]; (2) on the basis of global (rather than local) information on the parallel actors (or "walkers") [RossiCPL2006].

We conclude this section by simply mentioning a fascinating possibility which we believe will become a topic of great interest in the future: the use of external (in

particular electric) fields to modify charge transfer effects at a metal-nanoparticle/oxide-substrate interface and thus orient the physics and chemistry of adsorption and in turn the growth, the catalytic properties of the system, etc. In the case of an electric field, this possibility is particularly intriguing for thin or ultra-thin oxide films, as for such systems one can realize a very simple condenser set-up by exploiting the metal support as one of the electrodes (see Fig. 64), a possibility which is currently being investigated in collaboration with Netzer's experimental group in Graz.

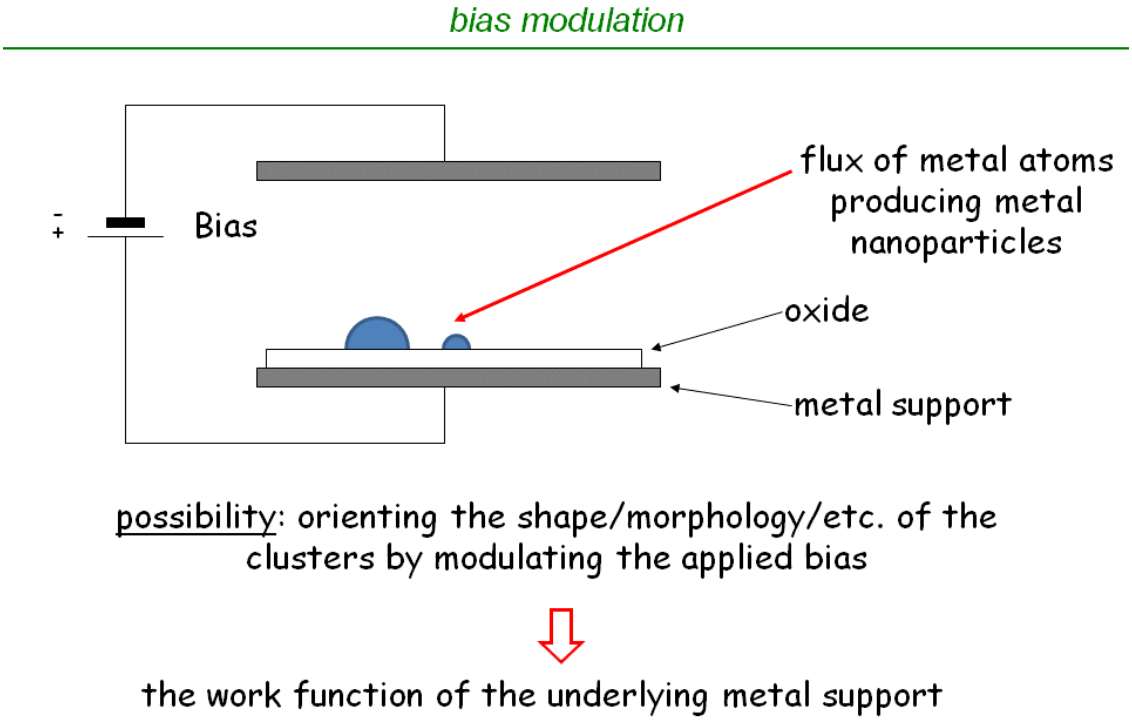

Fig. 64: Use of external electric fields to influence charge transfer effects at a metal/oxide interface and orient the physics and chemistry of adsorption.

5.5 Perspectives

In this Thesis, which is far from being exhaustive especially in terms of literature citation (and we apologize in advance with the colleagues whose important contributions have not been quoted for reasons of space or needs of presentation), we have presented what in our opinion are the specific (sometimes unique) features of the chemical bond in metal nanoclusters and nanoalloys from the theoretical point of view. We have discussed some of the techniques developed to model and simulate these systems, and pointed out their advantages and limitations. In particular, attention has also been focused on concepts and methods developed from a

theoretical point of view which can help rationalize the available information, provide a general framework for experimental investigations, and set the ground for a predictive computational science. We showed that interesting results have already been obtained in several cases and suggested that many more are likely to be expected in the next future, considering the increasing accuracy of first-principles methods, the advances in and the ever-increasing accessibility of computer hardware and software by which the application of first-principles approaches is becoming feasible in practice to a large set of users via commonly available computational resources. In particular in the field of the properties: catalytic, optical, magnetic, etc., we believe that rigorous computational methods are nowadays finally becoming able to treat realistic systems with sufficient accuracy and will give a decisive contribution to future advances in both basic and oriented research and industrial applications. Our hope is that the present work will represent a step in this direction, contributing to bringing theory closer to experiment, promoting interdisciplinary research, and advancing the general field of metal nanoclusters and nanoalloys.

List of publications

The list of selected publications relevant to the work described in the present Thesis and attached to it follow, arranged according to the year of publication. Publications not attached are available upon request.

[FortunelliJMS1999b] A. Fortunelli A. M. Velasco, J. Mol. Struct. (Theochem) 487, 251 (1999).

[ApraJMS2000] E. Aprà, A. Fortunelli, J. Mol. Struct. (TheoChem) 501-502, 251 (2000).

[BalettoJCP2002] F. Baletto, R. Ferrando, A, Fortunelli, F. Montalenti, C. Mottet, J. Chem. Phys. 116, 3856 (2002).

[ApraJPCA2003] E. Aprà A. Fortunelli, J. Phys. Chem. A 107, 2934 (2003).

[ApraPRL2004] E. Aprà, F. Baletto, R. Ferrando, A. Fortunelli, Phys. Rev. Lett. 93, 065502 (2004).

[RossiPRL2004] G. Rossi, A. Rapallo, C. Mottet, A. Fortunelli, F. Baletto, R. Ferrando, Phys. Rev. Lett. 93, 105503 (2004).

[BarcaroJCTC2005] G. Barcaro A. Fortunelli, J. Chem. Theory Comput. 1, 972 (2005).

[FerrandoPRB2005] R. Ferrando, A. Fortunelli, G. Rossi, Phys. Rev. B 72, 085449 (2005).

[BarcaroPRL2005] G. Barcaro, A. Fortunelli, F. Nita, R. Ferrando, Phys. Rev. Lett. 95, 246103 (2005).

[ApraPRB2006] E. Aprà, R. Ferrando, A. Fortunelli, Phys. Rev. B 73, 205414 (2006).

[BarcaroJPCB2006a] G. Barcaro A. Fortunelli, J. Phys. Chem. B 110, 21021 (2006).

[BarcaroJPCB2006b] G. Barcaro, A. Fortunelli, G. Rossi, F. Nita, R. Ferrando, J. Phys. Chem. B 110, 23197 (2006).

[BorbonJPCC2007] L. O. Paz-Borbon, R. L. Johnston, G. Barcaro, A. Fortunelli, J. Phys. Chem. C 111, 2936 (2007).

[BarcaroNJP2007] G. Barcaro A. Fortunelli, New J. Phys. 9, 22 (2007).

[BarcaroPRL2007] G. Barcaro, A. Fortunelli, G. Rossi, F. Nita, R. Ferrando, Phys. Rev. Lett. 98, 156101 (2007).

[BarcaroTCA2007] G. Barcaro, M. Causà , A. Fortunelli, Theor. Chem. Acc. 118, 807 (2007).

[BarcaroCEJ2007] G. Barcaro, E. Aprà , A. Fortunelli, Chem. Eur. J. 13, 6408 (2007).

[BarcaroJPCC2007] G. Barcaro A. Fortunelli, J. Phys. Chem. C 111, 11384 (2007).

[BarcaroPRB2007] G. Barcaro A. Fortunelli, Phys. Rev. B. 76, 165412 (2007).

[BorbonJCP2008] L. O. Paz-Borbon, R. L. Johnston, G. Barcaro, A. Fortunelli, J. Chem. Phys. 128, 134517 (2008).

[BarcaroPCCP2008] G. Barcaro, A. Fortunelli, G. Granozzi, Phys. Chem. Chem. Phys. 10, 1876 (2008).

[FerrandoPCCP2008] R. Ferrando, A. Fortunelli, R. L. Johnston, Phys. Chem. Chem. Phys. 10, 640 (2008).

[FerrandoACSN2008] R. Ferrando, G. Rossi, F. Nita, G. Barcaro, A. Fortunelli, ACS Nano 2, 1849 (2008).

[OlivierPRB2008] S. Olivier, R. Conte, A. Fortunelli, Phys. Rev. B 77, 054104 (2008).

[SedonaJPCL2008] F. Sedona, M. Sambi, L. Artiglia, G. A. Rizzi, A. Vittadini, A. Fortunelli, G. Granozzi, J. Phys. Chem. C 112, 3187 (2008).

[BarcaroJPCC2009] G. Barcaro, A. Fortunelli, G. Granozzi, F. Sedona, J. Phys. Chem. C 113, 1143 (2009).

[BarcaroTCA2009] G. Barcaro A. Fortunelli, Theor. Chem. Acc. 123, 317 (2009).

[FerrandoJCP2009] R. Ferrando, G. Rossi, A. C. Levi, Z. Kuntová , F. Nita, G. Barcaro, A. Fortunelli, A. Jelea, C. Mottet, J. Goniakowski, J. Chem. Phys. 130, 174702 (2009).

[GoniakowskiJCP2009] J. Goniakowski, A. Jelea, C. Mottet, G. Barcaro, A. Fortunelli, Z. Kuntová, F. Nita, A. C. Levi, G. Rossi, R. Ferrando, J. Chem. Phys. 130, 174703 (2009).

[FerrandoPRL2009] R. Ferrando, G. Barcaro, A. Fortunelli, Phys. Rev. Lett. 102, 216102 (2009).

[BorbonEPJD2009] L. O. Paz-Borbon, R. L. Johnston, G. Barcaro, A. Fortunelli, Eur. Phys. J. D 52, 131 (2009).

[FerrandoJPCM2009] R. Ferrando A. Fortunelli, J. Phys. Cond. Mat. 21, 264001 (2009).

[BarcaroJPCL2010] G. Barcaro, R. Ferrando, A. Fortunelli, G. Rossi, J. Phys. Chem. Lett. 1, 111 (2010).

[WestJPCC2010] P. West, R. L. Johnston, G. Barcaro, A. Fortunelli, J. Phys. Chem. C 114, 19678 (2010).

[BarcaroNL2011a] G. Barcaro, A. Fortunelli, M. Polak, L. Rubinovich, NanoLett. 11, 1766 (2011).

[MolinaCT2011] L. M. Molina, S. Lee,. Fortunelli, B. Lee, S. Seifert, R. E. Winans, J. W. Elam, M. J. Pellin, I. Barke, V. von Oeynhausen, Y. Lei, R. J. Meyer, J. A. Alonso, A. F. Rodriguez, A. Kleibert, S. Giorgio, C. R. Henry, K. H. Meiwes-Broer, S. Vajda, Cat. Today 160, 116 (2011) .

[DuranteJPCC2011] N. Durante, A. Fortunelli, M. Broyer, M. Stener, J. Phys. Chem. C 115, 6277 (2011).

[GavioliPSS2011] L. Gavioli, E. Cavaliere, S. Agnoli, G. Barcaro, A. Fortunelli, G. Granozzi, Prog. Surf. Sci., 86, 59 (2011).

[BarcaroNL2011b] G. Barcaro, L. Sementa, F. R. Negreiros, R. Ferrando, A. Fortunelli, NanoLett. 11, 5542 (2011).

[NegreirosNS2012] F. R. Negreiros, E. Aprà, G. Barcaro, L. Sementa, S. Vajda, A. Fortunelli, Nanoscale, 4, 1208 (2012).

List of figures

List of tables

Bibliography

[AbrikosovRPP2008] A. I. Abrikosov, Rep. Progr. Phys. 71, 046501 (2008).

[AdamoJCP1995] C. Adamo, V. Barone, A. Fortunelli, J. Chem. Phys. 102, 384 (1995)

[AdamoJCP1999] C. Adamo, V. Barone, J. Chem. Phys. 110, 6158 (1999).

[AgnoliJPCB2005] S. Agnoli, M. Sambi, G. Granozzi, J. Schoiswohl, S. Surnev, F. P. Netzer, M. Ferrero, A. M. Ferrari, C. Pisani, J. Phys. Chem. B 109, 17197 (2005).

[AguadoJCP2010] A. Aguado and J. M. Lopez, J. Chem. Phys. 133, 094302 (2010).

[AhlrichsPCCP1999] R. Ahlrichs, S. D. Elliott, Phys. Chem. Chem. Phys. 1, 13 (1999).

[AkolaJACS2008] J. Akola, M. Walter, R. L. Whetten, H. Hakkinen, H. Grönbeck, J. Am. Chem. Soc. 130, 3756 (2008).

[AltieriPRB2009] S. Altieri, M. Finazzi, H. H. Hsieh, M. W. Havekort, H. J. Lin, C. T. Chen, S. Frabboni, G. C. Gazzardi, A. Rot, S. Valeri, Phys. Rev. B 79, 174431 (2009).

[AMSHandbook1992] H. Baker, ed., Alloy Phase Diagrams (ASM International, Materials Park, OH, USA, 1992).

[AnisimovPRB1991] V. I. Anisimov, J. Zaanen, O. K. Andersen, Phys. Rev. B 44, 943 (1991).

[AnisimovPRB1993] V. I. Anisimov, I. V. Solovyev, M. A. Korotin, M. T. Czyzyk, G. A. Sawatzky, Phys. Rev. B 48, 16929 (1993).

[AokiPMS2007] M. Aoki, D. Nguyen-Manh, D. G. Pettifor, V. Vitek, Progr. Mat. Sci. 52, 154 (2007).

[ApraIJQC2004] E. Aprà, E. A. Carter, A. Fortunelli, Int. J. Quantum Chem. 100, 277 (2004).

[ApraJMS2000] E. Aprà, A. Fortunelli, J. Mol. Struct. (TheoChem) 501-502, 251 (2000).

[ApraJPCA2003] E. Aprà A. Fortunelli, J. Phys. Chem. A 107, 2934 (2003).

[ApraPRB2006] E. Aprà, R. Ferrando, A. Fortunelli, Phys. Rev. B 73, 205414 (2006).

[ApraPRL2004] E. Aprà, F. Baletto, R. Ferrando, A. Fortunelli, Phys. Rev. Lett. 93, 065502 (2004).

[ArenzCPC2006] M. Arenz, U. Landman, U. Heiz, ChemPhysChem 7, 1871 (2006).

[AtanasovEPJD2009] I. S. Atanasov, M. Hou, Eur. Phys. J. D 52, 51 (2009).

[AtanasovSS2009] I. S. Atanasov, M. Hou, Surf. Sci. 603, 2639 (2009).

[AustinS1970] I. G. Austin and N. F. Mott, Science 168, 71 (1970).

[BaePRB2005] Y. C. Bae, V. Kumar, H. Osanai, Y. Kawazoe, Phys. Rev. B 72, 125427 (2005).

[BalettoJCP2002] F. Baletto, R. Ferrando, A, Fortunelli, F. Montalenti, C. Mottet, J. Chem. Phys. 116, 3856 (2002).

[BalettoPRB2001] F. Baletto, C. Mottet, R. Ferrando, Phys.Rev. B 63, 155408 (2001).

[BalettoPRL2000] F. Baletto, C. Mottet, R. Ferrando, Phys. Rev. Lett. 84, 5544 (2000).

[BalettoRMP2005] F. Baletto R. Ferrando, Rev. Mod. Phys. 77, 371 (2005).

[BaoPRB2009] K. Bao, S. Goedecker, K. Koga, F. Lancon, A. Neelov, Phys. Rev. B 79, 041405 (2009).

[BarcaroCEJ2007] G. Barcaro, E. Aprà , A. Fortunelli, Chem. Eur. J. 13, 6408 (2007).

[BarcaroCPL2008] G. Barcaro A. Fortunelli, Chem. Phys. Lett. 457, 143 (2008).

[BarcaroFD2008] G. Barcaro A. Fortunelli, Faraday Disc. 138, 37 (2008).

[BarcaroJCP2010] G. Barcaro, I. O. Thomas A. Fortunelli, J. Chem. Phys. 132, 124703 (2010).

[BarcaroJCTC2005] G. Barcaro A. Fortunelli, J. Chem. Theory Comput. 1, 972 (2005).

[BarcaroJPCA2009] G. Barcaro A. Fortunelli, J. Phys. Chem. A 113, 14860 (2009).

[BarcaroJPCB2006a] G. Barcaro A. Fortunelli, J. Phys. Chem. B 110, 21021 (2006).

[BarcaroJPCB2006b] G. Barcaro, A. Fortunelli, G. Rossi, F. Nita, R. Ferrando, J. Phys. Chem. B 110, 23197 (2006).

[BarcaroJPCC2007] G. Barcaro A. Fortunelli, J. Phys. Chem. C 111, 11384 (2007).

[BarcaroJPCC2009] G. Barcaro, A. Fortunelli, G. Granozzi, F. Sedona, J. Phys. Chem. C 113, 1143 (2009).

[BarcaroJPCC2011] G. Barcaro, M. Broyer, N. Durante, A. Fortunelli, M. Stener, J. Phys. Chem. C 115, 24085 (2011).

[BarcaroJPCL2010] G. Barcaro, R. Ferrando, A. Fortunelli, G. Rossi, J. Phys. Chem. Lett. 1, 111 (2010).

[BarcaroNJP2007] G. Barcaro A. Fortunelli, New J. Phys. 9, 22 (2007).

[BarcaroNL2011a] G. Barcaro, A. Fortunelli, M. Polak, L. Rubinovich, NanoLett. 11, 1766 (2011).

[BarcaroNL2011b] G. Barcaro, L. Sementa, F. R. Negreiros, R. Ferrando, A. Fortunelli, NanoLett. 11, 5542 (2011).

[BarcaroPCCP2008] G. Barcaro, A. Fortunelli, G. Granozzi, Phys. Chem. Chem. Phys. 10, 1876 (2008).

[BarcaroPRB2007] G. Barcaro A. Fortunelli, Phys. Rev. B. 76, 165412 (2007).

[BarcaroPRL2005] G. Barcaro, A. Fortunelli, F. Nita, R. Ferrando, Phys. Rev. Lett. 95, 246103 (2005).

[BarcaroPRL2007] G. Barcaro, A. Fortunelli, G. Rossi, F. Nita, R. Ferrando, Phys. Rev. Lett. 98, 156101 (2007).

[BarcaroTCA2007] G. Barcaro, M. Causà , A. Fortunelli, Theor. Chem. Acc. 118, 807 (2007).

[BarcaroTCA2009] G. Barcaro A. Fortunelli, Theor. Chem. Acc. 123, 317 (2009).

[BardiSS1992] U. Bardi, A. Atrei, G. Rovida, Surf. Sci. 268, 87 (1992).

[BaroneJACS1998] V. Barone, A. Bencini, M. Cossi, A. Di Matteo, M. Mattesini, F. Totti, J. Am. Chem. Soc 120, 7069 (1998).

[BarthNT2006] C. Barth, O. H. Pakarinen, A. S. Foster, C. R. Henry, Nanotechnology 17, S128 (2006).

[BarthPRL2003] C. Barth C. R. Henry, Phys. Rev. Lett. 91, 196102 (2003).

[BaskesPRB1992] M. Baskes, Phys. Rev. B 46, 2727 (1992).

[BaskesPRL1987] M. Baskes, Phys. Rev. Lett. 59, 2666 (1987).

[BazinACA2000] D. Bazin, C. Mottet, G. Treglia, Appl. Cat. A, 200, 47 (2000)

[BeckeJCP1993] A. D. Becke, J. Chem. Phys. 98, 1372 (1993).

[BeckeJCP2005] A. D. Becke, J. Chem. Phys. 122, 064101 (2005).

[BeckerBBGPC1995] A. Becker, S. Benfer, P. Hofmann, K.-H. Jacob, E. Knozinger, Ber. Bunsen Ges. Phys. Chem. 99, 1328 (1995).

[BeckerTCC2009] C. Becker K. Wandelt, Top. Curr. Chem. 287, 45 (2009).

[BengtssonPRB1999] L. Bengtsson, Phys. Rev. B 59, 12301 (1999).

[BinnsSSR2001] C. Binns, Surf. Sci. Rep. 44, 1 (2001).

[BiswasPRL2010] A. Biswas, D. Siegel, D. N. Seidman, Phys. Rev. Lett. 105, 076102 (2010).

[BogicevicSS1999] A. Bogicevic D. Jennison, Surf. Sci. 437, L741 (1999).

[BogicevicSS2002] A. Bogicevic D. R. Jennison, Surf. Sci. 515, L481 (2002).

[BondBook1987] G. C. Bond, Heterogeneous Catalysis (Oxford University Press, Oxford, UK, 1987), 3rd ed.

[BondBook2006] G. C. Bond, C. Louis, D. T. Thomson, Catalysis by Gold (Imperial College Press, London, UK, 2006).

[BonnemannEJIC2001] H. Bonnemann, R. M. Richards, Eur. J. Inorg. Chem. 2455 (2001).

[BoothJCP2010] G. H. Booth, A. Alavi, J. Chem. Phys. 132, 174104 (2010).

[BorbonEPJD2009] L. O. Paz-Borbon, R. L. Johnston, G. Barcaro, A. Fortunelli, Eur. Phys. J. D 52, 131 (2009).

[BorbonJCP2008] L. O. Paz-Borbon, R. L. Johnston, G. Barcaro, A. Fortunelli, J. Chem. Phys. 128, 134517 (2008).

[BorbonJPCC2007] L. O. Paz-Borbon, R. L. Johnston, G. Barcaro, A. Fortunelli, J. Phys. Chem. C 111, 2936 (2007).

[BorbonPCCP2007] L. O. Paz-Borbon, T. V. Mortimer-Jones, R. L. Johnston, A. Posada-Amarillas, G. Barcaro, A. Fortunelli, Phys. Chem. Chem. Phys. 9, 5202 (2007).

[BorbonPRB2012] L. O. Paz-Borbon, G. Barcaro, A. Fortunelli, S. V. Levchenko, Phys. Rev. B 85, 155409 (2012).

[BornAP1927] M. Born, J. R. Oppenheimer, Ann. Phys. 84, 457 (1927).

[BornholmZPD1991] S. Bornholm, J. Borggreen, O. Echt, K. Hansen, J. Pedersen, H. D. Rasmussen, Z. Phys. D, Mol. Clusters 19, 47 (1991).

[BroyerFD2007] M. Broyer, E. Cottancin, J. Lermé, M. Pellarin, N. Del Fatti, F. Valle, J. Burgin, C. Guillon, P. Langot, Faraday Discuss. 138, 137 (2008).

[BruneN1998] H. Brune, M. Giovannini, K. Bromann, K. Kern, Nature 394, 451 (1998).

[BurdaCR2005] C. Burda, X. Chen, R. Narayanan, M. A. El-Sayed, Chem. Rev. 105, 1025 (2005).

[BurkeJCP1998] K. Burke, J. Perdew, M. Ernzerhof, J. Chem. Phys. 109, 3760 (1998).

[CarPRL1985] R. Car, M. Parrinello, Phys. Rev. Lett. 55, 2471 (1985).

[CaroBook2008] A. Caro, in "Materials Issues for Generation IV Systems" V. Ghetta et al. Eds.; Springer Science + Business Media B. V., Berlin, 2008.

[CarrascoJCP2006] J. Carrasco, N. Lopez, F. Illas, H.-J. Freund, J. Chem. Phys. 125, 074711 (2006).

[CarrascoPRL2004] J. Carrasco, N. Lopez, F. Illas, Phys. Rev. Lett. 93, 225502 (2004).

[CasidaBook1995] M. E. Casida, in "Recent Advances in Density-Functional Methods"; Chong, D. P., ed.; World Scientific: Singapore, 1995; p 155.

[CausaPS1988] M. Causà, R. Colle, R. Dovesi, A. Fortunelli, C. Pisani, Phys. Scripta 38, 194 (1988).

[CavalierePCCP2009] E. Cavaliere, I. Kholmanov, L. Gavioli, F. Sedona, S. Agnoli, G. Granozzi, G. Barcaro, A. Fortunelli, Phys. Chem. Chem. Phys. 11, 11305 (2009).

[CavalierePCCP2011] E. Cavaliere, L. Artiglia, G. Barcaro, G. A. Rizzi, F. Bondino, A. Fortunelli, L. Gavioli, G. Granozzi, Phys. Chem. Chem. Phys. 13, 17171 (2011).

[CCDB] The Cambridge Cluster Database, D. J. Wales, J. P. K. Doye, A. Dullweber, M. P. Hodges, F. Y. Naumkin F. Calvo, J. Hernandez-Rojas T. F. Middleton, URL http://www-wales.ch.cam.ac.uk/CCD.html.

[CerbelaudPCCP2011] M. Cerbelaud, R. Ferrando, G. Barcaro, A. Fortunelli, Phys. Chem. Chem. Phys. 13, 10232 (2011).

[ChakiJACS2008] N. K. Chaki, Y. Negishi, H. Tsunoyama, Y. Shichibu, T. Tsukuda, J. Am. Chem. Soc. 130, 8608 (2008).

[ChanNL2007] G. H. Chan, J. Zhao, E. M. Hicks, G. C. Schatz, R. P. Van Duyne, Nano Lett. 7, 1947 (2007).

[ChenJPCC2010] H. Chen, J. M. McMahon, M. A. Ratner, G. C. Schatz, J. Phys. Chem. C 114, 14384 (2010).

[ChenJPCM2008] M. S. Chen D. W. Goodman, J. Phys.: Condens. Matt. 20, 264013 (2008).

[ChenTC2007] M. S. Chen, D. W. Goodman, Top. Catal. 44, 41 (2007).

[ChiesaACR2006] M. Chiesa, M. C. Paganini, E. Giamello, D. M. Murphy, C. D. Valentin, G. Pacchioni, Acc. Chem. Res. 39, 861 (2006).

[ChiuPRL2006] Y. P. Chiu, L. W. Huang, C. M. Wei, C. S. Chang, T. T. Tsong, Phys. Rev. Lett. 97, 165504 (2006).

[ChoAP2007] Y. Cho, C. Kim, H.-S. Ahn, E. Cho, T.-E. Kim, S. J. Han, Appl. Phys. 101, 083710 (2007).

[ClaridgeACSN2009] S.A. Claridge, A. W. Castleman Jr., S. N. Khanna, C.B. Murray, A. Sen, P. S. Weiss, ACS Nano 3, 244 (2009).

[CococcioniPRB2005] M. Cococcioni, S. de Gironcoli, Phys. Rev. B 71, 035105 (2005).

[CohenBook2006] C. Cohen-Tannoudji, B. Diu, F. Laloe, "Quantum Mechanics", Wiley-Interscience, 2006.

[ColleTCA1975] R. Colle, O. Salvetti, Theoret. Chim. Acta, 37, 329 (1975).

[CoquetJMC2006] R. Coquet, G. J. Hutchings, S. H. Taylor, D. J. Willock, J. Mater. Chem. 16, 1978 (2006).

[CottancinPRB2000] E. Cottancin, J. Lermé, M. Gaudry, M. Pellarin, J. L. Vialle, M. Broyer, B. Prével M. Treilleux, P. Mélinon, Phys. Rev. B 62, 5179 (2000).

[DanielCR2004] M.-C. Daniel D. Astruc, Chem. Rev. 104, 293 (2004).

[DawPRB1984] M. Daw M. Baskes, Phys. Rev. B 29, 6443 (1984).

[deHeerRMP1993] W. A. deHeer, Rev. Mod. Phys. 65, 611 (1993).

[delCampoJCP2008] J. M. del Campo, A. M. Köster, J. Chem. Phys. 129 (2008) 024107

[DelFattiGB2008] N. Del Fatti, D. Christofilos, F. Vallée, Gold Bulletin 41, 147 (2008).

[DelVittoJPCB2005] A. Del Vitto, G. Pacchioni, F. Delbecq, P. Sautet, J. Phys. Chem. B 109, 8040 (2005).

[DietzJCP1981] T. G. Dietz, M. A. Duncan, D. E. Powers, R. E. Smalley, J. Chem. Phys. 74, 6511 (1981).

[DinsdaleCALPHAD1991] A. T. Dinsdale, CALPHAD 15, 317 (1991).

[DiracPCPS1930] P. A. M. Dirac, Proc. Cambridge Phil. Soc. 26, 376 (1930).

[DiracPRS1928] P. A. M. Dirac, Proc. R. Soc. 117, 610 (1928).

[DiValentinSS2006] C. Di Valentin, A. Scagnelli, G. Pacchioni, T. Risse, H.-J. Freund, Surf. Sci. 600, 2434 (2006).

[Dovesi2006] R. Dovesi, V. R. Saunders, R. Roetti, R. Orlando, M. Zicovich-Wilson, F. Pascale, B. Civalleri, K. Doll, N. M. Harrison, I. J. Bush, P. D'arco, M. Llunel, CRYSTAL06.

[DoyeJCP1995] J. P. K. Doye, D. J. Wales, R. S. Berry, J. Chem. Phys. 103, 4234 (1995).

[DoyePRL2001] J. P. K. Doye and D. Wales Phys. Rev. Lett. 86, 5719 (2001).

[DoyePRL2005] J. P. K. Doye L. Meyer, Phys. Rev. Lett. 95, 063401 (2005).

[DubostN1986] B. Dubost, J. M. Lang, M. Tanaka, P. Sainfort, M. Audier, Nature 324, 48 (1986).

[DunlapMP2010] B. I. Dunlap, N. Rosch, S. B. Trickey, Mol. Phys. 108, 3167 (2010).

[DuranteJPCC2011] N. Durante, A. Fortunelli, M. Broyer, M. Stener, J. Phys. Chem. C 115, 6277 (2011).

[EbertRPP1996] H. Ebert, Rep. Progr. Phys. 59, 1665 (1996).

[EkardtPRB1984] W. Ekardt, Phys. Rev. B 29, 1558 (1984).

[ErcolessiPRL1986] F. Ercolessi, E. Tosatti, M. Parrinello, Phys. Rev. Lett. 57, 719 (1986).

[ErtlPT1999] G. Ertl H.-J. Freund, Phys. Today 52, 32 (1999).

[FakenCMS1994] D. Faken H. Jónsson, Comput. Mat. Sci. 2, 279 (1994).

[FaradayPTRSL1857] M. Faraday, Philos. Trans. R. Soc. London 147, 145, (1857).

[FavrePRB2006] L. Favre, V. Dupuis, E. Bernstein, P. Melinon, A. Perez, Phys. Rev. B 74, 014439 (2006).

[FerrandoACSN2008] R. Ferrando, G. Rossi, F. Nita, G. Barcaro, A. Fortunelli, ACS Nano 2, 1849 (2008).

[FerrandoCR2008] R. Ferrando, J. Jellinek, R. L. Johnston, Chem. Rev. 108, 845 (2008).

[FerrandoJCP2009] R. Ferrando, G. Rossi, A. C. Levi, Z. Kuntová , F. Nita, G. Barcaro, A. Fortunelli, A. Jelea, C. Mottet, J. Goniakowski, J. Chem. Phys. 130, 174702 (2009).

[FerrandoJPCM2009] R. Ferrando A. Fortunelli, J. Phys. Cond. Mat. 21, 264001 (2009).

[FerrandoPCCP2008] R. Ferrando, A. Fortunelli, R. L. Johnston, Phys. Chem. Chem. Phys. 10, 640 (2008).

[FerrandoPRB2005] R. Ferrando, A. Fortunelli, G. Rossi, Phys. Rev. B 72, 085449 (2005).

[FerrandoPRL2009] R. Ferrando, G. Barcaro, A. Fortunelli, Phys. Rev. Lett. 102, 216102 (2009).

[FerrariPCCP1999] A. M. Ferrari, C. Xiao, K. M. Neyman, G. Pacchioni, N. Rösch, Phys. Chem. Chem. Phys. 1, 4655 (1999).

[FichthornPRB2003] K. A. Fichthorn, M. L. Merrick, M. Scheffler, Phys. Rev. B 68, 041404 (2003).

[FinazziSSR2009] M. Finazzi, L. Duò , F. Cicacci, Surf. Sci. Rep. 64, 139 (2009).

[FortunelliBook1992] Fortunelli A., Desalvo A., Salvetti O., Albertazzi E. “Cluster simulations of amorphous silicon, with and without an impurity

boron atom" In "Cluster Models for Surface and Bulk Phenomena", G. Pacchioni et al. eds., Plenum Press, New York, p. 595 (1992).

[FortunelliCPL1991] A. Fortunelli, O. Salvetti, Chem. Phys. Lett. 186, 372 (1991).

[FortunelliCPL1994] A. Fortunelli, M. Selmi, Chem. Phys. Lett. 223, 390 (1994).

[FortunelliCPL1996] A. Fortunelli, Chem. Phys. Lett. 248, 50 (1996).

[FortunelliIJQC2004] A. Fortunelli A. M. Velasco, Int. J. Quantum Chem. 99, 654 (2004).

[FortunelliJCC1991] A. Fortunelli, O. Salvetti, J. Comp. Chem. 12, 36 (1991).

[FortunelliJCP1997] A. Fortunelli, A. Painelli, J. Chem. Phys. 106, 8041 (1997).

[FortunelliJMS1995] A. Fortunelli, M. Selmi J. Mol. Struct. (TheoChem) 337, 25 (1995).

[FortunelliJMS1998] A. Fortunelli, J. Mol. Struct. (TheoChem) 428, 9 (1998).

[FortunelliJMS1999a] A. Fortunelli, J. Mol. Struct. (TheoChem) 493, 233 (1999).

[FortunelliJMS1999b] A. Fortunelli A. M. Velasco, J. Mol. Struct. (Theochem) 487, 251 (1999).

[FortunelliJMS2000] A. Fortunelli A. M. Velasco, J. Mol. Struct. (Theochem) 528, 1 (2000).

[FortunelliJMS2002] A. Fortunelli A. M. Velasco, J. Mol. Struct. (Theochem) 586, 17 (2002).

[FortunelliPRB1997] A. Fortunelli, A. Painelli, Phys. Rev. B 55, 16088 (1997).

[FortunelliSS1991] A. Fortunelli, O. Salvetti, G. Villani, Surf. Sci. 244, 355 (1991).

[FrankAC1958] F. C. Frank J. S. Kasper, Acta Cryst. 11, 184 (1958).

[FrankAC1959] F. C. Frank, J. S. Kasper, Acta Cryst. 12, 483 (1959).

[FreundBook2003] L. B. Freund, S. Suresh, "Thin Film Materials: stress, defect formation surface evolution", Cambridge University Press, 2003

[FreundCSR2008] H.-J. Freund G. Pacchioni, Chem. Soc. Rev. 37, 2224 (2008).

[FreundCT2005] H.-J. Freund, Catalysis Today 100, 3 (2005).

[FreundSS2002] H.-J. Freund, Surf. Sci. 500, 271 (2002).

[FreundSS2007] H.-J. Freund, Surf. Sci. 601, 1438 (2007).

[FreysoldtPRL2007] C. Freysoldt, P. Rinke, M. Scheffler, Phys. Rev. Lett. 99, 086101 (2007).

[FrondeliusNJP2007] P. Frondelius, H. Häkkinen, K. Honkala, New. J. Physics 9, 339 (2007).

[FurcheJCP2002] F. Furche, R. Ahlrichs, P. Weis, C. Jacob, S. Gilb, T. Bierweiler, M. Kappes, J. Chem. Phys. 117, 6982 (2002).

[GambardellaS2003] P. Gambardella, S. Rusponi, M. Veronese, S. S. Dhesi, C. Grazioli, A. Dallmeyer, I. Cabria, R. Zeller, P. H. Dederichs, K. Kern, C. Carbone, H. Brune, Science 300, 1130 (2003).

[GaoJACS2005] Y. Gao, S. Bulusu, X. C. Zheng, J. Am. Chem. Soc. 127, 15680 (2005).

[GauthierPRL2001] Y. Gauthier, M. Schmid, S. Padovani, E. Lundgren, V. Bus, G. Kresse, J. Redinger, P. Varga, Phys. Rev. Lett. 87, 036103 (2001).

[GavioliPSS2011] L. Gavioli, E. Cavaliere, S. Agnoli, G. Barcaro, A. Fortunelli, G. Granozzi, Prog. Surf. Sci., 86, 59 (2011).

[GhaziJPCA2009] S. M. Ghazi, S. Zorriasatein, D. G. Kanhere, J. Phys. Chem. A 113, 2659 (2009).

[GiannozziJPCM2009] P. Giannozzi, S. Baroni, N. Bonini, M. Calandra, R. Car, C. Cavazzoni, D. Ceresoli, G. Chiarotti, M. Cococcioni, I. Dabo, A. Dal Corso, S. De Gironcoli, S. Fabris, G. Fratesi, R. Gebauer, U. Gerstmann, C. Gougoussis, A. Kokalj, M. Lazzeri, L. Martin-Samos, N. Marzari, F. Mauri, R. Mazzarello, S. Paolini, A. Pasquarello, L. Paulatto, C. Sbraccia, S. Scandolo, G. Sclauzero, A. P. Seitsonen, A. Smogunov, P. Umari, R. M. Wentzcovitch, J. Phys.: Condens. Matter 21, 395502 (2009).

[GilbJCP2002] S. Gilb, P. Weis, R. A. M. Kappes, J. Chem. Phys. 116, 4094 (2002).

[GiordanoPRL2004] L. Giordano, C. D. Valentin, J. Goniakowski, G. Pacchioni, Phys. Rev. Lett. 92, 096105 (2004).

[GiordanoSS2005] L. Giordano G. Pacchioni, Surf. Sci. 575, 197 (2005).

[GiorgioPMB1993] S. Giorgio, C. Chapon, C. R. Henry, G. Nihoul, Phil. Mag. B 67, 773 (1993).

[GoedeckerRMP1999] S. Goedecker, Rev. Mod. Phys. 71, 1085 (1999).

[GoniakowskiJCG2005] J. Goniakowski C. Mottet, J. Cryst. Growth. 275, 29 (2005).

[GoniakowskiJCP2009] J. Goniakowski, A. Jelea, C. Mottet, G. Barcaro, A. Fortunelli, Z. Kuntová, F. Nita, A. C. Levi, G. Rossi, R. Ferrando, J. Chem. Phys. 130, 174703 (2009).

[GoniakowskiRPP2008] J. Goniakowski, F. Finocchi, C. Noguera, Rep. Progr. Phys. 71, 016501 (2008).

[GoringeRPP1997] C. M. Goringe, D. R. Bowlerand, E. Hernandez, Rep. Progr. Phys. 60, 1447 (1997).

[GracianiJPCB2006] J. Graciani, J. Oviedo, J. F. Sanz, J. Phys. Chem. B 110, 11600 (2006).

[GrimmeJCC2006] S. Grimme, J. Comput. Chem. 27, 1787 (2006).

[GronbeckJPCB2006] H. Grönbeck, J. Phys. Chem. B 110, 11977 (2006).

[GrueneS2008] P. Gruene, D. M. Rayner, B. Redlich, A. F. G. van der Meer, J. T. Lyon, G. Meijer, A. Fielicke Science 312, 674 (2008).

[GrunerPRL2008] M. E. Gruner, G. Rollmann, P. Entel, M. Farle, Phys. Rev. Lett. 100, 087203 (2008).

[HaasPRB2000] G. Haas, A. Menck, H. Brune, J. V. Barth, J. A. Venables, K. Kern, Phys. Rev. B 61, 11105 (2000).

[HaberlenJCP1997] O. D. Häberlen, S.-C. Chung, M. Stener, N. Rösch, J. Chem. Phys. 106, 5189 (1997).

[HakkinenACIE2003] H. Häkkinen, S. Abbet, A. Sanchez, U. Heiz, U. Landman, Angew. Chem. Intl. Ed. 42, 1297 (2003).

[HakkinenCSR2008] H. Hakkinen, Chem. Soc. Rev. 37, 1847 (2008).

[HakkinenJPCA2003] H. Hakkinen, B. Yoon, U. Landman, X. Li, H.-J- Zhai, L.-S. Wang, J. Phys. Chem. A 107, 6168 (2003).

[HakkinenPRL1996] H. Häkkinen M. Manninen, Phys. Rev. Lett. 76, 1599 (1996).

[HakkinenPRL2002] H. Häkkinen, M. Moseler, U. Landman, Phys. Rev. Lett. 89, 033401 (2002).

[HalasCR2011] N. J. Halas, S. Lal, W.-S. Chang, S. Link, P. Nordlander, Chem. Rev. 111, 3913 (2011).

[HammPRL2006] G. Hamm, C. Barth, C. Becker, K. Wandelt, C. R. Henry, Phys. Rev. Lett. 97, 126106 (2006).

[HandbookHetCat2008] “Handbook of Heterogeneous Catalysis”, G. Ertl, H. Knotziger, F. Schuth and J. Weitkamp Eds. (Wiley, NY, 2008, 2nd ed.)

[HaunschildJCP2010] R. Haunschild, G. E. Scuseria, J. Chem. Phys. 132, 224106 (2010).

[HeizBook2007] U. Heiz, U. Landman, Eds, “Nanocatalysis Series: Nanoscience Technology”, Springer Verlag, 2007.

[HenryPSS2005] C. R. Henry, Prog. Surf. Sci. 80, 92 (2005).

[HenrySSR1998] C. R. Henry, Surf. Sci. Rep. 31, 235 (1998).

[HerzingS2008] A. A. Herzing, C. J. Kiely, A. F. Carley, P. Landon, G. J. Hutchings, Science 321, 1331 (2008).

[HeydJCP2003] J. Heyd, G. E. Scuseria, M. Ernzerhof, J. Chem. Phys. 118, 8207 (2003).

[HinnemannJPCC2007] B. Hinnemann E. A. Carter, J. Phys. Chem. C 111, 7105 (2007).

[HohenbergPR1964] P. Hohenberg, W. Kohn, Phys. Rev. 136, 864B (1964).

[HoneycuttJPC1987] J. D. Honeycutt, H. C. Andersen, J. Phys. Chem. 91, 4950 (1987).

[HuangJCP2011] C. Huang, M. Pavone, E. A. Carter, J. Chem. Phys. 134, 154110 (2011).

[HubbardRMP1961] P. S. Hubbard, Rev. Mod. Phys. 33, 249 (1961).

[HutchingsACA2005] G. J. Hutchings, M. Haruta, Appl. Catal. A 291, 1 (2005).

[ImprotaCR2004] R. Improta, V. Barone, Chem. Rev. 104, 1231 (2004).

[InntamAPA2006] C. Inntam, L. V. Moskaleva, K. M. Neyman, V. A. Nasluzov, N. Rösch, Appl. Phys. A 82, 181 (2006).

[IannuzziPRL2003] M. Iannuzzi, A. Laio, M. Parrinello, Phys. Rev. Lett. 90, 238302 (2003).

[JaegerSS1991] R. M. Jaeger, H. Kuhlenbeck, H.-J. Freund, M. Wuttig, W. Hoffmann, R. Franchy, H. Ibach, Surf. Sci. 259, 235 (1991).

[JalboutJPCA2008] A. F. Jalbout, F. F. Contreras-Torres, L. A. Perez, I. L. Garzon, J. Phys. Chem. A 112, 353 (2008).

[JellinekCPL1996] J. Jellinek, E. B. Krissinel, Chem. Phys. Lett. 258, 283 (1996).

[JiACIE2005] M. Ji, X. Gu, X. Li, X. Gong, J. Li, L.-S. Wang, Angew. Chem. Intl. Ed. 44, 7119 (2005).

[JohanekS2004] V. Johánek, M. Laurin, A. W. Grant, B. Kasemo, C. R. Henry, J. Libuda, Science 304, 5677 (2004).

[JohanssonJPCC2008] M. P. Johansson, D. Sundholm, J. Vaara, J. Phys. Chem. C 112, 19311 (2008).

[JohnstonDT2003] R. L. Johnston, Dalton Trans. 22, 4193 (2003).

[JudaiJACS2004] K. Judai, S. Abbet, A. S. Worz, U. Heiz, C. R. Henry, J. Am. Chem. Soc. 126, 2732 (2004).

[KaishewPhDTh1952] R. Kaishew, PhD thesis, Arbeitstagung Festkoper Physik, Dresden (1952), p. 81.

[KantorovichSS1995] L. N. Kantorovich, J. M. Holender, M. J. Gillan, Surf. Sci. 343, 221 (1995).

[KarttunenCC2008] A. J. Karttunen, M. Linnolahti, T. A. Pakkanen, P. Pyykkö , Chem. Comm. 4, 465 (2008).

[KimJPCB2002] Y. D. Kim, J. Stultz, T. Wei, D. W. Goodman, J. Phys. Chem. B 106, 6827 (2002).

[KittelBook1996] C. Kittel, "Introduction to Solid State Physics", Seventh Edition, Wiley & Sons, 1996.

[KnightPRL1984] W. D. Knight, K. Clemenger, W. A. de Heer, W. A. Saunders, M. Y. Chou, M. L. Cohen, Phys. Rev. Lett. 52, 002141 (1984).

[KnozingerJMCA2000] E. Knozinger, O. Diwald, M. Sterrer, J. Mol. Catal. A 162, 83 (2000).

[KohnPR1965] W. Kohn, L. J. Sham, Phys. Rev. 140, 1133A (1965).

[KohnRMP1999] W. Kohn, Rev. Mod. Phys. 71, 1253 (1999).

[KokaljCMS2003] A. Kokalj, Comp. Mat. Sci. 28, 155 (2003).

[KolmakovJCP2000] A. Kolmakov, J. Stultz, D. W. J. Goodman, J. Chem. Phys. 113, 7564 (2000).

[KramerSS2002] J. Kramer, W. Ernst, C. Tegenkamp, H. Pfnur, Surf. Sci. 517, 87 (2002).

[KreibigBook1995] K. Kreibig M. Vollmer, Optical properties of metal clusters (Springer, New York, USA, 1995).

[LearyPRE1999] R. H. Leary J. P. K. Doye, Phys. Rev. E 60, 6320 (1999).

[LeeACIE2009] S. Lee, L. M. Molina, M. J. Lopez, J. A. Alonso, B. Hammer, B. Lee, S. Seifert, R. E. Winans, J. W. Elam, M. J. Pellina, et al., Angew. Chem. Int. Ed. 48, 1467 (2009).

[LeeAPL1998] C. Lee, A. L. Barabasi, Appl. Phys. Lett. 73, 2651 (1998).

[LeiS2010] Y. Lei, F. Mehmood, S. Lee, J. P. Greeley, B. Lee, S. Seifert, R. E. Winans, J. W. Elam, R. J. Meyer, P. C. Redfern, D. Teschner, R. Schlögl, M. J. Pellin, L. A. Curtiss, S. Vajda, Science 328, 224 (2010).

[LeroyPRL2005] F. Leroy, G. Renaud, A. Letoublon, R. Lazzari, C. Mottet, J. Goniakowski, Phys. Rev. Lett. 95, 185501 (2005).

[LewisCR1993] L. N. Lewis, Chem. Rev. 93, 2693 (1993).

[LibudaSSR2005] J. Libuda H.-J. Freund, Surf. Sci. Rep. 57, 157 (2005).

[LiechtensteinPRB1995] A. I. Liechtenstein, V. I. Anisimov, J. Zaanen, Phys. Rev. B 52, R5467 (1995).

[LiN2008] Z. Y. Li, N. P. Young, M. D. Vece, S. Palomba, R. E. Palmer, A. L. Bleloch, B. C. Curley, R. L. Johnston, J. Jiang, J. Yuan, Nature 451, 7174 (2008).

[LinPRL2009] X. Lin, N. Nilius, H.-J. Freund, M. Walter, P. Frondelius, K. Honkala, H. Häkkinen, Phys. Rev. Lett. 102, 206801 (2009).

[LiPNAS1987] Z. Li H. A. Sheraga, Proc. Natl. Acad. Sci. USA 84, 6611 (1987).

[LiPRL2002] J. L. Li, J. F. Jia, X. J. Liang, X. Liu, J. Z. Wang, Q. K. Xue, Z. Q. Li, J. S. Tse, Z. Zhang, S. B. Zhang, Phys. Rev. Lett. 88, 066101 (2002).

[LiS2003] J. Li, X. Li, H. J. Zhai, L. S. Wang, Science 299, 864 (2003).

[LopassoPRB2003] E. M. Lopasso, M. Caro, A. Caro, P. E. A. Turchi, Phys. Rev. B 68, 214205 (2003).

[LopezJCP1999] N. Lopez, F. Illas, N. Rosch, G. Pacchioni, J. Chem. Phys. 110, 4873 (1999).

[LordBook2006] E. A. Lord, A. L. Mackay, S. Ranganathan, New geometries for new materials (Cambridge University Press, Cambridge, UK, 2006).

[LunsfordJPC1966] J. Lunsford J. Jayne, J. Phys. Chem. 70, 3464 (1966).

[MaACSN2010] Y. Ma, W. Y. Li, E. C. Cho, Z. Y. Li, T. K. Yu, J. Zeng, Z. X. Xie, Y. N. Xia, ACS Nano 4, 6725 (2010).

[MahanBook2008] G. D. Mahan, "Quantum Mechanics in a Nutshell", Princeton University Press, 2008.

[MakovPRB1995] G. Makov M. C. Payne, Phys. Rev. B 51, 4014 (1995).

[MarchRPP1968] N. H. March, J. C. Stoddard, Rep. Prog. Phys. 31, 53 (1968).

[MarkovitsPRB2003] A. Markovits, J. C. Paniagua, N. Lopez, C. Minot, F. Illas, Phys. Rev. B 67, 115417 (2003).

[MarksPMA1984] L. D. Marks, Philos. Mag. A 49, 813 (1984).

[MarksRPP1994] L. D. Marks, Rep. Progr. Phys. 57, 603 (1994).

[MartinJCP1994] T. P. Martin, U. Naher, H. Schaber, U. Zimmermann, J. Chem. Phys. 100, 2322 (1994).

[MattheyS2007] D. Matthey, J. G. Wang, S. Wendt, J. Matthiesen, R. Schaub, E. Laegsgaard, B. Hammer, F. Besenbacher, Science 315, 1692 (2007).

[MatveevSS1999] A. V. Matveev, K. Neyman, I. Yudanov, N. R¨ sch, Surf. Sci. 426, 123 (1999).

[McWeenyBook1969] R. McWeeny, B. T. Sutcliffe, "Methods of Molecular Quantum Mechanics", Academic Press, 1969.

[McWeenyBook1980] R. McWeeny, Coulson's Valence (Oxford University Press, Oxford, 1980), 3rd ed.

[MeersonEPJD2005] O. Meerson, G. Sitja, C. Henry, Eur. Phys. J. D 34, 119 (2005).

[MilaniBook1999] P. Milani, S. Iannotta, Cluster Beam Synthesis of Nanostructured Materials, Springer, Berlin (1999).

[MillsPRL1994] G. Mills, H. Jonsson, Phys. Rev. Lett. 72, 1124 (1994).

[MolenbroekTC2009] A. M. Molenbroek, S. Helveg, H. Topsoe, B. S. Clausen, Top. Catal. 52, 1303 (2009).

[MolinaACA2005] L. M. Molina B. Hammer, Appl. Catal. A 291, 21 (2005).

[MolinaCT2011] L. M. Molina, S. Lee,. Fortunelli, B. Lee, S. Seifert, R. E. Winans, J. W. Elam, M. J. Pellin, I. Barke, V. von Oeynhausen, Y. Lei, R. J. Meyer, J. A. Alonso, A. F. Rodriguez, A. Kleibert, S. Giorgio, C. R. Henry, K. H. Meiwes-Broer, S. Vajda, Cat. Today 160, 116 (2011) .

[MolinaJCP2005] L. M. Molina B. Hammer, J. Chem. Phys. 123, 161104 (2005).

[MolinaPRB2004] L. M. Molina B. Hammer, Phys. Rev. B 69, 155424 (2004).

[MoriPRB2002] P. Mori-Sanchez, J. M. Recio, B. Silvi, C. Sousa, A. M. Pendas, V. Luana, F. Illas, Phys. Rev. B 66, 075103 (2002).

[MortonCR2011] S. M. Morton, D. W. Silverstein, L. Jensen, Chem. Rev. 111 3962 (2011).

[MoselerPRL2002] H. Moseler, H. Häkkinen, U. Landman, Phys. Rev. Lett. 89, 176103 (2002).

[MottetPhasT2004] C. Mottet, J. Goniakowski, F. Baletto, R. Ferrando, G. Tréglia, Phase Transit. 77, 101 (2004).

[MusolinoPRL1999] V. Musolino, A. Selloni, R. Car, Phys. Rev. Lett. 83, 3242 (1999).

[MusolinoSS1998] V. Musolino, A. Selloni, R. Car, Surf. Sci. 402-404, 413 (1998).

[NasluzovJCP2001] V. A. Nasluzov, V. V. Rivanenkov, A. B. Gordienko, K. M. Neyman, U. Birkenheuer, N. Rösch, J. Chem. Phys. 115, 8157 (2001).

[NavaPCCP2003] P. Nava, M. Sierka, R. Ahlrichs, 5, 3372 (2003).

[NayakPRB1997] S. K. Nayak, P. Jena, V. S. Stepanyuk, W. Hergert, K. Wildberger, Phys. Rev. B 56, 6952 (1997).

[NegreirosJCP2010] F. R. Negreiros, Z. Kuntová , G. Barcaro, G. Rossi, R. Ferrando A. Fortunelli, J. Chem. Phys. 132, 234703 (2010).

[NegreirosNS2012] F. R. Negreiros, E. Aprà, G. Barcaro, L. Sementa, S. Vajda, A. Fortunelli, Nanoscale, 4, 1208 (2012).

[NegreirosPrep2012] F. R. Negreiros, F. Taherkhani, A. Caro, A. Fortunelli, in preparation.

[NegreirosSS2011] F. R. Negreiros, G. Barcaro, Z. Kuntová , G. Rossi, R. Ferrando A. Fortunelli, Surf. Sci. 605, 483 (2011).

[NetzerSS2010] F. P. Netzer, Surf. Sci. 604, 485 (2010)

[NeymanCEJ2006] K. M. Neyman, C. Inntam, L. V. Moskaleva, N. Rösch, Chem. Eur. J. 12, 277 (2006).

[NeymanCT2005] K. M. Neyman F. Illas, Catal. Today 105, 2 (2005).

[NeymanJACS2005] K. M. Neyman, C. Inntam, A. V. Matveev, V. A. Nasluzov, N. Rösch, J. Am. Chem. Soc. 127, 11652 (2005).

[NeymanNC1997] K. Neyman, S. Vent, G. Pacchioni, N. R¨ sch, Nuovo Cimento 19, 1743 (1997).

[NeymanPCCP2007] K. M. Neyman, K. H. Lim, Z. X. Chen, L. V. Moskaleva, A. Bayer, A. Reindi, D. Borgmann, R. Denecke, H. P. Steinruck, N. Rosch, Phys. Chem. Chem. Phys. 9, 3470 (2007).

[NoltePRB2008] P. Nolte, A. Stierle, N. Kasper, N. Y. Jin-Phillipp, H. Reichert, A. Rühm, J. Okasinski, H. Dosch, S. Schöder, Phys. Rev. B 77, 115444 (2008).

[NunezPRB2006] M. Nuñez M. B. Nardelli, Phys. Rev. B 73, 235422 (2006).

[OjamaeJCP1998] L. Ojamae C. Pisani, J. Chem. Phys. 109, 10984 (1998).

[OlanderPRB2007] J. Olander, R. Lazzari, J. Jupille, B. Mangili, J. Goniakowski, G. Renaud, Phys. Rev. B 76, 075409 (2007).

[OlivierPRB2008] S. Olivier, R. Conte, A. Fortunelli, Phys. Rev. B 77, 054104 (2008).

[OlsenJCP2004] R. A. Olsen, G. J. Kroes, G. Henkelman, A. Arnaldsson, H. Jonsson, J. Chem. Phys. 121, 9776 (2004).

[OlsonJACS2005] R. M. Olson, S. Varganov, M. S. Gordon, H. Metiu, S. Chretien, P. Piecuch, K. Kowalski, S. A. Kucharski, M. Musial, J. Am. Chem. Soc., 127, 1049 (2005).

[OnidaRMP2002] G. Onida, L. Reining, A. Rubio, Rev. Mod. Phys. 74, 601 (2002).

[OsterlundBook2007] L. Osterlund, A. W. Grant, B. Kasemo, Lithographic Techniques in Nanocatalysis, in Nanocatalysis, Series: NanoScience Technology, U. Heiz U. Landman Eds., Chapter 4, 2007, ISBN: 978-3-540-74551-8 Springer Verlag.

[PacchioniCPC2003] G. Pacchioni, ChemPhysChem 4, 1041 (2003).

[PacchioniPRL2005] G. Pacchioni, L. Giordano, M. Baistrocchi, Phys. Rev. Lett. 94, 226104 (2005).

[PacchioniSS1998] G. Pacchioni P. Pescarmona, Surf. Sci. 412-413, 657 (1998).

[ParkerTC2007] S. C. Parker, C. T. Campbell, Top. Catal. 44, 3 (2007).

[ParkinNM2004] S. S. P. Parkin, C. Kaiser, A. Panchula, P. M. Rice, B. Hughes, M. Samant, S.-H. Yang, Nature Mater. 3, 862 (2004).

[PaulingBook1960] L. Pauling, The Nature of the Chemical Bond (Cornell University Press, New York, 1960).

[PauwelsPRB2000] B. Pauwels, G. V. Tendeloo, W. Bouwen, L. T. Kuhn, P. Lievens, H. Lei, M. Hou, Phys. Rev. B 62, 10383 (2000).

[PedersenN1991] J. Pedersen, S. Bjornholm, J. Borggreen, K. Hansen, T. P. Martin, H. D. Rasmussen, Nature 353, 733 (1991).

[PenuelasPRL2008] J. Penuelas, P. Andreazza, C. Andreazza-Vignolle, H. C. N. Tolentino, M. D. Santis, C. Mottet, Phys. Rev. Lett. 100, 115502 (2008).

[PerdewJCP2005] J. P. Perdew, A. Ruzsinszky, J. Tao, V. N. Staroverov, G. Scuseria, G. Csonka, J. Chem. Phys. 123, 062201 (2005).

[PerdewPRB1981] J. P. Perdew, A. Zunger, Phys. Rev. B 23, 5048 (1981).

[PerdewPRB1986] J. P. Perdew, W. Yue, Phys. Rev. B 33, 8800 (1986).

[PerdewPRL1985] J. P. Perdew, Phys. Rev. Lett. 55, 1665 (1985).

[PerdewPRL1996] J. P. Perdew, K. Burke, M. Ernzerhof, Phys. Rev. Lett. 77, 3865 (1996).

[PettiforMSEA2004] D. G. Pettifor, M. W. Finnis, D. Nguyen-Manh, D. A. Murdick, X. W. Zhou, H. N. G. Wadley, Mat. Sci. Eng. A 365, 2 (2004).

[PickettPRB1998] W. E. Pickett, S. C. Erwin, E. C. Ethridge, Phys. Rev. B 58, 1201 (1998).

[PileniCRC2003] M. P. Pileni, C. R. Chimie 6, 965 (2003).

[PileniNM2003] M. P. Pileni, Nature Mat. 2, 145 (2003).

[PittawayJPCC2009] F. Pittaway, L. O. Paz-Borbon, R. L. Johnston, H. Arslan, R. Ferrando, C. Mottet, G. Barcaro, A. Fortunelli, J. Phys. Chem. C 113, 9141 (2009).

[PolakSSR2000] M. Polak L. Rubinovich, Surf. Sci. Rep. 38, 127 (2000).

[PunPM2009] G. Pun Y. Mishin, Phil. Mag. 89, 34 (2009).

[PyykkoACIE2002] P. Pyykkö N. Runeberg, Angew. Chem. Int. Ed. 41, 2174 (2002).

[PyykkoACIE2004] P. Pyykkö, Angew. Chem. Intl. Ed. 43, 4412 (2004).

[PyykkoCSR2008] P. Pyykkö , Chem. Soc. Rev. 37, 1967 (2008).

[PyykkoICA2005] P. Pyykkö , Inorg. Chim. Acta 358, 4113 (2005).

[PyykkoNN2007] P. Pyykkö , Nature Nanotech. 2, 273 (2007).

[RanjanPRB2008] L. Yu, V. Ranjan, W. Lu, J. Bernholc, M. B. Nardelli, Phys. Rev. B 77, 245102 (2008).

[RaoultRSI1973] B. Raoult, J. Farges, Rev. Sci. Instrum. 44, 430, (1973).

[RapalloJCP2005] A. Rapallo, G. Rossi, R. Ferrando, A. Fortunelli, B. Curley, L. Lloyd, G. Tarbuck, R. Johnston, J. Chem. Phys. 122, 194308 (2005).

[RappeJPC1991] A. Rappe´ and W. Goddard, J. Phys. Chem., 95, 3358 (1991).

[ReinhardPRL1997] D. Reinhard, B. D. Hall, P. Berthoud, S. Valkealahti, R. Monot, Phys. Rev. Lett. 79, 1459 (1997).

[RenaudS2003] G. Renaud, R. Lazzari, C. Revenant, A. Barbier, M. Noblet, O. Ulrich, F. Leroy, J. Jupille, Y. Borensztein, C. R. Henry, et al., Science 300, 1416 (2003).

[ReppS2004] J. Repp, G. Meyer, F. E. Olsson, M. Persson, Science 305, 493 (2004).

[ReuterPRB2006] K. Reuter, M. Scheffler, Phys. Rev. B 73, 045433 (2006).

[RevenantNIMB2006] C. Revenant, G. Renaud, R. Lazzari, J. Jupille, Nucl. Instr. Meth. B 246, 112 (2006).

[RicciJCP2002] D. Ricci, G. Pacchioni, P. Sushko, A. L. Shluger, J. Chem. Phys. 117, 2844 (2002).

[RicciPRL2006] D. Ricci, A. Bongiorno, G. Pacchioni, U. Landman, Phys. Rev. Lett. 97, 036106 (2006).

[RizziPCCP2009] G. A. Rizzi, F. Sedona, L. Artiglia, S. Agnoli, G. Barcaro, A. Fortunelli, E. Cavaliere, L. Gavioli, G. Granozzi, Phys. Chem. Chem. Phys. 11, 2177 (2009).

[RobachPRB1998] O. Robach, G. Renaud, A Barbier, Phys. Rev. B 60, 5858 (1998).

[RodriguezPRL2004] J. L. Rodrıguez-Lopez, J. M. Montejano-Carrizales, U. Pal, J. F. Sanchez-Ramırez, H. E. Troiani, D. Garcıa, M. Miki-Yoshida, M. José-Yacamàn, Phys. Rev. Lett. 92, 196102 (2004).

[RosatoPMA1989] V. Rosato, M. Guillopé , B. Legrand, Philos. Mag. A 59, 321 (1989).

[RossiCPL2006] G. Rossi R. Ferrando, Chem. Phys. Lett. 423, 17 (2006).

[RossiFD2008] G. Rossi, R. Ferrando, C. Mottet, Faraday Disc. 138, 193 (2008).

[RossiJCP2005] G. Rossi, R. Ferrando, A. Rapallo, A. Fortunelli, B. Curley, L. Lloyd, R. Johnston, J. Chem. Phys. 122, 194309 (2005).

[RossiJPCB2006] G. Rossi, C. Mottet, F. Nita, R. Ferrando, J. Phys. Chem. B 110, 7436 (2006).

[RossiJPCM2009] G. Rossi R. Ferrando, J. Phys.: Condens. Matt. 21, 084208 (2009).

[RossiNT2007] G. Rossi R. Ferrando, Nanotechnology 18, 225706 (2007).

[RossiPCCP2010] G. Rossi, L. Anghinolfi, R. Ferrando, F. Nita, G. Barcaro, A. Fortunelli, Phys. Chem. Chem. Phys. 12, 8564 (2010).

[RossiPRL2004] G. Rossi, A. Rapallo, C. Mottet, A. Fortunelli, F. Baletto, R. Ferrando, Phys. Rev. Lett. 93, 105503 (2004).

[RoussetSRL1996] J. L. Rousset, A. M. Cadrot, F. S. Aires, A. Renouprez, P. Mélinon, A. Pérez, M. Pellarin, J. L. Vialle, M. Broyer, Surf. Rev. Lett. 3, 1171 (1996).

[RubinovichPRB2009] L. Rubinovich, M. Polak, Phys. Rev. B 80, 045404 (2009)

[SahimiCSE2010] M. Sahimi, H. Hamzehpour, Comp. Sci. Eng. 12, 74 (2010).

[SanchezJPCA1999] A. Sanchez, S. Abbet, U. Heiz, W. D. Schneider, H. Häkkinen, R. N. Barnett, U. Landman, J. Phys. Chem. A 103, 9573 (1999).

[SattlerPRL1980] K. Sattler, J. Mulhback, E. Recknagel, Phys. Rev. Lett. 45, 821 (1980).

[SchimkaJCP2011] L. Schimka, J. Harl, G. Kresse, J. Chem. Phys. 134 (2011) 024116

[SchrodingerPR1926] E. Schrödinger, Phys. Rev. 28, 1049 (1926).

[ScuseriaJPCA1999] G. E. Scuseria, J. Phys. Chem. A 103, 4782 (1999).

[SedonaJPCC2007] F. Sedona, S. Agnoli, M. Fanetti, I. Kholmanov, E. Cavaliere, L. Gavioli, G. Granozzi, J. Phys. Chem. C 111, 8024 (2007).

[SedonaJPCL2008] F. Sedona, M. Sambi, L. Artiglia, G. A. Rizzi, A. Vittadini, A. Fortunelli, G. Granozzi, J. Phys. Chem. C 112, 3187 (2008).

[SedonaPRB2008] F. Sedona, G. Granozzi, G. Barcaro, A. Fortunelli, Phys. Rev. B 77, 115417 (2008).

[SementaPrep2012] L. Sementa, A. Marini, F. R. Negreiros, G. Barcaro, N. Durante, A. Fortunelli, in preparation.

[ShapiroPRB1999] A. I. Shapiro, P. Rooney, M. Tran, F. Hellman, K. Ring, K. Kavanagh, B. Rellinghauss, D. Weller, Phys. Rev. B 60, 12826 (1999).

[ShechtmanPRL1984] D. Shechtman, I. Blech, D. Gratias, J. W. Cahn, Phys. Rev. Lett. 53, 1951 (1984).

[ShoemakerJPCA1999] J. R. Shoemaker, L. W. Burggraf, J. Phys. Chem. A 103, 3245 (1999).

[SilvestreJC2006] J. Silvestre-Albero, G. Rupprechter, H.-J. Freund, J. Catal. 240, 58 (2006).

[SlaterBook1972] J. C. Slater, "Statistical Exchange-Correlation in the Self-Consistent Field", in P. O. Lowdin, Ed., "Advances in Quantum Chemistry", Academic Press, 1972, p. 1

[SocaciuJACS2003] L. D. Socaciu, J. Hagen, T. M. Bernhardt, L. Woste, U. Heiz, H. Hakkinen, and U. Landman J. Am. Chem. Soc. 125, 10437 (2003).

[SolerSSC2001] J. M. Soler, I. L. Garzon, J. D. Joannopoulos, Solid State Commun. 117, 621 (2001).

[SousaJCP2001] C. Sousa F. Illas, J. Chem. Phys. 115, 1435 (2001).

[StaroverovPRB2004] V. N. Staroverov, G. E. Scuseria. J. Tao, J. P. Perdew, Phys. Rev. B (2004).

[SterrerACIE2006] M. Sterrer, M. Yulikov, E. Fischbach, M. Heyde, H.-P. Rust, G. Pacchioni, T. R. H.-J. Freund, Angew. Chem. Int. Ed. 45, 2630 (2006).

[SterrerPRL2005] M. Sterrer, E. Fischbach, T. Risse, H.-J. Freund, Phys. Rev. Lett. 94, 186101 (2005).

[SterrerPRL2007a] M. Sterrer, T. Risse, M. Heyde, H. P. Rust, H.-J. Freund, Phys. Rev. Lett. 98, 206103 (2007).

[SterrerPRL2007b] M. Sterrer, T. Risse, U. M. Pozzoni, L. Giordano, M. Heyde, H. P. Rust, G. Pacchioni, H.-J. Freund, Phys. Rev. Lett. 98, 096107 (2007).

[StierleMRSB2007] MRS Bulletin Vol. 32, pp. 1001-1050, A. Stierle A. M. Molenbroek Eds. (Mat. Res. Soc., Warrendale, 2007).

[StillingerS1984] F. H. Stillinger, T. A. Weber, Science 225, 983 (1984).

[StillingerS1995] F. H. Stillinger, Science 267, 1935 (1995).

[StrainS1996] M. C. Strain, G. E. Scuseria, M. J. Frisch, Science 271, 51 (1996).

[SurnevPSS2003] S. Surnev, M. G. Ramsey F. P. Netzer, Progr. Surf. Sci. 73, 117 (2003).

[SvenssonJPC1996] M. Svensson, S. Humbel, R. D. J. Froese, T. Matsubara, S. Sieber, K. Morokuma, J. Phys. Chem. 100, 19357 (1996).

[SzaboBook1996] A. Szabo, N. S. Ostlund, "Modern Quantum Chemistry", Dover Publications, 1996

[TadmorPM1996] E. Tadmor, M. Ortiz, R. Phillips, Phil. Mag. 73, 1529 (1996).

[TaherkhaniCPL2010] F. Taherkhani, F. Negreiros, G. Parsafar, A. Fortunelli, Chem. Phys. Lett. 498, 312 (2010).

[TaoPRL2003] J. Tao, J. P. Perdew, V. Staroverov, G. Scuseria, Phys. Rev. Lett. 91, 146401 (2003).

[TaoS2008] F. Tao, M. E. Grass, Y. Zhang, D. R. Butcher, J. R. Renzas, Z. Liu, J. Y. Chung, B. S. Mun, M. Salmeron, G. A. Somorjai, Science 322, 932 (2008).

[TianAPL2005] W. Tian, H. P. Sun, X. Q. Pan, J. H. Yu, M. Yeadon, C. B. Boothroyd, Y. P. Feng, R. A. Lukaszew, R. Clarke, Appl. Phys. Lett. 86, 131915 (2005).

[TimpNanotechnology1999] Nanotechnology, edited by G. L. Timp, Springer-Verlag, New York (1999).

[TkatchenkoPRL2009] A. Tkatchenko, M. Scheffler, Phys. Rev. Lett. 102, 073005 (2009).

[TranPRL2009] F. Tran, P. Blaha, Phys. Rev. Lett. 102, 226401 (2009).

[VajdaNM2009] S. Vajda, M. J. Pellin, J. Michael, J. P. Greeley, C. L. Marshall, L. Christopher, L. A. Curtiss, G. A. Ballentine, J. W. Elam, S. Catillon-Mucherie, et al., Nature Mat. 8, 213 (2009).

[ValeroJC2007] M. C. Valero, P. Raybaud, P.Sautet, J. Catal. 247, 339 (2007).

[VelevAM2009] O. D. Velev, S. Gupta, Adv. Mater. 21, 1897 (2009).

[VervischPRB2002] W. Vervisch, C. Mottet, J. Goniakowski, Phys. Rev. B 65, 245411 (2002).

[VinkAPL2002] T. J. Vink, A. R.Balkenende, R. G. F. A. Verbeek, H. A. M. van Hal, S. T. de Zwart, Appl. Phys. Lett. 80, 2216 (2002).

[VitaliPRL1999] L. Vitali, M. G. Ramsey, F. P. Netzer, Phys. Rev. Lett. 83, 316 (1999).

[VoterARMR2002] A. F. Voter, F. Montalenti, T. C. Germann, Ann. Rev. Mater. Res. 32, 321 (2002).

[WalesBook2003] D. J. Wales, Energy Landscapes with Applications to Clusters, Biomolecules Glasses (Cambridge University Press, Cambridge, UK, 2003).

[WalesJPCA1997] D. J. Wales J. P. K. Doye, J. Phys. Chem. A 101, 5111 (1997).

[WalesS1999] D. J. Wales H. A. Sheraga, Science 285, 1368 (1999).

[WalterPRB2005] M. Walter H. Häkkinen, Phys. Rev. B 72, 205440 (2005).

[WalterPRL2007] M. Walter, P. Frondelius, K. Honkala, H. Häkkinen, Phys. Rev. Lett. 99, 096102 (2007).

[WangJACS2007] L. Wang, X. Shi, N. N. Kariuki, M. Schadt, G. R. Wang, Q. Rendeng, J. Choi, J. Luo, S. Lu, C. J. Zhong, J. Am. Chem. Soc. 129, 2161 (2007).

[WangJPCM2001] Y. L. Wang M. Y. Lai, J. Phys. Cond. Mat. 13, R589 (2001).

[WangSM2001] Q. Wang, Q. Sun, Z. J. Yu, M. Sakurai, Y. Kawazoe, Scripta Mater. 44, 1959 (2001).

[WebParam] The numerical parameters for the metal-surface interaction can be found in http://www.cinam.univrs.fr/mottet/param/metalMgO.pdf http://h2.ipcf.cnr.it/alex/webparam.pdf.

[WeigendJCP2009] F. Weigend, M. Kattannek, R. Ahlrichs, J. Chem. Phys. 130, 164106 (2009).

[WendtPSS2003] S. Wendt, Y. D. Kim, D. W. Goodman, Prog. Surf. Sci. 74, 141 (2003).

[WestJPCC2010] P. West, R. L. Johnston, G. Barcaro, A. Fortunelli, J. Phys. Chem. C 114, 19678 (2010).

[WorzCPL2004] A. S. Wörz, K. Judai, S. Abbet, J. M. Antonietti, U. Heiz, A. D. Vitto, L. Giordano, G. Pacchioni, Chem. Phys. Lett. 399, 266 (2004).

[WorzJACS2003] A. S. Worz, K. Judai, S. Abbet, U. Heiz, J. Am. Chem. Soc. 125, 7964 (2003).

[WuCNS2009] Q.-H. Wu, Current Nanosci. 5, 58 (2009).

[WuIRPC2009] Q. Wu, A. Fortunelli G. Granozzi, Int. Rev. Phys. Chem. 28, 517 (2009).

[WulffZK1901] G. Wulff, Z. Kristallogr. 34, 499 (1901).

[XiePRB2001] Y. N. Xie J. A. Blackman, Phys. Rev. B 64, 195115 (2001).

[XiongACIE2007] Y. Xiong, B. J. Wiley, Y. Xia, Angew. Chem. Int. Ed. 46, 7157 (2007).

[XuPRL2005] L. Xu, G. Henkelman, C. T. Campbell, H. Jónsson, Phys. Rev. Lett. 95, 146103 (2005).

[YacamanJVSTB2001] M. J. Yacaman, J. A. Ascencio, H. B. Liu, J. Gardea-Torresdey, J. Vac. Sci. Technol. B 19, 1091 (2001).

[YacamanTC2002] J. Yacaman, J. A. Ascencio, S. Tehuacanero, M. Marin, Top. Catal. 18, 167 (2002).

[YangJCP1996] L. Yang, A. E. DePristo, J. Chem. Phys. 100, 725 (1996).

[YangJCP1998] W. Yang, J. Chem. Phys. 109, 10107 (1998).

[YangPRB2002] Z. Yang, R. Wu, Q. Zhang, D. W. Goodman, Phys. Rev. B 65, 155407 (2002).

[YanJACS2005] Z. Yan, S. Chinta, A. A. Mohamed, J. P. Fackler, D. W. Goodman, J. Am. Chem. Soc. 127, 1604 (2005).

[YoonS2005] B. Yoon, H. Häkkinen, U. Landman, A. S. Wörz, J.-M. Antonietti, S. Abbet, K. Judai, U. Heiz, Science 307, 403 (2005).

[YudanovCPL1997] I. Yudanov, S. Vent, K. Neyman, G. Pacchioni, N. R¨ sch, Chem. Phys. Lett. 275, 245 (1997).

[YudanovJCP2002] I. V. Yudanov, R. Sahnoun, K. M. Neyman, N. Rösch, J. Chem. Phys. 117, 9887 (2002).

[YulikovPRL2006] M. Yulikov, M. Sterrer, M. Heyde, H. P. Rust, T. Risse, H. J. Freund, G. Pacchioni, A. Scagnelli, Phys. Rev. Lett. 96, 146804 (2006).

[ZhangPCCP2008] Y. Zhang, L. Giordano, G. Pacchioni, J. Phys. Chem. C 112, 191 (2008).

[ZhuMP2011] B. E. Zhu, Z. Y. Pan, M, Hou, D. Cheng, Y. X. Wang, Mol. Phys. 109, 527 (2011)

[ZhuangPRB2004] J. Zhuang, Z. Sun, W. Zhang, M. Zhuang, X. Ning, L. Liu, Y. Li, Phys. Rev. B 69, 165421 (2004).

Acknowledgements

With the following lines I wish to acknowledge the people who in various ways have supported me in my recent research activity.
The work here described would not have been possible without intense and gratifying collaborations with many students, post-docs and colleagues, who along the way have become not only co-workers but most often also good friends. First of all I would like to thank my collaborators who spent many long hours in discussing and planning simulations, analyzing and making sense of their outcome, figuring out the way to overcome technical and in-principle difficulties. Among these, Giovanni Barcaro, whose help and support along these years have been invaluable and to whom I express my hearty wishes of a most successful career in research, Lauro-Oliver Paz-Borbòn, Francesca Baletto, Giulia Rossi, Paul S. West, Luca Sementa, Fabio Negreiros Ribeiro, Iorwerth Owain Thomas, Florin Nita, Stephane Olivier, Stefano Conte, Daojian Cheng, Farid Taherkhani, Manuella Cerbelaud, Zdenka Kuntovà. I am also in debt with many theoretician colleagues, first of all Riccardo Ferrando from Genoa University (IT), who has co-authored many of the publications reported in the above list in a very fruitful ten-year-long collaborative work, Roy. L. Johnston from Birmingham University (UK), collaboration with whose group has been made possible through many exchange visits supported by HPC-Europa and HPC-Europa2 Programmes, and Edoardo Aprà, who is also most gratefully thanked for support and consultancy with the NWChem code. My sincere thanks also go to Micha Polak and Leonid Rubinovich from Beer-Sheva University (IL), Christine Mottet from CNRS-CINAM in Marseille (FR), Mauro Stener from Trieste University (IT), Mauro Causà from Neaples University (IT), Marc Hou from Université Libre de Bruxelles (BE), Jean-Christophe Charlier from Louvain University (BE), Nicola Durante from CNR-IPCF (IT), Gholamabbas Parsafar at Teheran University (IR), Luis Molina and the people at Valladolid University (ES), Julius Jellinek from Argonne National Laboratory (USA), Jacek Goniakowski from Paris University (FR). I am also indebted to stimulating discussions and exchange of ideas and projects with many experimentalist collegues, in primis Gaetano Granozzi and his group at Padua University (IT), and Falko Netzer and his group at Graz University (AT), with many thanks to Svetlozar Surnev, Sergio Valeri and his group at Modena University (IT), with special thanks to Paola Luches, Luca Gavioli and his group at Brescia University (IT), Michel Broyer from Lyon University (FR), Stefan Vajda from Argonne National Laboratory (USA). Paolo Giannozzi from Udine University (IT) is gratefully acknowledged for support and consultancy with the Quantum Espresso code. I am also very grateful to the staff at the CINECA Supercomputing Center (Bologna, IT), among whom particular thanks go to Giovanni Erbacci and Carlo Cavazzoni.
Financial support from the Italian Consiglio Nazionale delle Ricerche (CNR) for the project "(Supra-)Self-Assembly of Transition Metal Nanoclusters" (SSA-TMN) within the framework of the ESF EUROCORES SONS and from the European

Community Sixth Framework Programme for the STREP project “Growth and Supra-Organization of Transition and Noble Metal Nanoclusters” (GSOMEN) (No. NMP4-CT-2004-001594), both of which projects I had the great pleasure and honor to coordinate, and from the European Community Seventh Framework Programme for the project “Search for Emergent Phenomena in Oxide Nanostructures” (SEPON) (No. ERC-2008-AdG-227457) within the Advanced Grants of the European Research Council are gratefully acknowledged. Many of the DFT calculations here described were performed at the CINECA Supercomputing Center within an agreement with Italian CNR, and at the CASPUR Supercomputing Center. Without this generous support much of the research work here described would have remained in the no-where land of dreams and conjectures. I would also like to sincerely thank partners of the SSA-TMN and GSOMEN projects not acknowledged above: Hans-Joachim Freund and his group at Fritz-Haber Institute in Berlin (DE), with special thanks to Thomas Risse and Shamil Shaikhutdinov, Claude Henry and his group at CNRS-CINAM in Marseille (FR), with special thanks to Clemens Barth, Marie-Paule Pileni from UPMC University in Paris (FR), with many thanks to Christophe Petit and Isabelle Lisieki, Gilles Renaud from ESRF at Grenoble (FR), Ueli Heiz from TUM University in Munich (DE), Gianfranco Pacchioni from Milano-Bicocca University (IT). Even though we did not collaborate on a specific project, I was very happy to be in touch and to learn from them along these years.

This Thesis would have not been written without the “Perfezionamento” Programme of the Scuola Normale Superiore in Pisa. I wish to heartly thank first and foremost Fabio Beltram who kindly offered me the opportunity of presenting my recent research work as a “Tesi di Perfezionamento”, and heartly also Vincenzo Barone who accepted to be the formal Thesis’ supervisor and to preside the evaluating committee. As a historical note, it is a weird coincidence that I had actually started a “Perfezionamento” Programme at Scuola Normale in January 1984 (without completing it as I got a permanent position after few months since then) so that I receive my PhD exactly 25 years since I had originally intended to …

Last but in no way least, I would like to thank my family and friends who have been close to me in these years, standing my harsh character and providing me with the joy and feelings without which work is just mechanical routine. The memory of my father, long passed away, still fills my hearth with the gratitude that my dedication but partially witnesses.

ELSEVIER

Journal of Molecular Structure (Theochem) 487 (1999) 251–266

THEO CHEM

Structural and electronic properties of Pt/Fe nanoclusters from EHT calculations

Alessandro Fortunelli*, Ana María Velasco

Istituto di Chimica Quantistica ed Energetica Molecolare del C.N.R., via del Risorgimento 35, 56126 Pisa, Italy

Received 17 July 1998; received in revised form 3 November 1998; accepted 24 November 1998

Abstract

Extended Hückel theory (EHT) calculations are presented for pure Pt and mixed Pt/Fe nanoclusters, with a number of atoms in the range $N_{at} = 13–309$. Icosahedral and single-crystal (cuboctahedral, truncated octahedral) geometries are considered, optimized through a many-body potential approach for pure Pt clusters. In the mixed Pt/Fe clusters, the Fe atoms simply replace Pt atoms in an otherwise unrelaxed structure. It is found that single-crystal configurations are generally preferred over icosahedral ones and that — up to an Fe content of ~30% — the Fe atoms segregate in the interior of the cluster and the mixing reaction is exothermic. The electronic properties of the clusters are analyzed and are found to rapidly converge to a quasi-metallic behaviour for a number of atoms larger than ~150. The theoretical results are compared with the known experimental data on these systems.

Keywords: Extended Hückel theory; Icosahedral; Nanostructures; Octahedral; Bimetallic alloys

1. Introduction

Interest in bimetallic catalysts has lasted for a long time (see Ref. [1] for a recent comprehensive review), where the main point has been the possibility of modifying the catalytic activity of the main element (e.g. Pt) by judiciously alloying it with a different metal (e.g. Fe).

More recently, such an interest has partly shifted from bulk alloys to nanopowders, due to: (a) the much more favourable surface/bulk ratio; and (b) specific properties which finite-size or similar effects may confer to nanostructured systems (see, for example, Ref. [2] and references cited therein).

In this context, the Pt/Fe system, both as a bulk alloy [3] and a nanopowder [4–10], have been experimentally studied.

However, despite the numerous applications of bimetallic catalysts and the intense experimental effort devoted to their structural and catalytic characterization, theoretical investigations on these systems are not frequent (see, for example, Refs. [11,12] and references therein) or, as for the Pt/Fe pair, even completely lacking.

In the present paper, a theoretical study of pure Pt and Pt/Fe nanoclusters with a number of atoms in the range $N_{at} = 13–309$, will be presented, in an attempt to elucidate the structural and electronic characteristics of this class of catalytically interesting binary compounds.

2. Some experimental results on the Pt/Fe alloy

Pt is completely miscible with γ-Fe and the mixing

* Corresponding author. Tel.: + 39-050-91-8398; Fax: + 39-050-502-270.

E-mail address: alex@hal.icqem.pi.cnr.it (A. Fortunelli)

0166-1280/99/$ - see front matter
PII: S0166-1280(98)00597-1

reaction is exothermic [13]. Ordered states are formed centering around the compositions Fe_3Pt, $FePt_3$ — both with the ordered fcc ($L1_2$) structure isotypic with $AuCu_3$ — and FePt — with the ordered fc tetragonal ($L1_0$) structure isotypic with AuCu. In the $L1_2$ structure, the minority and majority components occupy the corners and faces of the basic cube, respectively, while in the $L1_0$ structure, they occupy alternating (002) planes. The lattice constants [13] of Fe_3Pt ($a = 3.727$ Å), FePt ($a = 3.861$ Å, $c = 3.788$ Å) and $FePt_3$ ($a = 3.877$ Å) are between that of pure Pt ($a = 3.9242$ Å) and that of pure (fcc) Fe ($a = 3.666$ Å). It is interesting to note that the structure is close to that of pure Pt when Fe is not present in large amounts. This has been taken into account in the following section when choosing the distribution of the atoms in the mixed clusters.

Despite the fact that pure Pt and Fe have comparable surface energies [14], in $Fe_{0.2}Pt_{0.8}$, the ordered structure of the bulk extends to the (111) surface, where a *complete monolayer* of Pt, reconstructed according to a (2×2) pattern, has been found [3]: 3/4 of the surface Pt atoms are bonded to two Pt atoms and one Fe atom in the first sublayer, and are located slightly inside the mean position of the surface plane, which also includes the remaining 1/4 surface Pt atoms, with only Pt atoms as first neighbours. Together with the data on the miscibility of Pt and γ-Fe [13], these results suggest that, experimentally, the Pt-–Fe bond is strong enough to favor a thorough mixing of Pt and Fe. This is a very important fact which has been taken into account in the following section when choosing the distribution of the atoms in the mixed clusters. The catalytic efficiency and selectivity of the Pt/Fe (111) surface exhibit marked differences with respect to the (111) surface of both pure Pt and Pt/Ni or Pt/Co alloys [3]. However, in Ref. [3], it was not clear whether such differences should be attributed to electronic or geometrical factors.

The structure of Pt/Fe nanopowders, prepared according to the metal vapour deposition (MVD) method [5–10], has not been fully characterized, apart from the mean particle size which is around 20 Å. However, the corresponding particles of pure Pt are known to be non-amorphous [5–10], exhibiting clear diffraction patterns at about 2.275 and 1.975 Å, which closely correspond to the (111) and (200) spacings of pure fcc Pt: 2.266 and 1.962 Å, respectively. Again, the catalytic efficiency and selectivity of the Pt/Fe nanopowders is markedly different from that of pure Pt nanopowders prepared with the same method in similar experimental conditions [5–10].

Pt/Fe clusters had previously been obtained through a different procedure, i.e. by evaporation/calcination of solutions of Fe^{III} and Pt^{IV} over alumina and subsequent reduction with H_2 at high temperatures [4]. The results of Ref. [4] mainly relevant to the present investigation are that, at high (∼5:1) Pt:Fe ratios, all of the iron combined with platinum to form clusters. The iron in the Pt/Fe clusters was found to be catalytically inert and the clusters essentially exhibited the catalytic behaviour of platinum. At low Pt:Fe ratios (≤ 1.7:1) ferromagnetic iron, in addition to Fe^{++} ions and Pt/Fe clusters, was also produced. Mössbauer measurements at a Pt:Fe ratio of ∼5:1 indicated that Fe is in an oxidation state intermediate between Fe^0 and Fe^{II}, and occupies sites of non-cubic symmetry, which are not all equivalent. From the measured adsorption of H_2 or CO, the size of the clusters was estimated to be between 100 and 300 atoms. It was also supposed by the experimentalists [4], that the Fe atoms were at the surface, which in their opinion explains the fact that they occupy inequivalent sites of non-cubic symmetry. The possibility that Pt segregates to the surface of the Pt/Fe clusters could not be ruled out, but it was believed that the inert behaviour of Fe in Pt/Fe catalysts was due to an electronic effect of Pt on Fe (electron withdrawal from Fe to Pt and lower electron density on Fe). It is to be noted, however, that at a Pt:Fe ratio of ∼1.7, (a) about 12% Fe remains as Fe^{++} ions, and (b) the adsorption of H_2 or CO decreases. In our opinion, (a) seems to indicate that the formation of Pt/Fe clusters with a Pt:Fe ratio smaller than about 2.0 is less favourable, while (b) points to Pt rather than Fe atoms being at the surface because, if the iron atoms were at the surface, they would interact much more strongly with CO (see the discussion in Section 4).

3. The approach

All the calculations reported here were performed according to the extended Hückel theory (EHT) approach [15–17], utilizing a modified version of

the CACAO [18] set of programs (release 5.01). The parameters for both Pt and Fe atoms were taken from the original literature [19]. No spin-orbit effects were introduced. Other possible choices of parameters have been proposed, for example in Refs. [20,21], and have been utilized by us in preliminary calculations not reported here, because a comparison with density functional results on small Pt and Fe clusters did not show significant improvements over the previously proposed ones. An extensive comparison of EHT and ab initio calculations aimed at putting the choice of the tight-binding parameters on firm theoretical grounds is in progress in our laboratory along the lines of Ref. [22]: in this sense, the present results can be considered as preliminary calculations, aimed at setting the stage and defining the theoretical tools to be used in future, more accurate, work. In this context, it is important to stress that the density functional calculations show how important it is that the explicit treatment of the d-orbitals of platinum for a correct description of the metal–metal bond: in this respect EHT appears as the 'simplest' theoretical method which, if properly parametrized, can produce reliable predictions on Pt or Pt/Fe nanoclusters, while at the same time being sufficiently simplified to allow one to treat 'realistic' systems (several hundredths of atoms) with modest computational effort.

For a given geometrical arrangement of the atoms, the virtue of EHT lies in the possibility of obtaining a quick and usually reliable description of the electronic structure of the system under consideration, which — together with structural predictions — is the basis for an understanding of its catalytic, optical, magnetic, etc. properties.

In our calculations, the EHT one-electron energy levels have been empirically broadened using a Gaussian function: $g(x) = \sqrt{\gamma/\pi}\mathrm{e}^{-\gamma x^2}$. The total density of states (DOS) is thus defined, as usual, as:

$$\mathrm{DOS}(\varepsilon) = \sum_i 2g(\varepsilon - \varepsilon_i)$$

where the sum, $\sum_i$, runs over all molecular orbitals with energies, $\{\varepsilon_i\}$. The DOS, integrated from $-\infty$ up to a properly chosen energy called the Fermi level — $\varepsilon_\mathrm{F}(N)$ — gives the total number of electrons:

$$N = \int_{-\infty}^{\varepsilon_\mathrm{F}(N)} \mathrm{DOS}(\varepsilon)\mathrm{d}\varepsilon$$

The DOS(ε) can be given a spatial dependence by defining a local density of states (LDOS) as:

$$\mathrm{LDOS}(\varepsilon, \bar{r}) = \sum_i 2g(\varepsilon - \varepsilon_i)|\Psi_i(\bar{r})|^2$$

where $|\Psi_i(\bar{r})|^2$ is the square of the modulus of the ith molecular orbital — $\Psi_i(\bar{r})$ — with one-electron energy, ε_i.

The EHT total energy is defined as:

$$E_\mathrm{T}(N) = \sum_i \int_{-\infty}^{\varepsilon_\mathrm{F}(N)} 2g(\varepsilon - \varepsilon_i)\varepsilon_i \mathrm{d}\varepsilon = \sum_i n_i \varepsilon_i$$

where $n_i = 1 + \mathrm{erf}\{\sqrt{\gamma}[\varepsilon_\mathrm{F}(N) - \varepsilon_i]\}$ is the occupation number of the ith molecular orbital (erf is the error function). In the limit $\gamma \to \infty$, it is convenient to define the band width (BW) as the energy difference between the lowest and the highest occupied orbitals, an apparent gap, as the energy difference between the highest occupied and lowest unoccupied orbitals, and a true gap, with this same energy difference, but evaluated considering degenerate levels as a single one.

Finally, it is interesting to note that the following formulae are valid within the EHT approach:

$$\frac{\mathrm{d}\varepsilon_\mathrm{F}(N)}{\mathrm{d}N} = \frac{1}{\mathrm{DOS}[\varepsilon_\mathrm{F}(N)]}$$

$$\frac{\mathrm{d}^2\varepsilon_\mathrm{F}(N)}{\mathrm{d}N^2} = 2\gamma\frac{\varepsilon_\mathrm{F}(N)\mathrm{DOS}[\varepsilon_\mathrm{F}(N)] - \bar{\varepsilon}(N)}{\mathrm{DOS}[\varepsilon_\mathrm{F}(N)]^3}$$

$$\frac{\mathrm{d}E_\mathrm{T}(N)}{\mathrm{d}N} = \frac{\bar{\varepsilon}(N)}{\mathrm{DOS}[\varepsilon_\mathrm{F}(N)]} \approx -\frac{\mathrm{IP} + \mathrm{EA}}{2}$$

$$\frac{\mathrm{d}^2E_\mathrm{T}(N)}{\mathrm{d}N^2} = 2\gamma\frac{\overline{\varepsilon^2}(N) - \overline{\varepsilon}^2(N)/\mathrm{DOS}[\varepsilon_\mathrm{F}(N)]}{\mathrm{DOS}[\varepsilon_\mathrm{F}(N)]^2}$$

$$\approx \mathrm{IP} - \mathrm{EA}$$

$$\frac{\mathrm{dDOS}[\varepsilon_\mathrm{F}(N)]}{\mathrm{d}N} = -2\gamma\frac{\varepsilon_\mathrm{F}(N)\mathrm{DOS}[\varepsilon_\mathrm{F}(N)] - \bar{\varepsilon}(N)}{\mathrm{DOS}[\varepsilon_\mathrm{F}(N)]}$$

where

$$\bar{\varepsilon}(N) = \sum_i 2g[\varepsilon_\mathrm{F}(N) - \varepsilon_i]\varepsilon_i$$

$$\overline{\varepsilon^2}(N) = \sum_i 2g[\varepsilon_\mathrm{F}(N) - \varepsilon_i]\varepsilon_i^2$$

and the ionization potential (IP) and electron affinity

(EA) are defined for the neutral clusters, as usual, as:

$$\mathrm{IP} = E_T(N-1) - E_T(N)$$

$$\mathrm{EA} = E_T(N) - E_T(N+1)$$

It can be noted that $[dE_T(N)]/(dN)$ approximately corresponds to the Pauli electronegativity, while $[d^2E_T(N)]/(dN^2)$ can be identified with the 'hardness' of the system.

The main problem with EHT is due to the fact that, if the one-electron energy levels are satisfactorily reproduced by the semi-empirical calculation, the proper definition of the total energy of the system (and even more, its dependence on the geometrical parameters) lies on uncertain ground. To be more precise, the parameterization of the integrals, and therefore the one-electron energies, $\{\varepsilon_i\}$, partially accounts for the Coulombic potential, but this contribution is not counted correctly when calculating the energy as a sum of one-electron energy levels. Alternatively, if the energy is to be reproduced, the one-electron energy levels do not possess the usual meaning (not to speak of the lack of dependence on orbital occupation numbers). This explains why some quantities (in particular, the ionisation potential and electron affinity) may exhibit large discrepancies with respect to the experimental values, even though they are not deprived of any physical meaning. Finally, one usually finds it convenient to add an interatomic repulsion potential in order to study the dependence of the energy on geometrical parameters. We have therefore not attempted to determine the geometries of our clusters through an energy minimization process. However, we believe that, given a certain geometrical structure consisting of a fixed amount of Pt and Fe atoms, it is meaningful to ask within EHT which is the disposition of Fe atoms that minimises the total energy (defined as the sum of one-electron energy levels multiplied by occupation numbers).

The geometries of the clusters to be considered in the next section have thus been taken from those determined using a different approach, namely through many-body potential (MBP) optimizations [23]. In particular, as in Ref. [23], two fundamental types of structural forms will be contrasted: single-crystal structures (i.e. cuboctahedra and truncated octahedra) and Mackay's icosahedra [24]. We refer to Ref. [24] for a description of these structures and for an extensive discussion of the competition between single-crystal structures versus icosahedra or other nonperiodic (or even amorphous) structures. The main point to be remembered here is that, for small clusters, icosahedral or, in general, non-periodic structures, should be energetically favoured, whereas, as the size of the cluster increases, single-crystal structures, in particular the truncated octahedra (or even better, the Wulff polyedra), should become the most stable species. In the range $N_{at} = 13$–309, one finds four complete-shell icosahedra or cuboctahedra at $N_{at} = 13$, 55, 147, 309 (complete-shell icosahedra and cuboctahedra possess the same number of atoms), and one complete-shell atom-centered truncated octahedron at $N_{at} = 201$. The geometries of this set of nine clusters have been taken from Ref. [23], where MBP simulations of pure Pt clusters were performed. We believe that it is important to consider partially optimized structures such as those given in Ref. [23], because it is known that atom–atom distances tend to be shorter in nanoclusters with respect to the bulk situation, even though an MBP — as any two-body interaction potential — cannot account for the Jahn–Teller distortion which is likely to occur in relatively small, highly-symmetrical structures such as those considered in the present study. Indeed, we often found a degenerate Fermi level in our EHT calculations (see the next section), but density functional calculations on small clusters (not reported here) indicate that the corresponding Jahn–Teller distortion is not so large as to qualitatively modify the comparison between different structural forms.

It is useful to describe in more detail the shell structure of the clusters to be considered in the following section. Icosahedral and cuboctahedral structures of increasing size can be formed by successively adding 'shells' of atoms to the smaller structures. In these clusters, one can thus distinguish the atoms as belonging to the first ($N_{shell} = 1$, with N_{shell} the number of atoms in the shell), second ($N_{shell} = 12$), third ($N_{shell} = 42$), fourth ($N_{shell} = 92$), fifth ($N_{shell} = 162$) etc.

Table 1
The shell structures of the $N_{at} = 309$ icosahedron and cuboctahedron and $N_{at} = 201$ truncated octahedron. For each shell, the atoms are distinguished as lying on vertices, edges, (111) or (100) faces. See text for more details. At the bottom of the table, the distances (R, in Å) from the central atom of the cluster are reported for the pure Pt icosahedral and cuboctahedral clusters with $N_{at} = 309$

Shell	Vertices	Edges	(111) faces	(100) faces
	$N_{at} = 309$ icosahedron			
I	1	–	–	–
II	12	–	–	–
III	12	30	–	–
IV	12	60	20	–
V	12	90 = 30 + 60	60	
	$N_{at} = 309$ cuboctahedron			
I	1	–	–	–
II	12	–	–	–
III	12	24	–	6
IV	12	48	8	24
V	12	72 = 48 + 24	24	54 = 24 + 24 + 6
	$N_{at} = 201$ truncated octahedron			
I	1	–	–	–
II	12	–	–	–
III	12	24	–	6
IV	–	–	–	24
V	24	36 = 24 + 12	56 = 48 + 8	6
Pt_{309} icosahedron:				
Shell II				
R	2.620			
Shell III				
	Edges	Vertex		
R	4.542	5.250		
Shell IV				
	(111) faces	Edges	Vertex	
R	6.478	6.980	7.904	
Shell V				
	(111) faces	Edges (30 + 60)	Vertex	
R	8.743	(9.072 + 9.476)	10.473	
Pt_{309} cuboctahedron:				
Shell II				
R	2.751			
Shell III				
	(100) faces	Edges	Vertex	
R	3.923	4.773	5.483	
Shell IV				
	(100) faces	(111) faces	Edges	Vertex
R	6.216	6.776	7.290	8.202
Shell V				
	(100) faces (24 + 6 + 24)	(111) faces	Edges (24 + 48)	Vertex
R	(8.271 + 7.812 + 8.703)	9.131	(9.448 + 9.830)	10.776

shell, giving, as already mentioned, a total number of $N_{at} = 1, 13, 55, 147, 309$ atoms for the first five complete-shell clusters. Within each shell, the atoms can be further distinguished into atoms lying on vertices, edges and faces. These atoms will possess a different number of first neighbours (and thus, for example, a different catalytic activity when lying at the surface). In icosahedral clusters, there exist only (111) (distorted) faces, whereas in cuboctahedral clusters one can have both (111) and (100) faces (see Ref. [24] for a more extensive discussion): in general, in the following, a (100) face will indicate a (010) or (001) face, as well. The $N_{at} = 201$ truncated octahedral clusters can be obtained from the $N_{at} = 309$ cuboctahedron by removing the first layer of atoms on the eight (111) faces, thus producing a cluster with edges both between (100) and (111) faces (24 atoms) and between two (111) faces (12 atoms). The shell structures of the $N_{at} = 309$ icosahedron and cuboctahedron and $N_{at} = 201$ truncated octahedron are reported in Table 1 (the shell structures of smaller icosahedra or cuboctahedra can easily be derived from these). The MBP optimization substantially preserves such a shell structure, implying essentially only a reduction of the atom–atom distances, more pronounced for the atoms of the outer shells. To give an idea of the kind of structural relaxation involved, the atomic distances from the central atom are also reported in Table 1 for the pure Pt cuboctahedral and icosahedral clusters with $N_{at} = 309$.

It can be noted that an atom on a (100) face has four first-neighbours on the surface and four in the bulk, and one on a (111) face has six first-neighbours on the surface and three in the bulk. By denoting by (n, m) the number of first neighbours on the surface and in the bulk, respectively, one has $(n, m) = (4, 1)$ for a vertex of a cuboctahedron, (5, 1) for a vertex of an icosahedron or truncated octahedron, (5, 2) for an edge of a cuboctahedron, (6, 2) for an edge of an icosahedron, (5, 2) for an edge of a truncated octahedron between a (100) and a (111) face, and (6, 1) for an edge between two (111) faces. By associating a formal metal–metal bond with each pair of first-neighbours atoms, one thus obtains the total number of bond (N_{bond}) for each structure: $N_{bond} = 36, 216, 660, 1488$ for the cuboctahedra with $N_{at} = 13, 55, 147, 309$, respectively; $N_{bond} = 42, 234, 696, 1548$ for the icosahedra with $N_{at} = 13, 55, 147, 309$, respectively; and $N_{bond} = 1039$ for the truncated octahedron with $N_{at} = 201$.[1]

The previous considerations define the structure of pure Pt clusters (for the Pt_{309} cluster, in particular, the distances reported in Table 1 allow a more complete definition of the structure). When one considers mixed Pt/Fe clusters, one has the problem of optimizing the positions of the Fe atoms. In this regard, we have assumed that the partial substitution of Pt atoms with Fe atoms does not drastically modify the cluster structures. This is a fundamental point, but it is not an unreasonable assumption, since it is experimentally known (see the beginning of the previous section) that up to the $FePt_3$ phase, the Fe atoms are disposed so as to maximize the interaction with Pt atoms in a cubic structure whose cell parameters are close to those of pure bulk Pt (even for FePt, the cell parameter, a, is close to that of pure Pt, while c is intermediate between that of pure Pt and pure Fe). In any case, the small reduction in the Pt–Fe distances to be expected for low Fe contents should not produce any qualitative difference in the results. We will thus compare the EHT total energies of clusters with a fixed number of Fe atoms without modifying the atomic positions. However, when such a number is substantial, the number of non-equivalent configurations grows exponentially and it rapidly becomes very costly to fully optimize the positions of all the Fe atoms, even if leaving unaltered the overall cluster skeleton. We therefore performed a complete search of the optimal Fe sites only in the case of one and two Fe atoms, whereas in the other cases, approximately representative of ~30 and ~50% Fe content, we performed calculations only on a subset of the

[1] If n is the order of a given cuboctahedral or icosahedral structure, then $N_{at}(n) = (10n^3 - 15n^2 + 11n - 3)/3$ is the total number of atoms, divided into $N_{at}(n - 1)$ atoms, which are in the bulk and $10n(n - 2) + 12$ atoms, which are at the surface. For a cuboctahedron, the latter can be distinguished into 12 atoms lying on vertices (if $n > 1$), $24(n - 2)$ lying on edges, $4(n - 2)(n - 3)$ lying on (111) faces and $6(n - 2)^2$ lying on (100) faces, for a total of $N_{bond} = 6N_{at}(n - 1) + 30 + 84(n - 2) + 24(n - 2)^2 + 18(n - 2)(n - 3)$ first-neighbour bonds (if $n > 1$). Analogously, for an icosahedron, the surface atoms can be distinguished into 12 atoms lying on vertices (if $n > 1$), $30(n - 2)$ lying on edges and $10(n - 2)(n - 3)$ lying on (111) faces, for a total of $N_{bond} = 6N_{at}(n - 1) + 36 + 120(n - 2) + 45(n - 2)(n - 3)$ first-neighbour bonds (if $n > 1$).

Table 2
Atomization energies (AE) in eV are reported for pure Pt, pure Fe and Pt/Fe clusters with $N_{at} = 13$, 55, 147 (part a) and 201 (part b)

Pt_xFe_y	Position of Fe	AE (eV)	Position of Fe	AE (eV)
(part a)				
	cuboctahedron		icosahedron	
($x + y = 13$)				
Pt_{13}	–	11.63	–	11.07
$Pt_{12}Fe$	II	14.06	II	13.63
$Pt_{11}Fe_2$	I,II	16.40	I,II	16.26
$Pt_{10}Fe_3$	$I,II,II_{(opposite)}$	18.97	$I,II,II_{(opposite)}$	19.01
Fe_{13}	–	39.91	–	40.58
($x + y = 55$)				
Pt_{55}	–	57.50	–	55.87
$Pt_{43}Fe_{12}$	II	90.96	II	91.25
	III(v)	89.23	III(v)	89.00
Fe_{55}	–	196.20	–	197.51
($x + y = 147$)				
Pt_{147}	–	164.62	–	163.12
$Pt_{105}Fe_{42}$	$II,III(f_{100},e)$	285.73	II,III(e)	284.26
	III	284.17	III	282.62
	$II,III(f_{100},v),IV(v)$	283.16	III(e),IV(v)	281.31
	$II,III(f_{100}),IV(f_{100})$	283.02	II,IV(e/2)	279.47
	$III(f_{100},v),IV(f_{100})$	280.87	III(v),IV(e/2)	277.74
$Pt_{75}Fe_{72}$	$II,III(v,e),IV(f_{100})$	366.74	II,III(e),IV(e/2)	365.21
	$II,III(e),IV(f_{100},v)$	364.25	III,IV(e/2)	363.74
	II,III(v),IV(e)	359.87	III(e),IV(e/2,v)	361.52
	II,IV(v,e)	357.75	II,IV(e)	356.52
Fe_{147}	–	550.07	–	551.39
(part b)				
($x + y = 201$) truncated octahedron				
Pt_{201}	–	230.03		
$Pt_{200}Fe$	III	232.91		
	II	232.89		
	I	232.89		
	IV	232.83		
$Pt_{199}Fe_2$	II,II	235.76		
	I,II	235.75		
	I,V	235.72		
	V,V	235.69		
$Pt_{153}Fe_{48}$	II,III(e,v)	368.91		
	III(e),IV	367.11		
	II,III(v),IV	366.94		
	III(e),V(v)	365.28		
	II,V(e)	364.24		
$Pt_{105}Fe_{96}$	$II,III,IV,V(12e_{111/111},f_{100})$	503.11		
	II,III(e,v),IV,V(v)	502.14		
	$II,III(e,v),V(48f_{111})$	499.60		
	$III(e),IV,V(48f_{111})$	497.73		
	$IV,V(48f_{111},v)$	493.28		
$Pt_{99}Fe_{102}$	II,III,IV,V(v)	519.24		
	$II,III,V(48f_{111})$	516.57		
Fe_{201}	–	764.45		

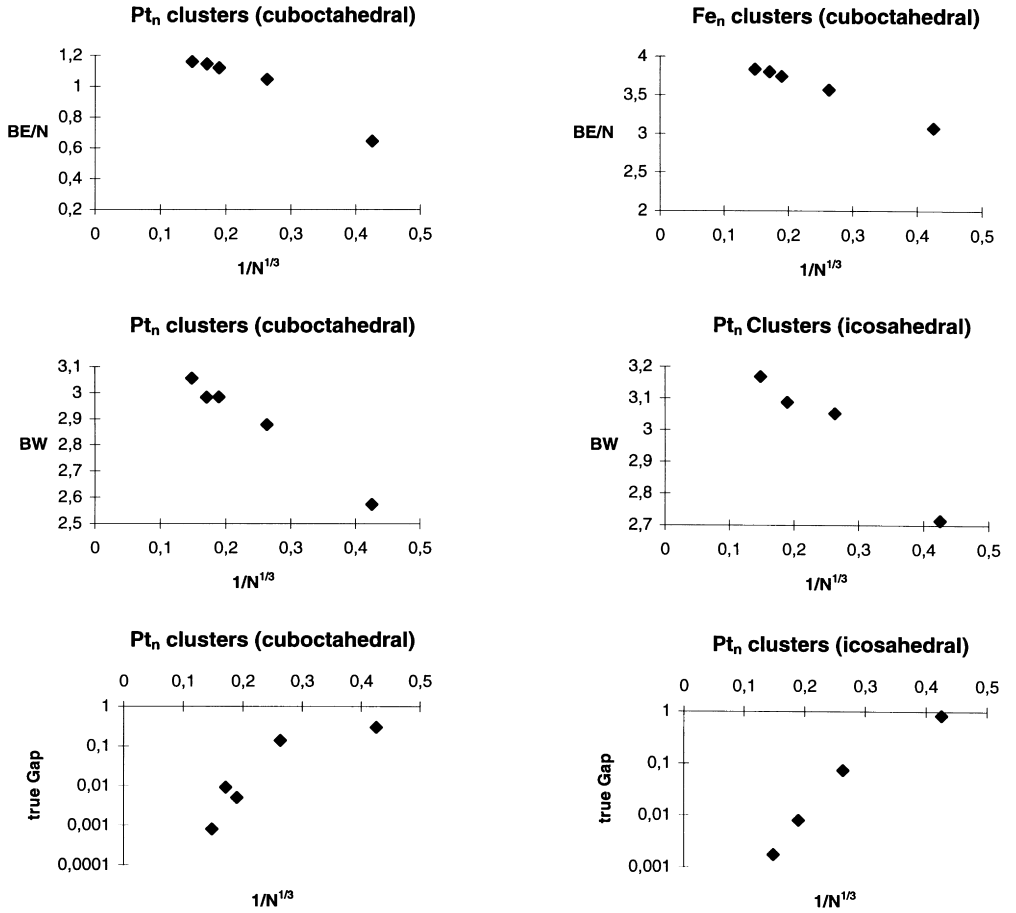

Fig. 1. The binding energies per atom (BE/*N*), the band width (BW) and 'true' gap values are shown as functions of $1/\sqrt[3]{N_{at}}$ (approximately, the inverse of the mean radius of the cluster). The first quantity, BE/*N*, is reported for the pure Pt and Fe octahedral clusters with $N_{at} = 13$, 55, 147, 201 and 309; the second and third quantities for the pure Pt octahedral clusters with $N_{at} = 13$, 55, 147, 201 and 309, and icosahedral ones with $N_{at} = 13$, 55, 147 and 309. The true gap values are presented in a logarithmic scale. All the quantities are in eV.

possible Fe configurations, selecting preferentially those in which entire shells or sub-shells of Pt atoms were replaced with Fe atoms (and which thus exhibited a substantial symmetry), without pretending to be complete and systematic, but choosing the most likely candidates among those which exhibited a substantial number of Fe–Fe and Pt–Fe bonds (the strongest bonds, according to the calculations reported in the next section). Each Pt/Fe cluster will thus be characterized by which shell or sub-shell of Pt atoms is replaced with Fe atoms. To give an example, the $Pt_{105}Fe_{42}$[II,III(f_{100},e)] cuboctahedral cluster will correspond to the $N_{at} = 147$ cuboctahedron in which the entire second (II) shell of 12 atoms (see Table 1) and the 24 atoms on the edges and the 6 atoms on the (100) faces of the third (III) shell are occupied with Fe atoms, giving a total of 42 replaced atoms. It should be remembered that, according to the chosen conventional hierarchy, an atom is considered to belong to an edge if it lies on an edge *and not* on a vertex, and it is considered to belong to a face, if it lies on that face *and not* on an edge or a vertex.

It is clear that such a procedure is not exhaustive, excluding, for example, all the configurations in which the Fe atoms are positioned at random, and, moreover, it limits the possible number of Fe atoms to those obtainable as sums of sub-shell numbers. However, we believe that such a procedure should

be sufficient to give the main structural features of the alloying process, particularly in the case of the Pt/Fe pair, in which random configurations do not seem to be favoured [13].

4. Results and discussion

The results of EHT total energy calculations for some selected cluster structures are given in Table 2. They are distinguished according to the size and geometry of the 'generating' pure Pt cluster, the number of Fe atoms, and their positions according to the nomenclature previously given. The Gaussian broadening factor, γ, was set equal to $556\ \mathrm{eV}^{-2}$, approximately corresponding to a pure 'thermal' broadening at room temperature, but completely analogous results were obtained with $\gamma = 5.56\ \mathrm{eV}^{-2}$ (one of the smallest values considered in the literature). Note again that even the pure Fe clusters are positioned according to the MBP geometries of pure Pt clusters.

Let us start by analyzing in some detail the energetics of cluster formation. One can define the EHT atomization energies (AE) for each cluster as the difference, $-\mathrm{AE}[\mathrm{Pt}_n\mathrm{Fe}_m] = \mathrm{E}[\mathrm{Pt}_n\mathrm{Fe}_m] - n\mathrm{E}[\mathrm{Pt}] - m\mathrm{E}[\mathrm{Fe}]$, where $\mathrm{E}[\mathrm{Pt}_n\mathrm{Fe}_m]$ is the EHT total energy of the cluster and E[Pt] and E[Fe] are the EHT energies of the Pt and Fe atoms, respectively. From this, one obtains the binding energy per atom (BE/N), i.e. $\mathrm{BE}/N[\mathrm{Pt}_n\mathrm{Fe}_m] = \mathrm{AE}[\mathrm{Pt}_n\mathrm{Fe}_m]/(n+m)$. The BE values per atom for pure Pt and Fe clusters as functions of $1/\sqrt[3]{N_{\mathrm{at}}}$ (approximately, the inverse of the mean radius of the cluster), are reported in Fig. 1. Starting with pure Pt clusters, one can notice first of all that BE/N is a smoothly increasing function of the cluster size, ranging between ~0.9 eV for Pt_{13} and ~1.16 eV for Pt_{309}. EHT thus seems to severely underestimate the experimental BE/N of pure Pt, which is ~5.8 eV [25]. This can be easily explained by thinking that, if there were no bonding s-orbitals available, the d-band would be fully occupied for Pt, and there would be no EHT bonding. It is the availability of bonding s-orbitals which produces an electron flow from the d- to the s-band (together with a minor stabilization of the entire d-band) and thus a (small) stabilisation of the system (for EHT bonding in a dimer system see, for example, Ref. [26]). However, it can be noted that the EHT energy does not correctly take into account the Coulombic repulsions among the electrons, so that the EHT atomic reference configuration for Pt is d^{10}. Electronic repulsion in reality makes the true atomic configuration for Pt d^9s^1 (neglecting spin-orbit effects). One can very roughly take into account this effect by choosing the d^9s^1 configuration as the atomic reference for Pt, while leaving unaltered the total energy values for larger clusters: Coulombic repulsions become more and more effectively screened with increasing cluster size. The BE/N values derived from the AE values reported in Table 2 (in a less approximate way, the larger the cluster size) may thus be all increased by a constant term equal to the difference between the s- and d-energy levels, that is ~3.5 eV, thus giving a value of ~4.7 eV for the Pt BE/N value extrapolated to the infinite crystal (which, in any case, remains still ~25% smaller than the experimental value).

The corresponding BE/N values for the fictitious Fe system (in which — we repeat again — the geometries are the same as those for pure fcc Pt, and therefore with atom–atom distances certainly larger than those appropriate for pure bcc or fcc iron) range between ~1.2 eV for Fe_{13} and ~3.8 eV for Fe_{309}. The predicted Fe BE/N is ~3.9 eV, i.e. about ~10% smaller than the experimental value (~4.3 eV for pure fcc iron) probably due to too large Fe–Fe distances. The theoretical value for the Fe BE/N is thus larger than the Pt one (which is contrary to experimental observations), for essentially two reasons: (a) even if there were no bonding s-orbitals available, the d-band for Fe would not be completely full (unlike in the Pt case), and would give rise to a substantial bonding (the availability of bonding s-orbitals adds an electron flow from the d- to the s-band, which further enforces the metallic bond); and (b) the EHT parameters are such that the bands are wider (and the associated energy stabilisation thus larger) for Fe than for Pt.

The BE/N values for both Pt and Fe might be improved by a proper re-parametrization of the EHT model [19–21,27]: for example, by adjusting the semiempirical one-electron atomic levels, or by modifying the Wolfsberg–Helmoltz formula for the orbital interaction and by including spin-orbit effects for platinum as in Ref. [27]. We believe however that — without a reparametrization of the method based on firm ab initio grounds — it may be dangerous to

introduce changes aimed at reproducing the experimental value of just one particular property, and it is meaningful to stick to parameters which at least found justification on a study of the atomic energy levels [15–17,19].

Still considering pure Pt clusters, it is also interesting to note that — according to the present EHT calculations — single-crystal structures (cuboctahedra) are preferred to icosahedral structures, even at very small cluster sizes ($N_{at} = 13$). This is at variance with the known behaviour of systems such as clusters of rare gas atoms, or atoms interacting through spherically symmetric potential, or many experimentally suggested structures of clusters of first-row transition metals (see the references cited in Ref. [24], for example). For these systems, it is known that icosahedral (in general, five-fold axes) or even amorphous structures should be favoured for clusters of low nuclearity. To understand this discrepancy, it can be noted that EHT calculations on cuboctahedral and icosahedral $N_{at} = 13$ clusters in which the atom–atom distances were not taken from the MBP optimized structures ($R = 2.618$ and 2.566 Å, for the cuboctahedron and icosahedron, respectively), but set equal to the bulk value, $R = 2.774$ Å [13], give the icosahedron as the most stable configuration. This can be rationalized by thinking that, as the atom–atom distances increase, the d–d orbital interactions rapidly become negligible with respect to the s–s ones, and therefore the atom–atom potential more and more resembles a spherically symmetric one (with the main difference being a variable number of s-electrons — taken from the d-reservoir when the s-levels go below the Fermi level $\varepsilon_F = \varepsilon_d$ — and the inclusion of an atom–atom repulsion term, also presumably spherically symmetric). The Pt preference for single-crystal structures is thus a consequence of the weight given in EHT model calculations to d–d interactions with respect to s–s ones. In an atom such as platinum, in which the relativistic contraction of the atomic s-orbital (even neglecting spin-orbit effects) makes the d-orbitals strongly involved in the chemical bonding, we believe that a proper treatment of such interactions is essential for a correct prediction of the electronic and geometrical structures of clusters. In this connection, the present calculations are just a preliminary step toward an accurate theoretical description of these systems. Experimentally, there is no general agreement on the structures of Pt nanoclusters, maybe due to a dependence on the method of preparation. However, it is interesting to note that clusters prepared via the MVD technique, in experimental conditions presumably close to equilibrium ones, seem to be ordered [5–10]. On the contrary, it can be noted that the fictitious Fe system seems to decidedly prefer icosahedral geometries, probably because of too large interatomic distances (calculations performed at Pt geometries).

Passing now to mixed Pt/Fe clusters, it is interesting to observe that for small clusters ($N_{at} \leq 55$) the substitution of Pt atoms with Fe atoms tends to shift the energy preference towards icosahedral structures. For the larger clusters ($N_{at} = 147$) this remains true up to a certain Fe composition, above which the cuboctahedral geometries again turn out to be the preferred ones.

In order to study the energetics of Fe dissolution into Pt clusters, it is useful to consider the following process:

$$(\mathrm{Pt/Fe})_{\mathrm{cluster}} + (\mathrm{Fe})_{\mathrm{cluster}} + (\mathrm{Pt})_{\mathrm{cluster}} \rightarrow (\mathrm{Pt}_{-1}\mathrm{Fe}_{+1})_{\mathrm{cluster}} + (\mathrm{Fe}_{-1})_{\mathrm{cluster}} + (\mathrm{Pt}_{+1})_{\mathrm{cluster}} \quad (1)$$

This corresponds to removing an Fe atom from a pure Fe cluster, inserting it in an (Pt/Fe) cluster in the place of a Pt atom, rearranging the new $(\mathrm{Pt}_{-1}/\mathrm{Fe}_{+1})_{\mathrm{cluster}}$ to the optimal configuration, and finally inserting the Pt atom extracted from the $(\mathrm{Pt/Fe})_{\mathrm{cluster}}$ into a pure Pt cluster. The ΔE of this reaction can be expressed as:

$$\Delta E = E[(\mathrm{Pt}_{-1}/\mathrm{Fe}_{+1})_{\mathrm{cluster}}] - E[(\mathrm{Pt/Fe})_{\mathrm{cluster}}] + E[\mathrm{Pt}] - E[\mathrm{Fe}] - \mathrm{BE/N[Pt]} + \mathrm{BE/N[Fe]}$$

where $E[(\mathrm{Pt}_i/\mathrm{Fe}_j)_{\mathrm{cluster}}]$ is the energy of the corresponding Pt/Fe cluster in the optimal configuration, E[Pt] and E[Fe] are the energies of the free atoms and BE/N[Pt] and BE/N[Fe] are the corresponding binding energies per atom. If one supposes for simplicity that only pure Fe or Pt clusters that are large enough to approach the bulk BE/N are considered, one can use BE/N values extrapolated for the infinite system, i.e. BE/N[Pt]∼1.2(4.7) eV and BE/N[Fe]∼3.9 eV, from our EHT calculations. The reaction, (1) will thus be exothermic if $\delta E = E[(\mathrm{Pt}_{-1}/\mathrm{Fe}_{+1})_{\mathrm{cluster}}] - E[(\mathrm{Pt/Fe})_{\mathrm{cluster}}] < 21.6$ eV, endothermic otherwise: in our calculation, 21.6 eV is the threshold for the purely electronic contribution (that given by EHT) to the

energetics of Fe dissolution into Pt. In order to compare clusters with a difference in the number of Fe atoms larger than one, say *m*, one has simply to divide δE by *m* and to compare the result with the 21.6 eV threshold. In terms of the AE values reported in Table 2, this corresponds to the inequality $AE(Pt_{-1}Fe_{+1}) - AE(PtFe) > 2.7$ eV for the mixing reaction to be exothermic. From an inspection of Table 2, one can thus see that — according to the present calculations — dissolution of Fe into Pt is an exothermic process, at least up to an Fe content of about 50%. For a larger Fe content, it may become an endothermic process, depending on the geometry of the clusters and other factors. This finding is very important, since it shows that — even though the present theoretical approach may give a Pt–Pt bond weaker than the Fe–Fe bond (which is contrary to experimental observations) — it predicts that the mixing reaction is exothermic, which means that the Pt–Fe bond is stronger than arithmetic mean of the Pt–Pt and Fe–Fe bonds (at least up to a certain Fe content), and this is in agreement with experimental data reported in 2.

It is now useful to analyze in more detail the results of Table 2 from the viewpoint of Fe positions. By an inspection of these results, the following conclusions can immediately be drawn:

1. When few Fe atoms are introduced, it is difficult to predict the most stable configuration. However, as the size of the cluster increases, the Fe preference seems to shift from the surface to the interior of the cluster, even though not exactly at the center, but in less symmetric positions.
2. When a substantial amount of Fe atoms is introduced (around the composition $FePt_3$), there appears a clear preference for internal and asymmetric configurations (in which there are no iron atoms at the surface) both within cuboctahedral and icosahedral structures. For example, in the cuboctahedral $Pt_{105}Fe_{42}$ cluster, the configurations with Fe atoms at the surface are less favourable with respect to the other ones [in the order $II,III(f_{100},v),IV(v) > II,III(f_{100}),IV(f_{100}) > III(f_{100},v),IV(f_{100})$], while — among the latter ones — the preferred configuration is $II,III(f_{100},e)$, which is less symmetrical and contains Fe atoms more ‘intermixed’ with Pt atoms with respect to the III configuration.
3. When still more Fe atoms are introduced (with the approximate composition of FePt), it becomes numerically impossible to put them all in the interior of the cluster, and a fraction of them will be found at the surface. However, the other features of Fe substitution remain the same.
4. The previous conclusions are true for both single-crystal (cuboctahedra or truncated octahedra) and icosahedral geometries.

One can thus summarize that the iron and platinum atoms distribute themselves, taking into account both the order of bond strengths (which is Fe–Fe > Fe–Pt > Pt–Pt from the theoretical calculations whereas it is Pt–Pt > Fe–Pt > Fe–Fe from experimental measurements) and the fact that the Fe–Pt bond strength is larger than the arithmetic mean of the Pt–Pt and Fe–Fe bond strengths (which is true both experimentally and theoretically). As a result, this produces a tendency for the iron atom to occupy the most internal shells, until this is numerically possible, with a large intermixing with platinum atoms and in non-symmetrical configurations. These conclusions, albeit possibly influenced by the choices of the EHT parameters, are in agreement with the experimental results reviewed in Section 2, i.e. the complete Pt monolayer at the (111) surface of $Fe_{0.2}Pt_{0.8}$ [3], the inert catalytic behaviour of iron in Pt/Fe clusters at high Pt:Fe ratio [4], and the fact that — according to Mössbauer measurements — iron atoms occupy sites of non-cubic symmetry which are not all equivalent in Pt/Fe nanoclusters [4]. In connection with the latter work, it can be noted that Pt segregation to the surface also explains the decrease of H_2 or CO adsorption with increasing Fe content: when more and more Fe atoms are present, some of them are not reduced and remain as ions, thus interacting weakly with H_2 and CO.

A further contribution to ΔE which is neglected in the EHT model is the Coulombic one (see the discussion of the approach in the previous section). A major component is thus the one associated with a charge transfer between Fe and Pt. To understand, qualitatively, the effect produced by such a charge transfer on the distribution of the different atoms, one can resort to a very simple model in which each atom is substituted by a point charge assumed equal for all like atoms (thus neglecting the minor differences associated with the difference in atomic sites). In the

Table 3
The quantities: Fermi level, $\varepsilon_F(N)$ (in eV); total energy, $E_T(N)$ (in eV); ionisation potential (IP, in eV); electron affinity (EA, in eV); and density of states calculated at the Fermi level, DOS[$\varepsilon_F(N)$], are reported for some selected clusters with $N_{at} = 201$ and for three different choices of the broadening parameter, γ (in eV^{-2})

γ	$\varepsilon_F(N)$	$E_T(N)$	DOS[$\varepsilon_F(N)$]	IP	EA
Pt_{201}					
5.56	− 11.0635	− 25 526.6557	277.3508	11.3019	11.2998
29.59	− 11.1811	− 25 533.0411	405.3812	11.2497	11.2482
556	− 11.2161	− 25 535.7279	567.9229	11.2228	11.2215
$Pt_{153}Fe_{48}$ [II,III(e,v)]					
5.56	− 11.2084	− 24 491.8564	401.8989	11.3192	11.3174
29.59	− 11.2493	− 24 504.5919	460.7002	11.2663	11.2643
556	− 11.2595	− 24 508.2013	483.4315	11.2632	11.2613
$Pt_{153}Fe_{48}$ [II,III(v),IV]					
5.56	− 11.2189	− 24 490.0128	415.8732	11.3291	11.3274
29.59	− 11.2571	− 24 502.5927	497.2323	11.2692	11.2675
556	− 11.2598	− 24 506.2002	622.9545	11.2643	11.2631
$Pt_{105}Fe_{96}$ [II,III(e,v),IV,V(v)]					
5.56	− 11.3541	− 23 454.4869	463.6031	11.4115	11.4096
29.59	− 11.3710	− 23 471.2344	464.0235	11.3756	11.3733
556	− 11.3736	− 23 475.0770	431.9663	11.3742	11.3723
Fe_{201}					
5.56	− 11.6197	− 21 164.1191	496.0730	11.6410	11.6391
29.59	− 11.6284	− 21 181.8045	508.7760	11.6295	11.6276
556	− 11.6215	− 21 185.7927	539.0942	11.6174	11.6153

resulting system of charges, the electrostatic interaction energy will be minimised by a configuration in which the minority charge component is positioned in the interior of the cluster and is largely intermixed with the majority charge component. The Coulombic contribution thus parallels the electronic one in not favouring Fe segregation at the surface (it is a general feature of alloying the fact that surface segregation of the minority component can only be caused by an electronic effect).

The last contribution to the dissolution free energy is the entropic one. This should be a minor one according to the present calculations: one finds substantial energy differences between the various configurations considered in Table 2, of the order of several tenths of an electron volt, and these should easily overwhelm the entropic contributions associated with disordered phases or frozen solutions. This is in agreement with the experimental tendency of Pt/Fe alloys to give ordered phases, not only in the bulk but also at interphases [3,13]. This tendency should be present also in small particles, according to the present calculations.

It can be noted, in conclusion, that calculations have also been performed with other possible choices of the parameters [20,21], qualitatively obtaining the same conclusions as those reported earlier.

Once the structural features of the Pt/Fe system have thus been characterized, the electronic structure of the energetically most stable clusters can be analyzed in more detail. For space reasons, such an analysis (which has been performed for all the most stable clusters of a given composition and geometrical arrangement of the atoms) will be presented only for selected clusters.

First of all, one can notice that the highest occupied molecular orbital is nearly always degenerate, thus implying an (albeit small) Jahn–Teller effect (see the previous discussion). Exceptions are the cuboctahedral Pt_{13}, Pt_{147} and Pt_{309} clusters, and the truncated octahedral Fe_{201} and $Pt_{153}Fe_{48}$ ones. In Fig. 1, the band-width and ‘true’ gap values for pure platinum

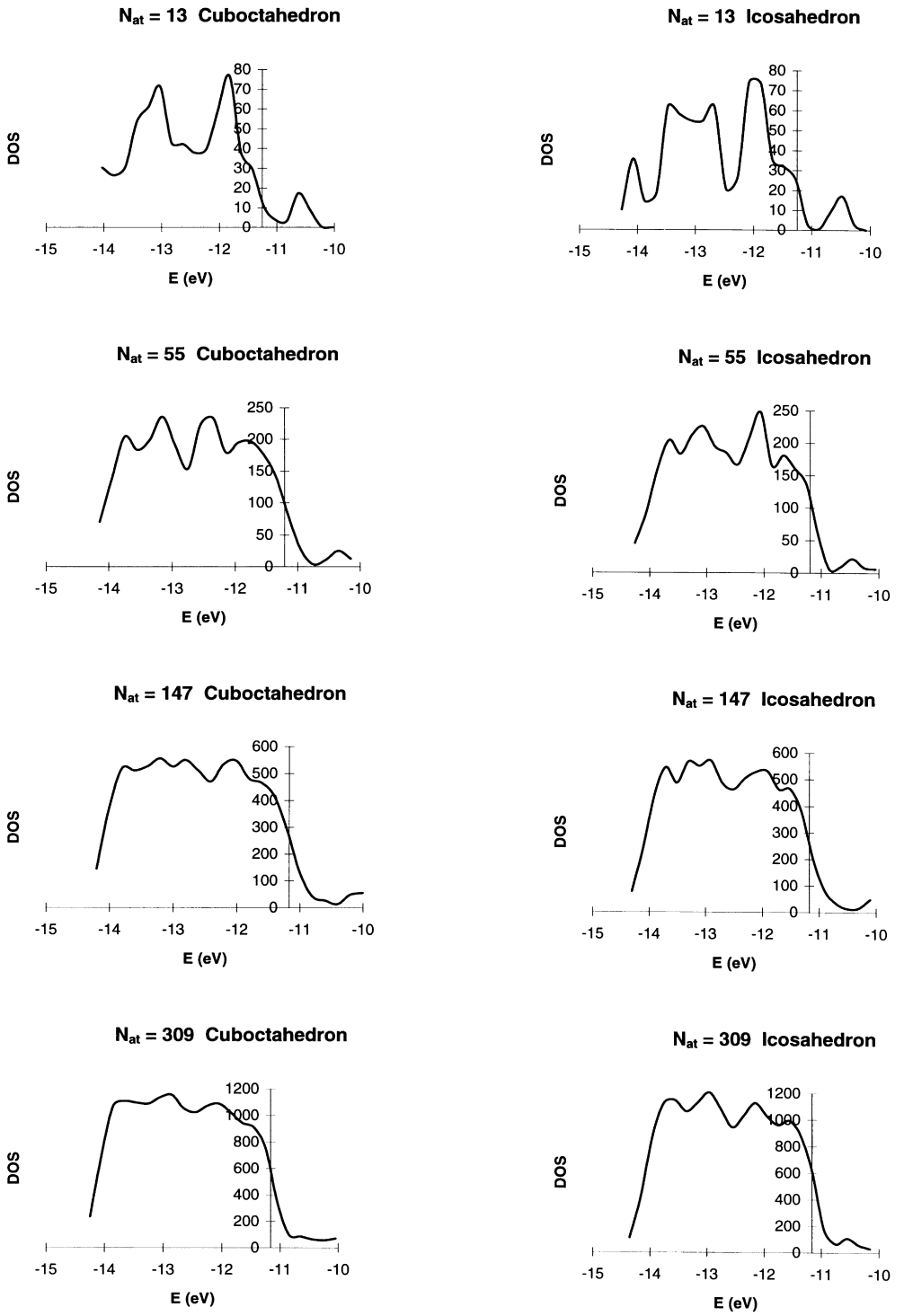

Fig. 2. DOS(ε) plots are shown for pure Pt clusters with $\gamma = 29.59\ \mathrm{eV}^{-2}$ as a function of the cluster size.

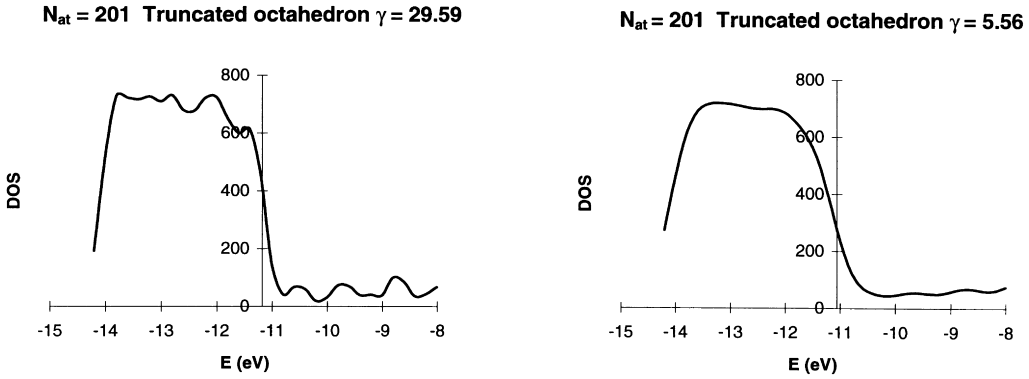

Fig. 3. DOS(ε) plots are shown for the Pt_{201} cluster and two different γ values (in eV^{-2}).

clusters are also reported. For $N_{at} \geq 147$, these quantities do not strongly depend on N_{at} (completely analogous results are found when considering Pt/Fe mixed clusters). From an inspection of Fig. 1, one can conclude that the smallest clusters ($N_{at} = 13$) still present a molecular-type appearance. For $N_{at} = 55$ one is probably in the intermediate *régime*, but already for $N_{at} = 147$ one expects a metallic-type behaviour, with a band gap smaller than ~0.01 eV. A bulk-like behaviour is thus approached at cluster sizes in the 100 to 200 atom range, in analogy with previous studies [28,29].

Further information can be drawn from Table 3, in which the quantities $\varepsilon_F(N)$, $E_T(N)$, IP, EA and DOS[$\varepsilon_F(N)$] are reported for selected clusters with $N_{at} = 201$ and for three different choices of the broadening parameter, γ. The following points are worth noticing:

1. The $\varepsilon_F(N)$, IP and EA values are nearly coincident, do not strongly depend on the composition of the cluster, and are roughly twice as large as the values of the pure platinum work function: WF(Pt) = 5.4 eV [25]. From results not reported in Table 3, one also finds that these values scarcely depend on the size of the cluster. This is in conflict with the known experimental behaviour of IP and EA as functions of the cluster size, etc. However, it should be remembered that the EHT energy does not correctly take into account the Coulombic contributions, which are mainly responsible for this behaviour, because one here compares systems with a different number of electrons.
2. The quantities, $E_T(N)$ and (especially) DOS[$\varepsilon_F(N)$], are very sensitive to the choice of the broadening parameter, γ. On the contrary, the relative stabilities of the clusters are much less dependent on γ, which makes us confident of the reliability of the structural predictions presented previously.
3. The formulae involving the derivatives of $\varepsilon_F(N)$, $E_T(N)$ and DOS[$\varepsilon_F(N)$] with respect to N presented in the previous section have been compared with the values for the corresponding quantities obtained through numerical differentiation using $\Delta N = \pm 1$. It has been found that the numerical values coincided with the analytical ones up to the limit of numerical accuracy for all the clusters considered in the present work, with a few exceptions concerning the smallest ones (i.e. $N_{at} = 13$).

To conclude the discussion of the electronic structure of Pt and Pt/Fe nanoclusters, we will present plots showing the DOS as a function of ε in some illustrative examples.

In Fig. 2, DOS(ε) plots are shown for pure Pt clusters with $\gamma = 29.59\ eV^{-2}$ as a function of the cluster size: one can clearly see, as N_{at} increases: (a) the evolution of the DOS function from complex shapes, which still keep the memory of the molecular origin, to rather smooth shapes which are typical of a metallic system; and (b) the progressive smoothing of the differences between cuboctahedral and icosahedral clusters, albeit that the latter generally exhibit more structured DOS patterns even for the larger sizes.

In Fig. 3, DOS(ε) plots are shown for the Pt_{201} cluster for two different γ values: one can see that

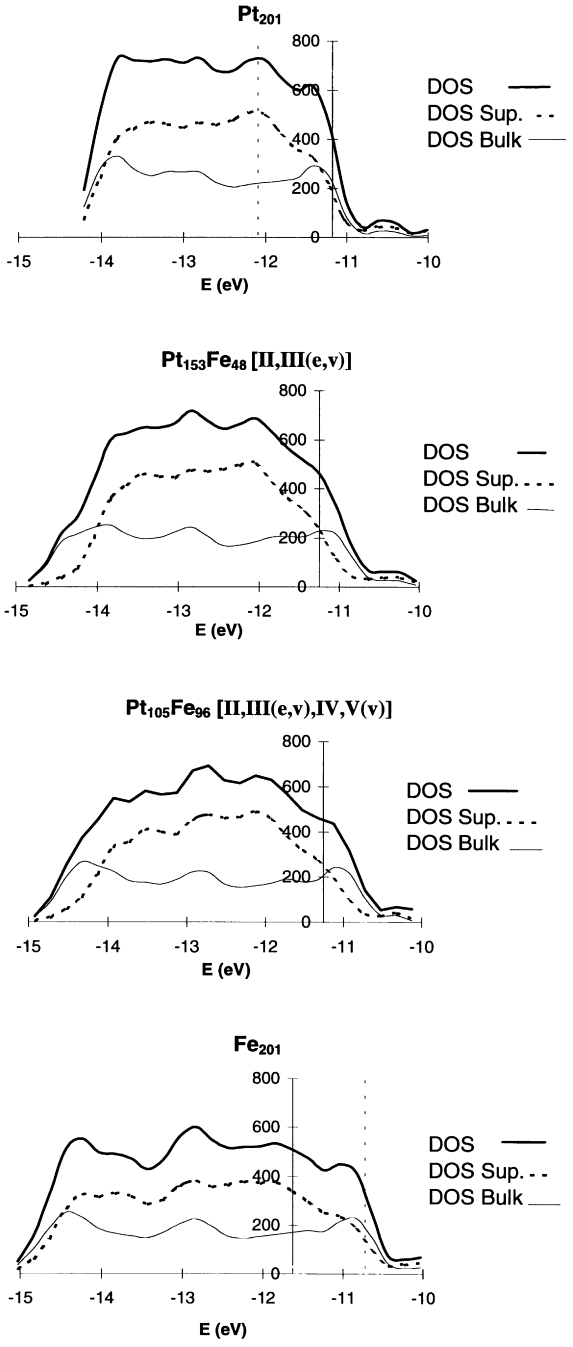

Fig. 4. DOS(ε) plots are shown for some selected truncated octahedral ($N_{at} = 201$) clusters. The bulk and surface contribution to the LDOS(ε) function are also separately shown. For comparison, in the case of the two pure systems, the Fermi level is also shown as a dotted line calculated with a number of electrons appropriate for the complementary pure system.

increasing the value of γ leads to a shape in which all the DOS peaks are smoothed out, but whose general appearance has not changed too much. It is clear, therefore, that quantities which depend only on cumulative sums of the DOS function may be reasonably evaluated using a small γ value which, in turn, gives a very smooth DOS function, easily represented — at least in this limited portion of the spectrum — in terms of a few moments with respect to ε; whereas quantities which depend substantially on the detailed shape of the DOS will be poorly represented by an expansion in terms of a few moments (or, equivalently, a small broadening parameter, γ). The range of ε in Fig. 3 has been slightly enlarged to give an idea of the first unoccupied levels: it is interesting to note that the DOS(ε) below the Fermi level mainly contains d-orbital states, whereas s-orbitals give a large contribution to the first DOS peaks above ε_F.

Finally, in Fig. 4, DOS(ε) plots are shown for some selected truncated octahedral ($N_{at} = 201$) pure and mixed nanoclusters. For comparison, the bulk and surface contributions to the LDOS(ε) function are also separately shown. These are defined as the sums over surface and bulk atoms, respectively, of the Mulliken gross atomic populations relative to the LDOS ($\varepsilon,\bar{r}$) function. From an inspection of Fig. 4, the following conclusions can be drawn:

1. The EHT parameters are such that the Fe band is wider and more structured than the Pt one. Nevertheless, there exists a similarity between the two: also the bulk and surface contributions to the total band structure are similar, although the Fermi levels are at different places.
2. The electron count, however, makes the Fermi level in the Pt case lie toward the end of the band, whereas in the Fe case it lies in the interior of the band. This implies that the DOS(ε_F) value is larger for Fe and that the surface and bulk contribution to DOS(ε_F) are nearly equal for Pt, whereas the surface contribution largely exceeds the bulk one for Fe.
3. For the mixed Pt/Fe systems, one finds an intermediate situation, in which the DOS(ε) functions and their surface and bulk contributions appear to be describable as linear combinations of the two pure (model) cases. In particular, with the composition, $Pt_{153}Fe_{48}$, representative of ~30% Fe

content, with only Pt atoms at the surface, the surface contribution is nearly superimposable on the corresponding contribution in the pure Pt cluster, whereas the bulk contribution does not exactly match either of the two model cases: for example, it is wider than the pure Pt one and narrower than the pure Fe one. Analogous considerations hold for the composition representative of ~50% Fe content.

The third point is especially worth noting, since it suggests the conclusion that Fe alloying does not drastically alter the electronic configuration of the surface atoms, and thus that its effects over the electronic properties of the clusters are subtle ones, in agreement with the fact that experimentalists have observed a fine modulation of the catalytic activity of these systems [3,5–10].

This concludes the analysis of the electronic structure of Pt/Fe nanoclusters from EHT calculations. A more detailed investigation of the relationships among the structural and electronic features with other properties of these systems (e.g. the catalytic ones) is in progress and will be published elsewhere.

Acknowledgements

We thank Dr. Carlo Mealli (ISSECC, CNR, Firenze) for providing us with the latest version of the CACAO set of programs; Dr. Andrea Ienco (ISSECC, CNR, Firenze) for precious technical assistance with the CACAO program; Dr. Gregorio D'Agostino (ENEA, Roma) for useful discussions and for providing us with the MBP optimized geometries; and Dr. Giovanni Vitulli (CSMSOA, CNR, Pisa) for enlightening discussions on the experimental results. Financial support from the Italian Consiglio Nazionale delle Ricerche (fellowship no. 201.03.25) granted to one of us (AMV) is gratefully acknowledged.

References

[1] V. Ponec, G.C.Bond, Catalysis by Metals and Alloys, Studies in Surface Science and Catalysis, Elsevier, Amsterdam, 1995.
[2] K.J. Klabunde, Free Atoms, Clusters, and Nanoscale Particles, Academic, London, 1994.
[3] J.C. Bertolini, J. Massardier, Catal. Lett. 9 (1991) 183.
[4] M.A. Vannice, R.L. Garten, J. Mol. Catal. 1 (1975) 201.
[5] G. Capanelli, A. Bottino, G. Gao, A. Grosso, A. Servida, G. Vitulli, A. Mastrantuono, R. Lazzaroni, P. Salvadori, Catal. Lett. 20 (1993) 287.
[6] G. Vitulli, R. Falorni, P. Salvadori, A. Parmaliana, F. Frusteri, N. Giordano, Catal. Lett. 17 (1993) 151.
[7] G. Vitulli, E. Pitzalis, R. Lazzaroni, P. Pertici, P. Salvadori, O. Salvetti, S. Coluccia, G. Martra, Mater. Sci. Forum 195 (1995) 93.
[8] G. Martra, S. Coluccia, O. Monticelli, G. Vitulli, Catal. Lett. 29 (1994) 105.
[9] G. Vitulli, E. Pitzalis, A. Verrazzani, P. Pertici, P. Salvadori, A. Giroir-Fendler, J.A. Dalmon, Procedings of the X Italian Congress of Catalysis, L'Aquila, 8–11 September 1996, Ed. SCI, Torino, 1996.
[10] G. Vitulli, E. Pitzalis, A. Verrazzani, P. Pertici, G. Martra, A. Fortunelli, A.M. Velasco, Catal. Lett., in preparation.
[11] L. Yang, A.E. DePristo, J. Catal., 148 (1994) 575; J.A. Rodriguez, M. Kuhn, J. Phys. Chem. 100 (1996) 381.
[12] P. Herman, D. Simon, P. Sautet, B. Bigot, J. Catal. 167 (1997) 33.
[13] J. Crangle, Phil. Mag. 7 (1962) 107.
[14] S.K. Overbury, P.A. Bertrant, G.A. Somorjai, Chem. Rev. 75 (1975) 547.
[15] R. Hoffmann, W.N. Limpscomb, J. Chem. Phys. 36 (1962) 2179.
[16] R. Hoffmann, W.N. Limpscomb, J. Chem. Phys. 37 (1962) 2872.
[17] R. Hoffmann, J. Chem. Phys. 39 (1963) 1397.
[18] C. Mealli, D.M. Prosepio, J. Chem. Ed. 67 (1990) 399.
[19] R.H. Summerville, R. Hoffrnann, J. Am. Chem. Soc. 98 (1976) 7240.
[20] J.-Y. Saillard, R. Hoffrnann, J. Am. Chem. Soc. 106 (1984) 2006.
[21] A.G. Gavezzotti, G.F. Tantardini, H. Miessner, J. Phys. Chem. 92 (1988) 872.
[22] A. Fortunelli, A. Painelli, J. Chem. Phys. 106 (1997) 8041.
[23] G. D'Agostino, Mater. Sci. Forum 195 (1995) 149.
[24] C.L. Cleveland, V. Landman, J. Chem. Phys. 94 (1991) 7376.
[25] C. Kittel, Introduction to Solid State Physics, Wiley, New York, 1968.
[26] A. Dedieu, R. Hoffmann, J. Am. Chem. Soc. 100 (1978) 2074.
[27] B. Bigot, C. Minot, J. Am. Chem. Soc. 106 (1984) 6615.
[28] R.C. Baetzold, M.G. Mason, J.F. Hamilton, J. Chem. Phys. 72 (1980) 366.
[29] M.G. Mason, in: G. Pacchioni, P.S. Bagus, F. Parmigiani (Eds.), Cluster Models for Surface and Bulk Phenomena, Nato ASI Series B, vol. 283, Plenum Press, New York, 1992, p. 115.

ELSEVIER

Journal of Molecular Structure (Theochem) 501–502 (2000) 251–259

THEO CHEM

www.elsevier.nl/locate/theochem

Density-functional study of Pt_{13} and Pt_{55} cuboctahedral clusters ☆

E. Aprà[a,1], A. Fortunelli[b,*]

[a]*Dipartimento di Scienza dei Materiali, via Emanueli 15, 20126 Milan, Italy*
[b]*Istituto di Chimica Quantistica ed Energetica Molecolare del CNR, via del Risorgimento 35, 56126 Pisa, Italy*

Abstract

The results of an accurate density-functional study of the structure and energetics of Pt_{13} and Pt_{55} cuboctahedral clusters are presented. The calculations utilize the Becke functional [A.D. Becke, Phys. Rev. A 38 (1988) 3098] for exchange and the Perdew–Wang functional [J.P. Perdew, Y. Wang, Phys. Rev. B 33 (1986) 12; J.P. Perdew, J.A. Chevary, S.H. Vosko, K.A. Jackson, M.R. Pederson, D.J. Singh, C. Fiolhais, Phys. Rev. B 46 (1992) 6671] for correlation, but comparison is made also with the Hartree–Fock approximation and a "hybrid" method, which employs a mixture of the Hartree–Fock and density functionals. A peculiar structural rearrangement is found for Pt_{55}, even imposing the cuboctahedral symmetry, which shows the tendency of the system toward "spherical" configurations. Comparison with previous atom–atom potential and extended Hückel findings shows the validity of the density-functional theory for describing the wave function of these nearly metallic systems. In contrast, the failure of the Hartree–Fock approximation on these systems is confirmed, whereas some doubts arise about the validity of the hybrid method for describing the electronic structure (if not the energetics) of platinum clusters.

Keywords: Density of states; Platinum nano clusters; Binding energies; Structural relaxation; Electron smearing

1. Introduction

Nanoscale clusters (with diameter ~1–100 nm) represent a state of matter which encompasses the transition from the molecule to the bulk state. As such, they have been intensively studied in recent years (see, e.g. Ref. [1]), with emphasis on their peculiar electronic, structural and catalytic properties. In this context, platinum clusters seem particularly interesting, in view of their applications in heterogeneous catalysis (see, e.g. Ref. [2]).

In the present article, density functional (DF) calculations on Pt_{13} and Pt_{55} cuboctahedral clusters are presented. Their results are analyzed in detail from the point of view of structural rearrangement, energetics of cluster formation and electronic structure, and compared with the results of atom–atom potential [3] and extended Hückel (EH) [4] calculations.

Pt_{13} and Pt_{55} have been chosen as sections of the fcc lattice of bulk platinum which exhibit body-centered cuboctahedral arrangements. This allows one to exploit the full O_h symmetry, which has been imposed also in the structural optimizations. The requirement of O_h symmetry excludes the possibility of investigating disordered structures, but the simplifications in the computational procedure assured by the use of symmetry make it possible to use a fully self-consistent DF approach with a good basis set and a computationally accurate (e.g. with regard to

☆ Dedicated to Professor R. Gáspár on the occasion of his 80th year.

* Corresponding author.

[1] Present address: Environmental Molecular Sciences Laboratory, Pacific Northwest National Laboratory, P.O. Box 999, Richland, WA 99352, USA.

0166-1280/00/$ - see front matter
PII: S0166-1280(99)00436-4

numerical integration) scheme. The aim of the present work is therefore also to furnish through extensive calculations a computational standard against which more simplified approaches (such as for example the corrected effective medium theory [5] or the Harris functional [6] among the DF ones) can be contrasted.

2. Computational details

All the calculations were carried out with the DFT module of the NW-Chem computational chemistry package [7] that uses Gaussian Type Orbitals (GTOs) for the solution of the Kohn–Sham equations.

The Atomic Orbital basis used in this work was derived from a (7s6p5d)/[6s3p2d] basis set [8]: we removed the most diffuse p function that causes numerical instabilities in these highly condensed systems and split the first p contraction of 4 GTOs to 2 contractions of 3 and 1 GTOs, respectively. In order to ease the computational burden, an Effective Core Potential (ECP) was used [9] to allow us to consider valence-electron-only wave functions.

This ECP incorporates spin–orbit averaged relativistic effects for the platinum atom. Despite the incomplete account of spin–orbit effects and the lack of Darwin and mass-polarization relativistic corrections in the ECP, the present computational approach described, in a reasonable way, the energetics of Pt–Pt bonds in small clusters [10,11].

In addition to the basis set for the Kohn–Sham orbitals, a charge density fitting basis was used to compute the Coulomb potential according to the method described in Ref. [12]. The basis set used was derived from the one described in Ref. [13] by removing the most diffuse p orbital. Numerical tests for Pt and Pt_{13} have shown that the effect of this approximation on the evaluation of the total energy is of the order of mHartrees.

A numerical integration is necessary for the evaluation of the exchange-correlation potential and energy. The scheme used in this work adopts well-known techniques that partition the density into atomic contributions [14]; this “atomic” density is then integrated using a radial quadrature [15] and a highly efficient angular quadrature [16].

To give an idea of the computational effort involved in the calculations, we quote that a single SCF cycle for Pt_{55} using the present methodology requires ~400 s when running on a CRAY-T3E computer (32 nodes).

In order to overcome the degeneracy problem that may arise in systems such as these, containing many heavy elements, a smearing technique for the fractional occupation of the energy levels was applied [17,18]; in our implementation, an error function was used with a broadening factor of 5.44×10^{-3} eV for the evaluation of the occupation numbers.

As for the geometry optimizations, they were stopped when maximum force on atoms was less than 4×10^{-4} a.u.

3. Method

The structural optimizations have been performed by using the DF theory, utilizing two approximate functionals: the Becke one [19] for exchange and the Perdew–Wang one [20,21] for correlation, hereafter referred to with the acronym BPW91. Spin unrestricted calculations have always been performed. The DF approach is the most reliable among the current theoretical methods for treating systems such as nanoclusters of transition metal atoms. The computational and in-principle difficulties of standard quantum chemical methods in describing exchange and correlation interactions in these systems are in fact well known, associated with the presence of at least two different open shells (s and d) with both localized and delocalized character and a vanishing gap. The results of the BPW91 method are representative of the whole class of “gradient-corrected” approaches (analogous results have been obtained in test calculations on Pt_{13}—not reported here—using other functionals). The BPW91 functional has been chosen in particular because on these systems it exhibits better convergence properties with respect to other possible choices. For comparison, calculations at a fixed geometry have been performed using also the Hartree–Fock (HF) or a “hybrid” method (B3PW91 approach), which mixes the HF and BPW91 functionals according to the prescription given in Ref. [22] (with the only difference that we use the VWN functional for the local density part [23]). The failure of the HF approximation on metallic systems is

Table 1
Absolute energies (E) at the BPW91 geometries; ΔE [Pt : $S = 1 \rightarrow 0$] : excitation energy from the $S = 1$ $5d^9 6s^1$ ground state to the $S = 0$ $5d^{10}$ excited state of the Pt atom; ΔE_{relax}: energy difference between the crystalline and the BPW91-optimized geometry; BE/N: Binding Energies per atom for a given cluster as calculated or extrapolated according to the various procedures explained in the text, are reported as obtained by using the HF, B3PW91 and BPW91 approaches. Absolute energies are in a.u., all other quantities are in eV

	HF	B3PW91	BPW91
E [Pt] ($S = 1$)	−118.39099	−119.35053	−119.38066
ΔE [Pt : $S = 1 \rightarrow 0$]	0.911	0.491	0.520
E [Pt_{13}]	−1538.79637	−1552.80424	−1553.46557
ΔE_{relax} [Pt_{13}]	−0.222	0.410	0.237
BE/N [Pt_{13}]	< 0	2.611	3.175
BE/N [$Pt_{13} \rightarrow Pt_\infty$]	–	5.7	6.9
E [Pt_{55}]	−6512.84069	−6571.33805	−6574.07347
ΔE_{relax} [Pt_{55}]	18.22	2.674	1.755
BE/N [Pt_{55}]	0.661	3.492	4.026
BE/N [$Pt_{55} \rightarrow Pt_\infty$]	1.0	5.3	6.1
BE/N [Pt_{13}, $Pt_{55} \rightarrow Pt_\infty$]	–	5.1	5.5

well known: HF results are reported here to check that this applies also to relatively small metal clusters. The B3PW91 approach has been chosen as representative of the class of "hybrid" methods, and has similarly been included to investigate whether the small percentage of HF exchange contained in this type of functionals may cause problems when applied to (quasi-)metallic systems.

The choice of cuboctahedral structures for Pt_{13} and Pt_{55} can be questioned, since "amorphous" structures might be the most stable ones for aggregates in this range of sizes (see, e.g. Refs. [24,25]; for other recent calculations on the Pt_{13} molecule, see Ref. [26]). Probably, a dependence on the experimental method of preparation can also be hypothesized. It can be noted, however, that nanoclusters of 100–300 atoms prepared according to the Metal Vapour Deposition technique [27], in experimental condition presumably close to equilibrium ones, have been found to be non-amorphous [27], exhibiting clear diffraction patterns at about 2.275 and 1.975 Å, which closely correspond to the (111) and (200) spacings of pure fcc platinum: 2.266 and 1.962 Å, respectively.

4. Results

First of all, structural optimizations on Pt_{13} and Pt_{55} clusters have been performed by using the BPW91 functional with the basis set and computational procedure defined in the previous section. The optimizations started from crystal geometries, i.e. the positions that the atoms assume in the clusters considered as sections of the bulk platinum fcc lattice (lattice constant $a = 3.9242$ Å [28]). Cuboctahedral symmetry has been imposed. The energetics of cluster formation has been analyzed, and compared with HF and B3PW91 results at fixed geometries (crystalline and BPW91-optimized ones), and those obtained through a many-body potential (MBP) [3] approach (which is an atom–atom potential approach and has been chosen as the simplest theoretical method applied to these systems).

The structural results have then been compared with the crystalline geometries and those obtained through the MBP approach.

Finally, the electronic structure of the clusters has been analyzed, and compared with those obtained by using the B3PW91 approach.

4.1. Energetics

The results of the energy calculations are reported in Table 1. Starting with the Pt atom, one finds that its electronic configuration is $5d^9 6s^1$ with total spin $S = 1$, in agreement with experimental data [29]. The $5d^{10}$ configuration lies at a higher energy by an amount indicated as ΔE[Pt : $S = 1 \rightarrow 0$], which should be compared with an experimental spin-averaged value of 0.478 eV [29]: it can thus be seen that—already at this level—the HF approach grossly overestimates the exchange-correlation interactions between d-electrons.

Table 2
Relevant atom–atom distances defining the structures of the clusters obtained as section of the crystal and from BPW91 and MBP optimizations. The BPW91 distances have been rescaled by the 1.93% reduction factor. Only non-equivalent values are reported. All distances are in Å

	II	IIIf	IIIe	IIIv
Crystal				
I	2.775	3.924	4.806	5.550
II	2.775	2.775	2.775	2.775
IIIf	–	–	2.775	–
IIIe	–	–	2.775	2.775
BPW91				
I	2.685	4.080	4.706	5.317
II	2.685	2.892	2.734	2.632
IIIf	–	–	2.656	–
IIIe	–	–	2.847	2.662
MBP				
I	2.735	3.888	4.692	5.308
II	2.735	2.749	2.696	2.572
IIIf	–	–	2.719	–
IIIe	–	–	2.690	2.656

This is confirmed with the Pt_{13} molecule, for which the HF approach gives a *negative* binding energy at both BPW91-optimized and crystalline geometries. Only for Pt_{55} one finds a (modest) binding energy per atom (BE/*N*) of 0.661 eV. The situation changes radically when considering the DF approaches: the $\Delta E[\mathrm{Pt}: S = 1 \rightarrow 0]$ energy is correctly estimated to be around 0.5 eV, while the clusters are predicted to be appreciably bound, with BE/*N* values ranging between 2.6 and 4.0 eV.

The structural relaxation is quantitatively appreciable, particularly in the Pt_{55} case, but it gives a minor contribution to the total binding energy of the clusters. The BE/*N* values for finite clusters can be extrapolated to the infinite crystal according to two different procedures. In the first instance, one can calculate the average coordination number (ACN) of the clusters, i.e. the total number of first-neighbor bonds multiplied by two and divided by the number of atoms, and extrapolate the BE/*N* value as if to each bond were associated an equal contribution (the ACN of the bulk is 12). The BE/*N* $[Pt_{13} \rightarrow Pt_{\infty}]$ and BE/*N* $[Pt_{55} \rightarrow Pt_{\infty}]$ values in Table 1 have been obtained through such a procedure. For example, in the Pt_{13} case one has 36 first-neighbor bonds, and therefore an ACN of 5.5385; in the Pt_{55} case, one has 216 first-neighbor bonds, and therefore an ACN of 7.8545. Alternatively, one can extrapolate linearly by considering the two values of ACN and BE/*N*: the BE/*N* $[Pt_{13},Pt_{55} \rightarrow Pt_{\infty}]$ values refer to such a procedure. By comparing the BPW91 and B3PW91 results of BE/*N* reported in Table 1, one sees that they compare favourably between each other. The major difference lies in the fact that the B3PW91 values are smaller by ~15–20% than the BPW91 ones, which implies that the corresponding extrapolated values are somewhat lower than the bulk platinum BE/*N*: 5.852 eV [28]. It does not seem however that the B3PW91 results degrade with increasing cluster size. In passing, it can be noted that very similar results are obtained by using the mean radius of the cluster—defined as $1/(N_{\mathrm{at}})^{1/3}$, with N_{at} the number of atoms—instead of the ACN as the abscissa: one obtains extrapolated BE/*N* values which differ by only ≈ 0.1 eV from those reported in Table 1.

For comparison, the corresponding extrapolated values obtained through an analysis of MBP results [3] are the following: BE/*N* $[Pt_{13} \rightarrow Pt_{\infty}] = 10.7$ eV, BE/*N* $[Pt_{55} \rightarrow Pt_{\infty}] = 8.1$ eV, BE/*N* $[Pt_{13}, Pt_{55} \rightarrow Pt_{\infty}] = 5.9$eV, showing that the constant term in the linear scaling of BE/*N* vs. ACN is much larger for the MBP approach than for the DF ones. An analogous behavior is found from an analysis of EH BE/*N* values for Pt_{13} and Pt_{55} clusters [4], but it can be noted that one finds a substantial dependence on the orbital occupancy, since the same extrapolation techniques give rather different results on systems such as iron clusters (iron possesses only 8 d electrons).

4.2. Structures

After having imposed the cuboctahedral symmetry to Pt_{13}, one is left with only one degree of freedom: the distance (*R*) between the central atom and its 12 first-neighbors, which corresponds to the "breathing" mode of the molecule. From BPW91 calculations, one finds a slight contraction of *R* in Pt_{13}: from $R = 2.775$ Å in the bulk [28] to 2.725 Å. In reality, the BPW91 method overestimates the bulk platinum lattice parameter as $a = 4.0$ Å [30] (calculation utilizing a basis set of plane waves and the PW91 exchange functional) instead of $a = 3.9242$ Å [28]. One can take in to account this fact by rescaling the BPW91 distances by ~1.93%, thus finding for Pt_{13}

$R = 2.674$ Å. For comparison, the MBP approach [3] gives a value of R decidedly smaller: $R = 2.618$ Å.

The Pt_{55} case is more interesting: here, after imposing the cuboctahedral symmetry, one has five inequivalent atoms: the central one (I), one among those of the second shell (II) of 12 atoms, and three belonging to the third shell of 42 atoms (III). The third-shell atoms can in fact be distinguished into 12 atoms lying on the vertexes (IIIv), 24 atoms lying on the edges (IIIe) and 6 atoms lying on the (100)-faces (IIIf) of the cluster surface. In Table 2, the relevant atom–atom distances are reported as derived from the crystalline structure and from BPW91 and MBP optimizations. The BPW91 distances have been rescaled by the previously introduced 1.93% reduction factor.

The most interesting feature resulting from an analysis of Table 2 is the *expansion* of the atoms on the (100)-faces. This is opposite to the usual expectation of a *contraction* of atom–atom distances in small clusters with respect to the bulk situation. Indeed, the distance of the vertex atoms from the central ones decreases by ~0.23 Å, that of the edge atoms by ~0.10 Å, whereas that of the (100)-face atoms increases by ~0.16 Å. This effect is not present in the MBP-optimized structures, in which all the atom–atom distances are contracted with respect to the crystal. For example, the corresponding MBP distances from the center are reduced by 0.24, 0.11 and 0.04 Å, respectively: in practice, the surface atoms contract the more the less they are bound (the lesser the number of first-neighbors).

This effect implies a clear tendency of the BPW91 method toward "spherical" arrangements. To give an idea, the angle between the lines joining a vertex between two (100)-faces and the corresponding atoms at the center of the faces, which is 90° in the crystal geometry, changes very little to 88.9° in the MBP-optimized geometry, but passes to 99.7° in the BPW91-optimized one.

It would be interesting to see whether this effect can be found also using more simplified DF approaches, such as the Corrected Effective Medium theory [5] or the Harris functional [6].

From the analysis of Table 2, it can also be observed that in the MBP approach the distance of the shell II of atoms from the center converge much more rapidly to the bulk value than in the BPW91 approach. This is reasonable, since using an atom–atom potential the atoms in the II shell—which have completed their shell of first-neighbors—essentially behave like bulk atoms.

From Table 2, one can calculate the average first-neighbor distance for the Pt_{55} cluster, which is 2.725 Å at the BPW91 level and 2.701 Å at MBP. These values can be extrapolated by using the Pt_{13} values and the ACN values to 2.82 and 2.85 Å for the BPW91 and MBP methods, respectively. It thus seems that the average first-neighbor distance does not scale linearly with the ACN.

4.3. Electronic structure

Let us start our analysis from the Pt_{13} molecule. In this case, the finite character of the system prevails, and one does not find extremely marked differences between the various theoretical methods, even though we recall that Pt_{13} is not bound at the HF level when the molecule is at the BPW91 equilibrium geometry (indeed, there it is in the repulsive part of the potential energy curve). Also the results at the crystalline and BPW91-optimized geometries are qualitatively very similar, which is reasonable, since only an overall reduction of the atom–atom distances is allowed for cuboctahedral Pt_{13}.

The spin value is predicted to be $S = 3$ using all three methods, with a very small spin symmetry breaking from our unrestricted calculations: for example, the value of $\langle S^2 \rangle$ is 12.04 at the B3PW91 level and 12.21 at the HF level at the BPW91-optimized geometry, to be compared with a value of 12.00 for a restricted calculation.

The band widths (BW), evaluated as the energy difference between the HOMO and the lowest occupied valence orbital, are very similar for both α and β spin-orbitals and from both BPW91 and B3PW91 approaches: around $7 \div 7.5$ eV at the optimized geometry. The Fermi energies analogously assume close values: $\epsilon_F = -4.35$ eV (HF), $\epsilon_F = -5.28$ eV($B3PW91$), $\epsilon_F = -5.31$ eV (BPW91) at the optimized geometry; these values compare very well with the experimental work function of bulk platinum: 5.3 eV [28].

The number of occupied orbitals belonging to a given irreducible representation is also conserved. The major differences between the two DF approaches are: (a) in the relative ordering of the

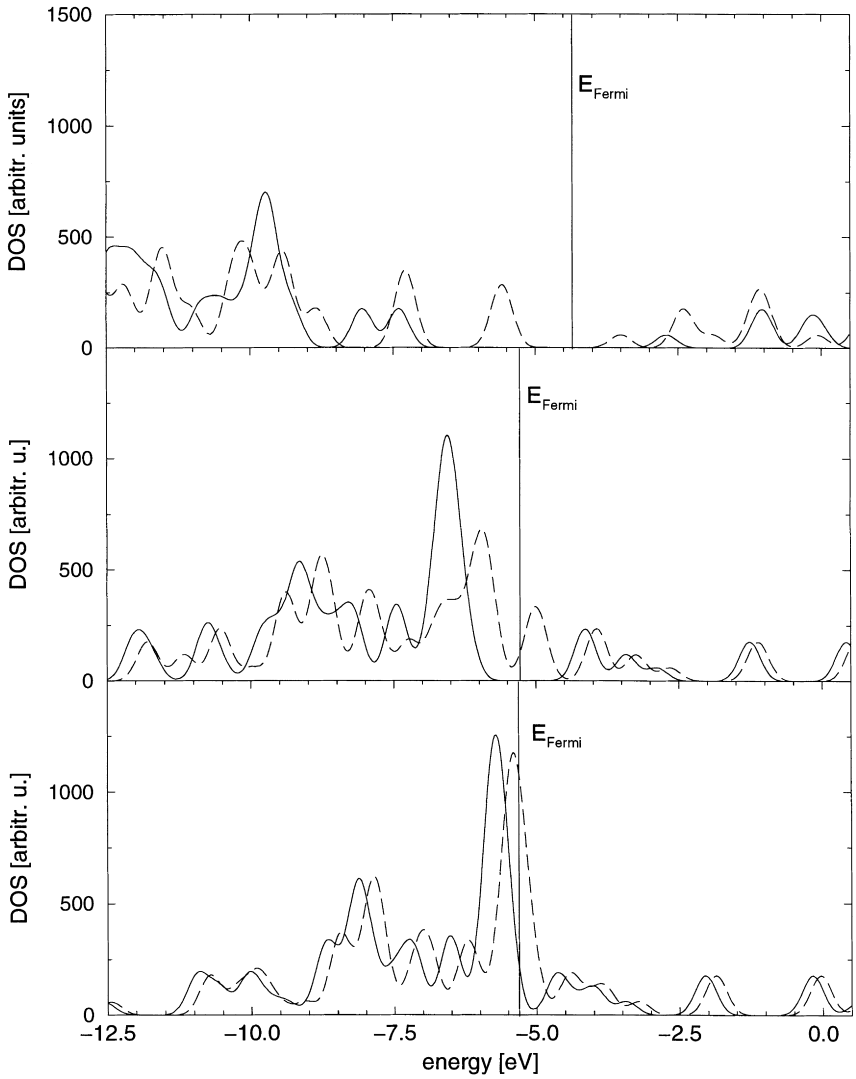

Fig. 1. Plots of the density of states (DOS) for the Pt_{13} molecule as derived from HF, B3PW91 and BPW91 calculations at the BPW91-optimized geometry. Continuous line: spin-majority (α) component; dashed line: spin-minority (β) component.

one-electron energy levels; an extensive rearrangement is observed, in which some levels are much more stabilized than others; (b) in the form of the occupied orbitals, in general, an increase in the s-character for the a_{1g} and t_{2g} orbitals is observed at the B3PW91 level; (c) in the energy gap values, i.e. in the energy difference between the HOMO and LUMO. One finds in fact a gap of 2.07 eV for α and 0.74 eV for β spin-orbitals from B3PW91 calculations at the optimized geometry, whereas the gap is 0.87 eV for α spin-orbitals but only 0.01 eV for β spin-orbitals from BPW91 calculations at the same geometry. The BPW91 β HOMO, which is of t_{2u} symmetry, and the β LUMO, which is of e_g symmetry, are thus so close in energy that they are both populated in virtue of the smearing procedure: $n_{t_{2u}} = 0.921$ and $n_{e_g} = 0.119$ at the BPW91-optimized geometry; $n_{t_{2u}} = 0.997$ and $n_{e_g} = 0.005$ at the crystal geometry. The next lowest β unoccupied orbital (which is of t_{2g} symmetry) lies at a higher energy by

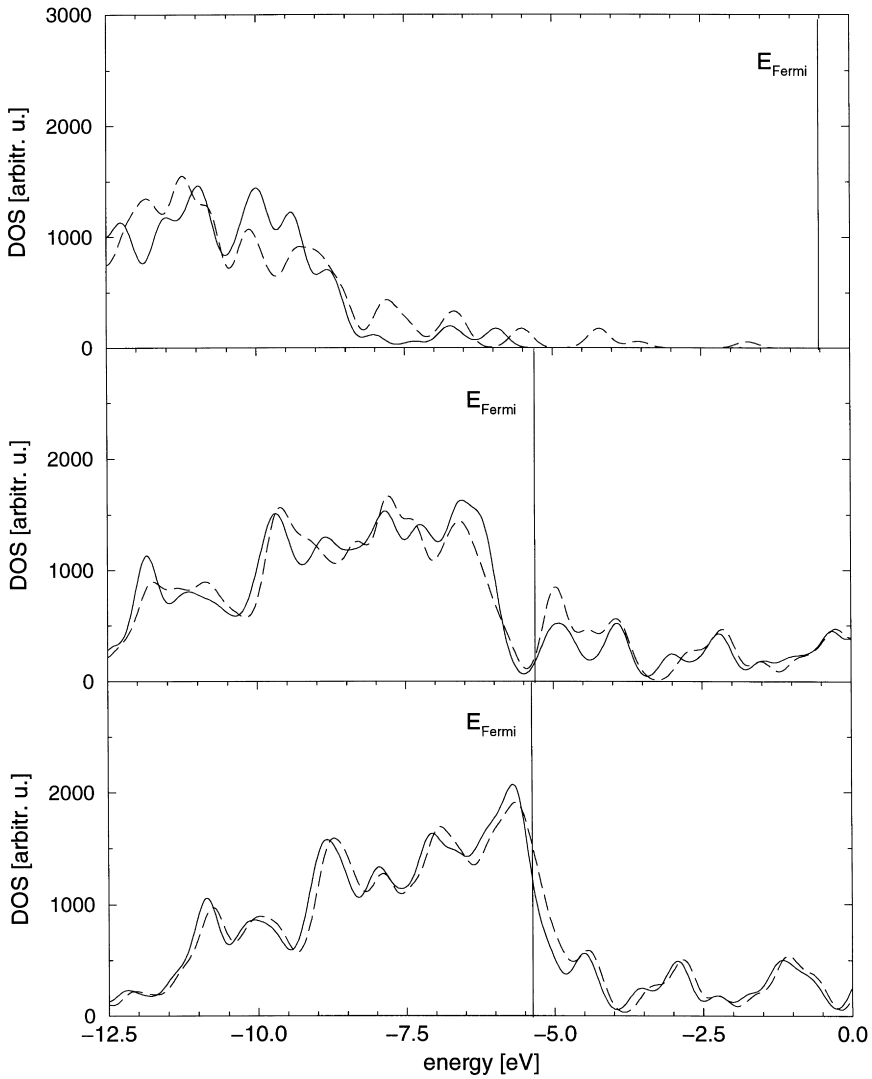

Fig. 2. Plots of the density of states (DOS) for the Pt_{55} molecule as derived from HF, B3PW91 and BPW91 calculations at the BPW91-optimized geometry. Continuous line: spin-majority (α) component; dashed line: spin-minority (β) component.

∼0.20 or ∼0.16 eV at the two geometries, respectively. In the BPW91 case, therefore, the smearing procedure is effective, even though not strictly necessary, to improve the convergence of the self-consistent procedure. It can be noted that the structural optimization "hardens" the system, i.e. brings it toward an increase of the energy gap (in the BPW91 case, an increase in the occupation number of the low-lying LUMO β orbital).

The Jahn–Teller effect is not present in cuboctahedral Pt_{13}; one does not find an incomplete occupancy of spatially degenerate orbitals from any of the three theoretical methods here considered.

To further investigate the electronic structure of the system, a plot of the density of states (DOS) as derived at the BPW91-optimized geometry using a Gaussian broadening factor of 0.184 eV (which has been chosen much larger than the value used in the smearing procedure for reasons of clarity), is shown in Fig. 1. The BPW91 curve qualitatively resembles

those obtained through EH calculations on Pt_{13} [4], much more than the B3PW91 one.

The Pt_{55} molecule represents a much more interesting case. First of all, the HF approach is here still less appropriate than for the smaller system. A huge spin contamination is a clear evidence of the inadequate HF description of this class of systems; one finds that all three methods predict a difference of 10 in the number of α and β orbitals, which should correspond to a spin value of $S = 5$, but the $\langle S^2 \rangle$ values are: $\langle S^2 \rangle = 30.11$ (BPW91) or $\langle S^2 \rangle = 31.43$ (B3PW91) from the DF approaches, whereas the HF result is $\langle S^2 \rangle = 50.84$, to be compared with a restricted value of 30.00. Also other descriptors turn out to be completely different (and unrealistic) from the HF approach: one finds $\epsilon_F = -1.70$ eV, BW = 10.91 (16.24) eV and Gap = 8.10 (4.26) eV for α (β) spin-orbitals at the HF level, whereas the corresponding values are: $\epsilon_F = -5.32$ eV, BW = 9.31 (9.34) eV and Gap = 0.63 (0.58) eV for α (β) spin-orbitals at the B3PW91 level, and $\epsilon_F = -5.38$ eV, BW = 8.65 (8.64) eV and Gap = 0.19 (0.10) eV for α (β) spin-orbitals at the BPW91 level; all these data referring to the BPW91-optimized geometry. It can be noted that the $\langle S^2 \rangle$ value is "worse" from the B3PW91 approach (as a consequence of the introduction of a HF exchange component into the approximate functional) but not in a dramatic way. Also the number of occupied orbitals belonging to a given irreducible representation is the same from BPW91 and B3PW91 approaches, but worth to be mentioned is the fact that the character of the electronic levels just below the gap gradually changes along the series BPW91–B3PW91–HF: at the gradient-corrected level only d-functions contribute to the molecular orbitals, at the hybrid level some s-orbital character appears and at the HF level there are almost 50% s- and 50% d-contributions.

A very important fact is that the energy gap at the BPW91-optimized geometry is larger than the smearing parameter, so that the smearing procedure is ineffective for all three methods at this geometry. However, this is not true at the crystal geometry, at which both the BPW91 and B3PW91 methods predict a HOMO β spin-orbital of e_u symmetry occupied by only one electron and—in the BPW91 case—very close to a LUMO β spin-orbital of t_{1g} symmetry. At the crystal geometry, therefore, one expects that both the smearing procedure is effective and the system undergoes a Jahn–Teller distortion.

In passing, it can be noted that this is essentially in line with EH calculations [4] which predict that Pt_{13} is a closed-shell, whereas Pt_{55} exhibits an incomplete occupancy of a spatially degenerate HOMO. This also confirms the prediction [4] that the Pt_{13} cluster still presents a molecular-type appearance, whereas for the Pt_{55} cluster one is probably in an intermediate regime toward the metallic transition (which was predicted to occur approximately above ~150 atoms in [4]).

The results presented in the previous sub-section in any case show that the Pt_{55} cluster possesses another way of removing the incomplete occupancy of the HOMO without breaking the cuboctahedral symmetry, i.e. by increasing its "sphericity". Such a peculiar structural rearrangement necessarily reflects on the electronic structure of the molecule. One finds in particular completely different orbital occupancies at the two geometries from both BPW91 and B3PW91 approaches, with a consistent electron flow of 18 electrons from t_{1g} and t_{1u} orbitals to e_g, e_u and t_{2u} orbitals.

A plot of the DOS function from the three approaches at the BPW91-optimized geometry is shown in Fig. 2. Here one finds major differences also between the two DF approaches. Many occupied energy levels are in fact shifted to lower energies in the B3PW91 calculation, whereas many unoccupied ones are destabilized, which nearly causes the appearance of an energy gap in which the Fermi energy falls (we recall the much larger gap values from the B3PW91 with respect to the BPW91 calculations; see the discussion above). The Pt_{55} cluster therefore appears electronically "harder" at the B3PW91 level, a fact which is certainly connected with the presence of a HF exchange component in the density functional (or better, the density–matrix functional). This should reflect on the *response* properties of the system. An investigation along these lines is currently in progress and will be published elsewhere.

Finally, it can be noted that the BPW91 DOS curve is qualitatively more similar to the EH one reported in [4] than the B3PW91 one: also the gap values are in better agreement with the EH ones. However, an important difference is that the BW values from the BPW91 approach are larger by more than a factor of two than the corresponding EH values. This strongly

points to a reparametrization of the EH method in order to accurately describe this class of systems.

Acknowledgements

The authors gratefully acknowledge the Italian INSTM (Istituto Nazionale per la Scienza e la Tecnologia dei Materiali) for a grant making available the resources of CINECA computing centre (Bologna, Italy), and Andrea Biagi (ICQEM, Pisa) for technical assistance.

References

[1] J. Klabunde, Free Atoms, Clusters and Nanoscale Particles, Academic Press, London, 1994.
[2] V. Ponec, G. Bond, Catalysis by metals and alloys, Studies in Surface Science and Catalysis, Elsevier, Amsterdam, 1995.
[3] G. D'Agostino, Mater. Sci. Forum 195 (1995) 149.
[4] A. Fortunelli, A.M. Velasco, J. Mol. Struct. (Theochem) 487 (1999) 251.
[5] M.S. Stave, A.E. DePristo, J. Chem. Phys. 97 (1992) 3386 and references therein.
[6] J. Harris, Phys. Rev. B 31 (1995) 1770.
[7] D.E. Bernholdt, E. Aprà, H.A. Früchtl, M.F. Guest, R.J. Harrison, R.A. Kendall, R.A. Kutteh, X. Long, J.B. Nicholas, J.A. Nichols, H.L. Taylor, A.T. Wong, G.I. Fann, R.J. Littlefield, J. Nieplocha, Int. J. Quantum Chem. Quantum Chem. Symp. 29 (1995) 475.
[8] A. Schafer, C. Huber, R. Ahlrichs, J. Chem. Phys. 100 (1994) 5829 Basis set retrievable from the following URL ftp://ftp.chemie.uni-karlsruhe.de/pub/basen/
[9] D. Andrae, U. Haeussermann, M. Dolg, H. Stoll, H. Preuss, Theor. Chim. Acta 77 (1990) 123.
[10] A. Fortunelli, J. Mol. Struct. (Theochem) (1999) in press.
[11] A. Fortunelli, in preparation.
[12] B.I. Dunlap, J.W.D. Connolly, J.R. Sabin, J. Chem. Phys. 71 (1979) 4993.
[13] K. Eichkorn, O. Treutler, H. Öhm, M. Häser, R. Ahlrichs, Chem. Phys. Lett. 242 (1995) 652.
[14] A.D. Becke, J. Chem. Phys. 88 (1988) 2547.
[15] C.W. Murray, N.C. Handy, G.L. Laming, Mol. Phys. 78 (1993) 997.
[16] B. Delley, J Comput. Chem. 17 (1996) 1152.
[17] C. Elsässer, M. Fähnle, C.T. Chan, K.M. Ho, Phys. Rev. B 49 (1994) 13975.
[18] R.W. Warren, B.I. Dunlap, Chem. Phys. Lett. 262 (1996) 384.
[19] A.D. Becke, Phys. Rev. A 38 (1988) 3098.
[20] J.P. Perdew, Y. Wang, Phys. Rev. B 33 (1986) 12.
[21] J.P. Perdew, J.A. Chevary, S.H. Vosko, K.A. Jackson, M.R. Pederson, D.J. Singh, C. Fiolhais, Phys. Rev. B 46 (1992) 6671.
[22] A.D. Becke, J. Chem. Phys. 98 (1993) 5648.
[23] S.J. Vosko, L. Wilk, M. Nusair, Can. J. Phys. 58 (1980) 1200.
[24] L. Yang, A.E. DePristo, J. Chem. Phys. 100 (1994) 725.
[25] S.H. Yang, D.A. Drabold, J.B. Adams, P. Ordejon, K. Glassford, J. Phys.: Condens. Matter 9 (1997) L39 and references therein.
[26] N. Watari, S. Ohnishi, Phys. Rev. B 58 (1998) 1665.
[27] G. Martra, S. Coluccia, O. Monticelli, G. Vitulli, Catal. Lett. 29 (1994) 105.
[28] C. Kittel, Introduction to Solid State Physics, Wiley, New York, 1968.
[29] C.E. Moore, Natl. Bur. Stand. (US) Circ. (1971) 467.
[30] G. Boisvert, L.J. Lewis, M. Scheffler, Phys. Rev. B 57 (1998) 1881.

Crossover among structural motifs in transition and noble-metal clusters

F. Baletto[a] and R. Ferrando[b]
INFM and CFSBT/CNR, Dipartimento di Fisica dell'Università di Genova, via Dodecaneso 33, 16146 Genova, Italy

A. Fortunelli[c]
Istituto per i Processi Chimico-Fisici del CNR, Via V. Alfieri 1, 56124, Pisa, Italy

F. Montalenti[d]
Theoretical Division, Los Alamos National Laboratory, Los Alamos, New Mexico 87545

C. Mottet[e]
CRMC2/CNRS, Campus de Luminy, Case 913, 13288 Marseille Cedex 9, France

BalettoJCP2002

(Received 25 October 2001; accepted 13 December 2001)

The energetics of nanoclusters is investigated for five different metals (Ag, Cu, Au, Pd, and Pt) by means of quenched molecular dynamics simulations. Results are obtained for two different semiempirical potentials. Three different structural motifs are considered: icosahedra (Ih), decahedra (Dh), and truncated octahedra (TO). The crossover sizes among structural motifs are directly calculated, considering cluster up to sizes $N \simeq 40\,000$. For all the systems considered, it is found that icosahedra are favored at small sizes, decahedra at intermediate sizes, and truncated octahedra at large sizes. However, the crossover sizes depend strongly on the metal: in Cu, the icosahedral interval is rather large, and it is followed by a very wide decahedral window; on the contrary, in Au, the icosahedral interval is practically absent, and the decahedral window is narrow. The other metals display intermediate behaviors, Ag being close to Cu, and Pd and Pt being close to Au. A simple criterion, which is based on the ratio between the bulk modulus and the cohesive energy per atom, is developed to account for the differences among the metals. © *2002 American Institute of Physics.* [DOI: 10.1063/1.1448484]

I. INTRODUCTION

Clusters provide a bridge between isolated atoms and bulk material, and, because of that, they can display unusual physical and chemical behaviors. The knowledge of the structure is the starting point to understand the peculiar characteristics of a cluster.[1,2] It is well known that nanometer-size clusters can present both crystalline (fcc for the elements that we shall consider in the following) and noncrystalline structures. The latter are very common at small sizes, and, in the case of noble and transition metals, they take the form of icosahedra (Ih) and of Marks truncated decahedra (*m*-Dh).[1–3] In Fig. 1, examples of Ih, Dh, and fcc clusters are shown. Icosahedra have a quasispherical shape and a close-packed surface with 20 distorted (111)-like facets.[1] The Ih structure is obtained by packing together twenty tetrahedra sharing a common vertex. This packing is possible only if the tetrahedra are distorted, and this causes the high internal strain of the structure. Icosahedra are thus expected to be favorable at small sizes, where the efficient minimization of the surface energy prevails over the strain contribution, which is proportional to the cluster volume. The decahedral structure is obtained by packing five tetrahedra so that they have a common edge. In this way, the surface is again close-packed, being formed by 10 (111)-like facets, but the resulting cluster shape is quite far form a spherical one. Better Dh structures can be obtained, however, by truncating the clusters. The Ino truncation[4] exposes five rectangular (100)-like facets. The latter facets are not close-packed, but the resulting shape is closer to a sphere. However, this is not usually the best decahedral shape, since the energetically costly (100) facets are rather large in the Ino Dh. A better solution to the problem of finding the best Dh structure was given by Marks,[5] who proposed further truncations, which are done in such a way to create (111)-like re-entrant facets. In this way, the cluster shape remains still close to a sphere, but smaller open (100)-like facets are exposed. From the point of view of the surface energy, icosahedra are still better for small clusters, but decahedra have less internal strain, and become more favorable than icosahedra at increasing sizes. Finally, fcc clusters are expected to be the most favorable in the macroscopic limit, because this is the bulk lattice symmetry for the metals considered in this paper. Fcc octahedra present only (111) facets, but are very far from the spherical shape. Truncated octahedra have a better surface/volume ratio, but expose large (100) facets. Therefore, fcc structures present a large surface energy, but they lack internal strain, and are thus expected to dominate at large sizes. These general trends are common to many fcc-bulk systems, ranging from metallic to Lennard-Jones clusters (as demonstrated by calculations[6–9] and

[a]Electronic mail: baletto@fisica.unige.it
[b]Author to whom correspondence should be addressed. Electronic mail: ferrando@fisica.unige.it
[c]Electronic mail: fortunelli@icqem.pi.cnr.it
[d]Electronic mail: montalenti@t12.lanl.gov
[e]Electronic mail: mottet@crmc2.univ-mrs.fr

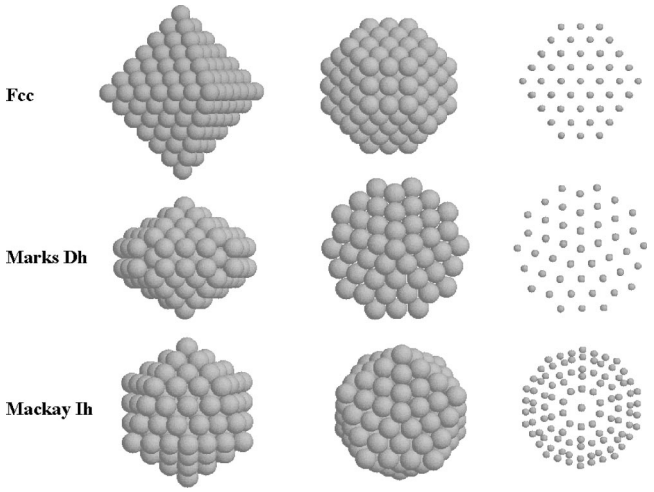

FIG. 1. Structural motifs of clusters. In the top row, at left a perfect octahedron is shown; in the middle panel and right panels, a truncated octahedron, obtaining truncating the six vertices of the octahedron, is shown. In the middle row, the (3,2,2) Marks decahedron is shown in different views. Note the rectangular (100)-like facets of size 3×2 ($m=3$, $n=2$), and the Marks re-entrance. In the bottom row, the fourth shell Icosahedron is shown in different views.

experiments[10,11]). We expect that they shall hold also for the metals treated in this paper, which are thus expected to show a crossover among structural motifs, from icosahedra, to decahedra and finally to fcc clusters. An interesting point is therefore to investigate quantitatively the crossover sizes for the different metals, looking at the best clusters for each structural motifs, and trying to devise general trends among the different elements and to give, if possible, some simple criteria for understanding *a priori* their behaviors. This is the purpose of the present paper, in which we shall treat explicitly Cu, Ag, Au, Pd, and Pt clusters. There are already several papers (see, for example Refs. 7, 8, 12, 13) dealing with crossover sizes in metallic clusters, but they either treat a single element (Ni in Ref. 7), or they are limited to rather small sizes, well below the crossover ones,[8] or they compare only Ih structures with cuboctahedra[13] [which are indeed very unfavorable fcc structures with large (100) facets] and truncated octahedra.[12] The present work synoptically treats several elements up to large sizes ($N\leqslant40\,000$), and searches for the best clusters for each structural motif.

The paper is structured as follows: in Sec. II we briefly describe the interaction potentials and the calculation method; in Sec. III we report the results of the energy minimization of the clusters for the three structural motifs comparing the five metals; Sec. IV develops a simple criterion to devise general trends among the different metals; Sec. V contains the conclusions.

II. THE MODEL

As anticipated in the Introduction, we calculate cluster energies by two different semiempirical many-body potentials. The first one was proposed by Rosato, Guillopè, and Legrand (RGL).[14,15] Then we check general trends by comparing with the results of an embedded atom method (EAM) potential[16] as parametrized by Voter.[17,18] The RGL potential has a very simple analytical expression depending on five parameters, and because of that, it is well suited for discussing general trends and for comparing the different metals in a rather easy way. In the following, we give a brief description of the RGL potential; for the EAM potential we refer to the original literature.[18] In the RGL potential, the cohesion of the crystal is given by an attractive many-body term (the band energy), which for an atom i is given by

$$E_b^i=-\left\{\sum_{j,r_{ij}<r_c}\xi^2\exp\left[-\frac{q}{\alpha}\left(\frac{r_{ij}}{r_0}-1\right)\right]\right\}^{\alpha}; \tag{1}$$

$\alpha=1/2$ in the second-moment approximation to the tight-binding model;[14] other exponents have been proposed in the literature.[13,19] The stability of the cluster is ensured by adding a phenomenological core-repulsion term E_b^r of the Born–Mayer-type,

$$E_r^i=\sum_{j,r_{ij}<r_c}A\exp\left[-p\left(\frac{r_{ij}}{r_0}-1\right)\right]. \tag{2}$$

In these expressions, r_{ij} is the distance between atoms i and j, r_c is the cutoff radius of the interactions (in the following calculations, we use the above form of the potential up to the second-neighbor distance, and link smoothly the potential to zero at the third-neighbor distance); r_0 is the nearest-neighbor distance in the bulk; A, ξ, p, q are parameters fitted on bulk properties of the metals, i.e., the cohesive energy, the bulk modulus and the annihilation of the energy gradient at r_0. Their values are given in Table I. It can be noted that, after fitting the bulk properties, one is left with only two independent parameters, say, p and q. p and q determine the range of the repulsive and of the attractive part of the potential, respectively; as we shall see in Sec. IV, these two parameters define the trends among the different metals.

TABLE I. Lattice constant a and RGL parameters for the different metals.

Metal	$a=\sqrt{(2)}r_0$ (Å)	ξ (eV)	A (eV)	p	q
Cu	3.62	1.280	0.0894	10.55	2.43
Ag	4.09	1.190	0.1031	10.85	3.18
Au	4.07	1.855	0.2197	10.53	4.30
Pd	3.89	1.702	0.1715	11.00	3.79
Pt	3.92	2.621	0.2477	10.71	3.85

The cohesive energy of a cluster of atoms is given by

$$E_c=\sum_i\,(E_b^i+E_r^i). \tag{3}$$

Detailed comparisons of RGL results for diffusion barriers on flat and stepped surfaces with experimental data, *ab initio*, and semiempirical calculations are reported in Ref. 20. It turns out that RGL results correctly predict the dominant diffusion mechanisms on noble and transition metal surfaces;[21,22] from the quantitative point of view, the agreement with experimental data and first-principle calculations is usually good, especially for silver. Moreover, the use of these potentials in the modeling of silver clusters growth[23,24] has lead to the explanation of the experimental phenomenology.[25]

Comparison with density functional calculations for noble-metal clusters are reported in Ref. 26, where once again a good agreement is found.

In the following, the total energy of the clusters is calculated by quenched molecular dynamics, which allows the complete relaxation of the structures around a local minimum. At the sizes which will be considered in the following, global optimization[27] is not feasible.

III. RESULTS

Here we report the results concerning the different structural motifs for the metals Ag, Au, Cu, Pd, and Pt. We report a thorough study of the energetics of the different structural motifs by RGL potentials, considering large clusters and determining crossover sizes. Then we check the general trends about the transition from icosahedra and decahedra by means of the EAM potentials. Ag is treated in greater details as a reference case.

Before showing the results we introduce few notations and indices related to the different structures, in order to facilitate their geometrical description, and we introduce the quantity Δ (see below), which is useful to discuss the relative stability of structures of different sizes.

Icosahedra: They are structured in shells, see Fig. 1. An Ih with k shells has

$$N_{\mathrm{Ih}}(k)=\frac{10}{3}k^3-5k^2+\frac{11}{3}k-1 \tag{4}$$

atoms (so that the series of magic numbers is 1, 13, 55, 147,...) and presents 20 triangular facets of side k.

Marks decahera: They are characterized by three indices (m, n, r) (in previous works,[23,24] the third index was named p instead of r, but here that choice would lead to a confusing notation because of the parameter p of the RGL potential). m and n are the length of the sides of the (100) facets, perpendicular and parallel to the fivefold axis, respectively (see Fig. 1); r is the depth of the Marks re-entrance ($r=1$ corresponds to no re-entrance i.e., to the Ino decahedron). A (m, n, r) marks Dh has $h=m+n+2r-3$ atoms along its symmetry axis and a total number of atoms $N_{\mathrm{Dh}}(m,n,r)$ given by

$$\begin{aligned}N_{\mathrm{Dh}}(m,n,r)=\tfrac{1}{6}\{&30r^3-135r^2+207r-102+[5m^3\\&+(30r-45)m^2+(60(r^2-3r)\\&+136)m]+n[15m^2+(60r-75)m\\&+3(10r^2-30r)+66]\}-1.\end{aligned} \tag{5}$$

fcc polyhedra: Starting from the octahedron (see Fig. 1), better fcc polyhedra are obtained truncating symmetrically the six vertices, thus obtaining square and hexagonal (triangular in the case of cuboctahedra) facets. In the following we characterize a given truncated octahedron (TO) by two indexes: n_l is the length of the edge of the complete octahedron; n_{cut} is the number of layers cut at each vertex. A TO has a number of atoms,

$$N_{\mathrm{TO}}(n_l,n_{\mathrm{cut}})=\tfrac{1}{3}(2n_l^3+n_l)-2n_{\mathrm{cut}}^3-3n_{\mathrm{cut}}^2-n_{\mathrm{cut}}, \tag{6}$$

and square facets with edges of $n_{\mathrm{cut}}+1$ atoms. Concerning the (111) hexagonal facets, they are not in general regular hexagons. In fact, three edges of the hexagons are in common with square facets, having thus $n_{\mathrm{cut}}+1$ atoms, while the remaining three edges have n_l-2n_{cut} atoms. Regular hexagons are thus possible if $n_l=3n_{\mathrm{cut}}+1$; in the following the TO with regular hexagonal facets will be referred to as regular TO. On the other hand, cuboctahedra are characterized by $n_l=2n_{\mathrm{cut}}+1$, which gives energetically unfavorable clusters with large (100) facets and triangular (111) facets; by substituting this relation into Eq. (6), and comparing with Eq. (4), one finds that a cuboctahedron with a given n_{cut} has the same number of atoms as an Ih with $k=n_{\mathrm{cut}}+1$.

The quantity, which we introduce to compare the energetics of clusters of different sizes N, is Δ,[3,7,8] defined as

$$\Delta=\frac{E_{\mathrm{tot}}-NE_{\mathrm{coh}}}{N^{2/3}}, \tag{7}$$

where E_{tot} is the total energy of the cluster after the relaxation of the structure and E_{coh} is the cohesive energy per atom in the bulk. Δ is thus the excess energy roughly divided by the number of surface atoms. In general, we expect the following expression to hold for Δ:[7,8]

$$\Delta=\frac{a+bN^{1/3}+cN^{2/3}+dN}{N^{2/3}}. \tag{8}$$

In the numerator (which is the excess energy), the constant comes from the vertices of the cluster, the term in $N^{1/3}$ from the edges, the term in $N^{2/3}$ from the facets, and the volume term in N is due to the internal strain. This last term is always present in Ih and Dh clusters, while in TO vanishes (at least in the limit of large sizes). Therefore, for TO clusters, Δ decreases with size and tends to a constant at $N\to\infty$, while for Ih and Dh Δ initially decreases, then reaches a minimum, and finally diverges at large sizes as $N^{1/3}$.

A. Ag clusters

Icosahedra: Silver icosahedra decrease their Δ up to $N=147$ (fourth shell Ih) according to the RGL potential (see Fig. 2).

Decahedra: The best Ag decahedra have $m=n$, which gives square (100) facets, and a more spherical cluster shape. Concerning the Marks reentrance, the best clusters have $r\simeq m/2$. As we shall see in the following, while the choice $m=n$ is common to all the metals treated here, the choice of r changes with the metal, and relative trends can be understood comparing the surface energies of the (100) and (111) surfaces [$\gamma_{(100)}$ and $\gamma_{(111)}$ respectively]. Indeed, increasing r, the proportion of (111) facets increases, and thus metals characterized by larger ratios $\gamma_{(100)}/\gamma_{(111)}$ (see Table II) prefer larger r than $m/2$. Once the sequence of the best decahedra is chosen ($m=n$, $r\simeq m/2$), Δ decreases up to sizes $N\simeq 15\,000$ for RGL potentials [where the best clusters are the (10, 10, 5) and the (10, 10, 6) Dh, at $N=10\,887$ and $N=13\,829$, respectively], and it decreases at least up to 1000 atoms for the EAM potential. According to RGL potentials, decahedra are the best structures in the interval $300<N<20\,000$.

fcc clusters: A criterion which can be helpful in finding the best TO structures is the Wulff construction (see, for example, Ref. 28), which was indeed developed to find the

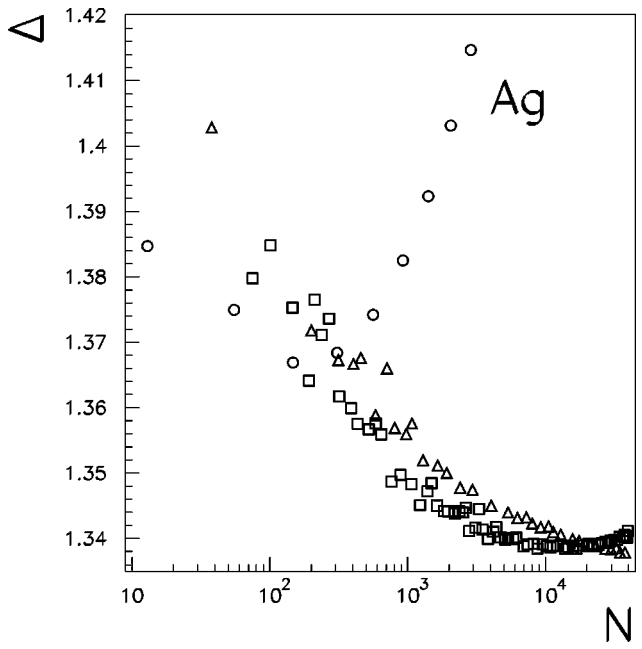

FIG. 2. The quantity $\Delta=(E_{\mathrm{tot}}-NE_{\mathrm{coh}})/N^{2/3}$ as a function of the size N, calculated by means of RGL potentials for silver clusters. Circles, squares, and triangles refer to icosahedra, decahedra, and truncated octahedra, respectively.

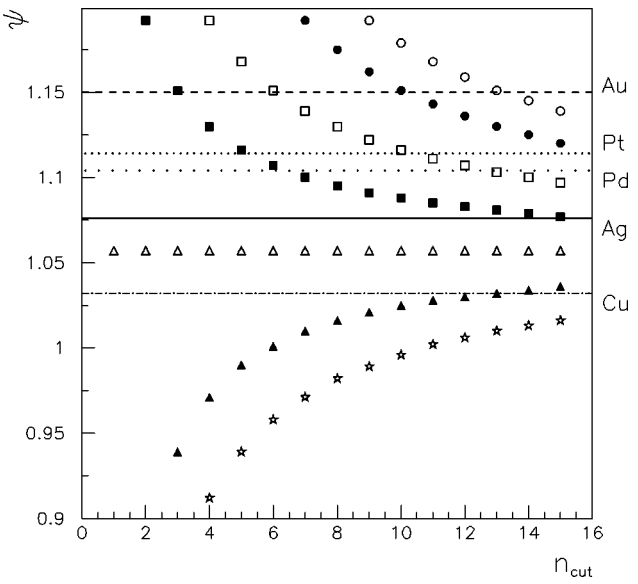

FIG. 3. Ratio $\psi=d_{(100)}/d_{(111)}$ as a function of n_{cut} for different series of truncated octahedra (TO). Each series is represented by different symbols: the open circles are related to TO structures with $n_l=3n_{\mathrm{cut}}+4$, the full circles to TO with $n_l=3n_{\mathrm{cut}}+3$, the open squares to TO with $n_l=3n_{\mathrm{cut}}+2$, the full squares to regular TO having $n_l=3n_{\mathrm{cut}}+1$, the open triangles to TO with $n_l=3n_{\mathrm{cut}}$, the full triangles to TO with $n_l=3n_{\mathrm{cut}}-1$, and the stars to TO with $n_l=3n_{\mathrm{cut}}-2$. The horizontal lines represent the ratio of surface energies $\gamma_{(100)}/\gamma_{(111)}$ for the five metals.

equilibrium shape of macroscopic crystals by the minimization of the surface energy for a crystal of a given volume. From the Wulff construction, the best TO structure should fulfill the following condition:

$$\frac{\gamma_{(100)}}{\gamma_{(111)}}=\frac{d_{(100)}}{d_{(111)}}, \tag{9}$$

where $\gamma_{(100)}$ and $\gamma_{(111)}$ are the (100) and (111) surface energies, respectively, whereas $d_{(100)}$ and $d_{(111)}$ are the distances from the center of the cluster. In Fig. 3, we report the ratio $\psi=d_{(100)}/d_{(111)}$ for the most significant unrelaxed TO structures in the nanometric size range, compared to the ratio of the surface energies for the different metals. The energy relaxation shows that either regular TO [characterized by n_{cut}^R and $n_l^R=3n_{\mathrm{cut}}^R+1$, see Fig. 3] or TO with slightly larger (100) facets than the regular TO (say with $n_l=n_l^R-1$ and $n_{\mathrm{cut}}=n_{\mathrm{cut}}^R$, which gives $n_l=3n_{\mathrm{cut}}$) are the most favorable at sufficiently large size, in good agreement with the Wulff construction criterion (compare the ratio of the surface energies in Table II with the data in Fig. 3), which turns out to be useful also for nanometer-size objects in the case of silver.

TABLE II. Ratio between the relaxed surface energies of (100) and (111) faces in the case of RGL potentials with $\alpha=\frac{1}{2}$.

Metal	$\gamma_{(100)}/\gamma_{(111)}$
Cu	1.032
Ag	1.076
Pd	1.104
Pt	1.114
Au	1.150

B. Other metals

In this section, we treat Cu, Au, Pd, and Pt clusters. Our results are reported in Fig. 4 using the RGL potential and in Fig. 5 for the EAM. In the latter case we consider a smaller size range ($N\simeq 1000$) just to analyze the crossover between icosahedra and decahedra. In the following we report in detail the results obtained with RGL potentials.

We find that the size interval in which a kind of structure is favored depends strongly on the metal. So we can find copper clusters which present icosahedral structures up to 1000 atoms and a very great size interval for decahedra (the crossover with fcc is at $N>30\,000$), while gold clusters prefer fcc structures already at sizes larger than 600 atoms. An intermediate behavior characterizes Pt and Pd clusters. In fact, for these metals, we find that icosahedra are favored only at very small sizes and the crossover between Dh and fcc is at $N\sim 6000-7000$ atoms.

Moreover, we find that the best choices for (m, n, r) for decahedra and n_l and n_{cut} for TO structures depend on metals. In the case of decahedral structures the choice $m=n$ is common to all metals, because in this way the cluster is much more spherical, while r is much larger in the case of Au clusters for which we have $r=m$ [the best Dh is the (3,3,3) at 433 atoms] than for Cu [decahedra decrease their Δ up to (10,10,5) at 10 887 atoms] and Ag clusters where $r\simeq m/2$. This means that Au clusters prefer to have deep reentrances or in other words, large (111) facets [remember that for gold a (111) facet presents a much better surface energy than a (100) facet (see Table II)]. Again Pt and Pd clusters present an intermediate choice: at small sizes $r\simeq m$ and at larger sizes $r=m-2$ or $r=m-3$ [for both metals the minimum is the (7,7,5) Dh at 5341 atoms].

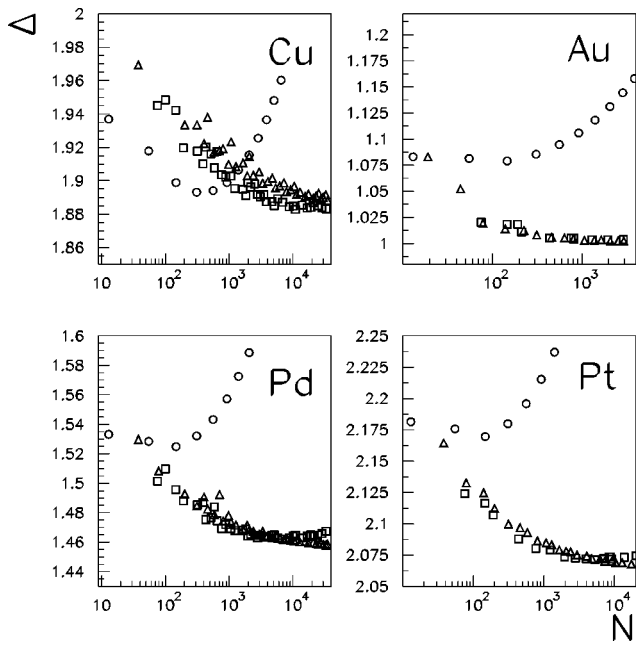

FIG. 4. Δ calculated by RGL potentials for Cu, Au, Pd, and Pt clusters. Symbols as in Fig. 2.

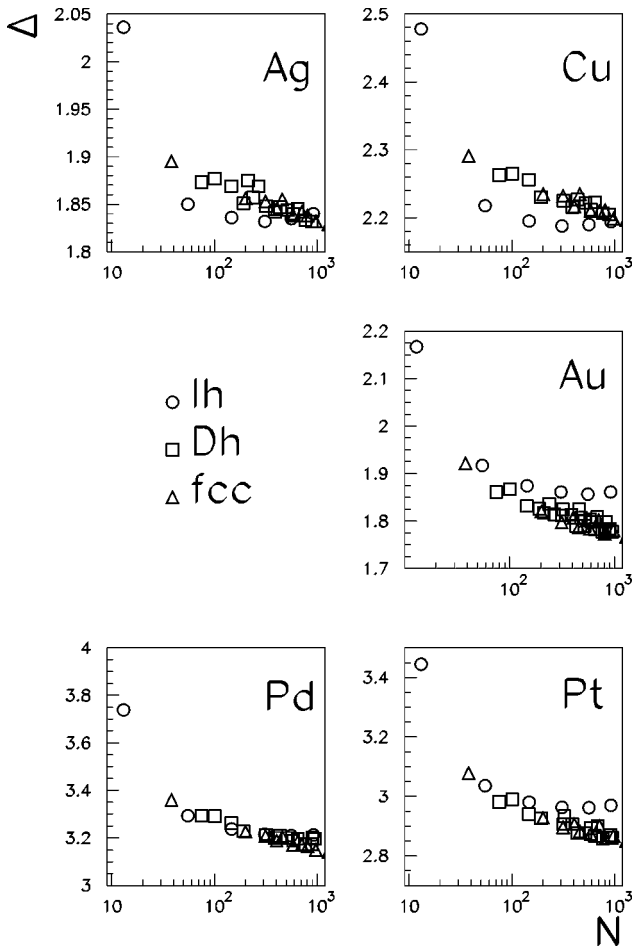

FIG. 5. Δ calculated by EAM potentials for Ag, Cu, Au, Pd, and Pt clusters. Symbols as in Fig. 2.

The best choice of n_l and n_{cut} satisfies generally the Wulff construction, especially when the cluster is not too small, as can be understood by the comparison of Table II and Fig. 3. Again we find that gold clusters are characterized by large hexagonal (111) facets (the best TO structures are characterized by $n_l=3n_{\mathrm{cut}}+3$ at small sizes and $n_l=3n_{\mathrm{cut}}+4$ at larger sizes) while Pt and Pd prefer $n_l=3n_{\mathrm{cut}}+2$ (for large Pt clusters also the choice $n_l=3n_{\mathrm{cut}}+3$ is very good), and Cu fcc clusters are characterized by $n_l=3n_{\mathrm{cut}}$. We remember that for Ag clusters we have regular TO, with $n_l=3n_{\mathrm{cut}}+1$. These results are in very good agreement with the ratio $\gamma_{100}/\gamma_{111}$ reported in Table II: in fact, we find that Cu and Ag, which present the lowest ratio, prefer smaller (111) facets than Au, which has the largest ratio.

Finally, we remark that, in the case of gold, it is known from literature[26] that, at small sizes, amorphous structures may play an important role. We do not consider them because the principal aim of our work is to make a comparison between different metals trying to find a simple method to devise *a priori* general trends about the crossover sizes between different structural motifs, whereas amorphous structures are favorable only for gold and maybe for platinum clusters.

C. Comparison of RGL and EAM results

Here we compare the results of the two potentials at sizes $N<1000$ (see Figs. 2, 4, 5). First of all, we notice that for each metal, the values of Δ obtained by the two potentials are rather different. However, the values in themselves are not of great importance. For example, we have made the following check. We have calculated Δ by means of a second parametrization of the RGL potential (the one in Ref. 15) which differs from the one used in Figs. 2 and 4 essentially because the cutoff distance for the interactions is larger. In that case, the curves of $\Delta(N)$ are shifted to higher values, but crossover sizes remain unaltered.

If we compare crossover sizes for the transition Ih $\rightarrow$Dh, we see that RGL results are in agreement with the EAM results from a qualitative viewpoint. In fact, also in this case we find that copper clusters present a broad size window in which Ih are the best structures (Δ decreases up to 309 atoms and the crossover with decahedra is at $N>1000$), which is followed by a large decahedral interval, while gold disfavors this kind of structures and prefers the fcc shape already at small sizes: there is a strong competition between Dh and fcc already at $N\simeq 400$. Silver has an intermediate behavior (closer to Cu than to Au) also according to EAM potentials, while Pt is closer to Au.

In conclusion, the major difference between RGL and EAM results is that, within the EAM potential description, palladium clusters present a behavior much more similar to Ag than to Pt (the icosahedral interval is wider: Ih are the best up to 150 atoms).

IV. DISCUSSION

In this section, we try to develop a simple criterion for explaining the trends shown by the different metals about the crossover sizes. Due to their rather simple analytical form,

TABLE III. Parameter $\sigma=\rho(\varepsilon)/\varepsilon^2$ in the cases of first ($\sigma_{1n}=pq/2$) and second neighbor (σ_{2n}, see Appendix for the formula) cutoff, sizes where Δ is minimum (N_Δ^{Ih} for icosahedra and N_Δ^{Dh} for decahedra), and crossover sizes ($N_{\mathrm{Ih}\to\mathrm{Dh}}$ and $N_{\mathrm{Dh}\to\mathrm{fcc}}$), in the case of the different metals and for the RGL potentials.

Metal	σ_{1n}	σ_{2n}	N_Δ^{Ih}	N_Δ^{Dh}	$N_{\mathrm{Ih}\to\mathrm{Dh}}$	$N_{\mathrm{Dh}\to\mathrm{fcc}}$	$N_{\mathrm{Ih}\to\mathrm{fcc}}$
Cu	13.1	14.4	309	20000	1000	>30000	1500
Ag	17.2	18.3	147	14000	<300	20000	400
Pd	20.9	21.8	147	5300	<100	6500	<100
Pt	20.6	21.5	147	5300	<100	6500	<100
Au	22.6	23.3	147	1300	<100	500	<100

RGL potentials are well suited to discuss general trends as functions of the potential parameters. An example is the (1×2) missing-row reconstruction. This reconstruction is adopted by Ir, Pt, and Au(110) surfaces (the $5d$ series, while the $3d$ and $4d$ series do not reconstruct) and it has been theoretically ascribed[29] to the increase of the parameter q, which governs the attractive interaction dependence with distance, when going from $3d$ to $5d$ metals. Such an increase in q for the fcc transition metals is consistent with the universal nature of binding-energy-distance relations.[30,31] A similar trend has been pointed out along the noble metal column concerning the vacancy stabilization in icosahedra.[12]

The question that we shall try to answer in the following is: Why are crossover sizes small for gold and large for copper? First of all, we notice that noncrystalline structures are distorted: even in the unrelaxed structure, nearest-neighbor atoms are placed at distances which are different from the nearest-neighbor distance in the bulk solid. Therefore, we expect that a crystal which increases strongly its energy for a change in interatomic distances (i.e., which has a ''sticky'' interatomic potential), would have small crossover sizes.[32] On the contrary, elements with less sticky interactions would have larger crossover sizes. Following this idea, we look for the effect on the total energy of a bulk crystal of changing all the interatomic distances by a factor, say

$$r_{ij}\to(1+\varepsilon)r_{ij}\,. \tag{10}$$

Then we develop the crystal energy per atom $E_i(\varepsilon)$ to the second order and divide it by the equilibrium value $|E_i(0)|$. We expect that the larger is the ratio,

$$\rho(\varepsilon)=\frac{E_i(\varepsilon)-E_i(0)}{|E_i(0)|}, \tag{11}$$

the smaller are the crossover sizes from icosahedra to decahedra and then from decahedra to fcc crystallites. $\rho(\varepsilon)$ is essentially the ratio between the bulk modulus and the cohesive energy per atom of the bulk crystal.

Let us now calculate $E_i(\varepsilon)$, and try to find a simple expression in terms of the parameters of the potential. We assume, for the moment, that interatomic interactions extend to first neighbors only. The inclusion of second neighbors introduces only minor changes (see the following). For first-neighbor interactions, we obtain [see Eqs. (1) and (2) with $\alpha=1/2$]:

$$\begin{aligned}E_i(\varepsilon)&=12A\exp(-p\varepsilon)-\sqrt{12}\xi\exp(-q\varepsilon)\\&\simeq12A-\sqrt{12}\xi-(12Ap-\sqrt{12}\xi q)\varepsilon\\&\quad+(6Ap^2-\sqrt{3}\xi q^2)\varepsilon^2.\end{aligned} \tag{12}$$

The first-order term is zero because of the equilibrium condition on the crystal; this gives

$$\sqrt{12}Ap=\xi q, \tag{13}$$

and therefore

$$\rho(\varepsilon)=\tfrac{1}{2}pq\varepsilon^2. \tag{14}$$

From the above arguments, this result would indicate that *the larger is pq, the smaller are the crossover sizes*. This is indeed the case, as can be seen in Table III, where also results for second-neighbor interactions are reported. In the latter case one finds again $\rho(\varepsilon)=f(p,q)\varepsilon^2$, with $f(p,q)$ of a rather complicated form (see the Appendix); however, the inclusion of second neighbors does not introduce significant changes. A simple interpretation to Eq. (14) follows from the fact that p and q determine the range of the repulsive and of the attractive parts of the potential, respectively [see Eqs. (1) and (2)]; smaller p and q give a longer range (and less sticky) potential. We can notice from Table I that, whereas p does not vary monotonically, q increases from $3d$ to $5d$ series as expected from the universal features of bonding in metals[30,31] so that pq is globally increasing from Cu to Au.

An equivalent way to correlate the metal-dependence of the stability domain of icosahedra relative to fcc-type structures with respect to the potential parameters is to give an analytical expression of the energies involved in the most simple cases: the 13 atoms clusters with icosahedral or cuboctahedral (TO with $n_l=2n_{\mathrm{cut}}+1$ and same atoms number as the Ih) symmetry. In these cases, the relaxed structures display only three different interatomic distances: one radial (r_1) and one tangential (r_2) for Ih_{13}, and only one (r_3) for

TABLE IV. Interatomic radial (r_1) and tangential (r_2) distances in the Ih_{13} and the one (r_3) in the TO_{13} after relaxation versus the equilibrium distance in the bulk (r_0).

Metal	$\frac{r_1}{r_0}$	$\frac{r_2}{r_0}$	$\frac{r_3}{r_0}$
Cu	0.928	0.976	0.950
Ag	0.924	0.972	0.945
Au	0.920	0.967	0.939

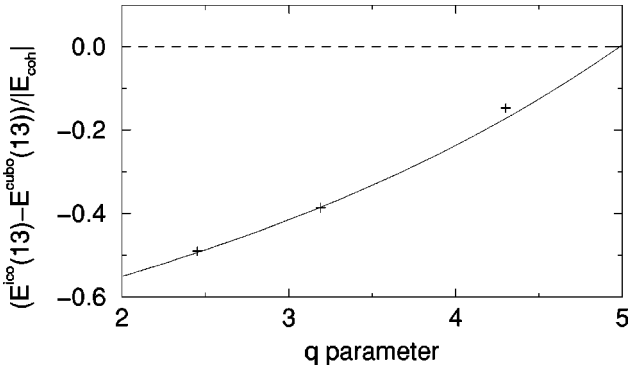

FIG. 6. Normalized energy difference between the Ih and the TO (cuboctahedron) of 13 atoms as a function of the parameter q.

the TO_{13}. If we note $P_i = e^{-p((r_i/r_0)-1)}$ and $Q_i = e^{-q((r_i/r_0)-1)}$ the distance dependencies of the repulsive and attractive terms of the potential, we can write the energy difference between Ih_{13} and TO_{13} normalized by the bulk cohesive energy as follows:

$$\frac{E_{Ih_{13}}-E_{TO_{13}}}{|E_{coh}|}=\frac{1}{p-q}\{-p[Q_1+2\sqrt{3Q_1^2+15Q_2^2} -(2\sqrt{15}+1)Q_3]+q(2P_1+5P_2-6P_3)\}. \tag{15}$$

The values of r_1, r_2, and r_3 are noted in the Table IV. For noble metals, we can notice from Tables III and IV that the p parameter and the interatomic distances are not so different from one metal to another, so that we use averaged values to plot Eq. (15) as a function of q; essentially, since p is not changing much, to look at variations in pq or in q is the same thing. We check in Fig. 6 that the points representing the ''exact'' values fit quite well the curve so that we get an evolution of the energy difference between Ih_{13} and TO_{13} which decreases appreciably when q increases, i.e., from Cu to Au. That means that the Ih is the most favorable for Cu then for Ag and at last for Au clusters. In order to extend this analysis to bigger sizes to evaluate the crossover transition from noncrystalline (Ih) to crystalline (TO) clusters in noble metals, we have compared the surface energy gain and the core energy loss of the Ih relatively to TO with the same atoms number for three different sizes: 13, 561, and 2057 in order to distinguish the trend in the crossover transition from one metal to another. Looking at Table V we notice that except for the 13-atoms clusters where core defect is increasing from Cu to Au along the series, the core energy loss is quasi constant for the three metals and independent of the size [this is coherent with the divergence as $N^{1/3}$ of Δ at large sizes, see Eq. (8)], whereas the surface energy gain is decreasing from Cu to Au so that Cu Ih are more favorable (in a larger size range) than Ag and Au ones. This second analysis confirms the first one related to the stickiness of the potential[32] in order to predict the crossover size transition from $3d$ to $5d$ transition and noble metals series.

V. SUMMARY AND CONCLUSIONS

In conclusion, we present a study of the energetics of five transition and noble metal clusters, and make a comparison among them trying to find simple ways to understand *a priori* general trends about crossover sizes among different structures.

We consider three structural motifs: icosahedra, truncated decahedra, and truncated octahedra for Cu, Ag, Au, Pd, and Pt.

We calculate the cluster energy by quenched molecular dynamics as a function of the cluster size N and considering both the RGL and EAM potential. Moreover, in the case of Dh and fcc structures we find a criterion to determine the best choice of the parameters which identify the cluster shape: (m, n, r) for decahedra and n_l and n_{cut} for TO. We find that their choice depends on metals according to the ratio $\gamma_{100}/\gamma_{111}$. In fact, we show that Au clusters, which present the largest ratio, prefer to have large (111) facet so they are characterized by $r=m$ and $n_l=3n_{cut}+3$. On the other hand, Cu and Ag clusters, which have the smallest ratio, present both $r=m/2$ and $n_l=3n_{cut}$, $n_l=3n_{cut}+1$, respectively. The best choice for Pd and Pt clusters is just in the middle: $r \simeq m-2$ and $n_l=3n_{cut}+2$.

Once we have found the best sequence for the three structural motifs, we can establish the crossover size among different structures and then make a comparison between metals. We demonstrate that copper and gold clusters have completely different behaviors. In fact, in the case of Cu clusters we find that non-crystalline structures are favored in wide intervals of size, while Au disfavors completely the icosahedral motif, with fcc clusters already at small sizes. The other metals present intermediate behaviors: silver is much more similar to copper while palladium and platinum are close to gold. The trends we find for different metals are in line with simple considerations based on the strain energy of the structures, due to the distortion of the interatomic distances in the noncrystalline structures. To estimate the effect of the strain on the excess energy, we introduce a small uniform expansion ε in the interatomic distances of the fcc bulk crystal, and we develop the crystal energy per atom $E_i(\epsilon)$ to the second order, subtract the equilibrium value $E_i(0)$ and divide by $|E_i(0)|$, thus obtaining the quantity $\rho(\epsilon)$, which is essentially the bulk modulus divided by the cohesive energy per atom in the bulk crystal. In this way, we can explain why

TABLE V. Energy difference between Ih and TO with same size for the surface energy gain and core energy loss divided by the total number of atoms (13, 561, 2057).

Metal	13 (surf.)	13 (core)	561 (surf.)	561 (core)	2057 (surf.)	2057 (core)
Cu	−0.081	0.019	−0.020	0.007	−0.012	0.007
Ag	−0.067	0.017	−0.014	0.006	−0.009	0.007
Au	−0.053	0.030	−0.005	0.006	−0.002	0.007

Cu has a wide size interval in which noncrystalline structures are favored while Au presents a very small crossover size interval. In fact, we find that $\rho(\epsilon)$ depends only on the product pq: a large pq (as happens for gold) suggests a sticky potential, so displacing atoms in noncrystalline positions costs a lot. On the other hand, small pq allows to displace interatomic distances and so the icosahedral and decahedral motifs are favored up to large sizes. Therefore, we can conclude that there is a simple way to determine the general trends in crossover sizes among different structures: a crystal which increases strongly its energy for a change in interatomic distances would have small crossover sizes while elements with less sticky interactions would have larger crossover sizes.

ACKNOWLEDGMENTS

The authors acknowledge financial support from the Italian MURST under project No. 9902112831. We thank A. F. Voter for permitting us to use his Molecular Dynamics code. The CRMC2 is associated to the Universities of Aix-Marseille II and III.

APPENDIX: FORMULA FOR $\rho(\epsilon)$ WITH SECOND-NEIGHBOR INTERACTIONS

Here we report the results for $\rho(\epsilon)$ in the case of interactions extended to the second neighbors for RGL potentials [see Eqs. (1) and (2) with $\alpha=1/2$]. Following the same procedure as in Sec. IV, one finds easily that $\rho(\epsilon)$ can be cast in the form $\rho(\epsilon)=f(p,q)\epsilon^2$ where $f(p,q)$ is given by

$$f(p,q)=\frac{pq}{2}\,\frac{p\dfrac{1+C}{1+\sqrt{2}C}-q\dfrac{1-(3-\sqrt{2})D+\dfrac{D^2}{2}}{\left(1+\dfrac{D}{2}\right)\left(1+\dfrac{D}{\sqrt{2}}\right)}}{p\dfrac{1+\dfrac{D}{2}}{1+\dfrac{D}{\sqrt{2}}}-q\dfrac{1+\dfrac{C}{2}}{1+\sqrt{2}C}}, \qquad \text{(A1)}$$

where

$$C=\exp[-p(\sqrt{2}-1)], \quad D=\exp[-2q(\sqrt{2}-1)]. \qquad \text{(A2)}$$

As seen in Table III the corrections to the first-neighbor result are in between 3–10%. They are larger for Cu and smaller for Au; this follows from the fact that the potential for Cu has the longest range (i.e., it is the least sticky) among the five metals, and the potential for gold has the shortest range. The result with first-neighbor interactions $[f(p,q)=pq/2]$ is recovered by putting $C=0$ and $D=0$ in the above formula.

[1] T. P. Martin, Phys. Rep. **273**, 199 (1996).
[2] L. D. Marks, Rep. Prog. Phys. **57**, 603 (1994).
[3] C. L. Cleveland, U. Landman, T. G. Schaaff, M. N. Shafigullin, P. W. Stephans, and R. L. Whetten, Phys. Rev. Lett. **79**, 1873 (1997).
[4] S. Ino, J. Phys. Soc. Jpn. **27**, 941 (1969).
[5] L. D. Marks, J. Cryst. Growth **61**, 556 (1984).
[6] B. Raoult, J. Farges, M. F. De Feraudy, and G. Torchet, Philos. Mag. B **60**, 881 (1989).
[7] C. L. Cleveland and U. Landman, J. Chem. Phys. **94**, 7376 (1991).
[8] J. Upperbrink and D. J. Wales, J. Chem. Phys. **96**, 8520 (1992).
[9] J. P. K. Doye, M. A. Miller, and D. J. Wales, J. Chem. Phys. **111**, 8417 (1999).
[10] D. Reinhard, B. D. Hall, P. Berthoud, S. Valkealahti, and R. Monot, Phys. Rev. Lett. **79**, 1459 (1997).
[11] J. Farges, M. F. De Feraudy, B. Raoult, and G. Torchet, Surf. Sci. **106**, 95 (1981).
[12] C. Mottet, G. Trèglia, and B. Legrand, Surf. Sci. **383**, L719 (1997).
[13] C. Barreteau, M. C. Desjonquères, and D. Spanjaard, Eur. Phys. J. D **11**, 395 (2000).
[14] V. Rosato, M. Guillopé, and B. Legrand, Philos. Mag. A **59**, 321 (1989).
[15] F. Cleri and V. Rosato, Phys. Rev. B **48**, 22 (1993).
[16] S. M. Foiles, M. I. Baskes, and M. S. Daw, Phys. Rev. B **33**, 7983 (1986).
[17] A. F. Voter, Los Alamos Unclassified Technical Report No. LA-UR 93-3901, 1993.
[18] C. L. Liu, J. M. Cohen, J. B. Adams, and A. F. Voter, Surf. Sci. **253**, 334 (1991).
[19] J. Guevara, A. M. Llois, and M. Weissmann, Phys. Rev. B **52**, 11509 (1995).
[20] F. Montalenti and R. Ferrando, Phys. Rev. B **59**, 5881 (1999).
[21] R. Ferrando, Phys. Rev. Lett. **76**, 4195 (1996).
[22] F. Montalenti and R. Ferrando, Phys. Rev. Lett. **82**, 1498 (1999).
[23] F. Baletto, C. Mottet, and R. Ferrando, Phys. Rev. Lett. **84**, 5544 (2000).
[24] F. Baletto, C. Mottet, and R. Ferrando, Phys. Rev. B **63**, 155408 (2001).
[25] D. Reinhard, B. D. Hall, D. Ugarte, and R. Monot, Phys. Rev. B **55**, 7868 (1997).
[26] K. Michaelian, N. Rendón, and I. L. Garzon, Phys. Rev. B **60**, 2000 (1999).
[27] J. P. K. Doye and D. J. Wales, New J. Chem. **22**, 733 (1998).
[28] A. Pimpinelli and J. Villain, *Physics of Crystal Growth* (Cambridge University Press, Cambridge, 1998).
[29] M. Guillopé and B. Legrand, Surf. Sci. **215**, 577 (1989).
[30] J. H. Rose, J. R. Smith, and J. Ferrante, Phys. Rev. B **28**, 1835 (1983).
[31] D. Spanjaard and M. C. Desjonqures, Phys. Rev. B **30**, 4822 (1984).
[32] J. P. K. Doye, D. J. Wales, and R. S. Berry, J. Chem. Phys. **103**, 4234 (1995).

Density-Functional Calculations on Platinum Nanoclusters: Pt_{13}, Pt_{38}, and Pt_{55}

Edoardo Aprà[†] and Alessandro Fortunelli*[,‡]

Theory, Modeling & Simulation, Environmental Molecular Sciences Laboratory, Pacific Northwest National Laboratory, P.O. Box 999, Richmond, Washington 99352, and Molecular Modeling Laboratory, Istituto per i Processi Chimico-Fisici (IPCF) del C.N.R., via V. Alfieri 1, 56010, Ghezzano (PI), Italy

Received: November 28, 2002; In Final Form: February 20, 2003

The results of an accurate density-functional study of the structure, energetics and electronic structure of Pt_n clusters (with $n = 13$, 38, and 55) are presented. For Pt_{38}, a truncated octahedral geometry is considered; for Pt_{13} and Pt_{55}, icosahedral, truncated decahedral, and cuboctahedral geometries are considered. In each case, the structure of the neutral and positively and negatively charged clusters is fully optimized within the given symmetry group. For Pt_{13}, allowing symmetry breaking starting from the symmetrical structures derives additional local minima. The computational procedure is thoroughly tested to keep numerical accuracy under control. From the electronic structure point of view, it is found that these systems start developing metallic characteristics, with ionization introducing small changes. From the structural point of view, for Pt_{13} the icosahedral configuration is not favored, whereas it becomes the ground state for Pt_{55}, in agreement with the predictions of atom−atom potentials. Moreover, the lowest energy configuration of Pt_{13} is a symmetry-broken D_{4h} one, while for Pt_{38} and Pt_{55} a peculiar rearrangement is found, corresponding to an expansion (reconstruction) of the atoms lying on (111) or (100) faces.

1. Introduction

The chemistry and physics of metal clusters have attracted much attention in recent years (see, for example, ref 1) for their peculiar structural, electronic, optical, etc., properties. The wealth of experimental data has prompted an intense theoretical effort devoted to elucidate the mechanisms at work in this class of systems. The theoretical literature on isolated metal clusters has dealt with both the structural and the electronic properties.[2−16] From the structural point of view, attention has usually concentrated on high-symmetry configurations. Structures corresponding to pieces of the bulk crystals (fcc, bcc, etc.), which should be the lowest energy ones for very large aggregates, have been compared with others containing C_5 axes (icosahedral or decahedral) which are incompatible with translational symmetry but are expected to be good competitors for smaller clusters, due to more favorable surface energies at the expense of introducing internal strain.[2−9,13] One thus expects a crossover among these structures with increasing size, with the icosahedral configurations dominating at small sizes, the decahedral configurations dominating at intermediate sizes, and the crystalline configurations eventually dominating at large sizes (see, for example, ref 7). More recently, "amorphous" arrangements have also been proposed as possible lowest energy structures for small clusters.[11,12,15] From the electronic point of view, the limitations of simplified approached such as the "jellium" model have been pointed out,[13] and various techniques have been proposed to analyze the shell structure of the one-electron energy levels[10] and to study the behavior of the cluster properties with size (and extrapolate them to the bulk limit).[8,9,13,14]

In this context, platinum clusters undoubtedly represent a class of systems of great importance because of the role they play in many catalytic processes (they are considered one of the most important materials in heterogeneous catalysis[1]). A theoretical understanding of their structural and electronic properties is essential to the first-principle prediction of their behavior. Moreover, platinum is especially interesting also from a purely theoretical point of view because the crossover between icosahedral, decahedral and crystalline structures is expected to occur at small size.[7] Despite this, in the literature one cannot find many calculations on Pt_n clusters with $n \geq 13$,[10−12,14] probably due to the fact that platinum (as a third-row transition metal) simultaneously presents all the difficulties connected with s/p-d mixing and relativistic effects.

Experimentally, the structure of Pt_n clusters with $n \leq 200$ is still unclear: for clusters with diameter >10 nm[17] or even ∼2 nm[18] crystalline geometries seem to be preferred, but other structural forms might be favorite for smaller aggregates.[19]

In the present article, density-functional (DF) calculations on Pt_{13}, Pt_{38}, and Pt_{55} neutral clusters and their singly charged ions will be presented. Highly symmetrical structures have been considered: truncated octahedron (O_h symmetry group) for Pt_{38}, cuboctahedron (O_h), truncated decahedron (D_{5h}), and icosahedron (I_h) for Pt_{13} and Pt_{55} (see Figure 1 for schematic pictures). All the structures have been fully optimized within the corresponding symmetry group. In the case of Pt_{13}, symmetry breaking starting from the symmetrical structures has been allowed, producing configurations corresponding to additional local minima. The chosen symmetrical structures are the most likely ordered candidates as the lowest energy ones for finite systems.[2,3] Moreover, from their comparison it is possible to predict the general crossover behavior among the different structural motifs (see, for example, ref 7 and references therein). Investigation on "amorphous" structures[11,12,15] is deferred to future work.

* Address for correspondence. IPCF-CNR, v. V. Alfieri 1, 56010, Ghezzano (PI), Italy. E-mail: fortunelli@icqem.pi.cnr.it. Phone: + 39-050-3152447. Fax: + 39-050-3152442.

[†] Pacific Northwest National Laboratory.

[‡] Molecular Modeling Laboratory IPCF-CNR.

10.1021/jp0275793 CCC: $25.00
Published on Web 04/01/2003

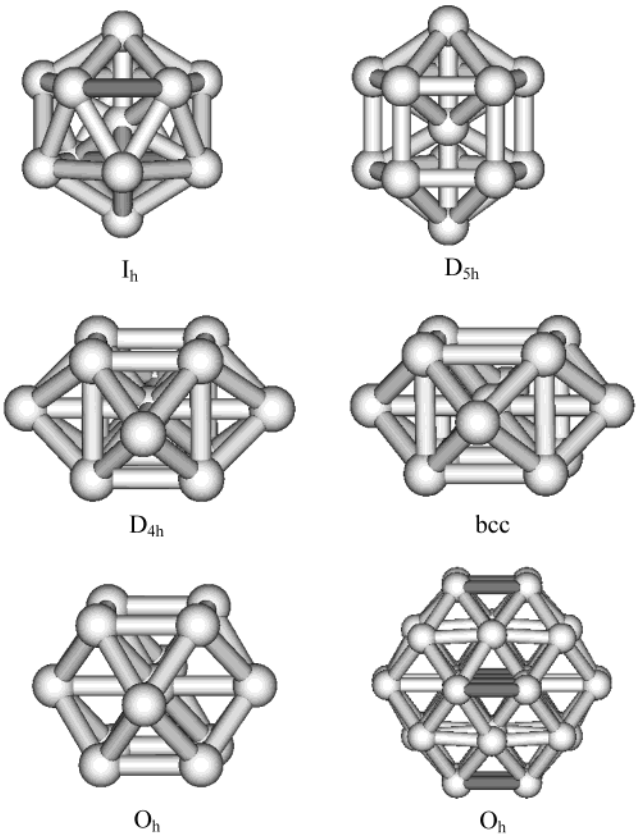

Figure 1. Schematic drawings of the Pt_{13} and Pt_{38} structures considered in the text.

From a computational point of view, symmetry is fully exploited to reduce the computational effort, so as to make a computationally accurate approach feasible on these large and complicated systems. This should also provide a standard against which more approximate approaches (many-body atom−atom potentials,[7,20] tight-binding methods,[21,22] etc.) can be contrasted and parametrized. Preliminary DF calculations on Pt_{13} and Pt_{55} cuboctahedral clusters have been previously presented.[14]

In section 2, the computational approach and the theoretical method will be detailed. In section 3, the results of the DF calculations will be presented and discussed. The main conclusions will be summarized in section 4.

2. Computational Details and Method

All the calculations were carried out with the DF module of the NWChem computational chemistry package (release 4.1)[23] that uses Gaussian-type orbitals (GTOs) for the solution of the Kohn−Sham equations.

An effective core potential (ECP)[24] was used to represent the nucleus plus inner-shell (up to the 4f shell) core electrons interactions with all valence electrons; thus only the outer-core (5s and 5p shells) plus valence electron wave function is solved for explicitly. This ECP incorporates spin−orbit-averaged relativistic effects. Two atomic orbital bases were used for describing the outer-core plus valence electrons, both derived from a (7s6p5d)/[6s3p2d] basis set.[25] In the first one (basis set A), the s-functions were left uncontracted, the first p- and d-contractions of 4 GTOs were split into three and one GTOs, corresponding to a (7s6p5d)/[7s4p3d] basis set. In the second one (basis set B), we removed the most diffuse p-function that causes numerical instabilities in these highly condensed systems, and split the first p-contraction as above, to get a (7s5p5d)/[6s3p2d] basis set.

All the calculations were performed spin-unrestricted, using the Becke functional[26] for exchange and the Perdew−Wang functional[27] for correlation, hereafter referred to with the acronym BPW91. The BPW91 functional has been selected as the gradient-corrected one which gives optimal values for the $5d^96s^1 \rightarrow 5d^{10}$ excitation energy of the Pt atom and dissociation energy of the Pt_2 molecule[28] (hybrid functionals should not be used for metal clusters[14]). We refer to refs 8−11, 14, and 16 for a discussion of the DF approach as applied to transition metal clusters.

In addition to the basis set for the Kohn−Sham orbitals, a charge density fitting basis was used to compute the Coulomb potential according to the method described in refs 29 and 30. The (9s3p3d2f2g) basis set used was derived from the one described in ref 31. Numerical tests on Pt_{13}, Pt_{38}, and Pt_{55} have shown that the effect of this approximation on the total energy differences among the various configurations is of the order of mhartree (care must be used in the choice of the auxiliary basis set, especially for the larger systems).

A numerical integration is necessary for the evaluation of the exchange−correlation potential and energy. The scheme used in this work adopts well-known techniques that partition the density into atomic contributions;[32] this "atomic density" is then integrated using a radial quadrature and a highly efficient angular quadrature.[33] One hundred twenty-three points were used for the radial part. Five hundred ninety points were used for the angular part, corresponding to the exact integration of all spherical harmonics up to $\ell = 41$. For the radial quadrature, the scheme of ref 34 has been rescaled[35] in order to better integrate the contribution coming from the diffuse functions present in the basis set. Such an extensive grid is necessary to keep numerical accuracy under control in these complicated systems, with s, p, and d mutually interacting open shells. Tests have shown that using lower quality numerical grids or charge density auxiliary basis sets may lead to even qualitatively incorrect results or slow convergence.

As in ref 14, the geometry optimization was stopped when maximum force on atoms was less than 4×10^{-4} au.

The exploitation of symmetry is obviously beneficial to reduce the computational effort. For example, the CPU time ratios among the different symmetries for Pt_{13} using basis set A on a single processor of a Compaq Alpha XP-1000 667 MHz computer are

O_h	D_{4h}	I_h	D_{5h}	C_{2h}	C_{2v}	C_1
1	1.7	2.2	2.7	4.6	4.8	16.9

It is to be noted that CPU time $I_h > D_{4h}$, O_h even though I_h is a higher group. This is due to the fact that the Lebedev angular grid[33] exhibits cubic symmetry, so that symmetry is not fully exploited when C_5 axes are present (the precise figure will in general depend on the ratio between the computational effort involved in the evaluation of the Coulomb potential and the numerical integration).

NWChem is a suite of programs specifically developed for parallel computers, and is based on a distributed memory approach for parallelism.[23] The use of an auxiliary charge density basis set can be particularly advantageous in this respect, because one expects super-linear scaling whenever the aggregate memory is sufficient to store all the three-center integrals in the memory available on the parallel hardware (which are therefore not recalculated at each iteration step). To give an idea of the computational effort involved in the calculations, we quote that a single SCF cycle for O_h Pt_{55} using the present

TABLE 1: The Results of DF Calculations Using Basis Set A on Pt_{13}^q ($q = 0, \pm 1$) in Various Structural Arrangements (Described in the Text) Are Reported[a]

system	ΔE	$N_\alpha - N_\beta$	BW (α/β)	gap (α/β)	ϵ_F	geometry
I_h	1.086	2	7.30/7.43	0.13/0.13 h_g^3	−5.242	2.671
I_h	1.065	8	7.57/7.49	0.82/0.03	−5.101	2.687
T_h	1.003	8	7.49/7.45	0.80/0.06 t_g^1	−5.098	2.684, 2.744, 2.842
O_h	0.720	6	6.96/7.04	0.86/0.19 $t_{2u}-e_g$ 0.001	−5.264	2.723
D_{5h}	0.230	4	7.12/7.17	0.36/0.18 e_{2g}^1	−5.082	2.906, 2.677 (0.463)
C_{2v}	0.186	4	7.12/7.09	0.30/0.15	−5.071	2.907, 2.63−2.72(0.465)
D_{4h}	3.297	2	7.48/7.36	0.11/0.31	−5.137	3.179, 2.526 (0.908)
I_h^+	1.295	3	7.39/7.43	0.10/0.10 h_g^2	−8.902	2.672
T_h^+	1.057	9	7.49/7.42	1.01/0.07	−8.786	2.684, 2.744, 2.842
O_h^+	0.902	7	6.85/7.05	1.1/0.17 $t_{2u}-e_g$ 0.008	−8.859	2.725
D_{5h}^+	0.264	5	7.15/7.15	0.35/0.06	−8.745	2.946, 2.672 (0.460)
D_{4h}^+	6.858	1	7.47/7.34	0.09/0.28	−8.652	3.158, 2.534 (0.902)
I_h^-	0.965	1	7.30/7.32	0.17/0.17 h_g^4	−1.674	2.810
C_{2h}^-	0.909	1	7.33/7.34	0.15/0.10	−1.609	2.63−2.70, 2.76−2.82, 2.80−2.83
O_h^-	0.566	5	6.91/6.97	0.70/0.22	−1.732	2.725
D_{5h}^-	0.250	3	7.07/7.10	0.36/0.18	−1.411	2.874, 2.685 (0.465)
D_{4h}^-	3.342	3	7.37/7.18	0.06/0.26	−1.585	3.145, 2.548 (0.898)

[a] $N_\alpha - N_\beta$ is the difference in the number of α and β electrons; BW and gap are the band width and the HOMO−LUMO energy difference for α/β electrons, respectively; ϵ_F is the Fermi energy; and geometry lists representative atom−atom distances as explained in the text. In the case of JT or pJT systems, HOMO symmetry labels are explicitly reported on the right of the gap value, together with their energy difference. The ΔE column has a mixed meaning, reporting the binding energy per atom BE/N in the case of the lowest energy minimum (D_{4h} for Pt_{13}), the electron affinity and ionization potential for the lowest energy ionic structures (D_{4h}^- and D_{4h}^+, respectively, for Pt_{13}), and the excitation energy with respect to the lowest energy configuration of each charge state for all other configurations. Energy-related quantities are in eV, distances in angstroms.

methodology requires ∼2300 s when running on a Compaq Alpha XP-1000 667 MHz computer.

To overcome the degeneracy problems that arise in systems such as these, containing many transition metals in low oxidation state, a Gaussian-smearing technique for the fractional occupation of the energy levels was applied.[36,37] This was not used to mimic Fermi−Dirac statistics at finite temperatures, nor was a many-determinantal wave function used to take into account long-range correlation effects.[38] However, smearing the one-electron levels is very beneficial if not strictly necessary to obtain a smooth convergence for such quasi-metallic systems, with very many levels extremely close in energy. The NWChem program has been purposely modified, and this new feature is available in the NWChem 4.1 release. Usually, the use of an error function with a broadening factor $\sigma = 0.006$ au is sufficient for obtaining a good convergence at the beginning of the SCF process, while $\sigma = 0.0003$ au was used for final convergence. All the results reported below have thus been obtained using $\sigma = 0.0003$ au and ∼0.01 eV.

If at convergence the HOMO−LUMO gap is appreciably larger than σ, then the use of smearing does not affect the final energy value (it is simply a tool to improve convergence). However, when restraining the system to have a definite (high) symmetry, one can find either an incomplete occupancy of a degenerate HOMO: Jahn−Teller systems (JT) or an accidental quasi-degeneracy between HOMO and LUMO in one spin symmetry: pseudo-Jahn−Teller systems (pJT). In such cases, the use of smearing makes a difference. For JT systems, in particular, it ensures an even occupation of all degenerate HOMOs, allowing one to perform calculations within the given symmetry group (no symmetry breaking). To be specific, for example, for neutral Pt_{13} we found one JT system (D_{5h}) and two pJT systems (O_h and I_h). In the case of Pt_{13}, starting from the geometry optimized at high symmetry, we have evaluated the gradient with respect to atomic displacements with the use of symmetry turned off; this gradient has resulted to be of a lower symmetry, which has finally been imposed in a further geometry optimization. This should guarantee that the final structures are local minima on the energy hyper-surface. Note that, for JT systems, $\sigma = 0$ has to be set in order to break symmetry.

A noteworthy advantage of the electron-smearing technique is that the difference in the number of α and β electrons takes its optimal value since no constraint is imposed on the spin multiplicity.[36,37] To check that this holds in a specific example, in analogy with ref 10 we have calculated for O_h Pt_{13} ($N_\alpha - N_\beta = 6$, see Tables 1 and 2 below) the solutions obtained without using the electron-smearing technique, but imposing a different value of $N_\alpha - N_\beta$, and found that these solutions existed at a higher energy.

Apart from the electron smearing, the exploitation of symmetry is extremely important to obtain a smooth convergence of the iterative process: for example, level-shifting techniques (with $\sigma = 0$) had to be used when dealing with low-symmetry configurations, such as C_{2v} Pt_{13}, as we were unable to obtain convergence even using electron smearing with high values of σ.

Unrestricted spin calculations have always been performed. The value of $\langle S^2 \rangle$ has been taken as an indicator of spin-symmetry breaking:[39] it usually differed from the spin-restricted value by less than 1%, except for few cases which will be explicitly indicated in the following.

3. Results

The results of DF/BPW91 calculations will be reported in this section, divided according to the number of atoms in the cluster.

Pt_{13}. Our results are collected in Table 1 (basis set A) and Table 2 (basis set B). For reasons of synthesis, the ΔE column in these and the following Tables has a mixed meaning, reporting the binding energy BE per atom BE/N in the case of the lowest energy minimum (D_{4h} for Pt_{13}), the electron affinity and ionization potential for the lowest energy ionic structures (D_{4h}^- and D_{4h}^+, respectively, for Pt_{13}), and the excitation energy with respect to the lowest energy configuration of each charge state for all other configurations.

The bandwidth BW reported in the tables is defined as the difference between the one-electron energies of the lowest and

TABLE 2: The Results of DF Calculations Using Basis Set B on Pt_{13}^q ($q = 0, \pm 1$) in Various Structural Arrangements (Described in the Text) Are Reported[a]

system	ΔE	$N_\alpha - N_\beta$	BW (α/β)	gap (α/β)	ϵ_F	E_{relax}	geometry
I_h	1.233	2	7.45/7.49	0.13/0.12 $\underline{h_g}^3$	−5.211	0.71	2.671
I_h	1.201	8	7.70/7.60	0.83/0.03	−5.081	0.74	2.686
O_h	0.701	6	7.00/7.09	0.90/0.21 $t_{2u}-e_g$ 0.009	−5.300	0.24	2.725
D_{4h}'	0.250	8	7.20/7.02	0.40/0.13	−5.081	1.86	3.147, 2.583 (0.965)
D_{5h}	0.221	4	7.20/7.27	0.36/0.16 $\underline{e}_{2g}^1$	−5.086	0.76	2.914, 2.678 (0.462)
D_{4h}	3.228	2	7.61/7.47	0.08/0.29	−5.189	2.11	3.181, 2.528 (0.905)
I_h^+	1.206	9	7.61/7.61	1.10/0.02 $\underline{h_g}^2$	−8.791		2.682
O_h^+	0.895	7	6.92/7.12	1.13/0.19 $t_{2u}-e_g$ 0.0006	−8.933		2.727
D_{5h}^+	0.248	5	7.26/7.26	0.36/0.07	−8.819		2.950, 2.673 (0.460)
D_{4h}^+	6.907	1	7.59/7.47	0.07/0.25	−8.724		3.166, 2.536 (0.903)
I_h^-	1.215	1	7.40/7.42	0.17/0.15 $\underline{h_g}^4$	−1.555		2.672
O_h^-	0.561	5	7.01/7.04	0.69/0.23 $t_{1g}-e_g$ 0.016	−1.713		2.726
D_{5h}^-	0.309	3	7.15/7.20	0.36/0.15	−1.357		2.881, 2.685 (0.464)
D_{4h}^-	3.359	3	7.38/7.26	0.06/0.26	−1.572		3.145, 2.550 (0.892)

[a] Notations are the same as those In Table 1, except for E_{relax}, which is the energy difference in eV between the "idealized" and optimized geometries. Energy-related quantities are in eV, distances in angstroms.

the highest occupied molecular orbitals. The gap value is defined as the difference between the one-electron energies of the HOMO and LUMO: a small value will be taken as an indication of the metallic character of the clusters. In the case of JT or pJT systems, all the (quasi-)degenerate orbitals have been considered as HOMOs, correspondingly taking average values of the various quantities. In these cases, the HOMO symmetry labels and energy differences are reported on the right of the gap values.

To avoid excessive duplications, not all states and quantities are reported in the two tables: in Table 2 only the basic states are reported, to be compared with the results for Pt_{38} and Pt_{55} using the same basis set. All the geometries have been fully optimized within the given symmetry group starting from "idealized" geometries, i.e., in which the basic Pt−Pt distance was set to $R_0 = 2.774$ Å (bulk crystal[40]). For O_h geometries, which correspond to a section of the face-centered cubic (fcc) crystal, this completely defines the atomic arrangement. Two distances characterize the I_h and D_{5h} geometries: the shorter one corresponds to the inter-shell distance for I_h and most of the distances for D_{5h}; the longer one to the intra-shell distance for I_h and a few distances for D_{5h}. The ratio between the two is

$$\sqrt{2(1 - 1/\sqrt{5})} \sim 1.05146$$

We set the shorter distance in idealized structures to 2.774 Å, which implies that the strained distance is equal to ∼2.915 Å. The relaxation energies E_{relax} reported in Tables 2, 4, and 5 refer to this choice of idealized geometries (for Pt_{13} the relaxation energy is only reported for basis set B).

As anticipated in section 2, for Pt_{13} the octahedral, icosahedral, and truncated decahedral geometries have been relaxed in the absence of symmetry until a local energy minimum was found. Let us start by looking at which kind of symmetry breaking one finds in each case.

Neutral D_{5h} Pt_{13} is a JT system, having a degenerate incompletely occupied e_{2g}^1 HOMO in the minority β spin symmetry. The structure deforms to a C_{2v} geometry. The energy gain is however small: only 0.044 eV. Adding or removing an electron from the e_{2g} orbital produces a system with a finite gap.

Neutral I_h Pt_{13} is a more complicated case, and very difficult to converge, because of an accidental quasi-degeneracy between a t_{2g} and a $\underline{h}_g$ orbitals close to the Fermi energy (here and in the following, β spin−orbitals will be denoted by underlining: $\underline{h}_g$), which implies a quasi-degeneracy between two electronic configurations:

high spin:	$h_g^5 t_{2g}^3 \underline{h}_g^0$	$N_\alpha - N_\beta = 8$
low spin:	$h_g^5 t_{2g}^0 \underline{h}_g^3$	$N_\alpha - N_\beta = 2$

differing in energy by ∼0.02−0.03 eV (see Tables 1 and 2). Of course, any change in the functional, but even in the basis set or the numerical procedure can reverse the order between the high- and low-spin states. By allowing symmetry breaking, the I_h configuration relaxes to a T_h or a C_{2h} one, depending on the charge state, but the energy lowering is again modest: 0.06 eV, except in the cation I_h (I_h^+) case, where however we were not able to converge to the high-spin state. An unusually high value of $\langle S^2 \rangle$ for C_{2h}^- Pt_{13}: $\langle S^2 \rangle = 1.152$ with $N_\alpha - N_\beta = 1$, testifies this quasi-degeneracy (the value of $\langle S^2 \rangle$ differs significantly from the spin-restricted one also for D_{4h}^- Pt_{13}: $\langle S^2 \rangle = 8.767$ with $N_\alpha - N_\beta = 3$).

Symmetry breaking is only important for the octahedral geometry, in which case one finds that a $O_h \rightarrow D_{4h}$ distortion lowers the energy by a substantial amount: 0.7, 0.9, and 0.5 eV for Pt_{13}^q with $q = 0, +1, -1$, respectively. The D_{4h} distorted geometry thus turns out to be the lowest energy one, surpassing the D_{5h} (C_{2v}) one by ≥0.2 eV at any charge state. In Table 2, therefore, only the D_{4h}, D_{5h}, O_h, and I_h states have been considered.

Before further relaxation, the order of the structure is: $D_{5h} < O_h < I_h$, irrespective of the charge state. This is at variance with the expectations of more simplified approaches[2,3,7] (atom−atom potentials, counting of the number of first neighbors, etc.) according to which the order should be $I_h < D_{5h} < O_h$: see below for a discussion. It is to be noted that low-spin states prevail, especially for the lowest energy configurations, in agreement with the fact that platinum is a nonmagnetic metal. The values of bandwidth BW and Fermi energy ϵ_F are similar for the different configurations, with the BW in the following order: $O_h < D_{5h} < D_{4h} \sim I_h$. Noteworthy is the variation of ϵ_F with the charge state.

By comparing the results with different charge, one finds that the addition or removal of an electron does not seem to affect much these clusters. All the characteristic quantities stay practically unchanged, apart from a "rigid-band" shift of all one-electron levels. In fact, we have checked that for each geometry even the electronic configuration stays the same, apart obviously from the orbitals directly involved in the charging process. Also the excitation energies of the various structural arrangements

do not change much: the order is $D_{4h} < D_{5h} < O_h < I_h$ for all cases, with D_{5h} at higher energy by 0.2−0.3 eV with respect to the D_{4h} ground state, O_h by ∼0.6−0.9 eV and I_h by ∼1.0−1.2 eV. The values of the geometrical parameters exhibit slightly larger differences, especially for I_h and D_{5h}.

By comparing the results of Tables 1 and 2, one sees that the smaller basis set (B) reproduces very well the results of the larger one (A). Apart from the binding energy BE per atom BE/*N*, which is larger for D_{4h} Pt_{13} by 0.07 eV when using basis set A, all the other energy differences, bandwidths, gaps, Fermi energies, and optimized geometrical parameters are accurately reproduced. We have also checked that the electronic configurations are the same using the two basis sets. Only the basis set B will thus be utilized for the calculations on the larger clusters: Pt_{38} and Pt_{55}.

Let us now discuss the structural results. The I_h and O_h structures have only one degree of freedom, which is the one reported in Tables 1 and 2: the distance between the central and the peripheral atoms. In the O_h structure, all the distances are the same. In the I_h structure, the distances among peripheral atoms are larger by a factor ∼1.051. The I_h structure can relax to a T_h or C_{2h} geometry. In the former (T_h) case, all peripheral atoms stay on a sphere, but six pairs of bonds in each of the plus/minus Cartesian directions shrink with respect to the other 30 surface bonds: these three distances are reported in Table 1. Note that T_h Pt_{13} is still a JT system, with a t_g^1 electronic configuration at the Fermi level. However, further symmetry breaking to C_{2h} geometry has a negligible effect on the energy, and has not been reported in Table 1. In the latter (C_{2h}) case, the original 12, 6, and 30 nearest-neighbor bonds of the T_h structure spread in such a way that it is difficult to describe. In Table 1 the range in which these bonds spread is reported.

The D_{5h} structure has three degrees of freedom which are reported in Tables 1 and 2: the distance of the two apical and of the 10 off-C_5 peripheral atoms from the central one, and the ratio between the absolute values of the *z*-coordinate of the off-C_5 atoms and the apical atoms (*z* is the C_5 axis). This ratio should be 0.5 in an idealized structure; its being smaller suggests that the (100) faces are larger than their optimal size, as expected on the basis of a Wulff construction reasoning.[2,3,7] When D_{5h} Pt_{13} relaxes to a C_{2v} structure, the two regular pentagons on which the ten C_5 atoms are distributed deform to two irregular ones. Again, the range in which the distances from the central atom spread is reported.

The most interesting case is the $O_h \rightarrow D_{4h}$ deformation. The O_h idealized cuboctahedron section of the fcc lattice is shown in Figure 1. The two (100) planes (or faces) along the *z*-axis are at a distance $(2)^{1/2}R_0 = 3.92$ Å, and are separated by a "crown" of four atoms in the $\pm x$ and $\pm y$ directions, at a distance $R_0 = 2.774$ Å from the central atom. For neutral Pt_{13} this structure is at 0.94 eV from the D_{4h} lowest energy state, and lowers to 0.72 eV after relaxation of the nearest-neighbor distance to 2.725 Å (results using basis set B from Table 2). The D_{4h} lowest energy configuration is also shown in Figure 1: with respect to the O_h structure, the (100) planes in the $\pm z$ directions get closer to each other (from 3.92 to 3.12 Å) and slightly enlarge (the nearest-neighbor distance increases from 2.774 to 2.82 Å), while the four "crown" atoms get further from the central one (from 2.774 to 3.17 Å). This structure may resemble an idealized body-centered cubic (bcc) structure (also shown in Figure 1), section of eight first and four second neighbors around the central atom of an hypothetical bcc crystal with nearest-neighbor distance set equal to 2.774 Å. However, in the bcc-like structure, the edges of the (100) faces are larger: 3.20 Å, so that the distance between atoms on the cube is the same as the second-neighbor distance (3.20 Å), and the bcc-idealized structure is at 2.11 eV over the D_{4h} ground state. The D_{4h} lowest energy structure therefore represents something between the bcc and fcc geometries, which differs substantially from both of them. This is confirmed by the fact that if one starts the geometry optimization from the bcc structure, one finds a different D_{4h} local minimum (denoted D_{4h}' in Table 2) in which the edge of the (100) faces is 2.95 Å; these faces are at a distance of 3.05 Å, and the peripheral atoms are at 3.15 Å from the central one (high spin: $N_\alpha - N_\beta = 8$). This structure resembles more the bcc idealized one, but is at 0.25 eV above the D_{4h} lowest energy configuration. The presence of low-lying local minima corresponding to structural isomers (even exhibiting the same symmetry) can have an influence on the mechanical properties of Pt nanoclusters. The peculiarity of the D_{4h} structure is also confirmed by the calculations reported in Table 3, where binding energies are reported for the sequence: Pt_9, Pt_{11}, Pt_{13}, and Pt_{15}, i.e., starting with a central atom surrounded by a cube of eight first-neighbors (Pt_9) and by progressively adding pairs of second neighbors on opposite faces of the cube. The BE increases by 8.34 eV from O_h Pt_9 to D_{4h} Pt_{11}, and by 8.63 eV from D_{4h} Pt_{11} to D_{4h} Pt_{13}, but only by 8.25 eV from D_{4h} Pt_{13} to D_{2h} Pt_{15}, which is moreover a pJT system, and, as such, is not particularly stable.

TABLE 3: Binding Energies BE in eV for the Sequence Pt_{9n}−Pt_{15}, from DF/BPW91 Calculations Using Basis Set A

system	BE	$N_\alpha - N_\beta$	degener
O_h Pt_9	25.91	2	no
D_{4h} Pt_{11}	34.23	0	no
O_h Pt_{13}	42.14	6	yes
D_{4h} Pt_{13}	42.86	2	no
O_h Pt_{15}	51.07	6	yes
D_{2h} Pt_{15}	51.11	6	yes

[a] The keyword "degener" indicates whether the systems are pJT ones (degener = yes) or have a finite gap at the Fermi level (degener = no). $N_\alpha - N_\beta$ Is the difference in the number of α and β electrons.

It is interesting to note that the relaxation energy, i.e., the difference between the idealized geometry and the optimized one, is minimal for the fcc (O_h) structure: ∼0.2 eV, intermediate for the C_5-axis structures, D_{5h} and I_h, ∼0.7 eV, and largest for the D_{4h} one, ∼2.1 eV. Even though the definition of idealized I_h and D_{5h} structures is not unique, these are the expected trends,[2] again with the only exception of the D_{4h} state.

The results for I_h and O_h Pt_{13} are comparable with those reported in the most recent work on these systems[10] (whose analysis of the orbital shell structure we refer to), after allowing for the differences due to the density functional, basis set, pseudopotential, and numerical approach. The main difference with respect to ref 10 is that the authors did not consider the D_{5h} structure and that a limited account of the Jahn−Teller distortion for the O_h structure hindered them from finding the D_{4h} ground state. In passing, it can be noted that the $I_h - O_h$ energy difference comes out to be much smaller from the calculations of ref 11, confirming the limitations of the Harris functional as applied to transition metal clusters.[9]

Pt_{38}. The results of DF calculations on Pt_{38}^q truncated octahedral cluster ($q = 0, \pm 1$) using basis set B are reported in Table 4. With respect to Pt_{13} one can observe a general increase in the BW, BE, and electron affinity values, and a decrease in the gap and ionization potential values, as expected. It is also to be noted the spin quenching effect, which now gives a closed-shell Pt_{38} neutral cluster. The value of $\langle S^2 \rangle$ differs significantly from the spin-restricted one only for O_h^+ Pt_{38}: $\langle S^2 \rangle = 1.001$ with $N_\alpha - N_\beta = 1$.

TABLE 4: The Results of DF Calculations on Truncated Octahedral Pt_{38}^q ($q = 0, \pm 1$) Are Reported[a]

system	ΔE	$N_\alpha - N_\beta$	BW (α/β)	gap (α/β)	ϵ_F	E_{relax}	geometry
O_h	3.876	0	8.19	0.07	−5.431	1.58	1.911, 4.311 (0.504), 3.631
O_h^+	6.760	1	8.20/8.21	0.09/0.08 $a_{1g}-t_{2u}^2$ 0.002	−8.059	-	1.914, 4.311 (0.504), 3.629
O_h^-(neu)	4.148	1	8.22/8.19	0.06 t_{1u}^1/0.06	−2.982	-	see fcc
O_h^-	4.202	7	8.24/8.14	0.02 t_{1g}^1/0.12	−2.998	-	1.908, 4.298 (0.501), 3.681
fcc							1.961, 4.386 (0.500), 3.397

[a] Notations are the same as those in Tables 1 and 2: in particular, the ΔE column reports the binding energy per atom BE/*N* in the case of the lowest energy neutral minimum, and the electron affinity and ionization potential for the lowest energy ionic structures. O_h^-(neu) stands for the result of a calculation on the Pt_{38}^- anion taken at the geometry of neutral O_h Pt_{38}. fcc is the "ideal" geometry corresponding to a section of the fcc crystal. Energy-related quantities are in eV, distances in angstroms.

TABLE 5: The results of DF Calculations On Cuboctahedral (O_h), Truncated Decahedral (D_{5h}), and Icosahedral (I_h) Pt_{55}^q ($q = 0, \pm 1$) Are Reported[a]

system	ΔE	$N_\alpha - N_\beta$	BW (α/β)	gap (α/β)	ϵ_F	E_{relax}	geometry
O_h	0.471	10	8.65/8.65	0.17/0.06	−5.379	1.703	2.734, 4.168, 4.792 (1.033), 5.420
D_{5h}	0.240	8	8.81/8.74	0.04 e^1_u/0.11	−5.364	2.183	2.72−2.79, 4.04, 4.71−4.86, 5.37−5.62
I_h	3.994	12	9.13/9.32	0.28/0.04	−5.511	3.807	2.651, 4.686, 5.233
O_h^+	0.364	11	8.61/8.63	0.20/0.04	−7.705		2.733, 4.201, 4.785 (1.032), 5.423
D_{5h}^+	0.010	7	8.78/8.76	0.05/0.09	−7.665		2.72−2.79, 4.04, 4.70−4.85, 5.37−5.61
I_h^+	6.545	13	9.13/9.31	0.29/0.03	−7.849		2.650, 4.686, 5.233
O_h^-	0.137	9	8.63/8.69	0.18/0.08 $e_u^{0.6}t_{2u}^{0.4}$	−3.082		2.735, 4.167, 4.792 (1.033), 5.421
D_{5h}^-	0.130	9	8.78/8.74	0.04/0.11	−3.081		2.72−2.80, 4.04, 4.72−4.86, 5.37−5.61
I_h^-	4.216	11	9.14/9.31	0.20/0.08 $t_{2g}^{2.2}g_g^{2.1}g_u^{0.7}$	−3.216		2.651, 4.686, 5.234

[a] Notations are the same as those In Tables 1 and 2: in particular, the ΔE column reports the binding energy per atom BE/N in the case of the lowest energy minimum (I_h for Pt_{55}), the electron affinity and ionization potential for the lowest energy Ionic structures (I_h^- and I_h^+, respectively, for Pt_{55}), and the excitation energy with respect to the lowest energy configuration of each charge state for all other configurations. Energy-related quantities are in eV, distances in angstroms.

We have checked also for Pt_{38} that the electronic configuration stays the same after the charging process, apart of course from the orbital directly involved. An exception is Pt_{38}^-. In this case, in fact, the electronic configuration of the anion changes in passing from the geometry optimized for the neutral molecule, $t_{1u}^1t_{1g}^0t_{2u}^3$, $N_\alpha - N_\beta = 1$, to that optimized for the anion itself, $t_{1u}^3t_{1g}^1t_{2u}^0$, $N_\alpha - N_\beta = 7$. This happens because the involved orbitals and corresponding configurations are all very close to the Fermi level, and a tiny structural rearrangement is sufficient to exchange their order: see Table 4. Apart from this, however, one finds that the charging process does not influence much the electronic and structural properties of O_h Pt_{38}, from a quantitative point of view even less than for Pt_{13}, as expected.

A very interesting result is the structural one. Pt_{38}, in fact, as a truncated octahedron should be a nearly optimal example of crystalline geometry, as the ratio between (100) and (111) faces is much more favorable than in the case of the cuboctahedral arrangement.[2,3,7] This is the reason Pt_{38} has been included in our analysis, even though we cannot compare it with other configurations of different symmetry containing the same number of atoms. One has three nonequivalent atoms for O_h Pt_{38}. In the first shell, one finds six atoms in an octahedral arrangement; in the second shell, one finds 24 atoms lying at the vertexes of the six (100) faces and eight atoms lying at the center of (111) faces (see Figure 1 for a schematic picture of the cluster). Correspondingly, one has four degrees of freedom: the distances of the three nonequivalent atoms from the center of the cluster, and the ratio of the minor over the major Cartesian components of the 24 (100) atoms (this ratio should be 0.5 for an idealized structure). From Table 2, one sees that this ratio has a value very close to the ideal one: this confirms that the (100) faces are only slightly larger than their optimal size.[7] However, the three nonequivalent atoms exhibit a very different (inhomogeneous) radial relaxation: the atoms in the first shell or on the (100) faces relax inward by 1.8−2.7%, whereas the atoms on the (111) faces relax outward by 6.8−8.4%. This peculiar structural rearrangement resembles that found for O_h Pt_{55} in ref 14 (and confirmed by the present calculations, see below), and seems to be a general feature of platinum nanoclusters, a feature not predicted by more simplified methods such as atom−atom potentials,[7] in which all the surface atoms tend to relax inward, the more the less bound they are. Such a behavior is probably connected with the tendency of Pt surfaces to peculiar reconstructions.[41−44]

Pt_{55}. The results of DF calculations on I_h, D_{5h}, and O_h Pt_{55}^q clusters ($q = 0, \pm 1$) using basis set B are reported in Table 5. The structures of these clusters can be obtained from those of the corresponding Pt_{13} clusters depicted in Figure 1 by adding another shell of atoms around the Pt_{13} "core". Their appearance is thus similar to the structures shown in Figure 1, with the only difference that all the edges contain three atoms instead of two, and there is a further atom at the center of the (100) faces. From an analysis of Table 5, several points are worth mentioning.

First, the order of the structures has changed with respect to Pt_{13} and is now $I_h < D_{5h} < O_h$. The energy differences are much smaller than for Pt_{13}. Furthermore, the lowest energy configuration is now the icosahedral one, in contrast with the expectations of more simplified approaches.[2,3,7] It is known in fact that icosahedral clusters have more favorable surface energies with respect to crystalline structures, but also larger strain for the interior atoms, due to the mismatch between intra- and intershell distances imposed by symmetry constraints. From general bonding considerations,[2,3,7] one thus expects icosahedral configurations to become less and less favored with increasing size. The fact that we found an opposite behavior implies that in our first-principles approach Pt_{13} presents peculiar characteristics of a finite system (e.g., occupation of unfavoured one-electron orbitals due to symmetry reasons) that are difficult to insert in a smooth behavior of the structural properties as functions of the cluster size. In contrast, Pt_{55} seems to conform reasonably well to atom−atom predictions,[7] and to be located about the crossover among 5-fold and crystalline structures (see the small values of the energy differences). The final DF/BPW91 predic-

TABLE 6: Number of Formal Nearest-Neighbor Bonds *B* and Extrapolated Values (in eV) of BE/*N* for the Various Structures Considered in the Present Work

system	B	extrapolated BE/N
I_h Pt_{13}	42	5.9
D_{5h} Pt_{13}	37	6.8
O_h Pt_{13}	36	6.9
O_h Pt_{38}	144	6.1
I_h Pt_{55}	234	5.6
D_{5h} Pt_{55}	219	6.0
O_h Pt_{55}	216	6.1

tion is thus that icosahedral arrangements are possible candidates (among the highly symmetrical ones) as the lowest energy structures for bare platinum nanoclusters with a number of atoms less than 100. This conclusion is attenuated by the fact that our comparison is taken at sizes which are optimal for the icosahedral structures, but not for the fcc or decahedral arrangements, which presents too large (100) faces at $N = 55$.[5] Better D_{5h} or O_h structures, with smaller (100) faces, can be obtained at other sizes through the Wulff construction,[2,3,7] which gives, for example, Pt_{38} for O_h or a particularly good D_{5h} candidate at $N = 75$.

Apart from the order of the structures, the other descriptors do not present surprises. The BW follows the same order as in Pt_{13}, i.e., $O_h < D_{5h} < I_h$, the gap values correspondently decrease, and charging the clusters does not produce qualitative modifications: we have checked also for Pt_{55} that the electronic configurations do not change with the charge state of the clusters (the only exception is I_h Pt_{55}, for which one finds a switch in the one-electron levels analogous to that for Pt_{38}^-).

The BE, electron affinities EA, and ionization potentials IP show the expected trend with respect to Pt_{13}.

The BE may be extrapolated to the bulk limit using the average coordination number ACN as in ref 14. One can calculate the ACN for the various clusters by counting the number of formal bonds, and then extrapolating to ACN = 12. The results of this extrapolation are given in Table 6. It can be noted that (a) despite the fact that BE(D_{5h} Pt_{13}) > BE(O_h Pt_{13}), the extrapolated value for the O_h structure is larger than that for the D_{5h} structure; (b) the extrapolated values for O_h Pt_{38} and O_h Pt_{55} coincide, despite the fact that Pt_{38} is a smaller cluster: this confirms that Pt_{55} is not a particularly stable fcc cluster.

It is useful to analyze the IP and EA values in terms of the spherical droplet model (SDM).[45] In this model, the intrinsic work function W_∞ of the metal is corrected for a cluster by the work to be done against the electric field of the charge remaining on the cluster (assumed to be at the surface of the cluster assimilated to a sphere of radius R), so that the formulas for IP(R) and EA(R) read as

$$\mathrm{IP}(R) = W_\infty + (\alpha + n - 1)\frac{e^2}{R}$$

$$\mathrm{EA}(R) = W_\infty - (\beta + n - 1)\frac{e^2}{R}$$

with W_∞ the intrinsic work function, n the ±charge, and α and β undefined parameters. The constraint $\alpha + \beta = 1$ is generally accepted, whereas there is no agreement on the ideal values for α and β, even though the ratio α/β is expected be around 3−4. We took the effective cluster radii as in ref 8 by averaging over all radial distances of the outermost shell nuclei and by adding half the nearest-neighbor bulk distance. The results derived from Table 2, 4, and 5 for the lowest energy state of each cluster size are presented in Figure 2. From this figure, it is apparent that the SDM fits the results reasonably well. The extrapolated value of the work function: $W_\infty \sim 6$. eV falls within the scattered range of experimental values.[46−51] The fitted value of the α/β ratio is about 3, as expected, and the overall appearance of Figure 2 is typical of this kind of plots.[45]

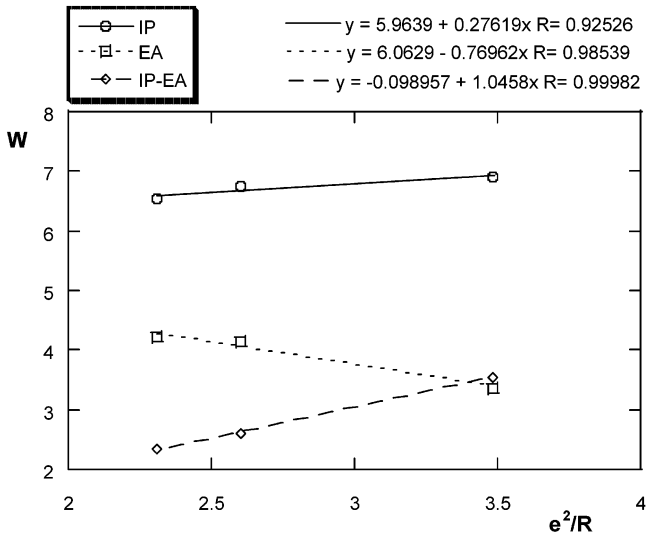

Figure 2. Ionization potential IP, electron affinity EA, and their difference (IP − EA) as functions of the inverse of the effective cluster radius R as defined in the text. In the equations, the results of a linear interpolation are shown, with y = fitted quantity (IP, EA, or IP − EA) in eV; $x = e^2/R$ in eV; and R = regression coefficient.

The structural results are again very interesting. For I_h Pt_{55} one has three nonequivalent atoms apart from the central one: 12 in the first shell, 12 at the vertexes, and 30 at the edges of the surface, whose distances from the central atoms are the degrees of freedom of the structure and are given in Table 5. For O_h Pt_{55}, one has four nonequivalent atoms apart from the central one: 12 in the first shell, 12 on the vertexes, 24 on the edges between (111) and (100) faces, and six at the center of the (100) faces of the surface. The degrees of freedom are the corresponding distances from the central atom, plus the ratio between the height of the (100) plane for the 24 edge atoms and the corresponding vertex atoms (the ideal value of this ratio is 1), and are given in Table 5. For D_{5h} Pt_{55}, one has eight nonequivalent atoms apart from the central one. In the first shell, we find two types of vertex atoms (10 + 2); in the second shell, two types of atoms at the vertexes (10 + 2), three types of atoms on the edges between (111) and (111), (111) and (100), and (100) and (100) faces, respectively, and one type of atom at the center of (100) faces of the surface. For the sake of simplicity, only the range of the distances from the central atom for first-shell atoms, and second-shell vertexes, edges, and faces is given in Table 5.

Two main points are worth noting,

(a) The geometries of the charged clusters are extremely similar to those of the neutral ones, with differences still smaller with respect to Pt_{38} and Pt_{13}, as expected.

(b) An *expansion* of the atoms at the center of (100) faces is found for O_h and D_{5h} Pt_{55}.

As for the latter point, to be specific for O_h Pt_{55}, the atoms in the first shell, the vertexes, and the edges of the surface shrink their distances from the center by 1.4%, 2.3%, and 0.3%, respectively, whereas the (100) atoms *expand* by 6.2%. Analogously, for D_{5h} Pt_{55} the angles *ABA* where B is a (100) atom and A is an atom at a vertex, or at an edge between (111) and (100) faces, or at an edge between two (100) faces, are 171.5°,

174.9°, and 169.5°, respectively. This kind of surface reconstruction is probably beneficial to release surface stress.[41−44] A similar but much smaller effect can be evinced for Pd_{55} from an inspection of Table 6 in ref 9.

We stress that the structural relaxation is strongly inhomogeneous,[6] with both a radial and a tangential pronounced character. It can be noted in particular the compression[6] of the inner shell in I_h Pt_{55} (from 2.686 to 2.651 Å), to be contrasted with the expansion in O_h Pt_{55} (from 2.725 to 2.734 Å), which is in agreement with the results of refs 6, 9, 52, and 53, using atom−atom or tight-binding approaches. This finding is in keeping with the well-known fact that the inner core of the crystalline structures progressively approach the bulk, whereas icosahedral structures remain something like a "giant molecule" at any size.[6,53] For D_{5h} Pt_{55}, one finds an intermediate situation: compression for the elongated v−c bonds, and expansion for the v′−c bonds, where v are the vertexes on the C_5 axis, v′ are the other vertexes, and c is the central atom.

4. Conclusions

We can summarize the conclusions of the present investigation in the following main points:

(a) Platinum clusters in this size range: Pt_n, $n = 13-55$, start developing metallic characteristics: we find a vanishing gap at the Fermi level, which produces in several cases quasi-degeneracies among different electronic configurations (see, for example, I_h Pt_{13} or O_h Pt_{38}^-). It is worth remarking that quasi-degeneracy between one-electron levels does not imply per se quasi-degeneracy between the corresponding electronic configurations, unless Coulomb interactions are effectively screened.

(b) The introduction of a ±charge produces small effects on Pt_{13} and even smaller on Pt_{38} and Pt_{55}; the optimized geometries are slightly affected, the order of the structures stays the same and the electronic configurations only change in the orbitals directly involved in the charging process, with the only exception of the quasi-degeneracy cases mentioned in point a.

(c) The energy order of the optimized symmetrical structure is $D_{5h} < O_h < I_h$ for Pt_{13} and $I_h < D_{5h} < O_h$ for Pt_{55}, even though the energy differences are smaller for Pt_{55} than for Pt_{13}. The anomalous behavior of Pt_{13} is interpreted as due to the small size of the molecule, while Pt_{55} seems to be intermediate between finite molecules and fully metallic systems.[54] In any case, the icosahedral structures seem to be possible competitors at these intermediate sizes, in agreement with the results of semiempirical potentials.[7] The presence of several structural isomers close in energy (see D_{4h}/D_{4h}' Pt_{13} above) may confer peculiar mechanical properties to these metallic clusters.

(d) For Pt_{13}, a D_{4h} configuration originating from the O_h one by symmetry breaking is predicted to be the lowest energy one. For Pt_{38} and Pt_{55}, a peculiar structural rearrangement is found, corresponding to an expansion (reconstruction) of the atoms lying on (111) or (100) faces. For Pt_{13} and Pt_{55}, the (100) faces tend to shrink whenever allowed by the symmetry constraints, whereas they seem to be at their optimal size for Pt_{38}.

(e) The spin is effectively quenched, especially for the most stable configurations, in agreement with the fact that platinum is a nonmagnetic metal.

(f) The binding energy per atom extrapolates reasonably well to the bulk value, and so do the ionization potential and electron affinity.

(g) A very accurate computational procedure is needed to keep numerical accuracy under control.

Acknowledgment. We gratefully acknowledge the Italian INSTM (Istituto Nazionale per la Scienza e Tecnologia dei Materiali) for a grant making available the resources of CINECA supercomputing center (Bologna, Italy) and Andrea Biagi (IPCF, Pisa, Italy) for technical assistance. A portion of the research described in this manuscript was performed at the W. R. Wiley Environmental Molecular Sciences Laboratory, a national scientific user facility sponsored by the U.S. Department of Energy's Office of Biological and Environmental Research and located at Pacific Northwest National Laboratory. Pacific Northwest National Laboratory is operated for the Department of Energy by Battelle.

References and Notes

(1) Klabunde, K. J. *Nanoscale Materials in Chemistry*; Wiley: New York, 2001.
(2) Marks, L. D. *Rep. Prog. Phys.* **1994**, *57*, 603.
(3) Martin, T. P. *Phys. Rep.* **1996**, *273*, 199.
(4) Cleveland, C. L.; Landman, U.; Schaaf, T. G.; Shafigullin, M. N.; Stephens, P. W.; Whetten, R. L. *Phys. Rev. Lett.* **1997**, *79*, 1873.
(5) Doye, J. P. K.; Wales, D. *J. New J. Chem.* **1998**, 733.
(6) Barretau, C.; Desjonquères, M. C.; Spanjaard, D. *Eur. Phys. J. D.* **2000**, *11*, 395.
(7) Baletto, F.; Ferrando, R.; Fortunelli, A.; Montalenti, F.; Mottet, C. *J. Chem. Phys.* **2002**, *116*, 3856.
(8) Haberlen, O. D.; Chung, J. C.;. Stener, M.; Rosch, N. *J. Chem. Phys.* **1997**, *106*, 5189.
(9) Jennison, D. R.; Schultz, P. A.; Sears, M. P. *J. Chem. Phys.* **1997**, *106*, 1856.
(10) Watari, N.; Ohnishi, S. *Phys. Rev. B* **1998**, *58*, 1665.
(11) Yang, S. H.; Drabold, D. A.; Adams, J. B.; Ordejòn, P.; Glassford, K. *J. Phys.: Condens. Matter* **1997**, *9*, L39.
(12) Yang, L.; DePriesto, A. E. *J. Chem. Phys.* **1994**, *100*, 725.
(13) Ahlrichs, R.; Elliot, S. *Phys. Chem. Chem. Phys.* **1999**, *1*, 13.
(14) Aprá, E.; Fortunelli, A. *J. Mol. Struct. (THEOCHEM)* **2000**, *501−502*, 251.
(15) Garzòn, I. L.; Posada-Amarillas, A. *Phys. Rev. B* **1996**, *54*, 11796.
(16) Häkkinen, H.; Moseler, M.; Landman, U. *Phys. Rev. Lett.* **2002**, *89*, 033401.
(17) Yeon-Wook, K.; Hong-Ming, L.; Kelly, T. F. *Acta Metall.* **1989**, *37*, 247.
(18) Martra, G.; Coluccia, S.; Monticelli, O.; Vitulli, G. *Catal. Lett.* **1994**, *29*, 105.
(19) . Contrata, W.; Mitchell M. J.; Mochel, J. M. *Ultramicroscopy* **1993**, *48*, 297.
(20) Rosato, V.; Guillopé M.; Legrand, B. *Philos. Mag. A* **1989**, *59*, 321.
(21) . Goringe, C. M.; Bowler, D. R.; Hernandez, E. *Rep. Prog. Phys.* **1997**, *60*, 1447.
(22) Fortunelli, A.; Velasco, A. M. *Int. J. Quantum Chem.* Submitted for publication.
(23) Harrison, R. J.; Nichols, J. A.; Straatsma, T. P.; Dupuis, M.; Bylaska, E. J.; Fann, G. I.; Windus, T. L.; Aprà, E.; Anchell, J.; Bernholdt, D.; Borowski, P.; Clark, T.; Clerc, D.; Dachsel, H.; de Jong, B.; Deegan, M.; Dyall, K.; Elwood, D.; Fruchtl, H.; Glendening, E.; Gutowski, M.; Hess, A.; Jaffe, J.; Johnson, B.; Ju, J.; Kendall, R.; Kobayashi, R.; Kutteh R.; Lin, Z.; Littlefield, R.; Long, X.; Meng, B.; Nieplocha, J.; Niu, S.; Rosing, M.; Sandrone, G.; Stave, M.; Taylor, H.; Thomas, G.; van Lenthe, J.; Wolinski, K.; Wong, A.; Zhang, Z. *NWChem, A Computational Chemistry Package for Parallel Computers*, version 4.1; Pacific Northwest National Laboratory, Richland, WA 99352-0999, 2002.
(24) Andrae, D.; Haeussermann, U.; Dolg, M.; Stoll, H.; Preuss, H. *Theor. Chim. Acta* **1990**, *77*, 123.
(25) Schaefer, A.; Huber, C.; Ahlrichs, R. *J. Chem. Phys.* **1994**, *100*, 5289.
(26) Becke, A. D. *Phys. Rev. A* **1988**, *38*, 3098.
(27) Perdew, J. P.; Wang, Y. *Phys. Rev. B* **1986**, *33*, 8800. Perdew, J. P.; Chevary, J. A.; Vosko, S. H.; Jackson, K. A.; Pederson, M. R.; Singh D. J.; Fiolhais, C. *Phys. Rev. B* **1992**, *46*, 6671.
(28) Fortunelli, A. *J. Mol. Struct. (THEOCHEM)* **1999**, *487*, 251.
(29) Dunlap, B. I.; Connolly J. W. D.; Sabin, J. R. *J. Chem. Phys.* **1979**, *71*, 4993.
(30) Fortunelli, A.; Salvetti, O. *J. Comput. Chem.* **1991**, *12*, 36.
(31) Eichkorn, K.; Treutler, O.; Öhm, H.; Häser M.; Ahlrichs, R. *Chem. Phys. Lett* **1995**, *242*, 652.
(32) Becke, A. D. *J. Chem. Phys.* **1988**, *88*, 2547.
(33) Lebedev, V. I.; Laikov, D. N. *Dokl. Math.* **1999**, *366*, 741. Delley, B. J. *Comput. Chem.* **1996**, *17*, 1152.
(34) Mura, M. E.and Knowles, P. J. *J. Chem. Phys.* **1996**, *104*, 9848. Murray, C. W.; Handy, N. C.; Laming, G. L. *Mol. Phys.* **1993**, *78*, 997.

(35) Aprà, E. Unpublished results. This rescaled grid is available in the 4.1 release of NWChem.
(36) Elsässer, C.; Fähnle, M.; Chan, C. T.; Ho, K. M. *Phys. Rev. B* **1994**, *49*, 13975.
(37) Warren, R. W.; Dunlap, B. I. *Chem. Phys. Lett.* **1996**, *262*, 384.
(38) Wang, S. G.; Schwartz, W. H. E. *J. Chem. Phys.* **1996**, *105*, 4641.
(39) Adamo, C.; Barone V.; Fortunelli, A. *J. Chem. Phys.* **1995**, *98*, 8648.
(40) Kittel, C. *Introduction to Solid State Physics*; Wiley: New York, 1968.
(41) Feibelman, P. J.; Nelson, J. S.; Kellogg, G. L. *Phys. Rev. B* **1994**, *49*, 10548. Feibelman, P. J. *Phys. Rev. B* **1995**, *51*, 17867.
(42) Oppo, S.; Fiorentini, V. *Phys. Rev. Lett.* **1998**, *81*, 4278.
(43) Filippetti, A.; Fiorentini, V. *Surf. Sci.* **1997**, *377*−*379*, 112; *Phys. Rev. B* **1999**, *60*, 14366.
(44) Fiorentini, V.; Methfessel, M.;. Scheffler, M. *Phys. Rev. Lett.* **1993**, *71*, 1051 and **1998**, *81*, 2184.
(45) Wood, D. M. *Phys. Rev. Lett.* **1981**, *46*, 749.
(46) Kiskinova, M.; Pirug, G.; Bonzel, H. P. *Surf. Sci.* **1983**, *133*, 321.
(47) Salmerón, R.; Ferrer, S.; Jazzar, M.; Somorjai, G. A. *Phys. Rev. B* **1983**, *28*, 6758.
(48) Derry, G. N.; Zhang, J.-Z. *Phys. Rev. B* **1989**, *39*, 1940.
(49) Alnot, M.; Ehrhardt, I. J.; Barnard, J. A. *Surf. Sci.* **1989**, *208*, 285.
(50) Cassuto, A.; Mane, M.; Hugenschmidt, M.; Dolle P.; Jupille, J. *Surf. Sci.* **1990**, *237*, 63.
(51) Kaack, M.; Fick, D. *Surf. Sci.* **1995**, *342*, 111.
(52) D'Agostino, G. *Mater. Sci. Forum* **1995**, *195*, 149.
(53) Fortunelli, A.; Velasco, A. M. *J. Mol. Struct. (THEOCHEM)* **2000**, *528*, 1.
(54) Fortunelli, A.; Velasco, A. M. *J. Mol. Struct. (THEOCHEM)* **1999**, *487*, 251.

Amorphization Mechanism of Icosahedral Metal Nanoclusters

E. Aprà,[1] F. Baletto,[2] R. Ferrando,[3] and A. Fortunelli[4,*]

[1]*William R. Wiley Environmental Molecular Sciences Laboratory, Pacific Northwest National Laboratory, Richland, Washington 99352, USA*

[2]*ICTP, Strada Costiera 11, 34014, Trieste, Italy*

[3]*INFM and IMEM-CNR, Dipartimento di Fisica dell'Università di Genova, via Dodecaneso 33, 16146 Genova, Italy*

[4]*Molecular Modeling Laboratory, Istituto per i Processi Chimico-Fisici (IPCF) del CNR, Via G. Moruzzi 1, 56124, Pisa, Italy*

(Received 4 March 2004; published 4 August 2004)

The amorphization mechanism of icosahedral Pt nanoclusters is investigated by a combination of molecular dynamics simulations and density functional calculations. A general mechanism for amorphization, involving rosettelike structural transformations at fivefold vertices, is proposed. In the rosette, a fivefold vertex is transformed into a hexagonal ring. We show that, for icosahedral Pt nanoclusters, this transformation is associated with an energy gain, so that their most favorable structures have a low symmetry even at icosahedral magic numbers, and that the same mechanism underlies the formation of amorphous structures in gold.

DOI: 10.1103/PhysRevLett.93.065502 PACS numbers: 61.46.+w

Clusters of transition and noble metals are interesting for their physical and chemical properties, and for technological applications [1]. In this context, platinum clusters are of great importance because of their role in many catalytic processes [2]. The starting point for understanding cluster properties is the determination of their structure, which is usually a nontrivial task, since clusters can assume a wide variety of structures. The simplest ones are pieces of the bulk crystal lattice, which is fcc for noble metals and Pt. Clusters can present also noncrystalline structures, such as icosahedra (Ih) and decahedra (Dh) [3], having fivefold symmetries. Interatomic distances in Ih and Dh differ with respect to the ideal bulk value, thus giving a volume contribution to the energy that is absent in fcc clusters. This volume contribution may be compensated by a lower surface energy: especially Ih structures, which present a close-packed surface and a low surface/volume ratio, can be more favorable than fcc structures at small sizes, where surface contributions to the energy are dominant. All these structures can be of special energetic stability at the so-called structural *magic numbers,* which are the numbers of atoms N needed to complete a perfect cluster of a given symmetry. For example, at $N = 13$ and 55 perfect Ih, truncated Dh, and fcc cuboctahedra (Oh) are obtained [3]. Several different calculations indicate that nickel, copper, and silver clusters adopt preferentially the Ih structure at $N = 55$ [4–6]. On the contrary, calculations on gold clusters show a preference for low-symmetry structures [7]. The latter are often called amorphous because their radial distribution functions resemble those of liquid clusters. These findings have been rationalized in terms of the bond order–bond length correlation in metallic systems [8,9]. In Au, bonds have a much stronger tendency to contract with decreasing coordination than in Ag, Cu, or Ni, and this favors the disordering of the cluster surface. From this point of view, Pt is intermediate between Au and Ag, and its behavior with respect to amorphization is still an open problem (see references to experimental controversy in [10]).

In this Letter we show that icosahedral Pt clusters have indeed a tendency towards amorphization, namely, to present low-symmetry structures at magic sizes. We propose a general amorphization mechanism of Ih clusters, which involves the formation of *rosettelike* structural excitations at the fivefold vertices. This mechanism also underlies the formation of amorphous clusters in Au. In the first step of our procedure we describe Pt by a many-body atom-atom potential (developed by Rosato, Guillopé, and Legrand (RGL) [11]; form and parameters are given in Ref. [6]) and perform a global minimum search by quenching $\sim 10^6$ snapshots from high-temperature molecular dynamics simulations. The results are checked by a genetic algorithm global optimization. In this way we are able to collect a huge catalog of minima, comprising hopefully the global minimum and all other low-lying minima. In the second part of the procedure, we locally optimize the most significant structures by density functional theory (DFT) calculations. These are carried out with the DFT module of the NWCHEM package [12], and use the Becke functional [13] for exchange and the Perdew-Wang functional [14] for correlation, a $(7s5p5d)/[6s3p2d]$ Gaussian-type-orbital basis set [15], and an effective core potential [16] incorporating spin-orbit averaged relativistic effects for the platinum atom. More details can be found in [10,17].

The global optimization results for Pt_{55} using the RGL potential indicate that the lowest minimum is an icosahedron (Ih_{55}; see Fig. 1). Oh and truncated Dh structures lie at higher energy, in agreement with DFT calculations [10]. Among the other low-lying minima, we single out a very peculiar structure, which is referred to as the *rosette*

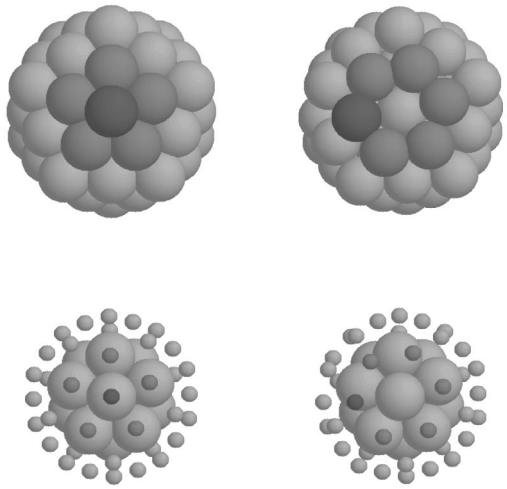

FIG. 1. Ih_{55} (left column) and rosette (right column) structures, as obtained within the RGL description. In the bottom row, the atoms of the external shell are represented with small spheres to show the 13 atoms forming the cluster core. The rosette is obtained from the Ih_{55} by displacing a vertex atom (dark gray) to form a hexagonal ring together with its five neighbors of the Ih_{55} surface.

in the following. The rosette is an elementary transformation of the Ih_{55} taking place at a single fivefold vertex. As shown in Fig. 1, a vertex atom is pushed out and inserted between its five neighbors on the surface, to form a sixfold ring centered around the original position of the vertex. This transformation breaks the Ih symmetry. However, the shell structure of the Ih is preserved in the rosette, which still has an inner core of 13 atoms—a somewhat distorted Ih_{13}—surrounded by an outer shell of 42 atoms, exactly as in the Ih_{55}. According to the RGL potential, the rosette is higher in energy than the Ih_{55} by $\Delta E = E^{\mathrm{ros}} - E^{\mathrm{Ih}} \sim 0.5$ eV, as shown in Table I.

What factors favor the rosette? We can try to give an answer by comparing the atomic energies E_i in the rosette and the Ih_{55}. In the rosette, the atoms of the outer shell have higher energies than in the Ih_{55}, whereas the opposite holds for the atoms of the inner core. Putting $E_{\mathrm{shell}}, E_{\mathrm{core}} = \sum_i E_i$, with i running on the 42 shell and the 13 core atoms, respectively, we find that $\Delta E_{\mathrm{shell}} = E^{\mathrm{ros}}_{\mathrm{shell}} - E^{\mathrm{Ih}}_{\mathrm{shell}} > 0$, whereas $\Delta E_{\mathrm{core}} = E^{\mathrm{ros}}_{\mathrm{core}} - E^{\mathrm{Ih}}_{\mathrm{core}} < 0$. This behavior is due to the peculiar interplay between the bond order–bond length correlation in metallic systems and the geometry of the Ih structure. In fact, highly coordinated atoms prefer larger first-neighbor distances than atoms with low coordination. Therefore, inner atoms would prefer to have neighbors at the ideal distance of the bulk fcc crystal, while surface atoms would better have contracted bonds. This is contrary of what happens in an Ih structure, where inner bonds are more compressed than surface bonds. In the rosette structure the surface is rearranged in such a way that there are fewer bonds than in the Ih_{55}, but these bonds are shorter on average. Moreover, the inner core is expanded, and its atoms are less compressed than in the Ih_{55}. The final result is that inner atoms lower their energy at the expense of surface atoms. Depending on the metal, the gain may either compensate the loss or not. As shown in Table I, for Ag, Pd, and Pt, the gain does not compensate the loss within the RGL description, but for Au the opposite happens, and the rosette is lower in energy than the Ih_{55}. The energy gain of core atoms can be rationalized using the concept of interaction *stickiness* [18]. A sticky potential is characterized by a high energetic penalty for changing the interatomic distances from their ideal bulk value. In a sticky metal, the highly coordinated core atoms gain more energy from the core expansion of the transformation $Ih_{55} \rightarrow$ rosette. Moreover, the rearrangement of the surface is less disadvantageous for systems with stronger bond contraction at decreasing coordination [8] because they present a weaker dependence of the energy on the number of bonds. This completely agrees with the normalized energy changes of shell and core atoms in Table I, since noble and quasinoble metals can be ordered with increasing stickiness and tendency to bond contraction as follows [6]: Ni, Cu, Ag, Pd, Pt, Au (with Pd and Pt essentially at the same level of stickiness). For Ni and Cu we have not succeeded in stabilizing the rosette, which probably does not even correspond to a local minimum. We have also investigated the behavior of Ih_{55} and rosette with temperature, by performing freezing and melting molecular dynamics simulations, and calculating the occupation probability of the two minima within the harmonic superposition approximation [19]. It turns out that the entropic effects favor the rosette against the Ih_{55} at temperatures above 600 K.

TABLE I. Results from the RGL potential modeling for Ih_{55} and rosette structures. Absolute energy differences (in eV) between rosette and Ih_{55} $\Delta E = E^{\mathrm{ros}} - E^{\mathrm{Ih}}$, and energy difference among external atoms $\Delta E_{\mathrm{shell}} = E^{\mathrm{ros}}_{\mathrm{shell}} - E^{\mathrm{Ih}}_{\mathrm{shell}}$ and among core atoms $\Delta E_{\mathrm{core}} = E^{\mathrm{ros}}_{\mathrm{core}} - E^{\mathrm{Ih}}_{\mathrm{core}}$. Normalized energy changes (i.e., divided by the value for the Ih_{55} structure) are also reported.

Metal	ΔE	$\Delta E/\lvert E^{\mathrm{Ih}}\rvert$	$\Delta E_{\mathrm{shell}}$	$\Delta E_{\mathrm{shell}}/\lvert E^{\mathrm{Ih}}_{\mathrm{shell}}\rvert$	ΔE_{core}	$\Delta E_{\mathrm{core}}/\lvert E^{\mathrm{Ih}}_{\mathrm{core}}\rvert$
Ag	0.584	4.10×10^{-3}	0.997	9.5×10^{-3}	−0.413	-1.11×10^{-2}
Pd	0.449	2.34×10^{-3}	1.139	8.0×10^{-3}	−0.690	-1.42×10^{-2}
Pt	0.483	1.66×10^{-3}	1.550	7.1×10^{-3}	−1.067	-1.46×10^{-2}
Au	−0.309	-1.59×10^{-3}	0.823	5.4×10^{-3}	−1.132	-2.38×10^{-2}

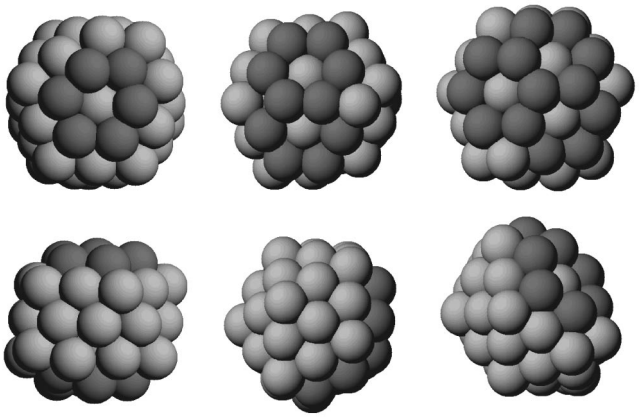

FIG. 2. From left to right, front (top row) and side (bottom row) views of the double opposite rosette (dor), of the double paired rosette (dpr), and of the triple rosette (tr), as obtained within the RGL description. Atoms belonging to the hexagonal rosette rings are depicted in darker gray.

An interesting question is whether the introduction of further rosette motifs on the surface can be energetically favorable. We thus investigate three multiple-rosette structures within the RGL description (see Fig. 2): the double opposite rosette (dor) with two rosettes at opposite fivefold vertices, the double paired rosette (dpr) with two rosettes at nearby fivefold vertices, and the triple rosette (tr) with three rosettes at nearby vertices. The energy differences of these structures with respect to the single rosette are given in Table II. For Au, the dpr structure is better than the single-rosette, and the tr structure is even lower in energy. Our global optimization confirms that these structures are the lowest-energy amorphous structures for Au clusters, in agreement with the findings in [5,7], thus showing that the amorphization mechanism of Au clusters occurs through *the generation of multiple rosettes*. In the case of Ag and Pd, multiple rosettes are always higher in energy than the single rosette. Platinum is in between, since the dpr structure is slightly better than the single rosette, while the tr structure is slightly worse. In all metals, rosettes at opposite vertices are always unfavorable (in Ag they are not even a stable local minimum). In summary, multiple rosettes are clearly favorable in Au, and unfavorable in Ag and Pd. The case of Pt is less clear.

TABLE II. Results from the RGL potential modeling for multiple-rosette structures. E^{ros}, E^{dor}, E^{dpr}, and E^{tr} are the energies of single rosette, double opposite rosette, double paired rosette, and triple rosette, respectively.

Metal	$E^{\mathrm{dor}} - E^{\mathrm{ros}}$	$E^{\mathrm{dpr}} - E^{\mathrm{ros}}$	$E^{\mathrm{tr}} - E^{\mathrm{ros}}$
Ag	⋯	0.206	0.453
Pd	0.910	0.017	0.155
Pt	1.743	−0.059	0.065
Au	0.640	−0.226	−0.329

The conclusion, within the RGL description, is that—apart from Au—the best candidate for amorphization is Pt, because it has the smallest relative energy difference between rosette and Ih_{55} (see Table I), and because in Pt multiple rosettes are as favorable as the single rosette. At the RGL level, Pt clusters are not amorphous. However, this description is approximate, as it does not take into account some features of bonding, such as its directionality, which play an important role in Pt [20]. Therefore, more accurate modeling is needed, and in the following we analyze both Ih_{55} and rosette clusters by DFT calculations.

To start, we optimize locally the symmetrical structures considered in [10]: Ih_{55}, Oh_{55}, and Dh_{55}, but removing any symmetry constraints. At variance with the Pt_{13} case, we do not find any significant symmetry breaking, and the relaxation energy is negligible, less than 0.1 eV, with the energy order ($Ih < Dh < Oh$) still holding. Quite different results are obtained from the local optimization of the RGL single-rosette structure: the energy drops below that of the Ih_{55} by more than 1.6 eV, and the structure undergoes a substantial rearrangement, finally producing the optimized configuration displayed in Fig. 3. The Ih arrangement is thus *metastable* at the DFT level with respect to the rosette deformation of one of its vertices. A possible explanation of the difference with respect to the RGL results follows from a comparison between the optimized RGL and DFT rosette structures of Figs. 1 and 3. It can be clearly seen that the rosette is conserved by the DFT optimization, but also that the atom at the center of the rosette, which lies well

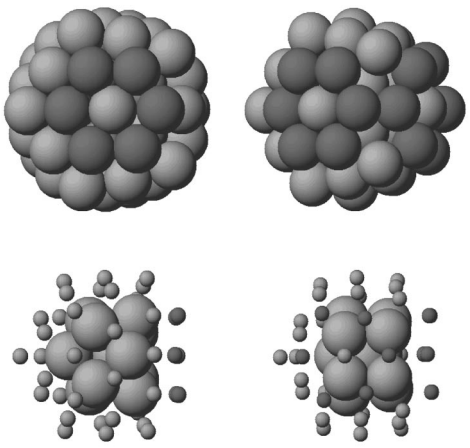

FIG. 3. Front (top row) and side (bottom row) views of the rosette (left) and double rosette (right) structures after DFT relaxation. In the side views, external atoms are represented by small spheres to show the inner part of the cluster. There are 12 and 11 internal atoms in the rosette and double rosette, respectively. Atoms belonging to the hexagonal rosette rings are depicted in darker gray.

inside the cluster in Fig. 1, *moves upward to the surface* in Fig. 3, thus producing what is essentially the typical seven-atom face of a (111) plane of a fcc crystal. The reason why the RGL potential misses this structural rearrangement cannot be due to an incorrect choice of the parameters, as it apparently derives from *anisotropic* or *bond directionality* [20] effects. Platinum, in fact, is a third-row metal, in which the relativistic contraction of the *s*-orbital brings it to substantially overlap with the *d* orbitals, decreasing the localized character of the latter and strongly increasing their contribution to chemical bonding [21]: see, for example, Ref. [20], in which this effect is discussed within the first-principles derivation of tight-binding parameters. This is in agreement with the ease of hex reconstruction formation on extended Au and Pt surfaces (at variance with, say, Pd and Ag surfaces). In passing, we note the quenching of the electron spin of the cluster: from $S = 6$ in the Ih_{55} to $S = 1$ in the ground state of the rosette (quasidegenerate with a $S = 0$ state). The gap in the one-electron energy spectrum is small, $\leq$ 0.1 eV, and the bandwidth is comparable with that of the Oh structure.

Are multiple-rosette structures favorable in Pt at the DFT level? To answer this question, we optimize a properly chosen multiple-rosette configuration, selecting the one that in principle should be the least favorable, namely, the double opposite rosette (similar to the one shown in Fig. 2). After local DFT optimization, the structure of Fig. 3 is obtained. Two points are worth noting. First, the minimized energy of this structure lies *below* the energy of the single rosette by ≈ 0.4 eV. The platinum tendency to form the rosette motif on the surface is so strong at the DFT level that even starting from an unfavorable arrangement of two rosettes, lying on opposite sides, one still decreases the energy with respect to a single rosette. Second, one of the two rosette motifs switches place during the optimization from being symmetrically opposite to the other rosette to moving on to a nearest-neighbor vertex, as the atom at the center of the rosette becomes a vertex of a pseudo-C_5 axis, and leaves a hole in the inner shell immediately below it. These subtle effects are apparently due to long-range interactions between different parts of the cluster. The spin is again effectively quenched (the ground state has $S = 0$), and the gap in the one-electron spectrum is ≈ 0.1 eV. We note that at the DFT level the cluster core, too, suffers a much stronger rearrangement than at the semiempirical level. A substantial rearrangement of the core (but of a different type), allowing the relief of local stress, was found in Ref. [9] for Au clusters.

In conclusion, our calculations show that icosahedral Pt clusters have, indeed, a tendency towards amorphization. The amorphization mechanism, which is effective also in gold clusters and generally in metallic systems with sticky potential and strong bond order–bond length correlation, takes place through the generation of (eventually multiple) rosette motifs at the fivefold vertices. The rosette motif allows an efficient relaxation of the internal atoms, which overcomes a surface energy penalty. In the case of platinum, the driving force favoring the rosette is enhanced by bond directionality effects due to *d-d* interactions.

We acknowledge financial support from the Italian CNR for the project "(Supra-)Self-Assemblies of Transition Metal Nanoclusters" within the framework of the ESF EUROCORES SONS. A. F. acknowledges the Italian INSTM for a grant at the CINECA supercomputing center. A portion of the research described in this manuscript was performed at the W. R. Wiley EMSL, a national scientific user facility sponsored by the U.S. DOE OBER and located at PNNL. PNNL is operated for the DOE by Battelle.

*Corresponding author.
Email address: fortunelli@ipcf.cnr.it

[1] *Progress in Experimental and Theoretical Studies of Clusters*, edited by T. Kondow and F. Mafuné (World Scientific, New York, 2003).
[2] K. J. Klabunde, *Nanoscale Materials in Chemistry* (Wiley, New York, 2001).
[3] T. P. Martin, Phys. Rep. **273**, 199 (1996).
[4] D. R. Jennison, P. A. Schultz, and M. P. Sears, J. Chem. Phys. **106**, 1856 (1997).
[5] K. Michaelian, N. Rendón, and I. L. Garzón, Phys. Rev. B **60**, 2000 (1999).
[6] F. Baletto *et al.*, J. Chem. Phys. **116**, 3856 (2002).
[7] I. L. Garzon *et al.*, Phys. Rev. Lett. **81**, 1600 (1998).
[8] J. M. Soler *et al.*, Phys. Rev. B **61**, 5771 (2000).
[9] J. M. Soler, I. L. Garzón, and J. D. Joannopoulos, Solid State Commun. **117**, 621 (2001).
[10] E. Aprà and A. Fortunelli, J. Phys. Chem. A **107**, 2934 (2003).
[11] V. Rosato, M. Guillopé, and B. Legrand, Philos. Mag. A **59**, 321 (1989).
[12] R. A. Kendall *et al.*, Comput. Phys. Commun. **128**, 260 (2000).
[13] A. D. Becke, Phys. Rev. A **38**, 3098 (1988).
[14] J. P. Perdew and Y. Wang, Phys. Rev. B **33**, 8800 (1986); J. P. Perdew *et al.*, Phys. Rev. B **46**, 6671 (1992).
[15] A. Schaefer, C. Huber, and R. Ahlrichs, J. Chem. Phys. **100**, 5829 (1994).
[16] D. Andrae *et al.*, Theor. Chim. Acta **77**, 123 (1990).
[17] E. Aprà and A. Fortunelli, J. Mol. Struct., Theochem **501/502**, 251 (2000).
[18] J. P. K. Doye, D. J. Wales, and R. S. Berry, J. Chem. Phys. **103**, 4234 (1995).
[19] J. P. K. Doye and F. Calvo, Phys. Rev. Lett. **86**, 3570 (2001).
[20] A. Fortunelli and A. M. Velasco, Int. J. Quantum Chem. **99**, 654 (2004).
[21] S. Taylor *et al.*, J. Chem. Phys. **89**, 5517 (1988).

Magic Polyicosahedral Core-Shell Clusters

RossiPRL2004

G. Rossi,[1] A. Rapallo,[2] C. Mottet,[3] A. Fortunelli,[4] F. Baletto,[5] and R. Ferrando[1]

[1]*INFM and IMEM/CNR, Dipartimento di Fisica, Via Dodecaneso 33, Genova, I16146, Italy*
[2]*ISMAC/CNR, Via Bassini 15, Milano, I20133, Italy*
[3]*CRMCN/CNRS, Campus de Luminy, Marseille, F13288, France*
[4]*IPCF/CNR, Via Alfieri 1, Ghezzano, I56010, Italy*
[5]*ICTP, Strada Costiera 11, Trieste, I34014, Italy*

(Received 15 April 2004; published 2 September 2004)

A new family of magic cluster structures is found by genetic global optimization, whose results are confirmed by density functional calculations. These clusters are Ag-Ni and Ag-Cu nanoparticles with an inner Ni or Cu core and an Ag external shell, as experimentally observed for Ag-Ni, and present a polyicosahedral character. The interplay of the core-shell chemical ordering with the polyicosahedral structural arrangement gives high-symmetry clusters of remarkable structural, thermodynamic, and electronic stability, which can have high melting points (they melt higher than pure clusters of the same size), large energy gaps, and (in the case of Ag-Ni) nonzero magnetic moments.

DOI: 10.1103/PhysRevLett.93.105503 PACS numbers: 61.46.+w, 71.15.Mb

Bimetallic nanoclusters have received considerable attention recently [1] for their peculiar properties, which can be very different from those of pure clusters of their constituents [2,3], and for a variety of applications, ranging from catalysis to optics [4,5]. What renders bimetallic nanoclusters very attractive is that their properties can vary dramatically not only with size, as happens in pure nanoclusters, but also with chemical composition. Controlling their structure and chemical ordering can be the starting point to prepare the building blocks for specifically tailored cluster-assembled materials [6]. For this application, a key step is to single out magic cluster structures, namely, those structures presenting special structural, as well as electronic and thermodynamic, stability. In recent experiments [7], it has been shown that silver-nickel nanoclusters adopt a core-shell configuration, where a well-defined outer silver shell embeds a nickel core. The analysis of low-energy ion scattering data has shown that the silver shell is often of monatomic thickness, but a more precise determination of their structure is not available yet.

Here we show theoretically that there is a whole family of new magic Ag-Ni and Ag-Cu nanoclusters, which are characterized by the common structural properties of being perfect core-shell clusters and polyicosahedra (pIh). Perfect core-shell clusters have all Ag atoms on the surface and all Ni or Cu atoms inside, so that the Ag shell is of monatomic thickness. pIh are clusters built by packing elementary Ih of 13 atoms (Ih13), as shown in Fig. 1. Previously [8,9], it has been shown that core-shell and multishell clusters can be kinetically favorable (but often metastable) structures in the growth of bimetallic clusters. Here we demonstrate that there is a new family of core-shell clusters of remarkable stability also from the energetic and thermodynamic point of view. In the following, a pIh of size N, made of N_1 Ag atoms and $N_2 = N - N_1$ Cu or Ni atoms, and comprising m interpenetrating Ih_{13}, are referred to as $(N_1, N_2)pIh^m$. We demonstrate that the interplay between the pIh structural ordering and the core-shell chemical ordering gives a net driving force for building up clusters of remarkable structural stability. Among these core-shell pIh we single out a few high-symmetry clusters presenting special thermodynamic and electronic stability, with high melting points and large highest occupied molecular orbital–lowest unoccupied molecular orbital (HOMO-LUMO) gaps. Some of these structures are also magnetic in their ground state.

Our computational procedure consists of several steps: (i) We model the clusters by realistic many-body atom-atom potentials [10], and search for the global energy minimum by genetic algorithm optimization [11] for some selected sizes and variable composition. (ii) At a given size, we look for the compositions corresponding to the most stable structures. (iii) We locally optimize the most significant structures using density functional theory (DFT) calculations [12] to confirm the trends obtained in (ii) and single out the clusters with high electronic stability. (iv) We check the thermodynamic stability of the magic structures by making molecular-dynamics melting simulations and calculating the temperature-dependent probabilities of the global minima by harmonic thermodynamics [13].

Why can core-shell pIh be magic structures? A driving force for the formation of high-stability clusters is the maximization of the number of nearest-neighbor bonds among the atoms. This favors compact quasispherical structures, such as the Ih_{13} and other Ih. However, interatomic distances in Ih are different from their ideal value in the bulk crystal, and this produces an internal strain. The competition between the maximization of the bond number and the accumulation of strain determines the most favorable structures in pure systems with pair inter-

actions [14], such as Lennard-Jones (LJ) and Morse. LJ clusters of 13 atoms prefer the Ih shape, and, adding further atoms, a series of compact polycosahedral clusters is produced at $N = 19, 23, 26, 29$ [15]. Above $N = 29$, the gain in the bond number does not compensate any more the internal strain so that LJ pIh become less favorable. For noble and transition metal pure clusters the situation is more complicated. The many-body part of the metallic bonding tends to disfavor Ih structures because it induces a significant *bond order–bond length correlation* [16], which means that the optimal bond length *increases with the coordination* of the atoms. This is exactly the opposite of what happens in Ih, where internal bonds are on the average shorter than surface bonds. In the Ih_{13}, internal bonds are 5% shorter than surface bonds. Compact pIh suffer from the same problem, since they have even more compressed internal distances, and a huge internal strain. Thus they are not expected to be of special stability for pure transition metal clusters.

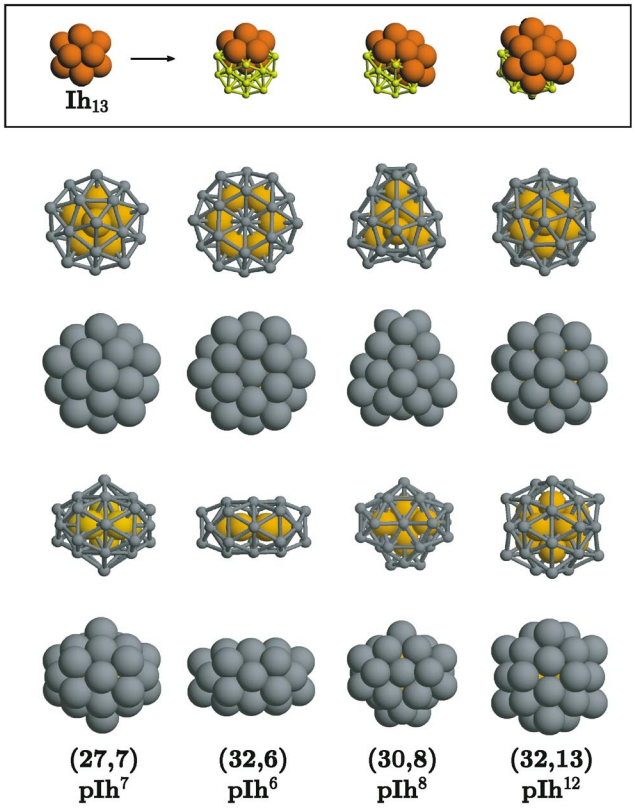

FIG. 1 (color). Magic core-shell pIh clusters. PIh clusters are built by packing elementary Ih_{13} clusters (see also Fig. S1), as shown in the top row, where three different fragments of the pIh^7 structure are given. From left to right, the fragments comprise one, two, and four interpenetrating Ih_{13}. Below, a selection of magic core-shell pIh is given. Each pIh is shown in four views; in two of them the Ag atoms (gray color) are represented by small points to show the arrangement of the core (Ni or Cu, orange color) atoms. The $(27, 7)pIh^7$ has a decahedral Ni or Cu core of 7 atoms, and the 27 Ag atoms are placed in an anti-Mackay overlayer. The $(32, 6)pIh^6$ is a *pancake* structure, with the six inner atoms placed on a regular hexagonal ring. The $(30, 8)pIh^8$ is the perfect core-shell structure including the maximum number of core atoms at size 38. The $(32, 13)pIh^{12}$ is the complete anti-Mackay icosahedron of size 45, including a perfect Ih_{13} core. It is made of 12 interpenetrating Ih_{13} sharing the central atom as a common vertex.

However, the situation can change drastically in binary systems. In fact, substituting the internal atoms in a pure pIh cluster with *smaller atoms,* the optimal bond lengths of both internal and surface atoms may be recovered, and the strain strongly decreased. This leads naturally to the idea of *core-shell pIh clusters,* which both maximize the bond number and minimize the strain. Other important factors favoring such clusters are that the large atoms must have a strong tendency toward segregating at the surface, and possibly the two elements should have a weak tendency toward mixing or alloying in the bulk phase. All these features are present in Ag-Ni and Ag-Cu. Ni and Cu atoms are 16% and 13% smaller than Ag atoms, Ag has a strong tendency to surface segregation with respect to both Ni and Cu [17], and Ag-Ni and Ag-Cu bulk systems present very extended miscibility gaps [18]. Our results demonstrate that the Ag-Ni and the Ag-Cu systems are really suitable for building up magic core-shell pIh. We shall show that, given the size, the most stable structures are obtained at the compositions corresponding to perfect core-shell pIh.

To compare the relative stability of clusters of different sizes and compositions, we monitor the quantities Δ and Δ_2 [19] adapted to binary clusters. Δ is the excess energy with respect to N bulk atoms, divided by $N^{2/3}$:

$$\Delta = \frac{E_{\mathrm{GM}}^{N,N_1} - N_1\varepsilon_1^{\mathrm{coh}} - N_2\varepsilon_2^{\mathrm{coh}}}{N^{2/3}}, \tag{1}$$

where N_1 and $\varepsilon_1^{\mathrm{coh}}$ are the number and the bulk cohesive energy of Ag atoms, whereas $N_2 = N - N_1$ and $\varepsilon_2^{\mathrm{coh}}$ are the same quantities of either Ni or Cu, and E_{GM}^{N,N_1} is the global-minimum energy at the given size and composition. Stable structures are identified by low Δ values. Δ_2 is the second difference in the energy:

$$\Delta_2^{N,N_1} = E_{\mathrm{GM}}^{N,N_1+1} + E_{\mathrm{GM}}^{N,N_1-1} - 2E_{\mathrm{GM}}^{N,N_1}. \tag{2}$$

Maxima of Δ_2 indicate structures of special relative stability compared to those of the same size and nearby compositions.

We start our analysis at $N = 38$, and look for the global energy minima at varying compositions. Size 38 is magic for the regular truncated octahedron, a high-symmetry piece of fcc bulk lattice, and thus is expected to correspond to pure clusters of good stability. Plotting Δ and Δ_2 vs N_1, for both Ag-Ni and Ag-Cu, the same conclusion follows (see Fig. 2): the minimum Δ and a high peak in Δ_2 correspond to the perfect core-shell structure which includes the maximum number of small atoms inside,

namely, 30 external Ag atoms and 8 inner Ni or Cu atoms. This structure (see Fig. 1) is a $(30, 8)\text{pIh}^8$, made up of 8 interpenetrating Ih_{13}. Other perfect core-shell pIh are the $(31, 7)\text{pIh}^7$ and the $(32, 6)\text{pIh}^6$. The latter is a highly symmetric (group D_{6h}) *pancake* structure.

At $N = 34$, the predominance of the core-shell pIh structure is even clearer. This is the right size for forming a high-symmetry (group D_{5h}) pIh made of 7 Ih_{13}. This structure underlies most of the minima at varying compositions, and attains its maximum stability when the perfect core-shell arrangement is formed, in $(27, 7)\text{pIh}^7$. It contains a compact decahedral nucleus of Ni or Cu, and all Ag atoms are placed in an anti-Mackay [20] shell (see Fig. 1). The special energetic stability of perfect core-shell pIh at $N = 34$ and $N = 38$ is nicely confirmed by our DFT calculations, whose results are reported in Fig. 2 and Table I. The atom-atom potential geometries are only slightly modified by the DFT relaxation, thus validating the accuracy of the semiempirical approach for these elements.

High-stability core-shell pIh constitute a rich family of different sized clusters. At $N = 45$ we find the so-called anti-Mackay (see [20]) Ih, $(32, 13)\text{pIh}^{12}$ which is the highest symmetry pIh. It is obtained by covering a Ni or Cu Ih_{13} with a complete anti-Mackay Ag shell. Moreover, there is a series of perfect core-shell pIh made of fragments of this anti-Mackay pIh^{12}. They are shown in the auxiliary material [21]. All the perfect core-shell pIh are well separated in energy from their homotops (homotops are defined as clusters of the same size, structure, and composition, and differ only in the chemical ordering). This separation is due to the high energetic cost of placing an Ag atom in the cluster core.

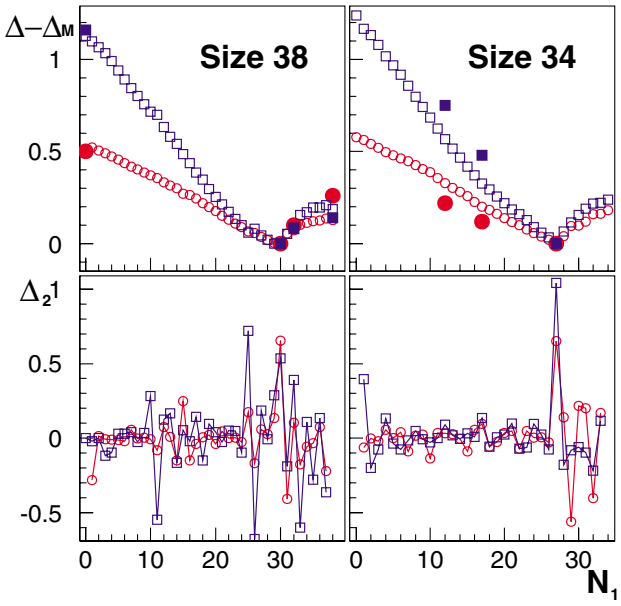

FIG. 2 (color online). Δ and Δ_2 (in eV) for clusters of fixed size vs the number of Ag atoms N_1. Δ_M is the minimum value of Δ at the given size. Circles and squares refer to Ag-Cu and Ag-Ni, respectively. Open symbols refer to the atom-atom potential results, while full symbols refer to the DFT results. Minima in Δ and maxima in Δ_2 both concur to single out the most stable structures, which are the perfect core-shell $(30, 8)\text{pIh}^8$ and $(27, 7)\text{pIh}^7$ (see Fig. 1) at sizes 38 and 34, respectively.

Among this family of core-shell pIh, now we focus on the $(27, 7)\text{pIh}^7$, which from Fig. 2 and Table I seems to have the most intriguing properties. For Ag-Cu, this cluster has a large gap (0.82 eV), indicating a strong electronic stability, and no magnetic moment. For Ag-Ni, the gap is still rather large (0.81 and 0.46 eV in the majority and the minority spin, respectively), and the ground state has a non-negligible magnetic moment. In both cases, the $(27, 7)\text{pIh}^7$ is also of remarkable thermodynamic stability, as follows from the analysis of its melting behavior. In fact (see Fig. 3), this core-shell cluster melts at considerably *higher* temperature than pure Ag, Cu, and Ni clusters in the same size range. This is at variance with the behavior of Ag-Cu and Ag-Ni bulk systems, where the melting point is depressed at mixed compositions [18]. The thermodynamic stability of the $(27, 7)\text{pIh}^7$ follows from two factors. First, this cluster is well separated from higher isomers [22], by at least 0.3 eV for Ag-Cu and 0.45 eV for Ag-Ni according to the atom-atom potential, but the DFT calculations give a much larger separation, of more than 0.8 eV. Second, our harmonic thermodynamics calculations show that

TABLE I. DFT calculations results. Values of spin (S) and HOMO-LUMO gap (in eV) for alpha/beta electrons. The symbol "JT" signals a Jahn-Teller system, with a degenerate HOMO. Pictures of the $(17, 17)\text{pIh}^7$ and $(12, 22)\text{pIh}^7$ are shown in [21]. For pure clusters, the DFT relaxation shows that defected decahedral structures are slightly lower in energy than the truncated octahedra.

System	Size	Cluster	S	Gap
Ag	38	Truncated octahedron	1	0.39/0.35 JT
Cu	38	Truncated octahedron	1	0.61/0.56 JT
Ni	38	Truncated octahedron	16	0.21/0.03 JT
Ag-Cu	38	$(32, 6)\text{pIh}^6$	0	0.34/0.34
	38	$(30, 8)\text{pIh}^8$	0	0.26/0.26
	34	$(27, 7)\text{pIh}^7$	0	0.82/0.82
	34	$(17, 17)\text{pIh}^7$	0	0.94/0.94
	34	$(12, 22)\text{pIh}^7$	0	0.88/0.88
	45	$(32, 13)\text{pIh}^{12}$	2.5	0.49/1.00
Ag-Ni	38	$(32, 6)\text{pIh}^6$	0	0.09/0.09
	38	$(30, 8)\text{pIh}^8$	0	0.05/0.05
	34	$(27, 7)\text{pIh}^7$	3.5	0.81/0.46
	34	$(17, 17)\text{pIh}^7$	6.5	0.19/0.07
	34	$(12, 22)\text{pIh}^7$	7	0.26/0.07 JT
	45	$(32, 13)\text{pIh}^{12}$	16	0.21/0.03 JT

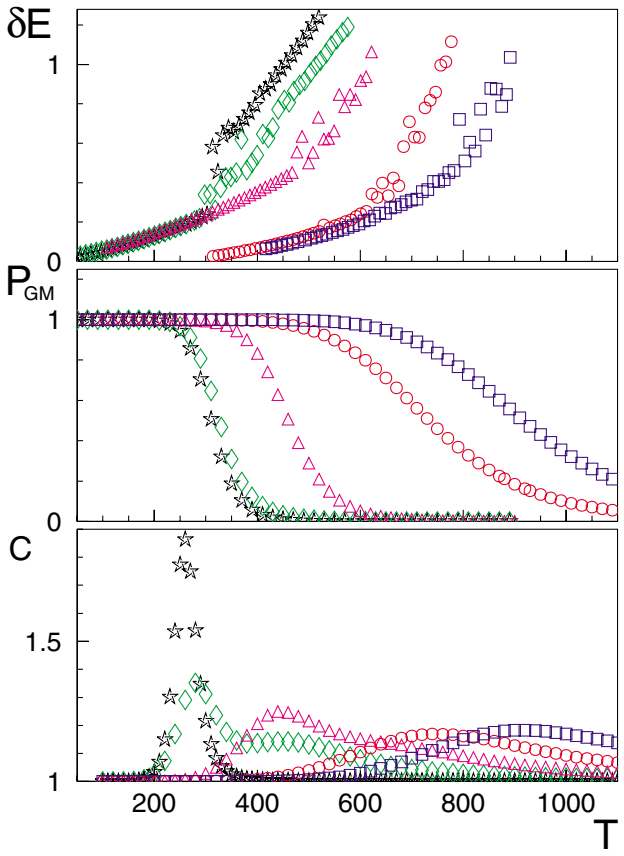

FIG. 3 (color online). Melting of pure clusters and of core-shell pIh. The top panel shows the molecular-dynamics caloric curves δE (in eV) vs temperature T (in K), where $\delta E = E - E_{GM} - 3(N-1)k_BT$, namely, δE is the total cluster energy minus the global-minimum energy E_{GM} and the harmonic contribution $3(N-1)k_BT$. The middle panel reports p_{GM} which is the probability of finding the cluster in its global-minimum structure as a function of T. The bottom panel reports the vibrational specific heat c per degree of freedom (in units of the Boltzmann constant k_B). p_{GM} and c are calculated in the harmonic superposition approximation. Stars, diamonds, and triangles refer to pure Ag_{38}, Cu_{38}, and Ni_{38} clusters; circles and squares refer to the (27, 7)pIh[7] of Ag-Cu and Ag-Ni. Core-shell pIh melt considerably higher than pure clusters.

the entropic contributions to the free energy are favorable to the (27, 7)pIh[7] structure.

The electronic and magnetic properties of this new family of magic clusters can be of great interest, and are currently under investigation. For example, the large gap and the stability of the Ag-Cu (27, 7)pIh[7] make this cluster potentially suitable for applications in optoelectronic and single-electron tunneling devices. On the other hand, the same cluster is a promising candidate for single-molecule magnetism in the case of Ag-Ni. Finally, since the requirements for these structures are of quite general character (size mismatch, large atoms segregating at the surface with respect to small atoms, possibly a weak tendency to mix in the bulk phase), we expect that magic core-shell polyicosahedra are likely to be encountered in a large variety of binary metallic systems, for example, Ag-Co, Au-Ni, Au-Co, and (with a weaker tendency) Ag-Pd and Au-Cu.

The authors thank J. P. K. Doye and R. L. Johnston for a critical reading of the manuscript. A. F. and R. F. acknowledge financial support from the CNR for the project SSA-TMN in the framework of the ESF EUROCORES SONS. A. F. acknowledges the INSTM for a grant at CINECA.

[1] J. Jellinek and E. B. Krissinel, in *Theory of Atomic and Molecular Clusters*, edited by J. Jellinek (Springer, Berlin, 1999), pp. 277–308.
[2] T. Shibata *et al.*, J. Am. Chem. Soc. **124**, 11 989 (2002).
[3] S. Darby *et al.*, J. Chem. Phys. **116**, 1536 (2002).
[4] A. M. Molenbroek, S. Haukka, and B. S. Clausen, J. Phys. Chem. B **102**, 10 680 (1998).
[5] U. Kreibig and M. Vollmer, *Optical Properties of Metal Clusters* (Springer, Berlin, 1995).
[6] P. Jensen, Rev. Mod. Phys. **71**, 1695 (1999).
[7] M. Gaudry *et al.*, Phys. Rev. B **67**, 155409 (2003).
[8] F. Baletto, C. Mottet, and R. Ferrando, Phys. Rev. B **66**, 155420 (2002).
[9] F. Baletto, C. Mottet, and R. Ferrando, Phys. Rev. Lett. **90**, 135504 (2003).
[10] Form and parameters are given in [8,9].
[11] For a general description of genetic algorithms for binary clusters optimization see [3].
[12] DFT calculations are carried out by the DFT module of the NWCHEM package [R. A. Kendall *et al.*, Comput. Phys. Commun. **128**, 260 (2000)]. $(7s6p6d)/(5s3p2d)$ Gaussian-type orbital basis sets and effective core potentials are used for all elements. A charge density fitting basis is used for the Coulomb integrals (courtesy of Dr. F. Weigend). More details are in E. Aprà and A. Fortunelli, J. Chem. Phys. **107**, 2394 (2003).
[13] J. P. K. Doye and F. Calvo, Phys. Rev. Lett. **86**, 3570 (2001).
[14] J. P. K. Doye, D. J. Wales, and R. S. Berry, J. Chem. Phys. **103**, 4234 (1995).
[15] See the Cambridge Cluster Database, http://www-wales.ch.cam.ac.uk/CCD.html.
[16] L. Pauling, *The Nature of the Chemical Bond* (Cornell University Press, New York, 1960).
[17] J.-M. Roussel *et al.*, Phys. Rev. B **55**, 10 931 (1997).
[18] M. Hansen, *Constitution of Binary Alloys* (McGraw-Hill, New York, 1958).
[19] C. L. Cleveland and U. Landman, J. Chem. Phys. **94**, 7376 (1991).
[20] J. A. Northby, J. Chem. Phys. **87**, 6166 (1987).
[21] See EPAPS Document No. E-PRLTAO-93-057434 for pictures of core-shell polyicosahedra structures. A direct link to this document may be found in the online article's HTML reference section. The document may also be reached via the EPAPS homepage http://www.aip.org/pubservs/epaps.html or from ftp.aip.org in the directory /epaps/. See the EPAPS homepage for more information.
[22] D. D. Frantz, J. Chem. Phys. **115**, 6136 (2001).

JCTC Journal of Chemical Theory and Computation

The Interaction of Coinage Metal Clusters with the MgO(100) Surface

Giovanni Barcaro and Alessandro Fortunelli*

Molecular Modeling Laboratory, Istituto per i Processi Chimico-Fisici (IPCF) del C. N. R., via V. Alfieri 1, 56010 Ghezzano (PI), Italy

Received March 22, 2005

Abstract: The results of a systematic study of the interaction of small coinage metal clusters (M_n, $n = 1-3$) and extended deposition (one and two MLs; ML = monolayer) with the regular and locally defected (F_s center and divacancy) neutral MgO(100) surface are presented. The calculations have been performed at the DFT level employing plane waves as a basis set and using a gradient-corrected exchange-correlation functional (PW91). The adhesion energy along the group follows a trend that can be rationalized in terms of the strength and "stickiness" of the metallic bond, electrostatic polarization effects, and chemical interactions. Coinage metal dimers and trimers are absorbed on the regular surface in an upright position with little modification with respect to the gas-phase structure and can easily diffuse from site to site (in the case of trimers, also because of their fluxional character). In the case of extended deposition, the adhesion energy increases when passing from one to two MLs because of a "metal-on-top" stabilization mechanism. Neutral localized defects on the surface such as the F_s center (generated by a missing O atom) and the double vacancy (generated by a missing MgO dimer) act as strong trapping centers for small clusters and remarkably increase the adhesion of metal slabs to the surface in the case of extended deposition. At variance with the F_s center, the double vacancy induces a strong structural and energetic modification of the surrounding oxide lattice, varying also as a function of the metal deposition. A peculiar structural rearrangement consisting of the segregation of the metal slab into "islands" on the surface is observed in the case of one ML Cu and (to a lesser extent) Au.

1. Introduction

Transition metal nanoclusters have gained increasing attention in science and application in the past several years as a result of the observation of properties that are unique to the nanoscale domain.[1−4] From a technological point of view, the process of stabilization of the metal clusters by coating with surfactants or through absorption on a substrate is an essential step to exploit the many potential applications of these materials. For this reason, a considerable experimental and theoretical effort has been dedicated to the study of the interaction and structural modifications induced in the metal aggregate by the presence of a supporting substrate[5−29] or surfactant and solvent molecules.[33−35] Moreover, the experimental conditions of the stabilization process can be tuned in order to induce the formation of supraorganized structures of single nanocluster units.[4,34−36] From a theoretical point of view, the characterization of transition metal clusters absorbed upon a supporting substrate has mainly concentrated on the study of static structures and has rarely dealt with the mechanism of nucleation and growth (see, however, refs 29−32, 100). Furthermore, despite the many contributions to this field, previous theoretical work lacks a systematic homogeneous comparison between elements belonging to the same group. The aim of the present paper is to provide such a comparison for the metals belonging to the group IB and the MgO(100) surface. Attention will be concentrated on the interaction of small coinage metal clusters and extended

* Corresponding author. Tel: +39-050-3152447, e-mail: fortunelli@ipcf.cnr.it.

10.1021/ct050073e CCC: $30.25
Published on Web 08/12/2005

deposition with the regular or localized defected neutral MgO(100) surface. These systems present several elements of interest. On one hand, nanoclusters formed by coinage metals (Cu, Ag, and Au), both mono- and bimetallic, exhibit interesting optical, electronic transport, and catalytic properties, both in the gas phase and when stabilized by a substrate or by surfactant molecules.[33,37−44] On the other hand, the MgO(100) surface both is experimentally well-characterized and has technological (e.g., catalytic) applications.[3,45] Moreover, its theoretical description is simplified by the fact that this surface does not present the complications associated with surface reconstruction, MgO being a simple ionic solid and the (100) surface being a nonpolar one. In discussing the results, we will highlight analogies and differences in the behaviors of the coinage metals in order to extract information on both static and dynamic properties of the metal/MgO interaction. These results can form the basis for (a) a comparison with experimental data on the growth of coinage metal clusters and thin films, (b) building semiempirical metal/oxide interaction potential, which can be used in the simulation of actual growth processes, and (c) improving other simplified (for example, thermodynamic) theoretical models.

Previous Work. During the past few years, several theoretical approaches have been used to study transition metal nanoclusters. First principles calculations have been performed on small metal aggregates in order to determine the minimum energy structure and structure/property relationship as a function of cluster size.[46−55] Numerical procedures based on genetic algorithms for single and bimetallic structures using atom−atom pair potentials[56] or many-body potentials[56−64] have been used to investigate a broader range of cluster sizes. Focusing on transition metal clusters supported on magnesia surfaces, in the past 10 years, a wealth of results has been collected on the interaction of single metal atoms on the regular and defected sites of the MgO(100) surface.[65−69] The extended and localized defected sites of the MgO surface have attracted remarkable attention because of their intrinsic chemical and physical properties[70−84] and because they can act as trapping centers for metal atoms absorbed on the oxide surface.[67,85] The results of such calculations have demonstrated that the choice of the model influences the description of the system[86] and that the metal/surface interaction changes primarily as a function of the electronic configuration and the dimensions of the metal species considered. For example, the coinage metals, which are characterized by a filled d shell plus an outer, unpaired s electron, are weakly bound to the surface (with adhesion energy less of 1 eV) because of the Pauli repulsion with the electron density of the oxide.[67] The catalytic properties of systems formed by a single atom or small clusters absorbed on the regular and defected MgO surfaces have been studied by monitoring the absorption of probe molecules on the metal atoms.[39,78,87−92] The real-time monitoring of cluster growth on MgO offered by GISAXS[9] has further promoted the study of the minimum structure configurations of metal clusters and extended deposition on regular and defected MgO(100) surfaces in order to extract information on the mechanism of nucleation and growth and on the modifications in structure and properties induced in the metal aggregate by absorption on the oxide surface.[42,65,93−102] In particular, the study of the small clusters and extended deposition of coinage metals (Cu and Ag) has been performed through standard DFT calculations,[103−109] Car Parrinello calculations,[29−32] and a thermodynamic model describing the metal/oxide system in terms of a solid solution.[83,110] The general conclusion is that the Cu and Ag interactions with the regular surface are weak. Small clusters are absorbed in an upright position with negligible modifications with respect to the gas-phase structure and are able to diffuse over the surface through leapfrog, twisting, and rolling movements. In the case of extended deposition, there is an increase of the adhesion energy to the surface when passing from one to two MLs, thanks to a polarization stabilization mechanism. Classical molecular dynamics calculations of the growth process have, until now, been performed only for Pd clusters absorbed on the regular MgO surface[111−113] thanks to the development of a specific metal/oxide potential, fitted on the results of first-principle calculations. An analogous potential is still lacking for the coinage metal clusters. One of our goals is to provide the theoretical input data for the construction of such a potential, accounting not only for the interaction with the regular surface sites but also for the interaction with localized neutral vacancies.

2. Computational Details

All the calculations reported here were performed at the DFT level employing the PWscf (Plane-Wave Self-Consistent Field) computational code[114]. For each atom, the interaction between the outer-shell electrons and the positive nucleus is shielded by a pseudopotential accounting for the influence of the inner-shell electrons. All the calculations were performed spin-unrestricted. The PW91 exchange-correlation functional was employed,[115] which is a gradient-corrected density functional. From previous experience, we do not expect qualitative changes when using other gradient-corrected density functionals. However, it has been shown (see, e.g., ref 86) that the use of hybrid density functionals produces an overall (roughly constant) reduction in the metal/surface interaction energies.

The geometry optimizations were stopped when maximum force on the atoms was less than 4×10^{-4} au. All of the configurations reported here were checked to insure that they were local minima in the energy hypersurface. Few saddle point configurations can be found among those reported in the Supporting Information.

The dimensions of the plane-wave basis set are determined by the kinetic energy cutoff, which was fixed at the value of 40 Ry for all of the calculations. The *k*-point sampling of the Brillouin zone was changed according to the conductive properties of the metal deposition absorbed on the oxide. In the case of the deposition of one and two ML metallic slabs, which are conductive (small energy gap between the HOMO and LUMO energy), it was necessary to increase the number of *k* points per unit cell and to apply a procedure of Gaussian smearing (a value of 0.002 Ry was chosen as the smearing parameter for every sampled point of the Brillouin zone).

The dimensions of the unit cell were modified according to the metal deposition, as specified in detail in the following sections. A common aspect of all the different cells employed is that the oxide surface was built by positioning the Mg and O atoms at the equilibrium lattice positions of the MgO rock-salt structure (isomorphic with NaCl) and cutting this bulk structure along 100 directions. The O atoms on the surface are surrounded by four Mg surface atoms plus one Mg bulk atom and vice versa. The distance between the two opposite surface layers of the oxide slab is about 10 Å. The lattice constant of the oxide corresponded to the experimental value of 4.208 Å (implying a Mg−O distance of 2.104 Å). When the oxide bulk structure is relaxed at the DFT level, the equilibrium lattice constant is overestimated by about 2%. However, the metal/surface interaction energies do not qualitatively vary when using the DFT-optimized lattice constant (unpublished results).

In the calculations involving the regular (undefective) oxide surface, the MgO structure was left frozen and only the atomic coordinates of the metallic atoms absorbed on the surface were optimized. In the case of the defected surfaces, we have followed two different approaches. In the case of a single F_s vacancy, we have relaxed the oxide lattice around the defect in the absence of metal atoms; such a structure has then been frozen, allowing only the relaxation of the metal atoms absorbed upon it. We have checked in test cases that there is a negligible difference between the results obtained following this approach and the results obtained allowing a further relaxation of the oxide surface upon metal deposition. In the case of the double vacancy (which can be thought of as a desorption of a neutral MgO dimer in the 100 direction), the relaxation plays a very important role,[100] and to obtain an accurate estimate of the metal absorption energies, we allowed a complete relaxation of the atoms of the defected oxide and all the metal atoms. For this reason, the calculations involving the double vacancy are, computationally, rather intensive.

3. Results and Discussions

This section is divided into three subsections: absorption (I) on the regular terrace of the MgO(100) surface, (II) on a neutral oxygen vacancy (F_s center), and (III) on a neutral divacancy

Each of these subsections will separately treat the case of the absorption of (A) isolated metal atoms, (B) metal dimers, (C) metal trimers, and (D) extended depositions (one and two MLs)

For each system, we report four values of energy:

(1) The Absorption Energy (E_{int}). This quantity is calculated by subtracting the ground-state energy of the isolated oxide and the isolated metal atoms from the value of the total energy of the system. The absorption energy corresponds to the energy gain achieved by moving the single cluster constituents from infinite distance to the equilibrium distance characterizing a particular configuration.

(2) The Adhesion Energy (E_{adh}). This quantity is calculated by subtracting the energy of the oxide surface and that of the metal cluster, both frozen in the interacting configuration, from the value of the total energy of the system.

(3) The Oxide Surface Distortion Energy (ΔE_{MgO}). This quantity corresponds to the "distortion energy" of the oxide surface. It is calculated by subtracting the energy of the oxide surface in the interacting configuration from the ground-state energy of the surface.

(4) The Metal Cluster Distortion Energy (ΔE_{met}). A quantity analogous to the previous one but for the metal cluster.

We report only a selection of the configurations that have been considered. Additional data can be found in the Supporting Information.

I. Interaction of Coinage Metal Clusters with the Regular Terrace of the MgO(100) Surface. As anticipated before, for this system, no relaxation of the MgO surface was allowed ($\Delta E_{MgO} = 0$). This is consistent with the experimental observation that this surface does not reconstruct. We optimized only the coordinates of the metal atoms because the surface structure modification induced by the absorbed metal is negligible.

I.A. Isolated Adatoms. The absorption of the isolated adatoms has been studied modeling the (100) terrace by a three-layer slab, each containing four Mg atoms and four O atoms (a five-layer-slab model gave essentially identical results). The minimum distance between metal atoms in neighboring unit cells was larger than 6 Å; this distance is sufficiently large to make the interaction between the metal atoms negligible.

Three characteristic sites of absorption have been considered: (1) the O^{2-} ion, (2) the Mg^{2+} ion, and (3) the hollow site (see Figure 1a). The results of the interaction energies are reported in Table 1. In Figure 1 of the Supporting Information, the absorption energies on the O^{2-} ion are reported for the three metals as functions of the metal−surface distance. The interaction is stronger for Cu and Au atoms, while it is weaker for Ag;[68] all three metals interact more strongly with the O^{2-} ion site of the surface, while the Mg^{2+} ion is the site characterized by the smallest value of adhesion energy.

The tendency of absorbing atop the O^{2-} site is a common trend among transition metal atoms.[32,65,66] The stabilizing contributions of the interaction can be of three types: (1) chemical bonding, (2) electrostatic stabilization, and (3) dispersion interactions. The Pauli repulsion between the metal cloud and the electronic density of the surface represents, instead, the mainly destabilizing contribution. This repulsion is certainly stronger for the coinage metal atoms that are characterized by a diffuse unpaired s electron, and this gives a rough explanation of the smaller adhesion energies of Cu, Ag, and Au with respect to other transition metal atoms such as Pd or Ni.[67] It is still under debate whether chemical bonding plays a significant role in the adhesion of the coinage metals; further studies need to be carried out to clarify this point.

I.B. Dimers. The formation of a dimer can be viewed as the first step in the process of the growth of metal clusters on the oxide surface. The unit cell was chosen, consisting of a three-layer MgO (each layer containing nine O atoms and nine Mg atoms) and two metal atoms. Two possible sites of absorption on the regular surface have been considered

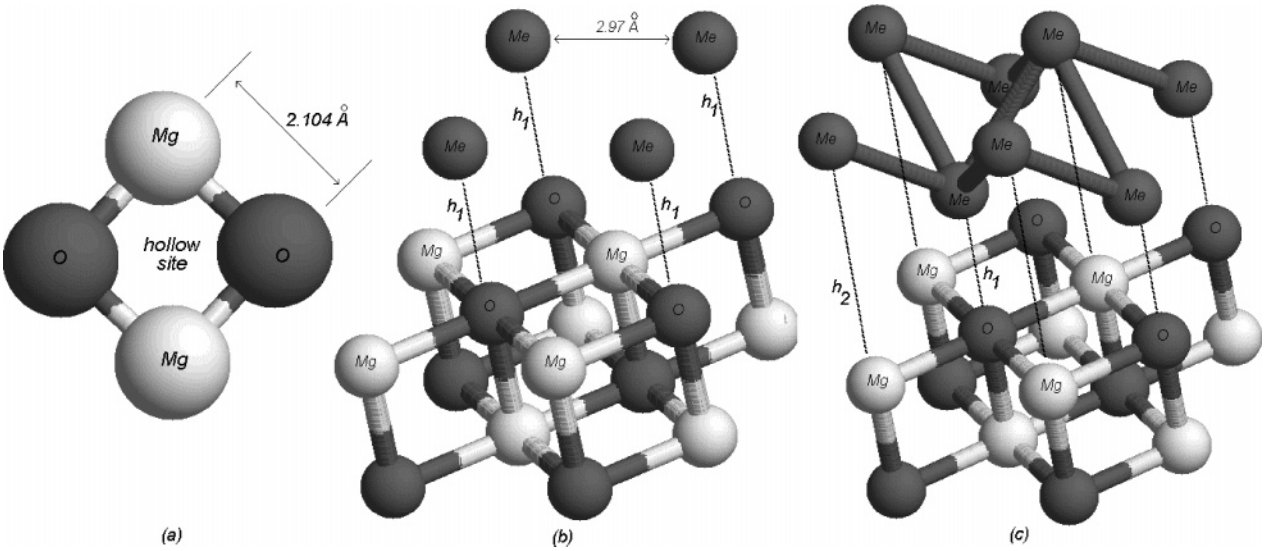

Figure 1. (a) Unit cell for a monolayer MgO slab. (b) One ML metal slab geometry absorption. (c) Two ML metal slab geometry absorption.

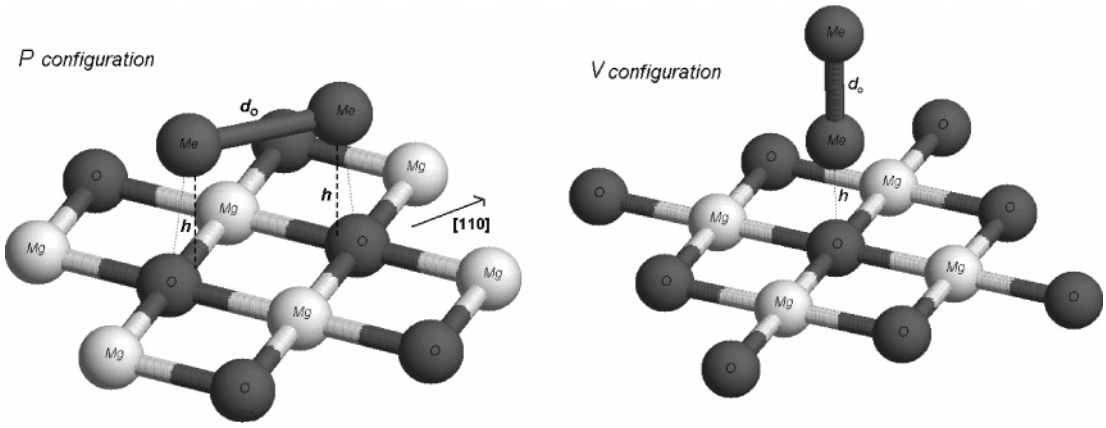

Figure 2. Dimer configurations on the regular MgO(100) surface.

Table 1. Interaction Energies and Distances Characterizing the Isolated Atom Absorption on the Regular MgO(100) Surface

adatoms		O site	Mg site	hollow site
Cu	E_{adh} (eV)	0.76	0.26	0.43
	d_o (Å)	2.1	2.8	2.3
Ag	E_{adh} (eV)	0.40	0.22	0.32
	d_o (Å)	2.5	2.9	2.6
Au	E_{adh} (eV)	0.87	0.49	0.67
	d_o (Å)	2.3	2.7	2.4

Table 2. (A) Characteristics of the Coinage Metal Dimers in the Gas Phase and (B) Geometric Parameters Characterizing the Geometric Configurations Shown in Figure 2

A. Characteristics of the Coinage Metal Dimers

	Cu_2	Ag_2	Au_2
binding energy (eV)	2.09	1.72	2.33
equilibrium bond length (Å)	2.25	2.59	2.52

B. Geometric Parameters

		d_0 (Å)	h (Å)	E_{int} (eV)	E_{adh} (eV)	ΔE_{met} (eV)
Cu_2	P	2.31	2.49	2.96	0.89	0.02
	V	2.26	2.16	3.24	1.15	0.00
Ag_2	P	2.61	2.79	2.18	0.46	0.00
	V	2.59	2.41	2.39	0.68	0.01
Au_2	P	2.56	2.63	2.92	0.61	0.02
	V	2.53	2.31	3.75	1.42	0.00

as interesting for a study of growth and diffusion (see Figure 2). The optimized values for the geometric parameters and the interaction energies are reported in Table 2b, while in Table 2a, the properties of the gas-phase dimers are reported.

The coinage metal dimers exhibit a similar behavior when absorbed on the regular surface. The values of the adhesion energy follow the same order characterizing the isolated adatoms: Au > Cu > Ag. The most stable geometry corresponds to the V configuration, in which the dimer is perpendicular to the surface atop the O^{2-} ion site. For Cu, this is in agreement with the results of refs 29−32, although we do not find any tilt angle with respect to the surface because we perform a symmetry-constrained relaxation along the surface normal direction. Although only one metal atom interacts with the surface, the adhesion energy of the dimer is *larger* than the value characterizing the isolated adatom.

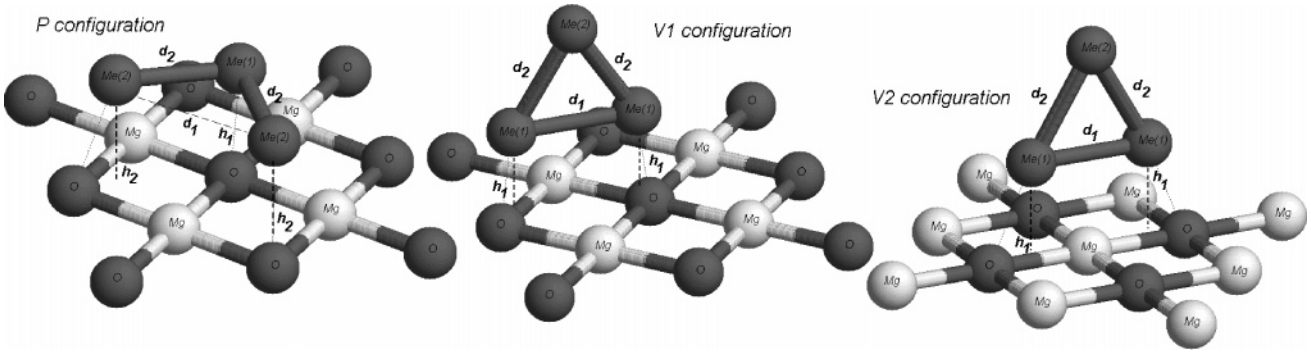

Figure 3. Trimer configurations on the regular surface. The last configuration on the right corresponds to the relaxation of the Au trimer on the F_s vacancy.

This result can be viewed as a first manifestation of the tendency of a vertical 3D growth of the coinage metal deposition on the oxide surface[29] and can be explained in terms of a stabilizing interaction between the dimer electron density and the field of the ionic surface.[103] In other words, the presence of metal atoms *above* those directly interacting with the surface *increases* the adhesion energy. This is what we call a "metal-on-top" stabilization mechanism. In the P configuration, the metal atoms can interact with two different O^{2-} ions, but the interaction energy is reduced because of the work needed to stretch the intermetal distance from the equilibrium value characterizing the isolated molecule. As a consequence, an almost identical intermetal distance is retained in all configurations considered and very small values of ΔE_{met} are observed.

To describe the diffusion process of the dimers on the surface, a leapfrog mechanism has been proposed for Cu, passing through the P configuration[29] with an activation energy barrier of 0.04 eV, although we find a larger energy difference between the V and P configurations.

It is interesting to note that, at variance with the coinage metal dimers, the most stable configuration for Pd_2 is the P one,[96] with the dimer parallel to the surface in a quasi-epitaxial geometry. This is due to a weaker metallic bond (especially noteworthy for the Pd_2 dimer) and a metal-on-top effect (probably because of a weaker polarizability of the d electrons with respect to the outer s electron).

I.C. Trimers. The chosen configurations are depicted in Figure 3. The unit cell was chosen, consisting of a three-layer MgO (each layer containing nine O atoms and nine Mg atoms) and three metal atoms. The values of the geometric parameters and of the interaction energies for each configuration are reported in Table 3b.

The trimers of the coinage metals are characterized by an s^3 electronic configuration, which produces a Jahn−Teller distortion and a consequent symmetry breaking from an equilateral triangle to an isosceles triangle. Looking at the optimized geometries of the three metals, we note that the distance between the central atom and the two lateral atoms is optimized at almost the equilibrium value of the gas-phase structure (reported in Table 3a), while the distance between the two lateral atoms is optimized in order to achieve the best interaction with the surface. Because of the Jahn−Teller effect, stretching the distance of the two lateral atoms does not imply any appreciable destabilization of the metal cluster.

Table 3. (A) Binding Energies and Geometric Parameters of the Coinage Metal Trimers in the Gas Phase and (B) Values of the Geometric Parameters Reported in Figure 4

A. Binding Energies and Geometric Parameters

	Cu_3	Ag_3	Au_3
binding energy (eV)	3.40	2.59	3.60
bond length d_1 (Å)	2.61	3.09	2.90
bond length d_2 (Å)	2.32	2.66	2.61

B. Values of Geometric Parameters

		d_1 (Å)	d_2 (Å)	h_1 (Å)	h_2 (Å)	E_{int} (eV)	E_{adh} (eV)	ΔE_{met} (eV)
	P	3.77	2.37	2.25	2.17	4.50	1.29	0.19
Cu_3	V1	2.61	2.33	2.10		5.00	1.60	0.00
	V2	3.50	2.36	2.06.		4.85	1.62	0.17
	P	4.33	2.69	2.73	2.67	3.27	0.72	0.04
Ag_3	V1	3.08	2.66	2.43		3.51	0.92	0.00
	V2	4.00	2.66	2.51		3.45	0.90	0.04
	P							
Au_3	V1	2.91	2.62	2.32		5.15	1.56	0.00
	V2	3.38	2.60	2.29		5.28	1.76	0.08

We refer to this behavior as *fluxional* (see the small values of ΔE_{met}). The larger values of ΔE_{met} for Cu are due to its shorter intermetal distances, which have to be stretched more to achieve a good interaction with the stabilizing sites of the surface.

As for the dimers, the preferred configurations of the trimers are the ones in which the cluster is perpendicular to the surface,[29] because of the metal-on-top stabilization mechanism. It can be noted that in the Au case, this effect is so strong that the P configuration relaxes toward the V2 configuration. These results are in fair agreement with those of ref 29 and suggest that the diffusion of the coinage trimers can take place through movements of "twisting" between the V1 and the V2 configurations, with low activation energy barriers especially for Ag and Au (slightly larger for Cu).

I.D. Extended Deposition. We built a unit cell assuming a pseudomorphic growth of the metal slab upon the oxide surface,[102,103] that is, positioning each metal atom above an O^{2-} (see Figure 1b), a Mg^{2+}, or a hollow site. Such a configuration corresponds to the growth of the (100) metal surface above the (100) oxide surface. Although the surface energy of the (100) surface is larger than the surface energy of the (111) surface for all the metals considered, the simplest metal configuration compatible with the symmetry of the

Table 4. Results for the Absorption of One and Two MLs on the Regular Surface[a]

		one ML			two ML		
		O site	Mg site	hollow site	O site	Mg site	hollow site
Cu	E_{int} (eV)	1.95	1.67	1.75	2.75	2.52	2.57
	E_{adh} (eV)	0.32	0.045	0.13	0.50	0.041	0.15
	h_1 (Å)	2.3	3.4	2.7	2.2	3.4	2.6
	h_2 (Å)				3.4	4.6	3.8
Ag	E_{int} (eV)	1.80	1.67	1.72	2.12	2.03	2.05
	E_{adh} (eV)	0.16	0.036	0.083	0.24	0.066	0.10
	h_1 (Å)	2.8	3.4	3.0	2.6	3.9	2.9
	h_2 (Å)				4.6	5.9	4.9
Au	E_{int} (eV)	2.26	2.20	2.24	2.66	2.59	2.62
	E_{adh} (eV)	0.15	0.095	0.13	0.22	0.084	0.15
	h_1 (Å)	2.9	3.1	2.9	2.8	3.3	2.9
	h_2 (Å)				4.8	5.3	4.9

[a] h_1 and h_2 respectively correspond to the heights of the first and the second metal layers on the MgO surface.

oxide cell is the one adopted here. The strict constraint of this assumption is that the first neighbor distance between the metal atoms of the slab is fixed at the value 2.975 Å. The chosen cell consists of three MgO layers, each containing only two Mg atoms, two O atoms, and two (four) metal atoms in the case of one (two) ML absorption (a five-layer slab model gave essentially identical results). In the two ML case, the atoms of the second metal slab were positioned in the interstitial sites of the first slab in such a way as to build the *fcc* structure of the bulk metals.

One ML. The results of one ML absorption are reported in Table 4, in which all energies are per atom. The values of ΔE_{met} are not reported because we did not perform a calculation by relaxing the reticular lattice parameter of the isolated metal ML.

From the results, which are in agreement with those reported in ref 103, we can derive the following observations:

(1) The order of stability of the three possible sites of absorption is the same as that found for the isolated atoms; the best configuration corresponds to all metal atoms on top of the O atoms on the surface.

(2) For all of the three system considered, there is a decrease of the adhesion energy per atom with respect to the case of the isolated atoms and a corresponding increase of the equilibrium distance between the metallic slab and the oxide surface.

(3) The absolute value of the adhesion energy decrease is remarkably large for Au on top of the O atoms; as a consequence, the stability order among the three metals is no longer Au > Cu > Ag (as for the isolated adatoms) but Cu > Ag ≈ Au.

To explain this behavior, two physical factors have to be taken into account: (1) the mismatch between the metal lattice constant and the reticular constant characterizing the pseudomorphic growth and (2) the strength of the metallic bond. The weak adhesion of the Au ML to the surface is due to the small mismatch between the reticular constant of bulk gold (2.885 Å) and the lattice parameter imposed by the pseudomorphic growth (2.975 Å), which implies a strong metal bond and, thus, a decreased interaction energy with the surface. Cu is characterized by a metal bond of strength comparable to Au, but the small value of the reticular constant of bulk copper corresponds to a large mismatch (about 16%) between the metal and the oxide lattice. The adhesion with the surface, thus, overcomes the metal binding energy.

Note, however, that these considerations neglect the change in the nearest-neighbor distances due to reduced coordination (from 12 to 4) in the one ML case. This determines a contraction of the lattice parameter,[57] consequently increasing the mismatch with the reticular constant of the oxide.

Two ML. The results for these systems are summarized in Table 4. Note that the adhesion energies are calculated normalizing the total interaction energy to the number of atoms in contact with the oxide surface (as we did in the case of the monolayer). [This is not a universally accepted convention, and some authors prefer to normalize the adhesion energy to the number of total atoms (considering those involved in the direct interaction with the surface and also the atoms in the second layer).] The general behavior is very similar to the one ML case: the order of stability among the three metals is Cu > Ag ≈ Au, and so forth. In passing from one to two ML deposition, however, one observes an increase in the adhesion energy (in a remarkable way, for the absorption atop the O^{2-} site). This increase in the adhesion energy has already been observed for Cu and Ag extended deposition[103] and explained in terms of the enhanced electrostatic polarization of the metallic electronic cloud in the surface field of the oxide, what we call a "metal-on-top" effect, in excellent agreement with the stabilization of the upright configurations reported in Sections I.B and I.C for the dimers and trimers. This happens despite the fact that the increase in the coordination number of the metal (from 4−8) increases its lattice constant, thus decreasing the mismatch with the lattice constant of the oxide and, consequently, enhancing the metallic bond in the slab.

We conclude this section by stressing that, when treating isolated atoms, among the coinage, we can distinguish between Cu and Au from one side and Ag on the other: Cu and Au are more strongly bound to the surface, while the interaction of Ag is much weaker. On the contrary, when passing to the extended deposition of one and two MLs, we observe a leveling of the adhesion energies among the three metals, with a pronounced resemblance between Ag and Au with respect to Cu.

II. Interaction of Coinage Metal Clusters with the an F_s Defect of the MgO(100) Surface. The F_s defect is formed when a neutral O atom leaves the MgO(100) surface but the two electrons carrying the negative charge of the O atom are kept in the vacancy. As the F_s vacancy constitutes a good candidate as a center of nucleation for the absorption of several transition metals on the oxide surface, this kind of defect has been extensively studied both experimentally and theoretically in recent years.

We considered the same unit cells used for the absorption on the regular surface: a three-layer MgO, each layer containing four or nine Mg and O atoms, depending on the size of the adsorbed metal cluster. Selected calculations using larger cells have also been performed, producing essentially comparable results.

Table 5. Adatoms Absorbed Atop the F_s Vacancy

adatoms	Cu	Ag	Au
$E_{adh} = E_{int}$ (eV)	1.76	1.59	3.04
h_o (Å)	1.80	2.00	1.81

Table 6. Dimer Geometries and Interaction Energies of the Coinage Dimers on the F_s Defect

		P	V		P	V
Cu_2	d_0 (Å)	2.33	2.34	E_{int} (eV)	4.13	4.16
	h_1 (Å)	1.55	1.68	E_{adh} (eV)	2.05	2.09
	h_2 (Å)	2.86	4.02	ΔE_{met} (eV)	0.01	0.02
Ag_2	d_0 (Å)	2.65	2.64	E_{int} (eV)	3.59	3.62
	h_1 (Å)	1.80	1.82	E_{adh} (eV)	1.89	1.92
	h_2 (Å)	3.91	4.46	ΔE_{met} (eV)	0.01	0.01
Au_2	d_0 (Å)	2.59	2.59	E_{int} (eV)		6.05
	h_1 (Å)	1.60	1.60	E_{adh} (eV)		3.75
	h_2 (Å)	4.19	4.19	ΔE_{met} (eV)		0.03

As anticipated before, the reconstruction of the MgO lattice around the F_s vacancy is negligible both in the absence and in the presence of metal absorption, in agreement with previous studies.[67,70] For this reason, we did not perform any relaxation of the MgO surface ($\Delta E_{MgO} = 0$).

II.A. Isolated Adatoms. The single atoms are trapped atop the F_s center. The values of the interaction energy and of the equilibrium distance are reported in Table 5 and are in fair agreement with the results reported in ref 67.

The order among the three metals is same as that for the adsorption on the regular surface. The atoms can get closer to the vacancy on the surface because of the decrease of the Pauli repulsion consequent to the removal of the O atom, thus experiencing a stronger electric field, with a consequent increase of the polarization interaction. The relative increase of the interaction energy is larger in the cases of Ag and Au with respect to Cu, probably because of chemical bond effects.

II.B. Dimers. We considered the same configurations used for the absorption on the regular surface (see Figure 2). In Table 6, the geometric parameters and the energies for each configuration are reported.

The results for the P configuration of Au_2 is not reported because it relaxes toward the perpendicular configuration atop the vacancy (V configuration).

As for the perfect surface, the intermetal distances are only slightly elongated with respect to the equilibrium gas-phase values; the distortion energies are consequently very small. Also, the differences in adhesion and interaction energies between the P and V configurations are very small; this can be explained by noting that the P configuration is remarkably tilted with respect to the surface, so the dimers in the two configurations probably experience a similar field.

The interaction mechanism is the same as that for the adsorption of a single atom on the F_s center. Only, the decrease in equilibrium distances and, thus, the stabilizing effect are still more pronounced, as a result of the metal-on-top mechanism.

II.C. Trimers. We chose two configurations: one is similar to V1 from Figure 3, in which the F_s vacancy is under a lateral metal atom, and the other one is a linear epitaxial configuration, in which the F_s vacancy is under one of the lateral atoms. The geometric parameters and the energies characterizing the absorption of the coinage metal trimers on the F_s vacancy are reported in Tables 7 and 8, from which it can be seen that an appreciable rearrangement of the metal atoms not directly bound to the defect occurs. The dominant contribution to the adhesion energy is given by the interaction of the metal atom atop the defect. As a result of the fluxionality of the trimers and the interplay between the metal-on-top effect and the direct metal−surface interaction, there exists a large set of different configurations very close in energy, among which we selected two representative ones, without being certain to have singled out the absolute energy minimum. As before, the energy differences are slightly larger for Cu, because of its reduced fluxionality. The order of stability among the three coinage metals is the same as that found in the previous sections. The adhesion energies for all three metals are still larger than for the dimers, as fluxionality allows the trimers to deform in such a way as to better interact with the surface and exploit the metal-on-top effect or the direct metal−surface interaction.

Table 7. Geometric Parameters for the Coinage Trimers Absorbed on the F_s Vacancy[a]

		d_{1-2} (Å)	d_{2-3} (Å)	d_{1-3} (Å)	h_1 (Å)	h_2 (Å)	h_3 (Å)
Cu_3	V1	2.58	2.36	2.40	1.68	2.17	3.90
	L1	2.47	2.37	4.80	1.91	2.48	2.43
Ag_3	V1	2.97	2.73	2.70	1.80	2.67	4.40
	L1	2.73	2.71	5.30	1.92	3.04	2.92
Au_3	V1	2.80	2.69	2.69	1.57	2.85	4.25
	L1	2.67	2.62	4.68	1.66	3.37	2.65

[a] The atom labeled 1 is the one absorbed atop the vacancy.

Table 8. Energies Involved in the Trimer Absorption on the F_s Vacancy

		E_{int} (eV)	E_{adh} (eV)	ΔE_{met} (eV)
Cu3	V1	6.12	2.75	0.03
	L1	5.58	2.48	0.31
Ag3	V1	4.96	2.39	0.02
	L1	4.78	2.25	0.07
Au3	V1	7.80	4.24	0.04
	L1	7.70	4.09	0.01

The main conclusion that we can extract from the results of the absorption of atoms, dimers, and trimers on the oxygen vacancy is that the defect acts as a strong trapping center for all the coinage metals. The differences in adhesion between several configurations are small with respect to the absolute values of the absorption energies found in the calculations. Every possible mechanism of diffusion of small clusters from the site of the vacancy to the neighboring regular sites is strongly disfavored; the more it is disfavored, the larger the metal cluster.

II.D. Extended Depositions. One ML. The mean values of the adhesion and adsorption energies are evaluated by calculating the total absolute value of the respective energies and dividing by the number of the atoms in contact with the surface (four both for one and two MLs). The word "mean" refers to the fact that the single atoms experience a different

Table 9. One and Two MLs Absorbed on the F_s Vacancy

	one ML			two ML		
	Cu	Ag	Au	Cu	Ag	Au
$\langle E_{int} \rangle$ (eV)	2.14	1.99	2.72	2.84	2.25	2.85
$\langle E_{adh} \rangle$ (eV)	0.54	0.41	0.84	0.68	0.47	0.79
$\langle \Delta E_{met} \rangle$ (eV)	0.03	0.06	0.20	0.01	0.01	0.09
h_1 (Å)[a]	1.79	2.00	1.71	1.83	2.31	1.80
h_2 (Å)[b]	2.41	2.84	2.90	2.17	2.74	2.69
h_3 (Å)[c]	2.54	2.96	2.99	2.18	2.77	2.73

[a] Distance of the metal atom atop the vacancy. [b] Distance of the metal atom atop an O ion at 2.97 Å away from the vacancy. [c] Distance of the metal atom atop an O ion at 4.21 Å away from the vacancy.

Table 10. Coinage Dimers on the Double Vacancy

	Cu_2	Ag_2	Au_2		Cu_2	Ag_2	Au_2
d_o (Å)	2.43	2.68	2.69	E_{int} (eV)	5.51	4.23	5.21
h_1 (Å)[a]	0.191	0.525	0.467	E_{adh} (eV)	4.56	3.21	3.89
h_2 (Å)[b]	1.59	2.10	2.04	ΔE_{met} (eV)	0.11	0.02	0.12
r_{1-Mg} (Å)	0.089	0.276	0.370	ΔE_{MgO} (eV)	1.03	0.68	0.89
r_{2-O} (Å)	0.028	0.336	0.442	ΔE_{relax} (eV)	0.86	0.60	0.73

[a] Height of the atom atop the Mg^{2+} empty site. [b] Height of the atom atop the O^{2-} empty site.

interaction with the surface. The sites of absorption are four: one atop the vacancy, two on regular O^{2-} ions at a distance of 2.97 Å from the defect, and one on a regular O^{2-} at a distance 4.21 Å from the defect. The results are reported in Table 9. The values reported as $\langle \Delta E_{met} \rangle$ correspond to the energy increase due to the corrugation of the metal slab.

The final relaxed topology of the metallic slab is characterized by a corrugation due to the different heights of the metal atoms upon the four different sites of the surface. The atom directly atop the vacancy lies almost at the equilibrium height characterizing the isolated adatom, which suggests that this atom is practically not involved in the metallic bond with the other metal atoms. By using the data of Table 4, we can give an estimate of the interaction energy of the lower metal atom with the vacancy: supposing that the three metal atoms on the regular sites interact with the surface with the same amount of adhesion energy characterizing the one ML on the regular surface, we get

- Cu: 1.44 eV (real value of the adatom: 1.76 eV)
- Ag: 1.28 eV (real value of the adatom: 1.59 eV)
- Au: 3.02 eV (real value of the adatom: 3.04 eV)

In the one ML system, the interaction of the lower atom with the vacancy is decreased by about 20% in the cases of Cu and Ag and only less than 1% in the case of Au.

Two ML. When studying the absorption of a second monolayer absorbed on the first one, we do not find any corrugation of the second metal layer. The results are reported in Table 9.

It can be noted that for Cu and Ag, we observe an increase of the adhesion energy and a corresponding decrease of the distance of the metal atoms on the regular sites from the surface. On the contrary, Au exhibits a decrease of the adhesion energy; the stabilization due to the metal-on-top effect does not manage to compensate for the loss of the metal bond energy due to the corrugation of the first layer.

III. Interaction of Coinage Metal Clusters with the a Double Vacancy of the MgO(100) Surface. Another surface defect that has attracted considerable interest in recent years is the double vacancy.[100] This is a neutral defect and corresponds to the removal of an MgO dimer in the 100 direction of the regular oxide terrace. Its surface concentration is estimated to be rather high.[7,72] The difference with respect to the F_s defect, which, as we will see, has important consequences in view of the nucleation process, is that the removal of an MgO dimer induces an appreciable modification in the structure of the oxide slab. In fact, allowing relaxation of the defected surface results in an increase of the dimensions of the cavity with a corresponding stabilization energy of about 2.90 eV. The distances between the prospicient atoms at the border of the cavity increase by up to 10% with respect to the nonrelaxed values (see Figure 4a, where some characteristic distances between the borders of the cavity are reported).

As anticipated above, we always relaxed all the geometric parameters upon absorption. The unit cell of the MgO slab is made of three layers containing a total of 52 atoms. This is the largest unit cell we have considered, and this, together with the need of optimizing the degrees of freedom also corresponding to the MgO surface, means that the calculations involving the divacancy are the most computationally intensive.

III.A. Isolated Atoms. The results of the absorption of single coinage metal atoms on the double vacancy are reported in Table 11. In the table, E_{int}, E_{adh}, ΔE_{MgO} are the quantities defined at the beginning of Section 3; ΔE_{relax} is a new quantity defined as the energy gain obtained by performing a relaxation of the cluster coordinates, keeping the coordinates of the lattice frozen in the position characterizing the relaxed isolated oxide, and it is useful in checking the validity of the quadratic expansion of the interaction energy (see below).

From the analysis of the data from Table 11, two common features can be derived: (1) All the metals adsorb near the site left empty by the removal of the Mg atom; all the adsorbed atoms go deeply into the cavity reaching almost the same height as the Mg and O atoms of the surface oxide layer. (2) The interaction energies with the divacancy are of the same order of magnitude as the energies characterizing the interaction with the F_s defect, suggesting that this defect is another good candidate as a nucleation site on the MgO-(100) terrace.[100]

Some quantitative differences can be evinced through a more detailed analysis: Cu has the smallest size and, thus, it gets closer than Ag or Au to the empty site of the Mg^{2+} ion. In such a way, it can interact with the O^{2-} ion beneath it and also with the other three O^{2-} ions at the borders of the vacancy. On the other hand, Ag and Au are too big to get close to the empty site of the Mg^{2+} ion and move toward the center of the vacancy, still keeping an appreciable interaction with the four O^{2-} surrounding ions. These considerations are confirmed by the amount of the MgO lattice "back relaxation", that is, the distortion energy of the lattice in the configuration optimally interacting with the metal atom with respect to the isolated relaxed defect,

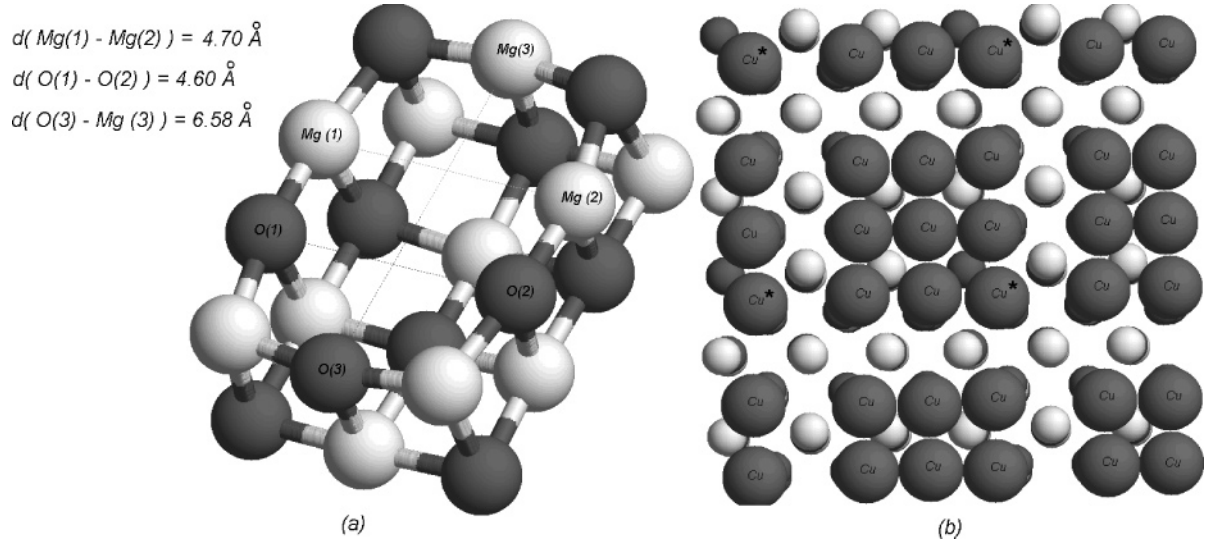

Figure 4. (a) Relaxed geometry of the oxide surface around the divacancy. (b) Cu_9 island formation; the Cu* atoms are the ones absorbed upon the vacancy.

Table 11. Interaction Energies and Characteristic Distances of the Isolated Adatoms on the Double Vacancy

adatoms	Cu	Ag	Au
E_{int} (eV)	2.83	1.95	2.34
E_{adh} (eV)	3.94	2.47	2.90
ΔE_{MgO} (eV)	1.11	0.522	0.568
ΔE_{relax} (eV)	0.778	0.454	0.481
h_o (Å)	0.189	0.547	0.501
distance from Mg site (Å)	0.176	0.585	0.781

expressed as ΔE_{MgO} in Table 11. In the case of Cu, the relaxed oxide lattice *closes* around the metal atom (ΔE_{MgO} has a value of 1.11 eV) much more than for Ag and Au. Finally, it can be noted that the values of ΔE_{relax} are roughly proportional to the values of ΔE_{MgO}, in agreement with a quadratic expansion of the interaction energy (see, e.g., ref 116).

III.B. Dimers. Whatever the starting configuration, all the coinage metal dimers relaxed to a configuration with the two atoms of the molecule atop the two empty sites of the vacancy. This behavior is analogous to the absorption of the Pd dimer on the double vacancy.[100] The remarkable stability of this configuration is due to the fact that the two atoms can interact with the three O^{2-} ions and the three Mg^{2+} ions at the border of the cavity; both atoms of the metal cluster can get close to the surface thanks to the big dimensions of the cavity. Our results are reported in Table 10.

The order of stability among the coinage metals is the same as that for the absorption of the single adatom; furthermore, also in this case, the smaller dimensions of the Cu dimer favor an enhanced backward movement of the oxide lattice around the cluster absorbed (see the values of ΔE_{MgO}). Again, the gain in interaction energy due to the relaxation of the oxide lattice (i.e., the values of ΔE_{relax}) are roughly proportional to ΔE_{MgO}, in fair agreement with the quadratic expansion theorem, showing that the system is roughly in the linear regime. This is further confirmed by the fact that the value of ΔE_{relax} is approximately proportional to the corresponding adhesion energy (ΔE_{adh}).

Table 12. Coinage Trimer Geometries on the Double Vacancy

	Cu_3		Ag_3		Au_3	
	A	B	A	B	A	B
d_{1-2} (Å)	2.49	2.44	2.68	2.70	2.63	2.64
d_{2-3} (Å)	2.47	2.61	2.76	2.82	2.65	2.61
d_{1-3} (Å)	2.38	2.39	2.80	2.79	2.81	2.91
h_1 (Å)[a]	0.217	0.255	0.789	0.808	1.13	1.15
h_2 (Å)[b]	1.56	1.67	2.17	2.17	1.82	1.84
h_3 (Å)	2.68	2.05	3.55	2.92	3.73	3.10

[a] Height of the atom atop the Mg^{2+} empty site. [b] Height of the atom atop the O^{2-} empty site

Table 13. Energies for the Trimers on the Double Vacancy

	Cu_3		Ag_3		Au_3	
	A	B	A	B	A	B
E_{int} (eV)	6.90	7.09	5.19	5.20	6.74	6.82
E_{adh} (eV)	4.65	5.00	3.23	3.28	4.11	4.26
ΔE_{met} (eV)	0.06	0.07	0.03	0.02	0.01	0.005
ΔE_{MgO} (eV)	1.09	1.24	0.60	0.65	0.96	1.03

III.C. Trimers. The geometries we considered are with two metal atoms on top of the two sites of the vacancy and the third metal atom either atop the other two (A), not in direct contact with the surface, or atop the O^{2-}(2) ion at the border of the cavity (B) (see Figure 4a for the nomenclature of the surface sites). The results of the calculations are reported in Tables 12 and 13.

The results for the three metals do not qualitatively differ very much: the two selected configurations are characterized by very similar values of the absorption energy, the distortion energies of the metallic clusters are quite small, and among the three coinage metals, the largest values are observed in the case of Cu, in agreement with the results of Sections I.C and II.C. As in the case of the interactions of the single atoms and dimers, the values of the distortion energy of the surface lattice are largest in the case of the absorption of Cu clusters

Table 14. One and Two MLs Absorbed on the Double Vacancy

	1 ML			2 ML		
	Cu	Ag	Au	Cu	Ag	Au
$\langle E_{int} \rangle$ (eV)	2.19	1.81	2.31	2.85	2.18	2.73
$\langle E_{adh} \rangle$ (eV)	0.47	0.25	0.31	0.78	0.32	0.50
$\langle \Delta E_{met} \rangle$ (eV)	−0.17	0.05	0.02	−0.02	−0.03	0.02
ΔE_{MgO} (eV)	0.70	0.29	0.67	1.37	0.67	1.00

[a] Distance of the metal atom atop the vacancy. [b] Distance of the metal atom atop an O ion at 2.97 Å away from the vacancy. [c] Distance of the metal atom atop an O ion at 4.21 Å away from the vacancy.

(because of the smaller dimensions of the Cu atom) and smallest in the case of Ag.

III.D. Extended Deposition. These results are reported in Table 14. The study of one (two) ML absorption above the double-vacancy defected MgO surface involves a heavy calculation implying the full relaxation of all the 61 (70) atoms per unit cell. For all three metals considered, a spin-restricted ground state was found. The chosen geometry is a pseudomorphic one with each metal atom atop a different O^{2-} ion of the surface layer. The particularity of this configuration is that one metal atom is put on top of the site of the vacancy with the weaker interaction (the empty O site).

The results of the calculations are discussed separately for the three coinage metals because of their peculiar behavior. Starting with Ag, for the which the discussion is simpler, we note that Ag is characterized by a good match between the lattice constant of the metallic layer and that of the oxide support. Moreover, Ag has a weaker interaction energy with the surface (both regular and defected) and a weaker metallic bond with respect to Au and Cu. The small value of ΔE_{MgO} (only 0.29 eV for one ML) and the fact that the metal atoms essentially maintain their starting positions suggest that the layer does not interact very much, even with the defected surface. In particular, the Ag atom atop the vacancy relaxes by simply decreasing its distance from the surface. The adhesion energy is quite low: 2.25 eV for nine atoms. If we take a value of 0.16 eV as the interaction energy of the eight atoms on the regular sites (the value characterizing the interaction with the regular surface), we obtain by difference that the atom atop the defect contributes about 0.9−1.0 eV, a value appreciably smaller than that for the absorption of the single atom on the divacancy (see Table 11).

Au, too, is characterized by a good match between the lattice constants of the metal and that of the oxide. However, Au interacts more strongly than Ag with the regular and defected surface sites of the surface and, at the same time, has a stronger metallic bond. The Au monolayer, thus, presents a more pronounced corrugation; in particular, the atom atop the empty O site remarkably decreases its distance from the surface (with a consequent weakening of its metal bonding), while the three Au atoms at the border of the vacancy move slightly inward. What we observe is a segregation of the metal slab with the formation of islands of nine atoms with the divacancy placed at one edge of the square (see Figure 4b for the case of Cu, in which this effect is even more pronounced). The stronger interaction with the surface is reflected in the larger value of the lattice distortion energy with respect to the Ag case.

The Cu monolayer exhibits the same behavior encountered in the Au case but in a more pronounced way. The larger mismatch between the Cu lattice constant and the surface lattice parameter and the stronger interaction of the Cu atom with the divacancy, in fact, determine a strong segregation of the metal slab with the formation of nine-atom islands (see Figure 4b). From the data of ΔE_{met} in Table 14, we observe that the formation of islands is accompanied by a strengthening of the metallic bond with respect to the pseudomorphic configuration. Segregation is also expected to occur in the absence of the divacancy defect, but it is significant that the defect places itself at a border of the metal islands; this suggests a peripheral growth of the metal cluster with respect to the double vacancy (at variance with the F_s center case, in which the cluster is expected to grow all around the defect).

The absorption of the second metal layer above the first one determines an increase of the values of ΔE_{MgO} and E_{adh} for all the three coinage metals, essentially because of the metal-on-top mechanism. In the case of Ag, the deposition of the second layer does not affect the geometry of the metal slab and the increase in adhesion energy is on the same order of magnitude as in the case of absorption on the regular surface and on the F_s defect. In the case of Cu and Au, the presence of the second metal layer above the first one prevents the segregation observed in the case of the single monolayer, thus increasing the direct interaction of the first metal slab with the surface and the metal-on-top effect. The increase in adhesion energy is consequently larger than in the case of absorption on the regular terrace and that on the single vacancy.

4. Conclusions

The results of a systematic study of the interaction of small coinage metal clusters (M_n, $n = 1-3$) and extended deposition (one and two ML) with the regular and locally defected (F_s center and divacancy) neutral MgO(100) surface are presented. These results can be summarized as follows, underlining analogies and differences between the three coinage metals.

In agreement with previous work,[65−67] the most stable site of nucleation on the regular surface for all the isolated adatoms is the O^{2-} ion. The interaction energy is larger in the case of Cu and Au with respect to Ag. This order of interaction energies is found to hold for nearly all the systems considered. In the dimers, the metal chemical bond is stronger than the interaction with the surface and the "sticky" character of the metallic bond prevents the stretching of the metal−metal distance from the equilibrium value characterizing the isolated dimers. The most stable configuration is perpendicular to the surface. Despite the fact that only one atom interacts with the surface, the adhesion energy of the cluster is larger than that for the single adatom, which suggests that the presence of metal atoms *on-top* of those directly interacting with the surface *increases* the adhesion energy ("metal-on-top" stabilization mechanism). A peculiar characteristic of the coinage metal trimers is their fluxional

behavior, originating from the Jahn−Teller symmetry breaking due to the electronic configuration of these molecules. As in the case of the dimers, the configurations perpendicular to the surface are the most stable ones ("metal-on-top" stabilization mechanism). Nevertheless, thanks to their fluxionality, the trimers manage to optimize both the metallic bond and the adhesion with the surface in several different configurations. The consequently small energy differences between the corresponding local minima allow the diffusion of the clusters on the surface even at rather low temperatures. This is particularly true for Ag and Au, which are characterized by longer intermetal bond lengths with respect to Cu and a, thus, smaller mismatch with the oxide lattice parameter.

For the absorption of extended pseudomorphic deposition (one and two ML), Ag[83,103,104] and Au are characterized by a good match between the bulk metal lattice constant and the lattice constant of the oxide pattern. The strength of the metallic bond then determines a decrease of the adhesion energy with the surface in passing from small clusters to extended deposition, especially in the case of Au, for the which the metallic bond is stronger and "stickier".[57] Instead, the mismatch between the lattice parameters of the Cu overlayer and the surface determines a smaller decrease of the adhesion energy with the surface.[83,103,104] For all three coinage metals, the thickening of the metal slab from one to two MLs determines an increase of the adhesion energy per atom in agreement with the "metal-on-top" stabilization mechanism.

In the case of the F_s center and the double vacancy, it is found that these defects act as strong trapping centers for small clusters and strongly increase the adhesion of metal slabs to the surface in the case of extended deposition.[67,108] The main difference between the two defects is that the presence of the double vacancy induces a strong structural and energetic modification in the surrounding oxide lattice;[67] moreover, such a structural relaxation changes according to the extent of the metal deposition upon the surface. On the contrary, the presence of the single vacancy induces negligible structural and energetic modifications of the oxide lattice both in the absence and in the presence of the metal deposition.

In the case of the single vacancy, the metal atoms can get closer to the surface because of the decreased Pauli repulsion consequent to the removal of the O atom.[103] The adhesion energy is stronger for Au than for Cu and Ag; since the dimensions and the polarizability of the gold atom are similar to those of Ag, this suggests that chemical bonding effects are important for Au. The most stable configurations of dimers and trimers are, again, those in which the cluster is perpendicular to the surface, with one of the lower atoms directly atop the vacancy. In the case of extended deposition, the atom atop the vacancy is weakly involved in the metallic bond. In the case of the two ML absorption, we observe an increase of the adhesion energy in the case of Cu and Ag but not for Au, for which the distortion of the metal structure overwhelms the stabilization as a result of the thickening of the metal slab.

In the case of the double vacancy, the metal atoms are free to choose between the two possible sites of the vacancy (the empty Mg site or the empty O site). Ag and Au, which are bigger than Cu, move toward the center of the cavity in order to reduce the Pauli repulsion with the O^{2-} ions at the border. Cu, instead, absorbs near the empty Mg site and, consequently, interacts much more strongly with the surface. In the case of the dimers and trimers, two metal atoms occupy the two empty sites of the surface. In the case of extended deposition, the pseudomorphic growth is disfavored by the fact that the metal atom directly above the cavity is atop the O empty site. For Cu and Au, this, together with the mismatch between the Cu lattice parameter of the metal and that of the oxide, induces the formation of segregated metal islands with the cavity at one of the corners. This effect is decreased in the two ML case, in which the adhesion energy increases appreciably for all three coinage metals.

To briefly summarize, we find that coinage metals can easily diffuse on the perfect MgO(100) surface, with small clusters diffusing even faster than single atoms, to be strongly trapped at local defects, such as the F_s center and the divacancy, which can, thus, act as nucleation centers. The presence of metal atoms above those directly interacting with the surface increases the adhesion energy, according to a "metal-on-top" mechanism, for both perfect and defected oxide. A peculiar structural relaxation is found for the divacancy, which suggests a "peripheral" growth of the metal clusters.

Acknowledgment. We thank Gianfranco Pacchioni (Milano, Italy) and Riccardo Ferrando (Genova, Italy) for useful discussions. We acknowledge financial support from the Italian CNR for the project "(Supra-)Self-Assemblies of Transition Metal Nanoclusters" within the framework of the ESF EUROCORES SONS and from the European Community Sixth Framework Programme for the STREP project "Growth and Supra-Organization of Transition and Noble Metal Nanoclusters" (Contract NMP4-CT-2004-001594). A.F. acknowledges the Italian INSTM for a grant at the CINECA supercomputing center. (After the manuscript was submitted, we learned of a related work on Au small clusters absorbed on regular and defected MgO surfaces[117]).

Acknowledgment. This section tagged Supporting Information

Supporting Information Available: Additional data on configurations. This material is available free of charge via the Internet at http://pubs.acs.org.

References

(1) Aiken, J. D., III; Finke, R. G. *J. Mol. Catal. A* **1999**, *145*, 1−44.

(2) Jensen, P. *Rev. Mod. Phys*. **1999**, *71*, 1695−1735.

(3) Henry, C. R. *Surf. Sci*. **1998**, *31*, 235−325.

(4) Pileni, M.-P. *J. Phys. Chem. B* **2001**, *105*, 3358−3371.

(5) Henry, C. R.; Meunier, M. *Mater. Sci Eng*., A **1996**, *A217/218*, 239−243.

(6) Leroy, F.; Revenant, C.; Renaud, G.; Lazzari, R. *Appl. Surf. Sci.* **2004**, *238*, 233−237.

(7) Revenant, C.; Leroy, F.; Lazzari, R.; Renaud, G.; Henry, C. R. *Phys. Rev. B* **2004**, *69*, 035411.

(8) Renaud, G. *Surf. Sci. Rep*. **1998**, *32*, 1−90.

(9) Renaud, G. *Science* **2003**, *300*, 1416−1419.

(10) Thornton, G. *Science* **2003**, *300*, 1378−1379.

(11) Hansen, K. H.; Ferrero, S.; Henry, C. R. *Appl. Surf. Sci.* **2004**, *226*, 167−172.

(12) Becker, C.; Rosenhahn, A.; Wiltner, A.; Von Bergmann, K.; Schneider, J.; Pervan, P.; Milun, M.; Kralj, M.; Wandelt, K. *New J. Phys*. **2004**, *4*, 75.1−75.15.

(13) Degen, S.; Becker, C.; Wandelt, K. *Faraday Discuss*. **2004**, *125*, 343−356.

(14) Becker, C.; Von Bergmann, K.; Rosenhahn, A.; Schneider, J.; Wandelt, K. *Surf. Sci.* **2001**, *486*, L443−L448.

(15) Wiltner, A.; Rosenhahn, A.; Schneider, J.; Becker, C.; Pervan, P.; Milun, M.; Kralj, M.; Wandelt, K. *Thin Solid Films* **2001**, *400*, 71−75.

(16) Xu, C.; Oh, W. S.; Liu, G.; Kim, D. Y.; Goodman, D. W. *J. Vac. Sci. Technol., A* **1997**, *15*, 1261−1268.

(17) Yoon, B.; Luedtke, W. D.; Gao, J.; Landman, U. *J. Phys. Chem. B* **2003**, *107*, 5882−5891.

(18) Bréchignac, C.; Cahuzac, P.; Carlier, F.; Colliex, C.; Leroux, J.; Masson, A.; Yoon, B.; Landman, U. *Phys. Rev. Lett.* **2002**, *88*, 196103.

(19) Moseler, M.; Hakkinen, H.; Landman, U. *Phys. Rev. Lett*. **2002**, *89*, 176103.

(20) Campbell, C. T.; Starr, D. *J. Am. Chem. Soc*. **2002**, *124*, 9212−9218.

(21) Kim, Y. D.; Stultz, J.; Wei, T.; Goodman, D. W. *J. Phys. Chem. B* **2002**, *106*, 6827−6830.

(22) Larsen, J. H.; Ranney, J. T.; Starr, D. E.; Musgrove, J. E.; Campbell, C. T. *Phys. Rev. B* **2001**, *63*, 195410.

(23) Suzuki, T.; Hishita, S.; Oyoshi, K.; Souda, R. *Surf. Sci.* **1999**, *442*, 291−299.

(24) Schaffner, M. H.; Patthey, F.; Schneider, W. D. *Surf. Sci.* **1998**, *417*, 159−167.

(25) Barbier, A.; Renaud, G.; Jupille, J. *Surf. Sci*. **2000**, *454*−*456*, 979−983.

(26) Stracke, P.; Krischok, S.; Kempter, V. *Surf. Sci.* **2001**, *473*, 86−96.

(27) Lagarde, P.; Colonna, S.; Flank, A. M.; Jupille, J. *Surf. Sci.* **2003**, *524*, 102−112.

(28) Abbet, S.; Ferrari, A. M.; Giordano, L.; Pacchioni, G.; Hakkinen, H.; Landman, U.; Heiz, U. *Surf. Sci.* **2002**, *514*, 249−255.

(29) Musolino, V.; Selloni, A.; Car, R. *Phys. Rev. Lett*. **1999**, *83*, 3242−3245.

(30) Musolino, V.; Selloni, A.; Car, R. *J. Chem Phys*. **1998**, *108*, 5044−5054.

(31) Musolino, V.; Del Corso, A.; Selloni, A. *Phys. Rev. Lett*. **1999**, *83*, 2761−2764.

(32) Musolino, V.; Selloni, A.; Car, R. *Surf. Sci.* **1998**, *402*−*404*, 413−417.

(33) Hakkinen, H.; Barnett, R. N.; Landman, U. *Phys. Rev. Lett*. **1999**, *82*, 3264−3267.

(34) Landman, U.; Luedtke, W. D. *Faraday Discuss.* **2004**, *125*, 1−22.

(35) Pileni, M.-P. *C. R. Chimie* **2003**, *6*, 965−978.

(36) Pileni, M. P.; Lalatonne, Y.; Ingert, D.; Lisiecki, I.; Coutry, A. *Faraday Discuss*. **2004**, *125*, 251−264.

(37) Shibata, T. *J. Am. Chem. Soc* **2002**, *124*, 11989−11996.

(38) Kreibig, U.; Vollmer, M. *Optical Properties of Metal Clusters*; Springer: Berlin, 1995.

(39) Sanchez, A.; Abbet, S.; Heiz, U.; Schneider, W. D.; Hakkinen, H.; Barnett, R. N.; Landman, U. *J. Phys. Chem. A* **1999**, *103*, 9573−9578.

(40) Hakkinen, H.; Landman, U. *J. Am. Chem. Soc*. **2001**, *123*, 9704−9705.

(41) Socaciu, L. D.; Hagen, J.; Bernhardt, T. M.; Woste, L.; Heiz, U.; Hakkinen, H.; Landman, U. *J. Am. Chem. Soc*. **2003**, *125*, 10437−10445.

(42) Del Vitto, A.; Sousa, C.; Illas, F.; Pacchioni, G. *J. Chem. Phys*. **2004**, *121*, 7457−7466.

(43) Garzon, I. L.; Beltran, M. R.; Gonzalez, G.; Gutierrez-Gonzales, I.; Michaelian, K.; Reyes-Nava, J. A.; Rodriguez-Hernandez, J. I. *Eur. Phys. J. D* **2003**, *24*, 105−109.

(44) Roman-Velasquez, C. E.; Noguez, C.; Garzon, I. L. *J. Phys. Chem. B*, **2003**, *107*, 12035−12038.

(45) Robach, O.; Renaud, G.; Barbier, A. *Surf. Sci*. **1998**, *401*, 227−235.

(46) *Progress in Experimental and Theoretical Studies of Clusters*; Kondow, T., Mafuné, F., Eds.; World Scientific: New York, 2003.

(47) Bravo-Perez, G.; Garzon, I. L.; Novaro, O. *THEOCHEM* **1999**, *493*, 225−231.

(48) Aprà, E.; Fortunelli, A. *J. Phys. Chem. A* **2003**, *107*, 2934−2942.

(49) Fortunelli, A.; Velasco, A. M. *THEOCHEM* **2002**, *586*, 17−27.

(50) Aprà, E.; Fortunelli, A. *THEOCHEM* **2000**, *501*−*502*, 251−259.

(51) Fortunelli, A. *THEOCHEM* **1999**, *493*, 233−240.

(52) Yannouleas, C.; Landman, U.; Herlert, A.; Schweikhard, L. *Phys. Rev. Lett*. **2001**, *86*, 2996−2999.

(53) Yoon, B.; Hakkinen, H.; Landman, U. *J. Phys. Chem. A* **2003**, *107*, 4066−4071.

(54) Hakkinen, H.; Landman, U. *Phys. Rev. B* **2000**, *62*, R2287−R2290.

(55) Cleveland, C. L.; Luedtke, W. D.; Landman, U. *Phys. Rev. B*, **1999**, *60*, 5065−507.7

(56) Wolf, M. D.; Landman, U. *J. Phys. Chem. A* **1998**, *102*, 6129−6137.

(57) Baletto, F.; Ferrando, R.; Fortunelli, A.; Montalenti, F.; Mottet, C. *J. Chem. Phys.* **2002**, *116*, 3856−3863.

(58) Baletto, F.; Mottet, C.; Ferrando, R. *Phys. Rev. Lett*. **2000**, *84*, 5544−5547.

(59) Baletto, F.; Mottet, C.; Ferrando, R. *Phys. Rev. B* **2002**, *66*, 1−11.

(60) Rossi, G.; Mottet, C.; Fortunelli, A.; Baletto, F.; Ferrando, R. *Phys. Rev. Lett*. **2004**, *93*, 105503.

(61) Garzon, I. L.; Kaplan, I. G.; Santamaria, R.; Novaro, O. *J. Chem. Phys*. **1998**, *109*, 2176−2184.

(62) Garzon, I. L.; Michaelian, K.; Beltran, M. R.; Posada-Amarillas, A.; Ordejon, P.; Artacho, E.; Sanchez-Portal, D.; Soler, J. M. *Phys. Rev. Lett.* **1998**, *81*, 1600−1603.

(63) Garzon, I. L.; Michaelian, K.; Beltran, M. R.; Posada-Amarillas, A.; Ordejon, P.; Artacho, E.; Sanchez-Portal, D.; Soler, J. M. *Eur. Phys. J. D* **1999**, *9*, 211−215.

(64) Michaelian, K.; Rendon, N.; Garzon, I. L. *Phys. Rev. B* **1999**, *60*, 2000−2010.

(65) Yudanov, I. V.; Vent, S.; Neyman, K.; Pacchioni, G.; Rosch, N. *Chem. Phys. Lett*. **1997**, *275*, 245−252.

(66) Neyman, K. M.; Vent, S.; Pacchioni, G.; Rosch, N. *Nuovo Cimento* **1997**, *19*, 1743−1748.

(67) Matveev, A. V.; Neyman, K. M.; Yudanov, I. V.; Rosch, N. *Surf. Sci*. **1999**, *426*, 123−139.

(68) Neyman, K. M., Inntam, C.; Nasluzov, V. A.; Kosarev, R.; Rosch, N. *Appl. Phys. A* **2004**, *78*, 823−828.

(69) Markovits, A.; Skalli, M. K.; Minot, C.; Pacchioni, G.; Lopez, N.; Illas, F. *J. Chem. Phys.* **2001**, *115*, 8172−8177.

(70) Menetrey, M.; Markovits, A.; Minot, C.; Del Vitto, A.; Pacchioni, G. *Surf. Sci*. **2004**, *549*, 294−304.

(71) Chiesa, M.; Paganini, M. C.; Giamello, E.; Di Valentin, C.; Pacchioni, G. *Angew. Chem., Int. Ed.* **2003**, *42*, 1759−1761.

(72) Pacchioni, G. *ChemPhysChem* **2003**, *4*, 1041−1047.

(73) Dominguez-Ariza, D.; Sousa, C.; Illas, F.; Ricci, D.; Pacchioni, G *Phys. Rev. B* **2003**, *68*, 054101.

(74) Ricci, D.; Di Valentin, C.; Pacchioni, G.; Sushko, P. V.; Shluger, A. L.; Giamello, E. *J. Am. Chem. Soc*. **2003**, *125*, 738−747.

(75) Ricci, D.; Pacchioni, G.; Sushko, P. V.; Shluger, A. L. *J. Chem. Phys*. **2002**, *117*, 2844−2851.

(76) Soave, R.; Ferrari, A. M.; Pacchioni, G. *J. Phys. Chem. B* **2001**, *105*, 9798−9804.

(77) Pacchioni, G. *Solid State Sci.* **2000**, 2, 161−179.

(78) Pacchioni, G.; Ferrari, A. M. *Catal. Today* **1999**, *50*, 533−540.

(79) Sousa, C.; Pacchioni, G.; Illas, F. *Surf. Sci*. **1999**, *429*, 217−228.

(80) Pacchioni, G.; Pescarmona, P. *Surf. Sci.* **1998**, *412/413*, 657−671.

(81) Pacchioni, G.; Ferrari, A. M.; Ieranò, G. *Faraday Discuss*. **1997**, *106*, 155−172.

(82) Giamello, E.; Paganini, M. C.; Murphy, D. M.; Ferrari, A. M.; Pacchioni, G. *J. Phys. Chem. B* **1997**, *101*, 971−982.

(83) Fucks, D.; Dorfman, S.; Kotomin, E. A.; Zhukovskii, Y. F.; Stoneham, M. *Phys. Rev. Lett*. **2000**, *85* (20), 4333−4336.

(84) Kuzovkov, V. N.; Popov, A. I.; Kotomin, E. A.; Monge, M. A.; Gonzalez, R.; Chen, Y. *Phys. Rev. B* **2001**, *64*, 1−5.

(85) Giordano, L.; Goniakowski, J.; Pacchioni, G. *Phys. Rev. B* **2001**, *75*, 1−9.

(86) Lopez, N.; Illas, F.; Rosch, N.; Pacchioni, G. *J. Chem. Phys*. **1999**, *110*, 4873−4879.

(87) Worz, A. S.; Judai, K.; Abbet, S.; Antonietti, J. M.; Heiz, U.; Del Vitto, A.; Giordano, L.; Pacchioni, G. *Chem. Phys. Lett.* **2004**, *399*, 266−270.

(88) Giordano, L.; Del Vitto, A.; Pacchioni, G.; Ferrari, A. M. *Surf. Sci*. **2003**, *540*, 63−75.

(89) Abbet, S.; Riedo, E.; Brune, H.; Heiz, U.; Ferrari, A. M.; Giordano, L.; Pacchioni, G. *J. Am. Chem. Soc*. **2001**, *123*, 6172−6178.

(90) Abbet, S.; Heiz, U.; Ferrari, A. M.; Giordano, L.; Di Valentin, C.; Pacchioni, G. *Thin Solid Films* **2001**, *400*, 37−42.

(91) Neyman, K.; Rosch, N.; Pacchioni, G. *Appl. Catal., A* **2000**, *191*, 3−13.

(92) Abbet, S.; Sanchez, A.; Heiz, U.; Schneider, W. D.; Ferrari, A. M.; Pacchioni, G.; Rosch, N. *J. Am. Chem. Soc*. **2000**, *122*, 3453−3457.

(93) Pacchioni, G.; Rosch, N. *J. Chem. Phys.* **1996**, *104*, 7329−7337.

(94) Neyman, K. M.; Vent, S.; Rosch, N.; Pacchioni, G. *Top. Catal*. **1999**, *9*, 153−161.

(95) Matveev, A. V.; Neyman, K. M.; Pacchioni, G.; Rosch, N. *Chem. Phys. Lett*. **1999**, *299*, 603−612.

(96) Ferrari, A. M.; Xiao, C.; Neyman, K. M.; Pacchioni, G.; Rosch, N.; *Phys. Chem. Chem. Phys*. **1999**, *1*, 4655−4661.

(97) Giordano, L.; Pacchioni, G.; Ferrari, A. M.; Illas, F.; Rosch, N. *Surf. Sci*. **2001**, *473*, 213−226.

(98) Giordano, L.; Pacchioni, G.; Illas, F.; Rosch, N. *Surf. Sci*. **2002**, *499*, 73−84.

(99) Di Valentin, C.; Giordano, L.; Pacchioni, G.; Rosch, N. *Surf. Sci.* **2003**, *522*, 175−184.

(100) Giordano, L.; Di Valentin, C.; Goniakowski, J.; Pacchioni, G. *Phys. Rev. Lett*. **2004**, *92*, 096105.

(101) Oviedo, J.; Sanz, J. F.; Lopez, N.; Illas, F. *J. Phys. Chem. B* **2000**, *104*, 4342−4348.

(102) Goniakowski, J. *Phys. Rev. B* **1998**, *58*, 1189−1192.

(103) Zhukovskii, Y. F.; Kotomin, E. A.; Fucks, D.; Dorfman, S. *Superlattices Microstruct.* **2004**, *36*, 63−72.

(104) Zhukovskii, Y. F.; Kotomin, E. A.; Jacobs, P. W. M.; Stoneham, A. M. *Phys. Rev. Lett*. **2000**, *84*, 1256−1259.

(105) Zhukovskii, Y. F.; Kotomin, E. A.; Fucks, D.; Dorfman, S.; Stoneham, A. M.; Sychev, O.; Borstel, G. *Appl. Surf. Sci*. **2004**, *226*, 298−305.

(106) Zhukovskii, Y. F.; Kotomin, E. A.; Fucks, D.; Dorfman, S. *Surf. Sci*. **2004**, *566−568*, 122−129.

(107) Zhukovskii, Y. F.; Kotomin, E. A.; Jacobs, P. W. M.; Stoneham, A. M.; Harding, J. H. *J. Phys: Condens. Matter* **2000**, *12*, 55−66.

(108) Zhukovskii, Y. F.; Kotomin, E. A. *Phys. Status Solidi* **2005**, *2*, 347−350.

(109) Herschend, B.; Hermansson, K.; Alfredsson, M.; Zhukovskii, Y. F.; Kotomin, E. A.; Jacobs, P. W. M. *J. Phys. Chem. B* **2003**, *107*, 11893−11899.

(110) Fucks, D.; Dorfman, S.; Zhukovskii, Y. F.; Kotomin, E. A.; Stoneham, A. H. *Surf. Sci.* **2002**, *499*, 24−40.

(111) Vervisch, W.; Mottet, C.; Goniakovskii, J. *Phys. Rev. B* **2002**, *65*, 245411.

(112) Vervisch, W.; Mottet, C.; Goniakovskii, J. *Eur. Phys. J. D* **2004**, *24*, 311−314.

(113) Mottet, C.; Goniakovskii, J. *Surf. Sci*. **2004**, *566*−*568*, 443−450.

(114) Baroni, S.; Del Corso, A.; de Gironcoli, S.; Giannozzi, P. *PWscf*; Scuola Internazionale Superiore di Studi Avanzati and DEMOCRITOS National Simulation Center: Trieste, Italy. http://www.pwscf.org.

(115) Perdew, J. P.; Chevary, J. A.; Vosko, S. H.; Jackson, K. A.; Pederson, M. R.; Singh, D. J.; Fiolhais, C. *Phys. Rev. B* **1992**, *46*, 6671−6687.

(116) Fortunelli, A. *J. Phys. Chem.* **1995**, *99*, 9056−9061.

(117) Del Vitto, A.; Pacchioni, G.; Delbecq, F.; Sautet, P. *J. Phys. Chem. B* **2005**, 109, 8040−8048.

CT050073E

Quantum effects on the structure of pure and binary metallic nanoclusters

R. Ferrando,[1] A. Fortunelli,[2,*] and G. Rossi[1]
[1]*INFM and IMEM/CNR, Dipartimento di Fisica, Via Dodecaneso 33, Genova, I16146, Italy*
[2]*Molecular Modeling Laboratory, IPCF/CNR, Via G. Moruzzi 1, Pisa, I56124, Italy*
(Received 26 April 2005; published 24 August 2005)

A family of high-symmetry bimetallic clusters—recently shown to give rise to "magic" structures in the case of Ag-Cu and Ag-Ni nanoclusters—is investigated also in the case of Ag-Pd, Ag-Co, Au-Cu, Au-Ni, and Au-Co. Cluster structures obtained by global optimization within a semiempirical potential model are then reoptimized via density functional calculations. Sizes up to 45 atoms are considered. Ag-Cu, Ag-Ni, and Au-Ni clusters have some common characteristics. They present polyicosahedral character and achieve maximum stability at the Ag- and Au-rich compositions, when the structural arrangement is associated to a Ni(Cu)core-Ag(Au)shell chemical ordering. This is due both to the huge size mismatch between the components and a clear tendency of the larger atoms to segregate at the surface. In Au-Cu and Ag-Pd, clusters achieve their best stability at intermediate compositions, in agreement with the tendency of these metals to mix in the bulk phase. Finally, for Ag-Co and Au-Co, peculiar quantum effects favor intermediate compositions despite the fact that these metal phases separate in the bulk. These results are rationalized in terms of the interplay between electronic and volumetric effects on the structure of metallic nanoclusters.

DOI: 10.1103/PhysRevB.72.085449 PACS number(s): 61.46.+w, 73.22.−f, 31.10.+z

I. INTRODUCTION

Bimetallic nanoclusters have recently attracted increasing interest for their peculiar catalytic, optical, magnetic, electric, and mechanical properties.[1,2] Especially intriguing is the possibility of finely tuning the properties of nanoclusters not only by varying their size, but also their composition. Bimetallic catalysts are important in a number of practical processes, including automobile exhaust conversion and petroleum naphtha reforming. One of the major problems which arises in the study of these systems is their structural characterization, a prerequisite for a deeper understanding and modeling of their properties. In this respect, theoretical approaches can give a useful contribution by restricting the search to few structural candidates. However, the determination of the most favorable structures of bimetallic clusters is a formidable task, due to the huge amount of combinatorial possibilities which exponentially complicates the theoretical prediction.[3] Particular importance is then assumed by the study of those structures which possess high energetic stability, that might serve as building blocks for cluster-assembled materials.

In a previous work,[4] a family of polyicosahedral structures has been described, and has been shown to give rise to "magic" clusters (i.e., clusters of remarkable structural, electronic and thermodynamic stability) for Ag-Cu and Ag-Ni bimetallic particles with a low fraction of Cu or Ni occupying the interior of a core-shell arrangement. The structural stability of these core-shell clusters was rationalized in terms of (a) reduction of internal and surface bond strain with respect to pure clusters due to the size mismatch between the larger Ag atom and the smaller Cu and Ni atoms, (b) smaller Ag surface energy which favors segregation of the Ag atoms at the surface. These factors cause the remarkable stability of the (27,7) [and also (30,8) and (32,6)] "magic" polyicosahedral clusters.

As the pairs gold/silver and cobalt/nickel have similar radii, it is worthwhile investigating whether these findings can be extended to the Ag-Co, Ag-Pd, Au-Cu, Au-Ni, and Au-Co combinations. In the present paper density functional (DF) calculations are employed to study these systems. Our results confirm the strong tendency of small bimetallic clusters to alloying.[4] For all systems considered here, even for those that present a very strong tendency against mixing in the bulk phase, mixed cluster are energetically more favorable than pure ones.

In addition, we find that subtle quantum effects can modulate this propensity giving rise to interesting variations. The behavior of Au-Ni is similar to the behavior of Ag-Cu and Ag-Ni, namely with a tendency to favor core-shell polyicosahedral structures, as indicated by both formation and excess energies which have lower values for Au-rich compositions (corresponding to the Ni-core–Au-shell arrangement). On the other hand, Au-Cu clusters do not single out the core-shell arrangement as being especially favorable, since formation energies are almost constant for compositions extending from the Au-rich to the Cu-rich side. This is consistent with the tendency of Au-Cu to mix in the bulk phase, forming a series of ordered alloys. Also for Ag-Pd both Ag-rich and intermediate compositions present low excess energies, and a clear tendency to form polyicosahedral structures. Finally, for Ag-Co and Au-Co we show that magnetic effects destabilize the core-shell arrangement. In this case, polyicosahedral structures are again very stable, but peculiar quantum effects bring the minimum in the formation energies from Au- or Ag-rich to intermediate compositions, presenting a much more thorough intermixing of the two atoms. This behavior is at variance with the tendency of Ag-Co and Au-Co to separate in the bulk phase, and is peculiar of finite or confined systems (see, for example, the observation of alloyed Ag-Co thin films on crystal surfaces[5]). Band structure and shell-closure effects on the geometries of pure metallic clusters are also found.

In Sec. II we briefly sketch the computational method. In Sec. III we describe polyicosahedral clusters and define the

quantities which are used to characterize the energetic stability of mixed clusters. Sections IV and V are devoted to the results. Before dealing with mixed systems, in Sec. IV we consider the pure clusters whose properties serve as a starting point for studying mixed clusters. Section V reports the results about mixed systems. Finally, Sec. VI contains the discussion and conclusions.

II. COMPUTATIONAL METHOD

The density functional calculations are carried out with the DF module of the NWChem package (release 4.5),[7] and use the Becke functional[8] for exchange and the Perdew-Wang functional[9] for correlation. $(7s6p6d)/[5s3p2d]$ Gaussian-type-orbital basis sets and effective core potentials are used for all elements, derived from Refs. 10 and 11 for Ag and Ref. 12 for Cu, Ni, and Co, and modified combining the suggestions in ftp://ftp.chemie.uni-karlsruhe.de/pub/basen and Ref. 13. Charge density fitting $(11s4p5d3f4g)/[11s4p4d3f2g]$ Gaussian-type-orbital basis sets were used to compute the Coulomb potential.[14] All the calculations have been performed spin-unrestricted, and using a Gaussian-smearing technique[15] for the fractional occupation of the one-electron energy levels, which improved the self-consistent convergence process, ensured that the final spin state was a local minimum in the spin space, avoided symmetry-breaking issues for Jahn-Teller systems, and did not affect the value of the energy as in almost all cases the one-electron energy gap was larger than the chosen smearing parameter $\sigma=0.02$ eV. A numerical grid of 65 radial points and 350 points for the angular part was used for evaluating the exchange-correlation potential and energy. The geometry optimization was stopped when the numerical force on atoms was less than 4×10^{-4} a.u. More details on the numerical procedure can be found in Ref. 13.

The initial configurations for DFT relaxation are provided by a genetic global-optimization procedure[4] unless otherwise specified.

III. STRUCTURAL FAMILIES AND ENERGETIC STABILITY INDEXES

The structures which are considered in the present work are depicted in Figs. 1–3. In particular, we focus attention on polyicosahedral (pIh) clusters, which are built by packing elementary icosahedra (Ih) of 13 atoms as described in Ref. 4. In the following, a pIh of size N, made of N_1 Ag or Au (large) atoms and $N_2=N-N_1$ Cu, Ni, Pd or Co (small) atoms, and comprising m interpenetrating Ih_{13} will be referred to as (N_1,N_2)pIh^m. These structures are very compact and exhibit a large number of bonds. However, inner atoms have nearest-neighbor distances which are very compressed with respect to the nearest-neighbor distance between surface atoms, so that these configurations are not favored in pure clusters. They become very competitive when their internal core is substituted with metal atoms of a smaller size, due to the combined effect of decrease in strain and the surface segregation of the metal with lower surface energy. Interestingly, the (27,7)pIh^7 structure—which in Ref. 4 resulted to be the stablest in the pIh family—has first been found as the lowest-energy isomer of pure Al_{34},[6] in this case the pIh structure is favored by the presence of a second minimum in the interaction potential at roughly the second-neighbor distance. As we shall see in the following also high-stability cagelike structures (which are found in gold clusters) are closely related to polyicosahedral structures.

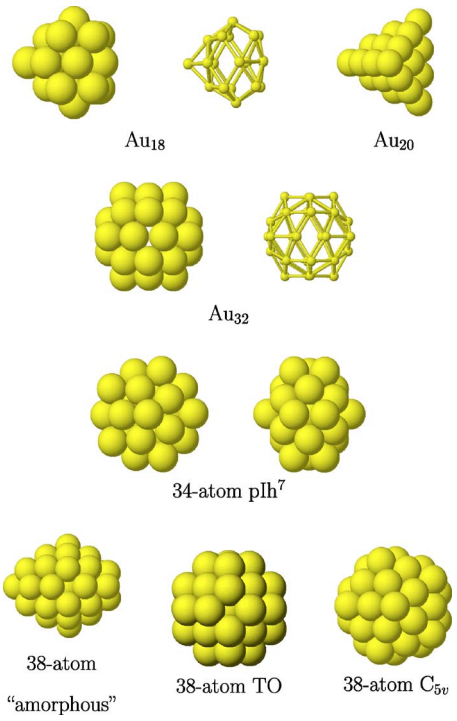

FIG. 1. (Color online) Schematic pictures of pure metallic clusters considered in this work.

Other structures of importance for clusters in this size range are the following. First of all, the truncated octahedron (TO) of 38 atoms (TO_{38}), which is simply a piece of fcc bulk

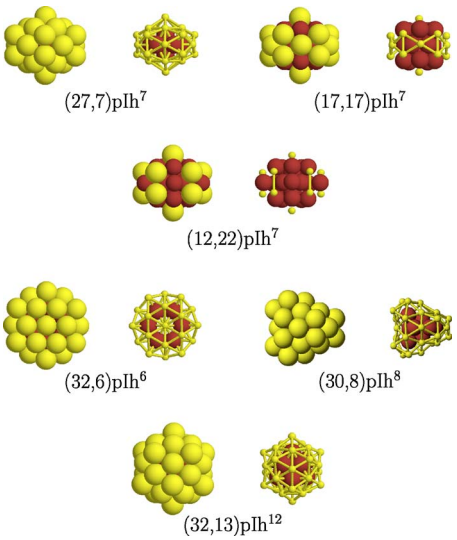

FIG. 2. (Color online) Schematic pictures of mixed bimetallic clusters considered in this work. Light grey atoms are either Ag or Au, whereas darker atoms are either Cu, Ni, Pd, or Co.

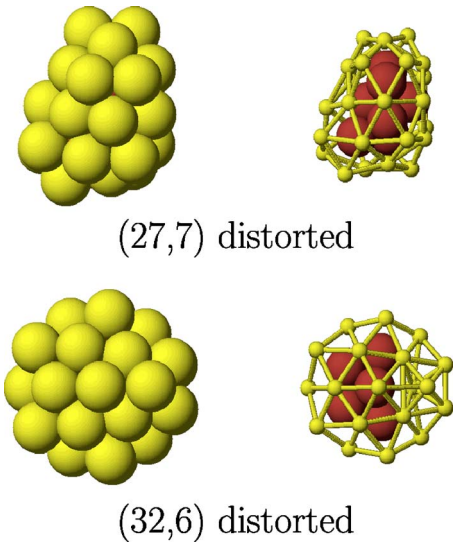

FIG. 3. (Color online) Schematic pictures of mixed bimetallic clusters considered in this work. Here the distorted structures are shown for the case Ag-Cu. Light grey atoms are either Ag, whereas darker atoms are Cu.

lattice and is a putative global minumum for silver, copper, and nickel clusters according to semiempirical potential calculations.[4,16] Then, the low-symmetry cluster of size 38, which is a putative global minimum for gold.[17] Finally, another cluster of size 38 which is obtained as a fragment of the icosahedron of 55 atoms. This fragment has C_{5v} symmetry group, and, according to semiempirical potential calculations,[18] is the second isomer for both Ag and Cu, being however quite close in energy to the TO_{38}.

The criterion that we use for comparing the relative stability of clusters with a different number of atoms is the excess energy with respect to N bulk atoms, divided by $N^{2/3}$,

$$\Delta = \frac{E_{\mathrm{DF}}^{N_1,N_2} - N_1\varepsilon_1^{\mathrm{coh}} - N_2\varepsilon_2^{\mathrm{coh}}}{N^{2/3}}, \qquad (1)$$

where N_1 and $\varepsilon_1^{\mathrm{coh}}$ are the number and the bulk cohesive energy of one metallic species, whereas $N_2=N-N_1$ and $\varepsilon_2^{\mathrm{coh}}$ are the same quantities for the other metallic species, and $E_{\mathrm{DF}}^{N_1,N_2}$ is the DF binding energy for the given cluster, identified by its size and composition. Stable structures are identified by low Δ values. For the cohesive energies we take the experimental values (in eV), $\varepsilon_{\mathrm{Cu}}^{\mathrm{coh}}=3.50, \varepsilon_{\mathrm{Ag}}^{\mathrm{coh}}=2.95, \varepsilon_{\mathrm{Au}}^{\mathrm{coh}}=3.82, \varepsilon_{\mathrm{Ni}}^{\mathrm{coh}}=4.47, \varepsilon_{\mathrm{Co}}^{\mathrm{coh}}=4.45, \varepsilon_{\mathrm{Pd}}^{\mathrm{coh}}=3.89$. Δ is the excess energy divided by $N^{2/3}$. $N^{2/3}$ is roughly proportional to the number of surface atoms in the cluster.

However, Δ may be a biased quantity when comparing clusters of the same size but different compositions. For example, as we shall see in the following, pure gold clusters present large Δ, whereas pure copper clusters have much lower Δ. This means that when comparing Au-Cu clusters, those with Au-rich compositions will present larger Δ. To avoid this bias, we use also other energetic stability indexes, Δ_{34} and Δ_{38}, defined in such a way that their value for pure clusters is zero (or small anyway) for sizes 34 and 38, respectively. Let us consider, for example, Δ_{38}. At this size, we consider pure TO_{38} clusters of the two species 1 and 2, and calculate their binding energies per atom $\varepsilon_1(TO_{38})$ and $\varepsilon_2(TO_{38})$. Then we define Δ_{38} as

$$\Delta_{38} = E_{\mathrm{DF}}^{N_1,N_2} - N_1\varepsilon_1(TO_{38}) - N_2\varepsilon_2(TO_{38}), \qquad (2)$$

Δ_{34} is defined in the same way, but taking the energies per atom of pure 34-atom pIh^7 clusters. Clusters with negative values of Δ_{34} or Δ_{38} are energetically favored over the 34-atom pIh^7 or the TO_{38}. The physical meaning of Δ_{34} and Δ_{38} is easy to understand, they represent the energy gain (or loss) for a mixed cluster with respect to pure clusters of size 38 or 34. Therefore Δ_{34} and Δ_{38} are the equivalent, in the case of nanoclusters, of the formation energy of bulk alloys.

IV. RESULTS FOR PURE CLUSTERS

Let us start by analyzing the DF results for pure clusters in Table I, whose schematic pictures are shown in Fig.1. The first noteworthy point is that the truncated octahedron configuration is not the lowest-energy one for pure coinage-metal M_{38} clusters. This is the first indication that quantum (in this case, band structure) effects can be important for medium-size clusters. The scheme of the one-electron energy levels is in fact very similar for Cu_{38}, Ag_{38}, and Au_{38}, and is such that they are not closed-shell systems, the majority-spin HOMO is degenerate and partially filled (Jahn-Teller systems). This non-shell-closure effect destabilizes the TO configuration, and because of that a lower energy is achieved with lower-symmetry isomers. However, there is a difference between Cu and Ag on the one hand and Au on the other hand. In fact the TO Au_{38} cluster is predicted to be at a higher energy with respect to a low-symmetry isomer (see Fig. 1) also using atom-atom potentials,[16,17] an example of amorphization of small clusters due to the increased "bond-stickiness" of the gold atom with respect to Cu and Ag atoms,[19] whereas the TO Cu_{38} and Ag_{38} clusters are predicted to be the lowest energy configurations by atom-atom potentials,[16,18] so that their being at a higher energy (even though by small amounts) with respect to a lower-symmetry isomer (essentially, a fragment of the Ih_{55} of C_{5v} symmetry group, which is also a capped decahedron with atomic islands on anti-Mackay stacking,[20], see Fig. 1) is an unexpected result due to a purely electronic effect.

Electronic effects are important also at size 34. At this size, the pure M_{34} pIh^7 configurations (see Fig. 1) have a lower Δ with respect to the TO_{38} for Cu and Ag, but a higher Δ for Au, due to the fact that pIh structures have very compressed internal bonds, and are thus highly disfavored in the case of "sticky" metals such as gold, which present in addition a very strong bond-order–bond-length correlation[21,22] as a further destabilizing factor for pIh structures. This trend about the energetic stability of M_{34} pIh^7 structures in coinage metals is thus in agreement with the predictions based on semiempirical potential modeling.[19,20]

This analysis, based on the interplay between electronic and ionic effects, can be further deepened by observing that $N=34$ is a magic number for the spherical hard-wall jellium electronic model.[23] In fact, an analysis of the one-electron spectrum of pure and mixed coinage metal $N=34$ clusters

TABLE I. DF calculations results for pure clusters. Values of spin (S), HOMO-LUMO energy difference (gap, in eV) for alpha/beta electrons, and excess energy (Δ, in eV) with respect to N bulk atoms, see Eq. (1). The symbol "JT" after the gap value signals a Jahn-Teller system, with a degenerate HOMO (symmetry breaking is not allowed during the DF relaxation in these cases).

System	Size	Structure	S	Gap	Δ	Δ_{38}	Δ_{34}
Cu	34	pIh^7	0	0.88	4.20	0.51	0.00
	38	TO	1	0.61/0.56 JT	4.30	0.00	−0.12
	38	C_{5v}	0	0.34	4.29	−0.09	−0.21
Ag	34	pIh^7	0	0.91	3.99	3.28	0.00
	38	TO	1	0.39/0.35 JT	4.06	0.00	−3.63
	38	C_{5v}	0	0.43	4.03	−0.28	−3.91
Au	18	C_{2v}(cage)	0	1.38	5.02	2.18	−0.02
	20	Td	0	2.10	5.02	0.97	−1.47
	32	Ih(cage)	0	1.78	5.55	−1.69	−5.60
	34	pIh^7	0	0.79	6.22	4.05	0.00
	38	TO	1	0.12/0.08 JT	6.05	0.00	−4.66
	38	"amorphous"	0	0.19	5.97	−0.92	−5.58
Ni	34	pIh^7	13.2	0.10/0.04 JT	5.09	2.29	0.00
	38	TO	16	0.21/0.03 JT	5.08	0.00	−2.59
Co	34	pIh^7	31	0.12/0.08 JT	5.39	2.56	0.00
	38	TO	32	0.43/0.08 JT	5.34	0.00	−3.28
Pd	38	TO	4	0.17/0.10	4.07	0.00	

shows that the s component can be described as a $1s1p1d2s1f$ jellium sequence. The shell-closure effects account for the large HOMO-LUMO gaps for all those clusters for size 34. Also the peculiar stability of the 34-atom mixed clusters, and especially of the (27,7)pIh^7 arrangement in the case of Ag-Cu, Ag-Ni, and Au-Ni (see the next section and Ref. 4) is partly attributable to this effect. Because of the electronic shell closure, Cu_{34} and Ag_{34} have a relatively low Δ, despite the fact that internal bonds are very compressed in pIh arrangements of pure clusters. In the case of Au_{34}, atom-atom interactions are more sticky, and the bond-order–bond-length correlation is stronger than in Ag and Cu. Therefore, the internal strain in Au_{34} is too high, and the cluster has a large excess energy.

Internal strain in pure Au polyicosahedra is so high that cagelike structures can become competitive, and as an example in Table I we report an Au_{32} cluster. This cluster is an Ih cage (see Fig. 1), corresponding to the external skeleton of the (32,13)pIh^{12} bimetallic anti-Mackay icosahedron (Fig. 2, see Ref. 4 and the following section) which has recently been shown[24] to possess remarkable stability. An analysis of the one-electron spectrum of Ih Au_{32} reveals that its s component can be well described as a $1s1p1d1f$ jellium sequence (one s shell of the spherical layered hard-wall jellium model is destabilized by the inner void). The analogous Ih Ag_{32} cagelike cluster is not favored because the larger spatial extent of the $5s$ orbital produces a destructive interference.

In this connection, one can predict for gold a very stable shell closing at $N=18$, corresponding to the $1s1p1d$ jellium sequence. In fact we were able to find a C_{2v} cagelike structure at $N=18$ (see Fig. 1) with a very low excess energy (especially considering that Δ usually increases with decreasing the size of the cluster), see Table I. This 18-atom cage has been found by genetic optimization of a cluster of size 20, made of 18 gold atoms and two copper atoms within a semiempirical potential modeling. This optimization has produced a core-shell structure with the two copper atoms inside, and a gold shell outside. After removing the copper atoms, the resulting gold shell has been relaxed by DF calculations.

Finally, it can be noted that the stability of the tetrahedral Au_{20} cluster[25] (which is reported for comparison in Table I and Fig. 1) can be explained by a shell closing effect within a tight-binding analysis framework.[26]

V. RESULTS FOR BINARY CLUSTERS

A. Ag-X clusters

The DF results for Ag-containing clusters are given in Table II. Here we consider four systems, Ag-Cu, Ag-Ni, Ag-Pd, and Ag-Co. First, we discuss Ag-Cu and Ag-Ni (in comparison with Ag-Pd), and then we focus on Ag-Co that presents a peculiar behavior.

1. Ag-Cu, Ag-Ni, and Ag-Pd

For Ag-Cu and Ag-Ni clusters of size 34, the excess energy as a function of the first-row transition metal composition has a minimum for the (27,7)pIh^7 structure (called fivefold pancake in the following), a minimum which is appreciably lower than the excess energy of the pure species.[4] In the Ag-Cu case, we have also locally optimized

TABLE II. DF calculations results for Ag-containing clusters. Values of spin (S), HOMO-LUMO energy difference (gap, in eV) for alpha/beta electrons, and excess energy (Δ, in eV) with respect to N bulk atoms, see Eq. (1). The symbol "JT" after the gap value signals a Jahn-Teller system, with a degenerate HOMO (symmetry breaking is not allowed during the DF relaxation in these cases).

System	Size	Structure	S	Gap	Δ	Δ_{38}	Δ_{34}
Ag-Cu	34	(27,7)pIh^7	0	0.82	3.68	−2.88	−5.55
	34	(27,7)distorted	0	0.24	3.77	−1.97	−4.47
	34	(17,17)pIh^7	0	0.94	3.80	−2.39	−4.00
	34	(12,22)pIh^7	0	0.88	3.90	−1.70	−2.84
	38	(32,6)pIh^6	0	0.34	3.90	−2.21	−5.26
	38	(32,6)distorted	0	0.18	3.87	−2.59	−5.64
	38	(30,8)pIh^8	0	0.26	3.80	−3.50	−6.35
	45	(32,13)pIh^{12}	2.5	0.49/1.00	3.98	−8.95	−13.03
Ag-Ni	34	(27,7)pIh^7	3.5	0.81/0.46	3.74	−3.93	−4.36
	34	(17,17)pIh^7	6.5	0.19/0.07	4.22	−1.99	−3.11
	34	(12,22)pIh^7	7	0.26/0.07 JT	4.49	−0.60	−2.07
	38	(32,6)pIh^6	0	0.09	4.00	−2.47	−5.76
	38	(30,8)pIh^8	0	0.05	3.92	−3.99	−7.18
	45	(32,13)pIh^{12}	4	0.59/0.06 JT	3.96	−8.23	−11.89
Ag-Co	34	(27,7)pIh^7	0	0.22	4.10	−0.64	−3.63
	34	(17,17)pIh^7	17	0.95/0.13 JT	4.38	−1.57	−4.53
	38	(32,6)pIh^6	6	0.36/0.22	4.10	−1.76	−5.09
	45	(32,13)pIh^{12}	10.5	0.80/0.31	4.12	−7.11	−11.03
Ag-Pd	38	(32,6)pIh^6	0	0.14	3.80	−2.97	
	38	(26,12)pIh^6	0	0.14	3.76	−3.45	

the energy of a (27,7) low-symmetry isomer, taking as starting structure the one predicted as the second isomer by a semiempirical atom-atom potential (for technical details, see Ref. 4), the corresponding result is reported as a 34-atom distorted cluster in Table II and depicted in Fig. 3. This low-symmetry isomer lies at 0.8 eV above the pIh structure, thus confirming the remarkable (magic) stability of this arrangement. The additional stability of the $N=34$ configuration due to the previously discussed jellium shell-closure effect also plays a role in favoring polyicosahedral structures. In the case of Ag-Cu, 34-atom polyicosahedra present large HOMO-LUMO gaps for all compositions. Shell-closure effects producing pronounced stability have been previously described in small bimetallic clusters, see, for example, Refs. 29–31. In the case of Ag-Pd, size mismatch is not large enough to stabilize the fivefold pancake according to the atom-atom potential, and therefore we have not considered this cluster.

Let us now consider size 38. Composition (32,6) is interesting for the competition of different possible structures. The global optimization by atom-atom potential[4] for this composition gives the (32,6)pIh^6 structure (called in the following sixfold pancake) as the global minimum for Ag-Cu, Ag-Ni, Ag-Pd and also in Au-Cu.[27,28] For Ag-Pd the same structure is found also for a wide range of compositions, extending to (20,18). Comparing fivefold and sixfold pancake structures, it can be noted that the sixfold pancake maximizes the number of mixed bonds, while the fivefold pancake has a compact nucleus of small atoms. Moreover, the fivefold pancake prefers a huge size mismatch, while the sixfold pancake prefers a somewhat smaller size mismatch. As a result, in systems such as Ag-Cu and Ag-Ni, which present huge size mismatch and no preferential tendency for making mixed bonds, there is a whole family of structures of size 38 which have close resemblance with the fivefold pancake, and that are in competition with the sixfold pancake already at the atom-atom potential level. After DF relaxation, one of these structures (the distorted cluster of size 38, see Fig. 3) becomes lower in energy than the sixfold pancake in Ag-Cu. In Ag-Pd, such distorted structure is completely unfavorable because the size mismatch is too small, and the two metals have a better tendency to form mixed bonds. Finally, in Au-Cu, there is both a strong tendency to form mixed bonds and a large size mismatch. These two features act in opposite direction on the stability of the sixfold pancake, so that it is not easy to understand whether this structure can retain the global minimum also at the DF level. This point is currently under investigation.

However, in agreement with the atom-atom calculations,[4] for Ag-Cu and Ag-Ni at size 38, the structure with the most favorable energetic stability indexes is not found at composition (32,6) but at composition (30,8). Here we find the (30,8)pIh^8, which is the perfect core-shell polyicosahedron with the largest Ni or Cu core. For Ag-Pd, the energetic stability indexes are favorable for a series of sixfold pancakes of different compositions. In agreement with the atom-

atom potential calculations, and with the tendency of Ag and Pd to mix, the (26,12)pIh[6] (which is not a core-shell structure, but presents an intermediate Pd layer) is more favorable than the core-shell (32,6)pIh[6].

2. Ag-Co

The results for the Ag-Co system present some peculiarity. Here we have not performed atom-atom global optimization, but simply taken the same structures of Ag-Cu and Ag-Ni and performed DF relaxation, in order to compare the same structures for different systems. From Tables I and II, we can see that Δ at size 34 is increasing from pure silver ($\Delta=3.99$) to pure cobalt ($\Delta=5.39$), without giving a preference for the clusters of intermediate composition. However, since Δ values for pure Ag and Co clusters differ significantly, it is better to consider the unbiased indicators Δ_{34} and Δ_{38}. Both Δ_{34} and Δ_{38} are negative for mixed Ag-Co clusters, confirming the general trend of nanoalloy clusters to a negative formation energy, even in systems where the bulk formation energy is positive. However, at variance with Ag-Cu and Ag-Ni, which present the most negative Δ_{34} and Δ_{38} in correspondence with perfect core-shell clusters (that is for silver-rich compositions), Ag-Co clusters present values of Δ_{34} and Δ_{38} which are smaller in absolute value and moreover reach their minimum for intermediate compositions. This indicates a somewhat reduced chemical interaction and a more pronounced tendency towards intermixing of Ag-Co with respect to Ag-Ni and Ag-Cu (see also the behavior of Au-Cu and Au-Co in the next section for comparison). Before discussing the origin of this behavior, we note that we even found severe convergence problems in the self-consistent process for the (30, 8)pIh[8] and (12,22)pIh[7] clusters, so that the corresponding results are not reported in Table II.

What is the origin of the different behavior of Ag-Co compared to Ag-Ni and Ag-Cu?

Ni and Co have very similar atomic radii, and the Ag-Co bulk phase diagram is similar to the Ag-Ni (and also Ag-Cu) phase diagram.[32] All these binary systems present a very limited miscibility in the bulk phase. However, magnetic effects are appreciably more important in Co than in Ni. It can be reminded, for example, that bulk Co has an hcp structure—at variance with the other metals considered in this work, which present an fcc structure in the bulk.

In this connection, it is instructive to analyze the DF-optimized geometries of pure M_{38} TO structures, reported in Table III. From this analysis, it can be seen that pure Cu_{38} and Ag_{38} TO clusters essentially correspond to a section of the fcc crystal, apart from a slight outward protrusion of the atoms on the (111) faces.[33] This protrusion is essentially due to the bond-order–bond-length correlation in metallic systems,[21,22] and quantitatively predicted by atom-atom potentials.[34] This outward protrusion is very pronounced in the Au_{38} TO, which is a sign of strong bond-directionality effects in gold clusters,[35] similar to those found for platinum clusters in Refs. 13 and 36. A completely analogous behavior to Cu_{38} and Ag_{38} is present in the Ni_{38} TO cluster, except that now the whole structure is "shrunk" by a larger factor with respect to the crystal. For the Co_{38} TO cluster, instead, the (111) faces become completely "flat," whereas the internal octahedral atoms expand by $\approx 4\%$, thus hinting at being in a "coordinatively unsaturated" situation. This thus suggests that the buried Co atoms in the core-shell pIh structures are less stable than the corresponding Ni or Cu atoms because of unfavorable magnetic interactions. This interpretation is supported by analysis of the DF-optimized (27,7)pIh[7] $Ag_{27}Co_7$ structure, which shows a large structural relaxation of the internal Co atoms. In fact, a comparison between the pIh[7] $Ag_{27}Co_7$ and $Ag_{27}Ni_7$ structures shows that the Ag external cage is practically unaltered in the two clusters (with differences in the interatomic distances of the order of 0.3%), whereas the Co atoms at the apexes of the fivefold bipyramid shrink their distance by $\approx 5.5\%$. In parallel, the electron spin is quenched to $S=0$, and the gap in the one-electron energy spectrum drops from 0.81/0.46 eV to 0.22 eV.

TABLE III. Values of geometrical parameters for M_{38} truncated octahedral (TO) clusters from DF calculations. In a TO cluster, one has an inner shell atom (I) surrounded by an outer shell composed of vertex (IIv) and (111) face (IIf) atoms. The values refer to representative atoms in the upper half of the cluster as ratios of Cartesian coordinates over the absolute value of the y coordinate of the IIv atoms (the D_4 axis of the cluster coincides with the z axis). The ratio of y_{IIv} with its "ideal" crystal value is also given. For a cluster which is a section of an "ideal" fcc lattice, these values should read 1.0, 2.0, 1.0, 1.0.

System	$z_{\mathrm{I}}/y_{\mathrm{IIv}}$	$z_{\mathrm{IIv}}/y_{\mathrm{IIv}}$	$z_{\mathrm{IIf}}/y_{\mathrm{IIv}}$	$y_{\mathrm{IIv}}^{\mathrm{crystal}}/y_{\mathrm{IIv}}$
Co_{38}	1.05	1.99	1.00	0.975
Ni_{38}	1.01	2.01	1.03	0.976
Cu_{38}	1.01	1.99	1.03	0.992
Ag_{38}	1.00	2.00	1.03	0.998
Au_{38}	0.99	1.99	1.08	0.996
Pt_{38}	0.99	1.99	1.09	0.987

B. Au-X clusters

The DF results for Au-containing clusters are given in Table IV. For Au-X clusters, we have preferred to relax (by DF calculations) the same structures that we found in Ag-Cu and Ag-Ni, instead of performing an indipendent global optimization by means of an atom-atom potential. However we remark that the core-shell polyicosahedra considered for Au-rich composition are indeed the global minima of the atom-atom potential in Au-Cu.[27]

Since pure gold clusters present a much larger excess energy than pure clusters of the other metals considered here,[37] it is better to consider Δ_{34} and Δ_{38} to discuss the energetic trends at fixed size and varying composition. In passing, we note that we found convergence problems in the self-consistent process for the (30,8)pIh[8] Au-Ni and Au-Co clusters, so that the corresponding results are not reported in Table IV.

The main outcome of these calculations is that (a) for Au-X clusters Δ_{34} and Δ_{38} show negative formation energies for any composition considered here, as found for Ag-X, but larger in absolute values. (b) The lowest value Δ_{34} and Δ_{38} is

TABLE IV. DF calculations results for Au-containing clusters. Values of spin (S), HOMO-LUMO energy difference (gap, in eV) for alpha/beta electrons, and excess energy (Δ, in eV) with respect to N bulk atoms, see Eq. (1). The symbol "JT" after the gap value signals a Jahn-Teller system, with a degenerate HOMO (symmetry breaking is not allowed during the DF relaxation in these cases).

System	Size	Structure	S	Gap	Δ	Δ_{38}	Δ_{34}
Au-Cu	34	(27,7)pIh^7	0	0.97	4.85	−6.65	−9.86
	34	(17,17)pIh^7	0	0.75	4.31	−7.13	−9.20
	34	(12,22)pIh^7	0	1.06	4.12	−6.58	−8.04
	38	(32,6)pIh^6	0	0.30	5.18	−6.78	−10.90
	38	(30,8)pIh^8	0	0.37	5.03	−7.39	−11.05
	45	(32,13)pIh^{12}	2.5	0.40/0.63	5.16	−8.95	−13.03
Au-Ni	34	(27,7)pIh^7	3.5	0.98/0.24	4.90	−7.04	−10.79
	34	(17,17)pIh^7	6.5	0.63/0.16	4.73	−6.71	−9.92
	34	(12,22)pIh^7	9	0.30/0.08 JT	4.79	−4.56	−7.51
	38	(32,6)pIh^6	3	0.28/0.05 JT	5.33	−6.43	−10.70
	45	(32,13)pIh^{12}	1	0.48/0.17 JT	5.19	−11.64	−16.37
Au-Co	34	(27,7)pIh^7	4	0.32/0.37	5.20	−5.11	−8.97
	34	(17,17)pIh^7	17	0.66/0.13 JT	4.80	−7.24	−10.93
	34	(12,22)pIh^7	22	0.95/0.17	4.81	−6.01	−9.32
	38	(32,6)pIh^6	6	0.29/0.29	5.38	−6.43	−10.70
	45	(32,13)pIh^{12}	10.5	0.45/0.33	5.26	−11.73	−16.69

obtained for gold-rich compositions in the case of Au-Ni clusters (see the results at size 34), so that the core-shell polyicosahedral structure is singled out as being of special stability, in analogy with Ag-Cu and Ag-Ni. However, in Ag-Ni, the tendency to favor core-shell polyicosahedra is stronger than in Au-Ni. (c) For Au-Cu, one finds that the three mixed compositions considered here give clusters of substantially comparable stability—with the preferred composition depending on the choice of the stability index (Δ, Δ_{34}, or Δ_{38}). (d) For Au-Co, the results are analogous to Ag-Co, with a preference for the intermediate composition, which is remarkable due to the tendency of Au and Co to phase separation in the bulk. However, formation energies are much more negative in Au-Co than in Ag-Co.

The following facts can help rationalize these findings.

As a general remark, chemical bonding effects play a more important role for Au than for Ag,[35] due to the more substantial contribution of the d orbitals to bonding (directionality effects[38]) and the smaller spatial extent of the s orbitals, which stengthens the Au chemical interaction with first-row transition metals such as Cu, Ni, and Co. This explains the larger absolute values of Δ_{34} and Δ_{38} for Au-X clusters with respect to Ag-X clusters.

Moreover, the Au-Cu bulk phase diagram is different from those of the Au-Ni, Au-Co, and Ag-X systems.[32] While the latter in fact show a very limited miscibility of the two components, the Au-Cu phase diagram presents three stable ordered alloys at compositions Au_3Cu, AuCu, and $AuCu_3$, with a larger melting temperature for the two phases with larger Cu concentration. This helps explaining point (c), i.e., the fact that in the Au-Cu case the cluster stability is substantially flat as a function of Au concentration. Also the somewhat larger surface energy of Au with respect to Cu (Refs. 39 and 40) contributes to disfavoring the segregation of a complete layer of Au to the surface.

In order to explain the somewhat weaker tendency of Au-Ni in favor of core-shell polyicosahedra with respect to Ag-Ni, it can be observed that—despite the fact that Au and Ag have very similar atomic radii—gold is a "stickier" metal than silver, and one in which directionality (chemical bonding) effects play a very important role.[35] These factors are against core-shell polyicosahedral structures (as seen already for pure Au clusters), and in principle could destabilize them. However, the driving forces towards core-shell polyicosahedra are so strong that these destabilizing factors eventually have a rather weak effect, which has some quantitative relevance but does not induce qualitative changes.

Au-Co clusters favor intermediate compositions as in Ag-Co. However, in the case of the (27,7) Au-Co clusters, the peculiar internal relaxation of the internal Co atoms is not taking place as in Ag-Co, and the spin is not quenched to zero. This explains why the values of Δ_{34} and Δ_{38} are much more negative than in Ag-Co.

Finally we remark that also 34-atom polyicosahedral Au-Cu clusters present large HOMO-LUMO gaps, due to the electronic shell-closing effect predicted by the hard-wall jellium model.

VI. CONCLUSIONS

A family of polyicosahedral bimetallic core-shell nanoclusters, recently shown to possess peculiar structural, thermodynamic, and electronic ("magic") stability in the case of the Ag-Cu and Ag-Ni nanoalloys,[4] has been investigated in the case of Ag-Pd, Ag-Co, Au-Cu, Au-Ni, and Au-Co via first-principles (DF) calculations.

The tendency of these structures to being "magic" has been rationalized in terms of general arguments considering the interplay of surface energy, size mismatch and bond-order–bond-length correlation.

On the basis of these general arguments, one would make the following predictions. The polyicosahedral core-shell arrangement should be especially favorable in those systems presenting size mismatch and tendency to phase separation in the bulk phase, with the large atoms segregating at the surface. These features are found in Ag-Co, Au-Ni, and Au-Co, besides the already studied[4] Ag-Cu and Ag-Ni. By contrast, Ag-Pd and Au-Cu tend to mix in bulk phases, so that intermixed clusters (obtained at intermediate compositions) as well as core-shell clusters (obtained at silver-rich composition for Ag-Pd and gold-rich compositions for Au-Cu) could be favored.

The DF results confirm the validity of the general arguments for Ag-Cu, Ag-Ni, Ag-Pd, Au-Ni, and Au-Cu, while in clusters containing cobalt, peculiar quantum effects cause a qualitatively different behavior.

In the case of Ag-Co, the interaction among the magnetic moments of the buried Co atoms oppose the gain in energy associated with the shrinking of the cluster size and the reduced strain. In the case of Au-Co, the latter effect is less evident, but chemical bonding effects (connected with the strong directionality of the Au-Au bonding[35]) combined with the "sticky" character of the Au-Au interaction[19] moves the maximum in the stability of the bimetallic clusters as a function of concentration from structures with a perfect core-shell arrangement to configurations with a substantial intermixing of the two atoms. Unfavorable magnetic interactions also contribute to destabilize Ni_{34} and Co_{34} clusters.

Apart from magnetic and chemical bonding effects, interesting electronic effects are also found for pure clusters.

In particular, band structure effects are found to disfavor "crystalline" (TO) arrangements in pure Cu_{38} and Ag_{38} clusters, nonsymmetrical structures (actually, defected decahedral M_{55} configurations) which appear as closely competing low-lying isomers from atom-atom calculations are predicted to be at lower energy from first-principles calculations, essentially because the TO clusters are found to be Jahn-Teller systems and, as such, not particularly favored.

This non-shell-closure effect can be contrasted with the additional stability imparted to $N=34$ pure and bimetallic clusters by shell closing within the spherical hard-wall jellium model, to Au_{18} or Au_{32} clusters within the spherical layered hard-wall jellium model, and to Au_{20} within a tight-binding approach. In general, a large value of the HOMO-LUMO gap is a signature of a shell-closure effect, which—in the case of gold—is amplified by the smaller extent and stronger interaction of the electronic wave function with respect to the Ag case.

We conclude by remarking that our results confirm the strong tendency of small bimetallic clusters to mixing,[4] for all systems considered here, even for those that present a very strong tendency against mixing in the bulk phase (such as Ag-Cu, Ag-Ni, Ag-Co, or Au-Co), mixed cluster are characterized by large negative values of formation energy (Δ_{34} and Δ_{38} in Tables II and IV). This can be understood in terms of the greater structural freedom which reduced symmetry systems (such as clusters and surfaces) possess with respect to the constraints due to translational invariance of predefined lattices in bulk systems. For example, this structural freedom helps nanoclusters in accommodating strain in size-mismatched systems.

Quantum effects are found to often reinforce the tendency to mixing. They are particularly important for nanoclusters (in general, confined systems) with respect to bulk systems due to the neater separation between electronic shells, and the reduction in interatomic distances due to bond-order–bond-length correlation, which strengthens chemical bonding.

ACKNOWLEDGMENTS

The authors acknowledge financial support from the Italian CNR for the project "(Supra-)Self-Assemblies of Transition Metal Nanoclusters" within the framework of the ESF EURO-CORES SONS, and from European Community Sixth Framework Programme for the project "Growth and Supra-Organization of Transition and Noble Metal Nanoclusters" (Contract No. NMP4-CT-2004-001594). One of the authors (A. F.) acknowledges the Italian INSTM for a grant at the CINECA supercomputing center (Bologna, Italy).

*Corresponding author. Electronic address: fortunelli@ipcf.cnr.it

[1] *Progress in Experimental and Theoretical Studies of Clusters*, edited by T. Kondow and F. Mafuné (World Scientific, New York, 2003).

[2] K. J. Klabunde, *Free Atoms, Clusters and Nanoscale Particles* (Academic, New York, 1994); K. J. Klabunde, *Nanoscale Materials in Chemistry* (Wiley, New York, 2001).

[3] J. Jellinek and E. B. Krissinel, "Alloy clusters: Structural classes, mixing, and phase changes," in *Theory of Atomic and Molecular Clusters with a Glimpse at Experiments*, edited by J. Jellinek (Springer, Heidelberg, 1999).

[4] G. Rossi, A. Rapallo, C. Mottet, A. Fortunelli, F. Baletto, and R. Ferrando, Phys. Rev. Lett. **93**, 105503 (2004).

[5] G. E. Thayer, V. Ozolins, A. K. Schmid, N. C. Bartelt, M. Asta, J. J. Hoyt, S. Chiang, and R. Q. Hwang, Phys. Rev. Lett. **86**, 660 (2001).

[6] J. P. K. Doye, J. Chem. Phys. **119**, 1136 (2003).

[7] R. A. Kendall, E. Aprà, D. E. Bernholdt, E. J. Bylaska, M. Dupuis, G. I. Fann, R. J. Harrison, J. Ju, J. A. Nichols, J. Nieplocha, T. P. Straatsma, T. L. Windus, and A. T. Wong, Comput. Phys. Commun. **128**, 260 (2000).

[8] A. D. Becke, Phys. Rev. A **38**, 3098 (1988).

[9] J. P. Perdew, J. A. Chevary, S. H. Vosko, K. A. Jackson, M. R. Pederson, D. J. Singh, and C. Fiolhais, Phys. Rev. B **46**, 6671 (1992).

[10] A. Schaefer, C. Huber, and R. Ahlrichs, J. Chem. Phys. **100**,

5289 (1994).
[11] D. Andrae, U. Haeussermann, M. Dolg, H. Stoll, and H. Preuss, Theor. Chim. Acta **77**, 123 (1990).
[12] M. Dolg, U. Wedig, H. Stoll, and H. Preuss, J. Chem. Phys. **86**, 866 (1987).
[13] E. Aprá and A. Fortunelli, J. Phys. Chem. **107**, 2934 (2003).
[14] Courtesy of Dr. Florian Weigend, Karlsruhe, Germany.
[15] C. Elsässer, M. Fähnle, C. T. Chan, and K. M. Ho, Phys. Rev. B **49**, 13975 (1994); R. W. Warren and B. I. Dunlap, Chem. Phys. Lett. **262**, 384 (1996).
[16] K. Michaelian, N. Rendón, and I. L. Garzón, Phys. Rev. B **B 60**, 2000 (1999).
[17] I. L. Garzon, K. Michaelian, M. R. Beltran, A. Posada-Amarillas, P. Ordejon, E. Artacho, D. Sanchez-Portal, and J. M. Soler, Phys. Rev. Lett. **81**, 1600 (1998).
[18] F. Baletto, A. Rapallo, G. Rossi, and R. Ferrando, Phys. Rev. B **69**, 235421 (2004).
[19] F. Baletto, R. Ferrando, A. Fortunelli, F. Montalenti, and C. Mottet, J. Chem. Phys. **116**, 3856 (2002).
[20] F. Baletto and R. Ferrando, Rev. Mod. Phys. **77**, 371 (2005).
[21] J. M. Soler, M. R. Beltrán, K. Michaelian, I. L. Garzón, P. Ordejón, D. Sánchez-Portal, and E. Artacho, Phys. Rev. B **61**, 5771 (2000).
[22] J. M. Soler, I. L. Garzón, and J. D. Joannopoulos, Solid State Commun. **117**, 621 (2001).
[23] M. Manninen, "Models of metal clusters and quantum dots," in *Atomic Clusters and Nanoparticles*, NATO ASI Les Houches LXXIII, edited by C. Guet, P. Hobza, F. Spiegelman, and F. David (Springer, Berlin, 2000).
[24] X. Gu, M. Ji, S. H. Wei, and X. G. Gong, Phys. Rev. B **70**, 205401 (2004).
[25] J. Li, X. Li, H.-J. Zhai, and L.-S. Wang, Science **299**, 864 (2003).
[26] A. Fortunelli (unpublished).
[27] A. Rapallo, G. Rossi, R. Ferrando, A. Fortunelli, B. C. Curley, G. M. Tarbuck, L. D. Lloyd, and R. L. Johnston, J. Chem. Phys. **122**, 194308 (2005).
[28] G. Rossi, R. Ferrando, A. Rapallo, A. Fortunelli, B. C. Curley, L. D. Lloyd, and R. L. Johnston, J. Chem. Phys. **122**, 194309 (2005).
[29] U. Heiz, A. Vayloyan, and E. Schumacher, J. Phys. Chem. **100**, 15033 (1996).
[30] M. Heinebrodt, N. Malinoski, F. Tast, W. Branz, I. M. L. Billas, and T. P. Martin, J. Chem. Phys. **110**, 9915 (1999).
[31] E. Janssens, H. Tanaka, S. Neukermans, R. E. Silverans, and H. Lievens, New J. Phys. **5**, 46.1 (2003).
[32] R. Hultgren, P. D. Deai, D. T. Hawkins, M. Gleiser, and K. K. Kelley, *Values of the Thermodynamic Properties of Binary Alloys* (American Society for Metals, Berkeley, 1981).
[33] E. Aprà and A. Fortunelli, J. Mol. Struct.: THEOCHEM **501/502**, 251 (2000).
[34] V. Rosato, M. Guillopé, and B. Legrand, Philos. Mag. A **59**, 321 (1989).
[35] A. Fortunelli and A. M. Velasco, Int. J. Quantum Chem. **97**, 654 (2004).
[36] E. Aprà, F. Baletto, R. Ferrando, and A. Fortunelli, Phys. Rev. Lett. **93**, 065502 (2004).
[37] Due to basis set limitations and especially to the fact that the quality of the DF approach is not homogeneous for all the metals, experimental bulk binding energies have been taken as a reference for evaluating Δ.
[38] S. Taylor, G. W. Lemire, Y. M. Hamrick, Z. Fu, and M. D. Morse, J. Chem. Phys. **89**, 5517 (1988).
[39] W. R. Tyson and W. A. Miller, Surf. Sci. **62**, 267 (1977).
[40] A. R. Miedema, Z. Metallkd. **69**, 287 (1978).

Diffusion of Palladium Clusters on Magnesium Oxide

BarcaroPRL2005

G. Barcaro,[1] A. Fortunelli,[1] F. Nita,[2,3] and R. Ferrando[2]
[1]*IPCF/CNR, Via Alfieri 1, Ghezzano, I56010, Italy*
[2]*Dipartimento di Fisica, INFM and IMEM/CNR, Via Dodecaneso 33, Genova, I16146, Italy*
[3]*I. G. Murgulescu Institute of Physical Chemistry of the Romanian Academy, 202 Splaiul Indipendentei, 060021 Bucharest - 12, POB 194, Romania*
(Received 19 July 2005; published 6 December 2005)

The diffusion of small palladium clusters on MgO(100) is theoretically investigated. It is found that small clusters can diffuse even faster than isolated adatoms by a variety of mechanisms (some of which are novel), such as dimer rotation, trimer walking, tetramer rolling, and sliding. The consequences of the diffusion of small clusters on the growth of Pd aggregates on MgO(100) are investigated, and it is shown that fast mobility of clusters larger than a single atom is essential to bring the theoretical results into agreement with the outcome of molecular beam epitaxy experiments.

DOI: 10.1103/PhysRevLett.95.246103 PACS numbers: 68.43.Jk, 68.35.Fx, 81.15.Aa

The study of metallic aggregates adsorbed on oxide surfaces is extremely important for technological applications, especially in the field of catalysis [1]. Aggregates are usually obtained by the molecular beam epitaxy technique [2], in which single atoms are deposited with a given flux, and aggregation takes place on the surface. In order to make aggregation possible, the deposited species should be able to diffuse significantly on the surface [3]. In this respect, the determination of diffusion pathways and activation barriers is a crucial step toward understanding the formation processes of the aggregates, and to control their size and shape.

Among metal-on-oxide systems, Pd/MgO(100) is one of the most studied, being probably the most well-known model catalyst system [1]. MgO(100) is a surface of square symmetry, presenting a checkerboard of alternating oxygen and magnesium atoms. Single palladium atoms adsorb on top of oxygen atoms (see Fig. 1) [4], and are more strongly bound to surface defects, such as oxygen vacancies (F_s centers), MgO divacancies, and steps [5].

Several experiments have been performed on the growth of palladium clusters on MgO(100) [1,6]. These experiments have shown that, at least for sizes above 1.5 nm of diameters (say above $\sim$100 atoms), Pd aggregates grow with fcc structure and pseudomorphically with the substrate, presenting (100) facets on their top. This clear epitaxial relation with the substrate indicates a quite strong adhesion between Pd clusters and MgO, so that the interpretation of nucleation experiments usually assumes that only palladium monomers diffuse, while clusters are immobile [7]. It has also been found that the nucleation of aggregates takes place only at surface defects down to low temperatures [1,7]. This implies a substantial mobility of palladium, to reach the defect sites. Despite the huge amount of experiments and calculations on the Pd/MgO(100) system, very little is known about the mobility of Pd on this surface.

In this Letter we address the problem of the diffusion of Pd on MgO(100) and show that the nucleation of Pd aggregates on MgO(100) is indeed controlled by the mobility of small clusters, which can be nonpseudomorphic with the substrate, and can diffuse faster than monomers. We show that small clusters diffuse by several different mechanisms (some of which are novel), ranging from dimer rotation, to trimer walking, and tetramer rolling and sliding.

In order to achieve this result, we set up a computational procedure consisting of several steps. The first step is the molecular-dynamics simulation of diffusion within an atom-atom potential model, whose parameters are fitted to first-principles calculations [8], to identify possible cluster structures and diffusion pathways. The results of this first step are the starting point of first-principles [density-

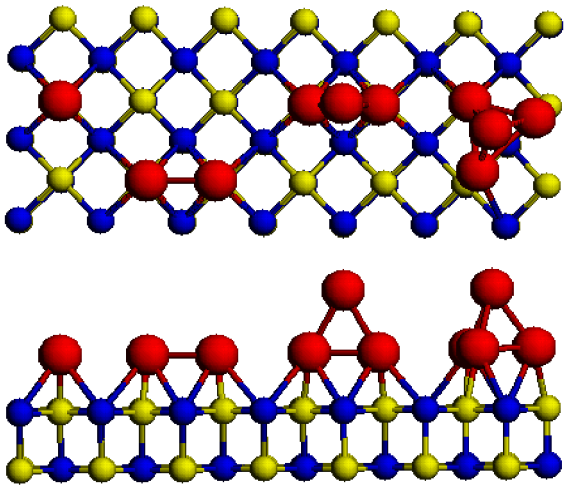

FIG. 1 (color online). Top and side view of the best structures of Pd clusters up to the tetramer. The light (yellow online) and dark (blue online) atoms on the surface are oxygens and magnesiums, respectively.

functional (DF)] calculations, which allow us to select the best cluster structures for each nuclearity and to calculate the activation barriers of the diffusion mechanisms. Once the diffusion mechanisms are determined together with their barriers, a kinetic Monte Carlo simulation [9] of island nucleation is performed, and its results are compared to the experimental data obtained by Haas *et al.* [7].

First-principle calculations to explore the potential energy surface of the system were performed at the DF level employing the PWSCF (Plane-Wave Self-Consistent Field) computational code [10], using ultrasoft pseudopotentials to describe the interaction between the outer shell electrons with the inner shell electrons and the nucleus. The PW91 exchange-correlation functional [11], which is a gradient-corrected functional, was employed. The kinetic energy cutoff for the selection of the plane-wave basis set was fixed at 40 Ry for all the calculations. Apart from local energy minimizations to determine the best possible structures and lowest-energy isomers of the Pd clusters adsorbed on the oxide surface, Nudged Elastic Band (NEB) [12] calculations were performed in order to determine the diffusion barriers. This method searches for the minimum-energy path between two local minima by creating a fixed number of intermediate configurations (images) which are linked to each other by elastic springs. The image highest in energy does not feel the spring forces along the band; instead, the true force at this image along the tangent is inverted. In this way, the image tries to maximize its energy along the band and so, when this image converges, it is at the exact saddle point [12].

Let us now discuss the diffusion pathway of monomers and small clusters. The only possible diffusion mechanism for monomers is hopping between neighboring oxygen sites, via the saddle point located at the bridge position. According to our calculations, the energy barrier for monomer hopping is of 0.39 eV [8].

The determination of the possible diffusion pathways for dimers is more complicated. The lowest-energy configuration turns out to be horizontal, with the dimer atoms placed above two nearest-neighbor oxygens (see Fig. 1), in agreement with Ref. [13]. The Pd-Pd distance is however contracted with respect to the distance between oxygens, down to 2.83 Å, and the spin state is a singlet. The vertical dimer configuration turns out to be much higher in energy, being 0.83 eV above the absolute minimum. This is at variance with the case of Cu on MgO(100), where the vertical dimer configuration was found to be the lowest in energy [14,15]. The diffusion of the dimer takes place by a combination of rotational moves, in which one of the atoms is practically at rest in its adsorption site, and the second performs a 90° rotation around a vertical axis passing through the first atom. In this rotational motion, the dimer passes through a first saddle point, then through a local minimum (after a 45° rotation) and a further symmetric saddle. The local minimum and the saddle are 0.28 eV and 0.39 eV higher than the absolute minimum, respectively. Therefore, the activation barrier for dimer diffusion is of 0.39 eV, the same numerical value of the barrier of monomers. This can be rationalized by considering the unusual weakness of the metal-metal bond in Pd_2 [16], which only slightly decreases its interaction with the oxide surface, at the same time being easily stretched.

The lowest-energy configuration of trimers on MgO(100) is triangular and vertical [17] (see 1) with triplet spin state, as the freestanding trimer. This configuration was found to be the most favorable also for Cu_3 on MgO(100) [14,15]. This is due to a ''metal-on-top'' effect [15], i.e., an increase in the metal-surface adhesion due to the presence of metal atoms above those directly interacting with the surface, an effect which is dominant in coinage metal clusters, but still appreciable in Pd clusters. This metal-on-top effect is sufficient to stabilize vertical Pd trimers compared to the two best (slightly tilted) horizontal trimers, which are higher in energy by 0.28 and 0.44 eV. Trimers diffuse keeping the vertical orientation by a mechanism which we refer to as *trimer walking*. Trimer walking is analogous to dimer rotation (see Fig. 2), and, in fact, it takes place through a series of 90° rotations around the atoms of the trimer basis. Again, a local minimum and two symmetric saddles are encountered during a 90° rotation, but in this case the local minimum and the saddle are only 0.19 and 0.30 eV higher in energy than the absolute minimum. This corresponds to an activation barrier of 0.30 eV, which is significantly lower than the barrier of monomers and dimers. The fact that the barrier for trimer walking is lower than the barrier for dimer rotation may be justified by noting that the total adhesion energy of the trimer is lower than the adhesion energy of the dimer (1.86 against 2.24 eV), due to the enhancement of metallic bonding in the trimer at the expense of the bonding with the oxide surface. Moreover, Pd_3 shares with coinage metal trimers [15] a *fluxional* character which allows it to select a nonsymmetrical, lower-energy path for diffusion that better takes advantage of the metal-on-top effect.

Trimer walking was found to appear also in *ab initio* molecular-dynamics simulations of Cu_3 diffusion on MgO(100) [14] but only at high temperatures. The activation barrier of the Cu_3 trimer walking was not calculated; however, it was concluded that Cu_3 trimer walking was a much slower diffusion process compared to the diffusion of Cu monomers. The situation for Pd is completely different, since trimer walking is the process with the lowest-energy barriers among the diffusion processes of monomers and small clusters (see Table I).

Several *ab initio* calculations indicate that gas-phase Pd tetramers assume a tetrahedral shape [16]. When adsorbed on the MgO(100) surface, this tetrahedral arrangement is preserved. As shown in Ref. [13], the square Pd_4 cluster, with the Pd atoms sitting above four oxygens, is higher in energy than the Pd_4 tetrahedron positioned as in Fig. 2(f). The lowest-energy configuration is, however, the (non-pseudomorphic) one reported in Figs. 1 and 2(d) [17], followed by the configuration in Fig. 2(e), while that in Fig. 2(f) is not a local minimum but a saddle point.

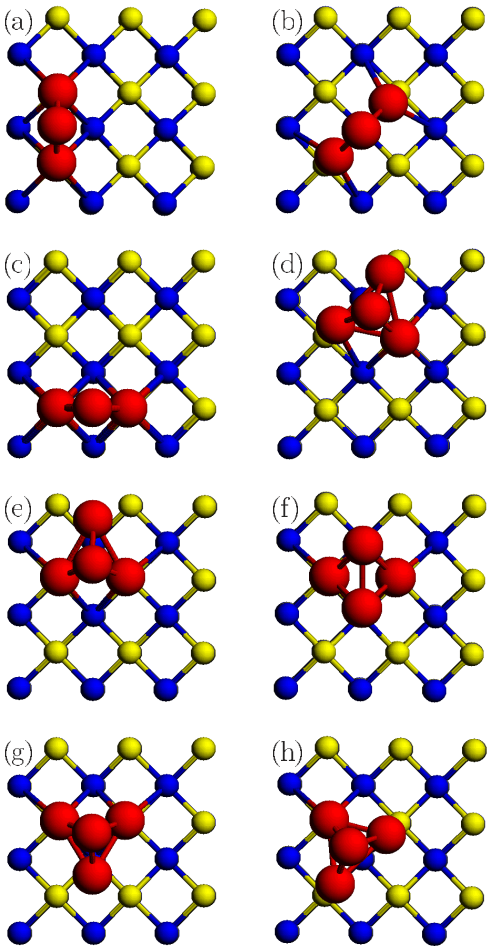

FIG. 2 (color online). Schematic representation of the trimer walking [(a) → (c)] and of tetramer rolling [(d) → (h)]. Trimer walking is composed by successive 90° rotations and is thus completely analogous to dimer rotation. From the absolute energy minimum (a), the trimer rotates by 45° degrees to the local minimum (b) passing through a saddle point which is roughly half way between (a) and (b). Another 45° rotation leads to the new absolute minimum (c). Tetramer rolling takes place through a series of consecutive rotations. The move (d) → (e) is close to a small-angle rotation around a vertical axis; the move (e) → (f) → (g) is a rotation around a horizontal axis; the move (g) → (h) is the reverse of (a) → (b).

Configurations in Figs. 2(d)–2(f) are triplet spin states. Pd_4 tetrahedra can diffuse by a novel mechanism, which we refer to as *tetramer rolling*. Tetramer rolling is a combination of rotational moves, as shown in the sequence in Figs. 2(d)–2(h). From the absolute minimum in Fig. 2(d), a small-angle rotation around a vertical axis (with some additional bond stretching) leads to the local minimum in Fig. 2(e). From this position, a rotation follows around a horizontal axis passing through the two Pd atoms which are positioned above the oxygens. This rotation leads to the saddle in Fig. 2(f) and then to the local minimum in Fig. 2(g), which is of the same kind as Fig. 2(e). Finally, a further small-angle rotation around a vertical axis leads to the new absolute minimum in Fig. 2(h). The activation energy for this sequence is given by the energy difference between Figs. 2(f) and 2(d), and turns out to be 0.38 eV, a value slightly lower than the activation energy of monomers. The metal-on-top effect contributes to stabilizing the saddle point in Fig. 2(f). Tetramers can also diffuse by a sliding motion. The sequence starts from the configuration in Fig. 2(d), then passes through Fig. 2(e). From Fig. 2(e), instead of rotating around a horizontal axis as in the rolling mechanism, the tetramer can translate rigidly along a oxygen row to the next cell, arriving at a local minimum and then performing a small-angle rotation to the absolute minimum. Tetramer sliding has a barrier of 0.45 eV and is thus more difficult than rolling.

TABLE I. Energy barriers for the diffusion processes described in the text.

Process	Energy barrier (eV)
Monomer hopping	0.39
Dimer rotation	0.39
Trimer walking	0.30
Tetramer rolling	0.38
Tetramer sliding	0.45

Our calculations have thus shown that dimers, trimers, and tetramers can diffuse even faster than adatoms. Let us now discuss the consequences of our findings on the interpretation of Pd nucleation experiments on MgO(100). Haas *et al.* [7] deposited Pd atoms with a flux $F = 0.032$ ML/min for about three minutes to reach a final coverage of 0.1 ML. They repeated the same experiment for a wide range of temperatures, and at each temperature measured the island density by taking atomic force microscope (AFM) images. They found that the island density is constant in the range from 200 to 500 K. This can only be explained if island nucleation is taking place exclusively at surface defects, whose number is temperature independent. Indeed, as mentioned in the introduction, Pd binds much more strongly at defects than at surface sites. However, if nucleation is taking place only at defects down to low temperatures, palladium must be sufficiently mobile to reach the defects.

Let us now show that our diffusion barriers can produce island densities in agreement with the experiment only if the mobility of small clusters is taken into account. We have performed a kinetic Monte Carlo (KMC) simulation in which monomers, dimers, trimers, and tetramers diffuse, while larger clusters are not mobile. In our simulation box, we randomly place defects with the same density of the experiment. When monomers or clusters reach a defect, they stick there. Activation barriers are given in Table I. Since we are interested in simulating the low-temperature range, we assume irreversible aggregation of Pd atoms and neglect the possibility of detaching monomers or aggregates from defect sites. These processes may become important above 500 K in the experimental conditions of Ref. [7]. Prefactors of diffusion precesses are calculated

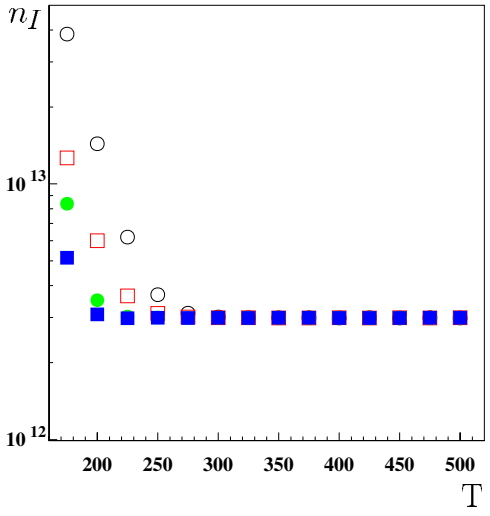

FIG. 3 (color online). Kinetic Monte Carlo results for the island density n_I (including monomers, in cm^{-2}) as a function of temperature (in K). Open circles: only monomers diffuse. Open squares: only monomers diffuse, but a post-deposition time of 3 minutes is allowed. Filled circles: monomers and small clusters diffuse. Filled squares: monomers and small clusters diffuse, and a post-deposition time of 3 minutes is allowed.

by means of molecular-dynamics simulations within the atom-atom model [8], and all fall in the range around 2×10^{12} s^{-1}.

The results of the KMC simulations are given in Fig. 3, where the island density n_I (which includes monomers) is reported as a function of the temperature T. If we consider that only monomers are mobile, we obtain a result which is in clear disagreement with the experiment. As already noted by Haas *et al.*, if only monomers move with a barrier of $\simeq 0.4$ eV, the island density begins to deviate from a constant for $T < 275$ K because of island nucleation at terrace sites and not only at defects. Also if we take into account 3 minutes of post-deposition time (a conservative estimate of the time needed to take the AFM image after stopping deposition) at the growth temperature, the results are still in disagreement with the experiment for $T \leq 250$ K, with large deviations at 200 K. In fact, if only monomers diffuse, the post-deposition time allows the aggregation of monomers to existing islands, but it has no effect on islands that nucleated outside defects, whose number cannot be reduced. On the contrary, if we allow the diffusion of dimers, trimers, and tetramers, the island density stays almost perfectly constant, and equal to the defect density, in the whole temperature range. Only a slight increase can be seen at 200 K, while the transition from the regime of nucleation at defects to the regime of nucleation at terrace sites is taking place just below 200 K. Experimental results for $T < 200$ K are not available to verify whether our prediction about the transition temperature is correct. However, we remark that the theoretical determination of the transition temperature should probably also take into account the mobility of clusters larger than the tetramer. In fact, our molecular-dynamics simulations indicate that also heptamers, octamers, and decamers could diffuse fast, thus contributing to a further decrease of the island density, and therefore to the extension of the range of constant island density to lower temperatures.

In conclusion, we have shown that even for a system such as Pd/MgO(100), which is characterized by a strong tendency to pseudomorphic growth, small clusters can diffuse faster than isolated adatoms, by means of a variety of mechanisms. This has been rationalized by considering that small clusters (a) often grow nonpseudomorphically (also due to a metal-on-top effect), (b) can exhibit a fluxional behavior less likely in larger aggregates, (c) metal-metal bonding competes with surface adhesion thus lowering activation barriers. The diffusion of small clusters has deep consequences on the nucleation of islands, which can thus take place at defects, and not on the flat terraces, down to low temperatures.

Financial support from the Italian CNR for the project "(Supra—) Self—Assemblies of Transition Metal Nanoclusters" within the framework of the ESF EUROCORES SONS and from the European Commission for the project GSOMEN (Contract No. NMP4-CT-2004-001594) is gratefully acknowledged.

[1] C. R. Henry, Surf. Sci. Rep. **31**, 231 (1998).
[2] H. Brune, Surf. Sci. Rep. **31**, 125 (1998).
[3] T. Ala-Nissila, R. Ferrando, and S. C. Ying, Adv. Phys. **51**, 949 (2002).
[4] I. Yudanov, G. Pacchioni, K. Neyman, and N. Rösch, Surf. Sci. **426**, 123 (1999), and references therein.
[5] L. Giordano, C. Di Valentin, J. Goniakowski, and G. Pacchioni, Phys. Rev. Lett. **92**, 096105 (2004).
[6] S. Giorgio, C. Chapon, C. R. Henry, and G. Nihoul, Philos. Mag. B **67**, 773 (1993).
[7] G. Haas, A. Menck, H. Brune, J. V. Barth, J. A. Venables, and K. Kern, Phys. Rev. B **61**, 11 105 (2000).
[8] W. Vervisch, C. Mottet, and J. Goniakowski, Phys. Rev. B **65**, 245411 (2002).
[9] M. Kotrla, Comput. Phys. Commun. **97**, 82 (1996).
[10] S. Baroni, A. Dal Corso, S. de Gironcoli, and P. Giannozzi, http://www.pwscf.org
[11] J. P. Perdew *et al.*, Phys. Rev. B **46**, 6671 (1992).
[12] G. Henkelman, B. P. Uberuaga, and H. Jónsson, J. Chem. Phys. **113**, 9901 (2000).
[13] A. M. Ferrari, C. Xiao, K. M. Neyman, G. Pacchioni, and N. Rösch, Phys. Chem. Chem. Phys. **1**, 4655 (1999).
[14] V. Musolino, A. Selloni, and R. Car, Phys. Rev. Lett. **83**, 3242 (1999).
[15] G. Barcaro, and A. Fortunelli, J. Chem. Theory Comput. **1**, 972 (2005).
[16] F. Baletto and R. Ferrando, Rev. Mod. Phys. **77**, 371 (2005) and references therein.
[17] L. Giordano and G. Pacchioni, Surf. Sci. **575**, 197 (2005).

Density-functional global optimization of gold nanoclusters

Edoardo Aprà,[1] Riccardo Ferrando,[2] and Alessandro Fortunelli[3,*]
[1]*William R. Wiley Environmental Molecular Sciences Laboratory, Pacific Northwest National Laboratory, Richland, Washington 99352, USA*
[2]*Dipartimento di Fisica dell'Università di Genova, Via Dodecaneso 33, Genova, I16146, Italy*
[3]*Molecular Modeling Laboratory, IPCF-CNR, Via G. Moruzzi 1, Pisa, I56124, Italy*
(Received 27 January 2006; revised manuscript received 30 March 2006; published 18 May 2006)

The structure of gas-phase gold clusters of size ~20 is studied by density-functional global optimization in the full configuration space. The putative global minimum of Au_{20} is confirmed to be a tetrahedron (T_d) independently of the choice of the exchange-correlation functional, whereas the structure of the low-lying excited states depends on the theoretical approach. The peculiar stability of T_d is rationalized in terms of the synergic effects of *s-d* hybridization and electronic shell closure. Calculations on Au_{16} and Au_{18} show that T_d Au_{20} possibly represents a "unicum" in the sequence of gold clusters.

DOI: 10.1103/PhysRevB.73.205414 PACS number(s): 61.46.Bc, 36.40.Mr, 73.22.−f

I. INTRODUCTION

The properties of metal clusters have attracted much attention in recent years (see for example, Ref. 1) for their interesting properties and potential applications in nanotechnology. In this context, an important role is expected to be played by "magic" clusters, i.e., those possessing peculiar stability due to structural and/or electronic shell closure, whose formation energy thus exhibits a pronounced concave "cusp" as a function of size or composition, which favors preferential accumulation during growth and confers them unusual properties. Gold-based clusters are promising candidates in the search for magic structures. Gold itself occupies a unique position at the borderline between transition and simple metals, at the same time exhibiting a very large relativistic effect[2] which brings the 6*s* orbital to overlap significantly with the 5*d* orbital. Even though bulk gold is the noblest of all metals,[3] a rich and often unexpected behavior shows up in gold nanoclusters,[4] ranging from selective low-temperature catalysis of industrially important reactions, to interesting optical and electrical properties, to applications in biosensors and drug delivery thanks to its full biocompatibility. Great interest has thus arosen in connection with the discovery and characterization through photoelectron spectroscopy of the gas-phase Au_{20} cluster,[5] exhibiting an unusually large highest occupied molecular orbital (HOMO)-lowest unoccupied molecular orbital (LUMO) gap: 1.77, 0.2 eV greater than in C_{60}. On the basis of the large gap and of first-principles calculations on few selected structures, a highly symmetric tetrahedral (T_d) configuration was hypothesized [see Fig. 1(f)]. This configuration represents a piece of the fcc bulk, it is a surface-only or "cage" structure (there are no inner atoms), and its surface exhibits only fcc (111) faces. The result was puzzling from a theoretical point of view, as no existing empirical potential predicts the T_d structure as the energy minimum.[1,6] Since then, a few first-principles calculations on selected structures of Au_{20} have appeared,[7–10] confirming that T_d is more stable than several plausible competitors. However, an unbiased search of the Au_{20} global minimum has not been attempted, and the definitive assignment of the Au_{20} structure still represents an open problem.

In this paper, we perform unbiased global optimization of Au clusters in the full configuration space within a density-functional basin-hopping (DF-BH) approach. We demonstrate that the T_d structure is indeed the putative global minimum of Au_{20}, irrespectively of the choice of the exchange-correlation functional, and perform a thorough analysis of the low-lying excited states, whose ordering, on the other hand, depends on the functional. Moreover, we discover putative global minima for Au_{18} and Au_{16}, which do not belong to the T_d structural motif.

II. RESULTS AND DISCUSSION

The difficulty in locating the global minima of (metal) clusters lies in the fact that commonly employed techniques such as simulated annealing[11] are very often not exhaustive, and one has to resort to global-optimization approaches. Among these the BH algorithm[12,13] has proved to be one of the most efficient and cost effective. In the BH algorithm, the potential energy hypersurface is deformed such that to every point in the catchment basin of each local minimum the energy of that minimum is assigned. The Monte Carlo search moves then allow the system to hop from one catchment basin to another.

A first-principles description of the energetics is necessary in our case since empirical potentials are apparently not able to correctly describe the energetics of small Au clusters. Our DF calculations utilizes the Becke[14] functional for exchange and the Lee-Yang-Parr[15] functional for correlation, within the NWChem[16] suite of programs.[17]

In the case of Au_{20}, three DF-BH runs have been performed, each comprising 300 Monte Carlo steps, starting from randomly chosen initial configurations.[18] The choice of 300 Monte Carlo steps is justified by considering that BH searches conducted on Au_{20} using several different atom-atom potentials always found the corresponding global minimum within the first 300 Monte Carlo steps. In addition, the 100 lowest-energy structures obtained through an extensive BH search using an empirical potential[19] have also been locally optimized. In all three DF-BH runs, the search singled out T_d as the lowest-energy structure, locating it after 233,

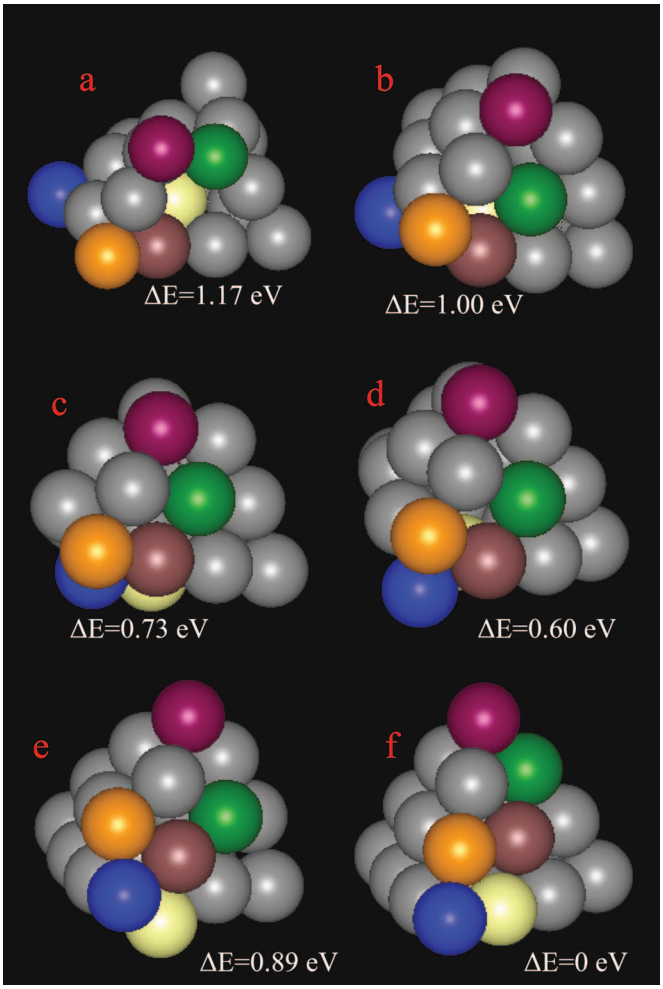

FIG. 1. (Color) Schematic pictures of selected local minima [(a)–(e)] and the T_d putative global minimum (f) from one particular DF-BH run (see text for details). ΔE represents the energy difference with respect to T_d in electron-volts (eV), according to the Becke-Lee-Yang-Parr *xc* functional.

28, and 177 steps, respectively.[20] The T_d minimum, apart from being the lowest-energy structure found by the DF-BH algorithm, also seems to have a rather large catchment basin, as proved by the fact that (1) it has been located as the putative global minimum in all the three DF-BH runs, and (2) after the algorithm locates the T_d structure, it takes 15–20 Monte Carlo steps before being able to escape from it: This is due to the large energy separation with respect to the first excited state, but also to the fact that in some of these steps the geometry optimization falls back into the T_d minimum after the random move.

Even though the BH random moves cannot be associated with real physical processes (the kinetics of the cluster reorganization), it is suggestive to interpret them as some kind of Monte Carlo jumps between basins of attraction. We thus show in Fig. 1 five configurations chosen among those 14 immediately preceding the location of the T_d putative global minimum in the third DF-BH run. These configurations have been chosen because they are highly representative examples of the low-lying excited states we encountered in our DF-BH searches, i.e., mainly cage structures, among which a substantial number of variously defective T_d. Different colors have been used to distinguish individual atoms, and allow one to follow their movements. The energy differences with respect to T_d are also shown. Figure 1(a) is a typical example of the "cage" structures that occur so frequently in our BH search: it has a relatively high energy (1.17 eV), but it is structurally not too far from a T_d. Indeed, after a BH step, it rearranges into a defective T_d [Fig. 1(b)] in which one apex atom (the blue colored one) has moved onto an edge of the tetrahedron. This is the simplest type of T_d defect, but also has a relatively high energy (1.0 eV). In the next step [Fig. 1(c)], the blue atom has inserted into the bottom fcc (111) face, giving another common type of a defective T_d. A further rearrangements [Fig. 1(d)] brings this atom onto the vertex of a triangular pyramid whose three basal atom lye in a corner of the bottom fcc (111) face. This configuration can also be described as a defective T_d, and, according to our calculations, it corresponds to the lowest-energy isomer above the T_d putative global minimum. From here, through an intermediate configuration slightly higher in energy [Fig. 1(e)], in which the blue atom has moved to an apex position, dragging the atom at the center of the fcc (111) face onto an edge of the tetrahedron, a configuration which is thus intermediate between a generic cage structure and a defective T_d, the T_d putative global minimum is finally attained [Fig. 1(f)]. It can be noted that the HOMO-LUMO gap of T_d Au_{20} is 1.96 eV, in agreement with previous calculations, but the defective T_d first excited state [Fig. 1(d)] also has a significant gap (1.49 eV).

Other low-lying excited states found in our DF-BH searches and different from those shown in Fig. 1 are reported in Fig. 2: They correspond to other defective T_d [Figs. 2(a) and 2(b)], doubly defective T_d [Figs. 2(c) and 2(d)], and a cage structure [Fig. 2(e)]. The most stable compact configuration [Fig. 2(f)] obtained via local minimization of the 100 lowest-energy structures obtained using an empirical potential[19] is also shown. It can be noted that Fig. 2(a) is taken from the second DF-BH run, Fig. 2(b) from the third, Fig. 2(c) from the first DF-BH run, Fig. 2(d) from the second DF-BH run, Fig. 2(e) from the third DF-BH run: This shows that there is a qualitative overlap among the three DF-BH runs. To give an idea of the statistics of our DF-BH searches, a histogram showing the cumulative energy distribution of the structures found in our BH searches is shown in Fig. 3: From this figure, it is apparent that the energy range beyond $\approx$1.7 eV above the T_d putative global minimum is more and more poorly sampled with increasing ΔE.

No compact, space-filled configurations could be located within 1 eV of the T_d putative global minimum: The most stable isomer obtained from the local geometry optimization of the empirical potential[19] structures [see Fig. 2(f)] lies at 1.28 eV. In contrast, a planar structure [a Au_{21} triangle cut out of an fcc (111) face and missing one apex atom] lies only slightly above the T_d-defected first excited state [Fig. 1(d)]: This is not surprising, as planar structures are the global minima of slightly smaller gold clusters and anions.[21,22] This explains why it is so difficult to find the T_d minimum via unbiased combined empirical potential/DF searches: At the

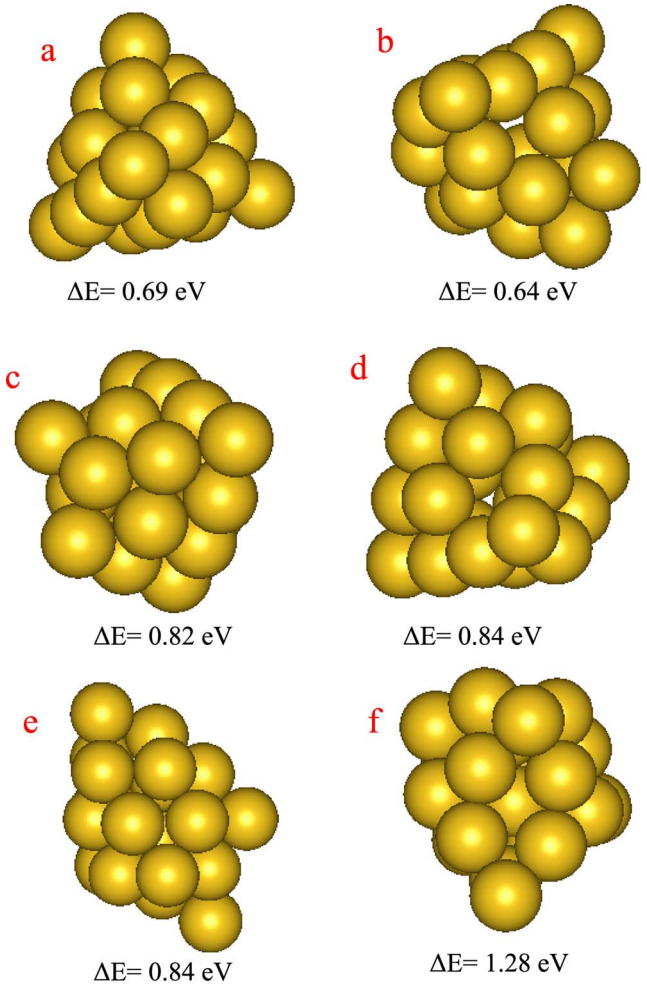

FIG. 2. (Color online) Schematic pictures of a few low-lying excited states from our BH searches different from those shown in Fig. 1: defective T_d [(a), (b)], doubly defective T_d [(c), (d)], and a cage structure (e). The most stable compact configuration (f) obtained via local minimization of the 100 lowest-energy structures obtained using an empirical potential (see Ref. 19) is also shown. ΔE represents the energy difference with respect to T_d in eV, according to the Becke-Lee-Yang-Parr *xc* functional.

empirical potential[19] level, T_d lies at 1.08 eV above the global minimum, and is estimated to be the 1300th excited state. Also biased empirical potential/DF searches often miss to predict the true lowest-energy structure. As an example, the defective T_d structures predicted by a biased combined empirical potential/DF search as global minima for Au_{18} and Au_{16} (Ref. 10) (i.e., Au_{20} tetrahedra missing two or four apex atoms, respectively) are not the lowest-energy structures according to our calculations. By performing a few tens of DF-BH steps using the same *xc* functional[23] as in Ref. 10 we could easily find several isotops, structurally different from the global minima proposed in Ref. 10, but either nearly degenerate with them (for Au_{18}) or more stable by $\geqslant$0.5 eV (for Au_{16}). In Fig. 4, the defective T_d missing four apex atoms proposed as global minimum in Ref. 10 and a low-symmetry cluster from our DF-BH search lying below the former by 0.71 eV are shown for Au_{16}. It can thus be

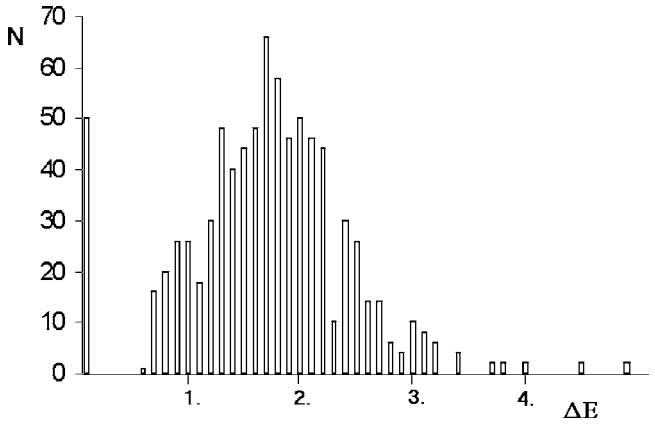

FIG. 3. Histogram showing the cumulative energy distribution of the structures found in our BH searches. The first peak contains the T_d putative global minimum. ΔE in eV.

concluded that only an unbiased, fully first-principles global-optimization approach like the one employed in the present work does furnish a reasonable guarantee that the true DF global minimum is located, at the same time providing with a set of candidates for the low-lying excited states.

The peculiar stability of the T_d can be rationalized in terms of three main reasons: (1) stickiness of the Au-Au bonding; (2) directionality effects in the Au-Au interaction; and (3) electronic shell closure.

Stickiness of the Au-Au bonding. The limited spatial extension of the Au 6*s* orbital (due to the relativistic contraction) translates into a shorter-range atom-atom interaction as compared to first-row and second-row transition metals, and thus to a high energetic penalty for changing the interatomic distances from their optimal (coordination-dependent) value.[24] This disfavors icosahedral configurations, which are competitive in this size range in terms of bond counting but present a large internal strain, and favors possibly amorphous or—for very small clusters such as Au_{20}—surface-only or cage structures, such as the T_d.

Directionality effects. The relativistic contraction of the *s* orbital brings it to substantially overlap with the *d* orbitals, decreasing the localized character of the latter and strongly increasing their contribution to chemical bonding. This in turn implies a substantial anisotropy of the Au-Au bonding: Not only the number, but also the spatial arrangement of the neighbors matters in terms of binding energy. For gold, in

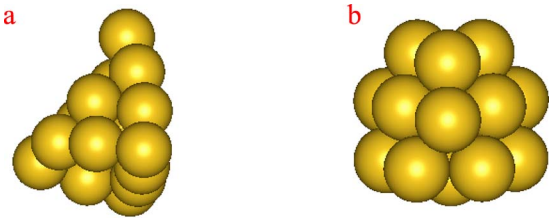

FIG. 4. (Color online) Schematic pictures of the Au_{16} defective T_d (b) and a structurally different configuration (a) lower in energy by 0.71 eV according to the PW91 *xc* functional (see Ref. 23) used in Ref. 10.

particular, this disfavors asymmetric arrangements. For example, a fcc (111) bilayer (coordination number=9, but strongly asymmetric bonding environment) has a binding energy per atom only 0.08 eV greater than that of a single fcc (111) monolayer (coordination number=6, but symmetric bonding environment). In other words, there is a small energy penalty in dissociating a fcc (111) bilayer into two fcc (111) monolayers, and this again favors surface-only or cage structures with low-coordinated atoms arranged according to local fcc patterns (see Ref. 25 for a more detailed discussion).

Electronic shell closure. $N=20$ and $N=18$ correspond to electronic magic numbers for various different models. For $N=20$: spherical electron gas,[26] tetrahedral electron gas.[27] For $N=18$: tensor surface harmonic Theory;[28] hard-well layered electron gas;[29] Hirsch $2(N+1)^2$ rule for spherical aromaticity.[30] It is thus not surprising to encounter clusters exhibiting large HOMO-LUMO gaps in this size range. This means that a large HOMO-LUMO gap does *not* automatically implies that the cluster is of high symmetry: As it happens, the information derived from electron spectroscopy measurements does not provide *per se* a complete structural characterization. The scheme of the one-electron energy levels of T_d indeed conforms to that predicted by jellium models.[4] However, here again the *s-d* interaction plays a significant role. First, by performing a *s-d* decomposition of the DF wave function[31] we found an appreciable *s-d* orbital mixing. Moreover, to provide a clearer evidence, we implemented an approach[32] in which the Au atom is described as a one-electron element, i.e., in which the *d* orbitals are separated from the *s* orbitals and included into the core, and we performed a DF-BH run. After a few tens of steps starting from the T_d configuration, the system evolved into low-symmetry compact, space-filled structures qualitatively similar to those predicted as global minimum or low-lying excited states by the empirical potential,[19] and more stable than T_d by 0.5–1.0 eV. It is interesting to note that in this approach the T_d HOMO-LUMO gap is 2.63 eV, i.e., even greater than that predicted by the all-electron approach, but that of several low-symmetry low-energy structures is also large: About 1.8 eV. This explains why T_d is not the global minimum of Cu_{20}, Ag_{20}, etc.[7,9] At the one-electron level, in the absence of *s-d* hybridization, the extra stability assured by tetrahedral aromaticity[27] is counteracted by other structural factors, such as the preference for compact arrangements (which are also favored by spherical aromaticity at $N=20$). In contrast, for T_d Au_{20} the stability induced by tetrahedral aromaticity (which can be quantified in 0.5–1.0 eV) is reinforced by the tendency of small gold clusters towards open, cage configurations, a tendency ultimately relying on *s-d* hybridization. As noted above, this is no more true for $N\neq 20$, so that T_d structures missing apex atoms are not the global minima for Au_{16} and Au_{18}. The T_d structure of Au_{20} thus possibly represents a "unicum" in the structural sequence of gold clusters.[9]

Finally, it has been observed that DF predictions of the structure of gold clusters are affected (sometimes appreciably) by the choice of the *xc* functional, the effective core potential and the numerical approach.[8,9,32] Under this respect, we found the Au_{20} T_d structure to be remarkably stable under a variety of DF approaches. We performed in fact further DF-BH test runs and properly selected local geometry optimizations using the local density approximation or a different *xc* functional,[23] employing more extended Gaussian-type orbital or plane wave basis sets, and we always found that T_d remains the ground state. Selected results from these calculations are reported in Table I. From this table, it can be seen that what changes when changing the *xc* functional is the nature of the lowest-energy excited states, switching from open (cage) arrangements for the Becke-Lee-Yang-Parr functionals, to compact, space-filled configurations (similar to those reported in Ref. 8) for the local density approximation. A more detailed study will be reported in the future.[25]

TABLE I. Relative energies of various structures of Au_{20} clusters from DF calculations. T_d is the putative tetrahedral global minimum [Fig. 1(f)], defective-T_d corresponds to Fig. 1(d), compact corresponds to Fig. 2(f). BLYP is the Becke-Lee-Yang-Parr *xc* functional, PW91 the Perdew-Wang *xc* functional (see Ref. 23), LDA is the local density approximation. GTO means Gaussian-type-orbitals (see Ref. 38), PW means plane waves (see Ref. 39).

Cluster	BLYP/GTO	PW91/GTO	PW91/PW	LDA/PW
T_d	0.00	0.00	0.00	0.00
Defective T_d	0.60	0.88	0.89	0.96
Compact	1.26	1.30	1.33	0.77

III. CONCLUSIONS

We have implemented a DF-BH approach, and applied it to the determination of the global minimum and low-energy excited state structures of gas-phase Au_{20}. Three DF-BH runs are conducted, each comprising 300 DF-BH steps, plus additional local geometry optimizations starting from the 100 lowest-energy structures according to an empirical potential. The putative global minimum of Au_{20} is confirmed to be a T_d, independently of the choice of *xc*-functional or the numerical approach, whereas the structure of low-lying excited states depends on the theoretical approach, switching from open (cage)—such as defective T_d—arrangements, to compact, space-filled configurations. The peculiar stability of T_d is rationalized in terms of the synergic effects of *s-d* hybridization, which makes the Au-Au interaction very sticky and directional, thus favoring open structures exhibiting local fcc patterns, and electronic shell closure, associated with tetrahedral aromaticity. Calculations on Au_{16} and Au_{18} using two different gradient-corrected *xc* funxtionals show that low-symmetry arrangements structurally different from defective T_d are either competitive or at an appreciably lower energy, suggesting that T_d Au_{20} possibly represents a unicum in the structural sequence of gold clusters.

ACKNOWLEDGMENTS

We acknowledge financial support from the Italian CNR for the project "(Supra-)Self-Assemblies of Transition Metal Nanoclusters" within the framework of the ESF EURO-

CORES SONS, and from European Community Sixth Framework Programme for the project "Growth and Supra-Organization of Transition and Noble Metal Nanoclusters" (Contract No. NMP4-CT-2004-001594). A portion of the research described in this manuscript was performed at the W.R. Wiley EMSL, a national scientific user facility sponsored by the U.S. DOE OBER and located at PNNL. PNNL is operated for the DOE by Battelle.

*Author to whom correspondence should be addressed; email address: fortunelli@ipcf.cnr.it

[1] F. Baletto and R. Ferrando, Rev. Mod. Phys. **77**, 371 (2005).
[2] P. Pyykkö, Angew. Chem., Int. Ed. **43**, 4412 (2004).
[3] B. Hammer and J. K. Norskov, Nature (London) **376**, 238 (1995).
[4] M.-C. Daniel and D. Astruc, Chem. Rev. (Washington, D.C.) **104**, 293 (2004).
[5] J. Li, X. Li, H.-J. Zhai, and L.-S. Wang, Science **299**, 864 (2003).
[6] N. T. Wilson and R. L. Johnston, Eur. Phys. J. D **12**, 161 (2000).
[7] J. Wang, G. Wang, and J. Zhao, Chem. Phys. Lett. **380**, 716 (2003).
[8] B. Soulé de Bas, M. J. Ford and M. B. Cortie, J. Mol. Struct.: THEOCHEM **686**, 193 (2004).
[9] E. M. Fernández, J. M. Soler, I. L. Garzón, and L. C. Balbás, Phys. Rev. B **70**, 165403 (2004).
[10] W. Fa, C. Luo, and J. Dong, Phys. Rev. B **72**, 205428 (2005).
[11] S. Kirkpatrick, C. D. Gelatt, Jr., and M. P. Vecchi, Science **270**, 671 (1983).
[12] Z. Li and H. A. Scheraga, Proc. Natl. Acad. Sci. U.S.A. **84**, 6611 (1987).
[13] D. J. Wales and J. P. K. Doye, J. Phys. Chem. A **101**, 5111 (1997).
[14] A. D. Becke, Phys. Rev. A **38**, 3098 (1988).
[15] C. Lee, W. Yang, and R. G. Parr, Phys. Rev. B **37**, 785 (1988).
[16] E. Aprà *et al.*, NWCHEM, A Computational Chemistry Package for Parallel Computers, Version 4.7, 2005, Pacific Northwest National Laboratory, Richland, WA 99352-0999.
[17] We use a $(7s,5p,5d)/[6s,3p,2d]$ Gaussian-type-orbital basis set (see Ref. 33), a scalar-relativistic effective-core potential (see Ref. 34), an auxiliary $(9s,4p,4d,3f,4g)/[8s,4p,3d,3f,2g]$ basis set (see Refs. 35 and 36) for the expansion of the electron density, a numerical grid of 65 radial points and 350 Lebedev angular points for evaluating the *xc* potential and energy, and a smearing factor of 0.005 a.u., see Ref. 37 for more details on the numerical procedure. All the calculations are spin unrestricted. The geometry optimizations were stopped after a threshold of 0.004 a.u./Å on the gradient and 0.019 Å on the difference in Cartesian coordinates of the atoms was reached.
[18] The initial states have been generated by randomly distributing the atoms in a sphere of 6 Å radius. A random move of up to 1 Å (positive or negative) in the Cartesian coordinates of each atom was allowed. A value of 0.5 eV was chosen as kT in the Monte Carlo check.
[19] V. Rosato, M. Guillopé, and B. Legrand, Philos. Mag. A **59**, 321 (1989). The following parameters have been used: $A=0.2197$ eV, $\xi=1.855$ eV, $p=10.53$, $q=4.3$, $r_0=2.885$ Å.
[20] The NWCHEM self-consistent algorithm proved to be rather robust, always converging in all the 1000 geometry optimizations we conducted. On average, the first scf process reached convergence in about 30–37 iterative steps in 90% of the cases (never exceeding 54 iterative steps in the remaining 10% cases), and typically in about ten iterative steps for the successive iterative processes. Note that our random moves do not exceed 1 Å in absolute value in each coordinate, which implies that the random configurations generated in the Monte Carlo steps usually do not have too small internuclear distances.
[21] H. Häkkinen, M. Moseler, and U. Landman, Phys. Rev. Lett. **89**, 033401 (2002).
[22] F. Furche, R. Ahlrichs, P. Weis, C. Jacob, S. Gilb, T. Bierweiler, and M. M. Kappes, J. Chem. Phys. **117**, 6982 (2002).
[23] J. P. Perdew, J. A. Chevary, S. H. Vosko, K. A. Jackson, M. R. Pederson, D. J. Singh, and C. Fiolhais, Phys. Rev. B **46**, 6671 (1992).
[24] J. P. K. Doye, D. J. Wales, and R. S. Berry, J. Chem. Phys. **103**, 251 (2000).
[25] S. Olivier and G. Barcaro, A. Fortunelli (unpublished).
[26] M. Brack, Rev. Mod. Phys. **65**, 677 (1993).
[27] S. M. Reimann, M. Koskinen, H. Häkkinen, P. E. Lindelof, M. Manninen, and Phys. Rev. B **56**, 12147 (1997).
[28] A. J. Stone, Inorg. Chem. **20**, 563 (1981).
[29] R. Ferrando, A. Fortunelli, and G. Rossi, Phys. Rev. B **72**, 085449 (2005).
[30] A. Hirsch, Z. Chen, and H. Jiao, Angew. Chem., Int. Ed. **39**, 3915 (2000).
[31] A. Fortunelli and A. M. Velasco, Int. J. Quantum Chem. **97**, 654 (2004).
[32] V. Bonačič-Koutecky, J. Burda, R. Mitrič, M. Ge, G. Zampella, and P. Fantucci, J. Chem. Phys. **117**, 3120 (2002).
[33] D. Andrae, U. Haeussermann, M. Dolg, H. Stoll, and H. Preuss, Theor. Chim. Acta **77**, 123 (1990).
[34] M. Dolg, U. Wedig, H. Stoll, and H. Preuss, J. Chem. Phys. **86**, 866 (1987).
[35] A. Fortunelli and O. Salvetti, J. Comput. Chem. **12**, 36 (1991).
[36] K. Eichkorn, O. Treutler, H. Öhm, M. Häser, and R. Ahlrichs, Chem. Phys. Lett. **240**, 283 (1995).
[37] E. Aprà and A. Fortunelli, J. Phys. Chem. **107**, 2934 (2003).
[38] The Kohn-Sham equations are solved on a large $(9s,8p,6d,3f,1g)/[7s,5p,4d,3f,1g]$ basis set of Gaussian-type-orbitals (see Ref. 33) using an auxiliary $(9s,4p,5d,4f,5g,3h)/[8s,4p,4d,4f,5g,3h]$ basis set (see Ref. 36) for the expansion of the electron density and a scalar-relativistic effective-core potential (see Ref. 34).
[39] The DF calculations are performed using the plane-wave self-consistent field (PWSCF) computational code (see Ref. 40), employing a plane-wave basis set, ultrasoft pseudopotentials, a kinetic energy cutoff for the selection of the plane-wave basis set of 40 Ry (1 Ry=13.6 eV), and the Gamma point for the *k*-point sampling of the Brillouin zone. The dimension of the unit cell is chosen so as to leave a distance of 6–8 Å between atoms on neighboring cell images.
[40] S. Baroni, A. Del Corso, S. de Gironcoli, and P. Giannozzi, http://www.pwscf.org

Rotational Invariance and Double Frustration in the Structures of Gold Clusters Growing around the F_s-Defected MgO (100) Surface

BarcaroJPCB2006a

Giovanni Barcaro and Alessandro Fortunelli*

Molecular Modeling Laboratory, Istituto per i Processi Chimico-Fisici (IPCF) del C.N.R., via G. Moruzzi 1, 56124, Pisa, Italy

Received: July 17, 2006

The interaction of small gold clusters (Au_n, $n = 1-4$, 20) and a gold monolayer with the MgO (100) surface surrounding a neutral oxygen vacancy (F_s center) is investigated using density-functional (DF) calculations. It is found that the presence of the defect modifies the interaction of gold not only with the vacancy itself, but also with the oxygen and magnesium atoms around it by increasing both the adhesion energy and the equilibrium bond distances. This is at variance with the interaction of metal atoms with the regular MgO (100) surface or the F_s defect itself, in which an increase of the adhesion energy is associated with a shortening of the metal−surface distance. The resulting double frustration and cylindrical invariance of the metal−surface interaction cause small gold clusters growing around an F_s nucleation center to be highly fluxional in terms both of rotational freedom and of multiple competing structural motifs. Fragmentation energies of the gold clusters are also discussed, finding that the lowest-energy pathway corresponds to the detachment of a dimer.

1. Introduction

Metal nanoclusters have attracted much attention in recent years as a result of properties that are unique to the nanoscale domain.[1−4] In this context, gold nanoclusters play an important role: even though gold is the noblest of all metals,[5] a rich and often unexpected behavior shows up in gold nanoclusters,[6−8] ranging from selective low-temperature catalysis of industrially important reactions,[9−13] to peculiar optical[14,15] and electrical[16] properties, etc. In technological applications, stabilizing the metal clusters by coating with surfactants or through absorption on a substrate is an essential step to exploit the many fascinating properties of these materials. The (100) surface of the MgO oxide is a good candidate as an inert template for the cluster absorption.[17] The same inert characteristics of this surface, however, cause the growth of metal clusters to be strongly influenced by the presence of defects.[18,19] In this connection, the growth of gold clusters on the MgO (100) surface obtained via molecular-beam epitaxy (MBE) has been recently studied in great detail,[20,21] analyzing the dependence of the cluster density on the substrate temperature and the morphology of the resulting particles. From a theoretical point of view, several previous studies have confirmed that the interaction of gold with the regular MgO (100) surface is rather weak (less than 1 eV per atom).[22−24] The consequent need of nucleation centers to anchor the growth of metal deposition has promoted the study of extended and localized surface defects. In this context, the neutral oxygen vacancy (also known as F_s center) has been shown to be at the same time a common surface defect and able to act as a nucleation center for several transition metal species, including gold.[22−25] The strength of the Au atom/F_s center bond in fact is estimated to be greater than 2.5 eV,[22,23] thus providing a site at which nucleation can occur, as confirmed by a recent combined EPR and theoretical characterization of a single gold atom interacting with the regular and defected MgO (100) surface.[26] However, the evolution of the geometric structures of the metal clusters growing around the F_s center has been studied only for the smallest clusters and not systematically. The attention has mainly focused on the catalytic activity of small gold clusters rather than on the study of the growth process. For Au_n clusters in the range $n = 2-11$, some selected local minima structures atop neutral and charged defects (F_s and F_s^+ centers) have been considered in the light of the absorption properties of probe molecules (like CO or O_2);[13,27,28] this kind of study has been extended to consider optical properties of supported gold clusters[29] (with or without probe molecules absorbed atop them) or bigger metal aggregates absorbed on the regular (100) MgO surface.[30]

Small metal clusters have been the subject of intensive research in the past few years because they often exhibit peculiar low-energy configurations, different from those of larger aggregates.[31] The interaction with the substrate and its defects adds another degree of freedom and can induce further modifications into the cluster structure,[32,33] a topic of great interest both in view of the unusual properties that are often a consequence of these structural modifications and because the low-energy structures of small metal clusters can orient the subsequent growth. In fact, as the time-scale of the growth process is typically of the order of seconds or minutes (see, for example, ref 20), while the time-scale of the reorganization of small clusters (up to 50 atoms) can be estimated to be of the order of nanoseconds,[34] the metal clusters have the possibility to readjust their configurations to their low-energy structures.

Our aim in the present work is to understand the low-energy structures of small metal clusters growing around an F_s defect of the MgO (100) surface, and their connection with the basic energetics of the metal/defected-surface interaction. In a previous work,[22] we have presented a general investigation of the interaction of small coinage metal clusters and extended depositions with the regular and locally defected (100) MgO

* Corresponding author. Tel.: +39-050-3152247. E-mail: fortunelli@ipcf.cnr.it.

10.1021/jp064519e CCC: $33.50
Published on Web 09/20/2006

surface. In the present work, we report the results of systematic density-functional (DF) calculations focusing on the study of the interaction of small Au_n clusters ($n = 1-4$, 20) with a neutral oxygen vacancy defect. We show that this defect induces a long-range modification of the metal absorption characteristics in its surrounding and that this perturbation is responsible for the fluxionality of small clusters growing around the vacancy, possibly connected with the peculiar catalytic properties of small Au clusters[9,11,12,20,21] or the formation of clusters exhibiting different structural motifs.[21] Additionally, we calculate the fragmentation energies of clusters grown around the defect, finding that the lowest-energy pathway corresponds to the detachment of a dimer and involves energies that might be accessible in MBE experiments at high temperatures.

2. Computational Details

Density-functional (DF) calculations are performed using the PWscf (Plane-Wave Self-Consistent Field) computational code[35] employing ultrasoft pseudopotentials. The PBE exchange-correlation functional,[36] which is a gradient-corrected functional, is used. The kinetic energy cutoff for the selection of the plane-wave basis set is set at 40 Ry (1 Ry = 13.6 eV) for all of the calculations. A (4,4,1) *k*-point sampling of the Brillouin zone is chosen, and a Gaussian smearing procedure (with a smearing parameter of 0.002 Ry) is applied. The geometry optimizations are stopped when maximum force on atoms is less than 10^{-4} au. The distance between atoms in replicated cells is about 8−10 Å. The regular MgO (100) surface is modeled by a three-layer slab (as it is customary), each containing 18 (3×3 cell) or 32 (4×4 cell) Mg and O atoms fixed at the equilibrium lattice positions characterizing the MgO rock-salt structure (frozen at the experimental lattice constant of 4.208 Å). To produce a neutral F_s-defected surface, we remove one O atom from a surface layer, keeping the positions of all of the other atoms in the cell fixed. Larger (5×5) cells have been considered to check that the results on adhesion energies were not biased by the size of the cell. A general remark is here in order. DF theory using gradient-corrected (GGA) xc-functionals (such as PBE) makes the MgO system rather soft, as is proven by the fact that its lattice parameter at the DF-relaxed geometry is overestimated by about 2%. Hybrid xc-functionals would improve the description of the oxide, but they cannot be used here because of their bad description of the metal clusters (see, for example, ref 37), a common problem in the study of interfacial systems. Our experience then shows that, lacking clear experimental data to settle this problem, freezing the geometry of the oxide substrate at its experimental equilibrium configuration is the best choice so as not to let the DF/GGA approach overestimate the structural relaxation around the oxygen vacancy upon metal absorption. Anyway, we also checked that in the case of gold absorption the results were not qualitatively altered when allowing the substrate to relax.

3. Results and Discussion

We start with considering the absorption of a single Au atom on the regular and defected MgO (100) surface. We fix the Au position in the plane parallel to the oxide surface and optimize its distance from the surface. Figure 1 shows the resulting absorption topography, that is, the equilibrium distance and absorption energy as a function of the in-plane position, for both the regular and the defected surfaces.

A completely different energy and equilibrium distance landscape is immediately apparent in the two cases.

On the regular surface, one finds a rather flat potential energy surface, exhibiting minima in correspondence of the oxygen atoms, maxima on the magnesium atoms, and saddle points on the hollow sites, with a maximum adhesion energy of 0.91 eV and energy barriers of about 0.2 eV for the diffusion between neighboring oxygen sites. Correspondingly, the equilibrium height exhibits minima at 2.30 Å on the oxygen sites, maxima at 2.71 Å on the magnesium sites, and saddle points at 2.40 Å on the hollow sites. The in-plane distance between the energy minima corresponds to the MgO lattice parameter of about 2.97 Å: this value is larger than the typical Au−Au distances (the Au−Au distance in the bulk is 2.885 Å; smaller distances are normally found in Au nanoclusters), thus inducing a frustration (mismatch) in the metal growth on the MgO (100) surface.[38,39]

The presence of the F_s defect completely alters this situation,[32] with the resulting potential energy and equilibrium height surfaces exhibiting three major features: (I) the energy minimum in correspondence of the defect site is much deeper, with an adhesion energy of 3.07 eV; (II) a large basin of attraction is produced around the defect, with an adhesion energy of 1.62 eV on the magnesium atoms first-neighbors to the vacancy (to be compared to a value of 0.5 eV for the regular surface), extending its influence up to third neighbors, and exhibiting an approximate cylindrical symmetry, which is due to a strong perturbation of the electrostatic potential outside the surface with respect to the regular, nondefected system, which affects the polarization and thus the adhesion characteristics of the metal atom, as will be shown in detail in future work; and (III) there is a large difference between the equilibrium distance atop the defect (about 1.8 Å), strongly reduced with respect to the absorption onto the regular surface, and that atop the neighboring sites (2.65 Å on the magnesium and 2.59 Å on the oxygen sites first-neighbors to the vacancy, respectively), for which an increase in the absorption energy unexpectedly corresponds to an almost general increase in the equilibrium distance. The equilibrium distance then slowly relaxes to the values typical of the absorption on the regular surface as the Au atom gets farther from the defect. The topography of r_{min} as a function of the in-plane coordinates thus corresponds to a "crater" around the F_s center.

These three features determine the characteristics of the metal growth around the F_s defect.

First, due to the strong interaction of gold with the oxygen vacancy (I), this defect can act as an efficient trapping center for the nucleation of metal clusters.[22−25]

Second, the approximate cylindrical symmetry of E_{adh} around the defect site (II) ensures the metal clusters a considerable rotational freedom, by which the clusters can rotate on the surface keeping the atom atop the defect fixed, as the adhesion energy to the surface is essentially determined by the distance of the site with which the metal atom is interacting from the defect, rather than by its chemical identity.

The strong variation of r_{min} around the defect site (III) finally entails that the growth of metal clusters is frustrated not only "horizontally" with respect to the surface, due to the mismatch between MgO and Au lattice parameters, but also "vertically", due to the appreciable difference in the equilibrium height for the atom interacting directly with the F_s center and the neighboring atoms interacting with the surrounding sites, a feature which can be described as a "double frustration".

Point (I) is already known from previous work.[22−25] We will illustrate points (II) and (III) via examples of optimized structures of small Au clusters growing around the F_s center.

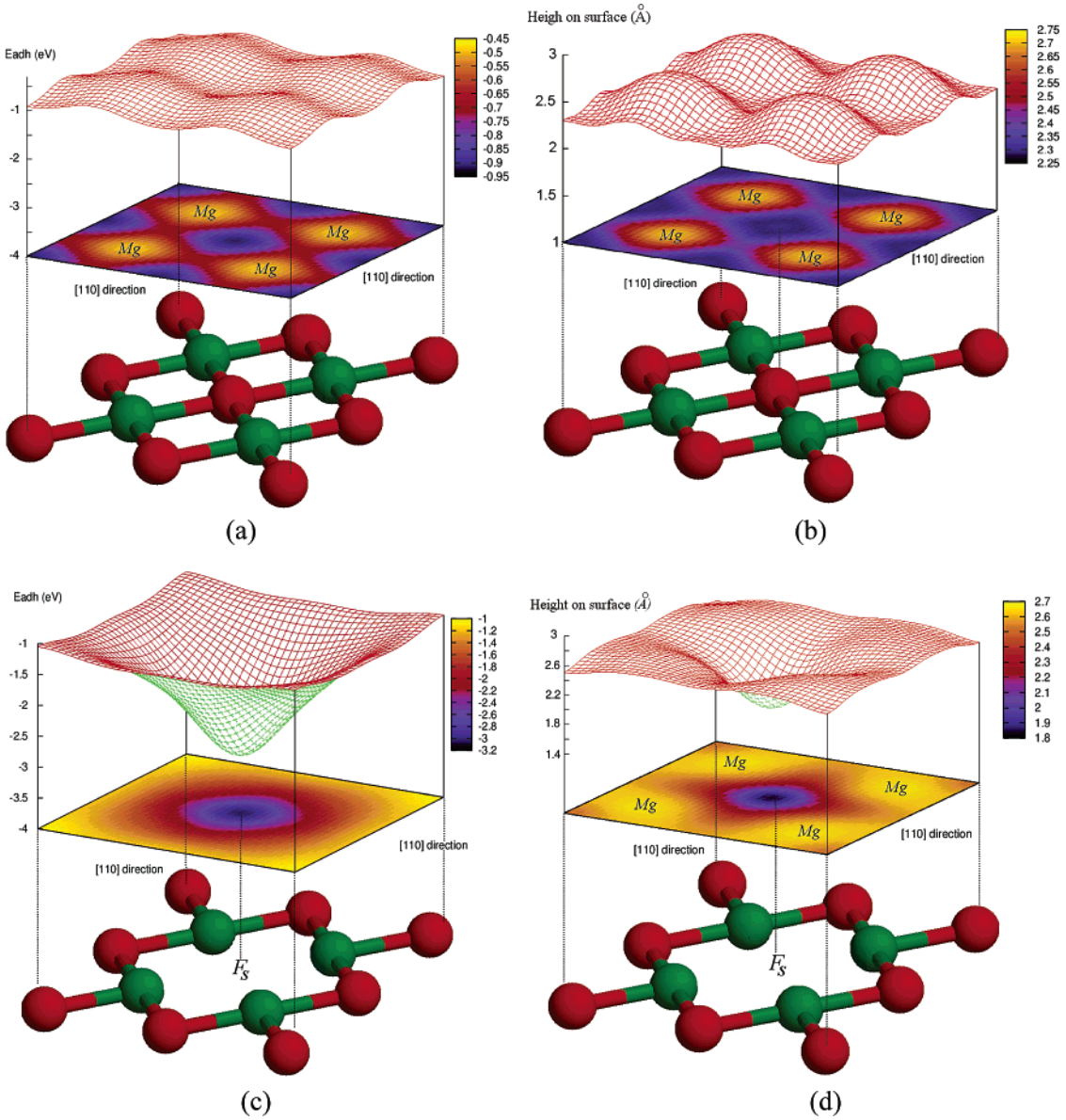

Figure 1. Topography of the absorption of an Au atom on the regular and defected MgO (100) surface: optimal adhesion energy (a) and equilibrium height (b) of a gold atom absorbed on the regular surface; optimal adhesion energy (c) and equilibrium height (d) of a gold atom absorbed on the F_s-defected surface.

The Au dimer minimum-energy structure is not shown, as it is known from previous work[22] to absorb on-top the F_s center in an upright position. In Figure 2, the Au_3 and Au_4 lowest-energy structures absorbed on the F_s-defected MgO (100) surface are shown, obtained through a search in which several (6−8) geometry optimizations starting from properly selected configurations have been conducted. In Table 1, the corresponding energies are reported. In addition, we also report in Figure 3 and Table 1 the structures and energy values for an Au_{20} cluster (a "magic" gold cluster recently characterized in the gas phase[40,41]) absorbed on the F_s center. This cluster has been chosen as an example of larger clusters and for its intrinsic interest: it is in fact a surface-only structure (no inner atoms), exhibiting a very large HOMO−LUMO gap of 1.77 eV, larger than that of C_{60},[40] an unusual stability and structure,[40,41] and peculiar optical[42,43] and catalytic[44] properties.

For each structure, we report in Table 1 four values of energy: (i) the adhesion energy (E_{adh}), calculated by subtracting the energy of the oxide surface and of the metal cluster, both frozen in their interacting configuration, from the value of the total energy of the system; (ii) the binding energy of the metal cluster (E_{met}), calculated by subtracting the energy of the isolated metal atoms from the total energy of the metal cluster in its interacting configuration; (iii) the metal cluster distortion energy (E_{dist}), which corresponds to the difference between the energy of the metal cluster in the configuration interacting with the surface, and the energy of the cluster in its lowest-energy gas-phase configuration; and (iv) the total energy (E_{tot}), which is the sum of the binding energy of the metal cluster and of the adhesion energy ($E_{tot} = E_{met} + E_{adh}$).

Let us start by illustrating the rotational freedom effect (II). The differences in total energy between configurations (b) and (c) of Au_3 or configurations (f) and (g) of Au_4 in Figure 2 (corresponding to the rotation of the trimer or tetramer around an axis perpendicular to the surface) are of the order of 0.02 eV. For such a "large" cluster as Au_{20}, one finds a similar situation, with an energy difference of 0.03 eV between configurations (a) and (b) in Figure 3, differing by a rotation around an axis perpendicular to the surface. For comparison, the energy differences among different Au_3 isomers on the

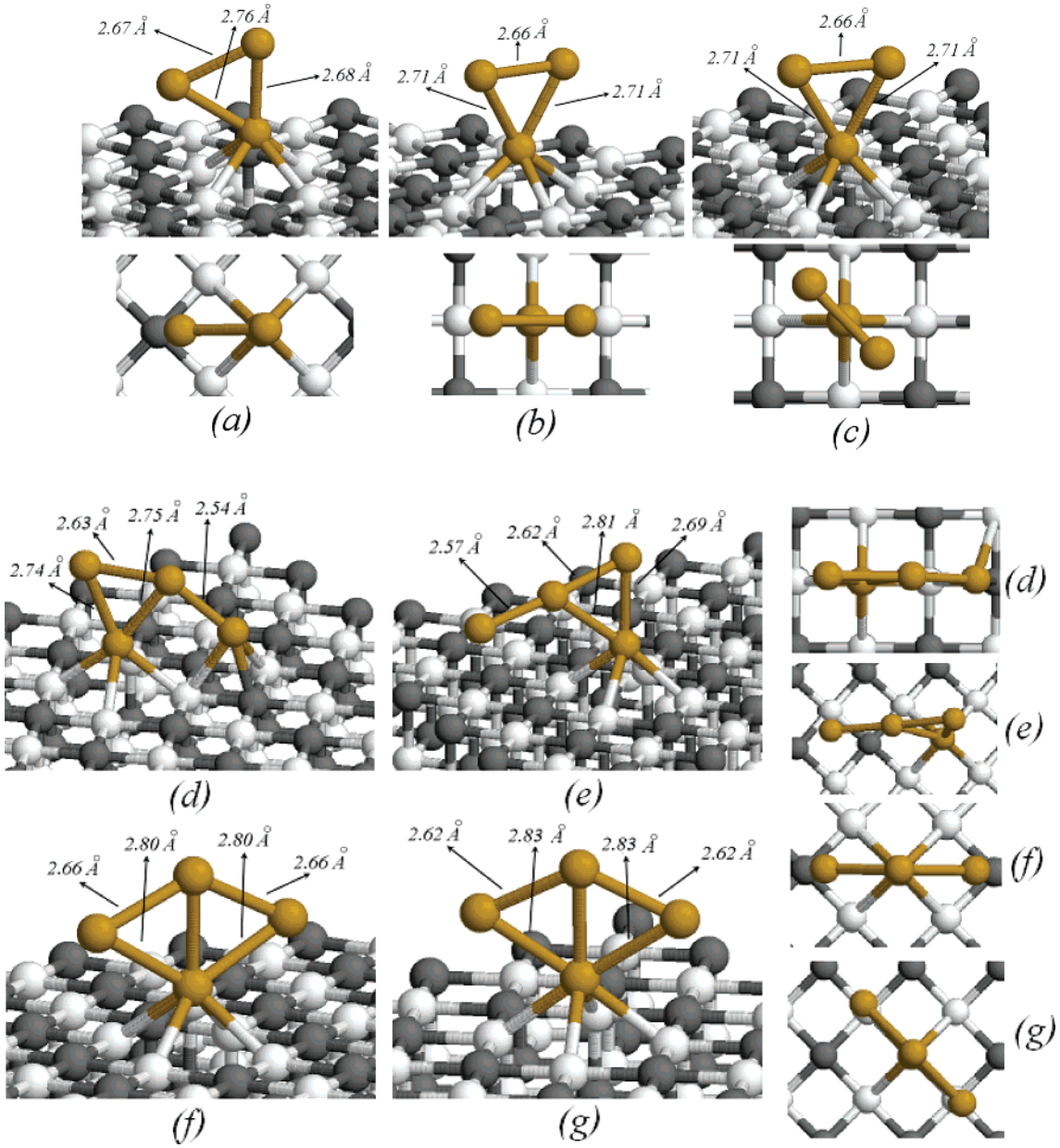

Figure 2. Lowest-energy local minima found for Au_3 and the Au_4 absorbed on an F_s defect from extensive DF searches. The corresponding energies are reported in Table 1.

TABLE 1: Energy Contributions Involved in the Absorption of Au_n (n = 3, 4, 20) Clusters on the F_s-Defected Oxide Surface[a]

	configuration	E_{adh} (eV)	E_{met} (eV)	E_{dist} (eV)	E_{tot} (eV)
Au_3	(a)	3.95	3.57	0.02	7.52
	(b)	3.96	3.56	0.03	7.52
	(c)	3.93	3.57	0.02	7.50
Au_4	(d)	4.57	5.80	0.46	10.37
	(e)	4.25	6.12	0.15	10.37
	(f)	4.04	6.20	0.06	10.24
	(g)	4.13	6.09	0.17	10.22
Au_{20}	(a)	4.33	46.25	0.72	50.58
	(b)	4.14	46.41	0.56	50.55

[a] The total energy of absorption (E_{tot}) is the sum of the metal bond contribution (E_{met}) and of the adhesion contribution (E_{adh}). The bigger is the value of E_{tot}, the more stable is the corresponding configuration. The metal distortion contribution (E_{dist}) is also reported.

regular surface are in the range 0.04−0.13 eV.[22] Small Au clusters absorbed on an oxygen vacancy are thus "rotationally fluxional" with respect to the absorption onto the surface.

The results in Figure 2 and Table 1 also illustrate the effects of the double frustration (III). A typical consequence is the fact that one finds configurations that are structurally different, but nearly isoenergetic; that is, one finds a competition between configurations with a reduced adhesion energy and a stronger metallic bond versus "doubly frustrated" configurations in which the metal cluster deforms appreciably with respect to the gas-phase situation to be in registry with the equilibrium energy and height topography shown in Figure 1 and thus increase its adhesion energy. Examples of this competition are structures (a) versus (b) of Au_3 and structures (d) versus (f) of Au_4. In the structures with a larger adhesion energy, the effect of the additional frustration produced by the F_s center is apparent: one finds an elongation of the metal−metal bond length between the atom atop the vacancy and its neighbors, as in structures (a) of Au_3, (d) of Au_4, and (a) of Au_{20}. These strained metal−metal bonds reflect in the larger values of E_{dist}. Alternatively, the cluster can essentially maintain its gas-phase equilibrium structure and adhere to the surface mainly through the atom

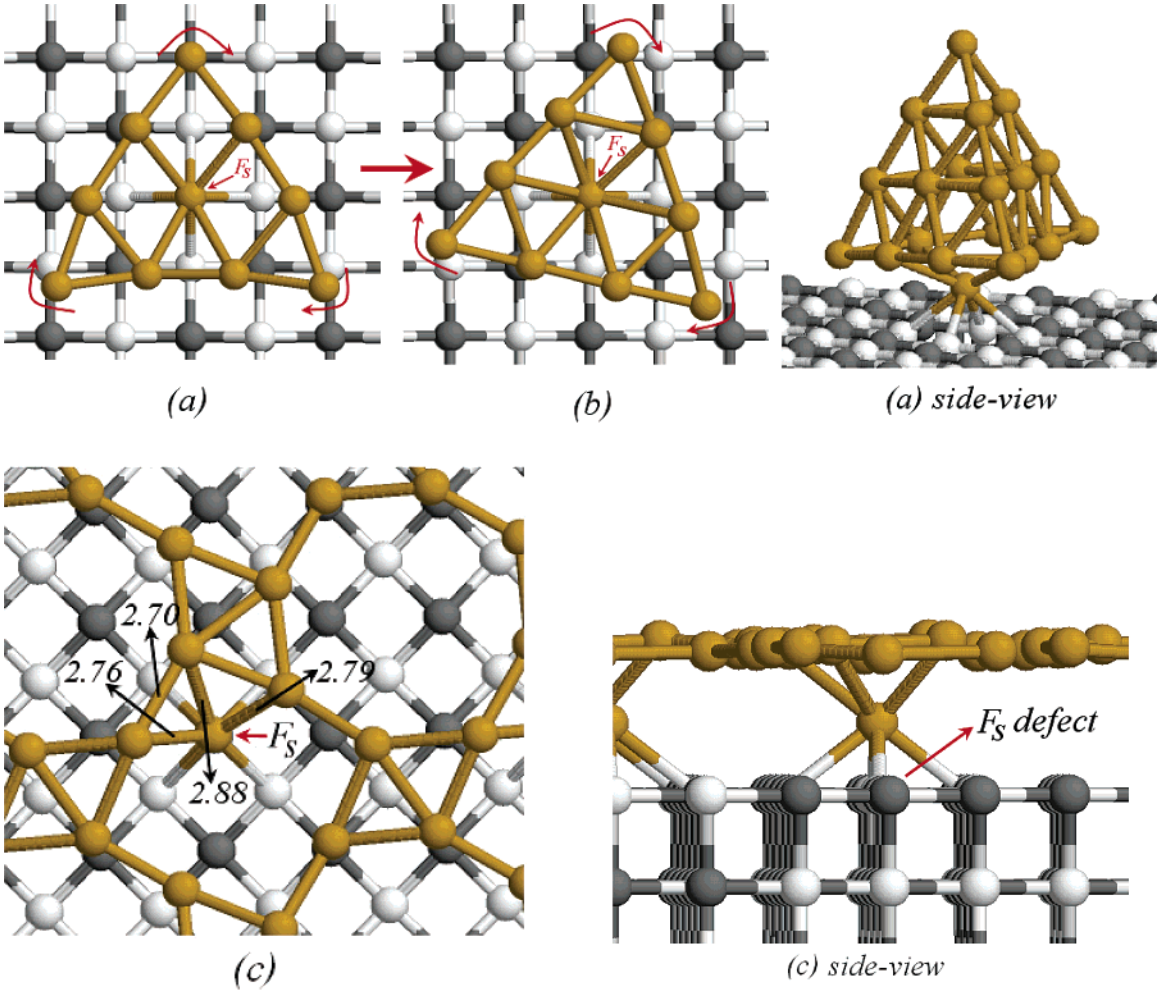

Figure 3. Low-energy configurations for Au_{20} (a,b) and a gold monolayer (c) are displayed: (b) is obtained from (a) through a rotation of about 30° around an axis perpendicular to the surface; on the right, a side-view of the (a) configuration is displayed to highlight the strong deformation of the basal fcc (111) face; (c) Au monolayer reconstruction around the F_s vacancy in the 3 × 3 cell; the elongated metal bond lengths shown are due to the frustration induced by the oxide defect.

directly atop the vacancy, as in structures (b) of Au_3 or (f) of Au_4. It is interesting to observe from Figure 3 that absorbed Au_{20} substantially maintains its "magic" tetrahedral structure, with the notable exception of the atom at the center of the basal fcc (111) face, which protrudes out and elongates its metal−metal bonds to better interact with the oxygen vacancy. One can also note that, despite the very similar values of the total absorption energy, the Au_{20} cluster is more deformed in structure (a), see especially the atoms at two basal apexes, with respect to structure (b). The metal distortion energy is, however, not large enough to overcome the extra stability associated with the electronic shell closure, cage-like and local-fcc-pattern effects,[41] so that the tetrahedral structure is a good candidate as the global minimum of Au_{20} absorbed on the MgO (100) F_s defect. If confirmed, this implies that tetrahedral Au_{20} absorbed on MgO (100) may possess peculiar optical and catalytic properties.[42−44] A further illustration of the effects of double frustration is given in Figure 3c, in which the configuration resulting from the geometry optimization of a gold monolayer in a 3 × 3 cell is shown: one finds a peculiar clusterization induced by the presence of the F_s defect. In particular, the Au atom atop the vacancy gets much closer to the surface (1.62 Å) with respect to the neighboring atoms (distances in the range 3.2−3.5 Å), as it is apparent from the side-view of Figure 3c, and this is the origin of the clusterization effect. We note in passing that this is an example of 2D structures, which have been advocated for gold deposition on oxide substrates.[12] To summarize point (III), we can say that the peculiar topography of r_{min} around the vacancy gives rise to a different form of cluster fluxionality, in which the cluster's energy landscape is populated with nearly isoenergetic, but qualitatively diverse structural motifs. A precise understanding of metal clusters' fluxionality is important as it can have a substantial influence, for example, on the clusters' catalytic properties,[13,20,21] or explain the experimentally observed formation of metal clusters exhibiting different structural motifs.[20,21]

In passing, we note that we have not discussed the configurations derived from our local energy minimizations lying at high energies. Kinetic trapping effects involving high-energy local minima could occur if the dynamics of the growth process is much faster than that of the cluster reorganization. However, the experimental flow (or deposition) rate is usually kept small to increase the reproducibility of the results, so the time-scale of the growth process is typically of the order of seconds or minutes (see, for example, ref 20), much larger than the time-scale of the reorganization of small clusters (of the order of nanoseconds[34]). Kinetic effects involving high-energy minima are therefore not likely in the usual experimental conditions.

To conclude the analysis of the results reported in Table 1, we consider the energetics of processes in which a metal cluster absorbed on an F_s center dissociates into two smaller clusters: one still absorbed on the defect, and the other one on the regular

TABLE 2: Energy Differences Corresponding to Metal Cluster Dissociation Processes[a]

process	energy difference (eV)
$Au_2(d) \rightarrow Au(d) + Au(r)$	1.87
$Au_3(d) \rightarrow Au_2(d) + Au(r)$	0.75
$Au_3(d) \rightarrow Au(d) + Au_2(r)$	0.70
$Au_4(d) \rightarrow Au_3(d) + Au(r)$	1.96
$Au_4(d) \rightarrow Au_2(d) + Au_2(r)$	0.79
$Au_4(d) \rightarrow Au(d) + Au_3(r)$	2.07

[a] $Au_n(d)$ and $Au_n(r)$ represent clusters lying on the F_s-defected or the regular surface, respectively. The energies used to calculate these differences are the total energies reported in Table 1 for the clusters absorbed on the defect. The total absorption energy of a dimer on the defect is 5.85 eV. The total cluster absorption energies on the regular surface are: Au_1, 0.91 eV; Au_2, 3.74 eV; Au_3, 5.30 eV.

surface. These processes can be important[33,45] for understanding detrapping and thus Ostwald ripening of small clusters by larger ones observed in MBE experiments at sufficiently high temperatures.[20,21] In Table 2, we report the energy differences corresponding to several fragmentation processes of Au_n clusters. $Au_n(d)$ and $Au_n(r)$ represent clusters lying on the defect or the regular surface, respectively. The most interesting finding from these results is that dissociation of a dimer (Au_2) fragment as a rule requires substantially less energy than that of a single atom or a trimer. This is due to two reasons: (a) an Au_2 dimer both on the regular surface or atop an oxygen vacancy is stabilized by the "metal-on-top" effect,[22] that is, by an increase in the metal−surface adhesion due to the presence of metal atoms above those directly interacting with the surface; and (b) the double frustration around the defect strains the Au−Au distance between the Au atom atop the defect and those atop neighboring sites and destabilizes the Au_3 and Au_4 clusters with respect to a single atom or a dimer on the oxygen vacancy, whose optimal geometry is in an upright position and does not involve the interaction of metal atoms with sites surrounding the vacancy. As a consequence, we see from Table 2 that extraction of an $Au_2(r)$ fragment from $Au_3(d)$ or $Au_4(d)$ requires 0.7/0.8 eV. This energy difference is not large as compared to k_BT in MBE experiments,[20,21] which suggests that fragmentation processes of small clusters may be active and should be taken into account in the growth and sintering of Au clusters at sufficiently high temperatures.[33,45]

4. Conclusions

We find that the presence of a neutral oxygen vacancy (F_s center) appreciably modifies the potential energy landscape of a gold atom moving in its surrounding, and that this has important consequences on the growth of small gold clusters atop the defect site. An accurate sampling of the single-atom absorption topography highlights that not only the interaction of the gold atom directly atop on the defect is strongly increased, and its equilibrium distance from the surface decreased, but the absorption over a larger region extending up to third- and fourth-neighbor sites is appreciably altered. Unexpectedly, (a) similar interaction energies are found for the neighboring oxygen and magnesium sites, which therefore lose their chemical identity, and (b) both the absorption energies and the equilibrium heights are increased with respect to the regular surface. The latter effect induces what can be described as a "double frustration", in the sense that it adds to the usual frustration due to the mismatch between oxide and bulk metal lattice parameters. All of this produces a rotational and structural fluxionality of the gold clusters absorbed on the F_s defect, by which (a) the clusters can almost freely rotate around an axis perpendicular to the surface, leaving the atom directly interacting with the defect site fixed; and (b) one finds a competition between metal cluster configurations with a reduced absorption energy, but a small distortion with respect to the gas-phase structure and thus a stronger metallic bond, and configurations in which the metal−metal distances between the atom atop the defect and its nearest neighbors are elongated (double frustration), but the overall configuration is stabilized by larger adhesion energies. This is explicitly shown for the Au_3 and Au_4 lowest-energy structures, and for the tetrahedral Au_{20} and a gold monolayer absorbed on an oxygen vacancy. This fluxionality can have a substantial influence, for example, on the clusters' catalytic properties,[13,20,21] or explain the experimentally observed formation of metal clusters exhibiting different structural motifs.[20,21]

Additionally, we also calculate cluster fragmentation energies, corresponding to partial detrapping from the defect site, and find that the extraction of a gold dimer involves energies around 0.7/0.8 eV, and might thus be active[45] in MBE experiments at sufficiently high temperatures[20] (Ostwald ripening).

Finally, we stress that this behavior is not peculiar of gold, but is qualitatively quite general, and has been verified by us also for other metals (e.g., Ag) growing around an MgO (100) oxygen vacancy, as will be reported in future work.

Acknowledgment. We acknowledge financial support from the Italian CNR for the project "(Supra-)Self-Assemblies of Transition Metal Nanoclusters" within the framework of the ESF EUROCORES SONS, and from the European Community Sixth Framework Program for the STREP project "Growth and Supra-Organization of Transition and Noble Metal Nanoclusters" (contract no. NMP4-CT-2004-001594).

References and Notes

(1) de Heer, W. A. *Rev. Mod. Phys*. **1993**, *65*, 611.
(2) *Chemisorption and Reactivity on Supported Clusters and Thin Films*; NATO Advanced Study Institute, Series E: Physics; Lambert, R. M., Pacchioni, G., Eds.; Kluwer: Dordrecht, 1997; Vol. 331.
(3) Klabunde, K. J. *Nanoscale Materials in Chemistry*; Wiley: New York, 2001.
(4) *Progress in Experimental and Theoretical Studies of Clusters*; Kondow, T., Mafuné, F., Eds.; World Scientific: New York, 2003.
(5) Hammer, B.; Norskov, J. K. *Nature* **1995**, *376*, 238.
(6) Schwerdtfeger, P. *Angew. Chem., Int. Ed.* **2003**, *42*, 1892.
(7) Daniel, M.-C.; Astruc, D. *Chem. Rev.* **2004**, *104*, 293.
(8) Pyykkö, P. *Angew. Chem., Int. Ed.* **2004**, *43*, 4412.
(9) Hutchings, G. J.; Haruta, M. *Appl. Catal., A* **2005**, *291*, 2.
(10) Remediakis, N.; Lopez, N.; Norskov, J. K. *Appl. Catal., A* **2005**, *291*, 13.
(11) Haruta, M. *Chem. Rec.* **2003**, *3*, 75.
(12) Chen, M. S.; Goodman, D. W. *Science* **2004**, *306*, 252.
(13) Häkkinen, H.; Abbet, S.; Sanchez, A.; Heiz, U.; Landman, U. *Angew. Chem., Int. Ed*. **2003**, *42*, 1297.
(14) Zheng, J.; Dickson, R. M. *J. Am. Chem. Soc*. **2002**, *124*, 13982.
(15) Brongersma, M. L. *Nat. Mater*. **2003**, *2*, 296.
(16) Chen, S.; Ingram, R. S.; Hostetler, M. J.; Pietron, J. J.; Murray, R. W.; Schaaff, T. G.; Khoury, J. T.; Alvarez, M. M.; Whetten, R. L. *Science* **1998**, *280*, 2098.
(17) Lee, Y. C.; Tong, P.; Montano, P. A. *Surf. Sci*. **1987**, *181*, 559.
(18) He, J.-W.; Moller, P. J. *Surf. Sci.* **1987**, *180*, 411.
(19) Haas, G.; Menck, A.; Brune, H.; Barth, J. V.; Venables, J. A.; Kern, K. *Phys. Rev. B* **2000**, *61*, 11105.
(20) Horup-Hansen, K.; Ferrero, S.; Henry, C. R. *Appl. Surf. Sci*. **2004**, *226*, 167.
(21) Meerson, O.; Sitja, G.; Henry, C. R. *Eur. Phys. J. D* **2005**, *34*, 119.
(22) Barcaro, G.; Fortunelli, A. *J. Chem. Theory Comput.* **2005**, *1*, 1972.
(23) Del Vitto, A.; Pacchioni, G.; Delbecq, F.; Sautet, P. *J. Phys. Chem. B* **2005**, *109*, 8040. The numerical differences of the absorption energies with respect to ref 22 are due to a different description of the oxide structural properties.
(24) Yudanov, I.; Pacchioni, G.; Neyman, K.; Rösch, N. *J. Phys. Chem. B* **1997**, *101*, 2786.

(25) Matveev, A. V.; Neyman, K.; Yudanov, I.; Rösch, N. *Surf. Sci.* **1999**, *426*, 123.
(26) Yulikov, M.; Sterrer, M.; Heyde, M.; Rust, H.-P.; Risse, T.; Freund, H.-J.; Pacchioni, G.; Scagnelli, A. *Phys. Rev. Lett.* **2006**, *96*, 146804.
(27) Sanchez, A.; Abbet, S.; Heiz, U.; Schneider, W.-D.; Häkkinen, H.; Barnett, R. N.; Landman, U. *J. Phys. Chem. A* **1999**, *103*, 9573.
(28) Molina, L. M.; Hammer, B. *J. Chem. Phys.* **2005**, *123*, 161104.
(29) Walter, M.; Häkkinen, H. *Phys. Rev. B* **2005**, *72*, 205440.
(30) Molina, L. M.; Hammer, B. *Phys. Rev. B* **2004**, *69*, 155424.
(31) Baletto, F.; Ferrando, R. *Rev. Mod. Phys.* **2005**, *77*, 371.
(32) Moseler, M.; Hakkinen, H.; Landman, U. *Phys. Rev. Lett.* **2002**, *89*, 176103.
(33) Giordano, L.; Di Valentin, C.; Goniakowski, J.; Pacchioni, G. *Phys Rev. Lett.* **2004**, *92*, 096105.
(34) Baletto, F.; Mottet, C.; Ferrando, R. *Phys. Rev. Lett.* **2000**, *84*, 5544.
(35) Baroni, S.; Del Corso, A.; de Gironcoli, S.; Giannozzi, P., http://www.pwscf.org.
(36) Perdew, J. P.; Burke, K.; Ernzerhof, M. *Phys. Rev. Lett*. **1996**, *77*, 3865.
(37) Aprà, E.; Fortunelli, A. *J. Mol. Struct. (THEOCHEM)* **2000**, *501*−*502*, 251.
(38) Vervisch, W.; Mottet, C.; Goniakovski, J. *Phys. Rev. B* **2002**, *65*, 245411.
(39) Leroy, F.; Renaud, G.; Letoublon, A.; Lazzari, R.; Mottet, C.; Goniakowski, J. *Phys. Rev. Lett.* **2005**, *95*, 185501.
(40) Jun, L.; Li, X.; Zhai, H. J.; Wang, L. S. *Science* **2003**, *299*, 864.
(41) Aprà, E.; Ferrando, R.; Fortunelli, A. *Phys. Rev. B* **2006**, *73*, 205414.
(42) Wu, K.; Li, J.; Lin, C. *Chem. Phys. Lett*. **2004**, *388*, 353.
(43) Xie, R.-H.; Bryant, G. W.; Zhao, J.; Kar, T.; Smith, V. H. *Phys. Rev. B* **2005**, *71*, 125422.
(44) Molina, L. M.; Hammer, B. *J. Catal*. **2005**, *233*, 399.
(45) Xu, L.; Henkelman, G.; Campbell, C. T.; Jonsson, H. *Phys Rev. Lett.* **2005**, *95*, 146103.

Electronic and Structural Shell Closure in AgCu and AuCu Nanoclusters

BarcaroJPCB2006b

Giovanni Barcaro,[†] Alessandro Fortunelli,*[,†] Giulia Rossi,[‡] Florin Nita,[‡,§] and Riccardo Ferrando*[,‡]

IPCF/CNR, Via G. Moruzzi 1, Pisa, I56124, Italy, Dipartimento di Fisica, Università di Genova, INFM and IMEM/CNR, Via Dodecaneso 33, Genova, I16146, Italy, and Institute of Physical Chemistry IG Murgulescu, Romanian Academy, Spl. Independentei 202, Bucharest, Romania

Received: July 20, 2006; In Final Form: September 19, 2006

The structures of AgCu clusters containing 40 atoms are investigated. The most promising structural families (fcc clusters, capped decahedra, and two types of capped polyicosahedra) are singled out by means of global optimization techniques within an atom−atom potential model. Then, representative clusters of each family are relaxed by means of density-functional methods. It is shown that, for a large majority of compositions, a complex interplay of geometric and electronic shell-closure effects stabilizes a specific polyicosahedral family, whose clusters are much lower in energy and present large HOMO−LUMO gaps. Within this family, geometric and quantum effects concur to favor magic structures associated with core−shell chemical ordering and high symmetry, so that these clusters are very promising from the point of view of their optical properties. Our results also suggest a natural growth pathway of AgCu clusters through high-stability polyicosahedral structures. Results for AuCu clusters of the same size are reported for comparison, showing that the interplay of the different effects is highly material specific.

1. Introduction

Metallic nanoclusters, namely aggregates of metal atoms of nanometric size, present physical and chemical properties which can be strongly size-dependent,[1−4] thus offering the possibility of tuning specific properties by selecting the cluster size. These size-dependent properties are interesting not only from the point of view of basic science but also for applications in nanotechnology and heterogeneous catalysis.

In this context, nanoscale clusters of coinage metals have been widely studied from both the experimental and theoretical point of view.[5−7] Their interaction with oxygen, carbon monoxide, methanol, and nitrogen in the gas phase has been intensively studied in view of understanding their role as catalysts in specific chemical reactions, such as CO and hydrocarbon oxidation.[8−12] They are also of great practical importance because of their peculiar optical properties,[13−15] especially when core−shell arrangements are achieved.

Recently, binary coinage metal clusters have attracted considerable attention.[16−22] In fact, binary clusters offer an extra degree of freedom for catalysis and nanotechnology applications, since in these clusters one can vary both size and composition.[23] The starting point for determining, and possibly tuning, the properties of a binary cluster of given size and composition is the knowledge of its structure. Pure clusters may present a large variety of possible structures, including high-symmetry structural motifs such as fcc-truncated octahedra, icosahedra, and decahedra.[4] Binary clusters offer an even wider spectrum of possible structural motifs, and within each motif, different kinds of chemical ordering are possible: intermixed, core−shell, and multishell.[24−26]

For these reasons, the determination of the best structures of binary clusters is a very challenging task. As a starting point, indications on the possible structures may come from geometric and electronic shell closure considerations, corresponding to geometric and electronic magic numbers. In the case of pure coinage metals, the photoelectron spectra of clusters containing a few tens of atoms have revealed electronic shell structures with clear closures corresponding to those of spherical electron gas models.[27−32] These results indicate that coinage metals behave, at least approximately, as simple metals, with each atom contributing a single quasi-free electron. The electronic shell closure has also been confirmed for Ag clusters doped by a single Cu impurity,[21] with the further indication that the inclusion of the impurity somewhat enhances the shell closure effect. However, these considerations are not sufficient for determining the actual structure of the clusters.

In this paper we analyze binary AgCu clusters of size $N = 40$ atoms at varying composition and compare the results to those for AuCu clusters of the same size. This size is especially important for two reasons. First of all, it is a magic electronic size for both the hard-wall and the harmonic jellium (spherical electron gas) model[33] and the Tensor Surface Harmonic Theory[34,35] (as modified to describe nonhollow clusters[36]); hence we expect quantum effects, possibly connected with spherical aromaticity,[37,38] to play a significant role. Second, at $N = 40$, there is a competition among several structural motifs, from bulklike fcc clusters, to capped decahedra, to two distinct families of polyicosahedra. Sizes $N = 34$ and $N = 38$, which were studied previously,[17−19,39] lack some of these features. Size 34 is magic for the hard-wall but not for the harmonic electron gas model. Moreover, at size 34, there is practically no competition among motifs, since there is a clearly dominant specific polyicosahedral family. Size 38 presents a competition among several motifs, but it is not an electronic magic size.

* Corresponding author: A.F., fortunelli@ipcf.cnr.it; R.F., ferrando@fisica.unige.it.
[†] IPCF/CNR.
[‡] Dipartimento di Fisica, Università di Genova, INFM and IMEM/CNR.
[§] Institute of Physical Chemistry IG Murgulescu, Romanian Academy.

10.1021/jp064593x CCC: $33.50
Published on Web 10/26/2006

In the following we show that the most stable structural motif of AgCu clusters arises from a complex interplay of different factors, including geometry, chemical ordering, and electronic shell closure. These factors concur in determining a single structural family which is magic from both the electronic and the geometric point of view and occurs at almost every possible composition, with special stability when the composition allows a high-symmetry core−shell arrangement. This structural family has polyicosahedral character,[17] compact shape, and not too strained bonds (especially at intermediate compositions) and at the same time presents quite large HOMO−LUMO gaps (of the order of 0.8 eV), indicating electronic shell closure. Other structural motifs could be in principle competitive but lack at least one of these favorable factors. The fact that geometric and quantum effects concur to favor magic structures associated with core−shell chemical ordering and high-symmetry render these clusters very appealing from the point of view of their optical properties.

Results for AuCu clusters of the same size are also reported, to highlight differences which mainly originate from the stronger tendency of Au and Cu to form heterogeneous bonds, compared to Ag and Cu, and to the shorter-range character of the atom−atom interaction for gold: these differences bring two different families of polyicosahedra in close competition.

2. Computational Method

An unbiased search of the lowest-energy structures of metallic clusters of this size can be performed on fully ab initio grounds only with an intense computational effort[40] due to the huge number of local minima on the potential energy surface.[4] The case of bimetallic clusters is even much more demanding, because of the inequivalence of homotops, namely of isomers presenting the same geometric structure but a different chemical ordering.[41] For this reason, a two-step procedure is employed. First, for each composition at size 40, global optimization is performed within a second-moment tight-binding (SMTB) atom−atom potential model[42,43] (see refs 19 and 44 for the form and parameters of the potential). Even though the parameters of the potential are fitted on bulk quantities, there are indications that the potential is reasonably accurate also in low-coordination situations, such as crystal surfaces. In fact, this potential was employed in the modeling of an Ag monolayer on Cu(111), obtaining a very good agreement with the experimental results.[45] This semiempirical potential was also able to select the most important structural motifs of AgCu clusters.[17] Representative clusters of each motif are then locally optimized by density-functional-theory (DFT) calculations.

Global optimization is performed by running three different algorithms, the basin-hopping,[46] the energy-landscape paving method (ELP),[47] and the parallel excitable walkers[48] (PEW) method. These algorithms adopt a Monte Carlo (MC) plus minimization scheme.[49] At each composition, a run of 10^6 MC steps is made for each algorithm. In these long runs, the elementary MC moves are performed by displacing each atom of the cluster within a sphere of radius 1.3 Å with uniform probability. After the MC runs, the best clusters pertaining to different structural motifs are reoptimized by running low-temperature basin-hopping simulations of 10^5 steps in which only exchange moves between Ag and Cu atoms, or moves displacing single surface atoms are performed. These further simulations are aimed at the optimization of the chemical ordering and of the surface of a given kind of structure.

Density-functional calculations are then carried out on selected configurations from each structural family with the DF

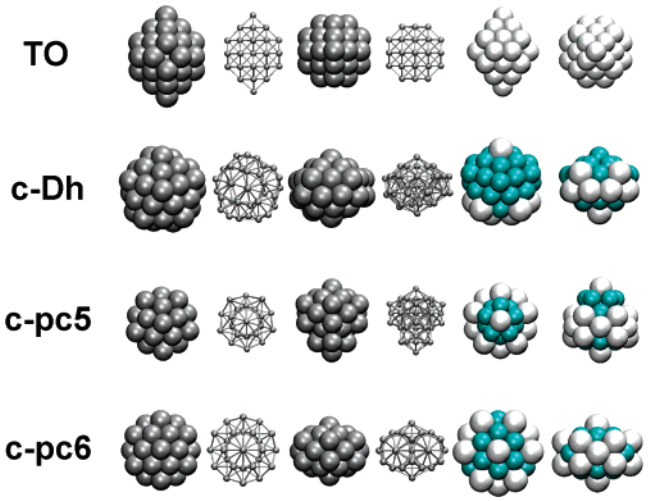

Figure 1. (First row) fcc-truncated octahedron (TO). This TO has D_{4h} symmetry. It can be obtained either by removing atoms from four vertexes over six of the complete octahedron of 44 atoms or by adding two atoms on opposite square facets of the 38-atom fully symmetric truncated octahedron. In the first four snapshots from left, the structure is shown from different viewpoints. In the fifth and sixth snapshots, the TO is shown at composition $Ag_{34}Cu_6$. Copper atoms are not visible because they form the inner core; silver atoms are in light gray. (Second row) Capped decahedron (c-Dh). This structure is obtained by adding an umbrella to the complete decahedron of 23 atoms. Depending on composition, the umbrella shape may change, but the structure is not highly symmetric, having at most a single reflection plane. In the fifth and sixth snapshots, the c-Dh is shown at composition Ag_8Cu_{32}. (Third row) Capped 5-fold pancake (c-pc5). This structure is a polyicosahedron obtained by adding an umbrella of 6 atoms on the 5-fold pancake of 34 atoms.[17] The first four snapshots show the structure from different viewpoints. In the fifth and sixth snapshots, the c-pc5 is shown at composition $Ag_{17}Cu_{23}$, where it has C_{5v} symmetry. (Fourth row) Capped 6-fold pancake (c-pc6). This structure is obtained by adding 2 vertex atoms to the 6-fold pancake,[17] a polyicosahedron of 38 atoms. In the fifth and sixth snapshots, the c-pc6 is shown at composition $Ag_{17}Cu_{23}$, where it has D_{3h} symmetry.

module of the NWChem package[50] (release 4.7) and use the Becke functional[51] for exchange and the Perdew−Wang functional[52] for correlation. Gaussian-type-orbital basis sets (7s6p6d)/[5s3p2d] and effective core potentials are used for all elements, derived from refs 53 and 54 for Ag and ref 55 for Cu, and modified combining the suggestions in refs 56 and 57. Charge density fitting (11s4p5d3f4g)/[11s4p4d3f2g] Gaussian-type-orbital basis sets were used to compute the Coulomb potential.[58] All the calculations have been performed spin-unrestricted and using a Gaussian-smearing technique[59] for the fractional occupation of the one-electron energy levels. A numerical grid of 65 radial points and 350 points for the angular part was used for evaluation of the exchange-correlation potential and energy. The geometry optimization was stopped when the numerical force on atoms was less than 4×10^{-4} au. More details on the numerical procedure can be found in ref 57.

3. Structural Motifs from Atom−Atom Potential Optimization

The global optimization runs using the Gupta-like potential have singled out four possible structural motifs (see Figure 1).

The first motif is represented by fcc clusters, namely pieces of fcc bulk crystal (Cu, Ag, and Au present the fcc lattice in their bulk form). This is the only motif which does not present any local 5-fold symmetry axis.

The clusters belonging to the second motif can be described as decahedra of 23 atoms capped by a distorted umbrella of 17

atoms. In the following, this motif will be referred to as the capped decahedral motif (c-Dh). Depending on composition, the umbrella can be of different shapes. In some cases, the umbrella is placed in such a way that this cluster is a fragment of the icosahedron of 55 atoms. Structures of this kind were found in the optimization of pure Sutton-Chen Ag_{40} and Cu_{40} clusters[60] and in the optimization of Cu_{40}, $Au_{10}Cu_{30}$, $Au_{20}Cu_{20}$ within the Gupta model.[16]

The clusters belonging to the third and fourth motifs are different families of polyicosahedra. Polyicosahedra are clusters built up by interpenetrating elementary icosahedra of 13 atoms.[17] The structures of the third motif are a 34-atom polyicosahedra (the 5-fold pancake, see Figure 1 of ref 17) capped by 6 atoms. These clusters will be referred to as capped 5-fold pancakes (c-pc5) in the following. When the cap is placed symmetrically around the 5-fold axis, these clusters can also be seen as incomplete anti-Mackay icosahedra missing 5 atoms, with a crown of atom vacancies placed symmetrically around the 5-fold axis. For some specific compositions (like $Ag_{27}Cu_{13}$, $Ag_{22}Cu_{18}$, $Ag_{17}Cu_{23}$) these clusters belong to the C_{5v} symmetry group. The clusters of the fourth motifs can be described as 6-fold pancake structures (see Figure 1 of refs 17 and 39) capped by two silver atoms along the 6-fold symmetry axis. For this reason, they will be referred to as capped 6-fold pancakes (c-pc6) in the following. For some specific compositions, these clusters can be of D_{6h} symmetry, thus being the most symmetric clusters found at size 40. A cluster of this structure was found to be the global minimum of $Au_{10}Cu_{30}$ within the Gupta model[16] and of Al_{40} using an embedded-atom potential.[61]

The results of the SMTB model indicate that, depending on composition, capped decahedra, c-pc5, and c-pc6 are the global minima. No fcc global minima are found, even though fcc clusters are in close competition with the other motifs for homogeneous clusters. Capped decahedral global minima are found for homogeneous Ag and Cu clusters,[7] for copper-rich compositions from Cu_{40} to $Ag_{11}Cu_{29}$, and for silver-rich compositions from Ag_{40} to $Ag_{37}Cu_3$. Capped 6-fold pancakes (c-pc6) are the global minima in the ranges from $Ag_{36}Cu_4$ to $Ag_{33}Cu_7$ and from $Ag_{20}Cu_{20}$ to $Ag_{12}Cu_{28}$. Finally, c-pc5 structures are the global minima in the range from $Ag_{32}Cu_8$ to $Ag_{21}Cu_{19}$. As we shall see below, the DFT local optimizations of the clusters belonging to the four families will reveal a different scenario, arising from the different electronic effects on the relative energetics of the structural motifs.

4. DFT Optimization of Homogeneous Ag and Cu Clusters

The DFT local relaxation of the structures described in the previous section shows that homogeneous Ag and Cu clusters exhibit a different energy ordering of the four motifs. For Ag, the capped Dh and the fcc cluster are almost degenerate, whereas polyicosahedra are clearly higher in energy, especially the c-pc6. For Cu, the c-pc5 is the lowest in energy, and it is appreciably separated from the capped decahedron and the fcc cluster. Even though we cannot claim that we have considered the best capped decahedron, there is a clear indication that the c-pc5 is competitive for Cu_{40}, whereas for Ag_{40} it is not. This result agrees with a qualitative trend derived from the semiempirical potential modeling. In fact, c-pc5 structures are highly strained, with strongly compressed inner atoms.[17] Compared to Ag, Cu is able to better accommodate this compression,[4] paying a smaller energy penalty, whereas for Au the energetic penalty would be larger. Inner atoms in c-pc6 structures are less compressed,[39] so the SMTB model would favor them compared to c-pc5 structures for homogeneous clusters. Surprisingly, the DFT calculations indicate the opposite. The reasons why the c-pc6 structures are destabilized with respect to c-pc5 structures are purely electronic in character and thus are not included in the SMTB approach. In fact, structures of type c-pc5 generally present an electronic shell closure effect, whereas c-pc6 structures present an electronic shell *un*closure effect.[18] Indeed, as shown in Table 1, c-pc5 structures present large HOMO−LUMO gaps, whereas c-pc6 clusters are Jahn−Teller structures with very small gaps. To further rationalize this point, we performed an extended Hückel (or tight-binding) calculation, i.e., we assigned to each atom an s-type atomic orbital, interacting with neighboring atomic orbitals through a distance-dependent Slater-like analytic form, $H_{ij} = -11.2\delta_{ij} - A \exp(-r_{ij}/r_0)$,[62] and we diagonalized the corresponding Hamiltonian matrix. This is the simplest model which can take into account quantum (shell closure/unclosure) effects. The density-of-states (DOS) typically obtained for c-pc5 and c-pc6 structures is shown in Figure 2. From an inspection of this figure, it is apparent that c-pc5 structures exhibit significant energy gaps at both 34 and 40 electrons, whereas c-pc6 structures do not. Assuming the usual ordering of electronic states in a spherical potential,[33,35,37] 1s1p1d2s1f2p1g..., with shell closures at $N = 34$ (1s1p1d2s1f) and $N = 40$ (1s1p1d2s1f2p), we see that the oblate deformation of c-pc6 structures destabilizes the 2p orbitals, bringing them to intermix with the 1g orbitals, thus destroying the shell closure at $N = 40$. We note in this connection that all the 2p orbitals are destabilized, also because their radial node is associated with antibonding interactions, more numerous in the c-pc6 structure due to the larger number of intershell contacts (this is also true for the 2s orbitals). The more oblate character of the c-pc6 structure implies a greater splitting of the 1g orbitals compared to the c-pc5 structure.

TABLE 1: Structure, Symmetry Group, Spin, HOMO−LUMO Gap, and Separation from the Lowest Minimum ΔE for Structures Pertaining to the Different Structural Motifs of Homogeneous Ag and Cu Clusters

composition	structure	group	spin	gap (eV)	ΔE (eV)
Cu_{40}	c-pc5[b]	C_{5v}	0	0.77	0.00
Cu_{40}	c-Dh[a]	C_i	1	0.25/0.17	0.36
Cu_{40}	TO[d]	C_{4v}	1	0.49/0.16	0.46
Ag_{40}	c-Dh	C_i	0	0.02	0.00
Ag_{40}	TO	D_{4h}	1	0.32/0.18	0.03
Ag_{40}	c-pc5	C_{5v}	0	0.73	0.64
Ag_{40}	c-pc6[c]	D_{6h}	0	0.05	1.19

[a]Capped decahedra. [b] Capped 5-fold pancakes. [c]Capped 6-fold pancakes. [d]fcc-truncated octahedra.

5. DFT Optimization of Binary AgCu Clusters

There are several reasons to expect that polyicosahedral structures become more favorable for binary than for homogeneous clusters. The difference in atomic radii (the atomic size mismatch, which is already effective for binary noble gas clusters[63]), bond-order/bond-length correlation of metallic bonding,[64] and the smaller surface energy of Ag with respect to Cu, producing a tendency to surface segregation of Ag, all concur to the formation of polyicosahedral core−shell clusters with considerably reduced internal tension. However, all these considerations apply to both c-pc5 and c-pc6 structures. Indeed, c-pc5 structures would be better stabilized by an even larger difference in atomic radii,[39] whereas for c-pc6 the difference in atomic radii between Ag and Cu atoms is close to optimal. We have seen that the results of the global optimization within the atom−atom SMTB potential confirm this prediction, since

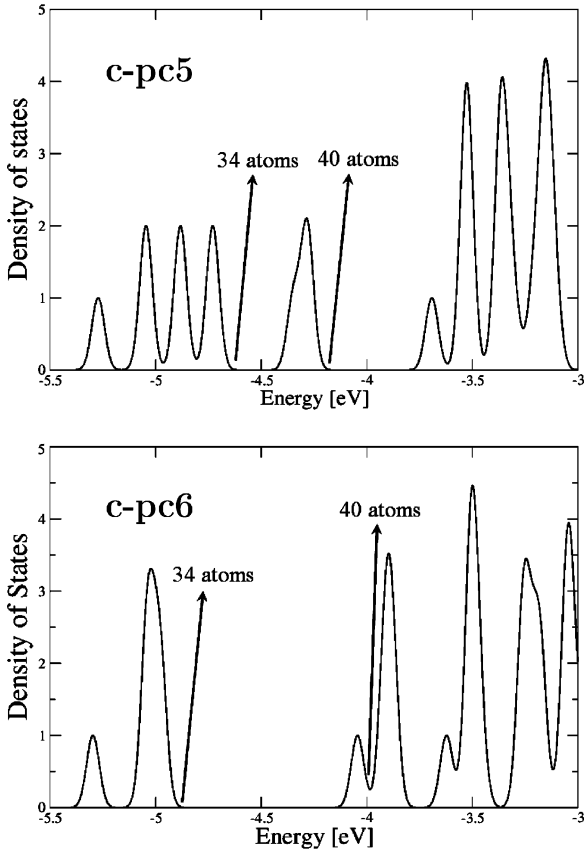

Figure 2. DOS derived from extended Hückel calculations on typical c-pc5 and c-pc6 structures. Energies in eV, DOS in arbitrary units. A broadening factor of 0.03 eV has been used to transform the delta functions into Gaussians. First 20 electrons are not shown for c-pc5; the first 22 electrons are not shown for c-pc6 (the lowest 1f orbital in c-pc6 lies at −6.3 eV). The occupations corresponding to $N = 34$ and $N = 40$ electrons are indicated by arrows. The peak of the c-pc6 DOS where the Fermi energy falls is a mixture of 2p and 1g states. The DFT DOS are qualitatively similar to those in the figure.

the majority of (putative) global minima have polyicosahedral character, and among polyicosahedral minima, there is a fair proportion of c-pc5 and c-pc6.

The DFT analysis leads to a different scenario. Polyicosahedral structures become even more dominant, and a specific polyicosahedral motif, the c-pc5 one, is clearly preferred at almost all compositions. As shown in Table 2, in fact, where the energy separation ΔE from the lowest isomer is reported, capped 5-fold pancakes are much lower in energy than the other structures. For example, for Ag_6Cu_{34}, the c-pc5 structure is separated from the c-Dh by more than 1 eV; for $Ag_{14}Cu_{26}$, ΔE is more than 1.7 eV below the c-Dh and the c-pc6, which are almost degenerate. Large ΔEs (of even more than 2 eV) are found also for several other compositions, from $Ag_{17}Cu_{23}$ to $Ag_{32}Cu_8$. For $Ag_{34}Cu_6$, ΔE is somewhat reduced, and the c-pc6 structure is separated by only 0.7 eV.

The enhanced stability of the c-pc5 structures can be explained in terms of the above-mentioned electronic shell closure effect: c-pc5 clusters present large HOMO−LUMO gaps at all compositions, even at those at which the C_{5v} symmetry cannot be attained. On the opposite, clusters pertaining to c-Dh, c-pc6, and TO motifs present small gaps, indicating electronic shell unclosure. The stability of c-pc5 clusters is thus due to the synergic effect of geometric magic arrangement and electronic shell closure. As we shall see in the following, this synergic effect is peculiar of AgCu and is not found in AuCu.

TABLE 2: Structure, Symmetry Group, Spin, HOMO−LUMO Gap, and Separation from the Lowest Minimum ΔE for Structures Pertaining to the Different Structural Motifs of Heterogeneous AgCu Clusters

composition	structure	group	spin	gap (eV)	ΔE (ev)	ΔE_{SMTB}[f]
Ag_6Cu_{34}	c-pc5	C_{5v}	0	0.74	0.00	0.00
Ag_6Cu_{34}	c-Dh[a]	C_i	0	0.06	1.11	−1.23
$Ag_{14}Cu_{26}$	c-pc5[b]	C_s	0	0.81	0.00	0.00
$Ag_{14}Cu_{26}$	c-Dh	C_s	0	0.17	1.41	−0.52
$Ag_{14}Cu_{26}$	c-pc6[c]	D_{6h}	1	0.39/0.22 JT	1.47	−0.65
$Ag_{16}Cu_{24}$	c-pc5	C_s	0	0.81	0.00	0.00
$Ag_{16}Cu_{24}$	c-pc6	D_{2h}	1	0.16/0.04	1.72	−0.49
$Ag_{16}Cu_{24}$	c-Dh	C_i	1	0.19/0.10	1.77	−0.32
$Ag_{17}Cu_{23}$	c-pc5	C_{5v}	0	0.79	0.00	0.00
$Ag_{17}Cu_{23}$	c-pc6	D_{3h}	1	0.38/0.13	1.87	−0.40
$Ag_{17}Cu_{23}$	c-Dh	C_s	0	0.13	1.88	−0.25
$Ag_{20}Cu_{20}$	c-pc5	C_s	0	0.77	0.00	0.00
$Ag_{20}Cu_{20}$	c-pc6	D_{6h}	0	0.09	2.38	−0.09
$Ag_{22}Cu_{18}$	c-pc5	C_{5v}	0	0.78	0.00	0.00
$Ag_{26}Cu_{14}$	c-pc5	C_s	0	0.77	0.00	0.00
$Ag_{27}Cu_{13}$	c-pc5	C_{5v}	0	0.80	0.00	0.00
$Ag_{28}Cu_{12}$	c-pc5	C_s	0	0.77	0.00	0.00
$Ag_{32}Cu_8$	c-pc5	C_{5v}	0	0.75	0.00	0.00
$Ag_{32}Cu_8$	c-pc6	D_{6h}	0	0.06 JT[e]	1.61	0.09
$Ag_{33}Cu_7$	c-pc5	C_{5v}	0	0.71	0.00	0.00
$Ag_{34}Cu_6$	c-pc5	C_s	0	0.75	0.00	0.00
$Ag_{34}Cu_6$	c-pc6	C_s	0	0.03	0.73	−0.56
$Ag_{34}Cu_6$	TO[d]	D_{4h}	1	0.54/0.11	2.03	1.34

[a]Capped decahedra. [b] Capped 5-fold pancakes. [c]Capped 6-fold pancakes. [d]fcc-truncated octahedra. [e] JT indicates Jahn−Teller systems. [f]ΔE_{SMTB} is the energy difference within the SMTB model potential (here the zero of the energy is the lowest isomer after DFT optimization). Within the SMTB model, the $Ag_{34}Cu_6$ TO turns out to be highly distorted.

Let us now compare the energetic stability of clusters of different compositions. To this end, we define the excess energy E^*_{exc} as follows

$$E^*_{exc}(Ag_nCu_{N-n}) = E(Ag_nCu_{N-n}) - n\frac{E(Ag_N)}{N} - (N-n)\frac{E(Cu_N)}{N} \quad (1)$$

where $E(Ag_nCu_{N-n})$ is the energy of Ag_nCu_{N-n}, whereas $E(Ag_N)$ and $E(Cu_N)$ are the energies of the homogeneous Ag_{40} and Cu_{40} clusters, respectively. Energy values are obtained by the DFT calculations. For each composition, the lowest-energy isomers are considered. E^*_{exc} is analogous to the formation energy of bulk alloys, adapted to the case of nanoclusters. This quantity is a good indicator of the cluster stability and of the tendency to mixing. As shown in Figure 3, the plot of E^*_{exc} singles out an especially stable composition, corresponding to $n = 27$, where a quite sharp minimum is found. $Ag_{27}Cu_{13}$ is a perfect core−shell cluster, with a central icosahedral Cu core, and an external Ag shell. This is the cluster with the largest inner Cu core, and its special stability is due to the concurrent factors mentioned at the beginning of this section. The special stability of $Ag_{27}Cu_{13}$ is analogous to that of $Ag_{27}Cu_7$ for clusters of size 34.[17]

We can thus hypothesize a natural pathway for the growth of AgCu nanoclusters passing through a series of polyicosahedral clusters of the same family, from pc5 clusters at size 34 (with preferred composition $Ag_{27}Cu_7$) to c-pc5 structures at size 40 (preferred composition $Ag_{27}Cu_{13}$) to the anti-Mackay icosahedron at size 45, of which the previous clusters are fragments.[18]

Finally, to quantify the energy gain due to the electronic shell closure, we have analyzed a series of isomers of $Ag_{27}Cu_{13}$. These isomers (see Figure 4) all belong to the c-pc5 motif. The lowest in energy is the perfect C_{5v} c-pc5 cluster, whereas the other

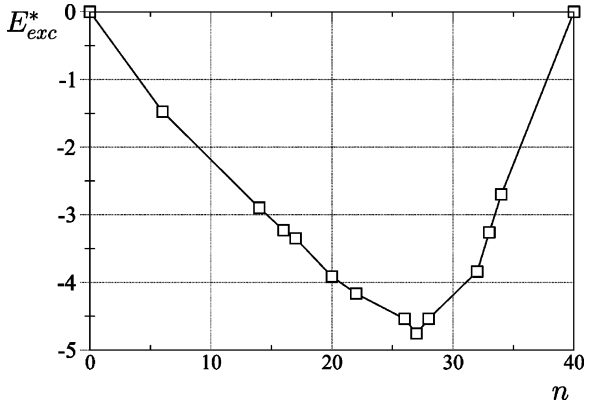

Figure 3. Excess energy E^*_{exc} (see eq 1) as a function of the number of Ag atoms n. Energies are given in eV.

seven isomers are different defected c-pc5 structures. According to the SMTB model, all these isomers are very close in energy, with a maximum ΔE of about 0.06 eV. At variance, at the DFT level, the eight isomers separate into two groups of four. In the first group, all isomers present electronic shell closure, with large gaps between 0.65 and 0.80 eV, and quasi-degenerate total energies (ΔE within 0.05 eV). In the second group, the clusters present small gaps (from 0.21 down to 0.13 eV) and correspondingly considerably higher total energies (ΔE from 0.62 to 1.27 eV). We can thus quantify in ≈0.7 eV the additional stabilization due to electronic shell closure.

6. Polyicosahedral Motifs in AuCu

In the following, we consider c-pc5 and c-pc6 motifs in AuCu 40-atom clusters, showing that the relative stability of the different structures is ruled by rather subtle effects. The qualitative considerations which single out $N = 40$ as a magic electronic size apply also in this case. Moreover, the difference in atomic radii is practically the same for AuCu and AgCu. However, there are two differences which play a key role in determining a different relative structural stability. First of all, compared to AgCu, AuCu has a considerably stronger tendency to form heterogeneous bonds (note that Ag and Cu have an extended miscibility gap in bulk crystals, whereas Au and Cu form a series of ordered alloys). The larger extent of the gold d orbitals (the d orbitals expand with respect to silver due to the relativistic contraction of the gold s orbitals) favors their participation to chemical bonding with copper d orbitals, thus producing a more defined directional character of the Au−Cu interaction with respect to the "isotropic" Ag−Cu interaction. Second, Ag atoms better accommodate bond elongation as compared to Au atoms,[4] due to the shorter-range character of the atom−atom interaction in gold with respect to silver, again ultimately relying on the limited spatial extension (relativistic contraction) of the Au s orbitals. Structures of c-pc5 type are more strained than c-pc6 structures; the latter present also a higher number of heterogeneous bonds at a given composition. These two factors are in favor of c-pc6 structures in the case of AuCu, whereas electronic shell closure is in favor of c-pc5 clusters but with somewhat reduced gaps (see Table 3). Depending on composition, either the geometric and chemical ordering effects or the shell closure effect may prevail, so that, at variance with AgCu, there is a close competition of the two motifs in AuCu clusters. As shown in Table 3, for $Au_{17}Cu_{23}$, the c-pc5 cluster is still lower in energy, but the energy separation ΔE is small. Analogously, for $Au_{28}Cu_{12}$, ΔE is less than 1 eV, which should be compared with the much larger ΔE in AgCu clusters in this composition range. Finally, for $Au_{34}Cu_6$, the stability is reversed, so that the c-pc6 cluster is lower than the c-pc5 by more than 1.5 eV.

TABLE 3: Structure, Symmetry Group, Spin, HOMO−LUMO Gap, and Separation from the Lowest Minimum ΔE for AuCu-Capped 5-Fold Pancakes (c-pc5) and Capped 6-Fold Pancakes (c-pc6)

composition	structure	group	spin	gap (eV)	ΔE (eV)
$Au_{17}Cu_{23}$	c-pc5	C_{5v}	0	0.53	0.00
$Au_{17}Cu_{23}$	c-pc6	D_{3h}	0	0.33	0.18
$Au_{22}Cu_{18}$	c-pc5	C_{5v}	0	0.52	0.00
$Au_{27}Cu_{13}$	c-pc5	C_{5v}	0	0.56	0.00
$Au_{28}Cu_{12}$	c-pc5	C_s	0	0.55	0.00
$Au_{28}Cu_{12}$	c-pc6	C_s	0	0.38	0.81
$Au_{34}Cu_6$	c-pc6	C_s	0	0.25	0.00
$Au_{34}Cu_6$	c-pc5	C_s	0	0.65	1.55

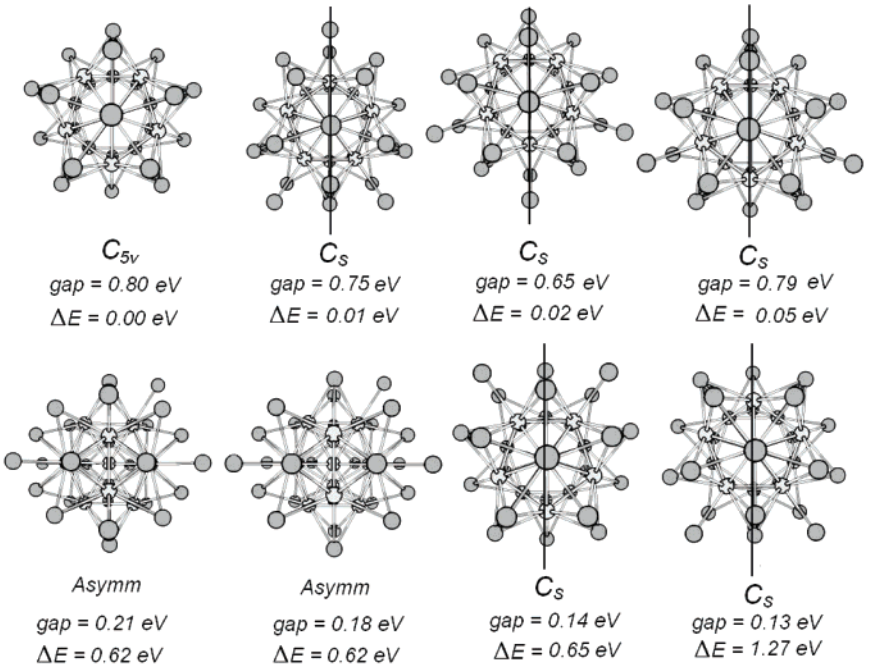

Figure 4. Isomers of $Ag_{27}Cu_{13}$, with HOMO−LUMO gaps and energy separation ΔE.

7. Conclusions

A combined empirical-potential/first-principles analysis of AgCu and AuCu clusters of 40 atoms has shown that the most stable structures originate from a nontrivial interplay of geometric and electronic effects.

Geometric effects include the selection of the structural motif and of the type of chemical ordering. In AgCu, chemical ordering is core−shell, since the larger surface energy of silver with respect to copper produces a tendency to surface segregation of Ag. This tendency is reinforced in polyicosahedral structures, since the relief of internal tension in these structures is favored when inner atoms are of small size compared to surface atoms.[17] These considerations are especially valid when the proportion of silver atoms is not too small. On the Cu-rich side, also, capped decahedral structures can give an efficient geometry optimization.

Moreover, the stability of a structure can be modulated by purely electronic effects. Indeed, the structural motif presenting an electronic shell closure becomes by far the dominant one in AgCu. This motif is the capped 5-fold pancake: thus c-pc5 clusters combine an optimal geometric structure with an optimal electronic structure. Conversely, an electronic shell unclosure effect destabilizes the c-pc6 and fcc-truncated octahedral structures. The high stability of c-pc5 structures suggests a natural growth pathways through polyicosahedral clusters leading to the anti-Mackay icosahedron of 45 atoms.

The fact that geometric and quantum effects concur to favor magic structures associated with core−shell chemical ordering and high symmetry renders these clusters very promising from the point of view of their optical properties (investigation along these lines is in progress in our labs).

In other cases one can find a delicate balance between geometric and electronic factors. In AuCu, in fact, c-pc5 structures are less optimal from the geometric point of view (both because of too strained bonds and of chemical ordering with too little intermixing), so that the gain due to electronic shell closure may not be sufficient for some compositions to compensate for these factors. Therefore, in AuCu, c-pc5 and c-pc6 structures are in close competition.

Acknowledgment. We acknowledge financial support from the Italian CNR for the project "(Supra)-Self-Assemblies of Transition Metal Nanoclusters" within the framework of the ESF EUROCORES SONS and from European Community Sixth Framework Program for the project "Growth and Supra-Organization of Transition and Noble Metal Nanoclusters" (Contract No. NMP4-CT-2004-001594).

References and Notes

(1) De Heer, W. A. *Rev. Mod. Phys.* **1993**, *65*, 611.
(2) Alonso, J. A. *Chem. Rev.* **2000**, *100*, 637.
(3) Heiz, W.; Schneider, W. D. *J. Phys. D: Appl. Phys.* **2000**, *33*, R85.
(4) Baletto, F.; Ferrando, R. *Rev. Mod. Phys.* **2005**, *77*, 371.
(5) Pyykkö, P. *Angew. Chem., Int. Ed.* **2004**, *43*, 4412.
(6) Schooss, D.; Blom, M. N.; Parks, J. H.; von Issendorf, B.,; Haberland, H.; Kappes, M. M. *Nano Lett.* **2005**, *5*, 1972.
(7) Xing, X.; Danell, R. M.; Garzón I. L.; Michaelian, K.; Blom, M. N.; Burns, M. M.; Parks, J. H. *Phys. Rev. B: Condens. Matter Mater. Phys.* **2005**, *72*, 081405.
(8) Knickelbein, M. B.; Koretsky, G. M. *J. Phys. Chem. A* **1998**, *102*, 580.
(9) Kim, Y. D. *Int. J. Mass Spectrom.* **2004**, *238*, 17.
(10) Bernhardt, T. M. *Int. J. Mass Spectrom.* **2005**, *243*, 1.
(11) Schmidt, M.; Masson, A.; Bréchignac C. *J. Chem. Phys.* **2005**, *122*, 134712.
(12) Ichihashi, M.; Corbett, C. A.; Hanmura, T.; Lisy, J. M.; Kondow, T. *J. Phys. Chem. A* **2005**, *109*, 7872.
(13) Nepijiko, S. A.; Ievlev, D. N.; Schulze, W. *Eur. Phys. J. D* **2003**, *24*, 115.
(14) Celep, G.; Cottancin, E.; Lermé, J.; Pellarin, M.; Arnaud, L.; Huntzinger, J. R.; Vialle, J. L.; Broyer, M.; Palpant, B.; Boisron, O.; Mélinon, P. *Phys. Rev. B*: *Condens. Matter Mater. Phys.* **2004**, *70*, 165409.
(15) Padeletti, G.; Fermo, P. *Appl. Phys. A: Mater. Sci. Process.* **2003**, *76*, 515.
(16) Darby, S.; Mortimer-Jones, T. V.; Johnston, R. L.; Roberts, C. *J. Chem. Phys.* **2002**, *116*, 1536.
(17) Rossi, G.; Rapallo, A.; Mottet, C.; Fortunelli, A.; Baletto, F.; Ferrando, R. *Phys. Rev. Lett.* **2004**, *93*, 105503.
(18) Ferrando, R.; Fortunelli, A.; Rossi, G. *Phys. Rev. B: Condens. Matter Mater. Phys.* **2005**, *72*, 085449.
(19) Rapallo, A.; Rossi, G.; Ferrando, R.; Fortunelli, A.; Curley, B. C.; Lloyd, L. D.; Tarbuck, G. M.; Johnston, R. L. *J. Chem. Phys.* **2005**, *122*, 194308.
(20) Pauwels, B.; Van Tendeloo, G.; Zhurkin, E.; Hou, M.; Verschoren, G.; Theil Kuhn, L.; Bouwen, W.; Lievens, P. *Phys. Rev. B: Condens. Matter Mater. Phys.* **2001**, *63*, 165406.
(21) Janssens, E.; Neukermans, S.; Wang, X.; Veldeman, N.; Silverans, R. E.; Lievens, P. *Eur. Phys. J. D* **2004**, *34*, 23.
(22) Cazayous, M.; Langlois, C.; Oikawa, T.; Ricolleau, C.; Sacuto, A. *Phys. Rev. B: Condens. Matter Mater. Phys.* **2006**, *73*, 113402.
(23) Kumar, V. *Comput. Mater. Sci.* **2006**, *36*, 1.
(24) Massen, C.; Mortimer-Jones, T. V.; Johnston, R. L. *J. Chem. Soc., Dalton Trans.* **2002**, 4375.
(25) Baletto, F.; Mottet, C.; Ferrando, R. *Phys. Rev. Lett.* **2003**, *90*, 135504.
(26) Fromen, M. C.; Morillo, J.; Casanove, M. J.; Lecante, P. *Europhys. Lett.* **2006**, *73*, 885.
(27) Katakuse, I.; Ichihara, T.; Fujita, Y.; Matsuo, T.; Sakurai, T.; Matsuda, H. *Int. J. Mass. Spectrom. Ion Proc.* **1985**, *67*, 229.
(28) Taylor, K. J.; Pettiette-Hall, C. L.; Cheshnovsky, O.; Smalley, R. E. *J. Chem. Phys.* **1992**, *96*, 3319.
(29) Jackschath, C.; Rabin, I.; Schulze, W. Z. *Phys. D*: *Amsterdam, Neth.* **1992**, *22*, 517.
(30) Alameddin, G.; Hunter, J.; Cameron, D.; Kappes, M. M. *Chem. Phys. Lett.* **1992**, *192*, 122.
(31) Cha, C.-Y.; Ganteför, G.; Eberhardt, W. J. *J. Chem. Phys.* **1993**, *99*, 6308.
(32) Handschuh, H.; Bechthold, P. S.; Ganteför, G.; Eberhardt, W. J. *J. Chem. Phys.* **1994**, *100*, 7093.
(33) Brack, M. *Rev. Mod. Phys.* **1993**, *65*, 677.
(34) Stone, A. J. *Inorg. Chem.* **1981**, *20*, 563.
(35) Wales, D. J.; Stone, A. J. *Inorg. Chem.* **1989**, *28*, 3120.
(36) Johnston, R. L.; Mingos, D. M. P. *J. Chem. Soc., Dalton Trans.* **1987**, 1445.
(37) Hirsch, A.; Chen, Z.; Jiao, H. *Angew. Chem., Int. Ed.* **2000**, *39*, 3915.
(38) Tsipis, C. A. *Coord. Chem. Rev.* **2005**, *249*, 2740.
(39) Rossi, G.; Ferrando, R.; Rapallo, A., Fortunelli, A.; Curley, B. C.; Lloyd, L. D.; Johnston, R. L. *J. Chem. Phys.* **2005**, *122*, 194309.
(40) Aprà, E.; Ferrando, R.; Fortunelli, A. *Phys. Rev. B*: *Condens. Matter Mater. Phys.* **2006**, *73*, 205414.
(41) Jellinek, J.; Krissinel, E. B. *Chem. Phys. Lett.* **1996**, *258*, 283.
(42) Gupta, R. P. *Phys. Rev. B*: *Solid State* **1981**, *23*, 6265.
(43) Cleri, F.; Rosato, V. *Phys. Rev. B: Condens. Matter Mater. Phys.* **1993**, *48*, 22.
(44) Baletto, F.; Mottet, C.; Ferrando R. *Phys. Rev. B: Condens. Matter Mater. Phys.* **2002**, *66*, 155420.
(45) Meunier, I.; Tréglia, G.; Gay, J. M.; Aufray, B.; Legrand, B. *Phys. Rev. B: Condens. Matter Mater. Phys.* **1999**, *50*, 10910.
(46) Doye, J. P. K.; Wales, D. J. *J. Phys. Chem. A* **1997**, *101*, 5111.
(47) Hansmann, U. H. E.; Wille, L. T. *Phys. Rev. Lett.* **2002**, *88*, 068105.
(48) Rossi, G.; Ferrando, R. *Chem. Phys. Lett.* **2006**, *423*, 17.
(49) ELP and PEW are especially suited for exploring potential energy surfaces exhibiting structurally different basins of attraction and require the use of an order parameter. As order parameter we have chosen the number of heterogeneous AgCu nearest-neighbor bonds to differentiate the various structural families.
(50) Aprà, E. et al. *NWChem, A Computational Chemistry Package for Parallel Computers*, Version 4.7; Pacific Northwest National Laboratory: Richland, WA, USA, 2005.
(51) Becke, A. D. *Phys. Rev. A* **1988**, *38*, 3098.
(52) Perdew, J. P.; Chevary, J. A.; Vosko, S. H.; Jackson, K. A.; Pederson, M. R.; Singh, D. J.; C. Fiolhais, C. *Phys. Rev. B* **1992**, *46*, 6671.
(53) Schaefer, A.; Huber, C.; Ahlrichs, R. *J. Chem. Phys.* **1994**, *100*, 5289.
(54) Andrae, D.; Haeussermann, U.; Dolg, M.; Stoll, H.; Preuss, H. *Theor. Chim. Acta* **1990**, *77*, 123.
(55) Dolg, M.; Wedig, U.; Stoll, H.; Preuss, H. *J. Chem. Phys.* **1987**, *86*, 866.
(56) ftp://ftp.chemie.uni-karlsruhe.de/pub/basen.

(57) Aprà, E.; Fortunelli, A. *J. Phys. Chem.* **2003**, *107*, 2934.
(58) Courtesy of Dr. Florian Weigend, Karlsruhe, Germany.
(59) (a) Elsässer, C.; Fähnle, M.; Chan, C. T.; Ho, K. M. *Phys. Rev. B: Condens. Matter Mater. Phys.* **1994**, *49*, 13975. (b) Warren, R. W.; Dunlap, B. I. *Chem. Phys. Lett.* **1996**, *262*, 384.
(60) Doye, J. P. K.; Wales, D. J. *New J. Chem.* **1998**, *22*, 733.
(61) Doye, J. P. K. *J. Chem. Phys*. **2003**, *119*, 1136.
(62) We chose $A = 10.9$ eV and $r_0 = 5.6$ Å, such that the Extended Hückel DOS around the Fermi level optimally matches the DFT DOS.
(63) Doye, J. P. K.; Meyer, L. *Phys. Rev. Lett.* **2005**, *95*, 063401.
(64) Pauling, L. *The Nature of the Chemical Bond*; Cornell University Press: Ithaca, NY, 1960.

A Mixed Structural Motif in 34-Atom Pd−Pt Clusters

BorbonJPCC2007

Lauro Oliver Paz-Borbón,[†] Roy L. Johnston,*[,†] Giovanni Barcaro,[‡] and Alessandro Fortunelli*[,‡]

School of Chemistry, University of Birmingham, Edgbaston, Birmingham, B15 2TT, United Kingdom and Istituto per i Processi Chimico-Fisici/Consiglio Nazionale delle Ricerche (IPCF/CNR), via G. Moruzzi 1, I-56124, Pisa, Italy

Received: November 9, 2006; In Final Form: December 11, 2006

Global optimizations via a genetic algorithm using the Gupta empirical potential are performed on 34-atom Pd−Pt binary clusters, finding a complex crossover among several structural motifs that are close in energy. The composition range is then restricted on the basis of stability criteria; (a) the Gupta global minima at each composition are subjected to density functional (DFT) local energy minimizations, and (b) at the 24−10 composition, the lowest-energy isomers of each structural family are locally optimized at the DFT level. It is found that the energetic ordering of the structural motifs predicted by the Gupta potential is not confirmed at the DFT level and that a new structural motif, a mixed decahedral/close-packed (Dh-cp(DT)) one, is the putative global minimum at all compositions. Finally, segregation effects of Pd atoms to the surface of the cluster are studied at the composition $Pd_{17}Pt_{17}$ and found to be corroborated by DFT calculations. The peculiar stability of the Dh-cp(DT) arrangement is rationalized in terms of an optimal compromise between core-segregated, and thus preferentially close-packed, Pt atoms and surface-segregated, and thus preferentially decahedral, Pd atoms.

Introduction

The desire to fabricate materials with well-defined, controllable, properties and structures on the nanometer scale coupled with the flexibility afforded by intermetallic materials has generated interest in bimetallic clusters or "nanoalloys".[1] Platinum and palladium are of particular interest because they are widely used as catalysts (often as finely divided metal particles) in elemental or alloy form in a number of important reactions. They are used, for example, in catalytic converters in automobiles for the reduction of exhaust gases.[2] It has been claimed that Pd−Pt alloy particles are more catalytically active for aromatic hydrocarbon hydrogenation and more resistant to sulfur poisoning than either of the pure metals (i.e., there is said to be "synergism"),[3] though there is some controversy over this viewpoint.[4,5] Renouprez et al. have performed extensive experimental studies of the structures, compositions, and catalytic activity of Pd−Pt particles generated by the laser vaporization of bulk alloys of various compositions.[4,5] Results obtained from a combination of experimental techniques indicate that the Pd−Pt nanoparticles (1−5 nm diameter) are truncated octahedra with a Pt-rich core surrounded by a Pd-rich shell.[4,5] In more recent studies, Pd−Pt systems were deposited on γ-alumina and by combining X-ray absorption spectroscopy with transmission electron microscopy (TEM) and volumetric H_2−O_2 titration it was shown that small Pd−Pt particles ($\sim$ 1 nm) have "cherry-like" structures with a distribution of Pd atoms on the surface of the cluster.[6] Computational studies, based on the Gupta many-body potential and a genetic algorithm search method, have given new insights into the geometries and segregation properties of Pd−Pt nanoalloys with up to 56 atoms.[7,8,9] Using parameters for the mixed (Pd−Pt) interactions that were derived based on considerations of the mixing behavior of the bulk Pd−Pt alloys, the experimentally observed tendency of Pt and Pd atoms to preferentially occupy interior (core) and exterior (surface) sites, respectively, has been confirmed in the computational simulations. Different types of structures (e.g., icosahedral, cubic close-packed, decahedral, or amorphous geometries) adopted by the lowest energy isomers for Pd, Pt, and Pd−Pt clusters also were identified. Recent calculations by Rossi et al.[10] based on the Gupta potential showed that pure 34-atom Pd and Pt clusters are incomplete decahedra, and in the case of mixed clusters they exhibit the same structural motif for several different compositions. Preliminary calculations by Fernandez et al.[11] have shown that the $Pt_{core}Pd_{shell}$ segregation predicted by the Gupta potential simulations are reproduced at higher levels of theory, although the energy ordering of the permutational isomers may differ from Gupta to density functional theory (DFT) calculations.

The objective of this work is to search for energetic competition between different structural families (motifs) at the DFT level. We focus on 34-atom clusters, and we start by determining the lowest energy isomers for all 34-atom Pd−Pt compositions at the empirical potential level. This size has been chosen as previous empirical potential calculations[10] singled out three clusters at compositions 21−13, 24−10, and 30−4, exhibiting high-symmetry and peculiar stability that thus lent themselves as promising candidates for a more accurate DFT analysis. The Birmingham Cluster Genetic Algorithm code[12] is used as a search technique of the potential energy surface (PES), coupled with the Gupta potential to model interatomic interactions. Then, the composition range is limited according to stability criteria, and at each composition the most stable isomer at the Gupta level is subjected to a DFT local relaxation.

* Corresponding authors. E-mail: (R.L.J.) r.l.johnston@bham.ac.uk; (A.F.) fortunelli@ipcf.cnr.it.
[†] University of Birmingham.
[‡] Istituto per i Processi Chimico-Fisici/Consiglio Nazionale delle Ricerche (IPCF/CNR).

10.1021/jp0674165 CCC: $37.00
Published on Web 01/26/2007

TABLE 1: Parameters of the Gupta Potential for Pt−Pt, Pd−Pd and Pd−Pt Interactions

parameters	Pt−Pt	Pd−Pd	Pt−Pd
A/*eV*	0.2975	0.1746	0.23
ζ/*eV*	2.695	1.718	2.2
p	10.612	10.867	10.74
q	4.004	3.742	3.87
r_o/Å	2.7747	2.7485	2.76

Furthermore, for the 24−10 composition, following a previously proposed protocol,[13] the energetic competition among the different structural motifs is studied in detail. It is found that a particular configuration (a mixed decahedral/close-packed motif) has a much lower energy than any of its competitors. This motif is found to be the putative global minimum at all compositions from 17−17 to 28−6. Finally, surface segregation of Pd atoms is investigated at the DFT level for the 17−17 composition.

Computational Details. At present, a systematic unbiased search[14] for optimal (global minimum, GM) structures for clusters with tens of atoms or more remains extremely demanding for high level calculations because of computational limitations on exploring vast areas of configurational space. For bimetallic clusters, such as Pd_mPt_n, the search is further complicated by the existence of homotops[15,16] (i.e., isomers with the same geometry and composition but with a different arrangement of the two types of atoms). Empirical atomistic potentials have been developed to overcome computational limitations in the search for optimal structures in configurational space. One such potential, the Gupta potential, is derived by fitting experimental values calculated using a potential of an assumed functional form. It is based on the second moment approximation to tight binding theory[17] and is constructed from an attractive many-body (V^m) term and a repulsive pair (V^r) term, obtained by summing over all *N* atoms

$$V_{\text{clus}} = \sum_{i}^{N} [V^r(i) - V^m(i)] \tag{1}$$

where $V^r(i)$ and $V^m(i)$ are defined as

$$V^r(i) = \sum_{j \neq i}^{N} A(a,b) \exp\left(-p(a,b)\left(\frac{r_{ij}}{r_0(a,b)} - 1\right)\right) \tag{2}$$

$$V^m(i) = \left[\sum_{j \neq i}^{N} \zeta^2(a,b) \exp\left(-2q(a,b)\left(\frac{r_{ij}}{r_0(a,b)} - 1\right)\right)\right]^{1/2} \tag{3}$$

In eqs 2 and 3, r_{ij} represents the distance between atoms *i* and *j* in the cluster. The parameters *A*, r_0, ζ, *p*, *q* are fitted to experimental values of the cohesive energy, lattice parameters, and independent elastic constants for the reference crystal structure at 0 K. The parameters for the interactions of Pt−Pt and Pd−Pd are taken from the work of Cleri and Rosato,[17] while the Pd−Pt parameters are obtained as reported by Massen et al.[7] (see Table 1).

For calculations using the Gupta potential, the Birmingham Cluster Genetic Algorithm (BCGA) code[12] was used to find the global minima and other higher-energy isomers at each size and composition. Genetic algorithms (GA's) work by evolving a population of trial solutions through a combination of evolutionary operators suchs as crossover, mutation, and natural selection. Details of the BCGA methodology have been presented elsewhere.[12]

The DFT calculations used the NWChem 4.7 quantum chemical package[18] and the Perdew and Wang exchange-correlation functional, PW91.[19,20] (7s6p5d)/[5s3p2d] Spherical Gaussian type-orbital basis sets[21] and effective core potentials (ECP)[22] were used for both elements. Moreover, charge density fitting (11s4p5d3f4g)/[11s4p4d3f2g] Gaussian type-orbital basis sets[23] were used to compute the Coulomb potential. All the calculations were performed spin-unrestricted, using a Gaussian smearing technique for the fractional occupation of the one-electron energy levels for improving the self-consistent field convergence process.[24,25]

Energetic Analysis. To analyze the energetics and compare the relative stability of Pd−Pt clusters, it is convenient to introduce three quantities. The first is the Δ index, originally introduced by Cleveland and Landman[26] for pure clusters. It is defined as the excess energy with respect to *N* bulk atoms, divided by $N^{2/3}$, and scales roughly as the number of surface atoms[1]

$$\Delta = \frac{E_{\text{exc}}(Pd_mPt_n)}{N^{2/3}} = \frac{E_{\text{total}}^{\text{Gupta}}(Pd_mPt_n) - m\epsilon_{\text{Pd}}^{\text{coh}} - n\epsilon_{\text{Pt}}^{\text{coh}}}{N^{2/3}} \tag{4}$$

where $E_{\text{total}}^{\text{Gupta}}(Pd_mPt_n)$ represents the total energy of a given cluster calculated at the Gupta level, and *m*, *n*, $\epsilon_{\text{A}}^{\text{coh}}$, and $\epsilon_{\text{B}}^{\text{coh}}$ are the number of atoms of each metallic element and their corresponding bulk cohesive energies, respectively.[17] Low values of excess energy as a function of composition characterize the most stable clusters.

One disadvantage is that Δ can be biased when comparing clusters of the same size but different composition, because metals with large cohesive energies tend to give clusters with higher excess energy. To obviate this problem, when studying clusters with fixed size but different composition the unbiased quantity, $\Delta_{34}^{\text{Gupta}}$, is introduced[27]

$$\Delta_{34}^{\text{Gupta}} = E_{\text{total}}^{\text{Gupta}}(Pd_mPt_n) - m\frac{E_{\text{total}}^{\text{Gupta}}(Pd_{34})}{34} - n\frac{E_{\text{total}}^{\text{Gupta}}(Pt_{34})}{34} \tag{5}$$

We emphasize that in eq 5 we subtract the binding energy per atom of the pure cluster of the same size instead of the bulk cohesive energy from the total energy of the cluster. In this way, $\Delta_{34}^{\text{Gupta}}$ is an unbiased quantity, which is zero for the pure clusters. Moreover, negative values of the excess energy mean that mixing is favorable. We can think of the excess energy as being analogous to the formation energy of bulk alloys, adapted now to the case of nanoclusters.[1] At the DFT level, Δ_{34}^{DFT} can be similarly defined as

$$\Delta_{34}^{\text{DFT}} = E_{\text{total}}^{\text{DFT}}(Pd_mPt_n) - m\frac{E_{\text{total}}^{\text{DFT}}(Pd_{34})}{34} - n\frac{E_{\text{total}}^{\text{DFT}}(Pt_{34})}{34} \tag{6}$$

where $E_{\text{total}}^{\text{DFT}}(Pd_mPt_n)$ is the DFT total energy for a given cluster, and $E_{\text{total}}^{\text{DFT}}(Pd_{34})/34$ and $E_{\text{total}}^{\text{DFT}}(Pt_{34})/34$ are the DFT energies per atom calculated for the pure Pd_{34} and Pt_{34} clusters. Clearly, Δ_{34}^{DFT} is most reliable when the GM for the pure clusters are correctly identified.

A final indicator of the relative stability of clusters is the second difference in binding energy, Δ_2E. In mixed clusters, for a fixed size and variable composition, Δ_2E is defined as

$$\Delta_2E = E_{\text{total}}^{\text{Gupta}}(Pd_{m+1}Pt_{n-1}) + E_{\text{total}}^{\text{Gupta}}(Pd_{m-1}Pt_{n+1}) - 2E_{\text{total}}^{\text{Gupta}}(Pd_mPt_n) \tag{7}$$

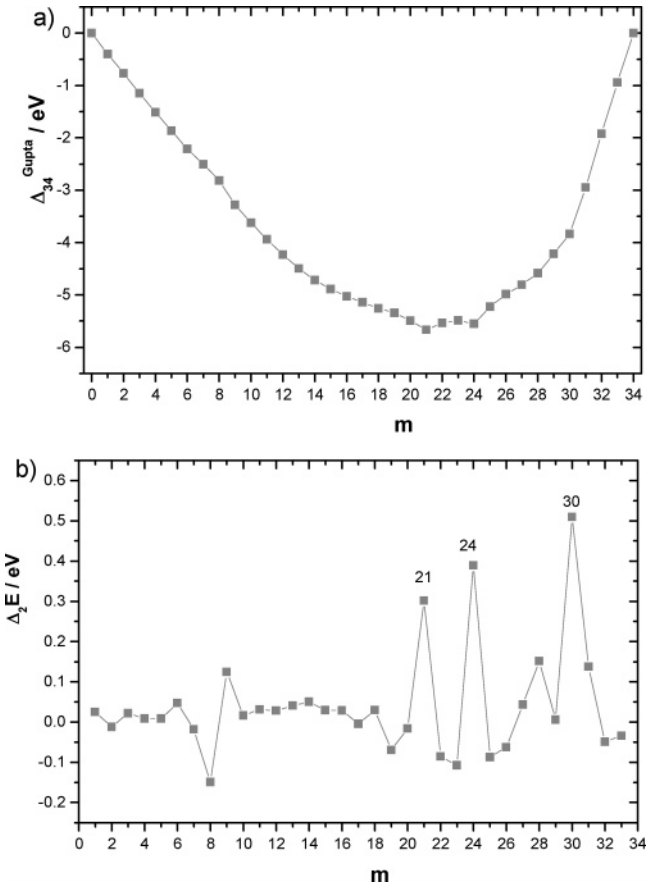

Figure 1. Excess energy (a) and second difference in energy (b) for 34-atom Pd_mPt_{34-m} clusters, modeled by the Gupta potential.

$\Delta_2 E$ can be used to compare the relative stabilities of clusters that are close both in size and composition.[7,28] Intense peaks in $\Delta_2 E$ correspond to structures of high relative stability.

Results and Discussion

Figure 1a shows a plot of Δ_{34}^{Gupta} against Pd content (m) for the Gupta potential GM for all compositions Pd_mPt_{34-m}. The lowest values of Δ_{34}^{Gupta} are found for the compositions $Pd_{21}Pt_{13}$ and $Pd_{24}Pt_{10}$, indicating that these are relatively stable GM. This is confirmed in Figure 1b, which shows the corresponding $\Delta_2 E$ plot, with peaks at $m = 21$, 24, and 30. This is because of the high-symmetry core−shell segregated nature of these GM, which exhibit polyhedral or polygonal cores of Pt (a centered icosahedron in $Pd_{21}Pt_{13}$, a tetrahedron in $Pd_{24}Pt_{10}$, and a rectangle in $Pd_{30}Pt_4$). According to the Δ_{34}^{Gupta} and $\Delta_2 E$ analysis (Figure 1), one should expect to find relatively stable Pd−Pt structures in the composition range Pd_mPt_{34-m} ($m \approx 17-28$).

Therefore, a detailed study of clusters in the range $Pd_{17}Pt_{17}$−$Pd_{28}Pt_6$ was undertaken. For each composition, 50 GA runs were performed at the Gupta potential level. A number of low-energy structural families (motifs) were identified. These structures are shown in Figure 2 for the particular case of the 24−10 composition. Figure 2a shows a mixed decahedral (Dh)/close-packed (cp) motif in which a tetrahedral (T) core of 10 atoms is surrounded by 12 atoms growing on the (111) faces and 12 atoms growing along the edges of the tetrahedron. Figure 2b shows a mixed Dh/cp motif, presenting a 14-atom core with the structure of a trigonal bipyramid (a "double tetrahedron", DT) surrounded by 18 atoms growing on the (111) faces and 2 atoms growing along one of the edges of the double tetrahedron. Figure 2c shows an incomplete, somewhat distorted 38-atom truncated octahedron (TO), lacking 4 atoms of a (100) face. Figure 2e shows a Marks decahedron.[1] Finally, Figure 2d,f, and g show three different polyicosahedral (pIh) structures,[29] of which Figure 2d is a low-symmetry configuration, Figure 2g is an incomplete and slightly distorted 38-atom 6-fold pIh[6] pancake, lacking two dimers on the basal ring, and Figure 2f is an incomplete 45-atom 5-fold pIh[5] (i.e., an incomplete anti-Mackay icosahedron) (see ref 29 for a more detailed description of the polyicosahedral structures).

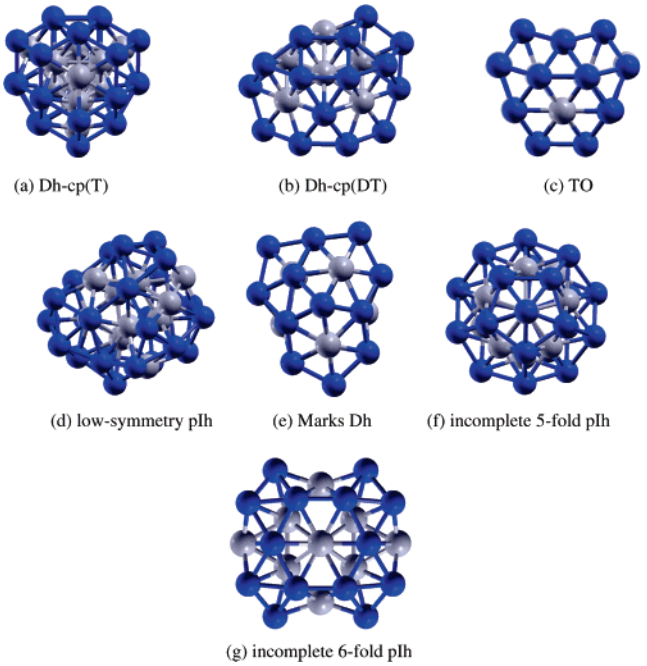

Figure 2. Different structural motifs found for the composition $Pd_{24}Pt_{10}$. Pd atoms are indicated by dark spheres.

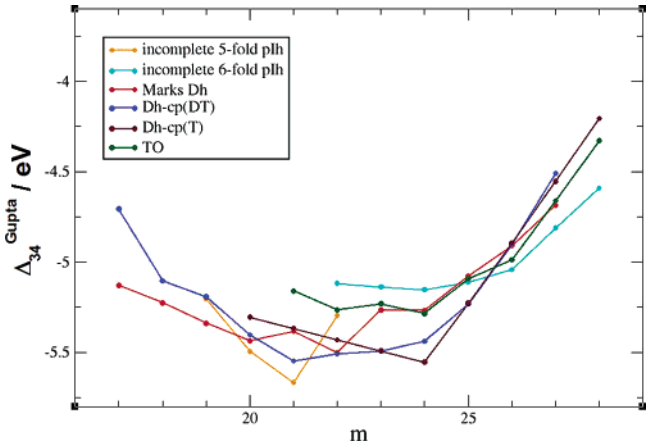

Figure 3. Plot of excess energy, Δ_{34}^{Gupta}, for different structural motifs at compositions Pd_mPt_{34-m} varying from $Pd_{17}Pt_{17}$ to $Pd_{28}Pt_6$.

In Figure 3, we plot the variation of Δ_{34}^{Gupta} with composition for the lowest energy homotop of each structural motif of Figure 2 with the exception of the low-symmetry pIh, which being a disordered structure is sometimes difficult to locate. As a general trend, decahedral motifs dominate for 34-atom Pd−Pt clusters. (See Tables 1−3 in the Supporting Information). Many incomplete Marks Dh motifs are found as global minima in the Pt-rich composition range. At the Gupta level, the lowest excess energy structure occurs for $Pd_{21}Pt_{13}$, which has a complete icosahedral Pt_{13} core. It is followed in energy by $Pd_{24}Pt_{10}$, which has a tetrahedral Pt_{10} core. Higher excess energy structures correspond to incomplete 6-fold pancakes as well as incomplete

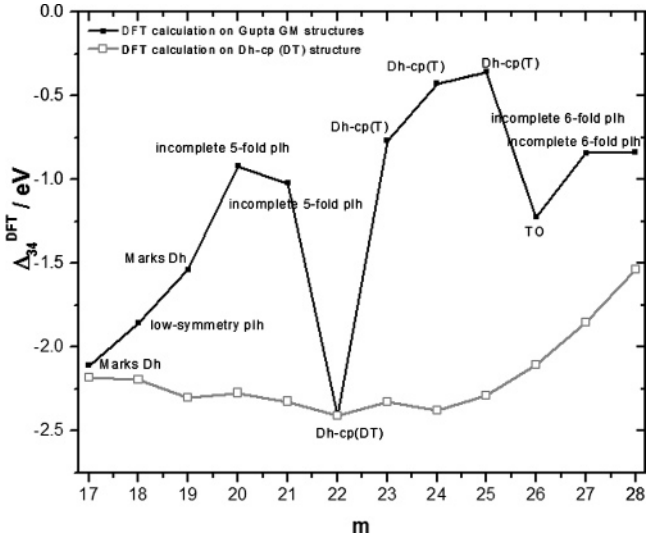

Figure 4. Δ_{34}^{DFT}curve obtained by local geometry optimizations of the global minima predicted at the Gupta potential level (cross marks) and of Dh-cp(DT) structures (square marks).

TO structures. The main conclusion of this analysis is that at the empirical potential level one finds a complex crossover between several different structural families that are rather close in energy: the energy difference between the GM and the first excited-state ranges from essentially zero to about 0.2 eV in the chosen composition interval.

We will now show that the DFT analysis significantly alters the empirical potential predictions. First of all, for each composition the most stable homotop at the Gupta level was locally optimized at the DFT level. Figure 4 shows a plot (dotted line) of the Δ_{34}^{DFT} values so obtained. The jagged nature of this plot makes it unlikely that these structures correspond to GM on the DFT energy hyperspace. It is interesting to note that the lowest Δ_{34}^{DFT} value is the Dh-cp(DT) core structure for $Pd_{22}Pt_{12}$, which was only obtained as GM for this composition at the Gupta level. Because of its high stability, the Dh-cp(DT) structure was then locally optimized at the DFT level for all compositions by taking the initial structures from the empirical potential searches. The solid line in Figure 4 is a plot of Δ_{34}^{DFT} values after DFT reoptimization of Dh-cp(DT) structures. The following analysis will show that this structure is the putative GM at the DFT level for all compositions $Pd_{17}Pt_{17}-Pd_{28}Pt_6$. A detailed study now will be presented for two particular compositions: $Pd_{24}Pt_{10}$ and $Pd_{17}Pt_{17}$ for which we conducted DFT local geometry optimization for structures representative of several families.[13]

$Pd_{24}Pt_{10}$. At the Gupta level, the GM at this composition corresponds to a highly symmetrical structure: a tetrahedral core of 10 Pt atoms surrounded by the remaining 24 Pd atoms (Figure 2a). An exhaustive search (1000 GA runs) then was performed at this composition using the GA code based on the Gupta potential. This search gave us a wide distribution of several structural arrangements. Following a previously proposed protocol,[13] each of the lowest energy homotops for each structural motif was subjected to DFT local optimization. Figure 2 shows the lowest energy homotops found for each of the seven low-energy structural arrangements (at the Gupta level) for this composition. Table 2 shows the energetic ordering of the different isomers as well as their corresponding symmetries. It is apparent that after performing the DFT local optimization a substantial change in the energetic ordering occurs. The highly symmetric Dh-cp(T) structure, which is the GM at the Gupta level, is found to be one of the motifs with the highest Δ_{34}^{DFT} value. In agreement with the results from the previous subsection, the new putative GM corresponds to the Dh-cp(DT) structure. We have performed a similar (though not quite as complete) analysis at other compositions by locally optimizing various higher-energy isomers; the result is that in the chosen composition interval the Dh-cp(DT) structure turned out to have the lowest-energy in all cases. In principle, following the complete protocol[13] one should locally optimize several low-energy configurations for each structural family, as it is found (see, e.g., ref 11) that DFT relaxation can change the energy ordering also within each family. However, this effect is usually less dramatic than when comparing different structural motifs, and we do not expect it to qualitatively modify our main conclusions. This also was confirmed by DFT calculations on several higher-energy configurations from selected structural families.

TABLE 2: Energy Ordering Predicted by the Gupta Potential and DFT at the $Pd_{24}Pt_{10}$ Composition[a]

motif	symmetry	Gupta potential E_{total}^{Gupta}/eV	DFT/PW91 E_{total}^{DFT}/au (S ≠ **0**; σ = **0.005**)
Dh-cp(DT)	C_s	−140.320	−4267.36912
TO	C_s	−140.164	−4267.34367
Marks Dh	C_1	−140.150	−4267.34142
incomplete 5-fold pIh	C_{5h}	−139.317	−4267.29345
incomplete 6-fold pIh	D_{4h}	−140.034	−4267.32287
low-symmetry pIh	C_1	−140.008	−4267.31167
Dh-cp(T)	T_d	−140.435	−4267.29754

[a] Lowest energy minima are highlighted in bold. S ≠ 0 corresponds to spin unrestricted calculations. σ indicats the smearing parameter in au. DFT total energies are expressed in au while Gupta potential total energies are in eV.

Analysis of the Dh-cp(DT) Structure. The Dh-cp(DT) structure is best described for the 20−14 composition in which the internal core of Pt atoms is a double tetrahedron or trigonal bipyramid (i.e., two tetrahedra sharing a face). Pd atoms can grow on the (111) faces of these two tetrahedra in a regular hcp (111) stacking. On each of the 6 faces of the Pt double tetrahedron (each one formed by 6 Pt atoms), three Pd atoms can grow, giving a total of 18 surface Pd atoms. The two remaining Pd atoms lie on an edge between two faces belonging to the same Pt tetrahedron, thus creating what it is locally a decahedron with its 5-fold axis coinciding with the shared edge. Simultaneously, there is a deformation of the 12 Pd atoms located next to the three edges shared by the two tetrahedra; these Pd atoms minimize their local energy by getting closer to each other and forming three other local decahedral motifs whose axes coincide with the three edges shared by the two tetrahedra. The growth mechanism of the Pd atoms on top of the Pt double tetrahedron is similar to that responsible for the interconversion between 5-fold structural families as theoretically predicted[32,33] and experimentally verified.[34] Figure 5 shows the internal core of the Dh-cp(DT) for all the compositions studied in this work. The peculiar stability of this structure is due to the fact that Pt segregates into the core, where it is highly coordinated and thus preferentially cp,[1] while Pd segregates to the surface, where it is low-coordinated and thus preferentially in decahedral arrangements.[1] The Dh-cp(DT) arrangement thus represents the best compromise for the frustration caused by the different tendencies of the component metals. Clearly, this is especially true for medium-sized clusters such as those considered in the present work, whereas the crystalline arrangements will eventually prevail for larger clusters.[4,5]

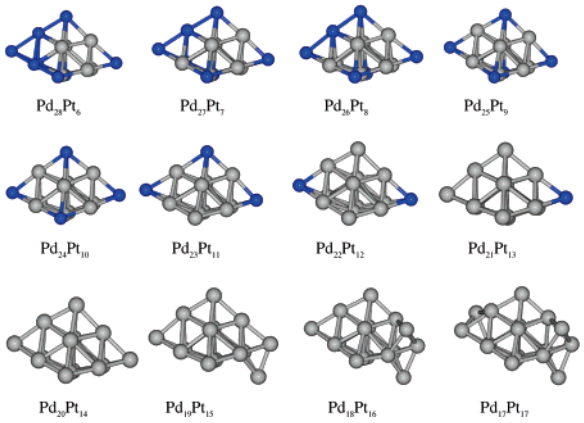

Figure 5. Double tetrahedral Pt (light color) core of the Dh-cp(DT) structure for various compositions. At low Pt compositions, some Pd (dark color) atoms are shown for completeness.

It is interesting to observe that the Dh-cp(DT) structure with the lowest Δ_{34}^{Gupta} and Δ_{34}^{DFT} value is realized at the composition $Pd_{22}Pt_{12}$. In this case, the two extremal (apical) vertices of the Pt double tetrahedron are replaced by two Pd atoms: this lowers the mixing energy of the structure by replacing those internal Pt atoms with fewer bonds with Pd atoms, that are less strained as the Pd potential is less "sticky" than Pt.[30] At the DFT level there is a further stabilizing contribution due to the fact that the replaced Pt atoms lie in a very asymmetrical bonding environment that is particularly disfavored as Pt has a large orientational (dipolar) energy.[31]

Compared to the Dh-cp(DT) arrangement, the TO structure is disfavored because the Pd atoms are not in a decahedral bonding environment, while the "pure" 5-fold noncrystalline structures are disfavored because the internal Pt atoms are not in a cp bonding environment. Finally, the Dh-cp(T) motif is disfavored because (a) there is a smaller proportion of atoms lying on (111) faces in cp stacking and (b) in going from size 32 to size 34, there is a difference between covering the first edge of the double tetrahedron (thus forming decahedral Pd arrangements and releasing strain) or the last edge of the single tetrahedron (thus increasing strain because of competition for decahedra formation with Pd dimers on the other edges).

We have performed further calculations (to be reported in more detail in future work) on Pd−Pt clusters with a number of atoms in the range 32−44. The preliminary result is that the mixed Dh-cp(DT) motif seems to be preferred in this size range with a somewhat enhanced stability at size 34 and 36. However, we were unable to single out a cluster in which structural stability was associated with electronic shell closure; the density of states around the Fermi level always came out rather smooth, confirming the metallic character of these systems.

$Pd_{17}Pt_{17}$. As mentioned previously, segregation of Pd atoms to the surface and Pt atoms to the core seems to be a general tendency for Pd−Pt clusters.[4−9] This is interesting as Pd−Pt clusters are among the few systems in which the lighter atoms tend to segregate to the surface. As $Pd_{17}Pt_{17}$ has a 50:50 composition of Pd and Pt atoms, it represents a good candidate to study surface segregation effects. Several structures were generated using the Gupta potential and the GA search technique. It was found that Dh-Marks type motifs are preferred over pIh structures at the Gupta potential level, with the Dh-cp(DT) structure somewhat higher in energy. The lowest-energy homotops corresponding to these three structural families then were selected and the Pd and Pt atom positions exchanged before performing local geometry optimization at the DFT level. In

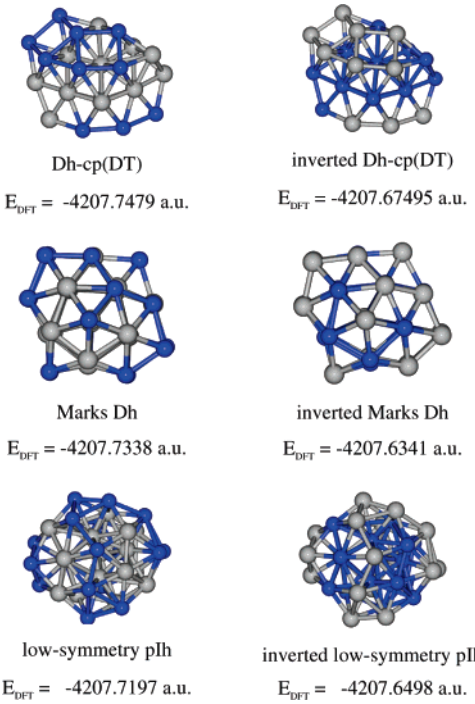

Figure 6. Structural motifs at the $Pd_{17}Pt_{17}$ composition. The left column shows low energy structures predicted by the Gupta potential and reoptimized at the DFT level. The right column shows the DFT reoptimized "inverted" structures in which the Pd (dark) and Pt (light) atoms have been swapped.

Figure 6 the three lowest-energy motifs for the $Pd_{17}Pt_{17}$ cluster, the corresponding inverted structures, and the relative energetics are shown. It can be seen that swapping Pd and Pt atoms always increases the total energy of the system, thus confirming that Pd segregation to the surface of the cluster is energetically favorable in the Pd−Pt system. Such a segregation is mainly ruled by two factors: maximization of the number of the strongest interatomic interactions and minimization of cluster surface energy. Experimentally, the surface energy of Pd (125−131 meV/Å^2) is lower than that of Pt (155−159 meV/Å^2) while having a core of Pt atoms also enables the maximization of the number of Pt−Pt interactions (which are the strongest according to both the Gupta potential and DFT). Thus, the DFT calculations on $Pd_{17}Pt_{17}$ show that surface segregation effects of Pd atoms in medium-sized clusters are supported at the higher level of theory in agreement with previous DFT calculations on Pd−Pt clusters.[11]

Conclusions

By combining Gupta potential global optimizations and DFT local energy minimizations,[13] we have identified a new particularly stable structural motif, a Dh-cp(DT) structure. In the case of the 34-atom Pd−Pt clusters studied in this work, the energetic ordering of global minimum structural motifs predicted by the Gupta potential is not confirmed at the higher level of theory (i.e., DFT). The Dh-cp(DT) motif is predicted to be the ground state only at composition 22−12 at the empirical potential level, whereas it corresponds to the lowest energy structure at the DFT level for all the compositions (17−17 to 28−6) studied here. This is rationalized in terms of an optimal compromise between core-segregated, and thus preferentially close-packed, Pt atoms and surface-segregated, and thus preferentially decahedral, Pd atoms. Mixed motifs such as the Dh-cp(DT) structure described in the present work have not been studied much in the literature, whereas they might be quite

common for medium-sized binary clusters, frustrated because of different bonding tendencies of the two component elements (other candidate systems are presently under investigation). Finally, segregation effects of Pd atoms to the surface of the cluster are studied at the composition $Pd_{17}Pt_{17}$ and are found to be corroborated by DFT calculations.

Acknowledgment. This work has been performed within the HPC-Europa Project (RII3-CT-2003−506079) with the support of the European Community Research Infrastructure Action under the FP6 "Structuring the European Research Area" Programme, which allowed us to perform most of the DFT calculations here described at the CINECA supercomputing center (Bologna, Italy). L.O.P.B. is grateful to CONACYT (Mexico) for the award of a Ph.D. scholarship. L.O.P.B. and R.L.J. acknowledge support from NSCCS EPSRC National Service for Computational Chemistry Software, U.K. (http://www.nsccs.ac.uk/). A.F. and G.B. acknowledge financial support from Italian CNR for the project SSA-TMN within the framework of the ESF EUROCORES SONS and from EC FP6 for the STREP project GSOMEN ("Growth and Supra-Organization of transition and noble Metal Nanoclusters").

Supporting Information Available: This material is available free of charge via the Internet at http://pubs.acs.org.

References and Notes

(1) Ferrando, R.; Jellinek, J.; Johnston, R. L. *Chem. Rev.*, submitted for publication, 2006.
(2) Coq, B.; Figueras, F. *J. Mol. Catal. A* **2001**, *173*, 117.
(3) Stanislaus, A.; Cooper, B. H. *Catal. Rev.—Sci. Eng.* **1994**, *36*, 75.
(4) Renouprez, A. J.; Rousset, J. L.; Cadrot, A. M.; Soldo, Y.; Stievano, L. *J. Alloys Compd.* **2001**, *328*, 50.
(5) Cadete-Santos-Aires, F. J.; Geantet, C.; Renouprez, A. J.; Pellarin, M. *J. Catal.* **2001**, *202*, 163.
(6) Bazin, D.; Guillaume, D.; Pichon, Ch; Uzio, D.; Lopez, S. *Oil and Gas Science and Technology*, Rev. No.5; IFP: Rueil-Malmaison, France, 2005; Vol 60, pp 801−813.
(7) Massen, C.; Mortimer-Jones, T. V.; Johnston, R. L. *J. Chem. Soc., Dalton Trans.* **2002**, 4375
(8) Lloyd, L. D.; Johnston, R. L.; Salhi, S.; Wilson, N. T. *J. Mater. Chem* **2004**, *14*, 1691.
(9) Lloyd, L. D.; Johnston, R. L.; Salhi, S. *J. Comput. Chem.* **2005**, *26*, 1069.
(10) Rossi, G.; Ferrando, R.; Rapallo, A.; Fortunelli, A.; Curley, B. C.; Lloyd, L. D.; Johnston, R. L. *J. Chem. Phys.* **2005**, *122*, 194309.
(11) Fernández, E. M.; Balbas, L. C.; Perez, L. A.; Michaelian, K.; Garzon, I. L. *Int. J. Mod. Phys. B* **2005**, *19*, 2339.
(12) Johnston, R. L. *J. Chem. Soc., Dalton Trans.* **2003**, 4193.
(13) Barcaro, G.; Fortunelli, A.; Rossi, G.; Nita, F.; Ferrando R. *J. Phys. Chem. B* **2006**, *110*, 23197.
(14) Aprà, E.; Ferrando, R.; Fortunelli, A. *Phys. Rev. B* **2006**, *73*, 205414.
(15) Jellinek, J.; Krissinel, E. B. *Theory of Atomic and Molecular Clusters;* Springer: Berlin, 1999.
(16) Krissinel, E. B.; Jellinek, J. *Int. J. Quantum Chem.* **1997**, *62*, 185.
(17) Cleri, F.; Rosato, V. *Phys. Rev. B* **1993**, *48*, 22.
(18) Kendall, R. A.; Aprà, E.; Bernholdt, D. E.; Bylaska, E. J.; Dupuis, M.; Fann, G. I.; Harrison, R. J.; Ju, J.; Nichols, J. A.; Nieplocha, J.; Straatsma, T. P.; Windus, T. L.; Wong, A. T. *Comput. Phys. Commun.* **2000**, *128*, 260.
(19) Perdew, J. P.; Wang, Y. *Phys. Rev. B* **1986**, *33*, 8800.
(20) Perdew, J. P.; Chevary, J. A.; Vosko, S. H.; Jackson, K. A.; Pederson, M. R.; Singh, D. J.; Fiolhaus, C. *Phys. Rev. B* **1992**, *46*, 6671.
(21) Schaefer, A.; Huber, C.; Ahlrichs, R. *J. Chem. Phys.* **1994**, *100*, 5289.
(22) Andrae, D.; Haeussermann, U.; Dolg, M.; Stoll, H.; Preuss, H. *Theor. Chim. Acta* **1990**, *77*, 123.
(23) Weigend, F.; Haser, M.; Patzel, H.; Ahlrichs, R. *Chem. Phys. Lett.* **1998**, *294*, 143.
(24) Elsässer, C.; Fähnle, M.; Chan, C. T.; Ho, K. M. *Phys. Rev. B* **1994**, *49*, 13975.
(25) Warren, R. W.; Dunlop, B. I. *Chem. Phys. Lett.* **1996**, *262*, 384.
(26) Cleveland, C. L.; Landman, U. *J. Chem. Phys.* **1991**, *94*, 7376.
(27) Ferrando, R.; Fortunelli, A.; Rossi, G. *Phys. Rev. B* **2005**, *72*, 085449.
(28) Rapallo, A.; Rossi, G.; Ferrando, R.; Fortunelli, A.; Curley, B. C.; Lloyd, L. D.; Tarbuck, G. M.; Johnston, R. L. *J. Chem. Phys.* **2005**, *122*, 194308.
(29) Rossi, G.; Rapallo, A.; Mottet, C.; Fortunelli, A.; Baletto, F.; Ferrando, R. *Phys. Rev. Lett.* **2004**, *93*, 105503.
(30) Baletto, F.; Ferrando, R.; Fortunelli, A.; Montalenti, F.; Mottet, C. *J. Chem. Phys.* **2002**, *116*, 3856.
(31) Aprà, E.; Baletto, F.; Ferrando, R.; Fortunelli, A. *Phys. Rev. Lett.* **2004**, *93*, 065502.
(32) Baletto, F.; Mottet, C.; Ferrando, R. *Phys. Rev. B* **2001**, *63*, 155408.
(33) Baletto, F.; Ferrando, R. *Rev. Mod. Phys.* **2005**, *77*, 371.
(34) Rodríguez-López, J. L.; Montejano-Carrizales, J. M.; Pal, U.; Sánchez-Ramírez, J. F.; Troiani, H. E.; García, D.; Miki-Yoshida, M.; José-Yacamán, M. *Phys. Rev. Lett.* **2004**, *92*, 196102.

New Journal of Physics
The open-access journal for physics

Structure and diffusion of small Ag and Au clusters on the regular MgO (100) surface

G Barcaro and A Fortunelli[1]
Molecular Modeling Laboratory, IPCF-CNR, Via G. Moruzzi 1, Pisa, I56124, Italy
E-mail: fortunelli@ipcf.cnr.it

New Journal of Physics **9** (2007) 22
Received 6 October 2006
Published 8 February 2007
Online at http://www.njp.org/
doi:10.1088/1367-2630/9/2/022

Abstract. The lowest energy structures and the diffusion energy barriers of small $M_N (N = 1–4)$ Ag and Au clusters absorbed on the regular MgO (100) surface are investigated via density-functional (DF) calculations, using two different xc-functionals (PBE and LDA). In agreement with previous work, it is found that the lowest-energy structures of Ag and Au clusters in this size-range exhibit a strong 'metal-on-top' effect, by which the clusters are absorbed atop oxygen ions in a linear (dimer) or planar (trimer and tetramer) configuration perpendicular to the surface. The corresponding diffusion mechanisms range from monomer hopping, to dimer leapfrog (Ag_2) or hopping (Au_2), trimer walking, tetramer walking (Ag_4) or rocking and rolling (Au_4), exhibiting interesting differences between Ag and Au. An analysis of the corresponding energy barriers shows that trimers can diffuse at least as fast as monomers, while tetramers and (especially in the case of gold) dimers present somewhat higher barriers, but are anyway expected to be mobile on the surface at the temperatures of molecular beam epitaxy (MBE) experiments. The calculated PBE diffusion energy barriers compare reasonably well with the values extracted from the analysis of recent MBE experimental data, with the LDA predicting slightly higher barriers in the case of gold.

[1] Author to whom any correspondence should be addressed.

PII: S1367-2630(07)34447-9

Contents

1. Introduction

Metal clusters absorbed on oxide surfaces [1, 2] have been the subject of growing attention in recent years due to their interest in many scientific and technological fields, ranging from catalysis and chemical sensing [3]–[10] to optoelectronic and electrical devices [11]–[14], etc. A key issue in this respect is represented by the control of the size and distribution of the clusters, i.e., of the growth process, in its various components: absorption, diffusion, nucleation and sintering. As the field grows mature, the initial emphasis on the energetics of static processes, such as absorption and nucleation [15]–[19], is gradually shifting and extending to more complex dynamical processes, such as diffusion [20, 21] and sintering [22]. In particular, as emphasized in [23], the role of small cluster diffusion in affecting the growth kinetics is not fully understood, and deserves further investigation. In close analogy with the field of the dynamical processes of metal atoms and clusters on metal surfaces [24, 25], the first studies have appeared [26]–[29] in which the mechanism and kinetics of diffusion of metal adatoms and metal clusters on oxide surfaces were investigated in detail. The main result of these studies [27, 28], as applied to the prototypical Pd/MgO (100) system—probably the most well-known metal-on-oxide model catalyst [30]—was that mobility of small clusters is important to understand the growth of Pd islands on MgO (100), and that only by explicitly considering these processes can theoretical predictions and experimental observations be fully reconciled. In this respect, it is therefore interesting to know whether the Pd/MgO (100) system represents an exceptional case, or whether the overall picture can be extended to other systems. In particular, it is of interest to know how fast dimers and larger clusters can move, and by which mechanisms. In the present study, we address these issues by reporting the results of density-functional (DF) calculations aimed at determining the lowest-energy structures and diffusion energy barriers of small $M_N (N = 1–4)$ silver and gold clusters on the regular MgO (100) surface. Gold and silver clusters absorbed on MgO (100) are of interest for their peculiar chemical [3], [5]–[7], [31, 32] and optical [11]–[14], [33] properties, and have thus been intensively studied in recent years [17], [32]–[44]. Moreover, silver and gold are noble metals, with an electronic configuration of the single atoms ($d^{10}s^1$)

different from that of Pd ($d^{10}s^0$), and thus represent interesting examples for testing whether small metal cluster mobility is confirmed in these cases.

The paper is organized as follows. In section 2, the computational details are presented. In section 3, the results of the DF calculations are reported, distinguished in terms of nuclearity to help the comparison between silver and gold and with the experimental data [21]. Finally, conclusions are summarized in section 4.

2. Computational details

The DF calculations for the determination of the lowest-energy structures are performed using the plane-wave self-consistent field (PWscf) computational code [45] employing ultrasoft pseudopotentials. The Perdew–Burke–Ernzerhof (PBE) exchange-correlation functional [46], which is a gradient-corrected (GGA) functional, is used; in some calculations also the local density approximation (LDA) functional [47] is used. The kinetic energy cutoff for the selection of the plane-wave basis set is fixed to 40 Ryd (1 Ryd ≈13.6 eV) for all the calculations. A (3,3,1) *k*-point sampling of the Brillouin zone is chosen, and a Gaussian smearing procedure (with a smearing parameter of 0.002 Ryd) is applied. The geometry optimizations are stopped when the maximum force on the atoms is less than 10^{-4} au. The regular MgO (100) surface is modelled by a three-layer slab (as is customary [38]), each layer containing 9 Mg and 9 O atoms fixed at the equilibrium lattice positions characterizing the MgO rock-salt structure (with lattice parameter equal to the experimental value of 4.208 Å). The distance between metal atoms in replicated cells is at least 4–6 Å.

The determination of the diffusion barriers is performed by applying the climbing image nudged elastic band (CI-NEB) [48, 49] module of the PWscf package. This method searches for the minimum-energy path between two local minima of the potential energy surface (PES) by creating a fixed number of intermediate configurations (images) which are linked to each other by elastic springs. After a few iterations, the band-tangent component of the force felt by the image highest in energy (the climbing image) is inverted and this image is set free to evolve towards the *true* saddle point along the pathway. In our calculations, five images have been chosen; the first and the last are two local minima singled out from the lowest-energy structures of the metal clusters located by the previous search.

It should be noted that we only evaluate the diffusion energy barriers and not the Arrhenius prefactors. A full evaluation of the kinetic constants for diffusion would in principle imply also an estimate of these entropic factors, for example—applying the transition state theory [50]—by calculating the ratio of the vibrational frequencies of the normal modes at the minima and at the saddle points [28, 29]. However, we chose not to perform the corresponding calculations because: (i) the entropic factors evaluated through the transition state theory using atom–atom potentials [51] were substantially constant for the diffusion processes investigated in the present study; (ii) in the case of Pd, the entropic factors did not qualitatively modify the results, bringing about differences smaller than the intrinsic accuracy of the DF approach (see later the differences between the LDA and PBE approaches). Along the same lines is the choice of not relaxing the MgO coordinates. Firstly of all, unconstrained DF theory using GGA (such as PBE) xc-functionals (at variance with hybrid xc-functionals [52]) makes the MgO system rather soft, whereas by employing a GGA xc-functional and fixing the oxide lattice parameter at the experimental value one partially recovers the hard character of the oxide [53]. Secondly,

we do not expect the relaxation of the oxide coordinates to qualitatively modify our results, as suggested by the comparison with the case of palladium clusters on MgO (100), both as far as the lowest-energy structures and the diffusion energy barriers are concerned [27, 28] (note that the Pd/surface interaction is even stronger than that of coinage metals). Indeed, as will be shown below, the DF/PBE energy barrier for the diffusion of a single Au atom is 0.22 eV from our calculations, in which the MgO surface is kept fixed, and 0.24 eV from the calculations of [38], obtained using an equivalent computational approach, but in which the oxide coordinates are fully relaxed.

3. Results and discussion

Our aim is to locate the lowest-energy local minima of small Ag and Au clusters on the MgO (100) surface and to find the lowest-energy diffusion pathways connecting them.

For each local minimum, it is convenient to define four quantities: (i) the adhesion energy (E_{adh}), calculated by subtracting the energy of the oxide surface and of the metal cluster, both frozen in their interacting configuration, from the value of the total energy of the system; (ii) the binding energy of the metal cluster (E_{met}), calculated by subtracting the energy of the isolated metal atoms from the total energy of the metal cluster in its interacting configuration; (iii) the metal cluster distortion energy (E_{dist}), which corresponds to the difference between the energy of the metal cluster in the configuration interacting with the surface, and the energy of the cluster in its lowest-energy gas-phase configuration; and (iv) the total binding energy (E_{bnd}), which is the sum of the binding energy of the metal cluster and of the adhesion energy ($E_{\mathrm{bnd}} = E_{\mathrm{adh}} + E_{\mathrm{met}}$).

For each diffusion pathway we report the value of the energy barrier, calculated using the CI-NEB method [49]. The results of subsections 3.1–3.4 have been obtained using the PBE xc-functional, those in subsection 3.5 using the LDA xc-functional.

To better compare the behaviour of silver and gold, the results are distinguished in terms of nuclearity (N) for the clusters Ag_N and Au_N, with $N = 1$–4.

3.1. Single atoms

As shown in [16, 17, 34, 37, 38, 40, 42, 44], for both Ag and Au single atoms the highest value of the adhesion energy to the regular surface corresponds to the absorption on top of an oxygen ion of the terrace. The preferential absorption on this site is a common feature of all neutral transition metal atoms, and, in the case of Au, it has been experimentally demonstrated [54]. In the case of the coinage metals (Cu, Ag and Au), the interaction is rather weak, less than 1 eV at the PBE level, because of the remarkable repulsion between the diffuse unpaired s electron of the metal and the charge density of the oxide surface, as discussed in [16, 17, 34, 40, 42]. Within the group, Au is characterized by the strongest adhesion (about 0.9 eV at the DF/PBE level), because the relativistic contraction of the s orbital brings it to overlap with the d orbitals of the metal [55]: the resulting s–d mixing means that the electronic density of the metal can be polarized away by the electric field of the surface in the outward direction, and, as a consequence, the metal orbitals are partially depleted and can accept charge density from the oxide surface [16, 17, 34, 38, 40, 42]. The total charge transfer between the Au atom and the MgO surface is however small [54]. On the contrary, Ag is characterized by the weakest interaction (about 0.4 eV) because of the poor hybridization between the s and d orbitals (for Ag, the low lying d orbitals are well separated

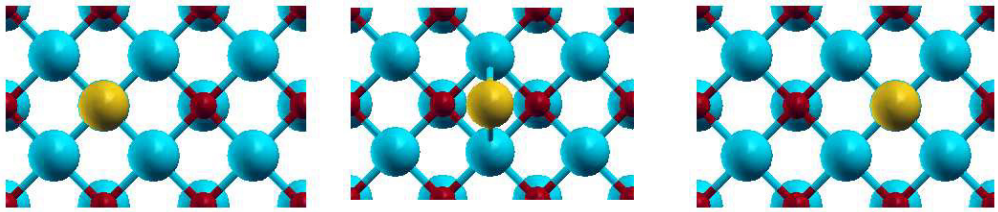

Figure 1. Schematic representation of the monomer hopping diffusion mechanism.

from the s orbital). The diffuse character of the valence s electron is further responsible for the stronger repulsion between the metal electronic cloud and the oxide charge density [34, 39, 42]. The diffusion of the single atom then takes place through a hopping mechanism (see figure 1) [38, 43]: the metal atom moves from one oxygen site to one of its four first neighbours passing above a hollow site, which represents the saddle point of the movement, in close analogy with the Pd case [27, 28, 56]. The diffusion energy barrier is thus easily determined by evaluating the difference in adhesion energy between the oxygen site and the hollow site. From our calculations, this difference amounts to 0.22 eV in the case of Au and 0.10 eV in the case of Ag, respectively (see tables 1 and 2), which compares very well with previous estimates [38, 43]. Thus the weaker adhesion of silver determines also a smaller value of the diffusion barrier. The value for Au is in reasonable agreement with the experimental data: it has been observed, in fact [62], that Au starts being mobile around 100–130 K on the regular MgO (100) surface, implying an energy barrier in the range 0.2–0.3 eV.

3.2. Dimers

At variance with the case of Pd_2 [57], the dimers of silver and gold are absorbed in an upright position perpendicular to the surface atop an oxygen site of the terrace, as already shown in [35, 37, 38, 42, 44]. This configuration is stabilized by an electrostatic contribution deriving from the increased polarization of the metal electronic density of the dimer in the field of the oxide. In general, it has been noted [36]–[39] that the presence of metal atoms above those directly interacting with the surface *increases* the adhesion energy (this effect is what we have called the 'metal-on-top' stabilization mechanism [37]).

The configurations that have been considered for the dimers and the corresponding diffusion pathways are displayed in figure 2. The energy analysis is reported in table 1.

In the case of gold, the metal-on-top effect in the ground-state configuration is so strong that the adhesion of the dimer is 1.41 eV, which corresponds to an *increase* of 0.5 eV with respect to the adhesion of the single atom, despite the fact that the atom interacting with the surface is involved in a strong metallic bond, which should *decrease* its availability to interact with the surface, in substantial agreement with previous analyses [35, 38]. The other two configurations that have been considered are: (b) an epitaxial one with two metal atoms absorbed atop two first neighbour oxygens on the surface, previously considered in [35]; (c) a configuration where the dimer is perpendicular to the surface but atop the hollow site. In configuration (b), which represents a local minimum, due to the stickiness of the metallic bond

Table 1. The values of the various energy quantities defined in the text are reported for the lowest-energy structures and saddle points for Ag_N and Au_N ($N = 1$–4) clusters, as calculated using the PBE xc-functional. The notation (a)–(e) refers to the configurations reported in figures 1–4.

Cluster	Configurations	E_{adh} (eV)	E_{met} (eV)	E_{dist} (eV)	E_{bnd} (eV)
Au_1	Oxygen	0.91	–	–	0.91
Au_1	Hollow	0.69	–	–	0.69
Ag_1	Oxygen	0.43	–	–	0.43
Ag_1	Hollow	0.33	–	–	0.33
	(a)	1.41	2.33	0.00	3.74
Au_2	(b)	0.56	2.31	0.02	2.87
	(c)	0.79	2.33	0.00	3.12
	(a)	0.66	1.73	0.00	2.39
Ag_2	(b)	0.44	1.73	0.00	2.17
	(c)	0.41	1.73	0.00	2.14
Au_3	(a)	1.52	3.58	0.01	5.10
	(b)	1.72	3.52	0.07	5.24
Ag_3	(a)	0.90	2.60	0.01	3.50
	(b)	0.91	2.58	0.03	3.49
	(a)	1.86	6.03	0.16	7.89
	(b)	2.18	5.86	0.32	8.04
Au_4	(c)	0.85	5.33	0.86	6.18
	(d)	1.44	6.16	0.03	7.60
	(e)	1.46	6.18	0.01	7.64
	(a)	1.00	4.55	0.03	5.55
	(b)	1.11	4.40	0.18	5.51
Ag_4	(c)	0.87	3.72	0.85	4.60
	(d)	0.92	4.58	0.00	5.50
	(e)	0.89	4.57	0.00	5.46

the equilibrium distance of the dimer (around 2.5 Å) is only slightly elongated with respect to the gas-phase, and the two metal atoms cannot match very well the two oxygens of the terrace (which are at a distance of about 2.97 Å). In this configuration the metal-on-top effect is completely absent and the adhesion energy (0.56 eV) is decreased by 0.85 eV with respect to the ground-state. In configuration (c), which represents a saddle point, the loss in adhesion energy (0.62 eV) is larger than the difference in adhesion between the oxygen site and the hollow site for the single atom (about 0.2 eV). The decrease in the adhesion is thus mainly due to a decrease of the metal-on-top effect when passing from the oxygen to the hollow site, probably because of the different form of the electric field above the two sites. The hopping mechanism with the dimer passing through the hollow site keeping the axis perpendicular

Table 2. The values of the energy barriers for the various diffusion mechanisms considered in the text are reported for Ag_N and Au_N ($N = 1$–4) clusters, as calculated using the PBE xc-functional.

Cluster	Mechanism	Barrier (eV)
Au_1	Monomer hopping	0.22
Au_2	Dimer hopping	0.62
Au_2	Dimer leapfrog	> 0.87
Au_3	Trimer walking	0.19
Au_4	Tetramer walking	0.60
Au_4	Tetramer rocking/rolling along [100]	0.44
Au_4	Tetramer rocking/rolling along [110]	0.42
Ag_1	Monomer hopping	0.10
Ag_2	Dimer hopping	0.25
Ag_2	Dimer leapfrog	0.22
Ag_3	Trimer walking	0.12
Ag_4	Tetramer walking	0.21
Ag_4	Tetramer rocking/rolling along [110]	0.58
Ag_4	Tetramer rocking/rolling along [100]	0.55

to the surface corresponds exactly to the energy difference between the ground-state and configuration (c), and amounts to 0.62 eV. Another possible diffusion mechanism is a 'leapfrog' movement with the dimer passing from the ground-state (a) to configuration (b) and again to the ground-state but atop an oxygen first neighbour of the starting one: the barrier has not been explicitly calculated using the CI-NEB approach, as it is necessarily higher than the energy difference between the ground-state and configuration (b), i.e., 0.87 eV. The leapfrog mechanism has previously been suggested as the lowest-energy diffusion mechanism for the Cu_2 dimer on a regular MgO (100) surface [26]; the dimer hopping mechanism, instead, has not been described before. We can thus conclude that the diffusion of the gold dimer is characterized by a barrier (0.62 eV) higher than the one characterizing the diffusion of the single atom (0.22 eV).

The case of silver is not qualitatively different as far as the static structures are concerned: the ground-state, configuration (a), is stabilized by the metal-on-top effect in the upright position perpendicular to the surface [42, 57]. The gain in adhesion with respect to the single atom is lower than in the case of gold, which implies that silver is characterized not only by a weaker direct interaction, but also by a weaker polarization contribution. This fact determines that configuration (b), the epitaxial one, and (c), the vertical one atop the hollow site, are characterized by a moderate loss of adhesion energy with respect to the ground-state: 0.22 and 0.25 eV, respectively (see the detailed analysis in table 1). The diffusion barrier for the vertical diffusion is equal to the difference between the ground-state and configuration (c), and amounts to 0.25 eV. The diffusion through the leapfrog mechanism, which in this case has been evaluated through the CI-NEB approach, is characterized by a barrier almost identical to the energy difference between the ground-state and configuration (b), i.e., 0.22 eV. As in the case of gold, the barrier for the diffusion of the dimer (0.22 eV) is thus higher than the one for the single atom (0.10 eV).

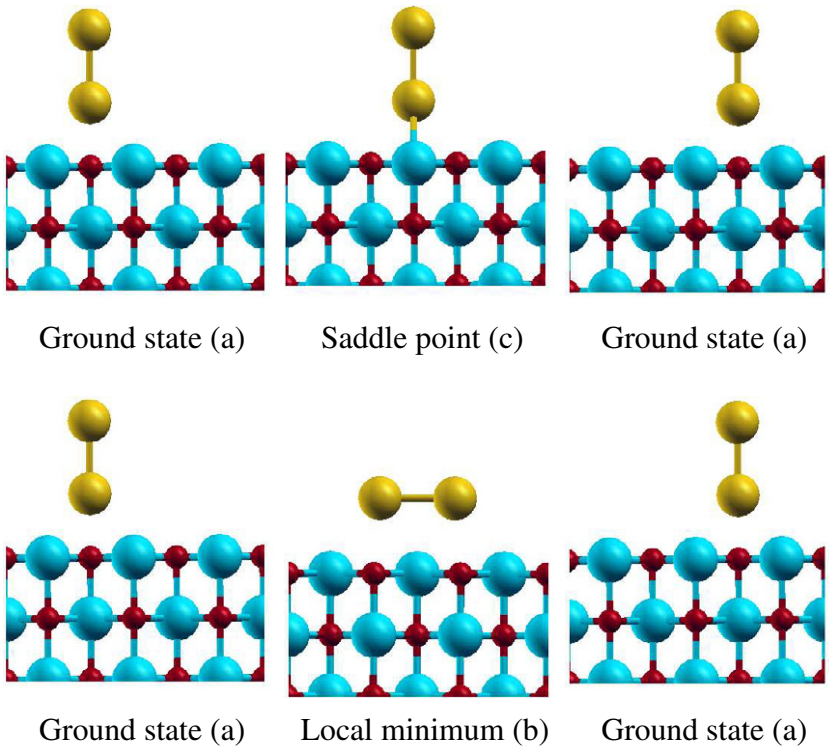

Figure 2. Schematic representation of the dimer hopping diffusion mechanism (first row) and of the dimer leapfrog diffusion mechanism (second row).

3.3. Trimers

In analogy with the Pd_3 case [58], the trimers of silver and gold are absorbed in an upright position with the cluster plane perpendicular to the surface and two metal atoms interacting with two oxygen ions of the terrace, as already shown in [35, 37]. The plane of the trimer can be oriented along the [110] direction—configuration (a), see figure 3—with the two basal metal atoms atop two first neighbour oxygens, or it can be oriented along the [100] direction—configuration (b)—with the two basal metal atoms pointing towards two oxygen atoms at a distance of 4.21 Å and with a magnesium atom underneath the centre of mass of the cluster. Configuration (a) has been considered in previous studies [35, 37], finding energy values in reasonable agreement with the present results, whereas, to our knowledge, configuration (b) has so far been neglected. The two configurations can be approximately interconverted through a rotation of 45° around an axis perpendicular to the surface and passing through one of the basal atoms of the cluster. In both the Ag and the Au case, the energy difference between the two configurations is very low: both structures are stabilized by the metal-on-top effect; moreover, the trimer, characterized by a doublet spin state, is a Jahn–Teller system with one electron occupying an anti-bonding orbital and is thus highly fluxional both in the gas-phase and when absorbed on the surface [37]. In the case of gold, configuration (b) is lower in energy than configuration (a) by 0.14 eV. In the case of silver, the two configurations have practically the same energy. An analysis of the energy contributions for the two configurations for both metals is reported in table 1.

Trimer diffusion can take place through successive transformations of configuration (a) into (b); this is obtained by a rotation of 45° around one of the two basal atoms, see figure 3. This

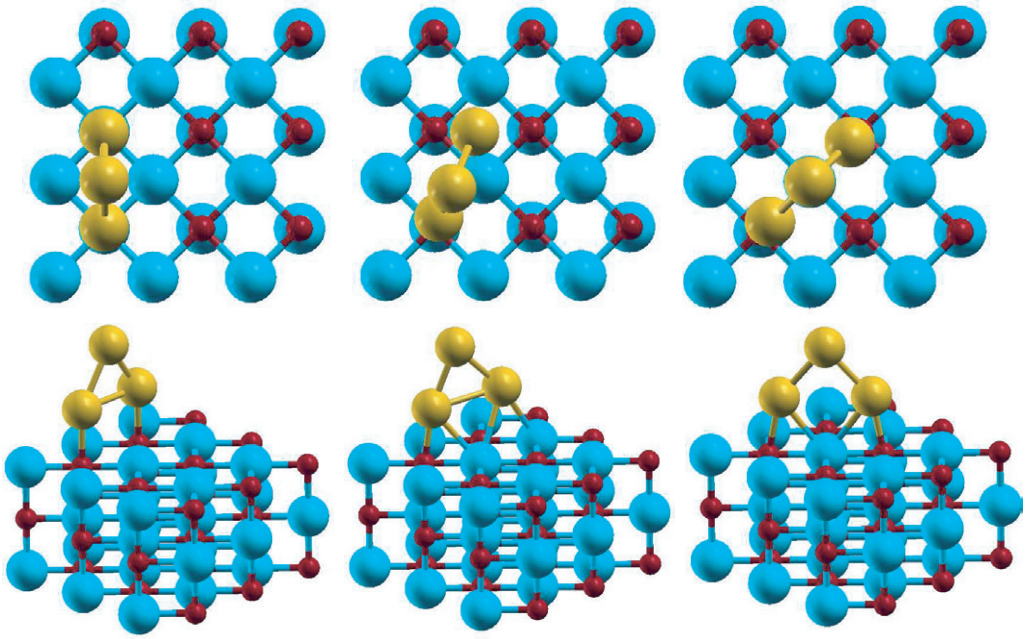

Figure 3. Schematic representation of the trimer walking diffusion mechanism.

kind of movement, already found in the case of the cluster Pd_3 [27, 28] on a (100) MgO surface, can be called *trimer walking*, and it takes place with the cluster keeping its plane perpendicular to the surface. The saddle point has been determined for the two metals by applying the CI-NEB method and corresponds to an intermediate angle of rotation between the two minima. The energy barrier amounts respectively to 0.19 eV in the case of Au_3 and 0.12 eV in the case of Ag_3, respectively. The two values are similar to the values found for the diffusion of the single atoms. In particular, in the case of gold, the barrier for the trimer is slightly lower than that of the monomer (0.19 eV versus 0.22 eV).

3.4. Tetramers

The lowest energy structures and saddle points of the gold and silver tetramers are displayed in figure 4, while the corresponding energies are reported in table 1.

The results for the tetramer are partly similar to the results found in the case of the trimer, but with interesting differences. We start the discussion by considering Au_4. In the two lowest-energy local minima, labelled (a) and (b) in figure 4, the cluster has the shape of a rhombus (the same shape characterizing the global minimum in the gas-phase) and interacts with the surface through two basal metal atoms. If the cluster plane is oriented along the [100] direction, we find the global minimum, configuration (b), whereas, if the plane is oriented along the [110] direction, we find a local minimum higher in energy by about 0.15 eV, configuration (a), which has been already considered in a previous study [36], which found energy values in reasonable agreement with the present results. These two configurations can be obtained from the configurations (a) and (b) of the trimer by absorbing a fourth atom in a metal-on-top position (not in direct contact with the surface). The ordering between the two configurations is the same as in the case

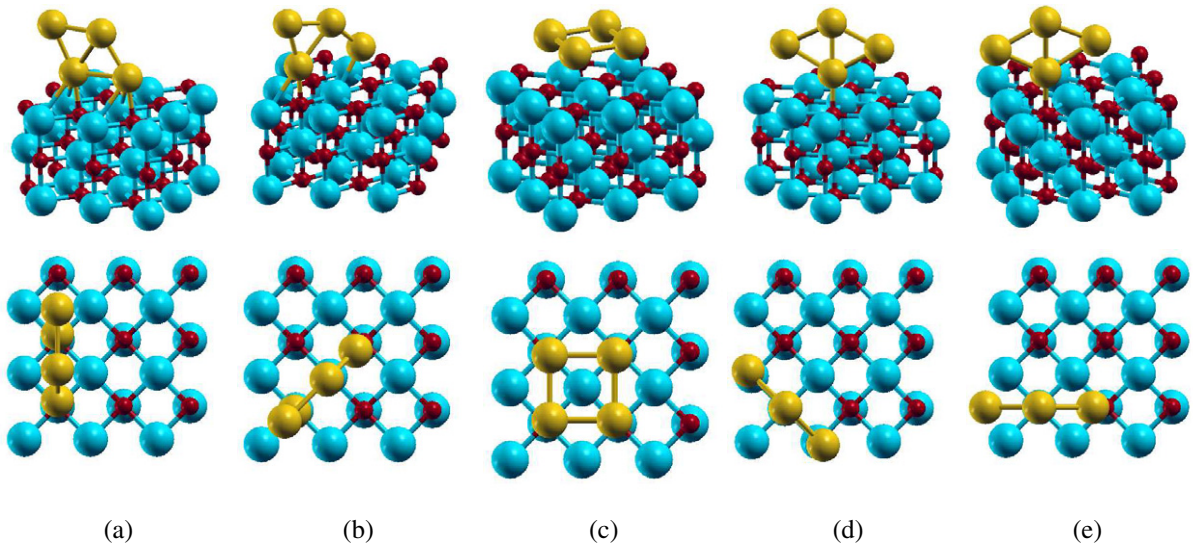

Figure 4. Schematic representation of the lowest-energy structures (a, b) and saddle points (d, e) of Ag and Au tetramers on a regular MgO (100) surface. Configuration (c) is a local minimum at higher energy.

of the trimer, and their energy difference is also very similar (0.15 eV versus 0.14 eV). The most significant difference with respect to the case of the trimer is that the tetramer undergoes a significant distortion, as can be noted in figure 4, in passing from the gas-phase to being absorbed on the surface, with distortion energies of 0.16 eV in configuration (a) and 0.32 eV in configuration (b), respectively. This is due to the fact that the tetramer is a closed shell with a reduced fluxional character with respect to the trimer. The loss of metallic energy is compensated in both configurations by the enhanced adhesion to the surface due to the metal-on-top effect. Another local minimum is configuration (c), where the tetramer has the shape of a square and is absorbed on four oxygen ions of the terrace. This configuration is strongly destabilized with respect to the previous ones, because of a significant loss in both metallic energy and adhesion energy. The low value of the adhesion energy of this structure is a further confirmation that the metal-on-top effect accounts for an important contribution to the adhesion: structure (c), with four atoms in direct contact with the surface, has an adhesion energy almost three times smaller than the adhesion of configuration (b), where the cluster is in direct contact with only two oxygen atoms. The last two configurations considered, (d) and (e), are saddle points: they have a C_{2v} symmetry, and interact with the surface with only one metal atom. They only differ between each other by the orientation of the cluster plane, which is along the [100] direction for configuration (d) and along the [110] direction for configuration (e). They are both characterized by lower values of distortion energies, but also lower values of the adhesion to the surface. Configuration (e) has already been considered in previous studies [36, 57].

The results for Ag_4 are qualitatively very similar. As can be noted from the values reported in table 1, all the configurations—except configuration (c)—are characterized by a value of the total binding energy of about 0.1 eV, because of a compensation between the metallic bond and the adhesion contributions. Also in this case, configurations (a) and (b) are the lowest-energy minima, but now, at variance with the case of Au, configuration (a) is the global minimum and configuration (c) is slightly higher in energy. Configurations (d) and (e), instead, are saddle

points. It is interesting to note that, for silver, the adhesion energy of configuration (c) is not much smaller than the adhesion of the other configurations and that the main loss is due to the destabilization of the metallic bond. This is again an indication that the metal-on-top effect is weaker in the case of silver with respect to gold and of the same order of magnitude as the direct interaction. The weak global adhesion to the surface is also suggested by the lower values of the distortion energies with respect to the gold tetramer: an appreciable loss of metallic bond is favourable only when it is compensated by a significant interaction with the surface.

The diffusion of the tetramer can take place through a variety of mechanisms, all of which are novel, as a rhombic configuration adhering through one of its edges is peculiar to silver and gold. One possibility is represented by a movement of 'tetramer walking' between configurations (a) and (b), a movement analogous to trimer walking. The difference with respect to the trimer is that the rotation of 45° can take place either around the vertex at higher coordination or around the vertex at lower coordination: the two movements have different barriers as it is energetically less costly to move the basal atom with lower coordination with respect to the basal atom with higher coordination, because the former loses less 'metal-on-top' or metal-bonding stabilization energy. In the case of gold, the values of the two energy barriers are 0.38 and 0.60 eV, respectively; in the case of silver 0.10 and 0.21 eV. Since a tetramer needs both movements for real diffusion (a single rotation does not allow the cluster to leave an area of four first-neighbour oxygen sites) the real value of the barrier is thus 0.60 eV for gold and 0.21 eV for silver. Therefore, despite the similarities between the walking mechanisms in the trimers and tetramers, the need to move an atom with higher coordination makes the diffusion energy barrier for the tetramer higher than that for the trimer. However, while in the case of silver the tetramer walking mechanism corresponds to the diffusion mechanism with the lowest barrier, in the case of gold we have found other processes characterized by lower activation energies. In figure 5, in fact, we can see how the configuration (b) can move along the [100] direction to another configuration (b) through a rocking mechanism, i.e., passing through the saddle point (1)—barrier of 0.39 eV—or through a rolling mechanism, i.e., passing through the saddle point given by configuration (d)—barrier of 0.44 eV. The rolling movement (to be distinguished from a qualitatively different movement of the Pd_4 tetrahedron [27, 28]) consists of revolving the cluster around the most coordinated atom in direct contact with the surface. The combination of these two movements determines a diffusion of the tetramer along the [100] direction; the barrier is given by the higher value between the the two values found: 0.44 eV. Still another possibility is that configuration (b) first rotates into configuration (a) through the first step of the walking mechanism, and that configuration (a) then diffuses through successive rocking/rolling movements along the [110] direction in a way completely analogous to the diffusion of configuration (b) along the [100] direction. Configuration (a) thus flips into another configuration (a) through the saddle point (2)—barrier of 0.27 eV—and rolls into another configuration (a) through the saddle point (e)—barrier of 0.25 eV.[2] The barrier for this mechanism is given by the sum of the energy difference between configuration (a) and (b)—0.15 eV—and the higher of the two rocking/rolling barriers—0.27 eV, for a total of 0.42 eV. The rocking/rolling processes in the two directions are thus energetically equivalent and both very favourable with respect to the walking mechanism. These rocking/rolling movements are not competitive in the case of silver because they pass through the saddle points (1) and

[2] We note that the energy difference between the (a) and (e) configurations obtained in [36] through a DF/BP86 method using a cluster approach is appreciably larger, probably due to the choice of the xc functional.

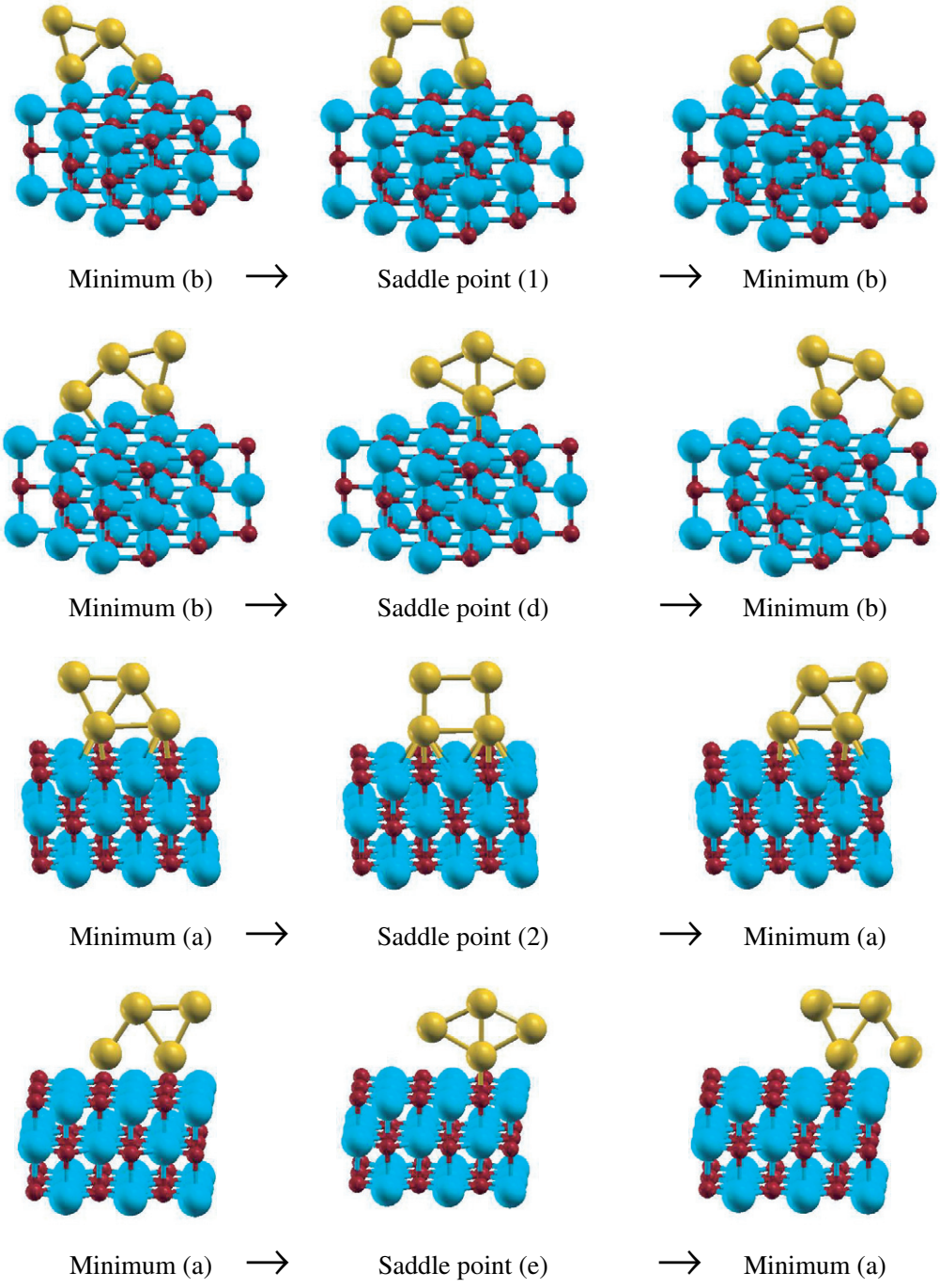

Figure 5. Schematic representation of the rocking/rolling diffusion mechanism along the [100] direction (first and second row) and along the [110] direction (third and fourth row).

(2) which present a remarkable distortion of the metal bonding, a distortion not compensated by an enhanced direct adhesion nor by the metal-on-top effect. Despite the similarities between Ag and Au, we can thus find subtle differences in the diffusion behaviour of the two metals.

Table 3. The values of the various energy quantities defined in the text are reported for the lowest-energy structures and saddle points for $Au_N (N = 1–4)$ clusters, as calculated using the LDA xc-functional; the notation (a)–(e) refers to the configurations reported in figures 1–4.

Cluster	Configurations	E_{adh} (eV)	E_{met} (eV)	E_{dist} (eV)	E_{bnd} (eV)
Au_1	Oxygen	1.54	–	–	1.54
Au_1	Hollow	1.26	–	–	1.26
	(a)	2.14	2.97	0.00	5.11
Au_2	(b)	1.44	2.93	0.04	4.37
	(c)	1.39	2.97	0.00	4.36
Au_3	(a)	2.71	4.87	0.04	7.58
	(b)	2.97	4.73	0.18	7.70
	(a)	3.11	8.13	0.21	11.24
	(b)	3.51	7.85	1.00	11.36
Au_4	(c)	2.23	7.34	1.47	9.57
	(d)	2.32	8.31	0.03	10.63
	(e)	2.36	8.34	0.00	10.70

The results of the energy barriers for the diffusion mechanisms described up to now are summarized in table 2. It can be noted that, for both metals, an odd/even oscillation in the values of the diffusion barriers exists, with the monomers and trimers being more mobile than the dimers and the tetramers. This is due to the doublet spin state and the consequent fluxional character of the odd nuclearities, which are thus able to rearrange their configuration without significant loss of metallic energy, simultaneously optimizing the interaction with the surface. In passing, we note that it can be hypothesized that bigger clusters are also mobile enough on the surface to contribute to the growth process through diffusion processes (work in progress).

3.5. LDA results for gold

In the case of gold, it is known that a change of the xc-functional can sometimes translate into a qualitative change in the theoretical predictions [59]–[61]. To increase our confidence about the soundness of our results, we have thus repeated (only for the Au clusters) the static and dynamics analysis discussed above by using the LDA xc-functional instead of the PBE xc-functional. The LDA xc-functional, in fact, it is thought to better describe the gold metallic bond [59]–[61]. The analysis of the configurations from monomer to tetramer is reported in table 3, while the values of the diffusion barriers are reported in table 4.

A general trend which can be immediately evinced from the results in tables 3 and 4 is that the adhesion energies are increased, in particular the component due to the chemical interaction between the metal atoms and the surface. For the dimer, for example, we see that the energy difference between the ground-state upright configuration and the horizontal configuration is reduced from 0.87 eV (PBE) to 0.74 eV (LDA): although the metallic bond is strengthened by the use of LDA, in the horizontal configuration the inter-metal distance is elongated with respect

Table 4. The values of the energy barriers for the various diffusion mechanisms considered in the text are reported for Au_N ($N = 1$–4) clusters, as calculated using the LDA xc-functional.

Cluster	Mechanism	Barrier (eV)
Au_1	Monomer hopping	0.28
Au_2	Dimer hopping	0.75
Au_2	Dimer leapfrog	> 0.74
Au_3	Trimer walking	0.30
Au_4	Tetramer walking	0.72
Au_4	Tetramer rocking/rolling along [100]	0.73
Au_4	Tetramer rocking/rolling along [110]	0.66

to the equilibrium value (by about 0.1 Å), in order to exploit the direct interaction with the two oxygen ions of the terrace. On the other hand, in the upright configuration, the polarization contribution due to the metal-on-top effect is not increased as much as the direct interaction, and the energy difference is thus decreased. At the same time, the vertical configuration atop the hollow site, in which the chemical bond is reduced, is destabilized (from 0.62 to 0.75 eV) and is almost isoenergetic with the horizontal configuration. Another indication that the direct interaction is strongly increased by the use of LDA is given by the larger values of the distortion energies: in the ground-state of the tetramer, for example, we have a distortion energy of 1 eV and, at the same time, a remarkable increase in the adhesion energy value. In general, we can conclude that, at the LDA level, in the interplay between metallic bond and metal–surface interaction, the latter prevails, with the additional qualification of an increased importance of the direct 'chemical' interaction with the surface with respect to the polarization (metal-on-top) effect. This also translates into a general increase of the diffusion energy barriers, mainly due to the increased importance of the chemical interaction with the surface, which destabilizes the hollow sites with respect to the epitaxial oxygen sites, and thus typically the saddle point configurations with respect to the ground-states configurations. This increase brings, for example, the energy barrier for the monomer hopping to 0.28 eV, a value which is anyway within the experimentally determined range: 0.2–0.3 eV [62]. It thus seems that—contrary to the Cu/MgO(100) case [41]—the DF approach does not overestimate the metal–surface interaction, and thus the diffusion energy barrier, for Au/MgO(100). Further study is needed to clarify this point.

Apart from these considerations, however, the use of LDA does not introduce a qualitative change in the picture drawn in the previous discussion. The values of the diffusion energy barrier are generally larger and we still observe an odd/even oscillation in these values as a function of the nuclearity of the metal cluster.

3.6. Comparison with experiment

In a previous study, the diffusion barriers for small clusters of palladium absorbed on a regular (100) MgO surface have been calculated using the same methodology as applied here [27]. From these results, monomers and trimers diffuse with the same mechanism as gold and silver, i.e., monomer hopping and trimer walking, with barriers of 0.39 and 0.30 eV, respectively (also in this case the high-spin state of the trimer and its consequent fluxionality decrease the diffusion

barrier with respect to monomer hopping). The dimer diffuses via a dimer rotation mechanism with a barrier of 0.39 eV. The tetramer is absorbed on the surface as a tetrahedron [58] and diffuses via a rolling mechanism (different from that described here) with a barrier of 0.38 eV.

The values found for the three metals suggest that the order of mobility on the regular surface is Pd $\approx$ 0.38 eV $<$ Au $\approx$ 0.22 eV $<$ Ag $\approx$ 0.10 eV, in a corresponding approximate ratio of 3–4 : 2 : 1, following the decreasing strength of the metal–surface interaction. This ordering is in qualitative agreement with 'effective energy barriers' derived from recent molecular beam epitaxy (MBE) experiments [21]. In these experiments, the density of the metal islands grown on the regular surface is measured as a function of temperature and interpolated using an Arrhenius law, i.e., an exponential decrease of the density as a function of temperature. The empirical effective energy barriers of the Arrhenius curve determined from these experiments are 0.22/0.16 eV for Pd, 0.12 eV for Au and 0.08 eV for Ag. Even though the interpretation of these energy barriers is not immediate, as several mechanisms can contribute to metal island growth (diffusion, detrapping from defects and Ostwald ripening, etc), the reasonable agreement between these values and the diffusion energy barriers calculated in the present study leads us to conclude that the experimentally determined values are intimately related to diffusion processes on the surface.

4. Conclusions

The lowest energy structures and the diffusion barriers of small M_N (N = 1–4) Ag and Au clusters absorbed on the regular MgO (100) surface are investigated via DF calculations, using the PBE xc-functional for both Ag and Au clusters and the LDA xc-functional for Au clusters only.

Concerning the lowest-energy structures, in agreement with previous studies [26, 36, 37], we find a predominance of planar configurations with the plane of the cluster perpendicular to the surface. This is rationalized in terms of a strong metal-on-top effect, particularly important for coinage metal clusters, due to the weakness of the direct metal–surface interaction and the large polarizability of the valence s electrons. The structures of the absorbed clusters thus resemble those in the gas-phase (which are also planar in this size range), even though the deformation with respect to the non-symmetric gas-phase structures can sometimes be appreciable in the case of gold.

Concerning the diffusion mechanisms, we find a variety of possibilities, some of which have been already previously described, such as monomer hopping (Ag and Au), dimer leapfrog (Ag_2, see Cu_2 in [26]) and trimer walking (Au_3 and Ag_3, see Pd_3 in [27, 28]); whereas some are novel, such as dimer hopping (Au_2), and tetramer walking (Ag_4) or tetramer rocking/rolling (Au_4). Diffusion being a subtler process than absorption, one finds appreciable differences between silver and gold. An analysis of the corresponding energy barriers also shows that trimers can diffuse at least as fast as monomers, while tetramers and, especially in the case of gold, dimers present somewhat higher barriers. Even though not dramatic, this even–odd alternation might be a general feature of Ag–Au/oxide systems and is anyway sufficiently large to be in principle exploitable in MBE soft-landing experiments at sufficiently low temperature [63, 64]. The main conclusion of the present study is, anyway, that at the temperatures of the MBE experiments [21] small clusters definitely contribute to the metal mobility on the MgO (100) surface, and that the calculated diffusion energy barriers compare reasonably well with the values extracted from the analysis of the MBE experimental data,

so that the effective energy barriers derived from this analysis should be essentially correlated with diffusion processes.

Finally, we note that the use of the LDA xc-functional for Au does not qualitatively modify the results, except for a general increase in the adhesion energies and diffusion energy barriers.

Acknowledgments

We acknowledge financial support from the Italian CNR for the project '(Supra-) Self-Assemblies of Transition Metal Nanoclusters' within the framework of the ESF EUROCORES SONS, and from the European Community Sixth Framework Project for the STREP Project 'Growth and Supra-Organization of Transition and Noble Metal Nanoclusters' (contract no. NMP-CT-2004-001594).

References

[1] Henry C R 1998 *Surf. Sci. Rep.* **31** 235
[2] Freund H J 2002 *Surf. Sci.* **500** 271
[3] Hutchings G J and Haruta M 2005 *Appl. Catal.* A **291** 2
[4] Campbell C T 1997 *Surf. Sci. Rep.* **27** 1
[5] Remediakis N, Lopez N and Norskov J K 2005 *Appl. Catal.* A **291** 13
[6] Chen M S and Goodman D W 2004 *Science* **306** 252
[7] Häkkinen H, Abbet S, Sanchez A, Heiz U and Landman U 2003 *Angew. Chem. Int. Edn. Engl.* **42** 1297
[8] de Oliveira A L, Wolf A and Schüth 2001 *Catal. Lett.* **73** 157
[9] Wang R, Hao J, Guo X, Wang X and Liu X 2004 *Stud. Surf. Sci. Catal.* **154** 2632
[10] Lim D C, Lopez-Salido I and Kim Y D 2005 *Surf. Sci.* **598** 96
[11] Nepijiko S A, Ievlev D N and Schulze W 2003 *Eur. Phys. J.* D **24** 115
[12] Celep G *et al* 2004 *Phys. Rev.* B **70** 165409
[13] Zheng J and Dickson R M 2002 *J. Am. Chem. Soc.* **124** 13982
[14] Brongersma M L 2003 *Nat. Mater.* **2** 296
[15] Moseler M, Häkkinen H and Landman U 2003 *Phys. Rev. Lett.* **89** 176103
[16] Yudanov I, Pacchioni G, Neyman K and Rösch N 1997 *J. Phys. Chem.* B **101** 2786
[17] Matveev A V, Neyman K, Yudanov I and Rösch N 1999 *Surf. Sci.* **426** 123
[18] Campbell C T and Starr D E 2002 *J. Am. Chem. Soc.* **124** 9215
[19] Henry C R 1996 *Mater. Sci. Eng. A: Struct.* **217/218** 239
[20] Haas G, Menck A, Brune H, Barth J V, Venables J A and Kern K 2000 *Phys. Rev.* B **61** 11105
[21] Højrup-Hansen K, Ferrero S and Henry C R 2004 *Surf. Sci.* **226** 167
[22] Revenant C, Renaud G, Lazzari R and Jupille J 2006 *Nucl. Instrum. Methods* B **246** 112
[23] Kyuno K, Golzhauser A and Ehrlich G 1998 *Surf. Sci.* **397** 191
[24] Linderoth T R, Horch S, Petersen L, Helveg S, Lægsgaard E, Stensgaard I and Besenbacher F 1999 *Phys. Rev. Lett.* **82** 1494
[25] Montalenti F and Ferrando R 1999 *Phys. Rev. Lett.* **82** 1498
[26] Musolino V, Selloni A and Car R 1999 *Phys. Rev. Lett.* **83** 3242
[27] Barcaro G, Fortunelli A, Nita F and Ferrando R 2005 *Phys. Rev. Lett.* **95** 246103
[28] Xu L, Henkelman G, Campbell C T and Jónsson H 2005 *Phys. Rev. Lett.* **95** 146103
[29] Xu L, Henkelman G, Campbell C T and Jónsson H 2006 *Surf. Sci.* **600** 1351
[30] Abbet S, Sanchez A, Heiz U, Schneider W D, Ferrari A M, Pacchioni G and Rösch N 2000 *J. Am. Chem. Soc.* **122** 3453

[31] Sanchez A, Abbet S, Heiz U, Schneider W D, Häkkinen H, Barnett R N and Landman U 1999 *J. Phys. Chem.* A **103** 9573
[32] Molina L M and Hammer B 2004 *Phys. Rev.* B **69** 155424
[33] Walter M and Häkkinen H 2005 *Phys. Rev.* B **72** 205440
[34] Neyman K M, Inntam C, Nasluzov V A, Kosarev R and Rösch N 2004 *Appl. Phys.* A **78** 823
[35] Inntam C, Moskaleva L, Neyman K M, Nasluzov V A and Rösch N 2006 *Appl. Phys.* A **82** 181
[36] Inntam C, Moskaleva L, Yudanov I V, Neyman K M, Nasluzov V A and Rösch N 2006 *Chem. Phys. Lett.* **417** 515
[37] Barcaro G and Fortunelli A 2005 *J. Chem. Theory Comput.* **1** 972
[38] Del Vitto A, Pacchioni G, Delbecq F and Sautet P 2005 *J. Phys. Chem.* B **109** 8040
[39] Zhukovskii Y F, Kotomin E A, Fucks D and Dorfman S 2004 *Superlatt. Microstruct.* **36** 63
[40] Yang Z, Wu R, Zhang Q and Goodman D W 2002 *Phys. Rev.* B **65** 155407
[41] Lopez N, Illas F, Rösch N and Pacchioni G 1999 *J. Chem. Phys.* **110** 4873
[42] Bogicevic A and Jennison D R 2002 *Surf. Sci.* **515** L481
[43] Ouahab A, Mottet C and Goniakowski J 2005 *Phys. Rev.* B **72** 035421
[44] Coquet R, Hutchings G J, Taylor S H and Willock D J 2006 *J. Mater. Chem.* **16** 1978
[45] Baroni S, Del Corso A, de Gironcoli S and Giannozzi P Online at http://www.pwscf.org
[46] Perdew J P, Burke K and Ernzerhof M 1996 *Phys. Rev. Lett.* **77** 3865
[47] Jones R O and Gunnarsson O 1989 *Rev. Mod. Phys.* **61** 689
[48] Mills G and Jónsson H 1994 *Phys. Rev. Lett.* **72** 1124
[49] Henkelman G, Uberuaga B P and Jónsson H 2000 *J. Chem. Phys.* **113** 9901
[50] Eyring H 1935 *J. Chem. Phys.* **3** 107
[51] Mottet C, Barcaro G and Fortunelli A, unpublished
[52] Becke A D 1993 *J. Chem. Phys.* **98** 5648
[53] Barcaro G and Fortunelli A 2006 *J. Phys. Chem.* B **110** 21021
[54] Yulikov M, Sterrer M, Heyde M, Rust H-P, Risse T, Freund H-J, Pacchioni G and Scagnelli A 2006 *Phys. Rev. Lett.* **96** 146804
[55] Pyykkö P 2004 *Angew. Chem. Int. Edn. Engl.* **43** 4412
[56] Vervisch W, Mottet C and Goniakowski J 2002 *Phys. Rev.* B **65** 245411
[57] Ferrari A M, Xiao C, Neyman K M, Pacchioni G and Rösch N 1999 *Phys. Chem. Chem. Phys.* **1** 4655
[58] Giordano L and Pacchioni G 2005 *Surf. Sci.* **575** 197
[59] Aprá E, Ferrando R and Fortunelli A 2006 *Phys. Rev.* B **73** 205414
[60] Fernandez E M, Soler J M, Garzón I L and Balbas L C 2004 *Phys. Rev.* B **70** 165403
[61] Bonačič-Koutecky V, Burda J, Mitrič R, Ge M, Zampella G and Fantucci P 2002 *J. Chem. Phys.* **117** 3120
[62] Yulikov M, Sterrer M, Risse T and Freund H J, submitted
[63] Moseler M, Häkkinen H and Landman U 2002 *Phys. Rev. Lett.* **89** 176103
[64] Antonietti J-M, Michalski M, Heiz U, Jones H, Lim K H, Rösch N, Del Vitto A and Pacchioni G 2005 *Phys. Rev. Lett.* **94** 213402

Epitaxy, Truncations, and Overhangs in Palladium Nanoclusters Adsorbed on MgO(001)

G. Barcaro,[1] A. Fortunelli,[1] G. Rossi,[2] F. Nita,[2,3] and R. Ferrando[2]

[1]*IPCF/CNR, G. Moruzzi 1, Pisa, I56124, Italy*

[2]*Dipartimento di Fisica and INFM, Via Dodecaneso 33, Genova, I16146, Italy*

[3]*Institute of Physical Chemistry IG Murgulescu, Romanian Academy, Splaiul Independentei 202, Bucharest, Romania*

(Received 12 January 2007; published 11 April 2007)

The structure of Pd clusters adsorbed on MgO(001) is determined by a combination of global-optimization methods using semiempirical potentials and density functional calculations. The transition to fcc clusters with (001) epitaxy is shown to take place in the size range $10 \leq N \leq 15$ atoms. Truncations of vertices and basal corners in fcc epitaxial clusters proceed in parallel, while overhangs are already formed at small sizes, below 30 atoms.

DOI: 10.1103/PhysRevLett.98.156101 PACS numbers: 68.43.Hn, 61.46.Bc, 61.46.Df, 68.43.Bc

Metal clusters on oxide surfaces are extremely important for technological applications, especially in the field of catalysis [1,2]. Recently, the deposition of mass-selected clusters on oxide surfaces has allowed us to demonstrate that the catalytic activity of metal clusters strongly depends on their size [2,3]. Shape dependence of cluster activity has also been demonstrated [4–6].

Small clusters containing few tens of atoms can present nanofacets of different symmetries and orientations, edges between nanofacets, corners (in some cases truncated corners), and overhangs at the interface with the support (see Fig. 1). These nanoscale features give a variety of adsorption sites, with different symmetries and properties, confined in a very small region of space. This can be very important for applications. For example, this may originate low-energy pathways for chemical reactions, as in the case of the CO + NO reaction on Pd clusters adsorbed on MgO, in which a low-temperature reaction mechanism is observed in small nanoclusters (below 30 atoms) but not in larger clusters or bulk surfaces [3]. On the other hand, overhangs in Au/MgO(001) clusters are very favorable sites for CO oxidation [4].

For Pd clusters on MgO(001), which is one of the most studied model catalysts, there is experimental evidence [1,7] of fcc structures in (001) epitaxy with the substrate for clusters of sizes $N \sim 100$ atoms and more. On the other hand, very small clusters, below $N = 10$, can present a different epitaxy, as shown by several density functional theory (DFT) calculations [8–10]. For example, the most stable form of Pd_4/MgO(001) is a tetrahedron, presenting a triangular facet in contact with the square-symmetry MgO(001) surface [11]. A transition to structures with (001) epitaxy should occur somewhere below 100 atoms, but the actual size is presently unknown. Global-optimization searches within atom-atom potential models give different answers depending on the model [12,13]. Some atomistic simulations indicate that overhangs could occur above $N = 30$ atoms [12] being definitely stabilized above $N \simeq 200$ [14]. In contrast, the Wulff-Kaischew theorem [6], valid in the macroscopic limit, predicts that truncations but no overhangs should appear with increasing size.

In this Letter we perform a systematic search for the lowest-energy structures of Pd/MgO(001) clusters by accurate DFT calculations. We show that in the size range $10 \leq N \leq 15$ there is a clear transition to structures which are in very good (001) epitaxy with the substrate. Moreover, we determine the sizes at which Pd clusters form truncations or overhangs, showing that overhanging atomic rows are already developed below $N = 30$. We consider clusters adsorbed on the flat regular oxide surface and not on surface defects, because size-selected clusters are often deposited at low temperatures [2,3]. For typical defect densities [1], these clusters are very likely to land on regular surface sites. Then, fcc(001) clusters are not expected to migrate to defects. Moreover, also in the case of deposition of single atoms by molecular beam epitaxy, deposition at sufficiently low temperatures or high fluxes may cause the growth of metal clusters on regular terrace sites [10,15].

In the following we consider a set of cluster sizes between 3 and 30 atoms ($N = 3$–15, 18, 20, 23, 25, 30) employing the following search strategy to locate low-

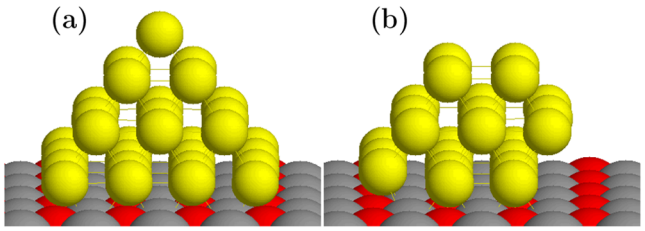

FIG. 1 (color online). (a) An fcc pyramidal cluster on MgO, with (001) epitaxy. (b) A cluster obtained from (a) after removal of some atoms to create truncations and overhangs. Truncations at the cluster vertex and at the left basal corner are shown. The removal of an atomic row from the right edge of the cluster basis forms an overhang, consisting of a row of three atoms in the second layer. In the substrate, red (dark gray) and gray (light gray) spheres correspond to O and Mg atoms, respectively.

energy isomers. First, we generate a large database of structures with the aid of basin-hopping and parallel-walker [16] global-optimization methods within two different atom-atom potential models (see Refs. [12,17] for the form and parameters of the potentials). The database is constructed to include clusters belonging to several different structural families (see below), and not simply the lowest-energy isomers of the prevailing family. At each size, we reoptimize the lowest-energy clusters of each structural family [18] by DFT calculations. For the smallest and largest sizes ($N = 3$–15 and 30) we consider clusters of all different structural families, whereas for intermediate sizes we restrict our reoptimization to fcc clusters with (001) epitaxy.

The DFT calculations are carried out using the PWSCF (plane-wave self-consistent field) computational code [19], employing the PBE xc-functional [20] and ultrasoft pseudopotentials in the spin-unrestricted formalism. The MgO(001) surface is modeled by a two-layer slab, each layer containing 25 Mg and 25 O atoms, 5×5 cell, fixed in the lattice positions of the rock-salt bulk structure (experimental value of the MgO distance of 2.104 Å). The distance between replicated cells in the direction perpendicular to the (001) surface is about 13 Å. The kinetic energy cutoff for the selection of the plane-wave basis set is fixed at 40 Ryd (1 Ryd = 13.6 eV) for all the calculations. Because of the large dimensions of the unit cell, eigenvalues and eigenvectors of the Kohn-Sham Hamiltonian are only evaluated at the Γ point. A Gaussian smearing technique [21] (with a smearing parameter of 0.002 Ryd) is applied. The DFT approach has been recently validated for small Pd/MgO clusters, for which it has been shown to predict diffusion energy barriers and hence a growth dynamics in full agreement with molecular beam epitaxy experiments [9,10,22].

The results of our calculations are shown in Table I and Figs. 2 and 3. There, the most significant clusters at different sizes are reported. For each cluster we report the total binding energy E_{bnd} and the energy difference ΔE from the lowest isomer of the same size. In the following we first discuss the competition between different structural families, and then the development of truncations and overhangs in structures with (001) epitaxy.

Structures of clusters for $N < 10$.—As a first step in the search of the transition to structures with (001) epitaxy, we have examined very small clusters, finding that, in the majority of cases, their lowest-energy structures do not present fcc(001) epitaxy: Pd_3 is a vertical isosceles triangle [10]; Pd_4 is a tetrahedron; Pd_6 is an octahedron leaning on the substrate with a triangular facet; Pd_7 is a distorted structure. fcc clusters with (001) epitaxy (Epi clusters in the following) are Pd_5 (a square pyramid) and Pd_8 (a rectangular pyramid).

Structural families of Pd/MgO(001) *clusters in the range $10 \leq N \leq 15$.*—In this size range, we find three main structural motifs in competition: Epi, icosahedral (Ih), and decahedral (Dh) clusters. For $N = 13$, the Ih family comprises the perfect Mackay icosahedron of 13 atoms (Ih^b_{13} in Fig. 2), and a distorted icosahedron (Ih^a_{13}), which presents a better matching with the substrate and a much lower energy (see Table I). For $N = 12$, the best icosahedral clusters are obtained by eliminating one atom from the distorted Ih^a_{13}. Ih^a_{12} is obtained after subtraction of the top vertex atom, whereas in Ih^b_{12} (which is slightly higher in energy) an atom of the basis is missing. For $N = 11$, Ih^a_{11} is obtained by removing the vertex atom from Ih^b_{12}. After removal, the cluster undergoes substantial rearrangement of its top layer. Ih^b_{11} is obtained by removing one basis atom from Ih^b_{12} and it is much higher in energy than Ih^a_{11}. The Dh family is made of fragments of a decahedron presenting a fivefold axis which runs parallel to the MgO(001) surface. All Dh clusters found in this size range can be obtained by removing atoms from the Dh_{15} cluster of Fig. 2. At $N = 13$ we find two Dh clusters. Dh^a_{13} is obtained by eliminating two top atoms from Dh_{15}. Dh^a_{13} is the buckled biplanar structure which has been recently proposed as the lowest-energy 13-atom Pd cluster in gas phase, in close competition with icosahedral and fcc clusters [23–25]. Dh^b_{13} is an Ino decahedron [26], which is, however, higher in energy than the buckled biplanar structure. For $N = 12$ and 11, the best Dh clusters are obtained by sequentially removing the side atoms of Dh^a_{13}. Epi clusters are obtained from the perfect square-basis pyramid of 14 atoms (not shown in the figure). An atom is added on a triangular facet of the pyramid to produce the cluster Epi_{15}. Epi^a_{13} and Epi^b_{13} are obtained by removing the top vertex atom and one basal corner atom of the pyramid,

TABLE I. Energies (in eV) of the clusters shown in Figs. 2 and 3. E_{bnd} is the total binding energy, ΔE is the energy separation from the lowest-energy isomer at a given size.

Cluster	E_{bnd}	ΔE	Cluster	E_{bnd}	ΔE
Ih^a_{11}	−28.57	0.00	Epi^a_{18}	−49.42	0.00
Epi_{11}	−28.42	0.15	Epi^b_{18}	−49.38	0.04
Ih^b_{11}	−28.03	0.54	Epi^a_{20}	−55.80	0.00
Dh_{11}	−27.92	0.65	Epi^b_{20}	−55.25	0.55
Epi_{12}	−31.69	0.00	Epi^a_{23}	−64.84	0.00
Ih^a_{12}	−31.32	0.37	Epi^b_{23}	−64.61	0.23
Ih^b_{12}	−31.29	0.40	Epi^c_{23}	−64.48	0.36
Dh_{12}	−30.98	0.71	Epi^a_{25}	−71.19	0.00
Epi^a_{13}	−34.61	0.00	Epi^b_{25}	−70.48	0.71
Epi^b_{13}	−34.47	0.14	Epi^a_{30}	−86.77	0.00
Ih^a_{13}	−34.41	0.20	Epi^b_{30}	−86.69	0.08
Dh^a_{13}	−34.20	0.41	Tl^a_{30}	−86.29	0.48
Dh^b_{13}	−33.69	0.92	Tl^b_{30}	−85.97	0.80
Ih^b_{13}	−32.90	1.71	Tl^c_{30}	−85.60	1.17
Epi_{15}	−40.55	0.00	Bl^a_{30}	−85.48	1.29
Dh_{15}	−40.29	0.26	Bl^b_{30}	−84.94	1.83

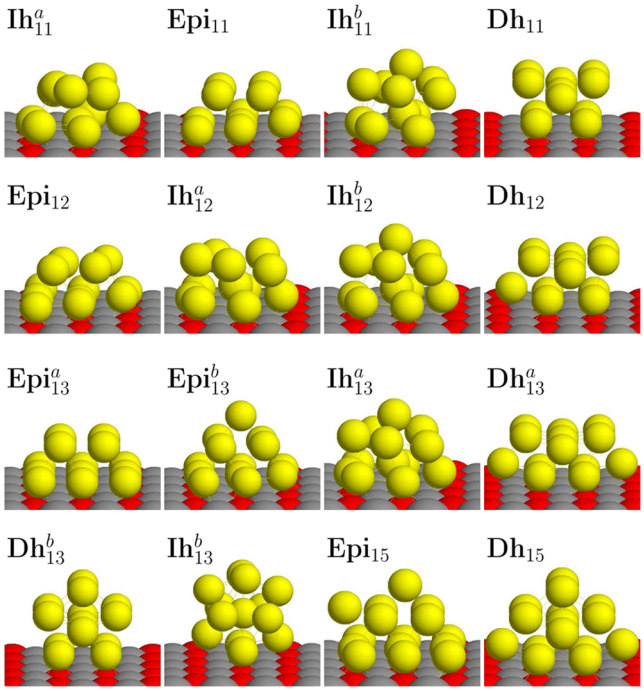

FIG. 2 (color online). Pd clusters on MgO(001) at sizes $11 \leq N \leq 15$. Energies are reported in Table I.

respectively. Epi_{12} and Epi_{11} are obtained by removing further basal corner atoms.

The data in Table I show that Epi structures clearly prevail for $N \geq 12$ (including $N = 14$, not shown in the figure). Epi^a_{12} is strongly distorted, while distortions in Epi clusters with $N \geq 13$ are small. For $N = 11$, a distorted cluster of the Ih family (Ih^a_{11}) is lower in energy than the best Epi structure. For $N = 10$ (not shown in the figure) the lowest-energy structure is a distorted bilayer not belonging to any of the Epi, Ih, or Dh families. As expected, metal-oxide interaction is not strong enough to cause a 2D cluster growth: the most stable cluster shapes are three dimensional. However, the metal-substrate interaction is crucial in determining the best cluster structures. In gas phase, for all sizes reported in Table I, Ih and Dh clusters are much better than fcc truncated pyramids. This is not sufficient to counterbalance the better adhesion to the substrate of Epi clusters for $N \geq 12$. For example, at size $N = 13$, neither the undistorted icosahedron, nor the buckled biplanar structure, which are favored in gas phase, can compete with the (001) epitaxy truncated pyramids. For very small clusters, the situation is different: for $N = 4$, the best Pd/MgO(001) cluster is the tetrahedron, which is also the best gas-phase structure.

Structural families of Pd/MgO(001) *for* $N = 30$.—As shown in Fig. 3, the most favorable Epi clusters are the perfect pyramid (Epi^b_{30}) and a structure presenting truncations and overhangs (Epi^a_{30}). Nonepitaxial structures are classified as trilayers (Tl) and bilayers (Bl). The best Tl structure (Tl^a_{30}) has its bottom layer in good (001) epitaxy with the substrate, but the second and third layers do not continue this arrangement. In Tl^b_{30} and Tl^c_{30}, also the bottom layer is not in registry with the oxide surface. Both Bl structures present (111) facets in contact with the substrate. We note that Epi structures are lower in energy, with larger differences than for $12 \leq N \leq 15$: (001) epitaxy is more and more favored as size increases. Among non-Epi structures, trilayers are lower in energy than bilayers, confirming the tendency to the formation of fully three-dimensional clusters.

Truncations and overhangs in Epi clusters.—Starting from a square-basis complete pyramid, we find that it is more favorable to remove a single atom from its top vertex than a basal corner atom (see clusters Epi^a_{13} and Epi^b_{13}). Semiempirical atomistic calculations [12] predict the opposite. On the other hand, from a rectangular pyramid (Epi^a_{20}) it is slightly more convenient to remove two basal corner atoms than the top vertex atoms (compare Epi^a_{18} and Epi^b_{18}). Finally, from the complete square pyramid Epi^b_{30}, the removal of a single atom from its top vertex and of all its four basal corner atoms is by far more favorable than the removal of a five-atom pyramid from the top vertex. In fact, the three-layer Epi^a_{25} structure is much lower in energy than the epitaxial bilayer Epi^b_{25}. Overhangs are already present for clusters in the size range $15 \leq N \leq 30$. A single overhanging atom is found in Epi_{15}. More significantly, well-developed overhanging atomic rows are present in Epi^a_{23}, which is clearly lower in energy than the structures without overhangs, and even in Epi^a_{30}, which is slightly better than the complete pyramid Epi^b_{30}. On the contrary, for $N = 20$, the structure with an overhanging dimer (Epi^b_{20}) is much higher in energy than the complete

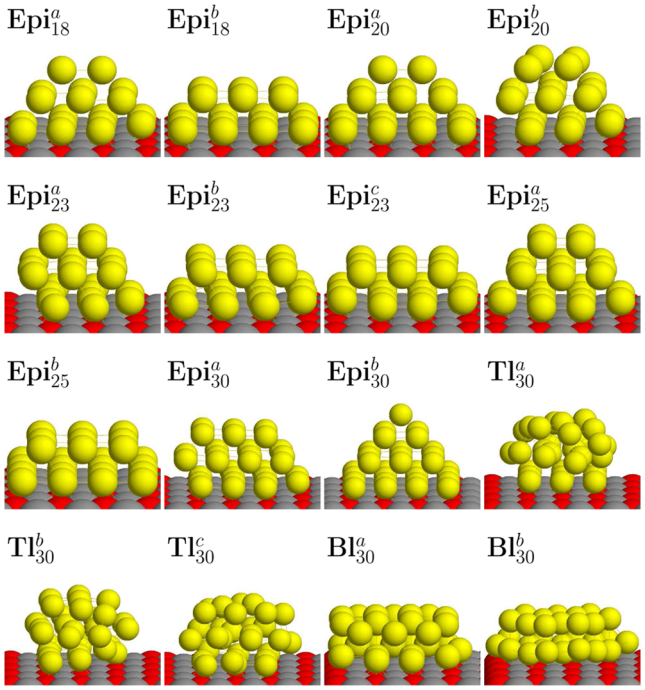

FIG. 3 (color online). Pd clusters on MgO(001) at sizes $18 \leq N \leq 30$. Energies are reported in Table I.

rectangular pyramid Epi^{a}_{20}. Structures with overhangs optimize metal-metal interactions at the expense of the adhesion with the substrate, since metallic bonding is improved by a more compact cluster shape, while adhesion suffers from the decrease of the number of atoms in the cluster basis. However, the ''metal-on-top effect'' [27] (i.e., the increase in the metal-surface interaction due to the presence of other metal atoms on top of the atom directly in contact with the substrate) partially compensates this decrease by a an improvement of the adhesion energy per basal atom: basal atoms on an edge below an overhang better adhere to the substrate than other basal edge atoms.

In summary, we have demonstrated that the transition towards fcc clusters in (001) epitaxy with the MgO substrate is taking place between sizes 11 and 13. At variance with the behavior of smaller clusters, from these sizes on, the metal-substrate interaction becomes crucial, so that the best Pd/MgO(001) clusters are not only different from the best gas-phase Pd clusters (as was found for Pd_7 and Pd_{13} deposited on oxygen vacancies [28]), but also grow in very good fcc (001) epitaxy with the underlying MgO lattice. All these Epi cluster are expected to present very small mobility on the surface compared to Pd_{1-4} [9,10], due to high activation barriers for diffusion. The results for $N = 30$ show that the energy difference between Epi and non-Epi clusters becomes larger with increasing size, which supports the transition from nonepitaxial to epitaxial configurations. In Epi clusters, overhanging atomic rows are developed already at quite small sizes, smaller than predicted by previous calculations.

Our results also serve as a validation test for atomistic approaches. In fact, we find that the atomistic model developed in Ref. [17] is a valuable tool, being qualitatively correct in predicting main cluster features, such as the transition towards Epi structures in the small-size range [12], and the development of overhangs well below $N = 100$ atoms. However, the atomistic model is not sufficiently accurate to quantitatively predict the actual structures of the most stable clusters for $10 \leq N \leq 15$, and the details of the shapes of larger clusters, such as preferential truncations and overhangs, due to the neglect of effects such as the metal-on-top one [27].

Finally, we plan to extend our calculations to other metals adsorbed on MgO, such as gold and silver. Compared to palladium, these metals present a weaker interaction with the substrate, so that the interplay of different structural motifs can be even more complex.

We acknowledge financial support from the Italian CNR for the project SSA-TMN within the framework of the ESF EUROCORES SONS, and from European Community Sixth Framework Programme for the project GSOMEN (No. NMP4-CT-2004-001594). The authors thank Christine Mottet for useful discussions. DFT calculations were performed at Cineca Supercomputing Center within an agreement with Italian INSTM.

[1] C. R. Henry, Surf. Sci. Rep. **31**, 231 (1998).
[2] K. Judai, S. Abbet, A. S. Wörz, U. Heiz, and C. R. Henry, J. Am. Chem. Soc. **126**, 2732 (2004).
[3] A. S. Wörz, K. Judai, S. Abbet, and U. Heiz, J. Am. Chem. Soc. **125**, 7964 (2003).
[4] L. M. Molina and B. Hammer, Appl. Catal., A **291**, 21 (2005).
[5] B. Huber, P. Koskinen, H. Hakkinen, and M. Moseler, Nat. Mater. **5**, 44 (2006).
[6] C. R. Henry, Prog. Surf. Sci. **80**, 92 (2005).
[7] S. Giorgio, C. Chapon, C. R. Henry, and G. Nihoul, Philos. Mag. B **67**, 773 (1993).
[8] A. M. Ferrari, C. Xiao, K. M. Neyman, G. Pacchioni, and N. Rösch, Phys. Chem. Chem. Phys. **1**, 4655 (1999).
[9] L. Xu, G. Henkelman, C. T. Campbell, and H. Jónsson, Phys. Rev. Lett. **95**, 146103 (2005).
[10] G. Barcaro, A. Fortunelli, F. Nita, and R. Ferrando, Phys. Rev. Lett. **95**, 246103 (2005).
[11] L. Giordano and G. Pacchioni, Surf. Sci. **575**, 197 (2005).
[12] G. Rossi, C. Mottet, F. Nita, and R. Ferrando, J. Phys. Chem. B **110**, 7436 (2006).
[13] J. Oviedo, J. F. Sanz, N. López, and F. Illas, J. Phys. Chem. B **104**, 4342 (2000).
[14] J. Goniakowski and C. Mottet, J. Cryst. Growth **275**, 29 (2005).
[15] M. Yulikov, M. Sterrer, M. Heyde, H.-P. Rust, T. Risse, H.-J. Freund, G. Pacchioni, and A. Scagnelli, Phys. Rev. Lett. **96**, 146804 (2006).
[16] G. Rossi and R. Ferrando, Chem. Phys. Lett. **423**, 17 (2006).
[17] W. Vervisch, C. Mottet, and J. Goniakowski, Phys. Rev. B **65**, 245411 (2002).
[18] G. Barcaro, A. Fortunelli, G. Rossi, F. Nita, and R. Ferrando, J. Phys. Chem. B **110**, 23 197 (2006).
[19] S. Baroni, A. Del Corso, S. de Gironcoli, and P. Giannozzi, http://www.pwscf.org.
[20] J. P. Perdew, K. Burke, and M. Ernzerhof, Phys. Rev. Lett. **77**, 3865 (1996).
[21] C. Elsässer, M. Fähnle, C. T. Chan, and K. M. Ho, Phys. Rev. B **49**, 13 975 (1994).
[22] G. Haas, A. Menck, H. Brune, J. V. Barth, J. A. Venables, and K. Kern, Phys. Rev. B **61**, 11 105 (2000).
[23] C. M. Chang and M. Y. Chou, Phys. Rev. Lett. **93**, 133401 (2004).
[24] T. Futschek, M. Marsman, and J. Hafner, J. Phys. Condens. Matter **17**, 5927 (2005).
[25] R. C. Longo and L. J. Gallego, Phys. Rev. B **74**, 193409 (2006).
[26] F. Baletto and R. Ferrando, Rev. Mod. Phys. **77**, 371 (2005), and references therein.
[27] G. Barcaro and A. Fortunelli, J. Chem. Theory Comput. **1**, 972 (2005).
[28] M. Moseler, H. Häkkinen, and U. Landman, Phys. Rev. Lett. **89**, 176103 (2002).

Theor Chem Account (2007) 118:807–812
DOI 10.1007/s00214-007-0324-4

REGULAR ARTICLE

A comparison between the absorption properties of the regular and F_s-defected MgO (100) surface

Giovanni Barcaro · Mauro Causà · Alessandro Fortunelli

Received: 30 January 2007 / Accepted: 25 April 2007 / Published online: 1 June 2007

Abstract The electron density, the electrostatic potential and the electric field of the MgO (100) surface, both regular and containing an oxygen vacancy (F_s center), are compared in order to understand the modifications induced in the surface-absorbate interaction by the presence of the defect, with particular attention to the metal-oxide case. The spin-density for a gold atom absorbing on the most characteristic sites of the regular and F_s-defected surface is also shown. It is found that in the defected surface the electron pair in the vacancy protrudes appreciably out of the surface, thus shifting the electrostatic potential to negative values (but producing a similar electric field) and being able to chemically interact with neighboring absorbed species. These results rationalize the rotational invariance and double frustration effects previously described for the metal/F_s-defected MgO (100) surface.

Keywords Oxide surfaces · Surface defects · Metal-on-oxide · Electrostatic potential · Electrostatic field

1 Introduction

Oxide surfaces are important for many scientific and technological applications, ranging from catalysis to chemical sensing, to their use as templates for the epitaxial growth of other oxides or for the deposition of nanosized metal clusters and other absorbates, etc. [1–8]. In this context, the MgO(100) surface has been intensively studied [9–13] for its technological (e.g., catalytic) applications, and for its potentialities as a support which is at the same time inert and able to modulate the absorbate charge distribution. Moreover, its theoretical description is simplified by the fact that this surface does not present the complications associated with surface reconstruction, MgO being a simple ionic solid and the MgO (100) surface being a non-polar one. Attention has been focused both on the regular surface, as it has been shown that MgO(100) films and single crystals of good quality can be prepared through various experimental protocols [12–14], and also on variously defected surfaces [9,15–17], with the goal of understanding the modifications induced by the defects on the adsorption properties of the oxide. Surface defectivity is particularly interesting in the case of MgO(100), as the defects can act as strong trapping (and thus nucleation) centers for the growth of absorbates: the same inert characteristics of this surface make that the absorbate growth is strongly influenced by the presence of defects. Among the possible surface defects, the neutral oxygen vacancy (also known as F_s center) has been intensively studied [18–30]: statical and dynamical properties, electron density, Bader and ELF maps, density of states plots, optical properties, etc. It has been shown that this defect is at the same time common on properly engineered surfaces [41] and able to act as a nucleation center for several species, such as for example gold clusters [19,31–33]. The strength of the Au atom/F_s-center bond in fact is estimated to be greater than 2.5 eV, thus providing a site at which nucleation can occur, as definitively confirmed by a recent combined EPR and theoretical characterization of a single gold atom interacting with the regular and defected MgO (100) surface [17]. In a previous work [35], we have performed systematic density-functional (DF) calculations focusing on the study of the interaction of small Au clusters with a neutral oxygen vacancy defect

G. Barcaro · A. Fortunelli (✉)
Molecular Modeling Laboratory, IPCF-CNR, Via G. Moruzzi 1, Pisa 56124, Italy
e-mail: fortunelli@ipcf.cnr.it

M. Causà
Università di Napoli "Federico II", Via Cintia, Napoli 80126, Italy

lying on a MgO(100) terrace. We have found that this defect induces a long-range modification of the metal absorption characteristics in its surrounding, and that this perturbation is responsible for the fluxionality of small clusters growing around the vacancy, possibly connected with the formation of clusters exhibiting different structural motifs. In the present work, we investigate in more detail the nature of the oxygen vacancy defect by comparing electron densities, electrostatic potentials and electric fields in presence and in absence of the defect, and the modifications the oxygen vacancy introduces in the absorbate/surface interaction, focusing attention on the absorption of a single gold atom as a prototypical case. This is achieved by decomposing the interaction energy in terms of repulsion, chemical bonding, electrostatic and polarization contribution, which allows us to show that the long-range enhancement in the absorbate/surface interaction induced by the F_s defect is due both to a chemical bonding effect and to an electrostatic effect.

2 Materials and methods

Density-functional (DF) calculations are performed using the CRYSTAL03 computational code [36]. The B3PW91 exchange-correlation functional [37], which is a hybrid functional, is used. A Gaussian-type-orbital basis set of double-zeta quality is used on both Mg and O. The contraction scheme (8-511G and 8-411G) is taken from refs. [38,40], and has been specifically derived for bulk MgO. This basis set can be found in the database of the CRYSTAL03 code (http://www.crystal.unito.it). In agreement with refs [38,40], we also found that such a basis set is able to produce a reasonable description of the MgO system and its electrostatic properties, even in the absence of polarization functions. The regular MgO (100) surface is modeled by a three layer-slab (as it is customary [23]), each containing 18 (3×3 cell) Mg and O atoms fixed at the equilibrium lattice positions characterizing the MgO rock-salt structure (frozen at the experimental lattice constant of 4.208 Å). To produce an F_s defected surface, we remove a neutral oxygen atom from a surface layer, keeping the positions of all the other atoms in the cell fixed.

All the pictures have been obtained by using the XCrySDen program [40].

3 Results

In the case of metal/defected-surface interaction, it has been previously shown [22,27,35] that the presence of an F_s center on the MgO (100) surface remarkably affects not only the interaction of the metal atoms on-top of the vacancy, but also the metal interaction with the surrounding surface sites in a region which extends up to 6–8 Å from the F_s center. For example, the absorption energy landscape of a single gold atom changes substantially when passing from the regular to the F_s-defected (100) surface. On the regular surface, one finds a rather flat potential energy surface, exhibiting minima on the oxygen atoms, maxima on the magnesium atoms, and saddle points on the hollow sites, with a maximum adhesion energy of 0.91 eV and energy barriers of about 0.2 eV for the diffusion between neighboring oxygen sites. Correspondingly, the equilibrium height exhibits minima at 2.30 Å on the oxygen sites, maxima at 2.71 Å on the magnesium sites, and saddle points at 2.40 Å on the hollow sites. The in-plane distance between the energy minima corresponds to the MgO lattice parameter of about 2.97 Å: this value is larger than the typical Au–Au distances (the Au–Au distance in the bulk is 2.885 Å; smaller distances are normally found in Au nanoclusters), thus inducing a frustration (mismatch) in the metal growth on the MgO (100) surface. The presence of the F_s defect completely alters this situation, with the resulting potential energy and equilibrium height surfaces exhibiting three major features: (i) the energy minimum in correspondance with the defect site is much deeper, with an adhesion energy of 3.07 eV; (ii) a large basin of attraction is produced around the defect, with an adhesion energy of 1.62 eV on the magnesium atoms first-neighbors to the vacancy (to be compared to a value of 0.5 eV for the regular surface), extending its influence up to third neighbors, and exhibiting an approximate *cylindrical symmetry*; (iii) there is a large difference between the equilibrium distance atop the defect (about 1.8 Å), strongly reduced with respect to the absorption onto the regular surface, and that atop the neighboring sites (2.65 and 2.59 Å on the magnesium and oxygen sites next to the defect, respectively), for which an increase in the absorption energy does not always correspond to a decrease of the equilibrium distances. This strong variation of $r_{\min}$ around the defect site entails that the growth of metal clusters is frustrated not only "horizontally" with respect to the surface, but also "vertically", due to the appreciable difference in the equilibrium height for the atom interacting directly with the F_s center and the neighboring atoms interacting with the surrounding sites, a feature which can be described as a *double frustration*.

In order to rationalize these features, we have performed a detailed analysis of the electronic density, the electrostatic potential and the electric field of the oxide in the case of the regular and of the F_s-defected MgO (100) surface.

We start with the analysis of the electron density. In Fig. 1 the HOMO orbital of the F_s-defected MgO (100) surface is displayed: this plot is obtained by performing a calculation at the Γ point of the Brillouin zone. The shape of this orbital, which lies in the band gap of the insulator oxide and presents a strong *s*-character, shows how the two electrons trapped in the cavity are not fully confined by the Madelung potential of

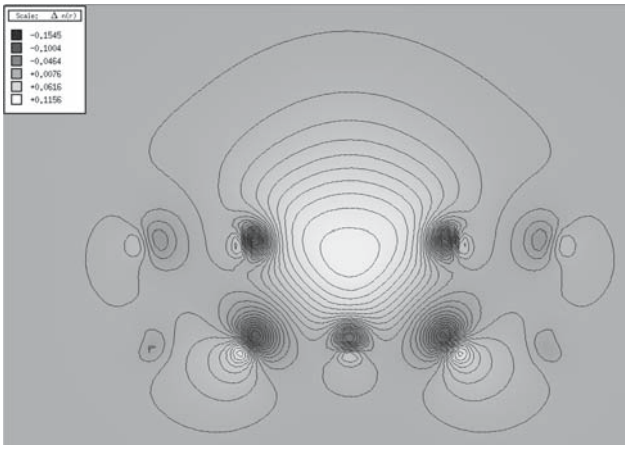

Fig. 1 Electron density contour of the HOMO orbital of the F_s defected MgO (100) surface: the two electrons in the vacancy are not well trapped by the Madelung potential and their density protrudes out of the cavity

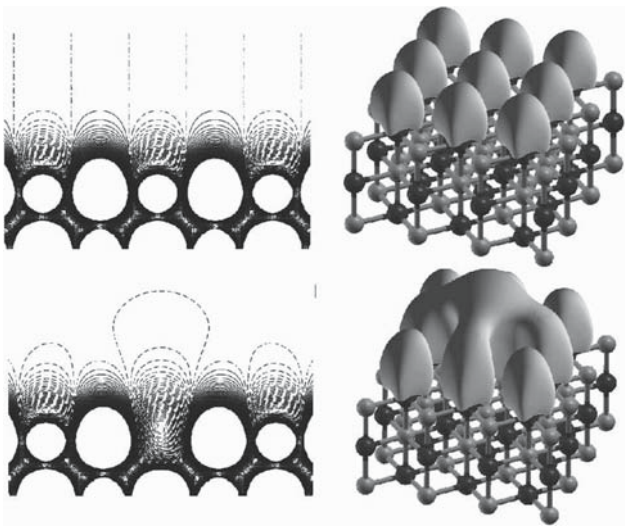

Fig. 2 Two dimensional and 3-D maps of the electrostatic potential generated by the regular (*first row*) and F_s-defected (*second row*) MgO (100) surface; in the 3-D maps, isosurfaces of value −0.0005 a.u. are shown

the solid; their density, on the contrary, protrudes out of the cavity and extends also above the sites around the vacancy [19,21,22].

This charge delocalization produces different patterns of electrostatic potential in the presence of the defect with respect to the regular surface. As can be observed in Fig. 2, in fact, in the case of the regular surface the absolute value of the electrostatic potential is almost the same on the oxygen and on the magnesium sites. This is due to the fact that, at a good approximation, this solid is ionic, with the same amount of positive and negative charge on the oxygen and magnesium sites. On the contrary, when the oxygen atom is missing and the negative charge protrudes out of the vacancy, an enhanced negative potential, which extends also to the neighbor sites around the defect, is observed.

To give a more quantitative estimate of this phenomenon, Fig. 3 illustrates the behavior of the electrostatic potential along the direction perpendicular to the (100) terrace and atop different sites of the regular and defected surfaces. Figure 3a refers to the regular surface: the dashed line shows the potential atop the magnesium site, whereas the continuous line shows the potential atop the oxygen site; as discussed above, the two behaviors are similar in absolute value, and opposite in sign. Figure 3b refers to the F_s-defected surface; the dashed line shows the potential directly atop the defect: this curve is strongly shifted towards negative values, because of the delocalization of the two electrons in the cavity. Since this delocalization implies spreading over the neighboring sites, also the other curves are negatively shifted: moreover, as the magnesium site is closer to the defect, the corresponding potential curve (dashed line) is more negatively shifted than the curve relating to the oxygen site first neighbor to the vacancy (continuous line) for distances greater than 3.7 Å. Finally, a further effect of the charge spreading out of the cavity is that all the potential curves go to zero much more slowly, and not monotonously, than in the case of regular surface.

When a metal atom is absorbed atop the defect, the remarkable increase of its interaction energy (which amounts, in the case of gold, to 3.07 eV instead of 0.91 eV) can be decomposed into three contributions: (i) The absence of the oxygen under the metal species determines a decrease of the Pauli repulsion energy; this is the main reason why the equilibrium metal/surface distance is decreased from 2.3 to 1.8 Å, which is the source of the double frustration effect [35]. (ii) A chemical bond is formed between the two electrons in the cavity and the metal orbitals [19,23]. As it will be explained in more detail in the following, this chemical bond is stronger than in the case of the regular surface, because the two delocalized electrons are more polarizable and can better overlap with the metal orbitals. (iii) Since the metal can get closer to the surface, it is subjected to a stronger electric field and thus the polarization contribution of the metal valence electrons is enhanced.

We now analyze how these three components of the metal/surface interaction change when the gold atom is absorbed on one of the neighboring sites of the defect (as usual, we limit our discussion to the first neighbor magnesium and the first neighbor oxygen). First of all, we remark that on these sites the interaction energy is stronger than in the case of the regular surface, being 1.62 eV on Magnesium and 1.19 eV on oxygen.

(i) The Pauli repulsion decreases only on top of the defect site. As a consequence, for example, the equilibrium height of the metal atom above the magnesium next to the defect does not change dramatically with respect to the regular surface. The decrease of Pauli repulsion

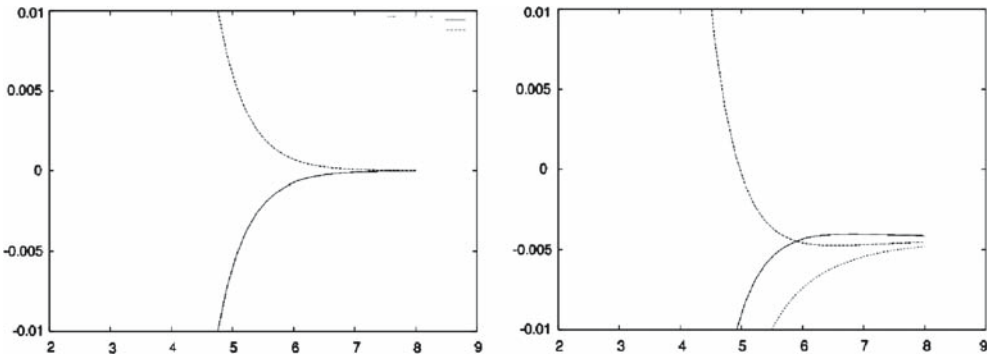

Fig. 3 Behavior of the electrostatic potential (in a.u.) along a direction perpendicular to the (100) terrace and on-top of the most characteristic sites of absorption on the surface. *Right* electrostatic potential on-top of the magnesium (*dashed line*) and oxygen (*continuos line*) sites of the regular surface. *Left* electrostatic potential on top of the vacancy (*dotted line*), of the magnesium first-neighbor (*dashed line*) and of the oxygen first-neighbor (*continuous line*) of the defect. Distances in a.u.

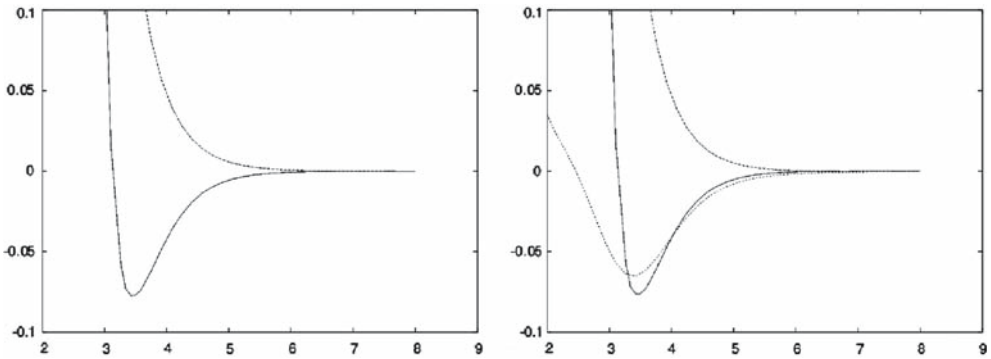

Fig. 4 Behavior of the electric field (in a.u.) along a direction perpendicular to the (100) terrace and on-top of the most characteristic sites of absorption on the regular and F_s-defected surface. *Right* electric field on-top of the magnesium (*dashed line*) and oxygen (*continuous line*) sites of the regular surface. *Left* electric field on top of the vacancy (*dotted line*), of the magnesium first-neighbor (*dashed line*) and of the oxygen first-neighbor (*continuous line*) of the defect. Distances in a.u.

thus does not account for the enhancement of the interaction energy.

(ii) The outward protrusion of the electron pair trapped in the vacancy generates an electrostatic potential in the neighborhood of the defect which is negatively shifted with respect to the regular surface. When a metal atom then approaches the surface, its valence electronic density is repelled far from the surface and a dipole, with its positive end pointing towards the surface, is formed. The interaction energy of such a dipole is thus enhanced by the negative shift of the electrostatic potential.

(iii) To analyze the polarization contribution, we show in Fig. 4 the electric field of the regular and defected surfaces. Somehow surprisingly, in spite of the overall negative shift of the potential, the behavior of the electric field appears to be very similar in the region relevant to metal absorption. The change in the polarization contribution is thus predicted to be of secondary importance in comparison to the stability enhancement due to the electrostatic potential — point (ii) — and to the chemical interaction — point (iv).

(iv) The chemical bonding contribution also plays an important role in explaining the observed behaviors.

To clarify this last point, it is useful to analyze the spin densities, reported in Fig. 5, that correspond to absorption of a single gold atom on the most significant sites of the regular and defective surface. In the first row of Fig. 5 we consider the absorption of the metal atom on the oxygen (left) and magnesium (right) sites of the regular surface. When gold interacts with the oxygen ion of the surface, a donation of electronic charge takes place from the surface to the partially depleted metal orbitals. For this reason, the spin density presents a *p*-character (centered on the surface oxygen) and a hybrid *s/d*-character (centered on the gold atom). On the contrary, when the gold atom is absorbed on the magnesium site, no chemical interaction occurs and the spin density is only

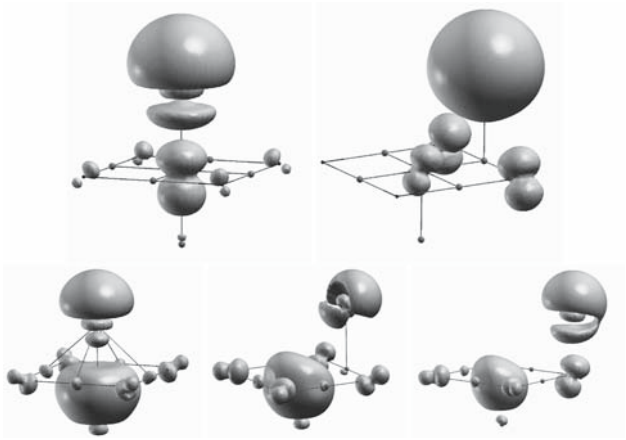

Fig. 5 Spin density isosurfaces of value −0.002 a.u. corresponding to the absorption of a gold atom on the most characteristic sites of the regular and of the F_s-defected surface. *First row* absorption on-top of the oxygen (*left*) and magnesium (*right*) sites of the regular surface. *Second row* absorption on-top of the vacancy (*left*), of the magnesium first-neighbor (*center*) and of the oxygen first-neighbor (*right*) of the defect

localized on the gold atom, where it approximately keeps the spherical shape of the unpaired valence s electron, as in the gas-phase.

The situation is remarkably different for the interaction with the F_s defect (second row of Fig. 5): in the case of absorption on-top of the vacancy (left), the strong interaction with the two electrons of the cavity is demonstrated by the fact that the spin density is concentrated both on the charge distribution in the cavity and on the metal atom. Analogously to what happens on the regular surface, a charge transfer takes place from the surface to the metal orbitals. With regard to the absorption on the magnesium site first-neighbor of the defect (center image), it is interesting to note that, differently from the regular surface, a noticeable chemical interaction still survives. As underlined above for the direct interaction with the defect, the possibility of forming stronger bonds is due to the delocalization of the two electrons of the vacancy. Furthermore, the chemical interaction survives, although a bit weaker, for the absorption of the gold atom on the oxygen first-neighbor of the defect. This chemical bonding contribution is substantially dependent only on the distance from the defect and the same is true for the negative shift of the electrostatic potential. This explains the *rotational invariance* observed for the metal/surface interaction [35].

In conclusion, we have shown that the presence of an F_s defect profoundly modifies the absorption features in the neighborhood of the defect. The surface Madelung potential is not sufficiently strong to confine within the vacancy the electron pair which protrudes out of the surface, thus: (a) decreasing the Pauli repulsion towards the electrons of absorbate species; (b) negatively shifting the electrostatic potential in a region around the defect extending up to 6–8 Å; (c) being able to form much stronger chemical bonds with incoming absorbates. This analysis rationalizes the double frustration and cylindrical invariance effect previously observed for the gold-oxide interaction. Finally, we stress that the results the results here reported are expected to hold not only in the case of gold-oxide interaction, but to be qualitatively true in general.

Acknowledgments GB and AF acknowledge financial support from the Italian CNR for the project SSA-TMN within the framework of the ESF EUROCORES SONS, and from the European Community Sixth Framework Project for the STREP Project GSOMEN (contract no. NMP-CT-2004-001594).

References

1. Osgood R (2006) Chem Rev 106:4379–4401
2. Barteau MA (1996) Chem Rev 96:1413–1430
3. Watanabe K, Menzel D, Nilius N, Freund HJ (2006) Chem Rev 106:4301–4320
4. Delmon B (2006) Catal Today 117:69–74
5. Lauritsen JV et al (2006) Nanotechnology 17:3436–3441
6. Schoiswohl J, Surnev S, Netzer FP (2005) Top Catal 36:91–105
7. Tada M, Iwasawa Y (2006) Chem Commun, pp. 2833–2844
8. Freund HJ (2002) Surf Sci 500:271–299
9. Barth C, Henry CR (2003) Phys Rev Lett 91:196102
10. Coluccia S, Baricco M, Marchese L, Martra G, Zecchina A (1993) Spectrochim Acta A 49:1289–1298
11. Mellor IM, Burrows A, Coluccia S, Hargreaves JSJ, Joyner RW, Kiely CJ, Martra G, Stockenhuber M, Tang WM (2005) J Catal 234:14–23
12. Sterrer M, Risse T, Freund HJ (2006) App Catal A 307:58–61
13. Sterrer M, Fischbach E, Heyde M, Nilius N, Rust HP, Risse T, Freund HJ (2006) J Phys Chem B 110:8665–8669
14. Barth C, Henry CR (2006) Nanotechnology 17:S155–S161
15. Barcaro G, Fortunelli A (2005) J Comp Theor Chem 1:972–985
16. Giordano L, Di Valentin C, Goniakowski J, Pacchioni G (2004) Phys Rev Lett 92:096105
17. Sterrer M, Yulikov M, Fischbach E, Heyde M, Rust HP, Pacchioni G, Risse T, Freund HJ (2006) Angew Chem Int Ed 45:2630–2632
18. Pacchioni G, Pescarmona P (1998) Surf Sci 412/413:657
19. Matveev AV, Neyman K, Yudanov I, Rösch N (1999) Surf Sci 426:123–139
20. Bogicevic A, Jennison DR (1999) Surf Sci 437:L741
21. Mori-Sanchez P, Recio JM, Silvi B, Sousa C, Martin Pendas A, Luana V, Illas F (2002) Phys Rev B 66:075103
22. Yang Z, Wu R, Zhang Q, Goodman DW (2002) Phys Rev B 65:155407
23. Del Vitto A, Pacchioni G, Delbecq F, Sautet P (2005) J Phys Chem B 109:8040
24. Yoon B, Häkkinen H, Landman U, Wörz AS, Antonietti JM, Abbet S, Judai K, Heiz U (2005) Science 307:403
25. Walter M, Häkkinen H (2005) Phys Rev B 72:205440
26. Neyman KM, Inntam C, Matveev AV, Nasluzov VA, Rosch N (2005) J Am Chem Soc 127:11652
27. Moseler M, Häkkinen H, Landman U (2002) Phys Rev Lett 89:176103
28. Pacchioni G (2003) Chem Phys Chem 4:1041
29. Sousa C, Illas F (2001) J Chem Phys 115:1435
30. Wendt S, Kim YD, Goodman DW (2003) Prog Surf Sci 74:141
31. Sanchez A, Abbet S, Heiz U, Schneider WD, Häkkinen H, Barnett RN, Landman U (1999) J Phys Chem A 103:9573–9578
32. Molina LM, Hammer B (2005) J Chem Phys 123:161104

33. Neyman K M, Inntam C, Moskaleva L V, Rösch N (2006) Chem Eur J 13:277
34. Yulikov M, Sterrer M, Heyde M, Rust HP, Risse T, Freund HJ, Pacchioni G, Scagnelli A (2006) Phys Rev Lett 96:146804
35. Barcaro G, Fortunelli A (2006) J Phys Chem B 110:21021–21027
36. Saunders VR, Dovesi R, Roetti C, Orlando R, Zicovich-Wilson CM, Harrison NM, Doll K, Civalleri B, Bush IJ, D'Arco P, Llunell M, CRYSTAL 2003 User Manual (2003) Turin University
37. Becke AD (1993) J Chem Phys 98:5648–5652
38. McCarthy MI, Harrison NM (1994) Phys Rev B 49:8574–8582
39. Dovesi R, Roetti C, Freyria-Fava C, Aprà E, Saunders VR, Harrison NM (1992) Philos Trans R Soc London Ser A 341:203
40. Kokalj A (1999) J Mol Graph Model 17:176
41. Sterrer M, Fischbach E, Risse T, Freund HJ (2005) Phys Rev Lett 94:186101

CHEMISTRY
A EUROPEAN JOURNAL

DOI: 10.1002/chem.200601796

Structure of Ag Clusters Grown on F_s-Defect Sites of an MgO(100) Surface

Giovanni Barcaro,[a] Edoardo Aprà,[b] and Alessandro Fortunelli*[a]

Abstract: The structure of Ag_N clusters ($N=1$–4, 6, 8, 10), both in the gas phase and grown on the MgO(100) surface containing F_s-defects, has been investigated by a density functional basin-hopping (DF-BH) approach. In analogy with what observed in the case of gold clusters, it is found that the presence of the defect implies a double frustration and a cylindrical invariance of the metal–surface interaction, causing small Ag clusters growing around the F_s defect to be highly fluxional. Nevertheless, two different structural crossovers are found to be induced by the metal–defect interaction for the adsorbed clusters such that: 1) planar structures prevail for $N \leq 4$ (as in the gas phase); 2) noncrystalline (fivefold symmetric) structures, which are the lowest energy ones in the gas phase for medium sized Ag_N clusters ($N \geq 7$), prevail for $N=6$ and $N=8$; 3) distorted face-centered cubic (fcc) structures grown pseudomorphically on the defected surface prevail for $N=10$. The transition from fivefold to fcc motifs is rationalized in terms of the double-frustration effect, which increases the bond strain of the noncrystalline structures. Detrapping energies from the defect were also calculated; the lowest energy pathway corresponds to the detachment of a dimer.

Keywords: adsorption · cluster compounds · density functional calculations · silver · structure elucidation · surface chemistry

Introduction

Metal-on-oxide systems have attracted increasing attention in recent years in both science and technology for their interesting properties and their applications in the fields of catalysis, opto–electronic devices, chemical sensors, and so forth.[1–14] The knowledge of the cluster structure is an evident pre-requisite for a deep understanding of these fascinating properties, and much theoretical effort has been devoted to this subject, primarily focusing on small clusters, especially when high accuracy was pursued through the use of sophisticated, first-principle approaches. In this context, the MgO(100) surface has often been studied for various reasons, ranging from its widespread use as an inert support, to the simplicity of its theoretical description.[15–18] MgO(100) is in fact an apolar, simple ionic surface without the complications associated with surface reconstruction, and so forth.[2,19,20] After initial studies of the interaction of metal atoms with the regular surface,[15,16,21,22] it was soon realized that the presence of kinks, corners, local defects, such as the oxygen vacancy (also called F_s or color center due to its optical absorption properties), and so forth, could substantially modify the metal–oxide interaction.[7,16,18,23–26,28–30,55] This assumes particular importance in the study of the growth process. Especially for metals such as silver, which presents a very weak adhesion to the regular surface ,[31] and hence diffuses rapidly even at low temperatures,[15,18,32–34] the presence of defects acting as trapping centers is reputed necessary for nucleation to occur, even more than, for example, in the Pd/MgO(100) case.[35] In this perspective, an important issue thus concerns the influence of the metal/defected-surface (rather than regular-surface) interaction on the cluster structure, i.e., whether the metal clusters keep their gas-phase structure, or whether the interaction with the defected site is strong enough to induce structural transitions.[7,18,23–26,55] In the present article, we tackle this issue by studying the structure of small (up to ten atoms) silver clusters both in the gas phase and adsorbed on the F_s-defective MgO(100) surface. The F_s defect on the MgO(100) surface is chosen as a prototypical example of a neutral local defect. We focus on clusters in the size range $N=1$–10 ($N=$number of Ag atoms), which are small enough to be computationally affordable and appreciably influenced by the presence of the local de-

[a] Dr. G. Barcaro, Dr. A. Fortunelli
Molecular Modeling Laboratory, IPCF-CNR
Via G. Moruzzi 1, Pisa, 56124 (Italy)
Fax: (+39) 050-3152442
E-mail: fortunelli@ipcf.cnr.it

[b] Dr. E. Aprà
Computer Science and Mathematics Division
Oak Ridge National Laboratory
Oak Ridge, TN 37831 (USA)

fects at the cluster–surface interface, but large enough to allow identification of structural motifs and to study their energetic crossover. We use a systematic search protocol within a first-principles approach: a density-functional basin-hopping (DF-BH) algorithm,[36] which is CPU-intensive, but gives us some confidence of having singled out the global minimum and the lowest energy excited states at each size. We find that indeed the presence of the defect substantially alters the potential-energy landscape of adsorbed Ag clusters, favoring (distorted) face centered cubic (fcc) structures with respect to noncrystalline fivefold symmetric configurations, which are the ground state for gas-phase Ag clusters of size $N \geq 7$.

The article is arranged as follows. After a brief review of previous work, the computational approach is described (Computation Methods). The results of the DF-BH calculations for both gas-phase and adsorbed clusters are presented, and distinguished in terms of the cluster size (Results and Discussion). Conclusions are summarized.

Previous work: Concerning previous work on the Ag and MgO(100) systems, a wealth of experimental and theoretical information exists on gas-phase Ag clusters. Extensive references to small ($N < 6$) clusters can be found in reference [37], while for larger clusters the main contributions are references [37–40], in which the structure of Ag clusters (and their ions) up to 12–13 atoms have been systematically investigated. Our calculations are in qualitative (and often quantitative) agreement with former DF calculations,[37,40] but a detailed comparison is not presented, as it would not be very informative.

The F_s center is one of the most studied defects of the MgO(100) surface.[16,27–30,41–60] Both static and dynamic properties have been studied: electron density maps and density of states plots,[29,46] formation energy and diffusion energy barriers,[27,41–44] and optical properties.[28,30] Intense study has also been conducted on metal clusters adsorbed on the F_s defect.[16,30,48–60] Despite recent suggestions that this type of defect might not be abundant on carefully annealed MgO(100) films,[61–65] it can be easily created by electron bombardment or other means[30,63] and it has been suggested that it can have an important effect on the catalytic activity of extremely small supported clusters.[58,63]

Computational Methods

The search for the lowest energy structures of Ag clusters was performed either by a biased search starting from selected configurations or by a density-functional basin-hopping (DF-BH) approach.[36] The basin-hopping algorithm[66–68] is defined in the following steps: 1) an initial random configuration was chosen, a local geometry optimization was performed, and the final energy (the fitness parameter) was registered as E_1; 2) starting from the relaxed configuration, the atoms of the metal cluster were randomly displaced,[69] a new local geometry optimization was performed, and the final energy is registered as E_2; 3) a random number (rndm) between 0 and 1 was generated and the movement of step 2 was accepted only if $\exp[-(E_2-E_1)/k_BT] > \text{rndm}$ (Metropolis criterion); 4) steps 2 and 3—the Monte Carlo steps—were repeated a given number of times. Depending on the k_BT parameter (which in this work is set to 1.0 eV in all the calculations), some high-energy configurations were accepted and the search was able to explore different structural motifs (belonging to different funnels of the potential-energy surface) of the metal cluster. In the DF-BH approach,[36] the determination of energies and forces was achieved by using a first-principles DF method: the number of Monte Carlo steps was limited by the CPU time available, and the DF-BH approach is practically unfeasible in the case of systems composed by more than few tens of atoms. In the present case, we deal with metal clusters composed of up to ten atoms, and we expected the global minimum for each cluster to be located in a small number of Monte Carlo steps.

The DF-BH calculations were carried out by employing a cluster approach[70] for the description of the MgO support. Either an ($Mg_{18}O_{18}$) cluster of C_{2v} symmetry or an ($Mg_{25}O_{25}$) cluster of C_{4v} symmetry (see Figure 1) were chosen, depending on the size of the metal aggregate.

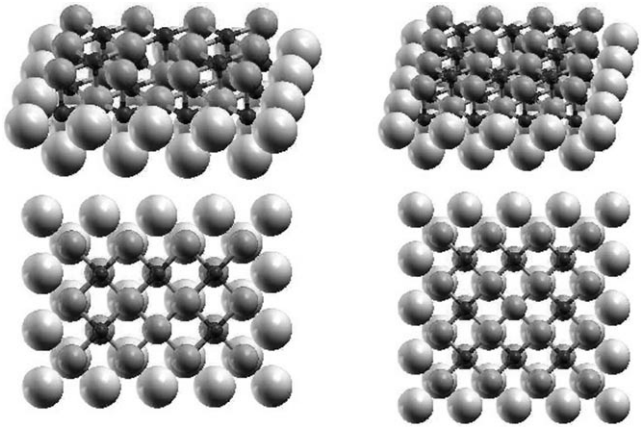

Figure 1. The systems used to model the F_s-defective MgO(100) surface in the cluster approach; small atoms represent oxygen atoms, larger atoms magnesium atoms, and largest atoms the positive charge sites on which a repulsive pseudopotential is added.

Both MgO clusters were embedded in an array of ± 2.0 au point charges[71] (about 1500) extending for four layers in the direction perpendicular to the surface and up to ≈ 10 Å from the borders of the cluster in the (100) surface plane. The atoms of the central cluster and the point charges around it were located at the lattice positions of the MgO rock-salt bulk structure at the experimental lattice constant of 4.208 Å. Moreover, a repulsive pseudopotential[72] was added on the positive point charges in direct contact with the cluster, in order to avoid an unphysical polarization of the charge density.[73] As shown in Figure 1, to create an F_s vacancy we erased a neutral oxygen atom from the surface keeping frozen the coordinates of all the Mg and O atoms around the defect. Structural relaxation around the F_s defect has been show to be undramatic[19,41,74,75] and we did not expect that the modest interaction of Ag clusters[76] with the surface would qualitatively modify the results (this has been actually been checked in selected cases). Moreover, freezing the geometry of the oxide substrate at its experimental equilibrium configuration was, in our opinion,[77] the best choice not to let the DF/GGA approach overestimate the structural relaxation around the oxygen vacancy upon metal adsorption. All the calculations with the cluster approach were carried out with the DF module of the NWChem package[78] by using the PW91 xc-functional[79] in the spin-unrestricted formalism. The geometry optimizations were performed by using Gaussian-type orbital basis sets of double-ζ quality,[80] while the total binding energy used in the Metropolis criterion energy was calculated from a single-point calculation on the relaxed geometry by using a triple-ζ plus polarization basis set.[80] A 19-valence-electron effective core potential was used for Ag.[81] The two electrons trapped in the cavity were described with a Gaussian-type orbital basis set of double-ζ quality for the optimization run and a set of triple-ζ quali-

ty plus d polarization functions in the single-point final calculation.[82] Charge-density-fitting Gaussian-type orbital basis sets were used to compute the Coulomb potential.[83] The calculations used a Gaussian-smearing technique[84] (with a smearing parameter of 0.001 a.u.) for the fractional occupation of the one-electron energy levels.

After having singled out the low-energy structures at each size by using the DF-BH approach with the NWChem software and a cluster description of the oxide, the obtained results were validated by performing local geometry optimizations with the PWscf (plane-wave self-consistent field) computational code,[85] employing the PBE xc-functional[86] and ultrasoft pseudopotentials in the spin-unrestricted formalism. This approach was computationally more demanding, but was essentially free of basis set limitations and thus represents a good check of localized basis set calculations. The kinetic energy cutoff for the selection of the plane-wave basis set was fixed at 20 au for all the calculations. A (3,3,1) *k*-point sampling of the Brillouin zone was chosen, and a Gaussian smearing technique (with a smearing parameter of 0.001 au) was applied. The MgO(100) surface was modeled by a three-layer slab, each layer containing 18 (3×3 cell) or 24 (4×3 cell) Mg and O atoms fixed in the lattice positions of the rock-salt bulk structure. The unit cell was chosen such that the distance between metal clusters belonging to replicated cells was greater than 6–8 Å. The F_s defect was created by removing a neutral oxygen atom from the surface and freezing the coordinates of all the other atoms of the substrate in the lattice positions.

It is important to stress that the two approaches: the cluster approach using NWChem and the periodic cell approach using PWscf, produced the same qualitative results with minor quantitative differences (partly due to the slightly different xc functionals adopted in the two cases). The energy values reported in the following are those obtained using the PWscf code.

Results and Discussion

In this section we report and discuss the results regarding the low-energy structures for Ag_N clusters (with $N=1$–4, 6, 8, 10) both in the gas phase and adsorbed on the F_s defect of the MgO(100) surface.

It is convenient to define four quantities: 1) the adhesion energy (E_{adh}), calculated by subtracting the energy of the oxide surface and of the metal cluster, both frozen in their interacting configuration, from the value of the total energy of the system, and by taking the absolute value; 2) the binding energy of the metal cluster (E_{met}), calculated by subtracting the energy of the isolated metal atoms from the total energy of the metal cluster in its interacting configuration, and by taking the absolute value; 3) the metal cluster distortion energy (E_{dist}), which corresponds to the difference between the energy of the metal cluster in the configuration interacting with the surface minus the energy of the cluster in its lowest energy gas-phase configuration (thus, a positive quantity); and 4) the total binding energy (E_{bnd}), which is the sum of the binding energy of the metal cluster and of the adhesion energy ($E_{bnd}=E_{adh}+E_{met}$).

In the following, the results are distinguished in terms of the Ag cluster size. For Ag_N with $N=2$–4, due to the small size of the metal clusters, we performed a biased DF search by locally optimizing a limited number of physically reasonable configurations, both in the gas phase and when adsorbed on the defected surface. The configurations of the adsorbed Ag_N clusters with $N=2$, 4 have been reported in previous work[49,50] with the exception of configuration (c1) of the tetramer (see below). The present results are in qualitative (and often quantitative) agreement with these earlier investigations, and are briefly reported in the following to set the stage for larger clusters and the sake of completeness. For Ag_6, three DF-BH runs were performed, each composed of 15 Monte Carlo steps; for Ag_8 and Ag_{10}, five DF-BH runs were performed, each composed of 15 Monte Carlo steps, both in the gas phase and when adsorbed on the defected surface. The starting configurations of each run were generated randomly in a sphere of radius 4 Å around the vacancy.

To our knowledge, this is the first time that a DF-BH approach has been applied to metal clusters adsorbed on a surface. The DF-BH approach is useful to sample the PES of these complicated systems in which biased searches often miss the ground-state structure for small clusters.

Single-atom adsorption topography: A single Ag atom interacts preferentially with the oxygen site of the regular (100) surface, with an adhesion energy of about 0.4 eV.[15,16,18,33,87] The presence of the F_s defect increases the interaction energy to 1.64 eV.[16,18,51] This increase can be rationalized in terms of two effects: first, the removal of an oxygen atom determines a remarkable reduction of the Pauli repulsion between the electronic cloud of the metal and that of the oxide substrate; second, the two electrons trapped in the cavity, being weakly bound by the Madelung potential, are very polarizable and able to form a stronger bond with the metal atom. The decrease of the Pauli repulsion determines also a reduction of the equilibrium distance of the metal atom from the surface (from a value of ≈2.5 Å on the oxygen site of the regular surface, to a value of ≈2.0 Å on top of the defect). The presence of the F_s defect not only modifies the adsorption on top of it,[16,18,51] but also the whole adhesion topography in an area which extends up to distances of 4–6 Å from the vacancy.[26,74,77] For example, the adhesion of the Ag atom on top of an Mg-atom nearest neighbor of the vacancy is 0.78 eV, much bigger than the value 0.22 eV characterizing the same site on the regular surface. In Figure 2, the topographic landscapes of the metal–surface interaction in the case of adsorption of a single Ag atom are displayed; for comparison, the topographic landscapes for the regular surface are also shown. The profiles in Figure 2 were obtained by performing a vertical relaxation of the Ag atom on top of several sites of the MgO regular and defective unit cell and interpolating the points obtained; in Figure 2a and 2c the adhesion energy and in Figure 2b and 2d the equilibrium distance from the surface are shown for the regular and defective surfaces, respectively. These profiles are qualitatively similar to those reported in reference [77] for the adsorption of a gold atom. As shown in Figure 2c, the presence of the defect produces a large basin of attraction, exhibiting an approximate cylindrical symmetry around the vacancy. Furthermore, on top of the defect the increase of the adhesion energy corresponds to a decrease of the equilibrium distance, whereas on the neighboring sites the increase of the adhesion often corre-

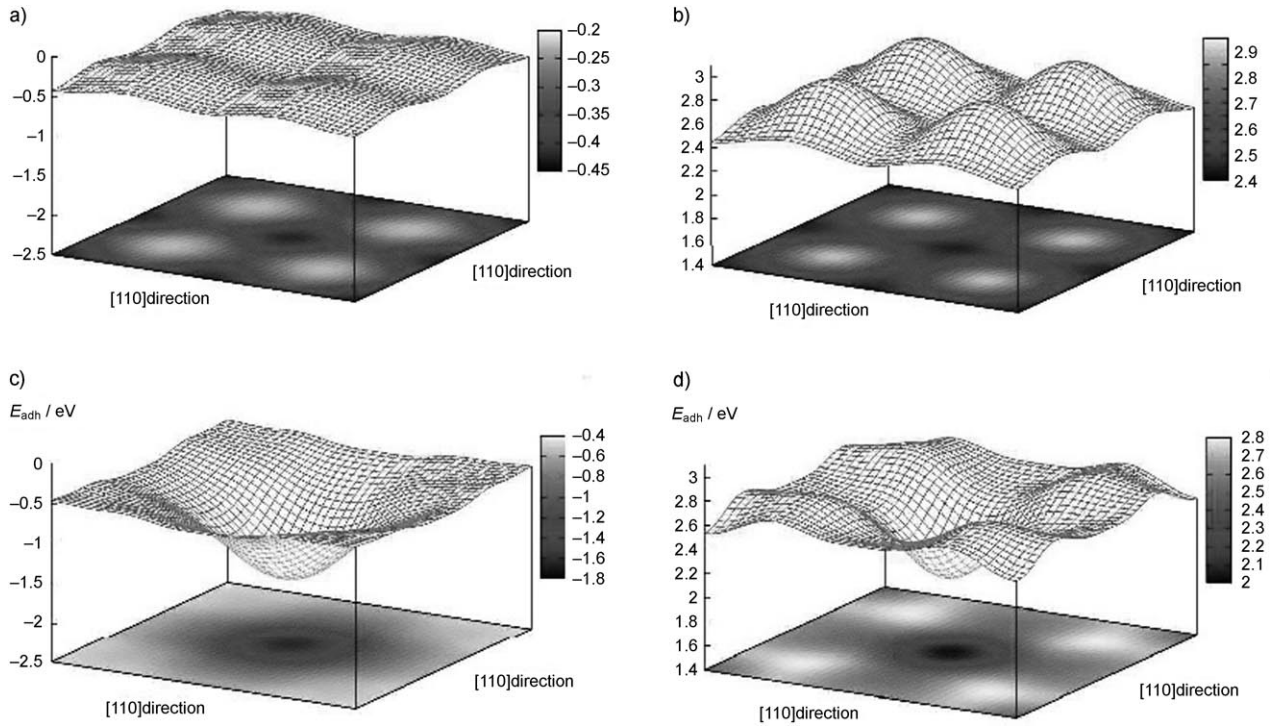

Figure 2. Topographic landscape of the adsorption of an Ag atom on the MgO(100) surface: the adhesion energy (a,c) and the equilibrium distance from the surface (b,d) are shown for the regular surface and the F_s-defective surface, respectively.

sponds to a lengthening of the metal–surface equilibrium distance. As we will see in the following discussion, the approximate cylindrical symmetry around the defect is also present when small clusters are adsorbed on the defect and implies a *rotational invariance* by which small clusters can rotate almost freely around an axis perpendicular to the surface, keeping one atom firmly bound to the defect. Moreover, the strong variation of the equilibrium distance around the defect implies that metal cluster growth is frustrated not only horizontally with respect to the surface (due to the mismatch between the lattice constants of the metal and of the support), but also vertically because of the difference between the equilibrium distance on top of the defect and that on top of the neighboring site around the vacancy, an effect that we have called *double frustration*.[77]

Ag_2, Ag_3, and Ag_4 clusters: The configurations considered for Ag_N ($N=2$–4) clusters adsorbed on the F_s defect are displayed in Figure 3, while the corresponding energy analysis is reported in Table 1.

When a second Ag atom reaches the defect, it binds to the first one in such a way that the dimer axis results perpendicular to the surface, as shown in previous work.[18,49,55] This configuration is stabilized by the electrostatic contribution coming from the increased polarization of the metal electronic density of the dimer in the field of the oxide. In general, it has been noted[18,49,55,56,87] that the presence of metal atoms above those directly interacting with the surface increases the adhesion energy: this effect is what we have called "metal-on-top" stabilization mechanism.[18] Thanks to the metal-on-top effect, the adhesion energy of the dimer is 1.79 eV, increased with respect to the adhesion of the single atom on the defect, despite the fact that the atom interacting with the surface is involved in a strong

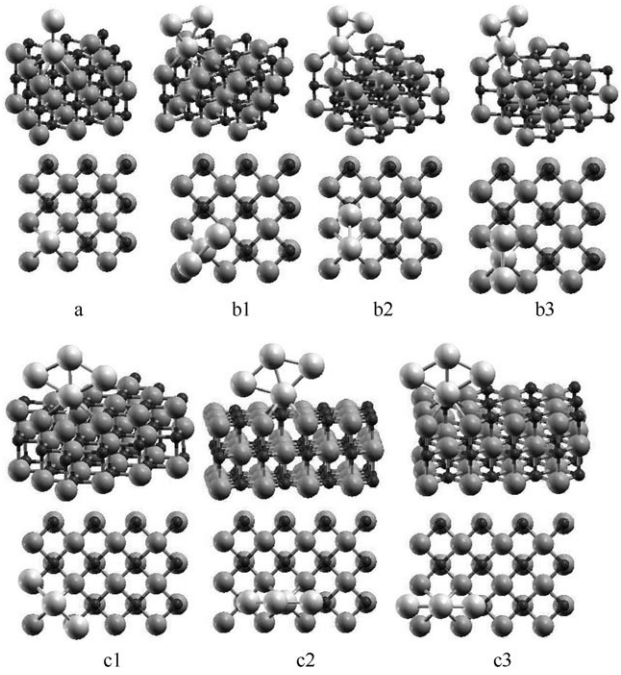

Figure 3. Schematic representation of the lowest energy structures and saddle points of Ag_N ($N=2$–4) clusters on the F_s-defective MgO(100) surface.

Table 1. The values of the various energy quantities defined in the text are reported for the lowest energy structures and saddle points of Ag_N ($N=1$–10) clusters. The notation used refers to the nomenclature defined in Figures 3–6. All energy values in eV.

Cluster	Conf.	E_{adh}	E_{met}	E_{dist}	E_{bnd}	Spin
Ag_1		1.64	–	–	1.64	1/2
Ag_2	a	1.79	1.72	0.01	3.51	0
Ag_3	b1	2.23	2.57	0.03	4.80	1/2
	b2	2.18	2.59	0.01	4.77	1/2
	b3	2.15	2.60	0.00	4.75	1/2
Ag_4	c1	2.46	4.55	0.02	7.01	0
	c2	2.48	4.52	0.05	7.00	0
	c3	2.43	4.55	0.02	6.98	0
Ag_6	d1	2.74	7.95	0.55	10.70	0
	d2	2.80	7.88	0.62	10.68	0
	d3	2.82	7.91	0.59	10.73	0
	d4	2.83	7.81	0.69	10.64	0
	d5	2.66	7.85	0.65	10.51	0
	d6	2.34	8.31	0.19	10.65	0
	d7	1.88	8.38	0.12	10.26	0
Ag_8	e1	2.02	12.29	0.06	14.31	0
	e2	2.19	12.09	0.25	14.28	0
	e3	2.14	12.13	0.22	14.27	0
	e4	2.03	11.99	0.35	14.02	0
	e5	2.07	12.21	0.14	14.28	0
	e6	2.30	11.53	0.82	13.83	0
Ag_{10}	f1	2.43	15.60	0.05	18.03	0
	f2	2.61	15.57	0.08	18.18	0
	f3	2.24	15.07	0.58	17.31	0
	f4	2.52	15.37	0.29	17.89	0
	f5	2.56	15.44	0.21	18.00	0
	f6	2.82	15.47	0.18	18.29	0

metallic bond, which should decrease its availability to interact with the surface.

The third atom is then added in a cluster plane perpendicular to the surface. When the cluster plane is oriented along the [100] direction, we obtain the ground-state configuration, exhibiting C_{2v} symmetry and labeled as b1. A 45° rotation brings the plane of the cluster along the [110] direction and the cluster slightly bends in order to make one of the two upper Ag atoms adhere to one oxygen ion of the surface nearest neighbor of the vacancy: this local minimum, labeled as b2, is higher in energy than the ground state by only 0.03 eV. The configuration b2 can be converted into another configuration b2 passing through the saddle point b3, in which the cluster is still oriented along the [110] direction with symmetry C_{2v} and which is higher in energy than the configuration b2 by 0.02 eV (thus is 0.05 eV higher than the ground state). The small energy differences between the three configurations confirm the rotational freedom of the metal cluster around an axis perpendicular to the surface and passing through the metal atom bound to the defect. The doublet spin state of the trimer is responsible for the fluxional character of the metal cluster and consequently for the small values of the metallic distortion energy for the three configurations.

The case of the tetramer is very similar to that of the trimer: Ag_4 adsorbs in a rhombic configuration (the same characterizing the gas phase at this size[88]) with one of the two highly coordinated vertices anchored to the vacancy and the cluster plane perpendicular to the surface. The ground-state configuration c1 corresponds to the cluster plane oriented along the [100] direction and has C_{2v} symmetry. Also in this case, a 45° rotation to the configuration c2 is accompanied by a bending of the cluster, so that one of the two lower coordinated vertices adheres to one oxygen ion of the surface nearest neighbor of the vacancy; this configuration has been previously found in reference [50]. The transition between two analogous configurations c2 is represented by the saddle point c3 with C_{2v} symmetry. As in the case of the trimer, the energy differences between the three configurations are very small (below 0.05 eV), thus confirming the rotational freedom of Ag_4.

Ag_6 cluster: The results concerning the Ag_6 cluster are reported in Table 1 and the corresponding structures are displayed in Figure 4. In the same figure, the three lowest energy configurations characterizing Ag_6 in the gas phase are also displayed.

The ground state of the cluster in the gas phase is represented by the planar structure a, with cohesive energy of

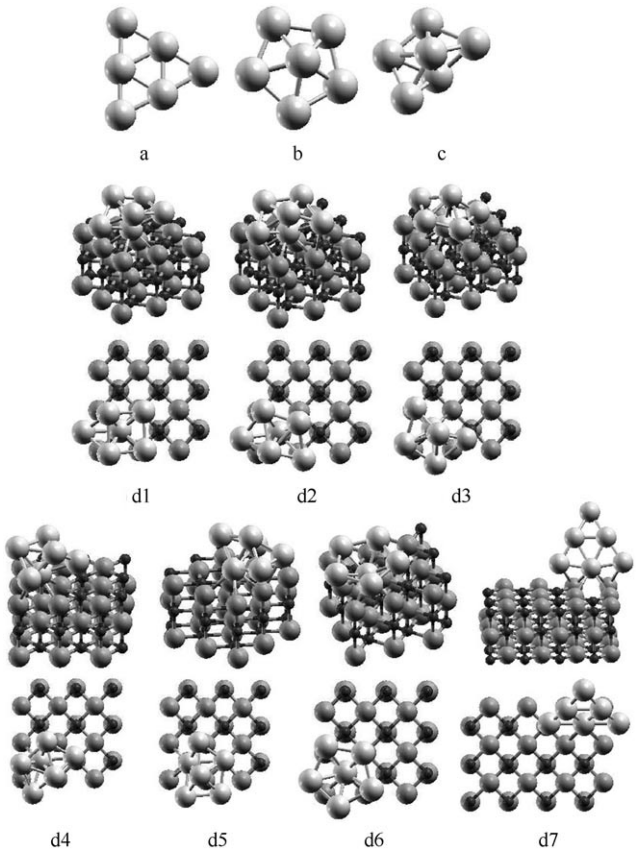

Figure 4. Schematic representation of the lowest energy structures of Ag_6 both in the gas phase (a–c) and on the F_s-defective MgO(100) surface (d1–d7).

8.50 eV; a pentagonal pyramid, structure b, has a cohesive energy a bit smaller than that of the ground state (8.30 eV), while structure c, an incomplete pentagonal bipyramid missing one equatorial atom, has a cohesive energy of 7.86 eV. These results are in keeping with the previous literature.[37,38,40] All three structures correspond to singlet spin states. At this size, the planar configuration has an enhanced stability as six is a magic number of the 2D triangular jellium model:[89] indeed, the HOMO–LUMO gap for this structure is 2.15 eV.

When Ag_6 adsorbs on the surface, we find three low-energy configurations, d2–d4, which belong to the same structural family, that is, the incomplete pentagonal bipyramid—the structure c of the gas phase. Among this family, configuration d3 is the ground state. The presence of the defect thus causes a first structural transition from a planar structure (favored in the gas phase) to noncrystalline (fivefold symmetric) structures (favored for adsorbed Ag_6). These three configurations can be obtained from each other through small rotations around an axis perpendicular to the surface and passing through the defect. From the energy values in Table 1, we can see that the small differences in the values of the total binding energies imply a rotational freedom of the metal cluster around the F_s vacancy.

In contrast, configurations d1 and d5 represent two local minima derived from a distortion of the motif of the incomplete bipyramid: they can be seen as two square pyramids with the square basis either on top to the atom directly bound to the defect (structure d1) or grown quasi-pseudomorphically on the defect and on three oxygen surface ions near the vacancy (structure d5). In both cases, the fifth atom is grown tetrahedrally on a triangular face of the pyramid. These two configurations have an increased metallic energy, but also a decreased adhesion to the surface. Configuration d1 turns out to be competitive with the global minimum, whereas structure d5 lies higher in energy by about 0.2 eV.

In structure d6 the metal cluster has the shape of a pentagonal pyramid (configuration b of the gas phase): in this motif the metallic bond results remarkably stabilized, but the adhesion to the surface is weaker. Thanks to compensation between these two contributions, this configuration is also competitive with the ground state.

Finally, in structure d7, the metal cluster is quasi-planar and adsorbed with three metal atoms interacting with the vacancy and two nearest-neighbor oxygen atoms (the cluster is slightly tilted with respect to the surface). This configuration is higher in energy by about 0.5 eV, despite the fact that this corresponds to the most stable structural motif characterizing the gas phase. This fact can be rationalized by considering the shape of the topography around the defect, which suggests a better adhesion for structure belonging to compact motifs, such as the pentagonal pyramid or the incomplete pentagonal bipyramid. The gain in adhesion is able to compensate for the loss of metallic energy in these motifs.

It can be noted that we discuss not only the putative global minimum, but also the putative lowest energy isomers. In principle, the DF-BH is also able to single out these higher energy configurations, even though longer and more numerous Monte Carlo runs would be necessary in order to ensure that the first, for example, three or four isomers have been correctly located, and assured that the intermediate configurations in the structural interconversion are not much higher in energy than the k_BT parameter. Due to the small size of the clusters here investigated, we are confident that most important structural motifs of these clusters are depicted in Figures 4–6.

We conclude that at this size the competition between metal bonding and adhesion, together with phenomena such as rotational invariance and double frustration, determine the presence of structures belonging to different structural motifs but exhibiting very similar values of the total binding energy: this implies a fluxionality of the metal cluster adsorbed on the defected surface. Nevertheless, a structural transition from planar to fivefold structures induced by the metal–defect interaction is clearly observed.

Ag_8 cluster: The results concerning Ag_8 are reported in Table 1 and the corresponding structures are displayed in Figure 5. In the same figure, four low-energy configurations

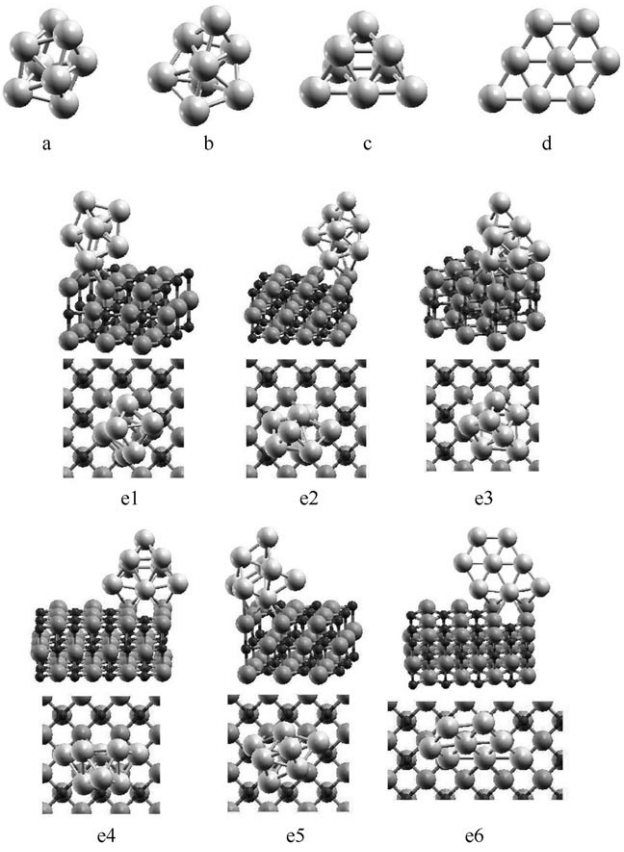

Figure 5. Schematic representation of the lowest energy structures of Ag_8 both in the gas phase (a–d) and on the F_s-defective MgO(100) surface (e1–e6).

characterizing Ag_8 in the gas phase are also displayed, which are in keeping with previous literature.[37,38,40] In the gas phase the ground-state, structure a, is represented by a pentagonal bipyramid in which one equatorial atom has been substituted by a dimer with the axis perpendicular to the equatorial plane (cohesive energy of 12.35 eV). Structure b belongs to the same structural motif, except that, in this case, the pentagonal bipyramid is perfect and the eighth atom is grown tetrahedrally on one of the ten triangular facets (cohesive energy of 12.21 eV). Structure c, almost isoenergetic with b, belongs to a crystalline motif: it is formed by a central octahedron with two atoms grown tetrahedrally on two opposite facets of the same square pyramid (cohesive energy of 12.19 eV). The planar structure d results destabilized with respect to the ground state and has a cohesive energy of 11.67 eV. For gas-phase Ag_8, thus, planar structures are no more the ground state, and a structural transition has occurred to noncrystalline (fivefold) configurations, in agreement with previous literature:[37,40] silver clusters behave not too differently from alkali clusters,[37] which have 3D structures for $N \geq 6$.[90]

For the structures adsorbed on the surface in the ground-state (structure e1), the metal cluster is adsorbed on the defect with the same structure as the ground state that characterizes the gas phase: in particular, one of the two atoms of the dimer perpendicular to the equatorial plane is bound to the defect, whereas the other one is adsorbed on one oxygen ion on a nearest-neighbor to the vacancy on the surface. In this configuration, only two atoms interact directly with the surface, and this fact determines the lower value of the adhesion energy with respect to neighboring sizes. In the configuration e2, the metal cluster is instead adsorbed with the same structure of the configuration b of the gas phase: thanks to a compensation between a reduced metallic energy and an increased adhesion, this configuration is nearly degenerate with the ground state.

In the structures e3 and e4, the cluster is adsorbed with the same structure as in the configuration c of the gas phase, that is, the crystalline motif. In structure e3, the metal cluster is remarkably distorted due to the formation of a (distorted) square facet through which the cluster adheres to the defect and to three oxygen ions of the surface next to the vacancy, as in the case of configuration d5 of Ag_6. This structure can also be seen as a tetrahedron of ten atoms lacking two basal atoms with the (111) epitaxy distorted to a quasi-(100) epitaxy, because of the tendency to a pseudomorphic growth on the defected surface. The structure e4 is less distorted with respect to the gas-phase structure, but, due to a loss of both metallic and adhesion energy, is the highest in energy among those considered (it lies about 0.3 eV higher than the ground state).

Configuration e5 can be seen either as a distortion of configuration a of the gas phase or as an alternative fcc crystalline structure, in which two metal atoms cover the central octahedral core by adsorbing on two vicinal facets belonging to different square pyramids. In this structure, both the metallic bond and the adhesion energy are strengthened and the configuration is thus competitive with the ground state, having a total binding energy similar to that of configurations e2 and e3.

Finally, in structure e6 the metal cluster is adsorbed in a planar configuration with three metal atoms interacting with the vacancy and two nearest-neighbor oxygen atoms. With respect to the other configurations considered, in this case the adhesion energy is enhanced, but the substantial destabilization due to the weak metallic energy makes this structure higher than the ground state by about 0.5 eV.

To conclude, we note that also Ag_8 exhibits a remarkable fluxionality: four of the configurations we have described (e1, e2, e3, e5) possess very similar values of the total binding energy, although they belong to completely different structural motifs. This confirms the ability of the DF-BH approach to explore different funnels of the adsorbed cluster potential energy surface.

Ag_{10} cluster: The results concerning Ag_{10} are reported in Table 1 and the corresponding structures are displayed in Figure 6. In the same figure, the lowest energy configurations characterizing Ag_{10} in the gas phase are also displayed.

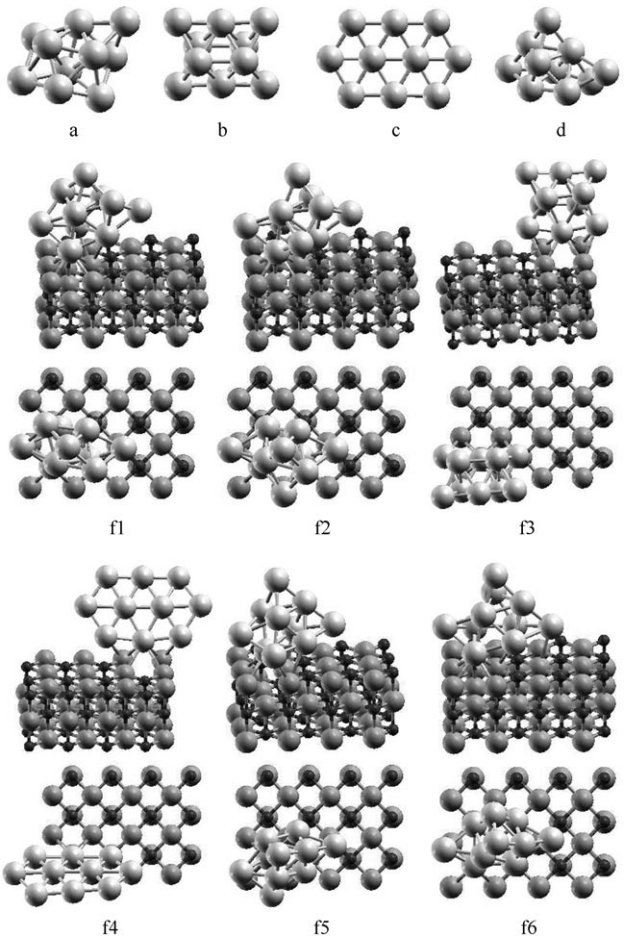

Figure 6. Schematic representation of the lowest energy structures of Ag_{10} both in the gas phase (a–d) and on the F_s-defective MgO(100) surface (f1–f6).

In the gas phase, as for Ag_8, the ground state still belongs to a noncrystalline fivefold motif: in structure a, with a cohesive energy of 15.65 eV, nine atoms constitute a fragment of the 13-atom icosahedron, while the tenth atom is external, growing on one of the (111) facets. Structure b, instead, with a cohesive energy of 15.30 eV, is a crystalline motif in which four atoms are grown symmetrically on the central octahedron core. Structure c, the cohesive energy of which is 15.53 eV, is a planar motif, portion of an fcc (111) layer. The energy difference of this planar structure with respect to the ground state is only 0.12 eV, which is not surprising because ten is a magic number for 2D circular jellium models (also due to the twofold angular degeneracy in the plane).[89] Finally, structure d, isoenergetic with structure c, can be described as a distorted fcc structure. These results are in keeping with previous literature.[37,38,40]

The ground state of Ag_{10} on the F_s-defective MgO(100) surface is given by configuration f6. Similar to configuration e3 of Ag_8, in this structure the metal cluster can be seen as a distorted tetrahedron adsorbed on the defect through one basal corner, in which the (111) epitaxy has converted to a quasi-(100) epitaxy to match the pattern of the oxygen ions of the surface; moreover, the corner of the tetrahedron more distant from the defect has moved in order to improve the adhesion to the surface. Configuration f5 is similar to f6, with the difference that the distorted metal tetrahedron is adsorbed on the vacancy through the central atom of a basal edge, and not through one basal corner: since the edge atom has a higher metal coordination, it has a weaker interaction with the defect and the adhesion energy is consequently lower with respect to the f6 ground state. The metallic energy is instead almost the same as that of the ground state and the total binding energy is lower (in absolute value) than the ground state by about 0.3 eV. Also the structure f3 belongs to the crystalline structural motif and is analogous to the configuration e4 of Ag_8. This configuration exhibits a loss of both metallic energy and adhesion to the surface and the total binding energy is lower than that of the ground state by about 1 eV.

Configuration f4 corresponds to the planar structure of the metal cluster in the gas phase: this configuration is destabilized by about 0.5 eV with respect to the ground state because of its poor adhesion to the surface.

Finally, in configurations f1 and f2 the metal cluster has the same noncrystalline structure characterizing configuration a of the gas phase. In spite of the increased metallic energy in these configurations, we have a decreased adhesion to the surface and, globally, this structural family is higher by 0.1–0.2 eV with respect to the ground state.

The main conclusion is thus that the ground-state structure of Ag_{10} adsorbed on the defected surface does not correspond to the gas-phase ground-state structure: in passing from Ag_8 to Ag_{10}, a structural transition from noncrystalline motifs, based on the pentagonal bipyramid, to distorted crystalline structures occurs. The reason of this is that the double frustration lengthens the interatomic distances between the atom adhered to the defect and its nearest-neighbors adhered to the nearby O and Mg sites; this effect disfavors noncrystalline fivefold symmetric structures, in which these distances are already strained because of the frustration inherent in decahedral or icosahedral clusters.[91] Despite the fluxionality inherent in such small clusters, this switch of preference towards crystalline structures can help explain why experimentally[31] only truncated octahedra are observed in MBE (molecular beam epitaxy) deposition experiments of Ag clusters on the MgO(100) surface, even at very small (height $\approx$1 nm, lateral width $\approx$1–2 nm) sizes, despite the fact that fivefold symmetric structures are the ground state for Ag clusters in the gas phase in this size range.[92] Even though larger clusters can be on the whole less affected by the presence of the neighboring defect, a kinetic trapping into fcc configurations might occur.

Is the cluster Ag_8 magic? It is interesting to observe that $N=8$ corresponds to an electronic magic number of the spherical jellium model.[93,94] We thus could expect a particular stability associated to this size, at least in the gas phase. Figure 7 shows the behavior of the excess energy for Ag_N clusters in the size range $N=4$–10 both in the gas phase and when adsorbed on the F_s-defective surface. The excess energy is defined in Equation (1), in which $E_b(N)$ is the metallic binding energy of the clusters in the gas phase, or the total binding energy (metallic energy plus adhesion energy) for the adsorbed clusters and ε_{coh} is the bulk fcc cohesive energy of the metal calculated within the DF/PWscf approach: 2.50 eV.

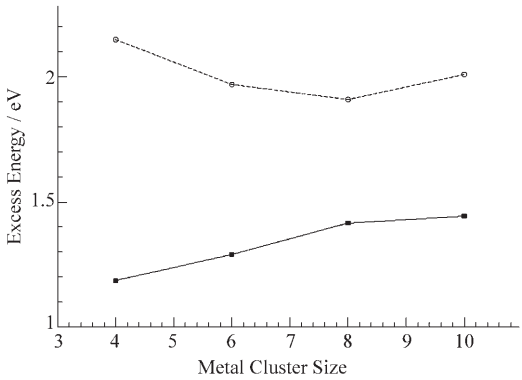

Figure 7. Excess energy as a function of cluster size for gas-phase structures (upper line with circles), and adsorbed structures (lower line with squares).

$$E_{exc}(N) = \frac{E_b(N) - N\varepsilon_{coh}}{N^{2/3}} \quad (1)$$

From Figure 7, we see that in the gas phase the cluster Ag_8 does not present an exceptional stability (somewhat at variance with the predictions of the jellium model), being only modestly favored with respect to sizes six and ten, even though a minimum in the excess energy is found at this size.

Table 2. Binding energies on the F_s [$E_{bnd}(F_s)$] and regular [E_{bnd}(reg)] surface and energy differences [$\Delta E(N \rightarrow i)$] related to the fragmentation process of an N-atom cluster into two smaller units, one (containing i atoms) still anchored to the defect and the other one (the complement of i to N) adsorbed on the regular surface. All energy values in eV.

N	$E_{bnd}(Fs)$	E_{bnd}(reg)	ΔE ($N \rightarrow 1$) Ag_1/F_s	ΔE ($N \rightarrow 2$) Ag_2/F_s	ΔE ($N \rightarrow 3$) Ag_3/F_s	ΔE ($N \rightarrow 4$) Ag_4/F_s	ΔE ($N \rightarrow 6$) Ag_6/F_s	ΔE ($N \rightarrow 8$) Ag_8/F_s
1	1.64	0.42	–	–	–	–	–	–
2	3.51	2.39	1.45	–	–	–	–	–
3	4.80	3.51	0.77	0.87	–	–	–	–
4	7.01	5.56	1.86	1.11	1.79	–	–	–
6	10.74	–	–	1.67	2.43	1.34	–	–
8	14.31	–	–	–	–	1.74	1.18	–
10	18.29	–	–	–	–	–	1.99	1.59

This is due to the fact that the valence 5s orbital of the silver atom is too expanded to fit the Ag–Ag interatomic distances, and the energy stabilization associated with the jellium shell closure is frustrated by a destructive interference of the electronic wavelength.[95] When the cluster is adsorbed on the defect, the situation is further worsened by the weak adhesion of this cluster with respect to the neighboring sizes. In order not to distort excessively with respect to the gas-phase structure, Ag_8 in fact adsorbs with only two atoms directly interacting with the surface. The final result is that the excess energy for the adsorbed clusters in this size range is an increasing function of the cluster size.

Cluster fragmentation: In analogy with previous work,[49,50,77,96] we have considered the energetics of processes corresponding to the fragmentation of the metal cluster into two pieces: the former still adsorbed on the defect, the latter adsorbed on the regular MgO(100) terrace. These processes can be important to understand the detrapping mechanism from this defect, and the process of Ostwald ripening of small clusters by bigger ones observed in MBE experiments at sufficiently high temperatures.[31] In Table 2 the energy differences corresponding to several fragmentation processes on the regular surface are reported. It is interesting to note that the lowest energy fragmentation process consists in the detachment of an Ag_2 dimer from a larger metal aggregate. This is due to the peculiar stability of Ag_2 on the regular surface. The energy associated with this process grows in an approximately monotonous way with the cluster size from 0.77 eV (the value for Ag_3 fragmentation) to 1.6 eV (the value for Ag_{10} fragmentation). With the exception of the smaller nuclearities, these processes are thus expected to be active at temperatures higher than room temperature.[31]

Conclusions

The structure of Ag_N clusters (N=1–4, 6, 8, 10) both in the gas phase and grown on the F_s-defective MgO(100) surface has been investigated by means of a density functional basin-hopping (DF-BH) approach.[36] In analogy with what already observed in the case of Au_N clusters on the F_s defect,[77] it is found that the presence of the defect implies a double frustration and a cylindrical invariance of the metal–surface interaction, causing small Ag clusters growing around the F_s defect to be highly fluxional.

For the gas-phase clusters, in agreement with the literature on the subject,[37,40] it is found that a structural transition occurs at $N=8$, such that the ground-states of Ag_N clusters are planar for $N=6$, and compact for $N=8$ and 10 with a predominance of noncrystalline, fivefold symmetric structures. The interaction with the F_s defect substantially modifies this scenario: 1) the crossover between planar and fivefold symmetric compact structures already occurs at $N=6$; 2) a further transition from fivefold symmetric to crystalline structures is found at $N=10$. The latter transition is rationalized by considering the additional strain that noncrystalline structures undergo, because of the double frustration effect due to the defect. Despite the fluxionality inherent in such small clusters, this tendency towards crystalline structures (possibly combined with kinetic trapping) could help explain why experimentally[31] only truncated octahedra are observed in MBE experiments of deposition of Ag clusters on the MgO(100) surface, even at very small (height $\approx$1 nm, lateral width $\approx$1–2 nm) sizes, despite the fact that fivefold symmetric structures are the ground state for Ag clusters in the gas phase in this size range.[92]

Moreover, Ag_8, which corresponds to a magic number of the spherical jellium model, is found to be slightly favored with respect to neighboring sizes in the gas phase, but not when adsorbed on the defected surface.

Fragmentation processes have also been investigated, finding that the lowest energy pathway corresponds to the detachment of a dimer, and that this process can be active for Ag_3 already at room temperature, or at higher temperatures for larger clusters.

Acknowledgements

G.B. and A.F. acknowledge financial support from the Italian CNR for the program "(Supra-) Self-Assemblies of Transition Metal Nanoclusters" within the framework of the ESF EUROCORES SONS, and from the European Community Sixth Framework Project for the STREP Project "Growth and Supra-Organization of Transition and Noble Metal Nanoclusters" (contract no. NMP-CT-2004-001594). E.A. was in part supported by Office of Basic Energy Sciences, U.S. Department of Energy under

Contract No. DE-AC05-00OR22725 with UT-Battelle, LLC. Calculations were performed at Cineca within an agreement with Italian CNR-INFM.

[1] H. J. Freund, *Surf. Sci.* **2002**, *500*, 271.
[2] C. R. Henry, *Surf. Sci. Rep.* **1998**, *31*, 235.
[3] G. J. Hutchings, M. Haruta, *Appl. Catal. A* **2005**, *291*, 2.
[4] C. T. Campbell, *Surf. Sci. Rep.* **1997**, *27*, 1
[5] N. Remediakis, N. Lopez, J. K. Norskov, *Appl. Catal. A* **2005**, *291*, 13.
[6] M. S. Chen, D. W. Goodman, *Science* **2004**, *306*, 252.
[7] H. Häkkinen, S. Abbet, A. Sanchez, U. Heiz, U. Landman, *Angew. Chem.* **2003**, *115*, 1335; *Angew. Chem. Int. Ed.* **2003**, *42*, 1297.
[8] A. L. de Oliveira, A. Wolf, F. Schüth, *Catal. Lett.* **2001**, *73*, 157.
[9] R. Wang, J. Hao, X. Guo, X. Wang, X. Liu, *Studies Surf. Sci. Catal.* **2004**, *154*, 2632.
[10] D. C. Lim, I. Lopez-Salido, Y. D. Kim, *Surf. Sci.* **2005**, *598*, 96.
[11] S. A. Nepijiko, D. N. Ievlev, W. Schulze, *Eur. Phys. J. D* **2003**, *24*, 115.
[12] G. Celep, E. Cottancin, J. Lermé, M. Pellarin, L. Arnaud, J. R. Huntzinger, J. L. Vialle, M. Broyer, B. Palpant, O. Boisron, P. Mélinon, *Phys. Rev. B* **2004**, *70*, 165409.
[13] J. Zheng, R. M. Dickson, *J. Am. Chem. Soc.* **2002**, *124*, 13982.
[14] M. L. Brongersma, *Nat. Mater.* **2003**, *2*, 296.
[15] I. Y. Yudanov, G. Pacchioni, K. Neyman, N. Rösch, *J. Phys. Chem. B* **1997**, *101*, 2786.
[16] A. V. Matveev, K. Neyman, I. Yudanov, N. Rösch, *Surf. Sci.* **1999**, *426*, 123.
[17] N. Lopez, F. Illas, N. Rösch, G. Pacchioni, *J. Chem. Phys.* **1999**, *110*, 4873.
[18] G. Barcaro, A. Fortunelli, *J. Chem. Theory Comput.* **2005**, *1*, 972.
[19] O. Robach, G. Renaud, A. Barbier, *Surf. Sci.* **1998**, *401*, 227.
[20] Y. C. Lee, P. Tong, P. A. Montano, *Surf. Sci.* **1987**, *181*, 559.
[21] F. Heifets, Y. F. Zhukovskii, E. A. Kotomin, M. Causà, *Chem. Phys. Lett.* **1998**, *283*, 395.
[22] J. Goniakowski, *Phys. Rev. B* **1998**, *58*, 1189.
[23] A. Sanchez, S. Abbet, U. Heiz, W. D. Schneider, H. Häkkinen, R. N. Barnett, U. Landman, *J. Phys. Chem. A* **1999**, *103*, 9573.
[24] L. Giordano, G. Pacchioni, *Surf. Sci.* **2005**, *575*, 197.
[25] L. M. Molina, B. Hammer, *J. Chem. Phys.* **2005**, *123*, 161104.
[26] H. Moseler, H. Häkkinen, U. Landman, *Phys. Rev. Lett.* **2002**, *89*, 176103.
[27] A. Bogicevic, D. R. Jennison, *Surf. Sci.* **1999**, *437*, L741.
[28] C. Sousa, F. Illas, *J. Chem. Phys.* **2001**, *115*, 1435.
[29] P. Mori-Sanchez, J. M. Recio, B. Silvi, C. Sousa, A. Martin Pendas, V. Luana, F. Illas, *Phys. Rev. B* **2002**, *66*, 075103.
[30] S. Wendt, Y. D. Kim, D. W. Goodman, *Prog. Surf. Sci.* **2003**, *74*, 141.
[31] C. Revenant, G. Renaud, R. Lazzari, J. Jupille, *Nucl. Instrum. Methods Phys. Res. Sect. B* **2006**, *246*, 112.
[32] G. Barcaro, A. Fortunelli, *New J. Phys.* **2007**, *9*, 22.
[33] A. Ouahab, C. Mottet, J. Goniakowski, *Phys. Rev. B* **2005**, *72*, 035421.
[34] H. M. Benia, N. Nilius, H. J. Freund, *Surf. Sci.* **2006**, *600*, L128.
[35] G. Haas, A. Menck, H. Brune, J. V. Barth, J. A. Venables, K. Kern, *Phys. Rev. B* **2000**, *61*, 11105.
[36] E. Aprà, R. Ferrando, A. Fortunelli, *Phys. Rev. B* **2006**, *73*, 205414.
[37] E. M. Fernández, J. M. Soler, I. L. Garzón, L. C. Balbás, *Phys. Rev. B* **2004**, *70*, 165403.
[38] V. Bonacic-Koutecky, L. Cespiva, P. Fantucci, J. Koutecky, *J. Chem. Phys.* **1993**, *98*, 7981.
[39] V. Bonacic-Koutecky, L. Cespiva, P. Fantucci, J. Pittner, J. Koutecky, *J. Chem. Phys.* **1994**, *100*, 490.
[40] R. Fournier, *J. Chem. Phys.* **2001**, *115*, 2165.
[41] L. N. Kantorovich, J. M. Holender, M. J. Gillan, *Surf. Sci.* **1995**, *343*, 221.
[42] G. Pacchioni, P. Pescarmona, *Surf. Sci.* **1998**, *412/413*, 657.
[43] J. Carrasco, N. Lopez, F. Illas, *Phys. Rev. Lett.* **2004**, *93*, 225502.
[44] J. Carrasco, N. Lopez, F. Illas, H. J. Freund, *J. Chem. Phys.* **2006**, *125* 074711.
[45] Z. Yan, S. Chinta, A. A. Mohamed, J. P. Fackler, D. W. Goodman, *J. Am. Chem. Soc.* **2005**, *127*, 1604.
[46] G. Pacchioni, *ChemPhysChem* **2003**, *4*, 1041.
[47] J. Kramer, W. Ernst, C. Tegenkamp, H. Pfnur, *Surf. Sci.* **2002**, *517*, 87.
[48] M. Sterrer, M. Yulikov, E. Fischbach, M. Heyde, H. P. Rust, G. Pacchioni, T. Risse, H. J. Freund, *Angew. Chem.* **2006**, *118*, 2692; *Angew. Chem. Int. Ed.* **2006** *45*, 2630.
[49] C. Inntam, L. V. Moskaleva, K. M. Neymanm V. A. Nasluzov, N. Rosch, *Appl. Phys. A* **2006**, *82*, 181.
[50] K. M. Neyman, C. Inntam, L. V. Moskaleva, N. Rösch, *Chem. Eur. J.* **2006**, *12*, 277.
[51] K. M. Neyman, C. Inntam, A. V. Matveev, V. A. Nasluzov, N. Rosch, *J. Am. Chem. Soc.* **2005**, *127*, 11652.
[52] L. M. Molina, B. Hammer, *Appl. Catal. A* **2005**, *291*, 21.
[53] R. Coquet, G. J. Hutchings, S. H. Taylor, D. J. Willock, *J. Mater. Chem.* **2006**, *16*, 1978.
[54] Y. F. Zhukovskii, E. A. Kotomin, P. W. M. Jacobs, A. M. Stoneham, *Phys. Rev. Lett.* **2000**, *84*, 1256.
[55] A. Bogicevic, D. R. Jennison, *Surf. Sci.* **2002**, *515*, L481.
[56] A. Del Vitto, G. Pacchioni, F. Delbecq, P. Sautet, *J. Phys. Chem. B* **2005**, *109*, 8040.
[57] A. S. Wörz, K. Judai, S. Abbet, J. M. Antonietti, U. Heiz, A. Del Vitto, L. Giordano, G. Pacchioni, *Chem. Phys. Lett.* **2004**, *399*, 266.
[58] M. Arenz, U. Landman, U. Heiz, *ChemPhysChem* **2006**, *7*, 1871.
[59] B. Yoon, H. Häkkinen, U. Landman, A. S. Wörz, J. M. Antonietti, S. Abbet, K. Judai, U. Heiz, *Science* **2005**, *307*, 403.
[60] M. Walter, H. Häkkinen, *Phys. Rev. B* **2005**, *72*, 205440.
[61] M. Sterrer, E. Fischbach, T. Risse, H. J. Freund, *Phys. Rev. Lett.* **2005**, *94*, 186101.
[62] M. Sterrer, M. Heyde, M. Novicki, N. Nilius, T. Risse, H. P. Rust. G. Pacchioni, H. J. Freund, *J. Phys. Chem. B* **2006**, *110*, 46.
[63] M. Chiesa, M. C. Paganini, E. Giamello, D. M. Murphy, C. Di Valentin, G. Pacchioni, *Acc. Chem. Res.* **2006**, *39*, 861.
[64] Y. D. Kim, J. Stultz, T. Wei, D. W. Goodman, *J. Phys. Chem. B* **2002**, *106*, 6827.
[65] A. Kolmakov, J. Stultz, D. W. Goodman, *J. Chem. Phys.* **2000**, *113*, 7564.
[66] Z. Li, H. A. Scheraga, *Proc. Natl. Acad. Sci. USA* **1987**, *84*, 6611.
[67] D. J. Wales, J. P. K. Doye, *J. Phys. Chem. A* **1997**, *101*, 5111.
[68] D. J. Wales, H. A. Scheraga, *Science* **1999**, *285*, 1368.
[69] Through movements of the metal atoms of up to ± 1 Å in each cartesian direction.
[70] K. Jug, T. Bredow, *J. Comput. Chem.* **2004**, *25*, 1551.
[71] G. Pacchioni, A. M. Ferrari, A. M. Marquez, F. Illas, *J. Comput. Chem.* **1997**, *18*, 617.
[72] P. J. Hay, W. R. Wadt, *J. Chem. Phys.* **1985**, *82*, 270; P. J. Hay, W. R. Wadt, *J. Chem. Phys.* **1985**, *82*, 299.
[73] I. V. Iudanov, V. A. Nasluzov, K. M. Neyman, N. Rösch, *Int. J. Quantum Chem.* **1997**, *65*, 975.
[74] Z. Yang, R. Wu, Q. Zhang, D. W. Goodman, *Phys. Rev. B* **2002**, *65* 155407.
[75] V. A. Nasluzov, V. V. Rivanenkov, A. B. Gordienko, K. M. Neyman, U. Birkenheuer, N. Rösch, *J. Chem. Phys.* **2001**, *115*, 8157.
[76] K. M. Neyman, C. Inntam, V. A. Nasluzov, R. Kosarev, N. Rösch, *Appl. Phys. A* **2004**, *78*, 823.
[77] G. Barcaro, A. Fortunelli, *J. Phys. Chem. B* **2006**, *110*, 21021.
[78] R. A. Kendall, E. Aprà, D. E. Bernholdt, E. J. Bylaska, M. Dupuis, G. I. Fann, R. J. Harrison, J. Ju, J. A. Nichols, J. Nieplocha, T. P. Straatsma, T. L. Windus, A. T. Wong, *Comput. Phys. Commun.* **2000**, *128*, 260.
[79] J. P. Perdew, J. A. Chevary, S. H. Vosko, K. A. Jackson, M. R. Pederson, D. J. Singh, C. Fiolhais, *Phys. Rev. B* **1992**, *46*, 6671.
[80] A. Schaefer, C. Huber, R. Ahlrichs, *J. Chem. Phys.* **1994**, *100*, 5289.
[81] D. Andrae, U. Haeussermann, M. Dolg, H. Stoll, H. Preuss, *Theor. Chim. Acta* **1990**, *77*, 123.
[82] The double-ζ basis is formed by two s functions with exponents $\alpha_s = 0.32$ and $\alpha_s = 0.12$, and a p function, contraction of two gaussians with exponents of $\alpha_p = 0.18$ and $\alpha_p = 0.05$; for the triple-ζ basis we

added an s function with $\alpha_s = 0.025$, we split the two contracted p functions and added a d function with exponent of $\alpha_d = 0.08$.
[83] F. Weigend, M. Haser, H. Patzel, R. Ahlrichs, *Chem. Phys. Lett.* **1998**, *294*, 143.
[84] C. Elsässer, M. Fähnle, C. T. Chan, K. M. Ho, *Phys. Rev. B* **1994**, *49*, 13975; R. W. Warren, B. I. Dunlap, *Chem. Phys. Lett.* **1996**, *262*, 384.
[85] S. Baroni, A. Del Corso, S. de Gironcoli, P. Giannozzi: http://www.pwscf.org.
[86] J. P. Perdew, K. Burke, M. Ernzerhof, *Phys. Rev. Lett.* **1996**, *77*, 3865.
[87] Y. F. Zhukovskii, E. A. Kotomin, D. Fucks, S. Dorfman, *Superlattices Microstruct.* **2004**, *36*, 63.
[88] C. W. Bauschlicher, S. R. Langhoff, H. Partridge, *J. Chem. Phys.* **1990**, *93*, 8133.
[89] E. Janssens, H. Tanaka, S. Neukermans, R. E. Silverans, P. Lievens, *New J. Phys.* **2003**, *5*, 46.
[90] I. A. Solov'yov, A. V. Solov'yov, W. Greiner, *Phys. Rev. A* **2002**, *65*, 053203.
[91] F. Baletto, R. Ferrando, *Rev. Mod. Phys.* **2005**, *77*, 371.
[92] F. Baletto, C. Mottet, R. Ferrando, *Phys. Rev. Lett.* **2000**, *84*, 5544.
[93] W. Ekardt, *Phys. Rev. B* **1984**, *29*, 1558.
[94] D. E. Beck, *Solid State Commun.* **1984**, *49*, 381.
[95] R. Ferrando, A. Fortunelli, G. Rossi, *Phys. Rev. B* **2005**, *72*, 085449.
[96] L. J. Xu, G. Henkelman, C. T. Campbell, H. Jonsson, *Surf. Sci.* **2006**, *600*, 1351.

Received: December 14, 2006
Published online: May 11, 2007

A Magic Pd−Ag Binary Cluster on the F_s-Defected MgO(100) Surface

BarcaroJPCC2007

Giovanni Barcaro and Alessandro Fortunelli*

Molecular Modeling Laboratory, IPCF - CNR, via G. Moruzzi 1, I-56124 Pisa, Italy

Received: March 21, 2007; In Final Form: May 21, 2007

The structure of Pd_1Ag_N clusters ($N = 1-8$), both in the gas-phase and adsorbed on an F_s-center of an MgO-(100) terrace, is investigated via a density-functional basin-hopping (DF-BH) approach. A structural transition from planar to noncrystalline 5-fold symmetric configurations is found for both free and adsorbed clusters in this size range. The Pd−Ag clusters are highly fluxional. In addition, Pd_1Ag_6 is found to be a magic cluster, exhibiting a large HOMO−LUMO gap (both in the gas-phase and adsorbed on the defect) and a peculiar structural stability (when adsorbed on the defect). To our knowledge, this is the first example of a magic metal cluster on an oxide surface. This is rationalized in terms of an electronic shell-closure, involving also the electrons trapped in the oxygen vacancy, coupled with a good adhesion to the defected surface. The low-energy Pd_1Ag_6 isomers (with excitation energies around 0.1−0.3 eV) adsorbed on the F_s-center also exhibit a large HOMO−LUMO gap.

Introduction

Metal clusters supported on oxide surfaces have been intensively studied for a long time, due to their important applications in fields as diverse as catalysis, optoelectronic and magnetic devices, chemical sensors, etc.[1−3] Much knowledge has been accumulated on these systems, in particular concentrating attention in recent years on the relationships between surface defects and metal cluster growth. It is by now clear that the presence of defects such as kinks, corners, vacancies, can have a dramatic effect on the metal/surface interaction, and thus on the characteristics of the oxide support with respect to the nucleation process, and for orienting the structure of metal clusters adsorbed on it. In this context, the MgO(100) surface is certainly one of the most studied systems, for its widespread use as an inert support and for its simplicity, MgO(100) being an apolar, simple ionic surface with no surface reconstruction.[2,4] Among its possible defects, the neutral oxygen vacancy (or F_s-center) on the regular terrace has often been chosen as a prototypical example in theoretical studies, and much effort has been devoted to its full characterization.[5−12] These studies have shown that the metal/surface interaction around such a defect presents peculiar features, namely rotational invariance and a large basin of attraction with a much reduced equilibrium distance on top of the defect with respect to neighboring sites ("double frustration").[13,14] As a consequence, metal clusters growing on the F_s-center exhibit a highly fluxional character, possibly connected with their catalytic activity,[15,46] and often a monotonic behavior of the formation energy as a function of cluster size.[16]

The situation is completely different in the case of gas-phase metal clusters, for which a number of "magic" clusters are known, i.e., clusters presenting a high stability (a differential formation energy much larger than that of neighboring clusters), as a rule associated with structural and/or electronic shell closure.[17−19] This is particular true for binary metal clusters, for which a wealth of magic clusters has been found in the past few years, both at the theoretical and experimental level.[20−24] It is thus of interest to ask whether magic clusters adsorbed on an oxide surface do exist, in particular a defected one.[25] In the present article, we explore such a possibility by studying Pd_1Ag_N ($N = 1-8$) clusters adsorbed on the F_s-defected MgO-(100) terrace. We show that Pd_1Ag_6 possesses the typical features of a magic cluster, i.e., a differential formation energy remarkably larger than that of neighboring clusters and a large HOMO−LUMO gap, signatures of both structural and electronic peculiar stability, simultaneously exhibiting a definite fluxional character. To our knowledge, this is the first example of a magic cluster on an oxide surface.

As for the choice of the system, we note that the type and abundance of defect sites on MgO(100) surfaces appreciably depends on the preparation method. Double vacancies are observed when MgO single crystals are cleaved under UHV.[26] Local defects in general seem to be nearly absent when thin MgO(100) films are grown by Mg reactive deposition on metal surfaces in an oxygen background and then annealed at high temperatures,[27] but both neutral and charged F_s-centers can be easily generated by postprocessing these films.[28] In particular, recent work has shown that F_s-defects (both neutral and charged) are common when thin MgO(100) films are subjected to electron bombardment and subsequent annealing,[29] and that these sites are trapping centers for the growth of metal clusters.[30] Probably due to the kinetics of the defect diffusion during annealing, F_s-centers are mostly found on kinks or steps rather than on regular terraces under such experimental conditions.[29,31] Our choice of an F_s-center on a MgO(100) terrace is due to technical reasons (i.e., to significantly speed-up calculations) and to our belief that anyway this is a reasonable structural model for metal clusters adsorbed on a locally defected MgO(100) surface. For example, for the Pd_1Ag_6 adsorbed magic cluster, we do not expect that its adhesion to the surface (which anyway is not the main driving force to its magicity) is spoiled by the change in the structural environment in passing from an F_s-center on a terrace to an F_s-center on a step, while the electron count (including the electrons in the vacancy) still holds in both cases

* Corresponding author. Address: IPCF - CNR, via G. Moruzzi 1, I-56124 Pisa, Italy. Tel: +39-050-3152447. Fax: +39-050-3152442. E-mail: fortunelli@ipcf.cnr.it. Home page: http://h2.ipcf.cnr.it/alex/af.html.

10.1021/jp072263m CCC: $37.00
Published on Web 07/11/2007

and thus should still produce an electronic shell closure. Charged defects are also possible both when MgO(100) surfaces are prepared by cleaving in UHV[26,32] or via reactive deposition,[29,31] but in this work we limit ourselves to the neutral F_s defect.

The choice of the Pd−Ag system is due to several reasons. First of all, a Pd atom interacts much more strongly than an Ag atom with the F_s-center (about 4 vs 1.7 eV).[5,9] Moreover, the surface energy of Pd is larger than that of Ag. It can thus be expected that Pd_1Ag_N clusters will adsorb on an F_s-center with the Pd atom pointing to the defect in a Pd-core/Ag-shell configuration. Second, the Pd atom in the gas phase has a $4d^{10}$-$5s^0$ electronic configuration, and about 0.5 eV is required to promote it to the $4d^95s^1$ state. This can give rise to peculiar electronic bi-stability effects when the Pd atom interacts with Ag clusters and the F_s-center. Third, due to the weak bonding in the Pd_2 dimer (related to the mentioned $4d^{10}5s^0$ configuration of the gas-phase Pd atom), the Pd dimerization energy on the F_s-center is very small,[5,33] and one can think of exploiting this in MBE experiments through a mechanism of sequential deposition, first saturating the F_s-defects with Pd atoms before depositing Ag atoms on top of these "saturated" defects. This suggests an explicit synthetic route to Pd_1Ag_N clusters which could be exploited experimentally. An alternative route would pass through the deposition of mass-selected binary clusters.[34] Finally, the Pd−Ag system is completely miscible in the bulk, and Pd−Ag alloys are known to exhibit peculiar properties, being for example commonly used in catalytic applications, see, e.g., ref[35] In this connection, it can be added that magic binary clusters have been suggested to possess interesting catalytic properties.[36]

Results and Discussion

The search for the lowest-energy structures of Ag−Pd clusters is performed via a density-functional basin-hopping (DF-BH) approach,[23,37] in which a basin-hopping (BH) algorithm[38−39] is implemented by determining energies and forces via a first-principles DF method. The DF-BH calculations were carried out using a Gaussian-type-orbital (GTO) basis set, the NWChem software,[40] and a cluster model for the MgO(100) surface[41] (the results have also been validated through a periodic boundary conditions approach,[12] as described in the Supporting Information). More computational details can be found in the Supporting Information. We note that our "static" results are only valid at 0 °K, even though the knowledge of the global minimum and low-energy isomers could provide information about relative populations as a function of temperature. For clusters up to $N = 4$ three DF-BH runs were performed, each composed of 15 Monte Carlo steps in the BH algorithm. For clusters with $N = 5-8$, five DF-BH runs were performed, each composed of 15 Monte Carlo steps. The starting configurations of each run were generated randomly in a sphere of radius 4 Å around the defect. Previous experience shows that such an approach is adequate to single out the global minimum in this size range. To our knowledge, this is the first time that a DF-BH approach is applied to binary metal clusters adsorbed on a (defected) surface. The DF-BH approach is useful to sample the potential energy surface of these complicated systems in which biased searches easily miss the global minimum already for small sizes.

It is convenient to define five quantities: (i) the adhesion energy (E_{adh}), calculated by subtracting the energy of the oxide surface and of the metal cluster, both frozen in their interacting configuration, from the value of the total energy of the system, and by taking the absolute value; (ii) the binding energy of the metal cluster (E_{met}), calculated by subtracting the energy of the isolated metal atoms from the total energy of the metal cluster in its interacting configuration, and by taking the absolute value; (iii) the metal cluster distortion energy (E_{dist}), which corresponds to the difference between the energy of the metal cluster in the configuration interacting with the surface minus the energy of the cluster in its lowest-energy gas-phase configuration; (iv) the total binding energy (E_{bnd}), which is the sum of the binding energy of the metal cluster and of the adhesion energy ($E_{bnd} = E_{met} + E_{adh}$); and (v) the incremental formation energy, defined as the energy gain (absolute value) for the addition of an Ag atom to a Pd_1Ag_{N-1} cluster, i.e., $E_{bnd}(N) - E_{bnd}(N-1)$. In Table 1 we report all these energy quantities for the adsorbed Pd_1Ag_N clusters obtained using a GTO basis set, the NWChem software,[40] and a cluster model for the MgO(100) surface. The total binding energy for the gas-phase clusters can be easily obtained by summing $E_{met} + E_{dist}$.

TABLE 1: Energetic Quantities (see Text for Their Definition) for Pd_1Ag_N Clusters Adsorbed on the F_s-Defected MgO(100) Surface Obtained Using GTO Basis Set and the NWChem Software[40] [a]

cluster	E_{adh}	E_{met}	E_{dist}	E_{bnd}	$E_{bnd}(N) - E_{bnd}(N-1)$
Pd_1Ag_1	3.48	1.50	0.05	4.98	1.08
Pd_1Ag_2	3.35	3.60	0.18	6.95	1.97
Pd_1Ag_3	3.21	5.20	0.03	8.41	1.46
Pd_1Ag_4	3.85	6.85	0.50	10.70	2.29
Pd_1Ag_5	3.64	8.83	0.22	12.47	1.77
Pd_1Ag_6	3.63	11.47	0.14	15.10	2.63
Pd_1Ag_7	3.53	12.99	0.40	16.52	1.42
Pd_1Ag_8	4.26	14.34	1.32	18.60	2.08

[a] Energies in eV.

Gas-Phase Clusters. The structures of the predicted global minima for Pd_1Ag_N clusters in the gas-phase are shown in Figure 1. The corresponding energy quantities can be derived from Table 1, with the incremental formation energy further displayed in Figure 3a. An inspection of Figure 1 shows a crossover between planar configurations, which are the predicted global minima up to Pd_1Ag_4, and compact, 5-fold symmetric configurations (pieces of an incomplete 13-atoms icosahedron), which are the predicted global minima for Pd_1Ag_7 and Pd_1Ag_8, and (presumably) larger clusters. This is in line with expectations based on previous experience, e.g., pure Ag clusters.[42−44] One important remark is however in order. While the ground state of Pd_1Ag_5 is already compact, that of Pd_1Ag_6 is planar, with the compact configuration (also shown in Figure 1) showing up as a first excited-state higher in energy by only 0.15 eV. The reason of this behavior lies in the electronic configuration bistability of the Pd atom and a peculiar electronic shell closure. We recall that the electronic ground-state configuration of a Pd single atom is $4d^{10}\ 5s^0$, with a $4d^95s^1$ state lying 0.5 eV higher in energy. When the Pd atom combines with Ag_N clusters, with N being even (and thus $S = 0$), it essentially keeps its $4d^{10}$ state, accepting electronic density from the Ag_N systems into its empty 5s orbital. The conduction electron count for Pd_1Ag_6 is thus 6, and corresponds to a magic number for the 2D jellium model.[24] This stabilizes the highly symmetric planar configuration, with a HOMO−LUMO gap of 1.5 eV, with respect to the compact configuration (a pentagonal bipyramid), with a HOMO−LUMO gap of 1.1 eV, thus making the former the ground-state for Pd_1Ag_6. Viceversa, when a Pd atom combines with an odd-numbered (and thus unpaired spin) Ag_N cluster, the promotion energy of a Pd d-electron to the conduction band is compensated by the formation of the metallic bond, and the unpaired spin remains essentially localized on the Pd d-system (as can be easily checked from electron spin density plots). The results displayed in Figure 3a further confirm this analysis. One

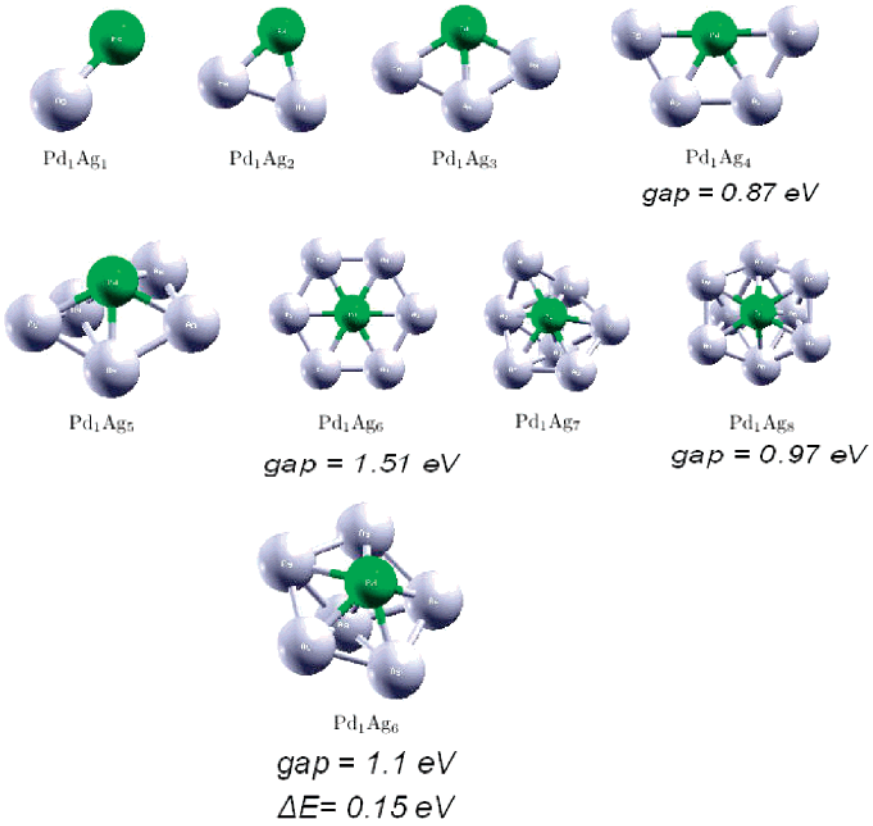

Figure 1. Predicted global minima of Pd_1Ag_N clusters in the gas phase. For Pd_1Ag_6, the first excited state (pentagonal bipyramid) is also shown, together with its excitation energy (ΔE). For $N = 4$, 6, 8 (closed shell systems), the HOMO−LUMO gas is reported.

observes the usual odd−even oscillation of Ag_N clusters,[16,43−44] further enhanced by the $4d^{10}\ 5s^0 \rightarrow 4d^95s^1$ promotion energy of the Pd atom. The fact that planar Pd_1Ag_6 achieves electronic shell closure in a region in which compact arrangements are already favored makes that its structural stability is not dramatically superior to that of the neighboring clusters. In passing, it can be noted that, based on the spherical jellium model, we would expect an electronic shell closure for Pd_1Ag_8. However, similarly to pure Ag_8,[16,43] this cluster does not exhibit a remarkable stability, due to the fact that the valence 5s orbital of the silver atom is too diffuse to fit the Ag−Ag interatomic distances, and the energy stabilization associated with the jellium shell closure is frustrated by a destructive interference of the electronic wavefunction.[45]

The issue of the fluxional character of the clusters deserves a separate comment. Our DF-BH search, in fact, generates not only a putative global minimum, but also a series of low-energy excited states. While an accurate description of these states would require longer and more numerous DF-BH runs, it is interesting to observe that we were able to identify for each size several candidates, often belonging to the same structural family, lying only 0.1−0.3 eV higher than the ground-state. The existence of these low-lying excited states, which can presumably be easily interconverted, makes gas-phase Pd_1Ag_N clusters highly fluxional, a phenomenon common for small metal clusters in the absence of peculiar directionality or electronic effects.[45]

Adsorbed Clusters. The structures of the predicted global minima for Pd_1Ag_N clusters adsorbed on the F_s-defected surface are shown in Figure 2. Note that the MgO system shown in this figure corresponds to the smaller of the two MgO systems employed in the calculations, and that for metal clusters larger than Pd_1Ag_4 a bigger MgO system was used, as detailed in the Supporting Information. The corresponding energy quantities are reported in Table 1, with the incremental formation energy further displayed in Figure 3b. First, we observe that the atom directly bound to the defect is always a Pd atom, in line with the expectations discussed above. We tried to locally optimize selected configurations starting from the ones reported in Figure 2 and switching a Pd and an Ag atom, but this always increased abnormally the energy or resulted in a collapse back to a "regular" F_s/Pd/Ag_N arrangement. The second point to be observed is that the transition from planar to 5-fold symmetric configurations occurs at Pd_1Ag_5 instead of Pd_1Ag_7 as in the gas-phase. In other words, Pd_1Ag6 is not "re-entrant" anymore, and the compact, pentagonal bipyramid arrangement lies much lower in energy than any planar or quasi-planar configurations. Planar configurations are still favored for adsorbed clusters up to Pd_1Ag_4 because they can arrange on the surface without any excessive distortion and moreover—by orienting the cluster plane perpendicular to the surface—take advantage of the "metal-on-top" effect.[12] Larger Pd_1Ag_N clusters ($N = 5-8$) then grow according to compact structures exhibiting a pentagonal bipyramid motif, i.e., they correspond to fragments of the 13-atom icosahedron for Pd_1Ag_N, $N = 5-7$ (with the Pd atom occupying the center of the icosahedron), or a fragment of the 13-atoms icosahedron plus an external atom on a (111) hcp hollow site for Pd_1Ag_8. With the exception of Pd_1Ag_8, these structures thus resemble the corresponding lowest-energy 5-fold symmetric arrangements in the gas-phase.

Moreover, Figure 3b shows that the odd−even alternation is confirmed and even enhanced for the adsorbed clusters. In analogy with the gas-phase, the N-even Pd_1Ag_N clusters have a closed-shell electronic configuration, with a Pd atom essentially in a $4d^{10}\ 5s^0$ state, and thus somewhat lengthened Pd−Ag distances which better match the requisite of double frustration, whereas those with N odd are spin 1/2 systems in which the spin density exhibits appreciable components on the Pd atom, as it can be checked from electron spin density plots and could

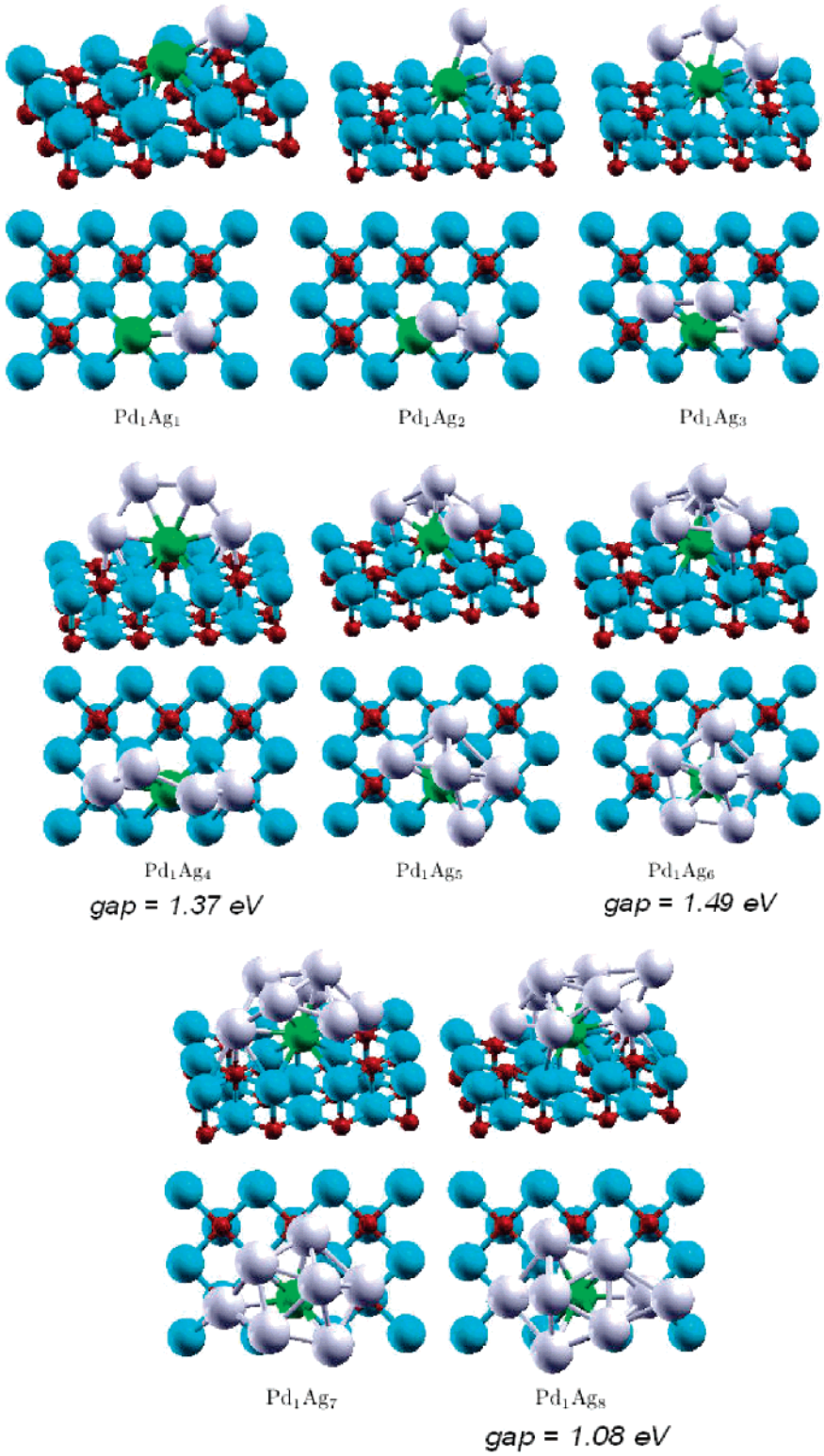

Figure 2. Predicted global minima of Pd_1Ag_N clusters adsorbed on the F_s-defected MgO(100) surface, as side and top views. For $N = 4, 6, 8$ (closed shell systems), the HOMO−LUMO gas is also reported.

be experimentally verified by EPR measurements.[29] This further destabilizes the N-odd clusters, in particular Pd_1Ag_1 and Pd_1Ag_7: it is known in fact that the interaction with the surface in general tend to quench the electron spin of the metal atoms.[6,13]

The most interesting observation is however that Pd_1Ag_6 adsorbed on the defect presents a remarkable structural stability, much larger than that of the neighboring clusters. In fact, it exhibits at the same time the highest incremental formation energy (2.63 vs 2.29 eV for Pd_1Ag_4) and the lowest incremental formation energy for the successive $N + 1$ cluster (1.42 vs 1.46 eV for Pd_1Ag_3). The pentagonal bipyramid configuration of Pd_1Ag_6, which was already stable in the gas-phase with respect to neighboring clusters and only 0.15 eV higher than the planar hexagonal global minimum, manages to achieve a fair adhesion to the defected surface by pointing the Pd atom toward the vacancy and adhering with its 5-fold symmetric "crown" to the potential energy well created by the defect.[13,14] In comparison, Pd_1Ag_8 is strongly disfavored by the need to

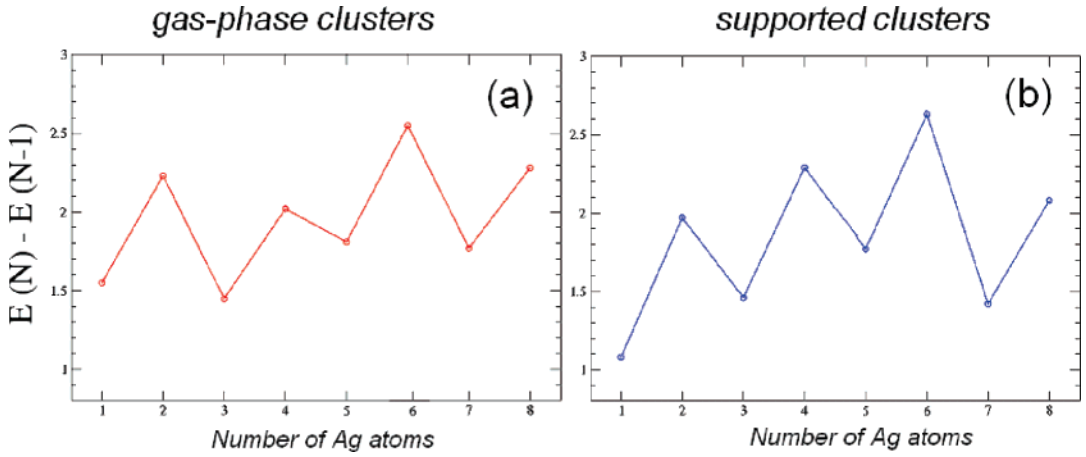

Figure 3. Plot of the incremental formation energy, $E_{bnd}(N) - E_{bnd}(N-1)$, for Pd_1Ag_N clusters: (a) in the gas phase, and (b) adsorbed on the F_s-defected MgO(100) surface.

deform to an asymmetric structure to better adhere to the surface, thus presenting a large metal distortion energy (E_{dist}) which appreciably decreases its stability. Moreover, what makes Pd_1Ag_6 stick out even more in the plot of Figure 3b is an electronic shell closure effect. The HOMO−LUMO gap for this cluster is in fact 1.49 eV, i.e., appreciably larger than that of the pentagonal bipyramid in the gas phase and comparable to the gas-phase planar hexagon. This can be rationalized by thinking that the two electrons in the cavity are strongly involved in the metal-surface interaction (see also the discussion about charge-transfer effects below),[7,8] so that the conduction electron count for Pd_1Ag_6 amounts to 8, which is a classical magic number for the spherical jellium model (as well as many other models).

Finally, the fluxional character observed in the gas-phase is kept, and even enhanced, for the adsorbed clusters, which may be important for catalytic activity.[46] The difference in energy between the putative global minimum and the first excited-state is always of the order of 0.1 − 0.3 eV. This also holds for Pd_1Ag_6, for which we were able to single out two low-lying excited states with excitation energies in the range 0.1−0.3 eV. In this connection, it is important to underline that these low-lying isomers also exhibit a large HOMO−LUMO gap, in the range 1.4−1.5 eV, whereas the first excited-state with a smaller HOMO−LUMO gap (about 0.7 eV) lies much higher in energy, about 1.4 eV higher than the ground-state. For Pd_1Ag_6 we thus encounter the peculiar situation of a cluster characterized by a substantial structural stability (structural magicity), which is simultaneously fluxional, i.e., with several low-lying excited states easily interconverted among each other, and electronically "hard" (electronic magicity, which corresponds to a large HOMO−LUMO gap) in both the ground-state and the low-lying excited states.

In connection with the catalytic activity of metal clusters, it is interesting to analyze in more detail the issue of the charge transfer between the electron pair in the vacancy and the metal clusters. A useful indicator of this effect can be given by the core level shift of the 4s orbital of the Pd and Ag atoms. In the adsorbed Pd_1Ag_6 cluster, for example, we find a core level shift of −0.5 and ∼−1.0 eV for the Pd atom and for the Ag atoms, respectively. These values can be compared with the value of +0.7 ÷ 0.9 eV, which is the core level shift of a single Pd atom on an oxygen site of the MgO(100) regular surface, while for a Pd atom on a magnesium site negligible (∼0.1 eV) values were found.[47] It can be noted that the direction of the charge transfer is of opposite sign in the case of Pd−Ag clusters adsorbed on the F_s center and of a Pd atom adsorbed on the regular surface, but the absolute values are similar, implying a quantitatively comparable (and not dramatic) size of the charge-transfer effect, at variance with the estimates for the case of gold clusters adsorbed on the F_s center.

Conclusions

The structure of Pd_1Ag_N clusters ($N = 1-8$), both in the gas phase and adsorbed on an F_s-center of an MgO(100) terrace, is investigated via a density-functional basin-hopping (DF-BH) approach. A structural transition from planar to noncrystalline 5-fold symmetric configurations is found for both free and adsorbed clusters in this size range. In analogy with gold and silver pure cases, the presence of the F_s-center causes the Pd−Ag clusters to be highly fluxional with the lowest-energy isomers lying at 0.1−0.3 eV above the global minimum. In addition, Pd_1Ag_6 is found to be a magic cluster, exhibiting a large HOMO−LUMO gap (both in the gas-phase and adsorbed on the defect) and a peculiar structural stability (when adsorbed on the defect) with respect to neighboring clusters. To our knowledge, this is the first example of a magic metal cluster on an oxide surface. This is rationalized in terms of an electronic shell-closure, involving also the electrons trapped in the oxygen vacancy, coupled with a good adhesion to the defected surface. Peculiarly, the low-energy Pd_1Ag_6 isomers (excitation energies around 0.1−0.3 eV) adsorbed on the F_s-center also exhibit a large HOMO−LUMO gap. An explicit synthetic route to the Pd_1Ag_6 cluster is proposed, passing through the sequential deposition of Pd and Ag atoms (exploiting the unfavorable dimerization of Pd on the F_s-center) or the deposition of mass-selected binary clusters (the latter is the more viable as the Pd_1Ag_6 cluster is magic in the gas phase, too). These features are expected to bring about promising consequences on the properties of this cluster, since it has been suggested, for example, that magic clusters can exhibit interesting catalytic properties.[36] Moreover, also the transition from planar to compact configurations is expected to appreciably modify their catalytic properties, such as the interaction of Pd_1Ag_N clusters with gases such as O_2 and CO.

Acknowledgment. This work was supported by the Italian CNR for the project SSATMN within the framework of the ESF EUROCORES SONS, and by the European Community Sixth Framework Program for the STREP Project GSOMEN. Part of the calculations have been performed at the Cineca Supercomputing Center within an agreement with Italian CNR-INFM.

Supporting Information Available: Choice of the cluster model for describing the MgO system, computational details such as GTO basis sets for the description of the molecular orbitals and charge density, effective core potentials, and numerical parameters for the Plane Wave basis set calculations. This material is available free of charge via the Internet at http://pubs.acs.org.

References and Notes

(1) Campbell, C. T. *Surf. Sci. Rep*. **1997**, *27*, 1.
(2) Henry, C. R. *Surf. Sci. Rep.* **1998**, *31*, 235.
(3) Freund, H. J. *Surf. Sci.* **2002**, *500*, 271.
(4) Robach, O.; Renaud, G.; Barbier, A. *Surf. Sci.* **1998**, *401*, 227.
(5) Bogicevic, A.; Jennison, D. R. *Surf. Sci.* **2002**, *515*, L481.
(6) Markovits, A.; Paniagua, J. C.; Lopez, N.; Minot, C.; Illas, F. *Phys. Rev. B* **2003**, *67*, 115417.
(7) A. Del Vitto A.; Pacchioni, G.; Delbecq, F.; Sautet, P. *J. Phys. Chem. B* **2005**, *109*, 8040.
(8) Yang, Z.; Wu, R.; Zhang, Q.; Goodman, D. W. *Phys. Rev. B* **2002**, *65*, 155407.
(9) Neyman, K. M.; Inntam, C.; Matveev, A. V.; Nasluzov, V. A.; Rosch, N. *J. Am. Chem. Soc.* **2005**, *127*, 11652.
(10) Yoon, B. Häkkinen, H.; Landman, U.; Wörz, A. S.; Antonietti, J. M.; Abbet, S.; Judai, K.; Heiz, U. *Science* **2005**, *307*, 403.
(11) Molina, L. M.; Hammer, B. *Appl. Catal., A* **2005**, *291*, 21.
(12) Barcaro, G.; Fortunelli, A. *J. Chem. Theory Comput.* **2005**, *1*, 972.
(13) Moseler, H.; Häkkinen, H.; Landman, U. *Phys. Rev. Lett.* **2002**, *89*, 176103.
(14) Barcaro, G.; Fortunelli, A. *J. Phys. Chem. B* **2006**, *110*, 21021.
(15) Yan, Z.; Chinta, S.; Mohamed, A. A.; Fackler, J. P., Jr; Goodman, D. W. *J. Am. Chem. Soc.* **2005**, *127*, 1604.
(16) Barcaro, G.; Aprà, E.; Fortunelli, A. *Chem.—Eur. J.* [Early online access]. DOI: 10.1002/Chem.200601796.
(17) Li, J.; Li, X.; Zhai, H.-J.; Wang, L.-S. *Science* **2003**, *299*, 864.
(18) Cui, L.-F.; Huang, X.; Wang, L.-M.; Li, J.; Wang, L.-S. *J. Phys. Chem. A* **2006**, *110*, 10169.
(19) Chen, Z.; Neukermans, S.; Wang, X.; Janssens, E.; Zhou, Z.; Silverans, R. E.; King, R. B.; von Ragué Schleyer, P.; Lievens, P. *J. Am. Chem. Soc.* **2006**, *128*, 12829.
(20) Rossi, G.; Mottet, C.; Fortunelli, A.; Baletto, F.; Ferrando, R. *Phys. Rev. Lett*. **2004**, *93*, 105503.
(21) Pyykko, P.; Runeberg, N. *Ang. Chem. Int. Ed*. **2002**, *41*, 2174.
(22) Li, X.; Kiran, B.; Li, J.; Zhai, H.-J.; Wang, L.-S. *Ang. Chem., Int. Ed.* **2002**, *41*, 4786.
(23) Gao, Y.; Bulusu, S.; Zeng, X. C. *J. Am. Chem. Soc.* **2005**, *127*, 15680.
(24) Janssens, E.; Tanaka, H.; Neukermans, S.; Silverans, R. E.; Lievens, P. *New J. Phys.* **2003**, *5*, 46.
(25) Goniakowski, J.; Mottet, C. *J. Cryst. Growth* **2005**, *275*, 29.
(26) Barth, C.; Henry, C. R. *Phys. Rev. Lett*. **2003**, *91*, 196102.
(27) Wendt, S.; Kim, Y. D.; Goodman, D. W. *Prog. Surf. Sci.* **2003**, *74*, 141.
(28) Kolmakov, A.; Stultz, J.; Goodman, D. W. *J. Chem. Phys.* **2000**, *113*, 7564.
(29) Sterrer, M.; Fischbach, E.; Risse, T.; Freund, H. J. *Phys. Rev. Lett*. **2005**, *94*, 186101.
(30) Sterrer, M.; Yulikov, M.; Fischbach, E.; Heyde, M.; Rust, H. P.; Pacchioni, G.; Risse, T.; Freund, H. J. *Angew. Chem., Int. Ed.* **2006**, *45*, 2630.
(31) Chiesa, M.; Paganini, M. Giamello, C.; Murphy, E.; Di Valentin, D. M.; C. Pacchioni, G. *Acc. Chem. Res.* **2006**, *39*, 861.
(32) Barth, C.; Claeys, C.; Henry, C. R. *Rev. Sci. Instrum*. **2005**, *76*, 083907.
(33) Giordano, L.; Di Valentin, C.; Goniakowski, J.; Pacchioni, G. *Phys. Rev. Lett*. **2004**, *92*, 096105.
(34) Judai, K.; Abbet, S.; Worz, A. S.; Heiz, U.; Henry, C. R. *J. Am. Chem. Soc.* **2004**, *126*, 2732.
(35) Wilhite, B. A.; Weiss, S. E.; Ying, J. Y.; Schmidt, M. A.; Jensen, K. F. *Adv. Mater.* **2006**, *18*, 1701.
(36) Graciani, J.; Oviedo, J.; Sanz, F. *J. Phys. Chem. B* **2006**, *110*, 1160.
(37) E. Aprà, R. Ferrando, A. Fortunelli, *Phys. Rev. B* **2006**, *73*, 205414.
(38) Li, Z.; Scheraga, H. A. *Proc. Natl. Acad. Sci. U.S.A.* **1987**, *84*, 6611.
(39) Wales, D. J.; Scheraga, H. A. *Science* **1999**, *285*, 1368.
(40) Kendall, R. A.; Aprà, E.; Bernholdt, D. E.; Bylaska, E. J.; Dupuis, M.; Fann, G. I.; Harrison, R. J.; Ju, J.; Nichols, J. A.; Nieplocha, J.; Straatsma, T. P.; Windus, T. L.; Wong, A. T. *Comp. Phys. Commun.* **2000**, *128*, 260.
(41) Matveev, A. V.; Neyman, K. M.; Yudanov, I. V.; Rösch, N. *Surf. Sci.* **1999**, *426*, 123.
(42) Bonacic-Koutecky, V.; Cespiva, L.; Fantucci, P.; Koutecky, J. *J. Chem. Phys*. **1993**, *98*, 7981.
(43) Fournier, R. *J. Chem. Phys.* **2001**, *115*, 2165.
(44) Fernández, E. M.; Soler, J. M.; Garzón, I. L.; Balbás, L. C. *Phys. Rev. B* **2004**, *70*, 165403.
(45) Ferrando, R.; Fortunelli, A.; Rossi, G. *Phys. Rev. B* **2005**, *72*, 085449.
(46) Häkkinen, H.; Abbet, S.; Sanchez, A.; Heiz, U.; Landman, U. *Angew. Chem., Int. Ed.* **2003**, *42*, 1297.
(47) Neyman, K. M.; Vent, S.; Rösch, N.; Pacchioni, G. *Top. Catal.* **1999**, *9*, 153.

Magic silver cluster on a MgO(100) terrace with defects

Giovanni Barcaro and Alessandro Fortunelli*
Molecular Modeling Laboratory, IPCF-CNR, Via G. Moruzzi 1, Pisa, I56124, Italy
(Received 24 August 2007; revised manuscript received 14 September 2007; published 11 October 2007)

The structure and energetics of Ag_N clusters ($N=2-10$) adsorbed on a double vacancy (DV) neutral defect of a MgO(100) terrace are investigated via a density-functional basin-hopping approach. It is found that Ag_8 is a surface magic cluster from both electronic and structural points of view, i.e., it exhibits enhanced stability with respect to neighboring sizes and a large highest occupied molecular orbital–lowest unoccupied molecular orbital gap. The possibility of synthesizing monodisperse Ag_8/DV/MgO(100) clusters is discussed. The first ionization potential, the electron affinity, and the interaction energies with atomic and molecular oxygen are evaluated for the adsorbed Ag clusters, showing that Ag_8 exhibits appreciable differences in its electronic and chemical properties with respect to neighboring sizes.

DOI: 10.1103/PhysRevB.76.165412 PACS number(s): 68.43.Hn, 61.46.Bc, 61.46.Df, 68.43.Bc

I. INTRODUCTION

Magic metal clusters are aggregates of metal atoms which possess peculiar stability due to electronic and/or structural shell closure. After their theoretical prediction[1] and experimental discovery as peaks of unusual abundance in the mass spectra of gas-aggregated alkali metal vapors,[2–4] many examples of gas-phase magic clusters have been experimentally discovered (see, e.g., Refs. 5–7) or theoretically predicted (see, e.g., Refs. 8 and 9). The jellium model or one of its variants,[10] i.e., a model in which nearly free valence electrons are assumed to move in a homogeneous ionic background, has often been invoked to rationalize electronic shell closure effects, with the predicted magic numbers of valence electrons for the spherical homogeneous jellium model at $N=2,8,20$, etc. For elements of the groups Ia and Ib, which can be considered as monovalent, these numbers immediately translate into the experimentally observed magic sizes, e.g., Ag_2, Ag_8, Ag_{20}, etc.[11] The great interest arisen by magic clusters lies in the expectation that their high stability favors the synthesis of fully monodisperse systems, while structural and electronic shell closures entail peculiar electron transport,[12] chemical,[13] optical,[14] etc., properties, which may lend themselves to technological applications. Prolonging the lifetime of gas-phase species by, e.g., adsorption onto a surface is a prerequisite for the exploitation of these properties in technological applications, and many efforts have been devoted in the search of surface magic clusters.[15] Many of the currently known examples concern metal-on-semiconductor[16,17] or metal-on-ionic-salt[18] systems, while metal-on-metal systems[19] are expected to be stable only at low temperatures due to a weaker strength of electronic and structural shell closures on metal surfaces.[15] Oxide surfaces are promising supports in this respect, as it has been shown that metal-surface interactions can be strong enough to preferentially orient cluster structures into configurations different from those prevailing in the gas phase already on regular surfaces,[20] and even more so on defected ones.[21–23] However, the same strength of the metal-surface interaction can represent a hindrance in the search for oxide surface magic clusters, as the magic character of gas-phase metal clusters can be lost once the clusters are adsorbed on the surface, due to structural frustration or electronic count mismatch. For example, it has recently been shown[23] that the adsorption of Ag_8 on an F_s-defected MgO(100) surface completely cancels its magic character. For these reasons, and also because of the great difficulties associated with the experimental and theoretical characterization of such systems, only one metal-on-oxide magic cluster has been predicted[24] until now.

In this work, the adsorption of small Ag_N ($N=2-10$) clusters on a simple but fully realistic system—a MgO(100) terrace exhibiting a double vacancy (DV) neutral local defect—is investigated, and it is shown that the cluster–defected-surface interaction strongly reinforces the magic character of Ag_8, thus producing a system with peculiar chemical and electronic properties. The choice of a DV-defected MgO(100) terrace—i.e., a regular surface in which a MgO dimer in the [100] direction is removed—is justified by the fact that MgO(100) is one of the most studied oxide supports for the growth of model metal catalysts,[25,26] that Ag clusters diffuse rapidly on the regular surface[27,28] and are thus able to reach surface defects which act as strong trapping centers,[21] and that the DV is the most common neutral local defect on UHV-cleaved MgO(100) terraces.[29] The relative abundance of defects clearly depends on the preparation protocol of the surface. Other types of defects, such as oxygen vacancies (also called F_s centers) at low-coordinated terrace sites,[30] can be created by postprocessing MgO(100) films prepared via reactive deposition of Mg on a metal surface.[31]

II. COMPUTATIONAL APPROACH

The search for the lowest-energy structures of Ag_N clusters adsorbed on a DV-defected MgO(100) terrace was performed using a density-functional basin-hopping (DF-BH) approach,[9,32] which combines the basin-hopping algorithm[33] for the exploration of the potential energy surface with a first-principles DF method for the calculation of energies and forces. Each BH run starts with a randomly chosen atomic configuration and is composed of a given number of Monte Carlo steps. In each of these, the starting configuration is first locally optimized to obtain an energy E_1, then subjected to a

random displacement of all the atoms up to ±1 Å in each Cartesian coordinates, and finally locally optimized to obtain a new energy E_2. If $\exp[(E_1-E_2)/k_BT]>\text{rndm}$, where rndm is a random number (Metropolis criterion), the new configuration is accepted (otherwise the old configuration is kept), and the process is iterated. For each size, we performed five BH runs, each one composed of 15–20 Monte Carlo steps, using a value of 0.5 eV as k_BT in the Metropolis criterion. Previous experience[23] showed us that this is sufficient to single out the global minimum for absorbed clusters of this size, while it is well known that the BH approach is more efficient as a search algorithm than other techniques such as simulated annealing[33] (in which the system often does not exit the starting structural basin in a time scale entailing a comparable computational effort). For example, in the present case, each BH run amounted to about 5000 elementary steps (each one composed of two energy and one electronic gradient evaluations). The MgO support was described via a $(Mg_{12}O_{12})$ cluster of C_s symmetry embedded in an array of ±2.0 a.u. point charges and repulsive pseudopotentials on the positive charges in direct contact with the cluster (see Ref. 23 for more details on the method). The atoms of the oxide cluster and the point charges were located at the lattice positions of the MgO rocksalt bulk structure at the experimental lattice constant of 4.208 Å. To account for the lattice relaxation around the vacancy, the coordinates of the three oxygens and of the three magnesium ions at the border of the cavity were relaxed as well as the coordinates of the atoms of the metal cluster, leaving the other atoms frozen. All the calculations were carried out with the DF module of the NWCHEM package[34] using the PW91 exchange-correlation (xc), functional[35] in the spin-unrestricted formalism. The geometry optimizations were performed by using Gaussian-type-orbital (GTO) basis sets of double-ζ quality,[36] while the total binding energy used in the Metropolis criterion was calculated via a single-point calculation on the relaxed geometry using a triple-ζ plus polarization basis set.[36] A 19-valence-electron effective-core potential was used for Ag.[37] Charge density fitting GTO basis sets were used to compute the Coulomb potential.[38] The calculations used a Gaussian-smearing technique with a smearing parameter of 0.001 a.u.

As in Ref. 23, the obtained results were validated by performing local geometry optimizations using the plane-wave self-consistent field (PWSCF) computational code,[39] employing the PBE xc functional[40] and ultrasoft pseudopotentials in the spin-unrestricted formalism. This plane-wave approach is periodic, employing a (3×3) unit cell, is essentially free of basis set limitations, and thus represents a good check of GTO calculations (even though it is more CPU demanding). The lowest-energy structures obtained with the cluster approach were considered, and a complete relaxation of the coordinates of the atoms of the metal cluster and of the first two layers of the oxide substrate was allowed in the periodic approach to check that structural relaxation around the DV was correctly described by the cluster approach. The results of the two approaches were in good agreement, with energy differences for the binding energies of the putative global minima of $Ag_{8,9}$ of the order of 0.1 eV (for Ag_{10}, a difference of 0.25 eV was found); only those obtained using the GTO basis set are thus reported in the following. It can be noted that the use of a (3×3) cell in the periodic approach is customary and can be justified in terms of cancellation of competing contributions.[41] However, to make sure that the results with the (3×3) cell are accurate also for the larger clusters, in the case of $Ag_{8,9,10}$, the putative global minima structures have also been locally optimized using a periodic approach and a (4×4) cell, finding binding energy differences smaller than 0.1 eV with respect to the (3×3) cell. The good agreement between GTO MgO-cluster and plane-wave periodic approaches is to be expected as (1) the back relaxation following the adsorption of metal atoms on the DV defect[42] much decreases the importance of surface rumpling around the defect,[43] (2) the size of the $(Mg_{12}O_{12})$ cluster is adequate, as compact configurations prevail for larger Ag clusters, so that each atom from the MgO(100) surface in contact with a metal atom is surrounded by first-neighbor surface atoms described at the quantum-mechanical level (thus satisfying the rule of thumb proposed in Ref. 23), and (3) the Ag-MgO interaction is small.

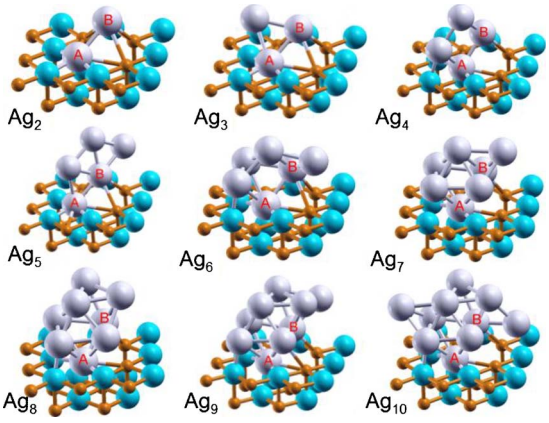

FIG. 1. (Color online) Schematic pictures of the putative global minima of Ag_N clusters adsorbed on the DV-defected MgO(100) surface. Silver atoms appear as gray (light) spheres, magnesium atoms as orange (small, dark) spheres, and oxygen atoms as light blue (big, dark) spheres. The silver atom occupying the empty Mg site is labeled with *A*, while the one above the empty O site is labeled with *B*.

III. RESULTS AND DISCUSSION

In Fig. 1, the lowest-energy structures of silver clusters adsorbed on the DV-defected MgO(100) are depicted. The structure of Ag_N $(N=2-3)$ clusters had been reported earlier.[42] It is interesting to observe that one Ag atom (indicated by *A* in the figure) fills up the empty Mg site of the DV, while a second Ag atom (indicated by *B*) is positioned outside the DV above the empty O site of the DV. Such an arrangement is always maintained in all the low-energy configurations generated by the DF-BH algorithm. In Table I, the distance of atom *A* from the empty magnesium site and the height of atom *B* above the oxide surface are reported. Apart from slight odd-even oscillations characterizing the smallest nuclearities, the structural parameters seem to stabilize

TABLE I. Structural parameters of the putative global minima of Ag_N clusters adsorbed on the DV-defected MgO(100) surface: distance of atom A from the empty magnesium site (d_A) and height of atom B above the oxide surface (h_B)—both in Å.

Cluster	d_A	h_B
Ag_2	0.55	2.00
Ag_3	0.43	2.02
Ag_4	0.52	2.25
Ag_5	0.43	1.96
Ag_6	0.53	2.18
Ag_7	0.59	2.27
Ag_8	0.59	2.20
Ag_9	0.57	2.15
Ag_{10}	0.55	2.18

around size 6, corresponding to the formation of a shell of neighbors around the dimeric pivotal silver unit filling the vacancy. An interesting similarity can be noted with the structure of the Ag_N clusters adsorbed on the F_s center[23] in that, once the first Ag atom has partially filled the DV, the next strongest interaction site is the one above the empty oxygen site of the vacancy, which has similar adsorption properties to the site above an F_s center, so that the metal growth follows a similar pattern. This, in turn, implies that the metal-surface interaction is characterized also in this case by a "double frustration" effect,[44] meaning that the metal growth around the local defect is frustrated not only horizontally by the mismatch of the lattice constant of the metal and of the oxide but also vertically by the difference in equilibrium lengths of the atoms adsorbed on the neighboring sites. The main difference with respect to the F_s case is that the valence electron count is different here, because the Ag atom inside the vacancy contributes with only one electron, whereas in the neutral F_s case, the defect contributes with two electrons. Apart from the transition from planar to compact configurations at $N=6$, which is expected for Ag clusters in this size range (see, e.g., Ref. 23 and references therein), one can observe that Ag_8 exhibits a more compact structure with respect to the neighboring sizes, with no Ag atoms hanging over the MgO surface, and this has consequences on its chemical properties, as discussed in the following.

In Fig. 2, the incremental formation energies, i.e., the differences $\Delta E_N = E(N) - E(N-1)$ for each N, where $E(N)$ is the total binding energy of the adsorbed Ag_N clusters, are shown as predicted by the DF-BH approach for both adsorbed and gas-phase[23] clusters. An inspection of this figure immediately conveys (a) even-odd oscillations in ΔE_N, which are typical of clusters of monovalent elements, (b) the fact that adsorbed Ag_8 sticks out as the cluster with the highest ΔE_N and the second lowest ΔE_{N+1} in this size range, and (c) the fact that the cluster–defected-surface interaction *strongly reinforces* the magic character of Ag_8. In other words, Ag_8 has the highest incremental formation energy, while Ag_9 has the second lowest incremental formation energy. Moreover, Ag_8 also has the largest highest occupied molecular orbital–

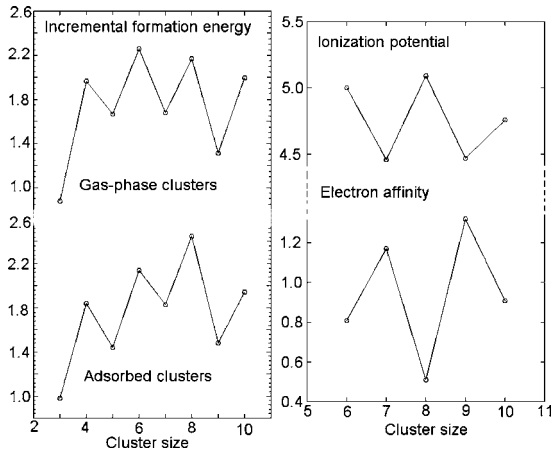

FIG. 2. Incremental formation energy of gas-phase and adsorbed Ag_N clusters, ionization potential, and electron affinity of adsorbed Ag_N clusters. All quantities in eV.

lowest unoccupied molecular orbital (HOMO-LUMO) gap, 1.7 eV (to put into perspective, comparable to that of fullerene), appreciably larger than that of Ag_4 (1.37 eV), Ag_6 (1.15 eV), and Ag_{10} (1.14 eV), and this should show up in its electronic response such as optical excitations, etc.

In Fig. 3, we show the structure of the lowest-lying isomers at each size, also reporting the energy differences with respect to the global minima. As can be noted from this figure, the fluxional character of Ag_8 is reduced with respect

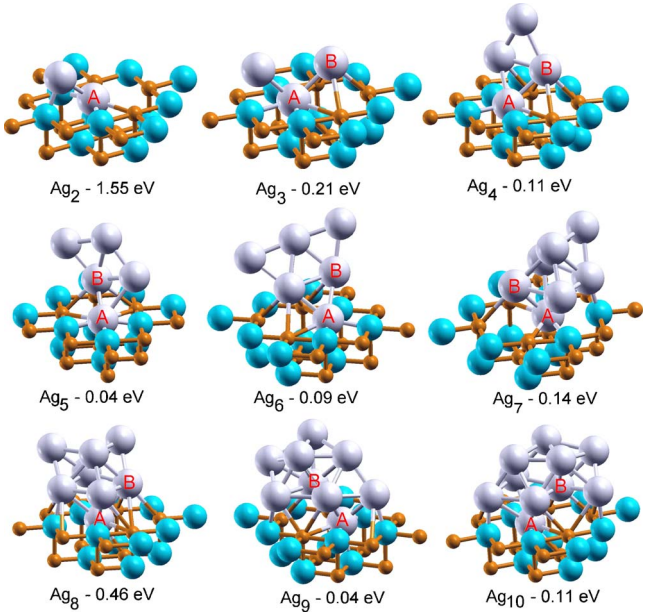

FIG. 3. (Color online) Schematic pictures of the lowest-lying isomers of Ag_N clusters adsorbed on the DV-defected MgO(100) surface with the corresponding energy differences with respect to global minima. Silver atoms appear as gray (light) spheres, magnesium atoms as orange (small, dark) spheres, and oxygen atoms as light blue (big, dark) spheres. The silver atom occupying the empty Mg site is labeled with A, while the one above the empty O site is labeled with B.

to neighboring sizes: the energy difference between the putative global minimum and the lowest-lying isomer is below 0.1 eV for Ag_6 and Ag_{10}, whereas in the case of Ag_8, it is 0.46 eV. Moreover, at this size, the lowest-lying isomer structure is obtained by a rearrangement of one of the uppermost Ag atoms, while the first isomer exhibiting a different structural motif is at 0.61 eV above the ground state. This could have an influence on the dynamic ("melting") behavior of Ag_8.[45] From Fig. 3, it can also be noted that the absorption of the second silver atom (the one indicated by *B* in Fig. 1) not on top of the empty oxygen site but above one of the oxygen atoms at the border of the vacancy as in Ag_2 corresponds to a huge decrease in the total binding energy (1.55 eV).

The magic character of Ag_8 suggests the possibility of selectively producing it via a properly devised synthetic method. Equilibrium conditions are not attained as a norm for metal-on-oxide molecular beam epitaxy growth.[25] In this perspective, especially important is not only the fact that the ΔE_N of Ag_8 is large (about 2.5 eV) but also that its ΔE_{N+1} is small, about 1.4 eV. As shown by test calculations, the energy barrier for the detachment of one Ag atom from Ag_9 is very close to the difference between initial and final states, i.e., ΔE_9 minus the adhesion of a single Ag atom to the regular surface [≈0.4 eV (Ref. 42)], so that the detachment energy barrier from Ag_9 is around 1 eV. If the deposition temperature is high enough and the deposition flux low enough, a condition of kinetic control can, in principle, be reached in which the metal cluster growth is stopped at Ag_8 (at high temperature and low flux, random nucleation on regular surface or weakly trapping defect sites is disfavored, as all atoms and small clusters are able to reach strongly trapping defect sites[28]). An alternative synthetic route passes through the deposition of size-selected gas-phase clusters.[46]

The peculiarity of the Ag_8/DV/MgO(100) cluster also shows up from an analysis of the adiabatic ionization energies and electron affinities for the adsorbed Ag_N clusters in Fig. 2. These values were obtained by locally relaxing the structures of Fig. 1 after removal or addition of one electron and then taking the corresponding energy differences.[49] From Fig. 2, one can see that Ag_8 has the highest (respectively, lowest) ionization potential (respectively, electron affinity) of the series, although such differences are not large, of the order of 0.1–0.3 eV. More marked differences are observed when the chemical behavior of the Ag_N clusters is investigated. We used a single oxygen atom or an O_2 molecule as chemical probes, and we studied their interaction with the adsorbed Ag_N clusters depicted in Fig. 1. For each cluster, O or O_2 were adsorbed on different sites of the cluster and local energy minimizations were performed, trying to find the optimal interaction site. The lowest-energy structures of the Ag_N/O and Ag_N/O_2 complexes are shown in Fig. 4, while the corresponding interaction energies are reported in Table II. From Table II, it can be seen that O binds preferentially to a triangular facet of the metal clusters, in agreement with the known behavior on crystal surfaces.[47] Moreover, the peculiarity of Ag_8 is apparent, as its reaction energy with O is more than 0.4 eV smaller than that of the other clusters (see Table II) and is due to both structural (shape of the cluster and exposed facets) and electronic effects. The results for the

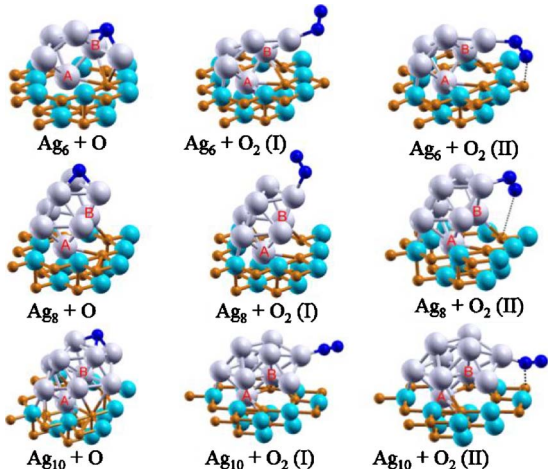

FIG. 4. (Color online) Interaction geometries of O and O_2 on Ag_N clusters. For O_2, two interaction modes are shown, mode (I) and mode (II), in which the O_2 molecule does or does not interact with the MgO surface, respectively. Silver atoms appear as gray (light) spheres, magnesium atoms as orange (small, dark) spheres, oxygen atoms of MgO as light blue (big, dark) spheres, and adsorbed oxygen atoms as dark blue (darkest) spheres. The silver atom occupying the empty Mg site is labeled with *A*, while the one above the empty O site is labeled with *B*. In interaction mode (II), a dotted line highlights the interaction of oxygens from the O_2 molecule with magnesium atoms at the surface.

interaction with O_2 are in line with these findings and present an additional structural effect. O_2, in fact, can adsorb on Ag_N essentially interacting through a single O atom, with the second O atom pointing away from the MgO surface (mode I) or with the second O atom pointing toward the surface and interacting with a Mg ion (mode II). Both interaction modes are possible for Ag_6, Ag_8, and Ag_{10}, but it is interesting to observe that in the case of Ag_6 and Ag_8, the interaction energy with O_2 is larger by ≈0.3–0.4 eV in interaction mode II with respect to interaction mode I, whereas in the case of Ag_8, modes I and II have practically the same interaction energy. This is due to the more compact structural arrangement of Ag_8, which does not present overhangs of metal atoms on the MgO(100) surface and, thus, does not favor the interaction of the O atom not directly bound to the metal cluster with the surface. This is interesting, as an interaction mode II connected with the presence of overhangs has been hypothesized to account for the catalytic activity of Au clusters.[48] Smaller interaction energies with incoming species can be useful when a fine tuning of the cluster catalytic activity is sought for.

TABLE II. Interaction energies (IE) in eV of adsorbed Ag_N clusters with O and O_2 (the latter according to modes I and II as explained in the text).

Cluster	Ag_N+O IE	Ag_N+O_2 IE (mode I)	Ag_N+O_2 IE (mode II)
Ag_6	4.09	0.65	1.00
Ag_8	3.34	0.48	0.49
Ag_{10}	3.78	0.82	1.20

IV. CONCLUSIONS

Surface magic clusters are clusters exhibiting enhanced stability on a particular surface. The structure and energetics of Ag_N clusters adsorbed on a neutral DV defect of a MgO(100) terrace are investigated using a DF-BH approach, and it is found that Ag_8 possesses the characteristics required for being such a cluster, having substantially larger stability and a larger HOMO-LUMO gap than neighboring sizes. These characteristics suggest that the selective synthesis of arrays of Ag_8/DV/MgO(100) clusters is, in principle, possible in properly chosen experimental conditions and makes that Ag_8 features the highest first ionization potential, the largest energy difference between the global minimum and the lowest-lying isomer, the lowest electron affinity, and the smallest interaction energies with atomic and molecular oxygen in the Ag_N (N=6–10) size range, thus being promising in terms of both electronic and chemical properties.

ACKNOWLEDGMENTS

We acknowledge financial support from the Italian CNR for the Project "(Supra-) Self-Assemblies of Transition Metal Nanoclusters," within the framework of the ESF EUROCORES SONS, and from the European Community Sixth Framework Project for the STREP Project "Growth and Supra-Organization of Transition and Noble Metal Nanoclusters" (Contract No. NMP-CT-2004-001594).

*fortunelli@ipcf.cnr.it

[1] W. Ekardt, Phys. Rev. B **29**, 1558 (1984).
[2] W. D. Knight, K. Clemenger, W. A. de Heer, W. A. Saunders, M. Y. Chou, and M. L. Cohen, Phys. Rev. Lett. **52**, 2141 (1984).
[3] J. Pedersen, S. Bjornholm, J. Borggreen, K. Hansen, T. P. Martin, and H. D. Rasmussen, Nature (London) **353**, 733 (1991).
[4] T. P. Martin, U. Naher, H. Schaber, and U. Zimmermann, J. Chem. Phys. **100**, 2322 (1994).
[5] Y. Yamada and A. W. Castleman, J. Chem. Phys. **97**, 4543 (1992).
[6] J. Li, X. Li, H. J. Zhai, and L. S. Wang, Science **299**, 864 (2003).
[7] Y. C. Bae, V. Kumar, H. Osanai, and Y. Kawazoe, Phys. Rev. B **72**, 125427 (2005).
[8] G. Rossi, A. Rapallo, C. Mottet, A. Fortunelli, F. Baletto, and R. Ferrando, Phys. Rev. Lett. **93**, 105503 (2004).
[9] Y. Gao, S. Bulusu, and X. C. Zheng, J. Am. Chem. Soc. **127**, 15680 (2005).
[10] W. A. deHeer, Rev. Mod. Phys. **65**, 611 (1993).
[11] E. Janssens, S. Neukermans, X. Wang, N. Veldeman, R. E. Silverans, and P. Lievens, Eur. Phys. J. D **34**, 23 (2005).
[12] Q. Wang, Q. Sun, Z. J. Yu, M. Sakurai, and Y. Kawazoe, Scr. Mater. **44**, 1959 (2001).
[13] J. Graciani, J. Oviedo, and J. F. Sanz, J. Phys. Chem. B **110**, 11600 (2006).
[14] K. Kreibig and M. Vollmer, *Optical Properties of Metal Clusters* (Springer, New York, 1995).
[15] Y. L. Wang and M. Y. Lai, J. Phys.: Condens. Matter **13**, R589 (2001).
[16] L. Vitali, M. G. Ramsey, and F. P. Netzer, Phys. Rev. Lett. **83**, 316 (1999).
[17] Y. P. Chiu, L. W. Huang, C. M. Wei, C. S. Chang, and T. T. Tsong, Phys. Rev. Lett. **97**, 165504 (2006).
[18] H. Hakkinen and M. Manninen, Phys. Rev. Lett. **76**, 1599 (1996).
[19] S. K. Nayak, P. Jena, V. S. Stepanyuk, W. Hergert, and K. Wildberger, Phys. Rev. B **56**, 6952 (1997).
[20] G. Barcaro, A. Fortunelli, G. Rossi, F. Nita, and R. Ferrando, Phys. Rev. Lett. **98**, 156101 (2007).
[21] M. Moseler, H. Hakkinen, and U. Landman, Phys. Rev. Lett. **89**, 176103 (2002).
[22] H. Hakkinen, S. Abbet, A. Sanchez, U. Heiz, and U. Landman, Angew. Chem., Int. Ed. **42**, 1433 (2003).
[23] G. Barcaro, E. Aprà, and A. Fortunelli, Chem.-Eur. J. **13**, 6408 (2007).
[24] G. Barcaro and A. Fortunelli, J. Phys. Chem. C. **111**, 11384 (2007).
[25] C. R. Henry, Surf. Sci. Rep. **31**, 235 (1998).
[26] H. J. Freund, Surf. Sci. **500**, 271 (2002).
[27] K. Højrup-Hansen, S. Ferrero, and C. R. Henry, Appl. Surf. Sci. **226**, 167 (2004).
[28] G. Barcaro and A. Fortunelli, New J. Phys. **9**, 22 (2007).
[29] C. Barth and C. R. Henry, Phys. Rev. Lett. **91**, 196102 (2003).
[30] S. Wendt, Y. D. Kim, and D. W. Goodman, Prog. Surf. Sci. **74**, 141 (2003).
[31] M. Sterrer, E. Fischbach, T. Risse, and H. J. Freund, Phys. Rev. Lett. **94**, 186101 (2005).
[32] E. Aprà, R. Ferrando, and A. Fortunelli, Phys. Rev. B **73**, 205414 (2006).
[33] D. J. Wales and H. A. Sheraga, Science **285**, 1368 (1999).
[34] R. A. Kendall *et al.*, Comput. Phys. Commun. **128**, 260 (2000).
[35] J. P. Perdew, J. A. Chevary, S. H. Vosko, K. A. Jackson, M. R. Pederson, D. J. Singh, and C. Fiolhais, Phys. Rev. B **46**, 6671 (1992).
[36] A. Schaefer, C. Huber, and R. Ahlrichs, J. Chem. Phys. **100**, 5829 (1994).
[37] D. Andrae, U. Haussermann, M. Dolg, H. Stoll, and H. Preuss, Theor. Chim. Acta **77**, 123 (1990).
[38] F. Weigend, M. Haser, H. Patzelt, and R. Ahlrichs, Chem. Phys. Lett. **294**, 143 (1998).
[39] S. Baroni, A. Del Corso, S. de Gironcoli, and P. Giannozzi, http://www.pwscf.org
[40] J. P. Perdew, K. Burke, and M. Ernzerhof, Phys. Rev. Lett. **77**, 3865 (1996).
[41] B. Ealet, J. Goniakowski, and F. Finocchi, Phys. Rev. B **69**, 195413 (2004).
[42] G. Barcaro and A. Fortunelli, J. Chem. Theory Comput. **1**, 972 (2005).
[43] L. Ojamäe and C. Pisani, J. Chem. Phys. **109**, 10984 (1998).
[44] G. Barcaro and A. Fortunelli, J. Phys. Chem. B **110**, 21021 (2006).
[45] H. Haberland, T. Hippler, J. Donges, O. Kostko, M. Schmidt, and B. von Issendorff, Phys. Rev. Lett. **94**, 035701 (2005).
[46] K. Judai, S. Abbet, A. S. Worz, U. Heiz, and C. R. Henry, J. Am.

Chem. Soc. **126**, 2732 (2004).
[47] A. Michaelides, K. Reuter, and M. Scheffler, J. Vac. Sci. Technol. A **23**, 1487 (2005).
[48] L. M. Molina and B. Hammer, Phys. Rev. B **69**, 155424 (2004).
[49] As a test of the quality of the theoretical approach, it can be mentioned that the predicted values of ionization potential and electron affinity of a Ag atom evaluated via a Δ(SCF) approach are 8.0 and 1.24 eV, respectively, to be compared with the experimental values of 7.6 and 1.31 eV.

Structural motifs, mixing, and segregation effects in 38-atom binary clusters

BorbonJCP2008

Lauro Oliver Paz-Borbón,[1] Roy L. Johnston,[1,a),b)] Giovanni Barcaro,[2] and Alessandro Fortunelli[2,a),c)]
[1]*School of Chemistry, University of Birmingham, Edgbaston, Birmingham B15 2TT, United Kingdom*
[2]*Molecular Modeling Laboratory, Istituto per i Processi Chimico-Fisici del Consiglio Nazionale delle Ricerche (IPCF-CNR), via G. Moruzzi 1, I-56124 Pisa, Italy*

(Received 16 November 2007; accepted 20 February 2008; published online 7 April 2008)

Thirty eight–atom binary clusters composed of elements from groups 10 and 11 of the Periodic Table mixing a second-row with a third-row transition metal (TM) (i.e., clusters composed of the four pairs: Pd–Pt, Ag–Au, Pd–Au, and Ag–Pt) are studied through a combined empirical-potential (EP)/density functional (DF) method. A "system comparison" approach is adopted in order to analyze a wide diversity of structural motifs, and the energy competition among different structural motifs is studied at the DF level for these systems, mainly focusing on the composition 24-14 (the first number refers to the second-row TM atom) but also considering selected motifs with compositions 19-19 (of interest for investigating surface segregation effects) and 32-6 (also 14-24 and 6-32 for the Pd–Au pair). The results confirm the EP predictions about the stability of crystalline structures at this size for the Au–Pd pair but with decahedral or mixed fivefold-symmetric/closed-packed structures in close competition with fcc motifs for the Ag–Au or Ag–Pt and Pd–Pt pairs, respectively. Overall, the EP description is found to be reasonably accurate for the Pd–Pt and Au–Pd pairs, whereas it is less reliable for the Ag–Au and Ag–Pt pairs due to electronic structure (charge transfer or directionality) effects. The driving force to core-shell chemical ordering is put on a quantitative basis, and surface segregation of the most cohesive element into the core is confirmed, with the exception of the Ag–Au pair for which charge transfer effects favor the segregation of Au to the surface of the clusters. © *2008 American Institute of Physics*. [DOI: 10.1063/1.2897435]

INTRODUCTION

Binary nanoalloys often present novel and interesting structures which are important when trying to understand their chemical and physical properties.[1] Density functional (DF) theory is the most convenient (and sometimes also the most accurate) approach to describe such effects. At present, a systematic search for global minimum (GM) structures for clusters involving more than 20 atoms is still extremely demanding for high-level calculations because of computation limitations in exploring vast areas of configuration space.[2–4] In the case of bimetallic clusters (A_mB_n), the search is even more complex due to the existence of homotops[5] (isomers with the same geometry and composition but with a different arrangement of the two types of atoms), and at the same time, more interesting as the greater structural freedom often translates into a substantial influence of alloying on the properties of the binary systems. Empirical potentials (EPs) have been developed to overcome the computational limitations presented by first-principle approaches. They are thought to be suitable for modeling noble and quasinoble metals but sometimes, electronic effects have been found to produce sizable changes.[2,6–8] It is, thus, important to check the predictions of EP using first-principles approaches. Combined DF-EP approaches are the only viable computational way to sort out the extremely expensive computational calculations for clusters containing more than 20 atoms and have been shown to be particularly efficient when coupled with structural recognition algorithms.[9,10] The need to explore a wide diversity of structural motifs to make the search of the GM successful has recently been underlined, and approaches such as system comparison[11] and hybrid genetic algorithm (GA) structural/basin-Hopping (BH) atom-exchange[12] among others have been proposed to enlarge the data set of structural candidates and sample more thoroughly the configurational space. For pure clusters, the competition between crystalline and fivefold-symmetric structural motifs (such as decahedra and icosahedra) has been traditionally analyzed,[13] finding that, in general, noncrystalline arrangements prevail at small sizes, whereas pieces of the bulk crystal progressively become dominant at larger sizes, with the crossover between these motifs[14] being directly related to the "stickiness"[15] of the metal-metal potential. An analysis in terms of structural families is particularly meaningful, as it allows one to roughly predict the order of stability among structural motifs on the basis of a minimal number of calculations. The set of competing structural families has been enlarged to include other possibilities, such as polyicosahedral (pIh) configurations,[15,16] which have been shown to be the GM at both EP and DF levels for several alloy systems involving (size-mismatched) second-row and first-row transition elements[17] but which have been predicted to be competitive

a)Authors to whom correspondence should be addressed.
b)Electronic mail: r.l.johnston@bham.ac.uk.
c)Electronic mail: fortunelli@ipcf.cnr.it.

at the EP level also for second-row/third-row pairs (see, e.g., Refs. 18 and 19 and the results depicted in Fig. 2 below). A more recent addition is represented by mixed fivefold-symmetric/close-packed motifs,[8,12,20] i.e., motifs exhibiting a close-packed core on which surface atoms grow according to fivefold symmetry axes, that in some cases realize an efficient compromise between the different tendencies of two metallic elements and have been predicted to be the lowest-energy structures at the DF level for, e.g., 34-atom Pd–Pt clusters over a wide composition range.[8]

In the present paper, we consider 38-atom binary clusters composed of elements from groups 10 and 11 of the periodic table obtained by combining a second-row with a third-row transition metal (TM), i.e., we consider the four binary TM pairs Pd–Pt, Ag–Au, Pd–Au, and Ag–Pt, and we try to extract useful structural information and insight into the modeling and design of the considered alloy systems from selected calculations combining EP and DF approaches.

Mixed alloys involving noble and quasinoble metals are interesting both for scientific reasons and in a number of applications, ranging from heterogeneous catalysis to optoelectronic devices.[1,21] Note that our set includes pairs with a practically zero (Pd–Pt, Ag–Au) or significant (Pd–Au, Ag–Pt) size mismatch, with a modest (Ag–Au, Pd–Au) or large (Ag–Pt, Pd–Pt) difference in the bulk cohesive energies and with differences in electronegativity ranging from large (Ag–Au) to negligible (Pd–Pt). The pure third-row TMs considered here are known to exhibit appreciable directionality effects (see, e.g., Refs. 2, 6, and 22) which are difficult to describe using empirical potentials but are here "diluted" by alloying with a second-row TM for which such effects are much less important. Au, especially, but also Pt and Pd possess a rather "sticky" interaction potential,[15] whereas this is less pronounced in the case of Ag. In short, this set allows us to explore in a systematic way a combination of different characteristics. We also observe that from an experimental point of view, mixing second- and third-row transition metals and the corresponding difference in atomic numbers make the investigation of segregation effects for these alloys easier using, e.g., x-ray spectroscopy, energy dispersive spectroscopy, and *Z*-contrast high-angle angular dark-field scanning transmission electron microscopy.[21]

Thirty-eight–atom clusters have been chosen for this study because 38 is a magic number for the truncated octahedral (TO) structure, which has fcc packing (the bulk crystalline structure for all of the metals considered here is fcc) and also for the pIh^6 structure (see below), and indeed, fragments of the fcc crystal or pIh structures are predicted to be the GM for 38-atom clusters by the EP.[18,19] We will, thus, be able to check whether these structures remain the lowest-energy ones at a higher level of theory or whether mixed fivefold-symmetric/close-packed or other structures can be competitive at this size and, thus, *a fortiori* in this size range for second-row/third-row transition element pairs in contrast with what is observed for first-row/second-row pairs.

We mainly focus here on the specific composition 24-14 (here and in the following, the first number always refers to the second-row TM atom and the second number to the third-row TM atom) but we also consider selected motifs at compositions 19-19 and 32-6. In addition, the compositions 14-24 and 6-32 are also considered for Pd–Au. The compositions 24-14 and 14-24 are chosen as they are predicted to be at or very close to the minimum in the mixing energy at the EP level (see below); i.e., they represent compositions at which the effect of alloying is at its maximum. Compositions 32-6 and 6-32 are included to sample the dependence of our results on this parameter, and 19-19 is of interest for investigating surface segregation effects. Note that 24-14 is also a magic number composition for TO and other structures, while 32-6 is a magic number for TO and pIh^6 structures.[18]

To study the energy competition between different structural families and to search for the lowest-energy structural motifs in 38-atom binary clusters, we use a system comparison approach.[9,11] In other words, we first perform systematic GA global optimization runs on the four TM pairs, we collect the lowest-energy structures (the putative GM and higher-energy isomers) for several compositions around 24-14, and we classify them into structural motifs. We then couple the GA structural search with a BH atom-exchange approach,[12] in which the putative GM candidates for the four TM pairs are subjected to BH-exchange-only calculations, in order to determine the optimal chemical ordering according to the EP. Finally, the lowest-energy configurations belonging to the different structural motifs so derived are subjected to local DF energy minimizations.

In a second step, the problem of the correct chemical ordering at the DF level is investigated in more detail. This is an important issue as it is known that surface segregation can influence the properties of nanoalloys.[1] The 19-19 composition is selected to investigate this issue as it allows one to compare the energies of configurations obtained by swapping the atomic positions of the two species in the cluster (passing, e.g., from a configuration in which *A* atoms are in the core and partly on the surface to a configuration in which the *B* atoms are in the core and partly on the surface). Selected structural motifs are considered and local energy optimizations are performed for both the structures with the chemical ordering obtained using the BH algorithm and those "inverted homotops" derived from the GM by swapping the positions of the two elements.[8] This allows one to obtain a quantitative estimate of the driving force to surface segregation at the DF level. It is found that the DF calculations confirm the EP predictions for the Pd–Pt, Ag–Pt, and Pd–Au pairs and that segregation effects in these cases are ruled by two factors: Maximization of the number of the strongest bonding interactions and minimization of cluster surface energy. However, for the Ag–Au pair, segregation of the heavier element (Au) to the surface is predicted by DF. This is counterintuitive, as Au has a larger surface energy than Ag. An analysis of the electronic wave function and of the one-electron energy levels clarifies that charging effects are the driving force for this segregation, based on the fact that Au is more electronegative than Ag, as observed in previous work.[23–26] For the other binary systems, charge transfer does not seem to play a significant role in directing segregation as electronegativity differences are smaller than for the Ag–Au case. Last, it is shown that directionality effects are also important for the Ag–Au and Ag-Pt pairs.

TABLE I. Gupta potential parameters used in this study (Refs. 10 and 21).

Parameters	Pd–Pd	Pt–Pt	Ag–Ag	Au–Au	Au–Au (in Ag–Au case only)	Ag–Au	Ag–Pt	Pd–Au	Pd–Pt
A (eV)	0.1746	0.2975	0.1031	0.2061	0.2096	0.1488	0.175	0.19	0.23
ζ (eV)	1.718	2.695	1.1895	1.790	1.8153	1.4874	1.79	1.75	2.2
p	10.867	10.612	10.85	10.229	10.139	10.494	10.73	10.54	10.74
q	3.742	4.004	3.18	4.036	4.033	3.607	3.57	3.89	3.87
r_0 (Å)	2.7485	2.7747	2.8921	2.884	2.885	2.8885	2.833	2.816	2.76

COMPUTATIONAL DETAILS

The empirical potential

We use the Gupta potential, as formulated by Cleri and Rosato,[27] to model the interatomic interactions. The Gupta potential is based on the second moment approximation to tight-binding theory and is constructed from an attractive many-body (V^m) term and a repulsive pair (V^r) term, obtained by summing over all N atoms,

$$V_{\text{clus}} = \sum_{i}^{N} [V^r(i) - V^m(i)], \tag{1}$$

where $V^r(i)$ and $V^m(i)$ are defined as

$$V^r(i) = \sum_{j \neq i}^{N} A(a,b) e^{(-p(a,b)(r_{ij}/r_0(a,b)-1))}, \tag{2}$$

$$V^m(i) = \left[\sum_{j \neq i}^{N} \zeta^2(a,b) e^{(-2q(a,b)(r_{ij}/r_0(a,b)-1))} \right]^{1/2}, \tag{3}$$

where a and b refer to the element type. In Eqs. (2) and (3), r_{ij} represents the distance between atoms i and j in the cluster. The parameters A, r_0, ζ, p, and q for the pure species are fitted to the experimental values of the cohesive energy, lattice parameters, and independent elastic constants for the reference crystal structure at 0 K. The Gupta potential parameters used in this study are listed in Table I.

The parameters for the heterogeneous interactions Pd–Pt, Ag–Pt, and Pd–Au were obtained as averages of the homonuclear parameters, as previously described for Pd–Pt.[28] The set of parameters for the Ag–Au case (including the parameters for the Au–Au interaction) have been fitted by Mottet.[11]

The genetic algorithm

The Birmingham cluster genetic algorithm (BCGA) code, which has been described elsewhere,[29] was used to find the GM on the potential energy surfaces of the investigated nanoalloy systems. The GA parameters adopted in this work were population size=40 clusters, crossover rate=0.8 (i.e., 32 offspring are produced per generation), crossover type =1-point weighted (the splice position is calculated based on the fitness values of the parents), selection=roulette (A random number r is generated in the range of 0.0–1.0; then a cluster is selected at random from the population. The cluster is accepted as a parent if the fitness is greater than the random number r), mutation rate=0.1, mutation type =mutate_move, number of generations=400, and number of GA runs for each composition=100. A large number of GA runs were performed due to the high number of homotops depending combinatorially on the composition.[5] For the worst case scenario, composition 19-19, we have $38!/(19)^2$, i.e., approximately 3.5×10^{10} homotops, although some of them may be symmetry equivalent. On the basis of previous experience,[29] we are confident that the present approach is able to find the GM of the potential energy surface of the investigated nanoalloy systems.

The basin-hopping algorithm

A more detailed homotop search was performed using a BH Monte-Carlo algorithm[30] which allows only atom exchange for a fixed structural configuration and composition. We carried out approximately 3000 Monte-Carlo steps, with a thermal energy k_BT of 0.02 eV. This low value is appropriate for performing a localized search of deep regions of the chosen structural funnel. We found that in some cases, the GA approach was not able to identify the most favorable chemical ordering, whereas this was easily found using the BH approach. This is in line with recent observations that the optimal strategy in configurational searches is to take initially only "structural" moves, and subsequently refine the lowest-energy structures via atom-exchange moves.[9,12,31]

Density Functional calculations

The DF calculations were performed using the NWCHEM 5.0 quantum chemistry package[32] and the Perdew–Wang exchange-correlation functional (PW91),[33] as in previous work.[8] Test calculations using other Perdew-Burke-Ernzerhof gradient-corrected exchange–correlation functionals produced qualitatively similar results (while hybrid functionals are not suitable for metallic systems[34]). Spherical Gaussian-type-orbital basis sets of double-zeta quality[35,36] were used for Pd $(7s6p5d)/[5s3p2d]$ Ag $(7s6p5d)/[5s3p2d]$ Pt $(7s6p5d)/[6s3p2d]$ and Au $(7s5p5d)/[6s3p2d]$ combined with effective core potentials.[37] Charge density fitting basis sets were used to speed up the evaluation of Coulombic contributions:[38] Pd $(8s7p6d5f4g)/[8s6p6d3f2g]$ Ag $(9s4p5d3f4g)/[7s4p4d3f2g]$ Pt $(9s4p3d3f4g)/[9s4p3d3f2g]$, and Au $(9s4p4d3f4g)/[8s4p3d3f2g]$. All the calculations were performed spin unrestricted, using a Gaussian smearing technique (with a smearing parameter of 1.36 eV) for the fractional occupation of the one-electron

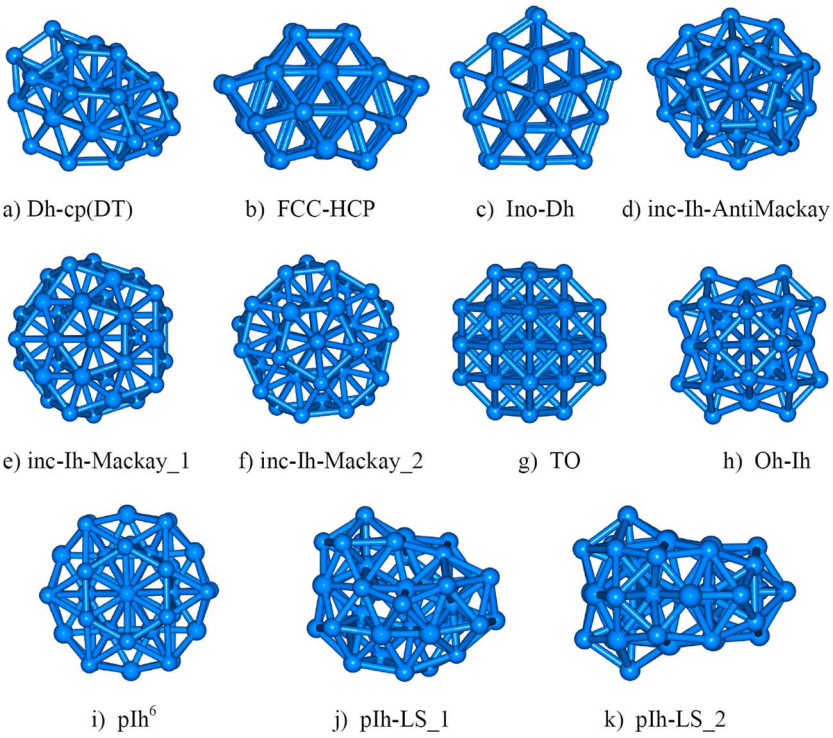

FIG. 1. (Color online) The eleven structural motifs studied in this work.

energy levels (see Ref. 22 for more computational details). Selected calculations were performed with basis sets of triple-zeta-plus-polarization quality[35,36] to evaluate DF mixing energies to be compared with Gupta values (see the next point). In contrast to the search of the EP potential energy surface using the GA method, we cannot guarantee that our combined EP/DF approach will be equally successful in the search of the GM at the DF level. For this reason, the expressions "putative GM" or "lowest-energy structure" are used when discussing the results of DF calculations.

Energetic analysis

The energetics of the four binary systems at the Gupta level were analyzed in terms of the mixing energy $\Delta_{38}^{\mathrm{Gupta}}$ defined as[6]

$$\Delta_{38}^{\mathrm{Gupta}} = E_{\mathrm{total}}^{\mathrm{Gupta}}(A_m B_n) - m\frac{E_{\mathrm{total}}^{\mathrm{Gupta}}(A_{38})}{38} - n\frac{E_{\mathrm{total}}^{\mathrm{Gupta}}(B_{38})}{38}, \tag{4}$$

where $E_{\mathrm{total}}^{\mathrm{Gupta}}(A_m B_n)$ represents the total energy of a given cluster calculated at the Gupta level and $E_{\mathrm{total}}^{\mathrm{Gupta}}(A_m)$ and $E_{\mathrm{total}}^{\mathrm{Gupta}}(B_m)$ represent the total energy of the GM of the pure metal clusters (Pt_{38}, Au_{38}, Pd_{38}, and Ag_{38}). $\Delta_{38}^{\mathrm{Gupta}}$ quantifies the energy associated with alloying: Negative values indicate that mixing is favorable. For selected structures and compositions, the DF mixing energy $\Delta_{38}^{\mathrm{DF}}$ was also calculated, defined in an analogous way as in Eq. (4) but with DF total energies replacing the Gupta ones.

RESULTS AND DISCUSSION

We initially performed a GA global structural optimization on the four systems for all compositions in order to explore the behavior of the mixing energy as a function of composition and then we focused mainly on the composition 24-14, chosen because it is exactly at (for the Pd–Pt and Ag–Au pairs) or very close (for Ag–Pt the minimum is reached at 25-13) to the minimum of the mixing energy at the EP level (see Fig. 2 below). For Pd–Au, the minimum is reached at the composition 14-24, which is, thus, also investigated for this pair, together with the corresponding 6-32 composition. We collected all the lowest-energy structures from the GA searches for all pairs following a "system comparison" philosophy.[9,11] Eleven structural motifs, shown in Fig. 1, were extracted from these searches and chosen as potential GM candidates for DF relaxation. The structures were then subjected to a BH atom-exchange optimization to determine the correct chemical ordering at the EP level for each structural motif.[12] Finally, local geometry relaxations at the DF level were performed on these structures. Note that imposing the chemical ordering of Pd–Pt for all of the four systems does not qualitatively change the results with respect to using the optimal chemical ordering at the Gupta level for each pair (implying differences of about 0.1–0.2 eV). In addition to the composition 24-14, the composition 32-6 was also considered in order to sample compositions with a low concentration of the third-row TM. At this composition, only high-symmetry structures were studied, i.e., TO (O_h), Oh-Ih (D_{4h}), inc-Ih-Mackay_1 (C_{5v}), and a pIh[6] (pancake-type) arrangement with a sixfold symmetry axis (D_{6h}).

The structural families

Eleven structural motifs (or "families") were singled out via a detailed examination of the GA-EP runs. These structures present a wide range of structural diversity, ranging from fcc crystalline arrangements (TO) to decahedral ones (Ino-Dh), mixed (Oh-Ih, Dh-cp) or pIh ones (inc-Ih-Mackay

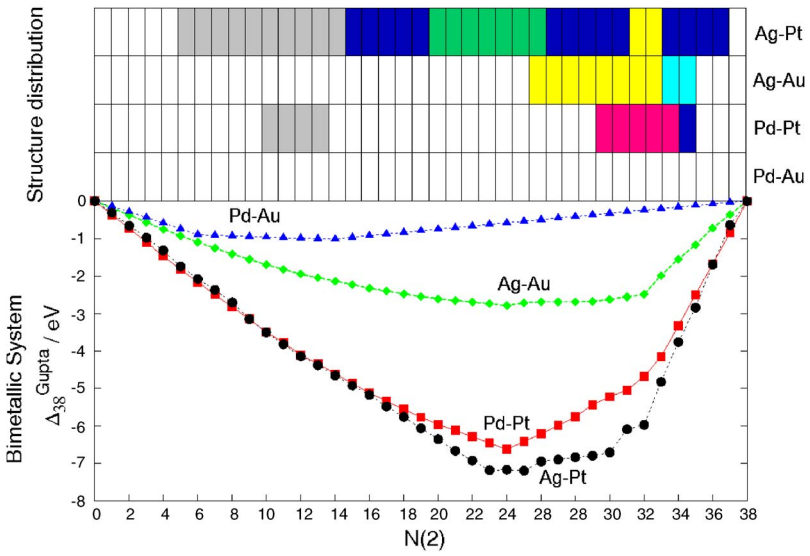

FIG. 2. (Color online) Bottom: Plot of the Gupta mixing energy Δ_{38}^{Gupta} for the four bimetallic systems as a function of the number of second-row TM atoms, $N(2)$. Black circles are used for Ag–Pt, red squares for Pd–Pt, green diamonds for Ag–Au, and blue triangles for Pd–Au. Top: The distribution of GM structures found in our GA search. The colors indicate the different structures: TO (white), Ino-Dh (gray), inc-Ih-AntiMackay (green), inc-Ih-Mackay (magenta), pIh[6] (yellow), and pIh-LS_1 and pIh-LS_2 (dark and light blue, respectively).

and inc-Ih-AntiMackay arrangements among others). These structural motifs are shown in Fig. 1. A detailed description of each of them is presented here.

(a) Dh-cp(DT): In our previous study of 34-atom Pd–Pt clusters, a novel structural motif was found based on a mixed decahedral/closed-packed arrangement[8] which was identified as the putative GM at the DF level for 34-atom Pd–Pt clusters over a wide range of compositions (from 17-17 to 28-6). The structure with 38 atoms is simply derived from that found in Ref. 8 by adding two Pd dimers along the edges of the two internal tetrahedral and possesses C_s symmetry. It consists of 14 closed-packed core atoms in a double tetrahedral or trigonal bypyramid arrangement (i.e., two tetrahedra sharing a face), further atoms growing on the (111) faces of the two internal tetrahedra in a regular hcp (111) stacking (three atoms per face, giving a total of 18 surface atoms), and 6 atoms, four lying on the edges of the same internal tetrahedron and two lying on an edge of the opposite internal tetrahedron. This atomic distribution creates local decahedra with their fivefold axes coinciding with the shared edge of the internal tetrahedra.

[(b) and (g)] TO and fcc-hcp: TO is the classic fcc-type truncated octahedron (O_h symmetry). Its surface presents eight hexagonal faces and six square ones. The fcc-hcp motif is a pseudocrystalline fcc-like structure with a hcp stacking fault and has C_{2v} symmetry. These two structures are similar as they both share an internal octahedron, but the distribution of eight internal atoms in the fcc-hcp structure is somewhat distorted compared to the TO as these atoms are not properly placed on top of each (111) face of the octahedron. A comparison of the internal cores of the TO, fcc-hcp, and Oh-Ih arrangements can be found in Fig. 1a of the Supplementary Information Material.[39]

(c) Ino-Dh: This is an incomplete Ino-decahedral structure. The complete structure is reached at 39 atoms and has ten rectangular (100) facets. In our case, the lack of one atom just gives nine rectangular facets and C_s symmetry.

(d) inc-Ih-AntiMackay: This structure corresponds to an incomplete anti-Mackay icosahedral structure (the complete structure is reached at size 45). It has an icosahedral (Ih_{13}) core surrounded by 20 atoms lying on top of each (111) face of the internal icosahedron, plus five atoms growing on top of the 12 vertex of the internal icosahedron in a perfect anti-Mackay arrangement, thus, creating five pseudo- (distorted) fivefold axes.

[(e) and (f)] inc-Ih-Mackay_1 and inc-Ih-Mackay_2: inc-Ih-Mackay_1 corresponds to an incomplete 55-atom Mackay icosahedron lacking its lower part when viewed from the five fold axis. It has five square (100) faces and an icosahedral core Ih_{13} lacking one atom. inc-Ih-Mackay_2 is similar, with the only difference that the vertex atom lying along the main symmetry axis has been moved to the opposite side of the cluster. Both structures possess C_s symmetry.

(h) Oh-Ih (octahedral-icosahedral): This peculiar structure has not been much considered in the literature before, although it has previously been identified as low-lying (non-GM) isomer for 38-atom homonuclear clusters of Ag, Ni, and Al, using the semiempirical Gupta [Ag, Ni (Ref. 40)] and Murrell–Mottram [Al (Ref. 41)] potentials. It is similar to the TO structure as it has an internal octahedral core. However, the surface atoms do not grow exactly on top of the (111) faces of the internal octahedron (as would happen in a TO arrangement) but are placed according to a distorted arrangement, in such a way that only two square faces (instead of six as in the TO) and no hexagonal faces are created. From an internal perspective, it resembles two double icosahedra joined by the central atoms [see Fig. 1b of the Supplement[39]], so that it can be considered as another example of a mixed fivefold-symmetric/closed-packed arrangement, which is being found with increasing frequency in medium-sized binary clusters.[8,12]

(i) pIh[6] (pIh sixfold pancake): 38 atoms represents a "magic" size for completing a sixfold "pancake" structure (D_{6h}).[6,11,17–19] These structures are found mainly at composition 32-6 where the species that tends to segregate to the surface is found in high concentrations (Pd in the case of Pd–Pt, Ag for Ag–Pt and Ag–Au). This structure is known to be favored among the pIh ones by a small size mismatch between the two metal atoms.[11]

[(j) and (k)] pIh-LS_1 and pIh-LS_2 (pIh low-symmetry

structures): These two structures share the same building principle: they both exhibit a quasidouble icosahedron as a pivotal frame with other pseudoicosahedra growing around it. The overall arrangement is rather distorted, hence, the name "pIh low-symmetry structures." pIh-LS_2 has a plane of symmetry (C_s), while pIh-LS_1 has no symmetry at all.

Composition dependence of the mixing energy and structures of the GM

Figure 2 shows the variation of the Gupta mixing energy $\Delta_{38}^{\mathrm{Gupta}}$ as a function of composition. The negative values of $\Delta_{38}^{\mathrm{Gupta}}$ indicate that the mixing is favored for all compositions. The minimum in $\Delta_{38}^{\mathrm{Gupta}}$ is reached at compositions 24-14 for Pd–Pt and Ag–Au and at 25-13 for Ag–Pt. For Pd–Au, the minimum occurs at 14–24 (i.e., at the Au rich side of the composition range). As will be shown later, this is because Pd–Au is the only system for which the third-row TM atom preferentially segregates to the cluster surface in the EP calculations.

Figure 2 also shows the GM structural motifs as a function of composition for all four systems. The TO structure predominates at the EP level, being the GM for all compositions for Pd–Au and for the majority of Pd–Pt and Au–Ag clusters. In these three cases, the minimum in $\Delta_{38}^{\mathrm{Gupta}}$ corresponds to a TO structure. The Ag–Pt system shows the greatest structural diversity, with a preponderance of decahedral, anti-Mackay, and pIh structures, with the minimum in $\Delta_{38}^{\mathrm{Gupta}}$ having an inc-anti-Mackay structure. In the following, the results of the DF local optimizations on the EP derived structural motifs are reported and analyzed for each pair.

Pd–Pt

The relative energies of the 11 structures for the Pd–Pt pair according to both EP and DF calculations are reported in Table II. An analysis of this table shows that the Gupta predictions are in overall fair agreement with the DF calculations, with the noteworthy exception than at the DF level, the Oh-Ih motif is lower in energy than the TO structure (predicted to be the GM by the EP), whereas it lies at high energy at the EP level (see Fig. 3). Note that the Oh-Ih structure was initially found as a high-energy isomer for the Ag–Au pair, which confirms the usefulness of the system comparison approach.[9,11] With respect to our previous work at size $N=34$,[8] we find similar trends, except that now Dh-cp and pIh structures are somewhat destabilized at the DF level. The Dh-cp structure, in particular, is destabilized by 2 eV relative to the TO. This is due to (a) $N=38$ being a magic number for TO and Oh-Ih and (b) the addition of two Pd dimers on the edges introduces a strain that was absent for $N=34$.[8] pIh structures such as pIh^6 are destabilized because Pd–Pt presents no size mismatch or electronic shell-closure effects.[7,18] For this composition and the Oh-Ih structure, $\Delta_{38}^{\mathrm{DF}}$ was also evaluated and found to be −4.8 eV, which compares reasonably well with the Gupta value $\Delta_{38}^{\mathrm{Gupta}}=-6.6$ eV (see Fig. 2) and confirms that the Gupta parametrization is reasonably accurate for the Pd–Pt pair.

In Table III, the same quantities are reported at composition 32-6 (higher Pd concentration). The TO structure is now found as the putative GM at the DF level, again in close competition (~0.04 eV) with the Oh-Ih structure. The other two structures (pIh^6 and inc-Ih-Mackay_1) are destabilized at the DF level and in the same order as at composition 24-14 but with smaller energy differences, which is reasonable since pure Pd clusters tend to be more fluxional and to exhibit smaller energy differences than pure Pt clusters. Moreover, as Pd and Pt present a small difference in electronegativity (both having a Pauling electronegativity of 2.2), one expects negligible charge transfer between the two species.

Segregation effects

As Pt has a higher cohesive energy and higher surface energy than Pd, while the atomic radii are practically the same, Pt segregation into the core of the cluster is expected. Indeed, $Pd_{shell}Pt_{core}$ is the preferred chemical ordering according to the EP. This ordering is confirmed by DF calculations on three different structural motifs at 19-19 composi-

TABLE II. Relative energies (in eV) of the 11 structures according to DF and Gupta calculations for the Pd–Pt, Ag–Pt, and Ag–Au pairs at the 24–14 composition.

Structure	Gupta	DF
	$Pd_{24}Pt_{14}$	
Oh-Ih	0.9282	0.0
TO	0.0	0.1306
Ino-Dh	1.1723	0.9441
fcc-hcp	0.8507	1.0675
inc-Ih-Mackay_1	0.8039	1.1319
Dh-cp(DT)	0.7833	1.3795
pIh-LS_2	1.1622	1.4394
inc-Ih-Mackay_2	1.081	1.6217
inc-Ih-AntiMackay	1.9233	2.4434
pIh^6	1.5826	2.4897
pIh-LS_1	1.4405	2.7563
	$Ag_{24}Au_{14}$	
Ino-Dh	0.5432	0.0
TO	0.0	0.3156
Oh-Ih	0.3552	0.4925
inc-Ih-Mackay_1	0.2084	0.7973
inc-Ih-AntiMackay	0.7707	1.1048
inc-Ih-Mackay_2	0.2979	1.1129
fcc-hcp	0.4533	1.6626
pIh-LS_1	0.5511	1.8259
pIh-LS_2	0.4618	2.0653
Dh-cp(DT)	0.4207	2.2966
pIh^6	0.2487	2.9552
	$Ag_{24}Pt_{14}$	
Oh-Ih	1.6474	0.0
inc-Ih-AntiMackay	0.0	0.4163
Dh-cp(DT)	0.7595	0.4979
TO	0.8957	0.5524
inc-Ih-Mackay_1	1.0823	0.6367
fcc-hcp	1.4142	0.8054
Ino-Dh	1.2216	0.9116
pIh-LS_1	1.5536	1.2000
inc-Ih-Mackay_2	1.4156	1.2027
pIh-LS_2	1.3946	1.2190
pIh^6	1.7793	1.3932

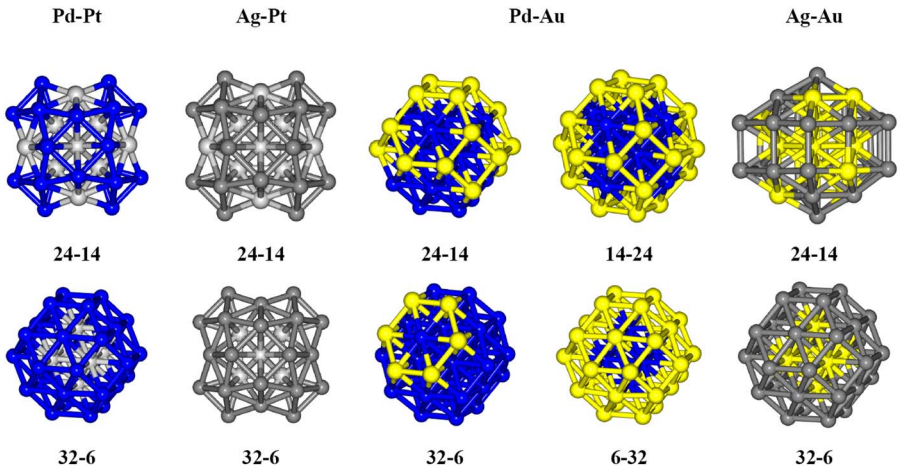

FIG. 3. (Color online) Putative GM structures found at the DFT level for the 24-14 and 32-6 compositions of all four bimetallic systems. For Pd–Au, compositions 14-24 and 6-32 are also shown. Color scheme: Pd (blue), Pt (light gray), Ag (dark gray), and Au (yellow).

tion [see Table IV and Fig. 2(a) in the Supplement[39]]. Segregation of Pd to surface sites for Pd–Pt clusters has previously been reported on the basis of EP and DF calculations.[8,28,42] It can also be noted that Oh-Ih is definitively at a lower energy than TO at this composition, which implies that Oh-Ih is the predicted GM at the DF level for compositions around 50%-50%.

Ag–Pt

For this pair, as can be seen from Table II, the Gupta potential predicts a strong preference for the inc-Ih-AntiMackay structure, with the other isomers well separated in energy. In contrast, at the DF level, we find that the Oh-Ih motif is the putative GM, as in the case of Pd–Pt system (see Fig. 3). It can also be observed that, contrary to what happens for the other TM pairs, DF calculations shrink instead of magnifying the energy differences, so that one finds several structurally very different motifs at 0.4–0.6 eV above the putative GM. Hence, considerable fluxional behavior is expected for this system at the DF level. Note that the Dh-cp motif is among the lowest-energy isomers at both the EP and DF levels: The size mismatch present in this system (the atomic radii are ~1.445 Å (Ag) and (~1.385 Å Pt) reduces the strain induced by the addition of Ag dimers along the edges of the internal tetrahedra with respect to the Pd–Pt case. The fact that the Gupta predictions are not confirmed at the higher level of theory is probably due to chemical or directionality effects associated with Pt–Pt interactions.[22] These effects are further enhanced by the size mismatch between the two atoms, which leads to shorter distances and, thus, stronger bonding between the Pt atoms. For this composition and the Oh-Ih structure, Δ_{38}^{DF} was also evaluated and found to be −2.7 eV. This value is much smaller than the Gupta value $\Delta_{38}^{Gupta}=-7.1$ eV (see Fig. 2) and suggests a reparametrization of the Gupta potential for the Ag–Pt pair. At composition 32-6, one finds similar results (see Table III), with the Oh-Ih motif as the putative GM and inc-Ih-Mackay_1 as a low-energy isomer.

Segregation effects

In Table IV, [see also Fig. 2b in the Supplement[39]], the total energies for selected structures at composition 19-19 (as predicted by the Gupta potential) and the "inverted" structures obtained by swapping Ag and Pt atoms are reported. In this case, the difference in electronegativities between Ag and Pt is not sufficient to favor Pt segregation at the surface, and the greater strength of Pt–Pt interactions and the larger surface energy of Pt both combine to favor Ag segregation at the surface, with energy differences for the inverted homotops of the order of 5–6 eV. It can also be noted that inc-Ih-Mackay_1 is practically isoenergetic with Oh-Ih and at a lower energy than TO at this composition (in the same way as at composition 32-6).

Pd–Au

The Gupta optimizations predict that TO is the preferred structure for all compositions for Pd–Au at size 38, with Au atoms segregating to the surface and Pd atoms occupying core positions (see Fig. 3). A thorough analysis is shown below for some specific compositions.

TABLE III. Relative energies (in eV) of selected structures according to DF and Gupta for the Pd–Pt, Ag–Pt, Pd–Au, and Ag–Au pairs at the 32–6 composition.

	$Pd_{32}Pt_6$		$Ag_{32}Pt_6$		Pd_6Au_{32}		$Pd_{32}Au_6$		$Ag_{32}Au_6$	
	Gupta	DF	Gupta	DF	Gupta	DF	Gupta	DF	Gupta	DF
Oh-Ih	0.7473	0.0435	2.2831	0.0	0.2699	0.4598	0.3007	0.1360	1.0132	0.2193
TO	0.2495	0.0	1.8506	0.5768	0.0	0.0	0.0	0.0	0.7078	0.0
inc-Ih -Mackay_1	0.0	0.4272	1.3508	0.1496	0.1753	0.1469	0.2215	0.6530	0.4331	0.4778
pIh[6]	0.0986	1.5184	0.0	1.7225	0.9146	1.9130	1.4499	1.5674	0.0	2.2711

TABLE IV. Segregation effects at composition 19-19 for the four pairs. Three structural motifs are investigated at the DF level (TO, Oh-Ih, and inc-Ih-Mackay_1). In each case, two homotops are studied: "EP" is the lowest-energy homotop found using the EP; "Inverted" is the homotop formed by swapping positions of A and B atoms. Both structures are minimized at the DF level and energies (in eV) are quoted relative to the putative DF GM. The negative values for $Ag_{19}Au_{19}$ indicate that the EP predicts the wrong segregation for this system.

	$Pd_{19}Pt_{19}$		$Ag_{19}Pt_{19}$		$Pd_{19}Au_{19}$		$Ag_{19}Au_{19}$	
	EP	Inverted	EP	Inverted	EP	Inverted	EP	Inverted
Oh-Ih	0.0	2.245	0.065	5.861	0.419	5.396	0.446	−0.963
TO	0.729	2.566	0.729	5.758	0.0	5.638	0.0	−0.863
inc-Ih-Mackay_1	0.811	3.526	0.0	6.221	0.871	6.310	0.078	−0.764

Compositions 14-24 and 6-32

Due to the interest in Pd–Au nanoparticles in catalytic applications[43,44] and also due to the very flat behavior of the mixing energy and the fact that the Gupta potential predicts the lowest mixing energy structures at composition $Pd_{14}Au_{24}$ (see Fig. 2), compositions with a high concentration of the third-row atom have also been investigated in this case (see Table V). The EP predicts an unusual surface segregation of the third-row atom for Pd–Au clusters (i.e., the $Pd_{core}Au_{shell}$ arrangement). Our DF calculations, as shown later for the specific case of the 19-19 composition, are in agreement with the EP prediction. At high Au concentrations, the TO structure is the lowest in energy at DF level, although the inc-Ih-Mackay_1 structure is also low in energy (difference of ~0.25 eV), whereas the Ino-Dh, Dh-cp(DT), and pIh structures are destabilized at both the EP and DF levels. For this composition and the TO structure, Δ_{38}^{DF} was also evaluated and found to be −2.3 eV, which is somewhat larger than the Gupta value $\Delta_{38}^{Gupta}=-1.0$ eV (see Fig. 2) and points to a fine tuning of the Gupta mixed parameters for the Pd–Au pair. At the 6-32 composition (see Table III), TO is still predicted to be the GM by both approaches, with inc-Ih-Mackay_1 and Oh-Ih as low-lying isomers (differences of around 0.1–0.4 eV).

Compositions 24-14 and 32-6

The results of the Gupta potential and DF calculations for the Pd–Au pair at the 24-14 composition (high Pd concentration) are reported in Table V. The predicted GM is again a TO structure at both the Gupta potential and the DF levels, followed by the Oh-Ih and fcc-hcp structures at ~0.6 eV and the other motifs at higher energies. DF, in general, amplifies the relative energy differences between the structural motifs, and this is due especially to the fact that pIh structures are strongly disfavored by DF. This is in line with previous results which indicate that Gupta overestimates the tendency of Au toward fivefold-symmetric structures because of an underestimation of chemical or directionality effects.[2,6] These expectations are confirmed at composition 32-6 (see Table III), where the TO structure is again predicted to be the putative GM by both approaches but now, icosahedral structures are less disfavored (inc-Ih-Mackay_1 lies at ~0.6 eV) and Oh-Ih lies at only 0.1–0.2 eV above the putative GM. This is probably due to the smaller size of the Pd atom with respect to the Au atom.

Segregation effects

The DF total energies for selected structures and their inverted homotops, obtained by swapping Pd and Au atoms, are reported in Table IV [see also Fig. 2(c) in the Supplement[39]]. The inverted structures are always disfavored, with energy differences of the order of 5–6 eV. This result is easily rationalized. The surface energy of Au is 98 meV/Å^2, whereas that of Pd is 131 meV/Å^2, the cohesive energies of the two species are roughly the same (3.81 vs 3.89 eV), the atomic radius of Au (1.44 Å) is larger than that of Pd (1.38 Å), and finally, the Pauling electronegativity of Au (2.4) is slightly larger than that of Pd (2.2), so that any charge transfer from Pd to Au reinforces the tendency to Au surface segregation. It is interesting to note in this respect that experimentally, the as-prepared Pd–Au particles present

TABLE V. Relative energies (in eV) of the 11 structures according to DF and Gupta for the Pd–Au pair at the $Pd_{14}Au_{24}$ and $Pd_{24}Au_{14}$ compositions.

Structure	Gupta	DF
	$Pd_{14}Au_{24}$	
TO	0.0	0
inc-Ih-Mackay_1	0.464	0.2530
inc-Ih-Mackay_2	0.709	0.4979
fcc-hcp	0.591	0.8707
Oh-Ih	0.352	1.2898
Ino-Dh	0.8188	1.6218
Dh-cp(DT)	1.598	1.9701
inc-Ih-AntiMackay	3.014	1.9864
pIh[6]	1.460	2.0545
pIh-LS_1	1.070	2.1497
pIh-LS_2	1.280	2.1796
	$Pd_{24}Au_{14}$	
TO	0.0	0.0
Oh-Ih	0.2869	0.6612
fcc-hcp	0.3855	0.6666
Ino-Dh	0.4123	1.4040
inc-Ih-Mackay_1	0.1227	1.5264
inc-Ih-Mackay_2	0.3804	1.6026
Dh-cp(DT)	0.5973	1.6951
pIh-LS_1	0.7428	2.4545
pIh-LS_2	0.9004	2.6041
pIh[6]	0.3450	2.6284
inc-Ih-AntiMackay	1.4332	2.925

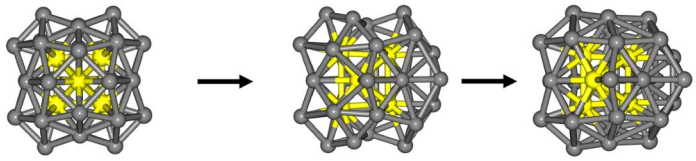

FIG. 4. (Color online) Schematic representation of the DF optimization for the Oh-Ih structure of $Ag_{32}Au_6$. The structural distortion, in which Au atoms (yellow) are displaced toward the surface, can be explained in terms of charge transfer effects which are not taken into account by the EP.

gold on the surface, but calcination brings Pd to the surface even after H_2 reduction, probably because of the higher affinity of Pd for oxygen.[43] It can be noted that TO is the putative GM also at this composition, and the energy of inc-Ih-Mackay_1 is intermediate between the values at 14-24 and 24-14 compositions, whereas that of Oh-Ih exhibits more erratic behavior. Anyway, it can be concluded that fcc configurations are definitely favored for Pd–Au particles, with this tendency reinforced around the minimum in the mixing energy, and that in this case, the EP description compares fairly well with the DF results.

Ag–Au

At the Gupta level, the minimum in the mixing energy is reached at composition 24-14 for a perfect TO structure. However, this minimum is not pronounced. Moreover, many structural motifs are predicted by Gupta to lie within an interval of 0.5 eV from the GM (see Table II). As the size mismatch between the two elements is very small (the atomic radii are 1.44 Å for Au and 1.445 Å for Ag), behavior similar to Pd–Pt is expected and, indeed, observed at the EP level.

At the DF level, the major differences are that (a) the energy separation between the different structural motifs is, in general, larger than at the EP level, (b) an Ino-Dh structure becomes the lowest-energy one for $Ag_{24}Au_{14}$ clusters (see Fig. 3), and (c) pIh structures are strongly disfavored by DF. Note that 38 is not a magic number for the Ino-Dh arrangement whose shell structure is completed at size 39. This reinforces the prediction of this structure as the putative GM in this size range. The TO and the Oh-Ih structures are found as lowest-energy metastable isomers at 0.3–0.4 eV above the Ino-Dh. For this composition and the Ino-Dh structure, Δ_{38}^{DF} was also evaluated and found to be −1.3 eV, which is smaller than the Gupta value $\Delta_{38}^{Gupta}=-2.7$ eV (see Fig. 2), probably also because of the underestimation of charge transfer effects for the Ag–Au pair (see the following discussion). An analogous remark can be made for the large energy differences between structural motifs found at the DF level with respect to the Gupta results, which could also be due to the wrong prediction of segregation effects by the EP. As shown in Table III, at high Ag concentrations (composition 32-6), the TO structure is found as the lowest-energy structure at the DF level, closely followed by the Oh-Ih structure (~0.20 eV). However, it is interesting to observe that the Oh-Ih structure undergoes a strong $D_{4h} \rightarrow C_s$ distortion after DF optimization, and some of the Au atoms in the core pop out to the surface (see Fig. 4). These factors prompted us to a closer investigation of segregation effects for this system.

Segregation effects

As can be seen from Table IV, the most important result obtained in our study of inverted structures is that the $Ag_{shell}Au_{core}$ segregation predicted by the Gupta potential is not confirmed by the DF calculations. Negative energy differences indicate that the inverted structures $Ag_{core}Au_{shell}$ correspond to the lowest-energy structures at the DF level [see Table IV and Fig. 2(d) in the Supplement[39]]. Thus, Au rather than Ag segregation to the surface is predicted by the first-principles approach. The difference must be due to electronic structure effects[6] and, considering that directionality effects associated with the Au atoms are diluted by the presence of Ag atoms and that electronic shell closure is not expected at size 38, the most likely explanation for this unexpected result is charge transfer effects, as underlined in previous works.[23–26] We recall that gold is more electronegative than silver (the Pauling electronegativities are 2.4 and 1.9 for Au and Ag, respectively). Au atoms can, thus, accept negative charge from silver atoms and, consequently, tend to occupy sites with low coordination, such as surface sites, in order to reduce Coulombic repulsion and charge compression. To confirm this interpretation, we have focused on the energies of the semicore 5*s* (for Au) and 4*s* (for Ag) levels (corresponding to states which are not heavily involved in chemical bonding). These values indicate the direction and the size of the charge transfer because an increase in the electronic density on one atom (negative charge) causes a destabilization of its core levels (increased positive charge leads to core level stabilization). To disentangle electronic and structural effects (which is possible as structural relaxation following Ag–Au exchange is a minor one), we follow a previously proposed protocol[45] and compare the values of the semicore levels for the mixed clusters with those of the pure silver and gold clusters at a frozen geometry. We found that in all the selected 19-19 structures, the gold atoms acquire negative charge (i.e., the energies of their 5*s* levels rise), while the silver atoms acquire a corresponding positive charge (i.e., their 4*s* levels drop in energy). Both energy shifts are of the order of 0.5 eV in absolute value and opposite in sign.

To perform a deeper analysis, we then focused on a particular structure, the 19-19 TO. TO is a crystalline structure, so size mismatch does not play a role in the stability of a particular chemical ordering (we recall that Au and Ag have very similar atomic radii and bulk lattice constants). Consequently, the two factors that contribute to the optimal chemical ordering are the number of mixed versus pure bonds (i.e., the number of Ag–Au versus Au–Au and Ag–Ag bonds) and charge transfer effects. To separate these two effects and quantify them independently, we have generated several structures characterized by a different chemical ordering and

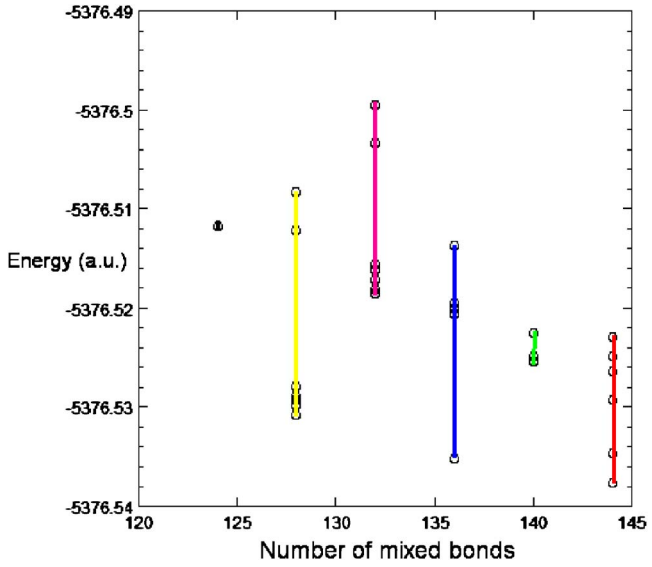

FIG. 5. (Color online) Cluster total energy as a function of the number of mixed bonds for several $Au_{19}Ag_{19}$ TO structures. Clusters presenting a variable number of mixed bonds are obtained by permuting the positions of the surface gold and silver atoms in the square (100) facets. The energy spread at a fixed number of mixed bonds gives an estimate of the charge transfer effects.

classified them on the basis of the number of pure and mixed bonds. The TO structures have been generated in the following way: The octahedral core is formed by six silver atoms, the atoms at the center of the eight (111) facets are also silver atoms, and the remaining five silver atoms and 19 gold atoms are randomly distributed over the 24 sites constituting the six (100) facets. Structures were selected and DF local optimizations were performed on them. In all the structures, the total number of bonds is equal to 240 (two atoms are considered to form a bond when their separation is less than 3.0 Å). The results of these calculations are reported in Fig. 5, where the clusters are classified according to the number of mixed bonds; note that we have chosen the structures in such a way that if two clusters have the same number of mixed bonds, the numbers of pure Ag–Ag and Au–Au bonds are also the same. As can be seen from an inspection of Fig. 5, the best chemical ordering (lowest energy) is obtained in correspondence with the maximum number of mixed bonds in the cluster (144); the total energy roughly increases when the number of mixed bonds decreases. However, charge transfer effects are also important: An estimate of their size can be made on the basis of the energy spread of clusters characterized by the same number of mixed bonds. From such an analysis, one finds that the maximum variations associated with charge transfer effects are of the order of 0.5–0.7 eV (these values being by chance very similar to the core level shifts of the two species). It, thus, seems necessary for a realistic description of the Ag–Au system to consider additional terms in the EP that take into account electrostatic contributions, as recently proposed.[25]

Another factor which can affect the cluster energy is the directionality of bonding. For example, by taking the lowest-energy structure and performing a simple exchange so that a gold atom is moved from a (100) facet to the center of a (111) facet, we found an increase in the energy of 0.33 eV, whereas the exchange between a gold atom at the surface and a silver atom in the core of the TO produces an increase in energy of only 0.08 eV. This is due to the fact that the directionality contributions in gold strongly destabilize asymmetric environments and are more important for sites of increased coordination, as it happens when a gold atom moves from the corner of a (100) facet to the center of a (111) facet.

CONCLUSIONS

The application of a combined EP/DF (system comparison) approach allowed us to single out reasonable candidates for the lowest-energy structures at selected compositions of 38-atom clusters of four bimetallic systems (Pd–Pt, Ag–Pt, Pd–Au, and Ag–Au). From the analysis of the results, the following main conclusions can be drawn:

(1) In general, the EP shows a preference for the TO arrangement except for the Ag–Pt pair, for which an inc-Ih-AntiMackay is predicted as the GM. This tendency is confirmed by DF for Pd–Au (at both 24-14 and 14-24 compositions), but an Ino-Dh arrangement is found as the lowest-energy structure for Ag–Au, while a novel Oh-Ih mixed arrangement is found as a low-energy isomer for Pd–Pt and as the lowest-energy structure for Ag–Pt: The fact that this occurs at $N=38$, which is a magic number for TO, strongly suggests that mixed fivefold-symmetric/close-packed or decahedral arrangements are favored in this size range for the Pd–Pt, Ag–Pt, and Ag–Au pairs.

(2) The EP energy differences between the structural motifs are generally amplified by DF for the Ag–Au and Pd–Au (at both 24-14 and 14-24 compositions) pairs, but the opposite is found for the Ag–Pt pair, while there is no significant trend for the Pd–Pt pair.

(3) pIh structures, which have been proven to be dominant for several pairs involving second-row and first-row transition elements[17] and are predicted to be important competitors by the EP for some of the second-row/third-row transition element binary pairs here investigated, are disfavored by DF for the Ag–Au, Pd–Pt and Pd–Au pairs at the 24-14 composition (the only exception is the Ag–Pt pair and is associated with a strong fluxional character of the potential energy surface of this system), while the pIh[6] structure is strongly disfavored for all the bimetallic pairs at the 32-6 and 6-32 compositions.

(4) Directionality effects for Au and Pt,[6] although diluted by the presence of the second-row metal, subtly modulate the energy ordering, thus, producing differences between EP and DF results.

(5) The DF prediction of segregation effects usually coincides with that from the EP calculations. The relative energy differences are found to be of the order of ~2 eV for Pd–Pt or 5–6 eV for Ag–Pt and Pd–Au. However, DF predicts Au rather than Ag segregation at the surface in Ag–Au particles because of charge transfer effects (as confirmed by an analysis of the energies of semicore levels for Ag–Au and pure Ag and Au clus-

ters), even though the corresponding energy differences are not large (of the order of 0.5–0.8 eV) and other effects, such as mixing and directionality effects, have been proven to be roughly of the same size.

(6) The difference between Gupta and DF mixing energies suggests the need for reparametrization of the mixed Gupta interaction parameters especially for the Ag–Pt pair and confirms the importance of including electrostatic contributions for the Ag–Au pair.[25]

It is interesting to underline that a peculiar Oh-Ih structure (originally found as a high-energy isomer for Ag–Au or pure Ag clusters[40]) corresponds to the putative GM for two of the systems studied in the present work (Pd–Pt and Ag–Pt) at composition 24-14. This confirms the usefulness of the system comparison approach in searching for the lowest-energy structures of nanoalloy clusters.[9,11] Note that the Oh-Ih and TO structures both have an internal octahedral core unit, but surface atoms do not grow in a fcc arrangement in Oh-Ih which is, thus, an example of the mixed fivefold fold-symmetric/close-packed motifs which are being found with increasing frequency in medium-sized binary clusters.[8,12] Their close energetic competition (~0.5 eV for all four systems) supports the prediction that fcc-based structures are important competitors for 38-atom size clusters, but mixed arrangements can be the preferred configurations in the neighborhood of this size. This can be rationalized in terms of the crossover between fcc and decahedral structures not yet being complete at size 38,[14] so that a compromise is for the "stickier" third-row transition metals to occupy the core, while the "less sticky" second-row transition metals grow on the surface, forming fivefold-symmetric motifs. Finally, when charge transfer effects are not strong, segregation is mainly determined by minimization of surface energy and maximization of the strongest bond interactions, with $Pd_{shell}Pt_{core}$, $Ag_{shell}Pt_{core}$, and $Pd_{core}Au_{shell}$ being the preferred segregation for these three systems.

ACKNOWLEDGMENTS

This work has been performed within the HPC-Europa Project (RII3-CT-2003-506079), with the support of the European Community—Research Infrastructure Action under the FP6 "Structuring the European Research Area" Programme, which allowed us to perform some of the DF calculations here described at the CINECA Supercomputing Center (Bologna, Italy). L.O.P.B. and R.L.J. acknowledge support from the EPSRC funded National Service for Computational Chemistry Software, UK (http://www.nsccs.ac.uk) for a 100 000 CPU hour grant on the Magellan supercomputer. A.F. and G.B. acknowledge financial support from Italian CNR for the project SSA-TMN within the framework of the ESF EUROCORES SONS and from EC FP6 for the STREP project GSOMEN (Growth and Supra-Organization of Transition and Noble Metal Nanoclusters). L.O.P.B. is grateful to CONACYT (México) for the award of a PhD scholarship. Benjamin Curley and Faye Pittaway are acknowledged for preliminary work on Ag–Au and Pd–Au clusters, respectively.

[1] R. Ferrando, J. Jellinek, and R. L. Johnston, Chem. Rev. **108**, 845 (2008).
[2] E. Aprà, R. Ferrando, and A. Fortunelli, Phys. Rev. B **73**, 205414 (2006).
[3] Y. Gao, S. Buluse, and X. C. Zeng, J. Am. Chem. Soc. **127**, 15680 (2005).
[4] G. Barcaro and A. Fortunelli, J. Phys. Chem. C **111**, 11384 (2007).
[5] J. Jellinek and E. B. Krissinel, *Theory of Atomic and Molecular Clusters*, edited by J. Jellinek (Springer-Verlag, Berlin, 1999), p. 277.
[6] R. Ferrando, A. Fortunelli, and G. Rossi, Phys. Rev. B **72**, 085449 (2005).
[7] G. Barcaro, A. Fortunelli, G. Rossi, F. Nita, and R. Ferrando, J. Phys. Chem. B **110**, 23197 (2006).
[8] L. O. Paz-Borbón, R. L. Johnston, G. Barcaro, and A. Fortunelli, J. Phys. Chem. C **111**, 2936 (2007).
[9] R. Ferrando, A. Fortunelli, and R. L. Johnston, Phys. Chem. Chem. Phys. **10**, 640 (2008).
[10] J. Cheng and R. Fournier, Theor. Chem. Acc. **112**, 7 (2004).
[11] A. Rapallo, G. Rossi, R. Ferrando, A. Fortunelli, B. C. Curley, L. D. Lloyd, G. M. Tarbuck, and R. L. Johnston, J. Chem. Phys. **122**, 194308 (2005).
[12] L. O. Paz-Borbón, T. V. Mortimer-Jones, R. L. Johnston, A. Posada-Amarillas, G. Barcaro, and A. Fortunelli, Phys. Chem. Chem. Phys. **9**, 5202 (2007).
[13] L. D. Marks, Rep. Prog. Phys. **57**, 603 (1994).
[14] F. Baletto, R. Ferrando, A. Fortunelli, F. Montalenti, and C. Mottet, J. Chem. Phys. **116**, 3856 (2002).
[15] J. P. K. Doye, D. J. Wales, and R. S. Berry, J. Chem. Phys. **103**, 4234 (1995).
[16] See the Cambridge Cluster Database (http://wwwwales.ch.cam.ac.uk/CCD.html).
[17] G. Rossi, A. Rapallo, C. Mottet, A. Fortunelli, F. Baletto, and R. Ferrando, Phys. Rev. Lett. **93**, 105503 (2004).
[18] G. Rossi, R. Ferrando, A. Rapallo, A. Fortunelli, B. C. Curley, L. D. Lloyd, and R. L. Johnston, J. Chem. Phys. **122**, 194309 (2005).
[19] B. C. Curley, G. Rossi, R. Ferrando, and R. L. Johnston, Eur. Phys. J. D **43**, 53 (2007).
[20] R. H. Leary and J. P. K. Doye, Phys. Rev. E **60**, R6320 (1999).
[21] "Nanoalloys: From Theory to Applications," edited by R. L. Johnston and R. Ferrando, Faraday Discuss. **138**, 1-441 (2008).
[22] E. Aprà and A. Fortunelli, J. Phys. Chem. A **107**, 2934 (2003).
[23] V. Bonačić-Koutecký, J. Burda, R. Mitrić, M. Ge, G. Zampella, and P. Fantucci, J. Chem. Phys. **117**, 7 (2002).
[24] R. Mitrić, C. Bürgel, J. Burda, V. Bonačić-Koutecký, and P. Fantucci, Eur. Phys. J. D **24**, 41 (2003).
[25] M. Zhang and R. Fournier, J. Mol. Struct.: THEOCHEM **762**, 49 (2006).
[26] P. Weis, O. Welz, E. Vollner, and M. M. Kappes, J. Chem. Phys. **120**, 677 (2004).
[27] F. Cleri and V. Rosato, Phys. Rev. B **48**, 22 (1993).
[28] C. Massen, T. V. Mortimer-Jones, and R. L. Johnston, J. Chem. Soc. Dalton Trans. **2002**, 4375.
[29] R. L. Johnston, J. Chem. Soc. Dalton Trans. **2003**, 4193.
[30] J. P. K. Doye and D. J. Wales, J. Phys. Chem. A **101**, 5111 (1997).
[31] R. Ferrando and G. Rossi, personal communication (4/5/2007).
[32] R. A. Kendall, E. Aprà, D. E. Bernholdt, E. J. Bylaska, M. Dupuis, G. I. Fann, R. J. Harrison, J. Ju, J. A. Nichols, J. Nieplocha, T. P. Straatsma, T. L. Windus, and A. T. Wong, Comput. Phys. Commun. **128**, 260 (2000).
[33] J. P. Perdew, J. A. Chevary, S. H. Vosko, K. A. Jackson, M. R. Pederson, D. J. Singh, and C. Fiolhaus, Phys. Rev. B **46**, 6671 (1992).
[34] E. Aprà and A. Fortunelli, J. Mol. Struct.: THEOCHEM **501**, 251 (2000).
[35] A. Schäfer, C. Huber, and R. Ahlrichs, J. Chem. Phys. **100**, 5829 (1994).
[36] See: ftp://ftp.chemie.uni-karlsruhe.de/pub/basen/
[37] D. Andrae, U. Haeussermann, M. Dolg, H. Stoll, and H. Preuss, Theor. Chim. Acta **77**, 123 (1990).
[38] F. Weigend, M. Haser, H. Patzel, and R. Ahlrichs, Chem. Phys. Lett. **294**, 143 (1998).
[39] See EPAPS Document No. E-JCPSA6-128-027813 for a view of the internal core of Oh-Ih, TO, and FCC-HCP arrangements [Fig. 1(a)], an analysis of the Oh-Ih structure [Fig. 1(b)], and the EP-predicted and "inverted" 19-19 homotops for the Pd–Pt [Fig. 2(a)], Ag–Pt [Fig. 2(b)], Pd–Au [Fig. 2(c)], and Ag–Au [Fig. 2(d)] pairs. This document can be

reached through a direct link in the online article's HTML reference section or via the EPAPS homepage (http://www.aip.org/pubservs/epaps.html).
[40] K. Michaelian, N. Rendón, and I. L. Garzón, Phys. Rev. B **60**, 2000 (1999).
[41] L. D. Lloyd, R. L. Johnston, C. Roberts, and T. V. Mortimer-Jones, ChemPhysChem **3**, 408 (2002).
[42] E. M. Fernández, L. C. Balbas, L. A. Perez, K. Michaelian, and I. L. Garzón, Int. J. Mod. Phys. B **19**, 2339 (2005).
[43] J. K. Edwards, A. F. Carley, A. A. Herzing, C. J. Kiely, and G. J. Hutchings, Faraday Discuss. **138**, 225 (2008).
[44] K. Luo, T. Wei, C.-W.Yi, S. Axnanda, and D. W. Goodman, J. Phys. Chem. B **109**, 23517 (2005).
[45] J. Jellinek and P. H. Acioli, *The Chemical Physics of Solid Surfaces*, Atomic Clusters: From Gas Phase to Deposited, Vol. 12, edited by D. P. Woodruff (Elsevier, Amsterdam, 2007); personal communication (9/3/2007).

PCCP
Physical Chemistry Chemical Physics

BarcaroPCCP2008

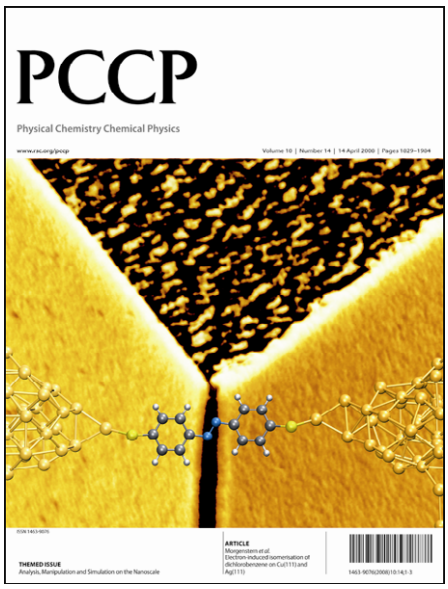

This article is part of a PCCP themed issue on:

Analysis, manipulation, and simulation on the nanoscale

Guest Editors: Harald Fuchs, Dominik Marx and Ulrich Simon

Other papers in the issue:

Metal adsorption on oxide polar ultrathin films

Giovanni Barcaro,[a] Alessandro Fortunelli*[a] and Gaetano Granozzi[b]

Received 14th December 2007, Accepted 25th January 2008
First published as an Advance Article on the web 19th February 2008
DOI: 10.1039/b719346g

The adsorption of Au and Pd atoms on two nanostructured titania monolayers grown on the Pt(111) surface is investigated *via* a computational approach. These phases present compact regions (zig-zag-like stripes) with titanium atoms at the oxide–metal interface and oxygen in the top-most overlayer, sometimes intercalated by point defects, *i.e.* holes exposing the bare metal support, and give rise to very regular patterns extending for large distances. A Pd atom experiences a rather flat energy landscape on the compact regions whereas it is strongly bound to the defects which act as nucleation centers, whence the interest of these substrates as nanotemplates for the growth of metal clusters. The interaction of a Au atom with these phases is peculiarly different: a charge transfer from the underlying Pt(111) support occurs so that Au gets negatively charged and strongly interacts with a titanium atom extracted from the interface in the compact regions, whereas it penetrates less easily than Pd into the defective holes due to its larger size. These results are discussed as paradigmatic examples of the interaction of metals with polar ultrathin films of oxides grown on metal supports, a novel and promising field in materials science.

I. Introduction

Metal clusters adsorbed on oxide surfaces have traditionally attracted considerable attention due to their scientific interest and technological applications in several fields, ranging from heterogeneous catalysis to opto-electronic and magnetic devices.[1] This attention has fueled a series of fundamental studies in which the complicated real-world systems are replaced by model systems obtained by controlled metal deposition on oxide single crystals in ultra-high vacuum.[2] More recently, the replacement of oxide single crystal surfaces with ultrathin films grown on metal supports[3,4] has brought basic research one step further away from the materials used in standard technology, simultaneously producing a wealth of fundamental knowledge and posing novel issues and challenges. The reasons behind this shift of interest toward ultrathin systems essentially lie in the higher level of characterization that can be achieved for them with respect to the traditional thick oxide layers. In way of example, at variance with many insulating bulk oxides, ultrathin films exhibit electric conductance to a degree sufficient for scanning tunneling microscopy (STM) measurements to be performed, and indeed STM images with impressive resolution have been obtained, of quality comparable with that of metal-on-metal systems (see *e.g.* ref. 5). Latest research, however, has found that the underlying metal support is not neutral and can actively participate in the adsorption process, to such an extent that these systems should better be described as metal-on-oxide-on-metal materials.[6] Among the novel phenomena arising as a consequence of the nanoscale thickness of the oxide and the vicinity of the metal support, one of the most intriguing is the possibility of a charge transfer between the metal surface and the deposited metal clusters, as recently theoretically predicted[7,8] and experimentally confirmed[9,10] (see also further theoretical analysis in ref. 11). This phenomenon was discovered for metal atoms adsorbed on oxide *non-polar* films grown on low-index metal single crystal surfaces, such as MgO on Mo(100) or Ag(100)[7–10,12,13] (species other than metals have also been investigated, see *e.g.* ref. 14). However, a rich variety of oxide *polar* nanophases[15,16] grown on compact metal surfaces has been discovered in latest years, and new additions are continuously enriching the field.[17–39] These new phases possess some common features: (a) the oxide film is few (one or two) monolayers thick; (b) the metal of the oxide is at the oxide-support interface while oxygen typically forms a top-most overlayer; (c) as a consequence, these systems are polar, *i.e.* they present a finite dipole moment perpendicular to the surface; (d) the oxide phase is often modulated into regular nanostructured patterns; (e) these patterns sometimes open up into point defects, *i.e.* holes which expose the bare metal support. These characteristics make these systems extremely promising as templates for the growth of ordered arrays of metal nanoclusters, and indeed their potentialities in this respect have already been convincingly demonstrated in selected examples.[28,36,37,40–47] Computational approaches are expected to play an important role in the study of these phenomena, both because they can help resolving the atomistic structure of the oxide ultrathin films and because they can provide invaluable information on the basic metal–oxide–metal interactions, which can hardly be derived *via* even the most advanced experiments.

In the present article, we focus on two such oxide polar ultrathin phases, namely two TiO_x (titania) monolayers grown on the Pt(111) surface exhibiting a zig-zag-like habitus in their

[a] *Molecular Modeling Laboratory, IPCF-CNR, Via G. Moruzzi 1, Pisa, I56124, Italy. E-mail: fortunelli@ipcf.cnr.it*
[b] *Dipartimento di Scienze Chimiche, Università di Padova, Via Marzolo, Padova, I35131, Italy*

STM images, whose structure has been recently elucidated,[38,39] and we investigate *via* a first-principles approach the characteristics of the adsorption of single Pd and Au atoms on them. The TiO_x/Pt(111) system is particularly interesting in this context as: (1) it presents a great variety of phases with different topographies providing a fairly complete representation of the various possibilities (compact regions, large holes, small holes *etc.*)[27] and (2) the dimension of the unit cells in these systems is not excessive, allowing one to limit the computational effort and develop systematic investigations. We show that this system presents phenomena that are novel with respect to non-polar ultrathin films but common to its polar analogues, thus allowing one to begin setting up a general framework for these fascinating systems.

II. Computational details

Density functional (DF) calculations were performed using the PWscf (plane-wave self-consistent field) computational code,[48] employing ultrasoft pseudopotentials[49] and the PW91 exchange–correlation functional.[50] Note that a gradient-corrected exchange–correlation functional is deemed appropriate for these oxide ultrathin phases, for which the presence of the underlying metal support and the resulting conductive character advise against[51] the use of hybrid methods that have recently been proposed for (defected) stoichiometric titania phases[52] (further studies would be helpful anyway to further clarify this point). As in ref. 38, a value of 30 Ryd for the energy cutoff on the wave function, a value of 150 Ryd for the energy cutoff on the electronic density, about 8–10 Å of empty space between replicated cells, and a (2,4,1) k_{mesh} grid for the sampling of the first Brillouin zone were used. All the calculations were performed spin-unrestricted. The support was mostly described using 2 layers of Pt, but this choice was validated by comparison with calculations using 4 layers of Pt, which produced qualitatively similar results (as it is reasonable, due to the minor importance of image-charge effects for these systems, see below) as shown in Table 1 (results obtained using 6 layers of Pt were practically coincident with those using 4 layers). The TiO_x/Pt(111) z-phase is shown in Fig. 1a. It has an incommensurate rectangular unit cell of 6.8×8.6 Å^2 aligned along a $\langle 1\bar{1}0 \rangle$ direction of the Pt(111) surface and stoichiometry Ti_6O_8. As in ref. 38, it has been modeled using an oblique $\begin{bmatrix} 5 & 0 \\ 6 & 7 \end{bmatrix}$ cell and slightly shearing the Pt substrate (by about 2%) to bring it into registry with the oxide phase (this cell was referred as "large" in ref. 38). The TiO_x/Pt(111) z′-phase is shown in Fig. 1b. It has a commensurate rectangular unit cell of 14.4×16.6 Å^2 aligned along a $\langle 1\bar{1}0 \rangle$ direction of the Pt(111) surface and stoichiometry $Ti_{24}O_{30}$.[39] Au and Pd atoms were positioned on top of selected oxygen or titanium atoms as a starting point and then the system was left free to fully relax until the forces were smaller than 0.01 eV Å^{-1} per atom.

Table 1 Adsorption energetics and geometry of Au and Pd atoms on the z-phase. The quantities: adhesion energy (E_{adh}), distortion energy (E_{dist}), and binding energy (E_{bnd}) are defined in the text. h_{eq} is the equilibrium distance from the Ti or O atoms directly interacting with the metal atom. The chosen interaction sites are illustrated in Fig. 1a, and are: tetracoordinated Ti atoms along the zig-zag-like motif (distinguished into $Ti_{4,ext}$ and $Ti_{4,int}$ as to their outer or inner location within the stripe), a tricoordinated Ti atom at the border of the stripe (Ti_3), and an oxygen atom at the center of the stripe

		4 Layers Pt				2 Layers Pt			
		$Ti_{4,ext}$	$Ti_{4,int}$	Ti_3	Oxygen	$Ti_{4,ext}$	$Ti_{4,int}$	Ti_3	Oxygen
Au	E_{adh}/eV	2.99	3.11	3.05	0.18	2.86	3.03	2.99	0.21
	E_{dist}/eV	1.53	1.95	1.94	0.02	1.26	1.69	1.69	0.02
	E_{bnd}/eV	1.46	1.16	1.11	0.16	1.60	1.34	1.30	0.19
	h_{eq}/Å	2.41	2.40	2.41	2.35	2.42	2.41	2.40	2.35

		2 Layers Pt			
		$Ti_{4,ext}$	$Ti_{4,int}$	Ti_3	Oxygen
Pd	E_{adh}/eV	1.28	1.27	1.27	1.15
	E_{dist}/eV	0.03	0.04	0.04	0.02
	E_{bnd}/eV	1.25	1.23	1.23	1.13
	h_{eq}/Å	2.45	2.45	2.53	2.04

III. Results and discussion

We start with a brief description of the adsorption template. The TiO_x/Pt(111) system presents a variety of phases: depending on the preparation conditions, several phases having different stoichiometries, structure and defect patterns can be isolated.[27] In particular, at low Ti coverage and in reducing conditions two different ultrathin wetting films are obtained, which, according to atomically resolved STM images, show a zig-zag-like contrast: the z-phase and the z′-phase.[27,38,39] They are constituted of TiO_x monolayers, with the Ti ions at the interface with the Pt(111) support and the O ions forming the top-most overlayer. The structure of the z-phase[38] can be described in terms of infinite stripes running along a $\langle 1\bar{1}0 \rangle$ direction of the underlying metal support. These stripes are linked to each other *via* bridging oxygen atoms (indicated as O_b in the bottom unit cell of Fig. 1a). Within each stripe, the Ti atoms form a (111) pattern distorted in such a way that oxygen-tetracoordinated Ti atoms (indicated as $Ti_{4,ext}$ or $Ti_{4,int}$ in the bottom unit cells in Fig. 1 according to their position within the stripe) determine a zig-zag-like motif. The remaining Ti atoms are coordinated by only 3 oxygen atoms (they are indicated as Ti_3 in the bottom unit cells in Fig. 1) and are located at the border of the stripes. The overall stoichiometry of the film is Ti_6O_8, and corresponds to an average oxidation state of +2.67 for the Ti atoms, in agreement with X-ray photoelectron spectroscopy (XPS) data collected on this system.[53] The z′-phase is less dense according to the STM images, and a variable degree of defectivity is observed, depending on the post-annealing time.[27,39] The major difference with the z-phase is that now the troughs are not constituted by bridging oxygen ions, but by irregular Ti_2O_3 units presenting two holes in each unit cell that expose the bare Pt(111) surface (see Fig. 1b). This is the structure that is obtained after 30 minutes' annealing time at 673 K and that has been tested as a template for the growth of metal clusters.[47] Further annealing produces a gradual transition to a similar structure in which the holes are finally filled with Ti atoms, but the system is under kinetic control and a mixture of the two phases is usually observed.[39]

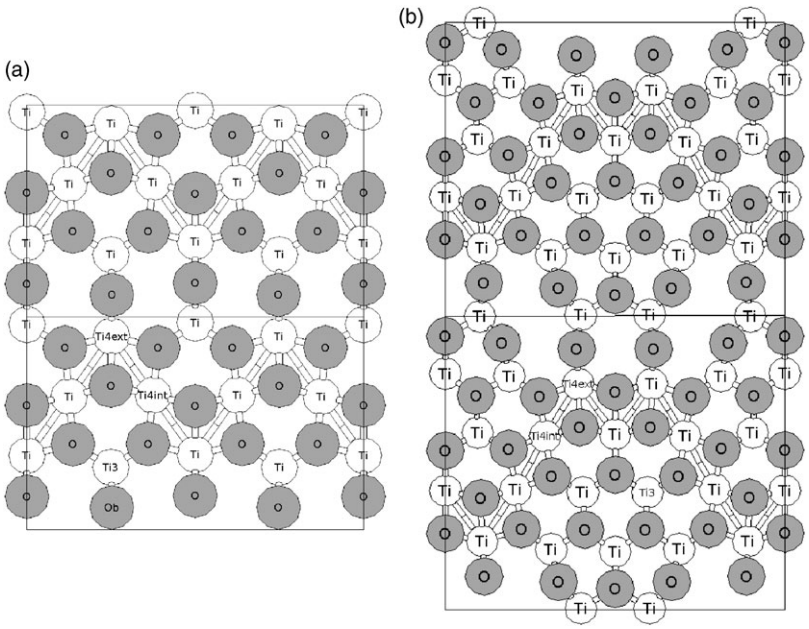

Fig. 1 Top views of the structures of the TiO_x (a) z- and (b) z′-phases grown on the Pt(111) surface (two units cells are shown). Tetracoordinated Ti atoms are indicated as Ti_4: the ones located at the edges of the zig-zag as $Ti_{4,ext}$, the inner ones as $Ti_{4,int}$; tricoordinated Ti atoms are indicated as Ti_3. Bridging oxygen atoms are indicated as O_b.

The results of interaction energies and equilibrium distances for the adsorption of Pd and Au atoms on the z- and z′-phases are collected in Tables 1 and 2, where three energy values are reported: the adhesion energy, E_{adh}, calculated by subtracting the energy of the isolated atom and of the isolated support (the latter in the interacting configuration) from the total energy of the system and by taking the absolute value; the distortion energy, E_{dist}, calculated as the difference between the energy of the isolated support in the interacting configuration and its lowest-energy (optimized) configuration; the binding energy, E_{bnd}, obtained by subtracting the value of the distortion energy from the value of the adhesion energy and corresponding to the energy gain achieved by carrying an atom from infinite distance to the interacting configuration. We now discuss these results, distinguished according to each atom/titania-phase pair.

Pd on the z-phase

As can be evinced from the results in Table 1, a Pd atom interacts with the atoms of the surface without a special preference for any specific site. One can only notice that the adsorption energy is slightly larger on Ti atoms than on O atoms and that there is a tiny difference for the adsorption above a Ti_4 site at the tip of the zig-zag. Due to this flat potential energy landscape, a fast diffusion of Pd atoms and presumably small clusters[54,55] can be expected, and no remarkable templating effect induced by the oxide nanostructuring. In other words, the z-TiO_x/Pt(111) phase should provide a very inert support for the growth of Pd clusters. Note however that we are considering here a coverage around 0.1 monolayers (ML), and that a much more systematic analysis would be needed to extrapolate the behavior at higher coverage.[56]

Table 2 Adsorption energetics and geometry of Au and Pd atoms in the hole located along the troughs of the z′-phase. Au is characterized by a double minimum landscape, so that two values are reported. The adhesion energy E_{adh} is defined in the text. h_{eq} is the equilibrium distance from the top-most Pt(111) plane

	Au^1		Au^2		Pd	
	E_{adh}/eV	h_{eq}/Å	E_{adh}/eV	h_{eq}/Å	E_{adh}/eV	h_{eq}/Å
z′-Phase hole	1.41	2.92	1.70	2.26	3.11	2.21

Au on the z-phase

The situation is completely different for Au adsorption on the same phase.

First of all the interaction with the Ti atoms is now much stronger than that with the O atoms. In particular, the values of the binding energy range between 1.1 and 1.6 eV in the case of adsorption on Ti atoms and only 0.1–0.3 eV in the case of adsorption on O atoms. An Au atom is thus expected to diffuse extremely rapidly on the oxygen overlayer except possibly at very low temperature. We can also note that the equilibrium height of the metal atom results smaller on the site characterized by a weaker adsorption, a behavior opposite to that observed on other oxide surfaces, such as, for example, bulk-terminated (100) MgO terraces.[57] Furthermore, from the data reported in Table 1, one can see that the template distortion energy is negligible (<0.05 eV) in the case of adsorption on O atoms, but quite big (up to nearly 2 eV) on Ti atoms. This is due to the fact that, in the case of the interaction with oxygen atoms, the substrate geometry is practically unperturbed as shown in Fig. 2a (in agreement with the negligible value of the distortion energy), whereas in the second case we observe a remarkable reconstruction in which the Ti atom interacting with the Au atom is "extracted"

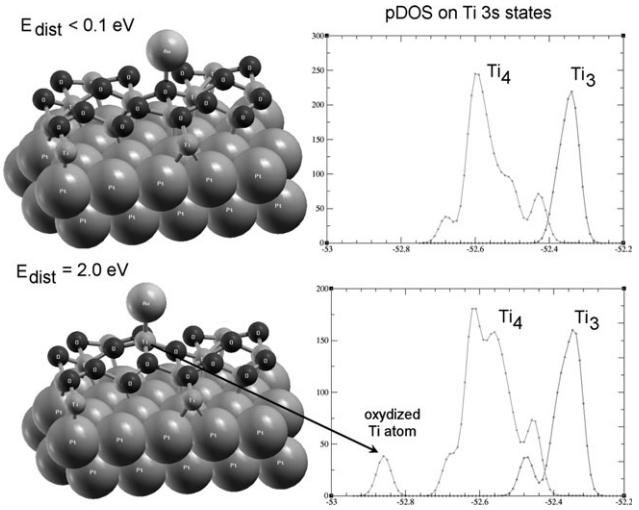

Fig. 2 Optimized structures (left) and pDOS (projected density of states, right) for the adsorption of a Au atom on two sites of the TiO_x/Pt(111) z-phase: an oxygen site (a) and a titanium site (b). The pDOS diagrams are obtained by projecting the total DOS on the Ti 3*s* (semicore) states. The pDOS of the Ti atom interacting with the adsorbed gold appears as a peak shifted at higher binding energies and is highlighted with an arrow.

from the film and brought well above the average height of the other atoms forming the oxide (see Fig. 2b). This accounts for the big value of E_{dist}, which roughly corresponds to the energy necessary to break the metallic bond between the Ti atom and the Pt atoms of the support. Note that the creation of this significant polaron distortion around adsorbed Au atoms (much larger than that found on MgO ultrathin films[7]) might have important consequences on the diffusion of these species and thus the characteristics of Au cluster growth.[54,55]

A second important observation is that the charge state of the Au atom changes when passing from the O to the Ti site: in the former case, Au is essentially neutral, whereas in the latter case it is negatively charged. This can be proven by a charge density analysis. A quick and useful indicator of the charge state of the Au atom is in fact given by the value of the electronic density of states projected on the 6*s* orbital of Au. When gold is adsorbed on Ti_4, one finds a values of 1.25, whereas for gold adsorbed on an oxygen site one finds a value of 0.75. These values can be compared with 1.33 for a gold adsorbed on the MgO(1-layer)/Mo(100) system, and 0.75 for a gold adsorbed on an unsupported MgO(100) film, for which it has been amply shown that Au gets charged in the former case but not in the latter.[7–10]

The situation thus seems to be peculiarly different from that found for Au atoms adsorbed on non-polar ultrathin (1–3 monolayer) MgO films supported on a Mo(100) slab. In the latter case, it has been shown that the charge compression effect due to the MgO film dramatically reduces the work function of the Mo(100) slab: from 4.2 to 2.1–2.5 eV.[58] The final value of the work function is thus not far from the electronic affinity of a gold atom (2.3 eV), and, taking into account that a negative charge on Au is further stabilized by the image charge induced in the Mo(100) metallic slab, this explains why it is energetically favorable for Au to extract an electron from the Mo support and get negatively charged. It should be noted that the image-charge stabilization effect is operative both when the Au atom is on top of a magnesium and when it is on top of an oxygen ion, although the more diffuse and polarizable charge density of the latter repels the Au^- electron cloud so that the final result is a slight preference of Au for the Mg site (2.3 *vs*. 2.0 eV for a 1-layer system from the calculations of ref. 7). The situation is completely different for a Au atom adsorbed on the z-phase. First of all, the fact that this is a polar and ultrathin phase produces a metallization of the oxide with a distortion of the Pt(111) electron density at the surface which partially cancels the surface dipole as in the analogous FeO/Pt(111) phase.[35,59] This has as a consequence that, as noted in ref. 38, there is no big shift of the Pt(111) work function that changes only slightly from 5.6 to 5.4 eV. This in turn means that the polarizability of the metal support and thus the image-charge stabilization effect are not large, and the final result is that the Au atom does not get negatively charged when it is adsorbed on top of an oxygen ion. In contrast, when the Au atom is on top of a Ti atom it is favourable for it to get negatively charged, and the interaction between Au and Ti is large enough to induce the previously described, energetically expensive structural rearrangement to a configuration in which the Ti atom is extracted from the interface and brought at the same level as the oxygen layer. It can be hypothesized, in passing, that at sufficiently high temperature a fast diffusion of the gold atoms on the oxygen overlayer may hinder the more favorable but energetically costly structural reconstruction before long lengths have been covered, suggesting a substantial dependence of Au cluster growth upon environmental parameters. We recall however that we are considering here a coverage around 0.1 ML, and further calculations would be required to investigate the interplay of metal–metal and metal–surface interactions and the corresponding epitaxial morphology.[56]

It can be asked what is the nature of the (charged)Au/(extracted)Ti interaction. An analysis of the pDOS (projected density of states) provides useful information in this sense. In Fig. 2, the pDOS projected on the Ti 3*s* (semicore) levels is shown for the Au/O and Au/Ti systems. As can be seen from this figure, the pDOS is undisturbed when Au adsorbs on top of an O ion and it essentially coincides with that of the bare oxide film (compare Fig. 2a with Fig. 5a in ref. 38), whereas a noticeable effect takes place when it is adsorbed on a Ti ion whose 3*s* level increases from 52.65 to 52.86 eV, a clear sign of an increase in its oxidation state due to the interaction with the Au^- ion (see Fig. 2b). It can be noted in this connection that in ref. 60 the adsorption of a Au atom on a Ti-doped SiO_2/Mo(112) ultrathin film has been studied, and a similar relaxation with the extraction of the Ti atom from the SiO_2 film due to Au adsorption has been observed and attributed to valence instability of Ti (which changes its oxidation state from +4 to +3) and to the formation of a covalent polar bond with Au. Even though it is not easy to quantify separately Coulombic and covalent contributions to the Au–Ti bond, Fig. 2 shows that the oxidation state of the Ti atom interacting with Au is changed, and suggests that electrostatic interactions might play a role in the Au/z-phase adsorption

(further analysis would anyway be useful). Finally, it is important to observe that this peculiar reconstruction is not specific to the TiO_x/Pt(111) phase: apart from the Ti-doped SiO_2/Mo(112) system, an analogous behavior seems to have been observed also for Au adsorption on FeO/Pt(111)[61] and AlO_x/NiAl(110) ultrathin films.[62] We can thus hypothesize that it is a general feature of the adsorption of Au atoms on polar ultrathin oxide films.

Pd on the z′-phase

As recalled above, the z′-phase exhibits zig-zag-like stripes which are very similar to those of the z-phase, but now the troughs are constituted of irregular Ti_2O_3 units presenting holes that expose the Pt(111) support, instead of bridging oxygens as in the z-phase. The interaction of Pd with the striped regions of the z′-phase is very similar to that with the striped regions of the z-phase, with a rather flat potential energy surface on both the oxygen and titanium sites. The corresponding results do not provide any significant information and are not reported here. The interaction of Pd with the troughs, instead, is very different. In particular, the Pd atom is strongly adsorbed and incorporated into the hole of the oxide layer, as can be seen from Table 2. The equilibrium configuration corresponds to a Pd which is practically at the metal/oxide interface at the same level with the Ti atoms, and gives rise to a large interaction energy of 3.1 eV. It can thus be expected that Pd atoms diffuse rapidly on the striped regions of the z′-phase until they get trapped on the defective hole. This is extremely important in view of the growth of metal clusters on these phases, as it allows one to use their regular nanostructured patterns as templates for the growth of ordered arrays of metal nanoclusters.[36,37,43,45–47] Also, a direct contact between metal clusters and the underlying metal support is created, but mediated by the ionic oxide layer, which could lead to novel effects. It can be observed, in passing, that the oxide layer slightly *increases* the Pd–Pt interaction energy (probably due to electrostatic contributions): a Pd atom adsorbed on the same site of the Pt(111) surface has an adsorption energy of 2.73 eV. Note that we are considering here a very low coverage (around 0.03 ML). At higher coverage, it can be expected that the epitaxy around the defect will be influenced by the perturbed electrostatic potential of the holes, whereas at larger distances from the defect the flat potential energy landscape of the striped regions should make that the oxide surface act as an inert support[56] (work to clarify this point is in progress in our lab).

Au on the z′-phase

The interaction of Au with the stripes of the z′-phase also strongly resembles that with the striped regions of the z-phase: one finds a very weak interaction with the oxygen ions and a rather more substantial one (0.8–1.0 eV) with the Ti ions, the latter, however, at the price of a remarkable surface reconstruction which brings the interacting Ti ion to the same height as the oxygen overlayer. The corresponding results do not provide any new information and are not reported here. The interaction of Au with the defective hole is now more subtle. We found in fact that Au interacts more strongly with the hole than with the rest of the oxide film, but also that (1) this interaction is smaller than in the case of the Pd atom (1.7 *vs.* 3.1 eV) and (2) it presents a double-well energy profile, with a first minimum at 2.9 Å from the metal support with an adhesion of 1.4 eV and a second, deeper minimum at 2.3 Å from the metal support with an adhesion of 1.7 eV (see Table 2). This different behaviour with respect to the Pd case is essentially due to the larger spatial extension of the Au $5d^{10}\ 6s^1$ wave function with respect to the Pd $4d^{10}\ 5s^0$ wave function, and strongly resembles an analogous effect observed for the SiO_2/Mo(112)[60] and AlO_x/Ni_3Al(111)[37,45] systems. It thus seems to be a general feature of such defective ultrathin films. This is interesting in view of the use of these oxide films as templates for the growth of metal clusters, as it suggests a seeding protocol in which the more strongly adsorbed element is deposited first and creates seeds that are then covered with a second species, as proposed in ref. 45 and rationalized in ref. 37 for the AlO_x/Ni_3Al(111) system. As observed in the Pd case, the direct contact between the metal clusters and the underlying metal support, mediated by the ionic oxide layer, could also lead to novel effects. It can be noted that in the Au case the presence of the oxide layer *decreases* the Au–Pt interaction energy: a Au atom adsorbed on the same site of the Pt(111) surface, in fact, has an adsorption energy of 2.42 eV. This is probably due to the energy taken up in the oxide rearrangement needed to accommodate the Au atom, or to electron density effects.[60] Note also that in other cases, such as the k-phase of the same TiO_x/Pt(111) system considered here,[63] the dimension of the hole is such that there is no steric hindrance barrier to the adsorption of Pd nor Au atoms. Finally, we recall that we are considering here a very low coverage (around 0.03 ML) and that systematic calculations are in progress in our lab aimed at investigating the epitaxial relationship of larger Au clusters adsorbed on the defective holes of the z′-phase and their effect on the oxide structure.[56,64]

IV. Conclusions

Au and Pd single atoms have been used to probe the energy landscape of metal adsorption on two nanostructured ultrathin films of titanium oxide grown on the Pt(111) surface. These films present compact regions—or stripes—exhibiting a zig-zag-like habitus in their STM images separated by less dense regions (which appear as dark troughs) formed by either bridging oxygens (z-phase) or defective Ti_2O_3 structures presenting holes which expose the bare Pt(111) support (z′-phase). Pd atoms are adsorbed according to a very flat potential energy landscape on the zig-zag-like stripes, and are thus expected to diffuse rapidly in these regions, whereas they are strongly adsorbed on the defective holes of the z′-phase (about 3 eV) where they penetrate into the oxide layer and get in contact with underlying metal. This confirms that these defective holes can act as strong trapping and nucleation centers for the growth of Pd clusters. On the contrary, a Au atom interacts with the zig-zag-like stripes according to two different régimes: (1) a weak interaction régime on top of overlayer oxygens, in which the Au atom remains essentially neutral and exhibits a rather low adsorption energy (less than 0.3 eV); (2) a

strongly interacting régime on top of the Ti atoms, in which Au acquires negative charge from the metal support and extracts a titanium atom from the interface, with a correspondingly much larger (around 1.3 eV) adsorption energy. It is argued that the driving force for the latter régime lies in the strength of the Au–Ti electrostatic interaction or covalent bond, rather than in an image-charge stabilization, which explains the differences of this phenomenon with respect to analogous charge transfer effects occurring in non-polar ultrathin films. Due to the large polaronic reconstruction of the oxide layer accompanying the strongly interacting régime, it is hypothesized that it may not be observed at sufficiently high temperatures on the z′-phase, when the Au atoms diffuse rapidly on the stripes and finally get trapped by the defective holes. The adsorption on these holes, however, is weaker than in the Pd case and presents a double-minimum energy profile, with a first energy minimum at a longer distance from the Pt(111) surface and with a smaller adhesion energy, and an inner minimum at a smaller distance and with a larger adhesion energy. These features are closely analogous to those exhibited by other oxide polar ultrathin phases, and suggest a general framework shared by metal adsorption phenomena on these phases.[65]

Acknowledgements

We acknowledge financial support from the Italian CNR for the project "(Supra-) Self-Assemblies of Transition Metal Nanoclusters" within the framework of the ESF EUROCORES SONS, and from the European Community Sixth Framework Project for the STREP Project "Growth and Supra-Organization of Transition and Noble Metal Nanoclusters" (contract no. NMP-CT-2004-001594). We thank the DEISA Consortium (co-funded by the EU, FP6 project 508830) for support within the DEISA Extreme Computing Initiative (www.deisa.org).

References

1 H. J. Freund, *Surf. Sci.*, 2002, **500**, 271.
2 C. R. Henry, *Surf. Sci. Rep.*, 1998, **31**, 235.
3 H. J. Freund, *Catal. Today*, 2005, **100**, 3.
4 H. J. Freund, *Surf. Sci.*, 2007, **601**, 1438.
5 M. Sterrer, E. Fischbach, T. Risse and H. J. Freund, *Phys. Rev. Lett.*, 2005, **94**, 186101.
6 C. Freysoldt, P. Rinke and M. Scheffler, *Phys. Rev. Lett.*, 2007, **99**, 086101.
7 G. Pacchioni, L. Giordano and M. Baistrocchi, *Phys. Rev. Lett.*, 2005, **094**, 226104.
8 D. Ricci, A. Bongiorno, G. Pacchioni and U. Landman, *Phys. Rev. Lett.*, 2006, **97**, 036106.
9 M. Sterrer, T. Risse, M. Heyde, H. P. Rust and H. J. Freund, *Phys. Rev. Lett.*, 2007, **98**, 206103.
10 M. Sterrer, T. Risse, U. M. Pozzoni, L. Giordano, M. Heyde, H. P. Rust, G. Pacchioni and H. J. Freund, *Phys. Rev. Lett.*, 2007, **98**, 096107.
11 M. Walter, P. Frondelius, K. Honkala and H. Hakkinen, *Phys. Rev. Lett.*, 2007, **99**, 096102.
12 P. Frondelius, H. Hakkinen and K. Honkala, *New J. Phys.*, 2007, **9**, 339.
13 S. Agnoli, M. Sambi, G. Granozzi, J. Schoiswohl, S. Surnev, F. P. Netzer, M. Ferrero, A. M. Ferrari and C. Pisani, *J. Phys. Chem. B*, 2005, **109**, 17197.
14 H. Grönbeck, *J. Phys. Chem. B*, 2006, **110**, 11977.
15 C. Noguera, *J. Phys.: Condens. Mat.*, 2000, **12**, R367.
16 J. Goniakowski, F. Finocchi and C. Noguera, *Rep. Progr. Phys.*, 2008, **71**, 016501.
17 R. M. Jaeger, H. Kuhlenbeck, H.-J. Freund, M. Wuttig, W. Hoffmann, R. Franchy and H. Ibach, *Surf. Sci.*, 1991, **259**, 235.
18 U. Bardi, A. Atrei and G. Rovida, *Surf. Sci.*, 1992, **268**, 87.
19 L. Zhang, J. van Ek and U. Diebold, *Phys. Rev. B: Condens. Matter Mater. Phys.*, 1998, **57**, R4285.
20 L. Zhang, J. van Ek and U. Diebold, *Phys. Rev. B: Condens. Matter Mater. Phys.*, 1999, **59**, 5837.
21 S. Surnev, M. G. Ramsey and F. P. Netzer, *Prog. Surf. Sci.*, 2003, **73**, 117.
22 N. Nilius, T. M. Wallis and W. Ho, *Phys. Rev. Lett.*, 2003, **90**, 046808.
23 G. Kresse, M. Schmid, E. Napetschnig, M. Shishkin, L. Kohler and P. Varga, *Science*, 2005, **308**, 1440.
24 E. D. L. Rienks, N. Nilius, H. P. Rust and H. J. Freund, *Phys. Rev. B: Condens. Matter Mater. Phys.*, 2005, **71**, 241404.
25 J. Weissenrieder, S. Kaya, J. L. Lu, H. J. Gao, S. Shaikhutdinov, H. J. Freund, M. Sierka, T. K. Todorova and J. Sauer, *Phys. Rev. Lett.*, 2005, **95**, 076103.
26 M. Bowker, P. Stone, P. Morrall, R. Smith, R. Bennett, N. Perkins, R. Kvon, C. Pang, E. Fourre and M. Hall, *J. Catal.*, 2005, **234**, 172.
27 F. Sedona, G. A. Rizzi, S. Agnoli, F. X. L. I. Xamena, A. Papageorgiou, D. Ostermann, M. Sambi, P. Finetti, K. Schierbaum and G. Granozzi, *J. Phys. Chem. B*, 2005, **109**, 24411.
28 M. Kulawik, N. Nilius and H. J. Freund, *Phys. Rev. Lett.*, 2006, **96**, 036103.
29 C. Franchini, V. Bayer, R. Podloucky, G. Parteder, S. Surnev and F. P. Netzer, *Phys. Rev. B: Condens. Matter Mater. Phys.*, 2006, **73**, 155402.
30 G. Hamm, C. Barth, C. Becker, K. Wandelt and C. R. Henry, *Phys. Rev. Lett.*, 2006, **97**, 126106.
31 J. L. Lu, S. Kaya, J. Weissenrieder, T. K. Todorova, M. Sierka, J. Sauer, H. J. Gao, S. Shaikhutdinov and H. J. Freund, *Surf. Sci.*, 2006, **600**, L164.
32 D. Stacchiola, S. Kaya, J. Weissenrieder, H. Kuhlenbeck, S. Shaikhutdinov, H. J. Freund, M. Sierka, T. K. Todorova and J. Sauer, *Angew. Chem., Int. Ed.*, 2006, **45**, 7636.
33 J. Schoiswohl, S. Surnev, F. P. Netzer and G. Kresse, *J. Phys. Chem. B*, 2005, **109**, 17197.
34 J. Schoiswohl, M. Sock, Q. Chen, G. Thornton, G. Kresse, M. G. Ramsey, S. Surnev and F. P. Netzer, *Top. Catal.*, 2007, **46**, 137.
35 L. Giordano, G. Pacchioni, J. Goniakowski, N. Nilius, E. D. L. Rienks and H. J. Freund, *Phys. Rev. B: Condens. Matter Mater. Phys.*, 2007, **76**, 075416.
36 M. Schmid, M. Shishkin, G. Kresse, E. Napetschnig, P. Varga, M. Kulawik, N. Nilius, H. P. Rust and H. J. Freund, *Phys. Rev. Lett.*, 2007, **97**, 046101.
37 M. Schmid, G. Kresse, A. Buchsbaum, E. Napetschnig, S. Gritschneder, M. Reichling and P. Varga, *Phys. Rev. Lett.*, 2007, **99**, 196104.
38 G. Barcaro, A. Fortunelli, F. Sedona and G. Granozzi, *J. Phys. Chem. C*, 2007, **111**, 6095.
39 F. Sedona, G. Granozzi, G. Barcaro and A. Fortunelli, *Phys. Rev. B: Condens. Matter Mater. Phys.*, 2008, in press.
40 B. K. Min, A. K. Santra and D. W. Goodman, *Catal. Today*, 2003, **85**, 113.
41 S. Degen, C. Becker and K. Wandelt, *Farad. Disc.*, 2004, **125**, 343.
42 B. K. Min, W. T. Wallace and D. W. Goodman, *J. Phys. Chem. B*, 2004, **108**, 14609.
43 N. Nilius, E. D. L. Rienks, H. P. Rust and H. J. Freund, *Phys. Rev. Lett.*, 2005, **95**, 066101.
44 A. Lehnert, A. Krupski, S. Degen, K. Franke, R. Decker, S. Rusponi, M. Kralj, C. Becker, H. Brune and K. Wandelt, *Surf. Sci.*, 2006, **600**, 1804.
45 G. Hamm, C. Becker and C. R. Henry, *Nanotechnology*, 2006, **17**, 1943.
46 N. Bernudov, G. Mariotto, K. Balakrishnan, S. Murphy and I. V. Shvets, *Surf. Sci.*, 2006, **600**, L287.
47 F. Sedona, S. Agnoli, M. Fanetti, I. Kholmanov, E. Cavaliere, L. Gavioli and G. Granozzi, *J. Phys. Chem. C*, 2007, **111**, 8024.
48 S. Baroni, A. D. Corso, S. de Gironcoli and P. Giannozzi, *PWscf (plane-wave self-consistent field)—a computer code for electronic-*

structure calculations within density-functional theory and density-functional perturbation theory, 2007, http://www.pwscf.org.
49 D. Vanderbilt, *Phys. Rev. B: Condens. Matter Mater. Phys.*, 1990, **41**, 7092.
50 J. P. Perdew, J. A. Chevary, S. H. Vosko, K. A. Jackson, M. R. Pederson, D. J. Singh and C. Fiolhais, *Phys. Rev. B: Condens. Matter Mater. Phys.*, 1992, **46**, 6671.
51 E. Aprà and A. Fortunelli, *THEOCHEM*, 2000, **501**, 251.
52 C. D. Valentin, *J. Chem. Phys.*, 2007, **127**, 154705.
53 P. Finetti, F. Sedona, G. A. Rizzi, U. Mick, F. Sutara, M. Svec, V. Matolin, K. Schierbaum and G. Granozzi, *J. Phys. Chem. C*, 2007, **111**, 869.
54 G. Barcaro, A. Fortunelli, F. Nita and R. Ferrando, *Phys. Rev. Lett.*, 2005, **95**, 246103.
55 L. J. Xu, G. Henkelman, C. T. Campbell and H. Jonsson, *Phys. Rev. Lett.*, 2005, **95**, 146103.
56 G. Barcaro, A. Fortunelli, G. Rossi, F. Nita and R. Ferrando, *Phys. Rev. Lett.*, 2007, **98**, 156101.
57 G. Barcaro and A. Fortunelli, *J. Phys. Chem. B*, 2006, **110**, 21021.
58 L. Giordano, F. Cinquini and G. Pacchioni, *Phys. Rev. B: Condens. Matter Mater. Phys.*, 2005, **73**, 045414.
59 J. Goniakowski, C. Noguera and L. Giordano, *Phys. Rev. Lett.*, 2007, **98**, 205701.
60 L. Giordano, A. D. Vitto and G. Pacchioni, *J. Chem. Phys.*, 2006, **124**, 034701.
61 L. Giordano, J. Goniakowski and G. Pacchioni, 2008, private communication.
62 N. Nilius, M. Ganduglia-Pirovana, V. Brazdova, M. Kulawik, J. Sauer and H.-J. Freund, *Phys. Rev. Lett.*, 2008, accepted.
63 F. Sedona, M. Sambi, L. Artiglia, G. A. Rizzi, A. Vittadini, A. Fortunelli and G. Granozzi, *J. Phys. Chem. C*, 2008, DOI: 10.1021/jp711801w.
64 A. Fortunelli, G. Barcaro, F. Sedona and G. Granozzi, 2008, unpublished results.
65 Note that we have not considered in this study electropositive metals (such as Fe) that might give rise to yet more novel effects.

Searching for the optimum structures of alloy nanoclusters†

Riccardo Ferrando,[a] Alessandro Fortunelli[b] and Roy L. Johnston[c]

Received 14th June 2007, Accepted 22nd August 2007
First published as an Advance Article on the web 5th September 2007
DOI: 10.1039/b709000e

FerrandoPCCP2008

Recent advances in computational methods for searching for the most stable structures of alloy nanoparticles are reviewed. A methodology based on extensive global optimization searches within an empirical potential model in conjunction with structure recognition algorithms and subsequent density-functional local relaxation of the lowest-energy structures pertaining to each different structural basin is proposed. Applications to different systems, including Cu–Ag, Cu–Au, Ni–Ag, Co–Ag, Co–Au, Ni–Au and Pd–Pt clusters, are presented.

1. Introduction

Alloy nanoclusters (or nanoalloys) are a subject of increasing interest both in basic science and in practical applications.[1,2] In fact, nanoalloys find applications in many different fields, from catalysis, to optics and magnetism. From the theoretical and computational point of view, the first problem that one is faced with is the determination of geometric and electronic structure: given the size (number of atoms, N) of an alloy nanocluster, and its composition, find the most stable cluster structure (*i.e.*, its geometry and chemical ordering).

Recent calculations and experiments have shown that nanoalloys can present non-trivial geometric structures[3–9] (exhibiting a much richer variety than pure clusters) and complex chemical ordering patterns.[10–15] From these results it follows that it is extremely difficult to simply guess what are the most stable structures on the basis, for example, of symmetry considerations, or some kind of physico-chemical intuition. What is needed to address the problem of the determination of the structure of a given alloy nanoparticle is a strategy for an accurate and possibly thorough exploration of its potential energy surface (PES).

[a] *Dipartimento di Fisica, Università di Genova, INFM and IMEM/CNR, Via Dodecaneso 33, I16146 Genova, Italy. E-mail: ferrando@fisica.unige.it*
[b] *IPCF/CNR, Via G. Moruzzi 1, I56124 Pisa, Italy. E-mail: fortunelli@ipcf.cnr.it*
[c] *School of Chemistry, University of Birmingham, Edgbaston, Birmingham, UK B15 2TT. E-mail: r.l.johnston@bham.ac.uk*

† The HTML version of this article has been enhanced with colour images.

Alessandro Fortunelli is senior researcher at the Istituto per i Processi Chimico-Fisici of the Italian CNR. His research in the field of theoretical chemistry has dealt with the description of the electronic structure of atoms, molecules and solids, with attention to methodologies which allow one to extend the theoretical treatment to realistic systems. Recent interests include structural, optical, catalytic and magnetic properties of metal nanoclusters and nanoalloys, ultra-thin oxide-on-metal films, and mechanical properties of polymers. He is author of roughly 100 journal articles.

Riccardo Ferrando is Professor of Condensed Matter Physics in the Physics Department of the University of Genova. His research activity is in the fields of theoretical and computational condensed matter physics and chemistry. Specific research interests range from the theory of activated processes, to diffusion on crystal surfaces, thin film and crystal growth, nanoparticle structural properties and dynamics, and aggregation phenomena in colloids. He is author of roughly 120 papers in peer reviewed journals.

Roy Johnston is Professor of Computational Chemistry in the School of Chemistry at the University of Birmingham. His research spans the fields of computational nanoscience and nature-inspired computation. Examples include the study of elemental and bimetallic clusters, the application of genetic and other nature-inspired algorithms to optimisation problems in chemistry and physics, and developing techniques for visualising and analysing the complexity of energy landscapes. He is the author of a book and over 120 journal articles.

When dealing with the problem of exploring a nanoalloy PES, one is faced with the problem of complexity. In fact, even for the simpler case of a free homogeneous cluster, the PES is incredibly complex.[16] The number of local minima (each one corresponding to a possible cluster structure) in the PES increases exponentially with cluster size.[17] This number becomes enormous even for quite small clusters. For example, the PES of a Lennard-Jones cluster of 55 atoms has more than 10^{12} minima.[18]

Binary clusters present even more complex PES than homogeneous clusters, due to the inequivalence of homotops.[19] Consider binary clusters made of atoms A and B. Homotops are defined as clusters with the same size, composition and geometrical arrangement, differing only in the way in which A and B-type atoms are arranged. For a cluster made of n_A and n_B atoms, with $n_A + n_B = N$, one finds that a single geometrical isomer comprises

$$\frac{N!}{n_A!n_B!} \tag{1}$$

different homotops (ignoring point group symmetry, which will cause some homotops to be equivalent). Therefore, the PES of a binary cluster can present a vastly larger number of local minima than the PES of a homogeneous cluster of the same size. For example, in the case of a 98-atom bimetallic cluster of composition $Pd_{49}Pt_{49}$, there are of the order of 10^{28} homotops for each geometrical structural motif![20] While it can never be guaranteed that the absolute lowest energy homotop has been found for a particular geometry, the combination of search methods described below should enable us to end up close to the global minimum.

For the above reasons, the direct exploration of the PES by first-principles methods, including density-functional theory (DFT), is today limited to small sizes. For pure clusters, there are examples of fully first-principles global optimization of clusters up to size 20.[21] In the case of binary clusters the limiting size is even smaller, around 10 atoms, and calculations are rather cumbersome.

In order to study larger alloy nanoclusters (and also to speed up the study of small clusters) we propose a two-step search strategy. The first step relies on the use of a more approximate model for the PES, which is thoroughly explored by global-optimization searches, in conjunction with structure recognition algorithms to construct an appropriate database of possible structures. In this way, the model PES is partitioned into basins corresponding to different structural motifs. The second step involves a reoptimization of the clusters in the database by DFT methods, selecting the lowest-energy candidates pertaining to each structural basin in order to explore as much structural diversity as possible. This methodoloy has recently been applied to gas-phase alloy nanoclusters (as described below) and to homogeneous Pd[22] and Ag[23] clusters supported on MgO. As such, it represents an extension of previous hybrid or hierarchical optimization approaches which use empirical potentials to guide optimization, followed by DFT minimization to refine the search (see, for example, ref. 24–28), to the more challenging problem of nanoalloys.

It should be noted that we here restrict ourselves to the static problem of identifying the global minimum and other low energy structural isomers, concentrating on the internal (binding) energy at 0 K. In future, it should be possible to extend this study to the exploration of the thermodynamic free energy landscape as a function of temperature, by calculating the vibrational, *etc*. contributions to the entropy at the DFT level. Moving from statics to dynamics, the energy differences between the global minimum and low energy isomers, when coupled with information about transition states (configurations and energy barriers)[16] can give important information about dynamical effects, including cluster rearrangement pathways and rates and cluster melting (see, for example, ref. 23, 29–31 and references therein).

In the following, we summarize our search methodology and present some examples to which it has been recently employed.

2. Computational methodology

2.1 Atom–atom potential model

First of all, the cluster PES is modelled by an empirical potential. Our choice is a many-body potential derived within the second-moment approximation to the tight-binding model, referred to in the following as the SMATB potential. This kind of potential has been derived and parametrized independently by several authors.[32–35]

Within this model, the configurational energy of a cluster is a function of the interatomic distances r_{kl} and it is written as the sum of atomic energies

$$E = \sum_{k=1}^{N} \sum_{i=A,B} d_k^i E_{k,i}, \tag{2}$$

where d_k^i is an occupation variable whose value is 1 if atom k is of species i, and 0 otherwise. The atomic energy $E_{k,i}$ of an atom k ($k = 1,\ldots,N$) of species i (i = A, B) includes a band-energy term $E_{k,i}^{band}$ and a repulsive term $E_{k,i}^{rep}$

$$E_{k,i} = E_{k,i}^{band} + E_{k,i}^{rep}. \tag{3}$$

$E_{k,i}^{band}$ and $E_{k,i}^{rep}$ are given by

$$\begin{aligned} E_{k,i}^{band} &= -\left\{ \sum_{l\neq k}^{N} \sum_{j=A,B} d_l^j \xi_{ij}^2 \exp\left[-2q_{ij}\left(\frac{r_{kl}}{r_{ij}^0} - 1 \right) \right] \right\}^{1/2} \\ E_{k,i}^{rep} &= \sum_{l\neq k}^{N} \sum_{j=A,B} d_l^j A_{ij} \exp\left[-p_{ij}\left(\frac{r_{kl}}{r_{ij}^0} - 1 \right) \right], \end{aligned} \tag{4}$$

where r_{kl} is the distance between the k-th and the l-th atoms. The parameters (A_{ij}, ξ_{ij}, p_{ij}, q_{ij}) are usually fitted to experimental properties of bulk metals and alloys,[32,33,35,36] or to bulk properties and those of the diatomic molecules of the corresponding elements.[36] r_{AA}^0 and r_{BB}^0 are the nearest-neighbour distances of the pure bulk elements. r_{AB}^0 is often taken as the average of the pure distances, *i.e.* $r_{AB}^0 = (r_{AA}^0 + r_{BB}^0)/2$, but it can also be taken as the experimental nearest-neighbor A–B distance in some specific ordered bulk alloy, as in ref. 35. The parameters of the potential for the systems presented below can be found in ref. 5.

It is important to note that the many-body character of the interaction potential is very important for a reasonably

accurate modelling of metallic systems. In fact, the potential must account for the bond-order/bond-length correlation, which gives shorter and stronger bonds for low-coordination atoms and is a many-body effect.

The main drawback of this type of empirical potential is the lack of specific quantum effects, such as shell-closure, magnetic, electronic wave function interference or directionality effects.[37] However, it can be noted that whereas shell-closure or magnetic effects are intrinsically of quantum origin and cannot be described within an empirical potential approach, directionality effects can be dealt with by introducing angular-dependent terms into the potential.[38] These terms can be important in stabilizing cage or even planar configurations for small clusters of third-row transition metals.[21,39]

2.2 Global optimization methods

Recent developments in computational techniques now allow the efficient exploration of the PES of homogeneous nanoclusters modelled by empirical potentials up to sizes of several hundred atoms.[40,41] For these sizes, putative global minima have been located for several systems. In the case of binary clusters, global optimization studies are fewer, and the present limiting sizes are somewhat lower. At present, putative global minima have been found for a series of systems at sizes below 100 atoms.[3–6,8,9,42–44]

Most studies in cluster global optimization have focused on the search for the global minimum and the lowest lying metastable isomers. However, in the case of metal clusters (and even more for nanoalloys) this is in general not sufficient. In fact, empirical potentials are often rather crude approximations to the real PES. For example, it may happen that the empirical potential does not give the correct energetic ordering for structures pertaining to different motifs. A striking example is tetrahedral Au_{20}.[21] According to the SMATB potential, the tetrahedral structure is the best in its energy funnel, but there are more than 10^3 structures belonging to other funnels which are lower in energy than the tetrahedron. Another example of incorrect energetic ordering of isomers within an empirical model is Pt_{55}, in which the SMATB potential underestimates the tendency of Pt icosahedra to form *rosettes* at vertices,[45] though it gives the correct increasing trend for rosette formation in clusters in the series Cu, Ag, Pt and Au.

A global optimization algorithm should, therefore, be able to explore all significant funnels on the empirical potential PES in order to increase the probability of finding all significant cluster structural motifs. For each funnel, the lowest-energy minima are collected to form the database of structures to be reoptimized by DFT methods.

The most widely used global optimization algorithms belong to two families. The first family is represented by genetic algorithms (GAs). Within the GA approach, a population of clusters is evolved, using evolutionary operators such as crossover, mutation and natural selection, which are analogues of natural processes in biological evolution.[46] GAs have been successfully applied to cluster geometry optimization problems for a variety of systems.[24,47–51] The results discussed below for Pd–Pt clusters were obtained using (in part) the Birmingham cluster genetic algorithm (BCGA) code, which has been described in detail elsewhere.[47]

The second family of algorithms comprises "Monte-Carlo-plus-minimization" schemes (also commonly known as basin-hopping Monte Carlo).[16,52] Within the basic basin-hopping approach, a single cluster is evolved. Starting with a given cluster configuration i, corresponding to a local minimum in the PES with energy E_i, a move is attempted, corresponding to a transformation of the cluster. For example, the *shake* move displaces all atoms in the cluster randomly by a certain amount around their present position. The *exchange* move swaps two atoms of different species. After performing the move, local minimization is applied to the cluster, and a tentative final configuration f with energy E_f (hopefully corresponding to a new local minimum), is obtained. The new configuration is either accepted or rejected, according to the Metropolis criterion at some simulation temperature T, *i.e.* with probability $\exp[-(E_f - E_i)/(k_B T)]$.

While basin-hopping is extremely efficient in exploring the PES within a given funnel, it may be less efficient in escaping from an initial funnel to explore other parts of the PES. Therefore, the search for structures belonging to different structural motifs might be difficult within this approach. In order to overcome this problem, different algorithms have been developed within the framework of the basin-hopping scheme. Some of them make use of an order parameter, which may be either related to the geometry or to the chemical ordering in the cluster. The parallel excitable walkers (PEW) algorithm evolves n_w Monte Carlo walkers in parallel.[53] These Monte Carlo walkers repel each other in the order parameter space. The order parameter should be chosen in such a way that structures belonging to different motifs present well-separated order parameter values. If this is the case, different walkers will explore different funnels and optimize structures within different motifs. An example of the output from a run of the PEW algorithm is given in Fig. 1. Order parameters can also be implemented within genetic algorithms, as a measure of population diversity or for evolving sub-populations within evolutionary niches.[54] Another possibility is to use the order parameter in memory-aided searching, to label parts of the PES which have already been visited, so they can be avoided in future,[55] as in tabu searching. Recently, a further global optimization approach called conformational space annealing has been developed by Lee *et al.*[56] which combines some features of the basin-hopping and the genetic algorithm approaches.

In our experience, there is no general rule for preferring a specific algorithm in all cases, since the efficiency of global optimization methods is rather strongly system-dependent. A good strategy is to perform optimization runs using different algorithms and different order parameters. Hybrid approaches, for example combining a genetic algorithm for geometry optimization and exchange-only Monte Carlo moves for homotop optimization, have also been adopted.[20] In the case of high-symmetry geometric shell structures, more restricted homotop searches may be carried out by only studying those homotops in which all atoms in a set of symmetry equivalent atoms in the parent homonuclear cluster (known as a "sub-shell" or "orbit"[16]) are constrained to be of the same element.[20,57]

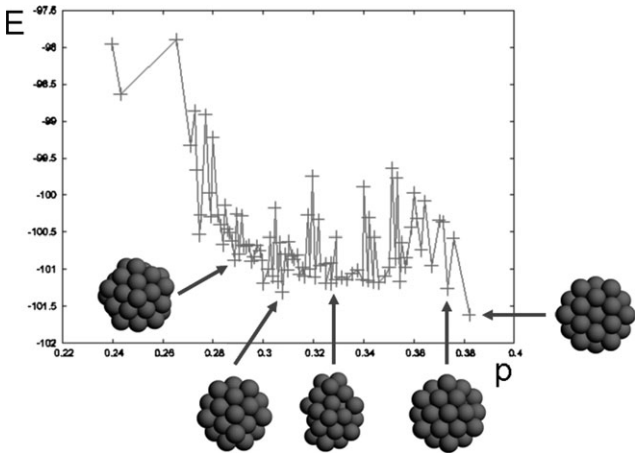

Fig. 1 Results of an optimization run by the PEW algorithm[53] for $Ag_{32}Cu_6$ modelled by SMATB potentials. Three walkers are used. These walkers repel each other in the space of the order parameter p, which is defined as the number of nearest-neighbour mixed bonds divided by the total number of nearest-neighbour bonds. For each p value, the configurational energy E of the most stable cluster is reported (in eV). Different ranges of p correspond to different structures, and some structures correspond to well-defined minima of $E(p)$. From left to right, a capped decahedron, two defective fivefold pancakes, a defective sixfold pancake and a perfect sixfold pancake are shown. The latter is the global minimum structure.

It has also been found that a combination of unseeded searches (which start from random atomic positions) and seeded searches (which may start for example from structures found for nearby sizes and/or compositions) is usually fruitful. For example, *system comparison* and *composition comparison* are often useful.[5,43,44]

System comparison is performed as follows. Once putative global minima have been identified for two clusters X_nY_m and X_nZ_m, two artificial clusters are constructed by replacing all the Y atoms of the X_nY_m cluster with Z atoms, and *vice versa*. These new clusters are then subjected to local minimization and compared to the old putative global minima, which are replaced if the new clusters have a lower energy.

Composition comparison starts from the putative global minima of three adjacent compositions, $X_{n-1}Y_{m+1}$, X_nY_m, and $X_{n+1}Y_{m-1}$. Then, the following test is made on the X_nY_m putative global minimum. The $X_{n-1}Y_{m+1}$ cluster is taken, and all Y atoms are substituted one by one by X atoms, obtaining $m + 1$ clusters of composition X_nY_m, which are locally minimized. This process is repeated by replacing each X atom of $X_{n+1}Y_{m-1}$ with a Y atom. Finally, all new clusters are compared to the old putative X_nY_m global minima.

The philosophy behind these and related approaches, such as varying the heteronuclear parameters of the SMATB potential within the range defined by the values for the pure metals,[58] is to use the empirical potential as a tool for exploring the diversity of the PES. In this spirit, rather than focusing on the accuracy and predictive capabilities of the empirical potential, it is often fruitful to use two different potentials which are able to "bracket" the experimental behaviour (*e.g.*, the tendency toward open or compact configurations) or where each one mimics different aspects of the experimental and/or sophisticated theoretical phenomenology.

2.3 Density-functional local relaxation

Density-functional relaxation is a very important step in obtaining an accurate description of the energetics of nanoalloys. As stated in the Introduction, for a given size and composition it is generally not very useful to relax the best n minima obtained in the global optimization of the empirical potential PES. Indeed, if there are f different structural motifs, it is much more effective to relax n/f clusters for each motif. This accounts for the cases in which empirical potentials predict in a sufficiently accurate way the energy ordering within each structural family, but for different reasons (some of them of electronic origin, such as electronic shell closure, magnetic or electronic wave function interference effects,[37] or due to an incorrect parametrization of the empirical potential) do not predict the correct relative energy ordering between different structural families. The importance of testing a wide diversity of empirical potential local minima using first-principles approaches has recently been underlined.[59]

In the following applications, density-functional calculations were carried out with the DF module of the NWChem package,[60] using the Becke functional[61] or the Perdew–Wang functional[62] for exchange and the Perdew–Wang functional[62] for correlation. Gaussian-type-orbital basis sets of double-zeta quality[63–66] and effective core potentials[67] were used for all elements. Charge density fitting (11s4p5d3f4g)/[11s4p4d3f2g] Gaussian-type-orbital basis sets were used to compute the Coulomb potential.[68] All the calculations were performed spin-unrestricted and using a Gaussian-smearing technique[69] for the fractional occupation of the one-electron energy levels. A numerical grid of 65 radial points and 350 points for the angular part was used for evaluation of the exchange–correlation potential and energy. The geometry optimization was stopped when the numerical force on atoms was less than 4×10^{-4} au. More details on the numerical procedure can be found in ref. 66.

3. Applications to specific systems

3.1 40-atom Cu–Ag and Cu–Au clusters

Here we review the results obtained in ref. 8 concerning Cu–Ag and Cu–Au clusters of size 40 and varying composition. For this size, we expect an interesting interplay of geometric and electronic effects. Size 40 is a magic electronic size for both the hard-wall and the harmonic spherical electron gas, and the tensor surface harmonic theory.[70–72] Therefore, quantum effects, possibly connected with spherical aromaticity, are likely to be important.[73,74] At $N = 40$, we also expect competition between several structural motifs, ranging from fcc to icosahedral, decahedral and polyicosahedral (pIh) clusters.[4–6,37] The latter are obtained by packing together elementary icosahedra of 13 atoms (which can share some atoms).

Let us consider Cu–Ag clusters first. Global optimization searches within the SMATB model potential have revealed that there are four structural families in competition, as can be seen in Fig. 2. The first family comprises fcc truncated

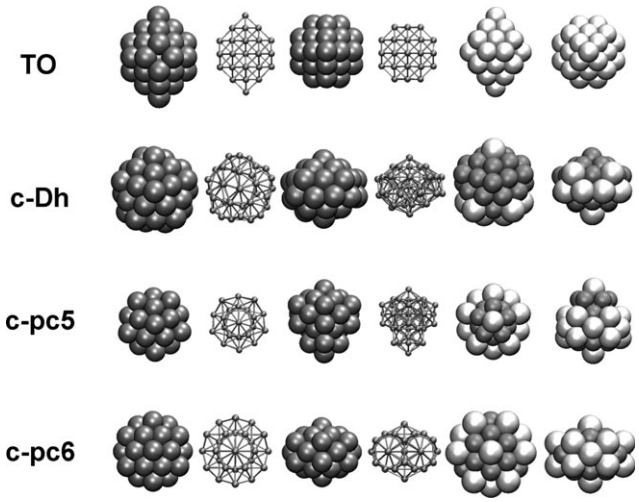

Fig. 2 Structural families of Cu–Ag nanoparticles of size 40 (From ref. 8, reprinted with permission of the American Chemical Society). Each row shows the same structure in six different representations. First row: fcc truncated octahedron (TO). It can be obtained either by removing atoms from four of the six vertices of the complete octahedron of 44 atoms, or by adding two atoms on opposite square facets of the 38-atom fully symmetric truncated octahedron. In the fifth and sixth snapshots, the TO is shown at composition $Ag_{34}Cu_6$. Copper atoms are not visible because they form the inner core; silver atoms are in light grey. This TO has D_{4h} symmetry. Second row: capped decahedron (c-Dh). This structure is obtained by adding an umbrella to the complete decahedron of 23 atoms. Depending on composition, the umbrella shape may change, but the structure is not highly symmetric, having at most a single reflection plane. In the fifth and sixth snapshots, the c-Dh is shown at composition Ag_8Cu_{32}. Third row: capped fivefold pancake (c-pc5). This structure is a polyicosahedron obtained by adding an umbrella of six atoms to the fivefold pancake of 34 atoms.[4] In the fifth and sixth snapshots, the c-pc5 is shown at composition $Ag_{17}Cu_{23}$, where it has C_{5v} symmetry. Fourth row: capped sixfold pancake (c-pc6). This structure is obtained by adding two vertex atoms to the sixfold pancake,[4] a polyicosahedron of 38 atoms. In the fifth and sixth snapshots, the c-pc6 is shown at composition $Ag_{17}Cu_{23}$, where it has D_{3h} symmetry.

octahedral (TO) clusters. The clusters belonging to the second family are decahedra of 23 atoms capped by a distorted umbrella of 17 atoms. In the following, these clusters will be referred to as capped decahedra (c-Dh). Depending on composition, the umbrella can be of different shapes. Structures of this kind were also found in the optimization of pure Sutton–Chen Ag_{40} and Cu_{40} clusters.[75]

Clusters belonging to the third and fourth families are capped polyicosahedra.[4] The third family is obtained by capping the 34-atom fivefold pancake[4] with an umbrella of 6 atoms to produce a 40-atom cluster with a fivefold symmetry axis. The 34-atom fivefold pancake is made of 7 interpenetrating icosahedra, and for that reason it was indicated as pIh^7 in ref. 4. Adding the six-atom cap preserves the polyicosahedral character of the structure, which is now made of 8 icosahedra. In the following, this 40-atom structure is referred to as the capped fivefold pancake (c-pc5). We note that this structure can also be obtained by eliminating five vertex atoms from the 45-atom anti-Mackay icosahedron.

The fourth family of clusters is obtained by capping the 38-atom sixfold pancake (see Fig. 1) by placing two atoms on opposite sides along the sixfold symmetry axis. The 38-atom sixfold pancake is a polyicosahedron made of six elementary icosahedra, and was denoted in ref. 4 as a pIh^6 structure. Adding two atoms on the symmetry axis does not preserve the polyicosahedral character of the structure. This 40-atom structure will be referred to as the capped sixfold pancake (c-pc6) in the following.

All Cu–Ag structures present silver segregation at the cluster surface, as would be expected from the tendency of these elements to phase separate in the bulk, and from the lower surface energy of silver.

The lowest-energy minima obtained within the SMATB model belong to different families depending on composition. No TO global minima are found for Cu–Ag binary clusters. Capped decahedral global minima are found for copper-rich compositions up to $Ag_{11}Cu_{29}$, and for silver-rich compositions from $Ag_{37}Cu_3$ onwards. Capped sixfold pancakes (c-pc6) are the global minima from $Ag_{367}Cu_4$ to $Ag_{33}Cu_7$, and from $Ag_{20}Cu_{20}$ to $Ag_{12}Cu_{28}$, while c-pc5 structures prevail from $Ag_{32}Cu_8$ to $Ag_{21}Cu_{19}$.

In order to analyze the results at varying composition, we define the excess energy E^*_{exc}

$$E^*_{exc}(A_mB_n) = E(A_mB_n) - m\frac{E(A_N)}{N} - n\frac{E(B_N)}{N}, \qquad (5)$$

where A = Ag, B = Cu, $n + m = 40$, and $E(A_mB_n)$ is the cluster configurational energy at the given composition. In the series of Cu–Ag global minima of the SMATB model, c-pc5 structures present the lowest excess energies. In fact, the absolute minimum of E^*_{exc} is obtained for composition $Ag_{27}Cu_{13}$, and corresponds to a perfect core-shell c-pc5 cluster, with an icosahedral copper core of 13 atoms and an external silver shell.

DFT local optimizations of the clusters belonging to the four families partially confirms the results of the SMATB model, though with some differences revealing the importance of electronic shell-closure effects. In fact, according to the DFT calculations, the composition range in which c-pc5 structures prevail is much wider, comprising almost all compositions. The DFT calculations confirm that the cluster with lowest excess energy is $Ag_{27}Cu_{13}$, as can be seen from Fig. 3.

Why do c-pc5 structures prevail strongly at the DFT level? The explanation follows from an electronic shell closure effect. In fact, the c-pc5 structure is the only motif which is able to close the electronic shell, giving clusters with large HOMO–LUMO gaps, in the range of 0.8 eV. In contrast, the gaps for fcc, c-Dh and c-pc6 clusters are very small, of the order of 0.1 eV.

In the case of Cu–Au clusters the situation is somewhat different. For Cu–Au clusters we might also expect the same kind of electronic shell-closure effects. However, already at the SMATB level, some differences come into play. In fact, when comparing gold and silver, one finds that gold is characterized by much *stickier*, shorter-ranged atom–atom interactions,[40,76] so that gold is less able to accommodate strain. The c-pc5 family presents the most strained structures,[6] and therefore these structures are less favoured for Cu–Au than for Cu–Ag.

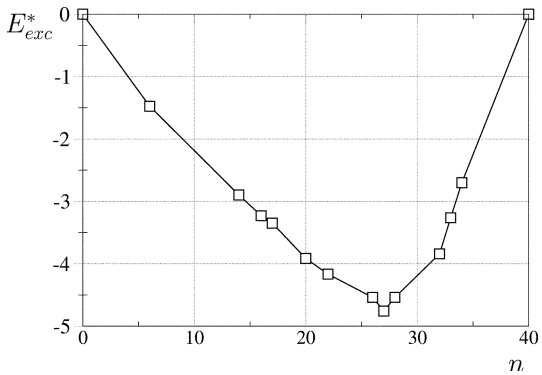

Fig. 3 Excess energy E^*_{exc} (see eqn (5)) as a function of the number of Ag atoms n for Cu–Ag nanoparticles of size 40, as obtained after DFT relaxation. The energies are given in eV. From ref. 8, reprinted with permission of the American Chemical Society.

Moreover, Cu and Au prefer to make mixed nearest-neighbour bonds, as can be expected from their tendency to form bulk ordered alloys. From this point of view, c-pc6 structures are optimal, because they maximize the number of mixed bonds.[6] For these reasons, c-pc5 and c-pc6 structures are in much closer competition for Cu–Au than for Cu–Ag, as confirmed also at the DFT level.[8] HOMO–LUMO gaps are approximately 0.5 and 0.3 eV for c-pc5 and c-pc6 clusters, respectively.

3.2 Intermixing in 34-atom fivefold pancakes

From the results shown in the previous section, it turns out that Cu–Ag clusters show a strong tendency to form perfect core-shell clusters. In fact, the perfect core-shell c-pc5 $Ag_{27}Cu_{13}$ structure exhibits the lowest excess energy in the whole composition range. Here we compare different binary systems with respect to this tendency. For this comparison we have chosen a specific 34-atom structure, the fivefold pancake (see Fig. 4, and also the previous section), and compare the excess energies of three different mixed compositions.[37] In the case of Cu–Ag fivefold pancakes, the perfect core-shell structure is obtained at composition $Ag_{27}Cu_7$ (27,7), with the 7 Cu atoms forming a central pentagonal bipyramid. At composition (27,7) a highly symmetric structure is thus obtained. Highly symmetric structures are possible also at compositions (17,17) and (12,22). Highly symmetric structures with these compositions have been analyzed for a series of systems (Cu–Ag, Ni–Ag, Co–Ag, Cu–Au, Ni–Au, Co–Au) by DFT relaxation. The results are presented in Table 1.

From Table 1, it is apparent that there is a very strong tendency towards core-shell structures for Cu–Ag and Ni–Ag. This tendency is still present, though less evident, in Cu–Au and Ni–Au. Finally, in both Co–Ag and Co–Au, the tendency is to favour intermediate compositions in which some Co atoms are in the external shell. The results obtained for Cu–Ag, Ni–Ag, Cu–Au and Ni–Au can be rationalized in terms of the energetic gain associated with a reduction of the strain in core-shell clusters.[4] This effect is well described already within the SMATB model. In the case of Co–Ag and Co–Au, specific quantum effects come into play.[37] For Ag–Co, the interaction between the magnetic moments of the buried Co atoms oppose the gain in energy associated with the shrinking of the cluster size and the reduced strain. For Au–Co, the latter effect is less evident, but chemical bonding effects connected with the strong directionality of the Au–Au bonding combined with the sticky character of the Au–Au interaction[76] moves the maximum in the stability of the bimetallic clusters as a function of concentration from structures with a perfect core-shell arrangement to configurations with a substantial intermixing of the two elements.

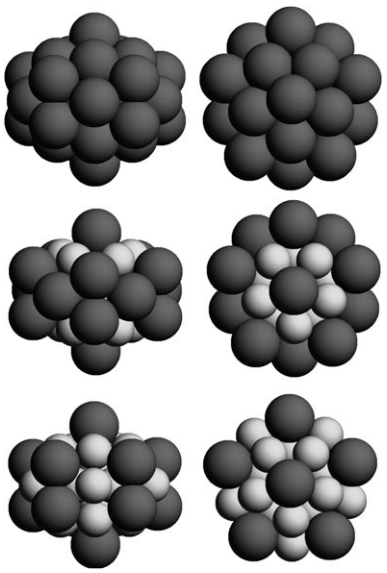

Fig. 4 34-atom fivefold pancakes with different compositions. Composition (27,7) is shown in the top row, compositions (17,17) and (12,22) are shown in the middle and bottom rows, respectively.

3.3 34-atom Pd–Pt clusters

Here we review the results obtained in ref. 9 concerning 34-atom Pd–Pt clusters with varying compositions. This cluster size was chosen as previous empirical potential calculations[6] identified three clusters, with (Pd,Pt) compositions (21,13), (24,10), and (30,4), as having high symmetry and high

Table 1 Excess energies E^*_{exc} (in eV) of 34-atom fivefold pancakes for different systems and compositions. Structures are shown in Fig. 4. Data are taken from ref. 37

Cluster	E^*_{exc}
$Ag_{27}Cu_7$	−5.55
$Ag_{17}Cu_{17}$	−4.00
$Ag_{10}Cu_{22}$	−2.84
$Ag_{27}Ni_7$	−4.36
$Ag_{17}Ni_{17}$	−3.11
$Ag_{10}Ni_{22}$	−2.07
$Ag_{27}Co_7$	−3.63
$Ag_{17}Co_{17}$	−4.53
$Au_{27}Cu_7$	−9.86
$Au_{17}Cu_{17}$	−9.20
$Au_{10}Cu_{22}$	−8.04
$Au_{27}Ni_7$	−10.79
$Au_{17}Ni_{17}$	−9.92
$Au_{10}Ni_{22}$	−7.51
$Au_{27}Co_7$	−8.97
$Au_{17}Co_{17}$	−10.93
$Au_{10}Co_{22}$	−9.32

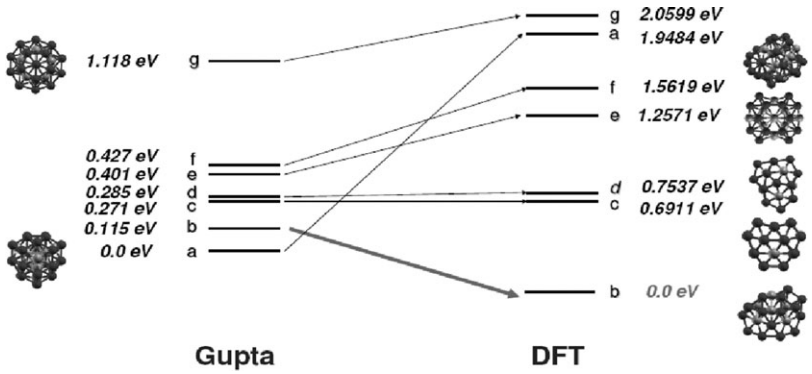

Fig. 5 Structures of seven low energy 34-atom structural motifs commonly found for Pd–Pt clusters. The examples shown are the lowest energy homotops identified (using the Gupta potential) for $Pd_{24}Pt_{10}$ (Pd atoms are shown in dark grey and Pt in light grey). The structures are: (a) Dh-cp(T); (b) Dh-cp(DT); (c) TO; (d) Marks Dh; (e) incomplete 6-fold pIh; (f) low-symmetry pIh; (g) incomplete 5-fold pIh. The figure also shows how the relative stabilities of these structures change on reoptimising the Gupta potential minima at the DFT level. (The numbers are the energies of the structural motifs, in eV, relative to the lowest energy structure, in each case. The thick arrow shows the relative stabilisation of the Dh-cp(T) motif at the DFT level.)

stability, making them promising candidates for a more accurate DFT analysis.

Global optimization searches, using the BCGA program, for the SMATB model potential revealed a large number of structural motifs with competitive energies across a wide range of compositions.[9] The most interesting region was found to be to the Pd-rich side of the composition range, from $Pd_{17}Pt_{17}$ to $Pd_{28}Pt_6$. The low-lying structural motifs identified in this region are shown in Fig. 5, for the composition $Pd_{24}Pt_{10}$ (in each case the lowest energy homotop found is shown). Fig. 5a shows a mixed decahedral (Dh)/closepacked (cp) motif in which a tetrahedral (T) core of 10 atoms is surrounded by 12 atoms growing on the (111) faces and 12 atoms growing along the edges of the tetrahedron. Fig. 5b shows a mixed Dh/cp motif, presenting a 14-atom core with the structure of a trigonal bipyramid (a double tetrahedron , DT) surrounded by 18 atoms growing on the (111) faces and 2 atoms growing along one of the edges of the double tetrahedron. Fig. 5c shows an incomplete 38-atom truncated octahedron (TO), lacking 4 atoms of a (100) face. Fig. 5d shows a Marks decahedron. Finally, Fig. 5e–g show three different polyicosahedral structures: Fig. 5e is an incomplete 38-atom sixfold pancake, lacking two dimers on the basal ring; Fig. 5f is a low-symmetry configuration; and Fig. 5g is an incomplete anti-Mackay icosahedron (which is however different from the c-pc5 structure of section 3.1).

Fig. 6 shows a plot of excess energy E^*_{exc} as a function of the number of Pd atoms n, in the composition range (17,17)–(28,6). The curves were constructed using a combination of genetic algorithm searching followed by homotop optimisation using an exchange-only basin-hopping program. At the level of the SMATB potential, the lowest excess energy structure is $Pd_{21}Pt_{13}$, which has a complete icosahedral Pt_{13} core. It is followed in energy by $Pd_{24}Pt_{10}$, which has a tetrahedral Pt_{10} core. Higher excess energy structures correspond to incomplete 6-fold pancakes as well as incomplete TO structures. It is evident, however, that at the empirical potential level there is a complex crossover in stability between several structural families that are rather close in energy: the energy differences between the putative GM and the first (geometric) excited state structures range from approximately 0–0.2 eV in this composition range.

In the initial DFT study of the 34-atom Pd–Pt clusters, for each composition the most stable homotop at the Gupta level was locally reoptimized at the DFT level. Fig. 7 shows a plot (black points) of the excess energies for these structures, calculated at the DFT level. The jagged nature of this plot makes it unlikely that these structures correspond to GM on the DFT energy surface. However, it was noted that the lowest E^*_{exc} value was found for the Dh-cp(DT) core structure for $Pd_{22}Pt_{12}$, which was only obtained as GM for this composition at the empirical potential level. Because of its high stability, the Dh-cp(DT) structure was then locally optimized at the DFT level for all compositions by taking the initial structures from the previous empirical potential searches. The lower line in Fig. 7 is a plot of E^*_{exc} values after DFT reoptimization of Dh-cp(DT) structures. The much smoother behaviour of E^*_{exc} *vs.* composition for this structure gives us greater confidence that the Dh-cp(DT) structure may be the actual GM on the

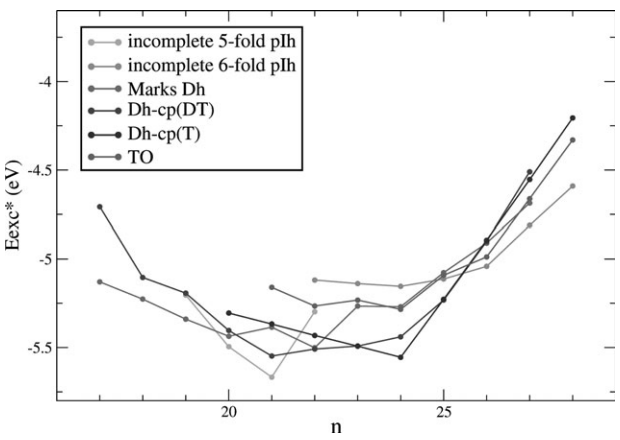

Fig. 6 Excess energies of 34-atom Pd–Pt clusters, as obtained within the SMATB model. n is the number of Pd atoms. From ref. 9, reprinted with permission of the American Chemical Society.

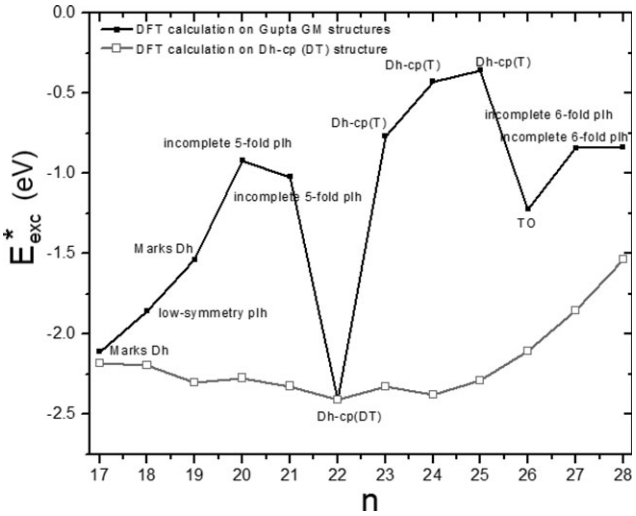

Fig. 7 Excess energies of 34-atom Pd–Pt clusters, as obtained after DFT relaxation. *n* is the number of Pd atoms. From ref. 9, reprinted with permission of the American Chemical Society.

DFT energy surface across the composition range studied. This conclusion was reinforced by a detailed study of $Pd_{24}Pt_{10}$, for which each of the lowest energy homotops of the seven structural families shown in Fig. 5 were reoptimized at the DFT level and the Dh-cp(DT) structure was found to be the most stable, by over 0.65 eV.

The change in relative ordering of the low-energy structural motifs, identified from the BCGA search of the SMTB (Gupta) PES, upon reminimisation at the DFT level is shown schematically in Fig. 5 for the composition $Pd_{24}Pt_{10}$. It is interesting to note that the relative ordering of most of the structural motifs is retained by the DFT calculations, with the exception of the above-mentioned stabilisation of the Dh-cp(DT) structure (indicated by the thick arrow) and a strong destabilisation of the Dh-cp(T) structure.

The Dh-cp(DT) structure is best described for the (20,14) composition in which the internal core of Pt atoms is a double tetrahedron or trigonal bipyramid (*i.e.*, two tetrahedra sharing a face). Pd atoms can grow on the (111) faces of these two tetrahedra in a regular hcp (111) stacking. On each of the 6 faces of the Pt double tetrahedron, three Pd atoms can grow, giving a total of 18 surface Pd atoms. The two remaining Pd atoms lie on an edge between two faces belonging to the same Pt tetrahedron, thereby creating what it is locally a decahedron with its 5-fold axis coinciding with the shared edge. Simultaneously, there is a deformation of the 12 Pd atoms located next to the three edges shared by the two tetrahedra; these Pd atoms minimize their local energy by getting closer to each other and forming three other local decahedral motifs whose axes coincide with the three edges shared by the two tetrahedra. The growth of the Pd atoms on top of the Pt double tetrahedron is similar to that responsible for the interconversion between 5-fold structural families as has been predicted theoretically[40,77] and verified experimentally.[78] The high stability of the Dh-cp(DT) structure is due to the fact that Pt segregates into the core, where it is highly coordinated and thus preferentially close packed, while Pd segregates to the surface, where it is low-coordinated and thus preferentially in a decahedral arrangement. The Dh-cp(DT) arrangement therefore represents the best compromise for the frustration caused by the different binding tendencies of the component metals. Clearly, this is especially true for medium-sized clusters such as those considered in the present work, whereas the crystalline arrangements will eventually prevail for larger clusters.

Previous experimental[79,80] and theoretical[13,81–83] studies of Pd–Pt nanoalloys have indicated that there is a tendency towards segregation of Pd atoms to the surface and Pt atoms to the core. This is interesting as Pd–Pt clusters are among the few systems in which the lighter atoms (*i.e.* Pd) segregate to the surface. The SMTB calculations reported in ref. 9 have confirmed this segregation preference, which is probably dominated by the lower surface energy of Pd.

As $Pd_{17}Pt_{17}$ has a 50 : 50 composition, it represents a good candidate to study surface segregation effects. Several structures were generated using the SMATB potential and the GA search technique. It was found that Dh-Marks type motifs are preferred over polyicosahedral structures at the Gupta potential level, with the Dh-cp(DT) structure somewhat higher in energy. The lowest-energy homotops corresponding to these three structural families were then locally optimized at the DFT level. The homotops were then inverted by swapping all Pd and Pt positions and reoptimized again.

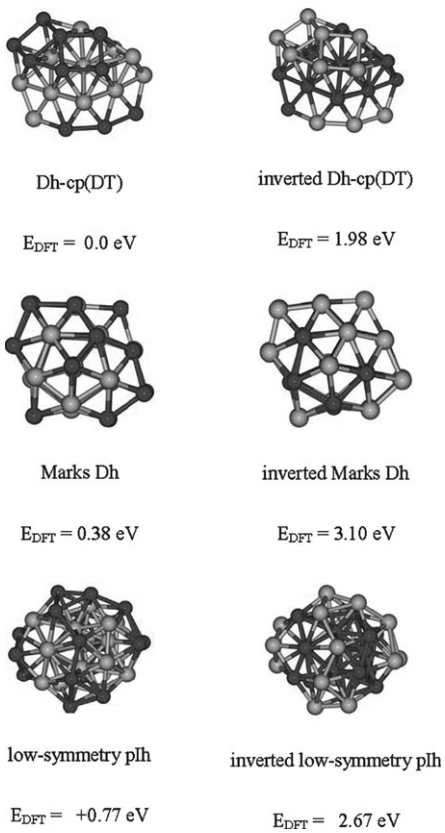

Fig. 8 Comparison of the relaxed DFT energies (relative to the putative GM) of the lowest energy homotops (for the three lowest energy structural motifs) of $Pd_{17}Pt_{17}$ and those obtained by inverting the homotops (swapping all Pd and Pt atoms). From ref. 9, adapted with permission of the American Chemical Society.

Fig. 8 shows the lowest energy homotops for the three lowest energy structural motifs found for $Pd_{17}Pt_{17}$, together with the inverted homotops. For each isomer, the DFT energy (in eV) is given, relative to the putative Dh-cp(DT) GM (top left). Swapping the Pd and Pt atoms always leads to a rise in energy, confirming the surface-segregation of Pd found at the empirical potential level. These calculations are in agreement with previous DFT calculations on smaller Pd–Pt nanoalloys, carried out by Fernández *et al.*[81]

4. Conclusions

As shown by the examples presented above, the structures of alloy nanoparticles are often highly non-trivial. These structures may arise from a complex interplay of geometric and electronic effects, whose relative importance strongly depends on material, size and composition. This is further complicated by the existence of non-equivalent permutational isomers (*i.e.*, homotops). Predicting the most stable structures of nanoalloys is therefore a very demanding task, which requires the development of sophisticated computational techniques.

Here we have reviewed recent advances in the field of structure optimisation of alloy nanoclusters. In particular we have considered a methodology based on extensive global-optimization searches within empirical potential models and subsequent DFT local relaxation of low-energy structures pertaining to different structural motifs (or basins on the energy landscape), rather than just the global minimum and the lowest-energy isomers from the empirical potential calculations. This methodology follows the general philosophy of using empirical potentials as tools for exploring the diversity of the free energy landscape and providing candidate structures for DFT reoptimisation, thus partially overcoming the limitations of empirical potentials, *e.g.*, in describing subtle electronic quantum effects, and pointing to the benefits of using several empirical potentials mimicking different aspects of the experimental and/or sophisticated theoretical phenomenology. This methodology has been successfully applied to gas-phase alloy nanoclusters in the size range up to 50 atoms.

Future challenges include the study of larger gas-phase alloy nanoclusters, and of supported and coated clusters, as well as moving from binary to ternary nanoalloys. As mentioned above, this work may also be extended by using angular-dependent empirical potentials to guide the DFT calculations and by including the calculation of entropy terms to allow searching of the free energy landscape. Finally, the study of dynamical processes, such as cluster rearrangements and cluster melting will also benefit from these methods.

Acknowledgements

A.F. and R.F. acknowledge financial support from the Italian CNR for the project "(Supra-)Self-Assemblies of Transition Metal Nanoclusters" within the framework of the ESF EUROCORES SONS, and from European Community Sixth Framework Programme for the project "Growth and Supra-Organization of Transition and Noble Metal Nanoclusters" (Contract no. NMP4-CT-2004-001594). R.L.J. acknowledges support from the Leverhulme Trust and EPSRC. Some of the work reported here was been performed within the HPC-Europa Transnational Access Programme and R.L.J. also acknowledges the EPSRC National Service for Computational Chemistry Software for a computer facility grant.

The authors would also like to acknowledge their research co-workers, mentioned in the relevant references, with special thanks to Dr Giovanni Barcaro (Pisa), Dr Giulia Rossi (Genova) and Oliver Paz-Borbón (Birmingham), who is also thanked for preparing Fig. 5.

References

1 R. Ferrando, J. Jellinek and R. L. Johnston, *Chem. Rev.*, submitted.
2 Faraday Discussion 138, *Nanoalloys: From Theory to Application*, University of Birmingham, United Kingdom, 3–5 September 2007, to appear in *Faraday Discuss.*, vol. 138.
3 S. Darby, T. V. Mortimer-Jones, R. L. Johnston and C. Roberts, *J. Chem. Phys.*, 2002, **116**, 1536.
4 G. Rossi, A. Rapallo, C. Mottet, A. Fortunelli, F. Baletto and R. Ferrando, *Phys. Rev. Lett.*, 2004, **93**, 105503.
5 A. Rapallo, G. Rossi, R. Ferrando, A. Fortunelli, B. C. Curley, L. D. Lloyd, G. M. Tarbuck and R. L. Johnston, *J. Chem. Phys.*, 2005, **122**, 194308.
6 G. Rossi, R. Ferrando, A. Rapallo, A. Fortunelli, B. C. Curley, L. D. Lloyd and R. L. Johnston, *J. Chem. Phys.*, 2005, **122**, 194309.
7 T. Van Hoof and M. Hou, *Phys. Rev. B*, 2005, **72**, 115434.
8 G. Barcaro, A. Fortunelli, G. Rossi, F. Nita and R. Ferrando, *J. Phys. Chem. B*, 2006, **110**, 23197.
9 L. O. Paz-Borbón, R. L. Johnston, G. Barcaro and A. Fortunelli, *J. Phys. Chem. C*, 2007, **111**, 2936.
10 D. Ferrer, A. Torres-Castro, X. Gao, S. Sepulveda-Guzman, U. Ortiz-Mendez and M. José-Yacamán, *Nano Lett.*, 2007, **7**, 1701.
11 M. C. Fromen, J. Morillo, M. J. Casanove and P. Lecante, *Europhys. Lett.*, 2006, **73**, 885.
12 F. Baletto, C. Mottet and R. Ferrando, *Phys. Rev. Lett.*, 2003, **90**, 135504.
13 L. D. Lloyd, R. L. Johnston, S. Salhi and N. T Wilson, *J. Mater. Chem.*, 2004, **14**, 1691.
14 T. Van Hoof and M. Hou, *Eur. Phys. J. D*, 2004, **29**, 33.
15 D. Cheng, W. Wang and S. Huang, *J. Phys. Chem. B*, 2006, **11**, 16193.
16 D. J. Wales, *Energy Landscapes with Applications to Clusters, Biomolecules and Glasses*, Cambridge University Press, Cambridge, 2003.
17 F. H. Stillinger, *Phys. Rev. E*, 1999, **59**, 48.
18 J. P. K. Doye, D. J. Wales and R. S. Berry, *J. Chem. Phys.*, 1995, **103**, 4234.
19 J. Jellinek and E. B. Krissinel, *Chem. Phys. Lett*, .1996, **258**, 283.
20 L. O. Paz-Borbón, T. V. Mortimer-Jones, R. L. Johnston, A. Posada-Amarillas, G. Barcaro and A. Fortunelli, *Phys. Chem. Chem. Phys.*, 2007, DOI: 10.1039/b707136a.
21 E. Aprà, R. Ferrando and A. Fortunelli, *Phys. Rev. B*, 2006, **73**, 205414.
22 G. Barcaro, A. Fortunelli, G. Rossi, F. Nita and R. Ferrando, *Phys. Rev. Lett.*, 2007, **98**, 156101.
23 G. Barcaro, E. Aprà and A. Fortunelli, *Chem.–Eur. J.*, 2007, **13**, 6408.
24 I. L. Garzón, K. Michaelian, M. R. Beltrán, A. Posada-Amarillas, P. Ordejón, E. Artacho, D. Sánchez-Portal and J. M. Soler, *Phys. Rev. Lett.*, 1998, **81**, 1600.
25 D. J. Wales and M. P. Hodges, *Chem. Phys. Lett.*, 1998, **286**, 65.
26 F. Calvo, S. Tran, S. A. Blundell, C. Guet and F. Spiegelmann, *Phys. Rev. B*, 2000, **62**, 10394.
27 B. Hartke, *Angew. Chem., Int. Ed.*, 2002, **41**, 1468.
28 J. M. Soler, M. R. beltrán, K. Michaelian, I. L. Garzón, P. Ordejón, D. Sánchez-Portal and E. Artacho, *Phys. Rev. B*, 2000, **61**, 5771.
29 E. B. Krissinel and J. Jellinek, *Chem. Phys. Lett.*, 1997, **272**, 301.
30 C. Mottet, G. Rossi, F. Baletto and R. Ferrando, *Phys. Rev. Lett.*, 2005, **95**, 035501.

31 F. Y. Chen, B. C. Curley, G. Rossi and R. L. Johnston, *J. Phys. Chem. C*, 2007, **111**, 9157.
32 R. P. Gupta, *Phys. Rev. B*, 1981, **23**, 6265.
33 V. Rosato, M. Guillopé and B. Legrand, *Philos. Mag. A*, 1989, **59**, 321.
34 A. P. Sutton and J. Chen, *Philos. Mag. Lett*., 1990, **61**, 139.
35 F. Cleri and V. Rosato, *Phys. Rev. B*, 1993, **48**, 22.
36 M. J. López and J. Jellinek, *J. Chem. Phys*., 1999, **110**, 8899.
37 R. Ferrando, A. Fortunelli and G. Rossi, *Phys. Rev. B*, 2005, **72**, 085449.
38 M. I. Baskes, *Phys. Rev. Lett*., 1987, **59**, 2666.
39 S. Bulusu, X. Li, L.-S. Wang and X. C. Zeng, *J. Phys. Chem. C*, 2007, **111**, 4190.
40 F. Baletto and R. Ferrando, *Rev. Mod. Phys*., 2005, **77**, 371.
41 See the Cambridge Cluster Database, http://www-wales.ch.cam.ac.uk/CCD.html.
42 P. J. Hsu and S. K. Lai, *J. Chem. Phys*., 2006, **124**, 044711.
43 J. P. K. Doye and L. Meyer, *Phys. Rev. Lett*., 2005, **95**, 063401.
44 F. Calvo and E. Yurtsever, *Phys. Rev. B*, 2004, **70**, 045423.
45 E. Aprà, F. Baletto, R. Ferrando and A. Fortunelli, *Phys. Rev. Lett*., 2004, **93**, 065502.
46 J. Holland, *Adaptation in Natural and Artificial Systems*, University of Michigan Press, Ann Arbor, MI, 1975.
47 R. L. Johnston, *Dalton Trans*., 2003, **4193**.
48 B. Hartke, *J. Phys. Chem*., 1993, **97**, 9973.
49 B. Hartke, Applications of evolutionary computation in chemistry, in *Structure and Bonding*, ed. R. L. Johnston, Springer-Verlag, Berlin, 2004, vol. 110, p. 33.
50 Y. Xiao and D. E. Williams, *Chem. Phys. Lett*., 1993, **215**, 17.
51 K. Michaelian, N. Rendón and I. L. Garzón, *Phys. Rev. B*, 2000, **60**, 2000.
52 D. J. Wales and J. P. K. Doye, *J. Phys. Chem. A*, 1997, **101**, 5111.
53 G. Rossi and R. Ferrando, *Chem. Phys. Lett*., 2006, **423**, 17.
54 B. Hartke, *J. Comput. Chem*., 1999, **20**, 1752.
55 U. H. E. Hansmann and L. T. Wille, *Phys. Rev. Lett*., 2002, **88**, 068105.
56 J. Lee, H. A. Scheraga and S. Rackovsky, *J. Comput. Chem*., 1997, **18**, 1222.
57 N. T. Wilson and R. L. Johnston, *J. Mater. Chem*., 2002, **12**, 2913.
58 A. Gupta, L. O. Paz-Borbón and R. L. Johnston, unpublished work.
59 J. Rogan, G. García, C. Loyola, W. Orellana, R. Ramírez and M. Kiwi, *J. Chem. Phys*., 2006, **125**, 214708.
60 E. Aprà, *et al*., *NWChem, A Computational Chemistry Package for Parallel Computers, Version 4.7*, 2005, Pacific Northwest National Laboratory, Richland, WA, USA, 2005..
61 A. D. Becke, *Phys. Rev. A*, 1988, **38**, 3098.
62 J. P. Perdew, J. A. Chevary, S. H. Vosko, K. A. Jackson, M. R. Pederson, D. J. Singh and C. Fiolhais, *Phys. Rev. B*, 1992, **46**, 6671.
63 A. Schaefer, C. Huber and R. Ahlrichs, *J. Chem. Phys*., 1994, **100**, 5289.
64 M. Dolg, U. Wedig, H. Stoll and H. Preuss, *J. Chem. Phys*., 1987, **86**, 866.
65 See ftp://ftp.chemie.uni-karlsruhe.de/pub/basen.
66 E. Aprà and A. Fortunelli, *J. Phys. Chem. A*, 2003, **107**, 2934.
67 D. Andrae, U. Haeussermann, M. Dolg, H. Stoll and H. Preuss, *Theor. Chim. Acta*, 1990, **77**, 123.
68 F. Weigend, M. Haser, H. Patzel and R. Ahlrichs, *Chem. Phys. Lett*., 1998, **294**, 143.
69 C. Elsaässer, M. Fähnle, C. T. Chan and K. M. Ho, *Phys. Rev. B*, 1994, **49**, 13975.
70 M. Brack, *Rev. Mod. Phys*., 1993, **65**, 677.
71 A. J. Stone, *Inorg. Chem*., 1981, **20**, 563.
72 D. J. Wales and A. J. Stone, *Inorg. Chem*., 1989, **28**, 3120.
73 A. Hirsch, Z. Chen and H. Jiao, *Angew. Chem., Int. Ed*., 2000, **39**, 3915.
74 C. A. Tsipis, *Coord. Chem. Rev*., 2005, **249**, 2740.
75 J. P. K. Doye and D. J. Wales, *New J. Chem*., 1998, **22**, 733.
76 F. Baletto, R. Ferrando, A. Fortunelli, F. Montalenti and C. Mottet, *J. Chem. Phys*., 2002, **116**, 3856.
77 F. Baletto, C. Mottet and R. Ferrando, *Phys. Rev. B*, 2001, **63**, 155408.
78 J. L. Rodríguez-López, J. M. Montejano-Carrizales, U. Pal, J. F. Sánchez-Ramírez, H. E. Troiani, D. García, M. Miki-Yoshida and M. José-Yacamán, *Phys. Rev. Lett*., 2004, **92**, 196102.
79 A. J. Renouprez, J. L. Rousset, A. M. Cadrot, Y. Soldo and L. Stievano, *J. Alloys Compd*., 2001, **328**, 50.
80 D. Bazin, D. Guillaume, Ch. Pichon, D. Uzio and S. Lopez, *Oil and Gas Science and Technology, Rev. No. 5*, IFP, Rueil-Malmaison, France, 2005, vol. 60, p. 801.
81 E. M. Fernández, L. C. Balbas, L. A. Perez, K. Michaelian and I. L. Garzón, *Int. J. Mod. Phys*., 2005, **19**, 2339.
82 C. Massen, T. V. Mortimer-Jones and R. L. Johnston, *J. Chem. Soc., Dalton Trans*., 2002, 4375.
83 L. D. Lloyd, R. L. Johnston and S. Salhi, *J. Comput. Chem*., 2005, **26**, 1069.

Interface-Stabilized Phases of Metal-on-Oxide Nanodots

Riccardo Ferrando,[†,*] Giulia Rossi,[†] Florin Nita,[†,‡] Giovanni Barcaro,[§] and Alessandro Fortunelli[§,*]

[†]Dipartimento di Fisica and INFM/CNR, Via Dodecaneso 33, Genova, I16146, Italy, [‡]Institute of Physical Chemistry IG Murgulescu, Romanian Academy, Spl. Independentei 202, Bucharest, Romania, and [§]IPCF/CNR, Via G. Moruzzi 1, Pisa, I56124, Italy

ARTICLE

ABSTRACT The control of the structure of oxide-supported metal nanoparticles is crucial in determining their properties and possible applications. Here, building principles are derived for predicting the epitaxies of metal nanoparticles on square-symmetry oxide surfaces. Unusual phases are found for an appropriate choice of the metal−oxide pair, where nanoparticles with hcp structure are stabilized for fcc metals such as Ni, Pd, and Pt, or for Co in a size range in which Co has typically nonhcp arrangements. These predictions are supported by a comparison with available experimental data on Ni/MgO(100) nanodots, and generalized to a whole class of metal−oxide systems of great potential interest, such as Pd and Pt on CaO, Ni on CoO, and Co on MgO. The atomistic features of the nanoparticles in turn suggest that these materials should possess peculiar properties; in particular, the facets exposed by the nanodots reveal adsorption sites with unusual geometry of possible effect on their catalytic properties, while the destabilization of stacking faults and the structural deformations observed for these particles are expected to influence their magnetic behavior.

KEYWORDS: nanoparticles · metals · oxides · surfaces · global optimization · density functional

As device miniaturization proceeds, attention is increasingly focusing on metal nanoparticles from a few tens to a few thousands of atoms, with applications ranging from catalysis to electronics, data storage, optics, and biological labeling.[1] The scientific and technological interest for these systems is further fueled by the discovery that at such small sizes unexpected structures may arise,[2−4] exhibiting novel and peculiar properties. In this context, oxide-supported metal nanoparticles have attracted great interest since a long time,[5] as they can be produced as dispersed objects with well-defined three-dimensional structures,[6] whose fine details are important in determining specific properties,[7−12] and whose control is crucial for developing new application devices. Their structure is ruled by a complex interplay of metal−metal and metal−oxide interactions,[13] but the possible scenarios and the corresponding building principles are far from being clarified.

Among oxide-supported metal systems, Pd/MgO(001) is one of the most extensively studied due to its importance as a model heterogeneous catalyst.[5] The MgO(001) surface is of square symmetry, with a checkerboard arrangement of alternating Mg and O atoms (lattice parameter 4.2072 Å, O−O distance 2.974 Å [14]). Metal atoms preferentially adsorb on top of oxygen atoms.[15] Bulk palladium is face-centered-cubic (fcc). Even though the nearest-neighbor distance in bulk Pd is smaller by about 7.5% than the distance between nearby adsorption sites on MgO(001), Pd nanoparticles easily grow in cube-on-cube fcc(001) epitaxy on the substrate.[5] Their morphology has been accurately determined,[13] and it has been shown that these nanoparticles present features, such as overhangs at the interface with the support, that can be strongly active sites for specific reactions.[11]

Metal−oxide systems presenting a larger size mismatch than Pd/MgO(001) have been much less investigated, despite their great potential interest. It can be expected, in fact, that a larger mismatch may cause the growth of "exotic" epitaxies, in which the nanodots have unusual morphologies. In the present work, we will focus on systems in which the mismatch between the bulk metal nearest-neighbor distance and the O−O distance in the substrate is in the range 15−20%, specifically considering Ni/MgO, Co/MgO, Pd/CaO, Pt/CaO, Au/CaO, and Ni/CoO(001), and we will show that, in an appropriate range of lattice mismatch, adhesion, and metallic energies, a general class of exotic hcp nanoparticle phases can be stabilized in a controlled way, even for metals that are not hcp in the bulk. In the following, Ni/MgO(001) is assumed as a

*Address correspondence to ferrando@fisica.unige.it, fortunelli@ipcf.cnr.it.

Received for review May 22, 2008 and accepted July 23, 2008.

Published online August 12, 2008.
10.1021/nn800315x CCC: $40.75

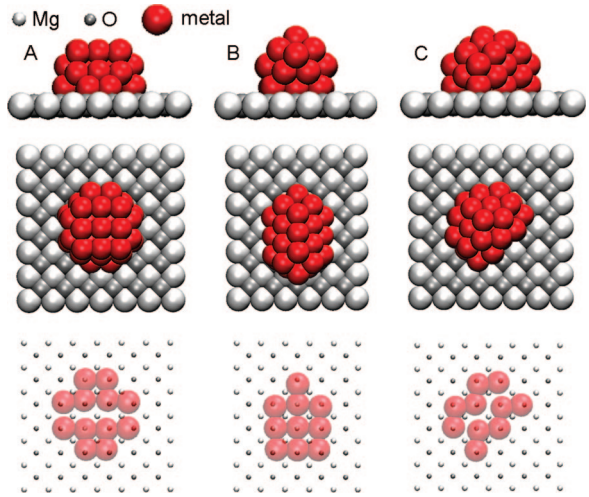

Figure 1. Representative structures of the three significant structural motifs of 40-atom Ni nanodots on MgO: (A) fcc(001) motif, (B) 5-fold motif, and (C) hcp motif. From top to bottom, side, top, and bottom views of the dots. The bottom view shows only the atoms that are in contact with the substrate. The energies of the nanoparticles are reported in Table 1.

testbed of our theoretical and computational approach. Electron-diffraction measurements have revealed the growth of small and medium-size Ni nanodots[16] that present vertical planes in hexagonal close-packed (hcp) stacking. The actual morphology of these nanodots and the nature of their exposed facets are, however, still unknown. At larger size, a transition toward the fcc(001) epitaxy occurs.[16,17] Our methodology will allow us to precisely determine the size-dependent morphology of the Ni/MgO(001) nanodots, and the size range in which hcp structures are energetically favorable, reproducing the size-dependent transition from hcp to fcc structures in remarkable agreement with the available experimental data.[16]

Pd and Pt are both bulk fcc metals of major interest in catalysis. CaO is an alkaline earth oxide as MgO, with which it shares the same bulk (rock salt) structure. However, apart from a larger lattice parameter (4.8032 Å [14]), CaO presents other interesting features as a support for the growth of metal particles, such as a stronger (by roughly ≈20%) metal−surface interaction and a more rugged energy landscape for metal adsorption. CoO in the rock salt form (lattice parameter 4.267 Å (ref 14)) can be stabilized in the form of thin or ultrathin films grown as buffer layers on the (100) surfaces of isomorphic oxides such as MgO or NiO.[18] An atomically sharp interface between a ferromagnetic metal and an antiferromagnetic oxide, as in Ni nanodots on CoO(100), is particularly interesting also as a model system in which to study the origin of the exchange bias effect.[19] Finally, the case of Co/MgO(001) is somewhat different. Even though bulk Co is hcp, the hcp phase is uncommon for nanoparticles of sizes below 4 nm (or even larger),[20,21] because Co nanoparticles prefer either icosahedral or fcc arrangements. If the substrate is properly chosen, its templating effect may stabilize the hcp phase also for small Co nanodots.

TABLE 1. DFT Results on the Energetics of Ni/MgO(001) Nanodots[a]

size	structure	E_{bind}	ΔE	E_{adh}	E_{met}
Ni_{30}	5-fold	−114.60	0.00	−7.46	−107.14
	hcp	−114.11	0.49	−7.15	−106.96
	fcc(001)	−113.91	0.69	−7.59	−106.32
Ni_{40}	hcp	−155.78	0.00	−8.71	−147.07
	5-fold	−155.42	0.35	−7.90	−147.52
	fcc(001)	−154.40	1.38	−8.68	−145.72
Ni_{50}	hcp	−197.70	0.00	−10.61	−187.09
	5-fold	−197.13	0.57	−9.51	−187.62
	fcc(001)	−196.64	1.06	−10.25	−186.39

[a] E_{bind} is the binding energy of the nanoparticle, ΔE is the energy difference from the lowest isomer, E_{adh} is the adhesion energy between the nanoparticle and the substrate, and E_{met} is the metallic atomization energy. All energies are in eV.

Our predictive computational methodology is based on an extensive search for structural motifs by means of global optimization methods[22] within many-body semiempirical potential models including metal−metal and metal−substrate interactions.[23] Sizes up to $N = 500$ atoms are considered. In the size range $N \leq 50$ atoms, the lowest-energy structures of each structural motif are then locally reoptimized by density-functional theory (DFT) calculations.[22]

RESULTS AND DISCUSSION

In the case of Ni/MgO(001), the global optimization searches in the size range $N \leq 50$ atoms single out three main structural motifs (see Figure 1). The first motif recalls the structure of bulk Ni. In fact, nanoparticles belonging to this motif are fcc nanocrystals which grow in (001) epitaxy with the oxide substrate. For this reason, this motif will be referred to as fcc(001) motif. However, due to the huge size mismatch between the nearest-neighbor distance in Ni and the O−O distance in the MgO substrate, these nanoparticles are often strongly distorted and/or dislocations between close-packed planes are observed. These dislocations, which appear already for very small sizes, help the structure in decreasing its strong internal strain. The second motif (referred to as 5-fold motif in the following) is noncrystalline. Nanoparticles belonging to this motif present at least one local 5-fold symmetry. Finally, the third motif is made of hcp nanocrystals, whose close-packed planes, alternating in ···ABAB··· stacking, are perpendicular to the oxide substrate and oriented along the [100] (or equivalently the [010]) direction of the substrate, thus in agreement with the electron-diffraction results.[16]

While for extremely small aggregates there is no clearly prevailing motif, as the size increases above ~40 atoms, the hcp motif becomes more and more favorable, so that the lowest-energy structures are hcp for almost all sizes. The prevalence of the hcp motif is clear

from the results of DFT calculations reported in Table 1. For Ni_{30}/MgO(001), a 5-fold structure is more stable than the best hcp structure, which is however lower in energy than fcc(001) structures. For Ni_{40} and Ni_{50}/MgO(001), hcp structures are the most favorable, with increasing energy differences.

In order to discuss which factors favor the stability of hcp nanodots for these small sizes, we decompose the binding energy E_{bind} of the nanoparticles into the metallic atomization energy E_{met} and the adhesion energy E_{adh} between the nanoparticle and the substrate. The metallic energy E_{met} is calculated by separating the nanoparticle from the surface and calculating its energy without any further relaxation. The adhesion energy E_{adh} is the difference between E_{bind} and E_{met}. 5-fold structures have favorable metallic energy, but a bad matching with the substrate, so that their adhesion is weak. On the contrary, fcc(001) structures can have strong adhesion with the substrate if a large number of metal atoms is in contact with it. This is possible only if the nanodot shape is not compact. Finally, hcp structures better match the substrate, so that their adhesion is as strong with fewer atoms in contact. Shapes of hcp structures are thus more compact than those of fcc(001) structures, with a better E_{met}.

The tendency favoring hcp structures becomes more and more evident with increasing size. Our global optimization runs show that, in the size range $50 \leq N \leq 100$, hcp structures without stacking faults are the lowest in energy for 50 sizes over 51. The 5-fold motif becomes rapidly much higher in energy of both hcp and fcc(001) motifs and for sizes larger than 100 atoms can be safely ignored. At the same time, hcp structures with stacking faults become competitive, in agreement with the experimental observation.[16] In Figure 2 we show the global minimum structures for sizes $N =$ 100, 200, and 300. All these structures belong to the hcp motif and do not present stacking faults, even though there are faulted structures that are quite close in energy to the global minimum. For $N = 500$, four different structures are also shown: a hcp nanoparticle, a hcp nanoparticle with a stacking fault, a fcc structure, and an icosahedral structure. In the fcc structure, the facet in contact with the substrate is a vicinal of the (110) surface. The global minimum is the faulted hcp nanoparticle, which is separated by a small energy difference (0.12 eV) from the unfaulted hcp structure. The fcc and icosahedral structures are much higher than the global minimum, by 4.37 and 6.30 eV, respectively. The appearance of stacking faults in the hcp nanodots is not related to a better strain relief of the faulted structures with respect to the unfaulted ones. In fact, the faulted structures present a worse matching with the substrate, but a better metallic energy, because they produce fcc regions in the hcp nickel nanoparticle.

From the structures shown in Figure 2 the morphology of the hcp nanodots is quite easily understood. In

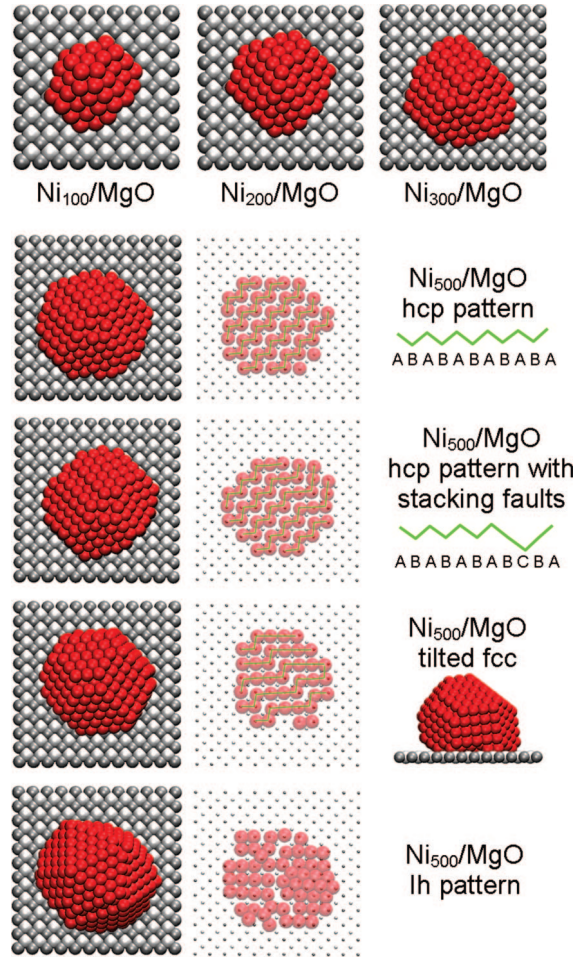

Figure 2. Global minima of Ni/MgO nanodots (of hcp structure) shown for $N = 100$, 200, and 300 atoms. For $N = 500$ we show, from top to bottom, an unfaulted hcp structure, a hcp structure with a stacking fault (global minimum), a fcc structure, and an icosahedral (Ih) structure.

fact, as better detailed in Figure 3, the hcp nanodots are truncated hexagonal bipyramids, whose axis coincides with the *c* axis of the hcp lattice. These bipyramids are cut to expose (0001), $(10\bar{1}1)$, and small $(11\bar{2}0)$ surfaces which offer a variety of adsorption sites of unusual geometry. In particular, the $(10\bar{1}1)$ facets present both 3-fold and 4-fold sites in close contact. A larger $(11\bar{2}0)$ face is in contact with the substrate, where Ni atoms assume a typical configuration in zigzag rows.

It is interesting to investigate the crossover from hcp to fcc(001) structures as size increases.[16,17] When size is above 500 atoms, full unseeded global optimization becomes more and more difficult, and practically not feasible for $N > 1000$.[22] Therefore we resort to the comparison of structures pertaining to the most competitive structural motifs: fcc(001) (in the form of truncated octahedra[17]) and hcp.

In order to compare the stability of the two motifs, we plot in Figure 4 the quantity $\Delta = (E_{bind} - N\epsilon_{Ni})/N^{2/3}$,[24] where E_{bind} is the total binding energy of the nanoparticle and ϵ_{Ni} is the binding energy per atom in bulk Ni. Δ is the excess energy of the nanoparticle with re-

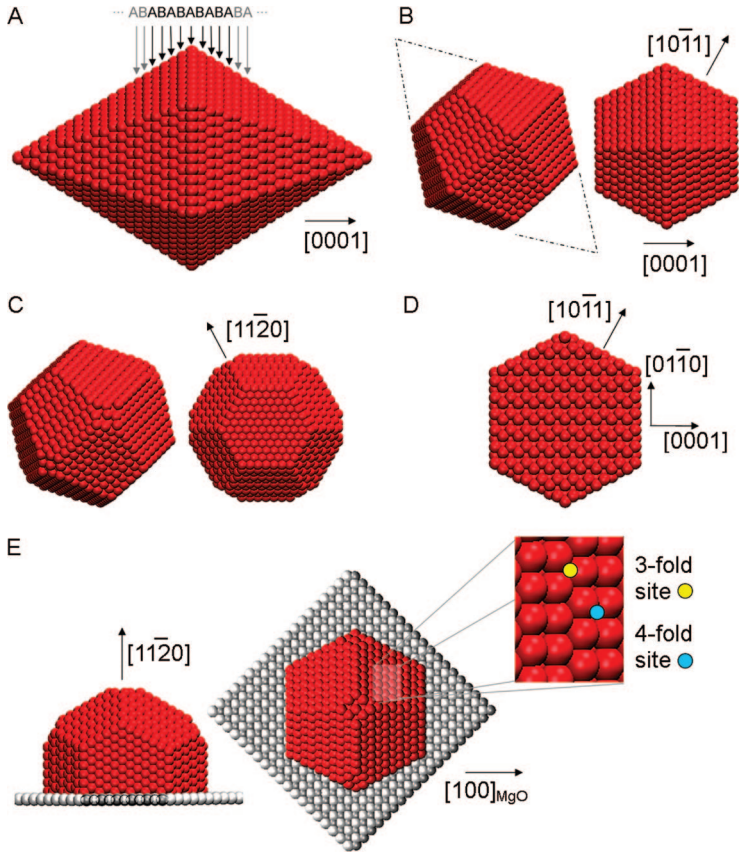

Figure 3. Morphology of the hcp motif. The hcp motif is obtained by truncating hexagonal bipyramids (A), whose axis is parallel to the *c*-axis of the hcp lattice of the metal. The first cut (B) eliminates top and bottom vertices of the pyramids, thus generating hexagonal (0001) faces. The second cut (C) eliminates lateral vertices, creating small (11$\bar{2}$0) facets, with their typical zigzag atomic arrangement. The final cut (D) is due to the contact with the substrate and generates a large (11$\bar{2}$0) face. Close-packed planes are perpendicular to the substrate. The nanodot is finally oriented in such a way that the [0001] direction of the hcp metal lattice is aligned with the [100] direction of the oxide substrate (E). The nanodot exposes also large (10$\bar{1}$1) facets, whose atomic arrangement is shown in the inset. These facets present a large number of 3-fold and 4-fold adsorption sites which are in close contact with each other.

which find the crossover for nanoparticles of thickness ~2.5 nm and lateral size ~5 nm.

What are the driving forces leading to the stabilization of the hcp nanodots? First of all, in these interface-stabilized phases, the hcp epitaxy is adopted to realize a good matching with the substrate. This geometric criterion is shown in Figure 5. Let d_1^{OO} and $d_2^{OO} = \sqrt{2}d_1^{OO}$ be the distances between first and second oxygen neighbors in the substrate, respectively. Let d^{MM} be the first neighbor distance in the bulk metal, $d^{apo} = \sqrt{3}d^{MM}$ the double of the apothema of 7-atom hexagons, and d^{AA} the distance between A planes in the hcp bulk. In an ideal hcp lattice, $d^{AA} = \sqrt{8/3}d^{MM}$. A good matching of the hcp phase is possible when both d^{apo}/d_2^{OO} and d^{AA}/d_2^{OO} are close to 1. For an ideal hcp lattice this implies that $d^{MM}/d^{OO} \simeq 0.8$. This condition warrants a bad matching of the fcc(001) epitaxy, for which $d^{MM}/d^{OO} \simeq 1$ should hold. Therefore, the fcc(001) epitaxy is automatically disfavored when the hcp (11$\bar{2}$0) epitaxy is favored. This makes it possible to stabilize hcp nanodots for fcc bulk metals, provided that the interaction with the substrate is sufficiently strong to overcome the energetic cost of building up the hcp phase. The second requirement to be fulfilled is that the hcp−fcc energy difference should not be too large. In this connection, we note that the above substrate-matching criterion is similar to that of the body-centered-cubic (bcc) (001) epitaxy. In fact, in the bcc(001) epitaxy, the metal atoms that are in contact with the substrate are at second neighbor distance $d_2^{MM} = 2d^{MM}/\sqrt{3}$. When $d^{apo}/d_2^{OO} \simeq 1$ and $d^{AA}/d_2^{OO} \simeq 1$, also $d_2^{MM}/d^{OO} \simeq 1$, so that a good hcp (11$\bar{2}$0) matching implies a good bcc(001) matching. However, bcc(001) epitaxy is strongly disfavored as a norm for metals which are not bcc in the bulk because of the much larger bcc−fcc energy difference with respect to the hcp−fcc one.[25] Finally, the (10$\bar{1}$1) faces should not be

spect to a bulk with the same number of atoms, approximately divided by the number of surface atoms. Lower values of Δ indicate more stable nanoparticles. The results in Figure 4 show that, for small sizes, the hcp motif presents lower Δ, as follows from the previously discussed global-optimization results. On the other hand, for large sizes, the fcc(001) motif must prevail[17] to recover the bulk fcc structure. A crossover between motifs is expected, and we find that it occurs between $N =$ 2000 and $N = 2500$ atoms, corresponding to nanodots 2.5 nm thick with lateral size of 4.5 nm, in very good agreement with the experimental results,[16]

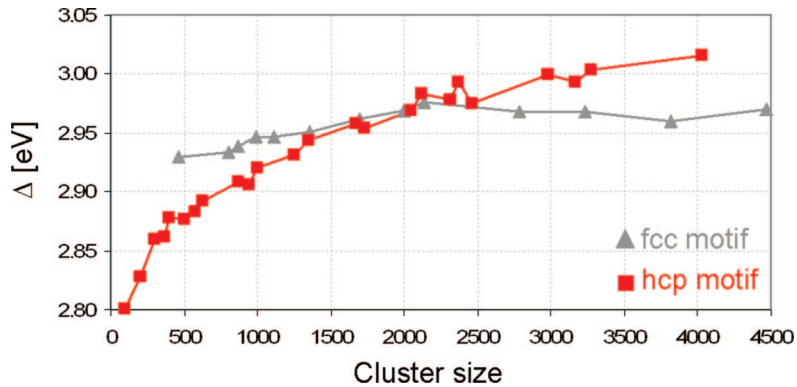

Figure 4. Crossover between structural motifs of nanodots. $\Delta = (E_{bind} - N\epsilon_{Ni})/N^{2/3}$ is plotted for the fcc(001) (A) and the hcp (B) motifs. A crossover from the hcp to the fcc(001) motif takes place for sizes between 2000 and 2500 atoms, corresponding to nanoparticle thickness of ~2.5 nm and width of ~4.5 nm.

too energetically disfavored with respect to (0001) faces, because the total area of the (10$\bar{1}$1) faces is large in the hcp nanodots.

Following these simple criteria, from the data reported in Table 2 we can predict the possible formation of hcp nanodots for several metal/substrate combinations, in particular Ni/MgO, Pd/CaO, Pt/CaO, Ni/CoO, and Co/MgO. The results of the DFT calculations nicely support these predictions: for each metal/oxide combination we have locally optimized several nanodot structures representative of the three main competitive structural families and found that the hcp motif is the lowest in energy for all systems at $N = 40$ and $N = 50$ for Co/MgO(001); see Table 3.

All these metals strongly adhere to their substrates. In Pd and Pt/CaO(001), the higher energy difference between hcp and fcc phases in Pd and Pt compared to Ni is partly compensated by the stronger adhesion to the CaO substrate and by the larger size mismatch of the fcc(001) epitaxy, which makes the latter quite unfavorable. The lattice parameter of CoO is very similar to that of MgO, so that the hcp Ni phase fits very well on the substrate, and the adhesion is even stronger than on MgO. As the nearest-neighbor distance in bulk Co is almost the same as in Ni, hcp Co/MgO(001) matches the substrate in the same way as Ni/MgO(001). The adhesion of Co to the substrate is comparable to that of Ni and moreover the hcp phase is marginally stable in Co bulk against the fcc phase (energy difference of about 0.004 eV/atom[25]).

In order to better discuss the factors determining the stability of hcp nanodots, we consider two more systems, for which we have not found evidence in favor of the hcp nanoparticle phase. The first counterexample is Pd/MgO. From Table 2 it follows that the fcc epitaxy better matches the substrate than the hcp epitaxy. In fact, as shown in ref 13, Pd/MgO nanodots are in fcc(001) epitaxy already starting from very small sizes, between 10 and 15 atoms. A second, and more interesting, counterexample is Au/CaO. Here, from the data in Table 2, the geometric criterion gives a very good matching of the hcp phase with the substrate. Moreover, the bulk hcp phase is only slightly higher in energy than the fcc phase. However, as reported in Table 3, the lowest energy Au_{40}/CaO cluster—a truncated rectangular pyramid—is in fcc(001) epitaxy with the substrate. This behavior of Au is due to the strong anisotropy of its surface energies, which favors clusters exposing close-packed surfaces. In Au, the ratio $\gamma_{(10\bar{1}1)}/\gamma_{(0001)}$ is large (see Table 2), disfavoring the hcp

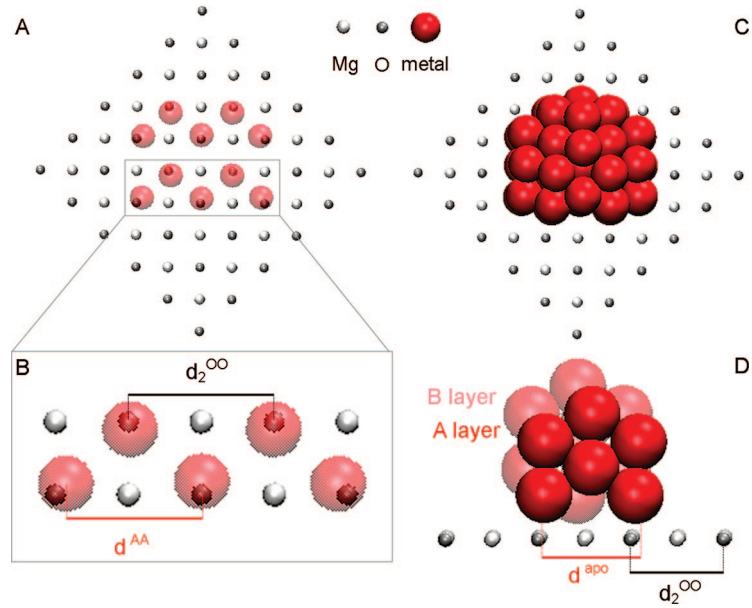

Figure 5. Matching of the hcp nanodots with the oxide surface. The criterion of good matching is that the distance between A planes in the hcp lattice (d^{AA}) and the apothema of 7-atom hexagons in the close-packed faces (d^{apo}) are both close to the distance between second-neighbor oxygens in the substrate (d_2^{OO}).

TABLE 2. Geometric Parameters for the Matching of the Nanodots with the Substrate[a]

metal	substrate	d^{apo}/d_2^{OO}	d^{AA}/d_2^{OO}	d^{MM}/d^{OO}	$\Delta E_{hcp-fcc}$	$\gamma_{(10\bar{1}1)}/\gamma_{(0001)}$
Ni	MgO(001)	1.024	0.964	0.837	1.1×10^{-2}	1.11
Co	MgO(001)	1.033	0.967	0.843	-4.4×10^{-3}	1.05
Pd	MgO(001)	1.135	1.068	0.927	2.1×10^{-2}	1.10
Pd	CaO(001)	0.992	0.935	0.810	2.1×10^{-2}	1.10
Pt	CaO(001)	1.001	0.943	0.817	2.6×10^{-2}	1.15
Au	CaO(001)	1.039	0.980	0.849	2.5×10^{-3}	1.22
Ni	CoO(001)	1.011	0.953	0.825	1.1×10^{-2}	1.11

[a]The data for calculating the geometric parameters are taken from ref 14. The experimental values of the energy difference (per atom) $\Delta E_{hcp-fcc}$ (in eV) between hcp and fcc bulk lattices are taken from ref 25. The ratios between surface energies $\gamma_{(10\bar{1}1)}/\gamma_{(0001)}$ are calculated by DFT.

TABLE 3. DFT Results on the Energetics of Co/MgO, Pd and Pt/CaO, and Ni/CoO Nanodots (All Energies in eV)

system and size	structure	E_{bind}	ΔE_{bind}	E_{adh}	E_{met}
Co_{30} /MgO(001)	fcc(001)	−111.22	0.00	−8.07	−103.15
	5-fold	−111.22	0.00	−7.56	−103.66
	hcp	−110.84	0.38	−7.14	−103.70
Co_{40} /MgO(001)	hcp	−151.18	0.00	−8.66	−142.52
	5-fold	−150.94	0.24	−8.41	−142.53
	fcc(001)	−149.62	1.56	−8.79	−140.83
Co_{50} /MgO(001)	hcp	−191.70	0.00	−10.72	−180.98
	5-fold	−191.39	0.31	−9.61	−181.78
	fcc(001)	−191.23	0.47	−10.15	−181.08
Pd_{40} /CaO(001)	hcp	−120.10	0.00	−10.55	−109.55
	fcc(001)	−119.30	0.80	−10.83	−108.47
	5-fold	−118.17	1.93	−8.58	−109.59
Pt_{40} /CaO(001)	hcp	−176.61	0.00	−14.46	−162.15
	fcc(001)	−174.64	1.97	−13.23	−161.41
	5-fold	−173.95	2.66	−12.89	−161.06
Au_{40} /CaO(001)	fcc(001)	−103.32	0.00	−7.20	−96.12
	hcp	−102.62	0.70	−6.87	−95.75
	5-fold	−102.50	0.82	−8.19	−94.31
Ni_{40} /CoO(001)	hcp	−158.90	0.00	−12.20	−146.70
	fcc(001)	−158.28	0.62	−12.57	−145.71
	5-fold	−158.09	0.81	−11.11	−146.98

nanodots with respect to fcc(001) pyramids, because the latter mostly expose close-packed faces.

Hcp metal-on-oxide nanodots are expected to present peculiar properties of interest in applications. As for the catalytic properties, recent research has clarified that catalysis is strongly affected not only by the type of nanoparticle facets (possibly in connection with the presence of particularly active sites[11]) but also by their relative orientation,[26] which can influence the mechanisms of mass transport over the nanoparticle surface. Shape is thus essential in determining the catalytic activity of metal nanoparticles, as shown, *e.g.*, by the enhanced catalytic activity of Pt nanocrystals with unconventional shapes, presenting facets of unusual geometries and orientations.[12] Moreover, the relative orientation of nanoparticle and substrate surfaces is known to play a role in both spillover and reverse spillover effects[27] and in adsorption modes of reacting molecules at the nanoparticle/oxide interface.[11] In this respect, the present hcp phases are very promising, as they exhibit unconventional features under all these viewpoints: the $(10\bar{1}1)$ facets have peculiar adsorption sites with unusual or strained coordination, they make unusual angles with the other, mostly close-packed, facets, and both the $(10\bar{1}1)$ and the close-packed facets present sharp interfaces with the oxide substrates, very different from the acute or obtuse angles of fcc pyramids or overhangs. The effect of all this on catalysis has still to be investigated.

As for magnetic properties, the easy magnetization axis in hcp structures is expected to be oriented along the *c* axis.[28] As a consequence of the 4-fold symmetry of the MgO(100) surface, the nanodot spin can thus be oriented along two different directions, making an angle of 90°. One can speculate that arrays of nanodots all oriented along the same direction could be obtained by applying a magnetic field during growth.[29] From the above discussion and Table 2, we also recall that a compression along the apothema and an elongation along the *c* axis are necessary to bring the nanodot structure in perfect registry with the oxide, and indeed these deformations are observed in the relaxed nanodot geometries, in perfect agreement with experiment. They should be beneficial in terms of magnetism, increasing the magnetic anisotropy of these systems.[28] Moreover, it is known that stacking faults decrease the magnetic anisotropy of hexagonal Co by provoking spin incoherence[30] and causing practical problems in applications, such as local bit storage instabilities and reading noise. The oxide substrate can stabilize against these phenomena, preventing the formation of fcc faults in the hcp lattice.

In conclusion, we have discussed a predictive computational methodology that allows one to study the size-dependent morphology of supported metal nanodots and applied it to metal particles on square-symmetry oxide surfaces in which the mismatch between the bulk metal nearest-neighbor distance and the O−O distance in the substrate is in the range 15−20%. We have shown that, in an appropriate range of adhesion and metallic energies, a general class of exotic hcp nanoparticle phases can be stabilized in a controlled way, even for metals that are not hcp in the bulk. These predictions have been supported by a comparison with available experimental data on Ni/MgO(100) nanodots, and generalized to a whole class of metal/oxide systems of great potential interest in catalytic and magnetic applications, such as Pd and Pt on CaO, and Ni and Co on CoO. To summarize, a morphological crossover has been quantitatively predicted, a general class of novel nanoparticle phases has been proposed, and the atomistic features of the particle structure have been unveiled for metal-on-oxide particles, features which in turn suggest that these materials might possess peculiar properties. This opens up a new avenue for predicting epitaxial relationships and tailoring structure and properties of supported metal nanoparticle nanophases *via* the substrate templating effect, a mechanism in principle extensible to other interfacial systems.

METHODS

As we deal with a very broad nanoparticle diameter range (1−8 nm), we use different computational methodologies depending on the size range considered. Three regimes can be spotted:

$N \leq 50$. Semiempirical model potentials are used within an unseeded global optimization approach to locate the most stable Ni/MgO(001) cluster structures. The significant structural motifs are singled out and, within each motif, several structures are locally relaxed by first-principle calculations.[22] Within this size range, DFT local minimizations extend the comparison among such motifs to the other metal/oxide systems considered in the paper;

$50 < N \leq 500$. The search for the lowest-energy structures is performed by an unseeded global optimization approach within semiempirical Ni/MgO(001) potential models;

$N > 500$. Candidate fcc and hcp clusters are built by truncating respectively fcc octahedra and hcp hexagonal bipyramids (see Figures 2 and 3). For each octahedron or bipyramid, several different truncations have been examined, in order to find the optimal one. Within semiempirical potential models, these nanoparticles are used as seeds for short global optimization searches, thus allowing full local structural relaxation and eventually small rearrangements of the structures, to accommodate the possible appeareance of dislocations.[17] The best structures that we have found have the same aspect ratios as those located by global optimization at smaller sizes, and are in reasonable agreement with the Wulff−Kaishew construction.[5]

In the following, the details of both energetic models and computational methods are discussed.

Energetic Modeling for Ni/MgO(001). In the global optimization searches, the energetic model is based on a tight-binding many-body potential for the metal−metal interactions and a surface energy potential approach fitted to *ab initio* calculations for the metal−oxide ones. The details of the energetic model description can be found in refs 17 and 23 together with the form of the metal−oxide interaction. The parameters for the Ni−MgO(001) interaction are listed in ref 31.

Concerning metal−metal interactions, their functional form is derived within the second-moment approximation to the

tight-binding model (SMATB potential). Within this approach, the total energy E_c of the system is obtained as[32]

$$E_c = \sum_i (E_b^i + E_r^i) \quad (1)$$

with

$$E_r^i = \sum_{j \neq i, r_{ij} < r_c} A \exp\left[-p\left(\frac{r_{ij}}{r_0} - 1\right)\right] \quad (2)$$

$$E_b^i = -\left\{\sum_{j \neq i, r_{ij} < r_c} \xi^2 \exp\left[-2q\left(\frac{r_{ij}}{r_0} - 1\right)\right]\right\}^{1/2} \quad (3)$$

where r_{ij} is the distance between atoms i and j, r_c is the cutoff radius, r_0 is the nearest-neighbor distance. The parameter set (A, ξ, p, q) fitted to experimental bulk quantities. We fit the equilibrium nearest-neighbor distance in bulk Ni, the bulk binding energy per atom E_{bind}, the bulk modulus B, and the experimental value of the energy difference (per atom) $\Delta E_{hcp-fcc}$ between hcp and fcc bulk lattices. The potential is smoothly linked to zero between the 5th and 6th neighbor distances by a polynomial function. The values of the parameters are A = 0.084 470 25 eV, ξ = 1.404 973 55 eV, p = 11.73, q = 1.93. The validity of our SMATB parametrization has been checked against experimental and DFT results for what concerns surface energies of high-index surfaces and equilibrium distances in small clusters, obtaining a good agreement.

Also other parametrizations of the SMATB potential[33,34] have been used in order to build up a richer database of oxide-supported structures by means of global optimization searches. For Pd and Pt/CaO(001) nanoparticles also motifs from our Pd and Pt/MgO(001) databases[13] were considered.

Density Functional Theory (DFT) Calculations. The DFT calculations are carried out using the PWscf (plane-wave self-consistent field) computational code,[35] employing the PBE xc-functional[36] and ultrasoft pseudopotentials in the spin-unrestricted formalism. The MgO(001) surface is modeled by a two-layer slab, each layer containing 25 Mg(Ca) and 25 O atoms, 5 × 5 cell, fixed in the lattice positions of the rock salt bulk structure of the various oxides. The distance between replicated cells in the direction perpendicular to the (001) surface is about 13 Å, and implies a distance of at least ≈6 Å between atoms in replicated cells. The kinetic energy cutoff for the selection of the plane-wave basis set is fixed at 30 Ryd (1 Ryd = 13.6 eV) for the energy and 150 Ryd for the density in all the calculations. Because of the large dimensions of the unit cell, eigenvalues and eigenvectors of the Kohn−Sham Hamiltonian are only evaluated at the Γ point. A Gaussian smearing technique[37] (with a smearing parameter of 0.002 Ryd) is applied. Bulk CoO has an antiferromagnetic spin ground state. As in analogous transition metal oxide systems, gradient-corrected xc-functionals, including the PBE one,[36] erroneously predict the ground state of CoO to be metallic,[38] a behavior usually cured *via* the use of DF+U[39] or hybrid-exchange[40] techniques within the DF formalism. To reduce the computational effort within the limit of our possibilities, we nevertheless chose to use the PBE xc-functional also in the CoO case: the antiferromagnetic state is anyway the ground state at the DF level, and a proper magnetic state for the oxide layer (even after the adsorption of ferromagnetic Ni clusters) can be simply obtained by doubling the unit cell (space group $R\bar{3}m$ in the bulk) and providing the right starting magnetization on each Co atom. This, however, implied that a 6 × 6 cell had to be used in this case. This choice is supported by selected calculations showing that the metal−surface interaction depends only marginally on the spin state of the oxide, and by the fact that the total density of the system is essentially correctly predicted by GGA approaches.[41]

Global Optimization Methods. The global optimization searches are performed by means of the basin hopping (BH) algorithm[42] and the parallel excitable walkers (PEW) algorithm.[43] For any nanoparticle size N below 100 atoms, 3−5 unseeded searches of 50 000 steps each are performed. Unseeded searches are started from random positions in a cubic box placed above the oxide surface. In the range $100 < N < 200$, we have considered only sizes 100, 110, 120,..., 200. For each size, at least 10 unbiased searches have been performed. We have run 15 unbiased searches for sizes N = 300 and 500. Moreover, several shorter seeded searches are performed. Seeded searches may either start from structures pertaining to motifs found at nearby sizes (typically $N - 1$ and $N + 1$ atoms), or from structures found at the same size within searches by means of a different potential parametrization (see ref 22 for a review on the global optimization methods). In the PEW searches, we use as an order parameter the fraction of atoms that are in contact with the substrate.

Acknowledgment. We thank Claude Henry for a critical reading of the manuscript. We acknowledge financial support from the European Community Sixth Framework Programme for the GSOMEN project (NMP4-CT-2004-001594). G.R. acknowledges *L'Oréal Italia e UNESCO per le Donne e la Scienza*, 2007 edition, for a research fellowship.

REFERENCES AND NOTES

1. Burda, C.; Chen, X.; Narayanan, R.; El-Sayed, M. A. Chemistry and Properties of Nanocrystals of Different Shapes. *Chem. Rev.* **2005**, *105*, 1025–1102.
2. Lord, E. A.; Mackay, A. L.; Ranganathan, S. *New Geometries for New Materials*; Cambridge University Press: Cambridge, UK, 2006.
3. Li, J.; Li, X.; Zhai, H.-J.; Wang, L. S. Au_{20}: a Tetrahedral Cluster. *Science* **2003**, *299*, 864–867.
4. Rossi, G.; Rapallo, A.; Mottet, C.; Fortunelli, A.; Baletto, F.; Ferrando, R. Magic Polyicosahedral Core-Shell Nanoclusters. *Phys. Rev. Lett.* **2004**, *93*, 105503-1–105503-4.
5. Henry, C. R. Morphology of Supported Nanoparticles. *Prog. Surf. Sci.* **2005**, *80*, 92–116.
6. Renaud, G.; Lazzari, R.; Revenant, C.; Barbier, A.; Noblet, M.; Ulrich, O.; Leroy, F.; Jupille, J.; Borensztein, Y.; Henry, C. R.; et al. Real-Time Monitoring of Growing Nanopar- ticles. *Science* **2003**, *300*, 1416–1419.
7. Libuda, J.; Freund, H.-J. Molecular Beam Experiments on Model Catalysts. *Surf. Sci. Rep.* **2005**, *57*, 157–298.
8. Valden, M.; Lai, X.; Goodman, D. W. Onset of Catalytic Activity of Gold Clusters on Titania with the Appearance of Nonmetallic Properties. *Science* **1998**, *281*, 1647–1650.
9. Campbell, C. T.; Parker, S. C.; Starr, D. E. The Effect of Size-Dependent Nanoparticle Energetics on Catalyst Sintering. *Science* **2002**, *298*, 811–814.
10. Judai, K.; Abbet, S.; Worz, A. S.; Heiz, U.; Henry, C. R. Low-Temperature Cluster Catal- ysis. *J. Am. Chem. Soc.* **2004**, *126*, 2732–2737.
11. Molina, L. M.; Hammer, B. Some Recent Theoretical Advances in the Understanding of the Catalytic Activity of Au. *Appl. Catal., A* **2005**, *291*, 21–31.
12. Xiong, Y.; Wiley, B. J.; Xia, Y. Nanocrystals with Unconventional Shapes—a Class of Promising Catalysts. *Angew. Chem. Intl. Ed.* **2007**, *46*, 7157–7159.
13. Barcaro, G.; Fortunelli, A.; Rossi, G.; Nita, F.; Ferrando, R. Epitaxy, Truncations and Overhangs in Palladium Nanoclusters Adsorbed on MgO(001). *Phys. Rev. Lett.* **2007**, *98*, 156101-1–156101-4.
14. *Landolt-Börnstein Tables*; Hellwege, K.-H., Hellwege, A. M., Eds.; Springer: Berlin, 1975; Group III, Vol. 7b.
15. Pacchioni, G.; Rosch, N. Supported Nickel and Copper Clusters on MgO(100): a First- Principles Calculation on the Metal/Oxide Interface. *J. Chem. Phys.* **1996**, *104*, 7329–7337.
16. Tian, W.; Sun, H. P.; Pan, X. Q.; Yu, J. H.; Yeadon, M.; Boothroyd, C. B.; Feng, Y. P; Lukaszew, R. A.; Clarke, R. Hexagonal Close-Packed Ni Nanostructures Grown on the (001) Surface of MgO. *Appl. Phys. Lett.* **2005**, *86*, 131915-1–131915-3.
17. Sao-Joao, S.; Giorgio, S.; Mottet, C.; Goniakowski, J.; Henry, C. R. Interface Structure of Ni Nanoparticles on MgO(100): a Combined HRTEM and Molecular Dynamics Study. *Surf. Sci.* **2006**, *600*, L86–L90.

18. Allegretti, F.; Parteder, G.; Ramsey, M. G.; Surnev, S.; Netzer, F. P. The Formation of Sharp NiO(100)-Cobalt Interfaces. *Surf. Sci.* **2007**, *601*, L73–L76.
19. Nogués, J.; Schuller, I. K. Exchange Bias. *J. Magn. Magn. Mat.* **1999**, *192*, 203–232.
20. Kitakami, O.; Sato, H.; Shimada, Y.; Sato, F.; Tanaka, M. Size Effect on the Crystal Phase of Cobalt Fine Particles. *Phys. Rev. B* **1999**, *56*, 13849–13854.
21. Morel, R.; Brenac, A.; Bayle-Guillemaud, P.; Portemont, C.; La Rizza, F. Growth and Properties of Cobalt Clusters Made by Sputtering Gas-Aggregation. *Eur. Phys J. D* **2003**, *24*, 287–290.
22. Ferrando, R.; Fortunelli, A.; Johnston, R. L. Searching for the Optimum Structures of Alloy Nanoclusters. *Phys. Chem. Chem. Phys.* **2008**, *10*, 640–649.
23. Vervisch, W.; Mottet, C.; Goniakowski, J. Theoretical Study of the Atomic Structure of Pd Nanoclusters Deposited on a MgO(100) Surface. *Phys. Rev. B* **2002**, *65*, 245411-1–245411-9.
24. Cleveland, C. L.; Landman, U.; Schaaff, T. G.; Shafigullin, M. N.; Stephens, P. W.; Whetten, R. L. Structural Evolution of Smaller Gold Nanocrystals: the Truncated Decahedral Motif. *Phys. Rev. Lett.* **1997**, *79*, 1873–1876.
25. Dinsdale, A. T. SGTE Data for Pure Elements. *CALPHAD* **1991**, *15*, 317–425.
26. Oŝterlund, L.; Grant, A. W.; Kasemo, B. Lithographic Techniques in Nanocatalysis. In *Nanocatalysis, Series: NanoScience and Technology*; Heiz, U., Landman, U., Eds.; Springer Verlag: Berlin, 2007.
27. Rottgen, M. A.; Abbet, S.; Judai, K.; Antonietti, J. M.; Worz, A. S.; Arenz, M.; Henry, C. R.; Heiz, U. Cluster Chemistry: Size-Dependent Reactivity Induced by Reverse Spill-Over. *J. Am. Chem. Soc.* **2006**, *129*, 9635–9639.
28. Hashimoto, A.; Saito, S.; Itagaki, N.; Takahashi, M. Pseudo-hcp Nonmagnetic Intermediate Layer for Granular Media with High Perpendicular Magnetic Anisotropy. *J. Phys. D: Appl. Phys.* **2008**, *41*, 012002−1012002−4.
29. Einax, M.; Heinrichs, S.; Maass, P.; Majhofer, A.; Dieterich, W. Simulation of MBE- Growth of Alloy Nanoclusters in a Magnetic Field. *Mater. Sci. Eng., C* **2007**, *27*, 1325–1327.
30. Sort, J; Suriñach, S.; Muñoz, J. S.; Bar, M. D.; Wojcik, M.; Jedryka, E.; Nadolski, S.; Sheludko, N.; Nogués, J. Role of Stacking Faults in the Structural and Magnetic Properties of Ball-Milled Cobalt. *Phys. Rev. B* **2003**, *68*, 014421-1–014421-7.
31. Mottet, C.; Goniakowski, J. http://www.cinam.univ-mrs.fr/mottet/param/metalMgO.pdf.
32. Gupta, R. P. Lattice Relaxation at a Metal Surface. *Phys. Rev. B* **1985**, *23*, 6265–6270.
33. Cleri, F.; Rosato, V. Tight-Binding Potentials for Transition Metals and Alloys. *Phys. Rev. B* **1993**, *48*, 22–33.
34. López, M-J.; Jellinek, J. On the Problem of Fitting Many-Body Potentials. I. The Minimal Maximum Error Scheme and the Paradigm of Metal Systems. *J. Chem. Phys.* **1999**, *110*, 8899–8911.
35. Baroni, S.; Dal Corso, A.; de Gironcoli, S.; Giannozzi, P. http://www.pwscf.org.
36. Perdew, J. P.; Burke, K.; Ernzerhof, M. Generalized Gradient Approximation Made Simple. *Phys. Rev. Lett.* **1996**, *77*, 3865–3868.
37. Elsässer, C.; Fähnle, M.; Chan, C. T.; Ho, K. M. Density-Functional Energies and Forces with Gaussian-Broadened Fractional Occupations. *Phys. Rev. B* **1994**, *49*, 13975–13978.
38. Dufek, P.; Blaha, P.; Sliwko, V.; Schwarz, K. Generalized-Gradient-Approximation Description of Band Splittings in Transition-Metal Oxides and Fluorides. *Phys. Rev. B* **1994**, *49*, 10170–10175.
39. Anisimov, V. I.; Zaanen, J.; Andersen, O. K. Band Theory and Mott Insulators: Hubbard U Instead of Stoner I. *Phys. Rev. B* **1991**, *44*, 943–954.
40. Feng, X. Electronic Structure of MnO and CoO From the B3LYP Hybrid Density Functional Method. *Phys. Rev. B* **2004**, *69*, 155107-1–155107-7.
41. Fritsche, L.; Koller, J.; Reinert, T. Borderline Cases in Density Functional Theory. *Int. J. Quantum Chem.* **2004**, *100*, 681–694.
42. Wales, D. J.; Doye, J. P. K. Global Optimization by Basin-Hopping and the Lowest Energy Structures of Lennard-Jones Clusters Containing up to 110 Atoms. *J. Phys. Chem. A* **1997**, *101*, 5111–5116.
43. Rossi, G.; Ferrando, R. Global Optimization by Excitable Walkers. *Chem. Phys. Lett.* **2006**, *423*, 17–22.

Derivation of an empirical potential for gold with angular corrections

Stéphane Olivier,* Riccardo Conte, and Alessandro Fortunelli†
Molecular Modeling Laboratory, IPCF-CNR, Via G. Moruzzi 1, Pisa, I56124, Italy
(Received 21 July 2007; published 19 February 2008)

From a detailed analysis of density-functional calculations on gold model clusters and surfaces, an empirical potential for gold, which includes angular corrections, is derived. This potential introduces higher-order nonlinear terms (specifically, the product dipole-quadrupole) that do not seem to have been previously used, but that are necessary to describe directionality effects in the gold-gold interaction. Preliminary tests show that the proposed empirical potential possesses novel features with respect to the existing ones, such as a strong tendency of small Au clusters toward cage configurations, and represents a good starting point for future investigations.

DOI: 10.1103/PhysRevB.77.054104 PACS number(s): 61.46.Bc, 31.50.Bc, 68.35.B−

I. INTRODUCTION

Several empirical potentials have been proposed and are often successfully used to describe the physics of the metal-metal interaction. Among these, the most popular are the Rosato, Guillopè, Legrand (RGL),[1] embedded atom model (EAM),[2] glue-model[3–5] potentials, and their variants. In general, in all these empirical schemes it is assumed that the total energy of the system can be expressed as the sum of site atomic energies with a many-body character, i.e., depending in an analytically compact form upon the number, distance, and orientation of the neighbors of each given metal atom:

$$E^{\mathrm{tot}} = \sum_{i}^{\mathrm{atoms}} E_i^{\mathrm{atomic}}(\vec{r}_{ij}, j \neq i), \tag{1}$$

where $\vec{r}_{ij}=\vec{r}_j-\vec{r}_i$, with $\vec{r}_i,\vec{r}_j$ the vectors of the coordinates of the atoms i and j. As a norm, the atomic energies E_i^{atomic} are assumed to depend on the coordinates of all the other atoms through generalized collective variables (GCV), i.e., functions which describe the distribution of neighbors around the given atom in a collective way. What distinguishes the various empirical potentials is then the choice of the GCV and the analytic form by which the E_i^{atomic} depend upon the GCV. As an example, the RGL energy expression reads[1]

$$E_i^{\mathrm{RGL}} = A \sum_{j\neq i}^{\mathrm{atoms}} \exp\left[-p\left(\frac{r_{ij}}{r_0}-1\right)\right] - \xi\left\{\sum_{j\neq i}^{\mathrm{atoms}} \exp\left[-2q\left(\frac{r_{ij}}{r_0}-1\right)\right]\right\}^{1/2}, \tag{2}$$

where A and ξ are positive coefficients, p and q are the exponents of the repulsive and attractive terms, respectively, r_0 is the first-neighbor distance in the bulk (for fcc gold, $r_0=2.885$ Å), and r_{ij} is the modulus of $\vec{r}_{ij}$. The glue-model energy expression similarly reads[3–5]

$$E_i^{\text{glue-model}} = \sum_{j\neq i}^{\mathrm{atoms}} V(r_{ij}) - F\left[\sum_{j\neq i}^{\mathrm{atoms}} n(r_{ij})\right], \tag{3}$$

where $V(r)$, $F(x)$, and $n(r)$ are functions often (but not necessarily) described as a set of points that are connected by cubic splines. Many empirical energy expressions (such as EAM and RGL) are just particular cases of the general glue-model expression. However, the GCV in Eq. (3) only depend on the moduli of the interatomic distances r_{ij}. Baskes[6,7] was the first to call for the introduction of angular terms into the potential, i.e., terms depending on the angular distribution of neighbors around a given atom. The form he proposed is based on the theory of the multipolar expansion of the density defined as a set of points. The lowest-order terms of this expansion are the dipole, the quadrupole and the octupole, whose analytic forms read

$$\text{dipole} = \sum_{\sigma=x,y,z}\left[\sum_{j\neq i}^{\mathrm{atoms}} \rho^{\mathrm{dipole}}(r_{ij})\frac{r_{ij}^{\sigma}}{r_{ij}}\right]^2, \tag{4}$$

$$\text{quadrupole} = \sum_{\sigma=x,y,z}\sum_{\sigma'=x,y,z}\left[\sum_{j\neq i}^{\mathrm{atoms}} \rho^{\mathrm{quadrupole}}(r_{ij})\frac{r_{ij}^{\sigma}r_{ij}^{\sigma'}}{r_{ij}^2}\right]^2 - \frac{1}{3}\left[\sum_{j\neq i}^{\mathrm{atoms}} \rho^{\mathrm{quadrupole}}(r_{ij})\right]^2, \tag{5}$$

$$\text{octupole} = \sum_{\sigma=x,y,z}\sum_{\sigma'=x,y,z}\sum_{\sigma''=x,y,z}\left[\sum_{j\neq i}^{\mathrm{atoms}} \rho^{\mathrm{octupole}}(r_{ij})\frac{r_{ij}^{\sigma}r_{ij}^{\sigma'}r_{ij}^{\sigma''}}{r_{ij}^3}\right]^2 - \frac{3}{5}\sum_{\sigma=x,y,z}\left[\sum_{j\neq i}^{\mathrm{atoms}} \rho^{\mathrm{octupole}}(r_{ij})\frac{r_{ij}^{\sigma}}{r_{ij}}\right]^2, \tag{6}$$

where $\rho^k(r)$ are functions of r, and the corresponding energy contributions are functions of these expressions. In Eqs. (4)–(6), the $\rho^k(r)$ functions can be given a simple exponential form[6–9] or described as a set of points that are connected by cubic splines in the spirit of glue models.[10] The corresponding modified EAM (MEAM) or modified glue models have proven to often give improved results with respect to the original spherical models.[7,10,11] It is worthwhile noting that there is often a cancellation of terms in Eq. (6), such that the octupole assumes appreciable values only when the dipole is zero. In general, it should be also recalled that these contributions are identically null for cubic systems (fcc, bcc, simple cubic).

The case of gold is particularly interesting in this context: it has been shown in fact that directionality effects are im-

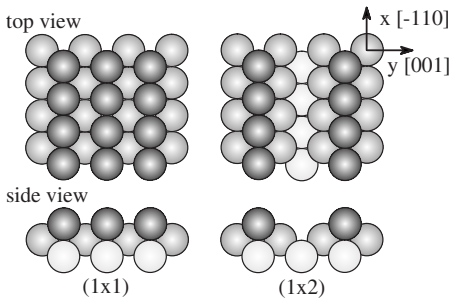

FIG. 1. Schematic representation of the Au(110) surface and its missing-row reconstruction.

portant in determining the structure and energetics of gold nanoclusters.[12–16] These effects can only be described within an empirical potential formalism through angular-dependent terms. Given the scientific and technological importance of gold clusters and surfaces it is therefore of great interest to search for an empirical potential which can describe directionality effects in the gold-gold interaction. This would open the way to a more realistic simulation of systems such as catalytically active supported gold clusters, organic monolayers self-assembled on gold surfaces, etc. There already exist empirical potentials which include angular corrections for gold. However, preliminary tests using two different MEAM potentials, the one proposed in Ref. 7 and one derived according to the protocol described in Ref. 17, have shown that the existing potentials do not improve in a qualitatively significant way with respect to the standard RGL or EAM approaches in the description of directionality effects in gold systems. Tight-binding approaches have also been proposed[18] but their results are also not fully satisfactory.

In this work, we pursue the derivation of a gold-gold empirical potential which includes angular-dependent terms. Through a detailed analysis of the energetics of model systems, we show that the reasons of the failure of existing empirical potentials to account for the peculiar directionality effects of Au-Au interactions are to be found in the lack of higher-order nonlinear terms (such as the product dipole-quadrupole). We include one such a term in our fit, thus deriving a new Au-Au potential with unusual characteristics, and producing results more in line with what is currently known about the structure and relaxation of gold clusters and surfaces.

In our analysis, we will often refer to a particular gold surface: the missing-row reconstructed Au(110) surface. Experimentaly, a missing row reconstruction has been observed on the Au(110) surface with several techniques such as low energy electron spectroscopy,[19–23] field ion microscopy,[24–26] ion scattering,[27–32] x-ray diffraction,[33] electronic microscopy,[34] and scanning tunneling microscopy.[35] The fcc (110) surface and its (1×2) reconstruction are shown in Fig. 1. This anisotropic surface orientation can be described with two inequivalent unit vectors along the $[\bar{1}10]$ and the [001] directions (which we call, respectively, x and y). The atom density in the x direction is higher than in the y direction (the interatomic distances are, respectively, $a/\sqrt{2}$ and a, with a the fcc lattice parameter). The missing row reconstruction consists in removing one every two dense rows (see Figs. 1 and 2), leading to a succession of (111) microfacets. Its interest in this context lies in its peculiar structural relaxation (experimentally observed and essentially in agreement with first-principles calculations) such that the (111) microfacets tend to assume a concave rather than a convex habitus.[36] This is shown in a pictorial way in Fig. 2: the atoms lying on the (111) microfacets, labeled as atom-2 in Fig. 2, tend to move slightly outwards, instead of inwards, and is put on a quantitative basis in Table I, where the structural parameters of the reconstructed and fully relaxed Au(110) surface are reported. This "rounding" of low-index faces in gold clusters and surfaces has been previously observed[14–16] and indicated as a signature of directionality or angular-dependent effects. As an example, in Table II the geometrical parameters for the Au_{38} truncated octahedral cluster are reported, as obtained from first-principles calculations, whence it is apparent that the atoms lying on the (111) faces tend to expand and protrude out of the surface plane.

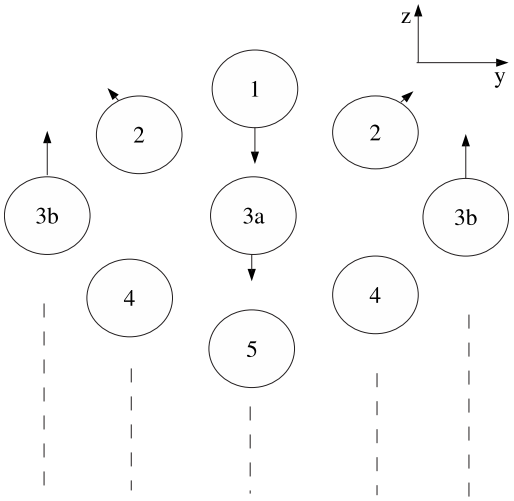

FIG. 2. Schematic picture (side-view) of the Au (110) missing-row reconstructed surface. The atoms explicitly shown are those selected in our simplified "surface-only" Au (110) system. The orientation of coordinates in the (y,z) plane is also shown. The arrows indicate the directions of the final reconstruction according to DF calculations.

II. COMPUTATIONAL DETAILS

Density-functional (DF) calculations are performed using the PWSCF (plane-wave self-consistent field) computational code,[37] and employing ultrasoft pseudopotentials to describe the interaction between the outer-shell electrons with the inner shell electrons and the nucleus. The PW91 exchange-correlation functional,[38] which is a gradient-corrected functional, is employed. The kinetic energy cutoff for the selection of the plane-wave basis set is set at 544 eV for all the calculations. A procedure of Gaussian broadening of the one-electron energy levels is applied (with a value of 0.68 eV as the smearing parameter). The k-point sampling of the Brillouin zone is changed according to the conductive properties of the systems. In the case of extended systems, which are conductive (small energy gap between HOMO and

TABLE I. Values of the differences in geometrical parameters with respect to the bulk structure for the complete fcc (110) surface (including 15 layers) or its simplified "surface-only" version, optimized through various empirical potential (RGL, POT) and first-principles (LDA, PW91) approaches. POT is the potential derived in the present work. The parameters for the RGL potential were taken from Ref. 1. LDA is the local-density exchange-correlation functional. PW91 is the Perdew-Wang exchange-correlation functional (Ref. 38). All values are in Å.

	Δz_1	Δz_2	Δz_{3a}	Δz_{3b}	Δy_2
complete (110) surface					
LDA	−0.229	0.028	−0.114	0.168	0.026
PW91	−0.335	0.014	−0.202	0.161	0.011
RGL	−0.199	−0.040	−0.042	0.065	−0.041
POT	−0.248	0.024	−0.163	0.319	0.027
simplified "surface-only" (110) surface					
PW91	−0.090	0.030	0	0	0.040
RGL	−0.196	−0.048	0	0	−0.004
POT	−0.197	0.002	0	0	0.046

LUMO), twelve k points are used in each extended direction. For finite systems (Au_{38} and Au_6 clusters), only the Gamma point is used. The geometry optimizations are stopped when maximum force on atoms are less than 0.005 eV/Å. The dimension of the unit cell is chosen so as to leave a distance of at least 6–8 Å between atoms on neighboring cells for finite systems. The PW91 results are reported after rescaling the energies by a factor 1.18794 and the distances by a factor 0.9786, so as to reproduce the experimental binding energy per atom of 3.83 eV and equilibrium first-neighbor distance of 2.885 Å for fcc gold. Note that the (110) surface is relaxed by fixing the lattice constant to the DF-relaxed value, not to the experimental value, and finally rescaled by the 0.9786 factor. The DF description of the energetics of gold systems is known to depend sometimes appreciably upon the choice of the exchange-correlation functional, the pseudopotential, and the numerical approach used for the solution of the DF equations.[16,39–42] In this context, the PW91 functional appears to produce results which are in reasonable agreement with the experimental data. The main qualitative points of the following analysis have anyway been found to hold also with a different choice of the exchange-correlation functional.

TABLE II. Values of the geometrical parameters for the Au_{38} truncated octahedral cluster optimized through various empirical potential (RGL, POT) and first-principles (PW91) approaches. POT is the potential derived in the present work. The parameters for the RGL potential were taken from Ref. 1. PW91 is the Perdew-Wang exchange-correlation functional (Ref. 38). All values are in Å.

	zcore	zvertex	yvertex	zface
RGL	2.006	1.954	3.900	2.067
PW91	1.974	1.993	3.963	2.294
POT	1.937	1.947	3.826	2.377

III. THE APPROACH

The approach we use in the derivation of the gold-gold potential is essentially based on a detailed analysis of the energetics of model systems. As in all empirical schemes, we assume that the total energy of the system can be expressed as the sum of site atomic energies E_i^{atomic}, see Eq. (1), which depend on the coordinates of all the other atoms through generalized collective variables (GCV). A basic GCV quantity which will be used to orient our analysis is the coordination number, i.e., the number of first neighbors, obtained by neglecting all atoms at a distance larger than, say, 15% of the first-neighbor distance in the bulk. Model systems are then chosen in which the coordination number and the internuclear distances span the range encountered in typical physical systems, and the corresponding energy results are carefully analyzed, trying to derive information on the analytic forms aptest to describe the physics of the metal-metal interaction. Our fitting set is thus a set of DF/PW91 energies of model systems in ideal configurations for different values of the first-neighbor internuclear distance. As "ideal configurations" we mean that all first-neighbor distances have the same value, and only an overall "breathing" of the structure is allowed (i.e., a multiplication of all the coordinates by the same factor). This choice allows us to keep the underlying physics under control. Once the physical range of the parameters has been found, a final refinement using a larger fitting set and the force-matching method[43,44] can be profitably used to improve accuracy. Our aim here is however to achieve a basic understanding of the factors at stake in the gold-gold interaction, trying to avoid that numerics obscure the physics underneath.

The model systems we have selected are as follows.

(1) fcc: the structure of bulk gold, with coordination number=12 and no bonding anisotropy.

(2) The fcc (111) bilayer (111BL), taken as a simplified example of the fcc (111) unreconstructed surface, with coordination number=9 and a strong bonding anisotropy.

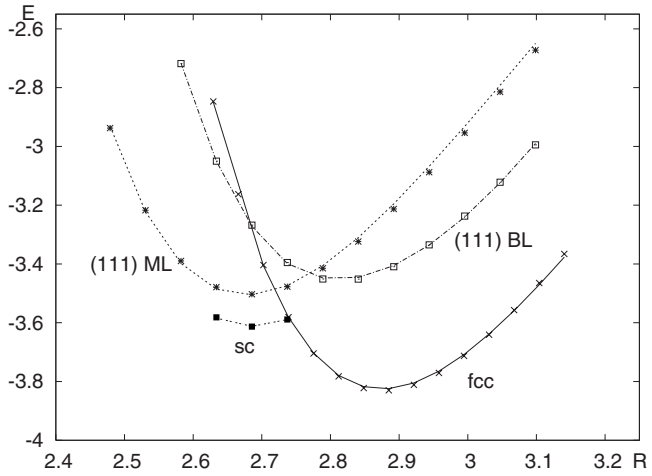

FIG. 3. The DF/PW91 (points) and our atom-atom potential (full-line) energies for several gold systems: fcc (crosses, continous line); (111) monolayer (asterisks, short-dotted line); (111) bilayer (empty squares, point-dotted line); simple cubic (sc, filled squares, long-dotted line). The energy (in eV) is reported as a function of the first neighbor distance (in Å).

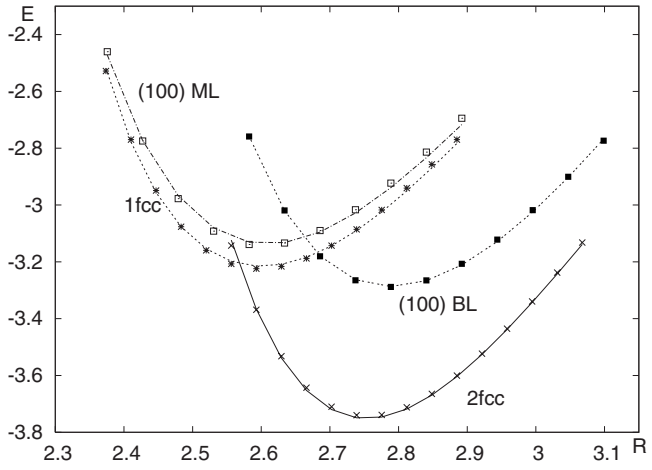

FIG. 4. The DF/PW91 (points) and our atom-atom potential (full-line) energies for several gold systems: (100) monolayer (empty squares, point-dotted line); (100) bilayer (filled squares, long-dotted line); fcc missing atoms on (100) and (010) faces (asterisks, short-dotted line); fcc missing atoms on (100) faces (crosses, continous line). The energy (in eV) is reported as a function of the first neighbor distance (in Å).

(3) The fcc (111) monolayer (111ML), a configuration which is also rather common (as argued below), with coordination number=6 and a small bonding anisotropy.

(4) The fcc (100) bilayer (100BL), taken as a simplified example of the fcc (100) unreconstructed surface, with coordination number=8 and a strong bonding anisotropy.

(5) The fcc (100) monolayer (100ML), with coordination number=4 and a small bonding anisotropy.

(6) Simple cubic (sc): the simple cubic arrangement, with coordination number=6 and no bonding anisotropy.

(7), (8) 2fcc and 1fcc: two 3D fcc-like structures obtained by taking the fcc four-atom simple cubic supercell and by deleting atoms on (100) faces for 2fcc, or atoms on both (100) and (010) faces for 1fcc, respectively, with coordination numbers=8 (respectively, 4) for 2fcc (respectively, 1fcc) and a small bonding anisotropy, chosen as counterparts of the fcc (100) bilayer and monolayer, respectively.

(9) A simplified "surface-only" fcc (110) surface: the system shown in Fig. 2, with coordination numbers=7 (atom 1), 9 (atom 2), 10 (atom 3b), and 12 (atom 3a), respectively, and a strong bonding anisotropy except for the 3a atoms.

(10) Au_{38}: the Au_{38} cluster in its truncated octahedral configuration, with coordination numbers=6 for the 24 apex atoms, 9 for the 8 atoms on the fcc (111) faces, and 12 for the 6 core atoms, respectively, and a strong bonding anisotropy except for the core atoms.

(11) Au_6: the Au_6 cluster in its octahedral configuration, with coordination number=4 and a strong bonding anisotropy.

We underline again that these structures are not fully relaxed, but are taken in ideal configurations, with all the first-neighbor distances equal, and are only allowed to "breathe" as a function of the first-neighbor distance. Figures 3–5 show the properly rescaled DF/PW91 energies for the selected model systems which have been used in the fit of the potential.

We start our analysis by justifying our choice of the fcc (111) monolayer as a fitting system. This is a very common structural motif, typical of many systems, including reconstructed surfaces and clusters. As an example, for the fcc (110) missing-row reconstructed surface, as a result of the appreciable structural relaxation of atoms 3a and 3b, with 3a penetrating deeply into the bulk and 3b moving upward to the surface, atom 2 in practice decreases its coordination number from 9—i.e., the value of an fcc (111) surface—to 6, i.e., the value of an fcc (111) monolayer. Analogously, in the rosettelike amorphization mechanism of the 55-atom icosahedron, described in Ref. 14 for Pt_{55} but common also to Au_{55}, a bulk atom below the reconstructed icosahedral vertex moves to the surface to form (together with its six first neighbors) what is essentially an fcc (111) monolayer. The reasons

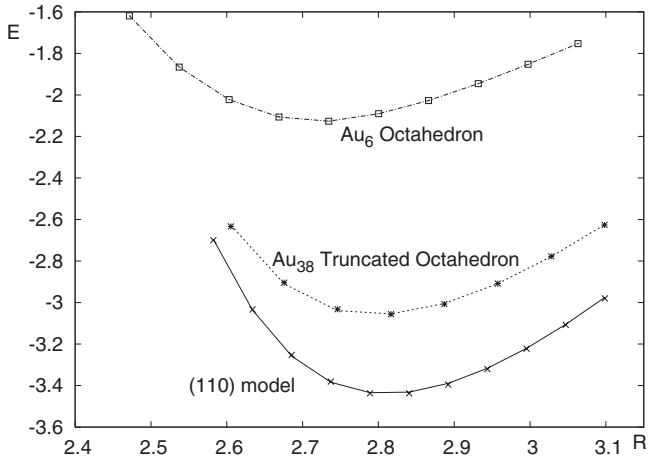

FIG. 5. The DF/PW91 (points) and our atom-atom potential (full-line) energies for several gold systems: simplified "surface-only" (110) system, see Fig. 2 (crosses, continous line); Au_{38} truncated octahedron (asterisks, dotted line); Au_6 octahedron (squares, point-dotted line). The energy (in eV) is reported as a function of the first neighbor distance (in Å).

of this ubiquitous presence are apparent from Fig. 3: if only a breathing is allowed, but no relaxation of the interlayer distance, the binding energy per atom of the fcc (111) bilayer (≈3.45 eV) is smaller than the binding energy per atom of the fcc (111) monolayer (≈3.50 eV). The bilayer is thus formally unstable with respect to dissociation into two monolayers (obviously, when interlayer relaxation is allowed, the bilayer energy drops below the monolayer energy, but only by 0.09 eV). This also explains why angular terms in the potential are necessary for an accurate description of gold-gold bonding: using a spherical coordination number as the only variable would either overestimate the binding energy of the fcc (111) bilayer (underestimate the surface energy), or underestimate the binding energy of the fcc (111) monolayer (i.e., overestimate the stability of compact vs planar configurations). As we will see below, among the angular terms, the dipolar one in particular will be necessary to describe such an effect.

The second point which can be drawn from an inspection of Fig. 3 concerns the weight of the quadrupolar term, through a comparison of the simple cubic and fcc (111) monolayer results. These two systems have the same coordination number, but a different number of second neighbors, and also different angular contributions: The dipolar and octupolar terms are zero by symmetry for both systems, whereas the quadrupolar term is zero for the simple cubic (as for all cubic systems), but nonzero for the fcc (111) monolayer. Indeed, the simple cubic energy lies below the 111ML energy in Fig. 3. However, this difference can be explained essentially in terms of second- and further-neighbor contributions, as confirmed by the fact that by fitting the 111 ML energy curve with an RGL-like expression, and using the RGL parameters so derived to evaluate the simple cubic energy, we found a good agreement with the true simple cubic results. This implies that the quadrupolar contribution is not large, presumably much smaller than the dipolar one, and we thus chose to ignore it altogether. Moreover, we only included three points of the simple cubic curve into our fitting set to give more weight to the fcc (111) monolayer arrangement, which is a much more common configuration. Analogously, we also ignore the octupolar contribution, which—by a similar analysis—we found to be much smaller than the dipolar one.

In passing, we report the result of a test of the assumption that the total energy can be expressed as the sum of site atomic energies: The energies of an fcc (111) trilayer (with three atoms in the unit cell) and the sum of the fcc bulk (with one atom in the unit cell) and the 111 BL (with two atoms in the unit cell) are within 0.02 eV up to a first-neighbor distance of 2.90 Å. This confirms that it is meaningful to analyze these systems in terms of a site-dependent energetics.

IV. PARAMETRIZATION OF THE SPHERICAL MODEL

We start from the parametrization of the spherical component of the potential, i.e., the terms which are nonzero for systems presenting a center of inversion, and thus lacking the dipolar term: fcc, 111 ML, sc, 2fcc, 100 ML, 1fcc. Preliminary tests showed that an RGL-like analytic form was able to reasonably describe the energy curves of Figs. 3 and 4, but that for improving the accuracy the coefficients of the repulsive and attractive terms should depend on the coordination number of the atoms involved, in a spirit analogous to that at the basis of glue models.[3–5]

We thus chose the following analytic form, which is a mixture of the RGL and glue-model energy expressions:

$$E^{\mathrm{tot}} = \sum_{i}^{\mathrm{atoms}} E_i^{\mathrm{sph}}, \tag{7}$$

$$E_i^{\mathrm{sph}} = A_i \sum_{j\neq i}^{\mathrm{atoms}} \exp\left[-p\left(\frac{r_{ij}}{r_0}-1\right)\right] - \xi_i \left\{ \sum_{j\neq i}^{\mathrm{atoms}} \exp\left[-2q\left(\frac{r_{ij}}{r_0}-1\right)\right]\right\}^{1/2}, \tag{8}$$

where the first (second) term on the right-hand-side is the usual repulsive (attractive) RGL-like contribution, but the linear coefficients A_i and ξ_i now depend upon effective coordination numbers (or GCV):

$$A_i = A^{(0)} + A^{(1)}c_i + A^{(2)}c_i^2 + A^{(3)}c_i^3, \tag{9}$$

$$\xi_i = \xi^{(0)} + \xi^{(1)}d_i + \xi^{(2)}d_i^2 + \xi^{(3)}d_i^3, \tag{10}$$

where c_i, d_i are GCV, defined as

$$c_i = \sum_{j\neq i}^{\mathrm{atoms}} f(r_{ij};\alpha_c,R_c), \tag{11}$$

$$d_i = \sum_{j\neq i}^{\mathrm{atoms}} f(r_{ij};\alpha_d,R_d) \tag{12}$$

with the weight function f defined as

$$f(r;\alpha,R) = \begin{cases} \{1+\exp[\alpha(r-R)]\}^{-1}, & r \leqslant R, \\ 0.5\cdot\exp[-\alpha(r-R)/2], & r \geqslant R. \end{cases} \tag{13}$$

Note that f is continuous with its derivative at R by construction and that (being a Fermi distribution for $r \leqslant R$) it "saturates" to 1 for $r \to 0^+$, while it decays exponentially for $r \to \infty$. The rationale for this choice of the f function is that saturation for $r \to 0^+$ prevents the GCV from growing without limit at small distances, while the junction with the exponential function for $r \geqslant R$ assures a slower decay than the Fermi distribution. We decided not to describe f in terms of general polynomials (as in glue models) to limit the number of nonlinear parameters in the fitting procedure (i.e., only p, q, α_c, α_d, R_c, R_d). We thus minimized Δ, the mean square-root deviation between the empirical potential energies and the DF/PW91 energies, for the spherical model systems. The linear parameters $A^{(0)}$, $A^{(1)}$, $A^{(2)}$, $A^{(3)}$, $\xi^{(0)}$, $\xi^{(1)}$, $\xi^{(2)}$, $\xi^{(3)}$ were obtained through a least-square fit, keeping the nonlinear parameters fixed. The nonlinear parameters were obtained through a basin-hopping global-optimization procedure,[45,46] which is known to be efficient and cost effective for this kind of problem. The final values of all parameters are reported in

TABLE III. Values of the optimized linear and nonlinear parameters for the spherical model. Radii are in Å.

parameter	value	parameter	value
p	12.40566	q	3.75564
α_c	8.2366	R_c	3.315329
α_d	4.436801	R_d	3.864539
$A^{(0)}$	0.197011	$\xi^{(0)}$	1.496829
$A^{(1)}$	−0.033297	$\xi^{(1)}$	0.026087
$A^{(2)}$	0.003679	$\xi^{(2)}$	−0.002991
$A^{(3)}$	−0.000116	$\xi^{(3)}$	0.0000886

Table III, and correspond to a value of $\Delta=0.0096$ eV (72 points).

V. PARAMETRIZATION OF THE DIPOLAR CONTRIBUTION

The dipolar contribution is by far the most delicate one. This is due to the fact that it is a differential contribution, in which all the inaccuracies of the spherical model are also hidden, and above all to the elusive nature of the directional, orientation-dependent interactions that this term is invoked to deal with.

As a first try, we chose an analytic form for the dipolar contribution along the lines of Eqs. (7) and (8):

$$E = \sum_{i}^{\text{atoms}} (E_i^{\text{sph}} + E_i^{\text{dip}}), \tag{14}$$

$$E_i^{\text{dip}} = D_i \sum_{\sigma=x,y,z} \left[\sum_{j\neq i}^{\text{atoms}} P(r_{ij};R_M) \frac{r_{ij}^{\sigma}}{r_{ij}} \right]^2, \tag{15}$$

where the sum over σ in the right-hand-side is the dipolar term, multiplied by a linear coefficient D_i expressed as a third-order polynomial of an effective coordination number e_i:

$$D_i = D^{(0)} + D^{(1)} e_i + D^{(2)} e_i^2 + D^{(3)} e_i^3 \tag{16}$$

with

$$e_i = \sum_{j\neq i}^{\text{atoms}} f(r_{ij};\alpha_e,R_e). \tag{17}$$

Moreover, to allow the dipolar contribution the maximum possible freedom (which is necessary, as the detailed energetics of gold clusters via empirical potentials is very sensitive to the choice of the dipolar term), we expressed the $P(r;R_M)$ function in terms of a sixth-order polynomial in $r-R_M$, as usual in glue models

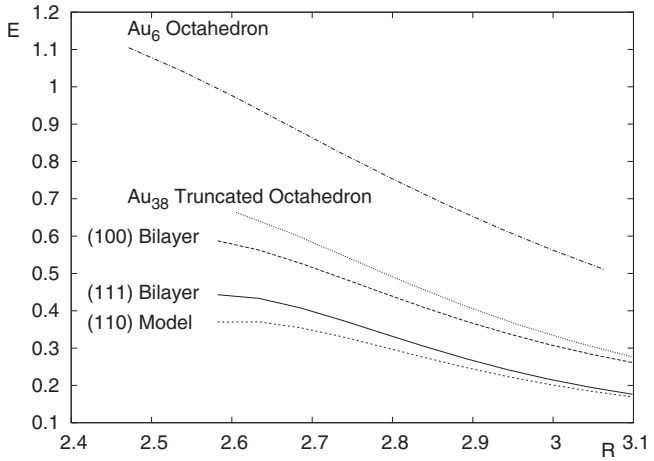

FIG. 6. Plots of the dipolar energy contribution, i.e., the difference between the DF/PW91 binding energy per atom and the spherical component per atom of our atom-atom potential for several gold systems: (111) bilayer (continous line); (100) bilayer (long-dotted line); simplified "surface-only" (110) system (medium-dotted line); Au_{38} truncated octahedron (short-dotted line); Au_6 octahedron (point-dotted line). Note that the contribution for the (110) system is smaller than for the other surface systems because the energy per atom is considered. Within the dipolar contribution, $E_i^{\text{dip-quad}}$ has a minimum around 3.3 Å representing roughly −10–16 % of the total dipolar contribution for the surface systems, is small (around −1%) for Au_{38}, and is roughly constant and around +20% for Au_6. Energies in eV, distances in Å.

$$P(r;R_M) = \begin{cases} p^{(2)}(r-R_M)^2 + p^{(3)}(r-R_M)^3 \\ + p^{(4)}(r-R_M)^4 + p^{(5)}(r-R_M)^5 \\ + p^{(6)}(r-R_M)^6 & \text{if } r \leqslant R_M, \\ 0 & \text{if } r \geqslant R_M. \end{cases} \tag{18}$$

Note that $P(r;R_M)$ is continuous with its derivative at R_M. As a technical aside, in glue models $P(r;R_M)$ is often defined in terms of polynomials over splinelike intervals. We found this unnecessary, as the choice of a polynomial over a single interval assures one to reach a comparable accuracy, at the same time reducing the number of nonlinear parameters.

With this choice of the analytic form for the dipolar term we conducted an extensive search (using the basin-hopping algorithm) for the best possible values of the nonlinear parameters, with the linear parameters obtained as before via a least-square fit. The main result of this extensive search was that it is impossible to accurately describe the energetics of the fitting set using only the dipolar term: Major discrepancies between DF and empirical potential results still remained. The reason for this failure is apparent from Fig. 6, where we plot the differences $E_i^{\text{DF/PW91}} - E_i^{\text{sph}}$ for the dipolar systems included in our fitting set. From an inspection of Fig. 6, one can see that (1) the dipolar contribution tends to level off at small r, and most importantly that (2) these differences do not scale even in an approximately linear way with the number of dipolar first-neighbors, calculated by limiting the sum over neighbors in the definition of the dipolar

term in Eq. (15) to first neighbors only, and assuming that they are all at the same distance, which gives a rough estimate of the size of the dipolar contribution. This number reads (for the dipolar systems included in our fitting set): six for 111BL, eight for 100BL, four for octahedral Au_6, nine for atom-1, six for atom-2, one for atom-3b, in the simplified version of the fcc (110) reconstructed surface. This led us to conclude that for an accurate reproduction of the dipolar contribution one needs to introduce a dependence of the coefficients D_i upon the distribution of the neighboring atoms. This represents a higher-order effect, but one that is apparently important. A rough analysis also shows that the square or the cube of the dipole are not appropriate, as a more subtle dependence is at play. The octupole is also excluded, as it is usually too small to produce a sizeable effect. At the same order in the multipolar expansion as the octupole and the cube of the dipole, one finds the product of the dipole by the quadrupole. We thus added to the empirical potential expression a product contribution of the form

$$E_i^{\text{dip-quad}} = DQ_i \,\text{dipole} \cdot \left\{ \sum_{\sigma=x,y,z} \sum_{\sigma'=x,y,z} \times \left\{ \sum_{j\neq i}^{\text{atoms}} \exp\left[-\alpha_q \left(\frac{r_{ij}}{r_0} - 1 \right) \right] \frac{r_{ij}^{\sigma} r_{ij}^{\sigma'}}{r_{ij}^2} \right\}^2 - \frac{1}{3} \left\{ \sum_{j\neq i}^{\text{atoms}} \exp\left[-\alpha_q \left(\frac{r_{ij}}{r_0} - 1 \right) \right] \right\}^2 \right\}, \quad (19)$$

where dipole is the usual dipolar term defined in Eq. (15) without the D_i factor, and the sum over σ, σ' and $j \neq i$ in the right-hand-side is the quadrupolar term, multiplied by a linear coefficient DQ_i which is expressed as a third-order polynomial in an effective coordination number e_i:

$$DQ_i = DQ^{(0)} + DQ^{(1)} e_i + DQ^{(2)} e_i^2 + DQ^{(3)} e_i^3. \quad (20)$$

Note that to avoid a proliferation of nonlinear parameters, and since the product (dipole times quadrupole) is only a correction term, we used a simple exponential for the radial dependence of the quadrupole, and that the coefficient DQ_i of the product term $E_i^{\text{dip-quad}}$ depends on the same effective coordination number e_i as the coefficient of the "pure" dipolar term.

As before, with this choice of the analytic form for the dipolar term we conducted an extensive search (using the basin-hopping algorithm) for the best possible values of the non-linear parameters, with the linear parameters obtained via a least-square fit. We found that in this case it was possible to obtain an excellent fit of all the energy curves in Figs. 3–5. It can also be noted in passing that—despite the fact that the coefficients of the $P(r;R_M)$ polynomial describing the radial part of the dipolar contribution were left completely unconstrained and only one interval was used in its definition—the resulting behavior, shown in Fig. 7, does not present any nonphysical oscillations, and tends to saturation for small values of the distance. The final optimal parameters for the dipolar term are given in Table IV, and correspond to a value of $\Delta = 0.0083$ eV (123 points). The quality of the final fit is shown in Figs. 3–5, and in our opinion can be considered as satisfactory, with absolute differences between DF and empirical potential energies of the order of 0.01 eV.

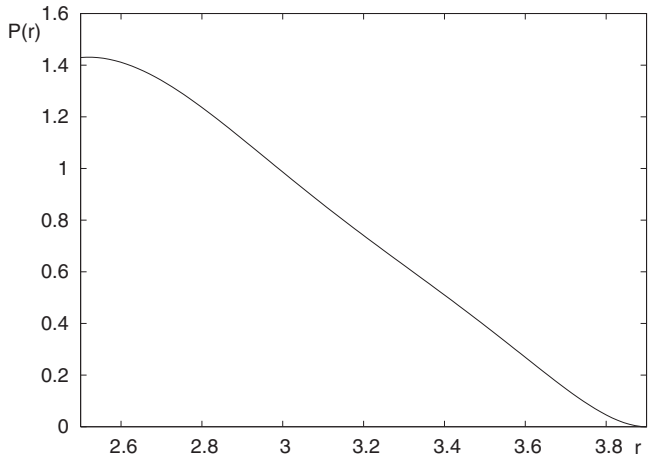

FIG. 7. Plot of $P(r;R_M)$, the polynomial describing the radial component of the dipolar contribution to the energy, as a function of r (in Å), see text for details.

VI. TEST OF THE EMPIRICAL POTENTIAL

The first test of the new potential consisted in evaluating the values of some bulk quantities and comparing them with experimentally derived values and with the results of calculations using our DF approach. This comparison is reported in Table V. From an inspection of this table, it can be seen that the new potential is in reasonable agreement with both experiment and DF results. The tendency to underestimate the stacking fault energy is typical of RGL-like approaches when this quantity is not explicitly introduced into the fitting set, while the overestimation of the vacancy formation energy with respect to DF witnesses an overshooting of the directional contribution at high coordination number which anyway goes in the direction of a better agreement with experiment.

TABLE IV. Values of the optimized linear and nonlinear parameters for the dipolar component. Radii are in Å.

parameter	value	parameter	value
α_e	5.747017	R_e	3.125850
α_q	4.008572	R_M	3.9
$D^{(0)}$	0.115741	$DQ^{(0)}$	0.133939
$D^{(1)}$	−0.035967	$DQ^{(1)}$	−0.061012
$D^{(2)}$	0.00606144	$DQ^{(2)}$	0.0087037
$D^{(3)}$	−0.00034804	$DQ^{(3)}$	−0.00039698
$p^{(2)}$	5.706506		
$p^{(3)}$	12.521950		
$p^{(4)}$	13.436660		
$p^{(5)}$	6.718205		
$p^{(6)}$	1.211088		

TABLE V. Comparison between some experimental bulk quantities (exp.) for gold and the same quantities as predicted by the potential (POT) derived in the present work, or evaluated via our density-functional (DF) approach (properly rescaled as detailed in the text). E_v^F, E_{sf} and the various σ are calculated at $T=0$ and include relaxation effects. $\sigma^{111}, \sigma^{100}$ refer to unreconstructed surfaces, σ^{110} refers to the missing-row reconstructed surface.

Quantity	POT	exp.	DF
Lattice parameter a (Å)	4.08	4.08	4.08
Cohesive energy E_c (eV/atom)	3.83	3.83	3.83
Stacking fault energy E_{sf} (mJ/m^2)	5	<55	26
Vacancy formation energy E_v^F (eV)	0.86	0.94	0.55
Bulk Modulus B (10^{12} dyne cm^{-2})	1.927	1.803	1.793
C_{11} (10^{12} dyne cm^{-2})	2.208	2.016	2.166
C_{12} (10^{12} dyne cm^{-2})	1.786	1.697	1.606
C_{44} (10^{12} dyne cm^{-2})	0.612	0.454	0.283
Surface energy σ^{111} (meV/Å^{-2})	58.1	96.8	57.3
Surface energy σ^{110} (meV/Å^{-2})	69.2	—	68.6
Surface energy σ^{100} (meV/Å^{-2})	128.2	—	123.0

The second test of the new potential consisted in fully relaxing the model structures which were used as fitting systems from their ideal configurations: the simplified "surface-only" Au(110) surface, the complete Au(110) surface and the Au_{38} truncated octahedral cluster. The results of such calculations are reported in Tables I and II. An inspection of these tables immediately shows that the present potential improves upon the description of the missing-row Au(110) surface and the truncated octahedral Au_{38} cluster with respect to the RGL potential. In particular, it can be noted how: (a) the "rounding" of the (111) face in the Au(110) surface—both the simplified "surface-only" system and the complete system (note that the latter has not been used as a fitting system)—is now described in a qualitatively correct way (see the sign of Δy_2 in Table I), (b) the z-coordinate of the atoms lying on (111) faces of the Au_{38} cluster are remarkably expanded, in agreement with the DF/PW91 results but at variance with the RGL results. The new potential thus seems to be able to describe the fitting systems also in a neighborhood of the ideal configurations which have been used in the fitting procedure.

As a further test of the new potential, the lowest-energy structures of small gold clusters (with size between 6 and 200 atoms) were investigated. Extracted from these calculations, the putative global minima of Au_{14}, Au_{20}, and Au_{32} according to the new potential are shown in Fig. 8, together with the corresponding binding energies. These structures were obtained through basin-hopping runs comprising 1000 Monte Carlo steps starting from randomly chosen initial configurations and allowing random moves of up to 1 Å (positive or negative) in the Cartesian coordinates of each atom (a value of $kT=0.5$ eV was chosen). It is interesting to note that for Au_{32} the proposed cage structure coincides with the highly symmetrical icosahedral structure proposed as the global minimum.[47] This does not hold for Au_{20}, for which the putative global minimum given by the potential is structurally different from the tetrahedral structure which is

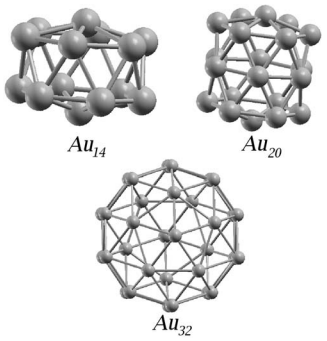

FIG. 8. Schematic representation of the putative global minima of Au_{14} (2.823 eV/atom), Au_{20} (3.007 eV/atom), and Au_{32} (3.210 eV/atom).

thought to be the ground state in the gas phase.[48] However, shell closure effects have been shown to be essential in stabilizing the Au_{20} tetrahedron with respect to cage structures[16] and, of course, we cannot aim at describing effects, such as quantum (shell closure/unclosure, electronic wave function or magnetic interference) effects, which are by definition outside the scope of empirical potential approaches. In general, we found that small gold clusters have a great tendency toward cage configurations according to the new potential: we estimated that the transition from cage to compact (fcc-like) structures only occurs around size $N=150$ atoms. This tendency is probably overestimated with respect to DF/PW91 predictions.[49]

VII. CONCLUSIONS

From a detailed analysis of DF/PW91 calculations on gold model clusters and surfaces, an empirical potential for gold, which includes angular corrections, has been derived in the present article. Its consists in the inclusion of higher-order nonlinear terms (specifically, the product dipole-quadrupole) that do not appear to have been used before, but that our analysis suggests to be necessary to describe directionality effects in the Au-Au interaction. Preliminary tests show that this potential is able to describe in a reasonably accurate way the systems used in the fitting procedure also in a neighborhood of the ideal configurations thereby used, and that it possesses some unusual features with respect to existing potentials, such as a strong tendency toward cage structures for small Au clusters.[16] It thus represents a good starting point for future investigations (currently in progress in our lab). In particular, we stress that even though the present formulation probably overestimates the tendency of gold to open structures, it is important to have a potential available which gives qualitatively different results with respect to the existing ones and can thus "bracket" the experimental behavior. This point should be particularly useful when using such potentials in combined empirical potential/first-principles systematic searches.[50] Another intriguing possibility is to use a weighted average (with weights to be optimized) of the new potential and, say, the RGL potential, which is known to favor in an excessive way compact structures.[16]

A final remark: even though we are reasonably confident to have singled out the main physical origin of the angular

corrections to the Au-Au potential, the present formulation is obviously not the only possible one, and the inclusion of a more extensive set of DF data is in order to further improve the accuracy of the proposed parametrization. Moreover, in the absence of really accurate and complete experimental data, we resorted to a parametrization based on DF/PW91 results (only properly rescaling lengths and energies to match the experimental bulk values of binding energy and lattice constant), so that the present potential obviously suffers from the limitations of the rescaled DF/PW91 approach.

ACKNOWLEDGMENTS

We thank Dr. Pietro Ballone (Belfast) for useful discussions. We acknowledge financial support from the Italian CNR for the program "(Supra-) Self-Assemblies of Transition Metal Nanoclusters" within the framework of the ESF EUROCORES SONS, and from the European Community Sixth Framework Project for the STREP Project "Growth and Supra-Organization of Transition and Noble Metal Nanoclusters" (Contract No. NMP-CT-2004-001594).

*Present address: LAAS-CNRS, Av. du Colonel Roche 7, 31077 Toulouse, France.

†Corresponding author. fortunelli@ipcf.cnr.it

[1] V. Rosato, M. Guillopé, and B. Legrand, Philos. Mag. A **59**, 321 (1989).
[2] M. S. Daw and M. I. Baskes, Phys. Rev. B **29**, 6443 (1984).
[3] F. Ercolessi, M. Parrinello, and E. Tosatti, Philos. Mag. A **58**, 213 (1988).
[4] F. Ercolessi, E. Tosatti, and M. Parrinello, Phys. Rev. Lett. **57**, 719 (1986).
[5] A. Bartolini, F. Ercolessi, and E. Tosatti, Phys. Rev. Lett. **63**, 872 (1989).
[6] M. I. Baskes, Phys. Rev. Lett. **59**, 2666 (1987).
[7] M. I. Baskes, Phys. Rev. B **46**, 2727 (1992).
[8] M. I. Baskes, J. S. Nelson, and A. F. Wright, Phys. Rev. B **40**, 6085 (1989).
[9] M. I. Baskes and R. A. Johnson, Modell. Simul. Mater. Sci. Eng. **2**, 147 (1994).
[10] Y. Mishin, M. J. Mehl, and D. A. Papaconstantopoulos, Acta Mater. **53**, 4029 (2005).
[11] B.-J. Lee, J.-H. Shim, and M. I. Baskes, Phys. Rev. B **68**, 144112 (2003).
[12] E. Aprà and A. Fortunelli, J. Mol. Struct.: THEOCHEM **501-502**, 251 (2000).
[13] A. Fortunelli and A. M. Velasco, Int. J. Quantum Chem. **99**, 654 (2004).
[14] E. Aprà, F. Baletto, R. Ferrando, and A. Fortunelli, Phys. Rev. Lett. **93**, 065502 (2004).
[15] R. Ferrando, A. Fortunelli, and G. Rossi, Phys. Rev. B **72**, 085449 (2005).
[16] E. Aprà, R. Ferrando, and A. Fortunelli, Phys. Rev. B **73**, 205414 (2006).
[17] P. Torelli, F. Sirotti, and P. Ballone, Phys. Rev. B **68**, 205413 (2003).
[18] P. Koskinen, H. Häkkinen, G. Seifert, S. Sanna, T. Frauenheim, and M. Moseler, New J. Phys. **8**, 1 (2006).
[19] D. G. Fedak and N. A. Gjostein, Acta Metall. **15**, 827 (1967).
[20] D. Wolf, Ph.D. thesis, Universität München, Munich, 1972.
[21] W. Moritz and D. Wolf, Surf. Sci. **88**, L29 (1979).
[22] D. Wolf, H. Jagodzinski, and W. Moritz, Surf. Sci. **77**, 265 (1978).
[23] D. Wolf, H. Jagodzinski, and W. Moritz, Surf. Sci. **77**, 283 (1978).
[24] Q. J. Gao and T. T. Tsong, J. Vac. Sci. Technol. A **15**, 761 (1987).
[25] K. Müller, J. Witt, and O. Schütz, J. Vac. Sci. Technol. A **5**, 757 (1987).
[26] G. L. Kellog, J. Vac. Sci. Technol. A **5**, 747 (1987).
[27] T. E. Jackman, J. A. Davies, D. P. Jackson, P. R. Norton, and W. N. Unertl, Surf. Sci. **120**, 389 (1982).
[28] H. Niehus, Surf. Sci. **145**, 407 (1984).
[29] J. Möller, K. J. Snowdon, W. Heiland, and H. Niehus, Surf. Sci. **176**, 475 (1986).
[30] S. H. Overbury, W. Heiland, D. M. Zehner, S. Datz, and R. S. Thoe, Surf. Sci. **109**, 293 (1981).
[31] P. Häberle, P. Fenter, and T. Gustafsson, Phys. Rev. B **39**, 5810 (1989).
[32] M. Copel, P. Fenter, and T. Gustafsson, J. Vac. Sci. Technol. A **5**, 742 (1987).
[33] I. K. Robinson, Phys. Rev. Lett. **50**, 1145 (1983).
[34] L. D. Marks, Phys. Rev. Lett. **51**, 1000 (1983).
[35] G. Binnig, H. Rohrer, C. Gerber, and E. Weibel, Surf. Sci. **131**, L379 (1983).
[36] S. Olivier, G. Tréglia, A. Saul, and F. Willaime, Surf. Sci. **600**, 5131 (2006).
[37] S. Baroni, A. Dal Corso, S. de Gironcoli, and P. Giannozzi, PWSCF site http://www.pwscf.org
[38] J. P. Perdew, J. A. Chevary, S. H. Vosko, K. A. Jackson, M. R. Pederson, D. J. Singh, and C. Fiolhais, Phys. Rev. B **46**, 6671 (1992).
[39] V. Bonačič-Koutecky, J. Burda, R. Mitrič, M. Ge, G. Zampella, and P. Fantucci, J. Chem. Phys. **117**, 3120 (2002).
[40] B. Soulé de Bas, M. J. Ford, and M. B. Cortie, J. Mol. Struct.: THEOCHEM **686**, 193 (2004).
[41] E. M. Fernández, J. M. Soler, I. L. Garzón, and L. C. Balbás, Phys. Rev. B **70**, 165403 (2004).
[42] F. Remacle and E. S. Kryachko, *Advances in Quantum Chemistry* (Elsevier, Amsterdam, 2004).
[43] F. Ercolessi and J. B. Adams, Europhys. Lett. **26**, 583 (1994).
[44] X. Y. Liu, F. Ercolessi, and J. B. Adams, Modell. Simul. Mater. Sci. Eng. **12**, 665 (2004).
[45] Z. Li and H. A. Scheraga, Proc. Natl. Acad. Sci. U.S.A. **84**, 6611 (1987).
[46] D. J. Wales and J. P. K. Doye, J. Phys. Chem. A **101**, 5111 (1997).
[47] M. P. Johansson, D. Sundholm, and J. Vaara, Angew. Chem., Int. Ed. **43**, 2678 (2004).
[48] J. Li, X. Li, H.-J. Zhai, and L.-S. Wang, Science **299**, 864 (2003).
[49] S. Bulusu, X. Li, L.-S. Wang, and X.-C. Zeng, J. Phys. Chem. C **111**, 4190 (2007).
[50] R. Ferrando, A. Fortunelli, and R. L. Johnston, Phys. Chem. Chem. Phys. **10**, 640 (2008).

THE JOURNAL OF PHYSICAL CHEMISTRY C LETTERS

2008, *112,* 3187−3190
Published on Web 02/07/2008

Mobility of Au on TiO_x Substrates with Different Stoichiometry and Defectivity

Francesco Sedona,[†] Mauro Sambi,[†] Luca Artiglia,[†] Gian Andrea Rizzi,[†] Andrea Vittadini,[‡] Alessandro Fortunelli,[§] and Gaetano Granozzi*,[†]

Dipartimento di Scienze Chimiche, Unità di Ricerca CNR-INFM and INSTM, Università di Padova, Via Marzolo 1, I-35131 Padova, Italy, Dipartimento di Scienze Chimiche, ISTM-CNR and INSTM, Università di Padova, Via Marzolo 1, I-35131 Padova, Italy, and IPCF-CNR, via Giovanni Moruzzi 1, I-56124 Pisa, Italy

Received: December 16, 2007; In Final Form: January 24, 2008

Au nanoparticles deposited on titania films, where two nanophases of different stoichiometry and defectivity are co-present, were imaged on the same spot by scanning tunneling microscopy. The observed sizes are rather dissimilar as a consequence of the different mobility of Au on the two surfaces. The role of the stoichiometry, which can influence the Au−substrate interaction, and of the defects, which can trap the metal atoms, is discussed on the basis of theoretical calculations of diffusion energy barriers on the two surfaces.

One important issue in surface chemistry and catalysis is to clearly identify the effect of dimensionality on the chemical reactivity of heterogeneous systems, and this has produced the new field of nanocatalysis.[1] It is well-known that new, or improved, chemical and catalytic properties are obtained when metallic nanoparticles (NPs) in the range of 1−5 nm are supported on a dispersing support, typically a metal oxide. A major general problem that needs to be overcome is related to the intrinsic instability of the NPs: due to their high surface/volume ratio, NPs tend to decrease their energy by coalescing into larger particles (Ostwald ripening and sintering processes). This makes their characterization difficult and the exploitation of their innovative properties on a long time scale or under realistic reaction conditions uncertain. Being intrinsically unstable, NPs can only survive in the presence of kinetic barriers which avoid mass transfer and agglomeration processes or when stabilized by specific NP−substrate interactions. As defects in oxides have been demonstrated to be effective in stabilizing NPs, ultrathin films containing ordered arrays of defects have been used as templates for the growth of size-selected and ordered NPs arrays.[2−8]

In this context, Au NPs supported on reducible metal oxides represent a case of particular relevance because they are very active catalysts for a variety of reactions. A paradigmatic example in this sense is the catalytic activity toward CO oxidation at low temperature discovered for Au grown on reduced titania surfaces, whose explanation, however, is still the object of debate.[9−14] Controlling the Au mobility on titania surfaces is particularly important in relation to the goal of stabilizing the Au NPs. Indirect evidence has been reported according to which Au NPs are less mobile on reduced titania surfaces with respect to stoichiometric ones, based on the NP size observation by scanning tunneling microscopy (STM) on surfaces of different stoichiometry,[15] but a direct and simultaneous observation of differently sized NPs on different TiO_x substrates having a well-defined stoichiometry is still lacking. In the present Letter, we report such a STM study, where Au NPs were deposited and observed on two ultrathin TiO_x films on Pt(111) which have well-defined and different stoichiometries and defect structures.[16] What is most interesting is that the two different oxide nanophases are co-present in the same STM images, thus allowing a direct comparison of both the Au NP size and mobility at different temperatures free from errors due to tip and scanning parameter differences.

In recent years, some of us have managed to prepare and characterize several nanophases of TiO_x on Pt(111) having rather different STM topographies and stoichiometries and distinct low energy electron diffraction (LEED) patterns.[16] For some of them, we have recently demonstrated that they are good templates for metal-cluster growth.[2] The two nanophases used in the present study have been termed as *k*-TiO_x (*k* stands for *kagomé*[17] and $x \approx 1.5$)[16] and *rect*′-TiO_2 (*rect*′ stays for rectangular),[16b] respectively.

The preparation and the structural characterization of the different TiO_x nanophases on Pt(111) have been reported in detail elsewhere.[16] Ti was evaporated at room temperature (RT) onto the clean Pt(111) surface, in an oxygen background pressure (P_{O_2}) of 1×10^{-4} Pa. In order to obtain a well-defined and ordered TiO_x nanophase, the amount of deposited Ti, the substrate temperature, and the oxygen pressure during the postannealing have to be optimized. However, if the preparation is carried out under nonoptimized conditions (in the present case 950 K $P_{O_2} = 10^{-6}$ Pa for 10'), different phases can be co-present and the LEED pattern may result in the superimposition of different patterns typical of each phase. In these cases, looking at the surface by STM, regions where the different nanophases are adjacent can be imaged.

Au has been evaporated from a filament basket on the substrate held at RT under UHV conditions (without further annealing), with a typical deposition rate of about 0.3 ML/min. The STM images have been obtained in constant-current mode

* To whom correspondence should be addressed. E-mail: gaetano.granozzi@unipd.it.
[†] Unità di Ricerca CNR-INFM and INSTM, Università di Padova.
[‡] ISTM-CNR and INSTM, Università di Padova.
[§] IPCF-CNR.

10.1021/jp711801w CCC: $40.75

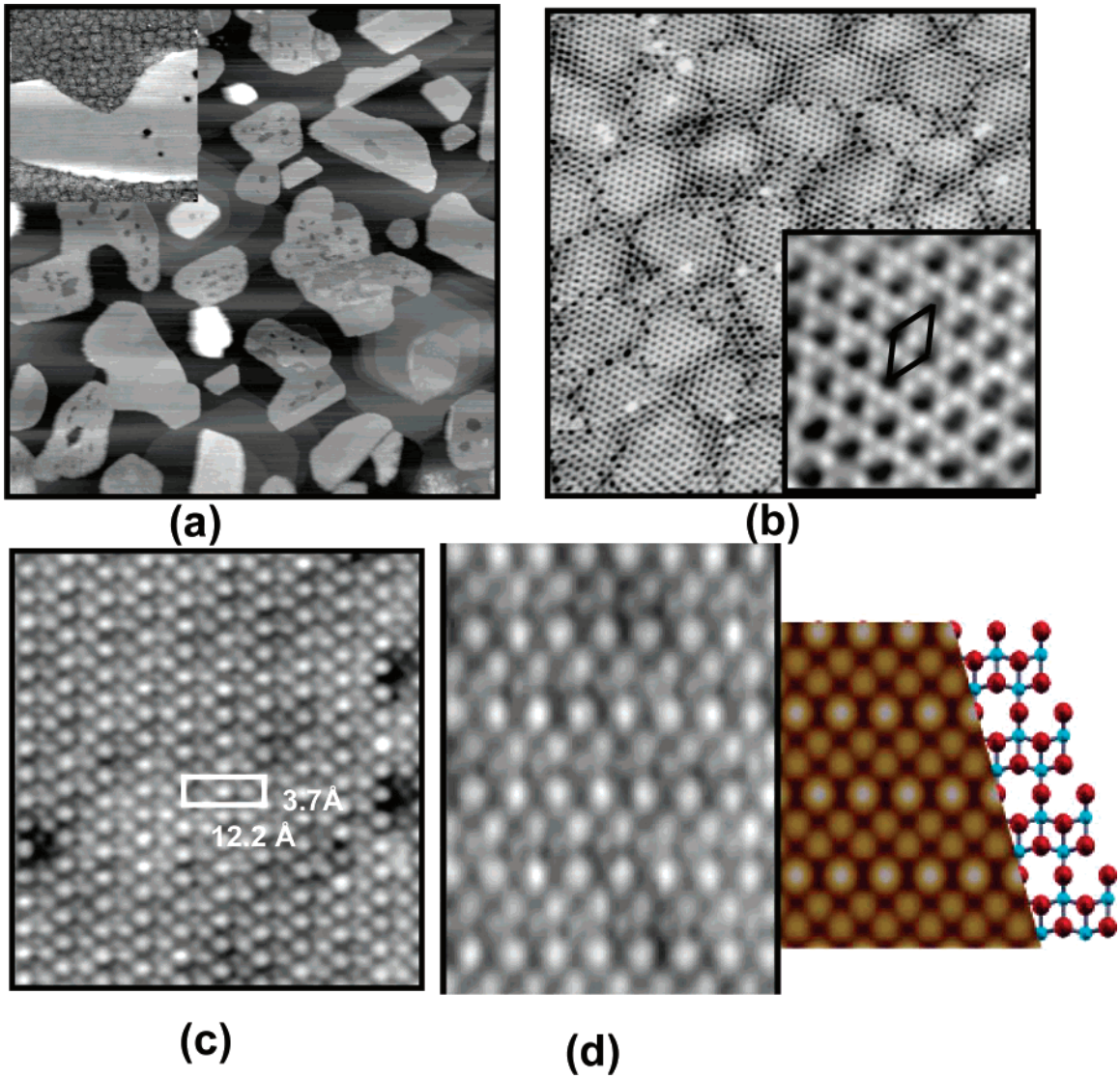

Figure 1. STM constant-current image of (a) *rect*′-TiO_2 islands grown on the *k*-TiO_x monolayer (500 × 500 nm^2; $V = 1.2$ V, $I = 1.2$ nA). In the inset, a close-up of an island is shown (80 × 80 nm^2; $V = 2.0$ V, $I = 1.0$ nA). (b) The wetting monolayer of *k*-TiO_x (30 × 30 nm^2; $V = 1$ V, $I = 1$ nA) and (inset) its atomically resolved image (3 × 3 nm^2; $V = -0.4$ V, $I = 1.06$ nA). (c) The top of a *rect*′-TiO_2 island (6.1 × 6.1 nm^2; $V = -0.7$ V, $I = 0.66$ nA). (d) The comparison between a close-up of a STM image and a simulation obtained from a "pentacoordinated nanosheet" model where Ti atoms are reported as light blue spheres and O atoms as red spheres.

at RT in an Omicron VT-STM system operating at a base pressure of 5×10^{-9} Pa. Tunneling voltages are given with respect to the sample. The tunneling parameters are reported in the corresponding captions of the reported STM images. Experimental details were similar to those in ref 16a.

In Figure 1a, we report the STM image of a spot of the sample where *rect*′-TiO_2 large islands are evident on a substrate covered by a wetting monolayer (ML) of the *kagomé-like* *k*-TiO_x phase. The *rect*′-TiO_2 islands have sizes in the range 50−100 nm and an apparent height in the order of 0.5 nm. If one looks carefully at the inset in Figure 1a, the typical pattern of the *k*-TiO_x nanophase can be easily recognized.[16a] For comparison, in Figure 1b, we report the STM image of the *k*-TiO_x phase, taken in a different experiment on a single *k*-TiO_x nanophase sample:[16a] a patched but clearly two-dimensional hexagonal overlayer with a long-range Moirè-like modulation is observed, where the surface mesh has a periodicity of approximately 6.0 Å, in good agreement with the hexagonal 2.15 × 2.15 mesh seen by LEED.[16a] Atomically resolved images (see the inset in Figure 1b) allowed us to demonstrate that a *kagomé-like* ML is present, based on hexagons which are interconnected through their vertices. A structural model implying a Ti_2O_3 stoichiometry for the *k*-TiO_x nanophases has been suggested, which has been recently corroborated by density functional theory (DFT) calculations.[18]

In Figure 1c, we report a close-up of the *rect*′-TiO_2 island, where the outlined centered rectangular unit cell (3.7 × 12.2 $Å^2$) is in good agreement with the LEED pattern of a single *rect*′-TiO_2 phase.[16b] A model of this phase has been recently proposed, which consists of a 2-ML-thick nanosheet composed of 5-fold coordinated cations connected by an intermediate layer of 2-fold coordinated oxygens. In spite of the low ion coordination number, this structure is remarkably stable (only 0.18 eV/TiO_2 above bulk anatase), and is readily obtained starting from a 4 ML (101)-oriented anatase slab.[19]

In Figure 1d, we report a comparison between the simulated and experimental STM map for the top of the *rect*′-TiO_2 island. We point out that the theoretical map was obtained from an unsupported film. To correct for the absence of the support−overlayer charge transfer, the empty states closest to the Fermi level were excluded from the Tersoff−Hamann procedure.

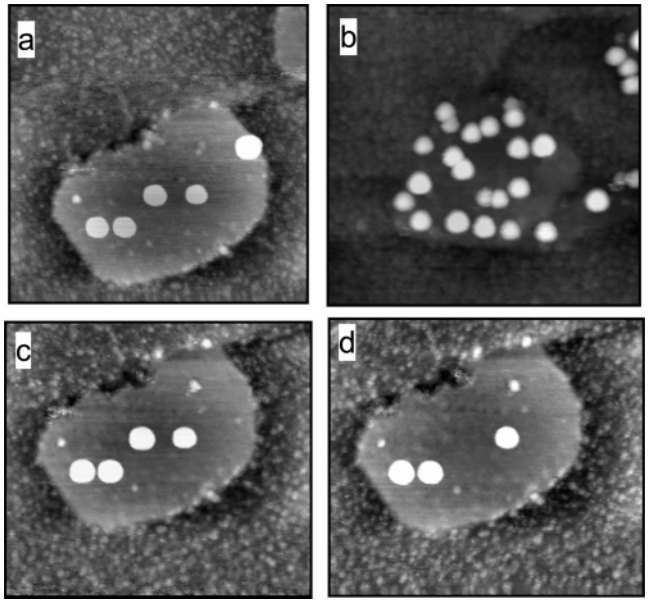

Figure 2. STM constant-current image of the *rect*′-TiO_2/*k*-TiO_x system after the deposition of Au NPs: (a) 0.2 ML of Au (82 × 82 nm^2; V = 1.5 V, I = 1.5 nA); (b) 0.8 ML of Au (82 × 82 nm^2; V = 1.5 V, I = 1.5 nA); (c and d) the same as part a in successive scans, demonstrating a tip-induced mobility.

As to the relevance to the present report, the important point is that we have the co-presence of two adjacent, well-characterized phases having rather different stoichiometry (i.e., Ti_2O_3 and TiO_2) and topography (a *kagomé-like* defective and a completely oxygen terminated surface, respectively). The STM image reported in Figure 2a shows the *rect*′-TiO_2/*k*-TiO_x system after the deposition of 0.2 ML of Au.[20] As it can be easily observed, there is a striking difference between the dimensions of the Au NPs imaged on the stoichiometric *rect*′-TiO_2 surface and those covering the reduced *k*-TiO_x surface. The particles deposited on the *rect*′-TiO_2 phase show an apparent height of ca. 1.5 nm and a diameter of ca. 5−6 nm. In contrast, on the reduced *k*-TiO_x phase, the Au NPs are characterized by a definitely smaller mean apparent height (0.2 nm) (with a larger spread in the height distribution) and diameter (1.5−2 nm). Since the flux of Au particles impinging on the sample surface is statistically the same (the *k*- and *rect*′-phases are co-present on the same spot of the Pt(111) surface), the fact that on the stoichiometric *rect*′ phase the Au NPs are characterized by a larger mean cluster size than on *k*-TiO_x strongly suggests a larger mobility of Au on the *rect*′-TiO_2 phase with respect to the *k*-phase, which favors the agglomeration and formation of larger Au NPs. When the Au coverage is increased to 0.8 ML, one observes an increase in the particle density of the NPs on the *rect*′-phase, even though their shape and dimensions are similar to those obtained at lower coverage (see Figure 2b). Considering the NPs on *k*-TiO_x, their mean apparent height (0.25 nm) and diameter (2.5 nm) are somewhat larger in the 0.8 ML system, even if the actual sizes are difficult to be precisely measured because many NPs are barely resolved.

To corroborate this analysis, adsorption energies and diffusion pathways and activation energy barriers for a single Au atom on both the *k*- and *rect*′-TiO_2 surfaces have been calculated via a DFT approach.[21,22] First, the optimal adsorption sites of Au atoms on the two titania surfaces have been found, and—starting from these sites—the diffusion mechanisms and the corresponding energy barriers have been calculated using a nudged elastic band (NEB) approach.[23] A striking difference was found for the two phases. A gold atom interacts very weakly with the *rect*′-phase, with a maximum adsorption energy on top of an oxygen atom of 0.30 eV. Correspondingly, the barriers for the two possible diffusion mechanisms by which the Au atom can jump from an oxygen site to the two neighboring ones are extremely small: 0.05 and 0.06 eV, respectively (see Figure 3a). It can be concluded that diffusion of Au single atoms (and presumably small clusters[21a]) is extremely fast on this phase, and that even medium-sized clusters can be mobile if subjected to sufficiently strong forces.

In contrast, a gold atom easily penetrates into the "holes" exposing the bare Pt(111) surface which characterize the *k*-phase and is strongly adsorbed there (with adsorption energies of 2.96 eV in the center of the hole), and the jump out of a hole into the nearest neighbor is energetically costly, with an activation energy barrier of about 2.4 eV (see Figure 3b). It is thus to be expected that significant diffusion of Au atoms on the *k*-phase can only occur at RT if they are not trapped into the holes but are kinetically hopping on top of the oxygen atoms in a metastable state (the corresponding adsorption energies and energy barriers were also calculated, finding values similar to those on the *rect*′-phase). Our results of a substantial influence of mobility on the growth of metal clusters are consistent with recent experimental data of MBE experiments of Au on the TiO_2(110) surface.[24] Note that the presence of some small and

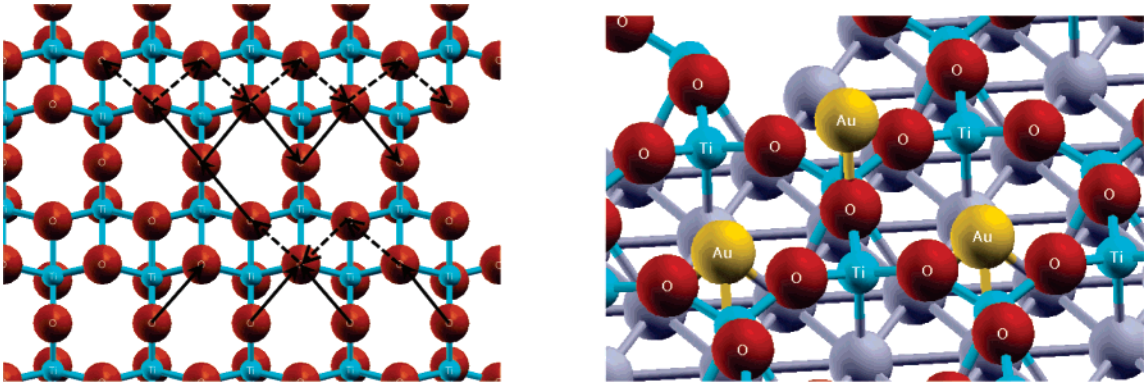

Figure 3. Diffusion mechanisms of a Au atom on the (a) *rect*′-TiO_2 and (b) *k*-TiO_x phases. Ti atoms are reported as light blue spheres, O atoms as red spheres, and Au atoms as golden spheres. On the *rect*′-phase, diffusion occurs through two different nearest-neighbor jumps, highlighted as full and dotted arrows in part a. On the *k*-phase, the initial, saddle-point, and final positions of a Au atom hopping from a hole into the next neighbor are shown in part b.

a few large Au NPs at the borders of the *rect′* islands in Figure 2 suggests that a step-edge (Ehrlich−Schwoebel) barrier is effective, which is consistent with the large mean size of the NPs and with a constant NP size as a function of coverage.[25]

Another interesting feature concerning the Au NP mobility on top of the *rect′*-TiO_2 surface is shown in Figure 2c and d, where we report the image of the same island taken after some tip passages: a tip-induced extraction of the NPs from the surface is clearly evident. This cannot be due to a simple movement out of the picture frame but is probably due to the fact that Au NPs can get attached to the STM tip.[26]

The present experimental data clearly show to what extent the different stoichiometry and defect structure of an oxide surface can influence the interaction with a metal.[27] In the case of Au on titania, a very weak interaction with TiO_2 stoichiometric surfaces is documented, with cluster nucleation occurring only in the presence of undercoordinated Ti atoms (e.g., step-edge decoration). It is quite clear from our data that undercoordinated Ti atoms are rare on the oxygen terminated surface of the stoichiometric *rect′*-TiO_2 islands. On the contrary, the peculiar *kagomé-like* structure of the wetting ML offers potential nucleation sites in the center of each hexagon. In this connection, we recall that an example of Au NPs deposited on a reduced *w′*-TiO_x ($x \approx 1.2$) ML phase has recently been published,[2] where the outermost layer is also a complete oxygen layer exhibiting a close-packed structure with virtually no defects. In that case, the mean diameter of the Au NPs was ≈3.5 nm, a value lower than that found on the *rect′*-TiO_2 island. The smaller size of the Au NP is to be attributed either to confinement effects[25] or to a lower Au mobility on the defect-free reduced *w′*-TiO_x phase with respect to the defect-free oxidized *rect′*-TiO_2 phase, a fact that can be rationalized by assuming a larger Au−substrate interaction in the reduced surface. A way to rationalize this larger interaction could be related to charging of the Au atoms on the *w′*-TiO_x phase, similar to what was proposed for analogous ultrathin systems.[28]

Acknowledgment. This work has been funded by European Community through two STRP projects (NanoChemSens, *Nanostructures for Chemical Sensors*, and GSOMEN, *Growth and Supra-organization of Transition and Noble Metal Nanoclusters*), by the Italian CNR through the project SSATMN within the framework of the ESF EUROCORES SONS, and by the Italian Ministry of Instruction, University and Research (MIUR) through the fund "Programs of national relevance" (PRIN-2003, PRIN-2005). Part of the calculations were performed at the Cineca Supercomputing Center within an agreement with Italian INFM-CNR.

References and Notes

(1) (a) Bell, A. T. *Science* **2003**, *299*, 1688. (b) Schlogl, R.; Abd, H. *Angew. Chem., Int. Ed.* **2004**, *43*, 1628. (c) Madey, T. E.; Pelhos, K.; Wu, Q.; Barnes, R.; Ermanoski, I.; Chen, W.; Kolodziej, J. J.; Rowe, J. E. *Proc. Natl. Acad. Sci. U.S.A.* **2002**, *99*, 6503.

(2) Sedona, F.; Agnoli, S.; Fanetti, M.; Kholmanov, I.; Cavaliere, E.; Gavioli, L.; Granozzi, G. *J. Phys. Chem. C* **2007**, *111*, 8024.

(3) Freund, H. J. *Surf. Sci.* **2002**, *500*, 271.

(4) Fallace, W. T.; Min, B. K.; Goodman, D. W. *Top. Catal.* **2005**, *34*, 17.

(5) Degen, S.; Becker, C.; Wandelt, K. *Faraday Discuss.* **2004**, *125*, 343.

(6) Berdunov, N.; Mariotto, G.; Balakrishnan, K.; Murphy, S.; Shvets, I. V. *Surf. Sci.* **2006**, *600*, L287.

(7) Hamm, G.; Becker, C.; Henry, C. R. *Nanotechnology* **2006**, *17*, 1943.

(8) Jordan, K.; Murphy, S.; Shvets, I. V. *Surf. Sci.* **2006**, *600*, 5150.

(9) Chen, M. S.; Goodman, D. W. *Science* **2004**, *306*, 252.

(10) Lopez, N.; Janssens, T. V. W.; Clausen, B. S.; Xu, Y.; Mavrikakis, M.; Bligaard, T.; Nørskov, J. K. *J. Catal.* **2004**, *223*, 232.

(11) Chen, M. S.; Goodman, D. W. *Acc. Chem. Res.* **2006**, *39*, 739.

(12) Chen, M.; Cai, Y.; Yan, Z.; Goodman, D. W. *J. Am. Chem. Soc.* **2006**, *128*, 6341.

(13) Hernandez, N. C.; Sanz, J. F.; Rodriguez, J. A. *J. Am. Chem. Soc.* **2006**, *128*, 15600.

(14) Kung, M. C.; Davis, R. J.; Kung, H. *J. Phys. Chem. C* **2007**, *111*, 11767.

(15) Chen, M. S.; Luo, K.; Kumar, D.; Wallace, W. T.; Yi, C.-W.; Gath, K. K.; Goodman, D. W. *Surf. Sci.* **2006**, *601*, 632.

(16) (a) Sedona, F.; Rizzi, G. A.; Agnoli, S.; Llabrés i Xamena, F. X.; Papageorgiou, A.; Ostermann, D.; Sambi, M.; Finetti, P.; Schierbaum, K.; Granozzi, G. *J. Phys. Chem. B* **2005**, *109*, 24411. (b) Finetti, P.; Sedona, F.; Rizzi, G. A.; Mick, U.; Sutara, F.; Svec, M.; Matolin, V.; Schierbaum, K.; Granozzi, G. *J. Phys. Chem. C* **2007**, *111*, 869.

(17) Mekata, M. *Phys. Today* **2003**, *56*, 12.

(18) Fortunelli, A.; Barcaro, G.; Sedona, F.; Granozzi, G. Manuscript in preparation.

(19) Vittadini, A.; Selloni, A.; Casarin, M. *Theor. Chem. Acc.* **2007**, *5−6*, 663. Vittadini, A.; Casarin M. *Theor. Chem. Acc.*, in press.

(20) The Au coverage has been determined by analyzing the STM images of Au on clean Pt(111). The typical deposition rate is about 0.3 ML/min.

(21) The computational details are similar to those used in previous work: (a) Barcaro, G.; Fortunelli, A.; Nita, F.; Ferrando, R. *Phys. Rev. Lett.* **2005**, *95*, 246103. (b) Barcaro, G.; Sedona, F.; Fortunelli, A.; Granozzi, G. *J. Phys. Chem. C* **2007**, *111*, 6095.

(22) Baroni, S.; dal Corso, A.; de Gironcoli, S.; Giannozzi, P.; Cavazzoni, C.; Ballabio, G.; Scandolo, S.; Chiarotti, G.; Focher, P.; Pasquarello, A.; Laasonen, K.; Trave, A.; Car, R.; Marzari, N.; Kokalj, A. http://www.p-wscf.org/.

(23) This method searches for the minimum energy path between two local minima by creating a fixed number of intermediate configurations (images) which are linked to each other by elastic springs. The image highest in energy does not feel the spring forces along the band; instead, the true force at this image along the tangent is inverted. In this way, the image tries to maximize its energy along the band, and thus, when this image converges, it is at the exact saddle point. See: Henkelman, G.; Uberuaga, B. P.; Jònsson, H. *J. Chem. Phys.* **2000**, *113*, 9901.

(24) Matthey, D.; Wang, J. G.; Wendt, S.; Matthiesen, J.; Schaub, R.; Laegsgaard, E.; Hammer, B.; Besembacher, F. *Science* **2007**, *315*, 1692.

(25) Krug, J.; Politi, P.; Michely, T. *Phys. Rev. B* **2000**, *61*, 14037.

(26) Durston, P. J.; Palmer, R. E.; Wilcoxon, J. P. *Appl. Phys. Lett.* **1998**, *72*, 176.

(27) Fua, Q.; Wagner, T. *Surf. Sci. Rep.* **2007**, *62*, 431 and references therein.

(28) Pacchioni, G.; Giordano, L.; Baistrocchi, M. *Phys. Rev. Lett.* **2005**, *94*, 226104.

THE JOURNAL OF PHYSICAL CHEMISTRY C

Letter

Cooperative Phase Transformation in Self-Assembled Metal-on-Oxide Arrays

Giovanni Barcaro, Alessandro Fortunelli, Gaetano Granozzi, and Francesco Sedona

J. Phys. Chem. C, **2009**, 113 (4), 1143-1146• DOI: 10.1021/jp808695r • Publication Date (Web): 07 January 2009

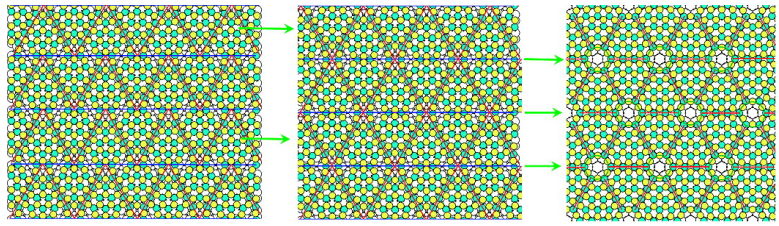

Phase transformation of a TiOx/Pt(111) film induced by Au deposition and heating

THE JOURNAL OF PHYSICAL CHEMISTRY C LETTERS

2009, *113,* 1143–1146
Published on Web 01/07/2009

Cooperative Phase Transformation in Self-Assembled Metal-on-Oxide Arrays

Giovanni Barcaro,[†] Alessandro Fortunelli,* Gaetano Granozzi,[‡] and Francesco Sedona[‡]

IPCF-CNR, Via G. Moruzzi 1, Pisa, 56124, Italy, and Dip. di Scienze Chimiche, Università di Padova, Via Marzolo 1, Padova, 35131, Italy

Received: October 01, 2008; Revised Manuscript Received: December 11, 2008

The thermal behavior of a composite system formed by gold nanoclusters self-organized on a TiO_x/Pt(111) ultrathin film is investigated via first-principles simulations. A cooperative phase transformation from a rectangular to an hexagonal phase occurs at high temperature, by which Au clusters do not coalesce, but rearrange their shape and positions together with the more mobile regions of the oxide. A model describing the atomistic processes behind this transformation is proposed that is in full agreement with available experimental data.

Ultrathin oxide films grown on metal supports have recently attracted great attention as substrates for studying the growth and reactivity of metal deposits.[1] With respect to bulk systems, they offer the advantage of being conductive to some extent and thus can be characterized with atomistic resolution by electron-based probe techniques.[2] Moreover, especially in the case of polar films they are often modulated into regular nanostructured patterns opening up into point defects that act as trapping and nucleation centers[3] and thus constitute nearly ideal nanotemplates.[4] However, when employed as model catalysts their thermal stability becomes a central issue, especially when the reactions to be catalyzed are strongly exothermic (as in the case of CO and NO oxidation catalyzed by gold particles),[5] as the evolved heat can induce particle detachment from the substrate, Ostwald ripening and sintering[6] leading to larger particles and/or to the loss of beneficial particle-substrate interactions,[7−9] and thus to deactivation of the catalyst.[10] The presence of the underlying metal support makes ultrathin substrates promising in terms of heat dispersion, but their nanoscale dimension is likely to originate novel phenomena, such as structural phase transformations of both the metal aggregates and the oxide layer. Herein we show through static and dynamic density functional (DF) simulations on Au clusters self-assembled on a titanium oxide TiO_x /Pt(111) polar ultrathin film[11,12] that the combined effect of metal adsorption and heating induces a peculiar transformation from a metastable rectangular to a stable hexagonal phase without implying a detachment of the metal clusters from their trapping centers. This is the first example of a cooperative phase transformation in self-assembled metal-on-oxide arrays of interest from the point of view of basic science and also as it suggests that these systems can be robust enough to cross the gap between model studies and practical applications.

The atomistic structure of a polar ultrathin titanium oxide film grown on the Pt(111) surface (named z′-phase in ref 13) is schematically shown in Figure 1a, together with a simulated STM image at positive bias (1 eV).[11] This film is constituted of (i) compact pseudoepitaxial regions where triangular islands of oxygen-tricoordinated titanium atoms are separated by zigzag-like lines of oxygen-tetracoordinated titanium atoms (the latter appear brighter in the STM images at positive bias, hence the z′ nomenclature), and (ii) defective troughs (appearing darker in the STM images) that are aligned along the $\langle 1\bar{1}0\rangle$ directions of the Pt(111) surface and are based on irregular Ti_2O_3 units that alternate with Ti vacancies or "holes" (highlighted with white circles in Figure 1a) exposing the bare metal support.[11] In Figure 2a, an STM image of the z′-phase after the deposition of 0.9 monolayer equivalent (ML) of Au is displayed;[14] the Au clusters nucleating on the holes along the troughs of the z′-phase[3] are very regular with a narrow size distribution despite their small size (the average number of atoms is roughly estimated to be around 25) and grow along a preferential orientation, highlighted with black lines in Figure 2a. It can be noted that the shape of the smaller clusters is elongated in the direction of the preferential orientation. The cluster/oxide/metal

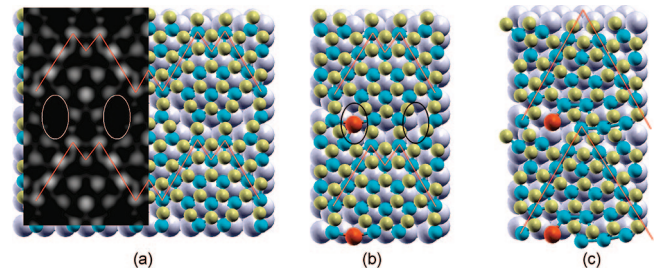

Figure 1. Atomistic structures of (a) the bare z′-phase at $T = 0$ K; (b) the same phase with a Au atom adsorbed inside the defective hole at $T = 0$ K; (c) the same system as in panel b, but now as a snapshot from a first-principles molecular dynamics simulation at $T = 600$ K. Pt, Ti, O, and Au atoms are represented as gray, yellow, light blue, and red colors, respectively. In panel a, an STM image at 1 eV bias simulated using the Tersoff−Hamann approach[21] at a height of 2 Å above the oxygen layer is also shown. The defective holes are highlighted with white circles in (a) and as black circles in (b). The simulations used the PW91 xc-functional[22] and ultrasoft pseudopotentials[23]

* To whom correspondence should be addressed. E-mail: (A.F.) fortunelli@ipcf.cnr.it; (G.G.) gaetano.granozzi@unipd.it.
[†] IPCF-CNR.
[‡] Università di Padova.

10.1021/jp808695r CCC: $40.75

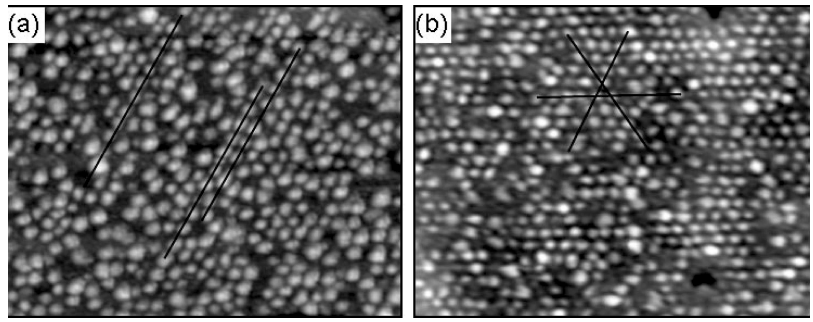

Figure 2. STM constant-current images of Au clusters deposited at 0.35 ML coverage on the z′-TiO_x phase: (a) as deposited at $T = 300$ K (50×40 nm^2, $V = 1$ V, $I = 0.5$ nA); (b) after a postdeposition annealing in UHV at $T = 600$ K for 15 min (50×40 nm^2, $V = 1$ V, $I = 0.5$ nA).

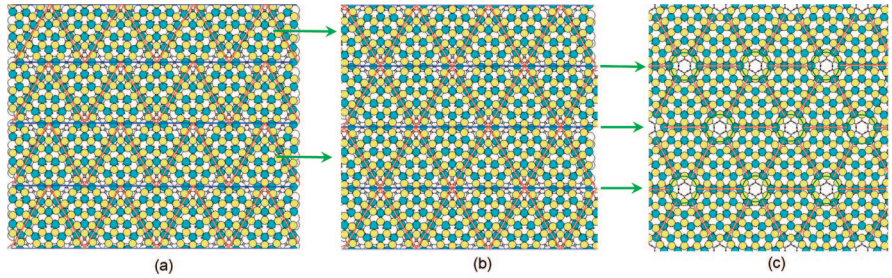

Figure 3. Schematic representation of the transformation from (a) the rectangular z′-TiO_x /Pt(111) phase to (b) an intermediate (hexagonal) z′-phase with still two holes per cell, to (c) an hexagonal z′-phase with only one hole per cell and full *p6m* symmetry. Color convention as in Figure 1.

system is quite stable; no change is observed after annealing in UHV for several minutes at temperatures up to 550 K. However, at higher temperatures a peculiar phenomenon is observed, by which the rectangular pattern of nanoclusters transforms into an hexagonal one, and the transformation is almost complete above 600 K.[12] In Figure 2b, an STM image obtained after annealing at 600 K for 15 min is shown.[14] Note that there are now three preferential orientations, highlighted with black lines in Figure 2b. Moreover, the Au clusters are more spatially separated, even though their density is roughly constant, and their shape (also for the smaller clusters) is more rounded. This transformation has no counterpart in the pure titanium oxide phases and is only observed for the composite metal-on-oxide-on-metal system.[15]

In order to rationalize the mechanisms behind such a peculiar transformation, first-principles molecular dynamics (Car−Parrinello, CP)[16] simulations were conducted on the TiO_x z′-phase both as a bare system and with a Au atom adsorbed inside the defective hole.[17] The z′-phase turned out to be thermally stable; CP runs were performed at $T = 300$ K and at $T = 600$ K, each one for a total time of 3−5 ps without any noticeable effect. An analogous result was obtained when a Au atom was adsorbed inside the hole and CP simulations were performed at $T = 300$ K, as can be appreciated from Figure 1b, where a schematic picture of the optimized structure obtained after a local energy minimization (using the PWscf code) is shown.[18] On the contrary, when the temperature was raised to 600 K, the system rapidly rearranged to a different configuration, shown in Figure 1c as a representative snapshot taken from the corresponding CP run. The two defective holes along the troughs merged into a single one, while the zigzag-like motifs of oxygen-tetracoordinated titanium atoms deformed from a W-shape into a triangular outline. This structural transformation is a purely entropic effect; a local energy minimization starting from the configuration of Figure 1c brings the system back to the configuration of Figure 1b. Its driving force lies in the fact that the Au atom is somewhat constrained in the hole,[3] and the associated tension increases with increasing kinetic energy of Au.

As cell dimensions and stoichiometry are held fixed in our simulations, a rectangular translational symmetry is imposed and the system is not free to relax to a different (e.g., hexagonal) periodicity. The structure shown in Figure 1c however is very suggestive. Note that the dimensions of the rectangular unit cell are such that the cell height (14.4 Å) is in a $\sqrt{3}/2$ ratio with the cell width (16.6 Å), so that the arrangement shown in Figure 1c can be viewed as a pattern of horizontally disposed stripes of equilater triangles (Figure 3a). Now, such a regular pattern can be transformed into an hexagonal arrangement by translating every second stripe by half an horizontal lattice parameter (Figure 3b). This new configuration is quite competitive; its energy per unit cell being only 0.42 eV higher than that of the rectangular structure at the DF level. Moreover, small displacements of the Ti_2O_3 units in the troughs produce a merging of the two holes into a single one and create a perfect hexagonal arrangement (Figure 3c). This last structure is a local energy minimum (at variance with the kinetically stabilized configuration of Figure 1c), has hexagonal symmetry (cell edge 16.6 Å), presents merged equidistant holes, is thermally stable within the constraints given by its geometry, and is isoenergetic with the structure of Figure 3b. The interconversion shown in Figure 3 thus represents a route for the experimentally observed rectangular-to-hexagonal transformation, taking place via atomic rearrangements in the oxygen overlayer and along the troughs.

Both the rectangular (Figure 1a) and hexagonal (Figure 1c) cells were then used as templates for density functional basin-hopping (DF-BH) calculations of the structure and energetics of Au_N clusters ($N = 1-8$) adsorbed on them (calculations on selected structures were also conducted up to Au_{11}). The DF-BH approach is a first-principles global optimization method[19] that allows one to explore the potential energy surface of complex systems and predict their global minima.[20] The binding

TABLE 1: Total Binding Energies of Au_N Clusters on the Rectangular and Hexagonal Phases

cluster	E_{bnd} (rect)	E_{bnd} (hex)
Au_1	1.76	1.43
Au_2	3.47	3.47
Au_3	5.63	5.57
Au_4	7.74	8.36
Au_5	9.91	10.81
Au_6	12.37	13.20
Au_7	14.40	14.67
Au_8	16.53	17.03

energies of the combined cluster/oxide/support systems from such calculations, i.e., the difference between the sum of the energies of the separated fragments in their equilibrium configurations (metal atoms in the gas-phase and supported titania film) and the energy of the composite system, are reported in Table 1. Note that the clusters on the rectangular phase are favored for few (up to three) Au atoms, but the situation is reversed for Au clusters with four or more atoms. The hexagonal metal-on-oxide phase thus become not only entropically but also *thermodynamically* more stable than the rectangular one, and this explains why this arrangement is maintained after the system is brought back to RT. The reasons for this energetic crossover lie in the better interaction of the Au clusters with the defective oxide surface in the hexagonal phase, obtained without sacrifying the cluster internal energy. It can be added that the clusters on the hexagonal phase have a more rounded aspect in agreement with experiment (Figure 2b). Even though computational limitations do not allow us to investigate clusters of the same size as in the experiments (the average number of atoms for the clusters of Figure 2 can be roughly estimated to be around 25 while we have tentative structures only up to Au_{11}), we believe that the prediction of an energetic crossover between metal-on-oxide rectangular and hexagonal phases can be extrapolated to the experimentally investigated régime (further experiments are in progress to verify this point).

Note from Table 1 that the binding energies of the clusters to the substrate are substantial, so that cluster coalescence from detrapping is unlikely under the given experimental conditions. This statement can be substantiated by the following arguments. The energy differences involved in the ($Au_N \rightarrow Au_{N-1} + Au$) fragmentation ($N \geq 2$) for Au clusters adsorbed on the rectangular phase range between 2.03 and 2.46 eV (actually, it can be noted in passing that with the exception of Au_6 these energy differences range in a very narrow interval of 2.03/2.17 eV and that one does not observe the usual even−odd oscillations in the incremental formation energy of noble metal clusters).[19] Setting the adsorption of a single Au atom on the neighboring oxygen atoms to 0.2 eV[3] and even neglecting any additional energy penalty due to transition state rearrangements, the energy barriers for the fragmentation of a single Au atom can be roughly estimated to be at least ≈1.83 eV. By assuming an Arrhenius prefactor of $\approx 10^{13}$ Hz (which is an upper bound to typical values), it turns out that fragmentation is predicted to occur on a time scale of hours. Ostwald ripening via single-atom fragmentation is thus unlikely for short (15 min) annealing even at 600 K. Fragmentation of larger species, such as a Au_2 dimer, can also be considered. Detachment of a dimer turns out to be more favorable than that of a single-atom, as in similar cases,[19] but still the corresponding energy barriers are predicted to be at least 1.6 eV (with the only exception of Au_3, which suffers from the scarce stability of the Au dimer adsorbed on the hole of the z′-phase, and Au_8, which suffers for the peculiar stability of the Au_6 cluster). Cluster sintering via disruption of small clusters is thus not viable according to our calculations under the given experimental conditions, in fair agreement with the experimental result that the dimensions of the Au clusters are not strongly perturbed by the annealing process.[12]

In conclusion, metal-on-ultrathin-oxide systems present a great potential interest in several fields, including heterogeneous catalysis, as the oxide acts as a protective layer, hindering alloying of metal particles with metal of the support, while the steric constraints and the electrostatic field generated by the charge-separated layer can trap metal atoms (surface nanopatterning) and orient the cluster growth into ordered metal arrays, in addition to originating novel phenomena. Given the nanoscale dimensions of the interface and the exothermal character of many catalytic processes, the thermal stability of these materials is a key issue. The present analysis unveils the atomistic processes behind the first example of a cooperative phase transformation in such systems, by which regular Au/TiO_x/Pt(111) arrays transform from a metastable rectangular to an hexagonal phase. This transformation is favored by both entropic and energetic factors, and occurs without cluster detrapping or alloying with the support, but via a rearrangement of their shapes and positions together with the more mobile and defective regions of the oxide to increase their relative distance and optimize cluster/substrate interactions. Given the growing activity in this field, the present results are expected to be followed by more such examples in the future.

Acknowledgment. We thank the DEISA Consortium (co-funded by the EU, FP6 project 508830) for support within the DEISA Extreme Computing Initiative (www.deisa.org) and for providing CPU time on the CSC supercomputing center. Carlo Cavazzoni and Paolo Giannozzi are gratefully acknowledged for porting the PWscf and CP codes and improving scalability for CPU and RAM requirements.

References and Notes

(1) Freund, H.-J. *Surf. Sci.* **2007**, *601*, 1438–1442.

(2) Sterrer, M.; Fischbach, E.; Risse, T.; Freund, H.-J. *Phys. Rev. Lett.* **2005**, *94*, 186101.

(3) Barcaro, G.; Fortunelli, A.; Granozzi, G. *Phys. Chem. Chem. Phys.* **2008**, *10*, 1876, and references therein.

(4) Hamm, G.; Becker, C.; Henry, C. R. *Nanotechnology* **2006**, *17*, 1943.

(5) Hutchings, G. J.; Haruta, M. *Appl. Catal., A* **2005**, *291*, 1.

(6) Parker, S. C.; Campbell, C. T. *Top. Catal.* **2007**, *44*, 3–13.

(7) Yoon, B.; Hakkinen, H.; Landman, U.; Wörz, A. S.; Antonietti, J.-M.; Abbet, S.; Judai, K.; Heiz, U. *Science* **2005**, *307*, 403–407.

(8) Chen, M. S.; Goodman, D. W. *Top. Catal.* **2007**, *44*, 41–47.

(9) Matthey, D.; Wang, J. G.; Wendt, S.; Matthiesen, J.; Schaub, R.; Laegsgaard, E.; Hammer, B.; Besenbacher, F. *Science* **2007**, *315*, 1692–1696.

(10) Goguet, A.; Burch, R.; Chen, Y.; Hardacre, C.; Hu, P.; Joyner, R. W.; Meunier, F. C.; Mun, B. S.; Thompsett, A.; Tibiletti, D. *J. Phys. Chem. C* **2007**, *111*, 16927–16933.

(11) Sedona, F.; Granozzi, G.; Barcaro, G.; Fortunelli, A. *Phys. Rev. B* **2008**, *77*, 115417.

(12) Sedona, F.; Agnoli, S.; Fanetti, M.; Kholmanov, I.; Cavaliere, E.; Gavioli, L.; Granozzi, G. *J. Phys. Chem. C* **2007**, *111*, 8024–8029.

(13) Sedona, F.; Rizzi, G. A.; Agnoli, S.; Xamena, F. X. L. I.; Papageorgiou, A.; Ostermann, D.; Sambi, M.; Finetti, P.; Schierbaum, K.; Granozzi, G. *J. Phys. Chem. B* **2005**, *109*, 24411.

(14) The pictures reported in Figure 2 were obtained during the same STM experiments reported in ref 12 to which the reader is referred to for more details. The TiO_x film was prepared by reactive deposition in the presence of oxygen ($p_{O_2} = 10^{-4}$ Pa) and successive annealing in UHV at 673 K.[11] Au was evaporated from a filament basket on the TiO_x substrate held at RT under UHV with a typical deposition rate of about 0.3 ML/minute. The sample preparation and characterization was performed using an OMICRON STM UHV system with a base pressure $< 5 \times 10^{-9}$ Pa. STM images were obtained in constant current mode at RT.

(15) In ref 12, this transformation was interpreted as into a different w-TiO_x/Pt(111) phase; the present analysis supersedes this previous hypothesis.

(16) Car, R.; Parrinello, M. *Phys. Rev. Lett.* **1985**, *55*, 2471.

(17) The CP calculations were performed using the ESPRESSO software (http://www.quantum-espresso.org). The time step was set to 25 au, the electron mass 3500 au, a CP run consisted of 500 minimization steps, 200 MD steps starting with null velocities at 300 K, and a variable number of production MD steps at the chosen temperature for a total simulation time between 3 and 5 ps using a Nosè thermostat for the kinetic energy of the electronic wave function. The CP runs were conducted at the Cray XT4 supercomputer of CSC ((http://www.csc.fi) in Espoo, Finland.

(18) The PWscf (http://www.pwscf.org) calculations used ultrasoft pseudopotentials, the PW91 exchange-correlation functional,[22] and the following computational parameters (identical to those used in ref 3): 30 Ryd for the energy cutoff on the wave function, 150 Ryd for the energy cutoff on the electronic density, about 8−10 Å of empty space between atoms in replicated cells, a (2,2,1) k_{mesh} grid for the sampling of the first Brillouin zone, and 2 layers of Pt for describing the metal support.

(19) Barcaro, G.; Aprà, E.; Fortunelli, A. *Chem.—Eur. J.* **2007**, *13*, 6408–6418.

(20) The DF-BH method is based on a basin-hopping algorithm for the exploration of the potential energy surface combined with a density-functional method for the calculation of energies and forces. Each BH run starts with a randomly chosen atomic configuration and is composed of a given number of Monte Carlo steps. In each of these, the starting configuration is first locally optimized to obtain an energy E_1, then subjected to a random displacement of all the atoms up to ± 1 Å in each Cartesian coordinates, and finally locally optimized to obtain a new energy E_2. If $\exp[(E_1 - E_2)/k_BT] >$ rndm, where rndm is a random number (Metropolis criterion), the new configuration is accepted; otherwise the old configuration is kept and the process is iterated. For each size, we performed three to five BH runs, each one composed of about 10−15 Monte Carlo steps, using a value of 0.5 eV as k_BT in the Metropolis criterion.

(21) Tersoff, J.; Hamann, D. R. *Phys. Rev. Lett.* **1983**, *50*, 1998–2001.

(22) Perdew, J. P.; Chevary, J. A.; Vosko, S. H.; Jackson, K. A.; Pederson, M. R.; Singh, D. J.; Fiolhais, C. *Phys. Rev. B* **1992**, *46*, 6671–6687.

(23) Vanderbilt, D. *Phys. Rev. B* **1990**, *41*, 7892–7895.

JP808695R

Theor Chem Acc (2009) 123:317–325
DOI 10.1007/s00214-009-0551-y

REGULAR ARTICLE

Structural and electronic properties of small platinum metallorganic complexes

Giovanni Barcaro · Alessandro Fortunelli

Received: 26 November 2008 / Accepted: 23 February 2009 / Published online: 25 March 2009

Abstract A theoretical first-principles study of Pt_n(ligand)$_m$ (n = 1–3) metallorganic complexes is performed, by varying the number of metal atoms and the nature and number of organic coordinate ligands (specifically, vinylic and arylic ligands). For each system, the nature of the bonding, the structure and the energetics of the metal/organic-species interaction are analyzed to derive information on the growth of coated metal clusters in solution. It is found that two régimes can be distinguished: a "coordinatively saturated" régime, in which the ratio among the number of ligands and the number of metal atoms is high and a ligand/organic π-interaction mode is preferred, and a "coordinatively unsaturated" régime, in which the ligand/metal ratio is low and a ligand/organic σ-interaction mode is preferred. Reactive channels, such as oxidative insertion of Pt into C–H bonds with the corresponding formation of platinum hydride species, can be opened in the latter régime.

Keywords Density-functional theory · Metallorganic complex · Solvated metal clusters · σ-interaction · π-interaction

Dedicated to the memory of Professor Oriano Salvetti and published as part of the Salvetti Memorial Issue.

G. Barcaro (✉) · A. Fortunelli
Molecular Modeling Laboratory,
Istituto per i Processi Chimico-Fisici (IPCF) del Consiglio Nazionale delle Ricerche (CNR), Area della Ricerca,
Via G. Moruzzi 1, 56124 Pisa, Italy
e-mail: barcaro@ipcf.cnr.it

1 Introduction

Colloidal suspensions of transition metals are formed by metallic particles, ranging in size between 1 and 50 nm, which are stabilized by protective shells/layers to prevent coalescence phenomena [1–4]. The possibility of effectively stabilizing nanometric metallic particles with a high surface/volume ratio in solution allows for a quickly growing number of technological applications of such colloidal suspensions, in particular (but not exclusively) in the field of catalysis [5–10]. Bottom-up methods to produce these systems are based on the synthesis of metallic particles starting from elementary constituents, i.e., single atoms, ions, or small clusters. These methods primarily consist on the reduction of metal salts via chemical processes, the use of electrochemical techniques, the controlled decomposition of organometallic metastable compounds or the aggregation of metallic species in low oxidation state. A large number of stabilizing species, donor ligands, polymers and surfactants are used to control the growth of the freshly formed metallic particles and to protect the growing units from coalescence into the thermodynamic equilibrium phase: the bulk crystal [11–14].

In this context, the use of olefinic complexes of metals in a low oxidation state proves to be a clean route for obtaining colloidal suspensions of mono- and bi-metallic particles. In particular, the technique of metal vapor deposition [1, 2, 15] is based on the co-condensation of vapors of one metal and of one or more organic solvents on the cold walls (−196 °C) of proper reactors in ultra-high vacuum (10^{-4}–10^{-6} mbar). The subsequent heating of the reactor determines the melting of the solvent to give solutions in which small atoms or very minute metallic clusters (containing no more than 10 atoms, normally less than 4) are coated by the solvent molecules or added

surfactants. An inconvenience of this technique is represented by the low thermical stability of the solvates, which quite often, even if kept at low temperatures, decompose slowly with the formation of insoluble aggregates. This determines a variation both in the concentration of the metal in solution as well as in the size of the particles and, as a consequence, in the catalytic properties. A possible solution to stabilizing the solvates consists in using emulsifying species (such as long chain aliphatic ammines or olefinic systems) capable of coordinating the metallic atoms in order to prevent the coalescence of the aggregates.

Given the high affinity of Pt towards unsaturated organic compounds, ligands based on C=C functional groups have been devised and tested [16, 17]: using the metal vapor deposition technique, colloidal suspensions of platinum have been obtained in the presence of deuterated benzene (C_6D_6) as solvent species and molecules of vinylsiloxanic compounds as stabilizing species [18]. In more detail, the surfactants used were 1,3-divinyl-1,1,3,3-tetramethyldisiloxane (DVS) and 1,3,5,7-tetravinyl-1,3,5,7-tetramethyl-cyclotetrasiloxane (TVS), whose structures are shown in Fig. 1. For both these compounds, the interaction with platinum occurs through the terminal olefinic groups. Experimental evidence has shown that in the presence of only the solvent molecules the stability of these suspensions at room temperature is limited to a few days, while with the use of surfactants the stability of metal aggregates is extended to a few months. The effective mechanisms by which growth eventually takes place, however, are not known, and are difficult to investigate experimentally, due to the lack of proper characterization tools able to furnish information on reactive processes in situ and in real time. Computational approaches can provide a very useful support in this sense, as it is nowadays possible to explore the structure, energetics and dynamics of aggregates of reasonable size with sufficient accuracy, see for example [19], a field into which one of us (AF) was introduced by Prof. Salvetti many years ago.

In the present article, such an enterprise is undertaken in the specific case of neutral small Pt clusters interacting with surfactants in which the ligand is based on unsaturated organic groups. The lowest-energy structures of $Pt_n ligand_m$ complexes where $n = 1$–3, $m = 1$–6, and ligand is a vinylic or arylic species, have been investigated via density-functional (DF) calculations. Our aim is to elucidate the nature of the interaction, the structure of the solvated species and the energetics of the metal/ligand detachment. It will be shown that it is possible to derive from such studies information useful to interpret experimental observations and suggestions with some general significance.

The article is structured as follows. In Sect. 2, the computational details will be given; the results will be discussed in Sect. 3 and the conclusions will be summarized in Sect. 4.

2 Computational details

Density-functional (DF) calculations have been performed using the DFT module of the NWChem software [20], adopting the B3LYP xc-functional [21] for the description of the exchange-correlation energy. It is known that this functional does not provide an adequate description of the metal bond, especially when this is fully developed in large clusters [22]. However, here we are dealing with small Pt units, for which the B3LYP functional is still appropriate. Moreover, some calculations have also been performed by employing the BPW91 [23, 24] exchange-correlation functional. The differences between the two functionals will be discussed in the next section. The structural search was mostly carried out via biased (or inspired) guesses, i.e., by setting up reasonable initial configurations and locally minimizing their energy at the DF level. However, in selected cases, a few steps of a density-functional basin-hopping (DF-BH) approach were also performed. In the DF-BH approach [25, 26], one

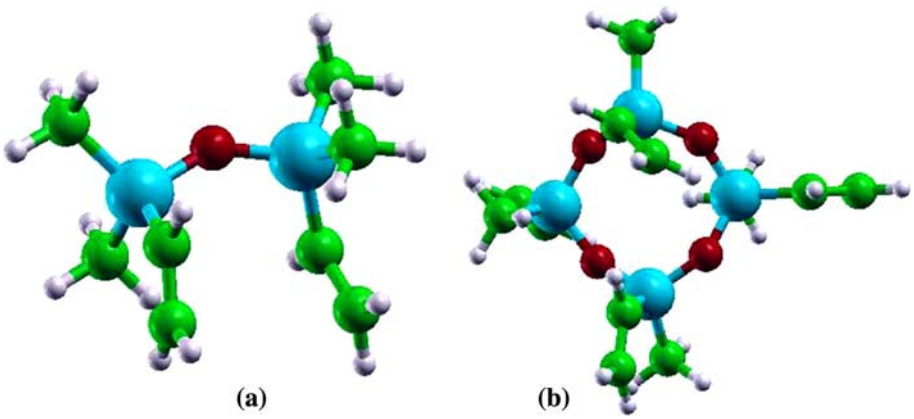

Fig. 1 **a** 1,3-divinyl-1,1,3,3-tetramethyldisiloxane (DVS) and **b** 1,3,5,7-tetravinyl-1,3,5,7-tetramethyl-cyclotetrasiloxane (TVS). Oxygens in *red*, carbons in *green*, hydrogens in *white* and silicons in *light blue*

starts from a random configuration and tries to explore the PES of the system by random moves followed by local minimizations whose acceptance is ruled by a Monte Carlo Metropolis criterion. Alternatively, one can start the DF-BH search from inspired guesses, in which selected plausible structures are set up and locally minimized, trying to exploit for the larger systems the experience acquired with small ones.

For the DF calculations, the chosen basis set included Gaussian functions of triple-ζ quality plus polarization functions (f on the platinum atom, d on the carbon, oxygen and silicon atoms and p on the hydrogen atom) [27, 28]. In the case of the platinum atom, a relativistic effective core potential (ECP) has been employed for the description of the 60 inner electrons [28]. All calculations have been performed spin-unrestricted and using a Gaussian-smearing technique [29] for the fractional occupation of the one-electron energy levels. The pictures have been obtained by using the XCrySDen program [30].

3 Results

Our aim is to elucidate the basic principles of the metal/ligand interaction from which models for the aggregation and coalescence of metal clusters can be developed. In the following, the results on $Pt_n(C_2H_4)_m$ complexes will be presented and discussed according to the number of Pt atoms in the complex.

3.1 $Pt_1(ligand)_m$

Before going further into the study of the structure of $Pt_n(ligand)_m$ complexes, it is useful to conduct a preliminary analysis of the Pt^0/C=C interaction (carbon–carbon double bond) in the simplest possible case: the interaction of one platinum atom with an ethylene molecule (C_2H_4), recalling some of the results obtained in [31]. In the gas phase, the electronic configuration of the platinum atom is a $5d^96s^1$ triplet state. When the Pt atom interacts with the ethylene molecule, there is a change from the $5d^96s^1$ triplet state to the $5d^{10}6s^0$ singlet state. In this transition the $6s$ platinum orbital is vacated, making it available for a *donation* of electron density from the organic species. The d orbitals, which now become completely filled and slightly more diffuse, are in turn available for *back-donating* electron density to the π^* orbitals of the double bond. This phenomenon is apparent in the density plots of the molecular orbitals of the $Pt(C_2H_4)$ complex shown in Fig. 2a–c. 0.5 eV are necessary to promote the Pt atom to its valence state (averaging spin–orbit contributions). Once the Pt atom is in its valence state, the formation of the chemical bond produces a significant amount of energy, 2.67 eV. Overall, the total variation of energy in the reaction:

$$Pt + C_2H_4 \rightarrow Pt(C_2H_4) \quad \Delta E = -2.17 \text{ eV} \tag{1}$$

is equal to 2.17 eV, see Table 1, where the results obtained on the energetics of small Pt systems are reported. When the platinum–ethylene distance is increased, one can observe a *spin-crossing* following bond breaking: the asymptotic state (with the two fragments at infinite distance) is characterized by a different spin from the bonding state.

The complex $Pt(C_2H_4)$ can bind a second and a third ethylene molecules, forming larger complexes, see Fig. 2d, e. In the final $Pt(C_2H_4)_3$ complex, approximately all of the carbon atoms lye in the same plane as the platinum atom. The bonding mechanism, with the interplay of the σ-donation and π-back-donation, is the same in the presence of a greater number of ethylene molecules, but the energy gains resulting from the addition of a second and third ligand molecule are smaller than that of the reaction (1)

$$Pt(C_2H_4) + (C_2H_4) \rightarrow Pt(C_2H_4)_2 \quad \Delta E = -1.36 \text{ eV} \tag{2}$$

$$Pt(C_2H_4)_2 + (C_2H_4) \rightarrow Pt(C_2H_4)_3 \quad \Delta E = -0.74 \text{ eV} \tag{3}$$

These interaction energies are approximately the same when the ethylene molecules are substituted by ligands with vinylic terminal groups, as in the case of the three complexes shown in Fig. 2f–h, where 1,3-divinyl-1,1,3,3-tetramethyldisiloxane (DVS) is the ligand species. The energies of the corresponding reactions are

$$Pt + DVS \rightarrow Pt(DVS)^{[2f]} \quad \Delta E = -2.16 \text{ eV} \tag{4}$$

$$Pt(DVS)^{[2f]} \rightarrow Pt(DVS_{chelate})^{[2g]} \quad \Delta E = -1.39 \text{ eV} \tag{5}$$

$$Pt(DVS_{chelate})^{[2g]} + DVS \rightarrow Pt(DVS_{chelate})(DVS)^{[2h]} \quad \Delta E = -0.65 \text{ eV} \tag{6}$$

This leads us to conclude that ethylene molecules are good models of ligands with vinylic terminals with a significant reduction of the computational cost. Note that the only significant difference is between Eqs. 3 and 6 is due to the steric effects.

In order to complete this preliminary analysis, we have calculated the dissociative barrier corresponding to the detachment of one of the three vinylic groups of the $Pt(DVS)_2$ complex, more specifically the detachment of the DVS non-chelated species, that is, bonded to platinum via just one vinylic group. The energy curve was obtained by progressively increasing the distance from the center of mass of the exiting vinylic part and the platinum atom. With this distance kept at a fixed value, a local optimization of all the other degrees of freedom of the system was carried out for every point. The obtained curve (not

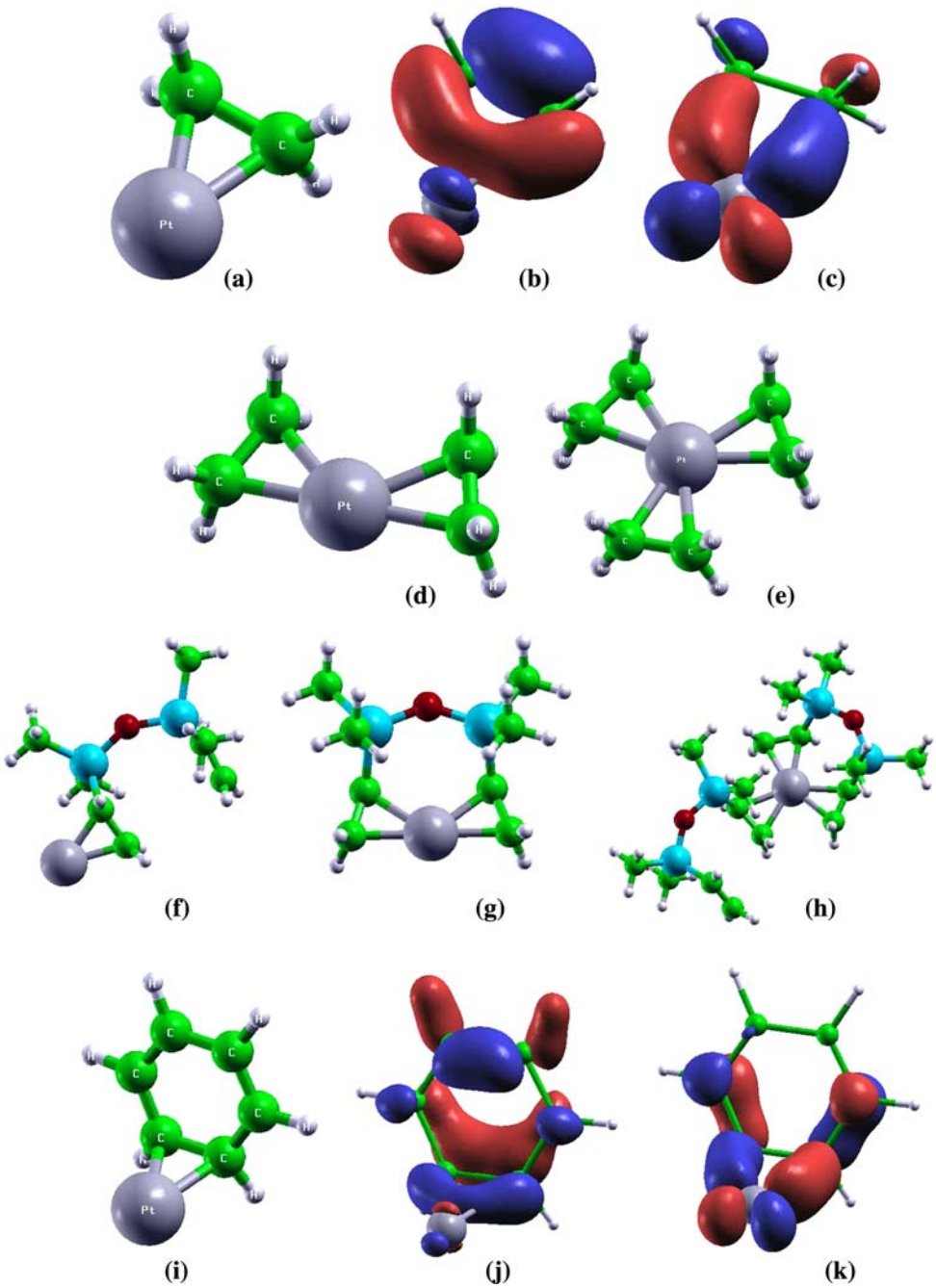

Fig. 2 **a** Structure of the $Pt(C_2H_4)$ complex and **b**, **c** two of its molecular orbitals; **b** donation process from the π orbitals of the organic species to a $d-s$ hybrid orbital of the metal; **c** back-donation process from the metal orbitals to the π^* orbitals. The two isosurfaces correspond to a density value of 0.07 a.u. Structure of the complexes (**d**) $Pt(C_2H_4)_2$, **e** $Pt(C_2H_4)_3$, **f** Pt(DVS) with only one C=C bond interacting, **g** Pt(DVS) with both C=C bonds interacting, and **h** $Pt(DVS)_2$. **i** Structure of the $Pt(C_6H_6)$ complex and **j**, **k** two of its molecular orbitals highlighting the **j** donation and **k** back-donation processes. *Color coding* as in Fig. 1, with platinums in *dark grey*

reported) shows that fragmentation of the complex occurs without any additional energy barrier with respect to the energy loss of the Pt/vinyl bond. As this barrier is not large (0.65 eV), this process is predicted to be already active at room or at a slightly higher temperature. The experimental evidence shows that solutions containing vinylic surfactants are stable for a time-span of some months at room temperature, but for much shorter periods even with minimal heating. This suggests that, once platinum becomes coordinately unsaturated (i.e., it loses a ligand), it can aggregate with other unsaturated species present in the solution, thus causing a progressive growth of the metal cluster. Once it reaches a critical size, growth accelerates, causing a precipitation of the metal aggregate, and consequently an instability of the solution.

The question that arises at this point is whether the detached DVS ligand is substituted by one of the surrounding solvent molecules (benzene or deuterated benzene). In such a case, platinum would not be in a coordinatively unsaturated state, therefore hindering the growth of the metal aggregate. A first hint to answer this question comes from the fact that if in the CVD process the

Table 1 Energetic analysis of the Pt/ligand interaction in the case of vinylic and arylic organic species

Complex	Binding energy (eV)
$Pt + C_2H_4$	2.17
$Pt + C_6H_6$	1.73
$Pt(C_2H_4) + C_2H_4$	1.36
$Pt(C_2H_4) + C_6H_6$	0.80
$Pt(C_6H_6) + C_2H_4$	1.71
$Pt(C_6H_6) + C_6H_6$	1.04
$Pt(C_2H_4)_2 + C_2H_4$	0.74
$Pt(C_2H_4)_2 + C_6H_6$	≤ 0
$Pt(C_6H_6)_2 + C_2H_4$	≤ 0
$Pt(C_6H_6)_2 + C_6H_6$	≤ 0

co-condensation of the metal vapors happens in the presence of the solvent vapors only (without any surfactant), the solution thus obtained is stable for a time span of few days, indicating that the interaction with the solvent molecules is much weaker than that with surfactants. To shed some light on this point, we carried out a study of the interaction of platinum atoms also with arylic organic ligands. The first system looked at was the Pt/benzene complex, see Fig. 2i–k. Figure 2j, k shows that the interaction between metal and organic part is very similar to the platinum/ethylene case with the major difference that the bond energetics is greatly reduced by the need of breaking the aromatic system and to localize the π electrons of benzene [32]. Benzene is thus a much weaker ligand than ethylene (see Table 1)

$$Pt + C_6H_6 \rightarrow Pt(C_6H_6) \quad \Delta E = -1.23 \text{ eV} \tag{7}$$

Mesethylene, $C_6H_3(CH_3)_3$, often used as a solvent, behaves in a completely analogous way with an almost identical reaction energy

$$Pt + C_6H_3(CH_3)_3 \rightarrow Pt(C_6H_3(CH_3)_3) \quad \Delta E = -1.21 \text{ eV} \tag{8}$$

The weakness of the Pt/aryl bonding is further confirmed by the addition of a second and third benzene in order to complete the coordination of the platinum atom, in analogy to what observed in the case of vinylic ligands. The second benzene binds with an interaction energy of 1.04 eV, while the third benzene does not bind to the complex. The latter fact is significant in view of the growth process in solution because it means that in the presence of an arylic solvent, or even an arylic surfactant, a complete saturation of the platinum coordination valence is not reached, thus allowing the growth of the metal cluster even at room temperature. The same behavior occurs when platinum is coordinated to vinylic groups and a benzene group attempts to attach itself: a benzene molecule binds to the $Pt(C_2H_4)$ complex with an interaction energy of 0.80 eV, but is not able to bind to the $Pt(C_2H_4)_2$ complex. This shows that in the case of the fragmentation of the $Pt(DVS)_2$ complex considered above, once platinum is in a coordinatively unsaturated state due to the loss of a surfactant molecule, an arylic solvent molecule (benzene or mesethylene) cannot replace the vinylic ligand and block the coordination of the metal: the only event that can take place is the addition of another fragment leading to the formation of a Pt–Pt bond and the consequent growth of the metallic aggregate. Eventhough the DF approach does not take into account dispersion interactions, the absence of covalent bonding implies small energy barriers for the opening of the Pt coordination shell.

3.2 $\mathbf{Pt_2(ligand)_m}$

In the gas-phase, Pt_2 is a triplet: the 5*d* and 6*s* orbitals are hybridized leading to the formation of a strong σ-bond. At the B3LYP level, the Pt-Pt bond energy is estimated to be 2.15 eV (bond distance of 2.53 Å). Note that at the BPW91 level, which is a better functional to describe neutral Pt clusters, the bond energy rises to 3.24 eV (close to the experimental value of 3.15 eV [33, 34]) and the bond length decreases to 2.37 Å. Nevertheless, as we will see, these quantitative differences do not seem to qualitatively affect the interaction of the metal cluster with the organic ligands.

In the case of the interaction with a single ethylene molecule, two different configurations can be obtained: the first, shown in Fig. 3a–c, is similar to the one observed for the single platinum atom (π-interaction mode) and is characterized by a σ-donation/π-back-donation interaction. For Pt_2, however, the Pt/ethylene interaction is much weaker (1.62 eV instead of 2.67 eV) and the formation of the bond is not accompanied by any spin-crossing (the spin state of the final complex is still a triplet): this is mainly due to the tendency of the system to optimize the metal–metal interaction at the expense of the weaker metal–ligand interaction. The second configuration (σ-interaction mode), shown in Fig. 3d–f, results more stable than the former by about 0.7 eV. In this configuration, the two platinum atoms form real σ-bonds with the two carbon atoms. This process is accompanied by a shortening of the Pt–C distances with respect to the π-configuration (2.02 Å instead of 2.16 Å) and a corresponding elongation of the C–C distance in the organic ligand (from 1.40 to 1.51 Å) due to the fact that the double bond basically becomes a single bond. A deeper analysis reveals that the carbon atoms are now sp^3 hybridized with a tetrahedral disposition of the H atoms around the carbons. The coupling of the unpaired *d* electrons of the two platinum atoms with the carbons valence electrons makes that the spin state of this complex is zero (singlet state) and thus implies that Pt_2 is in a valence state

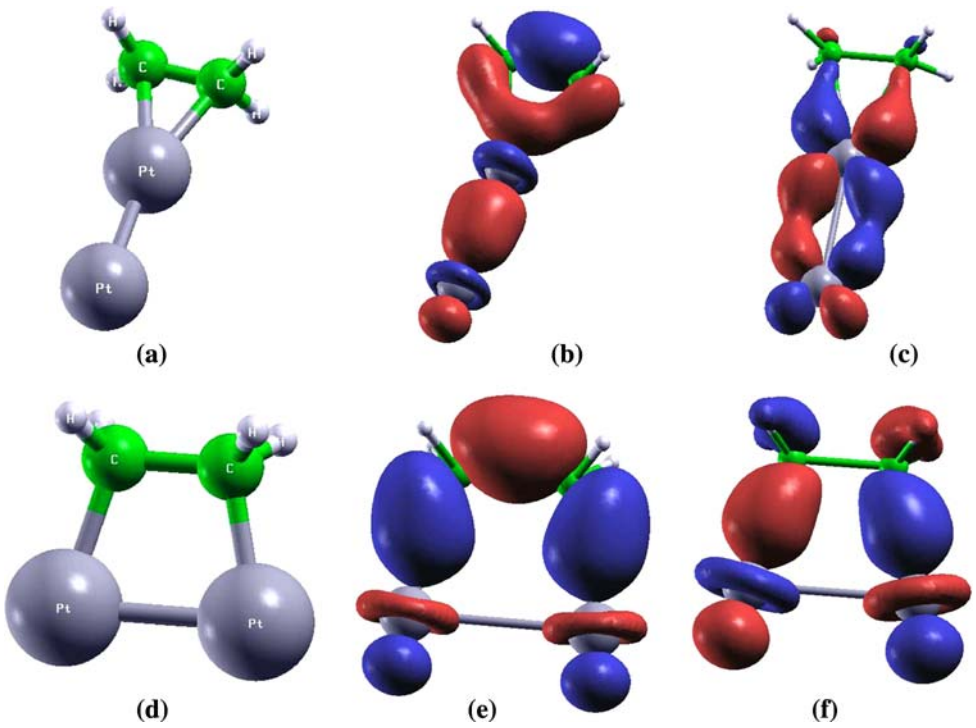

Fig. 3 **a–c** π-configuration of the $Pt_2(C_2H_4)$ complex (total spin S = 0) and two of its molecular orbitals, where the mechanism of **b** donation and **c** back-donation is clarified. **d–f** σ-configuration of the $Pt_2(C_2H_4)$ complex (total spin S = 1) and two of its molecular orbitals, where it is shown how the donation/back-donation mechanisms are accompanied by the formation of σ-bonds among platinum and carbon atoms. *Color coding* as in Fig. 2

(d^{10}–d^{10}) that can be estimated to be at least 1 eV higher in energy than the triplet ground state [34]. The interaction of the ethylene molecule with the dimer is indeed stronger than in the previous case (2.32 eV = 1.62 eV + 0.70 eV). These results were obtained employing the B3LYP xc-functional. By repeating the calculation with the BPW91 functional, the greater strength of the Pt–Pt bond makes that the interaction with the organic molecule is weaker. In fact the σ-configuration (interaction energy of 2.20 eV) is still favored over the π-configuration (interaction energy of 1.74 eV), but by only 0.46 eV, determining a quantitative but not a qualitative difference among the two approaches. An analysis of the molecular orbitals (MO) of the resulting complexes highlights the electronic differences between σ- and π-interaction modes. In the π-configuration (Fig. 3b, c) the situation is similar to that found in the case of a single Pt atom: Fig. 3b shows the σ-donation and Fig. 3c shows the π-back-donation mechanisms. In contrast, the MO plots of the σ-configuration show that the orbitals consist of a symmetric (Fig. 3e) and anti-symmetric (Fig. 3f) combinations of true (although distorted) Pt–C covalent bonds.

In the case of the interaction of the platinum dimer with two ethylene molecules, several configurations can be realized. The most significant are those shown in Fig. 4a–d. All of them are characterized by a zero net value of the total spin, thus implying a promotion of 1 eV to the valence state of the dimer. In the case of Fig. 4a, a double π-configuration takes place; by pairing the unpaired *d* electrons, the system sacrifices part of the metallic bond to better interact with the organic species: this is reflected in the elongation of the Pt–Pt distance (from 2.53 to 2.78 Å). The interaction of the $Pt_2(C_2H_4)$ complex with the second ethylene molecule is strongly decreased (0.57 eV instead of 1.62 eV), but this decrease is also due to the spin-crossing energy penalty. Among the four configurations shown, the lowest in energy is Fig. 4b, where we observe a copresence of a σ- and a π-configuration. The ethylene in the π-configuration interacts with 1.12 eV, this value being decreased by the presence of the first group in σ-configuration. Also in this case, the functional BPW91 does not lead to any qualitative changes of the described results, as shown by the numbers in parentheses in Fig. 4. It is interesting to observe that, starting from the lowest energy configuration of the species $Pt_2(C_2H_4)$, the addition of the second organic group takes place in π-configuration, whereas the formation of a second σ-configuration is higher in energy by 0.77 eV.

For the complex $Pt_2(C_2H_4)_3$, as shown in Fig. 4e–g, the third organic molecule adds to the lowest configuration of the previous complex via a π-configuration. In general, this addition determines a global decrease of the σ character of the interaction in favor of the π-interaction; this is due to the fact that the π-configuration is characterized by a more delocalized character and is thus favored in the case of a larger number of ligands. These considerations also hold in the case of the complex $Pt_2(C_2H_4)_4$, see Fig. 4h, i, where the interaction of the dimer with the four ligands in the lowest-energy structure (4*h*) takes place only through π-configurations.

It is important to note that in this case the configuration in which all the four (C_2H_4) units interact in the

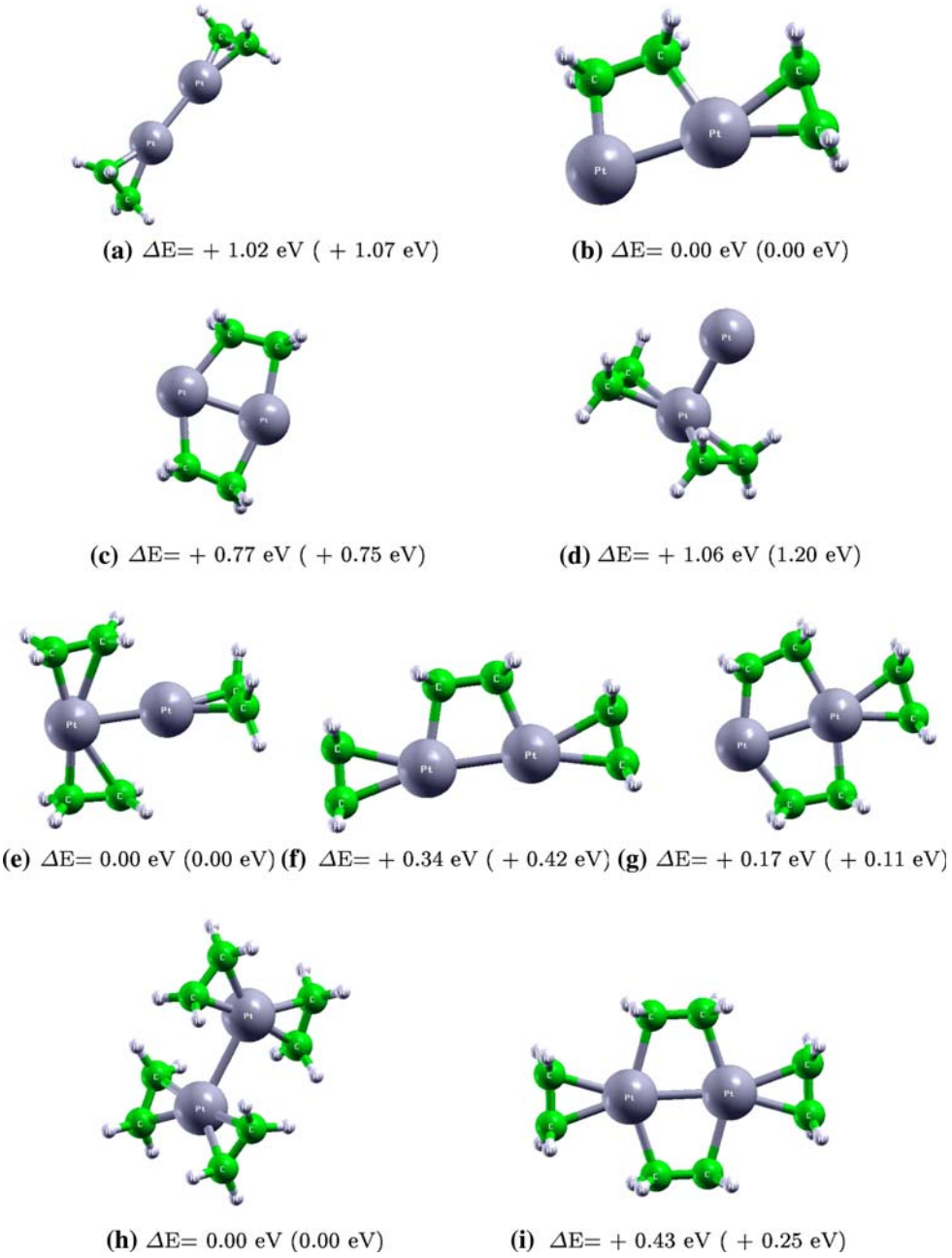

Fig. 4 **a–d** Configurations of the $Pt_2(C_2H_4)_2$ complex; **e–g** configurations of the $Pt_2(C_2H_4)_3$ complex; **h**, **i** configurations of the $Pt_2(C_2H_4)_4$ complex. For each structure, the relative energy is indicated at the B3LYP level and, in parenthesis, at the BPW91 level. The total spin is S = 0 for all the configurations shown. *Color coding* as in Fig. 2

π-configuration mode is favored with respect to the one in which two of the (C_2H_4) molecules interact in the σ-configuration mode. A *transition* from σ-configuration to π-configuration thus occurs as a function of the number of ligands. We can translate this finding into information useful for studying the growth process by distinguishing two régimes: a "coordinatively saturated" régime, in which the ratio among the number of ligands molecule and the number of metal atoms is high, and a "coordinatively unsaturated" régime, when this ratio is low. Our calculations imply that the π-interaction mode is energetically favored in the coordinatively saturated régime, whereas the σ-interaction mode is favored in the coordinatively unsaturated régime.

3.3 $\mathbf{Pt_3(ligand)}_m$

The putative global minimum of the $Pt_3(C_2H_4)_6$ complex is shown in Fig. 5a. By comparison with other σ-interacting configurations (not shown), it is confirmed that σ-interaction is disfavored when the number of coordinating (C_2H_4) units is high. The average interaction energy of each ethylene molecule with the Pt trimer is now 0.92 eV (for a total ΔE of 5.52 eV). Figure 5b, c show another

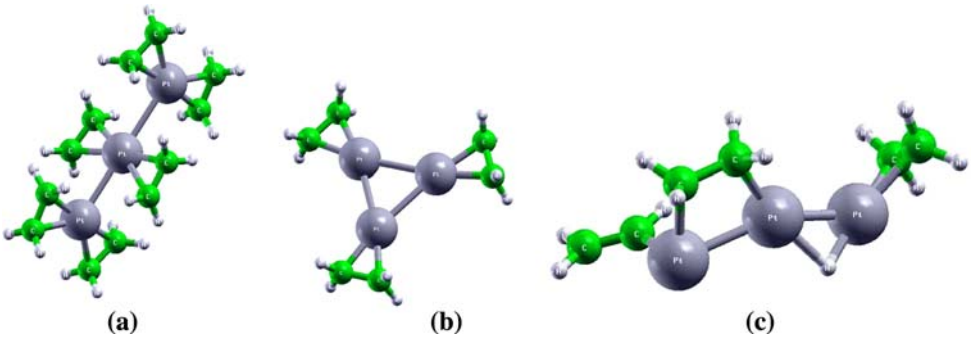

Fig. 5 **a** Putative global minimum of the $Pt_3(C_2H_4)_6$ complex; **b** π-configuration of the $Pt_3(C_2H_4)_3$ complex; **c** insertion of a Pt in the C–H bond to give an hydride complex. At the B3LYP level, **c** is lower in energy by 0.33 eV with respect to **b**. The total spin is S = 0 for all the configurations shown. *Color coding* as in Fig. 2

interesting effect. Figure 5b represents the lowest-energy configuration of the complex $Pt_3(C_2H_4)_3$ obtained imposing the π-coordination mode, with an average interaction energy of each ethylene molecule with the Pt trimer in the triangular configuration of 0.51 eV (for a total ΔE of 1.53 eV). If, however, one relaxes this geometrical constraint and performs a few steps of a DF-BH algorithm, the structure of Fig. 5c results. It can be noted that Fig. 5c corresponds to the oxidative insertion of Pt into a C–H bond, and, at the B3LYP level, is lower in energy by 0.33 eV with respect to the Fig. 5b. We can thus predict that in the coordinatively unsaturated régime, reactive channels can be opened, with the formation of Pt hydrides. This rationalizes the experimental NMR observation of signals in the hydride regions especially in non-controlled surfactant-poor conditions [17, 35]. It can also be noted that the total spin for all the configurations shown in Fig. 5 is S = 0: again, the interation with the ligands promotes the Pt cluster to a valence state in which the local spin is quenched (the ground state of the Pt trimer is a triangular triplet, even though a triangular singlet is only 0.03 eV higher in energy, while the linear arrangement has S = 2 and is 1.04 eV higher in energy with respect to the ground state [34]).

4 Conclusions

In this work, a theoretical first-principles study of the $Pt_n(ligand)_m$ ($n = 1, 3$) metallorganic complexes has been performed, by varying the number of metal atoms and the nature and number of organic coordinate ligands (specifically, vinylic and arylic ligands). From the analysis of the results, several conclusions can be drawn.

First of all, ethylene has been shown to be a good model (at least, at the electronic level) for the vinylic functional groups of the DVS ligand. Clearly, the *steric* properties are different: in the case of DVS, steric hindrance can disfavor the achievement of full coordination thus favoring growth or, on the opposite, can impose constraints on reactive processes.

Second, the Pt/carbon–carbon double bond interaction has a many-body character, i.e., the binding energy appreciably decreases with the number of interacting C=C units.

Third, aromatic species are much weaker ligands than vinylic species, due to the need of disrupting π-electron conjugation. This fact, coupled with the many-body character of the Pt/ligand interaction, makes that a third aromatic molecule does not bind to a doubly coordinated Pt center, thus leaving it free for further aggregation.

Fourth, the many-body character of the Pt/ligand interaction also makes that the detachment energy barriers of a fully coordinated Pt center are not high, and can be overcome at room or slightly higher temperatures.

Fifth, when considering metal dimers or larger clusters, there exist two metal/organic binding mechanisms: one involving the formation of σ bonds between Pt and C atoms (σ-interaction mode) and one in which the metal/ligand interaction takes place through a donation/back-donation mechanism (π-interaction mode). The latter mechanism is the only one occurring for a single Pt atom. It can be noted that the need to locally vacate the Pt *s* orbitals in the π-interaction mode or to make this orbital available to covalent bonding in the π-interaction mode, entails a promotion of the Pt atom to a valence "interaction" state with a corresponding quenching of the local spin. This promotion, which for small clusters corresponds to a weakening of the metal–metal bonds, has an energy cost that must be taken into account when evaluating or predicting the Pt/ligand binding energy or parametrizing Pt/ligand empirical potentials, and represent the metal analogue of the preparation of the fragments in the interacting state discussed in [36].

Sixth, two régimes can be distinguished: a "coordinatively saturated" régime, in which the ratio among the number of ligands and the number of metal atoms is high and the ligand/organic π-interaction mode is preferred, and a "coordinatively unsaturated" régime, in which this ratio is low and the ligand/organic σ-interaction mode is preferred. The coordinative unsaturation typical of the latter régime favors more complicated, reactive processes, such as oxidative insertion of Pt atoms into a C–H bond.

These conclusions are in tune with available experimental data, and suggest a positive role of theoretical simulations in the study of the nuclation and growth of metal clusters in the homogeneous phase in terms of accurate prediction of the energetics and of the kinetic growth parameters.

Acknowledgments We acknowledge financial support from the Italian CNR for the program "(Supra-) Self-Assemblies of Transition Metal Nanoclusters" within the framework of the ESF EUROCORES SONS, and from the European Community Sixth Framework Project for the STREP Project "Growth and Supra-Organization of Transition and Noble Metal Nanoclusters" (contract no. NMP-CT-2004-001594).

References

1. Klabunde KJ (1994) Free atoms, clusters and nanoscale particles. Academic Press, San Diego
2. Bradley JS (1994) Clusters and colloids. Wiley, Wienheim
3. Bonnemann H, Richards RM (2001) Eur J Inorg Chem 2455
4. Pileni MP (2003) C R Chimie 6:965
5. Schmid G (1996) Applied homogeneous catalysis with organometallic compounds, vol 2. Wiley, Wienheim, pp 636–644
6. Herrmann WA, Cornils B (1996) Applied homogeneous catalysis with organometallic compounds, vol 2. Wiley, Wienheim, pp 1171–1172
7. Bonnemann H, Brijoux W (1996) Advanced catalysts and nanostructured materials, chap 7. Academic Press, San Diego, pp 165–196
8. Schmidt TJ, Noeske M, Gasteiger HA, Behm RJ, Britz P, Brijoux W, Bonnemann H (1997) Langmuir 13:2591
9. Gotz M, Wendt H (1998) Electrochim Acta 43:3637
10. Schmidt TJ, Noeske M, Gasteiger HA, Behm RJ, Britz P, Bonnemann H (1998) J Electrochem Soc 145:925
11. Faraday M (1857) Philos Trans R Soc Lond 147:145
12. Aiken III JD, Finke RG (1999) J Mol Catal A 145:1
13. Toshima N, Yonezawa T (1998) New J Chem 22:1179
14. Leisner T, Rosche C, Wolf S, Granzer F, Woste L (1996) Surf Rev Lett 3:1105
15. Blackborrow JR, Young D (1979) Metal vapor synthesis. Springer, New York
16. Hitchcock PB, Lappert MF, Warhurst NJW (1991) Ang Chem Int Ed 30:438
17. Uccello-Barretta G, Balzano F, Evangelisti C, Raffa P, Mandoli A, Nazzi S, Vitulli G (2008) J Organomet Chem 693:1276
18. Lewis LN, Colborn RE, Grade H, Bryant GL, Sumpter CA, Scott RA (1995) Organometallics 14:2202
19. Ciacchi LC, Pompe W, DeVita A (2001) J Am Chem Soc 123:7371
20. Kendall RA, Aprà E, Bernholdt DE, Bylaska EJ, Dupuis M, Fann GI, Harrison RJ, Ju J, Nichols JA, Nieplocha J, Straatsma TP, Windus TL, Wong AT (2000) Comput Phys Commun 128:260
21. Becke AD (1993) J Chem Phys 98:1372
22. Aprá E, Fortunelli A (2000) J Mol Struct/Theochem 501–502:251
23. Becke AD (1988) Phys Rev A 38:3098
24. Perdew JP, Chevary JA, Vosko SH, Jackson KA, Pederson MR, Singh DJ, Fiolhais C (1992) Phys Rev B 46:6671
25. Aprà E, Ferrando R, Fortunelli A (2006) Phys Rev B 73:205414
26. Barcaro G, Aprà E, Fortunelli A (2007) Chem Eur J 13:6408
27. Schaefer A, Huber C, Ahlrichs R (1994) J Chem Phys 100:5829
28. Andrae D, Haussermann U, Dolg M, Stoll H, Preuss H (1990) Theor Chim Acta 77:123
29. Elsasser C, Fahnle M, Chan CT, Ho KM (1994) Phys Rev B 49:13975
30. Kokalj A (1999) J Graph Model 17:176
31. Fortunelli A, Velasco AM (2002) J Mol Struct/Theochem 586:17
32. Roszak S, Balasubramanian K (1995) Chem Phys Lett 234:101
33. Taylor S, Lemire GW, Hamrick YM, Fu ZW, Morse MD (1988) J Chem Phys 89:5517
34. Fortunelli A (1999) J Mol Struct/Theochem 493:233
35. Evangelisti C, Raffa P, Balzano F, Uccello-Barretta G, Vitulli G, Salvadori P (2008) J Nanosci Nanotech 8:2096
36. Carter EA, Koel BE (1990) Surf Sci 226:339

Structures of metal nanoparticles adsorbed on MgO(001). I. Ag and Au

Riccardo Ferrando,[1,a)] Giulia Rossi,[1] Andrea C. Levi,[1] Zdenka Kuntová,[1,2] Florin Nita,[1,3] Andrei Jelea,[3,4] Christine Mottet,[4] Giovanni Barcaro,[5] Alessandro Fortunelli,[5] and Jacek Goniakowski[6,b)]

[1]*Dipartimento di Fisica, CNISM and INFM/CNR, Via Dodecaneso 33, Genova 16146, Italy*
[2]*Institute of Physics, AS CR, v.v.i., Na Slovance 2, 182 21 Prague 8, Czech Republic*
[3]*Institute of Physical Chemistry Ilie Murgulescu, Romanian Academy, 202 Spl Independentei St., 060021 Bucharest-12, Romania*
[4]*CINaM/CNRS, Campus de Luminy, Marseille 13288, France*
[5]*IPCF/CNR, via G. Moruzzi 1, Pisa 56124, Italy*
[6]*INSP/CNRS and Université Paris VI, Campus Boucicaut, Paris 75015, France*

FerrandoJCP2009

(Received 4 November 2008; accepted 8 December 2008; published online 1 May 2009)

The structure of metal clusters supported on a MgO(001) substrate is investigated by a computational approach, with the aim to locate stable structural motifs and possible transition sizes between different epitaxies. Metal-metal interactions are modeled by a second-moment approximation tight-binding potential, while metal-oxide interactions are modeled by an analytic function fitted to first-principles calculations. Global optimization techniques are used to search for the most stable structural motifs at small sizes ($N \leq 200$), while at larger sizes different structural motifs are compared at geometric magic numbers for clusters up to several thousand atoms. Metals studied are Ag, Au, Pd, and Pt. They are grouped according to their mismatch to the oxide substrate (lattice constant of the metal versus oxygen-oxygen distance on the surface). Ag and Au, which have a smaller mismatch with MgO, are studied in Paper I, while Pd and Pt, with a larger mismatch, are investigated in Paper II. For Ag the cube-on-cube (001) epitaxy is favored in the whole size range studied, while for Au a transition from the (001) to the (111) epitaxy is located at $N=1200$. The reliability of the model is discussed in the light of the available experimental data. © *2009 American Institute of Physics*. [DOI: 10.1063/1.3077300]

I. INTRODUCTION

Metal clusters supported on oxide surfaces have traditionally attracted considerable attention due to their scientific interest and technological applications in several fields, ranging from heterogeneous catalysis to optoelectronic and magnetic devices.[1] This attention has fueled a series of fundamental studies in which the complicated real-world systems are replaced by model systems obtained by controlled metal deposition on oxide single crystals in UHV.[2,3] The aim of these studies was to derive accurate knowledge on model systems in ideal conditions that can then help in clarifying the complex phenomena occurring in real-world systems, with the final goal of achieving (at least, qualitative) understanding of structure-property relationships. Characterizing, predicting, and controlling the structure of supported metal particles and their epitaxial relationship to the underlying oxide substrate represent a key step in this perspective, and much theoretical and experimental efforts has been devoted in this direction. Recent developments suggest that such an effort is finally being met with success. On the experimental side, advances have been recently realized that allow one to characterize with a good degree of certainty the structure and morphology of supported metal particles.[4–10]

On the theoretical side, computational approaches are expected to play an important role because, if sufficient accuracy is achieved, they can provide structural information, which nicely complements that derived via experiments. Effective tools have been recently introduced to explore and predict the structural properties of metal nanoparticles, finding results generally in good agreement with experiments.[11–17]

Mere knowledge of the global minimum structure is obviously not sufficient to predict the behavior of metal particles in complex environments and/or under kinetic conditions. For example, it has been shown that metal particles can undergo structure fluctuations and bistabilities during experiments reproducing typical catalytic conditions.[18] However, structure determination is a necessary step of great importance both as a preliminary check for validation purposes in the study of more complicated processes and in view of "static" phenomena and properties such as optical and magnetic (but even chemical) ones under mild conditions. Another issue is connected with substrate defectivity. It has been shown that, for several systems in a range of substrate preparation and metal deposition conditions, cluster nucleation occurs at defect sites rather than on regular terraces, see, e.g., Ref. 19. An interesting problem is thus represented by the influence of the underlying defect on the structure of the particles. Here, however, we focus on medium-sized or large metal particles, for which the influence of, e.g., a local

a)Author to whom correspondence should be addressed. Electronic mail: ferrando@fisica.unige.it.
b)Author to whom correspondence should be addressed. Electronic mail: jacek.goniakowski@insp.jussieu.fr.

TABLE I. Parameters of the metal-metal part of the interaction [see Eqs. (3)–(5)].

Metal	r_0 (Å)	A (eV)	ξ (eV)	p	q
Au	2.885	0.209 57	1.8153	10.139	4.033
Ag	2.890	0.103 10	1.1895	10.850	3.180
Pd	2.751	0.171 49	1.7019	11.000	3.794
Pt	2.770	0.274 43	2.6209	10.710	3.845

defect is expected to be negligible, unless kinetic trapping into structural funnels takes place, as recently hypothesized for specific systems.[20–22]

In the present work we develop a systematic investigation of the structural motifs of metal nanoparticles adsorbed on MgO(001) and their energetic crossover. This work follows the general philosophy adopted in Ref. 23, and translates it from gas-phase to supported metal clusters. In particular, in this article (Paper I), we present a systematic study of Ag and Au on MgO(001) terraces, while the following article (Paper II) contains the results about Pd and Pt/MgO(001) and a discussion concerning all the investigated systems.

These metal/oxide pairs are interesting in themselves: MgO(001) is one of the most studied models of single crystal oxide surfaces,[1,3] supported Pd and Pt particles (in pure form or as alloys) play an important role in many catalytic applications,[24] and so does Au (and—to a more limited extent—Ag) in the nanoscopic régime,[25] while Ag and Au particles are also of interest for their optical (plasmonic) response.[26] In addition, in the context of the structural prediction of supported metal particles these systems have general significance as they are representative of metal/oxide pairs where the oxide is of square symmetry and which span a range of adhesion from weak to moderate while exhibiting a small (about 3% for Ag and Au) or medium (about 8% for Pd and Pt) mismatch between the oxide and bulk metal lattice parameters. We will find that in this range of metal/oxide interactions the main phenomenology is represented by the competition between (001) or (111) epitaxies and noncrystalline structures, which present local fivefold symmetries. The latter structures are especially decahedral fragments. In particular, we shall focus on the competition between fcc(001) and fcc(111) epitaxies. This competition has been observed in several experiments but the theoretical interpretation is still lacking. More "exotic" epitaxies have been proposed to occur for larger lattice mismatch still on square-symmetry oxides[27,28] or can be hypothesized on oxides with different symmetries (work is in progress in our laboratories to explore these possibilities).

Paper I is divided as follows. Section II contains the description of the model and of the simulation methods that are common for both this Paper and Paper II. Sections III and IV are devoted to the results for Au/MgO and Ag/MgO, respectively. Section V contains a brief summary and discussion of the results concerning these two systems only.

II. MODEL AND METHODS

A. Model potential

Following Ref. 29, the binding energy E of a cluster of N atoms is written as the sum of atomic contributions E_i

$$E = \sum_{i=1}^{N} E_i, \tag{1}$$

with

$$E_i = E_i^{mm} + E_i^{mo}, \tag{2}$$

where E_i^{mm} and E_i^{mo} model the metal-metal and metal-oxide interactions, respectively.

The functional form of E_i^{mm} is derived within the second-moment approximation to the tight-binding model (SMATB potential),[30–32]

$$E_i^{mm} = E_i^b + E_i^r \tag{3}$$

with

$$E_i^r = \sum_{j\neq i, r_{ij}<r_c} A \exp\left[-p\left(\frac{r_{ij}}{r_0}-1\right)\right], \tag{4}$$

$$E_i^b = -\left\{\sum_{j\neq i, r_{ij}<r_c} \xi^2 \exp\left[-2q\left(\frac{r_{ij}}{r_0}-1\right)\right]\right\}^{1/2}, \tag{5}$$

where r_{ij} is the distance between atoms i and j, r_c is the cutoff radius, and r_0 is the nearest-neighbor distance. The parameter set (A,ξ,p,q) is fitted to experimental bulk quantities. The potential is smoothly linked to zero between the second and third neighbor distances by a polynomial function. The values of the parameters are given in Table I. The reliability of our SMATB parametrization has been checked against experimental and density-functional (DF) results in several cases for the systems studied here.[13,14,33–35] However we remark that this kind of potential cannot account for the structure of very small clusters, especially in the case of gold, where planar and cage clusters have been found in gas phase.

For E_i^{mo}, a many-body potential energy surface (PES) for metal-MgO(001) interactions has been fitted on first-principles calculations in order to take into account the main energetic characteristic of the metal-oxide interaction in the case of nonreactive interfaces.[11] This is a weak metal-oxide interaction, with no interdiffusion and small interfacial charge transfer, which is due principally to polarization effects and van der Waals interactions, with only a small contribution from covalent metal-oxygen bond. This interaction presents a many-body character, i.e., it depends on the metal

coverage, so that a metal atom surrounded by other metal atoms has a weaker interaction with the substrate than an isolated adatom. Assuming a rigid metal-oxide PES, we model the interaction energy between the metal cluster and the MgO(001) surface as a sum of interactions of each metal atom with the substrate. The dependence of this interaction on the distance from the substrate (z) is reproduce via a Morse-like function, whereas a periodic cosine function is used to model the dependence of the interaction energy on x and y coordinates. The functional form of E_i^{mo} is[29]

$$E_i^{mo}(x_i,y_i,z_i,Z_i) = a_1(x_i,y_i,Z_i)\{e^{-2a_2(x_i,y_i,Z_i)[z_i-a_3(x_i,y_i,Z_i)]} - 2e^{-a_2(x_i,y_i,Z_i)[z_i-a_3(x_i,y_i,Z_i)]}\},$$

$$a_j(x_i,y_i,Z_i) = b_{j1}(x_i,y_i) + b_{j2}(x_i,y_i)e^{-Z_i/b_{j3}(x_i,y_i)} \quad (6)$$

$$b_{jk}(x_i,y_i) = c_{jk1} + c_{jk2}\{\cos(\chi x_i) + \cos(\chi y_i)\} + c_{jk3}\{\cos(\chi(x_i+y_i)) + \cos(\chi(x_i-y_i))\}.$$

In Eq. (6), Z_i is the number of metal nearest neighbors of atom i and $\chi=2\pi/a$, with a the oxygen-oxygen distance in the substrate. The x and y coordinates are parallel to the $\langle 110\rangle$ directions. Z_i is calculated including all neighbors within 1.25 r_0, with r_0 the nearest-neighbor distance in the bulk metal. Equation (6) contains 27 parameters c_{jkl}.

The fitting procedure for the c_{jkl} parameters, developed along the lines of Ref. 29, is system dependent. It is based on (i) the choice of three ideal fitting systems (selected among the single atom, the (001) epitaxial pseudomorphic monolayer, the (001) epitaxial multilayer, and small clusters) and three surface sites (on top of oxygen and magnesium ions and in the hollow site positioned halfway between two O ions), (ii) the derivation of the interaction energy curves in the corresponding nine cases, and (iii) their analysis to extract the values of interaction energy, distance, and curvature at equilibrium, which are directly related to the c_{jkl}. In the case of Pd, the fitting systems are the single atom, the (001) epitaxial monolayer, and the (001) epitaxial bilayer.[29] The empirical potential derived through such an approach produced results in good agreement with the DF calculations[13,36] for clusters of sizes up to 30 atoms. An analogous procedure has been followed for the Pt/MgO system.

However, a drawback of such a model is that it does not take into proper account the "metal-on-top" effect,[37] i.e., the enhancement of adhesion energy due to the stabilizing contribution of metal atoms above the one directly interacting with the substrate. Such an effect, already present in the Pd/MgO and Pt/MgO systems, becomes dominant for Ag and Au, to such a degree that the behavior of the adhesion energy as a function of coordination is not monotonic any more: the adhesion energy of the (001) monolayer is smaller in absolute value than that of the (001) bilayer (for analogous reasons, for example Pd or Pt dimers on MgO(001) lie horizontally on the substrate, whereas Ag and Au dimers are vertical[37]). To circumvent this problem without abandoning the simplicity of the original model, a straightforward possibility is to select in the fitting procedure ideal systems in which the metal-on-top effect is implicitly included. In particular, in the Ag and Au cases we found that replacing the (001) monolayer with the five-atom square pyramid is sufficient to obtain a smooth behavior of the adhesion energy with coordination.

The resulting empirical potentials have been checked against DF calculations on selected supported metal clusters, finding results of quality comparable to that obtained in the Pd/MgO case. For example, in the case of Au, where, as we show in the following, there is a close competition between fcc(001) and fcc(111) epitaxies, we have considered size 31. This size is a geometric magic size for the fcc(111) epitaxy. However, both our model potential and our density functional theory calculations agree in finding that fcc(001) clusters are more favorable. The parameters c_{jkl} in Eq. (6) can be found on the Web.[38] Finally we note that our metal-substrate interaction model does not include van der Waals terms. Their contribution should amount to a few hundredths of eV for an atom in contact with the surface, and they decay as $1/z^3$.

B. Global optimization procedure

The global optimization searches are performed by means of the basin hopping algorithm[39] and the parallel excitable walkers (PEW) algorithm.[40] In these algorithms, Metropolis Monte Carlo walks are performed on the modified PES, which is obtained by associating to each point of the configuration space the energy of its closest local minimum. Two kinds of elementary moves have been used in the Monte Carlo simulations. In the *shake* move each atom is randomly displaced within a sphere of radius 1.4 Å centered on its position. In the *dynamics* move, a short molecular-dynamics run at high temperature (in the range 2000–3000 K) is performed. In the PEW searches, we use as an order parameter the fraction of atoms that are in contact with the substrate.

For any nanoparticle size, at least six unseeded searches of 200 000 elementary moves each are performed. Unseeded searches are started from random positions in a cubic box placed above the oxide surface. Moreover, several shorter seeded searches are performed. Seeded searches may either start from structures belonging to motifs found at nearby sizes, when possible, or from structures found at the same size for other metals (see Ref. 12 for a review of global optimization methods). Local atomic defects are then eliminated by runs in which the elementary move displaces single atoms on the cluster surface.

C. Comparison of selected structural motifs by local structural optimization

Global optimization becomes very cumbersome for sizes above 500 atoms. As we shall see in the following, important morphology transitions can take place well above that size. These morphology transitions are therefore studied by local structural optimization of selected structural motifs.

The goal of the local structural optimization is to generate complete families of clusters of a given form/morphology/epitaxy in a wide range of sizes and independently of their actual stability. Such an approach enables a precise determination of the relative stabilities of clusters belonging to different families and facilitates the analysis of

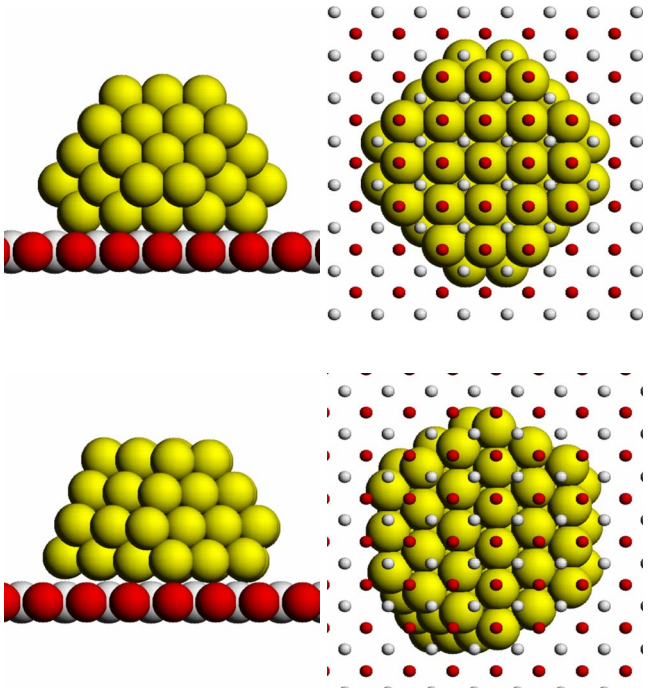

FIG. 1. (Color online) First row: Side and bottom views of a fcc(001) cluster. Second row: Side and bottom views of a fcc(111) cluster. In all panels, oxygen atoms are in dark gray (red) and magnesium atoms are in white (light gray). In the bottom views (right column), substrate atoms are represented by small spheres so that the contact epitaxy of the cluster is visible.

behavior of family-specific characteristics as a function of cluster size, and thus the prediction of their energetic crossover.[23]

In the present study we have focused on closed atomic-shell, truncated octahedral, and truncated decahedral metal clusters. The truncated octahedral clusters can be either in (001)‖(001) or (111)‖(001) epitaxy relation with the MgO(001) substrate (see Fig. 1). The initial structures, corresponding to various Wulff polyhedra and exposing different proportions of (111) and (001) facets, were obtained by various sequences of truncations of perfect octahedra and decahedra. Upon deposition on the substrate further truncations were applied, in the spirit of the Wulff–Kaischew construction. For each of the initial clusters, a series of quenched molecular dynamics runs of different lengths and at various temperatures were performed in order to find the local energy minimum corresponding to the 0 K equilibrium state for the given cluster form/morphology/epitaxy. Except for the smallest particles, which will not be considered here, the above procedure does indeed preserve the initial form of the metal particles and their initial epitaxy relation with the substrate. It thus enables an efficient construction of the complete distinct families of deposited metal clusters.

Due to a variety of applied sequences of truncations, each of the cluster families generated in this way contains thousands of particles, including both stable and very unlikely ones. In the following, within each family we will focus principally on the minimum energy clusters, corresponding to the lowest total energy for each given size. Note that, following the analysis of Ref. 16, within each structural family it is interesting to focus on "magic clusters," i.e., those clusters that realize structural shell closure and show enhanced stability compared to clusters of similar sizes. The envelope of the excess energy as a function of size for these optimal-shape configurations provides the minimum of the excess energy for that particular motif, and thus allows one to study the ideal crossover among different motifs. Moreover, these clusters may also represent the most abundant particles in proper experimental conditions.

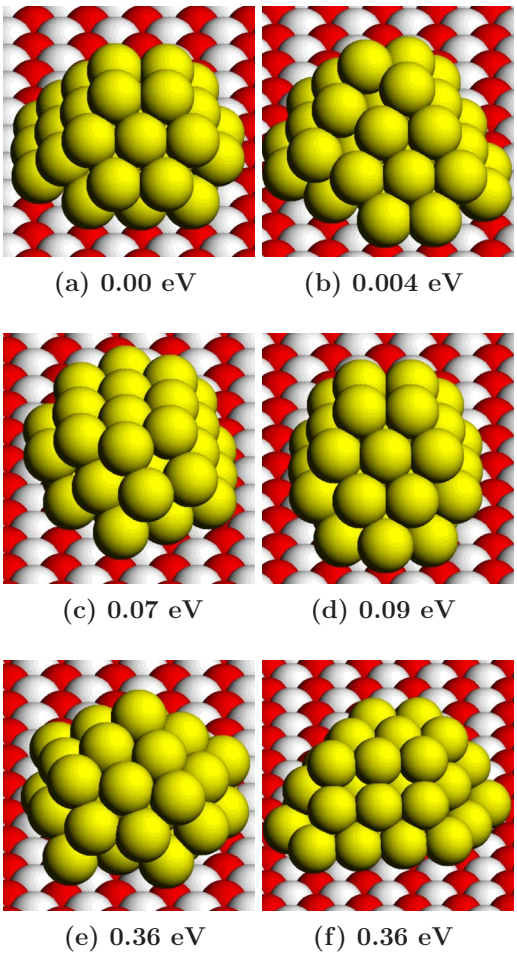

FIG. 2. (Color online) Ag/MgO(001) nanoparticles of size $N=40$.

III. AG NANOPARTICLES

A. Global optimization results

The lowest-energy structures of Ag/MgO(001) clusters have been searched for the following sizes $N=30,40,50,60,70,90,100,150,200,300,500$. The global optimization runs have found a variety of structural families, which are in close competition for the smallest sizes considered here.

For example, in the case of $N=40$ (see Fig. 2), six different families have been singled out. The global minimum [Fig. 2(a)] is a fcc truncated pyramid in (001) epitaxy with the substrate. This cluster presents overhangs at the interface with the substrate, in analogy to what has been found for small Pd/MgO(001) nanoparticles.[13] The global minimum is in very close competition with three clusters: a fcc(001) structure with a stacking fault, a fcc(111) cluster, and a frag-

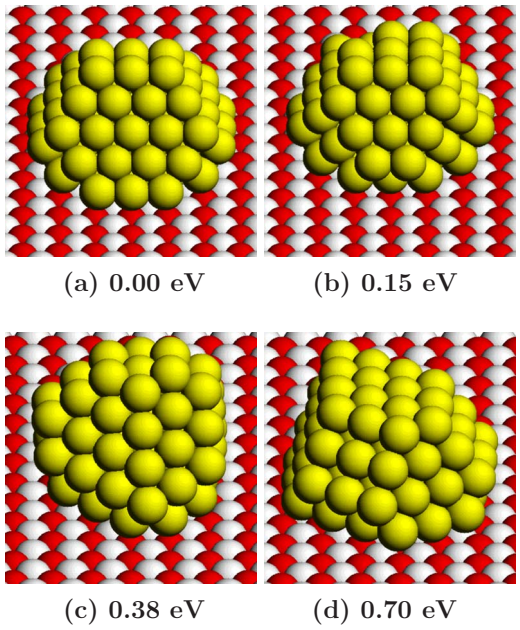

FIG. 3. (Color online) Ag/MgO(001) nanoparticles of size $N=90$.

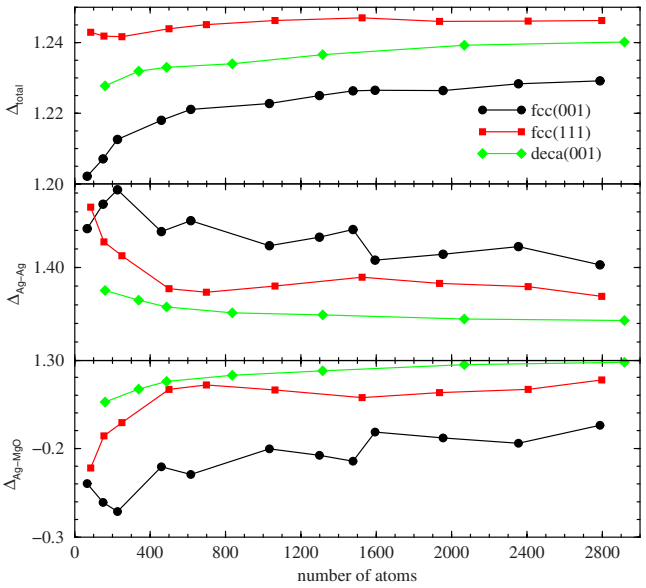

FIG. 4. (Color online) Δ_{total}, Δ_{Ag-Ag}, and Δ_{Ag-MgO} (in eV) for fcc(001), fcc(111), and decahedral Ag nanoparticles.

ment of a decahedron [Figs. 2(b)–2(d), respectively]. For all these structures, the energy differences from the global minimum are less than 0.1 eV. Two more nanoparticles are noteworthy, even though somewhat higher in energy. Cluster (e) is a slightly distorted fragment of the 55 atom icosahedron. Cluster (f) is hcp, since it is made of three horizontal close-packed planes in (111) epitaxy with the substrate and ABA stacking. The hcp structure has been found only in clusters made by three close-packed layers. These hcp clusters are different from those found in the case of Ni/MgO(001).[27] In Ni clusters, hcp nanoparticles present close-packed planes that are perpendicular to the substrate and are formed mainly because of the large size mismatch between Ni and MgO.

For $N=90$, three motifs are in competition (see Fig. 3). The global minimum [structure (a) in the figure] is fcc in (001) epitaxy, and it is close in energy to other fcc(001) structures, as the structure in (b). The second motif at this size is decahedral. The lowest-energy decahedral fragment is shown in Fig. 3(c), and it is separated from the global minimum by about 0.4 eV. Finally, fcc clusters in (111) epitaxy are higher in energy. The best structure of this family is shown in (d) and has an energy difference of 0.7 eV.

Size 90 is representative of the behavior of larger sizes. In fact, for $N>90$ we have always found the same three structural motifs with the same energetic ordering. On average, energy differences from the global minimum tend to increase with size for both decahedral fragments and fcc(111) structures. In the range up to 500 atoms, the best decahedral clusters are separated from fcc(001) global minima by differences from 0.4 to 1.3 eV. The best fcc(111) clusters are higher in energy, with differences from 0.7 to 1.7 eV depending on size and not showing any tendency to decrease with increasing size. In fact, the energy difference is always above 1 eV from size 180 on. Other motifs, such as icosahedra, are much less favorable, and they are seldom found in the optimization runs. For example, the best icosahedral fragment of size 200 is separated from the global minimum by more than 3 eV.

It can be noted that the preference for fcc motifs can be reinforced by the influence of local defects, such as an oxygen vacancy; in Ref. 20 it was found that the corresponding structural frustration induces a transition from fivefold-symmetry to distorted fcc configurations already at size $N=10$.

B. Comparison of selected structural motifs for large sizes

From the results of global optimization, it turns out that three motifs are relevant as cluster size increases: fcc(111), fcc(001) and decahedral [dec(001), since these decahedra lie on the surface with a pseudo-(001) facet] clusters. In order to compare their size-dependent stability, we use the quantity Δ_{total},[41] which is defined as follows:

$$\Delta_{total} = \frac{E - N\varepsilon_b}{N^{2/3}}, \tag{7}$$

where E is the cluster energy and ε_b is the binding energy per atom in the bulk solid. Δ is the excess energy of the cluster with respect to a bulk fragment with the same number of atoms, divided by approximately the number of surface atoms in the cluster. Low Δ_{total} values correspond to energetically favorable structures. The behavior of Δ_{total} for the three motifs is reported in Fig. 4, which clearly shows that fcc(001) structures are consistently the lowest in energy, fcc(111) structures are the highest in energy and decahedra are in between. There is no indication of any tendency to a crossover between fcc(001) and fcc(111) structures. Since decahedral structures present an internal strain, which give a volume contribution to their energy,[23,42] we expect that decahedra should become less favorable than both fcc epitaxies in the limit of large sizes. However, from the data in Fig. 4, we cannot extrapolate the actual crossover size with (111) struc-

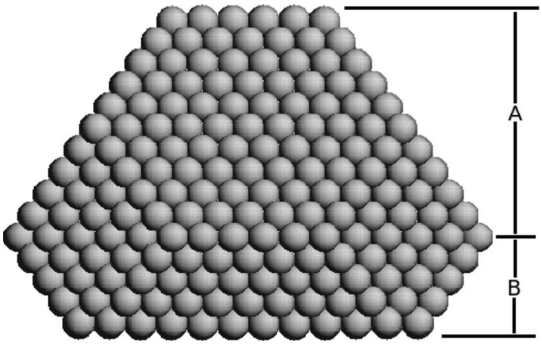

FIG. 5. Side view of a truncated octahedral fcc(001) cluster. The quantity r_H is defined as the ratio A/B.

tures. If a crossover between decahedra and (111) structures takes place, the crossover size should be quite large.

The energy of each nanoparticle can be decomposed into a metal-metal contribution $E_{\mathrm{Ag-Ag}}$ and a metal-oxide contribution $E_{\mathrm{Ag-MgO}}$, so that $E=E_{\mathrm{Ag-Ag}}+E_{\mathrm{Ag-MgO}}$. In Fig. 4 we report the quantities $\Delta_{\mathrm{Ag-Ag}}$ and $\Delta_{\mathrm{Ag-MgO}}$ defined as follows:

$$\Delta_{\mathrm{Ag-Ag}}=\frac{E_{\mathrm{Ag-Ag}}-N\varepsilon_b}{N^{2/3}},\quad \Delta_{\mathrm{Ag-MgO}}=\frac{E_{\mathrm{Ag-MgO}}}{N^{2/3}}, \tag{8}$$

so that their sum is equal to Δ_{total}. From the analysis of $\Delta_{\mathrm{Ag-Ag}}$ and $\Delta_{\mathrm{Ag-MgO}}$ it turns out that decahedral structures present the lowest metallic energy, in agreement with the findings on free clusters,[23,42] while fcc(001) are the highest in energy except for very small sizes. However, the interaction with the substrate clearly favors fcc(001) clusters so that they become the most stable. For what concerns fcc(111), a better interaction with the substrate compared to decahedra is not sufficient to compensate their higher metallic energy.

From Fig. 4, it turns out that $\Delta_{\mathrm{Ag-Ag}}$ and $\Delta_{\mathrm{Ag-MgO}}$ are strikingly in antiphase as functions of the cluster size for each structural motif: when the former increases, the latter drops down and vice versa, so that they compensate to a good extent. This is a clear sign that the shape of the clusters is the result of the competition between metallic bond and metal-substrate interaction. Typically, within each structural motif, the clusters tend to grow according to a given shape, which, for example, optimizes a quantity as the metal-substrate interaction energy until this requires too high an energetic prize, at which point the competing quantity (in the present example the metal-metal interaction energy) sets in, overcoming the corresponding energy penalty and the structure "collapses" or better realizes a transition into a different shape. This behavior is common to all metals that we shall consider in the following.

The experiments on the growth of Ag nanoparticles on MgO are in favor of fcc(001) structures for all sizes.[43,44] This is in qualitative agreement with our results, which indeed clearly favor the fcc(001) epitaxy. A more quantitative comparison with experiment can be carried out by considering the shape of the fcc(001) particles, i.e., the quantities H/d and r_H. H is the height of the cluster and d its lateral size. r_H is the octahedral aspect ratio,[44] defined as $r_H=A/B$ (see Fig. 5). These quantities were experimentally measured in Ref. 44. In the size range of our simulated clusters, the experiments give $H/d=0.57\pm0.03$ and $r_H=3.0\pm0.3$. For our simulated clusters, the average values of these quantities are $H/d=0.64$ and $r_H=2.5$, therefore in reasonable agreement with experiment.

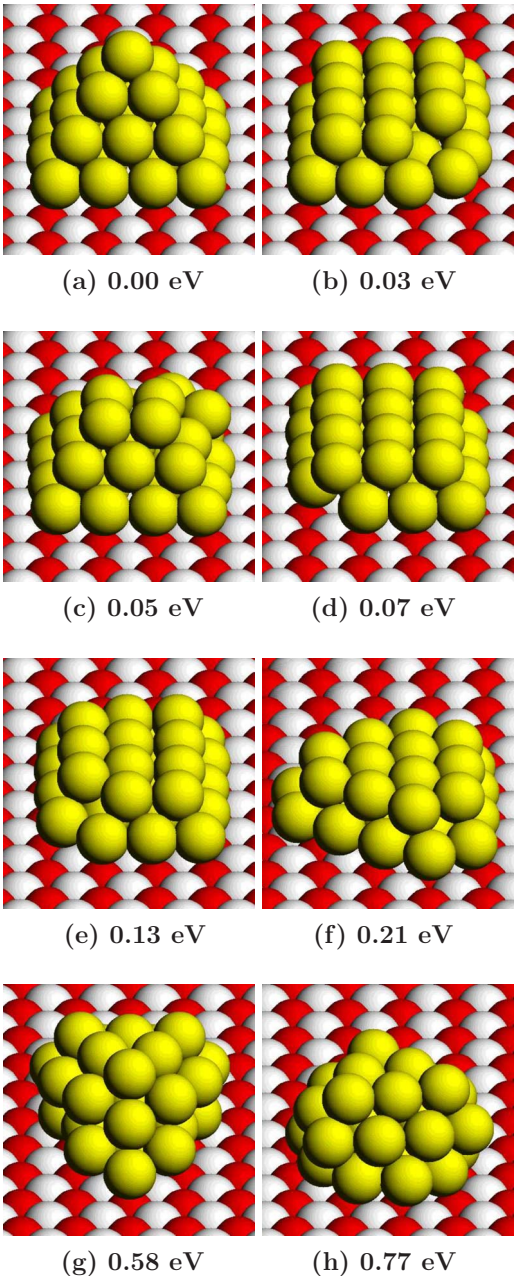

FIG. 6. (Color online) Au/MgO(001) nanoparticles of size $N=30$.

IV. AU NANOPARTICLES

A. Global optimization results

Global optimization of Au/MgO(001) clusters has been performed for the same sizes as in Ag. Different structural motifs have been singled out also in this case.

For $N=30$, the global minimum is a complete square pyramid [see Fig. 6, structure (a)], which is in fcc(001) epitaxy with the substrate. There are however several other structures that are almost degenerate with the global minimum. These structures are either distorted/truncated pyra-

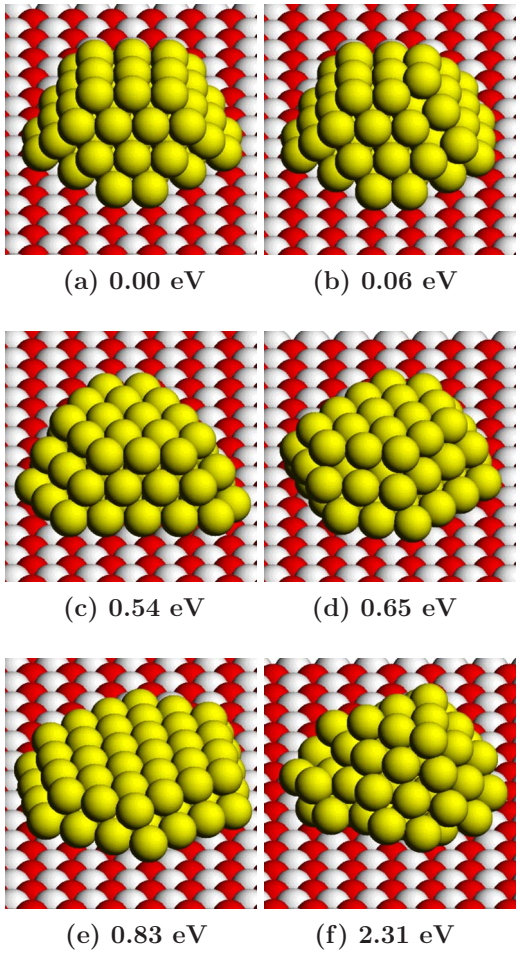

FIG. 7. (Color online) Au/MgO(001) nanoparticles of size $N=70$.

mids [as structure (c)] or fcc(001) bilayers [structures (b)–(e)]. Clusters with fcc(111) epitaxy [as (f)] are separated from the global minimum by slightly more than 0.2 eV. Distorted icosahedral or icosahedral fragments [structures (g) and (h), respectively] are somewhat higher in energy. At this size, no favorable decahedral fragment has been found.

For $N=70$, the global minimum is a truncated square fcc(001) pyramid [see Fig. 7, structure (a)], which is close in energy to the same kind of pyramid but with an Au plane in stacking fault [structure (b)]. fcc(111) and hcp(1000) trilayers [(c) and (d), respectively] are separated from the global minimum by about 0.5 eV, while (111) bilayers (e) are clearly higher in energy. Finally, icosahedral fragments [as in (f)] are very high in energy, separated by more than 2 eV from the global minimum. Again, no favorable decahedra are found.

As size increases up to 500 atoms, one finds that fcc(001) clusters are consistently the lowest in energy, followed by fcc(111) clusters. The latter are less separated in energy from fcc(001) clusters than in the case of Ag, with energy differences in the range of 0.3–1 eV, with a tendency to decrease the difference as size increases. As in Ag, icosahedra become largely unfavorable with increasing size, so that they become even worse than decahedra. This is expected from the weak tendency of gold to form icosahedra also in gas phase.[23,42] However, even decahedra are much higher in energy than both fcc(001) and fcc(111) clusters, with energy differences from the global minimum of the order of 2 eV at least.

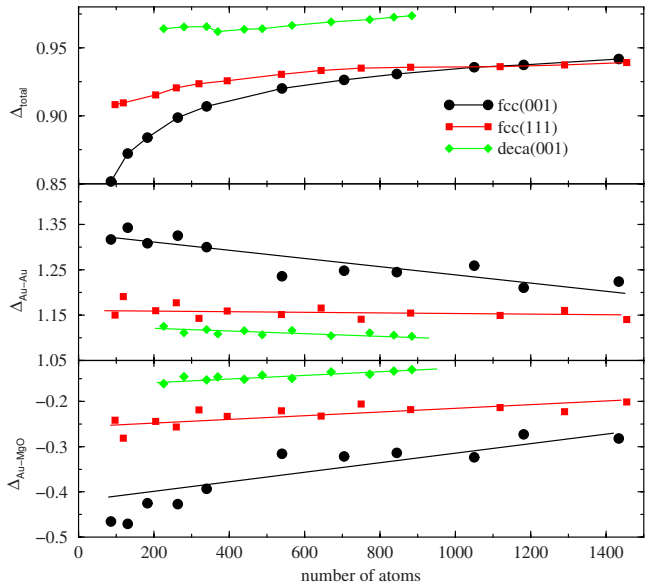

FIG. 8. (Color online) Δ_{total}, Δ_{Au-Au}, and Δ_{Au-MgO} (in eV) for fcc(001), fcc(111), and decahedral Au nanoparticles.

B. Comparison of selected structural motifs for large sizes

From the global optimization results, it turns out that also for gold the most significant motifs are fcc(001), fcc(111), and decahedra. We compared these three motifs for $N>500$ in order to check whether there is a crossover from fcc(001) to fcc(111) structures. This is indeed the case, with the crossover size N_{cr} of about 1200 atoms as shown in Fig. 8. This prediction is in good qualitative agreement with the experiments. At variance with silver, Au clusters grown on MgO(001) present both fcc(001) and fcc(111) epitaxies,[9] even though the crossover size has not yet been measured. Our results confirm that it is possible to produce fcc(111) particles already at rather small sizes because fcc(111) structures are quite close in energy to fcc(001) already at small size and become dominant when size exceeds N_{cr}.

The decomposition of Δ_{total} into Δ_{Au-Au} and Δ_{Au-MgO} shows that, at small sizes, the high metallic energy of fcc(001) structures is compensated by a stronger adhesion to the substrate. However, as size increases, fcc(001) clusters improve their metallic energy compared to fcc(111) clusters, while their adhesion gets worse. The latter is stronger in Au–MgO than in Ag–MgO (see the much lower values of Δ_{Au-MgO} compared to Δ_{Ag-MgO}), and this is sufficient to cause a crossover toward fcc(111) structures with increasing size. The more important role of adhesion for Au compared to Ag is confirmed by the fact that decahedral structures present the lowest metallic energy, but due to their small contact area with the substrate are the highest in energy in the whole size range. Note however that for small clusters under the influence of an underlying point defect a quasidegeneracy among structural motifs can be induced[21] that could entail possible kinetic trapping effects.

A semiquantitative comparison with the experiments is possible considering the data by Pauwels *et al.*,[10] who deposited Au clusters on MgO(001) in the small size range (diameters below 3 nm, corresponding to sizes below 1000 atoms) obtaining structures in (001) epitaxy with the substrate. This well agrees with our prediction of a crossover size above 1000 atoms. Moreover, Pauwels *et al.*[10] measured the aspect ratios of their clusters. They considered as cluster width w the size viewed along the [011] direction, and compared it to the height H of the clusters. They found a population with H/w values scattered in a wide interval, between 0.4 and 1. For our lowest-energy simulated clusters H/w is in a narrower range, between 0.5 and 0.6. This is fully compatible with the experimental data, with however the indication that our clusters are on average slightly flatter than the experimental ones.

V. SUMMARY

The structure of Ag and Au/MgO(001) clusters has been studied to single out the relevant structural motifs in a size range from a few tens to a few thousands atoms. For both metals, small clusters ($N<100$) present a variety of structures that are rather close in energy. As size increases, three structural motifs prevail: fcc(001), fcc(111), and decahedral clusters. The latter adhere to the substrate with a pseudo-(001) facet but with a weaker metal-substrate interaction energy as compared to the other epitaxies, due to the smaller area of the facet.

In Ag, fcc(001) clusters are always dominant and well separated from decahedra and fcc(111) clusters. Our results do not show any sign of a crossover from fcc(001) to other motifs with increasing size. For $N\leq 3000$, decahedral clusters are lower in energy than fcc(111) clusters, even though the energy difference between these motifs is decreasing with increasing size, indicating that a crossover between these two motifs might occur.

In Au, fcc(001) clusters are the lowest in energy up to $N\simeq 1200$, where a crossover in favor of fcc(111) clusters occurs. Moreover, at small sizes, the energy separation of these two motifs is smaller than in silver. At variance with silver, decahedral clusters are always higher in energy than both fcc motifs. In the case of Au, the transition size to the (111) epitaxy could be somewhat displaced if fcc(001) clusters with stacking faults were considered. However, we expect that this might change the transition size of a few hundred atoms without modifying the general picture.[27]

Our results are generally in good agreement with experiments. In the case of Au, there is a clear qualitative agreement, since we find that both epitaxies are in close competition for all sizes, with preference for the (001) epitaxy at small size, in agreement with the experimental findings.[9,10] Unfortunately, we cannot be more quantitative in the comparison with experiments because data about the crossover size between epitaxies are, to our knowledge, not yet available. Concerning the aspect ratios of fcc(001) clusters below 1000 atoms, our findings are again in good agreement with experiments, even though there is some indication that our simulated clusters are on average slightly flatter than the experimental ones. This might be due to an underestimate of gold surface energies in our model.

In the case of Ag, there is again a good qualitative agreement because we predict that only the (001) epitaxy should be produced at least for sizes up to 3000 atoms, and this is indeed what is experimentally observed. The agreement is also quantitatively good because the aspect ratios of our simulated clusters are close to those measured in the experiments, showing that our model well reproduces not only the epitaxy but also the cluster shape. However, also for Ag, it is likely that our metal-metal interaction underestimates surface energies, so that a good agreement about cluster shapes indicates that also the metal-substrate interaction might be underestimated. Work is in progress on this point.

ACKNOWLEDGMENTS

We acknowledge financial support from the European Community Sixth Framework Programme for the GSOMEN project (Grant No. NMP4-CT-2004-001594), from the French National Agency for Research under the project SIMINOX (Grant No. ANR-06-NANO-009-01) and from the Università Italo-Francese under the program Galileo. G.R. acknowledges *L'Oréal Italia e UNESCO per le Donne e la Scienza*, 2007 edition, for a research fellowship.

[1] H. J. Freund, Surf. Sci. **500**, 271 (2002).
[2] G. Ertl and H.-J. Freund, Phys. Today **52**, 32 (1999).
[3] C. R. Henry, Surf. Sci. Rep. **31**, 231 (1998).
[4] G. Renaud, R. Lazzari, C. Revenant, A. Barbier, M. Noblet, O. Ulrich, F. Leroy, J. Jupille, Y. Borensztein, C. R. Henry, J.-P. Deville, F. Scheurer, J. Mane-Mane, and O. Fruchart, Science **300**, 1416 (2003).
[5] C. Barth, O. H. Pakarinen, A. S. Foster, and C. R. Henry, Nanotechnology **17**, S128 (2006).
[6] A. Stierle and A. M. Molenbroek, MRS Bull. **32**, 1001 (2007).
[7] M. J. Yacaman, J. A. Ascencio, S. Tehuacanero, and M. Marin, Top. Catal. **18**, 167 (2002).
[8] J. Silvestre-Albero, G. Rupprechter, and H.-J. Freund, J. Catal. **240**, 58 (2006).
[9] C. R. Henry, Prog. Surf. Sci. **80**, 92 (2005).
[10] B. Pauwels, G. Van Tendeloo, W. Bouwen, L. Theil Kuhn, P. Lievens, H. Lei, and M. Hou, Phys. Rev. B **62**, 10383 (2000).
[11] J. Goniakowski, C. Mottet, and C. Noguera, Phys. Status Solidi B **243**, 2516 (2006).
[12] R. Ferrando, A. Fortunelli, and R. L. Johnston, Phys. Chem. Chem. Phys. **10**, 640 (2008).
[13] G. Barcaro, A. Fortunelli, F. Nita, G. Rossi, and R. Ferrando, Phys. Rev. Lett. **98**, 156101 (2007).
[14] G. Rossi and R. Ferrando, Nanotechnology **18**, 225706 (2007).
[15] C. Mottet, J. Goniakowski, F. Baletto, R. Ferrando, and G. Tréglia, Phase Transitions **77**, 101 (2004).
[16] J. Goniakowski and C. Mottet, J. Cryst. Growth **275**, 29 (2005).
[17] J. Oviedo, J. F. Sanz, N. López, and F. Illas, J. Phys. Chem. B **104**, 4342 (2000).
[18] V. Johánek, M. Laurin, A. W. Grant, B. Kasemo, C. R. Henry, and J. Libuda, Science **304**, 1639 (2004).
[19] G. Haas, A. Menck, H. Brune, J. V. Barth, J. A. Venables, and K. Kern, Phys. Rev. B **61**, 11105 (2000).
[20] G. Barcaro, E. Aprà, and A. Fortunelli, Chem. Eur. J. **13**, 6408 (2007).
[21] G. Barcaro and A. Fortunelli, Chem. Phys. Lett. **457**, 143 (2008).
[22] G. Barcaro and A. Fortunelli, Phys. Rev. B **76**, 165412 (2007).
[23] F. Baletto, R. Ferrando, A. Fortunelli, F. Montalenti, and C. Mottet, J. Chem. Phys. **116**, 3856 (2002).
[24] G. C. Bond, *Heterogeneous Catalysis*, 3rd ed. (Oxford University Press, Oxford, 1987).
[25] G. C. Bond, C. Louis, and D. T. Thomson, *Catalysis by Gold* (Imperial College Press, London, 2006).

[26] K. Kreibig and M. Vollmer, *Optical Properties of Metal Clusters* (Springer, New York, 1995).
[27] R. Ferrando, G. Rossi, F. Nita, G. Barcaro, and A. Fortunelli, ACS Nano **2**, 1849 (2008).
[28] M. Nuñez and M. B. Nardelli, Phys. Rev. B **73**, 235422 (2006).
[29] W. Vervisch, C. Mottet, and J. Goniakowski, Phys. Rev. B **65**, 245411 (2002).
[30] R. P. Gupta, Phys. Rev. B **23**, 1981 (1985).
[31] V. Rosato, M. Guillopé, and B. Legrand, Phys. Mag. **59**, 321 (1989).
[32] F. Cyrot-Lackmann and F. Ducastelle, Phys. Rev. B **4**, 2406 (1971).
[33] F. Baletto, C. Mottet, and R. Ferrando, Phys. Rev. Lett. **84**, 5544 (2000).
[34] F. Baletto, C. Mottet, and R. Ferrando, Phys. Rev. B **63**, 155408 (2001).
[35] J. Olander, R. Lazzari, J. Jupille, B. Mangili, J. Goniakowski, and G. Renaud, Phys. Rev. B **76**, 075409 (2007).
[36] G. Barcaro, A. Fortunelli, F. Nita, and R. Ferrando, Phys. Rev. Lett. **95**, 246103 (2005).
[37] G. Barcaro and A. Fortunelli, J. Chem. Theory Comput. **1**, 972 (2005).
[38] See http://www.cinam.univ-mrs.fr/mottet/param/metalMgO.pdf for more information on the parameters used in Eq. (6).
[39] D. J. Wales and J. P. K. Doye, J. Phys. Chem. A **101**, 5111 (1997).
[40] G. Rossi and R. Ferrando, Chem. Phys. Lett. **423**, 17 (2006).
[41] C. L. Cleveland and U. Landman, J. Chem. Phys. **94**, 7376 (1991).
[42] F. Baletto and R. Ferrando, Rev. Mod. Phys. **77**, 371 (2005).
[43] O. Robach, G. Renaud, and A. Barbier, Phys. Rev. B **60**, 5858 (1989).
[44] C. Revenant, G. Renaud, R. Lazzari, and J. Jupille, Nucl. Instrum. Methods Phys. Res. B **246**, 112 (2006).

Structures of metal nanoparticles adsorbed on MgO(001). II. Pt and Pd

Jacek Goniakowski,[1,a)] Andrei Jelea,[2,3] Christine Mottet,[2] Giovanni Barcaro,[4] Alessandro Fortunelli,[4] Zdenka Kuntová,[5,6] Florin Nita,[5,3] Andrea C. Levi,[5] Giulia Rossi,[5] and Riccardo Ferrando[5,a)]

[1]*INSP/CNRS and Université Paris VI, Campus Boucicaut, Paris, 75015, France*
[2]*CINaM/CNRS, Campus de Luminy, Marseille, 13288, France*
[3]*Institute of Physical Chemistry Ilie Murgulescu, Romanian Academy, 202 Spl Independentei St., 060021 Bucharest-12, Romania*
[4]*IPCF/CNR, via G. Moruzzi 1, Pisa, 56124, Italy*
[5]*Dipartimento di Fisica, CNISM and INFM/CNR, Via Dodecaneso 33, Genova, 16146, Italy*
[6]*Institute of Physics, AS CR, v.v.i., Na Slovance 2, 182 21 Prague 8, Czech Republic*

(Received 4 November 2008; accepted 30 March 2009; published online 1 May 2009)

The structure of metal clusters on MgO(001) is searched for by different computational methods. For sizes $N \leq 200$, a global optimization basin-hopping algorithm is employed, whereas for larger sizes the most significant structural motifs are compared at magic sizes. This paper is focused on Pt and Pd/MgO(001), which present a non-negligible mismatch between the nearest-neighbor distance in the metal and the oxygen-oxygen distance in the substrate. For both metals, a transition from the cube-on-cube (001) epitaxy to the (111) epitaxy is found. The results of our simulations are compared to experimental data, to results found for Au and Ag in the previous paper (paper I), and to predictions derived from the Wulff–Kaischew construction. © *2009 American Institute of Physics*. [DOI: 10.1063/1.3121307]

I. INTRODUCTION

In the previous paper (I),[1] we searched for the lowest-energy structures of Au and Ag nanoparticles supported on MgO(001) by global optimization methods and by comparing the most significant structural motifs at large sizes. Since the nearest-neighbor distance in bulk Au and Ag is of 2.88 and 2.89 Å, respectively, these metals present a rather small lattice mismatch with the oxygen-oxygen distance in the substrate, about 3%. In this paper (II) we focus on Pt and Pd, whose bulk lattice spacings are smaller so that their lattice mismatch with the substrate is more important, being 7.0% and 7.6%, respectively. A larger lattice mismatch can have strong effects on the preferred epitaxy on the substrate. For example, in the cases of Ni/MgO(001), Pd/CaO(001), and Pt/CaO(001), which present an even larger mismatch, the interaction with the substrate stabilizes hcp phases.[2,3] For Pd and Pt/MgO(001) we do not expect this behavior.[2] Nevertheless, we expect that lattice mismatch can play a role in determining structural transitions between fcc epitaxies. In addition, Pd and Pt differ from Ag and Au also because they present a stronger interaction with the substrate.

The computational methodology is described in paper I. Here, in Secs. II and III we discuss the global optimization results and the comparison of structural motifs for Pt and Pd, respectively. In Sec. IV, the results are rationalized in terms of the Wulff–Kaischew construction,[4,5] modified in order to take into account the variation in adhesion energy with the size of the clusters.[6] Section V contains an overall discussion of all the systems treated in papers I and II.

II. PT NANOPARTICLES

A. Global optimization results

In the size range up to 200 atoms, we considered the following sizes: $N=30,40,50,60,70,90,100,150,200$, finding that fcc(001) structures are always the lowest in energy, followed by decahedral and fcc(111) clusters. The only exception is $N=200$, at which the fcc(111) motif is slightly lower in energy than decahedra. Icosahedral particles are higher in energy. Only for $N=50$ we find an icosahedron whose energy is close (but still higher) than the best fcc(111) cluster. These results show once more the importance of the substrate in determining the most stable cluster structures. In fact, within the same model potential, free Pt clusters would be preferentially decahedral in this size range.[7,8]

In Fig. 1 we report an example of this behavior, for size $N=90$. At this size, the global minimum [Fig. 1(a)] is an fcc(001) cluster, which presents stacking faults (one of them gives a twin boundary). Clusters of this kind are often the global minima, at variance with the results for Au and Ag.[1] However, we note that our model for the Pt–Pt interaction underestimates the stacking fault energy, so that the appearance of such faults might be facilitated by this feature. In any case, fcc(001) clusters without faults are also found [Fig. 1(b)] and they are lower in energy than decahedra and fcc(111) structures [Figs. 1(c) and 1(d), respectively]. Especially the latter are much higher in energy, not only for $N=90$ but in the whole size range up to 200 atoms.

[a)]Authors to whom correspondence should be addressed. Electronic addresses: jacek.goniakowski@insp.jussieu.fr and ferrando@fisica.unige.it.

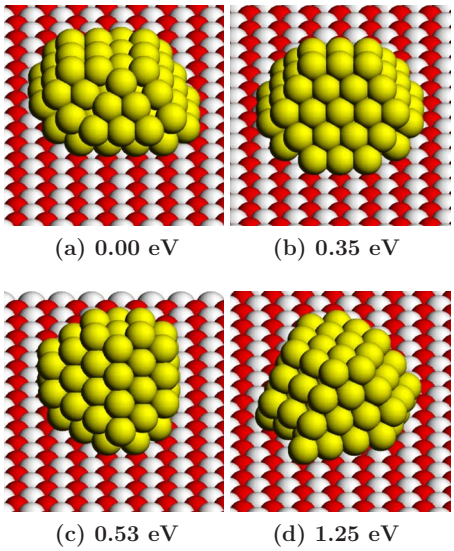

FIG. 1. (Color online) Pt/MgO(001) nanoparticles of size $N=90$.

B. Comparison of selected structural motifs for large sizes

The comparison of fcc(001), fcc(111), and decahedral structures (see Fig. 2) confirms that, for $N<200$, fcc(001) clusters are the lowest in energy, followed by decahedra and fcc(111) clusters. A first crossover between fcc(111) and decahedral clusters takes place around size 200, while the crossover between fcc(001) and fcc(111) structures is around $N=550$. From this size on, the fcc(111) structures are the most stable. This estimate, deduced from results on the magic clusters only, is necessarily approximative. Indeed, a detailed set of results (inset of Fig. 2) shows very similar energies of the two motifs in a relatively large zone of cluster sizes, where an addition or subtraction of a single atom may change their relative stability, as checked also by global optimization runs in the vicinity of size 400. Even though the crossover zone is broadened in a size range of more than 100

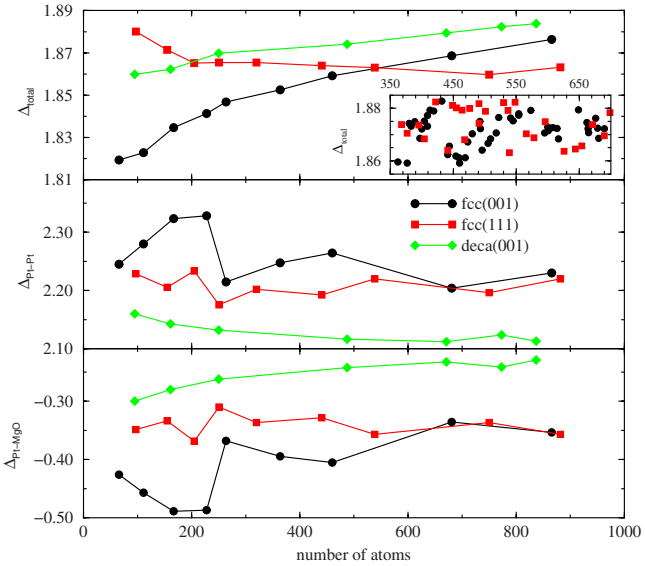

FIG. 2. (Color online) Δ_{total}, Δ_{Pt-Pt}, and Δ_{Pt-MgO} (in eV) for fcc(001), fcc(111); and decahedral Pt nanoparticles. A detailed representation of the fcc(001)→fcc(111) transition zone is given in the inset.

atoms, the crossover is however much sharper than in gold,[1] where epitaxies compete in a range of width of about 10^3 atoms at least.

Decomposing the energy into a metal-metal part and a metal-oxide part, we find that decahedral structures present the lowest metallic energy (as expected for free clusters[7,8]) and the weakest interaction with the substrate. On the other hand fcc(111) clusters are better than fcc(001) clusters for what concerns the metallic energy and worse for what concerns the interaction with the substrate.

This is a general behavior, which is similar to the Ag and Au cases as described in paper I.[1] However, in Pt, the adhesion of fcc(111) clusters becomes almost as good as the adhesion of fcc(001) clusters as size increases. In fact, at variance with Ag and Au, the adhesion energy of the (001) epitaxy does not evolve in a monotonic way: Around 250 atoms in size, the adhesion energy decreases abruptly in absolute value because of a partial relaxation of the epitaxial strain due to the variation in size of the surface in contact with the support (the full strain release by interfacial dislocations[9,10] takes place at larger size than those displayed in Fig. 2). This partial relaxation is sufficient to make (001) adhesion energy of the same magnitude as the (111) adhesion energy. This behavior also appears in Pd (as we will show in the following) and leads to a structural crossover.

Platinum films have been grown on the MgO(001) surface by a variety of techniques, including pulsed laser deposition,[11–14] electron beam evaporation,[15–17] and sputtering.[18–21]

As a general trend, it has been found that the (111) and (001) epitaxies coexist at low temperature and the (001) one tends to dominate in films obtained at higher temperatures. For example, *in situ* analysis by grazing incident small angle x-ray scattering (GISAXS) of Pt grown by physical evaporation shows that for growth at 1000 K and even after annealing at 1500–1600 K, the cluster epitaxy is the (001) whereas the clusters grown below 1000 K display preferentially the (111) epitaxy.[22] Nanoparticle structural transformations depending on coverage (which determines the cluster size) or temperature have been observed also in other systems, such as In/Si(111) growth[23] or Ni/MgO(001).[2] For In/Si(111), it was possible to determine experimentally the kinetic pathways for the fcc(111)→bct(101) transformation obtained by either increasing the thickness of the deposited In film or the temperature. In the case of Pt/MgO(001) experimental information on a possible epitaxy change depending on cluster size is not yet available and therefore a direct quantitative comparison with our simulations is not yet possible.

However, our results are in qualitative agreement with the experimental findings in predicting that both epitaxies should be observed as low-temperature structures, provided that the structures observed below 1000 K are close to those expected at equilibrium. In any case, it is difficult to rule out possible kinetic or thermodynamic effects[8] in order to establish whether the experimentally produced clusters really represent the low-temperature equilibrium structures.

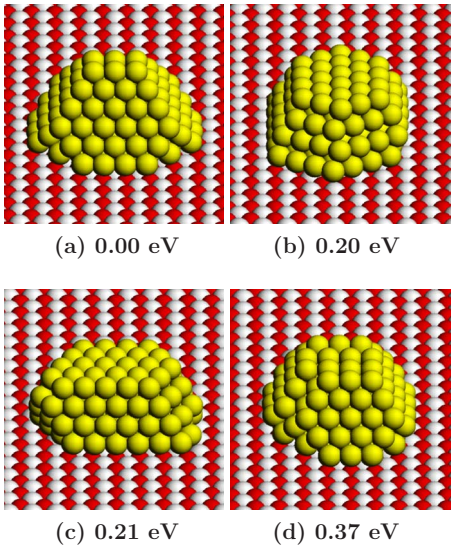

FIG. 3. (Color online) Pd/MgO(001) nanoparticles of size $N=150$.

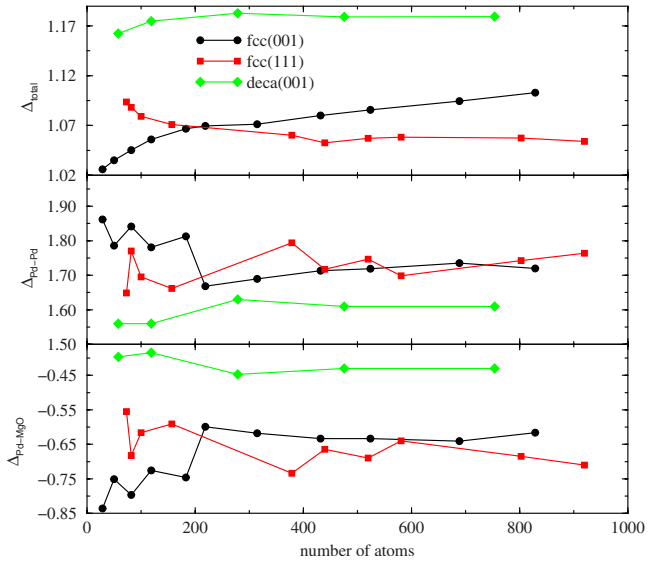

FIG. 4. (Color online) Δ_{total}, Δ_{Pd-Pd}, and Δ_{Pd-MgO} (in eV) for fcc(001), fcc(111), and decahedral Pd nanoparticles.

In fact, kinetic trapping effects are very difficult to avoid in low-temperature experiments. Growing clusters tend to get trapped into metastable structures that belong to the same motif, which is produced at lower sizes. A clear example has been found in the growth of gas-phase silver clusters simulated by molecular dynamics.[24] There, icosahedral clusters are produced for large sizes, at which icosahedra are much higher in energy than decahedra or fcc clusters. These metastable structures can have quite long lifetimes. Even though the growth on surfaces takes place on longer time scales than aggregation in gas phase, we expect for example that the (111) clusters predicted by our model for sizes of about 400 atoms would be very difficult to observe, since smaller clusters (and also some larger clusters) are in (001) epitaxy.

Finally, we note that, since average surface energies calculated for clusters in (001) and (111) epitaxy differ by a few hundredths of J/m^2 only, one cannot exclude that our energetic model is not precise enough. Such a small inaccuracy may indeed be related to the anisotropy factor $\gamma_{(001)}/\gamma_{(111)}$ being underestimated by the present Pt–Pt potential. This factor may play a role in determining the transition size between epitaxies, as will be discussed in Secs. IV and V.

III. PD NANOPARTICLES

A. Global optimization results

The structures of Pd/MgO nanoparticles of sizes $N \leq 120$ have been searched for in Ref. 25 within the same model considered here. In that size range, a clear prevalence of fcc(001) truncated pyramids has been found. These results have been confirmed also by density-functional (DF) theory calculations for $N \leq 34$.[26] In the following we focus on sizes $N > 120$.

For $N=150$, the global minimum is a fcc(001) structure, shown in Fig. 3(a). However, the structures in Figs. 3(b) and 3(c) present close-packed planes in contact with the substrate and are separated from the global minimum by only 0.2 eV. Structure (b) is indeed a hcp cluster with four close-packed planes in *ABAB* stacking. This cluster is obtained by truncating a hexagonal pyramid.[2] The occurrence of hcp clusters in our model might be overemphasized by the fact that our metal-metal interaction produces a small energy difference between fcc and hcp bulk phases. However, structure (c), which is almost degenerate with (b), is a fcc(111) cluster, which is thus in rather close competition with the global minimum. Structure (d) is fcc(001) with an island in stacking fault.

B. Comparison of selected structural motifs for large sizes

From a comparison among structural motifs, a crossover from fcc(001) to fcc(111) structures is predicted for sizes around 200 atoms, as shown in Fig. 4. Decahedral structures are always the highest in energy. The decomposition into metal-metal and metal-substrate contributions shows that, as in the other metals, decahedra present the most favorable metal-metal interaction, which however is overcompensated by a weak adhesion to the substrate.

For small sizes, metallic energy is compensated by the adhesion energy to favor the (001) epitaxy as in the other metals. For $N > 200$, fcc(001) metallic energy falls abruptly, symmetrically compensating the strengthening of the adhesion to the substrate. This corresponds to a partial strain release as in the Pt/MgO case due to the large lattice mismatch. As a result, metallic energies are comparable for both fcc epitaxies, but fcc(111) clusters better adhere to the substrate, which is a particularity of the Pd case because it has never been observed for the other metals. In fact, at best, Pt adhesion energy becomes equivalent for the two fcc epitaxies. This result will be rationalized in Sec. IV in terms of size-dependent adhesion energies per unit area.

The experimental results on Pd/MgO(001) report the observation of mostly fcc(001) nanoparticles,[27] with some evidence in favor of the formation of fcc(111) epitaxy clusters as cluster size increases. This evidence has been reported in recent experiments,[28] in which fcc(111) clusters are observed

TABLE I. Values of σ, τ_1, and τ_2 for the four metals.

Metal	σ	τ_1	τ_2
Ag	0.88	0.58	0.50
Au	0.86	0.71	0.69
Pt	0.85	0.59	0.64
Pd	0.87	1.11	1.21

even for the smallest sizes (4–5 nm). However, these (111) clusters are much larger than our transition size (a few thousand atoms at least compared to 200 atoms). The possible origin of this disagreement will be discussed in Sec. V.

IV. WULFF–KAISCHEW CONSTRUCTION FOR FCC(001) AND FCC(111) EPITAXIES

The shapes and energies of supported clusters can easily be computed in the limit of large clusters by means of the Wulff–Kaischew construction.[4,5] Here we apply this construction not only to Pd and Pt, but also to the metals treated in paper I (Ag and Au). In such limit no reference to the atomic structure is necessary and the shape and energy of a cluster depends on few parameters, i.e., on the surface energies per unit area γ and on the adhesion energy ε, again per unit area, to the substrate. ε is negative being an energy gain. Moreover, it is easy to convince oneself that for the noble and quasinoble metals only facets in the (001) and (111) orientations occur at equilibrium, all other orientations leading to considerably higher surface energies. Within this approach, contributions due to edges and vertices are neglected. Energy contributions due to dislocations are not considered either. Therefore, we expect the Wulff–Kaischew approach to be valid in the limit of large clusters. We do not consider noncrystalline structures because they are not expected to be favorable at large sizes due to their internal strain.

Under these conditions, as shown in detail in the Appendix, all relevant cluster properties, in particular, the equilibrium shape and energy of a cluster, depend on the three ratios

$$\sigma = \frac{\gamma_{(111)}}{\gamma_{(001)}}, \quad \tau_1 = \frac{|\varepsilon_{(001)}|}{\gamma_{(001)}}, \quad \tau_2 = \frac{|\varepsilon_{(111)}|}{\gamma_{(111)}}. \tag{1}$$

A relevant question is whether the cluster prefers to lie on a (001) facet (orientation 1) or on a (111) facet (orientation 2). An answer to this question can be obtained by calculating the energies $E_1(\sigma,\tau_1,\tau_2)$ and $E_2(\sigma,\tau_1,\tau_2)$ of clusters with the same volume but with (001) and (111) epitaxies, respectively. The formulas for E_1 and E_2 are rather cumbersome and are given in the Appendix, along with their derivation.

In the cases studied in the present work (noble and near-noble metal clusters adsorbed on magnesium oxide) the effect of σ is relatively unimportant, because for all considered metals our model predicts that σ values lie in a narrow range $0.85 \leq \sigma \leq 0.88$, while there is much more spread in τ_1 and τ_2, as can be seen in Table I. A convenient way of presenting the results is to consider the (τ_1,τ_2) plane at fixed σ (see Fig. 5).

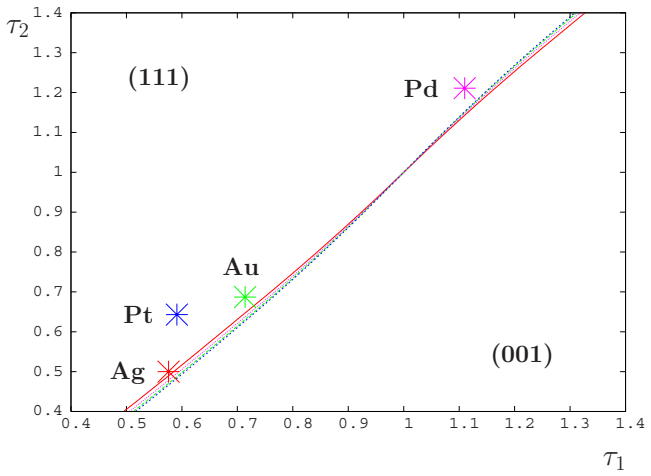

FIG. 5. (Color online) (τ_1,τ_2) plane at fixed σ. The lines separate the upper left part of the plane [where (111) epitaxy is favored] and the lower right part [where (001) epitaxy is favored] for the different metals. The points correspond to the actual values of (τ_1,τ_2) reported in Table I.

This plane is subdivided into two regions, separated by a line which runs near the diagonal $\tau_1=\tau_2$. This line is obtained by imposing that the energies of the two epitaxies are equal, $E_1=E_2$, for the same cluster volume. The line is slightly different for the different metals, corresponding to the small differences in σ. In the upper left region (high τ_2) of the plane, (111) epitaxy is favored, while in the lower right region (high τ_1) (001) epitaxy prevails.

From this plot it turns out that the condition for having the (001) epitaxy preferred over the (111) epitaxy is not simply $\varepsilon_{(001)} > \varepsilon_{(111)}$, but $\tau_1 > \tau_2$. As we shall see below, a larger ε does not translate automatically into a larger τ, because, in metal-oxide systems, a large ε is correlated with a large γ.

The (τ_1,τ_2) values of Table I fall in the region in which (111) epitaxy is favorable for all metals. This means that, asymptotically in the limit of large clusters, all four metals should present a crossover to (111) epitaxy. Note however that the point corresponding to Ag is very close to the separation line, indicating that the stability of the (111) epitaxy should be marginal. These results are in agreement with our simulations, which show a clear crossover toward the (111) epitaxy for Au, Pt, and Pd, while in the case of Ag, the crossover, if any, should be for $N > 3000$.[1]

The Wulff–Kaischew construction simply gives the prevailing structure in the limit of large sizes. In the following we show that this construction can be extended by incorporating size-dependent interface energies[6] to predict the size dependence of the epitaxy. In particular, we demonstrate that, by introducing size-dependent adhesion energies, we are able to reproduce the transition between epitaxies in the correct size range.

First of all, we note that the observed transitions are at rather large sizes, and therefore the contribution of edges and vertices should not be very important, so that the functional form of $E_1(\sigma,\tau_1,\tau_2)$ and $E_2(\sigma,\tau_1,\tau_2)$ can be taken as in the large-size limit discussed before. The size dependence can be introduced in first approximation by letting the parameters σ, τ_1, and τ_2 depend on size, so that also γ and ε depend on size.

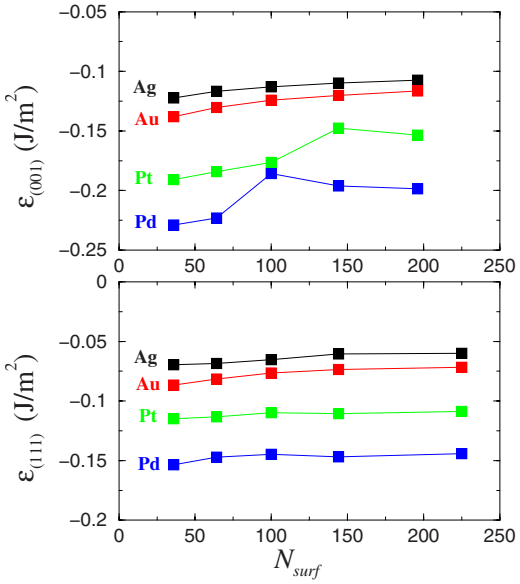

FIG. 6. (Color online) Variation in $\varepsilon_{(001)}$ and $\varepsilon_{(111)}$ with N_{surf} (the number of atom in contact with the substrate) for all metals. Energies are given in J/m^2.

Size-dependent adhesion energies have been calculated considering truncated octahedral clusters at different geometric magic sizes and with aspect ratios corresponding to the lowest energy in each size range. The adhesion energies $\varepsilon_{(001)}$ and $\varepsilon_{(111)}$ significantly depend on size, as shown in Fig. 6, while surface energies γ present a weaker change, at least until clusters become very small. Therefore τ_1 and τ_2 vary with size, with σ remaining constant. In Fig. 6 we report $\varepsilon_{(001)}$ and $\varepsilon_{(111)}$ as a function of the number of cluster atoms in contact with the substrate, N_{surf}. It turns out that decreasing N_{surf} the adhesion energies tend to increase in absolute value, indicating a stronger adhesion per unit area. This is due to an easier accommodation of strain when the number of contact atoms decreases.

For $\varepsilon_{(111)}$ the change with N_{surf} is rather small. For $\varepsilon_{(001)}$ this change is larger, especially in the cases of Pd and Pt, which present a non-negligible lattice mismatch with the substrate. In these cases, the change in the slope around $N_{surf}=100$ corresponds to the introduction of interfacial dislocations.[9,10]

If these variations in $\varepsilon_{(111)}$ and $\varepsilon_{(001)}$ are taken into account a size-dependent crossover from fcc(111) epitaxy at large sizes to fcc(001) epitaxy at small sizes is predicted for all metals, as can be seen in Fig. 7. In this figure, the starting points, which are in the fcc(001) region of the (τ_1,τ_2) plane, move to the left with increasing cluster size due to the variation in the ε values, to end up in the fcc(111) region for sufficiently large sizes. Looking at the crossover sizes predicted by this method, we find good agreement with those found within our atomistic calculations.

V. DISCUSSION AND CONCLUSIONS

In papers I and II, the low-energy structures of metal clusters adsorbed on MgO(001) have been investigated by a combination of computational methods. Simulation results have been compared also to those derived from the Wulff–Kaischew construction. Here we focus on summarizing the results for Pt and Pd, even though some comparison with Ag and Au will be made.

For all metals, the preferred structures of clusters at small sizes is in fcc(001) cube-on-cube epitaxy with the substrate. These fcc(001) clusters may either be in competition with fcc(111) clusters (in the case of Au and Pd) or with decahedral fragments (as in Ag and Pt). As size increases, metals behave differently.

In Ag, the fcc(001) clusters are favorable up to $N=3000$ at least. In Au the crossover is around $N=1200$, but both epitaxies are in close competition in the whole size range. As shown in Ref. 1, these results well agree with the available experimental observations.

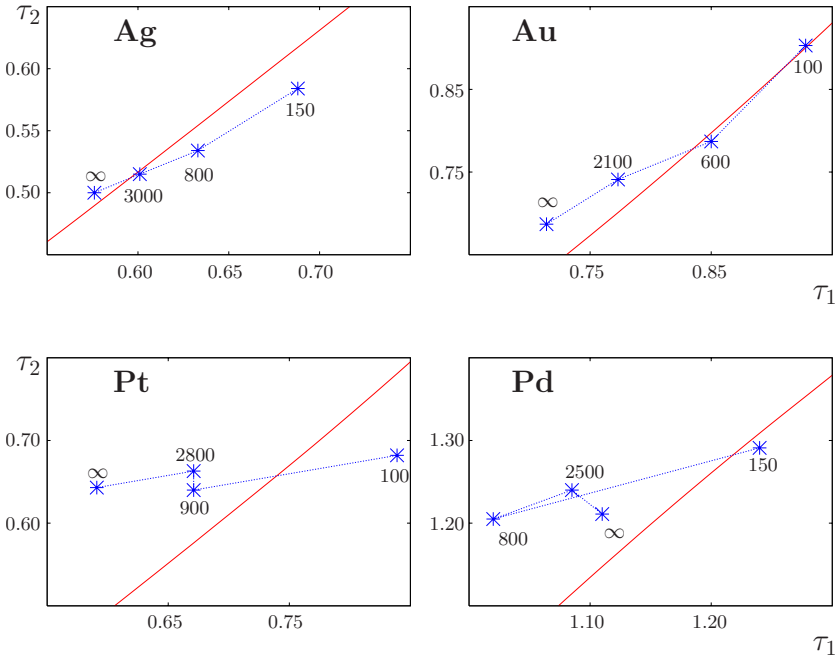

FIG. 7. (Color online) Same as in Fig. 5, but now four points correspond to each system, to take into account the variation in the adhesion energies with cluster size. For each point, we indicate the corresponding approximate cluster size. For $N\to\infty$ the points are in the upper left part of the (τ_1,τ_2) plane for all metals, corresponding to the (111) epitaxy, as follows from Fig. 5. With decreasing size, the points approach the dividing line of the plane and end in the lower right part, which corresponds to the (001) epitaxy. The irregular behavior of the Pt and Pd points is due to the appearance of dislocations. These appear at sizes which are far above the crossover size between epitaxies.

According to our calculations, Pt/MgO(001) clusters are fcc(001) at small sizes. For $N<200$, these are followed by decahedral clusters, while fcc(111) clusters are the highest in energy. A first crossover between decahedra and fcc(111) clusters is found around size 200, followed by a second crossover between (001) and (111) clusters at $N\simeq 550$. The latter becomes clearly the most favorable for large sizes. Such a rather sharp crossover is common to Pd, but not to Au. It can be interpreted by noting that Pt and Pd present a lattice mismatch, which induces a strong size dependence of the adhesion energy of (001) facets. When comparing with experiments,[22] the comparison is not completely straightforward. The fact that in clusters grown below 1000 K both epitaxies are observed is in qualitative agreement with our findings, which predict a competition between them. However, the experimentally observed transition to fcc(001) structures at high temperatures is not easily interpreted by our calculations. More studies are necessary.

The case of Pd/MgO(001) presents the most problematic comparison with the experiments for large sizes, while for sizes below 200 atoms the results agree well with experiments and DF calculations.[25,26] In fact, our calculations predict a crossover from (001) to (111) epitaxy around $N=200$. Some experimental data indeed indicate the presence (in some cases marginal) of fcc(111) clusters,[28–31] but at larger sizes.[28] Other experiments are in favor of the (001) epitaxy only,[27,32–34] up to the largest observed sizes (of several nanometers, thus containing many thousands of atoms).

This discrepancy between our results and the experiments may originate from different causes. Pd has a strong interaction with the substrate and the largest lattice mismatch. This causes a rather strong dependence of the adhesion energy on size in the (001) epitaxy (see Fig. 6). Compared to DF data, our metal-metal interactions underestimate surface energies, while the metal-substrate interaction is fitted on DF values. From the Wulff–Kaischew construction it follows that our simulated clusters are flatter than those that one would find from a full DF calculation, and probably flatter than those produced in experiments. Therefore, our simulated clusters adhere to the substrate with larger facets. This disfavors the (001) epitaxy, which worsens its adhesion per unit area as the contact area increases. In order to verify this effect we reparametrized the metal-metal part of the interaction potential in order to obtain higher surface energies that are in good agreement with the DF calculations. As can be seen in Fig. 8, there is a neat effect, which shows that crossover sizes are quite sensitive to changes in surface energies. In fact, the results of the new parametrization shift the transition size from 200 to about 750 atoms, thus going in the direction of a better agreement with the experimental data.

Furthermore, we note that it is not easy to disentangle thermodynamic, kinetic, support, etc. effects[8,35,36] and compare our low-energy structures with the outcome of experiments in a straightforward way. For example, a possible hypothesis to solve the discrepancy between experiment and theory is that in conditions of high flux and on surfaces rich in local defects (whose influence on the cluster structure can be expected to be minor in the limit of large sizes) the clusters nucleate on regular terraces or local defects and are thus free to realize a transition from (001) to (111) epitaxy, whereas when the clusters grow on extended defects such as steps (as those shown in Ref. 37) the influence of the support is sufficient to invert the energetic preference between (001) and (111) epitaxies. More studies are however necessary to support this hypothesis.

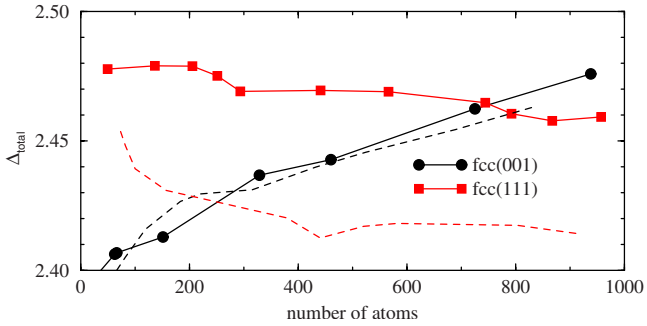

FIG. 8. (Color online) Comparison of the crossover between fcc(001) and fcc(111) epitaxies in Pd/MgO(001), according to different parametrization of the metal-metal interaction potential. Δ_{total} is given in eV. The results of the reparametrized Pd–Pd potential correspond to the full lines, which cross at about 750 atoms. Dashed lines reproduce the results of Fig. 4, with a crossover at about 200 atoms. The dashed lines have been shifted rigidly upwards by the same amount to achieve a more evident comparison with the full lines.

Finally we note that the transition between different epitaxies can be treated within the framework of the Wulff–Kaischew construction. This construction predicts that the asymptotic epitaxy for large cluster sizes should be (111), not only for Pd and Pt, but also for the metals, Ag and Au, treated in paper I. By incorporating into the Wulff–Kaischew framework size-dependent adhesion energies, we were able to reproduce the crossover toward the (001) epitaxy in the correct size range. This shows that the size dependence of the adhesion energy per unit contact area has a key role in driving the transition between epitaxies.

ACKNOWLEDGMENTS

We acknowledge financial support from the European Community Sixth Framework Program for the GSOMEN project (Project No. NMP4-CT-2004-001594), from the French National Agency for Research under the project SIMINOX (Project No. ANR-06-NANO-009-01), and from the Université Franco-Italienne under the program Galileo. G.R. acknowledges *L'Oréal Italia e UNESCO per le Donne e la Scienza*, 2007 edition, for a research fellowship. A.F. is grateful to Clemens Barth for interesting and useful discussions.

APPENDIX: WULFF-KAISCHEW CONSTRUCTION FOR (001) AND (111) EPITAXIES

Here we derive the formulas for the energy of fcc(001) and fcc(111) clusters by means of the Wulff-Kaischew construction.

1. In vacuum

In vacuum the clusters have the shape of truncated octahedra. An ideal octahedron is formed of two pyramids of height h with a square basis; from a truncated octahedron six little pyramids of height $q=xh$ are missing. x depends on

$$\sigma = \frac{\gamma_{(111)}}{\gamma_{(001)}}; \tag{A1}$$

by Wulff's theorem

$$x = 1 - \frac{1}{\sqrt{3}\sigma}. \tag{A2}$$

The inequalities

$$\frac{1}{\sqrt{3}} < \sigma < \frac{1}{\sqrt{3}-1} \tag{A3}$$

must hold; indeed for $\sigma \leq 1/\sqrt{3}$ the cluster would be an ideal octahedron, for $\sigma > 1/(\sqrt{3}-1)$ a cube, while in between these values the cluster is a truncated octahedron.

A truncated octahedron has 14 facets, 6 of type (001) and 8 of type (111). Letting $s_{(001)}$ and $s_{(111)}$ be their respective areas, we find

$$s_{(001)} = 2x^2h^2, \quad s_{(111)} = \frac{\sqrt{3}}{2}(1-3x^2)h^2. \tag{A4}$$

The volume is

$$V = V_0 = \tfrac{4}{3}(1-3x^3)h^3 \tag{A5}$$

and (using here and in the following $\gamma_{(001)}$ as the unit of energy/area) the total surface energy is

$$E_0 = 4\frac{1-3x^3}{1-x}h^2\gamma_{(001)} = \frac{[36(1-3x^3)]^{1/3}}{1-x}V^{2/3}\gamma_{(001)}. \tag{A6}$$

2. On the surface

On the surface, not only σ, but also τ_1 and τ_2,

$$\tau_1 = \frac{|\varepsilon_{(001)}|}{\gamma_{(001)}}, \quad \tau_2 = \frac{|\varepsilon_{(111)}|}{\gamma_{(111)}} \tag{A7}$$

are important parameters. When the cluster is adsorbed on the surface, a further cutting of its free vacuum shape takes place. For a given h, a part of the cluster is cut. The (negative) volume of this part is ΔV, which can be calculated by

$$\Delta V = -\int_0^p S(z)dz, \tag{A8}$$

where p is the height of the part which is cut and S is the area of the x-y cross section of the volume which is cut. S depends on z, with $0 \leq z \leq p$.

A remark is necessary here. In comparing the two epitaxies, clusters of the same size must be considered. In fact, the question that we wish to answer in the following is: Given surface and adhesion energies, what is the best epitaxy for a truncated octahedral cluster of a given size?

This means that the volume of the cluster after all cuts (at free and supported surfaces) must be the same for both epitaxies. Therefore, clusters corresponding to different values of h will be compared, because h will be determined in order to produce the same volume for both epitaxies.

In the subsequent formulae we suppose τ to be less than 1. The quantity τ is positive and its value can be both larger and smaller than one. When $\tau < 1$, less than half of the unsupported cluster is cut due to its contact with the substrate. There is, however, a duality property which allows us to suppose $\tau < 1$ and pass to the case of $2-\tau$ when required by $\tau > 1$ (this is the case of Pd).

Letting energy and volume to be

$$E = A(\tau)h^2\gamma_{(001)}, \quad V = B(\tau)h^3, \tag{A9}$$

the duality is expressed by

$$A(2-\tau) + A(\tau) = A(0), \quad B(2-\tau) + B(\tau) = B(0), \tag{A10}$$

where, as we have seen,

$$A(0) = 4\frac{1-3x^3}{1-x}, \quad B(0) = \frac{4}{3}(1-3x^3). \tag{A11}$$

We will compare explicitly two situations, evaluating the surface energy of two clusters of the same volume but with different facets adhering to the substrate, namely, type (001) (orientation 1) or type (111) (orientation 2).

a. fcc(001) epitaxy

When the cluster is supported on (001) (orientation 1) there are:

-One (001) facet at the cluster bottom (in contact with the substrate, of area $S_{(001)}$),
-One (001) facet on top of the cluster (of area $s_{(001)}$),
-Four lateral (001) facets (of area $s'_{(001)}$ each),
-Four lateral (111) facets in the lower half of the cluster (of area $s'_{(111)}$ each), and
-Four lateral (111) facets in the upper half of the cluster (of area $s_{(111)}$ each).

Therefore, the total cluster energy is given by

$$E_1 = 4(s_{(111)} + s'_{(111)})\gamma_{(111)} + (s_{(001)} + 4s'_{(001)})\gamma_{(001)} + S_{(001)}(\gamma_{(001)} - |\varepsilon_{(001)}|). \tag{A12}$$

Let $y = p/h = \tau_1(1-x)$. Here two cases must be distinguished:

First case: $\tau_1 < (1-2x/1-x)$. In this case, the four lateral (001) facets are not cut by the contact with the substrate. Then

$$s'_{(001)} = s_{(001)}, \tag{A13}$$

$$s'_{(111)} = \frac{\sqrt{3}}{2}(1-3x^2-2xy-y^2)h^2, \tag{A14}$$

$$S_{(001)} = 2(x+y)^2h^2, \tag{A15}$$

$$\Delta V = -\tfrac{2}{3}[(x+y)^3 - x^3]h^3. \tag{A16}$$

Second case: $(1-2x/1-x)<\tau_1<1$ In this case the four lateral (001) facets are cut

$$s'_{(001)}=[2x^2-(y+2x-1)^2]h^2<s_{(001)}, \tag{A17}$$

$$s'_{(111)}=\frac{\sqrt{3}}{2}(3-5x-y)(1-x-y)h^2, \tag{A18}$$

$$S_{(001)}=[2(x+y)^2-4(y+2x-1)^2]h^2, \tag{A19}$$

$$\Delta V=-\tfrac{2}{3}[(x+y)^3-x^3-2(y+2x-1)^3]h^3. \tag{A20}$$

In both cases the volume is obtained by subtracting $V=V_0-|\Delta V|$ (ΔV is negative), V is found as $V=V(h,x,y)$, which also means $V=V(h,\sigma,\tau_1)$. Inverting with respect to h, one finds $h=h(V,\sigma,\tau_1)$, from which the total interface energy of the (001) epitaxy $E_1=E_1(V,\sigma,\tau_1)$ follows.

b. fcc(111) epitaxy

When the cluster is supported on (111) (orientation 2) there are:

-One (111) facet at the cluster bottom (in contact with the substrate, of area $S_{(111)}$),
-One (111) facet on top of the cluster (of area $s_{(111)}$),
-Three lateral (001) facets in the lower half of the cluster (of area $s'_{(001)}$ each),
-Three lateral (001) facets in the upper half of the cluster (of area $s_{(001)}$ each),
-Three lateral (111) facets in contact with the facet at the cluster bottom (of area $s'_{(111)}$ each), and
-Three lateral (111) facets in contact with the facet at the cluster top (of area $s''_{(111)}$ each).

The energy is given by

$$E_2=(s_{(111)}+3s'_{(111)}+3s''_{(111)})\gamma_{(111)}+3(s_{(001)}+s'_{(001)})\gamma_{(001)}+S_{(111)}(\gamma_{(111)}-|\varepsilon_{(111)}|). \tag{A21}$$

Two cases must again be distinguished.

First case: $\tau_2<2x$. In this case, the three lateral (111) facets that are in contact with the cluster top are not cut. Then

$$s'_{(001)}=x(2x-\tau 2)h^2, \tag{A22}$$

$$s'_{(111)}=\frac{\sqrt{3}}{8}[(2-\tau_2)^2-4x^2-2(2x-\tau_2)^2]h^2, \tag{A23}$$

$$s''_{(111)}=s_{(111)} \tag{A24}$$

$$S_{(111)}=\frac{\sqrt{3}}{2}\left[\left(1+\frac{1}{2}\tau_2\right)^2-3x^2\right]h^2, \tag{A25}$$

$$\Delta V=-\tfrac{1}{24}\tau_2(12+6\tau_2+\tau_2^2-36x^2)h^3. \tag{A26}$$

Second case: $2x<\tau_2<1$. In this case, the three lateral (111) facets that are in contact with the cluster top are cut. Then

$$s'_{(001)}=0, \tag{A27}$$

$$s'_{(111)}=\frac{\sqrt{3}}{8}[(2-\tau_2)^2-4x^2]h^2, \tag{A28}$$

$$s''_{(111)}=\frac{\sqrt{3}}{8}(4-8x^2-\tau_2^2)h^2 \tag{A29}$$

$$S_{(111)}=\frac{\sqrt{3}}{4}[2+2\tau_2-\tau_2^2]h^2, \tag{A30}$$

$$\Delta V=-\left[\tfrac{1}{12}\tau_2(6+3\tau_2-\tau_2^2)-2x^3\right]h^3. \tag{A31}$$

In analogy with the case of E_1, $E_2=E_2(V,\sigma,\tau_2)$ can be calculated.

[1] R. Ferrando, G. Rossi, A. C. Levi, Z. Kuntová, F. Nita, G. Barcaro, A. Fortunelli, A. Jelea, C. Mottet, and J. Goniakowski, J. Chem. Phys. **130**, 174702 (2009).
[2] R. Ferrando, G. Rossi, F. Nita, G. Barcaro, and A. Fortunelli, ACS Nano **2**, 1849 (2008).
[3] W. Tian, H. P. Sun, X. Q. Pan, J. H. Yu, M. Yeadon, C. B. Boothroyd, Y. P. Feng, R. A. Lukaszew, and R. Clarke, Appl. Phys. Lett. **86**, 131915 (2005).
[4] C. R. Henry, Prog. Surf. Sci. **80**, 92 (2005).
[5] B. Mutaftschiev, *The Atomistic Nature of Crystal Growth* (Springer-Verlag, Berlin, 2001).
[6] C. Mottet and J. Goniakowski, J. Comput. Theor. Nanosci. **4**, 326 (2007).
[7] F. Baletto, R. Ferrando, A. Fortunelli, F. Montalenti, and C. Mottet, J. Chem. Phys. **116**, 3856 (2002).
[8] F. Baletto and R. Ferrando, Rev. Mod. Phys. **77**, 371 (2005).
[9] W. Vervisch, C. Mottet, and J. Goniakowski, Phys. Rev. B **65**, 245411 (2002).
[10] W. Vervisch, C. Mottet, and J. Goniakowski, Eur. Phys. J. D **24**, 311 (2003).
[11] J. F. M. Cillessen, R. M. Wolf, and D. M. de Leeuw, Thin Solid Films **226**, 53 (1993).
[12] J. Narayan, P. Tiwari, K. Jagannadham, and O. W. Holland, Appl. Phys. Lett. **64**, 2093 (1994).
[13] Y. Takai and M. Sato, Supercond. Sci. Technol. **12**, 486 (1999).
[14] M. Morcrette, A. Guitierrez-Llorente, W. Seiler, A. Laurent, and P. Barboux, J. Appl. Phys. **88**, 5100 (2000).
[15] R. Farrow, D. Weller, R. Marks, M. Toney, A. Cebollada, and G. Harp, J. Appl. Phys. **79**, 5967 (1996).
[16] P. McIntyre, C. Maggiore, and M. Natasi, Acta Mater. **45**, 869 (1997).
[17] P. McIntyre, C. Maggiore, and M. Natasi, Acta Mater. **45**, 879 (1997).
[18] B. M. Lairson, M. R. Visokay, R. Sinclair, S. Hagstrom, and B. M. Clemens, Appl. Phys. Lett. **61**, 1390 (1992).
[19] J. L. Menéndez, P. Caro, and A. Cebollada, J. Cryst. Growth **192**, 164 (1998).
[20] P. Andreazza, C. Andreazza-Vignolle, J. Rozenbaum, A.-L. Thomann, and P. Brault, Surf. Coat. Technol. **151–152**, 122 (2002).
[21] C. Gatel, P. Baules, and E. Snoeck, J. Cryst. Growth **252**, 424 (2003).
[22] J. Olander, R. Lazzari, J. Jupille, B. Mangili, J. Goniakowski, and G. Renaud, Phys. Rev. B **76**, 075409 (2007).
[23] J. Chen, M. Hupalo, M. Ji, C. Z. Wang, K. M. Ho, and M. C. Tringides, Phys. Rev. B **77**, 233302 (2008).
[24] F. Baletto, C. Mottet, and R. Ferrando, Phys. Rev. Lett. **84**, 5544 (2000).
[25] G. Rossi, C. Mottet, F. Nita, and R. Ferrando, J. Phys. Chem. B **110**, 7436 (2006).
[26] G. Barcaro, A. Fortunelli, F. Nita, G. Rossi, and R. Ferrando, Phys. Rev. Lett. **98**, 156101 (2007).
[27] C. R. Henry, Surf. Sci. Rep. **31**, 231 (1998).
[28] P. Nolte, A. Stierle, N. Kasper, N. Y. Jin-Phillipp, H. Reichert, A. Rühm, J. Okasinski, H. Dosch, and S. Schöder, Phys. Rev. B **77**, 115444 (2008).
[29] H. Fornander, J. Birch, L. Hultman, L. G. Petersson, and J. E. Sundgren, Appl. Phys. Lett. **68**, 2636 (1996).
[30] H. Fornander, L. Hultman, J. Birch, and J. E. Sundgren, J. Cryst. Growth **186**, 189 (1998).

[31] C. Revenant, F. Leroy, R. Lazzari, G. Renaud, and C. R. Henry, Phys. Rev. B **69**, 035411 (2004).
[32] G. Renaud and A. Barbier, Surf. Sci. **433–435**, 142 (1999).
[33] G. Renaud, A. Barbier, and O. Robach, Phys. Rev. B **60**, 5872 (1999).
[34] G. Renaud, R. Lazzari, C. Revenant, A. Barbier, M. Noblet, O. Ulrich, F. Leroy, J. Jupille, Y. Borensztein, C. R. Henry, J.-P. Deville, F. Scheurer, J. Mane-Mane, and O. Fruchart, Science **300**, 1416 (2003).
[35] G. Barcaro, E. Aprà, and A. Fortunelli, Chem. Eur. J. **13**, 6408 (2007).
[36] J. Oviedo, J. Fernandez-Sanz, N. Lopez, and F. Illas, J. Phys. Chem. B **104**, 4342 (2000).
[37] O. H. Pakarinen, C. Barth, A. S. Foster, and C. R. Henry, J. Appl. Phys. **103**, 054313 (2008).

Surface-Supported Gold Cages

FerrandoPRL2009

R. Ferrando,[1] G. Barcaro,[2] and A. Fortunelli[2]

[1]*Dipartimento di Fisica and CNISM, Via Dodecaneso 33, Genova, I16146, Italy*

[2]*IPCF/CNR, via G. Moruzzi 1, Pisa, I56124, Italy*

(Received 24 January 2009; published 28 May 2009)

It is shown, by density-functional theory calculations, that gold clusters on the MgO(001) surface prefer cage structures in the size range between 23 and 42 atoms. These structures belong to a new structural family, the open pyramidal hollow cages, which has no counterpart in gas-phase clusters. These cages are possible because of the peculiar features of the Au-Au and Au-MgO interactions, which include strong many-body and directional effects. These effects reinforce the tendency of Au to produce cage structures with respect to the gas phase.

DOI: 10.1103/PhysRevLett.102.216102 PACS numbers: 68.43.Hn, 61.46.Bc, 61.46.Df, 68.43.Bc

Stimulated by the discovery of C_{60} [1], the recent years have witnessed a surge of activity in the search for cagelike configurations of noncarbon elements (see, e.g., Ref. [2]). In cage structures, all atoms belong to the surface of the cluster, which is a shell of monoatomic thickness. Gold nanoparticles have attracted much attention (almost exclusive among metals) due to their unique structural behavior [3]. In Au, relativistic effects [4] stabilize 6*s* and destabilize 5*d* orbitals, inducing significant *s*-*d* hybridization and strong directionality effects in bonding [5]. Until now, this attention has concentrated on gas-phase clusters [6]. A well-known example is Au_{20}, which is tetrahedral [7,8] and of great structural and electronic stability [9]. Also hollow cages have been proposed [10–17], such as Au_{32}, which is icosahedral and could accommodate several guest atoms in its empty inner part. However, these studies deal with structures in free space, while much less is known about the possibility of stabilizing cage structures when gold nanoparticles are put in contact with some sort of environment, such as a crystal surface.

In this Letter, we address the issue of the stabilization of supported gold cages. As a substrate, we choose the MgO(001) surface for its widespread use as a prototypical oxide support in the study of model nanocatalysts [18]. By density-functional theory (DFT) calculations, we show that, in the size range between 25 and 40 atoms, hollow gold cages are the most favorable structures on the MgO(001) surface. In particular, we show that the interaction with the substrate stabilizes a novel class of hollow cage nanoparticles, the open pyramidal hollow cages, which have no counterpart in free-space clusters. The substrate plays a key role in inducing the formation of cages, which become favorable even for sizes and charge states for which gas-phase clusters are expected to be compact.

Our calculations are developed along the methodology of Ref. [19]. Global optimization searches within an empirical potential model [20] are performed to build up a vast database of compact (noncage) Au/MgO(001) clusters. This semiempirical model is able to reproduce the experimentally observed cluster epitaxies and shapes of larger Au/MgO(001) nanoparticles [21]. Cage structures are built up either by accommodating on the substrate the gas-phase structures, or by building up pyramidal cages (see below). All structures are locally relaxed by DFT. The DFT calculations are carried out using the PWscf (Plane-Wave Self-Consistent Field) code [22], with the Perdew-Burke-Ernzerhof (PBE) exchange-correlation (xc) functional [23] and ultrasoft pseudopotentials. For comparison, results obtained by other xc functionals are reported in [24]. The MgO(001) surface is modeled by a two-layer slab. Each layer contains either 36 Mg and 36 O atoms (6×6 cell) or 35 Mg and 35 O atoms (7×5 cell), fixed in the lattice positions of the MgO bulk structure. The kinetic energy cutoff is 40 Ry for the energy and 160 Ry for the density for all calculations. Because of the large unit cells, eigenvalues and eigenvectors of the Kohn-Sham Hamiltonian are only evaluated at the Γ point. A Gaussian smearing technique (smearing parameter of 0.002 Ry) is applied.

In the following we focus on the size range $23 \leq N \leq 42$.

Let us consider compact structures, i.e., clusters containing at least one inner atom, without any void inside. Several compact motifs are found by the empirical potential search (see Fig. 1). Pyramidal clusters, in fcc(001) epitaxy with the substrate, are either based on the square pyramid of size 30 [1(a) and 1(b)], with (4×4) basis and a single inner atom, or on the rectangular pyramid of size 40 [1(c) and 1(d)], with (5×4) basis and two inner atoms. In the (001) epitaxy, Au atoms are placed above oxygens. These pyramids may be truncated at the basal corners, at the top vertex or may present overhangs at the interface with the substrate. Truncation of the basal corners is favored over truncation of the top vertex by a larger amount than in Pd/MgO [19], due to the weaker adhesion to MgO of Au. Overhangs are more favorable than top vertex truncation.

Compact fcc clusters can be also in (111) epitaxy, as observed in experiments for larger sizes [18]. In Fig. 1(e) we report a truncated octahedron of size 31, which adheres to MgO with a (111) hexagonal facet. These clusters are

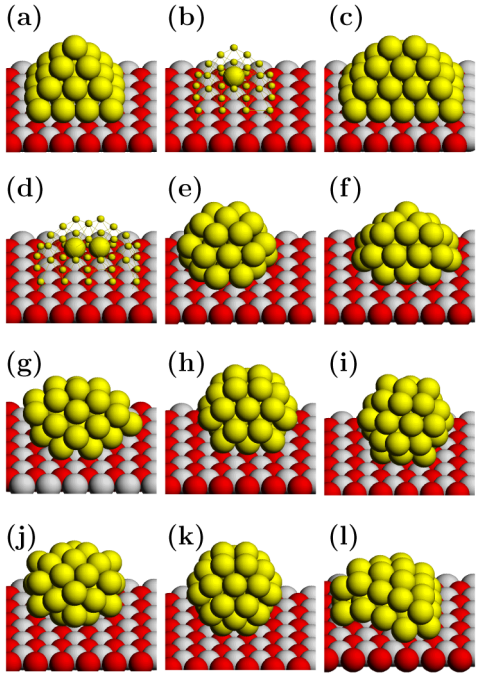

FIG. 1 (color online). Compact structures of Au/MgO(001) (a),(b) Square pyramid of 30 atoms. (c),(d) Rectangular pyramid of 40 atoms. In (b),(d) surface atoms of the pyramids are represented by small spheres, so that inner atoms are visible. (e) fcc cluster of 31 atoms—a truncated octahedron in (111) epitaxy with the MgO. (f),(g) Noncrystalline structures—icosahedral and decahedral fragments of 32 atoms, respectively. (h) Fcc truncated octahedron of 34 atoms, in (001) epitaxy with the substrate. (i) Icosahedral hollow cage. (j) D_{6h} hollow cages. (k) Truncated octahedral hollow cage. (l) Bilayer structure.

much higher in energy than fcc(001) compact pyramids, due to a much worse matching with the substrate. Even for $N = 31$, a geometrical magic size of fcc(111) clusters, the energy difference with the best pyramid is more than 0.4 eV.

Also icosahedral and decahedral compact fragments [Figs. 1(f) and 1(g), respectively] are found, but they are higher in energy than the previous fcc structures. Finally, fcc(001) clusters occur also in the form of truncated octahedra, as in Fig. 1(h). A highly symmetric truncated octahedron is at $N = 34$. It is higher by 0.37 eV than a rectangular pyramid with truncations at basal corners and overhangs. In summary, we find that compact structures are dominated by the fcc(001) pyramids.

It is now interesting to compare compact and cage structures. In gas phase, there is evidence in favor of gold cages for $N = 32$. This is an electronic magic number for the jellium model on a spherical shell [25], and a geometrical magic size for high-symmetry cage structures, in particular, for an icosahedral cage, corresponding to the external shell of the 45-atom anti-Mackay icosahedron [26]. This gas-phase cage is separated from other structures by at least 0.3 eV [6,10,11,14]. When deposited on MgO(001), as in Fig. 1(i), this cage matches the substrate reasonably well, with four gold atoms on oxygen sites. This is sufficient to prevail by 0.64 eV over the best compact pyramid, even though the latter has 12 gold atoms on oxygen sites. Other 32-atom cages are the cluster of Fig. 1(j), of D_{6h} symmetry in gas phase, and higher in energy than the icosahedral cage by about 1 eV. The cluster in Fig. 1(k) is a truncated-octahedral cage, obtained by removing the six inner atoms of the 38-atom truncated octahedron. In gas phase, this is 0.88 eV higher than the icosahedral cage. Because of a better matching with the substrate, this difference decreases to 0.71 eV on MgO. Deposited icosahedral and truncated-octahedral cages retain considerable HOMO-LUMO gaps—1.19 and 1.23 eV, respectively—showing that their magic electronic character is preserved to a good extent. Bilayer cages [Fig. 1(l)] are much higher in energy.

These results demonstrate that 32-atom hollow cages can be formed on the substrate with the same structure of gas-phase clusters. Unfortunately, 32 is a special size. In fact, the peculiar stability of the icosahedral cage is due to the combined effects of electronic and geometrical shell closure, effects that disappear when size is changed by a few atoms. This holds in gas phase [25] and on MgO. In fact, for $N = 33$ the icosahedral cage—with one atom added at the interface with MgO—is still lower by 0.17 eV than the best compact pyramid, but already for $N = 31$ and 34, compact structures clearly prevail.

However, other cage structures, unknown in the gas phase, come into play. The key to their formation is in the structure of Fig. 2(a). This is a 38-atom rectangular cage pyramid obtained by removing the two inner atoms from the compact pyramid of Figs. 1(c) and 1(d). This structure matches the substrate with 20 atoms and is in close competition with the best compact structures [see Fig. 3(a)]. However, we note that its basal layer presents a substantial reconstruction, as shown in the right panel of Fig. 2(a). In fact, while the atoms of the perimeter of the basal layer are in close contact with MgO, the six central atoms (in white in the figure) are pushed up, with their z coordinates in average higher by almost 0.3 Å, as if they were repelled by the substrate. The same effect is observed in the bilayer of Fig. 1(l), and, to a smaller extent, in compact clusters. This observation suggests the possibility of building up a new cage motif by simply removing the atoms in the interior of the basal layer. This leads to the open pyramidal hollow cages of Figs. 2(b) and 2(c), whose basis is reduced to atoms along the perimeter only. The rectangular cage of Fig. 2(b) has size 32; complete square open cages are at $N = 25$ [Fig. 2(c)] and 41; a rectangular open cage with 6×4 basis is at $N = 39$. The range $23 \leq N \leq 42$ can be covered by cutting basal corners or adding adatoms on the lateral close-packed facets. This motif is by far the most stable in this size range (with a single exception, see below), as follows from the results of Fig. 3(a). For example, at $N = 32$, the open cage of Fig. 2(b) is lower than the icosahedral cage of Fig. 1(i) by 0.53 eV, being thus more stable than compact structures by almost 1.2 eV.

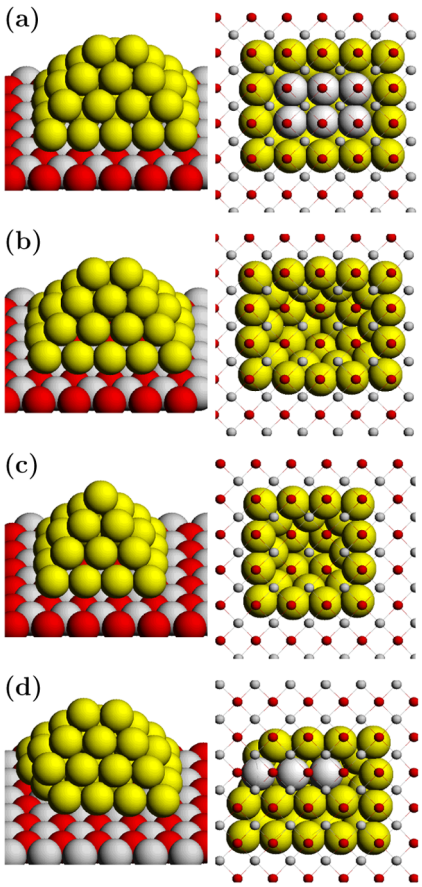

FIG. 2 (color online). Substrate-stabilized cages. (a) Rectangular pyramidal cage of 38 atoms, obtained by removing the two inner atoms of the compact pyramid of Fig. 1(b). In the right column, bottom view of this cluster, where O and Mg atoms are small spheres, to show the basal layer of the cage. This plane consists of 20 atoms, of which 14 belongs to its perimeter, and 6 (in white) belong to its inner part. (b) Rectangular *open cage* of 32 atoms obtained by removing six basal atoms from (a). (c) Square open cage of 25 atoms. (d) Rectangular cage with distorted basal plane—in the right column, the three atoms in white are in bridge positions between neighboring oxygens.

Results obtained by other xc functionals confirm this finding [24]. Large energy differences with respect to compact structures are found for several nuclearities $23 \leq N \leq 39$. Then open cages prevail also for $40 \leq N \leq 42$, but by smaller amounts. This indicates that a transition towards compact structures is likely to take place just above this size range. The only size at which the best structure is not an open pyramidal cage is $N = 34$, where a different new cage motif prevails. This is obtained by distorting the basal plane of the cages of Fig. 2(a) as shown in Fig. 2(d). In this way, the number of Au-Au nearest-neighbor bonds in the basal layer is increased to the expense of a modest decrease of the adhesion with MgO. In summary, for $23 \leq N \leq 42$, pyramidal cages are the lowest in energy, and open cages always prevail with a single exception.

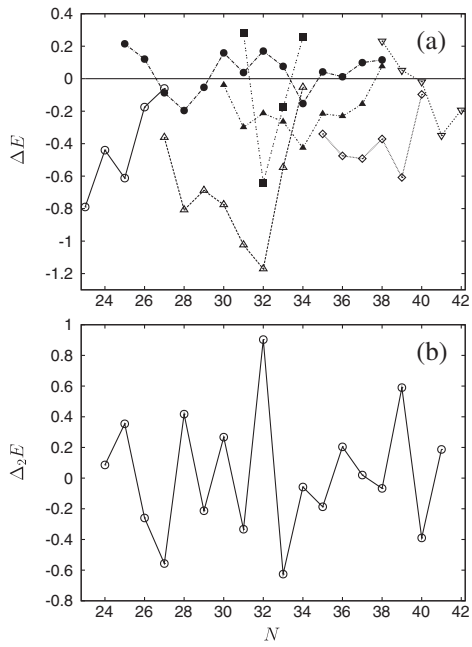

FIG. 3. (a) Energy difference ΔE (in eV) between cage structural motifs and the best compact structures, depending on size N. Negative values of ΔE correspond to cage structures that are more stable than compact structures of the same size. Open pyramidal cages correspond to open symbols. Four series of open pyramidal cages are considered—with 4×4, 5×4, 6×4, and 5×5 basis (open circles, upward triangles, diamonds, and downward triangles, respectively). Full symbols correspond to other cage motifs: closed pyramidal cages with (001) basis (full circles); icosahedral cages (full squares); closed pyramidal cages with distorted basis (full triangles). (b) Second difference in the energy $\Delta_2 E$ (in eV, see text) vs size N. Positive peaks single out the most stable sizes.

Two reasons (specific to the physics of Au bonding) concur to determine the special stability of pyramidal open cages.

First, gold has a ubiquitous tendency to form close-packed monolayers in undercoordinated systems [5]. This is due to that fact that this metal looses only 8% of its binding energy in passing from the bulk 12-coordinated situation to close-packed 6-coordinated monolayers, a fact that reverberates in the planarity of small clusters [27], the reconstruction of low-index Au surfaces [5], and stabilizes the compact facets of supported pyramidal cages.

Second, the Au/surface interactions also present peculiar features with a directional and strongly many-body character [28]. In fact, a single Au atom interacts appreciably with the oxygen ions of MgO also via a chemical bond component. However, the strength of this interaction drops rapidly with Au coordination, as a result of the competition with metal-metal bonds. This shifts the interaction mechanism of higher coordinated clusters to a largely prevailing polarization component with a strong ''metal-on-top'' effect (i.e., an increased metal-surface interaction due to the presence of metal atoms on top of the atom directly in contact with the substrate) [28]. The net result is that highly

coordinated Au atoms dislike being in contact with the oxide surface, whereas the interaction of low-coordinated atoms is much more favorable, especially if enhanced by the ''metal-on-top'' effect. The open pyramidal cages perfectly meet these features, presenting low-coordinated perimetral basal atoms with a proper set of on-top neighbors.

To quantify the stability of cage structures as a function of N, in Fig. 3(b) we report the second difference in energy $\Delta_2 E(N) = E(N-1) - 2E(N) + E(N+1)$, which compares the stability of clusters of neighboring sizes. Positive peaks of $\Delta_2 E$ single out structures of special stability. The highest peak is at $N = 32$, indicating a magic structure; other relevant peaks occur for $N = 25$, 28, 39, and 41. In the size range around 32, $\Delta_2 E$ displays odd-even oscillations, which, however, become even-odd around 25 and 39–41, showing that their occurrence is not simply due to the filling of electronic levels. This is also shown by the fact the Au_{32} pyramidal open cage wins over the icosahedral one even though the latter has a much larger HOMO-LUMO gap (1.19 vs 0.47 eV).

It is interesting to note that the same mechanism by which neutral pyramidal hollow cages are stabilized is operative also for *charged* clusters. We have compared in fact the energies of the anionic Au_{32} species for three motifs: the pyramidal open cage, the icosahedral hollow cage, and the compact pyramid, and found that the pyramidal open cage is still lower in energy than any of the other two. Indeed, charging even increases the energy difference in favor of the open pyramid by 0.07 eV. At variance with the gas phase, where negatively charging the Au_{32} cluster induces a transition from the icosahedral cage to compact low-symmetry structures [6,14,29], supported pyramidal open cages resist charging. This can be explained by the fact that their stabilization mechanism is not simply connected to electronic shell closure, but to the general physics of the Au-Au and Au-surface interaction, and is thus more robust than in gas phase.

Here we have considered only regular, nondefected MgO(100) terraces. We expect however that the general picture should not change on more realistic MgO surfaces. On the contrary, extended defects such as steps, that are thought to be the most abundant defects on MgO(100) crystals or thick slabs [18], should further stabilize pyramidal cage arrangements and their simple (001) epitaxy with respect to noncrystalline configurations or more complex epitaxial relationships. Open pyramidal cages are likely to be stable also on other square-symmetry oxide surfaces.

In conclusion, we have shown that a new family of cage structures is stabilized by the combined effects of the Au-Au and Au-oxide interactions. These cages prevail in a wide range of sizes, showing thus that a properly chosen substrate can have a clear active effect in reinforcing the tendency of gold to produce cage structures. These systems are of interest both from a fundamental point of view and also in view of potential applications. For example, endohedral filling with dopants can tune the cluster electronic structure [25] and produce, e.g., novel catalytic [30] or optical [31] properties.

R. F. acknowledges support from Italian MIUR for the PRIN Project No. 2007LN873M_003. The authors acknowledge support from CINECA and CNR-INFM for the project ''Properties of Exotic Phases of Metal-on-Oxide Nanodots'' and from the European Community Sixth Framework Programme for the GSOMEN project (NMP4-CT-2004-001594).

[1] H. W. Kroto *et al.*, Nature (London) **318**, 162 (1985).
[2] S. F. Li *et al.*, J. Phys. Chem. C **112**, 13 200 (2008).
[3] M.-C. Daniel and D. Astruc, Chem. Rev. **104**, 293 (2004).
[4] P. Pyykkö, Angew. Chem., Int. Ed. **43**, 4412 (2004).
[5] S. Olivier, R. Conte, and A. Fortunelli, Phys. Rev. B **77**, 054104 (2008).
[6] M. P. Johansson, D. Sundholm, and J. Vaara, J. Phys. Chem. C **112**, 19311 (2008).
[7] J. Li *et al.*, Science **299**, 864 (2003).
[8] P. Gruene *et al.*, Science **321**, 674 (2008).
[9] E. Aprà, R. Ferrando, and A. Fortunelli, Phys. Rev. B **73**, 205414 (2006).
[10] M. P. Johansson, D. Sundholm, and J. Vaara, Angew. Chem., Int. Ed. **43**, 2678 (2004).
[11] X. Gu *et al.*, Phys. Rev. B **70**, 205401 (2004).
[12] Q. Sun *et al.*, Phys. Rev. B **70**, 245411 (2004).
[13] S. Bulusu *et al.*, Proc. Natl. Acad. Sci. U.S.A. **103**, 8326 (2006).
[14] A. F. Jalbout *et al.*, J. Phys. Chem. A **112**, 353 (2008).
[15] Y. Gao and X. C. Zeng, J. Am. Chem. Soc. **127**, 3698 (2005).
[16] D. X. Tian and J. J. Zhao, J. Phys. Chem. A **112**, 3141 (2008).
[17] A. J. Karttunen *et al.*, Chem. Commun. (Cambridge) 04 (2008) 465.
[18] C. R. Henry, Prog. Surf. Sci. **80**, 92 (2005).
[19] G. Barcaro *et al.*, Phys. Rev. Lett. **98**, 156101 (2007).
[20] W. Vervisch, C. Mottet, and J. Goniakowski, Phys. Rev. B **65**, 245411 (2002).
[21] R. Ferrando *et al.*, J. Chem. Phys. **130**, 174702 (2009).
[22] S. Baroni, A. Del Corso, S. de Gironcoli, and P. Giannozzi: http://www.pwscf.org.
[23] J. P. Perdew, K. Burke, and M. Ernzerhof, Phys. Rev. Lett. **77**, 3865 (1996).
[24] See EPAPS Document No. E-PRLTAO-102-020924 for a comparison of PBE results with those of other xc functionals. For more information on EPAPS, see http://www.aip.org/pubservs/epaps.html.
[25] P. Pyykkö, Nature Nanotech. **2**, 273 (2007).
[26] G. Rossi *et al.*, Phys. Rev. Lett. **93**, 105503 (2004).
[27] M. Moseler, H. Häkkinen, and U. Landman, Phys. Rev. Lett. **89**, 176103 (2002).
[28] G. Barcaro and A. Fortunelli, J. Chem. Theory Comput. **1**, 972 (2005).
[29] S. F. Li *et al.*, Angew. Chem., Int. Ed. **44**, 7119 (2005).
[30] Y. Gao *et al.*, J. Phys. Chem. C **112**, 8234 (2008).
[31] M. L. Brongersma, Nature Mater. **2**, 296 (2003).

Surface-supported gold cages - Auxiliary online material

R. Ferrando[a], G. Barcaro[b], and A. Fortunelli[b]

[a] *Dipartimento di Fisica and CNISM,*

Via Dodecaneso 33, Genova, I16146, Italy,

[b] *IPCF/CNR, via G. Moruzzi 1, Pisa, I56124, Italy.*

Here we report the comparison between the results of different gradient-corrected xc-functionals on selected structures of sizes 25 and 32. For size 25, we consider the best compact clusters and the pyramidal open cage. For size 32, also the icosahedral cage is considered. In the Table below we compare PW91 [1], BP86 [2, 3] and BLYP [3, 4] results to those of the PBE [5] functional. All functionals agree in predicting that cage structures prevail over compact structures. Energy differences in favor of cage structures are even larger than for PBE.

TABLE I: Energy differences ΔE (in eV) between cage and compact structures. All values of ΔE are negative, indicating that cage structures are lower in energy than compact structures. The BLYP functional does not even stabilize compact pyramids for size 25, while open pyramids are stabilized.

size	and structure	ΔE PBE	ΔE PW91	ΔE BP86	ΔE BLYP
25	open pyramid	-0.61	-0.74	-0.94	–
32	icosahedral cage	-0.64	-0.76	-1.30	-3.23
32	open pyramid	-1.17	-1.40	-1.69	-3.01

[1] J. P. Perdew, J. A. Chevary, S. H. Vosko, K. A. Jackson, M. R. Pederson, D. J. Singh, and C. Fiolhais, Phys. Rev. B **46**, 6671 (1992).

[2] J. P. Perdew, Phys. Rev. B **33**, 8822 (1986).

[3] A. D. Becke, Phys. Rev. A **38**, 3098 (1988).

[4] C. Lee, W. Yang, and R. G. Parr, Phys. Rev. B **37**, 785 (1988).

[5] J. P. Perdew, K. Burke, and M. Ernzerhof, Phys. Rev. Lett. **77**, 3865 (1996).

Eur. Phys. J. D (2009)
DOI: 10.1140/epjd/e2009-00041-9

THE EUROPEAN PHYSICAL JOURNAL D

Regular Article

Chemisorption of CO and H on Pd, Pt and Au nanoclusters: a DFT approach

L.O. Paz-Borbon[1], R.L. Johnston[1,a], G. Barcaro[2], and A. Fortunelli[2]

[1] School of Chemistry, University of Birmingham, Edgbaston, Birmingham, B15 2TT, UK
[2] Molecular Modeling Laboratory, Istituto per i Processi Chimico-Fisici del Consiglio Nazionale delle Ricerche (IPCF-CNR), via G. Moruzzi 1, 56124 Pisa, Italy

Received 19 September 2008
Published online 13 February 2009 –

Abstract. We have performed a theoretical study of pure metal nanoparticles (Pd/Pt/Au) and their interaction with CO molecules and atomic hydrogen, in order to investigate chemisorption effects of relevance to catalysis by nanoparticles. First-principles density-functional local relaxations are used to investigate the effect of CO and H adsorption on six structural motifs. The results of the energetic crossover and structural deformations are analyzed in terms of the interplay between metal-metal interactions (including internal and surface stress) and CO-metal and H-metal interactions. It is found that H adsorption releases surface stress, thus favoring 5-fold symmetry motifs, whereas CO adsorption produces a flattening of the potential energy surface of the metal clusters.

PACS. 61.46.Bc Structure of clusters – 71.20.Be Transition metals and alloys – 31.15.es Applications of density-functional theory

1 Introduction

One of the important characteristics of nanoparticles is their high surface/volume ratio. This makes them very attractive as catalysts, as most chemical reactions occur at surfaces sites. Moreover, an important difference between studying reactions on a finite cluster rather than on a periodic infinite surface, is that clusters present chemically active coordination sites which are not present on an ideal extended surface. The nature and number of active surface sites vary with particle shape, packing and size. Computational studies of chemisorption of small molecules on such active sites represent a first step towards a deeper understanding of nanoparticle catalysis, and this is the subject of the present work.

This subject has been considered in the literature before. For example, recent DFT calculations on H adsorption on small Pt clusters have shown that dissociative H_2 chemisorption energies and H desorption are strongly coverage dependent, showing a general decrease with increasing hydrogen coverage, with the a-top position preferred over edge or hollow sites [1]. Chen et al. performed DFT calculations on a Pt_6 cluster and its interactions with H_2, finding a preference for a-top positions, sequential dissociative chemisorption of H_2 and that this adsorption is governed by charge transfer effects from the Pt cluster to the hydrogen molecules ($5d/1\sigma^*$ orbital overlap) [2]. For larger clusters, Calvo and Carré have studied the stability of Pd icosahedral and fcc clusters under H adsorption by means of Monte Carlo simulations using empirical potentials. High H concentrations were found to favour fcc structures relative to icosahedral ones, suggesting a structural transition induced by H adsorption [3]. Concerning CO, Feibelman et al. have highlighted the importance of how the different approximations used in DFT theory (e.g. pseudo-potentials, exchange-correlation functional, basis set size) can lead to results in which different adsorption sites are preferred (e.g. the CO/Pt(111) puzzle) [4]. Hvolbæk et al. [5], used a Au_{10} cluster to model the CO oxidation process and showed that low-coordinated Au atoms are able to bind CO and O_2 and that the direct reaction between O_2 and CO is favoured with respect to O_2 dissociation prior to reaction. Neyman and coworkers [6,7] studied the adsorption site-energetics of CO on Pd 1–2 nm particles via DFT calculations, finding results in good agreement with experimental data in UHV. In recent work [8], morphology changes in Au clusters induced by CO adsorption have been predicted. Thus, high-level computational techniques, such as DFT, have been shown to play an important role in understanding the effect of atomic and electronic structure on the chemisorption of small molecules on nanoparticles.

[a] e-mail: r.l.johnston@bham.ac.uk

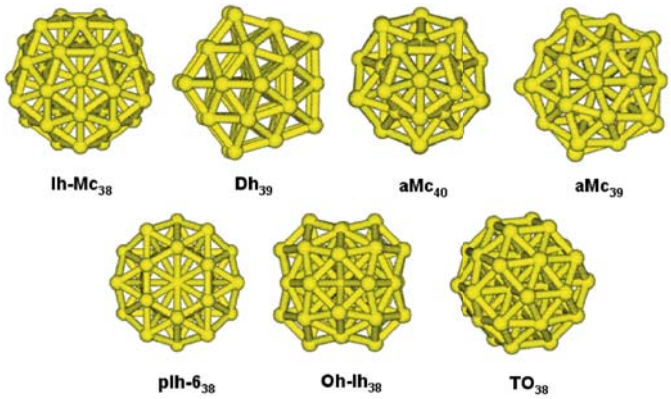

Fig. 1. (Color online) Structural motifs used as models of Pd, Pt and Au clusters (see text for details).

2 Methodology

Six structural motifs for Pd, Pt and Au clusters have been found from a previous thorough investigation [9] to be energetically the most competitive, and are used in this study. These structural motifs, which are shown in Figure 1, can be described as follows: (a) Ih-Mc (38 atoms) is a fragment of a 55-atom Mackay icosahedron; (b) Dh (39 atoms) is an Ino decahedron; (c) aMc (40 and 39 atoms) is a polyicosahedral (anti-Mackay) motif with 5-fold symmetry: aMc_{40} is the original structure [10], while aMc_{39} is a distorted decahedral-type configuration resulting from the local optimization of the aMc_{40} Au cluster which has a single atom protruding out of the cluster tip: the aMc_{39} structure is obtained by removing the segregated atom; (d) pIh-6 (38 atoms) is a polyicosahedral motif with 6-fold symmetry [11]; (e) Oh-Ih (38 atoms) is a hybrid 5-fold-symmetry/close-packed structure [9]; (f) TO (38 atoms) is a truncated octahedron. Note that – to speed up calculations – only motifs with structural shell-closure have been considered.

These structures were fully covered with H or CO adsorbed in a-top positions on all the 32 surface metal atoms, and subjected to local energy minimizations at the DFT level. As some of these structures have different numbers of metal atoms, for a proper comparison of the energetics rescaled energies have been considered, i.e., the **binding energy per atom** for the pure metal clusters and the **interaction energy per adsorbate unit** for the chemisorbed species. For the chemisorbed clusters, the **distortion energy** was also defined as the difference between the energy of the metal cluster relaxed bare and frozen in the configuration obtained after chemisorption.

DFT calculations were performed using the NWChem 5.0 quantum chemistry software package [12] and the PW91 exchange-correlation functional [13]. Computational details were identical to reference [9], with the addition of the basis sets for the light atoms, chosen as standard H $(4s)/[2s]$ and C and O $(8s4p)/[4s2p]$ basis sets for the structural optimizations [14]. After the optimization step, all the energy values to be reported in the following were obtained using a triple-zeta-plus-polarization basis set as in reference [9], with the addition of H $(5s1p)/[3s1p]$ and C and O $(11s6p1d)/[5s3p1d]$ basis sets [14]. All calculations were performed spin unrestricted.

3 Results and discussion

The DFT energy ordering of the structural motifs, before and after chemisorption of 32 CO molecules or H atoms (i.e. full coverage of a-top sites) are compared in Figure 2 for Pd, Pt and Au. One can immediately observe very different qualitative behaviour upon H and CO adsorption, so these will be analyzed separately.

For bare Au clusters, all the structural motifs are rather close in energy, except for pIh-6, which suffers from internal strain [15]. Upon H adsorption, the spread in energy is much increased, with the energy differences between chemisorbed and bare clusters being in the order of $aMc_{39} > \text{pIh-6} \approx \text{Ih-Mc} > \text{Dh} > \text{Oh-Ih} > \text{TO}$. Remembering that fcc Au does not interact favorably with hydrogen (gold is the only metal that does not dissociate the H_2 molecule in macroscopic form), the effect of H adsorption can be easily rationalized in terms of larger interaction for the more exposed (less coordinated or less "fcc-like") sites.

Pt, being a very "sticky" metal, tends to disfavor structures entailing substantial surface stress, such as Ih-Mc or Dh. With respect to Au, it interacts more strongly with hydrogen, see Table 1 (the interaction energies tend to be similar for different motifs). The effect of H adsorption is to increase coordination of surface atoms and to decrease surface stress, thus favouring Ih-Mc and Dh with respect to less strained configurations. This is consistent with the initial favoring of icosahedra with respect to fcc clusters at low H content (occupation of outer sites) in reference [3]. pIh-6 is a different case, because H coordination cannot reduce its internal stress.

Finally, Pd is similar to Pt, but with the difference that, being a less "sticky" metal, the TO structure does not correspond to an ideal shape for Pd, so that it is also significantly stabilized by H coverage.

In contrast to hydrogen, the interaction with CO molecules appreciably changes the cluster potential energy landscape, with non-crystalline structures being stabilized relative to fcc-type motifs. This can be better appreciated by an analysis of distortion energies reported in Table 2. The main effect that one can observe from this table is a much larger (more than doubled) value of the distortion energies for CO with respect to H for Pd and Pt clusters. This is because CO interacts much more strongly with Pd and Pt atoms, via a σ-donation/π-back-donation mechanism [6,8]. Substantial CO coordination, such as considered here (see Fig. 3), thus brings about a partial disruption of the metal-metal bonds and a "flattening" of the potential energy surface of the metal clusters, with energy differences between them reduced to within 2 eV. The behaviour of Au is somewhat different, in that fcc-like structures (TO and Oh-Ih) interact less strongly with CO because of increased coordination and are thus destabilized.

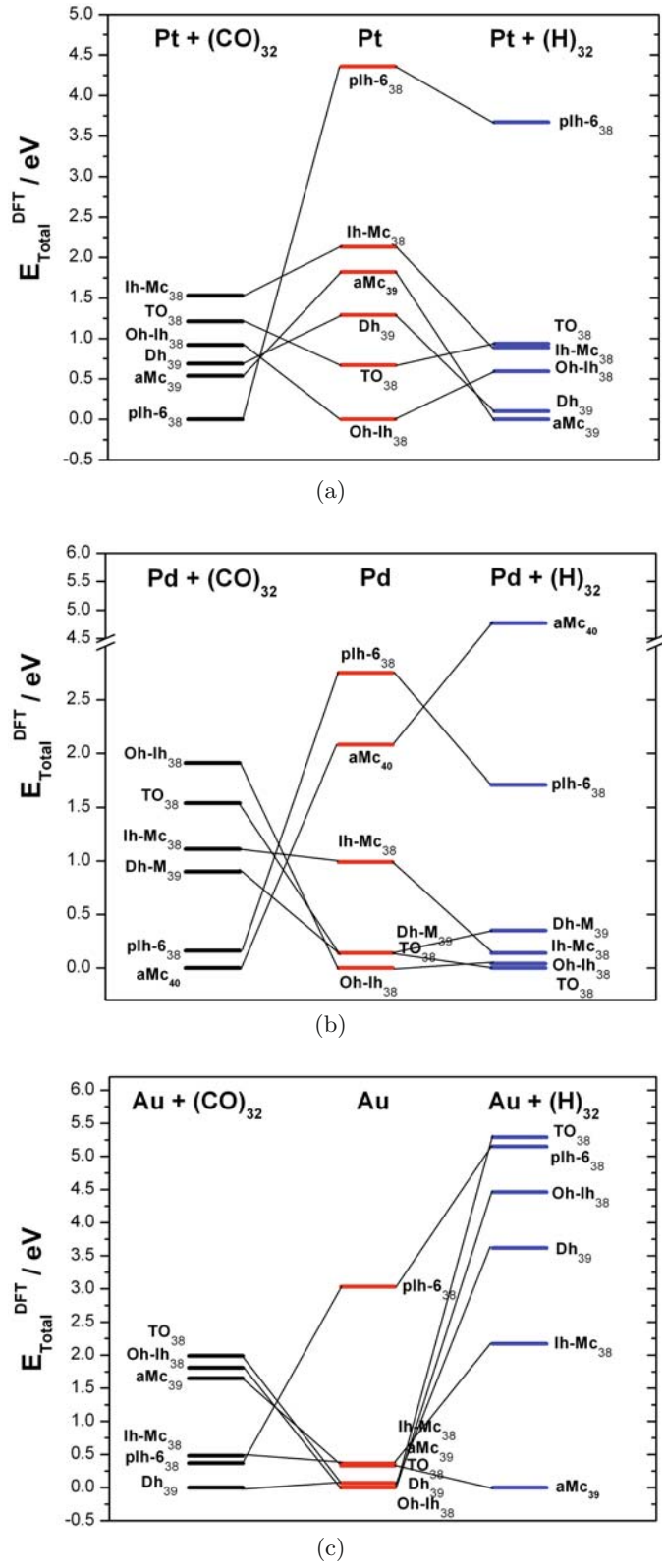

(a)

(b)

(c)

Fig. 2. (Color online) Comparison of relative energies of structural motifs for Pd, Pt and Au clusters before and after a-top chemisorption of 32 CO molecules or H atoms. E^{DFT}_{Total} is rescaled when necessary for 38-atom metal clusters by using the binding energy per atom.

Table 1. Interaction energies (eV) for H/CO adsorption. Dashes indicate SCF failure.

Motif	Pt	Pd	Au
Oh-Ih	–2.67/–1.84	–2.19/–1.42	–1.97/–0.61
TO	–2.68/–1.85	–2.20/–1.43	–1.95/–0.61
Dh	–2.73/–1.89	–2.19/–1.45	–2.00/–0.67
Ih-M	–2.73/–1.89	–2.22/–1.47	–2.01/–0.67
pIh-6	–2.71/–2.01	–2.21/–1.54	–2.04/–0.75
aMc_{40}	–/–	–2.13/–1.56	–/–
aMc_{39}	–2.75/–1.91	–/–	–2.12/–0.63

Table 2. Distortion energies (eV) for H/CO adsorption. Dashes indicate SCF failure.

Motif	Pt	Pd	Au
Oh-Ih	1.52/3.58	0.63/1.36	2.69/1.78
TO	1.04/4.03	0.41/1.42	1.97/2.09
Dh	0.99/3.01	0.48/1.34	1.08/1.56
Ih-M	1.26/3.24	0.57/1.29	2.41/1.51
pIh-6	1.81/3.90	0.16/1.15	1.16/2.07
aMc_{40}	–/–	0.32/1.20	–/–
aMc_{39}	2.01/4.00	–/–	3.58/1.25

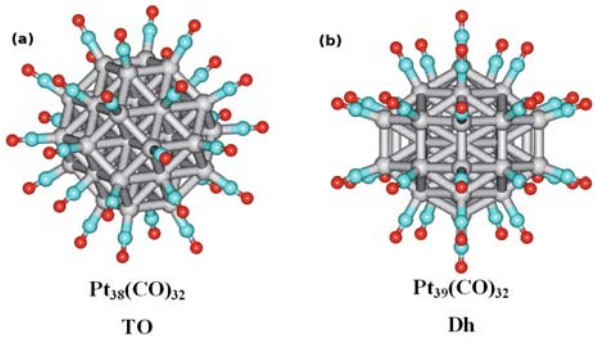

Fig. 3. (Color online) Structures of (a) TO (Pt_{38}) and (b) Dh (Pt_{39}) with 32 CO molecules adsorbed on surface a-top sites.

A more detailed analysis confirms the previous description. The interaction energies per adsorbate unit for the TO, pIh-6 and Dh Pt clusters are plotted against the number of a-top adsorbate ligands in Figure 4 for: (a) CO (only TO and pIh-6 structures) and (b) H adsorption. The choice of adsorption sites (always full occupation of sites equivalent by symmetry) is the following: for TO, 8 (111)-centroid or 24 vertex sites; for Dh_{39}, 10 sites on edges connecting apices to off-axis vertices or 20 off-axis vertex sites; for pIh-6, 6 sites in the equatorial symmetry plane, 12 sites off this symmetry plane (but close to it) or 24 sites consisting of the previous 12 plus 12 sites further from the equatorial plane. In the case of H adsorption, comparing the decahedral (Dh) structure with the truncated octahedral (TO) motif, we notice that the distortion energies are similar, see Table 2. Figure 4b shows that the last 12 H atoms (i.e. going from $Pt_{38}H_{20}$ to $Pt_{38}H_{32}$) allow the structures to relax. The TO structure undergoes a small relaxation of the (111) facets, while the Dh structure undergoes a larger reconstruction, leading to a more rounded shape. It is known that the Dh structure has internal elastic strain: surface Pt coordination allows this strain to be

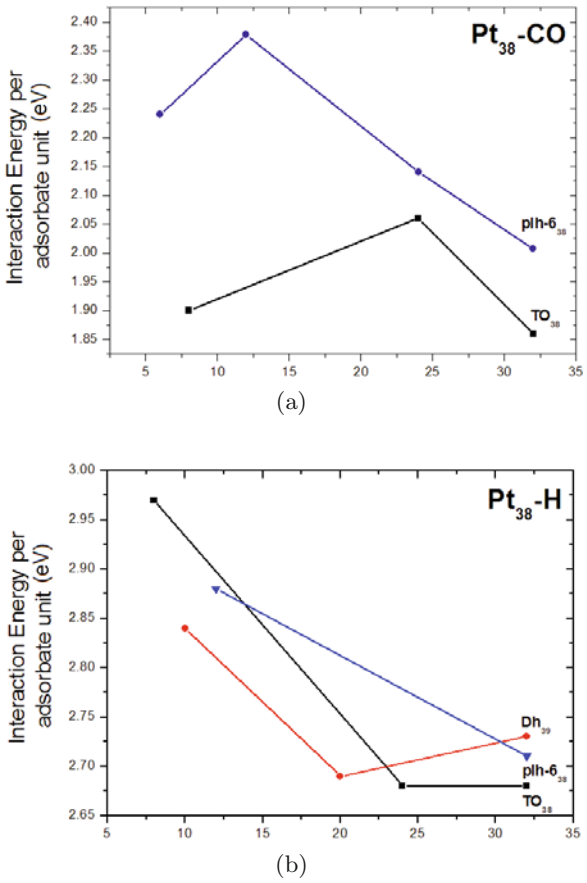

Fig. 4. (Color online) Magnitudes of interaction energies as a function of coverage for three structural motifs of Pt_{38} with (a) CO and (b) H.

released via expansion of the radial Pt–Pt bonds. Similar results have been found for $Pd_{38}H_m$ clusters.

Turning now to CO adsorption, we observe in Figure 4a a smoother behaviour of the ligand interaction energies as a function of coverage, consistent with previous results [6,8]. Moreover, from the structural point of view a significant expansion of the central octahedral core of the TO upon CO adsorption is found, with the Pt–Pt bond length increasing from 2.78 Å to 2.92 Å and a disappearance of the protrusion of atoms on (111) facets, a sign of the decreased importance of directionality effects [15], see Figure 3. For the polyicosahedral (pIh-6) structure, CO adsorption induces a compression along the 6-fold symmetry axis and an expansion in the plane perpendicular to this axis, thereby increasing the eccentricity or oblateness of the cluster. Again, there is an overall inflation of the cluster and a weakening of the metal-metal bonds.

4 Conclusions

The DFT energy ordering of the structural motifs of Pd, Pt and Au clusters of size around 38 is altered by CO and H chemisorption. CO chemisorption is found to induce a "flattening" of the metal cluster PES, however favouring non-crystalline (e.g., polyicosahedral) structures, whereas the effect of H adsorption is mostly connected with the release of surface stress. These findings are in tune with experimental observations of structural changes under catalytic conditions [16–18]. Moreover, these general trends could be further supported by an electronic structure analysis, quantifying, e.g., charge transfer between metal clusters and the adsorpted molecules or the changes in the local density of states of the metal *d*-shells [6,8].

LOPB is grateful to CONACYT (Mexico) for the award of a PhD scholarship. Much of this work was carried out under the HPC-Europa Project (RII3-CT-2003-506079), with the support of the European Community Research Infrastructure Action under the FP6 Structuring the European Research Area Programme. The EPSRC-funded National Service for Computational Chemistry Software (NSCCS http://www.nsccs.ac.uk) is also acknowledged for a 100 000 cpu hour grant to LOPB and RLJ.

References

1. C. Zhou, J. Wu, A. Nie, R.C. Forrey, A. Tachibana, H. Cheng, J. Phys. Chem. C **111**, 12773 (2007)
2. L. Chen, A.C. Cooper, G.P. Pez, H. Cheng, J. Phys. Chem. C **111**, 5514 (2007)
3. F. Calvo, A. Carré, Nanotechnology **17**, 1292 (2006)
4. P.J. Feibelman, B. Hammer, J.K. Nørskov, F. Wagner, M. Scheffler, R. Stumpf, R. Watwe, J. Dumesic, J. Phys. Chem. B **105**, 4018 (2001)
5. B. Hvolbæk, T.V.W. Janssens, B.S. Clausen, H. Falsig, C.H. Christensen, J.K. Nørskov, Nanotoday **2**, 14 (2007)
6. I.V. Yudanov, R. Sahnoun, K.M. Neyman, N. Rösch, J. Chem. Phys. **117**, 9887 (2002)
7. I.V. Yudanov et al., J. Phys. Chem. B **107**, 255 (2003)
8. K.P. McKenna, A.L. Schluger, J. Phys. Chem. C **111**, 18848 (2007)
9. L.O. Paz-Borbón, R.L. Johnston, G. Barcaro, A. Fortunelli, J. Chem. Phys. **128**, 134517 (2008)
10. G. Barcaro, A. Fortunelli, G. Rossi, F. Nita, R. Ferrando, J. Phys. Chem. B **110**, 23197 (2006)
11. G. Rossi, A. Rapallo, C. Mottet, F. Baletto, A. Fortunelli, R. Ferrando, Phys. Rev. Lett. **93**, 105503 (2004)
12. R.A. Kendall, E. Aprà, D.E. Bernholdt, E.J. Bylaska, M. Dupuis, G.I. Fann, R.J. Harrison, J. Ju, J.A. Nichols, J. Nieplocha, T.P. Straatsma, T.L. Windus, A.T. Wong, Comput. Phys. Commun. **128**, 260 (2000)
13. J.P. Perdew, J.A. Chevary, S.H. Vosko, K.A. Jackson, M.R. Pederson, D.J. Singh, C. Fiolhaus, Phys. Rev. B **46**, 6671 (1992)
14. ftp://ftp.chemie.uni-karlsruhe.de/pub/basen/
15. R. Ferrando, A. Fortunelli, G. Rossi, Phys. Rev. B, **72**, 085449 (2005)
16. M.A. Newton et al., Nature Mater. **6**, 528 (2007)
17. J. Evans, M. Tromp, J. Phys.: Cond. Mat. **20**, 184020 (2008)
18. G. Rupprechter, C. Weilhach, J. Phys.: Cond. Mat. **20**, 184019 (2008)

IOP PUBLISHING JOURNAL OF PHYSICS: CONDENSED MATTER

J. Phys.: Condens. Matter **21** (2009) 264001 (12pp) doi:10.1088/0953-8984/21/26/264001

Diffusion of adatoms and small clusters on magnesium oxide surfaces

Riccardo Ferrando[1] **and Alessandro Fortunelli**[2]

[1] Dipartimento di Fisica, Università di Genova, Via Dodecaneso 33, I-16146 Genova, Italy
[2] IPCF/CNR, via G Moruzzi 1, I-56124 Pisa, Italy

E-mail: ferrando@fisica.unige.it and fortunelli@ipcf.cnr.it

Received 30 October 2008, in final form 14 November 2008
Published 11 June 2009
Online at stacks.iop.org/JPhysCM/21/264001

Abstract

The diffusion of isolated adatoms and small clusters is reviewed for transition and noble metals adsorbed on the (001) surface of magnesium oxide. While isolated adatoms diffuse by hopping among adsorption sites, small clusters such as dimers, trimers and tetramers already display a variety of diffusion mechanisms, from cluster hopping to rotation, sliding, leapfrog, walking, concertina, flipping, twisting, rolling and rocking. Since most of the available results are computational, the review is mostly related to theoretical work. Connection to experiments is discussed where possible, mostly by dealing with the consequences that adatom and small cluster mobility may have on the growth of larger aggregates on the MgO(001) surface.

(Some figures in this article are in colour only in the electronic version)

1. Introduction

The adsorption of metals on oxide surfaces has been extensively studied in recent years, especially in the context of the preparation of model nanocatalysts. Among oxide surfaces, the (001) surface of magnesium oxide has received a great deal of attention. Well-defined MgO(001) surfaces can be prepared with a low density of defects [1, 2].

The flat MgO(001) surface presents a perfect checkerboard of alternating oxygen and magnesium atoms. It is believed that most of the defects on this surface are oxygen vacancies (F_s centers), double vacancies (in which a magnesium–oxygen dimer is missing) and steps. When adsorbed on a flat MgO(001) surface, metal atoms preferentially sit on top of oxygen atoms [3]. Defect sites can provide some extra binding [4, 5].

Metals on MgO(001) very often tend to form well-defined three-dimensional aggregates, because the interactions between metal atoms are usually stronger than the interactions between metal atoms and the substrate [1, 6]. The shape of the aggregates depends on a complex interplay between metal–metal and metal–oxide interactions [7–9]. Depending on the metal and on the size of the nanoparticle, fcc structures can be produced in different epitaxies with the substrate, such as cube-on-cube (001) [1, 10] and (111) epitaxy [2, 11], as in the cases of Ag, Au, Pd and Pt. If the mismatch between the bulk metal lattice spacing and the oxygen–oxygen distance is large, as in Ni/MgO(001), even hcp clusters can be produced [12, 9].

A key step for understanding how these aggregates form on the surface is the study of the diffusion of single atoms and small clusters. In fact, their mobility is crucial in determining whether nucleation occurs preferentially at defects or on the flat surface. Fast diffusion causes nucleation at defects only, whereas slow diffusion allows nucleation also on flat terraces.

At variance with metal-on-metal diffusion [13], we do not expect complicated diffusion mechanisms for single atoms, which should simply hop among lattice sites separated by a distance $a = 2.977$ Å. However, for metal-on-metal epitaxy, small clusters are flat, i.e. they are one-layer-thick islands. For metals on MgO, already dimers and trimers may not stay flat on the surface in their lowest-energy configuration [14]. For example, neutral copper, silver and gold dimers prefer to stay vertical on regular MgO(001) terraces [15, 16], even though the situation can be different on ultrathin films, where gold clusters can be charged [17]. Palladium dimers stay horizontal, but already trimers prefer the vertical configuration [14, 18, 19]. Therefore, we expect that small clusters could present a variety of interesting diffusion mechanisms.

In this paper we review the results on the diffusion of isolated adatoms and small metal clusters on the surface of MgO(001). Due to the difficulty of directly measuring diffusion coefficients and of imaging diffusion processes in experiments, most of the available results have been obtained

in the domain of theory and simulations. For this reason, our review will mostly be focused on theoretical results. However, information about the mobility of adatoms and small clusters can be inferred from the effects that such mobility has on quantities that can be more easily measured at the experimental level. When possible, we shall thus compare the predictions that can be inferred from the theoretical results with the experimental observations.

This paper is structured as follows. Section 2 deals with the diffusion of isolated adatoms. Sections 3.1 and 3.2 consider the diffusion of dimers and trimers, while section 3.3 treats the diffusion of tetramers and larger clusters. Section 4 contains the discussion and the conclusions.

2. Diffusion of isolated adatoms

2.1. Energy barriers for diffusion on the flat surface

Isolated adatoms on the flat MgO(001) surface diffuse by *hopping* among oxygen sites, which are the most stable for adsorption. The saddle point for diffusion between neighboring oxygen sites is located at the bridge position, which stays in between two magnesium atoms, as shown in figure 1. This has been demonstrated by nudged elastic band (NEB) [20] calculations for several adsorbed metal atoms, including Pd, Ag and Au at least [18, 19, 16]. The energy barrier E_d for this jump process is thus the difference in adsorption energy between oxygen and bridge positions.

Pd/MgO(001) has probably received the greatest attention, so that several calculations of the diffusion barrier for isolated adatoms on the flat terrace are available in the literature. These calculations are all in the framework of density functional theory (DFT), but differ in some aspects, such as in the choice of the exchange–correlation (xc) functional, in either relaxing or not relaxing substrate atoms, in either using a cluster approach for modeling the surface + adatom system or in using supercells. In spite of the different approaches adopted, the values obtained for this barrier are quite similar to each other, thus reinforcing their validity.

Judai *et al* [21] and then Giordano *et al* [22] performed DFT calculations employing the B3LYP xc-functional [23]. They modeled the surface + adatom system by a clusters approach. They also let the substrate neighbors of the adatom relax. From their calculated adsorption energies at oxygen and bridge sites, one can deduce an energy barrier of 0.41 eV for the adatom hopping process.

Vervisch *et al* [7] and Barcaro *et al* [18] adopted a supercell approach, kept the substrate atoms rigid in their bulk-terminated position, with the experimental value of the MgO lattice parameter, and employed the PBE xc-functional [24]. They obtained a barrier of 0.39 eV, thus differing by only 0.02 eV from the value in [21, 22]. Finally, Xu *et al* [19] also used the PBE functional with a supercell, but let the atoms of the top substrate layer relax. They obtained a somewhat lower barrier, of 0.34 eV. This result shows that the relaxation of the substrate does not introduce major changes in diffusion on the flat surface. As we shall see later, substrate relaxation is more important for processes at defects.

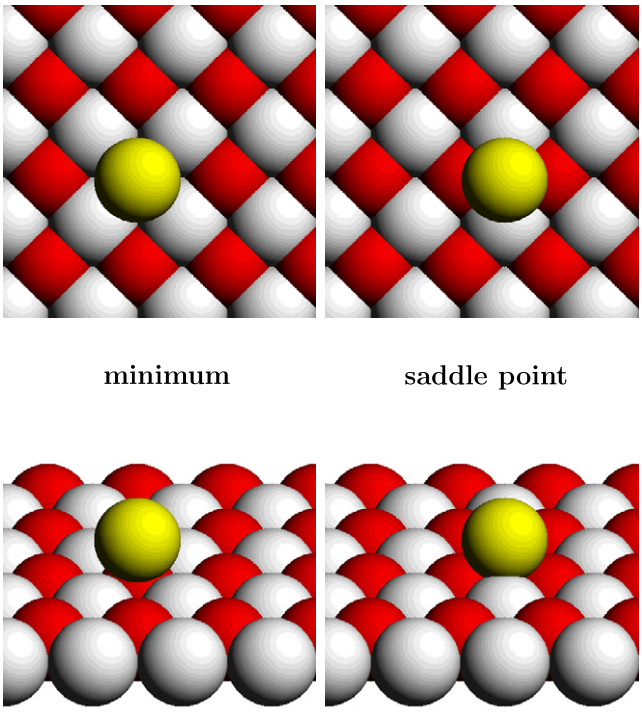

Figure 1. Minimum and saddle point positions for hopping diffusion of metal monomers on MgO(001). In the substrate, red (dark gray) and white (light gray) atoms correspond to oxygen and magnesium, respectively. Each position is shown twice, in top and side views.

The diffusion of noble metal atoms has also received some attention. In a pioneering work: Musolino *et al* [15] performed DFT calculations with the PW91 exchange and correlation functional [25] for copper. They obtained a diffusion barrier of 0.36 eV for Cu adatoms on the flat surface. This is a high barrier, practically of the same magnitude as the hopping barrier of Pd, which has, however, a considerably larger adsorption energy than copper. Barcaro and Fortunelli [16] considered the diffusion of Ag and Au within the same computational approach of [18], i.e. with the PBE xc-functional and a rigid substrate. They obtained barriers of 0.10 and 0.22 eV for Ag and Au, respectively. These barriers are much lower than the barrier for Pd atom hopping, as might be expected from the smaller adsorption energy of Ag and Au compared to Pd. In the case of gold it is known that, by changing the xc-functional, calculated properties may vary significantly [26–33]. For this reason, Barcaro and Fortunelli [16] performed calculations within the local-density approximation (LDA) approach for the xc-functional and obtained a somewhat larger barrier of 0.28 eV. On the other hand, Del Vitto *et al* [34] employed the PW91 xc-functional and obtained a barrier of 0.24 eV by relaxing the substrate. This shows again that relaxation of the substrate has no major effect on the diffusion barriers of transition and noble metals on MgO(001).

A detailed study has recently been conducted on the adsorption and diffusion of small Ca clusters on MgO(100) [35]. A Ca monomer was found to diffuse by hopping between nearest-neighbor oxygen sites with a barrier of 0.45 eV, a sizable fraction of its adsorption energy (0.84 eV),

probably due to the loss of charge transfer interactions at the saddle point (the direction of the charge transfer in Ca/MgO is opposite to the Pd/MgO or noble metal/MgO cases).

It should be stressed that here we are considering neutral atoms on thick MgO(100) terraces. Diffusion of charged species can, in principle, present qualitatively different features. In this connection it can be noted that gold atoms have been shown to become negatively charged on properly selected ultrathin ionic films [36, 37]. To the best of our knowledge, the diffusion of the corresponding polaronic species has not been studied at the computational level, while a systematic investigation of cluster formation as a function of temperature has not yet been conducted at the experimental level, even though preliminary results [38] seem to suggest that diffusion coefficients of single atoms might not be too different from those of neutral atoms on thick substrates.

Finally, we recall that diffusion through hopping of adatoms among favorable adsorption sites has been considered on many other oxide surfaces in addition to MgO(100), usually by calculating static energy landscapes whence diffusion energy barriers, see, e.g., [39–41], or occasionally via NEB calculations [42]. Note that the presence of adsorbed species can strongly influence the mobility of metal adatoms, and thus cluster sintering, as shown experimentally for Pd carbonyl-like species on an ultrathin silica film [43].

2.2. Long jumps of isolated adatoms

An interesting issue concerning the diffusion of isolated metal adatoms on MgO(001) (and possibly also on other non-polar oxide surfaces) is the possible occurrence of long jumps. In a long jump, the adatom starts from a given adsorption site, travels on the surface and finally thermalizes in a site which is not a nearest neighbor of the site of departure [44, 13, 45, 46]. Long jumps have been observed in the case of metal-on-metal diffusion for several systems [47–51] and also in the diffusion of small and large molecules on metal surfaces [52, 53]. In general, long jumps are favored by a weak dynamic coupling between the substrate and the diffusing adatom, which indeed might be the case of metals on oxides. Let us try to evaluate quantitatively the probability of long jumps for Pd, Ag and Au adatoms.

The MgO(001) substrate is very rigid compared to the above-mentioned metals. For example, the melting temperature of MgO is above 3000 K, while melting temperatures of the adsorbed metals are much lower, from 1235 K (Ag) to 1828 K (Pd). Therefore the typical phonon frequencies of MgO are quite high. In contrast, the frequencies related to the frustrated translations of the adatom on the surface are significantly smaller [19]. This should rule out memory effects in diffusion [54, 13], because the latter are expected to be important when substrate and adatom frequencies are close to each other. This allows the treatment of diffusion within a simple Langevin approach, in which the dynamic coupling between adatom and substrate is described by a simple friction parameter η, which, together with the temperature, determines also the magnitude of the white noise caused by the substrate [55].

The friction η can be decomposed into the sum of a phononic contribution $\eta_{\rm ph}$ and an electronic contribution $\eta_{\rm el}$. The latter is essentially due to the possible creation of electron–hole pairs in the substrate [56]. Due to the insulating nature of the substrate, this process is very unlikely, so that $\eta_{\rm el}$ should be very small, negligible with respect to $\eta_{\rm ph}$. The phononic friction can be easily evaluated by a simple formula which holds for a harmonic substrate, as MgO is expected to be for the temperatures of interest in growth experiments, which are much lower than its melting temperature. The formula for $\eta_{\rm ph}$ follows from an elastic continuum model treatment of the substrate and is [57]

$$\eta_{\rm ph} = \frac{3m}{8\pi\rho}\left(\frac{\omega_{\rm osc}}{c_{\rm T}}\right)^3 \omega_{\rm osc}, \tag{1}$$

where m is the mass of the adatom, $\omega_{\rm osc}$ is the frequency of the frustrated translation of the adatom, ρ is the mass density of the substrate and $c_{\rm T}$ is the transverse sound velocity in the substrate. According to equation (1), $\eta_{\rm ph}$ does not depend on temperature, and this should hold as far as anharmonic effects are negligible. However, within the Langevin model, and assuming that jumps essentially follow straight lines [44] (i.e. assuming that the motions in different directions are uncoupled [58]), the probability of long jumps depends on the dissipation parameter Δ [59, 44, 60, 61], which can be evaluated as

$$\Delta = \eta_{\rm ph}\frac{2\sqrt{2}a}{\pi k_{\rm B}T}\sqrt{mE_{\rm d}}. \tag{2}$$

The dissipation Δ is dimensionless and corresponds to the ratio between the energy loss in crossing a single lattice spacing and the thermal energy $k_{\rm B}T$.

Let us discuss the occurrence of long jumps in Pd, Au and Ag on MgO(001).

In the case of Pd, from the model potential of [7] it follows that $\omega_{\rm osc} = 8.76 \times 10^{12}$ rad s^{-1}. Taking $c_{\rm T} = 6.62 \times 10^3$ m s^{-1} [62, 63] and $\rho = 3.5761 \times 10^3$ Kg m^{-3}, one obtains $\eta_{\rm ph} = 1.25 \times 10^{11}$ s^{-1}. This value of the friction is rather low and leads to small dissipation Δ. For example, taking $E_{\rm d} = 0.39$ eV [18], $\Delta = 8.6 \times 10^{-1}$ at $T = 300$ K. Such a value of the dissipation leads to a significant percentage of long jumps [64]. In fact, the model predicts that about 45% of jumps should be long, so that only 55% of the jumps ends in a nearest-neighbor cell. On the other hand, at $T = 200$ K, $\Delta = 1.3$, with a fraction of long jumps of about 40%. This leads to a mean square jump length $L^2 \sim 10a^2$. This might have some consequences on the magnitude of the diffusion coefficient D, because the latter is given by

$$D = rL^2 \tag{3}$$

where r is the jump rate in a given direction. The latter assumes the usual Arrhenius form:

$$r = \nu \exp\left(-\frac{E_{\rm d}}{k_{\rm B}T}\right), \tag{4}$$

where ν is the frequency prefactor, which is often estimated by the transition state theory (TST) [65]. However, TST strongly

overestimates r at low friction, where an energy diffusion regime holds. In the case of Pd, we expect TST to overestimate r by at least a factor of 5.

For Ag, the interaction potential is less corrugated [16, 66], so that $\omega_{\rm osc} = 4.66 \times 10^{12}$ rad s^{-1}, which, according to equation (1), leads to a much smaller friction, $\eta_{\rm ph} = 9.77 \times 10^9$ s^{-1}, than for Pd. At $T = 300$ K, with $E_{\rm d} = 0.10$ eV [16], $\Delta = 3.4 \times 10^{-2}$, corresponding to a percentage of long jumps of about 90% [64]. At $T = 200$ K, $\Delta = 5.2 \times 10^{-2}$, so that the percentage of long jumps slightly decreases to about 85%. Therefore, the diffusion of single Ag atoms almost completely occurs by long jumps down to very low temperatures, with large percentages of them well below 100 K.

For Au, the interaction potential has intermediate corrugation [16, 66], but the atomic mass is larger, giving $\omega_{\rm osc} = 3.69 \times 10^{12}$ rad s^{-1}, which, according to equation (1), leads to an even smaller friction, $\eta_{\rm ph} = 6.99 \times 10^9$ s^{-1}, than the friction of Ag. However, mass and corrugation compensate for the lower friction when comparing with Ag. In fact, at $T = 300$ K, with $E_{\rm d} = 0.22$ eV [16], $\Delta = 4.9 \times 10^{-2}$, corresponding to a percentage of long jumps close to 85% [64]. At $T = 200$ K, $\Delta = 7.4 \times 10^{-2}$, so that the percentage of long jumps is nearly 80%. As in Ag, diffusion of single Au is thus expected to be dominated by long jumps down to very low temperatures.

We note that we assumed that all jumps occur in straight lines. This is not true in a multidimensional coupled potential [67, 58], in which there is energy transfer between the x, y and z degrees of freedom of the adatom. This energy transfer decreases the percentage of long jumps [58]. According to the model interaction of [7], the coupling between the directions is, however, not strong. Therefore our values of the long jump fraction may be overestimated, but not by a large amount, so that a non-negligible fraction of long jumps should be expected for Pd, Au and Ag on MgO(001).

In the low-friction regime, the jump-length probability distribution of single atoms displays deviation from the exponential decay behavior for short jump distances, while the exponential decay is recovered asymptotically [44]. This rules out the possibility of anomalous diffusion for single adatoms. Anomalous diffusion may occur for larger clusters, which may diffuse by a stick and slip mechanism [68].

Finally we remark that long jumps should be taken into account when calculating the prefactor for adatom diffusion of Pd, Ag and Au. In the case of Pd, the increase of the prefactor due to long jumps is partially compensated by the decrease of the jump rate, so that major effects are not expected. However, for Ag and Au dissipation is considerably weaker and the effect should be more important. In fact, in the limit of $\Delta \ll 1$, the jump rate r decreases as Δ, but $L \propto \Delta^{-2}$, with an increasing effect on the prefactor as follows from equation (3).

2.3. Diffusion in the presence of defects

The influence of defects, such as steps and point defects, on diffusion is crucial for understanding the nucleation, growth and phase ordering of adsorbates on crystal surfaces [69–71] in general. In the case of metals on oxides this is even more crucial, since nucleation is often occurring at defects only [72].

The adsorption of Pd, Rh and Ag atoms on steps, edges and corners of MgO has been studied by Judai *et al* [21] and Giordano *et al* [22]. It has been found that oxygen ions are still the preferred adsorption sites for these defects, and that decreasing oxygen coordination usually results in an increase of the metal binding energy to these sites. It can thus be expected that diffusion is inhibited in the presence of these defects, and that they act as trapping and nucleation centers for the growth of metal clusters, as suggested, for example, by the experimental observation of the nucleation of Pd particles along MgO(100) steps [1, 2]. However, it should also be noted that (i) a substantial increase of the binding energy was only observed for Rh atoms adsorbed on steps (about 2 eV instead of about 1 eV on the regular surface) and (ii) real diffusion mechanisms with the corresponding energy barriers and Arrhenius prefactors were not studied explicitly, so that nucleation at such defects might depend on the experimental conditions. A detailed study has instead been conducted for Ca/MgO(100) by Xu and Henkelman [35]. In addition to a rough doubling of the binding energy of Ca atom to steps with respect to flat terraces, it has been found that Ca monomers do not readily diffuse along steps: according to the predicted lowest-energy-barrier mechanism, a Ca atom first leaves the step by crossing a barrier of 1.4 eV to an oxygen site near the step and then hops back to the next site on the step. Steps thus act as strong traps for Ca atoms. Note that, on a different oxide surface, a step-edge (Ehrlich–Schwoebel) barrier has been invoked to rationalize the experimental evidence of increased nucleation at island borders and constant nanoparticle size as a function of coverage [42].

A vast literature exists on the interaction of metal atoms and small clusters with point defects such as the (charged and neutral) oxygen vacancy and the MgO dimer vacancy. It has been shown both theoretically (see, e.g., [73–76] and references therein) and experimentally (see, e.g., [77, 78]) that these defects can act for most metals and cluster sizes as trapping centers, with binding energies for single atoms that can easily surpass 2–3 eV. As far as growth is concerned, the question thus becomes to quantify the detrapping energy barriers corresponding to the dissociation of pieces of clusters adsorbed on the defect (fragmentation). These processes are believed to be the basic mechanisms by which Ostwald ripening and then sintering takes place. A lower bound to fragmentation energy barriers can be derived from the difference between cluster binding energies at defects and on the regular surface. For small clusters, such quantities can be found in several publications for different metal/defect combinations, see, e.g., [79, 4, 80–86, 76, 87, 35]. For Ag clusters on a single oxygen vacancy, due to the peculiar stability of Ag_2 on the regular surface, the lowest-energy fragmentation process consists in the detachment of a dimer from a larger metal aggregate. The energy associated with this process was found to grow in an approximately monotonic way with the cluster size from 0.77 eV (the value for Ag_3 fragmentation) to 1.6 eV (the value for Ag_{10} fragmentation). A similar behavior was found for Au clusters adsorbed on a single oxygen vacancy, for which fragmentation of a dimer was equally found to be favored (even though with obviously

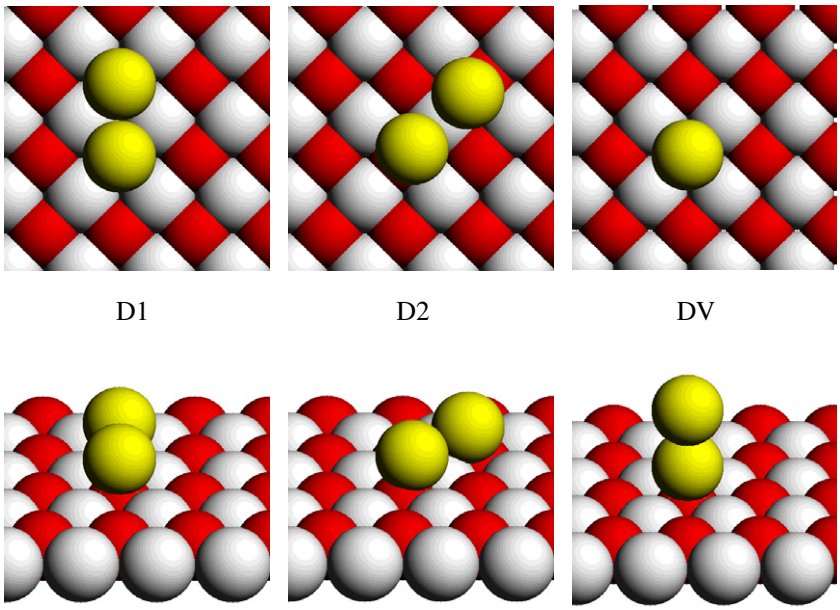

Figure 2. Positions D1, D2 and DV (see text) for dimers on MgO(001). In the substrate, red (dark gray) and white (light gray) atoms correspond to oxygen and magnesium, respectively. Each position is shown twice, in top and side views.

different actual values). On the double vacancy, however, the presence of a magic cluster for size $N = 8$ makes that for $N = 9$ the dissociation of a single atom is definitively favored [86], while this is not observed for Au clusters on the same defect due to the lack of magic numbers [87]. In general, dissociation energy differences present a non-monotonic behavior in correspondence with magic clusters and this holds also for binary clusters [85, 76]. The situation is different for the fragmentation of Pd clusters adsorbed on the single vacancy, as a Pd dimer is only marginally stable on the flat terrace or on the oxygen vacancy defect with respect to dissociation into monomers, so that fragmentation of a monomer or of larger clusters, leaving a single Pd atom adsorbed on the defect, can be expected. It should be remarked, however, that the actual barriers can be larger than the static differences between cluster binding energies at defects and on the regular surface, as the dissociating fragment may be forced to pass through unfavorable routes in which contact to the surface (and thus adhesion energy) is lost. To our knowledge, the only example of a full calculation is given in [86] for the '$Ag_9 \rightarrow Ag_8 + Ag$' fragmentation, a special case in which anyway no significant additional barrier was found.

3. Diffusion of dimers, trimers and tetramers

3.1. Dimers

A metal dimer on the MgO(100) surface exhibits basically three local minima: one in which the dimer axis is perpendicular to the surface and the basal atom stands on top of an oxygen ion (DV), one in which the dimer axis is parallel to the surface with two metal atoms on nearest-neighbor oxygen atoms (D1) and one in which the dimer axis is parallel to the surface with the metal–metal bond across a magnesium ion (D2), see figure 2. Depending on the relative energetics of these three states one finds different diffusion mechanisms.

For Pd, D1 and D2 are about 1 eV lower in energy than DV and the diffusion takes place via a *rotation* between D1 and D2 involving the motion of one atom at a time, resulting in an intermediate state with an elongated Pd–Pd bond. The weakness of this bond due to intersystem crossing between the d^{10} and d^9s^1 atomic configuration of the Pd atom facilitates this mechanism, even though it should be noted that the Pd–Pd distance is contracted with respect to the distance between oxygens and the spin state is a singlet and not a triplet as in the gas-phase species (the metal/surface interaction is often found to quench the cluster spin moment [88]). The barrier for this mechanism is 0.43 eV [19, 83] or 0.39 eV [18] and its Arrhenius prefactor is 2.5×10^{11} s^{-1} [19, 83]. Another mechanism involves a concerted *sliding* of the dimer along [110] directions with an energy barrier of 0.60 eV or a dissociation into two monomers with an energy barrier of 0.80 eV [19, 83].

For noble metal atoms, we found an opposite situation with the energy ordering: DV < D1 < D2, due to the 'metal-on-top' stabilization mechanism [5]. For Cu, the energy difference between the DV and D1 configurations, ΔE (DV–D1), is 0.04 eV [15] or 0.28 eV [5] (this is one of the rare cases in which we find a significant discrepancy between calculations using similar xc-functionals but different computational methods). Accordingly, the Cu_2 dimer can diffuse, either remaining in the DV configuration and hopping between nearest-neighbor oxygen sites with a barrier of 0.56 eV, or via a *leapfrog* [89] mechanism in which DV rotates into D1 that in turn rotates back into a DV on a nearest-neighbor site with a barrier of 0.17 eV [15]. Even taking into account discrepancies in the calculation of ΔE (DV–D1), the final energy barrier for this mechanism should not be larger than 0.4 eV, and thus comparable with that of the monomer. For Ag, ΔE (DV–D1) is 0.22 eV and Ag_2 can diffuse either via dimer hopping with a barrier of 0.25 eV or via a leapfrog

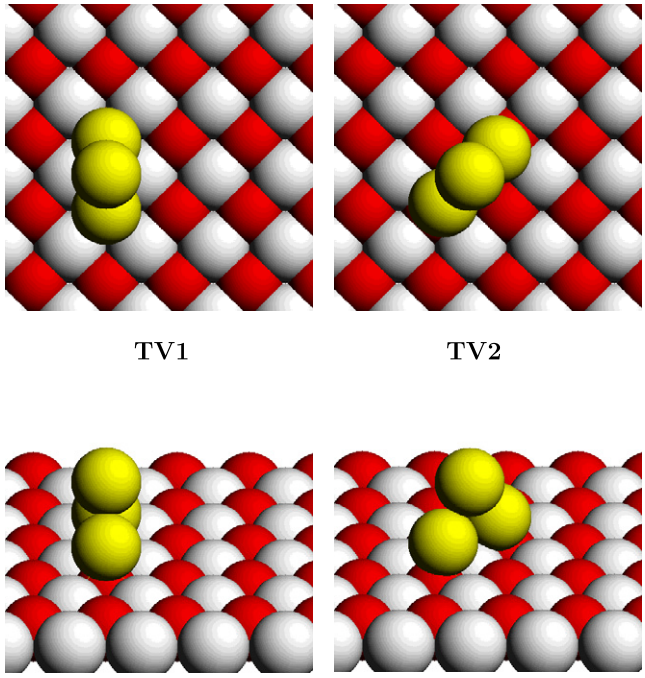

Figure 3. Positions TV1 and TV2 (see text) for vertical trimers on MgO(001). In the substrate, red (dark gray) and white (light gray) atoms correspond to oxygen and magnesium, respectively. Each position is shown twice, in top and side views.

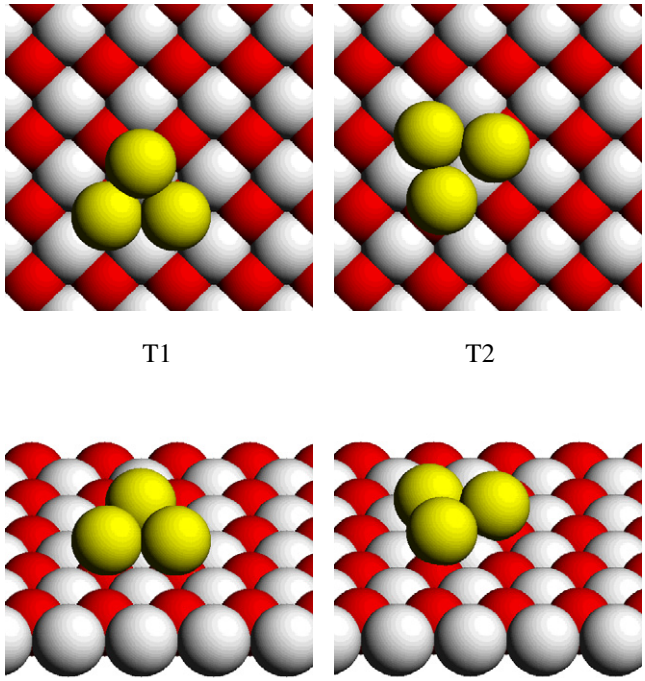

Figure 4. Positions T1 and T2 (see text) for flat trimers on MgO(001). In the substrate, red (dark gray) and white (light gray) atoms correspond to oxygen and magnesium, respectively. Each position is shown twice, in top and side views.

mechanism with a barrier of 0.22 eV, practically coincident with ΔE (DV–D1) [16]. Analogously for Au ΔE (DV–D1) is 0.87 eV and Au_2 can diffuse either via dimer hopping with a barrier of 0.62 eV or via a leapfrog mechanism with a barrier that has not been calculated explicitly but must be larger than 0.87 eV, i.e. the ΔE (DV–D1) energy difference [16]. We thus find that in the Ag and Au cases the dimer, although not epitaxial, has diffusion energy barriers appreciably larger than the monomer.

A still different case is that of an alkali-earth element such as Ca. In this case, the Ca_2 bond is really weak. The maximum adsorption energy (0.88 eV/atom) is achieved in the D2 configuration and is only marginally stable than the sum of two Ca monomers (0.84 eV), while the D1 configuration has an adsorption energy of 0.78 eV/atom and is thus metastable. Ca_2 in the D2 configuration can either diffuse via rotation to D1 with a barrier of 0.50 eV or via dissociation into monomers with a barrier of 0.30 eV, and thus with a mobility comparable with that of a monomer.

3.2. Trimers

A metal trimer on the MgO(100) surface exhibits at least five local minima: a linear one with a metal atom on top of an O ion and the other two atoms along a [110] direction (L); two vertical ones (see figure 3), in which the trimer is adsorbed in an upright position and the cluster plane can be either oriented along a [110] direction with the two basal metal atoms on top of nearest-neighbor oxygen ions (TV1) or oriented along a [100] direction with the two basal metal atoms pointing towards two next-nearest-neighbor oxygen ions and a magnesium atom beneath the center of mass of the cluster (TV2); and finally two flat ones, in which the cluster plane is lying on the surface and two metal atoms can either be adsorbed on top of nearest-neighbor oxygen ions while the third one points towards a magnesium ion (T1) or can be across a magnesium ion while the third one sits on an oxygen ion (T2), see figure 4. The diffusion mechanisms again depend on the relative energetics of these five configurations.

The metal-on-top effect stabilizes upright configurations with respect to planar ones for both Pd and noble metal trimers. The lowest-energy minimum is TV1, with TV2 higher in energy by 0.19–0.27 eV for Pd [18, 19, 83], 0.15–0.25 eV for Cu [15, 5], 0.01–0.06 eV for Ag [5, 16] and 0.12–0.14 eV for Au [5, 16]. The T1 planar configuration lies higher in energy: the TV1–T1 energy difference is 0.28 eV for Pd [19, 83], 0.50–0.56 eV for Cu [15, 16] and 0.24 eV for Ag, while it is not even a local minima for Au [5] (T2 is even higher in energy for Pd: 0.44 eV [19, 83]). Cu is the only metal for which the linear configuration is competitive with the planar ones, being 0.33 eV higher than T1 [15]. The upright character of the lowest-energy structures, added to the fluxional character of the trimer for these metals, i.e. the possibility of stretching metal–metal bonds due to their anti-bonding components, makes that trimer diffusion on MgO(100) is facile.

In particular, for Ag and Au the metal-on-top effect stabilizes the upright configurations so much that TV1–TV2 rotation or trimer *walking* represents by far the lowest-energy mechanism, with barriers of 0.12 eV for Ag and 0.19 eV for Au [16], i.e. fully comparable to those of the monomers. For Cu, the barrier for trimer walking was not calculated in [15], but a different *concertina* mechanism was found in which the

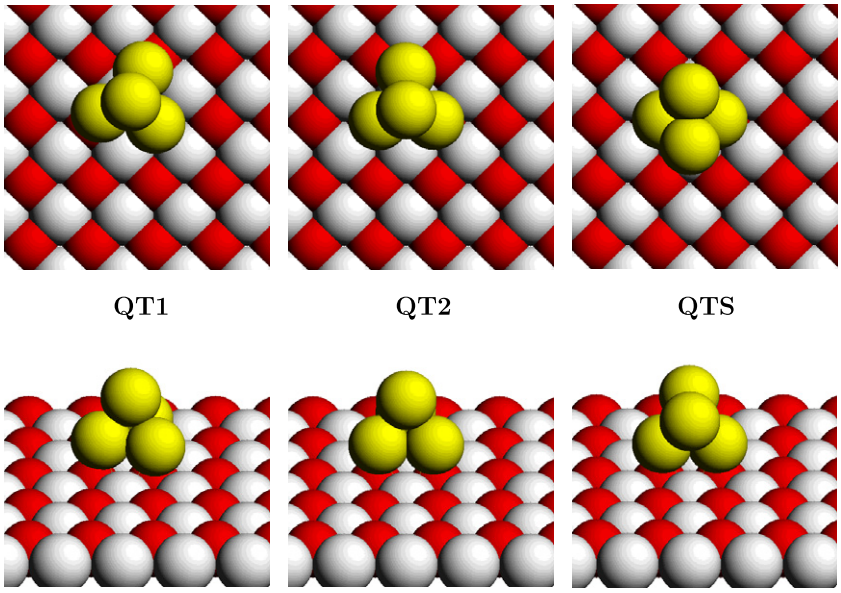

Figure 5. Positions QT1, QT2 and QTS (the latter is a saddle point configuration, see text) for tetrahedral tetramers on MgO(001). The diffusion of Pd tetrahedra takes place through the sequence QT1 → QT2 → QTS → QT2 → QT1 and so on. In the substrate, red (dark gray) and white (light gray) atoms correspond to oxygen and magnesium, respectively. Each position is shown twice, in top and side views.

top atom of TV1 moves down to a surface oxygen to form an L configuration and then the Cu atom at the other end of the line moves up to form a TV1 triangle displaced by one lattice unit. The barrier for this process was found to be 0.50 eV. For Pd, instead, the metal-on-top effect is less important and the situation is more varied. TV1–TV2 rotation still represents a low-energy mechanism with a barrier of 0.30 [18] or 0.48 and a prefactor of 5.4×10^{10} s^{-1} [83] eV. However, there is a *flipping* mechanism in which the top atom of TV1 flips down to the surface forming T1, from which a different atom can lift onto the other two, forming TV1 in a different location. According to [19, 83], the barrier for this process is 0.50 eV, but its prefactor is much larger than the walking mechanism: 1.1×10^{13} s^{-1} so that it is expected to dominate at high (and even low) temperatures. Flat trimers can also diffuse but with high barriers (at least 1–1.4 eV) [83].

For Ca, the lowest-energy trimer configurations are flat, but their adsorption energy is smaller than three times the monomer adsorption energies, so that they represent metastable states [35].

3.3. Tetramers and larger clusters

Four local minima are mostly involved in the diffusion mechanisms of metal tetramers studied in the previous literature: two tetrahedral arrangements lying on the surface with three contact atoms in which the basal atoms are either positioned as in the T2 configuration (QT1) or as in the T1 configuration (QT2) (see figure 5), and two vertical arrangements, in which the cluster has a rhomboidal shape, interacts with the surface through two basal atoms and the cluster plane is either oriented along the [100] direction (QV1) or the [110] direction (QV2), see figure 6.

For Pd, the tetrahedral structures QT1 and QT2 (with QT1 being the absolute minimum) are lower in energy than flat configurations by more than 1 eV [83] (and are also lower in energy than vertical configurations). The latter thus do not have a role in tetramer diffusion, which occurs via a *rolling* mechanism involving tetrahedral configurations only. QT1, in fact, first transforms into QT2 by a small-angle rotation around a vertical axis, after which QT2 rotates around a horizontal axis passing through the two Pd atoms positioned on top of the oxygens (this is the saddle point configuration QTS in figure 5) ending up in a different QT2 configuration displaced by one lattice spacing with respect to the initial one [18, 19, 83]. From this position, another small-angle rotation can produce a new QT1 configuration. The barrier for this sequence of moves is 0.38 eV [18] or 0.42 eV and a prefactor of 1.3×10^{14} s^{-1} [19, 83]. An identical mechanism is effective for Ca_4 diffusion on MgO(100), in which case the energy barrier is only 0.12 eV, an absolute minimum among the barriers involving small Ca clusters [35]. QT1 can also diffuse by sliding with a global barrier of 0.45 eV [18] or 0.51 eV and a prefactor of 1.0×10^{13} s^{-1} [19, 83], but this mechanism is not favored with respect to tetramer rolling.

A weaker metal/surface interaction favors vertical arrangements (QV1 and QV2) with respect to compact ones (QT1 and QT2) for noble metal clusters, thus giving rise to quite different diffusion mechanisms. Actual values for energy barriers and prefactors were not calculated for Cu_4 on MgO in [15], but snapshots from Carr–Parrinello simulations were reported, showing planar arrangements not heavily linked to the substrate, and it was pointed out that the observation of diffusion at low temperature (100 K) and in short runs (a few ps) implied that diffusion barriers are quite small for this system, of the same order as those of the dimer and thus smaller than the barriers for the monomer and trimer. In this system metal bonding prevails and Cu_4 diffuses via *twisting* mechanisms in which an adatom first detaches from the

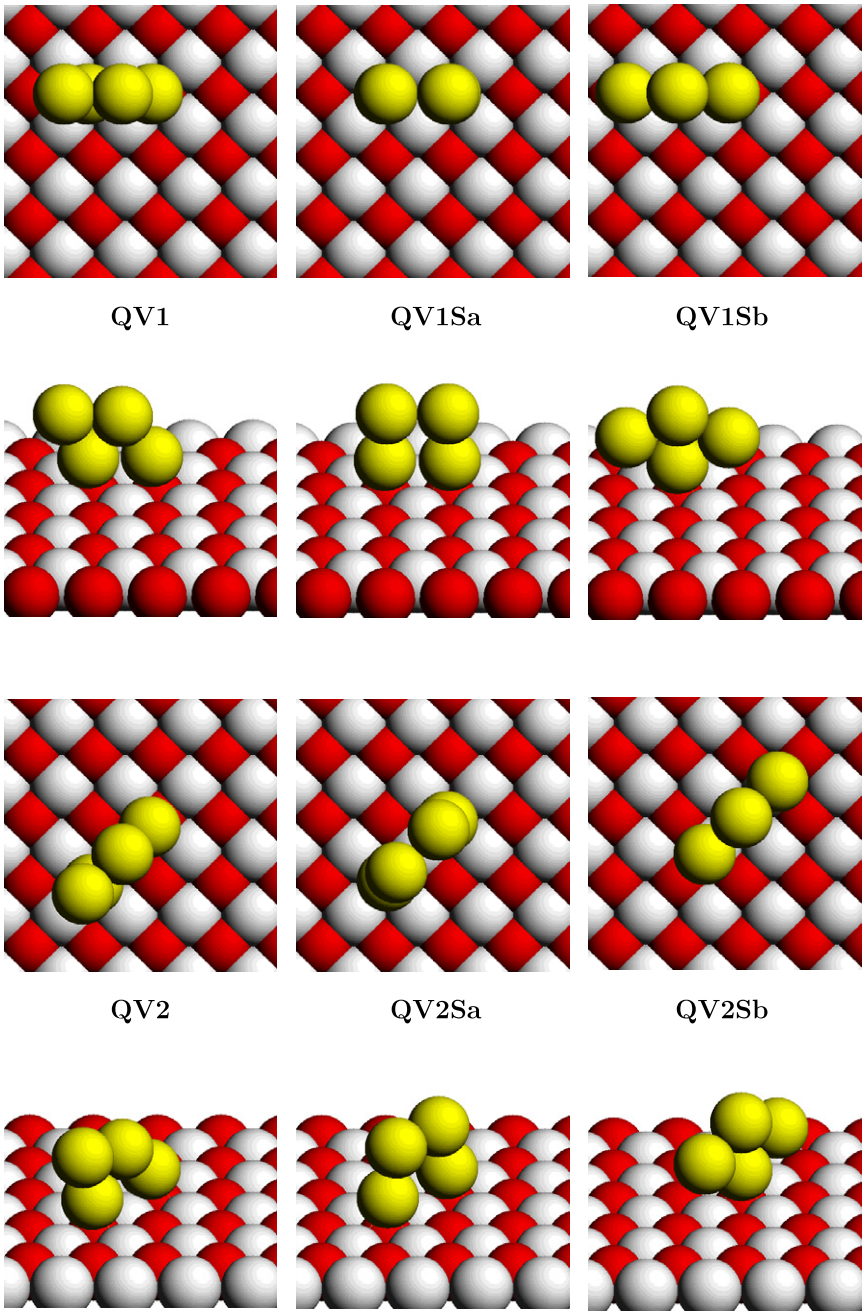

Figure 6. Positions QV1, QV1Sa, QV1Sb, QV2, QV2Sa and QV2Sb (see text) for vertical tetramers on MgO(001). QV1 and QV2 are minimum positions, whereas QV1Sa, QV1Sb, QV2Sa and QV2Sb are saddle point positions. In the substrate, red (dark gray) and white (light gray) atoms correspond to oxygen and magnesium, respectively. Each position is shown twice, in top and side views.

surface, rotates around a 'pivot' adatom which remains bonded to the surface, and finally readsorbs in a different position on the surface. A more detailed analysis was conducted for Ag and Au in [16]. It can be noted that for both metals the tetramer is a closed-shell system with a reduced fluxional character with respect to the trimer. However, silver and gold presents subtle differences, despite their similarities, in the energetics of their local minima and thus of their diffusion behavior. To begin with, QV2 is found as the global minimum for Au, with QV1 at a slightly higher energy (ΔE of 0.15 eV), whereas QV1 is the global minimum for Ag, with QV2 at a slightly higher energy ($\Delta E = 0.04$ eV). Moreover, the diffusion of Ag and Au tetramers can take place through a variety of mechanisms, which are different in the two cases. One possibility is represented by a movement of tetramer walking between configurations QV1 and QV2, a movement analogous to trimer walking. The difference with respect to the trimer is that the rotation of 45° can take place either around the vertex at higher coordination or around the vertex at lower coordination: the two movements have different barriers as it is energetically less costly to move the basal atom with lower coordination with respect to the basal atom with higher coordination, because the

former loses less metal-on-top or metal-bonding stabilization energy. In the case of gold, the values of the two energy barriers are 0.38 and 0.60 eV, respectively; in the case of silver 0.10 and 0.21 eV. Since a tetramer needs both movements for real diffusion (a single rotation does not allow the cluster to leave an area of four first-neighbor oxygen sites) the real value of the barrier is thus 0.60 eV for gold and 0.21 eV for silver. Therefore, despite the similarities between the walking mechanisms in the trimers and tetramers, the need to move an atom with higher coordination makes the diffusion energy barrier for the tetramer higher than that for the trimer. However, while in the case of silver the tetramer walking mechanism corresponds to the diffusion mechanism with the lowest barrier, in the case of gold other processes have a lower activation energy. The QV2 configuration, in fact, can move along the [100] direction to another QV2 configuration through a first *rocking* mechanism, i.e. passing through the saddle point QV2Sa—barrier of 0.39 eV—and then through a *rolling* mechanism, i.e. passing through the saddle point given by the configuration QV2Sb—barrier of 0.44 eV. This rolling movement (to be distinguished from the qualitatively different movement of the tetrahedron) consists of revolving the cluster around the most coordinated atom in direct contact with the surface. The combination of these two movements determines a diffusion of the tetramer along the [100] direction; the barrier is given by the higher value between the two values found: 0.44 eV. Still another possibility is that QV2 first rotates into QV1 through the first step of the walking mechanism, and that QV1 then diffuses through successive rocking/rolling movements along the [110] direction in a way completely analogous to the diffusion of QV2 along the [100] direction. A QV1 configuration thus rocks into another QV1 configuration through the saddle point QV1Sa—barrier of 0.27 eV—and rolls into another QV1 configuration through the saddle point QV1Sb—barrier of 0.25 eV. The barrier for this mechanism is given by the sum of the energy difference between QV2 and QV1—0.15 eV—and the higher of the two rocking/rolling barriers—0.27 eV—for a total of 0.42 eV. The rocking/rolling processes in the two directions are thus energetically equivalent and both very favorable with respect to the walking mechanism. These rocking/rolling movements are not competitive in the case of silver because they pass through the saddle points QV1Sa and QV2Sa which present a remarkable distortion of the metal bonding, a distortion not compensated by an enhanced direct adhesion to the surface nor by the metal-on-top effect.

To conclude this section, we recall that the mobility of large metal clusters on MgO(100) is a fascinating subject which, however, has not yet been investigated at the computational level. Experimental observations as well as theoretical simulations on different (especially non-epitaxial) systems indicate that large aggregates can be mobile under given conditions [90–93]. Experiments seem to suggest that similar phenomena can occur also on oxides, see, e.g., [94, 95] (and references therein), where surface diffusion rather than static coalescence has been invoked to rationalize observed power-law behavior of the growth of Pt nanoclusters on MgO(100) and Au nanoclusters on $TiO_2(110)$. All this is left for future work.

4. Discussion and conclusions

From the analysis of the existing literature on the subject, it can be concluded that the diffusion of metal adatoms and small clusters on the (001) surface of magnesium oxide can occur via a variety of processes. Apart from simple hopping between favorable adsorption sites, rotation, sliding, leapfrog, walking, concertina, flipping, twisting, rolling and rocking mechanisms have been shown to take place, depending on the type of metal (i.e. the features of its interaction with the surface) and the size of the cluster. It is difficult to predict *a priori* which mechanism will be dominant in each specific case, as the actual values of the energy barriers and prefactors strongly depend on fine details of the interplay between metal–metal and metal–surface interaction. As far as the latter is concerned, charge transfer effects from/to the surface, relative components of covalent bond versus electrostatic polarization of the electronic cloud and metal-on-top effects can all play a role.

A general statement can, however, be made in all the considered cases. Small clusters at least up to the tetramer have been found to exhibit diffusion coefficients comparable with, and in some cases even appreciably larger than, that of the monomer. Since aggregation of deposited atoms into small clusters as well as detachment of small fragments from a cluster trapped on a defect are common phenomena, diffusion of small clusters is extremely significant in the effect of growth understanding and simulation, and should not be ignored, as we discuss below in connection with the interpretation of Pd growth experiments.

Once diffusion coefficients and detrapping probabilities as a function of the cluster size together with the topography of the surface adsorption and nucleation sites are given, the kinetics of cluster nucleation, growth and sintering can then be simulated [96, 18, 19, 83, 97–101, 97, 102–105] and the results compared to experiments.

An experiment that has stimulated much theoretical work was performed by Haas *et al* [72], who epitaxially deposited Pd adatoms on MgO(001) in a wide range of temperatures, from 200 to 800 K, and measured the temperature-dependent island density n_I. They found that n_I is constant from 200 to about 600 K, and drops suddenly down above this temperature.

The constant island density was an indication of nucleation at defects down to low temperatures, with a negligible proportion of terrace nucleation. From this result, Haas *et al* deduced that there should be a substantial mobility of palladium down to 200 K. They attributed the mobility to palladium monomers diffusing and, assuming a prefactor $\nu = 3 \times 10^{12}$ s^{-1}, estimated $E_d < 0.3$ eV. The assumed prefactor for the jump frequency was larger than the one calculated by Xu *et al* [19], who obtained $\nu = 7.4 \times 10^{11}$ s^{-1}. However, in calculating the diffusion coefficient, that difference could be compensated by the occurrence of long jumps. The experimental estimate of E_d was at variance with all DFT calculations, which give 0.34 eV $\leqslant E_d \leqslant$ 0.41 eV [7, 21, 22, 19, 18]. The discrepancy between the experimental estimate and the calculations was solved by noting that small clusters, up to the tetramer, also strongly contribute to the mobility of palladium down to

200 K [19, 18], so that trimers or tetramers may be even more mobile than monomers. Therefore, in determining whether nucleation occurs either on terrace sites or at defects, the mobility of monomers and of small clusters must be taken into account [18].

Nucleation at defects imply that defects should act as traps for palladium monomers and clusters. Haas *et al* deduced a high trapping energy $E_t \geqslant 1.2$ eV for monomers, so that the drop of the island density at high temperatures was attributed to the breaking of clusters at traps, followed by incomplete condensation, and not to the detachment of monomers from the traps. This picture is consistent with the theoretical results mentioned in section 2.3, which give large values for E_t, even in the range of 2–3 eV, but much lower fragmentation energies for at least some small clusters at defects. Finally, rate-equation calculations [105], based on DFT detrapping and fragmentation energies, explained the drop in island density at high temperatures in terms of nucleation at F_s^+ and divacancy centers, obtaining a very good agreement with the experimental results.

When comparing with experiments, a warning should be kept in mind. Diffusion of metal adatoms and clusters on MgO(001) is a low-friction phenomenon, and this renders the theoretical evaluation of the frequency prefactors r (equation (4)) and of the mean square jump lengths L^2 more difficult. These quantities have an important role in determining diffusion coefficients, as follows from equation (3), and therefore nucleation rates and sites.

In fact, the discussion in section 2 has shown that long jumps of isolated adatoms can be numerous (or even dominant) with respect to nearest-neighbor ones. This could be expected to reinforce the role of monomer, rather than cluster, diffusion, but it should be taken into account that long jumps may occur equally well for small clusters. To our knowledge, however, such an analysis has not been conducted until now. Arrhenius prefactors and their influence on diffusion are also difficult to assess. At low friction, transition state theory can strongly overestimate the rates. Moreover, anharmonic effects may come into play when temperature is raised, so that the harmonic approximation to TST may become questionable.

A further remark concerns the strongly non-monotonic behavior of the diffusion energy barriers with cluster size: see, e.g., the Ag and Au cases with the odd/even alternation of barrier values, or the Ca/MgO case, in which Ca_4 diffuses with an energy barrier that is 3.7 times smaller than that of the isolated adatom. Collective movements can thus make diffusion more facile rather than hindering it.

Naturally, the conclusion about the importance of small cluster diffusion can be influenced by the fact that we are considering here the extreme non-scalable regime, i.e. the size range in which 'each atom counts' and in which most of the lowest-energy structures are non-epitaxial. It could be expected that in passing to larger, epitaxial systems cluster mobility should eventually be quenched. It can be noted, however, that in dynamic conditions, such as those typical during growth, metal clusters cannot be considered as static objects with a fixed (frozen) shape. Rather, incorporation of incoming adatoms is likely to pass via defective local minima, which will eventually rearrange to more stable configurations through dynamic processes, possibly involving movement of the center of mass of the cluster. Moreover, the heat evolved in the 'cluster + adatom' reaction will also take some time before being dissipated and in this period provide energy to facilitate overcoming activation barriers. These and other possible effects seem to be necessary to rationalize experimental observations concerning the diffusion of large clusters under typical growth conditions [94, 95].

To conclude, metal diffusion on oxide surfaces is a subject of apparent importance in the general field of supported nanoparticles. Despite recent progress, several unanswered questions still exist in this subject, ranging from the role of long jumps to diffusion mechanisms of charged species or in non-equilibrium conditions, opening the way for future investigations to stimulate, which is one of the aims of the present review.

References

[1] Henry C R 1998 *Surf. Sci. Rep.* **31** 235
[2] Henry C R 2005 *Prog. Surf. Sci.* **80** 92
[3] Li C, Wu R, Freeman A J and Fu C L 1993 *Phys. Rev.* B **48** 8317
[4] Giordano L, Di Valentin C, Goniakowski J and Pacchioni G 2004 *Phys. Rev. Lett.* **92** 096105
[5] Barcaro G and Fortunelli A 2005 *J. Chem. Theory Comput.* **1** 972
[6] Musolino V, Dal Corso A and Selloni A 1999 *Phys. Rev. Lett.* **83** 2761
[7] Vervisch W, Mottet C and Goniakowski J 2002 *Phys. Rev.* B **65** 245411
[8] Barcaro G, Fortunelli A, Nita F, Rossi G and Ferrando R 2007 *Phys. Rev. Lett.* **98** 156101
[9] Ferrando R, Rossi G, Nita F, Barcaro G and Fortunelli A 2008 *ACS Nano* **2** 1849
[10] Rossi G, Mottet C, Nita F and Ferrando R 2006 *J. Phys. Chem.* B **110** 7436
[11] Olander J, Lazzari R, Jupille J, Mangili B, Goniakowski J and Renaud G 2007 *Phys. Rev.* B **76** 075409
[12] Tian W, Sun H P, Pan X Q, Yu J H, Yeadon M, Boothroyd C B, Feng Y P, Lukaszew R A and Clarke R 2005 *Appl. Phys. Lett.* **86** 131915
[13] Ala-Nissila T, Ferrando R and Ying S C 2002 *Adv. Phys.* **51** 949
[14] Yudanov I, Pacchioni G, Neyman K and Rösch N 1999 *Surf. Sci.* **426** 123
[15] Musolino V, Selloni A and Car R 1999 *Phys. Rev. Lett.* **83** 3242
[16] Barcaro G and Fortunelli A 2007 *New J. Phys.* **9** 22
[17] Simic-Milosevic V, Heyde M, Nilius N, König T, Rust H-P, Sterrer M, Risse T, Freund H-J, Giordano L and Pacchioni G 2008 *J. Am. Chem. Soc.* **130** 7814
[18] Barcaro G, Fortunelli A, Nita F and Ferrando R 2005 *Phys. Rev. Lett.* **95** 246103
[19] Xu L, Henkelman G, Campbell C T and Jönsson H 2005 *Phys. Rev. Lett.* **95** 146103
[20] Henkelman G, Uberuaga B P and Jonsson H 2000 *J. Chem. Phys.* **113** 9901
[21] Judai K, Abbet S, Wörz A S, Heiz U, Giordano L and Pacchioni G 2003 *J. Phys. Chem.* B **107** 9377
[22] Giordano L, Del Vitto A, Pacchioni G and Ferrari A M 2004 *Surf. Sci.* **540** 63
[23] Becke A D 1996 *Phys. Rev.* A **38** 3865

[24] Perdew J P, Burke K and Ernzerhof M 1996 *Phys. Rev. Lett.* **77** 3865
[25] Perdew J P, Chevary J A, Vosko S H, Jackson K A, Pederson M R, Singh D J and Fiolhais C 1992 *Phys. Rev.* B **46** 6671
[26] Bonačič-Koutecky V, Burda J, Mitrič R, Ge M, Zampella G and Fantucci P 2002 *J. Chem. Phys.* **117** 3120
[27] Fernandez E M, Soler J M, Garzón I L and Balbas L C 2004 *Phys. Rev.* B **70** 165403
[28] Soulé de Bas B, Ford M J and Cortie M B 2004 *J. Mol. Struct. (Theochem)* **686** 193
[29] Pyykkö P and Runeberg N 2004 *Angew. Chem. Int. Edn* **41** 2174
[30] Pyykkö P 2005 *Inorg. Chim. Acta* **358** 4113
[31] Remacle F and Kryachko E S 2004 *Advances in Quantum Chemistry* (Amsterdam: Elsevier)
[32] Remacle F and Kryachko E S 2005 *J. Chem. Phys.* **122** 044304
[33] Aprà E, Ferrando R and Fortunelli A 2006 *Phys. Rev.* B **73** 205414
[34] Del Vitto A, Pacchioni G, Delbecq F and Sautet P 2005 *J. Phys. Chem.* B **109** 8040
[35] Xu L and Henkelman G 2008 *Phys. Rev.* B **77** 205404
[36] Repp J, Meyer G, Olsson F E and Persson M 2004 *Science* **305** 493
[37] Pacchioni G, Giordano L and Baistrocchi M 2005 *Phys. Rev. Lett.* **94** 226104
[38] Heyde M, Rust H-P, Sterrer M, Risse T and Freund H-J 2007 *Phys. Rev. Lett.* **98** 206103
[39] Corral Valero M, Raybaud P and Sautet P 2006 *J. Phys. Chem.* B **110** 1759
[40] Katsiev K, Batzill M, Diebold U, Urban A and Meyer B 2007 *Phys. Rev. Lett.* **98** 186102
[41] Matthey D, Wang J G, Wendt S, Matthiesen J, Schaub R, Laegsgaard E, Hammer B and Besenbacher F 2007 *Science* **315** 1692
[42] Sedona F, Sambi M, Artiglia L, Rizzi G A, Vittadini A, Fortunelli A and Granozzi G 2008 *J. Phys. Chem.* C **112** 3187
[43] Lu J-L, Kaya S, Weissenrieder J, Gao H-J, Shaikhutdinov S and Freund H J 2006 *Surf. Sci.* **600** L153
[44] Ferrando R, Spadacini R and Tommei G E 1993 *Phys. Rev.* E **48** 2437
[45] Miret-Artes S and Pollak E 2005 *J. Phys.: Condens. Matter* **17** S4133
[46] Antczak G and Ehrlich G 2007 *Surf. Sci. Rep.* **62** 39
[47] Frenken J W M, Hinch B J, Toennies J P and Wöll C 1990 *Phys. Rev.* B **41** 938
[48] Ellis J and Toennies J P 1993 *Phys. Rev. Lett.* **70** 2118
[49] Cowell-Senft D and Ehrlich G 1995 *Phys. Rev. Lett.* **74** 294
[50] Linderoth T R, Horch S, Laegsgaard E, Stensgaard I and Besenbacher F 1997 *Phys. Rev. Lett.* **78** 4978
[51] Antczak G and Ehrlich G 2004 *Phys. Rev. Lett.* **92** 166105
[52] Alexandrowicz G, Jardine A P, Fouquet P, Dworski S, Allison W and Ellis J 2004 *Phys. Rev. Lett.* **93** 156103
[53] Schunack M, Linderoth T R, Rosei F, Laegsgaard E, Stensgaard I and Besenbacher F 2002 *Phys. Rev. Lett.* **88** 156102
[54] Cucchetti A and Ying S C 1996 *Phys. Rev.* B **54** 3300
[55] Risken H 1989 *The Fokker–Planck Equation* (Berlin: Springer)
[56] Persson B N J 1998 *Sliding Friction—Physical Principles and Applications* (Berlin: Springer)
[57] Persson B N J and Rydberg R 1985 *Phys. Rev.* B **32** 3586
[58] Ferrando R, Spadacini R, Tommei G E and Caratti G 1996 *Phys. Rev.* E **54** 4708
[59] Melnikov V I 1991 *Phys. Rep.* **209** 1
[60] Ferrando R, Spadacini R, Tommei G E and Caratti G 1994 *Surf. Sci.* **311** 411
[61] Ferrando R, Spadacini R, Tommei G E and Caratti G 1993 *Physica* A **195** 506
[62] Singh R K and Upadhyaya K S 1972 *Phys. Rev.* B **6** 1588
[63] Sangster M J L, Peckham G and Saunderson D H 1970 *J. Phys. C: Solid State Phys.* **3** 1026
[64] Ferrando R, Spadacini R and Tommei G E 1995 *Phys. Rev.* E **51** 126
[65] Hanggi P, Talkner P and Borkovec M 1990 *Rev. Mod. Phys.* **62** 251
[66] Goniakowski J, Jelea A, Mottet C, Barcaro G, Fortunelli A, Kuntová Z, Nita F, Levi A C, Rossi G and Ferrando R 2009 *J. Chem. Phys.* submitted
[67] Chen L Y, Baldan M R and Ying S C 1996 *Phys. Rev.* B **54** 8856
[68] Luetdtke W D and Landman U 1999 *Phys. Rev. Lett.* **82** 3835
[69] Masin M, Vattulainen I, Ala-Nissila T and Chvoj Z 2003 *Surf. Sci.* **544** L703
[70] Chvoj Z, Masin M and Ala-Nissila T 2006 *J. Stat. Mech.* P10003
[71] Masin M, Vattulainen I, Ala-Nissila T and Chvoj Z 2007 *J. Chem. Phys.* **126** 114705
[72] Haas G, Menck A, Brune H, Barth J V, Venables J A and Kern K 2000 *Phys. Rev.* B **61** 11105
[73] Neyman K M, Inntam C, Matveev A V, Nasluzov V A and Rösch N 2005 *J. Am. Chem. Soc.* **127** 11652
[74] Barcaro G, Causà M and Fortunelli A 2007 *Theor. Chem. Acc.* **118** 807
[75] Florez E, Mondragòn F, Fuentealba P and Illas F 2001 *Phys. Rev.* B **63** 155408
[76] Barcaro G and Fortunelli A 2008 *Faraday Discuss.* **128** 37
[77] Sterrer M, Fischbach E, Risse T and Freund H J 2005 *Phys. Rev. Lett.* **94** 186101
[78] Barth C and Henry C R 2003 *Phys. Rev. Lett.* **91** 196102
[79] Bogicevic A and Jennison D R 2002 *Surf. Sci.* **515** L481
[80] Inntam C, Moskaleva L V, Neyman K M, Nasluzov V A and Rösch N 2006 *Appl. Phys.* A **82** 181
[81] Neyman K M, Inntam C, Moskaleva L V and Rösch N 2006 *Chem. Eur. J.* **12** 277
[82] Barcaro G and Fortunelli A 2006 *J. Phys. Chem.* B **110** 21021
[83] Xu L, Henkelman G, Campbell C T and Jönsson H 2006 *Surf. Sci.* **600** 1351
[84] Barcaro G, Aprà E and Fortunelli A 2007 *Chem. Eur. J.* **13** 6408
[85] Barcaro G and Fortunelli A 2007 *J. Phys. Chem.* C **111** 11384
[86] Barcaro G and Fortunelli A 2007 *Phys. Rev.* B **76** 165412
[87] Barcaro G and Fortunelli A 2008 *Chem. Phys. Lett.* **457** 143
[88] Markovits A, Paniagua J C, Lopez N, Minot C and Illas F 2003 *Phys. Rev.* B **67** 115417
[89] Montalenti F and Ferrando R 1999 *Phys. Rev. Lett.* **82** 1498
[90] Bardotti L, Jensen P, Hoareau A, Treilleux M and Cabaud B 1995 *Phys. Rev. Lett.* **74** 4694
[91] Deltour P, Barrat J-L and Jensen P 1997 *Phys. Rev. Lett.* **78** 4597
[92] Jensen P 1999 *Rev. Mod. Phys.* **71** 1695
[93] Carrey J, Maurice J-L, Petroff F and Vaurès A 2001 *Phys. Rev. Lett.* **86** 4600
[94] Olander J, Lazzari R, Jupille J, Mangili B, Goniakowski J and Renaud G 2007 *Phys. Rev.* B **76** 075409
[95] Lazzari R, Renaud G, Jupille J and Leroy F 2007 *Phys. Rev.* B **76** 125412
[96] Campbell C T, Parker S C and Starr D E 2002 *Science* **298** 811
[97] Xu L, Campbell C T, Jönsson H and Henkelman G 2007 *Surf. Sci.* **601** 3133
[98] Parker S C and Campbell C T 2007 *Phys. Rev.* B **75** 035430
[99] Parker S C and Campbell C T 2007 *Top. Catal.* **44** 3
[100] Chen P, Wang T Y and Luo M F 2007 *J. Chem. Phys.* **127** 144714

[101] Vasco E and Sacedòn J L 2007 *Phys. Rev. Lett.* **98** 036104
[102] Zhdanov V P 2008 *Surf. Rev. Lett.* **15** 217
[103] Zeng Q H, Wong K, Jiang X C and Yu A B 2008 *Appl. Phys. Lett.* **92** 103109
[104] Zhu J, Farmer J A, Ruzycki N, Xu L, Campbell C T and Henkelman G 2008 *J. Am. Chem. Soc.* **130** 2314
[105] Venables J A, Giordano L and Harding J H 2006 *J. Phys.: Condens. Matter* **18** S411

THE JOURNAL OF PHYSICAL CHEMISTRY Letters

BarcaroJPCL2010

pubs.acs.org/JPCL

Exotic Supported CoPt Nanostructures: From Clusters to Wires

Giovanni Barcaro,[†] Riccardo Ferrando,*[,‡] Alessandro Fortunelli,*[,†] and Giulia Rossi[‡]

[†]Molecular Modeling Laboratory, IPCF-CNR, Via Giuseppe Moruzzi 1, Pisa, I56124, Italy and [‡]Dipartimento di Fisica, Università di Genova, Via Dodecaneso 33, Genova, I16146, Italy

ABSTRACT A bottom-up computational approach for designing exotic phases of supported metallic nanostructures is proposed and exemplified for the CoPt/MgO(100) system. Magic polyicosahedral CoPt clusters, Frank−Kasper motifs that have no counterpart in bulk CoPt, are singled out in the gas phase and then deposited on a substrate that enhances their stability via a mechanism rationalized in terms of the many-body character of the metal/surface interaction. Both finite-size (nanoclusters) and one-dimensional (nanowires) structures can be so constructed, where one-layer Co interfacial segregation and the small size of the clusters suggest that their peculiar morphology can be reached and maintained via self-organization, while the wires appear to be robust with respect to necking instabilities.

SECTION Nanoparticles and Nanostructures

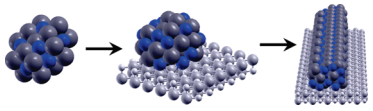

Predicting a material's structure from the knowledge of interactions at the atomic level is one of the most important and long-standing open problems in condensed matter science,[1,2] both from the point of view of basic knowledge and for its practical implications related to the ab initio design of novel structures and phases tailored for specific technological applications.[3,4] In the recent years, important advances have been made in the field[2] due to the development of effective methodologies for the exploring energy landscapes[5] and to the explosive increase of computing power. However, the problem is still far from being solved, so that the development of fresh approaches trying to tackle the complexity of computer-aided materials design is desirable.

In this paper, we propose a bottom-up computational approach for designing exotic structures of supported nanoparticles and nanowires for a material, CoPt, which is of great interest for applications in magnetism[6] and catalysis[7] and is being widely studied at the nanoscale.[8,9] In this computational approach (the computational methodology is described in detail in the Supporting Information), we first look for the most important structural motifs of gas-phase clusters by means of a combination of global optimization searches[5] and density functional (DF) calculations. In particular, we are interested in singling out structures possessing a magic character,[10] that is, presenting an uncommon energetic stability, often associated with highly symmetric configurations. Then, we choose a substrate such that it can enhance the stability of these structures once they are deposited. It turns out that an appropriate substrate is the MgO(001) surface, an oxide support widely used in both model studies and applications.[11] As a final step, we use the supported nanoclusters as building blocks to produce extended nanostructures in the form of nanowires. As we show below, both of these types of nanostructures are exotic in the sense that they have no counterpart in the bulk phases of CoPt alloys but can be described as either finite-size (clusters) or one-dimensional (wires) analogues of Frank−Kasper phases[12] and are thus related to quasicrystals.[13,14]

We recall that at 50−50% composition, bulk solid CoPt presents an ordered phase of $L1_0$ structure, with tetragonal crystal lattice, alternating homogeneous Pt and Co planes along a (001) axis. The structures of CoPt binary nanoparticles (referred to as nanoalloys in the following) are however much more complex; as has been shown both theoretically[8,15] and experimentally,[6,9] that they can present both crystalline (bulk-like) and noncrystalline structures. Our results below confirm these predictions.

To begin with, we focus on free CoPt nanoparticles in the size range of N_{tot} = 20−50 (with N_{tot} as the total number of atoms) at 50−50% composition. This size range corresponds to an interval in which polyicosahedral (pIh) structures[10,15] are expected. pIh are made up of several interpenetrating elementary icosahedra of 13 atoms (see an example in Figure 1). pIh free clusters with five-fold symmetry have been shown to be of special energetic stability in binary systems with atomic size mismatch,[10] such as Ag−Cu and Ag−Ni, but the origin of the stability of other classes of pIh structures is still unclear, and no theoretical predictions of surface-supported pIh structures have been reported so far.

A nice example of an unsupported magic pIh structure is a cluster of 38 atoms, $Co_{18}Pt_{20}$, shown in the top row of Figure 1. This is a Frank−Kasper polyhedron[12] with a disclination line

Received Date: October 1, 2009
Accepted Date: November 2, 2009

DOI: 10.1021/jz900076m | *J. Phys. Chem. Lett.* **2010**, *1*, 111–115

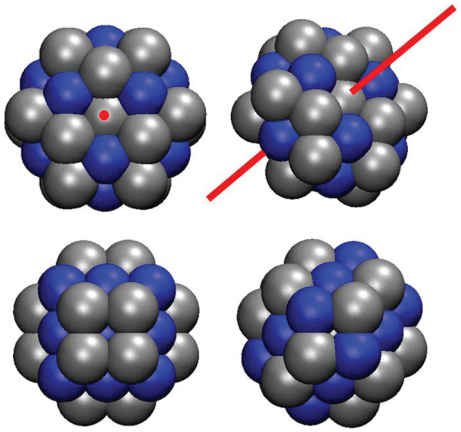

Figure 1. Schematic pictures of free polyicosahedral (pIh6, top row) and $L1_0$ truncated octahedron (TO, bottom row) structures at a composition of $Co_{18}Pt_{20}$. Top and side views are shown on the left and right side, respectively. The disclination line in the Frank−Kasper pIh6 cluster is indicated. Cobalt atoms are displayed in blue, and platinum atoms are in dark gray.

running along its symmetry axis and can be identified with the "six-fold pancake" (a pIh structure exhibiting a six-fold symmetry axis, hereafter pIh6).[10] This size and composition is simultaneously magic for $L1_0$ bulk-like structures because it is possible to build up a perfect cluster with (tetragonally distorted) truncated octahedral shape and $L1_0$ ordering (see the bottom row of Figure 1). However, even in this case, DF calculations predict that the pIh6 structure prevails by more than 1 eV.

Let us now consider supported CoPt nanoparticles. We anticipate the finding that the lowest-energy structures are dominated by one-layer Co segregation at the interface with the substrate. We expect this to be a common occurrence in supported nanoalloys with a sufficiently strong adhesion to the substrate, as for CoPt particles on MgO(100), and its driving force can be explained in terms of novel epitaxial concepts and the physics of the metal bonding. The metal−surface interaction in fact, as any other metal bonding mechanism, possesses a definite many-body character, that is, the adhesion strength of a metal atom to the surface depends appreciably on its coordination number (the number of first-neighbor metal atoms surrounding the interacting one). Such a many-body character is much more pronounced for Pt than for Co; the strong Pt/Pt bonds compete with and quickly weaken the Pt/MgO interaction, quenching it from values appreciably higher than the Co/MgO interaction in the case of a single atom (∼2.5 eV for the Pt atom versus ∼1 eV for the Co atom on the O site) to definitely smaller values already for coordination number = 4 (∼0.45 eV for Pt versus ∼0.75 eV for Co on the O site). This entails that, once a cluster reaches a critical size such that the adhesion energy favors the formation of an interface involving a substantial number of atoms thus exhibiting non-negligible coordination numbers, there will be a strong tendency for Co to form a segregated layer at the interface. Experimental evidence for small CoPt particles is not conclusive in this respect, as it concerns, for example, particles embedded in amorphous carbon or MgO matrixes[6] where matrix−cluster interaction (and possible interfacial oxidation) might play a decisive role. For fcc-like particles, we concurrently find that Pt has a strong tendency to form a segregated layer at the topmost (100) facet, in agreement with experimental observations.[6,16] For these particles, then, one-layer Co surface segregation at the interface together with one-layer Pt surface segregation at the topmost facet translates into $L1_0$ chemical ordering and entails that even numbers of layers possess a magic character; the presence of a pure Co first layer in fact favors the formation of a pure Pt second layer, and so on, thus strongly reinforcing the tendency already present in suspended particles.[8] However, this also implies that bulk-like gas-phase clusters must be cut to be accommodated on the substrate, as shown in Figure 2. On the contrary, pIh clusters can be satisfactorily accommodated on the substrate while preserving their gas-phase shape, simply segregating cobalt at the interface. As a counterintuitive result, the square-symmetry MgO(001) substrate does not favor the $L1_0$ phase but, on the contrary, enhances the stability of Frank−Kasper cluster structures.

The most representative cluster structures obtained for N_{tot} = 20, 40, 48, 50, 62, 64, and 80 are depicted in Figure 2, and the corresponding energy results are reported in Table 1 of the Supporting Information.

Scrutinizing the results, for small sizes (N_{tot} = 20), we find that the putative global minimum is a double icosahedron (N = 19) plus a lateral atom (Figure 2a), while an $L1_0$-type motif (Figure 2b) and an incomplete pIh (Figure 2c) lie at more than 2 eV. By increasing the size to N_{tot} = 40, a sharp crossover occurs, pure icosahedral motifs such as that in Figure 2f are still competitive in terms of adhesion energies but are drastically prevailed at the metal bonding level by a pIh motif, which is the gas-phase pIh6 cluster plus two lateral Co atoms at the interface (Figure 2d). In this size range, $L1_0$-type motifs such as Figure 2e present an excellent adhesion energy but are higher in energy due to a too low metal binding. The latter can be improved by introducing overhangs and thus better approximating the ideal shape predicted by the Wulff−Kaischev construction,[11,17] but at the expense of the adhesion energy, so that the resulting structures are even less stable.

One could think that sizes around 38 are somewhat special as they correspond to the perfect, closed-shell pIh6, but it turns out that pIh structures manage to be competitive at larger sizes by combining the pIh6 building block with novel epitaxial forms. For example, at N_{tot} = 48, the optimal $L1_0$-type arrangements are a truncated pyramid (Figure 2i) or a structure exhibiting a stacking fault and an overhang at the interface (not shown). However, the putative global minimum is a peculiar pIh-like structure (Figure 2g,h) still based on the perfect 38 atom pIh6 motif but now adsorbed on the surface by tilting its six-fold symmetry axis and by inserting further atoms to fill up the void so created; the added atoms produce a (100) pseudomorphic epitaxy with the substrate to realize the best match with the oxide surface (see a detailed view in Figure 2h). By increasing N_{tot} to 62−64, a novel type of pIh structure comes into play that can be denoted as double pIh6. It is in fact possible and energetically favorable to match a tilted pIh6 with an adjacent one tilted in the opposite way, creating a structure (shown in Figure 2l,m) which achieves

DOI: 10.1021/jz900076m | J. Phys. Chem. Lett. 2010, 1, 111–115

THE JOURNAL OF PHYSICAL CHEMISTRY Letters

pubs.acs.org/JPCL

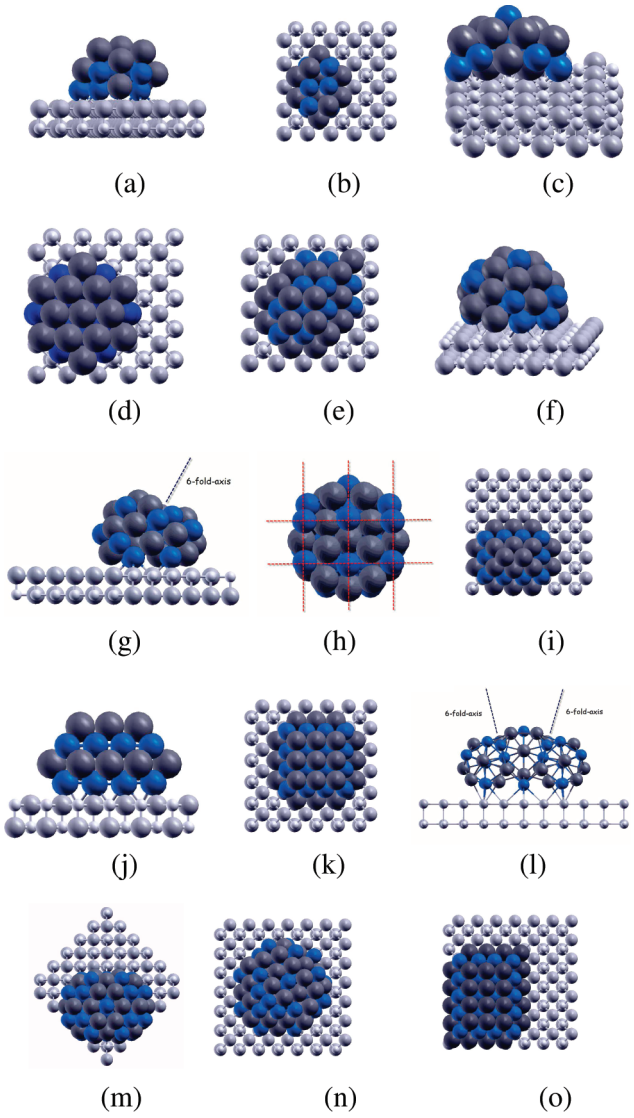

Figure 2. Schematic pictures of various supported CoPt clusters: (a) $Co_{10}Pt_{10}$ double icosahedron (N = 19) plus a lateral Co atom lying on the surface; (b) $Co_{10}Pt_{10}$ $L1_0$-type structure; (c) $Co_{10}Pt_{10}$ incomplete pIh; (d) $Co_{20}Pt_{20}$ pIh6-based structure; (e) $Co_{20}Pt_{20}$ $L1_0$-type structure; (f) $Co_{20}Pt_{20}$ incomplete pIh; (g) $Co_{24}Pt_{24}$ pIh6-based structure with its disclination axis indicated; (h) bottom view of (g) to better show its epitaxial relationship to the substrate; (i) $Co_{20}Pt_{20}$ $L1_0$-type structure; (j) side view of a $Co_{32}Pt_{30}$ $L1_0$-type structure; (k) top view of (j); (l) side view of a $Co_{32}Pt_{32}$ double-pIh6-based structure with its two disclination axes indicated; (m) top view of (l); (n) $Co_{40}Pt_{40}$ structure based on the double pIh6 plus fcc-type surface growth; and (o) $Co_{40}Pt_{40}$ $L1_0$-type truncated pyramid. Color coding is as that in Figure 1, plus oxygen atoms in light gray and magnesium atoms in white.

shell closure at N_{tot} = 64. At this size, $L1_0$-type configurations are appreciably higher in energy (by ~1.8 eV; see Table 1 of the Supporting Information). Even at N_{tot} = 62, which is a magic size for $L1_0$ motifs (see Figure 2j,k), an incomplete double pIh6 is still the putative global minimum, although by a smaller amount, ~0.4 eV. For larger sizes, our predictions become more uncertain. However, at N_{tot} = 80, we still find that a double pIh6 hybridized with a lateral fcc-type surface

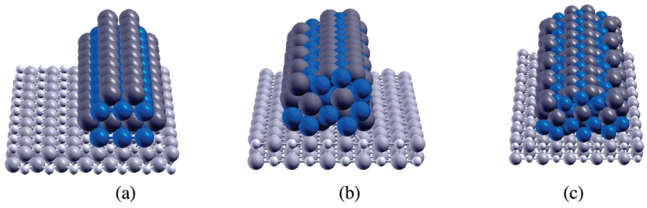

Figure 3. Schematic pictures of supported CoPt nanowires: (a) (16,16) $L1_0$-type wire; (b) (22,22) wire based on the single pIh6; and (c) (29,30) wire based on the double pIh6. The labeling convention is (N_{Pt},N_{Co}), where N_{Co} and N_{Pt} are the number of Co and Pt atoms in the repetitive unit. Color coding is as that in Figure 2.

growth (Figure 2n) is at lower energy than the best pure $L1_0$ structure (Figure 2o).

The tilted pIh6 motifs (Figure 2g,h and l,m) lend themselves to interesting speculations in terms of 1D systems, as one can ask whether these motifs can be the seeds of extended systems. As the regular interfacial pattern shown in Figure 2h points to a simple translational symmetry, we investigate this possibility by replicating neighboring tilted pIh6 motifs along the [100] direction of the MgO(100) substrate and joining them together to create stable periodic pIh nanowires, which are extended 1D Frank−Kasper phases. To this aim, we conduct EP global optimizations on systems composed of two adjacent (Figure 2g and l) configurations and a variable number of Pt or Co atoms added in between. From such calculations, the structures depicted in Figure 3b,c result.

They belong to two families, one based on the tilted single pIh6 (22,22) and one based on the tilted double pIh6 (29,30). These structures can be compared with unfaulted $L1_0$ wires. In Figure 3a, the best (16,16) candidate of the $L1_0$ family in this size range, as obtained from the Wulff−Kaischev construction, is also shown. The labeling convention is (N_{Pt},N_{Co}), where N_{Co} and N_{Pt} are the numbers of Co and Pt atoms in the repetitive unit. As it is well-known, nanowires are kinetically stabilized objects, on whose synthesis experimental conditions (temperature, mass transport, etc.) play a dominating role. Nevertheless, thermodynamic considerations at 0 K such as the present ones can be helpful to orient the search for novel structures and morphologies. In order to compare the thermodynamic stability of 1D systems, the excess energy per unit length (E_{exc}) can be usefully defined

$$E_{exc} = \frac{E_{bnd} - n_{Pt}E_{Pt} - n_{Co}E_{Co}}{\sqrt{n_{tot}}} \qquad (1)$$

where n_{Pt} and n_{Co} are the number of Pt and Co atoms per unit length of the wire, $n_{tot} = n_{Pt} + n_{Co}$, E_{Pt} and E_{Co} are the bulk binding energies of pure Pt and Co, respectively, and E_{bnd} is the wire binding energy per unit length. The most stable 1D structures correspond to the lowest values of the wire excess energy. The E_{exc} values for several trial configurations are reported in Figure 4.

The main result that can be drawn from an inspection of this figure is that the best pIh nanowires present an appreciably lower excess energy with respect to their $L1_0$ competitors, which in turn suggests that they might be selectively

DOI: 10.1021/jz900076m | J. Phys. Chem. Lett. 2010, 1, 111–115

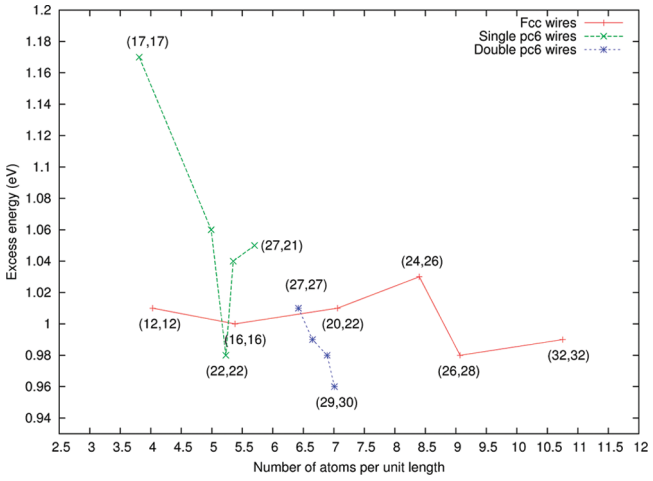

Figure 4. Wire excess energy per unit length (in eV) as a function of the number of atoms per unit length for supported wires.

synthetized under proper experimental conditions. This occurs despite the fact that pIh6 nanowires are oriented along the (100) direction of the substrate whereas the fcc ones are oriented along (110), so that structures with a comparable cross-sectional size have a higher number of atoms per unit length and are thus expected to possess a lower wire excess energy.

It can be noted in passing that for the $L1_0$-type wires, one observes a transition with increasing cross section from structures exhibiting a single overhang [(12,12), (16,16), and (24,26)] to those exhibiting a double [(20,22) and [(26,28)] and finally a triple [(32,32)] overhang, in agreement with the Wulff–Kaischev construction[11,17,18] (we emphasize that $L1_0$ chemical ordering is by far energetically favored in all cases).

In view of the mechanical stability of these objects, which is a general key issue when dealing with nanowires,[19] it is important to emphsize that for the pIh systems, a proper junction between the pIh6 motifs is of primary importance as structures with a minimum number of atoms between them, such as (17,17) or (27,27), possess a much higher excess energy than those with a more homogeneous cross section, such as (22,22) or (29,30); see Figure 3b,c. This suggests a greater stability of the pIh nanowires with respect to $L1_0$-type ones. $L1_0$-type nanowires in fact present a larger lattice mismatch with the substrate that, on the regular MgO(100) surface, will eventually be relieved by developing interfacial dislocations. This will decrease their excess energy, but at the same time, it will also increase the instability of the wires with respect to necking.[20] In contrast, the much greater stability of, for example, (22,22) with respect to (17,17) or of (29,30) with respect to (27,27) suggests that pIh6-based nanowires present a uniform stress along their length and should be less liable to breaking or necking phenomena and thus more relevant from the technological point of view once synthetic issues are solved.

What is the driving force to pIh structures?

Five-fold symmetry core–shell pIh structures have been found in several instances,[10] and their stability has been interpreted as originating from size mismatch and the difference in surface energies among the two elements, both favoring core–shell chemical ordering. The ubiquitous occurrence of pIh motifs in isolated binary clusters (see, e.g., ref 21) can however have a different, so far unexplored, origin. Certain classes of pIh structures, in fact, particularly those exhibiting six-fold symmetry axes such as pIh6, have been shown to maximize the number of mixed bonds.[21] This implies that pIh configurations will be favorable also for those binary alloys, such as, for example, CoPt, whose phase diagram[22] is characterized by ordered phases essentially driven by the strength of the mixed bonds and thus be expected to be of common occurrence in the field of nanoalloys.

Our computational approach is thus able to construct exotic phases of CoPt nanomaterials. These phases are possible because of a specific mechanism by which noncubic structures can be selectively stabilized on checkerboard/square-symmetry cubic surfaces. This mechanism arises from the many-body character of Pt versus Co/surface interaction. Its steeper decrease in Pt with increasing coordination number favors one-layer Co interfacial segregation. pIh structures can accommodate Co segregation without significantly distorting their geometry, whereas this is more difficult for $L1_0$ structures, thus leading to the interfacial stabilization of polyicosahedra.

From the point of view of technological applications, two points can be underlined. First, considering that atom exchange kinetics in such small clusters is expected to be faster than that in larger particles[23] and considering the substantial thermodynamic driving force toward these structures, it is to be expected that both the morphology and the chemical ordering can be reached and maintained via self-organization without invasive postsynthetic treatments (ion bombardments, plasmonic heating, etc.) that are needed for larger systems with the corresponding unwanted side effects (roughening, contamination, etc.). Second, from energetic considerations, it can be gathered that pIh-based nanowires present a uniform stress along their length, in contrast to the lattice mismatch and the formation of stress-relieving dislocations expected for fcc-type nanowires, and might thus be less liable to breaking or necking phenomena that are fatal to their possible technological use.

SUPPORTING INFORMATION AVAILABLE

Details of the computational methodology. This material is available free of charge via the Internet at http://pubs.acs.org.

AUTHOR INFORMATION

Corresponding Author:

*To whom correspondence should be addressed.

ACKNOWLEDGMENT A.F. acknowledges financial support from the EC VII FP within the ERC-AG SEPON project (ERC-2008-AdG-227457). R.F. acknowledges support from Italian MIUR for the PRIN Project No. 2007LN873M_003. DF calculations were performed at Cineca Supercomputing Center (Bologna, Italy) within an agreement with Italian CNR.

DOI: 10.1021/jz900076m | J. Phys. Chem. Lett. 2010, 1, 111–115

REFERENCES

(1) Maddox, J. Crystals from First Principles. *Nature* **1998,** *335*, 201.
(2) Woodley, S. M.; Catlow, R. Crystal Structure Prediction from First Principles. *Nat. Mater.* **2008,** *7*, 937–946.
(3) Lord, E. A.; Mackay, A. L.; Ranganathan, S. *New Geometries for New Materials*; Cambridge University Press: Cambridge, U.K., 2006.
(4) Xiong, Y.; Wiley, B. J.; Xia, Y. Nanocrystals with Unconventional Shapes—A Class of Promising Catalysts. *Angew. Chem., Int. Ed.* **2007,** *46*, 7157–7159.
(5) Wales, D. J. *Energy Landscapes with Applications to Clusters*; Cambridge University Press: Cambridge, U.K., 2003.
(6) Favre, L.; Dupuis, V.; Bernstein, E.; Melinon, P.; Perez, A. Structural and Magnetic Properties of CoPt Mixed Clusters. *Phys. Rev. B* **2006,** *74*, 014439.
(7) Gauthier, Y.; Schmid, M.; Padovani, S.; Lundgren, E.; Bus, V.; Kresse, G.; Redinger, J.; Varga, P. Adsorption Sites and Ligand Effect for CO on an Alloy Surface: A Direct View. *Phys. Rev. Lett.* **2001,** *87*, 036103.
(8) Gruner, M. E.; Rollmann, G.; Entel, P.; Farle, M. Multiply Twinned Morphologies of FePt and CoPt Nanoparticles. *Phys. Rev. Lett.* **2008,** *100*, 087203.
(9) Penuelas, J.; Andreazza, P.; Andreazza-Vignolle, C.; Tolentino, H. C. N.; Santis, M. D.; Mottet, C. Controlling Structure and Morphology of CoPt Nanoparticles through Dynamical or Static Coalescence Effects. *Phys. Rev. Lett.* **2008,** *100*, 115502.
(10) Rossi, G.; Rapallo, A.; Mottet, C.; Fortunelli, A.; Baletto, F.; Ferrando, R. Magic Polyicosahedral Core−Shell Clusters. *Phys. Rev. Lett.* **2004,** *93*, 105503.
(11) Henry, C. R. Morphology of Supported Nanoparticles. *Prog. Surf. Sci.* **2005,** *80*, 92–116.
(12) Frank, F. C.; Kasper, J. S. Complex Alloy Structures Regarded As Sphere Packings. I. Definitions and Basic Principles. *Acta Crystallogr.* **1958,** *11*, 184–190.
(13) Shechtman, D.; Blech, I.; Gratias, D.; Cahn, J. W. Metallic Phase with Long-Range Orientational Order and No Translational Symmetry. *Phys. Rev. Lett.* **1984,** *324*, 1951–1953.
(14) Dubost, B.; Lang, J. M.; Tanaka, M.; Sainfort, P.; Audier, M. Large AlCuLi Single Quasicrystals with Triacontahedral Solidification Morphology. *Nature* **1986,** *324*, 48–50.
(15) Rossi, G.; Ferrando, R.; Mottet, C. Structure and Chemical Ordering in CoPt Nanoalloys. *Faraday Disc.* **2008,** *138*, 193–210.
(16) Shapiro, A. I.; Rooney, P.; Tran, M.; Hellman, F.; Ring, K.; Kavanagh, K.; Rellinghauss, B.; Weller, D. Growth-Induced Magnetic Anisotropy and Clustering in Vapor-Deposited Co−Pt Alloy Films. *Phys. Rev. B* **1999,** *60*, 12826.
(17) Wulff, G. Zur Frage Der Geschwindigkeit Des Wachstums Unter Auflosung Der Kristallfiachen. *Z. Kristallogr.* **1901,** *34*, 499–530.
(18) Molina, L. M.; Hammer, B. Theoretical Study of COOxidation on Au Nanoparticles Supported by MgO(100). *Phys. Rev. B* **2004,** *69*, 155424.
(19) Tosatti, E.; Prestipino, S.; Kostlmeier, S.; Corso, A. D.; Tolla, F. D. D. String Tension and Stability of Magic Tip-Suspended Nanowires. *Science* **2001,** *291*, 288–290.
(20) Burki, J.; Stafford, C. A.; Stein, D. L. Theory of Metastability in Simple Metal Nanowires. *Phys. Rev. Lett.* **2005,** *95*, 090601.
(21) Rossi, G.; Ferrando, R.; Rapallo, A.; Fortunelli, A.; Curley, B.; Lloyd, L.; Johnston, R. Global Optimization of Bimetallic Cluster Structures. Ii. Size-Matched Ag−Pd, Ag−Au, and Pd−Pt Systems. *J. Chem. Phys.* **2005,** *122*, 194309.
(22) Baker, H., Ed. *Alloy Phase Diagrams*; ASM International: Materials Park, OH, 1992.
(23) Müller, M.; Albe, K. Concentration of Thermal Vacancies in Metallic Nanoparticles. *Acta Mater.* **2007,** *55*, 3237–3244.

DOI: 10.1021/jz900076m | *J. Phys. Chem. Lett.* **2010,** *1*, 111–115

Supporting Information (SI) for

Exotic CoPt supported nanostructures: from clusters to wires

Giovanni Barcaro[(a)], *Riccardo Ferrando*[(b)*], *Alessandro Fortunelli*[(a)*] *and Giulia Rossi*[(b)]

[a] *Molecular Modeling Laboratory, IPCF-CNR, Via Giuseppe Moruzzi 1, Pisa, I56124, Italy*

[b] *Dipartimento di Fisica, Università di Genova, Via Dodecaneso 33, Genova, I16146, Italy*

Our methodology follows a combined empirical-potential (EP)/density-functional (DF) predictive protocol to explore the structure, ordering pattern and epitaxial relationships of free and supported nanoparticles [1–3].

Extensive global optimization (GO) searches are performed within an atom-atom energetic model. In this model, metal-metal interactions are described by a many-body tight-binding EP [4], while metal-oxide interactions are described by a potential energy surface fitted to ab initio calculations [5, 6].

GO searches employ the basin-hopping algorithm [7] and the parallel walkers algorithm [8] for optimizing the structural part plus exchange-only basin-hopping [9] and shell-restricted systematic searches [9, 10] for compositional ordering. Searches are performed both in the case of gas-phase free clusters and of supported clusters, for several sizes. 50-50% composition is mainly considered, but also 25-75% and 75-25% compositions in selected cases. Typically, for each size, 10 unseeded searches of 60.000 steps each are performed starting from random positions in a cubic box (either in free space or placed above the oxide surface). The GO searches are able to produce a large database of candidate structures exhibiting wide structural diversity, and single out the most competitive structural motifs for the specific system under consideration and, among these, the low-energy structures pertaining to each motif. We then locally optimize these low-energy structures at the first-principles (DF) level, and analyze the changes brought about by the higher-level of theory on the predicted structural crossover, self-consistently refining the EP by introducing the DF binding energies of the most representative clusters positioned in a variety of cluster/surface distances and arrangements into the fitting procedure. Candidate structures for DF optimization are thus taken as the low-energy configurations of each structural motif from EP GO searches at 50-50% composition, but also translating those obtained at different compositions by optimizing the chemical ordering via an exchange-only approach [9, 10], or as fcc-like configurations built via the Wulff-Kaischew construction [11, 12] with $L1_0$ chemical ordering that is predicted to be the most favorable one by DF calculations [13]. System comparison techniques are so utilized to maximize structural diversity and thus the thoroughness of the search [1].

DF calculations calculations are carried out using the PWscf (Plane-Wave Self-Consistent Field) computational code [14], employing the PBE xc-functional [15] and ultrasoft pseudopotentials in the spin-unrestricted formalism. The MgO(001) surface is modeled by a

two-layer slab, each layer containing 25 Mg(Ca) and 25 O atoms, 5×5 cell, fixed in the lattice positions of the rock salt bulk structure of the various oxides. In selected cases a 6×6 cell is used to validate the results on the smaller cell. The distance between replicated cells in the direction perpendicular to the (001) surface is about 13 Å, and implies a distance of at least ≈ 6 Å between atoms in replicated cells. The kinetic energy cutoff for the selection of the plane-wave basis set is fixed at 30 Ryd (1 Ryd = 13.6 eV) for the energy and 150 Ryd for the density in all the calculations. Because of the large dimensions of the unit cell, eigenvalues and eigenvectors of the Kohn-Sham hamiltonian are only evaluated at the Γ point, having verified in several cases that this approximation does not influence the accuracy of the obtained results with respect to the employment of denser k_{mesh} grids. A Gaussian smearing technique [16] (with a smearing parameter of 0.002 Ryd) is applied.

In Table I, we report the energy values corresponding to the the most representative cluster structures obtained for $N_{\rm tot} = 20, 40, 48, 50, 62, 64, 80$ and depicted in Fig. 2 of the main text. Note that we decompose the total binding energy (E_{bnd}) into its adhesion (E_{adh}) and metallic (E_{met}) components.

---

[1] Ferrando, R.; Fortunelli, A.; Johnston, R. L. *Phys. Chem. Chem. Phys.* **2008,** *10,* 640.

[2] Barcaro, G.; Fortunelli, A.; Rossi, G.; Nita, F.; Ferrando, R. *Phys. Rev. Lett.* **2007,** *98,* 156101.

[3] Ferrando, R.; Rossi, G.; Nita, F.; Barcaro, G.; Fortunelli, A. *ACS Nano* **2008,** *2,* 1849.

[4] Rossi, G.; Ferrando, R.; Mottet, C. *Faraday Disc.* **2008,** *138,* 193-210.

[5] Vervisch, W.; Mottet, C.; Goniakowski, J. *Phys. Rev. B* **2002,** *65,* 245411.

[6] The numerical parameters for the metal-surface interaction can be found in http://h2.ipcf.cnr.it/alex/webparam.pdf.

[7] D. J. Wales, J. P. K. Doye *J. Phys. Chem. A* **101**, 5111 (1997).

[8] Rossi, G.; Ferrando, R. *Chem. Phys. Lett.* **2006,** *423,* 17.

[9] Paz-Borbon, L. O.; Mortimer-Jones, T. V.; Johnston, R. L.; Posada-Amarillas, A.; Barcaro, G.; Fortunelli, A. *Phys. Chem. Chem. Phys.* **2008,** *9,* 5202.

[10] Fortunelli, A.; Velasco, A. M. *J. Mol. Struct. - Theochem* **1999,** *487,* 251.

[11] Wulff, G. *Z. Kristallogr.* **1901,** *34,* 499-530.

[12] Henry, C. R. *Prog. Surf. Sci.* **2005,** *80,* 92-116.

[13] Rollmann, G.; Gruner, M. E.; Hucht, A.; Meyer, R.; Entel, P.; Tiago, M. L.; Chelikowsky, J. R. *Phys. Rev. Lett.* **2007,** *99,* 083402.

[14] S. Baroni, A. Dal Corso, S. de Gironcoli and P. Giannozzi, http://www.pwscf.org.

[15] Perdew, J.; Burke, K.; Ernzerhof, M. *Phys. Rev. Lett.* **1996,** *77,* 3865.

[16] Elsasser, C.; Fahnle, M.; Chan, C. T.; Ho, K. M. *Phys. Rev. B* **1994,** *49,* 13975.

TABLE I: Energy decomposition (see text for definitions) for selected CoPt/MgO(100) nanoparticles with $N_{\rm tot}$ = 20, 40, 48, 50, 62 and 64. $\mathbf{\Delta E}$ are the energy differences with respect to the putative global minimum. Energies in eV.

Cluster	Motif	$\mathbf{E}_{adh}$	$\mathbf{E}_{met}$	$\mathbf{E}_{bnd}$	$\mathbf{\Delta E}$
$Co_{10}Pt_{10}$	fig(2a)	5.04	74.66	79.70	0.00
	fig(2b)	5.88	71.53	77.41	+2.29
	fig(2c)	5.66	71.71	77.37	+2.33
$Co_{20}Pt_{20}$	fig(2d)	6.33	164.37	170.70	0.00
	fig(2e)	10.72	157.44	168.16	+2.54
	fig(2f)	7.28	160.50	167.78	+2.92
$Co_{24}Pt_{24}$	fig(2g-h)	7.81	198.20	206.01	0.00
	fig(2i)	9.29	195.12	204.40	+1.61
$Co_{25}Pt_{25}$	pIh6-type	8.06	206.49	214.55	0.00
	$L1_0$-type	14.17	199.69	213.86	+0.69
	$L1_0$'-type	11.49	202.15	213.64	+0.91
$Co_{32}Pt_{30}$	pIh6-type	9.13	259.79	268.92	0.00
	fig(2j-k)	13.58	254.97	268.55	+0.37
$Co_{32}Pt_{32}$	fig(2l-m)	9.78	269.10	278.88	0.00
	$L1_0$-type	14.35	262.71	277.06	+1.82

The Effect of CO and H Chemisorption on the Chemical Ordering of Bimetallic Clusters

Paul S. West,[†] Roy L. Johnston,*[,†] Giovanni Barcaro,[‡] and Alessandro Fortunelli*[,‡]

School of Chemistry, University of Birmingham, Edgbaston, Birmingham, B15 2TT, United Kingdom, and Molecular Modeling Laboratory, Istituto per i Processi Chimico-Fisici del Consiglio Nazionale delle Ricerche (IPCF-CNR), via G. Moruzzi 1, I-56124, Pisa, Italy

Received: September 2, 2010; Revised Manuscript Received: October 7, 2010

The effect of alloying on ligand adsorption energies and how this can modify the segregation patterns of selected binary nanoalloys is studied via first-principles total energy calculations. A model setup is considered, in which high-symmetry 38-atom truncated-octahedral (TO) clusters with compositions A_6B_{32} and B_6A_{32} are used as substrates to bind a single CO molecule or H atom in centroid sites for the following (A,B) pairs: (Au,Pd), (Pd,Pt), and (Cu,Pt), and the relative changes in the energetics of the systems upon ligand coordination are analyzed. We find qualitative similarities but quantitative differences between the CO and H cases (as examples of reducing agents), and a wide variety of behavior for the three (A,B) pairs. In AuPd, Pd−CO bonding is not strongly affected by neighboring Au atoms but the $Pd_{core}Au_{surface}$ segregation pattern (favored for bare particles) is expected to be inverted in the presence of CO coordinating species. At the other extreme, in CuPt, both Pt−CO and Pt−H bonding is strongly enhanced by neighboring Cu atoms, but the predicted segregation pattern differs from that expected on the basis of results for extended systems due to finite-size effects.

Introduction

Nanoparticles have a high surface to volume ratio, making them ideal for heterogeneous catalysis as most chemical reactions happen on surfaces, and they often have different properties to their corresponding bulk counterparts.[1] Multimetallic nanoclusters ("nanoalloys") have even greater potential, as additional structural motifs can be created and the chemical and physical properties can be tuned by varying the composition and degree of atomic mixing ("chemical ordering"), as well as the number of atoms.[2] In addition, some of the best catalysts tend to be expensive noble metals (e.g., platinum), so mixing with another, cheaper metal can decrease the cost of the catalyst without decreasing, and sometimes even improving, activity.

In this context, one of the issues currently under debate concerns the extent and the degree by which the particles' structures are modified by the presence of reacting species under working conditions. This is a crucial issue, as catalytic activity is expected to vary considerably depending on the nanoparticle geometry, particularly for small sizes (tens or hundreds of atoms).[3,4] For example, we have previously shown for pure Pd, Pt, and Au clusters that the energy ordering of various structural isomers can be changed quite dramatically upon coordinating CO molecules and H atoms.[5]

Considering bimetallic systems, chemical ordering in particular can have a large effect on the catalytic activity, and it has been shown, both experimentally and theoretically, that nanoparticles, thin films, and bulk surfaces can change their structure or surface composition when ligands are added.[5−12] Tao et al.[9] have shown that RhPd nanoalloys can undergo reversible core−shell inversion, depending on whether the environment is oxidizing (in which case the $Pd_{core}Rh_{shell}$ configuration is favored, with the Rh shell being preferentially oxidized) or reducing (where the $Rh_{core}Pd_{shell}$ configuration is observed). The authors suggest that this behavior can be utilized in the development of smart catalysts, where different reactions can take place on the same catalyst depending on the reaction conditions. In another work, Andersson et al.[6] have shown that for a Pt monolayer on top of Cu, the Cu migrates to the surface when CO is added. Since the CO binds preferentially on-top to Pt, Cu is not involved in direct binding to the CO, but rather it surrounds the Pt−CO unit. Moreover, DFT calculations have also shown that surface Pd−Au mixing increases the catalytic activity (for CO oxidation) of Pd/Au(111),[7] while both experimental and theoretical results show that alloying Pd with Zn can produce efficient catalysts for methanol steam reforming.[11] Reverse segregation of AgPd particles due to hydrogen adsorption has been investigated in pioneering work.[10,12]

In the present work, we focus on the effect of alloying on ligand adsorption energies and how this can modify the segregation patterns of selected binary nanoalloys. We set up a model system, by keeping a fixed geometrical structure and alloy composition and varying the chemical ordering, and investigate the relative changes in the energetics of the systems upon ligand coordination. Specifically, we study 38-atom truncated-octahedral (TO) clusters with compositions A_6B_{32} and B_6A_{32}, for the following (A,B) pairs: (Au,Pd), (Pd,Pt), and (Cu,Pt). CO and H are then chosen as prototypical examples of reducing ligands, and their adsorption atop (111) centroid sites of the TO structure is investigated for a number of high-symmetry isomers. Even though hybrid[35] or polyicosahedral[36] configurations can be competitive for 38-atom binary clusters,[17] the TO structure possesses a high symmetry, thus simplifying the analysis of ligand adsorption, and is among the lowest-energy isomers of the bare metal clusters,[17] always representing a local minimum (also after adsorption). Moreover, it can be taken as a model of crystalline-like structures and thus also as representative of larger clusters: hexagonal local arrangements are a common occurrence

* Corresponding authors, (RLJ) r.l.johnston@bham.ac.uk and (AF) fortunelli@ipcf.cnr.it.
[†] School of Chemistry, University of Birmingham.
[‡] Molecular Modeling Laboratory, Istituto per i Processi Chimico-Fisici del Consiglio Nazionale delle Ricerche.

10.1021/jp108387x
Published on Web 10/29/2010

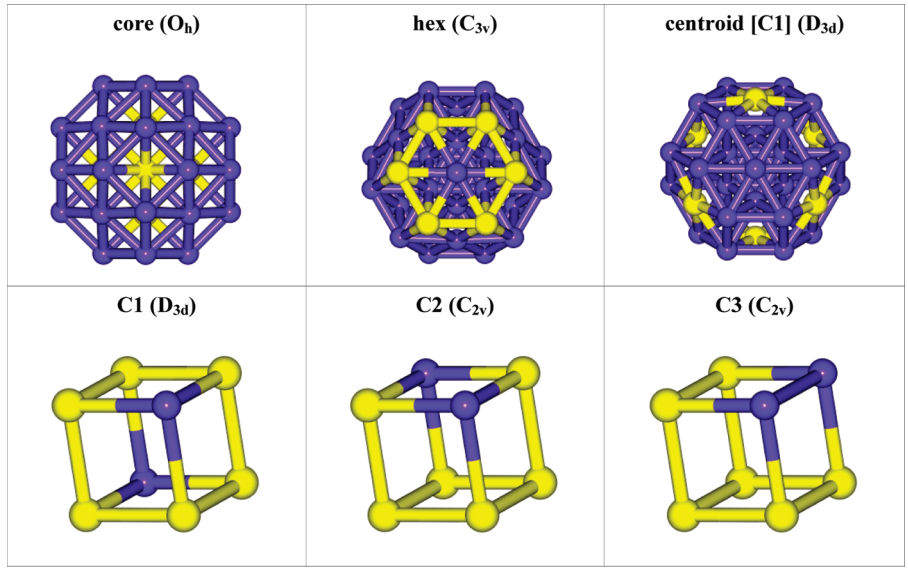

Figure 1. (Top) Definition of the homotops of the bare A_6B_{32} TO clusters studied here. (Bottom) The three different homotops of the centroid isomers: only the atoms at the centers of the (111) faces are shown.

on the surface of nanoparticles[38] and on-top ligand coordination is an important chemisorption mode. The proposed model setup then allows us to monitor ligand adsorption energies as a function of the surrounding chemical environment and to extract information useful to investigate nanoalloy structural rearrangements under reducing conditions. We find a wide variety of behavior for the three (A,B) pairs here considered, ranging from the AuPd pair, in which Pd−CO (or Pd−H) bonding is not strongly affected by neighboring Au atoms but the $Pd_{core}Au_{surface}$ segregation pattern—favored for bare particles—is expected to be inverted in the presence of coordinating species, to the CuPt pair, in which both Pt−CO and Pt−H bonding is strongly enhanced by neighboring Cu atoms in the presence of coordinating species, with similarities but also differences with respect to thin film surfaces.[6] Some qualitative analogies between the effect of H and CO adsorption point to general features of the behavior of nanoalloys in the presence of reducing agents. However, differences in segregation patterns are also found, most notably the predicted absence of segregation inversion from $Pd_{core}Au_{surface}$ to $Pd_{surface}Au_{core}$ configurations under H, which is at variance with the predicted behavior under CO, and an opposite prediction for the PdPt pair.

The article is organized as follows. In section II the adopted methodology is described in detail. In section III the results are presented and discussed, divided into bare (III.1), CO-ligated (III.2), and H-ligated (III.3) clusters. Conclusions are outlined in section IV.

II. Methodology

II.1. Cluster Structures Studied. A 38-atom truncated octahedron (TO), see Figure 1, was chosen as a model for chemisorption on bimetallic nanoparticles, due to the high symmetry of the parent TO structure (O_h) and the fact that it has (111) facets with (111)-centroid atoms on which a CO molecule or an H atom can bind in an atop fashion. Multiple adsorption of H and CO on the TO and other 38−40-atom clusters of Pd, Pt, and Au have previously been reported.[5,11]

(a) Bare A_6B_{32} Clusters. Bimetallic TO isomers with composition A_6B_{32} were studied, for the following (A,B) pairs: (Au,Pd), (Pd,Pt), and (Cu,Pt). In all cases we considered both elements as minority (A) and majority atoms (B)—e.g., we studied both Pd_6Au_{32} and Au_6Pd_{32}. This composition was chosen because it allows us to study a number of different A−B segregation patterns, while maintaining reasonably high symmetry. The following TO homotops[13] (inequivalent isomers of the same geometry and composition, but having different patterns of A and B atoms) of A_6B_{32}, which are shown in Figure 1, were considered:

1. **core**. A core−shell configuration, in which the 6 A atoms form an octahedral core surrounded by a shell of 32 B atoms. This homotop has the full O_h symmetry of the parent TO.

2. **hex**. The 6 A atoms form a hexagonal ring surrounding the centroid of one of the (111) facets, mimicking the local structure found by Andersson et al. on the (111) CuPt surface after CO adsorption.[6] This homotop has C_{3v} symmetry.

3. **centroid**. The 6 A atoms occupy 6 of the 8 (111) centroids. The 8 (111) centroids define a cube and there are three ways in which 6 A and 2 B atoms can decorate a cube: (a) **C1**, the 2 B atoms are arranged across a body-diagonal of the cube (i.e., diametrically opposed)—this homotop has D_{3d} symmetry; (b) **C2**, the 2 B atoms are arranged across a face-diagonal of the cube—this homotop has C_{2v} symmetry; (c) **C3**, the 2 B atoms are arranged along an edge of the cube—this homotop also has C_{2v} symmetry. The three **centroid** homotops (**C1**−**C3**) have identical distributions of A−A, A−B, and B−B bonds and are expected to have very similar energies. This was indeed found to be the case, with total energy differences ranging from 0 to 0.07 eV, both for the bare and ligated clusters, so only results for the **C1** homotop—hereafter referred to as "**centroid**" will be presented here.

TABLE 1: The Number of Nearest-Neighbor Contacts ("bonds") in TO Homotops of A_6B_{32}

	core	centroid	hex
A−A	12	0	6
A−B	48	54	24
B−B	84	90	114

The numbers of nearest-neighbor contacts ("bonds"), of type A−A, A−B, and B−B, in the **core**, **hex**, and **centroid** homotops of TO A_6B_{32} are compared in Table 1. Although the bonding in these homotops is not restricted to nearest-neighbor interactions, we would expect these to dominate, as discussed in the following.

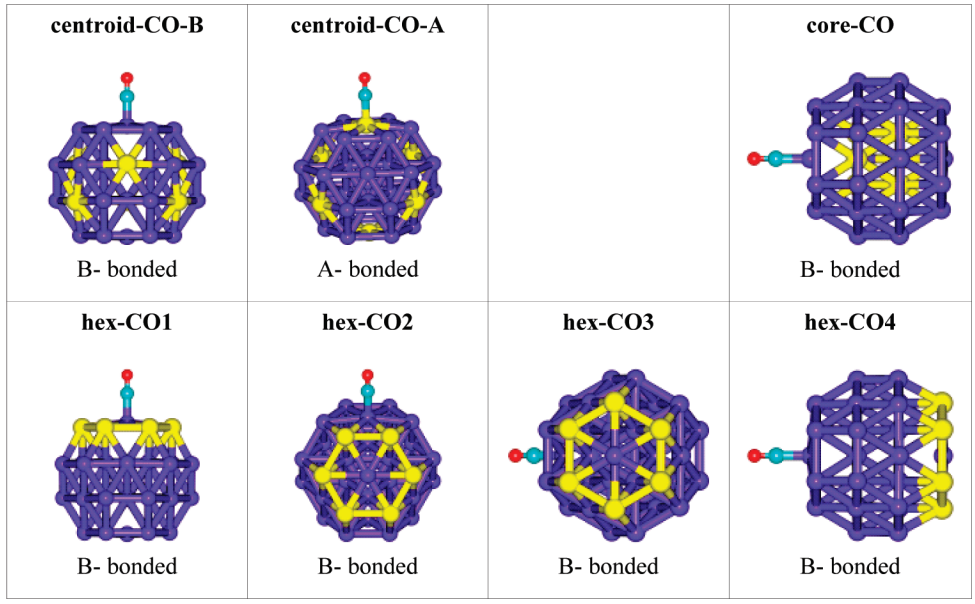

Figure 2. Definition of the possible isomers of $A_6B_{32}CO$ with CO bonded atop a (111) centroid.

The initial TO structures were generated manually, by doping six minority atoms into pure 38-atom Cu, Au, Pd, and Pt TO, and then locally optimizing the geometries using Density Functional Theory (DFT), as described below. As for the metal-cluster + ligand-molecule complexes, we stress that in all cases they were found to be local minima in the energy hypersurface (with the only constraint of on-top adsorption) and that ligand adsorption only produces a minor structural relaxation (consisting mainly of an outward protrusion of the binding metal atom), as shown in Figure 2.

(b) CO and H Chemisorbed on A_6B_{32}. The possible isomers of A_6B_{32}(CO), having CO bonded in an atop fashion on a (111) centroid atom on the **core**, **hex**, and **centroid** (**CO-A** and **CO-B**) homotops of A_6B_{32}, are defined in Figure 2. The corresponding A_6B_{32}(H) isomers are defined in the same way. This enables a comparison to be made of the strength of binding of CO and H to both A and B atoms, without modifying the cluster structure. We stress that our aim is not to study the most stable binding site for ligand adsorption but the changes in adsorption energies upon alloying. The following isomers can be identified:

1. **core-CO**. The CO is bonded to a (111) centroid B atom in the outer shell. Due to the high symmetry of the core−shell homotop, only one isomer (with C_{3v} symmetry) arises.

2. **hex-CO**. There are four distinct isomers, all with CO bonded to B, since all the (111) centroids are B atoms. In order of increasing distance from the hexagonal A_6 ring, these are as follows: (a) **hex-CO1**, the CO is bonded to the B atom in the center of the A_6 ring, this isomer has C_{3v} symmetry; (b) **hex-CO2**, the CO is bonded to a B atom in the center of a (111) facet adjoining the A_6 ring, this isomer has C_s symmetry; (c) **hex-CO3**, the CO is bonded to a B atom in the center of a (111) facet which is two faces away from the A_6 ring, this isomer has C_s symmetry; (d) **hex-CO4**, the CO is bonded to the B atom at the center of the (111) facet on the opposite side of the cluster to the A_6 ring, this isomer has C_{3v} symmetry.

3. **centroid-CO**. There are only two distinct isomers, depending on whether the CO is bonded to a B or A atom: (a) **centroid-CO-B**, the CO is bonded to a B atom (111) centroid, this isomer has C_{3v} symmetry; (b) **centroid-CO-A**, the CO is bonded to an A atom centroid, this isomer has C_s symmetry.

Concerning the information that can be extracted from an analysis of the energetics of these clusters (and that will be applied in sections III.2 and III.3), a few general remarks are in order, here specified for the case of the CO ligand (but valid also for the H ligand):

(i) Since all the (111) centroids of the **hex** and **core** homotops and one of the centroids of the **centroid** homotop of A_6B_{32} are majority (B) atoms, for a given composition the six isomers **core-CO**, **centroid-CO-B**, and **hex-CO1−4** are all bound to the same type of atom, but in different A environments.

(ii) The stronger binding of CO to one metal of an (A,B) pair results in a splitting of the energies of the isomers arising from CO binding to the **centroid** homotop of A_6B_{32}. If A-CO bonding is stronger than B-CO, then the **centroid-CO-B** isomer is more stable, with the **centroid-CO-A** isomer higher in energy. The splitting is reversed when B−CO bonding is stronger than A−CO.

(iii) There is some CO-induced splitting of the **hex-CO** isomers, due to the different chemical environment of the B−CO unit. Assuming that **hex-CO4** is a good model of CO binding to a pure B_{38} cluster (as basically confirmed by the results for pure, non-alloyed clusters reported in the Supporting Information), then a comparison with **hex-CO1** directly gives the effect on the B-CO bond of nearest-neighbor surface alloying with A atoms. Analogously, recalling point (i), comparison with **core-CO** and **centroid-CO-B** gives one the effect on the B−CO bond of core and second-neighbor surface alloying with A atoms.

In summary, the chosen model setup allows us to study not only the effect of CO (and H) bonding on the A/B segregation pattern but also B−CO (respectively, B−H) binding in different environments: subsurface A atoms (**core-CO**), surface first-neighbor A atoms (**hex-CO1**), surface second-neighbor A atoms (**centroid-CO-B**), surface far-neighbor A atoms (**hex-CO4**), when B is the majority species, and surface first-neighbor A atoms (**centroid-CO-A**) when B is the minority species, with minor modulations for the **hex-CO2** and **hex-CO3** clusters.

II.2. Density Functional Theory Calculations. DFT calculations were performed using the NWChem 5.1 quantum chemistry package,[14] which is efficiently parallelized and fully exploits point group symmetry, with the Perdew−Wang exchange-correlation (xc-)functional (PW91).[15] Other gradient-corrected xc-functionals were tested to produce similar results. During the geometry optimization stage, spherical Gaussian-type-orbital basis sets of double-ζ quality were used for the

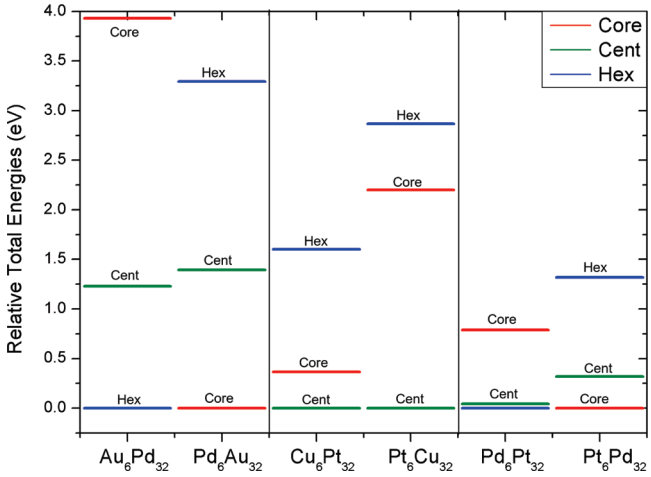

Figure 3. The relative energies (in eV) of the bare clusters. In the color version, different colors represent the different structures: **core** (red), **centroid** (green), **hex** (blue).

metal atoms: Pd (7s6p5d)/[5s3p2d], Pt (7s6p5d)/[6s3p2d], Cu (8s7p6d)/[6s5p3d], and Au (7s5p5d)/[6s3p2d], combined with relativistic effective core potentials,[16] and for hydrogen, carbon, and oxygen atoms: H (4s)/[2s]; C and O (8s4p)/[4s2p]. After geometry optimization, single point calculations using triple-ζ-plus-polarization basis sets were performed: Pd (7s6p5d1f)/[5s3p3d1f], Pt (7s6p5d1f)/[6s3p3d1f], Au (7s6p5d1f)/[6s3p3d1f], Cu (8s7p6d1f)/[6s5p3d1f] H (5s1p)/[3s1p], C and O (11s6p1d)/[5s3p1d]. Coulomb charge fitting was used and all calculations were performed spin unrestricted, using a Gaussian smearing technique (smearing parameter of 0.14 eV for the final energy calculations) for the fractional occupation of the one-electron energy levels. Note that the use of smearing ensures an even occupation of all degenerate molecular orbitals, allowing one to perform calculations within the given symmetry group (no symmetry breaking).[37]

III. Results and Discussion

III.1. Bare A_6B_{32} Clusters. The relative total energies of the bare TO A_6B_{32} clusters are shown in Figure 3 for the three bimetallic systems here considered. Detailed energetics are also reported in Table S-I of the Supporting Information. As segregation patterns of nanoalloys have been studied before,[17−19] we will briefly analyze the present results to provide a basis for comparison with ligated clusters.

(a) AuPd. For AuPd nanoalloys (left-hand side of Figure 3), $Pd_{core}Au_{surface}$ configurations are favored by: the lower surface energy of Au (96.8 meV Å^{-2}) compared to Pd (131 meV Å^{-2}, experimental values from refs 20 and 21 obtained as averages over polycrystalline samples); the higher cohesive energy of Pd (3.89 eV/atom) compared to Au (3.81 eV/atom)[2]; and the smaller atomic radius of Pd (1.375 Å) compared to Au (1.44 Å)[2]. This explains why for Pd_6Au_{32} the **core** homotop (having an octahedral Pd_6 core) is the most stable homotop (by ≈1.4 eV with respect to the isomer second lowest in energy) whereas for Au_6Pd_{32} the **core** homotop (with an octahedral Au_6 core) is the least stable homotop (by nearly 4 eV compared to the best homotop). It should be noted that the **core** TO homotop was previously identified, based on DFT calculations, as the putative global minimum for the composition Pd_6Au_{32}.[17]

The lowest-energy homotop for Au_6Pd_{32} is calculated to be the **hex** structure, which has surface-segregated Au atoms. The reason why **hex** is lower in energy than the **centroid** homotop is because the formation of only six Au−Au bonds in the **hex** homotop causes less disruption of the Pd bonding and allows one to maximize the number of the stronger Pd−Pd bonds (114), as seen in Table 1. It should again be noted that the **hex** TO homotop was previously identified as the putative DFT global minimum for the composition Au_6Pd_{32}.[17] The **hex** structure, however, is the highest energy homotop for Pd_6Au_{32}, since, in addition to exposing Pd atoms on the surface, it leads to maximization of the weaker Au−Au bonds. For both compositions, the more mixed **centroid** homotop, which has surface-segregated but isolated A atoms, lies between the **core** and **hex** homotops, so the relative energy plot for Au_6Pd_{32} is inverted with respect to Pd_6Au_{32}.

(b) PdPt. For PdPt nanoalloys (right-hand side of Figure 3), $Pt_{core}Pd_{surface}$ configurations are favored by: the lower surface energy of Pd (131 meV Å^{-2}) compared to Pt (151 meV Å^{-2})[20,21] and the higher cohesive energy of Pt (5.84 eV/atom) compared to Pd (3.89 eV/atom)[2], while the atomic radii of Pd and Pt are almost identical.[2] This explains the stability of the **core** isomer for Pt_6Pd_{32} and its higher energy for Pd_6Pt_{32}. The core homotop was previously identified as the putative global minimum, at the DFT level, for Pt_6Pd_{32}.[17] The lowest-energy homotop calculated for Pd_6Pt_{32} is the **hex** structure, though the **centroid** homotop lies very close in energy (with a relative energy of +0.05 eV).[22] The **hex** homotop is favored by the stronger Pt−Pt bonds, while the centroid homotop, although it has fewer Pt−Pt bonds, has none of the weakest Pd−Pd bonds. In contrast to Pd_6Pt_{32}, the **hex** structure is the highest energy homotop for Pt_6Pd_{32}, lying approximately 1 eV above the **centroid** homotop.

The energy ordering for the PdPt clusters is the same as for the AuPd system, though the energetic spacings are different for the two compositions and the spread of relative energies is smaller (less than a half) for PdPt than AuPd. This is in part due to the smaller ratio of surface energies for PdPt: $E_{surf}(Pt)/E_{surf}(Pd) = 1.15$, compared to AuPd: $E_{surf}(Pd)/E_{surf}(Au) = 1.35$, overcoming the cohesive energy—the corresponding ratios of cohesive energies are $E_{coh}(Pt)/E_{coh}(Pd) = 1.50$ and $E_{coh}(Pd)/E_{coh}(Au) = 1.02$—for such small clusters, where the surface energy effect is likely to dominate. The small size mismatch (almost zero) between Pd and Pt also tends to decrease the energy difference between homotops[18,23]—by contrast the atomic radius of Au is 5% larger than Pd. Moreover, $Pd_{core}Au_{surface}$ configurations are stabilized by Pd-to-Au charge transfer,[24] which is not the case for PdPt (the values of the Pauling electronegativity are 2.4 for Au and 2.2 for both Pd and Pt). Finally, it should be recalled that the PdPt bulk phase diagram presents a series of solid solutions, in contrast to the several ordered phases observed for the AuPd and CuPt pairs.[25]

(c) CuPt. The spread of relative homotop energies for CuPt, shown in Figure 3 (center), is intermediate between those of PdPt and AuPd, with Cu_6Pt_{32} displaying an energy range of 1.6 eV and Pt_6Cu_{32} a range of 2.9 eV. The most striking difference with respect to the previous two cases is that the ordering of the homotops for Cu_6Pt_{32} and Pt_6Cu_{32} are the same (**hex** > **core** > **centroid**), not inverted as for AuPd and PdPt. The greater stability of the **centroid** homotop reflects the energetic preference for Cu and Pt to mix,[26] since this isomer has the highest number (54) of Cu−Pt bonds (see Table 1). This also explains why the **hex** homotop lies at highest energy for both compositions, as this has the fewest Cu−Pt bonds (24). The favorable Cu−Pt mixing is consistent with the stability of ordered mixed Cu_3Pt, CuPt, and $CuPt_3$ bulk phases.[25] It is interesting to note that for Pt_6Cu_{32} the strong exothermic Cu−Pt mixing overcomes the greater surface energy (151 meV Å^{-2}) and cohesive energy (5.84 eV/atom) of Pt compared to Cu ($E_{surf} = 113.9$ meV Å^{-2};

E_{coh} = 3.49 eV/atom),[17,20,27] both of which should favor $Pt_{core}Cu_{surface}$ segregation. However, the greater atomic radius (1.385 Å) and electronegativity (2.2) of Pt compared to Cu (atomic radius = 1.28 Å; electronegativity = 1.9)[20,22] would tend to favor surface segregation of Pt, so perhaps this conflict of chemical ordering effects and the strongly exothermic Cu−Pt mixing[26] combine to favor mixing even in small CuPt clusters. In fact, Figure 3 shows that the relative energy of the **core** homotop is higher (+2.20 eV) for Pt_6Cu_{32} than for Cu_6Pt_{32} (+0.37 eV).

III.2. A_6B_{32}(CO) Clusters. The relative energies of A_6B_{32} clusters with CO bound atop (111) centroid atoms are shown in Figure 4, with detailed energetics reported in Table S-II of the Supporting Information. These will be discussed in detail for each A−B pair, along the lines of the general remarks outlined in section II.1.

(a) AuPd(CO). For AuPd (Figure 4a), two main observations can be made. First, CO binds more strongly to Pd than Au (the binding energy for CO atop Pd is 1.47 eV for Pd(111), while CO does not bind to the Au(111) surface[23]). This shows up most clearly for CO bound to the **centroid** homotops of Au_6Pd_{32} and Pd_6Au_{32}, giving rise to a low-energy Pd−CO isomer and a higher energy Au−CO isomer in both cases. The splitting of the **centroid-CO** isomers (i.e., the energy difference between the **centroid-CO-Au** and the **centroid-CO-Pd** isomers) is 0.97 eV for Au_6Pd_{32}(CO) and 0.87 eV for Pd_6Au_{32}(CO). Second, the energy differences between the isomers in which CO is bound to the same (majority) atom are very little modified upon CO-adsorption for both Au_6Pd_{32} and Pd_6Au_{32}; i.e., the CO binding energy is fairly constant.

An important consequence of the stronger binding of CO to Pd compared to Au is observed for Pd_6Au_{32}(CO), where the **centroid-CO-Pd** isomer lies close in energy (0.15 eV) to the **core-CO** isomer (compared with a **core-centroid** separation of 1.39 eV for the bare cluster). The **core-CO** isomer is favored due its Pd_6 core but it has weak Au−CO bonding. It is then to be expected that by coordinating further CO molecules to Pd_6Au_{32} a ligand-induced core/surface segregation inversion will occur, allowing the CO molecules to interact with surface Pd, rather than Au atoms. Indeed, we found that increasing the number (n) of adsorbed CO molecules, already for $n = 2$ there is a crossover between the **core** and **centroid** configurations. This is in agreement with the findings of Shan et al., whose DFT calculations indicate that increasing CO coverage of a AuPd alloy induces surface segregation of Pd atoms, driven by the greater strength of Pd−CO bonding.[29]

Considering in detail the low-energy **hex-CO** isomers of Au_6Pd_{32}(CO), the least stable is **hex-CO1**, which has CO bound to the Pd at the center of the Au_6 hexagon, followed by **hex-CO4**, where the CO is bound to the opposite face. This ordering is consistent with DFT calculations reported by Shan et al., who found that the binding energy of CO atop a Pd atom on an extended Pd/Au(111) surface is nearly 0.4 eV greater when the Pd−CO is surrounded by six other Pd atoms rather than six Au atoms (with the binding energy decreasing upon successive substitution of a neighboring Pd by Au).[29] In our calculations on finite clusters, however, we find that the energy spread of the **hex-CO** isomers is only around 0.16 eV. For Pd_6Au_{32}(CO), where the **hex-CO** isomers are the highest in energy and there is an even smaller spread of energies (less than 0.1 eV), the isomer energies simply increase as the Au−CO unit gets closer to the Pd_6 ring, with the lowest- and highest-energy isomers being **hex-CO4** (Au_6 environment) and **hex-CO1** (Pd_6), respectively. This is in qualitative agreement with the findings of Shan et al. for CO binding to Pd/Au(111) surfaces, where Au−CO atop binding was calculated to be stabilized by 0.2 eV when Au−CO is surrounded by six Pd atoms.[29]

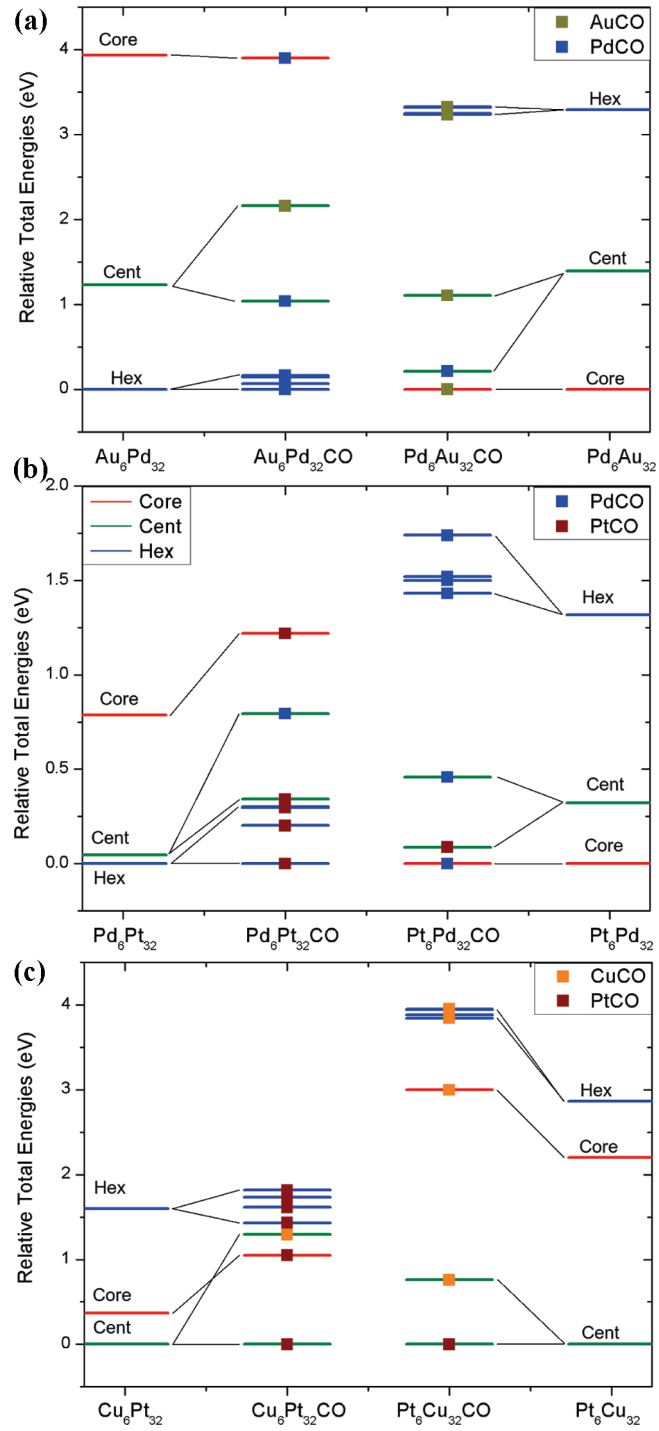

Figure 4. Comparison of the energies of the bare clusters A_6B_{32} clusters (far left and right of each diagram), with the corresponding CO-bound clusters (central columns): (a) Au_6Pd_{32} and Pd_6Au_{32}; (b) Pd_6Pt_{32} and Pt_6Pd_{32}; and (c) Cu_6Pt_{32} and Pt_6Cu_{32}. Squares indicate which element the CO is bound to: light = Au and Cu (orange in color), dark = Pd (blue in color) and Pt (red in color). Color coding of the different structures is the same as in Figure 3.

In contrast to our findings, however, DFT calculations by Zhang et al. for CO on Pd/Au(111) indicate that the atop Pd−CO binding energy increases from 0.97 (Au_6 environment) to 1.07 (Pd_2Au_4 environment), while the calculated Au−CO atop binding energy is 0.23 eV.[7] Surface enrichment by Au is said

to increase the catalytic activity of AuPd nanoparticles for CO oxidation due to an Au-induced ligand effect. According to Yuan et al., isolated Pd atoms on (111) faces—i.e., surrounded by 6 Au atoms—have a sharp localized electronic density of states, with this arrangement being favored in AuPd nanoparticles.[30]

(b) PdPt(CO). For PdPt (Figure 4b), CO binds slightly more strongly to Pt than to Pd: the atop binding energies reported by Norskov and co-workers[23] are 1.5 eV on Pt(111) and 1.47 eV on Pd(111). Relativistic effects obviously play an important role: Baerends and co-workers calculated the difference in binding energy between Pt−CO and Pd−CO to vary between −0.19 eV (Pd−CO more strongly bound—for nonrelativistic calculations) to +0.21 (Pt−CO more strongly bound—for scalar relativistic calculations), with values of approximately +0.1 eV for relativistic calculations including spin−orbit coupling.[31] The Pt−CO/Pd−CO difference is amplified in the splitting of the **centroid-CO** isomers, with the Pt−CO isomer favored over the Pd−CO isomer by approximately 0.4 eV, for both compositions. This is our main finding for the PdPt pair, implying that Pd−CO bonding is weakened in the presence of surface Pt atoms, whereas Pt−CO bonding is strengthened in the presence of surface Pd atoms.

This finding is consistent with the fact that the spread of the **hex-CO** isomers is greater for PdPt than for AuPd, being approximately 0.3 eV for both $Pd_6Pt_{32}(CO)$ and $Pt_6Pd_{32}(CO)$, and with the energy ordering of the **hex-CO** isomers. For $Pd_6Pt_{32}(CO)$, in fact, the lowest-energy isomer (by 0.2 ev) is **hex-CO1**, where the Pt−CO is in the center of a Pd_6 ring, with the energy increasing with increased distance from the ring. In contrast, for $Pt_6Pd_{32}(CO)$, **hex-CO1**, with the Pd−CO in the center of a Pt_6 ring, is the highest energy isomer (by over 0.2 eV). Thus, the relatively large spread of energies for **hex-CO** isomers in the PdPt system is due to the considerable stabilization or destabilization of the **hex-CO1** isomer, depending on the composition.

For the same reason, the relative energy of the least favored **core** homotop of Pd_6Pt_{32} increases (from around 0.8 eV to over 1.2 eV) upon coordination of CO, as it does not possess surface Pd atoms. Finally, in an analogous situation to that discussed above for AuPd, the weaker Pd−CO bonding compared with Pt−CO results in a small energy difference (0.09 eV) between the Pd−CO **core-CO** and **centroid-CO-Pt** isomer of $Pt_6Pd_{32}(CO)$. Again, it is interesting to speculate that the adsorption of additional CO molecules could induce a core−shell inversion in Pt_6Pd_{32}. This was suggested by preliminary calculations in which we find a crossover between the **core** and **centroid** configurations upon coordination of only two CO molecules. However, the great sensitivity of Pd−CO bonding to electronic effects suggests use of some caution in drawing such a conclusion, as there might be a subtle interplay of effects implying a dependence of the predictions upon cluster composition and CO chemical potential.

(c) CuPt(CO). For CuPt (Figure 4c), CO binds much more strongly to Pt than Cu—with an atop binding energy of 1.5 eV for Pt(111) compared with 0.5 eV for Cu(111).[23,28,32] This is apparent in the Pt_6Cu_{32} case, in which the energy differences of the Cu−CO bonded structures stay nearly constant and the only remark concerns the **centroid-CO-Cu/Pt** splitting, which is 0.7 eV, a little smaller than that predicted from the difference in Cu−CO and Pt−CO bond strengths.

The most interesting finding concerns the Cu_6Pt_{32} composition, for which we observe: (i) a **centroid-CO-Cu/Pt** splitting of ≈1.25 eV; (ii) a destabilization of the **core-CO** isomer by ≈0.7 eV. Both these effects point to a strengthening of Pt−CO bonding in the presence of surface Cu atoms, which is further confirmed by an analysis of the splitting of the **hex-CO** isomers. We find in fact a substantial spread of energies (nearly 0.4 eV) of the **hex-CO** isomers of $Cu_6Pt_{32}(CO)$, with the energy being lowest (by nearly 0.2 eV) for **hex-CO1**, where the Pt−CO is in the center of the Cu_6 ring and increasing with increasing distance from the ring, so that **hex-CO4** is the highest energy isomer. These findings can be compared with those of recent literature. Andersson et al.[6] have studied a CO-induced transition from a near-surface alloy (Cu layer beneath Pt) to a surface alloy consisting of 2/3 ML Cu (ordered, with isolated Pt atoms), and have shown that it is due to strengthened Pt−CO atop binding (the DFT calculated binding energy increases from 1.38 eV for pure Pt(111) to 2.03 eV for 2/3 ML Cu) though the surface segregation of Cu is endothermic (0.3−0.4 eV). In contrast, earlier DFT results reported by Knudsen et al.[8] indicated higher Pt−CO binding for subsurface Cu—as found for Ag and Au.[6] The Pt-bound **hex-CO** isomer is the closest cluster model of the surface coordination observed by Andersson et al.[6] However, it turns out not to be the lowest-energy configuration, not even after CO adsorption. In a 38-atom cluster in fact the **hex** structure, although stabilized by Pt−CO bonding, is relatively unstable, and CO bonding is not sufficient to reverse the energy order with respect to the lowest-energy **centroid-CO-Pt** structure. This points to an interesting difference between nanoparticles and extended surfaces: a larger cluster is necessary in order to stabilize the Cu−Pt surface alloy in the presence of CO for nanoparticles as well as thin films.

III.3. $A_6B_{32}(H)$ Clusters. The relative energies of A_6B_{32} clusters with H bound atop (111) centroid atoms are shown in Figure 5, with detailed energetics reported in Table S-III of the Supporting Information. Some features of these plots are similar to those for $A_6B_{32}(CO)$, which is interesting, as it suggests that qualitatively similar features exist concerning the effect of adsorption of different reducing agents on nanoalloy segregation patterns. However, significant differences in the energy splittings and in the fine details of the homotop ordering can also be observed, and are worth analyzing in detail.

(a) AuPd(H). For AuPd (Figure 5a), H binds more strongly to Pd than Au, which again leads to the relative stabilization in $Au_6Pd_{32}(H)$ of the **centroid-H-Pd** isomer with H bound to Pd. For $Pd_6Au_{32}(H)$, the **centroid-H-Pd** isomer is likewise stabilized. The main finding is here obtained from a comparison of Figures 4a and 5a, showing that the splitting of the centroid isomers after H-adsorption (0.40 and 0.25 eV for Au_6Pd_{32} and Pd_6Au_{32}, respectively) is very much smaller than for CO adsorption (1.12 and 0.89 eV). This entails a lower energetic preference for H bonding to Pd rather than Au, as compared with CO. This explains why the energy gap between the lowest-energy **core-H** isomer and the Pd-bound **centroid-H-Pd** isomer is much larger for $Pd_6Au_{32}(H)$ (1.24 eV) than for $Pd_6Au_{32}(CO)$ (0.21 eV), suggesting that core−shell segregation inversion of AuPd clusters under H_2 may not be favorable. Preliminary calculations indicate that we do find an energetic crossover, but only for six adsorbed H atoms.

The lowest-energy isomers for $Au_6Pd_{32}(H)$ are **hex-H** isomers, which follow a similar order to that for CO adsorption: **hex-H3** < **hex-H4** < **hex-H2** < **hex-H1**, so again placing the adsorbed species on the (111) Pd site in the center of the Au_6 ring is relatively unfavorable (the energy spread is slightly larger than in the CO case: 0.25 eV vs 0.16 eV). Interestingly, the ordering of the high energy **hex-H** isomers of $Pd_6Au_{32}(H)$ (**hex-H1** < **hex-H2** < **hex-H3** < **hex-H4**) is the exact opposite of the ordering for $Pd_6Au_{32}(CO)$, suggesting that the Au−H bonding

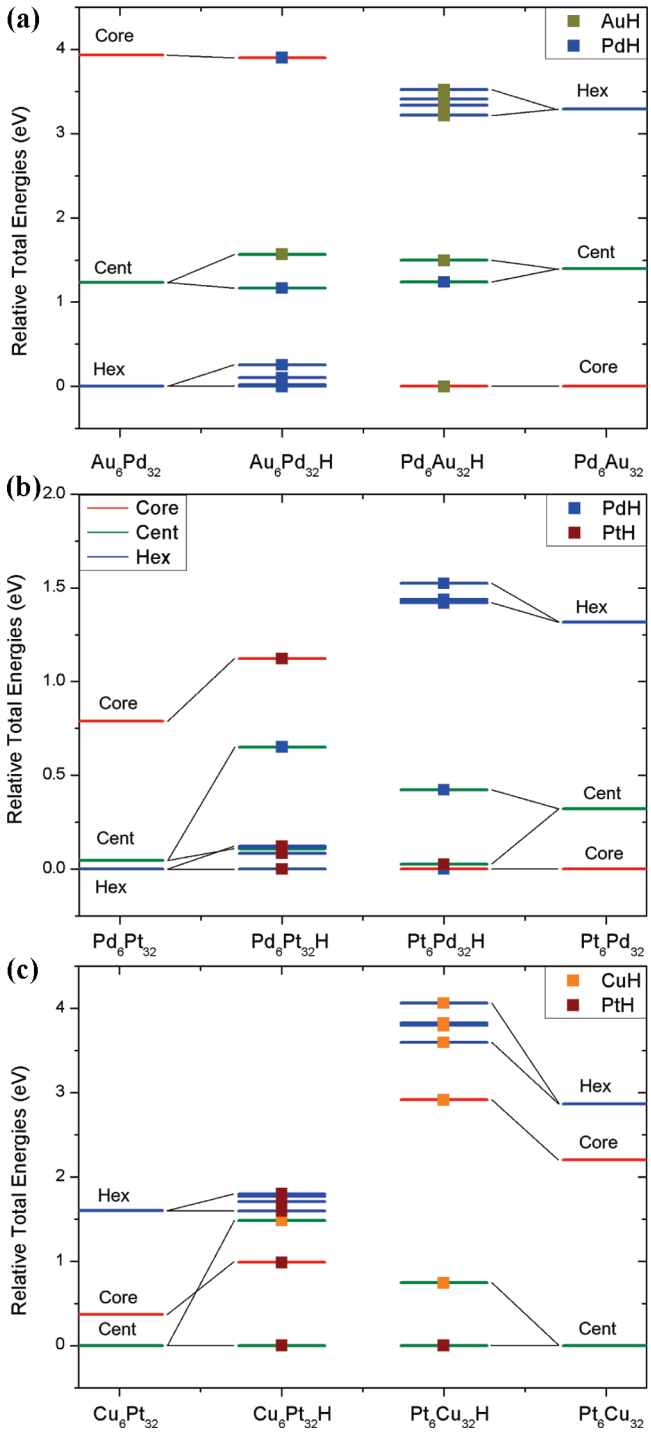

Figure 5. Comparison of the energies of the bare clusters A_6B_{32} clusters (far left and right of each diagram), with the corresponding H-bound clusters (central columns): (a) Au_6Pd_{32} and Pd_6Au_{32}; (b) Pd_6Pt_{32} and Pt_6Pd_{32}; and (c) Cu_6Pt_{32} and Pt_6Cu_{32}. Squares indicate which element the CO is bound to: light = Au and Cu (orange in color), dark = Pd (blue in color) and Pt (red in color). Color coding of the different structures is the same as in Figure 3.

is enhanced in the presence of surface Pd atoms, whereas Au-CO bonding is weakened. The spread of the **hex-H** isomers (0.31 eV) is again larger than that for the **hex-CO** isomers (0.09 eV), confirming the greater sensitivity of the Pd−H bonding strength to the environment than observed for CO.

(b) PdPt(H). For PdPt (Figure 5b), H binds more strongly to Pt than Pd, which again shows up in a splitting of the **centroid-H** isomers, with the Pt−H isomer favored over the Pd−H isomer. The ligand-induced centroid splitting for $Pd_6Pt_{32}(H)$ (0.54 eV) is slightly greater than for $Pd_6Pt_{32}(CO)$ (0.45 eV), and both are slightly greater than the splittings for $Pt_6Pd_{32}(H)$ (0.40 eV) and $Pt_6Pd_{32}(CO)$ (0.37 eV). This implies that the differences in the strengths of Pt−H and Pd−H bonding are slightly greater than for M−CO bonding.

The lowest-energy isomers for $Pd_6Pt_{32}(H)$ are **hex-H** isomers, which follow a similar order to that for CO adsorption: **hex-H1** < **hex-H2** < **hex-H4** < **hex-H3**, so again placing the adsorbed species on the (111) Pt site in the center of a Pd_6 ring is favorable. The ordering of the high energy **hex-H** isomers for $Pt_6Pd_{32}(H)$ is identical to that for $Pt_6Pd_{32}(CO)$. However, for both compositions the spread of energies of the **hex-H** isomers (approximately 0.1 eV) is significantly smaller than for the **hex-CO** isomers (0.3 eV), implying that Pd−H and Pt−H bond strengths are less sensitive to the presence of surface minority atoms.

One consequence of the relatively large stabilization of the **centroid-H** isomer with H bound to Pt is that the **centroid-H-Pt** isomer of $Pt_6Pd_{32}(H)$ lies only 0.03 eV above the **core-H** isomer, in which the H atom is bound to Pd, rather than Pt. This compares with a gap of around 0.09 eV between the **core-CO** and **centroid-CO-Pt** isomers of $Pt_6Pd_{32}(CO)$. In analogy with the CO case, it therefore seems likely that further hydrogenation of the Pt_6Pd_{32} cluster will result in core−shell inversion, with one or more Pt-centroid structures dropping below the core−shell structure, driven by the greater strength of Pt−H compared with Pd−H bonding. This is confirmed by preliminary multiple-adsorption calculations which predict such an inversion for just two adsorbed H atoms.

(c) CuPt(H). For CuPt (Figure 5c), H binds more strongly to Pt than Cu, which is again manifest in the splitting of the Pt−H and Cu−H **centroid-H** isomers. The centroid splitting for $Cu_6Pt_{32}(H)$ is 1.48 eV, greater than that calculated for CO adsorption (1.29 eV), suggesting that surface Cu atoms in a Pt-rich environment are s-depopulated and do not bind to H. The splitting of the **centroid-H** isomers for $Pt_6Cu_{32}(H)$ (0.74 eV), instead, is similar to that for $Pt_6Cu_{32}(CO)$ (0.76 eV).

The relative energies of the **core-H** isomers for both compositions are smaller (by 0.1−0.2 eV) than the **core-CO** isomers. For $Cu_6Pt_{32}(H)$—as found previously for $Cu_6Pt_{32}(CO)$—the **core-H** isomer, which has H bound to Pt, lies between the Pt−H and Cu−H **centroid-H** isomers. Due to the greater importance of Pt−H bonding for this composition, the energy gap between the **core-H** isomer and the **centroid−H-Cu** isomer for $Cu_6Pt_{32}(H)$ (0.50 eV) is more than twice as large as in the CO analogue (0.24 eV).

Considering the high-energy **hex-H** isomers, the spread of energies for $Cu_6Pt_{32}(H)$ (0.29 eV) is slightly smaller than that calculated for $Cu_6Pt_{32}(CO)$ (0.39 eV), with a similar ordering: **hex-H1** < **hex-H2** < **hex-H4** < **hex-H3**. This ordering is identical to that for $Pd_6Pt_{32}(H)$. In contrast, the spread of energies for the **hex-H** isomers of $Pt_6Cu_{32}(H)$ (0.47 eV) is much larger than that for $Pt_6Cu_{32}(CO)$ (0.11 eV), and the stability order: **hex-H4** < **hex-H3** < **hex-H2** < **hex-H1** (indicating a decrease in stability as the Cu−H gets closer to the Pt_6 ring) is very different from that for CO (**hex-CO3** < **hex-CO4** < **hex-CO1** < **hex-CO2**). The larger splitting for $Pt_6Cu_{32}(H)$ is due to a particular stabilization of **hex-H4** and destabilization of **hex-H1**, with the other two **hex-H** isomers lying within 0.03 eV of each other, and is consistent with the large centroid splitting of the $Cu_6Pt_{32}(H)$ isomer noted above. Therefore, comparing H and CO adsorption on the metastable hex homotops for the CuPt system, we see that for Cu_6Pt_{32}, both H and CO prefer to bind

to Pt(111) centroids which are surrounded by Cu, while for Pt_6Cu_{32}, H and, to a lesser extent, CO prefer to bind to Cu(111) centroids which are remote from the surface Pt atoms.

IV. Conclusions

In this work we have focused on the effect of alloying on ligand adsorption energies and how this can modify the segregation patterns of selected binary nanoalloys. The proposed model setup, which considers a fixed geometrical structure (TO_{38}) and alloy compositions (A_6B_{32} and B_6A_{32}) and varies the chemical ordering to investigate the binding energies of ligand species (CO and H) atop centroid sites, has some general features (hexagonal local arrangements are a common occurrence on the surface of nanoparticles[38] and on-top ligand coordination is an important chemisorption mode) and allows one to monitor ligand adsorption energies as a function of the coordination environment and extract information useful to investigate nanoalloy structural rearrangements under reducing conditions. The following (A,B) pairs: (Au,Pd), (Pd,Pt), and (Cu,Pt), were studied, and a wide variety of behaviors for the three (A,B) pairs was found.

CO bonding to AuPd is little sensitive to electronic and structural effects due to alloying, as confirmed by the fact that the spread of the **hex-CO** homotops is small: less than 0.16 eV, whereas the large splitting of the **centroid-CO** homotops (around 0.9−1. eV) points to the possibility of an inversion in the segregation pattern in the presence of CO: from $Pd_{core}Au_{surface}$ to $Au_{core}Pd_{surface}$, in agreement with experimental results.[29,33] In contrast, the spread of the **hex-H** homotops is larger (around 0.3 eV) and the splitting of the **centroid-H** homotops is much smaller (0.25−0.4 eV), implying a possible reversible switching depending on the reaction conditions when the two species are present simultaneously.

PdPt clusters present a nearly opposite behavior, with an appreciable spread of the **hex-CO** homotops (around 0.3 eV) and an intermediate splitting of the **centroid-CO** homotops (0.4 eV), to be contrasted with the small spread of the **hex-H** homotops (around 0.1 eV) and a slightly larger splitting of the **centroid-H** homotops (around 0.5 eV). Pd−CO bonds are in fact weakened by the presence of neighboring surface Pt atoms, whereas the opposite happens for Pt−CO bonds. PdPt might thus give segregation inversion from $Pt_{core}Pd_{surface}$ to $Pd_{core}Pt_{surface}$ in the presence of hydrogen, but a weaker tendency in the presence of CO (as is experimentally found for the latter[9]), possibly depending upon composition and chemical potentials (partial pressure, temperature) of CO and H_2 (a result awaiting experimental confirmation).

The CuPt pair presents the largest effects of alloying upon ligand adsorption, and also ones in which CO and H behave in exactly the same way. Both Pt−CO and Pt−H bonding is in fact strongly enhanced by neighboring surface Cu atoms, in agreement with previous results for thin film surfaces,[6] whereas both Cu−CO and Cu−H bonding is strongly weakened by neighboring surface Pt atoms. The spread of the hex homotops is as a rule substantial (0.3−0.5 eV, with the exception of Pt_6Cu_{32}−CO for which it is 0.11 eV), as well as the splitting of the centroid homotops, ranging from 0.75 to 1.48 eV. The simultaneous presence of these two phenomena produce the peculiar feature of centroid homotops being the putative global minima for both Pt_6Cu_{32} and Cu_6Pt_{32}, and strongly reinforcing their relative stability upon adsorption of CO or H species. In fact, at variance with extended systems, in small clusters the energy gain due to Pt−CO enhancement is not sufficient to overcome the tendency of Cu atoms to avoid sites with very low coordination and with a small number of mixed Cu−Pt bonds, and the main net result is to disfavor subsurface Cu with respect to surface segregation.

It should be underlined that the inverse correlation which is found in the effect of alloying on metal−ligand bond strengths, such that the increase in the metal−ligand bonding of one element of the pair corresponds to a weakening for the other element, seems to be a general phenomenon.

Finally, we underline that the proposed model setup (and its future generalizations, e.g., to consider multiple adsorption coupled with free energy calculations) provides a coherent framework in which to discuss and analyze the interplay of chemical ordering and ligand adsorption in nanoalloy clusters and seems to be able to provide some insight on this important theme in contemporary nanocatalysis.[1]

Acknowledgment. P.S.W. would like to thank The University of Birmingham and the EPSRC for PhD funding. P.S.W. is grateful to Dr Oliver Paz-Borbón for help in the initial stages of this work. This work has been performed in part within the HPC-Europa2 project, funded by the European Commission - DG Research in the Seventh Framework Programme under Grant Agreement Number 228398, which allowed us to perform some of the DFT calculations at the CINECA supercomputing center (Bologna, Italy). Computer resources on the HPCx service were also provided to P.S.W. and R.L.J. via their membership of the U.K.'s HPC Materials Chemistry consortium and funded by EPSRC (Portfolio Grant EP/D504872). Other calculations were performed on the University of Birmingham's BlueBEAR high-performance computer,[34] and at CINECA via an agreement with Italian CNR. A.F. acknowledges financial support from EC FP7 for the SEPON project within the ERC Advanced Grants.

Supporting Information Available: The detailed energetics of bare A_{38} and A_6B_{32} metal clusters and their interaction with a CO molecule and a H atom. This material is available free of charge via the Internet at http://pubs.acs.org.

References and Notes

(1) Haruta; Kobayashi, T.; Sano, H.; Yada, N. *Chem. Lett.* **1987**, 405–408.
(2) Ferrando, R.; Jellinek, J.; Johnston, R. L. *Chem. Rev.* **2006**, *103* (3), 845–910.
(3) Lei, Y.; Mehmood, F.; Lee, S.; Greeley, J. P.; Lee, B.; Seifert, S.; Winans, R. E.; Elam, J. W.; Meyer, R. J.; Redfern, P. C.; Teschner, D.; Schlögl, R.; Pellin, M. J.; Curtiss, L. A.; Vajda, S. *Science* **2010**, *328*, 224.
(4) Judai, K.; Wörz, A. S.; Abbet, S.; Heiz, U. *J. Am. Chem. Soc.* **2004**, *126*, 2732.
(5) Paz-Borbon, L. O.; Johnston, R. L.; Barcaro, G.; Fortunelli, A. *Eur. Phys. J. D* **2009**, *52*, 131–134.
(6) Andersson, K. J.; Calle-Vallejo, F.; Rossmeisl, J.; Chorkendorff, I. *J. Am. Chem. Soc.* **2009**, *131*, 2404–2407.
(7) Zhang, J.; Jin, H.; Sullivan, M. B.; Lim, F. C. H.; Wu, P. *Phys. Chem. Chem. Phys.* **2009**, *11*, 1441.
(8) Knudsen, J.; Nilekar, A. U.; Vang, R. T.; Schnadt, J.; Kunkes, E. L.; Dumesic, J. A.; Mavrikakis, M.; Besenbacher, F. *J. Am. Chem. Soc.* **2007**, *129*, 6485.
(9) Tao, F.; Grass, M. E.; Zhang, Y.; Butcher, D. R.; Renzas, J. R.; Liu, Z.; Chung, J. Y.; Mun, B. S.; Salmeron, M.; Somorjai, G. A. *Science* **2008**, *322*, 932–934.
(10) Lovvik, O. M.; Opalka, S. M. *Surf. Sci.* **2008**, *602*, 2840.
(11) Neyman, K. M.; Lim, K. H.; Chen, Z. X.; Moskaleva, L. V.; Bayer, A.; Reindl, A.; Borgmann, D.; Denecke, R.; Steinrück, H.-P.; Rösch, N. *Phys. Chem. Chem. Phys.* **2007**, *9*, 3470.
(12) González, S.; Neyman, K. M.; Shaikhutdinov, S.; Freund, H.-J.; Illas, F. *J. Phys. Chem. C* **2007**, *111*, 6852.
(13) Jellinek, J.; Krissinel, E. B. *Chem. Phys. Lett.* **1996**, *258*, 283.
(14) Bylaska, E. J.; de Jong, W. A.; Govind, N.; Kowalski, K.; Straatsma, T. P.; Valiev, M.; Wang, D.; Apra, E.; Windus, T. L.; Hammond, J.; Nichols, P.; Hirata, S.; Hackler, M. T.; Zhao, Y.; Fan, P.-D.; Harrison, R. J.; Dupuis,

M.; Smith, D. M. A.; Nieplocha, J.; Tipparaju, V.; Krishnan, M.; Wu, Q.; Van Voorhis, T.; Auer, A. A.; Nooijen, M.; Brown, E.; Cisneros, G.; Fann, G. I.; Fruchtl, H.; Garza, J.; Hirao, K.; Kendall, R.; Nichols, J. A.; Tsemekhman, K.; Wolinski, K.; Anchell, J.; Bernholdt, D.; Borowski, P.; Clark, T.; Clerc, D.; Dachsel, H.; Deegan, M.; Dyall, K.; Elwood, D.; Glendening, E.; Gutowski, M.; Hess, A.; Jaffe, J.; Johnson, B.; Ju, J.; Kobayashi, R.; Kutteh, R.; Lin, Z.; Littlefield, R.; Long, X.; Meng, B.; Nakajima, T.; Niu, S.; Pollack, L.; Rosing, M.; Sandrone, G.; Stave, M.; Taylor, H.; Thomas, G.; van Lenthe, J.; Wong, A.; Zhang, Z. *NWChem, A Computational Chemistry Package for Parallel Computers, Version 5.1*,Pacific Northwest National Laboratory, Richland, WA, 2007.

(15) Perdew, J. P.; Chevary, J. A.; Vosko, S. H.; Jackson, K. A.; Pederson, M. R.; Singh, D. J.; Fiolhais, C. *Phys. Rev. B* **1992**, *46*, 6671.

(16) Andrae, D.; Haeussermann, U.; Dolg, M.; Stoll, H.; Preuss, H. *Theor. Chim. Acta* **1990**, *77*, 123. ftp://ftp.chemie.uni-karlsruhe.de/pub/basen.

(17) Paz-Borbon, L. O.; Johnston, R. L.; Barcaro, G.; Fortunelli, A. *J. Chem. Phys.* **2008**, *128*, 134517.

(18) Reyes-Nava, J. A.; Rodriguez-López, J. L.; Pal, U. *Phys. Rev. B* **2009**, *80*, 161412.

(19) Menning, C. A.; Chen, J. G. *J. Chem. Phys.* **2009**, *130*, 174709.

(20) Tyson, W. R.; Miller, W. A. *Surf. Sci.* **1977**, *62*, 267.

(21) Pauling, L. *The Nature of the Chemical Bond*, 3rd ed.; Cornell University Press: Ithaca, NY, 1960.

(22) Rubinovich, L.; Polak, M. *Phys. Rev. B* **2009**, *80*, 045404.

(23) Hammer, B.; Morikawa, Y.; Norskov, J. K. *Phys. Rev. Lett.* **1996**, *76* (12), 2142.

(24) Zhang, M.; Fournier, R. *J. Mol. Struct. (THEOCHEM)* **2006**, *762*, 49.

(25) Miedema, A. R. *Z. Metallkd.* **1978**, *69*, 287.

(26) Strasser, P.; Koh, S.; Greeley, J. *Phys. Chem. Chem. Phys.* **2008**, *10*, 3670–3683.

(27) Kittel, C. *Introduction to Solid State Physics*, 6th ed.; Wiley: New York, 1986.

(28) *Landolt-Börnstein Group IV Physical Chemistry Vol. 5d*; Springer-Verlag: Berlin, 1994; p 1.

(29) Shan, B.; Hyun, J.; Kapur, N.; Cho, K. *2009 MRS Proceedings, Spring*, 2009.

(30) Yuan, D.; Gong, X.; Wu, R. *Phys. Rev. B* **2008**, *78*, 035441.

(31) Philipsen, P. H. P.; van Lenthe, E.; Snijders, J. G.; Baerends, E. J. *Phys. Rev. B* **1997**, *56*, 13556.

(32) Vollmer, S.; Witte, G.; Woll, C. *Catal. Lett.* **2001**, *77*, 97–101.

(33) Edwards, J. K.; Carley, A. F.; Herzing, A. A.; Kiely, C. J.; Hutchings, G. J. *Faraday Discuss.* **2008**, *138*, 225–239.

(34) http://www.bear.bham.ac.uk.

(35) Paz-Borbon, L. O.; Johnston, R. L.; Barcaro, G.; Fortunelli, A. *J. Phys. Chem. C* **2007**, *111*, 2936.

(36) Barcaro, G.; Fortunelli, A.; Rossi, G.; Nita, F.; Ferrando, R. *J. Phys. Chem. B* **2006**, *110*, 23197.

(37) Aprà, E.; Fortunelli, A. *J. Phys. Chem. A* **2003**, *107*, 2934.

(38) Aprà, E.; Baletto, F.; Ferrando, R.; Fortunelli, A. *Phys. Rev. Lett.* **2004**, *93*, 065502.

JP108387X

Supporting Information for
"The effect of CO and H chemisorption on the chemical ordering of bimetallic clusters"

Paul S. West[1], Roy L. Johnston[1], Giovanni Barcaro[2] and Alessandro Fortunelli[2]

[1]School of Chemistry, University of Birmingham, Edgbaston, Birmingham, B15 2TT, UK

[2]Molecular Modeling Laboratory, IPCF-CNR, via G. Moruzzi 1, I-56124, Pisa, Italy

All the energies reported in the following were obtained via DFT/PW91 calculations using a TZVP basis set on DZV-optimized geometries and the numerical approach detailed in the main text. The cluster nomenclature also corresponds to the definition given in the main text.
For the bare clusters we report the total energy (E_{tot}) of the clusters as derived from the DFT calculations, the relative energies (E_{rel}) of the various isomers with respect to the lowest-energy isomer of that composition, the cohesion (or atomization) energy (E_{coh}), and the mixing (or excess) energy (Δ_{mix}). The atomic energies at the DFT/PW91/TZVP level are: E_{at}(Au) = -135.801490 au (S=1/2); E_{at}(Cu) = -196.796583 au (S=1/2); E_{at}(Pd) = -127.908653 au (S=0); E_{at}(Pt) = -119.356896 au (S=1).

The cohesion energy is defined as:

$E_{coh}\ (A_6B_{32}) = E_{tot}\ (A_6B_{32}) - 6\ E_{at}\ (A) - 32\ E_{at}\ (B)$

while the mixing energy is defined as (see Ref. [1]):

$\Delta_{mix}\ (eV) = E_{tot}\ (A_6B_{32}) - 6\ [\ E_{tot}\ (A_{38})/38\ ] - 32\ [\ E_{tot}\ (B_{38})/38\ ]$

Negative values of Δ_{mix} indicate that mixing is favorable.

For the ligated clusters we report the total energy (E_{tot}) of the clusters as derived from the DFT calculations, the relative energies (E_{rel}) of the various isomers with respect to the lowest-energy isomer of that composition, and the binding (or chemisorption) energy (E_{bind}). The energy of the CO molecule at the DFT/PW91/TZVP level is -113.313939 au. The energy of the H atom at the DFT/PW91/TZVP level is about -0.5 au.

The binding energy, for example for a A_6B_{32} cluster, is defined as:

$E_{bind}\ (A_6B_{32}\text{-Ligand}) = E_{tot}\ (A_6B_{32}\text{-Ligand}) - E_{tot}\ (A_6B_{32}) - E\ (\text{Ligand})$

Cluster	E_{tot} (au)	E_{coh} (au)
Cu38	-7481.711406	-3.441
Au38	-5163.602223	-3.146
Pd38	-4864.662954	-4.134
Pt38	-4541.119402	-5.557

Cluster	E_{tot} (au)	E_{bind} (eV)
Cu38-H	-7482.280695	-1.885
Cu38-CO	-7595.038247	-0.350
Au38-H	-5164.175623	-1.997
Au38-CO	-5276.924161	-0.217
Pd38-H	-4865.250867	-2.391
Pd38-CO	-4978.025774	-1.330
Pt38-H	-4541.726928	-2.926
Pt38-CO	-4654.502971	-1.895

Cluster	E_{tot} (au)	E_{rel} (eV)	E_{coh} (au)	Δ_{mix} (eV)
Au6Pd32 centroid	-4911.868210	1.230	-3.982	
Au6Pd32 core	-4911.768935	3.931	-3.883	
Au6Pd32 hex	-4911.913400	0.000	-4.028	-1.35
Pd6Au32 centroid	-5116.519798	1.395	-3.420	
Pd6Au32 core	-5116.571051	0.000	-3.471	-4.62
Pd6Au32 hex	-5116.450080	3.292	-3.350	
Cu6Pt32 centroid	-5005.542945	0.000	-5.343	-3.25
Cu6Pt32 core	-5005.529458	0.367	-5.329	
Cu6Pt32 hex	-5005.484096	1.601	-5.284	
Pt6Cu32 centroid	-7017.613288	0.000	-3.981	-5.60
Pt6Cu32 core	-7017.532355	2.202	-3.900	
Pt6Cu32 hex	-7017.507970	2.866	-3.876	
Pd6Pt32 centroid	-4592.221997	0.045	-5.349	
Pd6Pt32 core	-4592.194716	0.788	-5.322	
Pd6Pt32 hex	-4592.223665	0.000	-5.351	-0.50
Pt6Pd32 centroid	-4813.615039	0.320	-4.397	
Pt6Pd32 core	-4813.626809	0.000	-4.409	
Pt6Pd32 hex	-4813.578413	1.317	-4.360	-1.35

Table S-I. For the bare metal clusters, total energies (E_{tot}, in au), relative energies (E_{rel}, in eV) with respect to the lowest-energy isomer of that composition, atomization energies (E_{coh}, in au), and mixing energies (Δ_{mix}, in eV, as defined in the text) for the lowest-energy isomers are reported.

Cluster	E_{tot} (au)	E_{rel} (eV)	E_{bind} (eV)
Au6Pd32 cent-COB	-5025.23954	1.0391	-1.5616
Au6Pd32 cent-COA	-5025.19832	2.1606	-0.4401
Au6Pd32 core-CO	-5025.13446	3.8984	-1.4038
Au6Pd32 hex-CO1	-5025.27171	0.1636	-1.2075
Au6Pd32 hex-CO2	-5025.27530	0.0660	-1.3051
Au6Pd32 hex-CO3	-5025.27772	0.0000	-1.3711
Au6Pd32 hex-CO4	-5025.27247	0.1431	-1.2280
Pd6Au32 cent-COB	-5229.85107	1.1058	-0.4716
Pd6Au32 cent-COA	-5229.88387	0.2133	-1.3642
Pd6Au32 core-CO	-5229.89171	0.0000	-0.1828
Pd6Au32 hex-CO1	-5229.76954	3.3243	-0.1503
Pd6Au32 hex-CO2	-5229.76968	3.3204	-0.1541
Pd6Au32 hex-CO3	-5229.77247	3.2445	-0.2301
Pd6Au32 hex-CO4	-5229.77285	3.2343	-0.2403
Cu6Pt32 cent-COB	-5118.93058	0.0000	-2.0054
Cu6Pt32 cent-COA	-5118.88307	1.2928	-0.7126
Cu6Pt32 core-CO	-5118.89197	1.0506	-1.3217
Cu6Pt32 hex-CO1	-5118.87794	1.4325	-2.1742
Cu6Pt32 hex-CO2	-5118.87127	1.6139	-1.9928
Cu6Pt32 hex-CO3	-5118.86693	1.7319	-1.8748
Cu6Pt32 hex-CO4	-5118.86382	1.8165	-1.7902
Pt6Cu32 cent-COB	-7130.95524	0.7588	-0.7622
Pt6Cu32 cent-COA	-7130.98313	0.0000	-1.5210
Pt6Cu32 core-CO	-7130.87293	2.9985	-0.7248
Pt6Cu32 hex-CO1	-7130.83828	3.9413	-0.4456
Pt6Cu32 hex-CO2	-7130.83795	3.9505	-0.4364
Pt6Cu32 hex-CO3	-7130.84198	3.8407	-0.5462
Pt6Cu32 hex-CO4	-7130.84046	3.8820	-0.5049
Pd6Pt32 cent-COB	-4705.60270	0.3418	-1.8168
Pd6Pt32 cent-COA	-4705.58607	0.7945	-1.3641
Pd6Pt32 core-CO	-4705.57045	1.2194	-1.6816
Pd6Pt32 hex-CO1	-4705.61527	0.0000	-2.1133

Pd6Pt32 hex-CO2	-4705.60786	0.2015	-1.9118
Pd6Pt32 hex-CO3	-4705.60439	0.2959	-1.8173
Pd6Pt32 hex-CO4	-4705.60422	0.3004	-1.8128
Pt6Pd32 cent-COB	-4926.97890	0.4581	-1.3585
Pt6Pd32 cent-COA	-4926.99255	0.0868	-1.7298
Pt6Pd32 core-CO	-4926.99574	0.0000	-1.4963
Pt6Pd32 hex-CO1	-4926.93182	1.7394	-1.0739
Pt6Pd32 hex-CO2	-4926.93990	1.5195	-1.2937
Pt6Pd32 hex-CO3	-4926.94311	1.4321	-1.3812
Pt6Pd32 hex-CO4	-4926.94062	1.4998	-1.3135

Table S-II. Total energies (E_{tot}, in au), relative energies (E_{rel}, in eV) with respect to the lowest-energy isomer of that composition, and CO binding energies (E_{bind}, in eV) for the CO-bound clusters.

Cluster	E_{tot} (au)	E_{rel} (eV)	E_{bind} (eV)
Au6Pd32 cent-HB	-4912.45745	1.16428	-2.4283
Au6Pd32 cent-HA	-4912.44264	1.56733	-2.0253
Au6Pd32 core-H	-4912.35693	3.89942	-2.3946
Au6Pd32 hex-H1	-4912.49087	0.25487	-2.1081
Au6Pd32 hex-H2	-4912.49651	0.10138	-2.2616
Au6Pd32 hex-H3	-4912.50024	0.00000	-2.3629
Au6Pd32 hex-H4	-4912.49959	0.01755	-2.3454
Pd6Au32 cent-HB	-5117.08626	1.49516	-1.8086
Pd6Au32 cent-HA	-5117.09568	1.23888	-2.0649
Pd6Au32 core-H	-5117.14121	0.00000	-3.3038
Pd6Au32 hex-H1	-5117.02306	3.21491	-1.9860
Pd6Au32 hex-H2	-5117.01872	3.33313	-1.8678
Pd6Au32 hex-H3	-5117.01604	3.40615	-1.7947
Pd6Au32 hex-H4	-5117.01182	3.52098	-1.6799
Cu6Pt32 cent-HB	-5006.15568	0.00000	-3.0676
Cu6Pt32 cent-HA	-5006.10120	1.48240	-1.5852
Cu6Pt32 core-H	-5006.11947	0.98527	-2.4494
Cu6Pt32 hex-H1	-5006.09711	1.59382	-3.0752
Cu6Pt32 hex-H2	-5006.09285	1.70976	-2.9592
Cu6Pt32 hex-H3	-5006.08955	1.8	-2.8697
Cu6Pt32 hex-H4	-5006.09061	1.77067	-2.8983
Pt6Cu32 cent-HB	-7018.18367	0.74335	-1.9152
Pt6Cu32 cent-HA	-7018.21099	0.00000	-2.6586
Pt6Cu32 core-H	-7018.10392	2.91355	-1.9473
Pt6Cu32 hex-H1	-7018.06175	4.06088	-1.4635
Pt6Cu32 hex-H2	-7018.07045	3.82418	-1.7002
Pt6Cu32 hex-H3	-7018.07150	3.79568	-1.7287
Pt6Cu32 hex-H4	-7018.07886	3.59553	-1.9289
Pd6Pt32 cent-HB	-4592.82974	0.10876	-2.9318
Pd6Pt32 cent-HA	-4592.80983	0.65042	-2.3901
Pd6Pt32 core-H	-4592.79249	1.12239	-2.6605
Pd6Pt32 hex-H1	-4592.83373	0.00000	-2.9951

Pd6Pt32 hex-H2	-4592.83065	0.08403	-2.9111
Pd6Pt32 hex-H3	-4592.82926	0.12175	-2.8734
Pd6Pt32 hex-H4	-4592.82946	0.11619	-2.8789
Pt6Pd32 cent-HB	-4814.20252	0.42184	-2.3805
Pt6Pd32 cent-HA	-4814.21710	0.02504	-2.7773
Pt6Pd32 core-H	-4814.21802	0.00000	-2.4821
Pt6Pd32 hex-H1	-4814.16201	1.52419	-2.2748
Pt6Pd32 hex-H2	-4814.16515	1.43879	-2.3602
Pt6Pd32 hex-H3	-4814.16585	1.41983	-2.3792
Pt6Pd32 hex-H4	-4814.16562	1.42594	-2.3731

Table S-III. Total energies (E_{tot}, in au), relative energies (E_{rel}, in eV) with respect to the lowest-energy isomer of that composition, and H binding energies (E_{bind}, in eV) for the H-bound clusters.

References

[1] R. Ferrando, A. Fortunelli and G. Rossi, *Phys. Rev. B* **72**, 085449 (2005)

NANO LETTERS

LETTER

pubs.acs.org/NanoLett

Patchy Multishell Segregation in Pd−Pt Alloy Nanoparticles

Giovanni Barcaro,[†] Alessandro Fortunelli,*[,†] Micha Polak,[‡] and Leonid Rubinovich[‡]

[†]CNR-IPCF, Istituto per i Processi Chimico-Fisici, I-56124 Pisa, Italy

[‡] Department of Chemistry, Ben-Gurion University, Beer-Sheva 84105, Israel

Supporting Information

ABSTRACT: Chemical ordering in face-centered-cubic-like PdPt nanoparticles consisting of 38−201 atoms is studied via density-functional calculations combined with a symmetry orbit approach. It is found that for larger particles in the Pd-rich regime, Pt atoms can segregate at the center of the nanoparticle (111) surface facets, in contrast with extended systems in which Pd is known to segregate at the surface of alloy planar surfaces. In a range of compositions around 1:1, a novel multishell chemical ordering pattern was favored, in which each shell is a patchwork of islands of atoms of the two elements, but the order of the patchwork is reversed in the alternating shells. These findings are rationalized in terms of coordination-dependent bond-energy variations in the metal−metal interactions, and their implications in terms of properties and applications of nanoscale alloy particles are discussed.

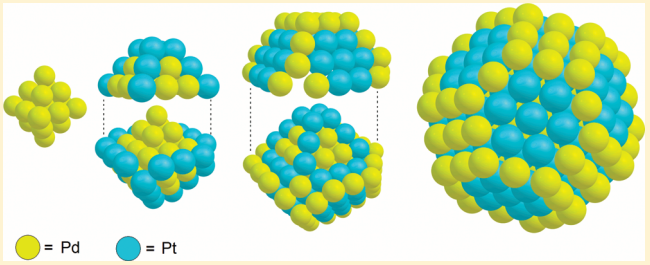

KEYWORDS: Nanoalloys, chemical ordering, surface segregation, metal nanoparticles, DFT calculations

In addition to structural morphology, the chemical ordering or compositional structure (i.e., the distribution of the different chemical species within a given structure)[1,2] plays a fundamental role in determining the properties of multicomponent metallic nanoparticles—or nanoalloys.[3,4] AgAu particles, for example, exhibit a different optical response depending on whether they are core−shell or random solutions.[5] Mechanical properties are equally known to be strongly affected by surface segregation.[6,7] The precise arrangement of the species in the particle is also important in catalysis, dominated by processes occurring at surface or subsurface shells, and changes in the segregation pattern under operating conditions have been observed.[8] Several mixing patterns have been described in the literature,[4] such as core−shell or in general multishell ordering (in which concentric shells of different elements alternate), random solutions, ordered arrangements (more or less related to the known ordered phases of bulk alloys), and Janus-like segregation typical of immiscible components.[9] In this context, theoretical methods can provide relevant information which nicely complements and sometimes prefigures experiment, but the prediction of the correct chemical ordering is not an easy task, especially at the first-principles level, due to the combinatorial increase in the number of possible "homotops" (isomers sharing the same skeletal structure and composition but differing in the mixing pattern).[3] Neglecting the reduction due to point group symmetry, for a cluster with given structure and N_{tot} atoms of which N_A of species A and N_B of species B, one has $(N_{tot})!/((N_A)!(N_B)!)$ possible different homotops. A possible solution to this problem is to consider "magic" structures,[10] i.e., arrangements exhibiting structural shell closure and thus exhibiting high symmetry. In this approach[10] the full point group symmetry is exploited to partition the atoms into "symmetry orbits",[11] i.e., groups of symmetry-equivalent species. The degrees of freedom of the system are thus reduced from N_{tot} to the number of symmetry-inequivalent orbits, N_{orb}, and correspondingly the number of distinct homotops is exponentially decreased.

In this work we adopt this symmetry orbit approach and apply it at a first-principles density-functional theory (DFT) level to study the segregation patterns of face-centered-cubic-like (fcc-like) PdPt nanoparticles in the size range between 38 and 201 atoms and over a broad range of compositions. We find that the interplay of metal−metal homo- and heterointeractions produces an unusual Pt surface segregation in Pd-rich particles (in spite of the larger Pt bulk energy) and a novel multishell pattern around equimolar composition in which each shell is decorated by "patches" of like atoms. We conclude by speculating on possible implications of these findings.

Plane-wave DFT calculations were performed using the QuantumEspresso package[12] employing ultrasoft pseudopotentials[13] and the Perdew−Burke−Ernzerhof (PBE) exchange-correlation (xc-) functional[14] (more details in the Supporting Information). Our structural models consist of fcc-like truncated octahedra (TO) configurations. Starting from octahedra, fcc polyhedra are obtained by truncating symmetrically their six vertices, obtaining square and hexagonal (or triangular) facets; see Figures 1 and 2. A given TO is characterized by two indexes: n_L, i.e., the length of the edge of the complete octahedron and n_{cut}, i.e., the number of layers cut at each vertex, and will be denoted as TO(n_L, n_{cut}) in the following. fcc-like structures are reasonable for PdPt particles at this size: the transition from icosahedral structures to less strained

Received: January 27, 2011
Published: March 02, 2011

structures is expected to occur at relatively small sizes for both Pd and Pt bare clusters,[15] and the only competitors to fcc motifs are decahedral or "hybrid" ones.[16] We select the site population within these models by applying the symmetry orbit approach in the O_h symmetry group. Broken-symmetry (such as Janus-like[9]) configurations have been explored but found very disfavored due to the strong mixing tendency of the Pd−Pt pair. The use of symmetry reduces the degrees of freedom of the system to N_{orb}, the number of symmetry-inequivalent orbits, which is 12 for a TO particle of 201 atoms. Considering that a full exploration of all possible symmetry-constrained segregation pattern is achieved by performing $2^{N_{orb}}$ calculations, it follows that this task is feasible using tight-binding Hamiltonians[10] or empirical potentials[11,16,17] but remains heavy to accomplish at the first-principles level due to limitations in computational resources. We have thus further reduced the number of possible homotops by focusing on selected compositions: the two regimes characterized by a small amount of one of the two elemental components and around 1:1 composition. An issue with the orbit approach is that the number of atoms in each orbit presents an nonhomogeneous distribution, being 1, 6, 12, or 24 in the cases here investigated. This puts constraints on the cluster chemical composition by limiting the number of homotops. To explore a broader range, a suborbit approach has been used, in which each orbit is divided into equivalent suborbits of six atoms. By properly choosing the populations of the suborbits in order to keep as high a symmetry as possible and to avoid repeated calculation of homologous configurations, it is possible to enlarge the scope of significant results still keeping the computational effort within reasonable limits. Four different sizes with N_{tot} = 38, 79, 116, 201 have been investigated, and total energy results for all selected homotops are reported in the Supporting Information.

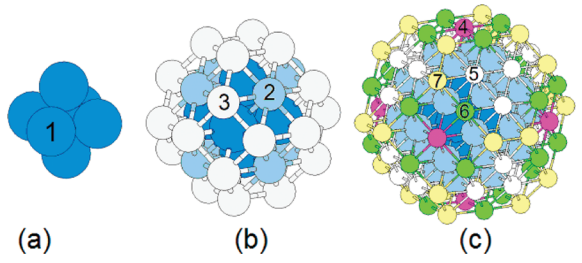

Figure 1. Orbit structure of the even-numbered truncated octahedra considered in this work: (a) 6-atom TO(2,0); (b) 38-atom TO(4,1), obtained adding 32 atoms to (a); (c) 116-atom TO(6,2), obtained adding 78 atoms to (b). Different symmetry orbits are singled out by different colors and numbers.

38-Atom Particle. This structure corresponds to the TO(4,1) shown in Figure 1b. It is made by an inner shell of 6 atoms (Figure 1a) and an outer shell of 32 atoms. The number of orbits is three: orbit-1 is formed by atoms of the inner shell; orbit-2 by the 8 atoms at the center of the (111) facets, and orbit-3 by the 24 atoms on the (100) facets.

A single Pd impurity in a nearly pure Pt cluster is best positioned on the surface, almost isoenergetically on the (111) or the (100) facets, while moving the Pd impurity into the core costs 0.23 eV. This is coherent with the lower surface energies of Pd, which thus prefers to segregate to the surface of the cluster.[18,19] At variance, a single Pt impurity can stay almost isoenergetically in the first or in the second orbit (i.e., in the core or on one of the 111 facets), whereas the occupation of the third orbit (one of the corners of the TO) increases the energy by 0.24 eV. This unexpected result (one could think that surface occupation by Pt is always disfavored with respect to the core) is the first indication of the Pt tendency to (111)-surface segregation. Increasing the number of impurity atoms to six changes the situation which turns out to be more in line with previous work,[20] as the six Pt atoms in fact preferentially go inside the cluster resulting in a core−shell structure.

79-Atom Particle. This structure corresponds to the TO(5,1) shown in Figure 2c. It is composed of three shells: the first shell is formed by the central atom (Figure 2a); the second shell by the surface of the internal (3,0) octahedron (Figure 2b); the third shell by the remaining 60 surface atoms. There are six orbits: orbit-1 corresponds to the central atom; orbit-2 to the surface of the inner TO(3,1) and contains 12 atoms; orbit-3 by the 6 vertices of the TO(3,0). The orbits from the fourth to the sixth contain the 60 surface atoms of the third shell: 24 on (111) facets (orbit 4), 12 on edges (orbit 5), and 24 on (100) facets (orbit 6).

For a single impurity the results are similar to those found in the 38 atoms case: a single Pt prefers to stay in the first inner-shell orbit, while moving it toward the surface corresponds to a gradual increase in the energy, with the situation mirrored in an inverse way for the Pd impurity. At the 6-73 composition, in Pt-rich structures the six Pd atoms prefer to populate corners, as expected, but for Pd-rich structures the landscape is more interesting. The lowest-energy configuration is one in which the Pt atoms populate part of the second orbit, which is not surprising as these sites are internal ones. However, this configuration is nearly isoenergetic with the occupation of the third and fourth orbit, which latter corresponds to a surface segregation of the Pt atoms in the middle of the external (111) facets. This behavior is definitively more marked at composition 12-67. Again, the Pt-rich panorama does not bear any surprise and the 12 Pd atoms preferentially populate the (100) facets. On the contrary, in the

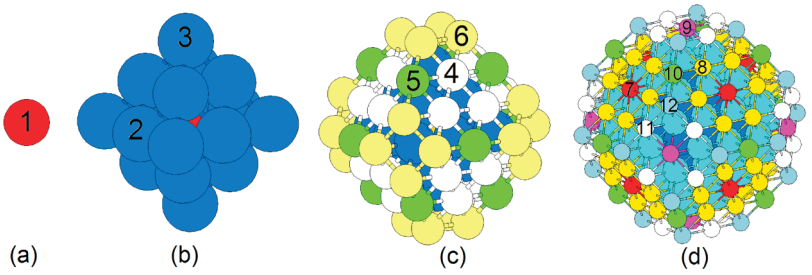

Figure 2. Orbit structure of the odd-numbered truncated octahedra considered in this work: (a) 1-atom TO(1,0); (b) 19-atom TO(3,0), obtained adding 18 atoms to (a); (c) 79-atom TO(5,1), obtained adding 60 atoms to (b); (d) 201-atom TO(7,2), obtained adding 122 atoms to (c). Different symmetry orbits are singled out by different colors and numbers.

dx.doi.org/10.1021/nl200322s |*Nano Lett.* 2011, 11, 1766–1769

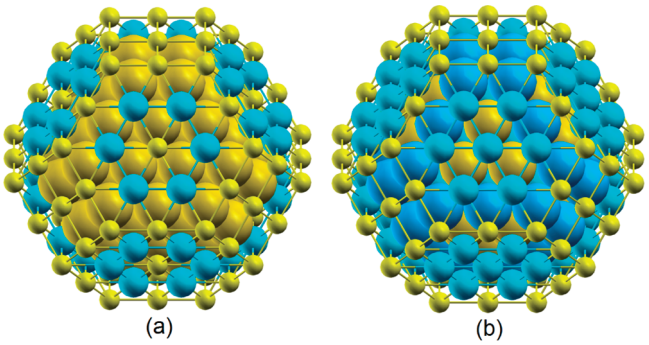

Figure 3. Optimal chemical ordering in a PdPt nanoparticle of size N_{tot} = 201: (a) composition $Pd_{153}Pt_{48}$; (b) composition $Pd_{110}Pt_{91}$ (around 1:1). The view represents atoms of different sizes to highlight the patchy multishell pattern in (b). Atom coloring: yellow for Pd and blue for Pt, with slightly darker shades for the inner shells.

Pd-rich case the 12 Pt atoms preferentially populate the fourth orbit, occupying half of the (111) surface sites, even though the competition with deeper segregation is still strong. In short, doubling the number of Pt atoms changes the segregation sites: there is a close energetic competition between internal and surface or subsurface segregation sites, and this competition is moved in favor of surface with increasing Pt content.

One can wonder whether a different theoretical method may change these results, as it is known that the precise energetics of systems containing third-row transition metals is very sensitive to the details of the theoretical approach.[22] We have thus used an approach involving norm-conserving pseudopotentials and localized basis sets[23] and found that this behavior is fully confirmed (more details in the Supporting Information). Note that in this case the use of symmetry is also beneficial to greatly speed up DFT calculations: we use the NWChem 5.1 quantum chemistry package,[23] which is efficiently parallelized and fully exploits point group symmetry.

116-Atom Particle. The TO(6,2) shown in Figure 1c has also been analyzed, finding results in line with those for the other sizes (more details in the Supporting Information).

201-Atom Particle. The largest (201-atom) nanoparticles here considered exhibit the most outstanding results. This structure corresponds to the TO(7,2) depicted in Figure 2d which is obtained by adding a further shell to the 79-atom TO(5,1). The structure is thus formed by four shells: the inner three are those of the 79-atom cluster, while the fourth one is composed of 116 surface atoms, distinguished into five orbits. As shown in Figure 2d, the (111) facets are regular hexagons.

The results for a single impurity and composition 6-195 show an even more marked tendency of Pt to populate the surface, in agreement with a coordination-dependent bond-energy variations (CBEV) study of 923-atom cuboctahedral PtPt particles.[21] Already a single or few Pt atoms now segregate at the (111) surface, whereas few Pd atoms in a Pt-rich cluster segregate at the corners of the (100) facets. The tendency of Pt to (111)-surface segregation in Pd-rich clusters thus increases with cluster size: at slight variance with CBEV predictions, the (111) surface segregation of a single Pt impurity is only clearly realized when the (111) facets are large enough. Also, with respect to the CBEV, at low Pt contents the center of the facets rather than the near-edge positions is favored (see Table 4 of the Supporting Information). However, similarly to the CBEV results, the tendency of Pt to occupy near-edge sites at (111) is apparent at composition $Pd_{153}Pt_{48}$: the 48 Pt preferentially occupy all the hexagon sites of the (111) surfaces, see Figure 3a, while the structure exhibiting Pt subsurface segregation is higher in energy by 3.82 eV. Thus, the tendency of Pt to (111)-surface segregation is now very strong.

A new picture emerges around composition 1:1. The lowest-energy chemical ordering pattern, e.g., at composition 110-91 is reported in Figure 3b, and it is clearly a multishell arrangement, but of a different kind. As can be drawn from an inspection of this figure, the structure of the fourth shell is such that Pt atoms occupy the center of surface (111) facets, whereas Pd atoms occupy the (100) facets and the edges of the surface shell. However, for the subsurface shell the chemical order is reversed with respect to that of the surface shell: Pd atoms occupy the three central positions of the (111) facets, whereas Pt occupies the (100) facets and the edges. In other words, in correspondence with segregation of Pt at the center of surface facets, we find a segregation of Pd at the center of the underlying facets, and so on. In this segregation pattern, which—to the best of our knowledge—has not been reported before, each shell is a "patchwork" of islands of atoms of the two elements, but the order of the patchwork is reversed in the alternating shells. This is realized in a clear way starting at a sufficiently large size (1.7−1.9 nm) and around composition ≈50−50%. However, this arrangement is not bound to a precise number of atoms but is stable in a *range* of compositions around the equimolar one. As shown in Table 5 of the Supporting Information, we find it favored not only for the nearly equimolar $Pd_{99}Pt_{102}$ and $Pd_{102}Pt_{99}$ particles but also for $Pd_{90}Pt_{111}$ and $Pd_{117}Pt_{84}$. CBEV calculations (which are essentially in tune with DFT results) confirm that this remains true also in the intermediate compositions which are not accessible to our orbit approach, so that we predict it to be stable between at least 45−55% and 58−42% compositions. It can also be recalled in this context that the minimum in the mixing energy (see ref 10 for its definition) for PdPt clusters in this size range at the DFT level is realized at compositions between 30% and 50% in Pt,[20] i.e., in the range in which patchy multishell arrangements are favored.

The origins of this unique chemical ordering can be rationalized in terms of the different behavior of site-energetics of the two elements as a function of the coordination number,[24] i.e., the preferential strengthening of Pt−Pt (and Pt−Pd) intrasurface and Pd−Pd (and Pt−Pd) surface-subsurface bonds, as predicted by the CBEV method.[21] Furthermore, as shown in Table 6 of the Supporting Information in the $Pd_{99}Pt_{102}$ case, the multishell patchy arrangements allow the system to minimize the number of weak Pd−Pd bonds with respect to the stronger Pt−Pt and heterobonds between the two elements, which is energetically advantageous as Pd−Pt mixing is exothermic:[20,30] in a way, the subsurface order is driven by the chemical order of the outer shell.

This peculiar compositional structure can have interesting consequences on the properties of Pd−Pt nanoalloys. Mechanical response[6,7] is expected to be reinforced by a thermodynamically robust and thorough intermixing of the two metals as realized in the patchy arrangement and will be investigated in future work. Catalytic properties of Pd−Pt nanoclusters are likely to be influenced as well.[26] It has been shown in fact that the preference of Pd and Pt clusters toward TO structures is not strongly affected or is even increased[27] in the presence of H adsorption and that Pt−ligand bonding in TO clusters (where Pt lies on a 111 facet) is strengthened by the presence of neighboring Pd atoms.[28] This implies that patchy multishell patterns are

robust to ligand adsorption in realistic conditions, which can even enhance their stability. This may explain the increase in the activity of Pd nanoparticles when Pt is added in the Pd-rich range of compositions.[29]

To conclude, the orbit approach here employed is a powerful tool to explore segregation patterns in nanoscale alloy particles at the first-principles level and will be used in the future also in conjunction with and to further validate effective Hamiltonian methods (e.g., the CBEV approach). The novel type of chemical ordering in nanoalloy clusters (patchy multishell segregation) revealed by first-principle computations is of general interest and is expected to have a significant impact on their properties and on current research in the corresponding area. Indeed, the fact that unusual segregation patterns can occur in nanoparticles even for a pair such as Pd−Pt which presents a nearly ideal solid−solution behavior in the bulk sheds new light on the unexpected possibilities arising at the nanoscale. Experimental verification[1] of the unusual surface segregation of the constituent having larger bulk energy (Pt), and of the corresponding patchy pattern, are desirable.

■ ASSOCIATED CONTENT

Supporting Information. Computational details and tables with a complete set of DFT results. This material is available free of charge via the Internet at http://pubs.acs.org.

■ AUTHOR INFORMATION

Corresponding Author
*E-mail: fortunelli@ipcf.cnr.it.

■ ACKNOWLEDGMENT

A.F. acknowledges financial support from the SEPON project within the ERC-AG programme and from ESF for the workshop on "Computational Nanoalloys" and the MP0903 COST action. DFT calculations were performed at the CINECA Supercomputing Center within the SCONA ISCRA project.

■ REFERENCES

(1) Rousset, J. L.; Renouprez, A. J.; Cadrot, A. M. *Phys. Rev. B* **1998**, *58*, 2150.
(2) Lim, B.; Wang, J.; Camargo, P. H. C.; Jiang, M.; Kim, M. J.; Xia, Y. *NanoLett.* **2008**, *8*, 2535.
(3) Jellinek, J.; Krissinel, E. B. *Chem. Phys. Lett.* **1996**, *258*, 283.
(4) Ferrando, R.; Jellinek, J.; Johnston, R. L. *Chem. Rev.* **2008**, *108*, 845.
(5) Broyer, M.; Cottancin, E.; Lermé, J.; Pellarin, M.; Del Fatti, N.; Vallée, F.; Burgin, J.; Guillon, C.; Langot, P. *Faraday Discuss.* **2008**, *138*, 137.
(6) Chen, H. P.; Kalia, R. K.; Kaxiras, E.; Lu, G.; Nakano, A.; Nomura, K.; van Duin, A. C. T.; Vashishtaa, P.; Yuan, Z. S. *Phys. Rev. Lett.* **2010**, *104*, No. 155502.
(7) Biswas, A.; Siegel, D. J.; Seidman, D. N. *Phys. Rev. Lett.* **2010**, *105*, No. 076102.
(8) Tao, F.; Grass, M. E.; Zhang, Y.; Butcher, D. R.; Renzas, J. R.; Liu, Z.; Chung, J. Y.; Mun, B. S.; Salmeron, M.; Somorjai, G. A. *Science* **2008**, *322*, 932–934.
(9) Paz-Borbón, L. O.; Gupta, A.; Johnston, R. L. *J. Mater. Chem.* **2008**, *18*, 4154.
(10) Fortunelli, A.; Velasco, A. M. *J. Mol. Struct. (THEOCHEM)* **1999**, *487*, 251.
(11) Wales, D., *Energy Landscapes: Applications to Clusters, Biomolecules and Glasses*; Cambridge University Press: Cambridge, 2004.
(12) Giannozzi, P.; et al. *J. Phys.: Condens. Matter* **2009**, *21*, No. 395502.
(13) Vanderbilt, D. *Phys. Rev. B* **1990**, *41*, 7892.
(14) Perdew, J. P.; Burke, K.; Ernzerhof, M. *Phys. Rev. Lett.* **1996**, *77*, 3865.
(15) Baletto, F.; Ferrando, R.; Fortunelli, A.; Montalenti, F.; Mottet, C. *J. Chem. Phys.* **2002**, *116*, 3856.
(16) Paz-Borbòn, L. O.; Mortimer-Jones, T. V.; Johnston, R. L.; Posada-Amarillas, A.; Barcaro, G.; Fortunelli, A. *Phys. Chem. Chem. Phys.* **2007**, *9*, 5202.
(17) Wilson, N. T.; Johnston, R. L. *J. Mater. Chem.* **2002**, *12*, 2913.
(18) Bazin, D.; Guillaume, D.; Pichon, Ch.; Uzio, D.; Lopez, S. *Oil Gas Sci. Technol.* **2005**, *60*, 801.
(19) Cadete-Santos-Aires, F. J.; Geantet, C.; Renouprez, A. J.; Pellarin, M. *J. Catal.* **2001**, *202*, 163.
(20) Fernandez, E. M.; Balbas, L. C.; Perez, L. A.; Michaelian, K.; Garzon, I. L. *Int. J. Mod. Phys. B* **2005**, *19*, 2339.
(21) Rubinovich, L.; Polak, M. *Phys. Rev. B* **2009**, *80*, No. 045404.
(22) Bonačič-Koutecky, V.; Burda, J.; Mitrič, R.; Ge, M.; Zampella, G.; Fantucci, P. *J. Chem. Phys.* **2002**, *117*, 3120.
(23) Bylaska, E. J. et al. *NWChem, A Computational Chemistry Package for Parallel Computers, Version 5.1*; Pacific Northwest National Laboratory: Richland, WA, 2007.
(24) Yang, L.; DePristo, E. *J. Chem. Phys.* **1994**, *100*, 725.
(25) Doye, J. P. K.; Wales, D. J.; Berry, R. S. *J. Chem. Phys.* **1995**, *103*, 4234.
(26) Gonzalez, S.; Neyman, K. M.; Shaikhutdinov, S.; Freund, H.-J.; Illas, F. *J. Phys. Chem. C* **2007**, *111*, 6852.
(27) Calvo, F.; Carre, A. *Nanotechnology* **2006**, *17*, 1292.
(28) West, P. S.; Johnston, Roy L.; Barcaro, G.; Fortunelli, A. *J. Phys. Chem. C* **2010**, *114*, 19678.
(29) Toshima, N.; Yonezawa, T. *New J. Chem.* **1998**, *1179*, 1179.
(30) Paz-Borbon, L. O.; Johnston, R. L.; Barcaro, G.; Fortunelli, A. *J. Phys. Chem. C* **2007**, *111*, 2936.

■ NOTE ADDED AFTER ASAP PUBLICATION

The TOC and abstract artwork was modified in the version of this paper published March 2, 2011. The correct version published March 8, 2011.

Supporting Information for

"Patchy multi-shell segregation in Pd-Pt alloy nanoparticles"

Giovanni Barcaro[1], Alessandro Fortunelli[1], Micha Polak[2] and Leonid Rubinovich[2]

[1] Molecular Modeling Laboratory, Istituto per i Processi Chimico-Fisici (IPCF-CNR), I-56124 Pisa, Italy

[2] Department of Chemistry, Ben-Gurion University, Beer-Sheva 84105, Israel

Computational Details

DFT calculations were performed using the QuantumEspresso package [1], employing a basis set of Plane Waves, ultrasoft pseudopotentials [2] and the Perdew-Burke-Ernzerhof (PBE) exchange-correlation (xc-) functional [3]. Values of 30 Ry and 150 Ry were chosen as the energy cutoff for the selection of the plane waves for the description of the wave function and the electronic density, respectively. The first Brillouin zone was k-sampled at the Γ point only by employing a Gaussian smearing of each level of about 0.03 eV. All the structural relaxations were performed spin-polarized until the forces on the atoms resulted smaller than 0.01 eV/ Å. We employed cubic unit cells of side between 35 a.u. and 50 a.u. (1 a.u. = 0.529 Å), ensuring a minimal distance between atoms in replicated cells of about 7 – 8 Å in each direction.

One can wonder whether a different theoretical method may change these results, as it is known that the precise energetics of systems containing 3rd-row transition metals is very sensitive to the details of the theoretical approach [6]. Selected calculations were thus also performed using the same PBE xc-functional but a different approach involving norm-conserving pseudopotentials [4] and localized basis sets through the NWChem 5.1 quantum chemistry package [5]. Single point calculations on the relaxed geometries obtained using the QuantumEspresso package were performed using triple-zeta-plus-polarisation Gaussian-type-orbital basis sets [4] of (7s6p5d1f)/[5s3p3d1f] quality for both Pd and Pt. A Coulomb charge fitting procedure was used and all calculations were performed spin unrestricted, using a Gaussian smearing technique (smearing parameter of 0.03 eV) for the fractional occupation of the one-electron energy levels. Note that in this case the use of symmetry is also beneficial to greatly speed up DF calculations: the NWChem code is efficiently parallelized and fully exploits any point group symmetry. Using this approach we found that the tendency of Pt to surface segregation is qualitatively the same and quantitatively even more pronounced, with larger energy differences among the homotops with respect to the plane-wave/ultrasoft-pseudopotential approach. For example, full core segregation in $Pd_{67}Pt_{12}$ is 0.35 eV higher in energy using this approach instead of 0.1 eV from PWscf.

A detailed comparison with the CBEV approach [7] was also pursued and will be reported in future work. We can anticipate that we found a close similarity between the predictions of the two approaches but also a few differences. At variance with the predictions of the CBEV approach, in fact, at the DFT level the (111) surface segregation of a single Pt impurity is only clearly realized when the (111) facets are large enough (201-atom particle). Note in this connection that we have applied the same CBEV approach (used in Ref. [7] on a 923-atom particle) on the 201-atom and 116-atom TO clusters and found Pt surface segregation also in these cases. Another difference with

respect to the CBEV results lies in that the center of the facets rather than the near-edge positions are favored at the DFT level.

[1] P. Giannozzi, S. Baroni, N. Bonini, M. Calandra, R. Car, C. Cavazzoni, D. Ceresoli, G. Chiarotti, M. Cococcioni, I. Dabo, A. Dal Corso, S. De Gironcoli, S. Fabris, G. Fratesi, R. Gebauer, U. Gerstmann, C. Gougoussis, A. Kokalj, M. Lazzeri, L. Martin-Samos, N. Marzari, F. Mauri, R. Mazzarello, S. Paolini, A. Pasquarello, L. Paulatto, C. Sbraccia, S. Scandolo, G. Sclauzero, A. P. Seitsonen, A. Smogunov, P. Umari, R. M. Wentzcovitch, J. Phys.: Condens. Matter, 21, 395502, (2009)

[2] D. Vanderbilt, Phys. Rev. B, 41, 7892 (1990)

[3] J. P. Perdew, K. Burke, M. Ernzerhof, Phys. Rev. Lett., 77, 3865 (1996)

[4] D. Andrae, U. Haeussermann, M. Dolg, H. Stoll, H. Preuss, Theor. Chim. Acta 77, 123 (1990); ftp://ftp.chemie.uni-karlsruhe.de/pub/basen

[5] E. J. Bylaska, W. A. de Jong, N. Govind, K. Kowalski, T. P. Straatsma, M. Valiev, D. Wang, E. Apra, T. L. Windus, J. Hammond, P. Nichols, S. Hirata, M. T. Hackler, Y. Zhao, P.-D. Fan, R. J. Harrison, M. Dupuis, D. M. A. Smith, J. Nieplocha, V. Tipparaju, M. Krishnan, Q. Wu, T. Van Voorhis, A. A. Auer, M. Nooijen, E. Brown, G. Cisneros, G. I. Fann, H. Fruchtl, J. Garza, K. Hirao, R. Kendall, J. A. Nichols, K. Tsemekhman, K. Wolinski, J. Anchell, D. Bernholdt, P. Borowski, T. Clark, D. Clerc, H. Dachsel, M. Deegan, K. Dyall, D. Elwood, E. Glendening, M. Gutowski, A. Hess, J. Jaffe, B. Johnson, J. Ju, R. Kobayashi, R. Kutteh, Z. Lin, R. Littlefield, X. Long, B. Meng, T. Nakajima, S. Niu, L. Pollack, M. Rosing, G. Sandrone, M. Stave, H. Taylor, G. Thomas, J. van Lenthe, A. Wong, and Z. Zhang, "*NWChem, A Computational Chemistry Package for Parallel Computers, Version 5.1*", Pacific Northwest National Laboratory, Richland, Washington 99352-0999, USA (2007)

[6] V. Bonačič-Koutecky, J. Burda, R. Mitrič, M. Ge, G. Zampella and P. Fantucci, *J. Chem. Phys.* 117, 3120 (2002)

[7] L. Rubinovich and M. Polak, Phys. Rev. B 80, 045404 (2009)

Complete list of results

The results will be distinguished according to the size (total number of atoms) of the Pd-Pt cluster: 38, 79, 116, and 201.

38-atom PdPt cluster (see Fig. 1b in the main text)

There are three orbits, composed of 6, 8 and 24 atoms, respectively:
Orbit 1: central TO core 6 atoms
Orbit 2: centers of the (111) faces 8 atoms
Orbit 3: corners of the (100) faces 24 atoms

Composition	*O1*	*O2*	*O3*
Pd 01 Pt 37	+0.23	**+0.00**	< +**0.01**
Pd 06 Pt 32	+0.76	+0.12	**+0.00**
Pd 32 Pt 06	**+0.00**	+0.26	+1.54
Pd 37 Pt 01	**+0.00**	< +**0.01**	+0.24

Table 1. Energy differences with respect to the lowest energy homotop set as zero (in bold) for various compositions of a 38-atom Pd-Pt TO cluster. O1-3 stand for Orbit 1 to Orbit 3 and indicate where minority atoms are placed.

79-atom PdPt cluster (see Fig. 2c in the main text)

The orbits in this case are 6 [number of orbit atoms: 1 + 12 + 6 + 24 + 12 + 24]:

Orbit 1: central atom	1 atom
Orbit 2: internal TO surface	12 atoms
Orbit 3: vertex of the internal TO	6 atoms
Orbit 4: atoms on the (111) faces	24 atoms
Orbit 5: atoms on the edges	12 atoms
Orbit 6: corners of the (100) faces	24 atoms

With the exception of the first, each orbit can be further divided into suborbits of 6 atoms each, as in the following scheme: [1 + (6 + 6) + 6 + (6 + 6 + 6 + 6) + (6 + 6) + (6 + 6 + 6 + 6)]

Composition	*O1*	*O2*	*O3*	*O4*	*O5*	*O6*
Pd 01 Pt 78	+0.30	+0.09	+0.10	+0.14	+0.10	**+0.00**
Pd 06 Pt 78	-	+0.73	+0.46	+0.40	+0.25	+**0.00**
Pd 73 Pt 06	-	+**0.00**	+0.04	+0.08	+0.61	+1.40
Pd 78 Pt 01	**+0.00**	+0.08	+0.13	+0.12	+0.23	+0.34

Composition	*O2A O2A*	*O2A O3A*	*O2A O4A*	*O2A O5A*	*O2A O6A*	*O3A O4A*	*O3A O5A*	*O3A O6A*	*O4A O4A*	*O4A O5A*	*O4A O6A*	*O5A O5A*	*O5A O6A*	*O6A O6A*
Pd 12 Pt 67	+1.12	+0.38	+1.36	+1.00	+0.27	+1.24	+0.68	+0.19	1.47	+1.22	+0.73	+0.92	+0.37	**+0.00**
Pd 67 Pt 12	+0.09	+0.02	+0.05	+0.63	+1.36	+0.02	+0.72	+1.56	**+0.00**	+0.62	+1.27	+0.90	+1.87	+2.71

Table 2. Energy differences with respect to the lowest energy homotop set as zero (in bold) for various compositions of a 79-atom Pd-Pt TO cluster. O1-6 stand for Orbit 1 to Orbit 6 and indicate where minority atoms are placed. Suborbits are indicated by the suffix “A” (thus, O1A, etc.).

116-atom PdPt cluster (see Fig. 1c in the main text)

The orbits in this case are 7 [number of orbit atoms: 6 + 8 + 24 + 6 + 24 + 24 + 24]:

Orbit 1: central TO core	6 atoms
Orbit 2: centers of the internal (111) faces	8 atoms
Orbit 3: internal (100) faces corners	24 atoms
Orbit 4: centers of the (100) faces	6 atoms
Orbit 5: atoms on the (111) faces	24 atoms
Orbit 6: edges of the (100) faces	24 atoms
Orbit 7: corners of the (100) faces	24 atoms

With the exception of the second, each orbit can be further divided into suborbits of 6 atoms each, as in the following scheme: [6 + 8 + (6 + 6 + 6 + 6) + 6 + (6 + 6 + 6 + 6) + (6 + 6 + 6 + 6) + (6 + 6 + 6 + 6)]

Composition	*O1*	*O2*	*O3*	*O4*	*O5*	*O6*	*O7*
Pd 001 Pt 115	+0.21	+0.13	+0.07	**+0.00**	+0.13	+0.08	< +**0.01**
Pd 006 Pt 110	+1.44	-	+0.39	**+0.01**	+0.78	+0.40	**+0.00**
Pd 110 Pt 006	**+0.00**	-	+0.15	+0.97	+0.18	+0.97	+1.24
Pd 115 Pt 001	**+0.00**	+0.02	+0.05	+0.18	+0.07	+0.19	+0.23

Composition	*O1A O3A*	*O1A O4A*	*O1A O5A*	*O1A O6A*	*O1A O7A*	*O3A O3A*	*O3A O4A*	*O3A O5A*	*O3A O6A*	*O3A O7A*
Pd 104 Pt 12	+0.08	+0.94	**+0.00**	+0.80	+0.98	+0.25	+1.03	+0.23	+1.02	+1.28
	O4A O5A	*O4A O6A*	*O4A O7A*	*O5A O5A*	*O5A O6A*	*O5A O7A*	*O6A O6A*	*O6A O7A*	*O7A O7A*	
	+1.03	+1.84	+2.16	+0.18	+1.00	+1.28	+1.74	+2.07	+2.39	

Table 3. Energy differences with respect to the lowest energy homotop set as zero (in bold) for various compositions of a 116-atom Pd-Pt TO cluster. O1-7 stand for Orbit 1 to Orbit 7 and indicate where minority atoms are placed. Suborbits are indicated by the suffix "A" (thus, O1A, etc.).

201-atom PdPt cluster (see Fig. 2d in the main text)

There are 12 orbits [number of orbit atoms: 1 + 12 + 6 + 24 + 12 + 24 + 8 + 48 + 6 + 12 + 24 + 24]:

Orbit 1: central atom	1 atom
Orbit 2: internal 13-atom TO surface	12 atoms
Orbit 3: vertex of the internal 13-atom TO	6 atoms
Orbit 4: atoms on the internal 79-atom (111) faces	24 atoms
Orbit 5: atoms on the internal 79-atom edges	12 atoms
Orbit 6: corners of the internal 79-atom (100) faces	24 atoms
Orbit 7: centers of the external (111) faces	8 atoms
Orbit 8: crowns on the external (111) faces	48 atoms
Orbit 9: centers of the external (100) faces	6 atoms
Orbit 10: external edges between (111) faces	12 atoms
Orbit 11: external edges between (100) and (111) faces	24 atoms
Orbit 12: external corners of the (100) faces	24 atoms

With the exception of the first and the seventh, each orbit can be further divided into suborbits of 6 atoms each, as in the following scheme: [1 + (6 + 6) + 6 + (6 + 6 + 6 + 6) + (6 + 6) + (6 + 6 + 6 + 6) + 8 + (6 + 6 + 6 + 6 + 6 + 6 + 6 + 6) + 6 + (6 + 6) + (6 + 6 + 6 + 6) + (6 + 6 + 6 + 6)]

Composit.	*O1*	*O2*	*O3*	*O4*	*O5*	*O6*	*O7*	*O8*	*O9*	*O10*	*O11*	*O12*
Pd 200 Pt 001	+0.09	+0.02	+0.03	+0.07	+0.08	+0.07	**+0.00**	+0.09	+0.11	+0.19	+0.24	+0.27
Pd 195 Pt 006	-	+0.14	+0.09	+0.38	+0.41	+0.41	**+0.00**	+0.52	+1.31	+1.10	+1.37	+1.57

Table 4. Energy differences with respect to the lowest energy homotop set as zero (in bold) for various compositions of a 201-atom Pd-Pt TO cluster. O1-12 stand for Orbit 1 to Orbit 12 and indicate where minority atoms are placed.

Pd90 Pt111	*O1*	*O2*	*O3*	*O4*	*O5*	*O6*	*O7*	*O8*	*O9*	*O10*	*O11*	*O12*
+0.00	**Pt**	**Pt**	**Pt**	**Pt**	**Pt**	**Pd**	**Pt**	**Pt**	**Pd**	**Pd**	**Pd**	**Pd**
+1.00	**Pt**	**Pd**	**Pt**	**Pt**	**Pd**	**Pt**	**Pt**	**Pt**	**Pd**	**Pd**	**Pd**	**Pd**
+1.10	**Pt**	**Pt**	**Pd**	**Pd**	**Pt**	**Pt**	**Pt**	**Pt**	**Pt**	**Pd**	**Pd**	**Pd**
+1.69	**Pt**	**Pt**	**Pt**	**Pt**	**Pt**	**Pd**	**Pt**	**Pt**	**Pd**	**Pd**	**Pd**	**Pd**
+2.26	**Pt**	**Pt**	**Pd**	**Pt**	**Pt**	**Pd**	**Pt**	**Pt**	**Pt**	**Pd**	**Pd**	**Pd**
+2.44	**Pt**	**Pd**	**Pd**	**Pt**	**Pd**	**Pt**	**Pt**	**Pt**	**Pt**	**Pd**	**Pd**	**Pd**

Pd99 Pt102	*O1*	*O2*	*O3*	*O4*	*O5*	*O6*	*O7*	*O8*	*O9*	*O10*	*O11*	*O12*
+0.00	**Pd**	**Pt**	**Pt**	**Pd**	**Pt**	**Pt**	**Pd**	**Pt**	**Pd**	**Pd**	**Pd**	**Pd**
+0.73	**Pd**	**Pt**	**Pd**	**Pd**	**Pt**	**Pt**	**Pd**	**Pt**	**Pt**	**Pd**	**Pd**	**Pd**
+1.13	**Pd**	**Pd**	**Pt**	**Pt**	**Pd**	**Pt**	**Pd**	**Pt**	**Pd**	**Pd**	**Pd**	**Pd**
+1.34	**Pd**	**Pt**	**Pt**	**Pt**	**Pt**	**Pd**	**Pd**	**Pt**	**Pt**	**Pd**	**Pd**	**Pd**
+1.65	**Pd**	**Pt**	**Pd**	**Pt**	**Pt**	**Pd**	**Pd**	**Pt**	**Pt**	**Pd**	**Pd**	**Pd**
+2.11	**Pd**	**Pd**	**Pd**	**Pt**	**Pd**	**Pt**	**Pd**	**Pt**	**Pt**	**Pd**	**Pd**	**Pd**

Pd102 Pt99	*O1*	*O2*	*O3*	*O4*	*O5*	*O6*	*O7*	*O8*	*O9*	*O10*	*O11*	*O12*
+0.00	**Pt**	**Pt**	**Pt**	**Pd**	**Pd**	**Pt**	**Pt**	**Pt**	**Pd**	**Pd**	**Pd**	**Pd**
+1.17	**Pt**	**Pd**	**Pt**	**Pd**	**Pt**	**Pt**	**Pt**	**Pt**	**Pd**	**Pd**	**Pd**	**Pd**
+1.57	**Pt**	**Pt**	**Pt**	**Pt**	**Pd**	**Pd**	**Pt**	**Pt**	**Pd**	**Pd**	**Pd**	**Pd**
+1.71	**Pt**	**Pt**	**Pd**	**Pd**	**Pd**	**Pt**	**Pt**	**Pt**	**Pt**	**Pd**	**Pd**	**Pd**
+2.38	**Pt**	**Pt**	**Pd**	**Pt**	**Pd**	**Pd**	**Pt**	**Pt**	**Pt**	**Pd**	**Pd**	**Pd**
+2.39	**Pt**	**Pd**	**Pd**	**Pd**	**Pt**	**Pt**	**Pt**	**Pt**	**Pt**	**Pd**	**Pd**	**Pd**

Pd117 Pt84	*O1*	*O2*	*O3*	*O4*	*O5*	*O6*	*O7*	*O8*	*O9*	*O10*	*O11*	*O12*
+0.00	**Pd**	**Pt**	**Pd**	**Pd**	**Pd**	**Pt**	**Pd**	**Pt**	**Pd**	**Pd**	**Pd**	**Pd**
+0.61	**Pd**	**Pt**	**Pd**	**Pt**	**Pd**	**Pd**	**Pd**	**Pt**	**Pd**	**Pd**	**Pd**	**Pd**
+1.12	**Pd**	**Pt**	**Pt**	**Pd**	**Pt**	**Pd**	**Pd**	**Pt**	**Pt**	**Pd**	**Pd**	**Pd**
+1.18	**Pd**	**Pd**	**Pd**	**Pd**	**Pt**	**Pt**	**Pd**	**Pt**	**Pd**	**Pd**	**Pd**	**Pd**
+1.72	**Pd**	**Pd**	**Pt**	**Pd**	**Pd**	**Pt**	**Pd**	**Pt**	**Pt**	**Pd**	**Pd**	**Pd**
+1.82	**Pd**	**Pd**	**Pt**	**Pt**	**Pd**	**Pd**	**Pd**	**Pt**	**Pt**	**Pd**	**Pd**	**Pd**

Pd153 Pt48	*O1*	*O2*	*O3*	*O4*	*O5*	*O6*	*O7*	*O8*	*O9*	*O10*	*O11*	*O12*
+0.00	**Pd**	**Pd**	**Pd**	**Pd**	**Pd**	**Pd**	**Pd**	**Pt**	**Pd**	**Pd**	**Pd**	**Pd**
+3.82	**Pd**	**Pt**	**Pd**	**Pd**	**Pt**	**Pt**	**Pd**	**Pd**	**Pd**	**Pd**	**Pd**	**Pd**
+4.13	**Pd**	**Pd**	**Pd**	**Pt**	**Pd**	**Pt**	**Pd**	**Pd**	**Pd**	**Pd**	**Pd**	**Pd**
+5.30	**Pd**	**Pt**	**Pd**	**Pt**	**Pt**	**Pd**	**Pd**	**Pd**	**Pd**	**Pd**	**Pd**	**Pd**

Table 5. Energy differences with respect to the lowest energy homotop set as zero (in bold) for various compositions of a 201-atom Pd-**Pt** TO cluster. O1-12 stand for Orbit 1 to Orbit 12. The various homotops are indicated by the population of the orbit with Pd atoms (in red for clarity) or Pt atoms (in blue for clarity).

Pd99 Pt102	N_{tot}	N_{mix}	N_{Pt-Pt}	N_{Pd-Pd}
+0.00	948	528	276	144
+0.73	948	504	288	156
+1.13	948	552	252	144
+1.34	948	384	348	216
+1.65	948	456	300	192
+2.11	948	528	264	156

Table 6. The number of nearest-neighbor bonds for homotops at composition $Pd_{99}Pt_{102}$ is reported, distinguished in terms of total (N_{tot}), Pd-Pd (N_{Pd-Pd}), Pt-Pt (N_{Pt-Pt}) and mixed (N_{mix}) bonds. Each homotop is denoted by its energy (see Table 5 of this Supplementary Information for a complete structural description).

MolinaCT2011

Catalysis Today 160 (2011) 116–130

Contents lists available at ScienceDirect

Catalysis Today

journal homepage: www.elsevier.com/locate/cattod

Size-dependent selectivity and activity of silver nanoclusters in the partial oxidation of propylene to propylene oxide and acrolein: A joint experimental and theoretical study

Luis M. Molina[a,1], Sungsik Lee[b,1], Kristian Sell[c,1], Giovanni Barcaro[d,1], Alessandro Fortunelli[d,1], Byeongdu Lee[b], Soenke Seifert[b], Randall E. Winans[b], Jeffrey W. Elam[e], Michael J. Pellin[f], Ingo Barke[c], Viola von Oeynhausen[c], Yu Lei[f,g], Randall J. Meyer[g], Julio A. Alonso[a], Arantxa Fraile Rodríguez[h,2], Armin Kleibert[h], Suzanne Giorgio[i], Claude R. Henry[i], Karl-Heinz Meiwes-Broer[c], Stefan Vajda[f,j,k,*]

[a] Departamento de Física Teórica, Atómica y Óptica, Universidad de Valladolid, 47011 Valladolid, Spain
[b] X-ray Sciences Division, Argonne National Laboratory, 9700 South Cass Avenue, Argonne, IL 60439, USA
[c] Institut für Physik, Universität Rostock, Universitätsplatz 3, D-18051 Rostock, Germany
[d] Molecular Modeling Laboratory, IPCF-CNR, Via Giuseppe Moruzzi 1, Pisa I56124, Italy
[e] Energy Systems Division, Argonne National Laboratory, 9700 South Cass Avenue, Argonne, IL 60439, USA
[f] Materials Science Division, Argonne National Laboratory, 9700 South Cass Avenue, Argonne, IL 60439, USA
[g] Department of Chemical Engineering, University of Illinois at Chicago, 810 South Clinton Street, Chicago, IL 60607, USA
[h] Swiss Light Source, Paul Scherrer Institut, CH-5232 Villigen PSI, Switzerland
[i] CINaM-CNRS and Aix-Marseille Université, Campus de Luminy, Case 913, 13288 Marseille, Cédex 09, France
[j] Center for Nanoscale Materials, Argonne National Laboratory, 9700 South Cass Avenue, Argonne, IL 60439, USA
[k] Department of Chemical Engineering, Yale University, 9 Hillhouse Avenue, New Haven, CT 06520, USA

ARTICLE INFO

Keywords:
Silver clusters
Propene
Propylene
Propylene oxide
Acrolein
Density-functional calculations
Oxametallacycle complex
Cluster reshaping

ABSTRACT

Model silver nanocatalysts between 9 and 23 nm in size were prepared by size-selected cluster deposition from a free cluster beam on amorphous alumina films and their size-dependent catalytic performance studied in the partial oxidation of propylene under realistic reaction conditions. Smaller clusters preferentially produced acrolein, while the 23 nm particles were considerably more selective towards the formation of propylene oxide, at reaction rates far exceeding those previously reported for larger silver particles. The activity of clusters dropped significantly with increasing particle size. First-principle calculations, of the activation energies for oxygen adsorption and its dissociation, at variable surface coverage yielded surface energies which resulted in particle shapes resembling the experimentally observed shapes of partially oxidized silver clusters. The calculated activation barriers for propylene oxide and acrolein formation on various facets and on the edges of the nanoparticles provided detailed information about the energetics of the competing reaction pathways. The size- and corresponding morphology dependent theoretical activity and selectivity are in good accord with experimental observations.

1. Introduction

Propylene oxide (PO) and acrolein (Acr) are important precursors for a variety of commodity chemicals [1]. Traditional processes to produce propylene oxide are energy-intensive, inefficient and environmentally unfriendly since the processes involve multiple steps and create large quantities of by-products and waste. Therefore, the heterogeneously catalyzed direct oxidation of propylene by molecular oxygen has received increased attention [1–9]. Silver-based catalysts have been successfully used in the epoxidation of ethylene on both the laboratory [3] and industrial scale [10], but no viable catalyst for propylene epoxidation has been identified that would use molecular oxygen. Much of the effort so far has been centered on the nature of the active oxygen species [11] and size-dependent selectivity and reactivity [2]. However, the use of silver in propylene epoxidation has been hampered by either low conversion or poor selectivity towards propylene oxide. Moreover, to date a detailed atomic level understanding of this process is still lacking [2,5,8,9,12].

* Corresponding author at: Argonne National Laboratory, Materials Science Division and Center for Nanoscale Materials, 9700 S Cass Avenue, Building 200, Room A109, Argonne, IL 60439, USA. Tel.: +1 630 252 8123; fax: +1 630 252 4954.
E-mail address: vajda@anl.gov (S. Vajda).
[1] Equally contributing (first) authors.
[2] Current address: Departament de Física Fonamental i Institut de Nanociència i Nanotecnologia, Universitat de Barcelona, E-08027 Barcelona, Spain.

0920-5861/$ – see front matter © 2010 Elsevier B.V. All rights reserved.
doi:10.1016/j.cattod.2010.08.022

In the case of heterogeneous catalysts dispersed on supports, it is a challenging task to elucidate the structure–reactivity relationship with the traditional catalyst preparation methods which introduce variations in mean particle size and particle size distribution. Therefore, size-selected cluster deposition methods are well positioned to contribute to the understanding of the effect of catalyst particle size on its catalytic reactivity and selectivity by providing highly uniform supported model catalyst systems for such studies [13–29]. In general, the activity of the catalytic metals can be optimized when used in a form of small sub-nanometer clusters or small nanoparticles [15,19,26,27,30–42]. In the epoxidation of propylene to propylene oxide on silver and gold nanoparticles these catalysts exhibit strongly size-dependent catalytic activity and selectivity [2,7,43,44]. However, none of the nanometer sized catalysts reported to date possess both high conversion and selectivity towards propylene oxide. For example, Haruta and co-workers discovered a highly selective propylene epoxidation catalyst based on titania-supported 2–4 nm gold nanoparticles when hydrogen is co-fed with the oxygen and propylene mixture [7]. However, the selectivity of these gold nanoparticles is extremely sensitive to their size and shape, with particles smaller than 1.5–2.0 nm mainly producing propane and particles larger than 4–5 nm preferentially catalyzing oxidation of propylene to CO_2 and H_2O. Size-preselected sub-nanometer gold clusters stabilized on amorphous alumina exhibit highly selective catalysis for this reaction [23], while sub-nanometer Ag clusters and their aggregates possess high activity [25]. In order to make a correlation between the shape/morphology of the catalyst and its function, it is necessary to track changes in nanoparticle shape induced by temperature and exposure to reactive gases *in situ*, under realistic reaction conditions. In the present study, grazing incidence small-angle X-ray scattering (GISAXS) [22,24,44–46] was used to monitor the change in size and shape of supported silver nanoparticles, while the catalytic performance was followed simultaneously by temperature-programmed reaction (TPRx) under atmospheric pressure.

On the theoretical side, modern developments in computational software and hardware allow one to investigate adsorption mechanisms and elementary reaction steps on realistic metal systems, and studies have been conducted on the oxidation of extended Ag surfaces and the interaction of alkenes with both bare and oxidized Ag substrates in previous work [47–56]. For oxygen adsorption on the (1 0 0) surface, a close competition has been found between oxygen-induced reconstruction and simple oxygen chemisorption in hollow sites [47] and it has been shown that at medium/high oxygen coverage the formation of subsurface oxygen species is energetically favoured. In contrast, alkenes bind rather weakly on bare extended silver surfaces, mainly through the interaction of the π orbitals of the organic species with the *d* orbitals of the metal atoms [49], even though the binding energy can increase in the proximity of extended defects (steps) and adatoms [50,51]. Co-adsorption with oxygen promotes the interaction of alkenes. Chemisorbed oxygen adatoms interact with olefinic molecules giving rise to oxametallacycle intermediates [52] which act as precursors for the formation of epoxide or aldehyde species, while surface reconstructions induced by subsurface oxygen atoms produce an increase of the interaction energy of ethylene molecules with the surface due to a *push-out* effect [48]. The formation of π-bonded olefinic species and oxametallacycle intermediates has been shown to take place also on the silver (1 1 1) surface [53]. The involved bonding mechanisms are similar to those on the (1 0 0) surface in the case of mild oxidation with the formation of chemisorbed species. At high temperature (above 100 °C) in an oxygen atmosphere the (1 1 1) surface reconstructs with the formation of mixed silver–oxygen phases [54–56], and the formation of oxametallacycle intermediates can occur as well due to the presence of surface oxygen atoms [54].

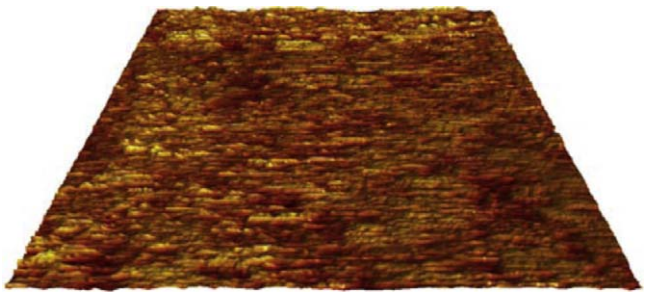

Fig. 1. Topographic STM image of the amorphous alumina support layer (500 nm × 500 nm, $U_T = -1.8$ V, $I_T = -0.5$ nA). The RMS roughness is about 0.69 nm.

In the present joint experimental and theoretical work, a study of the catalytic activity and selectivity of size-selected silver clusters of 9–23 nm size in the direct partial oxidation of propylene using molecular oxygen to preferentially produce propylene oxide and acrolein was undertaken. The very strong effect of size on catalyst performance is presented, along with the evolution of the morphology of the catalyst under reaction conditions. Accompanying first-principle simulations are then used to clarify the adsorption and reaction mechanisms of oxygen and alkene species on extended silver surfaces and finite-size models. Theoretical studies, here supplement prior results and explore cluster reshaping under realistic conditions. The cooperative effects in surface/oxygen/alkene interaction are investigated and compared with experimental results on nanometer clusters. Differences in the structural features of the nanometer sized silver clusters between room temperature and 200 °C are highlighted, focusing in particular on the presence and availability of reactive oxygen species, and are used to set up models providing a coherent mechanistic framework for the restructuring of clusters and its influence on selectivity, which is in excellent agreement with the experimental catalytic data.

2. Experimental methods

2.1. Support preparation: atomic layer deposition of thin amorphous alumina films

Atomic layer deposition (ALD) was used to deposit the alumina support layer on top of a naturally oxidized silicon wafer. ALD is a thin film growth technique that uses alternating cycles of saturating reactions between gaseous precursor molecules and the surface of the substrate to deposit films. In the case of Al_2O_3 it uses alternating exposures to trimethyl aluminum (TMA) and water [57]:

$$Al{-}OH* + Al(CH_3)_3 \rightarrow Al{-}O{-}Al(CH_3)_2* + CH_4 \quad (1)$$

$$Al{-}CH_3* + H_2O \rightarrow Al{-}OH* + CH_4 \quad (2)$$

The asterisks represent surface species, and the reactions have been simplified to show only a single functional group. In Eq. (1), the surface hydroxyl species OH* reacts with TMA to attach methyl-terminated Al atoms and liberate methane gas. In Eq. (2), the resulting $-CH_3{}^*$ surface groups react with water to restore the hydroxyl-termination and again liberate methane. In an iterative fashion, films of well-controlled thickness can be grown. In this study, six ALD cycles were used to coat the silicon. The thickness of the ALD Al_2O_3 layer was 7.2 Å based on a growth rate of 1.2 Å per cycle determined by spectroscopic ellipsometry. From the known density of ALD Al_2O_3 of 3.0 g/cm^3, we estimate a monolayer thickness of 3.0 Å so that the Al_2O_3 used in this study had a thickness of 2–3 monolayers. With a scanning tunneling microscope (Omicron LT-STM) the rough and amorphous surface of the created support layer was revealed (Fig. 1). The surface roughness of about

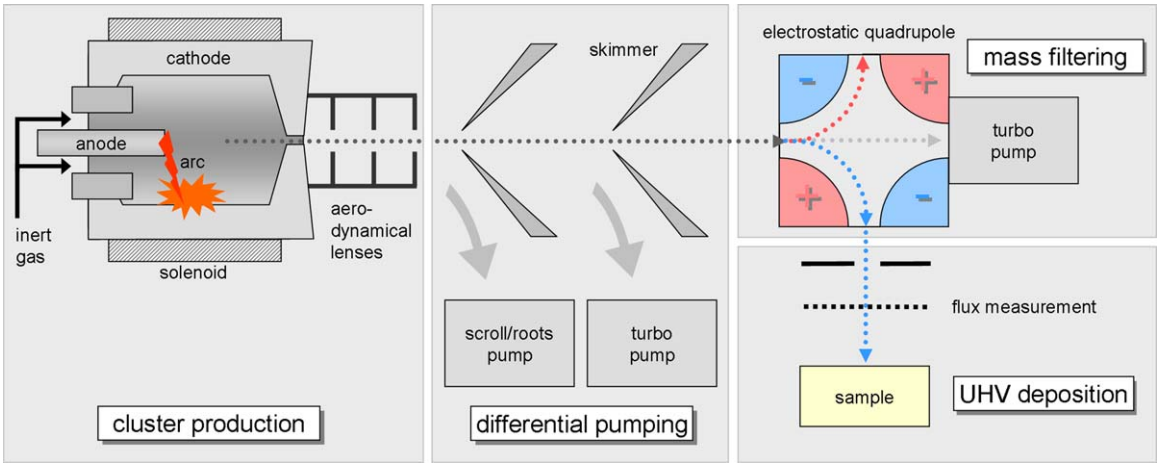

Fig. 2. Schematic view of the arc cluster ion source (ACIS) used for cluster production and deposition.

0.69 nm (RMS) is to be viewed as a lower limit due to convolution effects with the tip geometry. Uniform appearance and absence of large protrusions are characteristics of the substrates. Much of the roughness arises from the incomplete second monolayer. Supporting low energy electron diffraction (LEED) investigations showed no evidence of a periodic crystal structure at the sample surface.

2.2. Size-selected cluster deposition

Deposition of Ag clusters was performed in Rostock using an arc cluster ion source (ACIS) that is connected to a ultrahigh vacuum (UHV) preparation chamber [18]. The clusters are deposited from the free beam onto a flat 10 mm × 10 mm substrate produced by ALD as described above.

The wafers are transferred into the UHV chamber with a load-lock system and positioned in front of the ACIS. The schematic set-up of the deposition process is shown in Fig. 2.

In a cylindrical Ag cathode an arc is ignited between the water-cooled anode and the target-material. As a result, metal-vapor plasma is formed in the high temperature area. The cluster aggregation takes place in an inert gas atmosphere of about 80% He and 20% Ar with a total pressure of about 3 kPa within the cathode. Around the cathode a solenoid is mounted to ensure a rotation of the arc so that the cathode is eroded uniformly in all radial directions. The cluster beam passes an expansion channel, a system of aerodynamical lenses [58] and two skimmers where it is separated from the large part of the rare gas. An electrostatic quadrupole is used to deflect the charged clusters by 90° and to select the particle size. The latter is adjusted by the voltage applied to the four quadrupole plates. For this work voltages between 100 and 2000 V are used for sizes between 9 and 23 nm. The cluster current measured at a highly transparent metal grid is proportional to the cluster flux at the location of the sample. It has been calibrated for various cluster sizes by determining the cluster density utilizing TEM. One main challenge during deposition is to reduce the gas pressure from 2.96×10^{-2} atm in the cathode to UHV conditions at the support to obtain pure and well-defined particle deposits [58,59]. Several differential pumping stages are used for this purpose as shown in Fig. 2. For cluster sizes used in this work the kinetic energy per atom is less than 20 meV which is estimated based on a spherical cluster shape with measured cluster diameters. These energies are well within the regime of soft-landing conditions observed experimentally [60,61] and obtained from simulations [62,63]. Since no fragmentation or implantation takes place under such conditions, the number of atoms is not expected to change upon deposition. The absence of fragments was confirmed by scanning electron microscopy. The particles therefore maintain their gas-phase size and shape, but may experience a flattening upon impact and with interaction with the substrate [64]. The deposition process further leads to a random orientation of particles in the present size range [65]. For the sample coverage a cluster density of about 10^8 clusters per cm^2 was applied to avoid particle aggregation upon landing. As determined by scanning electron microscopy and X-ray scattering (see below for details), the lateral diameter of the supported size-selected clusters was around 9, 12 and 23 nm on the three samples, respectively.

2.3. Scanning electron microscopy

After the deposition process the samples were transferred to air and transported to scanning electron microscopy (SEM) at the Paul Scherrer Institut to determine the lateral diameter and number of clusters on the support before they continued to the Advanced Photon Source at Argonne National Laboratory for X-ray scattering and reactivity studies. After the reactivity studies, the samples were sent back to the Paul Scherrer Institut for SEM in order to verify particle size after the reactivity studies. The high resolution SEM measurements were performed on a Zeiss FE-SEM Supra VP55 apparatus.

2.4. In situ high-resolution environmental transmission electron microscopy

For the *in situ* observation in a high-resolution environmental transmission electron microscopy (HRETEM) at CINaM Marseille, the silver clusters were directly deposited on special copper discs covered with a transparent 6–8 nm thick carbon film. The copper discs had a diameter of 3 mm and were pierced at the center by 7 adjacent holes of 0.15 mm in diameter in a hexagonal arrangement. With a continuous carbon film covering the pierced area, the discs are gas proof and were tested up to a pressure difference of 3.95×10^{-1} atm on each side before use. The samples were mounted in a closed environmental TEM sample holder from JEOL, described in details in previous work [66,67]. This sample holder can be used with a standard microscope (JEOL 3010) equipped with a large gap pole piece (Cs = 1.4 mm). Under these conditions, the point resolution is 0.21 nm. A similar copper disc with a clean carbon film was used to close the sample holder. The clusters were sandwiched between the two carbon films; the gas was circulated between the carbon films at the level of the sample. In this simple closed environmental cell, the gas pressure must be lower than 2.96×10^{-2} atm at room temperature. In this work, sil-

ver clusters were imaged at room temperature and a gas pressure of 3.95×10^{-3} atm in pure H_2 and pure O_2. The images were recorded with a fast CCD camera to minimize exposure times. In order to reduce undesired effects caused by the electron beam, which after long exposures can cause a degradation of the sample, the adjustments of the electron beam optics were done on different areas than the working area of interest.

2.5. Grazing incidence small-angle X-ray scattering

Grazing incidence small-angle X-ray scattering (GISAXS) has been proved to be very powerful to study particles at surfaces and their transformations under vacuum conditions and low-pressure reactive gas environments at the nanometer [24,25,44,45,68–71] and sub-nanometer scale [22,23,25,41,72]. In addition to the determination of the size and shape of clusters, GISAXS can also provide information about faceting of nanoparticles [44,71] and structure of fractals [73,74]. The GISAXS experiments were performed at the 12-ID-C beamline of the Advanced Photon Source using X-rays of 12.0 keV energy in a reaction cell of our own design. The internal volume of the cell is approximately 25 ml, with the sample mounted on a ceramic heater in the center of the cell. The cell was sealed with mica windows and mounted on a computer controlled goniometer and equipped with gas feedthroughs mounted in the side walls of the cell. The reactant gas mixture was premixed in a remotely controlled gas-mixing unit with calibrated mass flow controllers (Brooks model SLA5850). The reaction temperature was controlled using a ceramic heater, and the sample temperature measured with a K-type thermocouple attached to the edge of the heater surface. As shown in Fig. 3, the X-ray beam was scattered off the surface of the sample at near the critical angle ($\alpha_c = 0.18^\circ$) of the substrate. A 1024×1024 pixel two-dimensional MarCCD detector was used for recording the GISAXS images from the sample. GISAXS data were collected as a function of reaction temperature and time. The two-dimensional X-ray images were analyzed by taking cuts in the q_y direction for horizontal information and in the q_z direction for vertical information. Scattering vectors q are calculated from $(4\pi/\lambda)\sin\theta_f$ where θ_f is the scattering half angle and λ is the wavelength of the X-rays. The data were analyzed by Guinier analysis [75], providing the horizontal and vertical particle radii of gyration R_{gH} and R_{gV}, respectively. The diameter and height of the nanoparticles can be calculated from the radii of gyration as $2.58 \times R_{gH}$ and R_{gV}, respectively. The uncertainty in the particle size was estimated to be ± 0.2 nm or better, which is 2% of the particle size or less. In this study, GISAXS was used to determine the diameter of clusters size under vacuum conditions before and after the reaction as well as to monitor changes in particle morphology under reaction conditions.

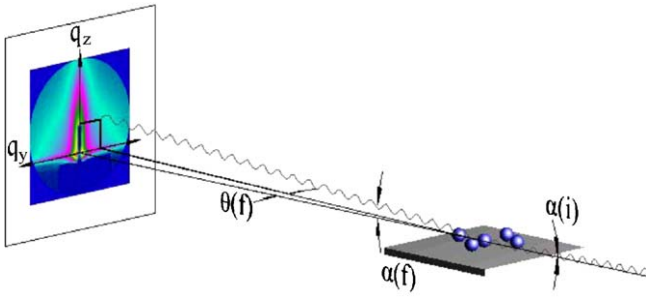

Fig. 3. The schematic of the GISAXS experiment: incident angle $\alpha_i = 0.18^\circ$ and scattered beam angle α_f.

2.6. Temperature-programmed reaction

The catalytic tests were performed in the reaction cell designed for the GISAXS experiments (see above) using temperature-programmed reaction (TPRx) at 1.3 atm pressure and total gas flow of 30 sccm. To achieve thermal equilibrium between the heater and sample during the application of a temperature ramp, a low heating rate (<1.5 °C/min.) was used. The gas mixture used consisted of 0.67% C_3H_6 and 0.33% O_2 in helium. The reaction products were analyzed on a differentially pumped quadrupole mass spectrometer (Pfeiffer Prisma). $m/z = 58$ was chosen to monitor the propylene oxide, as has been used by several other groups [76–79]. Theoretical and experimental work has shown that during the oxidation of propylene a variety of partial oxidation products can in principle form, some of which having the same molecular formula and mass as propylene oxide (the parent ions of acetone and propenol also have $m/z = 58$), a careful analysis of the mass spectra of the gas mixture exiting from the reaction cell was performed. Based on fragment patterns of the NIST mass spectra of these species the formation of acetone and propenol could be excluded based on the following. For the on-line analysis of the gas mixture exiting from the reaction cell during the course of the reaction, the mass spectrometer was operated in multi-ion-detection mode (MID). This operation mode allows for a simultaneous monitoring of the ion current corresponding to up to 24 m/z values. In our experiments a

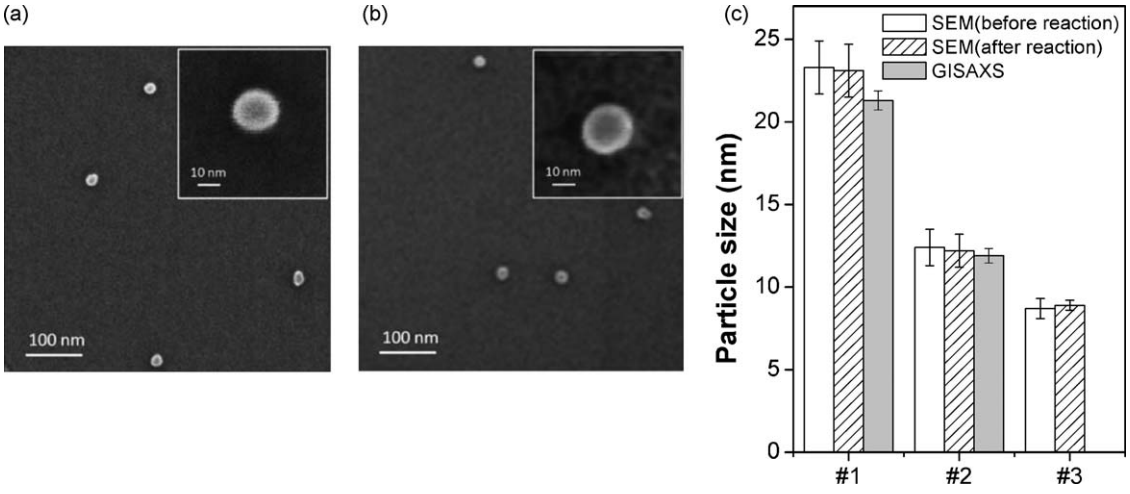

Fig. 4. Representative HRSEM images of silver nanoclusters of 23.3 nm (sample #1) in size (a) before the epoxidation reaction and (b) after reaction cycles. (c) Particle lateral size and size distribution (indicated by bars) at room temperature from SEM images before and after the reaction, and average lateral diameter and uncertainty from data fitting (error bars) from GISAXS before reaction (average sizes #1 = 23.3 nm, #2 = 12.0 nm, #3 = 8.7 nm).

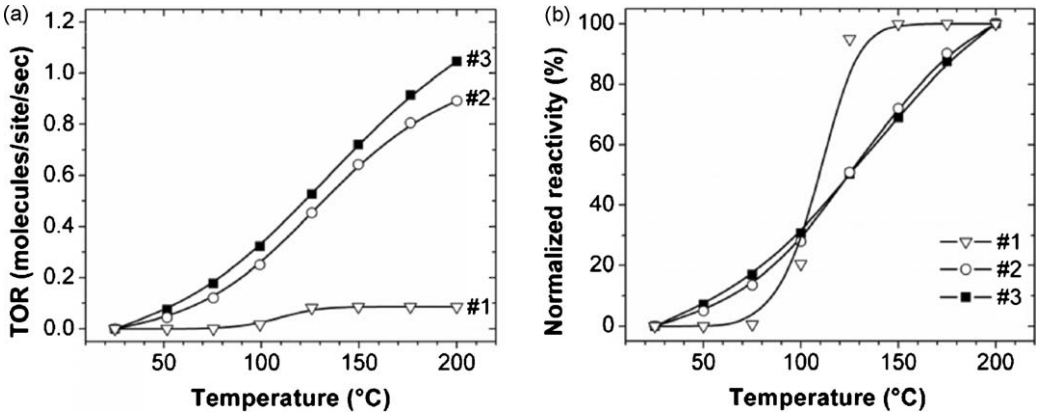

Fig. 5. (a) Background-corrected temperature dependent per surface atom turn-over rate of propylene oxide formation in the partial oxidation of propylene for three cluster sizes. (b) Normalized TORs of propylene oxide as a function of temperature (average lateral diameter of clusters: #1 = 23.3 nm, #2 = 12 nm, #3 = 8.7 nm). The signals plotted are background-corrected ones, using a support of the same size and composition without catalytic particles, and tested under identical conditions as the catalyst-containing sample. The background ion signal intensity for propylene oxide measured on a blank alumina support were below 4% of the signal intensity measured in the presence of silver nanoclusters, respectively. The mass spectrometer was calibrated using certified gas mixtures of the reactants and products in balance helium gas under identical flow conditions as in the TPRx experiments.

total of 20 m/z values were monitored, including the m/z values corresponding to the mass peaks of acetone and propenol, leading to the following conclusions: (1) propenol could be excluded because the mass spectrometer's MID signal corresponding to $m/z = 57$, the major peak of propenol, was below the detection limit during the entire temperature-programmed reaction cycle. Acetone could be excluded because there was no change in the mass spectrometer signal (MID) corresponding to $m/z = 43$, the major peak of acetone [80]. The uncertainty in the mass spectrometer signal has been estimated from standard deviation of 11–23 readout points which includes points both below and above the plotted reaction temperature. The uncertainty is estimated to be ~2% of the ion current. Taking into consideration an estimated 10% uncertainty in the determination of the number of deposited atoms, the uncertainty in determination of the turn-over rates is estimated to be about 10% of the reported values. This approach is analogous to the one reported by the Anderson group [81].

An estimate of the number of accessible surface silver atoms to the reactants was done by assuming hemispherical particle shape for the supported particles, with the lateral diameter and aspect ratio determined by SEM and GISAXS. The exposed surface area of the particles was calculated from the average height and diameter of particles. (This excluded the Ag atoms sitting on the alumina support which were inaccessible to the reactant molecules.) The number of accessible atoms of the hemisphere was calculated by taking into consideration the 2.88 Å Ag–Ag distance in Ag(1 1 1) with a fcc structure [82].

3. Computational methods

Density-functional (DF) calculations on the oxidation of Ag surfaces were performed using the QuantumEspresso computational code [83], employing ultrasoft pseudopotentials [84] and the Perdew, Burke, and Ernzerhof (PBE) [85] exchange-correlation functional. Values of 40 and 240 Ryd were employed as the energy cut-offs for the selection of the plane wave basis set for the description of the wave-function and the electronic density, respectively. DF calculations were performed spin-polarized by applying a Gaussian smearing technique with a broadening of the one-particle levels of 0.03 eV. To describe the silver surfaces, a supercell approach with a 7-layer metal slab was employed. To describe oxygen adsorption at increasing coverage, (3×3) and (2×2) cells were used; namely the (3×3) cell has been used in the case of 1/9 coverage, whereas the (2×2) cell for 1/4 and 1/2 coverages. A (4 4 1) k-grid was used to sample both the (2×2) and the (3×3) cells. In the case of the (1 1 0) surface, where the two in-plane lattice vectors of the unit cell do not have the same length, we have adopted a (4 3 1) k-grid. The silver atoms were positioned at the crystal sites of the fcc structure at a first-neighbour distance of 2.947 Å, corresponding to the equilibrium value predicted for fcc silver by our DF/PBE approach. The inner three layers were kept fixed in the crystal positions, whereas the outer two were allowed to relax. A symmetric adsorption on both sides of the metal slab was adopted to cancel the dipole moment developed by the adsorption process. Empty space between replicated cell was chosen between 10 and 15 Å.

The DF calculations for the partial oxidation of propylene were carried out using the DACAPO code [86], which also employs ultrasoft pseudopotentials. The set-up is slightly different: the PW91 functional [87] was used for exchange-correlation, and in order to keep the computational cost low (due to the large number of simulations which these type of studies of reaction pathways requires) the energy cut-off for the plane wave basis was slightly lower (25 Ryd). For the same reason, the Ag(1 1 1) surface was modeled using a 3-layer metal slab (relaxing only the first layer). Energy barriers were calculated by a constrained minimization method, involving several simulations where the reaction coordinate (C–O or C–H bond distance) was restricted at increasingly smaller values, while allowing the rest of the system to freely relax [88].

4. Experimental results and discussion

4.1. Characterization of the size of the supported clusters by SEM and GISAXS

Representative SEM images obtained on a silver sample before and after reaction are shown in Fig. 4a and b, respectively. The average lateral diameter of the clusters is determined by using the *Scion Image* software. The error bar is the standard deviation of the corresponding particle size counted from several SEM images on different areas of the given sample. The samples #1, #2 and #3 consisted of discrete silver clusters with an average size of 23.3, 12 and 8.7 nm, respectively, with a very narrow size distribution (<5%) as shown with bars in Fig. 4c. No noticeable change is observed in the mean cluster size and its distribution before and after the reaction. Cluster lateral diameters determined by GISAXS for samples #1 and #2 are also very well matched with SEM results. The density of the silver particles on sample #3 is too low for accu-

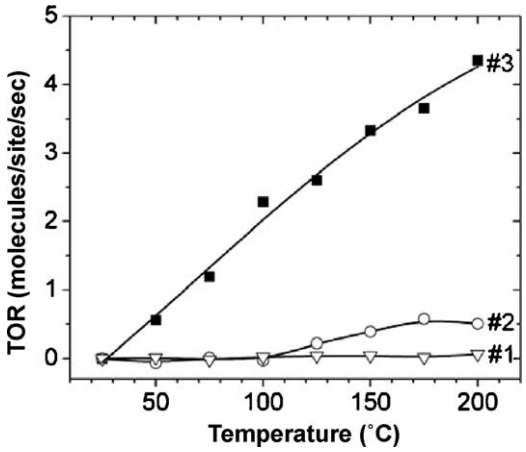

Fig. 6. Background-corrected temperature dependent per surface atom turn-over rate of acrolein formation in the partial oxidation of propylene for three silver cluster sizes (average lateral diameter #1 = 23.3 nm, #2 = 12 nm, #3 = 8.7 nm). The background ion signal intensity for acrolein measured on a blank alumina support was below 15% of the signal intensities measured in the presence of the silver clusters.

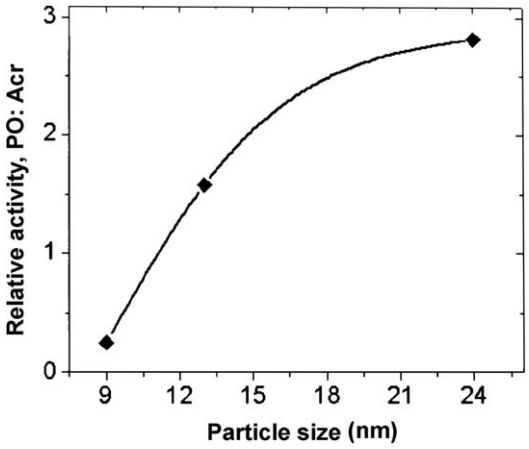

Fig. 7. Selectivity of silver catalyst (ratio propylene oxide/acrolein) at 200 °C as the function of particle size.

rate GISAXS measurements. Cluster lateral diameters and heights are determined from the Guinier analysis of the GISAXS images collected at room temperature under pure helium. The results show an average aspect ratio of about 1.6. The uncertainty of the dimensions obtained by the analysis of the GISAXS data (~0.2 nm) is calculated based on the counting statistics, which provides errors of data fitting (linear regression in this case). As discussed in detail in Ref. [24], the aspect ratio of the silver nanoclusters undergoes dramatic changes after the exposure of the particles to the reactant gas mixture and further evolves with temperature. Similar changes were observed for the smaller cluster sizes reported here.

The alumina-supported silver nanoclusters are very stable catalysts—they retain their size over the course of 4–6 reaction hours, as determined by GISAXS and by the analysis of SEM images collected before and after the reaction cycles (see Fig. 4a and b). Thus we could exclude both aggregation and Ostwald ripening [89] under our reaction conditions for all three particle sizes—an important aspect in the light of potential future applications.

4.2. TPRx: size-dependent activity and selectivity

Fig. 5a shows turn-over rates (TOR) of propylene oxide formation per surface atom on various size silver cluster catalysts. The smaller size silver clusters #2 and #3 (12 and 8.7 nm lateral diameter, respectively) start to react at much lower temperature than the largest particles #1 (23.3 nm); the latter start to show catalytic activity at ~80 °C and reaching maximum activity at ~150 °C [24]. At temperatures above 100 °C, the smaller silver clusters #2 and #3 exhibit about an order of magnitude higher reactivity than the largest size clusters #1. These results, along with the comparison of the trends exhibited by the normalized TORs (Fig. 5b) indicate that the reaction mechanism may change when crossing the ~20 nm size range.

It should be noted that 100 °C is reported to be the required temperature to form subsurface oxygen in silver via dissociation of molecular oxygen, which plays important role on extended silver surfaces [90–92], and Lu et al. identified an increased Ag_2O phase with decreasing particle size during the epoxidation of ethylene [5]. As reported by Savio et al. [93] in their study of O_2 adsorption at stepped surfaces, open steps favour the dissociation of oxygen and provide a gateway through which subsurface sites can be accessed.

Fig. 6 shows the turn-over rate of the acrolein, the main co-product identified, as a function of reaction temperature. High reactivity towards acrolein formation, about 4 times of propylene oxide production, is observed on smallest size clusters #3 (8.7 nm). The rate of acrolein production sharply decreases with increasing cluster size, dropping to about 1/3 of the TOR of propylene oxide on the largest particles (23.3 nm) at 200 °C.

The surface-atom based TORs show an interesting, non-linear decrease of activity with increasing size and corresponding surface area and volume. Considering the two smallest Ag clusters (average lateral diameters #3 = 8.7 nm and #2 = 12 nm), the surface-atom based TOR for PO decreases by about only 10% while acrolein production drops by about 90% with the slightly increased cluster size. For the largest Ag cluster (average lateral diameter #1 = 23.3 nm), the surface-atom based TORs drop by about a factor of 10 for both propylene oxide and acrolein. Thus, as we found above for the TOR's as a function of temperature, the reaction specificity also suggests that the mechanism for the catalytic reaction is significantly different for the larger clusters. We note that the smaller clusters have a much higher structural fluxionality, than their larger cousin.

The observed high TOR for propylene oxide formation at 200 °C on the ~9 nm particles reported here is only about ~30% lower than that observed for 2 nm tall and 4 nm in diameter silver particles made by aggregation of size-selected sub-nanometer silver trimer clusters [25], thus potentially indicating a new, sub-10 nm size range for highly active silver-based alkene partial oxidation catalysts. In comparison with reported silver-based propylene

Table 1
Turn-over rates of propylene oxide and acrolein formed at 200 °C per total and exposed silver surface atom basis.

Cluster sample	Ag cluster mean lateral diameter (nm)	TOR of propylene oxide produced		TOR of acrolein produced	
		[PO molecules × total Ag atoms^{-1} s^{-1}]	[PO molecules × exposed surface Ag atoms^{-1} s^{-1}]	[Acr molecules × total Ag atoms^{-1} s^{-1}]	[Acr molecules × exposed surface Ag atoms^{-1} s^{-1}]
#1	23.3	3.7×10^{-3}	8.5×10^{-2}	2.0×10^{-3}	4.8×10^{-2}
#2	12.0	7.2×10^{-2}	8.9×10^{-1}	7.9×10^{-2}	5.2×10^{-1}
#3	8.7	1.2×10^{-1}	1.1	5.0×10^{-1}	4.3

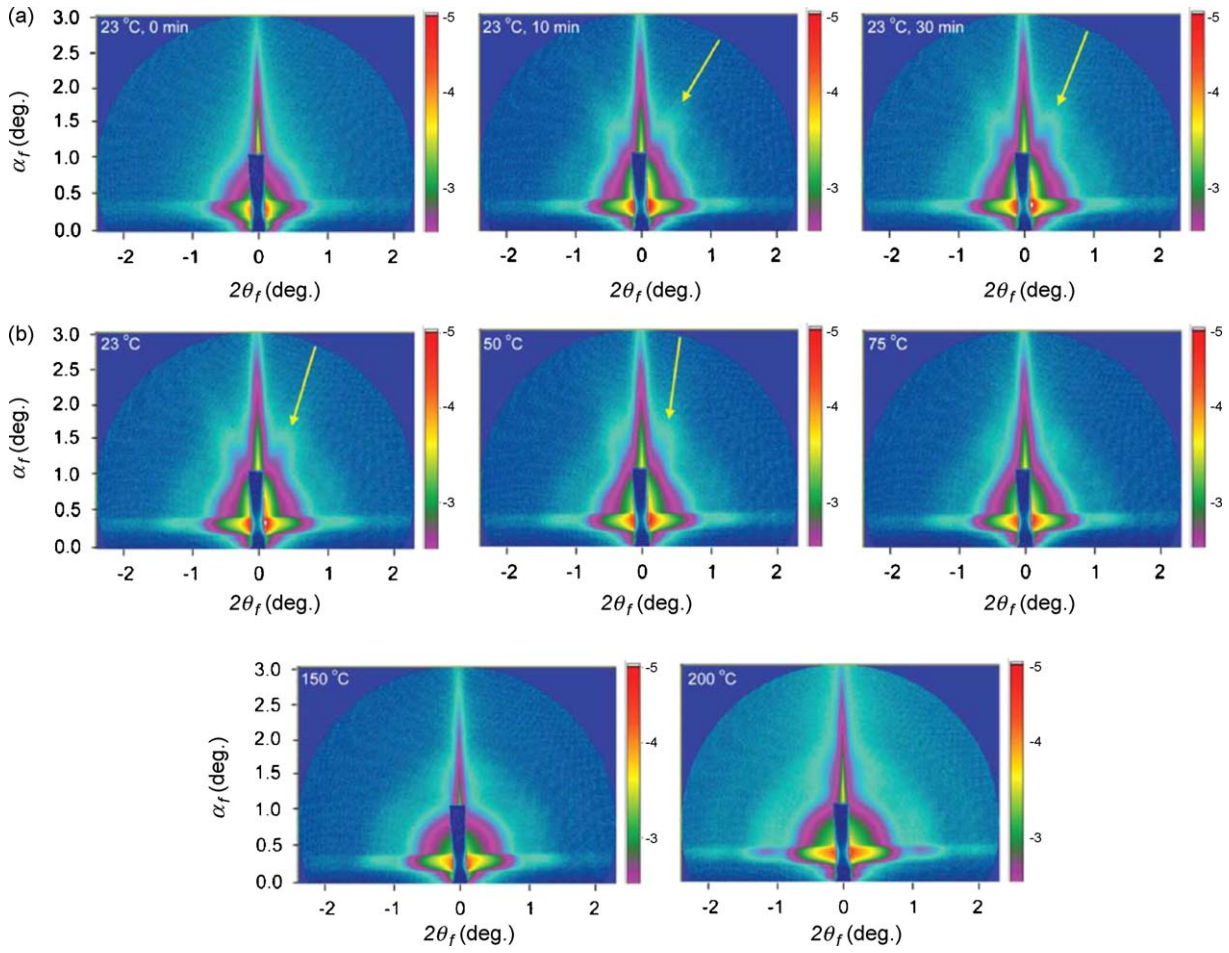

Fig. 8. GISAXS images on ~9 nm large particles. (a) At room temperature, from left to the right: image recorded at the time of the inlet of the propylene–oxygen mixture, after 10 min of exposure and after 30 min of exposure. (b) Change of the scattering pattern during ramping the temperature from 23 to 200 °C. The arrows indicate the angle of the most intense component of the directional scattering.

epoxidation catalysts, the TOR for the 9 nm sized clusters per surface atom or per atom is high. For instance, the rate of propylene oxide molecule formation per surface silver atom is about 1.1 s^{-1} at 200 °C for the 9 nm particles, which is much greater than that reported for larger silver particles. For example, turn-over rates per surface atom ($\leq 10^{-4}$ per total atom) is reported to be 1×10^{-2} s^{-1} for 50–660 nm unpromoted silver particles at 220 °C [5] and about 5×10^{-3} s^{-1} for a 3:1 weight ratio Ag/Ni catalyst tested in the 150–300 °C temperature range [94]. Thus, the turn-over rates in this work are more than an order of magnitude higher than the previously reported data by other groups (for reference data see Supplemental Online Material of reference [25] for TORs on either a per surface atom or a per atom basis).

The propylene oxide to acrolein ratio at 200 °C is plotted in Fig. 7, showing a change in selectivity by over an order of magnitude in the cluster size range ~9 to ~23 nm, reinforcing the conclusions drawn from Table 1. It is noteworthy that acrolein formation occurs at lower temperature than the temperature for propylene oxide formation, and no onset temperature could be found for this reaction, indicating that acrolein formation has a very low activation barrier and that surface oxygen may be involved in the production of acrolein, rather than subsurface oxygen whose formation requires higher temperatures [1,2,91,95]. Particle size-dependent oxidation properties have been reported by Bukhtiyarov and Kaichev [91] in the epoxidation of ethylene. Their results show that concentration of oxygen in silver catalysts is particle size dependent, and reactive (subsurface) oxygen appeared for particle sizes greater than 30 nm, which was associated with the rate of epoxidation of ethylene. Also it has been reported that adsorbed molecular oxygen is responsible for the formation of acrolein, whose formation is favoured on isolated silver sites [1].

As shown in Fig. 7, there is a pronounced effect of particle size on the selectivity. The smaller size silver clusters may stabilize adsorbed molecular oxygen more efficiently than the bigger clusters, on which O_2 dissociatively adsorbs to form subsurface oxygen preferentially. Surface oxide structure of silver has been in long debate [54,55,96–99] and high pressure subsurface oxide formation is not clearly understood [100]. Our results may indicate that, under given reaction conditions of steady state oxygen concentration, the silver oxide formation and equilibrium between surface and subsurface oxygen is particle size dependent, which can represent a key factor in controlling the selectivity in the oxidation of propylene. No change in the mass signal corresponding to carbon dioxide is observed during the temperature ramp. Presumably, low oxygen to propylene ratio (1:2) of the reaction gas effectively suppresses total oxidation.

4.3. *In situ GISAXS and HRETEM: change in faceting of the particles*

Fig. 8 shows a sequence of *in situ* GISAXS images of ~9 nm large silver particles recorded during the oxidation of propylene. Fig. 8a shows the change in scattering pattern at room temperature caused by the reactants. Few minutes after the inlet of the

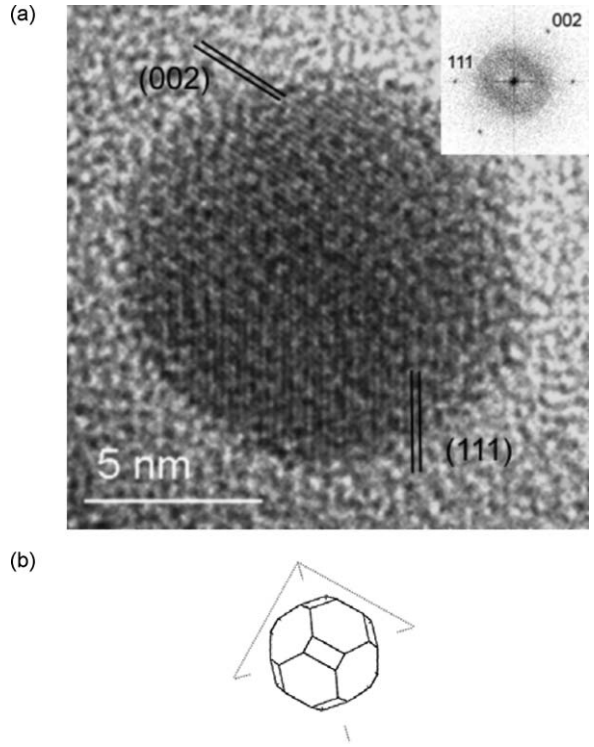

Fig. 9. (a) HRETEM of silver cluster under hydrogen. (b) Wulff shape reconstruction.

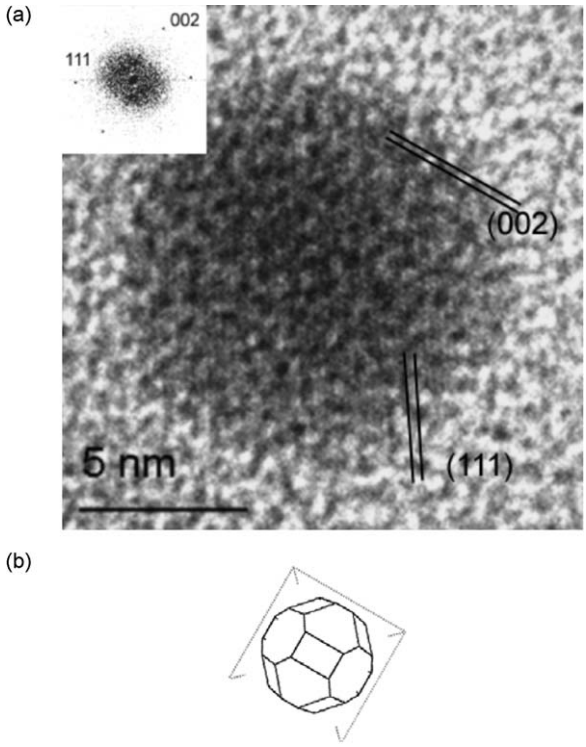

Fig. 10. (a) HRETEM of silver cluster under oxygen. (b) Wulff shape reconstruction.

reactants a directional scattering emerges (indicated by arrows), with its angle changing with time. As discussed below, we ascribe this to the growth of (1 1 1) facets—a reshaping accompanied by the reorientation of the particles. Fig. 8b shows the further evolution of the scattering pattern with temperature as the reaction proceeds. The directional scattering vanishes above 75 °C and the symmetrical scattering pattern at 200 °C is indicative of the formation of spherical particles at this temperature. Such directional scattering is observed for example on much larger palladium and silver nanoparticles [45,72].

In order to unambiguously attribute the observed pattern to facets, we have imaged silver nanoparticles in environmental HR TEM (HRETEM) under oxygen and hydrogen. Hydrogen was chosen instead of propylene to mimic competition for oxygen binding with propylene on the surface of the particles in order to avoid possible contamination of the environmental TEM cell.

The results are shown in Fig. 9 and reveal faceted particles. A reversible change in faceting structure is observed when alternating between oxygen and hydrogen environment. Fig. 9a shows a silver cluster under H_2 at a pressure of 3.95×10^{-3} atm. According to the high-resolution images and their calculated Fast Fourier-Transforms, the cluster is (1 1 0) oriented. In such an orientation, the lateral faces parallel to the electron beam are (0 0 2) and (1 1 1) faces.

The shape is limited by extended (1 0 0) and (1 1 1) surfaces, and by (1 1 0) small surfaces. The Wulff shape fitting to the external shape is represented in Fig. 9b. The series of Wulff shapes of an fcc cluster in the same (1 1 0) orientation were simulated for varying ratios between the surface free energies σ_{111}, σ_{001} and σ_{110}. The σ values were used with increasing steps of 0.1 J m^{-2}, from 0.9 to 1.3 J m^{-2} (see for example Ref. [101]). The comparison between the calculated shapes and experimental ones allows the estimation of the ratios $\sigma_{001}/\sigma_{111}$, and $\sigma_{110}/\sigma_{111}$. According to this shape, the central distances to the limiting (1 0 0), (1 1 1) and (1 1 0) facets are evaluated. According to the Wulff theorem, $h_i/h_j = \sigma i/\sigma j$, their ratio corresponds to the ratio between the surface free energies σ_{100}, σ_{111} and σ_{110}. The values of the anisotropy ratios are yield $\sigma_{100}/\sigma_{111} = 1.00$ and $\sigma_{110}/\sigma_{111} = 1.11$.

Fig. 10a shows the HRETEM image of the same silver cluster in pure O_2 at the same pressure after a few minutes. The cluster is still (1 1 0) oriented but the shape limited by (1 0 0), (1 1 1) and (1 1 0) faces is more isotropic. The Wulff shape fitting to the external shape observed in O_2 is represented in Fig. 10b. In this case, the values of the anisotropy ratios are evaluated to $\sigma_{100}/\sigma_{111} = 1.00$ and $\sigma_{110}/\sigma_{111} = 1.055$.

The effect of pure oxygen has previously been observed by the same technique on Au clusters of the same size, supported on carbon [67] or TiO_2 [102]. At variance with what was observed for Ag clusters, the effect of pure O_2 on Pt clusters on carbon [103] and Pd clusters supported on MgO [66], induces an extension of the (0 0 1) faces at the expense of the (1 1 1) faces. In the case of small Pd and Au clusters [104], the experimental values from HRETEM observations in vacuum were also found to have extended the (0 0 1) facets ($\sigma_{100}/\sigma_{111} = 1.15$). The electron beam effect on the morphology of the particles has been studied for example in Ref. [105].

In the case of the Ag clusters, the variations of the anisotropy ratio between the (1 0 0) and (1 1 1) facets in H_2 and O_2 at a pressure of 4×10^{-1} kPa, at room temperature were very small. On the opposite side, the more open faces (1 1 0) are extended with O_2 exposure. The HRETEM results provided very important proof about the existence of facets and their alteration caused by changes in the gas composition at lower temperatures, as indicated by GISAXS. However, due to differences between the gas composition and pressure in the GISAXS and HRETEM experiments, as well as the different composition of the support used, a direct quantitative comparison between both experiments would be difficult.

Fig. 11 shows a representative GISAXS image with facet scatterings from ~9 nm large nanoparticles. The blue solid arrows denote all possible contributions from (1 1 1) facet scatterings from a single crystalline nanoparticle oriented in a way that their (2 1 1) plane is parallel to the substrate surface but randomly oriented in the sample plane. The black dotted arrows indicate the possible con-

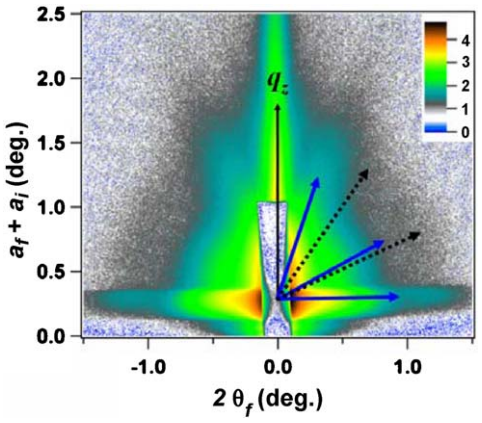

Fig. 11. Analysis of the GISAXS pattern of a ~9 nm large silver particles when exposed to the mixture of propylene and oxygen. The arrows indicate scattering from various facets. The blue solid arrows denote possible contributions from (1 1 1) facet scattering from single crystalline nanoparticles. The black dotted arrows denote the possible contributions from (1 1 0) facet scatterings from the same particles. Note that arrows are shown only on the right half of the image, since the GISAXS pattern is symmetrical with respect to the q_z axis.

tributions from (1 1 0) facet scatterings from the same particles. The azimuthal angles (the angle between q_z and facet scattering) of (1 1 1) facet scattering are 19.5°, 61.9°, and 90° [106]. Facet scatterings in the measured GISAXS images are well matched with the calculated (1 1 1) facet direction shown by arrows suggesting that (1 1 1) plane is a dominant facet of Ag nanoparticles under the mixture of propylene and oxygen. The disappearance of the directional scattering at higher temperatures (cf. Fig. 8) demonstrates the loss of (1 1 1) faceting and may be indicative of changes of the surface energies in the presence of catalytic reactions leading to more spherical particle shapes and/or the formation of disordered surface structures.

5. Results of theoretical calculations and discussion

5.1. Oxygen adsorption

The Ag particles as deposited are left in air for several days. Under these conditions, O_2 molecules dissociate over silver surfaces, and some degree of surface oxidation can be assumed. We argue that at room temperature and atmospheric pressure the exposure of the silver clusters to oxygen produces only chemisorbed species. Under mild conditions, in fact, the energy barriers for complex surface reconstructions leading to the formation of subsurface oxygen species are too high to overcome. This assumption is supported by experiment, which shows that oxygen-induced reconstructions of compact surfaces are formed only above at least 100 °C [107] or in the presence of defects [93]. We focus on the adsorption of oxygen atoms over the most compact metal surfaces, namely the (1 1 1), (1 0 0) and (1 1 0) ones (which are those experimentally observed by HRETEM) and at low coverages (up to 0.5 ML). At higher coverages, the occupation of subsurface sites becomes favoured [97,108].

Detailed studies of the oxygen adsorption process on the (1 0 0) and (1 1 1) surfaces have been already carried out in the literature [97,108]. Our calculations on these surfaces aim at validating our approach and for assuring consistency with the calculation performed on the (1 1 0) surface.

We evaluate the adsorption energy (ΔE_{ads}) of an oxygen atom according to the relation [108]:

$$\Delta E_{ads} = \frac{1}{N_o}\left[E_{tot} - E_{Ag} - \frac{N_o}{2}E_{O_2}\right]$$

where E_{tot} is the total energy of the composite system, E_{Ag} is the energy of the clean silver surface, E_{O_2} is the energy of an oxygen molecule and N_o is the number of oxygen atoms adsorbed on the surface. Recall that our DF/PBE approach overestimates the binding energy of the oxygen molecule (6.6 eV against the experimental value of 5.1 eV), and we expect that the oxygen/silver interaction is similarly overestimated, as suggested by comparison with experiment on strongly oxidized surfaces [54,55] . To evaluate the Gibbs free energy corresponding to the adsorption process (ΔG_{ads}), the O_2 molar Gibbs free energy is calculated in the perfect gas approximation, e.g., 0.54 eV at room temperature (298 K) and standard pressure (1 atm). Both ΔE_{ads} and ΔG_{ads} are reported in Table 2 for selected cases.

5.1.1. Oxygen adsorption on Ag (1 0 0) surface

In the case of the (1 0 0) surface, the most favourable adsorption site for oxygen is a four-fold hollow position. In this site, oxygen is surrounded by eight metal atoms (four in-plane and four below the surface). Looking at the results reported in Table 2, we can see that the adsorption energy is not appreciably modified in passing from 1/9 to 1/4 coverage, but is reduced from 0.70 to 0.57 eV due to the Coulombic repulsion between the negatively charged adatoms when the concentration is increased to 1/2 (and the atoms are arranged according to a $c(2\times2)$ pattern (see Fig. 12a) At higher coverage, configurations involving the occupation of subsurface sites become energetically favoured with respect to simple chemisorption. The values of ΔG_{ads} are negative, implying that the adsorption process occurs spontaneously. From Table 2 a coverage of 1/2, characterized by a $c(2\times2)$ arrangement of the adatoms (Fig. 12a), results as a good estimate of the real coverage of the (1 0 0) surface.

5.1.2. Oxygen adsorption on Ag (1 1 1) surface

On the (1 1 1) surface, which has also been the subject of previous studies (e.g. [97,109]), the most favourable adsorption sites for oxygen atoms are three-fold hollow sites. In these sites the interac-

Table 2
Adsorption energies (ΔE_{ads}) and Gibbs free energies (ΔG_{ads}) related to oxygen adsorption on the lowest-energy silver surfaces. The coverage is defined by the ratio between the number of adatoms and the number of surface hollow sites.

Surface	Coverage	Unit cell	# of adatoms	ΔE_{ads} (eV)	ΔG_{ads} (eV)	Figure
(1 0 0)	1/9	(3×3)	1	0.71	0.44	
	1/4	(2×2)	1	0.70	0.43	
	1/2	(2×2)	2	0.57	0.30	Fig. 12a
(1 1 1)	1/9	(3×3)	1	0.38	0.11	
	1/4	(2×2)	1	0.35	0.08	
	1/2	(2×2)	2	~0	<0	Fig. 12b
(1 1 0)	1/9	(3×3)	1	0.45	0.18	
	1/4	(2×2)	1	0.42	0.15	
	1/2 checkboard	(2×2)	2	0.30	0.03	Fig. 12c
	1/2 [1 1 0]-row	(2×2)	2	0.41	0.14	Fig. 12d
	1/2 [1 1 1]-row	(2×2)	2	0.08	<0	

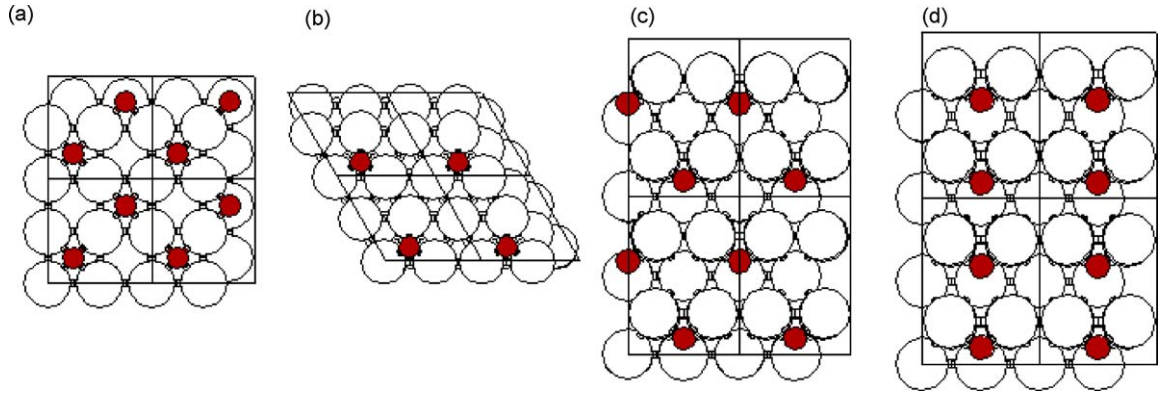

Fig. 12. Oxygen adatoms on the (a) (1 0 0) surface according to a 1/2 coverage and a $c(2 \times 2)$ pattern; (b) (1 1 1) surface according to a 1/4 coverage and a $p(2 \times 2)$ pattern; (c) (1 1 0) according to a 1/2 coverage and a $c(2 \times 2)$ pattern; (d) (1 1 0) surface according to a 1/2 coverage and a [1 1 0]-row pattern. Silver atoms are displayed in white, oxygen atoms in red. Four unit cells are displayed in each case.

tion with the surface is decreased with respect to the (1 0 0) surface, as metal atoms have higher coordination and the number of Ag–O bonds is smaller. Looking at the numbers of Table 2, we can see that at coverage of 1/9 and 1/4 on the (1 1 1) surface the interaction energy is decreased by a factor of 2 with respect to the case of the (1 0 0) surface (for example, 0.35 eV instead of 0.70 eV at 1/4), whereas at a coverage of 1/2 the adsorption process results energetically unfavourable. The values of the corresponding Gibbs free energies are consequently reduced with respect to the (1 0 0) surface, so that adsorption is spontaneous only up to a coverage of 1/4 (this structure is shown in Fig. 12b). This implies also that the density of oxygen adatoms on the (1 1 1) surface is decreased with respect the (1 0 0) case.

5.1.3. Oxygen adsorption on Ag (1 1 0) surface

The (1 1 0) surface exhibits an intermediate behavior between the previous two cases. The most favourable adsorption sites are the three-fold hollow sites, as in the (1 1 1) surface, but the metal coordination of the three first-neighbour atoms is reduced, so that the adsorption energy is a bit higher than on the (1 1 1) surface (0.42 eV instead of 0.35 eV at 1/4, see Table 2) and is only slightly decreased in passing from 1/9 to 1/4 coverage. In Fig. 12c and d we show two possibilities of adsorption at coverage of 1/2 among the several cases investigated. The checkboard pattern (Fig. 12c) is similar to the $c(2 \times 2)$ arrangement of the (1 0 0) surface and corresponds to a drastic reduction of the adsorption energy with respect to lower coverage. A better arrangement is realized in the configuration shown in Fig. 12d, in which the oxygen atoms are organized in rows running along the [1 1 0] direction. The same row pattern along the [1 1 1] direction (rows perpendicular to the former ones) is disfavoured, as the adsorption energy is only 0.08 eV per adatom. The 1/2 coverage in the [1 1 0]-row arrangement is thus a reasonable model for the oxygen adsorption on this surface.

5.2. Cluster reshaping

In Table 3, we report the values of surface energy for the (1 1 1), (1 0 0) and (1 1 0) surfaces when they are clean and in case of oxygen adsorption at room temperature and $p(O_2) = 1$ atm and $p(O_2) = 5 \times 10^{-3}$ atm, respectively, as evaluated using our DF/PBE energy values. In the presence of oxygen adsorption, the surface energies are decreased, due to stabilization via oxidation. This stabilization is strongest in the case of the (1 0 0) surface, characterized by the largest interaction with the oxygen atoms and by a high density of adatoms: the surface energy is decreased from 801 to 525 mJ/m^2 at $p(O_2) = 1$ atm. On the contrary, the (1 1 1) surface is the one experiencing the smallest energy gain: its surface energy changes from 742 to 700 mJ/m^2 at $p(O_2) = 1$ atm, due to the weaker interaction with oxygen atoms and to the lower density of adatoms. It should be recalled however, as noted above, that our DF/PBE approach probably overestimates the ratio of Ag–O vs Ag–Ag binding energies, and correspondingly the stabilization of (1 0 0) vs (1 1 1) surface.

Such changes in surface energies are reflected in a reshaping of the supported silver clusters in the absence or presence of oxygen. We apply the Wulff–Kaishev construction to derive the equilibrium shape of the supported metallic particles. In Fig. 13, we show the equilibrium shape of representative supported silver particles in the case of clean surfaces (Fig. 13a) and in the case of oxygen adsorption at $p(O_2) = 1$ atm (Fig. 13c) and at $p(O_2) = 5 \times 10^{-3}$ atm (Fig. 13b). For simplicity, we take into account only (1 1 1) and (1 0 0) surfaces. Furthermore, we assume a (1 1 1) epitaxy with an adhesion energy equal to 0.20 eV per interacting atom (a reasonable estimate for a simple ionic oxide, see e.g. Ref. [110]. The interaction with the substrate translates into a further energy gain for the surface in contact with the support, and as a consequence an increase of the contact area with respect to the opposite face. For clean particles, the anisotropy ratio between the energy of the (1 0 0) and (1 1 1) surfaces is 1.08, entailing that the area of the (1 1 1) faces

Table 3
Energies of the (1 1 1), (1 0 0) and (1 1 0) silver surfaces in the case of clean surface and in the presence of oxygen adatoms at $p(O_2) = 1$ atm and $p(O_2) = 5 \times 10^{-3}$ atm. In the table, the equilibrium oxygen coverage is also reported, with the corresponding Gibbs free energy per oxygen adatom.

	Surface	(1 1 1)	(1 0 0)	(1 1 0)
$p(O_2) = 0$ atm	Clean surface (mJ/m^2)	742	801	891
	Oxygen coverage	1/4	1/2	1/2
	ΔG_{ads} (eV)	0.08	0.30	0.14
$p(O_2) = 1$ atm	Energy gain (mJ/m^2)	42	276	91
	Covered surface (mJ/m^2)	700	525	800
	ΔG_{ads} (eV)	–	0.23	0.07
$p(O_2) = 5 \times 10^{-3}$ atm	Energy gain (mJ/m^2)	–	211	46
	Covered surface (mJ/m^2)	742	590	845

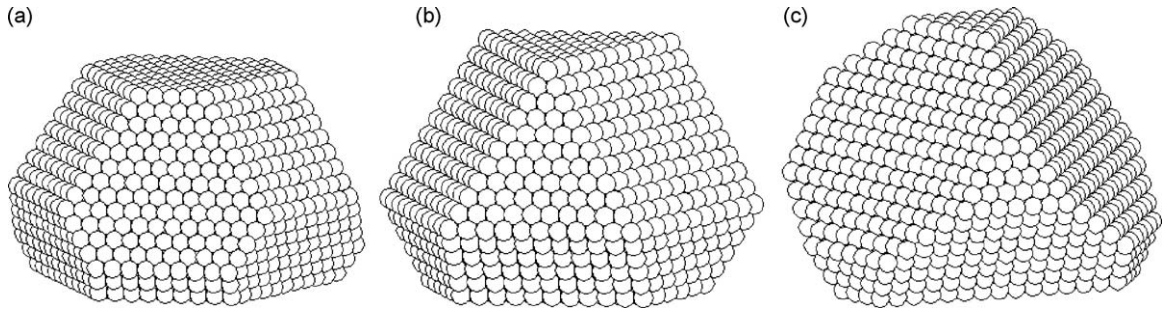

Fig. 13. Morphology of supported silver particles in case of (a) non-oxidized surfaces, and oxygen-covered surfaces at (b) $p(O_2) = 5 \times 10^{-3}$ atm and (c) $p(O_2) = 1$ atm. The lateral dimension of the clusters is about 6 nm.

is larger than that of the (1 0 0) faces—see Fig. 13a. In contrast, in the presence of oxygen adatoms, the ratio is decreased to 0.80 at $p(O_2) = 5 \times 10^{-3}$ atm or to 0.75 at $p(O_2) = 1$ atm, entailing an increase in the area of the (1 0 0) faces—see Fig. 13b and c. The calculated aspect ratio of the cluster, i.e., the ratio between the lateral dimension and the height of the cluster is 1.75 in the absence of oxygen adsorption, whereas it becomes 1.44 and 1.53 at $p(O_2) = 1$ atm and $p(O_2) = 5 \times 10^{-3}$ atm, respectively.

If we assume that propylene in the absence of oxygen produces a removal of oxygen atoms from the surface and thus a morphology change to the gas-phase shape of the particles, our predicted aspect ratio is 1.75 for the clean particles. The predicted aspect ratio of 1.53 for the oxidized particles at $p(O_2) = 5 \times 10^{-3}$ atm is somewhat smaller than the experimentally determined ~1.6 aspect ratio of the oxidized silver particles in the absence of propylene (but see the warning above). When propylene and oxygen are co-fed in the reaction mixture, a steady state will be reached, which will depend on the flux, the propylene/oxygen ratio, etc., and in which the oxidation state of the particles' surfaces will probably be intermediate between the two limit conditions (pure propylene and pure oxygen).

The situation is much more complex at $T > 100\,^{\circ}C$. In such conditions, in fact, formation of complex surface reconstructions is thermodynamically and kinetically favoured, on both the (1 0 0) [111] and the (1 1 1) [55,56,106] surfaces. However the formation of a thick shell of silver oxide is excluded by HRETEM and GISAXS data as well as XPS on ~3.5 nm size silver aggregates [25]. In particular, XPS data set an upper limit of ~5% to the oxygen content of the surface on small nanoparticles [25]. This is compatible with the formation of oxidized surface layers, but not with a thick AgO shell. Formation of structurally complex surface reconstructions in which a mixture of different phase is realized are discussed in Refs. [55,56,97,107,111] and is also consistent with the experimental observation at GISAXS that the particles lose faceting at higher temperatures (c.f. Fig. 8).

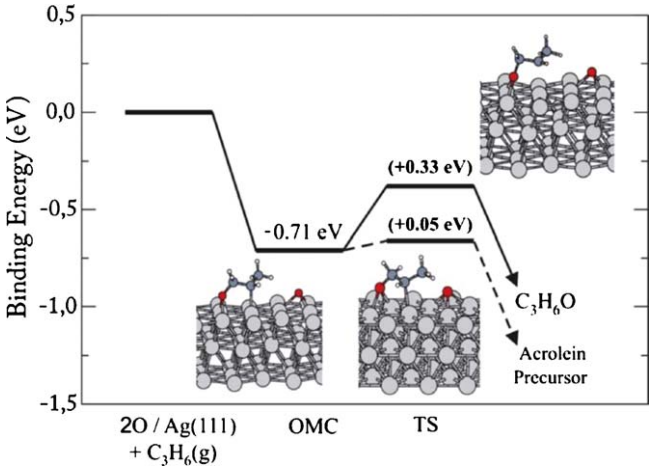

Fig. 14. Structures (see insets) and binding energies for the reaction of propylene with oxygen adatoms at the Ag(1 1 1) surface. The filled and dashed lines represent the pathways for propylene oxide or acrolein formation, respectively. In bold and parenthesis, values for the activation barriers. OMC and TS represent, respectively, the reaction steps involving propene oxametallacycle formation and the Transition State for either acrolein or propene oxide formation. Upper inset shows TS for C_3H_6O formation; lower inset to the right the TS for acrolein formation (involving hydrogen transfer from propene methyl group to oxygen surface adatoms). Red, white, dark gray and light gray spheres represent, respectively, O, H, C and Ag atoms. We take as reference energy (0.0 eV) the energy of gas-phase propene and of two oxygen adatoms on the Ag(1 1 1) surface.

5.3. Catalysis

5.3.1. Interaction of propylene or propylene/oxygen mixture with Ag particle surface

In order to gain a better understanding of the experimental results under catalytic conditions, the interaction of propylene with various models of oxygen-covered silver nanoparticles have been studied, considering cases with both small and large concentrations of surface oxygen (in the latter case, leading to the effective formation of a thin surface oxide). In the first place, we use the Ag(1 1 1) surface as a reasonable approximation of facet sites on large (~10 nm) nanoparticles. Two oxygen adatoms are then placed on the surface, and pathways for either propylene oxide (C_3H_6O) or acrolein (C_3H_4O) formation are evaluated, starting from a propylene oxametallacycle (OMC) intermediate. The

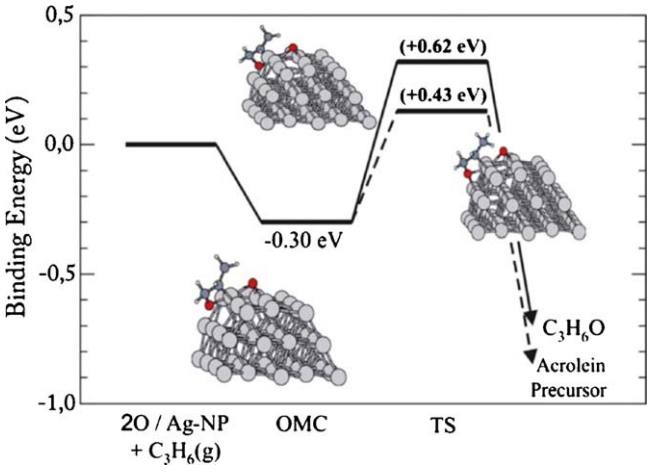

Fig. 15. Structures (see insets) and binding energies for the reaction of propylene with oxygen adatoms at a model of the edge sites in a Ag nanoparticle. Same convention as in Fig. 14. The upper inset represents the Transition State for propylene oxide formation, whereas the inset to the right represents the TS for acrolein formation. The lower inset to the left shows the equilibrium structure of the adsorbed propene oxametallacycle (OMC). Values for reaction barriers are shows as bold and in parenthesis.

results in Fig. 14 show a relatively high stability (0.7 eV) of the propylene OMC intermediate; this fact can be understood in terms of a quite high reactivity of the supported oxygen adatoms. This value is somewhat larger than the ones found for the analogous ethene OMC on Ag(1 1 1), which has been extensively studied in the past [52,107,112–115], being of the order of 0.4 eV. Then, starting from the OMC intermediate, we have calculated the energy barriers for the competitive steps of either closing the cycle (propylene oxide formation) or hydrogen transfer from the propylene methyl group towards a neigbouring oxygen adatom, which represents the first step of acrolein formation. We find a sizable barrier of 0.33 eV for the formation of propylene oxide, much higher than the one for hydrogen transfer, which is almost a barrierless process (only 0.05 eV barrier). Similar results were found for the (1 0 0) and (1 1 0) surfaces. We can therefore conclude that, at low oxygen coverage, facet sites will be more selective towards acrolein production than towards propylene oxide formation.

5.3.2. Interaction of propylene or propylene/oxygen mixture at Ag particle edges

In the case of nanoparticle edge sites, the situation is somewhat changed. To obtain a relatively accurate model of this type of sites, at a reasonable computational cost, we employed a one-dimensional silver rod, which takes advantage of the periodic symmetry requirements introduced by our plane-wave-based DF approach. The insets in Fig. 15 show perspective views of the unit cell for the relaxed rod structure, 4 Ag atoms long (a size that we estimate large enough to minimize intercell interaction). Then, dissociation of O_2 at the edge leads to a configuration with two oxygen adatoms placed at both sites of the silver edge (several conformations of the two oxygen adatoms were tested, in order to find the most stable structure).

The higher reactivity of these sites causes chemisorbed oxygen atoms to bind more strongly to silver, with a binding energy (with respect to gas-phase O_2) of 0.73 eV (the binding energy at Ag(1 1 1) is only 0.31 eV). Then, we have again analyzed the propylene interaction with the slightly oxidized model catalyst. The results in Fig. 15 show a weaker propylene OMC–silver interaction (0.30 eV formation energy); this is due to the stronger binding of oxygen to silver at these more reactive sites, which causes in turn a weakening of the C–O bond strengths. Then, starting from the OMC intermediate, we have calculated the energy barriers for either propylene oxide or acrolein formation (again, by hydrogen transfer from the propylene methyl $-CH_3$ group to the second oxygen adatom). In both cases, the barriers rise (with respect to the Ag(1 1 1), i.e., facet sites case), and, although selectivity towards acrolein is larger, the difference in barrier height is now much reduced.

5.3.3. Interactions of propylene or propylene/oxygen mixture with Ag particle surface: high oxygen coverage

We now move to the case of high oxygen coverages (which can induce formation of a thin surface oxide). As a model of the highly oxidized silver Ag(1 1 1) surface (presumably, with a similar structure to the one of the facets of relatively large silver nanoparticles), we take the $Ag_{1.83}O$/Ag(1 1 1) thin silver oxide found in STM-UHV experiments by Bocquet et al. [107]. This structure has been also identified through DF simulations as particularly stable by Li et al. [97], being likely to form at temperatures above 100 °C. Fig. 16a shows the side and top view of the p(4 × 4) unit cell; the surface oxide structure is based on a honeycomb-like lattice of alternating O–Ag–O bonds, where half of the oxygen atoms are placed on top of the first Ag layer and another half below it. Next, half of the hexagons are filled by Ag atoms placed in their centers. In agreement with DF simulations by Bocquet and Loffreda [112], we find a 0.15 eV binding energy of "intact" propylene (i.e., with a double C=C bond) to the oxide, bonded to a Ag atom. Formation of

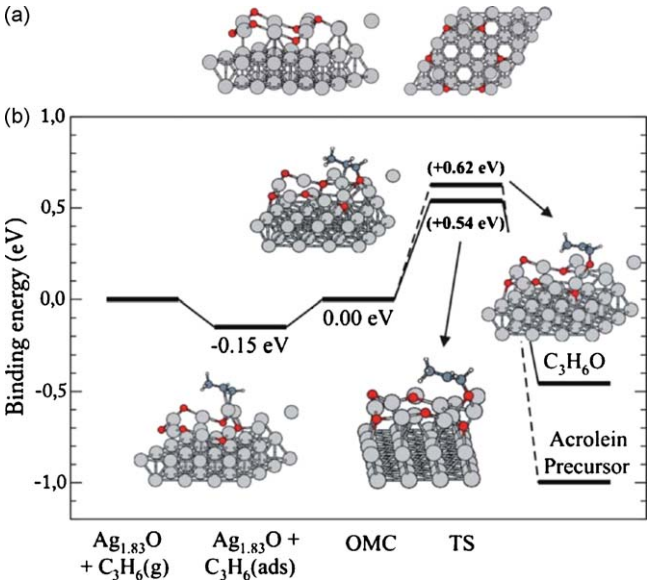

Fig. 16. (a) Top and side views of the model for the oxidized silver surface, being a $p(4 \times 4)$ unit cell of the $Ag_{1.83}O$/Ag(1 1 1) surface oxide. (b) Structures (see insets) and binding energies for the reaction of propylene with the oxidized Ag(1 1 1) surface. The first reaction step (C_3H_6 adsorption) is included. Same atom coloring as in Fig. 14. We take as energy reference (0.0 eV) the energy of gas-phase propene plus the energy of the oxidized silver surface. The two insets to the right show the structures of the Transition States for either acrolein (dashed line) or propylene oxide (full line) formation. The lower inset to the left shows the structure for propene adsorption, whereas the upper left inset shows the relaxed structure for the propene oxametallacycle (OMC). Values for energy barriers shown in bold and between parentheses.

the propylene OMC intermediate is thermoneutral, with a 0.0 eV binding energy (with respect to gas-phase propylene), which indicates a much less reactive character of the oxygen atoms which are now part of the surface oxide. All these facts indicate a relatively inert character of the surface, which agrees well with the experimentally observed low reactivity of the larger Ag nanoparticles. As for the selectivity, we find a completely different behavior with respect to the low oxygen coverage situation; now the energy barrier towards acrolein production is actually higher (0.62 eV) than the one for propylene oxide production (0.54 eV). We interpret this finding in terms of the absence of reactive oxygen species in the vicinity of the OMC intermediate, caused by the special structure of the surface oxide. The only oxygen atom available for oxygen transfer lies actually subsurface, and it costs a sizable amount of energy to drive it upwards towards the propylene OMC methyl group. In addition, we have also checked other reaction pathways involving direct reaction between the methyl group of "intact" adsorbed propylene (inset to the right in Fig. 16b) and neighboring oxygen atoms, but they turned out to be unfeasible due to the lack of a C–O covalent bond (present in the OMC case) which helps on stabilizing the final state.

5.3.4. Interactions of propylene or propylene/oxygen mixture at Ag particle edges: high oxygen coverage

Finally, we have considered the case of nanoparticle edge sites at high oxygen coverage; we employ again the one-dimensional rod model system, saturating one of its edges with adsorbed oxygen atoms. The results are shown in Fig. 17. We find that, after fully relaxing the model system, very important surface reconstructions occur, although the local chemical features at the edge atoms are not qualitatively changed; as in the case of low coverage, two oxygen atoms are placed at each of the sides of the Ag edge atoms. Interestingly, the overall features of the edge reactivity and selectivity do not strongly change with respect to the

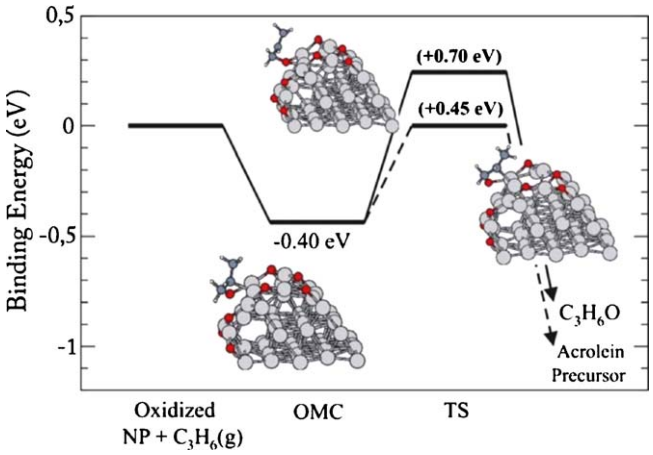

Fig. 17. Structures (see insets) and binding energies for the reaction of propylene with a model of oxidized nanoparticle edge sites. Same atom coloring as in Fig. 14. Dashed and full lines represent, respectively, pathways for acrolein or propylene oxide formation. The inset to the right shows the Transition State for acrolein formation, and the upper inset the TS for propene oxide formation. The lower inset to the left shows the relaxed structure for the propylene oxametallacycle (OMC). Values for energy barriers are shown in bold and between parentheses.

low coverage case, with a similar propylene OMC stability, and a preference towards acrolein formation (with, actually, a larger difference between the values of the barriers). Comparing this situation with the $Ag_{1.83}O$/Ag(1 1 1) case, the most striking difference (which causes the selectivity towards acrolein to drastically change) is the availability of exposed reactive oxygen adatoms in the vicinity of the propylene OMC. This fact is caused, as it can be seen in the relaxed structures, by the special topology and irregularities introduced by the presence of such defect-like edge sites.

5.3.5. Discussion of the theoretical results

Overall, the results from the DF simulations agree with the behavior observed in the experiments. At low temperature, where the oxygen coverage is relatively low, and surface oxides do not form, propylene oxide formation is hindered by large activation barriers, compared to the ones involved for acrolein formation. We must remark, however, that the process of hydrogen abstraction from the propene methyl group involves the presence of two neighbouring oxygen adatoms (one being involved in the propene oxametallacycle formation, and another one reacting with the $-CH_3$ group), suggesting that moderate oxygen coverages are necessary to make this process feasible. On silver nanoparticle edges, we find a similar preference for acrolein formation, although the difference in reaction barrier heights for both processes is now much smaller.

Above 100 °C we have the formation of surface oxides on the particle surfaces. Unfortunately, the situation is very complex: experiments [55,56,97,111] show that there is probably a mixture of different structures. We can reasonably hypothesize the presence of a substantial number of subsurface oxygen atoms. In our simulations, we find the energy barrier for acrolein formation larger than the barrier for the formation of propylene oxide. This is due to the extensive rearrangements that must take place for H-abstraction on these extended (1 1 1) surfaces. The formation of propene oxametallacycle intermediates involves reaction with oxygen adatoms in the topmost layer, with only subsurface oxygen neighbours. The formation of acrolein must necessarily occur through diffusion of subsurface oxygen species, which requires a large amount of energy. It is important to remark that reaction pathways for acrolein formation involving direct reaction of adsorbed propene with neigbouring oxygen surface adatoms were also studied, but the barriers involved were even larger; from this fact, an important conclusion can be reached: the OMC complex serves as a reaction intermediate for both propylene oxide and acrolein formation. Therefore we can conclude that in the case of large particles, where such extended surfaces are dominant, PO desorption becomes competitive with H-abstraction and hence the PO/acrolein ratio strongly increases above 100 °C, in agreement with experimental observations. For the smaller particles, the greater presence of edges, kinks, defects in general, probably implies a more irregular oxygen distribution making that oxygen atoms are still (at least in part) available for H-abstraction. PO formation in the final products hence increases but does not become dominant. Upon modelling a small oxidized Ag nanoparticle (see insets in Fig. 17), we find a strong stability for oxygen adatoms placed at both sides of the nanoparticle edge. The existence of such special arrangement allows now for reduced energy barriers in the process leading to acrolein formation, which effectively results in a reduced PO/acrolein ratio, in agreement with experimental observations.

In passing we note that the reaction mechanisms by very small, sub-nanometer size clusters can be very different from those occurring on few-nanometer particles or extended surfaces. The presence of a dominant number of under-coordinated sites is in fact known to modify substantially the chemistry of these systems [23,25,26,116]. These concepts have been refined by a more detailed analysis of the cluster frontier orbitals, from which basic principles for alkene epoxidation by very small Au clusters have been derived by Metiu and co-workers [34], while the question of the relevance of surface defectivity on the cluster catalytic activity has also been the subject of some attention, see e.g. Ref. [117]. It is also important to note that this study was focused on the catalytic oxidation of propene to propylene oxide with molecular oxygen, in the absence of any additives or promoters. The only co-product observed was acrolein, another valuable commodity chemical. Our results show that by proper choice of the size of the silver clusters either propylene oxide or acrolein can be efficiently produced, with high selectivity and under mild reaction conditions.

6. Summary

Highly monodispersed model silver nanocatalyst with three average lateral diameters (23.3, 12, and 8.7 nm) were prepared by size-selected cluster deposition on amorphous alumina films and their size-dependent catalytic performance was studied for the partial oxidation of propylene under realistic reaction conditions. All clusters tested were very stable up to 200 °C, without any signs of sintering under reaction conditions. Smaller clusters (8.7 and 12 nm) preferentially produced acrolein, while the 23.3 nm large particles were considerably more selective towards the formation of propylene oxide. The observed reaction rates considerably exceeded previously reported rates for larger silver particles. The activity of clusters dropped significantly with increasing particle size, with an about order of magnitude change in the ratio between propylene oxide and acrolein produced. The different specificities and temperature dependences of the TOR for the smaller versus the larger clusters studied indicate a change in reaction mechanism as a function of size.

Using HRETEM and GISAXS, the surface crystallinity of the clusters were investigated both in vacuum and under realistic catalytic conditions. These results indicate a changing surface crystal structure for the particles under reaction conditions. Density-functional calculations of the activation energies for oxygen adsorption and its dissociation, at variable surface coverages on each silver plane yielded surface energies which resulted in particle shapes consistent with experimentally observed morphologies of the partially oxidized silver clusters. Moreover, the changing crystal plane stabilities are consistent with particle shape changes due to changing plane areas.

The activation barriers calculated for the formation of propylene oxide and acrolein on various facets and on the edges of the silver clusters provided detailed insights into the competing reaction pathways leading to the size/morphology dependent theoretical activity and selectivity, in good agreement with experimental observations. The combined experimental and theoretical results point towards a new class of highly selective silver-based partial oxidation catalysts that works under mild reaction conditions and with molecular oxygen.

Acknowledgements

The work at Universidad de Valladolid was supported by Ministerio de Ciencia e Innovación (MAT2008-06483-C03-01 project) and Junta de Castilla y León (VA017A08 and GR23 projects). LMM acknowledges fruitful discussions with Paulina Martin. The work at IPCF-CNR was supported by the EC VII FP within the ERC-AG SEPON project (ERC-2008-AdG-227457) and the computational support by the CASPUR Supercomputing Center (Rome, Italy) within the "Competitive HPC Grant 2009" E-MOON project. The work at the Universität Rostock was supported by the Deutsche Forschungsgemeinschaft, Schwerpunktprogramm 1153 "Cluster in Kontakt mit Oberflächen" (German Science Foundation, Priority Program "Clusters at Surfaces"). Y.L. and R.J.M would like to acknowledge support from the American Chemical Society Petroleum Research Fund. The work at Argonne National Laboratory was supported by the US Department of Energy, BES-Materials Sciences and BES-Chemical Sciences, and BES-Scientific User Facilities under Contract DE-AC-02-06CH11357 with UChicago Argonne, LLC, Operator of Argonne National Laboratory. S.V. gratefully acknowledges the support by the Air Force Office of Scientific Research.

References

[1] T.A. Nijhuis, M. Makkee, J.A. Moulijn, B.M. Weckhuysen, Ind. Eng. Chem. Res. 45 (2006) 3447–3459.
[2] F.W. Zemichael, A. Palermo, M.S. Tikhov, R.M. Lambert, Catal. Lett. 80 (2002) 93–98.
[3] R.M. Lambert, F.J. Williams, R.L. Cropley, A. Palermo, J. Mol. Catal. A: Chem. 228 (2005) 27–33.
[4] H.-J.A.K. Weissermel, Industrial Organic Chemistry, Wiley-VCH, Weinheim, Germany, 2003.
[5] J.Q. Lu, J.J. Bravo-Suarez, A. Takahashi, M. Haruta, S.T. Oyama, J. Catal. 232 (2005) 85–95.
[6] T.A.R. Nijhuis, T. Visser, B.M. Weckhuysen, Angew. Chem. Int. Ed. 44 (2005) 1115–1118.
[7] T. Hayashi, K. Tanaka, M. Haruta, J. Catal. 178 (1998) 566–575.
[8] M.F. Luo, J.Q. Lu, C. Li, Catal. Lett. 86 (2003) 43–49.
[9] W. Yao, Y.L. Guo, X.H. Liu, Y. Guo, Y.Q. Wang, Y.S. Wang, Z.G. Zhang, G.Z. Lu, Catal. Lett. 119 (2007) 185–190.
[10] J.G. Serafin, A.C. Liu, S.R. Seyedmonir, J. Mol. Catal. A: Chem. (1998) 157–168.
[11] J.T. Ranney, S.R. Bare, Surf. Sci. 382 (1997) 266–274.
[12] M.A. Barteau, R.J. Madix, J. Am. Chem. Soc. 105 (1983) 344–349.
[13] D.M. Cox, B. Kessler, P. Fayet, W. Eberhardt, Z. Fu, D. Sondericher, R. Sherwood, A. Kaldor, Nanostruct. Mater. 1 (1992) 161–165.
[14] T. Leisner, C. Rosche, S. Wolf, F. Granzer, L. Woeste, Surf. Rev. Lett. 3 (1996) 1105–1108.
[15] F. Vanolli, U. Heiz, W.-D. Schneider, Chem. Phys. Lett. 277 (1997) 527–531.
[16] W. Bouwen, E. Kunnen, K. Temst, P. Thoen, M.J. Van Bael, F. Vanhoutte, H. Weidele, P. Lievens, R.E. Silverans, Thin Solid Films 354 (1999) 87–92.
[17] S.J. Carroll, S. Pratontep, M. Steun, R.E. Palmer, S. Hobday, R. Smith, J. Chem. Phys. 113 (2000) 7723–7727.
[18] R.P. Methling, V. Senz, E.-D. Klinkenberg, T. Diederich, J. Tiggesbaumker, G. Holzhuter, J. Bansmann, K.H. Meiwes-Broer, Eur. Phys. J. D 16 (2001) 173–176.
[19] K. Judai, A.S. Wörz, S. Abbet, U. Heiz, J. Am. Chem. Soc. 126 (2004) 2732–2737.
[20] S. Lee, C. Fan, T. Wu, S.L. Anderson, J. Chem. Phys. 123 (2005), 124710-1-13.
[21] D.C. Lim, R. Dietsche, M. Bubek, G. Gantefor, Y.D. Kim, ChemPhysChem 7 (2006) 1909–1911.
[22] S. Vajda, R.E. Winans, J.W. Elam, B.D. Lee, M.J. Pellin, S. Seifert, G.Y. Tikhonov, N.A. Tomczyk, Top. Catal. 39 (2006) 161–166.
[23] S. Lee, L.M. Molina, M.J. López, J.A. Alonso, B. Hammer, B. Lee, S. Seifert, R.E. Winans, J.W. Elam, M.J. Pellin, S. Vajda, Angew. Chem. Int. Ed. 48 (2009) 1467–1471.
[24] S. Vajda, S. Lee, K. Sell, I. Barke, A. Kleibert, V. von Oeynhausen, K.H. Meiwes-Broer, A.F. Rodriguez, J.W. Elam, M.J. Pellin, B. Lee, S. Seifert, R.E. Winans, J. Chem. Phys. 131 (2009), 121104-1-7.
[25] Y. Lei, F. Mehmood, S. Lee, J.P. Greeley, B. Lee, S. Seifert, R.E. Winans, J.W. Elam, R.J. Meyer, P.C. Redfern, D. Teschner, R. Schlögl, M.J. Pellin, L.A. Curtiss, S. Vajda, Science 328 (2010) 224–228.
[26] S. Vajda, M.J. Pellin, J.P. Greeley, C.L. Marshall, L.A. Curtiss, G.A. Ballentine, J.W. Elam, S. Catillon-Mucherie, P.C. Redfern, F. Mehmood, P. Zapol, Nat. Mater. 8 (2009) 213–216.
[27] Z. Xu, F.S. Xiao, S.K. Purnell, O. Alexeev, S. Kawi, S.E. Deutsch, B.C. Gates, Nature 372 (1994) 346–348.
[28] X. Tong, L. Benz, P. Kemper, H. Metiu, M.T. Bowers, S.K. Buratto, J. Am. Chem. Soc. 127 (2005) 13516–13518.
[29] K. Bromann, C. Felix, H. Brune, W. Harbich, R. Monot, J. Buttet, K. Kern, Science 274 (1996) 956–958.
[30] M.S. Chen, D.W. Goodman, Science 306 (2004) 252–255.
[31] C. Lemire, R. Meyer, S. Shaikhutdinov, H.-J. Freund, Angew. Chem. Int. Ed. 43 (2004) 118–121.
[32] A.T. Bell, Science 299 (2003) 1688–1691.
[33] F. Tao, M.E. Grass, Y. Zhang, D.R. Butcher, J.R. Renzas, Z. Liu, J.Y. Chung, B.S. Mun, M. Salmeron, G.A. Somorjai, Science 322 (2008) 932–934.
[34] S. Chrétien, S.K. Buratto, H. Metiu, Curr. Solid Opin. St. M. 11 (2007) 62–75.
[35] L. Benz, X. Tong, P. Kemper, Y. Lilach, A. Kolmakov, H. Metiu, T. Bowers Michael, K. Buratto Steven, J. Chem. Phys. 122 (2005), 81102-1-4.
[36] U. Heiz, U. Landman (Eds.), Nanocatalysis, Springer-Verlag, Berlin, Heidelberg, New York, 2007 (ISBN-13 978-3-540-32645-8).
[37] B. Yoon, H. Häkkinen, U. Landman, A.S. Wörz, J.-M. Antonietti, S. Abbet, K. Judai, U. Heiz, Science 307 (2005) 403–407.
[38] S. Lee, C. Fan, T. Wu, S.L. Anderson, J. Phys. Chem. B 109 (2005) 11340–11347.
[39] S. Lee, C. Fan, T. Wu, S.L. Anderson, J. Am. Chem. Soc. 126 (2004) 5683–5684.
[40] M. Aizawa, S. Lee, S.L. Anderson, Surf. Sci. 542 (2003) 253–275.
[41] S. Lee, B. Lee, F. Mehmood, S. Seifert, J.A. Libera, J.W. Elam, J. Greeley, P. Zapol, L.A. Curtiss, M.J. Pellin, P.C. Stair, R.E. Winans, S. Vajda, J. Phys. Chem. C 114 (2010) 10342–10348.
[42] K. Luo, X. Lai, C.W. Yi, K.A. Davis, K.K. Gath, D.W. Goodman, J. Phys. Chem. B 109 (2005) 4064–4068.
[43] A.L. de Oliveira, A. Wolf, F. Schuth, Catal. Lett. 73 (2001) 157–160.
[44] G. Renaud, R. Lazzari, C. Revenant, A. Barbier, M. Noblet, O. Ulrich, F. Leroy, J. Jupille, Y. Borensztein, C.R. Henry, J.-P. Deville, F. Scheurer, J. Mane-Mane, O. Fruchart, Science 300 (2003) 1416–1419.
[45] R.E. Winans, S. Vajda, B. Lee, S.J. Riley, S. Seifert, G.Y. Tikhonov, N.A. Tomczyk, J. Phys. Chem. B 108 (2004) 18105.
[46] S.A. Wyrzgol, S. Schäfer, S. Lee, B. Lee, M. Di Vece, X. Li, S. Seifert, R.E. Winans, M. Stutzmann, J.A. Lercher, S. Vajda, Phys. Chem. Chem. Phys. (2010) 5585–5595.
[47] G. Cipriani, D. Loffreda, A. Dal Corso, S. de Gironcoli, S. Baroni, Surf. Sci. 501 (2002) 182.
[48] A. Kokalj, A.D. Corso, S.D. Gironcoli, S. Baroni, Surf. Sci. 532–535 (2003) 191–197.
[49] A. Kokalj, A. Dal Corso, S. de Gironcoli, S. Baroni, Surf. Sci. 507–510 (2002) 62–68.
[50] A. Kokalj, A. Dal Corso, S. de Gironcoli, S. Baroni, J. Phys. Chem. B 106 (2002) 9839–9846.
[51] A. Kokalj, A. Dal Corso, S. de Gironcoli, S. Baroni, Surf. Sci. 566–568 (2004) 1018–1023.
[52] A. Kokalj, P. Gava, S. de Gironcoli, S. Baroni, J. Phys. Chem. C 112 (2008) 1019–1027.
[53] S. Linic, M.A. Barteau, J. Am. Chem. Soc. 125 (2003) 4034–4035.
[54] M.-L. Bocquet, A. Michaelides, D. Loffreda, P. Sautet, A. Alavi, D.A. King, J. Am. Chem. Soc. 125 (2003) 5620–5621.
[55] M. Schmid, A. Reicho, A. Stierle, I. Costina, J. Klikovits, P. Kostelnik, O. Dubay, G. Kresse, J. Gustafson, E. Lundgren, J.N. Andersen, H. Dosch, P. Varga, Phys. Rev. Lett. 96 (2006), 146102-1-4.
[56] J. Schnadt, A. Michaelides, J. Knudsen, R.T. Vang, K. Reuter, E. Laegsgaard, M. Scheffler, F. Besenbacher, Phys. Rev. Lett. 96 (2006), 146101-1-4.
[57] A.W. Ott, J.W. Klaus, J.M. Johnson, S.M. George, Thin Solid Films 292 (1997) 135–144.
[58] J. Passig, K.-H. Meiwes-Broer, J. Tiggesbäumker, Rev. Sci. Instrum. 77 (2006), 093304-1-5.
[59] R. Schaub, H. Jödicke, F. Brunet, R. Monot, J. Buttet, W. Harbich, Phys. Rev. Lett. 86 (2001) 2590–2593.
[60] W. Harbich, Philos. Magn. B 79 (1999) 1307–1320.
[61] U. Heiz, W.-D. Schneider, J. Phys. D: Appl. Phys. 33 (2000) R85–R102.
[62] H.-P. Cheng, U. Landman, Science 260 (1993) 1304–1307.
[63] M.O. Watanabe, N. Uchida, T. Kanayama, Phys. Rev. B 61 (2000) 7219–7222.
[64] M. Getzlaff, A. Kleibert, R. Methling, J. Bansmann, K.-H. Meiwes-Broer, Surf. Sci. 566–568 (2004) 332–336.
[65] A. Kleibert, A. Voitkans, K.H. Meiwes-Broer, Phys. Rev. B 81 (2010), 073412-1-4.
[66] S. Giorgio, S.S. Joao, S. Nitsche, D. Chaudanson, G. Sitja, C.R. Henry, Ultramicroscopy 106 (2006) 503–507.
[67] P.L. Gai, E.D. Boyes, S. Helveg, P.L. Hansen, S. Giorgio, C.R. Henry, MRS Bull. 32 (2007) 1044–1050.
[68] B. Lee, S. Seifert, S.J. Riley, G.Y. Tikhonov, N.A. Tomczyk, S. Vajda, R.E. Winans, J. Chem. Phys. 123 (2005), 074701-1-7.
[69] S. Vajda, R.E. Winans, J.W. Elam, B. Lee, M.J. Pellin, S.J. Riley, S. Seifert, G.Y. Tikhonov, N.A. Tomczyk, Prepr. Am. Chem. Soc. Div. Fuel Chem. 50 (2005) 190–191.
[70] S. Vajda, G.P. Wiederrecht, A. Bouhelier, G.Y. Tikhonov, N. Tomczyk, B. Lee, S. Seifert, R.E. Winans, Collect. Czech. Chem. C 72 (2007) 121–128.

[71] A. Barbier, G. Renaud, J. Jupille, Surf. Sci. 454–456 (2000) 979–983.
[72] R.E. Winans, S. Vajda, G.E. Ballentine, J.W. Elam, B.D. Lee, M.J. Pellin, S. Seifert, G.Y. Tikhonov, N.A. Tomczyk, Top. Catal. 39 (2006) 145–149.
[73] R. Wengeler, F. Wolf, N. Dingenouts, H. Nirschl, Langmuir 23 (2007) 4148–4154.
[74] A. Turkovic, Mater. Sci. Eng. B: Solid B 75 (2000) 85–91.
[75] A. Guinier, G. Fournet, C.B. Walker, K.L. Yudowitch, Small Angle Scattering of X-Rays, Wiley, New York, 1955.
[76] J.T. Ranney, S.R. Bare, J.L. Gland, Catal. Lett. 48 (1997) 25–29.
[77] K.A. Davis, D.W. Goodman, J. Phys. Chem. B 104 (2000) 8557–8562.
[78] J. Chou, E.W. McFarland, Chem. Commun. (2004) 1648–1649.
[79] T.A. Nijhuis, E. Sacaliuc-Parvulescu, N.S. Govender, J.C. Schouten, B.M. Weckhuysen, J. Catal. 265 (2009) 161–169.
[80] W.X. Huang, J.M. White, Catal. Lett. 84 (2002) 143–146.
[81] W.E. Kaden, T. Wu, W.A. Kunkel, S.L. Anderson, Science 326 (2009) 826–829.
[82] S. Orisaka, T. Minobe, T. Uchihashi, Y. Sugawara, S. Morita, Appl. Surf. Sci. 140 (1999) 243–246.
[83] P. Giannozzi, S. Baroni, N. Bonini, M. Calandra, R. Car, C. Cavazzoni, D. Ceresoli, G.L. Chiarotti, M. Cococcioni, I. Dabo, A. Dal Corso, S. de Gironcoli, S. Fabris, G. Fratesi, R. Gebauer, U. Gerstmann, C. Gougoussis, A. Kokalj, M. Lazzeri, L. Martin-Samos, N. Marzari, F. Mauri, R. Mazzarello, S. Paolini, A. Pasquarello, L. Paulatto, C. Sbraccia, S. Scandolo, G. Sclauzero, A.P. Seitsonen, A. Smogunov, P. Umari, R.M. Wentzcovitch, J. Phys. Condens. Mater. 21 (2009), 395502-1-18.
[84] D. Vanderbilt, Phys. Rev. B 41 (1990) 7892–7895.
[85] J.P. Perdew, K. Burke, M. Ernzerhof, Phys. Rev. Lett. 77 (1996) 3865–3868.
[86] DACAPO, See DACAPO web page at Danish Technical University: https://wiki.fysik.dtu.dc/dacapo.
[87] J.P. Perdew, J.A. Chevary, S.H. Vosko, K.A. Jackson, M.R. Pederson, D.J. Singh, C. Fiolhais, Phys. Rev. B 46 (1992) 6671–6687.
[88] A. Alavi, P. Hu, T. Deutsch, P.L. Silvestrelli, J. Hutter, Phys. Rev. Lett. 80 (1998) 3650–3653.
[89] A.K. Santra, B.K. Min, D.W. Goodman, Surf. Sci. 515 (2002) L475–L479.
[90] M. Rocca, L. Vattuone, L. Savio, F.B.D. Mongeot, U. Valbusa, G. Comelli, S. Lizzit, A. Baraldi, G. Paolucci, J.A. Groeneveld, E.J. Baerends, Phys. Rev. B 63 (2001), 081404-1-4.
[91] V.I. Bukhtiyarov, V.V. Kaichev, J. Mol. Catal. A: Chem. 158 (2000) 167–172.
[92] C.T. Campbell, Surf. Sci. 157 (1985) 43–60.
[93] L. Savio, L. Vattuone, M. Rocca, Appl. Phys. A: Mater. 87 (2007) 399–404.
[94] A. Takahashi, N. Hamakawa, I. Nakamura, T. Fujitani, Appl. Catal. A: Gen. 294 (2005) 34–39.
[95] F. Buatier de Mongeot, A. Cupolillo, M. Rocca, U. Valbusa, Chem. Phys. Lett. 302 (1999) 302–306.
[96] A. Michaelides, K. Reuter, M. Scheffler, J. Vac. Sci. Technol. A 23 (2005) 1487.
[97] W.X. Li, C. Stampfl, M. Scheffler, Phys. Rev. B 67 (2003), 045408-1-16.
[98] D.S. Su, T. Jacob, T.W. Hansen, D. Wang, R. Schlögl, B. Freitag, S. Kujawa, Angew. Chem. Int. Ed. 47 (2008) 5005.
[99] A.J. Nagy, G. Mestl, R. Schlögl, J. Catal. 188 (1999) 58–68.
[100] A. Reicho, A. Stierle, I. Costina, H. Dosch, Surf. Sci. 601 (2007) L19–23.
[101] L. Vitos, A.V. Ruban, H.L. Skriver, J. Kollár, Surf. Sci. 411 (1998) 186–202.
[102] S. Giorgio, M. Cabie, C.R. Henry, Gold Bull. 41 (2008) 167–173.
[103] M. Cabie, S. Giorgio, C.R. Henry, M.R. Axet, K. Philippot, B. Chaudret, J. Phys. Chem. C 114 (2010) 2160–2163.
[104] S. Giorgio, C.R. Henry, B. Pauwels, G. Van Tendeloo, Mater. Sci. Eng. A: Struct. 297 (2001) 197–202.
[105] S. Giorgio, C.R. Henry, C. Chapon, G. Nihoul, J.M. Penisson, Ultramicroscopy 38 (1991) 1–12.
[106] T. David, D. Buttard, T. Schülli, F. Dallhuin, P. Gentile, Surf. Sci. 602 (2008) 2675–2680.
[107] M.-L. Bocquet, P. Sautet, J. Cerda, C.I. Carlisle, M.J. Webb, D.A. King, J. Am. Chem. Soc. 125 (2003) 3119–3125.
[108] A. Kokalj, A. Dal Corso, S. de Gironcoli, S. Baroni, J. Phys. Chem. B 110 (2006) 367–376.
[109] C.I. Carlisle, T. Fujimoto, W.S. Sim, D.A. King, Surf. Sci. 470 (2000) 15–31.
[110] R. Ferrando, G. Rossi, A.C. Levi, Z. Kuntova, F. Nita, A. Jelea, C. Mottet, G. Barcaro, A. Fortunelli, J. Goniakowski, J. Chem. Phys. 130 (2009) 174702-1-9.
[111] I. Costina, M. Schmid, H. Schiechl, M. Gajdos, A. Stierle, S. Kumaragurubaran, J. Hafner, H. Dosch, P. Varga, Surf. Sci. 600 (2006) 617–624.
[112] M.-L. Bocquet, D. Loffreda, J. Am. Chem. Soc. 127 (2005) 17207–17215.
[113] S. Linic, M.A. Barteau, J. Am. Chem. Soc. 124 (2001) 310–317.
[114] S. Linic, H. Piao, K. Adib, M.A. Barteau, Angew. Chem. Int. Ed. 43 (2004) 2918–2921.
[115] J. Greeley, M. Mavrikakis, J. Phys. Chem. C 111 (2007) 7992–7999.
[116] N. Lopez, T.V.W. Janssens, B.S. Clausen, Y. Xu, M. Mavrikakis, T. Bligaard, J.K. Nørskov, J. Catal. 223 (2004) 232–235.
[117] A.M. Joshi, W.N. Delgass, K.T. Thomson, J. Phys. Chem. C 111 (2007) 7841–7844.

THE JOURNAL OF PHYSICAL CHEMISTRY C

ARTICLE

pubs.acs.org/JPCC

Optical Properties of Au Nanoclusters from TD-DFT Calculations

Nicola Durante,[†] Alessandro Fortunelli,[†] Michel Broyer,[‡] and Mauro Stener[§,⊥]

[†]CNR-IPCF, Istituto per i Processi Chimico-Fisici del Consiglio Nazionale delle Ricerche, Molecular Modeling Laboratory, via G. Moruzzi 1, I-56124, Pisa, Italy

[‡]Université de Lyon, Université de Lyon 1, CNRS, LASIM UMR 5579, F-69622, Villeurbanne, France

[§]Dipartimento di Scienze Chimiche, Università di Trieste, via L. Giorgieri 1, I-34127, Trieste, Italy

[⊥]Consorzio Interuniversitario Nazionale per la Scienza e Tecnologia dei Materiali, INSTM, Unita' di Trieste

ABSTRACT: A time-dependent density-functional-theory (TD-DFT) approach is employed to investigate theoretically the optical response of Au nanoclusters of size around $N = 150$ atoms as a function of: (a) the approximation used for the DFT exchange-correlation (xc-) functional, (b) the shape of the nanocluster. The results of the local-density-approximation (LDA) and the van Leeuwen−Baerends (LB94) xc-functionals are compared on a set of 4 structural motifs: octahedral ($N = 146$), cuboctahedral ($N = 147$), icosahedral ($N = 147$), and cubic ($N = 172$), representative of both crystalline and noncrystalline motifs commonly encountered in the study of metal nanoclusters. It is found that the position of the peak in the photoabsorption spectrum is weakly dependent on the shape of the cluster but is strictly related to its size and to the DFT xc-functional used in the calculations, with the finding that the predictions of the LB94 xc-functional compare better with the available experimental data on the absorption spectrum of Au particles in this size range with respect to those of the LDA xc-functional. The detailed shape of the cluster becomes apparent in the form of the absorption spectrum, which can be symmetric or asymmetric in two different forms.

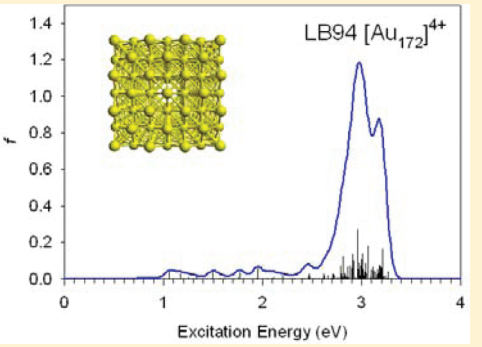

1. INTRODUCTION

The optical response properties of metal particles with nanometric size (nanoparticles) are a subject of great interest both in terms of basic science and for their technological applications (optoelectronic devices, thermal treatment of cancer, cell imaging, that is colorimetric probes for DNA detection, etc.).[1−3] The reason of such interest is due to the fact that nanoparticles of specific metals exhibit a surface plasmonic resonance (SPR), that is a very intense optical absorbance in the UV−vis region, due to the coherent and collective oscillation of electrons involved in the metallic bond subjected to electromagnetic radiation of proper wavelength. Au metal nanoparticles are frequently utilized in this context, pure or alloyed with other metals. Despite the great body of experimental evidence, fundamental questions still exist in this field. In particular, there is not much unambiguous information on the dependence of the shape and peak of SPR upon nanoparticle size and shape. From a theoretical point of view, empirical models such as the DDA (Discrete Dipole Approximation) (e.g., ref 4) or electrodynamical models[5−8] have been mostly used. For example, DDA methods have been successfully employed to correlate the SPR position and intensity with the structure of gold nanorods with average diameters from 35 up to 100 nm.[9] However, the validity of these mesoscopic models and especially their proper parametrization for the smaller nanoparticles is still debated. First-principles calculations, in particular those based on time-dependent density-functional-theory (TD-DFT), could provide rigorous answers but the computational effort soon exceeds common available resources, already for clusters of some tens of atoms. For example, it has been practicable by TD-DFT to monitor the spectral evolution from discrete excited states to plasmons in a series of silver clusters with increasing size, up to 120 atoms,[10] or to discuss the role of geometry, solvent, and ligand nature on the optical absorption of Au_{25} cluster protected by thiolates.[11] More simplified DFT approaches, consisting in the calculation of the photoabsorption spectrum from dipole transition moments between occupied and virtual single particle eigenstates (orbitals), have been employed to simulate the spectrum of large metal clusters, up to Ag_{586}.[7] A promising approach to tackle large systems is the multiscale hybrid quantum mechanics/classical electrodynamics method.[12] Another way to treat large-size gold clusters with standard TD-DFT methods has been explored in ref 13 and consists in focusing on high-symmetry clusters. The use of symmetry (e.g., the O_h point group of 48 elements for octahedral configurations or the I_h point group of 120 elements for icosahedral ones) allows one to drastically reduce the computational effort and to feasibly treat clusters of 150−200 atoms, large enough to start observing a resonance peak that will lead to the SPR. The work performed in ref 13 was limited to fcc-like configurations. Here, we carry out a systematic analysis at the

Received: December 23, 2010
Revised: February 10, 2011
Published: March 10, 2011

TD-DFT level of the optical response of Au nanoclusters (between 146 and 172 atoms) with high symmetry and various shapes (corresponding to those of interest in appplications), with the purpose of comparing the form and frequency of their resonance peak with available experimental data. Clusters with icosahedral ($N = 147$), cuboctahedral ($N = 147$), octahedral ($N = 146$), and cubic ($N = 172$) shapes are studied. The aim is to produce rigorous knowledge on the dependence of the SPR of Au particles upon the particle shape and to validate by comparison with experiments which DFT xc-functional is most appropriate for investigating the optical response of these systems. This represents one of the first TD-DFT investigations of the optical response of Au nanoclusters in this size range. It can be added that the results of the present study can form the basis of further developments. For example, they can be analyzed in terms of semiempirical Hamiltonians, thus allowing one to rigorously control the parametrization process of such approaches,[8,14] which can then be used to predict the optical response of larger systems containing thousands of atoms.

The article is structured as follows. The theoretical method is described in section 2. Computational details are given in section 3. Results are presented and discussed in section 4. Section 5 summarizes the main conclusions.

2. THEORETICAL METHOD

A scalar relativistic (SR) self-consistent field (SCF) Kohn−Sham (KS) formalism has been employed to describe the cluster electronic structure at the DFT level. It is well-known that relativistic effects play a crucial role in the quantum chemistry of gold compounds.[15] In the present work they have been included at the SR zeroth-order regular approximation (ZORA) level.[16]

The KS eigenvalues and orbitals so obtained were successively employed in the TD-DFT step. The TD-DFT scheme for valence excitations as well as its implementation in the ADF code[17,18] has been described previously,[19] so here we just recall the salient steps.

The general problem is cast in the following eigenvalue equation:[20]

$$\Omega \mathbf{F}_I = \omega_I^2 \mathbf{F}_I \tag{1}$$

where Ω is a four indexes matrix with elements $\Omega_{ia\sigma,jb\tau}$, the indexes consisting of products of occupied-virtual (ia and jb) KS orbitals, whereas σ and τ refer to the spin variable. The eigenvalues ω_I^2 correspond to squared excitation energies while the oscillator strengths are extracted from the eigenvectors $\mathbf{F}_I$.[20] The Ω-matrix elements can be expressed in terms of KS eigenvalues (ε) and the coupling matrix K:

$$\Omega_{ia\sigma,jb\tau} = \delta_{\sigma\tau}\delta_{ij}\delta_{ab}(\varepsilon_a - \varepsilon_i)^2 + 2\sqrt{(\varepsilon_a - \varepsilon_i)}K_{ia\sigma,jb\tau}\sqrt{(\varepsilon_b - \varepsilon_j)} \tag{2}$$

the elements of the coupling matrix K are given by:

$$K_{ia\sigma,jb\tau} = \int d\mathbf{r} \int d\mathbf{r}' \varphi_{i\sigma}(\mathbf{r})\varphi_{a\sigma}(\mathbf{r}) \left[\frac{1}{|\mathbf{r}-\mathbf{r}'|} + f_{xc}^{\sigma\tau}(\mathbf{r},\mathbf{r}',\omega)\right] \varphi_{j\tau}(\mathbf{r}')\varphi_{b\tau}(\mathbf{r}') \tag{3}$$

where φ are the KS orbitals and $f_{xc}^{\sigma\tau}(\mathbf{r},\mathbf{r}',\omega)$ is the exchange-correlation kernel. In this work, the adiabatic local density approximation (ALDA)[21] for the kernel has been employed.

3. COMPUTATIONAL DETAILS

In the present work, gold nanoclusters with both unrelaxed and relaxed geometries have been considered. For the unrelaxed geometries, the clusters were built at the positions of the crystal fcc lattice using the nearest-neighbor Au−Au interatomic distance of 2.88 Å taken from the experimental value of bulk gold. For the relaxed geometries, a geometry optimization was performed starting from the unrelaxed geometry as starting point. To this end, the scalar relativistic ZORA formalism and the ADF program were used, with the 4f frozen-core double zeta (DZ) ZORA basis set of Slater-type orbitals (STO) included in the ADF database, implying that inner shells are frozen up to the 4f one included. This basis set contains two STO functions for each of the 5s, 6s, 5d, and 5p shells, as well as one STO function for the 6p shell. For all of the geometry optimizations, we have employed the local density approximation (LDA) to the exchange correlation functional, according to the VWN parametrization.[22] The very good perfomances of the LDA geometry optimization with respect to the experimental bulk limit interatomic distance for gold clusters of increasing size has been demonstrated previously.[23] The TD-DFT calculations were performed at both unrelaxed and relaxed geometries, and also in this case the same DZ 4f frozen core ZORA basis set was employed. The reliability of the DZ basis set for TDDFT calculations of gold clusters has been checked and confirmed previously, in fact enlargement of the basis set to triple zeta plus polarization (TZP) did not change appreciably the calculated photoabsorption spectrum.[13] In the TD-DFT calculations, two different exchange-correlation (xc-) functionals have been considered, namely the LDA[22] and the LB94[24] ones. These two xc-functionals were considered with the aim of validating their results with respect to available experimental data. LDA and LB94 were chosen in particular because LDA represents the simplest option, while LB94 is expected to be more accurate in TD-DFT because of its correct asymptotic behavior.[25] As it will be explained in the next section, all calculations (geometry optimization as well as TD-DFT optical spectra) have been performed employing the O_h point group symmetry for octahedral, cubic and cuboctahedral clusters, while the icosahedral clusters have been calculated using the D_{5d} point group symmetry as the complete I_h one is not supported by ADF. Available point symmetry groups are fully exploited in the ADF code, and greatly speed up the calculations.

A delicate point of the present TD-DFT approach is the high number of the lowest roots (eigenvalues) to be extracted from eq 1. Such a number has a decisive impact on the computational effort required for the calculation and must be adequate to have a proper description of the calculated spectrum, as it controls the upper limit of the excitation energy range. In the present work, the calculated TD-DFT spectra have been obtained extracting 300 roots, keeping the whole space of virtual orbitals. Attempts to extract an appreciably larger ($\geq$400) number of roots have shown to bring about numerical problems in the Davidson algorithm used to diagonalize eq 1, whereas the choice to extract no more than 300 roots has been checked to be numerically consistent and physically informative, as the corresponding spectra coincide with spectra obtained by extracting a smaller number of roots in their range of validity (the low-energy part of the spectrum) and the form of the peak well beyond the peak

maximum is not affected by increasing the number of extracted roots. A stricter criterion for the SCF convergence has been found to help in this respect, so that we have employed a threshold of 10^{-8} for the maximum element of the commutator between the Fock and the density matrix in the representation of the basis functions. A single TD-DFT calculation on a 150−200 atom Au high-symmetry cluster consumes about 1000 CPU-hours on an IBM SP6 supercomputer and need up to 4−8 GB RAM/processor for about 32 CPU-hours on 32 cores. For an easier comparison, all the calculated discrete spectra have been broadened with Gaussian functions of fwhm = 0.12 eV.

4. RESULTS AND DISCUSSION

Four cluster structural motifs, shown in Figure 1, were investigated in the present work: (a) a cuboctahedron of 147 atoms (147-CO); (b) an octahedron of 146 atoms (146-Oh); (c) a cubic configuration of 172 atoms (172-CU); (d) an icosahedron of 147 atoms (147-Ih). All of these structures exhibit high (O_h or I_h) point-group symmetry. (a), (b), and (c) are representative of a fcc-like (crystalline) motif, but taken with different cuts exposing only (111) facets in the case of 146-Oh or only (100) facets in the case of 172-CU, with 147-CO representing an intermediate case. 147-Ih, instead, is representative of noncrystalline structures exhibiting 5-fold symmetry axes. All of these structures have been observed in Au nanoparticles.[26−30] In general, the electronic structure of neutral Au clusters can present an incomplete occupation of the highest-occupied molecular orbitals (HOMO), which would give rise to a Jahn−Teller structural distortion. To prevent this effect and to speed-up calculations, charged systems were considered so as to achieve electronic shell closure (thus performing spin restricted calculations): 147-CO (+5), 146-Oh (+2), 172-CU (+4), 147-Ih (−1). This simplification is effective in keeping symmetry high and in reducing the computational effort (section 3) but hardly affects the photoabsorption spectrum, as discussed below in one typical case (147-CO). For all of the 4 structures, the cluster geometry was optimized using the LDA xc-functional, and on the geometry obtained from these optimizations the absorption spectrum was calculated using both the LDA and LB94 xc-functionals. LDA geometries were chosen as it is known that, for gold clusters, they are more accurate than those predicted by gradient-corrected xc-functionals, as demonstrated in a previous analysis[23] where the extrapolation of the optimized nearest-neighbor Au−Au distance to the bulk limit gave an error of only 0.01 Å at the LDA level, whereas the error was 0.09 Å at the GGA level. As discussed below, in selected cases calculations were also performed at unrelaxed geometries cut from the Au fcc crystal lattice (all Au−Au distances set to 2.88 Å) finding that geometry optimization makes a minor difference in the optical properties of clusters of this size. When relaxing the cluster structures, we found that surface atoms were the most affected ones. In particular the atoms which occupy vertex positions are shrunk inward, as an effect of the reduced coordination number which implies a major involvement of valence electrons in the remaining chemical bonds (this effect can be pictured as a surface tension phenomenon). In particular, the Au−Au relaxed distances at vertexes are 2.80, 2.75, and 2.70 Å for 147-CO (+5), 146-Oh (+2), and 172-CU (+4), respectively. For 147-Ih (−1), the relaxed distance is 2.86 Å, giving only a minor reduction with respect to the bulk Au fcc lattice. This is due to the noncrystalline arrangement as well as to the negative charge of this cluster,

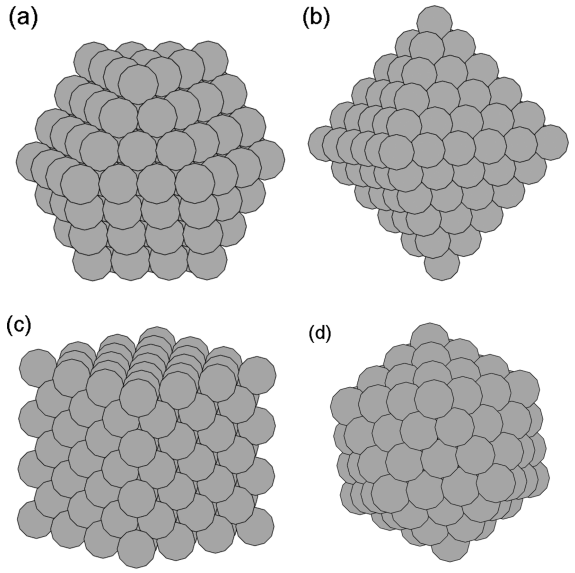

Figure 1. Pictorial view of the 4 structures here investigated: (a) 147-atom cuboctahedron (147-CO), (b) 146-atom octahedron (146-Oh), (c) 172-atom cube (172-CU), (d) 147-atom icosahedron (147-Ih).

which may favor a geometry expansion. Also the nearest-neighbor Au−Au distance along edges are reduced with respect to bulk for the clusters with crystalline structure, being in the range 2.70−2.80 Å, whereas for 147-Ih (−1) the two nonequivalent nearest-neighbor Au−Au distance along edges are 2.85 and 2.86 Å. Moreover, it is also observed that distances between atoms belonging to the (111) surface of the clusters tend to increase up to 2.95 Å in 146-Oh (+2). This effect has been already observed in Au and Pt clusters and has been assigned to bonding directionality caused by the hybridization between 6s and 5d atomic functions in the valence band[31,32] giving to the optimized structure a typical swelled appearance. The LDA approximation was chosen as the simplest possible one within DFT, whereas LB94 was proposed as a more accurate xc-functional specifically to predict the optical response of materials due to its correct asymptotic behavior at large distances from the nuclei.[24]

The main results of the present study are reported in parts a−d of Figure 2, where the absorption spectra of the 4 structures here considered obtained using the LDA and LB94 xc-functionals are shown, and Table 1, where the position and the height of the maximum and the center position at half-maximum of the absorption peak are reported for convenience of the reader. In Figure 2, the steep decline of photoabsorption peak toward high energies is the consequence of the limited number (300) of eigenvalues actually calculated, therefore the spectrum is obtained up to the maximum eigenvalue. The LB94 maximum eigenvalues are 3.58, 3.59, 3.27, 3.21 eV, whereas the LDA maximum eigenvalues are 2.88, 2.89, 2.63, and 2.55 eV for 147-CO (+5), 146-Oh (+2), 172-CU (+4), and 147-Ih (−1), respectively. The first and most important observation that can be drawn from an inspection of Figure 2 and Table 1 is that the position of the absorption peak, defined equivalently as the position of the maximum or the center of the peak, depends weakly on the cluster shape but is appreciably dependent on the choice of the xc-functional employed in the calculations. In detail, the position of the peak maximum varies in the range from 3.0 to

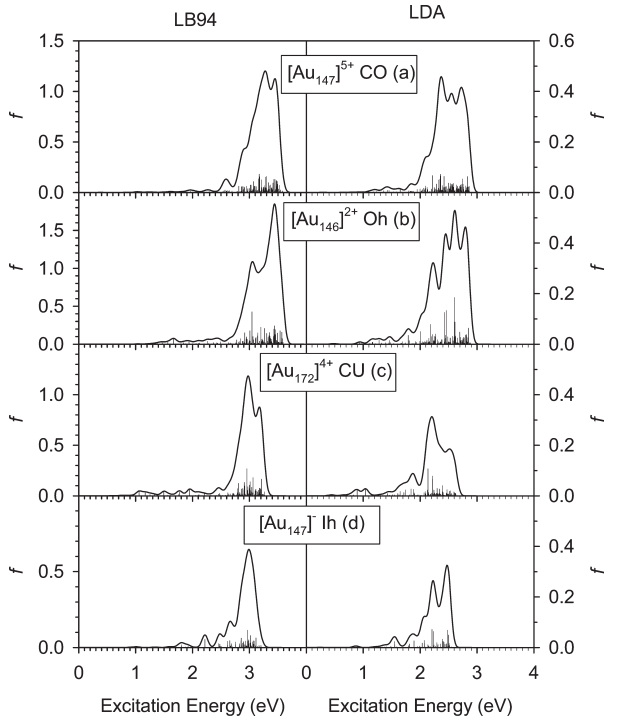

Figure 2. Photoabsorption spectra simulated at the LB94 and LDA level for Au nanoclusters at LDA-relaxed geometries.

Table 1. Position and the Height of the Maximum of the Absorption Peak are Reported for the 4 Structures Described in Figure *1* Using LDA and LB94 xc-Functionals

system	peak position (eV)	peak center (eV)	peak height (*f*)
146-Oh LB94	3.4	3.25	1.80
147-CO LB94	3.2	3.25	1.20
147-Ih LB94	2.95	2.95	0.65
172-CU LB94	2.95	3.00	1.20
146-Oh LDA	2.6	2.50	0.55
147-CO LDA	2.3	2.55	0.47
147-Ih LDA	2.5	2.35	0.35
172-CU LDA	2.1	2.35	0.30

3.4 eV at the LB94 level, whereas it ranges between 2.3 and 2.6 eV at the LDA level. This provides the possibility of validating the xc-functional (i.e., to determine which is the most appropriate to predict the optical response of Au clusters) by comparison with available experimental data.[33−35,8] In detail, from an inspection of Figure 3 from ref 8 one finds that Au particles of roughly 2 nm diameter exhibit a maximum in the absorption spectrum positioned at about 2.58 eV. A correction is due to the dielectric constant of Al_2O_3 (the medium where the experiment has been performed), and can be estimated using formula (4) of ref 8 with a dielectric constant of the medium ∼3 and a real part of the interband dielectric function ∼11: the peak position is decreased by a factor ∼1.08, so that in the gas phase it should occur at 2.78 eV. A further correction is due to the reduced size of the present clusters (diameter of roughly 1.7−1.8 nm). When both effects are included, one expects that experimental peak for particles similar to thise considered in the present study should be around 2.9−3.0 eV. Therefore, it can be concluded that the LB94 values

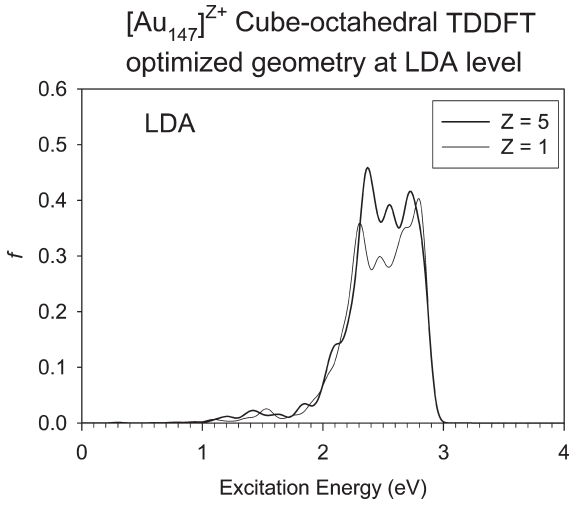

Figure 3. Comparison of the photoabsorption spectra simulated at the LDA level for a 147-CO Au nanocluster with two different total charges: +5 and +1.

for the absorption maximum seem to be in better agreement with experiment than the LDA ones. This conclusion corroborates the important role of asymptotically correct xc-potentials in TDDFT applications to gold clusters, in particular for locating the correct position of the interband/intraband transitions in bulk Au.[36]

The dependence of the center of the absorption peak on the cluster shape is instead weak. Basically, one can observe only a shift of this position to lower binding energy by ∼0.2 eV at both the LDA and LB94 level for the 147-Ih noncrystalline structure and the 172-CU structure. The latter shift can be justified by the larger size of the 172-CU cluster, in agreement with the expected decrease of the position of the absorption peak with increasing cluster size,[33] whereas the former shift is due to the higher symmetry of the I_h group, which narrows and reduces the number of electron−hole pairs in the excitation spectrum.

The maximum of the absorption peak instead is somewhat more dependent on the cluster shape. This is due to an appreciable dependence of the *form* of the absorption onto the shape of the particle: especially at the LDA level, one can clearly see that the absorption spectrum has a roughly symmetric form for 147-CO, and asymmetric forms for the other clusters, with a positive skewness for 146-Oh and 147-Ih (with the position of the maximum thus at higher energy than the center of the peak) and a negative skewness for 172-CU (with the position of the maximum at lower energy than the center of the peak). This is the reason of the greater sensitivity to the cluster shape of the maximum of the absorption peak with respect to its center.

Further considerations can also be done on the intensity of the optical response, roughly correlated with the height of the absorption peak. At the LB94 level, this height changes drastically in the range of structural motifs here considered, varying by nearly a factor of 3 from the minimum reached for 147-Ih to the maximum reached for 146-Oh. A much more contained oscillation is found at the LDA level, but nevertheless the overall intensity measured as the cumulative integral of the absorption peak can apparently be distinguished into two quite distinct cases, with the intensity of the 147-Ih and 172-CU structures roughly halved with respect to that of 146-Oh and 147-CO. This can essentially be traced back again to the more stringent selection rules in the 147-Ih and 172-CU clusters, which decrease

dx.doi.org/10.1021/jp112217g |*J. Phys. Chem. C* 2011, 115, 6277–6282

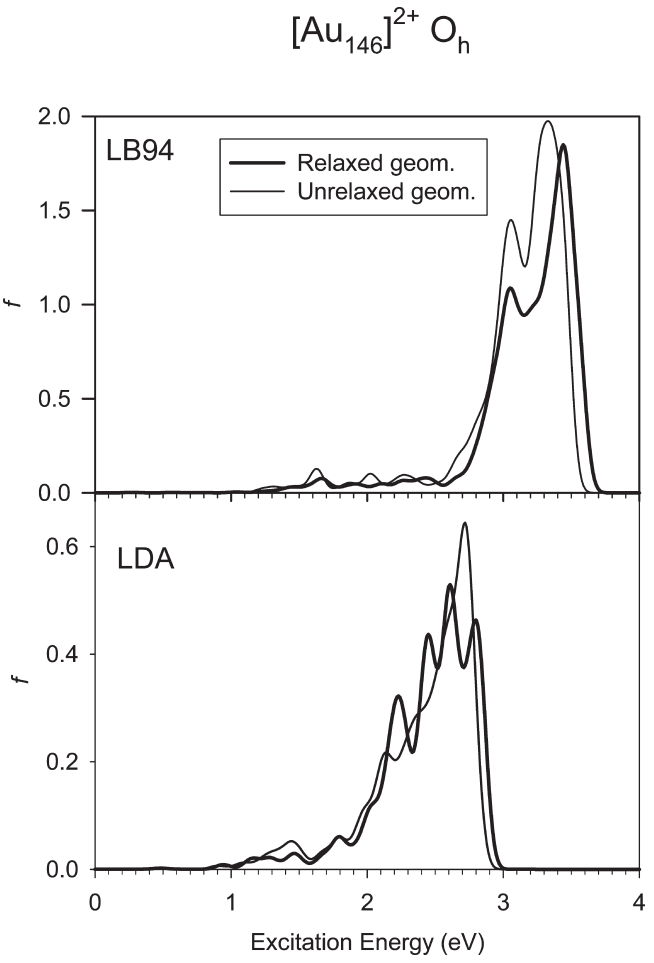

Figure 4. Comparison of the photoabsorption spectra simulated at both the LDA and LB94 level for a 146-Oh Au nanocluster at relaxed and unrelaxed (bulk) geometries.

the intensity as well as the width and the position of the optical response. Whereas this effect is probably overestimated at the LB94 level, a reduction of intensity for noncrystalline but higher-symmetry structure is in tune with experimental information.[37] It must be recalled in this connection that the Thomas−Kuhn−Reiche (TKR) sum rule dictates that the sum of the oscillator strengths over the whole energy interval (up to infinite) equals the number of electrons, so it is expected that for 147-Ih and 172-CU the intensity is actually redistributed from low to higher energy. On the low-energy part of the spectrum, sparse transitions appear that are due to the finite size of the cluster. We have not discussed them as they are rather weak and thus experimentally not very significant (and likely to be very sensitive to environment). A question which has not been answered so far is whether the use of charged clusters, which allows one to keep symmetry high and strongly reduces the computational effort, introduces any artifact into our analysis. That this is not the case can be clearly seen in Figure 3, where the absorption spectra at the LDA level of 147-CO with charge +5 (taken from part a of Figure 2) and charge +1 are compared. Despite the very different charge in the two cases, there is hardly any difference in the position, height and width of the resonance, with only a minor redistribution of the intensity within the peak toward its bottom in the more highly charged case.

Analogously, the details of the structural relaxation do not affect the optical response to a significant degree, as shown in Figure 4, where the absorption spectra at both LB94 and LDA levels of 146-Oh with charge +2 at the relaxed (taken from part b of Figure 2) and unrelaxed geometries are reported. It can be appreciated that very small differences are found by relaxing the cluster geometry, with a minor shift ($\leq$0.1 eV) of the peak position toward higher excitation energies and a minor redistribution of the intensity. This shift toward higher energy is found in both LDA and LB94 spectra and can be qualitatively rationalized in terms of an extra stabilization of the occupied orbitals with respect to the virtual ones. This effect enlarges the diagonal terms of the Ω matrix (eq 2) and therefore the resulting eigenvalues and excitation energies are increased. Apparently, the spectrum calculated with the LDA functional seems to be slightly more sensitive to the structural relaxation than the LB94 one.

5. CONCLUSIONS

Following a strategy based on the use of high-symmetry structures,[13] the optical response of Au nanoclusters between 150 and 200 atoms of various shapes (corresponding to those of interest in applications) is studied at the TD-DFT level, and the form and frequency of their resonance peak as a function of their shape and the approximation used for the DFT exchange-correlation (xc-) functional is investigated. Clusters with cuboctahedral (N = 147), octahedral (N = 146), cubic (N = 172), and icosahedral (N = 147) shapes were studied, producing rigorous knowledge on the SPR of Au nanoclusters of this size.

Two main conclusions can be drawn from the present investigation:

(i) The predictions of the LB94 xc-functional compare better with the available experimental data on the absorption spectrum of Au particles in this size range with respect to those of the LDA xc-functional, which tends to underestimate the position of the peak in the absorption. This validates the LB94 approximation for the prediction of the optical response of Au nanoclusters

(ii) The detailed shape of the cluster, which has little influence on the position of the absorption peak, is instead apparent in the form of the absorption spectrum, with the possibility of having a symmetric or two different asymmetric forms of the spectrum depending on the cluster specific structural arrangement or structural motif.

Finally, we note that, in perspective, the approach here explored lends itself to interesting developments. For example, the effect of alloying[38] on the nanoparticle optical response can be studied by focusing on high-symmetry particles composed by two different metals arranged in different chemical ordering patterns (e.g., core−shell vs homogeneous mixing). This would produce rigorous knowledge on the SPR dependence upon composition and segregation patterns, of great interest for the possibility of modulating SPR using alloying, and combining optical and magnetic effects. Additionally, the present results can be analyzed in terms of a semiempirical tight-binding (TB) model, whose quantum mechanical character would allow one to fully control the parametrization process,[14] whereas its simplified character would enable one to predict optical response of systems with thousands of atoms (5−10 nm), and thus the evolution of the SPR of large particles with nanoparticle size and morphology in the full range of interest in applications.

■ ACKNOWLEDGMENT

Computational support from CINECA supercomputing centre within the Au-SPR ISCRA project is gratefully acknowledged. A.F. acknowledges financial support from the SEPON project within the ERC Advanced Grants. This work has been supported by MIUR (Programmi di Ricerca di Interesse Nazionale PRIN 2006 and 2008) of Italy

■ REFERENCES

(1) Kreibig, K.; Vollmer, M. *Optical Properties of Metal Clusters*; Springer: New York, USA, 1995.
(2) Zhang, C.; Noguez, J. Z. *Plasmonics* **2008**, *3*, 1157.
(3) Burda, C.; Chen, X.; Narayanan, R.; El-Sayed, M. A. *Chem. Rev.* **2005**, *105*, 1025.
(4) Chen, F. Y.; Johnston, R. L. *Plasmonics* **2009**, *4*, 147.
(5) Bruzzone, S.; Malvaldi, M.; Arrighini, G. P.; Guidotti, C. *J. Phys. Chem. B* **2005**, *109*, 3807.
(6) Arrighini, G. P.; Durante, N.; Guidotti, C.; Lamanna, U. T. *Theor. Chem. Acc.* **2000**, *104*, 327.
(7) He, Y.; Zeng, T. *J. Phys. Chem. C* **2010**, *114*, 18023.
(8) Cottancin, E.; Celep, G.; Lermé, J.; Pellarin, M.; Huntzinger, J. R.; Vialle, J. L.; Broyer, M. *Theor. Chem. Acc.* **2006**, *116*, 514.
(9) Schmucker, A. L.; Harris, N.; Banholzer, M. J.; Blaber, M. G.; Osberg, K. D.; Schatz, G. C.; Mirkin, C. A. *ACS Nano* **2010**, *4*, 5453.
(10) Aikens, C. M.; Li, S.; Schatz, G. C. *J. Phys. Chem. C* **2008**, *112*, 11272.
(11) Aikens, C. M. *J. Phys. Chem. A* **2009**, *113*, 10811.
(12) Chen, H.; McMahon, J. M.; Ratner, M. A.; Schatz, G. C. *J. Phys. Chem. C* **2010**, *114*, 14384.
(13) Stener, M.; Nardelli, A.; De Francesco, R.; Fronzoni, G. *J. Phys. Chem. C* **2007**, *111*, 11862.
(14) Fortunelli, A.; Velasco, A. M. *Int. J. Quantum Chem.* **2004**, *99*, 654.
(15) Pyykkö, P. *Angew. Chem., Int. Ed.* **2004**, *43*, 4412.
(16) van Lenthe, E.; Baerends, E. J.; Snijders, J. G. *J. Chem. Phys.* **1993**, *99*, 4597.
(17) Baerends, E. J.; Ellis, D. E.; Ros, P. *Chem. Phys.* **1973**, *2*, 41.
(18) Fonseca Guerra, C.; Snijders, J. G.; te Velde, G.; Baerends, E. J. *Theor. Chem. Acc.* **1998**, *99*, 391.
(19) van Gisbergen, S. J. A.; Snijders, J. G.; Baerends, E. J. *Comput. Phys. Commun.* **1999**, *118*, 119.
(20) Casida, M. E. *Recent Advances in Density-Functional Methods*; Chong, D. P., ed.; World Scientific: Singapore, 1995; p 155.
(21) Gross, E. K. U.; Kohn, W. *Adv. Quantum Chem.* **1990**, *21*, 255.
(22) Vosko, S. H.; Wilk, L.; Nusair, M. *Can. J. Phys.* **1980**, *58*, 1200.
(23) Häberlen, O.; Chung, S. C.; Stener, M.; Rösch, N. *J. Chem. Phys.* **1997**, *106*, 5189.
(24) Van Leeuwen, R.; Baerends, E. J. *Phys. Rev. A* **1994**, *49*, 2421.
(25) van Gisbergen, S. J. A.; Kootstra, F.; Schipper, P. R. T.; Gritsenko, O. V.; Snijders, J. G.; Baerends, E. J. *Phys. Rev. A* **1998**, *57*, 2556.
(26) Ma, Y. Y.; Li, W. Y.; Cho, E. C.; Li, Z. Y.; Yu, T. K.; Zeng, J.; Xie, Z. X.; Xia, Y. N. *ACS Nano* **2010**, *4*, 6725.
(27) Li, W. Y.; Xia, Y. A. *Chemistry – An Asian Journal* **2010**, *5*, 1312.
(28) Xia, H. B.; Bai, S. O.; Hartmann, J.; Wang, D. Y. *Langmuir* **2010**, *26*, 3585.
(29) Tsuji, M.; Yamaguchi, D.; Matsunaga, M.; Alam, M. *J. Cryst. Growth Design* **2010**, *10*, 5129.
(30) Wu, C. M.; Li, C. Y.; Kuo, Y. T.; Wang, C. W.; Wu, S. Y.; Li, W. H. *J. Nanoparticle Res.* **2010**, *12*, 177.
(31) Aprà, E.; Fortunelli, A. *J. Phys. Chem. A* **2003**, *107*, 2934–2942.
(32) Aprà, E.; Baletto, F.; Ferrando, R.; Fortunelli, A. *Phys. Rev. Lett.* **2004**, *93*, 065502.
(33) Palpant, B.; Prével, B.; Lermé, J.; Cottancin, E.; Pellarin, M.; Treilleux, M.; Perez, A.; Vialle, J. L.; Broyer, M. *Phys. Rev. B* **1998**, *57*, 1963.
(34) Cottancin, E.; Lermé, J.; Gaudry, M.; Pellarin, M.; Vialle, J. L.; Broyer, M.; Prével, B.; Treilleux, M.; Mélinon, P. *Phys. Rev. B* **2000**, *62*, 5179.
(35) Gaudry, M.; Lermé, J.; Cottancin, E.; Pellarin, M.; Vialle, J. L.; Broyer, M.; Prével, B.; Treilleux, M.; Mélinon, P. *Phys. Rev. B* **2001**, *64*, 085407.
(36) Romaniello, P.; de Boeij, P. L. *J. Chem. Phys.* **2007**, *127*, 174111.
(37) Pileni, M. P. *J. Phys. Chem. C* **2007**, *111*, 9019.
(38) Ferrando, R.; Fortunelli, A.; Johnston, R. L. *Phys. Chem. Chem. Phys.* **2008**, *10*, 640.

Progress in Surface Science 86 (2011) 59–81

Contents lists available at ScienceDirect

Progress in Surface Science

journal homepage: www.elsevier.com/locate/progsurf

Review

Template-assisted assembly of transition metal nanoparticles on oxide ultrathin films

Luca Gavioli [a,b], Emanuele Cavaliere [a,b], Stefano Agnoli [c], Giovanni Barcaro [d], Alessandro Fortunelli [d], Gaetano Granozzi [c,*]

[a] Dipartimento di Matematica e Fisica, Università Cattolica del Sacro Cuore, via dei Musei 41, I-25121 Brescia, Italy
[b] Istituto Officina dei Materiali – CNR, Laboratorio TASC, Area Science Park – Basovizza, Strada Statale 14, Km.163.5 I-34149 Trieste, Italy
[c] Dipartimento di Scienze Chimiche and INSTM research Unit, via Marzolo 1, University of Padova, Italy
[d] CNR-IPCF, Istituto per i Processi Chimico-Fisici del Consiglio Nazionale delle Ricerche, via G. Moruzzi 1, 56124, Pisa, Italy

ARTICLE INFO

Commissioning Editor: Prof. C. Woell

Keywords:
Metal nanoparticles
Oxide layers
Templating effect
Defects
Directed-assembly
Metal/oxide interaction

ABSTRACT

In this work we analyse three paradigmatic examples of directed self-assembling and self-organisation of transition metal nanoparticles (NPs) on oxide ultrathin layers grown on single crystal metal surfaces. The major driving forces considered in the description of the NPs assembling process on these nanotemplate systems are the presence in the oxide layer of trapping centres in the form of defects and the metal/oxide interaction. We first summarise the structure of the different oxide nanotemplates, and then we discuss the role of geometric and electronic factors in the formation of ordered NP arrays on the selected systems. It turns out that a defective nanostructured oxide template can drive the organisation of the NPs if the metal NPs are efficiently trapped by the defects and these are accessible via the diffusion of metal adatoms on the surface, which is in turn strongly dependent on the metal/oxide interaction.

Contents

* Corresponding author.
E-mail address: gaetano.granozzi@unipd.it (G. Granozzi).

0079-6816/$ - see front matter © 2011 Elsevier Ltd. All rights reserved.
doi:10.1016/j.progsurf.2011.02.001

1. Introduction

Transition and noble metal nanoparticles (NPs) of size ranging from 1 to about 20 nm are currently the object of a huge amount of research work. In this dimensionality range, the electronic, optical, magnetic and chemical properties of the particles can be tuned by varying the NP physical size, leading to new phenomena, e.g. superparamagnetism of magnetic NPs, surface plasmon resonance and rather unexpected catalytic properties [1–6]. Some of these phenomena have already had an impact on applications in field far from surface science, as biology and medicine: as an example, taking advantage of the enhanced surface plasmon resonances, the sensitivity of biological markers has been strongly enhanced [5].

Because the specific properties are critically dependent on the NP size and shape, one major issue is devising methods and procedures which are effective in preparing NPs possessing well-defined size and shape. Colloidal chemistry is actually very efficient in obtaining such a task, and literature is full of creative methods to reach this goal [7]. However, matter at the nanoscale is intrinsically very unstable because of the high specific surface area which strongly increases the surface energy contribution, so that one further unavoidable step to exploit the new interesting properties is the stabilization of the NPs with respect to spontaneous coarsening processes (i.e. Ostwald ripening and sintering). In this respect, it was soon realised that using a substrate where to anchor, and thereby stabilize, the NPs is an effective way to prevent such adverse phenomena, and oxide surfaces represent a good substrate choice, as demonstrated by the common practice of preparing heterogeneous catalysts by dispersing active metal NPs on an oxide powder acting as support. The effective metal/oxide interaction plays a relevant role in this framework, and consequently many efforts have been devoted, and are currently in progress, to study metal/oxide interfaces at an atomic level [8–10]. Thence, the understanding of the fundamental aspects regulating the metal/oxide heterojunctions has become a crucial issue, and such studies have a tremendous impact in many other different fields, such as microelectronics and material science [11].

In the field of heterogeneous catalysis, the metal/oxide interfaces can be efficiently studied by using planar model catalyst, by examining two rather different model frameworks, i.e. metal films/particles on oxide surfaces or oxide films/particles on metal surfaces. Because of their relevance in real catalysts, the former type of systems has been studied first and a well known phenomenon, often referenced as the strong metal–support interaction (SMSI), has been described in great detail [12–19]. The SMSI acronym was first proposed by Tauster in 1978 [12] to describe the suppression of both H_2 and CO chemisorption ability for noble metals (group VIIIA) NPs, when adsorbed on TiO_2 or other reducible oxides [12,20]. Subsequently, a similar SMSI effect has been observed in other metal/oxide catalytic systems [12,15,18–20], and discussed by the action of two different factors: an electronic and a geometric factor. The first is determined by a perturbation of the electronic structure of the metal catalyst, deriving from charge transfer between the metal and the oxide. The second results from the presence of an ultrathin (UT) layer of the reduced oxide, originating from the support, that physically covers the metal NPs (encapsulation model), which actively blocks catalytic sites at the metal surface [21,22].

The SMSI effect can also be investigated using the second type of model systems, often called the inverse catalyst model, i.e. oxide films/particles on metal surfaces. Actually, it is now well recognised

that a way to achieve a detailed information on the NPs/oxide interactions is to carry out surface science experiments on a composite system, where the metal NPs are deposited on UT oxide films epitaxially grown on metal single crystals [23,24]. Such a methodology presents experimental advantages: (i) due to the intrinsic conductivity of the UT film, Scanning Tunnelling Microscopy (STM) experiments become feasible and informative, and (ii) UT oxide films with a well defined defectivity can be prepared, where the role of defects can be studied in detail. However, as explained in Section 2, the UT oxide films can have rather different properties with respect to bulk oxides, so that the validity of extrapolating the results of investigations obtained using metal NPs/UT oxide films to metal NPs/oxide(bulk) systems is not to be taken for granted.

A further important point to be considered is related to the new properties that can arise when arrays of metal NPs are created. In this situation, a hierarchical material is obtained where the primary building blocks (the NPs) are organised to create a regular secondary structure, a superlattice describing the long range order of the primary building blocks. In such hierarchical material, nanoscale forces between the building blocks are active [25], which can generate new collective functionalities originated by the *ensemble* of the metal NPs [26,27]: as an example, regular arrays of metal NPs allow to control the resonance frequency of the localised surface plasmon [28] and they are good candidates for sensors and extremely high-density data storage devices [29].

Thence, one main current issue is finding viable routes to prepare ordered arrays of metal NPs. One possibility is to rely on a *sequential* top-down approach, e.g. nanolithographic methods or by atomic manipulation via STM [30]. However, the current frontier is associated with obtaining such nanostructures by a *parallel* assembly (often indicated either as self- or directed-assembly) fast process.

One of the most simple and promising approach to obtain long-range assembled structures is related to the use of ordered arrays of defects, which act as templates for the preferential nucleation phenomenon [31]. It has been shown both theoretically [32] and experimentally [33] that an ordered array of defect trapping centres can narrow the size distribution of metal NPs growing on a support down to 5–10% with respect to 30–40% expected for random nucleation. Templating the NP growth by adsorbate induced surface reconstructions of bulk metal surfaces and by employing vicinal metal surfaces has been already largely explored in the past [33–35]. However, using metal based templates has weaker perspectives in applications, due to the intrinsic instability of the template itself under realistic conditions. On the contrary, two dimensional (2D) UT oxide films are expected to be more promising for some applications, thanks to their higher thermal stability [34,36–39]. The way the UT oxides layers on metals can act as effective 2D nanotemplates is connected with the presence of defects, which can operate as preferential nucleation sites for the directed-assembling process of the metal NPs. Due to the lattice mismatch between the oxide UT film and the metal substrate, ordered arrays of defects (e.g. ordered arrays of holes or dislocation lines), that can form the motif of the 2D template, are often present [23,34,40]. However, as discussed in the following, also electronic effects play a role in directing the NP assembly process. In addition, the affinity with oxygen of the deposited metal NPs is an important issue to be taken into consideration, since the 2D template itself can be partially destroyed by the deposited metal, thus influencing the effective NPs ordering [37].

In this article, we report a comparison of the 2D templating capabilities of three prototypical oxide UT films epitaxially grown on metal substrates, i.e.

a) A TiO_x bi-layer on Pt(1 1 1), where, according to the preparation procedure, both a defect-free film and a film with an ordered array of topographical defects can be achieved.
b) A defect-free FeO bi-layer on Pt(1 1 1) where a long-range Moiré pattern is apparent.
c) A thicker layer of AlO_x on Ni_3Al(1 1 1) with various types of topographical defects, where a rather complex templating effect is observed.

We will first summarise the structure of the different UT oxide layers, outlining their different electronic and morphological features. Thereafter we will examine the formation of NPs arrays obtained by UHV evaporation of the corresponding metals. The effects due to the different nature of the metal, i.e. a noble metal or a transition metal, will then be discussed. This approach will provide a general framework of the templating behaviour in these systems by critically assessing the role of different factors affecting the NP assembling. In a previous review article the experimental results on the same

triad of model systems has been very briefly described [34], whereas the templating behaviour of the AlO_x films with respect to several different metals has been discussed in detail in another review [41]. In both cases, however, no attempt was done to discuss the driving forces of the directed-assembling process.

2. The structure of the ultrathin oxide layers on metals

In recent years, much attention has focused on oxide model systems in the form of UT epitaxial films grown on single-crystal metal surfaces [23,40,42–49]. In the following, by the term UT we mean films characterised by thickness in the range up to a few monolayers (MLs), i.e. thickness $\leqslant$1–2 nm. While the results to date have demonstrated that films with thickness of the order of several MLs are adequate to simulate bulk-terminated oxide surfaces, more and more examples are reported of UT films with radically new structures, stoichiometries and properties. UT oxide films thus represent a potentially new class of materials where innovative properties with respect to bulk phases are obtained, due to the interaction with the substrate (metal proximity effects) and/or to the confinement of atomic-scale structures in at least one dimension [50–52]. For example, in order to find a local equilibrium with the substrate, the film can adjust to a structure different from the bulk one, resulting in the generation of strain, that is maintained until a critical thickness is reached, after which the film recovers the thermodynamically stable bulk structure. Indeed, most of the recent focus on UT films is related to the possibility of stabilizing phases and structures which are not obtainable in bulk form due to thermodynamic and/or kinetic constraints.

A number of review articles have appeared in literature in the field of UT oxide films: they have been mainly focused on the epitaxial growth procedures of oxide UT films [40,44,53] or on their relevance in catalysis [54,55]. In many cases, the metal/oxide interactions result in interface-stabilized reduced oxide phases [40,44,56–62]. The body of this work has shown that compact (1 1 1) metallic surfaces are best suited to grow UT oxide phases. In particular, a common observed feature is the presence of a wide variety of reconstructions with respect to the bulk phases, depending on different factors such as the lattice mismatch, the metal overlayer/oxygen ratio during deposition, and kinetic effects determined by the preparation procedure [40,44,57,61,63].

Concerning the oxide/metal interaction, several effects are expected. For example, the contact between a metal and an oxide can result in charge redistribution at the interface at the local scale and/or on the long range (see for instance [8] and Refs. reported therein). The electron redistribution is driven by principles of energy minimisation of the system and continuity of the electric potential in the solid. Moreover, the close proximity of the oxide to a highly polarizable medium, i.e. the metal support, can modify substantially the physico-chemical properties of the oxide itself. The charged atoms in the oxide e.g. induce image charges in the substrate, resulting in strong polarisation interactions, especially if the oxide phase has a polar character. All these effects can modify the work function of the system, as well as the electronic properties of the UT film, such as the on-site Coulomb repulsion or the charge transfer energy [64,65]. Strictly connected to the formation of the aforementioned interfacial dipole is the bending of the oxide bands at the interface leading to the formation of a Schottky-type heterojunction [23].

In the following, we present a short description of the structures of three different prototypical oxide UT films, i.e. TiO_x/Pt(1 1 1), FeO/Pt(1 1 1) and AlO_x/NiAl(1 1 1). They have been chosen because they represent suitable case studies to test the role of defects and of the metal/oxide interaction in templating metal NPs. For a more detailed description of each oxide system we refer the reader to the specific references.

2.1. TiO_x/Pt(1 1 1)

A comprehensive report on the structure and preparation procedures of several different TiO_x UT films grown on Pt(1 1 1) is part of a recent review article [40]. They were prepared by depositing Ti atoms in oxygen reactive atmosphere on the Pt(1 1 1) surface, held at room temperature (RT) under initial UHV conditions. A successive heat treatment of the surface at suitably high temperature,

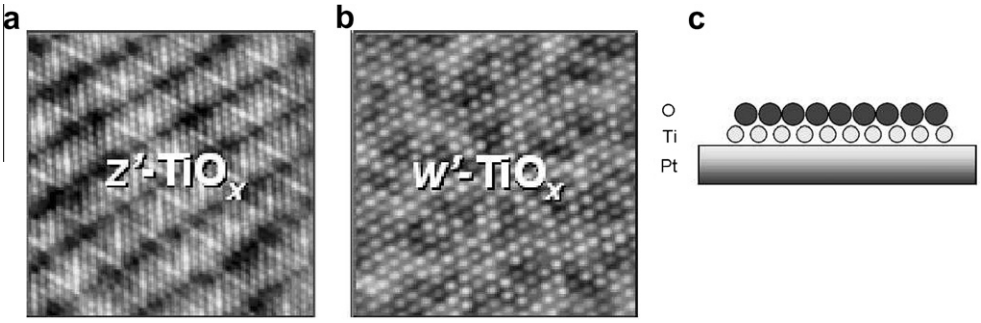

Fig. 1. STM images of the two different TiO_x/Pt(1 1 1) phases discussed in the present work. (a) z' phase, 9×9 nm^2, $V = 0.8$ V, $I = 1.5$ nA. (b) w' phase, 6×6 nm^2, $V = 0.2$ V, $I = 1.0$ nA. (c) Schematic drawing of the Pt/Ti/O stacking sequence. Adapted from Ref. [61].

performed in controlled oxidising or reducing environment (from P $O_2 = 5 \times 10^{-6}$ mbar to UHV), yields the desired surface structure. A more detailed description of the preparative conditions can be found in Refs. [61,66].

The atomistic structures of several TiO_x phases were derived from combined low energy electron diffraction (LEED), STM, X-ray photoemission spectroscopy (XPS) and photoelectron diffraction (XPD) measurements [61] and density functional theory (DFT) simulations [62,66]. The main morphological differences among these phases can be traced back to the different stacking of titanium and oxygen atoms in the film, and to the presence of ordered arrays of defects. In the present report we will restrict our attention to two UT phases, named z'-TiO_x and w'-TiO_x in Ref. [61], whose STM images are reported in Fig. 1a and b. Both of them are formed by a Ti–O bi-layer (Fig. 1c), where the Ti atoms are at the interface with the substrate and the oxygen atoms form the topmost layer. The two films have a similar stoichiometry ($x \approx 1.2$ [62]), but the main difference between the two with respect to a templating effect is associated to the presence in the z'-TiO_x phase of an ordered array of defects (see the description below and Figs. 1a and 2b) [66]. In contrast, in the w'-TiO_x film few defects are only randomly distributed and the structure has been described in terms of a Moiré pattern [67].

In Fig. 2, the LEED pattern and a representative STM image of the z'-TiO_x/Pt(1 1 1) system are shown. The STM image (Fig. 2b) shows that the z'-TiO_x/Pt(1 1 1) layer is constituted by bright stripes separated by darker rows. On the stripes, one can observe a *zigzag-like* motif (brighter atoms). The dark rows, parallel to the $[1\,\bar{1}\,0]$ direction of Pt(1 1 1), are present at both positive and negative bias, suggesting that these are true topological features, named *troughs*, as confirmed by DFT calculations [66]. The arrangement of the Ti layer would continue the fcc stacking of Pt, but the mismatch between the TiO_x lattice parameter (ranging around 0.3 nm) and the Pt one ($a = 0.277$ nm) and the O overcrowding due to the $TiO_{1.2}$ stoichiometry results in the creation of denser stripes separated by lower density regions, thus originating the *troughs* [66]. The characteristic *zigzag-like* STM motif observed on the stripes can be explained in terms of different coordination of Ti atoms: fourfold coordinated Ti atoms are separated by dislocation lines from defective Ti threefold coordinated atoms, arranged in triangles near the stripe edge. Fourfold coordinated Ti atoms are more positively charged, have a higher density of empty states above the Fermi level, and are imaged as brighter protrusions in STM images acquired with positive bias [61,66].

DFT calculations allowed to interpret the different types of defects which were detected by STM along the *troughs* (Fig. 2b), whose density depends on the preparation procedures [66]: wide *troughs* are characterised by defects constituted by a titanium vacancy, defined as *picoholes*, (single in Fig. 2b), that can merge to form larger *picoholes* (double in Fig. 2b), while narrow *troughs* do not show titanium vacancy defects [66].

Such data show that from a morphological point of view this oxide layer is very heterogeneous and thus potentially useful to act as nanotemplate for self-organisation of metal NPs: the *picoholes* are the best candidate as nucleation sites for deposited metal atoms during the NP assembling process.

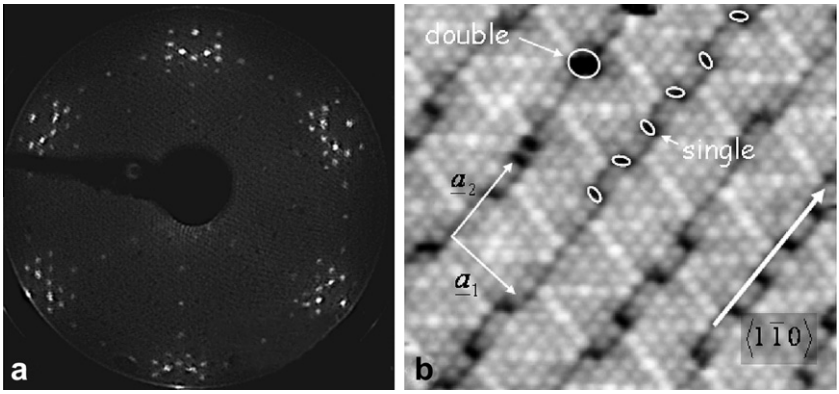

Fig. 2. (a) LEED pattern of z'-TiO_x/Pt(1 1 1) with its three domains. (b) z'-TiO_x lattice and high resolution STM image (7.5×6.8 nm^2) showing the characteristic *zigzag-like* contrast and orientation with respect to substrate lattice. The single and double *picoholes* (see text) are indicated by white ellipsis. Adapted from Ref. [66].

Moreover, such defects may also act as preferential channels for adatoms diffusion towards the substrate, something similar to the holes in a membrane (nanosieves) [68].

2.2. FeO/Pt(1 1 1)

In analogy to the TiO_x phases, a suitable substrate for preparing FeO UT films is Pt(1 1 1). Fe deposition at RT on the Pt(1 1 1) surface and subsequent heating to 1030 K in an oxygen pressure of 10^{-5} torr for ~30 s. [69] result in a FeO UT film with a morphology shown in the STM image of Fig. 3a. This phase is constituted by a FeO bilayer with an internal periodicity of 0.309 nm, slightly larger than that of the bulk FeO(1 1 1) plane (0.304 nm) [69–71]. XPD data show that the O atoms occupy hollow sites with respect to the iron layer underneath, confirming that STM is imaging Fe atoms at positive bias voltages [70].

The incommensurability between the oxide layer (0.31 nm periodicity) and the Pt(1 1 1) substrate (0.277 nm periodicity) gives rise to the formation of a Moiré pattern, shown on a larger scale STM image in Fig. 3b, and resulting in a very large unit cell (2.6 nm), misaligned by 0.6°, as schematized in Fig 3c. The registry of the Moiré pattern is described by Fe atoms either on top of the Pt atoms, or in bridge sites and, in still other regions, in fcc or hcp sites (see Fig. 3b) [69,71,72]. STM images, taken in the near-field emission regime, suggest that the modulated Fe–Pt stacking is responsible for a corresponding modulation of the surface potential [73].

It is important to observe that the corrugation of this oxide layer is very low (below 0.01 nm) and no periodic defect is visible inside the domains forming the oxide layer. Hence this UT film is different from a topographical point of view from the z'-TiO_x film, but somewhat similar to the w'-TiO_x one (Fig. 1b) which is also described as a Moiré pattern [67].

2.3. AlO_x/Ni_3Al(1 1 1)

As for TiO_x, AlO_x UT films can also be grown on several different metallic substrates and the topic has been recently reviewed [40]. One of the most suitable substrates for the growth of AlO_x UT films is Ni_3Al(1 1 1). To obtain closed and long-range ordered UT films, the oxidation process, consisting in clean surface exposure to 40 L of oxygen with the substrate at 1000 K, followed by annealing to 1050 K for 5 min, is performed twice [74,75].

The structure of the AlO_x film, although commensurated to the Ni_3Al substrate, is rather complex [75–77]. The STM real space topography of the AlO_x superstructure is strongly dependent on the bias voltage, as shown in Fig. 4a and b. At bias voltage of 3.2 V one can observe the so called "network" structure, which can be described as a hexagonal arrangement of dark holes, which are surrounded

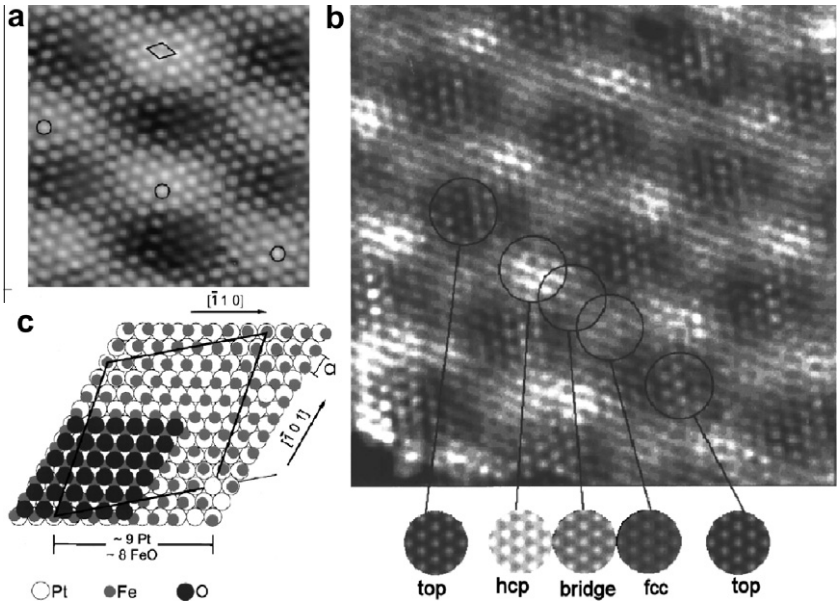

Fig. 3. (a) 5.5×5.5 nm^2 STM image of the FeO/Pt(1 1 1) system. An atomic periodicity of 0.31 nm is modulated by a large 2.6 nm periodicity creating a Moiré superstructure. The direction of this superstructure indicated by the marked atoms is rotated by about 11° against the small FeO(1 1 1)-(1×1) unit cell that is also indicated. ($V = 0.9$ V, $I = 0.3$ nA). (b) 6×6 nm^2 STM image showing the Moiré structure. The small circular images at the bottom are calculated images using the ESQC (electron scattering quantum chemistry) method for the various high-symmetry epitaxial configurations and associated with the circled regions in the image. (c) Model of the FeO(1 1 1) bilayer on Pt(1 1 1). Adapted from Refs. [69,71].

by smaller hexagonal rings of bright dots (Fig. 4a). Note that not all the holes present the same apparent depth, as shown in the constant current profile of Fig 4c. At a bias voltage of 2.0 V, the STM image in Fig. 4b, taken at the same spot as in Fig. 4a, shows a contrast reversal, with bright protrusions that are defined as the "dot" structure. The profiles taken at the two different biases are compared in Fig. 4c, and the superstructure unit cell present in both images is identical. Its lattice constant is $b_{dot} = 4.07$ nm, in good agreement with spot profile analysis of low energy electron diffraction (SPA-LEED) measurements [75].

The described contrast reversal is apparently not only due to an electronic state in the oxide band gap [78], but must be related to a different topography of the AlO_x film at these sites. The comparison with SPA-LEED data indicates that the "dot" structure is the only true superstructure of the AlO_x film, and the two different superstructures are schematized in Fig. 4d.

A combined STM and DFT study of this surface has revealed the atomic geometry of the oxide layer [39], even though refinements have been recently proposed [77]. In Fig. 5a the STM data taken on the same system at very low bias voltage are shown, in which the yellow triangles correspond to the black dots of the scheme in Fig. 4d, while the black hexagon corresponds to the open circles of Fig. 4d. The white protrusions with triangular arrangement observed in the STM image represent oxygen atoms (see the ball model obtained from comparison with DFT calculations reported in Fig. 5b). Here, the lattice rotation of 23.1° with respect to the substrate, and the stacking sequence of the UT oxide (Al–O–Al–O) is schematized, with the two surface layers (named Al_s and O_s in Fig 5c) being almost coplanar [39]. The comparison with DFT calculations revealed that the hexagonal structure with the brightest spot is an actual geometric hole in the AlO_x layer, reaching down the $Ni_3Al(1\ 1\ 1)$ substrate (*picoholes*) [39]. Quite important in the discussion in the next chapter are also the oxygen vacancies at the three-fold coordination sites (triangles in Fig 5). Finally, random defects are present, located close to the threefold coordination sites, that can also act as trapping centres for metals [39,79], see the discussion in the next chapter.

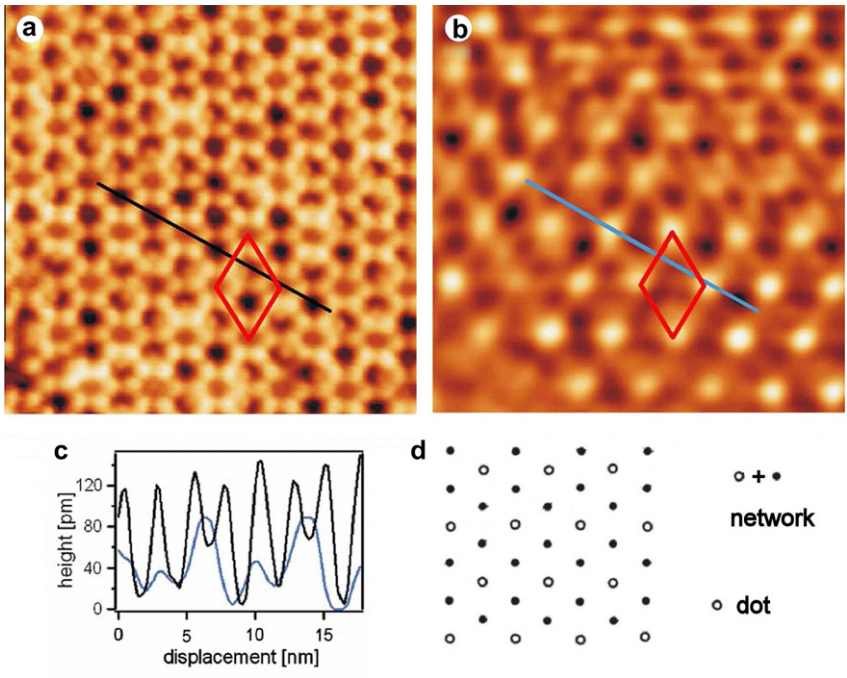

Fig. 4. STM topography (image size $27.8 \times 27.8\ nm^2$) of the $AlO_x/Ni_3Al(1\ 1\ 1)$ "network" structure (a) taken at + 3.2 V bias voltage and of the "dot" structure (b) taken at 2.0 bias voltage. The red rhombus represents the unit cell. In (c) the line profile taken from the black (a) and blue (b) line are plotted. (d) Schematic representation of the "network" and "dot" structure. The open circles correspond to the white spots of the STM image in (b), while the black circles correspond to the dark holes observed in (a). Adapted from Refs. [75,76]. (For interpretation of the references to colour in this figure legend, the reader is referred to the web version of this article.)

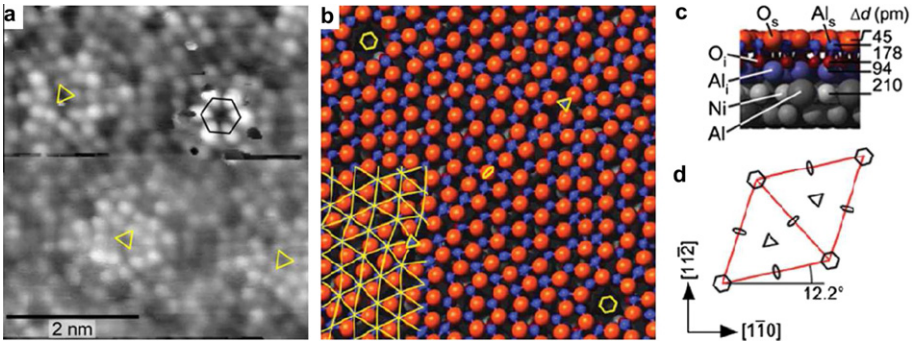

Fig. 5. (a) STM image of the $AlO_x/Ni_3Al(1\ 1\ 1)$ surface taken at bias voltage of 58 mV, with yellow triangles corresponding to the black dots of the scheme in Fig 4d and the black hexagon corresponding to the open circles of Fig. 4d. (b) Top view of the ball model of the system. Red indicates oxygen atoms, while blue reveal Al atoms. (c) Side view of the ball model obtained from DFT calculations. (d) Unit cell of the oxide layer. Adapted from Ref. [39]. (For interpretation of the references to colour in this figure legend, the reader is referred to the web version of this article.)

The *picoholes* in the network structure are analogous to the *picoholes* of the *z*′-TiO_x/Pt(1 1 1) film, but with a different spatial arrangement and symmetry on the surface. In particular, the *picoholes* of the AlO_x UT film have a hexagonal distribution and follow the surface symmetry of the oxide layer,

while the *picoholes* of the z'-TiO_x system are arranged along the one dimensional *troughs*, giving rise to a slightly less ordered arrangement of defects. Moreover, while the z'-TiO_x film also bears larger topographical defects (the double holes), the AlO_x UT film presents only this single type of geometrical defects and a smaller unit cell. A further difference between TiO_x and FeO systems and the AlO_x one lies in that the former are single layer oxides with a stacking sequence substrate/metal/oxygen, whereas the latter is a bilayer with a stacking sequence substrate/metal/oxygen/metal/oxygen. This difference translates in a lower structural freedom of the AlO_x with respect to the TiO_x and FeO systems, that will have an important role in the discussion of metal deposition.

3. Metal nanoparticles growth on the oxide layers

Prior to the discussion of specific systems, it is convenient to point out the main factors directing the growth of metal adsorbates on UT oxide films.

The defects in the structure of the oxide film (i.e. domain boundaries, steps, kinks, dislocations and point defects) can drive the nucleation of the adsorbed metals. Such kind of templating effect can be referenced as *topographical directed assembly* (TDA). As a typical example of TDA, we can mention the preferential adsorption of Au on colour centre defects induced by electron bombardment on highly regular UT films like MgO/Ag(1 0 0) [80]. However such artificially induced defects are randomly distributed on the film surface, resulting in a disordered distribution of adatoms, which finally result in a disordered array of NPs. As already mentioned in the Introduction, the ability to control or tune the system properties require a growth of NP arrays where both the size and spatial distribution over the substrate are controlled. Hence a necessary step is to obtain a large density of defects on the substrate surface, with a periodic, regular and long-range ordered distribution. Such kind of array would allow one to investigate the role of NP-NP distance and geometry and enlighten the mutual interactions between the NPs and their effect over the NP array properties.

Besides TDA, also an *electronic directed assembly* (EDA) can be envisioned. Actually, both experimental data and calculations have clearly shown that in UT oxide films a local modulation of the electronic structure is present. As an example, band bending at the metal/oxide interface and modification of the work function (WF) of the oxide-on-metal system can be considered [23]. In the case of a monolayer (ML) thick SiO_2/Mo(1 1 2) oxide, a 0.42 eV increase of the WF is predicted by DFT calculations [81] and an even higher value (0.8 eV) is experimentally observed [82], while 1 ML of MgO on Mo(1 0 0) significantly lowers the WF value. We will discuss the role of this factor in the specific case of polar oxide films, like FeO, where the surface dipole layer associated to the reduced and oxygen-terminated film modulates the WF of the Pt(1 1 1) substrate. At this point we underline that when metal NPs are deposited on an oxide UT film the situation becomes even more complex, because a further metal/oxide interface is generated with consequent charge transfer or polarisation phenomena.

Another interesting phenomenon to be taken into account is the possibility of a direct electron tunnelling via the UT oxide film from the metal substrate to the adsorbed metal NPs. This can happen if the Fermi level (E_F) of the metal single crystal lies above the empty states of the adsorbate [83–85]. The modified charge state determines a profound change on the electronic properties and even the geometry of the supported NPs [86].

Therefore the nature of the metal/oxide interface (relative position of the metal E_F with respect to the band structure of the oxide, interfacial hybridization, possibility of undergoing a polaronic distortion etc.), type of oxide material (degree of covalence/ionicity), thickness of the oxide layer, can be actively used as tools to control the properties of the metal NPs. The modified charge states of the NPs may have a strong effect both on the electronic properties and the geometry of the single NP, but also on their spatial arrangement, due to possible charge induced repulsions between them [83,87,88].

Finally, the local modification of the diffusion barriers landscape on the UT film can play a major role during the self-assembly of the NPs [37]. In this respect, the oxygen-affinity of the adsorbed metals can indeed critically affect the templating behaviour of the UT film, as it will be evidenced in the following.

The previous discussion is clearly valid in the limit of a rigid substrate. This assumption becomes less and less realistic as the temperature is raised. Thermal transformations of the composite

metal-support/oxide-UT-film/deposited-metal systems have been rarely investigated. In one of the few examples [37,89], Au NPs nucleated on the z'-TiO_x/Pt(1 1 1) phase were subjected to gradual heating. A cooperative phase transformation from a rectangular to a hexagonal phase was found to occur at high temperature (600 K), by which the Au NPs did not coalesce, but rearranged their shape and positions together with the more mobile regions of the oxide (see the end of Section 3.1 for more details). Other more complex but fascinating examples of thermal transformations have been very recently discovered for Fe NPs deposited on the same substrate [90].

3.1. Au and Fe nanoparticles on TiO_x/Pt(1 1 1)

Our group has investigated in detail the templating effect of the z'-TiO_x UT film with respect to two different metals, i.e. Au and Fe, as examples of metals with rather different affinity toward oxygen. They were deposited at RT, and the STM images were acquired at the same temperature [36,37].

Fig. 6a shows that starting from the very onset of nucleation no Au adatom or aggregates are found on the oxide stripes (see Section 2.1), and that all Au NPs are pinned inside the *troughs* with a narrow size dispersion. Note that the apparent morphology of the single NP is droplet-like with a 10% elongation along the direction of the *trough,* maintained also at higher coverage. The apparent diffuse glow can be interpreted as due to the overlap of featureless 6s orbitals of the Au atoms. At higher coverage regime (Fig. 6b), the behaviour is not modified, and the fast Fourier transform (FFT) reported in the inset shows that the alignment of the NPs along the *troughs* on the z'-TiO_x phase is preserved. The broader view of the same region, shown in Fig. 6c, confirms the alignment of Au NPs in the oxide *troughs*, which reflects the symmetry of the three equivalent [1 $\bar{1}$ 0] directions of the Pt substrate. Moreover, the coverage increase does not modify the size dispersion of the NP (Fig. 6d).

One can also note that, on uncovered Pt(1 1 1) areas, Au is forming 2D wetting islands, typical of Au/Pt(1 1 1) growth mode [91]. On the basis of these data it has been proposed that the *picoholes* within the *troughs* can act as effective nucleation sites, driving the formation of Au NPs which are ordered along straight lines with the same periodicity of the *troughs*. The highly preferred nucleation in the *troughs* is also demonstrated by an accurate analysis of the location of the NPs close to the step edges: quite unusually, they always appear at the upper rim of the step edge, indicating that nucleation at the step edges itself is highly disfavoured with respect to the one in the *troughs* [36].

Such experimental data find a rational view by considering both thermodynamic data and DFT calculations. The former suggest a low affinity of Au to oxygen. DFT simulations confirm that Au adatoms experience weak adsorption energy (0.1 eV) and a flat diffusion landscape on the oxygen terminated stripes, with a negligible distortion of the oxide film [92]. Actually, at low temperature (LT) a different

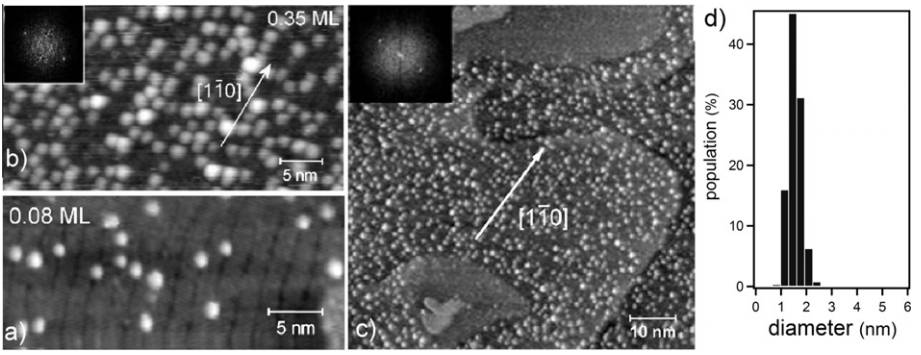

Fig. 6. Au NPs on z'-TiO_x/Pt(1 1 1) UT film: (a) at low coverage (θ = 0.08 ML) (V = +0.6 V, I = 0.6 nA) all NPs are nucleated in the *troughs*; (b) at θ = 0.35 ML, the NPs arrangement into linear arrays following the oxide *troughs* becomes more clear, as shown in the FFT transform of the image in the upper left inset frame; (c) extended view of the region of frame. The orientation of the z'-TiO_x film and of the *troughs* is given with respect to the main Pt(1 1 1) crystal direction [1 $\bar{1}$ 0]; (d) Histogram of the distribution of Au NPs obtained assuming a circular shape. Adapted from Ref. [36].

adsorption regime was identified (see the discussion at the end of this subsection), with a stronger interaction and reconstruction of the oxide film. In any case, diffusion energy barriers are predicted to be below 0.4 eV, and the DFT calculations suggest that, at RT, Au adatoms quickly reach the *picoholes* located along the *troughs* where the adsorption energy is the highest (1.7 eV) [92]. These results validate the hypothesis that the defects of the z'-TiO_x phase are effective as NP nucleation centres, and that the NP ordering is directed by the substrate template, at least for a metal with a low oxygen-affinity such as gold.

The deposition of a more oxygen–affine metal, such as iron ($\Delta H_{f\,Fe-O}$ = 250–300 kJ/mol) yields a different picture. At first sight a large scale STM image (Fig. 7a) shows again nm-sized Fe NPs aligned and pinned in the oxide *troughs* [37]. Portions of Pt(1 1 1) substrate not decorated by the oxide film show the quasi 2D growth of Fe islands [93]. At a more accurate inspection, however, the Fe NPs appear to be less regularly shaped and they exhibit a granular contrast in the STM image (Fig. 7b). This behaviour is already visible in the very low coverage regime (θ = 0.03 ML, (Fig. 7c), where some larger Fe NPs are pinned in the *troughs*, but also smaller particles (adatoms or dimers outlined in the figure) are adsorbed on the stripes [37]. A more careful analysis of the NPs positions indicates that the alignment of the NPs with respect to the *troughs* centre-lines is quite effective for Au NPs but much fuzzier for Fe (see the comparison in Fig. 8). In particular, the reported histograms are obtained by measuring how much every single NP centre is displaced (Δx) with respect to the *trough* centreline, i.e. a quantitative measure of the actual alignment effect along the *troughs*. It is evident that the Au NPs are mostly located within 0.15 nm from the *trough* line, while Fe NPs are much less aligned along the ideal *trough*.

The presence of adsorbate adatoms or tiny aggregates on the oxide stripes is coherent with the high oxygen affinity of Fe. DFT calculations yield substantially higher diffusion barriers for Fe adatoms, from 0.74 to 2.0 eV, depending on the position within the stripe [94]. Though the Fe adsorption energies on the stripes, ranging from 2.2 to 3.5 eV, are higher than those of Au on the same stripe sites, nevertheless, the behaviour of the NP formation is not very different from the Au case, i.e. the *picoholes* are yet the most favoured adsorption sites (4.66 eV) also for the Fe aggregates. In the case of Fe, however, higher adhesion energies of Fe adatoms on the oxygen landscape, terminating the oxide surface, are also associated to a partial oxidation of the adsorbed Fe [95]. The 4s valence electrons of Fe are in fact partially transferred to the oxygens, in analogy with the FeO/Pt(1 1 1) case (see the next subsection). The depletion of electron density from the Fe 4s orbitals means that there are little s electrons to "glue" one metal centre to a neighbouring one, and this is a possible explanation for the apparent granularity of Fe NPs found both in experimental and simulated STM images [94]: the appearance of the granularity of dimers adsorbed on the stripes [37] is outlined in Fig. 7c.

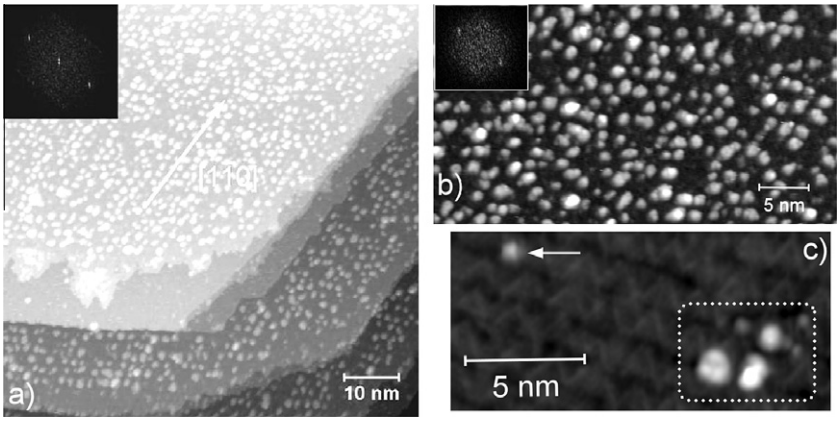

Fig. 7. Fe NPs on z'-TiO_x/Pt(1 1 1): (a) (θ = 0.3 ML, V = −1.61 V, I = 0.25 nA) [16]; (b) a magnified region of frame (a) shows less aligned Fe NPs with more irregular shapes; (c) at the very low coverage θ = 0.03 ML (V = +0.89 V, I = 0.48 nA) one can see granularity of the NPs in the *troughs* (dotted rectangle) and tiny aggregates pinned on the oxygen terminated stripes (white arrow). Adapted from Ref. [37].

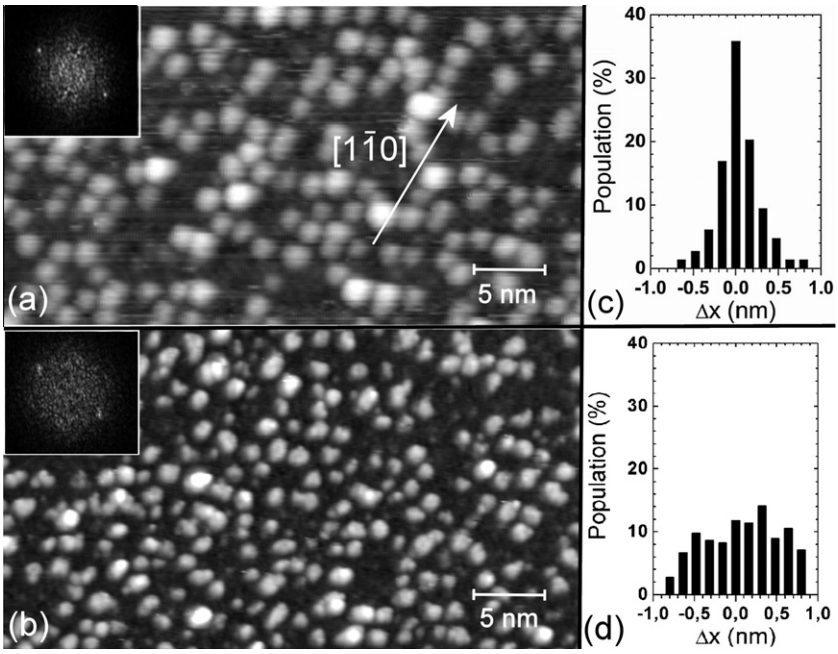

Fig. 8. Constant current STM data of Au and Fe NPs nucleated on the z'-TiO_x phase. (a) θ_{Au} = 0.35 ML, V = 0.6 V, I = 0.6 nA. (b) θ_{Fe} = 0.3 ML, V = −1.6 V, I = 0.25 nA. Panels (c) and (d) show the distributions of the Au and Fe NPs displacements (Δx) from the *trough* axis, in the direction orthogonal to the *trough*, respectively. Adapted from Ref. [37].

Despite these differences, the average NP lateral size and size dispersion are very narrow for both metals: 1.3 ± 0.4 nm for Au and 1.1 ± 0.4 nm for Fe [37]. Kinetic Monte Carlo simulations of metal NPs growth at RT [96] using the values of adsorption energies and diffusion energy barriers derived above, produce a narrow size distribution in fair agreement with experimental data for both Au and Fe NPs, confirming the templating effect of the z'-TiO_x film. They also rationalise the irregular, fractal-like shape of the Fe NPs at higher coverage vs. the homogeneous shape of the Au NPs as a result of kinetic trapping into non-equilibrium configurations [97].

Hence, the adsorption and nucleation of metals on the z'-TiO_x/Pt(1 1 1) film seem to be substantially determined by the interplay between the diffusion barrier landscape and defectivity of the oxide film. The presence of the picoholes is the basic ingredient that drives the ordering of the NPs, thanks to the high adsorption energy, but the long-range order and the shape of the NPs are dictated by the growth kinetics and thus ultimately by the metal affinity to oxygen, which is poor for Au and strong and Fe, respectively.

The role of the defects, i.e. the *picoholes*, in the ordered nucleation of metal NPs observed on the defective z'-TiO_x film is clearly evidenced by the comparison with the adsorption behaviour of the same metals on the flat, non-defective, w'-TiO_x/Pt(1 1 1) UT film [36]. In the w'-TiO_x/Pt(1 1 1) case, a spread of the Au NPs on the substrate is observed (Fig. 9a): the NPs are quite randomly distributed and have a definitely larger size (3.0 nm average versus 1.3 nm, compare Figs. 6d and 9c) with respect to the corresponding z'-TiO_x case. On the contrary, Fe NPs (Fig. 9b), though randomly nucleated on the oxide surface, show a size distribution similar to the one previously found on z'-TiO_x film (Fig. 8d), in agreement with the expected lower mobility of Fe on w'-TiO_x [36,37].

Thence, we can conclude that the ordered array of *picoholes* is an effective template for metals with a low oxygen-affinity, for which weak adsorption and small diffusion barriers do not hamper the path of impinging adatoms toward the *troughs*. The growth of metals more reactive toward oxygen is limited by kinetics, due to the strong interactions and high diffusion barriers on the oxygen landscape on these UT films.

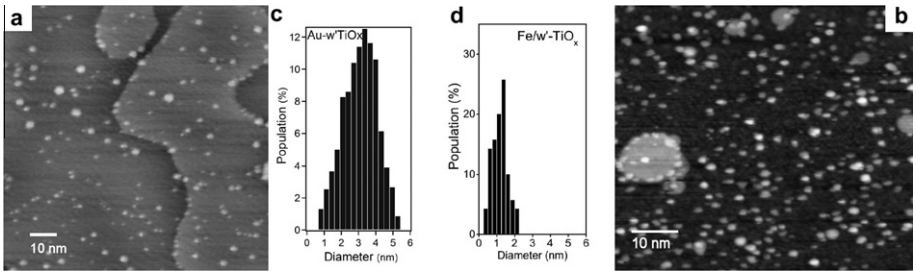

Fig. 9. (a) Au NPs (θ = 0.2 ML, V = 1.5 V, I = 0.2 nA) and (b) Fe NPs (θ = 0.35 ML, V = 1.6 V, I = 0.2 nA) on w'-TiO_x/Pt(1 1 1). Histograms of size dispersion of Au (c) and Fe (d) NPs are shown. Adapted from Ref. [36].

It should be noted however that the situation could change at LT. In particular in the case of Au a reduced mobility could switch the adsorption mode of Au adatoms on the regular TiO_x stripes from a weak to a strong interaction regime. In the latter, a Au adatom is able to extract a Ti ion from the oxide layer and create a Ti–Au bond in which both covalent and ionic components are present [92] and the Au adatom is negatively charged, at variance to the situation in which it is in direct contact with the Pt substrate as in the *picohole* [98]. In this regime, subtle electronic effects associated with the modulation of the surface potential could drive NPs self-organisation also on non-patterned substrates, such as the w'-TiO_x phase. This expectation is actually fulfilled on a different system: the FeO/Pt(1 1 1) phase discussed in the next subsection.

The theoretical prediction is quite different for Fe adatoms, that maximise the coordination with the oxygens, with a preferential adsorption on the O-hollow coordinated sites along the TiO_x stripes. The Ti on-top sites are on the contrary saddles in the diffusion barrier landscape and, due to oxidation, Fe adatoms and particles pinned on the stripes are positively charged [37].

The discussion so far assumes that the substrate is rigid. As already mentioned, thermal transformations of the composite metal-support/oxide-UT-film/deposited-metal systems have been investigated in the case of Au NPs adsorbed on the z'-TiO_x/Pt(1 1 1) phase [36,89]. It was found that the presence of Au NPs nucleated on the *picoholes* along the *troughs* can induce the transformation of the z'-phase into an hexagonal analogue in which every second stripe is shifted by half a horizontal lattice parameter. This reconstruction allows the system to merge two *picoholes* into a single one, thus making more room for the deposited Au atoms. In [89] it was shown that this change is entropically favoured even in the presence of a single Au atom, and becomes also thermodynamically favoured already for small clusters.

3.2. Metal nanoparticles on FeO/Pt(1 1 1)

The FeO/Pt(1 1 1) phase does not exhibit arrays of ordered defects and displays a low surface corrugation, resulting in significant metal adatom mobility at RT. Because of the high mobility of Au adatoms, the adsorption of this metal on the FeO/Pt(1 1 1) system has been investigated via LT STM (5 K) and in a very low coverage regime. We remark that, in clear contrast to the described experiments so far, at this temperature the diffusion coefficients of metal adatoms are extremely low, and single Au atoms or perhaps small aggregates are expected to form upon adsorption.

The FeO UT film shares some structural characters with the above discussed TiO_x films: they are both polar oxygen terminated bilayers where the metal (Fe or Ti) is at the interface with Pt and, as in the w'-TiO_x case, the oxide layer-Pt lattice mismatch gives rise to a Moiré pattern observed in the STM images of the bare oxide surfaces (see Section 2.2). A hard-sphere model of the film predicts that also the surface dipole within the FeO Moiré cell is modulated by the varying Fe–O distance: the largest dipole is expected for Fe atoms bound to Pt hcp hollow sites and O on Pt on-top sites (largest Pt–O distance), while the smallest dipole is expected for Fe on-top and O fcc hollow arrangement. This model of the surface dipole modulations inside the Moiré cell is also confirmed through STM barrier-height and field emission resonance images of the bare FeO film [73].

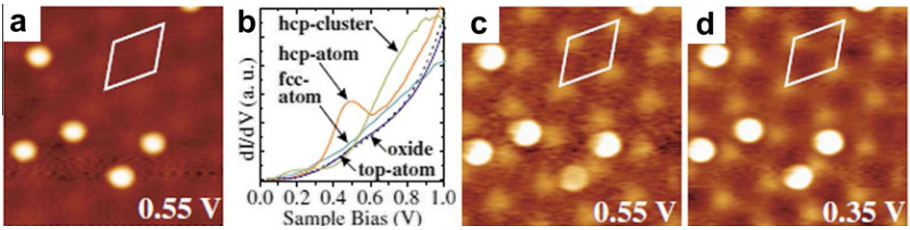

Fig. 10. (a) low temperature STM topographic image of Au adatoms on FeO/Pt(1 1 1) taken at 0.55 V and 0.1 nA. (b) Conductance spectra of bare FeO and Au adatoms bound to different domains of the Moiré cell. (c) Conductance images of the same area as in (a) taken at 0.55 V and (d) 0.35 V. All images are 130 × 130 Å^2 in size. Adapted from Ref. [99].

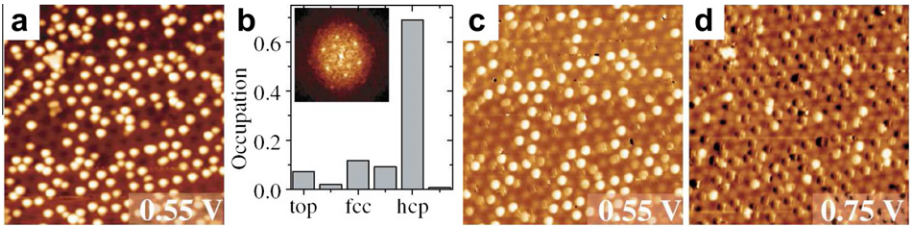

Fig. 11. (a) STM topographic image of Au adatoms on FeO/Pt(1 1 1) taken at 0.55 V and 0.1 nA. (b) Histogram of the occupation probability of different domains in the FeO Moiré cell determined from roughly 700 adatom positions. The inset shows a power spectrum of (a). (c) Conductance images of the same area as in (a) taken at 0.55 V and (d) 0.75 V. The current was set to 0.1 nA. All images are 430 × 430 Å in size. Adapted from Ref. [99].

Differential conductance dI/dV scanning tunnelling spectra (STS) [99] reveal a fingerprint of Au adatoms and aggregates adsorbed on hcp sites, in the form of a resonance located at $V = +0.5$ V bias for adatoms and of a broader feature centred around $V = +0.75$ V bias for larger aggregates (Fig. 10b). Consequently, conductance images acquired at $V = +0.55$ V in the region of Fig. 10a outline an enhanced contrast of Au adatoms adsorbed on hcp regions versus a depressed apparent height of adatoms adsorbed, for example, in fcc sites on the Moiré cell (Fig. 10c), whereas conductance images acquired at $V = +0.35$ V do not show any contrast difference between the adsorbed adatoms (Fig. 10d) (due to the very similar dI/dV spectral features of all objects adsorbed at biases out of the resonance region).

When the nominal coverage reaches roughly 1 Au adatom per Moiré cell ($\theta = 0.012$ ML), LT STM images (see Fig. 11a) show that the adsorbate is self-organised into a hexagonal network. The pitch of this pattern (0.26 nm) corresponds to the period of the Moiré superstructure of the FeO film. The FFT transform of the STM image, reported in the inset frame of Fig. 11b, clearly outlines this long-range ordered pattern of adatoms, even up to the second nearest neighbours. The authors also performed a statistical analysis aimed at finding not only a long-range ordering of the adsorbate monomers and NPs, but also the preferred adsorption sites along the Moiré cell of the FeO film.

The histogram of occupation frequency of adatoms versus cell sites (Fig. 11b) depicts a neat preference for the adsorption of Au atoms on hcp sites (70% probability), in contrast with the value around 10% for all other kinds of adsorption sites. Quite unexpectedly, the conductance images in Fig. 11c and d, that enhance the contrast of adatoms and aggregates, respectively, show a limited coalescence of Au adatoms into larger particles, even at the coverage corresponding to one adatom per Moiré cell. This apparent blocking of the Au aggregation on the FeO film is in sharp contrast to the nucleation behaviour observed on non-polar oxide surfaces, suggesting an effective repulsion between the adatoms [43,100,101].

The self-organisation of Au adatoms preferentially adsorbed on hcp domains of the FeO film has been explained by the interplay of: (i) periodic modulations of the surface potential and dipole in the cell of the Moiré superstructure, (ii) the high electronegativity of Au atoms (2.54 in the Pauling's

scale), to be compared with the values of 1.83 for Fe and 3.44 for O [102]. The adsorption of Au adatoms on the hcp sites of the FeO film can partially decrease the larger surface dipole on these specific regions and locally lower the surface free energy. Such adsorption-induced stabilization mechanism has been observed for other polar oxide surfaces before [38,103,104].

Considering the nature of the adsorption, polarisation mechanisms could be invoked to explain it. However, a simple polarisation of Au adatoms cannot explain the resonance observed at $V = +0.5$ V in the empty states region of the differential conductance STS curves. Such a resonance is more in tune with a charge transfer from the oxide film to adatoms and a hybridization of valence Au 6s electrons with the electronic states of FeO, generating a new bonding and antibonding state in close analogy with the strongly interaction regime of Au adatom adsorption on the compact stripes of TiO_x/Pt(1 1 1) phases discussed in the previous subsection [92]. An analogous antibonding state has already been mapped as a resonance above E_F in the STS spectra of Au adatoms and dimers adsorbed on the NiAl(1 1 0) substrate [105].

The electrostatic repulsion between charged Au atoms can also explain the long-range ordering of Au monomers and the suppressed aggregation into NPs. The self-organisation of the adsorbate driven by the Coulomb repulsion is already known for alkali atoms on metal [106] or semiconductor surfaces [107,108], where adsorption is accompanied by electron transfer from alkali atom to the substrate [109]. A recent review article addresses in detail this point [110]. The adatom interaction on the FeO film is then attributed to either dipole–dipole repulsion in the case that polarisation dominates the Au–FeO bond, or repulsion between negatively charged Au atoms assuming partial electron transfer upon adsorption. This mechanism is not active only on polar UT oxide films. A similar Coulomb repulsion between charged Au adatoms, upon electron tunnelling from the metal substrate through the UT oxide film has been predicted by DFT calculations [83,87] and experimentally observed [88] for Au atoms absorbed on a non polar 3 ML thick MgO(1 0 0)-like film grown on Ag(1 0 0) or Mo(1 0 0) substrates. Such a phenomenon is in any case peculiar to UT oxide layers: charging of deposited neutral Au atoms is nor predicted neither observed on the bulk-terminated MgO(0 0 1) oxide surface, though a polarisation of electronegative Au adatoms occurs [111].

As previously mentioned in Section 2, another driving force for charge transfer is the formation of heterojunctions at the interfaces, both between the oxide film and the metal substrate, and between the oxide film and adsorbed metal adatoms, entailing that the Fermi energies of the bare UT oxide-on-metal and metal adatoms or NPs have to be aligned at the interface. The electrical contact implies several mechanisms like band bending, the rise of a Schottky-like junction at NP-oxide interface [8], possibly stimulating polarisation and charge transfer from or to the adatoms. Also the surface work function of the metal–oxide–metal system will change due to the surface charge redistribution [87].

As already mentioned, the experiments of the adsorption of Au adatoms on FeO [99] were conducted with LT-STM at 5 K, so the diffusion of the adsorbate is expected to be marginal. Nilius and coworkers evaluated also the surface potential landscape felt by Au adatoms and found adsorption energy on hcp sites of FeO of 10 ± 2 meV higher than elsewhere. In addition, they observed that the hexagonal arrangement of Au nano-objects and blocked coalescence of NPs persists up to 50 K. At RT, where the thermal energy is $kT = 25$ meV, hence higher than the calculated diffusion barriers for Au adatoms on the FeO landscape, a very facile diffusion and nucleation of Au into larger NPs along the surface should reasonably be expected.

This hypothesis is confirmed by further STM studies [112,113]. In fact, low coverage deposition of gold at 120 K (and subsequent warming to 300 K for STM measurements) results in decoration of substrate steps and defects of the oxide film, while at increasing coverage small Au clusters of different sizes start to nucleate also on terraces. Fig. 12a indicates that Au NP grow in size by further increasing the deposited Au amount, and at high coverage Au particles are essentially homogeneously and randomly distributed on the FeO surface (Fig 12b). On average, the particle size increases with increasing Au coverage. Such data indicate that substantial Au diffusion is taking place at the surface of the oxide layer as soon as the temperature is raised. This is consistent with the few meV difference in the experimental evaluation of the energy landscape obtained for Au on FeO [99].

The 3D Volmer-Weber growth mode of Au NPs on the FeO/Pt(1 1 1) film is also in good agreement with experimental data on the nucleation at RT of Au on the TiO_x/Pt(1 1 1) films, especially the w'-TiO_x

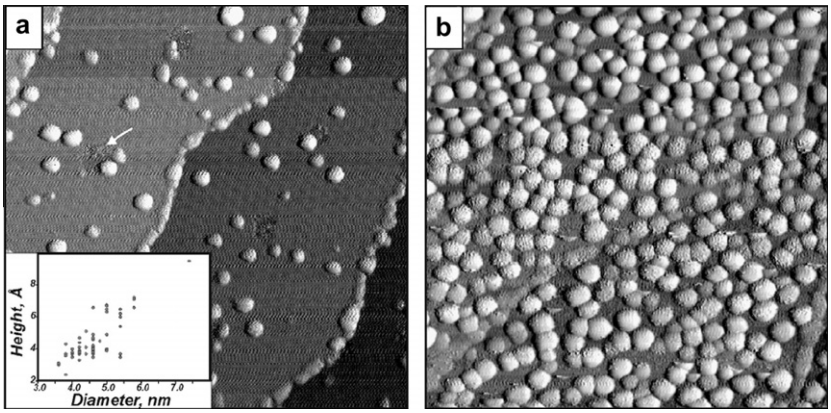

Fig. 12. 100×100 nm^2 STM images of gold particles deposited on an FeO(1 1 1)/Pt(1 1 1) film at 120 K and measured at RT for a nominal Au thickness of (a) 0.2 and (b) 2 Å, respectively. The images are presented with differentiated contrast. White arrows mark the defects of the oxide film, identified as large holes. The inset presents the size distribution of the particles imaged in (a), which show that growing particles keep their aspect ratio. Adapted from Ref. [113].

films. These results are well explained by considering both the low oxygen-affinity of Au and the substantially flat energy landscape that favours surface diffusion of adatoms.

Berdunov and coworkers investigated also the nucleation at small coverage of Fe and V on a FeO/Pt(1 1 1) film [114]: the nominal coverage referred to a (1 1 0) surface of bcc Fe and V are respectively θ_{Fe} = 0.099 ML and θ_V = 0.023 ML. The LEED pattern acquired upon deposition of this Fe amount shows that the structure of the FeO film is not disrupted (Fig. 13c). Fe NPs show a rather narrow size distribution and a partial order in the NPs arrangement is suggested by the FFT transform shown in the inset of Fig. 13a, following the Moiré superstructure with a 2.5–2.6 nm lattice parameter. The degree of the spatial order of Au NPs adsorbed on the FeO film is much sharper than for the Fe adsorbate, as one can deduce from the comparison of the FFT transform of the STM images in Figs. 11b and 13a, but it should be recalled that Fe and V are deposited at RT, while Au is deposited and measured at 5 K. In Fig. 13b the onset of V nucleation is shown. From STM simulations [69] the bright protrusions highlighted by hollow arrows are identified as the hcp sites on the Moiré cell of the FeO film. The unit cell of the superstructure of the film is also outlined (black rhomb). V NPs, pointed by the solid arrows, are pinned where the FeO layer forms fcc stacking sequence with the Pt surface, i.e. the darker regions between the hcp sites [114]. DFT simulations predict only a small difference (about 0.1 eV) for the adsorption sites with hcp and fcc stacking on undistorted FeO layer. However, when a stretching of the oxide layer is allowed, due to the interaction of Fe and V with O, the adsorption energy difference between hcp and fcc sites increases up to 1 eV, and the charge transfer between the Fe and O inside the oxide layer is modified. This indicates that the local distortion due to interaction with oxygen has a greater effect on the metal adatom binding energy than the stacking sequence variations [114], and that when employing a substrate without an ordered array of defects, such as FeO, the role of the metal/oxide interaction becomes more important in the determination of the spatial arrangement of the NP, that can be enhanced even at RT when a more oxygen–affine metal is deposited on the substrate.

The results presented for this UT oxide film, lacking geometrical defects, can be summarised as follows: at LT, for a low oxygen-affine metal (e.g. Au) the residual adatom mobility allows the metal/oxide interaction to trigger the organisation of the NPs by charge transfer and polarisation effects, resulting in an ordered NP array, mainly dictated by the oxide layer geometry that results from the interaction with the supporting substrate metal. At RT, where diffusion is much higher, Au NPs grow in size and result in little or no order on the surface. On the contrary, the higher oxygen-affinity of metals like Fe and V result in an increased diffusion barrier that favours the organisation of the NPs in a quite ordered array.

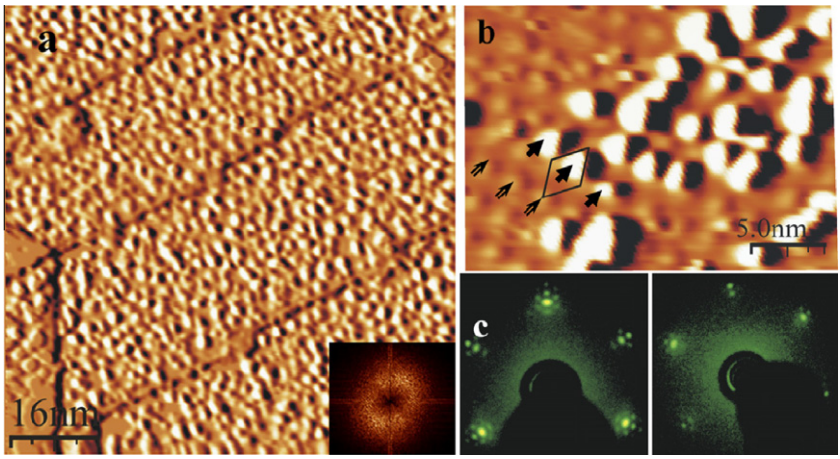

Fig. 13. (a) STM image of 0.2 Å Fe film grown on FeO/Pt(1 1 1) template. NPs of 1 ML thickness nucleate following the long-range surface superstructure of 2.6 nm periodicity. The image is presented in differentiated contrast. 2D Fourier transformation image shows preferred NP's periodicity of 2.6 ± 0.6 nm. (b) Demonstration of 'site selective' nucleation of vanadium NPs (white spots) after depositing a 0.05 Å vanadium film. The smaller corrugation seen on the image is the surface superstructure. Three hollow arrows point out the hcp sites of FeO/Pt(1 1 1) and the solid arrows indicate the vanadium NPs nucleated at fcc sites. Unit cell of FeO/Pt(1 1 1) superstructure is indicated. C) LEED pattern of Au (left) and Fe (right) NP deposited on FeO/Pt(1 1 1). Adapted from Ref. [114].

This behaviour is coherent with the data reported for the TiO_x system. On the w'-TiO_x UT film, which does not present any geometrical defect like FeO, the behaviour of adsorbed metals can be explained considering the higher (Fe) or lower (Au) oxygen-affinity. On the z'-TiO_x layer, which has an ordered array of geometrical defects, the NPs arrangement at RT is partly dictated by the defects and partly by the interaction with oxygen, that modify the surface diffusion barriers for metal adatoms.

3.3. Metal nanoparticles on $AlO_x/Ni_3Al(1\ 1\ 1)$

By far the most studied oxide nanotemplates are UT AlO_x films on metals, and a recent review article has covered the field [41]. In order to compare with the cases reported in the previous subsections, we have chosen the $AlO_x/Ni_3Al(1\ 1\ 1)$ case. This UT film present two types of templating sites: the hexagonal pattern of the "network" structure with a 2.6 nm pitch, and the "dot" structure, having a 4.07 nm pitch, and corresponding to an ordered network of *picoholes* reaching down the $Ni_3Al(1\ 1\ 1)$ substrate (see Section 2.2).

Becker et al. [38] first explored the behaviour of several metals on this AlO_x film, i.e. from noble metals, like Ag, Au and Cu, through Mn toward the most reactive (oxygen–affine) V. STM images of the very early growth of Au and Ag show a preferential pinning of the metal NPs into the "dot" structure. These data suggest that preferential nucleation occurs in the *picoholes*, like on the z'-TiO_x film above discussed. However, when larger amounts of Au or Ag are deposited, coalescence of NPs occurs and there is no further evidence of ordered spacing of the NPs related to the oxide substrate "dot" structure (see Fig. 14a). Also tip induced mobility of Ag NPs was observed, suggesting weak metal/oxide film interactions. These observations are again in tune with the fact that the low oxygen-affinity of the noble metals plays a definite role in affecting the formation and ordering of NP arrays. The weak adhesion to the *picohole* nucleation centres of Ag and Au NPs can also be explained in terms of a size effect. It can in fact be recalled that the interaction of Au with the z'-TiO_x/Pt(1 1 1) *picohole* presents a double-well energy profile [92], with a first shallower energy minimum (interaction energy of 1.4 eV) at a larger distance from and a negligible reconstruction of the oxide slab, and a second deeper energy minimum (interaction energy of 1.7 eV) at a closer distance from and with a more substantial

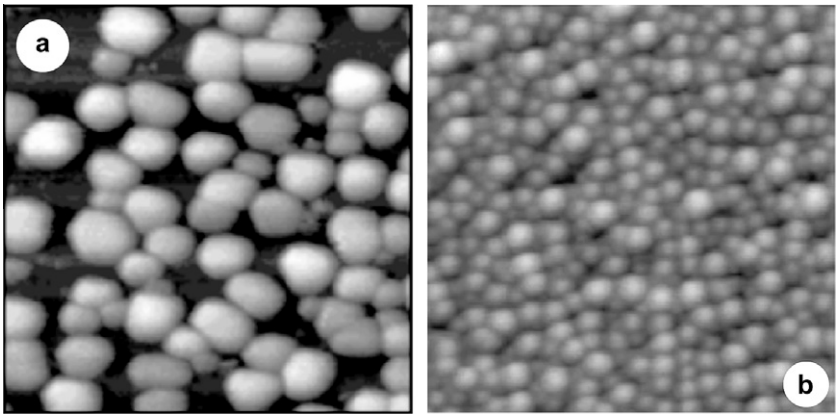

Fig. 14. Au (a) and Cu (b) NPs on $AlO_x/Ni_3Al(1\,1\,1)$. Size of the frames is 60×60 nm^2 and 72×72 nm^2, respectively. Adapted from Ref. [38].

reconstruction of the oxide UT film. The large extension of the Au electronic wave function is responsible for this behaviour. It can be recalled in this connection that this is also the first source of the thermal phase transformation induced by Au adsorption as discussed in the previous subsection [89]. It may be expected that the $AlO_x/Ni_3Al(1\,1\,1)$ oxide film, being a bilayer, is structurally less flexible than the single layer TiO_x phase and does not allow such a reconstruction, thus limiting the templating characters of this phase with respect to Au or Ag nucleation.

When Cu is deposited on the AlO_x film, initial nucleation on the "dot" structure is found, as in the case of Ag and Au, confirming that the growth is governed by the topographic features of the "dot" structure, i.e. the *picoholes*. However, in contrast to the Au and Ag growth mode, at higher coverages more ordered and size controlled Cu NPs are grown, following the periodicity of the "dot" structure (see Fig. 13b), while the coalescence into larger NPs is not observed. Such a behaviour suggests that in this case metal-defect interaction is dictating the NP formation and the degree of ordering of the NPs array. The difference with respect to the Ag and Au case can be explained by thinking that that the smaller Cu atoms can be better accommodated inside the *picoholes* of the "dot" structure with respect to the larger Ag and Au atoms without a significant and energetically expensive structural reconstruction. The trend toward effective templating action is confirmed by the experimental data obtained by depositing metals with higher oxygen-affinity, like Mn, Fe and V, on the AlO_x oxide layer (see Fig. 15 from left to right) [38,79,115,116]. Improved long-range order and size control in the NPs pattern and shape is associated with the increasing metal/oxide interaction of the adatoms.

The adsorption of more reactive metals [79] outlines also a new feature, deduced from the analysis of the radial distribution function of the nearest-neighbour NPs, especially for the most reactive V metal: the appearance of another pattern in the NPs spacing, an hexagonal mesh with a 2.6 nm periodicity. This pitch indicates a clear relation to the "network" structure of the underlying UT AlO_x film.

In the case of Fe adsorption, in spite of the apparently disordered nucleation (Fig. 15b), the pattern related to the "network" structure is still observed in the FFT of the STM data (inset of Fig 14b) [38,116]. This observation is explained by the presence of random defects, acting as trapping centres for Fe, located close to the threefold sites of the bare AlO_x film (triangles in Fig. 5a and d) [39], and observed in the STM images at positive biases like bright protrusions near threefold oxide sites. Therefore the Fe NPs arrangement is only affected in term of higher background in the FFT, while the hexagonal structure is still visible. This effect is much less pronounced for Co, that nucleates only in the "network" structure sites with a more ordered arrangement [39,82]. The threefold sites and the point defects occurring close to these sites on the compact regions of the AlO_x film can thus act as trapping centres for more oxygen–affine elements such as Fe < Co < V.

The case of vanadium is particularly interesting, since the deposition of this metal at 550 K results in an almost perfect arrangement of the NPs on the "network" structure sites, with a degree of order

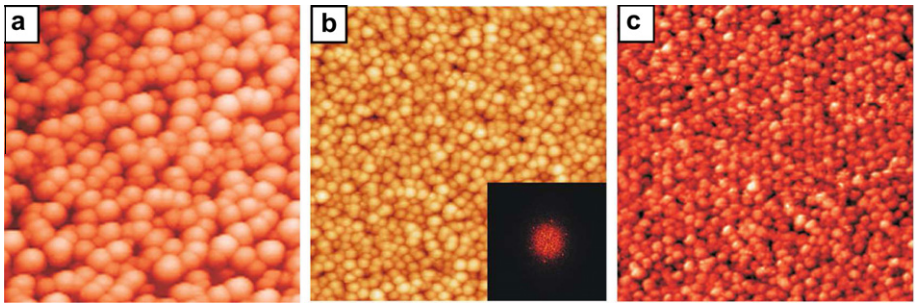

Fig. 15. 68 × 68 nm^2 STM images of (a) Mn (V = 0.7 V, I = 0.11 nA), (b) Fe (V = 0.7 V, I = 0.078 nA) and (c) V (V = 0.7 V, I = 0.33 nA) NPs on AlO_x/Ni_3Al(1 1 1). Inset of frame (b) is the FFT of the image, outlining the honeycomb-like arrangement of the NPs, with a 2.4 nm pitch. Adapted from Refs. [38,115,116].

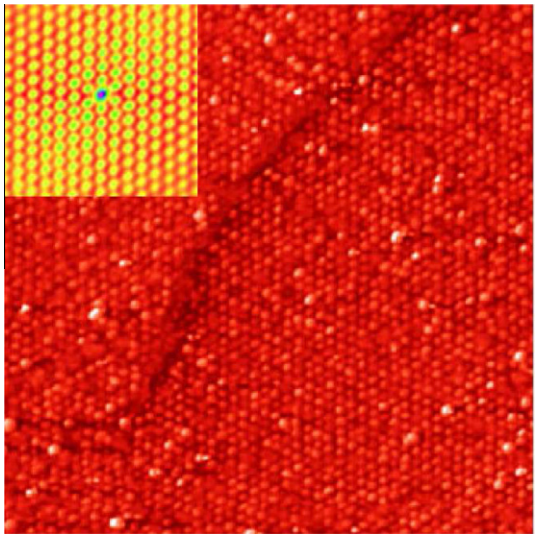

Fig. 16. (a) STM image (V = 0.7 V, I = 100 pA) of V NPs on AlO_x/Ni_3Al(1 1 1) grown at a substrate temperature of Tsub = 550 K. The image size is 125 nm × 125 nm^2. Inset: autocorrelation function of the image Adapted from Ref. [38].

much higher than that obtained at RT (Fig. 16). This observation is clearly related to the role played by kinetics in determining the actual structure of the metal film, through the different diffusion barriers that the adatoms and/or NPs are experiencing on the oxide layer in analogy with a similar behaviour of Co [79].

The deposition of Pd on the AlO_x/Ni_3Al(1 1 1) film, has also been thoroughly investigated. In this case it is possible to obtain a hexagonal array of size selected NPs, simply because the heterogeneous nucleation of metal nuclei on the "dot" structure is energetically very favoured. It has also been demonstrated that a careful tuning of temperature and flux of incoming metal atoms is of pivotal importance to obtain a good order of the metal NPs [117]. The d^{10} electronic configuration of the Pd atom, implying a low interaction with the oxygen ions and a small atomic size [68], allows one to rationalise the strong adsorption in the *picoholes* [39], in complete analogy with the behaviour on the z'-TiO_x/Pt(1 1 1) phase [92].

Taking the cue from the basic knowledge gained in these studies, more complex systems like array of bimetallic NPs have been tackled. Hamm et al. used a two-step procedure to grow ordered PdAu bimetallic NPs [118]: in the first step, Pd is deposited on the "dot" structure so that an ordered

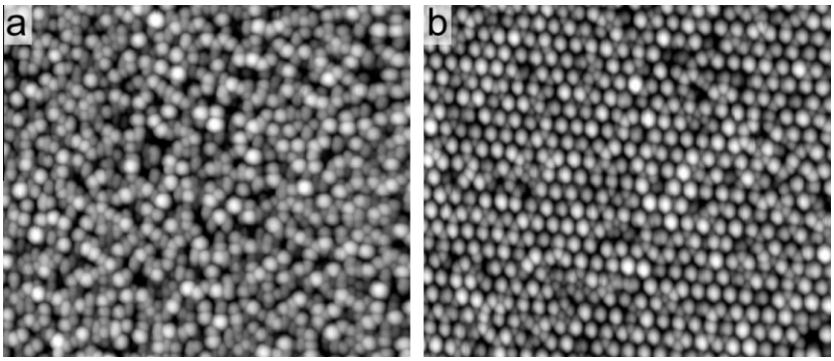

Fig. 17. STM images (80 nm wide) after deposition of 1 Å of Fe (a) without and (b) with predeposition of a 0.03 Å Pd seed layer. Adapted from Ref. [39].

arrangement of stable nuclei is obtained; in the second step, Au is evaporated on top of this seeding layer. The incoming atoms are then captured by the NPs formed during the first deposition, before they have time to nucleate any pure single metal NP [118]. This same procedure based on sequential deposition has been adopted to grow Fe–Pd [39] and Co–Pd bimetallic NPs [79].

The latter study, supported by DFT calculations [39], suggested a rationale for a good templating effect: the key factor is associated to the possibility of single atoms to have an easy access to the *picoholes* that constitute the "dot" structure. A kind of Ehrlich–Scwoebel barrier has been invoked [39] preventing atoms like Fe or Co to jump into the hole, which is energetically the most favourable nucleation site, even though more complicated mechanisms, such as penetration inside the defect and closure of the *picohole* could also be thought of. Accordingly they nucleate on less favourable sites of the oxide such as the threefold sites or the random defects (Fig. 17a). On the contrary, in the case of Pd the diffusion barrier almost vanishes and indeed this hole has quite a large capture radius (0.4 nm) (Fig. 17b).

The situation discussed in this subsection is different as compared to the case of Fe deposited on the z'-TiO_x phase [37], since in the latter case Fe finds a number of adsorption sites on the stripes that increase the diffusion barriers, resulting in the nucleation of the adatoms either on the stripes or inside the *picoholes*. At variance with the TiO_x/Pt(1 1 1) case, Fe adatoms on the AlO_x film are able in most cases to reach the defects at RT, implying that Fe adsorption on this substrate must be substantially weaker [79], while the fact that no thermal transformation is observed up to 600 K entails that the AlO_x film is structurally more rigid than its TiO_x counterpart. The presence of favourable adsorption sites on the regular stripes of the TiO_x phases is also in agreement with the fact that the Fe NPs on these phases are irregular and grainy, while on the AlO_x phase they present a regular shape, even in the absence of Pd pre-seeding [79]. It is unfortunate (but perhaps not surprising in view of the huge size of the unit cell) that, despite the interest of the AlO_x substrate as a nanopatterned surface, only one DFT study is available in the literature on the topic of metal adsorption on it [39].

In summary, the examples discussed in this subsection indicate that a good templating substrate should indeed posses nucleation sites that are geometrical in nature, but the data also show that these sites are effective in templating metal NPs if the energy landscape for surface diffusion of metal, in part determined by the oxygen-affinity, allows the diffusing species to actually reach the most energetically favourable adsorption sites and if these are able to effectively trap the metal NPs. Moreover, the layer stiffness with respect to modifications induced by the metal wavefunctions to allow accommodation of adatoms in the geometrical defects should also be taken into account to explain the behaviour of such a double layer system.

4. Conclusions

In this work we have discussed some significant examples of directed-assembling of transition metals on ultrathin oxide layers grown on single crystal metal surfaces acting as nanopatterned

surfaces. Different factors contribute to the formation of ordered arrays of metal NPs on such systems, determining the effectiveness of the oxide layer as a template: the presence of topographical defects (e.g. the *picoholes*) and their effectiveness as trapping centres, the metal/oxygen-affinity of the adsorbed metal, and the diffusion barrier landscape of the metal adatoms.

For low oxygen–affine metals (e.g. Au), two regimes can be distinguished, depending on the deposition temperature. At RT, the assembling is usually directed by the presence of geometrical defects, since the diffusion energy barriers are unable to limit the adatom diffusion at the surface, and the *picoholes* can accommodate in most cases even large adatoms as Au, with the $AlO_x/Ni_3Al(1\,1\,1)$ phase representing a borderline case. At LT, the templating effects can again be dictated by the structure of the film, but mediated by the surface potential of and the charge transfer from/to the ultrathin system, that allows the self-organisation of the adatoms inside the layer unit cell. For high oxygen–affine metals (e.g. Fe, V) the diffusion barriers play a major role in the resulting organisation of the metal NPs. In fact on a UT film with geometrical defects depending on the deposition conditions (temperature, flux) not all the metal adatoms do reach the lowest-energy adsorption sites, the *picoholes*, as part of them get trapped on other favourable adsorption sites resulting in a less ordered array. When topographical defects are not present, it is the oxygen-affinity that becomes the most important factor.

The most complicated case is represented by the AlO_x film on $Ni_3Al(1\,1\,1)$, characterised by the presence of three different types of defects (only two of which are regularly distributed on the surface), by a higher stiffness with respect to structural rearrangement of the oxide layer, and by a decreased metal/oxide interaction (due to the high chemical affinity between Al and O [79]) likely leading to smaller diffusion energy barriers. In practice, although for a low oxygen–affine metal (Au) the geometrical defects can act as trapping sites, this effect is limited by the size of the Au adatoms, resulting in a less ordered system, while this is less evident for smaller metals such as Cu. When more reactive metals are deposited, the resulting order is increased, due to the increased importance of diffusion barriers and nucleation on other type of defects present in the AlO_x unit cell. However, when diffusion is enhanced by increasing the deposition temperature, a very good templating effect following the geometrical defects is observed, as metal atoms can de-trap from the more weakly interacting nucleation centres, indicating that also this system follows the previously mentioned main driving factors for templating metal adsorption.

Acknowledgements

This work was supported by the project "Sviluppo di Film Fotocatalitici Nanostrutturati" of the CARIPLO foundation, by the University and Research (MIUR) through the program PRIN 2005 and 2006, and by the University of Padova, through the grant CPDA071781 and the Progetto Strategico PLATFORMS (PLAsmonic nano-Textured materials and architectures FOR enhanced Molecular Sensing). AF acknowledges financial support from the SEPON project within the ERC-AG programme and computational support at CINECA supercomputing centre within an agreement with Italian CNR and the ISCRA initiative.

References

[1] E. Ozbay, Science 311 (2006) 189–193.
[2] C. Desvaux, C. Amiens, P. Fejes, Ph. Renaud, M. Respaud, P. Lecante, E. Snoeck, B. Chaudret, Nat. Mater. 4 (2005) 750–753.
[3] A.T. Bell, Science 299 (2003) 1688–1691.
[4] M.C. Daniel, D. Astruc, Chem. Rev. 104 (2004) 293–346.
[5] P.K. Jain, X. Huang, I.H. El-Sayed, M.A. El-Sayed, Acc. Chem. Res 41 (2008) 1578–1586.
[6] M.S. Chen, D.W. Goodman, Science 306 (2004) 252.
[7] D.V. Talapin, J.-S. Lee, M.V. Kovalenko, E.V. Shevchenko, Chem. Rev. 110 (2010) 389–458.
[8] Q. Fu, T. Wagner, Surf. Sci. Rep. 62 (2007) 431–498.
[9] C.R. Henry, Prog. Surf. Sci. 80 (2005) 92–116.
[10] M. Bowker, Surf. Sci. 603 (2009) 2359–2362.
[11] F. Ernst, Mater. Sci. Eng. R14 (1995) 97–156.
[12] S.J. Tauster, S.C. Fung, J. Garten, J. Am. Chem. Soc. 100 (1978) 170–175.
[13] G.M. Schwab, Electronics of supported catalysts, Advances in Catalysis, Vol. 27, Academic Press, London, 1978.
[14] G.L. Haller, D.E. Resasco, Adv. Catal. 36 (1989) 173–235.
[15] O. Dulub, W. Hebenstreit, U. Diebold, Phys. Rev. Lett. 84 (2000) 3646–3649.

[16] G.L. Haller, J. Catal. 216 (2003) 12–22.
[17] C.G. Vayenas, S. Brosda, C. Pliangos, J. Catal. 216 (2003) 487–504.
[18] D.W. Goodman, Catal. Lett. 99 (2005) 1–4.
[19] Q. Fu, T. Wagner, S. Olliges, H.D. Carstanjen, J. Phys. Chem. B 109 (2005) 944–951.
[20] S.J. Tauster, S.C. Fung, R.T.K. Baker, J.A. Horsley, Science 211 (1981) 1121–1125.
[21] R.A. Bennett, C.L. Pang, N. Perkins, R.D. Smith, P. Morrall, R.I. Kvon, M. Bowker, J. Phys. Chem. B 106 (2002) 4688–4696.
[22] S. Bernal, J.J. Calvino, M.A. Cauqui, J.M. Gatica, C.L. Cartes, J.A.P. Omil, J.M. Pintado, Catal. Today 77 (2003) 385–406.
[23] H.J. Freund, G. Pacchioni, Chem. Soc. Rev. 37 (2008) 2224–2242.
[24] N. Nilius, Surf. Sci. Rep. 64 (2009) 595–659.
[25] K.J.M. Bishop, C.E. Wilmer, S. Soh, B.A. Grzybowski, Small 5 (2009) 1600–1630.
[26] S.A. Claridge, A.W. Castleman Jr., S.N. Khanna, C.B. Murray, A. Sen, P.S. Weiss, ACS Nano. 3 (2009) 244–255.
[27] O.D. Velev, S. Gupta, Adv. Mater. 21 (2009) 1897–1905.
[28] G.H. Chan, J. Zhao, E.M. Hicks, G.C. Schatz, R.P. Van Duyne, Nano Lett. 7 (2007) 1947–1952.
[29] L. Wang, X. Shi, N.N. Kariuki, M. Schadt, G.R. Wang, Q. Rendeng, J. Choi, J. Luo, S. Lu, C.J. Zhong, J. Am. Chem. Soc. 129 (2007) 2161–2170.
[30] R. Garcia, R.V. Martinez, J. Martinez, Chem. Soc. Rev. 35 (2006) 29.
[31] M. Grzelczak, J. Vermant, E.M. Furst, L.M. Liz-Marzan, ACS Nano. 4 (2010) 3591–3605.
[32] C. Lee, A.L. Barabási, Appl. Phys. Lett. 73 (1998) 2651–2653.
[33] H. Brune, Surf. Sci. Rep. 31 (1998) 121–229.
[34] C. Becker, K. Wandelt, Top. Curr. Chem. 287 (2009) 45–86.
[35] J.V. Barth, G. Costantini, K. Kern, Nature 437 (2005) 671–679.
[36] F. Sedona, S. Agnoli, M. Fanetti, I. Kholmanov, E. Cavaliere, L. Gavioli, G. Granozzi, J. Phys. Chem. C 111 (2007) 8024–8029.
[37] E. Cavaliere, I. Kholmanov, L. Gavioli, F. Sedona, S. Agnoli, G. Granozzi, G. Barcaro, A. Fortunelli, Phys. Chem. Chem. Phys. 11 (2009) 11305–11309.
[38] C. Becker, A. Rosenhahn, A. Wiltner, K. von Bergmann, J. Schneider, P. Pervan, M. Milun, M. Kralj, K. Wandelt, New J. Phys. 4 (2002) 75.
[39] M. Schmid, G. Kresse, A. Buchsbaum, E. Napetschnig, S. Gritschneder, M. Reichling, P. Varga, Phys. Rev. Lett. 99 (2007) 196104.
[40] Q.H. Wu, A. Fortunelli, G. Granozzi, Int. Rev. Phys. Chem. 28 (2009) 517–576.
[41] Q.H. Wu, Curr. Nanosci. 5 (2009) 58–68.
[42] R.M. Lambert, G. Pacchioni (Eds.), Chemisorption and Reactivity on Supported Clusters and Thin Films, NATO ASI Series, Series E: Applied Sciences, Vol. 331, Kluwer, 1997.
[43] M. Baumer, H.J. Freund, Prog. Surf. Sci. 61 (1999) 127–198.
[44] S.A. Chambers, Surf. Sci. Rep. 39 (2000) 105–180.
[45] S. Surnev, M.G. Ramsey, F.P. Netzer, Prog. Surf. Sci. 73 (2003) 117–165.
[46] S. Schintke, W.D. Schneider, J. Phys. Condens. Matter 16 (2004) R49–R81.
[47] M.S. Chen, D.W. Goodman, J. Phys. Condens. Matter 20 (2008) 264013.
[48] H.J. Freund, Surf. Sci. 601 (2007) 1438–1442.
[49] J. Goniakowski, F. Finocchi, C. Noguera, Rep. Prog. Phys. 71 (2008) 016501.
[50] D.K. Fork, J.M. Phillips, R. Ramesh, R.W. Wolf, Epitaxial oxide thin films and heterostructures, Mat. Res. Soc. Symp. Proc. 341 (1994).
[51] J.S. Speck, D.K. Fork, R.W. Wolf, T. Shiosaki, Epitaxial oxide thin films II, Mat. Res. Soc. Symp. Proc. 401 (1995).
[52] G. Granozzi, H.J. Freund, S. Chambers (Eds.), E-MRS Spring Conference Proceedings, Thin Sol. Films 400 (2001) 1–8.
[53] R. Franchy, Surf. Sci. Rep. 38 (2000) 199–294.
[54] J. Schoiswohl, S. Surnev, F.P. Netzer, Top. Catal. 36 (2005) 91–105.
[55] J. Schoiswohl, M. Sock, Q. Chen, G. Thornton, G. Kresse, M.G. Ramsey, S. Surnev, F.P. Netzer, Top. Catal. 46 (2007) 137–149.
[56] S. Surnev, L. Vitali, M.G. Ramsey, F.P. Netzer, G. Kresse, J. Hafner, Phys. Rev. B 61 (2000) 13945–13954.
[57] J. Schoiswohl, G. Kresse, S. Surnev, M. Sock, M.G. Ramsey, F.P. Netzer, Phys. Rev. Lett. 92 (2004) 206103.
[58] F.P. Netzer, Surf. Rev. Lett. 9 (2002) 1553–1563.
[59] J. Schoiswohl, M. Sock, S. Eck, S. Surnev, M.G. Ramsey, F.P. Netzer, G. Kresse, Phys. Rev. B 69 (2004) 155403.
[60] J. Schoiswohl, S. Surnev, M. Sock, S. Eck, M.G. Ramsey, F.P. Netzer, G. Kresse, Phys. Rev. B 71 (2005) 165437.
[61] F. Sedona, G.A. Rizzi, S. Agnoli, F.X. Llabrés i Xamena, A. Papageorgiou, D. Ostermann, M. Sambi, P. Finetti, K. Schierbaum, G. Granozzi, J. Phys. Chem. B 109 (2005) 24411.
[62] G. Barcaro, S. Agnoli, F. Sedona, G.A. Rizzi, A. Fortunelli, G. Granozzi, J. Phys. Chem. C 113 (2009) 5721.
[63] F. Sedona, M. Eusebio, G.A. Rizzi, G. Granozzi, D. Ostermann, K. Schierbaum, Phys. Chem. Chem. Phys. 7 (2005) 697.
[64] S. Altieri, L.H. Tjeng, G.A. Sawatzky, Thin Sol. Films 400 (2005) 9–15.
[65] G. Barcaro, I.O. Thomas, A. Fortunelli, J. Chem. Phys. 132 (2010) 124703.
[66] F. Sedona, G. Granozzi, G. Barcaro, A. Fortunelli, Phys. Rev. B 77 (2008) 115417.
[67] F. Sedona, S. Agnoli, G. Granozzi, J. Phys. Chem. B 110 (2006) 15359–15367.
[68] S. Ulrich, N. Nilius, H.-J. Freund, U. Martinez, L. Giordano, G. Pacchioni, Surf. Sci. 603 (2009) 1145–1149.
[69] H.C. Galloway, P. Sautet, M. Salmeron, Phys. Rev. B 54 (1996) R11145–R11148.
[70] S.K. Shaikhutdinov, R. Meyer, D. Lahav, M. Baümer, T. Klüner, H.-J. Freund, Phys. Rev. Lett. 91 (2005) 076102.
[71] M. Ritter, W. Ranke, W. Weiss, Phys. Rev. B 57 (1998) 7240–7251.
[72] Y.J. Kim, C. Westphal, R.X. Ynzunza, H.C. Galloway, M. Salmeron, M.A. Van Hove, C.S. Fadley, Phys. Rev. B 55 (1997) R13448–R13451.
[73] E. Rienks, N. Nilius, H.P. Rust, H.J. Freund, Phys. Rev. B 71 (2005) 241404.
[74] U. Bardi, A. Atrei, G. Rovida, Surf. Sci. 239 (1990) L511–L516.
[75] S. Degen, A. Krupski, M. Kralj, A. Langner, C. Becker, M. Sokolowski, K. Wandelt, Surf. Sci. 576 (2005) L57–L64.
[76] S. Degen, C. Becker, K. Wandelt, Faraday Discuss. 125 (2004) 343.
[77] E. Vesselli, A. Baraldi, S. Lizzit, G. Comelli, Phys. Rev. Lett. 104 (2010) 046102.

[78] T. Maroutian, S. Degen, C. Becker, K. Wandelt, R. Berndt, Phys. Rev. B 68 (2003) 155414.
[79] A. Buchsbaum, M. De Santis, H.C.N. Tolentino, M. Schmid, P. Varga, Phys. Rev. B 81 (2010) 115420.
[80] M. Sterrer, M. Yulikov, E. Fischbach, M. Heyde, H. Rust, G. Pacchioni, T. Risse, H.J. Freund, Angew. Chem. Int. Ed. 45 (2006) 2630–2632.
[81] L. Giordano, D. Ricci, G. Pacchioni, P. Ugliengo, Surf. Sci. 584 (2005) 225–236.
[82] S. Wendt, E. Ozensoy, T. Wei, M. Frerichs, Y. Cai, M.S. Chen, D.W. Goodman, Phys. Rev. B 72 (2005) 115409.
[83] J. Repp, G. Meyer, F.E. Olsson, M. Persson, Science 305 (2004) 493.
[84] G. Pacchioni, L. Giordano, M. Baistrocchi, Phys. Rev. Lett. 94 (2005) 226104.
[85] H. Gronbeck, J. Phys. Chem. B 110 (2006) 11977.
[86] D. Ricci, A. Bongiorno, G. Pacchioni, U. Landman, Phys. Rev. Lett. 97 (2006) 036106.
[87] L. Giordano, G. Pacchioni, Phys. Chem. Chem. Phys. 8 (2006) 3335–3341.
[88] M. Sterrer, T. Risse, M. Heyde, H.P. Rust, H.J. Freund, Phys. Rev. Lett. 98 (2007) 206103.
[89] G. Barcaro, A. Fortunelli, G. Granozzi, F. Sedona, J. Phys. Chem. C 113 (2009) 1143–1146.
[90] 90 E. Cavaliere, L. Artiglia, G. Barcaro, G. A. Rizzi, F. Bondino, A. Fortunelli,L. Gavioli, G. Granozzi, submitted.
[91] S. Ogura, K. Fukutani, M. Matsumoto, T. Okano, M. Okada, T. Kawamura, Phys. Rev. B 73 (2006) 125442.
[92] G. Barcaro, A. Fortunelli, G. Granozzi, Phys. Chem. Chem. Phys. 10 (2008) 1876.
[93] D. Repetto, T.Y. Lee, S. Rusponi, J. Honolka, K. Kuhnke, V. Sessi, U. Starke, H. Brune, P. Gambardella, C. Carbone, A. Enders, K. Kern, Phys. Rev. B 74 (2006) 054408.
[94] G. Barcaro, A. Fortunelli, J. Phys. Chem. A 113 (2009) 14860–14866.
[95] L. Artiglia, E. Cavaliere, G.A. Rizzi, L. Gavioli, G. Granozzi, J. Phys. Chem. Lett. 1 (2010) 1660–1665.
[96] G. Barcaro, A. Fortunelli, F. Nita, R. Ferrando, Phys. Rev. Lett. 95 (2005) 246103.
[97] A.L. Barabasi, H.E. Stanley, Fractal Concepts in Surface Growth, University of Cambridge, New York, 1995.
[98] G.A. Rizzi, F. Sedona, L. Artiglia, S. Agnoli, G. Barcaro, A. Fortunelli, E. Cavaliere, L. Gavioli, G. Granozzi, Phys. Chem. Chem. Phys. 11 (2009) 2177–2185.
[99] N. Nilius, E.D.L. Rienks, H.P. Rust, H.J. Freund, Phys. Rev. Lett. 95 (2005) 066101.
[100] S.C. Street, C. Xu, D.W. Goodman, Ann. Rev. Phys. Chem. 48 (1997) 43–68.
[101] G. Haas, A. Menck, H. Brune, J.V. Barth, J.A. Venables, K. Kern, Phys. Rev. B 61 (2000) 11105–11108.
[102] F.L. Boca Raton, CRC Handbook of Chemistry and Physics, 81st ed., Chemical Rubber Company Press, 2001.
[103] A. Barbier, C. Mocuta, G. Renaud, Phys. Rev. B 62 (2000) 16056–16062.
[104] O. Dulub, U. Diebold, G. Kresse, Phys. Rev. Lett. 90 (2003) 016102.
[105] N. Nilius, T.M. Wallis, M. Persson, W. Ho, Phys. Rev. Lett. 90 (2003) 196103.
[106] J. Kliewer, R. Berndt, Surf. Sci. 477 (2001) 250–258.
[107] L. Gavioli, M.G. Betti, V. Corradini, M. Sancrotti, Phys. Rev. B 70 (2004) 125317.
[108] L.J. Whitman, J.A. Stroscio, R.A. Dragoset, R.J. Celotta, Phys. Rev. Lett. 66 (1991) 1338–1341.
[109] J. Hebenstreit, M. Heinemann, M. Scheffler, Phys. Rev. Lett. 67 (1991) 1031–1034.
[110] M. Ternes, M. Pivetta, F. Patthey, W.-D. Schneider, Prog. Surf. Sci. 85 (2010) 1–27.
[111] M. Yulikov, M. Sterrer, M. Heyde, H.P. Rust, T. Risse, H.J. Freund, G. Pacchioni, A. Scagnelli, Phys. Rev. Lett. 96 (2006) 146804.
[112] C. Lemire, R. Meyer, S.K. Shaikhutdinov, H.J. Freund, Surf. Sci. 552 (2004) 27–34.
[113] S.H. Shaikhutdinov, R. Meyer, M. Naschitzki, M. Baümer, H.J. Freund, Catal. Lett. 86 (2003) 211–219.
[114] N. Berdunov, G. Mariotto, K. Balakrishnan, S. Murphy, I.V. Shvets, Surf. Sci. 600 (2006) L287–L290.
[115] C. Becker, K. von Bergmann, A. Rosenhahn, J. Schneider, K. Wandelt, Surf. Sci. 486 (2001) L443–L448.
[116] A. Lehnert, A. Krupski, S. Degen, K. Franke, R. Decker, S. Rusponi, M. Kralj, C. Becker, H. Brune, K. Wandelt, Surf. Sci. 600 (2006) 1804–1808.
[117] S. Degen, C. Becker, K. Wandelt, Farad. Discuss. 125 (2004) 343–356.
[118] G. Hamm, C. Becker, C.R. Henry, Nanotechnology 17 (2006) 1943–1947.

NANO LETTERS

LETTER

pubs.acs.org/NanoLett

Interface Effects on the Magnetism of CoPt-Supported Nanostructures

Giovanni Barcaro,[†] Luca Sementa,[†] Fabio R. Negreiros,[†] Riccardo Ferrando,[‡] and Alessandro Fortunelli*[,†]

[†]CNR-IPCF, Istituto per i Processi Chimico-Fisici, Via G. Moruzzi 1, Pisa, I56124, Italy

[‡]Physics Department, Via Dodecaneso 33, Genoa, I16146, Italy

ABSTRACT:

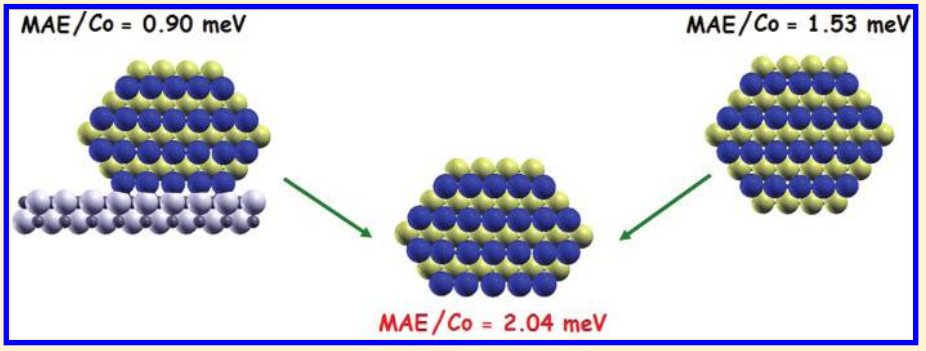

The magnetism of CoPt nanostructures supported on the MgO(100) surface is investigated via first-principles simulations using 1D models. Nanostructures with $L1_0$ chemical ordering and cube-on-cube epitaxy are predicted to possess large magnetic moments and easy magnetization axis perpendicular to the surface. However, their magnetic anisotropy energy is roughly halved with respect to the bulk alloy due to a peculiar mixing of particle and support electronic states. The general factors at play in determining this behavior and the implications of these findings are discussed in view of designing room-temperature magnetic bits.

KEYWORDS: Magnetic anisotropy energy, density functional theory, oxide supports, substrate effect, nanoparticles, nanowires

In the strive for the ultimate limit of miniaturization of memory bits, nanospintronics[1] represents a fascinating path. Magnetic nanostructures bearing a spin unit could be manipulated and exploited in ultrahigh-density recording devices.[2] Two requirements have so far hindered progress in this field: the magnetic anisotropy energy (MAE), that is, the energy barrier to the reorientation of the spin direction, should be large enough to overcome the superparamagnetic regime at room temperature, and for supported particles the easy magnetization axis should preferentially be perpendicular to the substrate surface.[3] CoPt nanoparticles at 1:1 composition in the $L1_0$ ordered phase are promising candidates in this perspective, as the CoPt alloy exhibits among the largest known bulk MAE,[2] so that properly oriented CoPt particles of few thousands of atoms could effectively function as room-temperature memory bits. The environment (such as the support) used to orient the particles however plays a crucial role in determining their structural and electronic features;[4] rigorous knowledge on this topic is available for the case of metal supports[5] but basically lacking for the more interesting oxide ones. Here, we investigate at the first-principles level interfacial effects on the structural and magnetic properties of oxide-supported CoPt nanostructures. We show that $L1_0$-ordered nanostructures with easy magnetization axis perpendicular to the surface can indeed be stabilized on MgO(100), however, at the price of a substantial reduction of the MAE. From this analysis, the general factors at play in determining this behavior are singled out, providing a framework for the design of nanospintronics devices.

For a full understanding and control of the physics of metal/support interface, we focus on a model system: the single-crystal MgO(100) surface as the substrate of CoPt nanostructures. Oxide surfaces are commonly used for the growth of metal nanoparticles and nanoalloys, and the MgO(100) surface is one of the best characterized and is widely used in both model studies and applications.[6] CoPt particles are interesting not only for magnetic[7] but also for catalytic[8] applications. The first issue to be faced when studying the magnetism of metal nanodots concerns the preferred particle structure. It is known in fact that peculiar structural phenomena can occur when reaching the nanoscale regime.[9] In the present case, both experimental evidence for particles embedded in weakly interacting substrates such as amorphous carbon[10] and theoretical simulations for free clusters[11] show that noncrystalline structures are favored for CoPt and FePt particles up to ~3−4 nm in diameter. Interface effects change the situation drastically; for CoPt mixed aggregates deposited on MgO(100), extensive simulations using many-body empirical potentials[12] (see also Methods section) indicate that a transition from noncrystalline (polyicosahedral) supported motifs to face-centered cubic (fcc)-like $L1_0$ configurations with cube-on-cube epitaxy is expected around 1:1 Co/Pt composition when the number of atoms exceeds roughly ~200. A further important structural information is that the

Received: October 3, 2011
Revised: November 14, 2011
Published: November 16, 2011

dx.doi.org/10.1021/nl203449y | *Nano Lett.* 2011, 11, 5542–5547

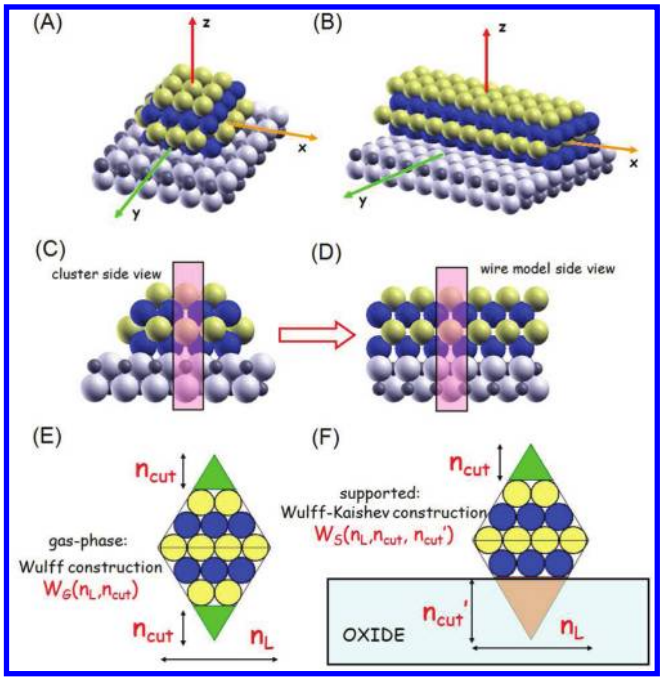

Figure 1. One-dimensional (wire) modeling of supported binary particles. A 0D particle (A) and a side view with its cross-section (C) are shown, together with a piece of the corresponding 1D wire model (B) and a side view with its cross-section (D). The Cartesian axes are also indicated in (A,B). Side views are along *y*-axis. The truncations of a free (E) and supported (F) wire viewed along the *x*-axis are also shown, defining the n_L, n_{cut}, and n_{cut}' quantities, respectively.

lowest-energy $L1_0$ configurations are dominated by the segregation of Co at the interface. This is because the Pt/MgO interaction, which is stronger than the Co/MgO one at low metal coordination (the number of first-neighbor metal atoms), drops abruptly with increasing coordination as Pt/Pt bonds compete with and quickly weaken the Pt/MgO ones, whereas this effect is much less pronounced for Co. Already at coordination number $Z = 4$, the Co/MgO interaction largely surpasses the Pt/MgO one. Co thus preferentially occupies interfacial sites as soon as their coordination is high enough to "quench" the Pt/MgO adhesion.[12] This interfacial effect in turn strongly reinforces the tendency of CoPt particles to $L1_0$ ordering:[11,13,14] the presence of a Co first layer in fact favors the formation of a pure Pt second layer, and so on.

Even assuming an fcc-like $L1_0$ morphology, however, a thorough investigation at the first-principles level of supported particles with a number of atoms between, for example, 200 and 3000 is beyond available computational resources. To overcome this problem, we resort to a 1D modeling,[15] that is, we focus on nanowires (1D systems) and take these as models of 0D nanoparticles with the same cross-section and aspect ratio. In Figure 1A−D, the correspondence between a truncated octahedral 0D cluster supported on a square-symmetry oxide surface to a 1D wire in which the section of the cluster is replicated ad infinitum is shown. Periodic symmetry is exploited to reduce the number of nonequivalent atoms in the unit cell used in the simulations (and also of the degrees of freedom of the system) and correspondingly the computational effort to a manageable size. Through the use of such models, 1D systems with a unit cell of 110−120 atoms can be constructed mimicking 0D particles

Table 1. Excess Energies E_{exe} (in eV) of Selected Suspended and Supported Nanowires[a]

suspended wires	E_{exe}	supported wires	E_{exe}
$W_G(3,0)_{Pt}$	0.94	$W_S(3,0,1)$	1.04
$W_G(3,1)_{Pt}$	1.48	$W_S(3,0,2)$	1.30
$W_G(3,1)_{Co}$	1.05	$W_S(3,1,1)$	1.25
$W_G(4,0)_{Pt}$	0.93	$W_S(4,1,3)$	1.19
$W_G(4,1)_{Pt}$	0.86	$W_S(4,1,2)$	1.01
$W_G(4,1)_{Co}$	1.22		
$W_G(4,2)_{Pt}$	1.57		
$W_G(4,2)_{Co}$	1.01		
$W_G(5,1)_{Pt}$	1.03	$W_S(5,2,2)$	1.19
$W_G(5,2)_{Pt}$	0.75	$W_S(5,2,3)$	1.00
$W_G(5,2)_{Co}$	1.24	$W_S(5,2,4)$	1.26
$W_G(5,3)_{Pt}$	1.65		
$W_G(5,3)_{Co}$	0.97		
$W_G(6,1)_{Pt}$	0.68	$W_S(6,2,3)$	0.98
$W_G(6,3)_{Pt}$	0.67	$W_S(6,3,2)$	0.96
		$W_S(6,3,4)$	1.03
$W_G(7,0)_{Pt}$	0.63	$W_S(7,2,3)$	0.94
$W_G7,2)_{Pt}$	0.56	$W_S(7,2,5)$	1.04
$W_G(8,1)_{Pt}$	0.54	$W_S(8,2,3)$	0.96
$W_G(8,3)_{Pt}$	0.46	$W_S(8,3,4)$	0.92
$W_G(9,2)_{Pt}$	0.37	$W_S(9,2,3)$	0.91
$W_G(9,4)_{Pt}$	0.38	$W_S(9,2,5)$	0.93
		$W_S(9,3,4)$	0.91

[a] The wire nomenclature is explained in the text with the addition that the chemical element composing the largest layer of suspended wires is specified as a subscript (for supported wires this is always Pt).

with 7−8 times this number of atoms, which would otherwise be hardly affordable with present computational facilities. Except for very small particles, this has proven to be an effective tool to enlarge the scope of systems accessible to first-principles simulations.[15]

The lowest-energy wire configurations can then be constructed as follows. For suspended wires, starting from a rhomboidal (octahedral) section, fcc polyhedral sections are obtained by truncating the two outermost vertices, obtaining square (100) planes. A given wire is then characterized by two indexes: n_L, the length of one of the two diagonals of the rhombus (largest layer), and n_{cut}, the number of layers cut at each vertex, and will be denoted as $W_G(n_L, n_{cut})$ in the following, see Figure 1E. For supported wires, a further degree of freedom is given by the truncation at the interface: the number of layers cut in this case will be n_{cut}' and the corresponding wire will be denoted as $W_S(n_L, n_{cut}, n_{cut}')$, see Figure 1F.

For a proper comparison of the energetic stability of 1D systems, the excess energy per unit length (E_{exc}) or wire excess energy can be defined as[16]

$$E_{exc} = \frac{E_{bnd} - N_{Pt}E_{Pt} - N_{Co}E_{Co}}{\sqrt{N_{tot}}} \quad (1)$$

where N_{Pt} and N_{Co} are the number of Pt and Co atoms per unit length (section) of the wire, $N_{tot} = N_{Pt} + N_{Co}$, E_{Pt}, and E_{Co} are the bulk density functional (DF) total energies per atom of pure fcc Pt and hcp Co, respectively, and E_{bnd} is the wire binding energy per unit length, evaluated as the total energy of the

dx.doi.org/10.1021/nl203449y |*Nano Lett.* 2011, 11, 5542–5547

Table 2. Magnetic Moment per Co Atom (m_S) in Bohr Magnetons μ_B and Magnetic Anisotropy Energy per Co Atom (MAE) in meV of Optimal-Shape Suspended and Supported Nanowires (Nomenclature Detailed in the Text)

suspended wire	m_S	MAE	supported wire	m_S	MAE
$W_G(3,0)$	2.00	1.46	$W_S(3,0,1)$	1.88	3.22
$W_G(4,1)$	1.95	0.71	$W_S(4,1,2)$	1.86	4.31
$W_G(5,2)$	1.90	1.16	$W_S(5,2,3)$	1.85	2.41
$W_G(6,3)$	1.94	1.06	$W_S(6,3,2)$	1.85	2.14
$W_G(7,2)$	1.89	1.43	$W_S(7,2,3)$	1.85	1.25
$W_G(8,3)$	1.88	1.53	$W_S(8,3,4)$	1.84	0.90
$W_G(9,2)$	1.88	1.53	$W_S(9,3,4)$	1.85	0.82

wire/support combined system minus the energy of the MgO-(100) support in its equilibrium configuration. The most stable 1D structures correspond to the lowest values of the wire excess energy.

The energetics of selected free and supported nanowires are reported in Table 1. From an analysis of this table, in the gas-phase one observes a transition with increasing wire cross-section from optimal structures exhibiting no truncations [$W_G(3, 0)$] to one [$W_G(4, 1)$] and higher truncations. In particular, for $5 \leq n_L \leq 9$, structures with n_L odd and two truncations [$W_G(5, 2)$; $W_G(7, 2)$; $W_G(9, 2)$] alternate with structures n_L even and three truncations [$W_G(6, 3)$; $W_G(8, 3)$]. For supported wires, one correspondently observes a transition with increasing wire cross-section from structures exhibiting a single overhang [$W_S(3, 0, 1)$; $W_S(4, 1, 2)$; $W_S(5, 2, 3)$], to those exhibiting a triple [$W_S(6, 3, 2)$; $W_S(7, 2, 3)$; $W_S(8, 3, 4)$] and finally a quadruple or quintuple [$W_S(9, 3, 4)$; $W_S(9, 2, 3)$] overhang. Some general rules can be derived. For free nanowires, the outmost (100) layers are always terminated with Pt atoms, which in agreement with experiment[7,17] and results for 0D particles.[11,12] A further preference is for wires with Pt on the largest layer, as it can also be drawn from an analysis of Table 1. The best gas-phase wires thus present odd ($4n + 1$) magic numbers. For supported nanowires, the best truncations are found as a rule by combining the optimal suspended cuts with the simple rule: $n_{cut}' = n_{cut} + 1$. As discussed above, in fact, Co segregation replaces Pt segregation at the interface, entailing that the best supported arrangements are obtained by removing the outmost Pt layer in contact with the substrate. The best supported wires thus present even ($4n$) magic numbers. The only exception to this rule is $W_G(6, 3)$ for which $W_S(6, 3, 2)$ is preferred over $W_S(6, 3, 4)$ [it can be noted that $W_S(6, 2, 3)$ is also very close in excess energy, suggesting that at this size a transition among different morphologies occurs]. This is in tune with the Wulff (for free particles) or Wulff–Kaishev (for supported particles) construction,[6] that is, the optimal shape predicted by proportioning the truncations to the surface[18] and interface (or adhesion)[12] energies. In passing, it can be observed that the mismatch of the wire and substrate lattice parameters induces the development of interfacial dislocations[19] (not shown).

Once the lowest-energy structures have been ascertained, their magnetic properties can be investigated. We recall that in the bulk CoPt alloys at 1:1 composition exhibit a $L1_0$ structure with an a axis of 3.793 Å and a c/a ratio of 0.969,[20] while the MAE is 0.8 meV per Co atom.[2] Our DF approach reasonably reproduces the structural features: the predicted values are 3.829 Å and 0.979 for the a axis and c/a ratio, respectively. The MAE instead is

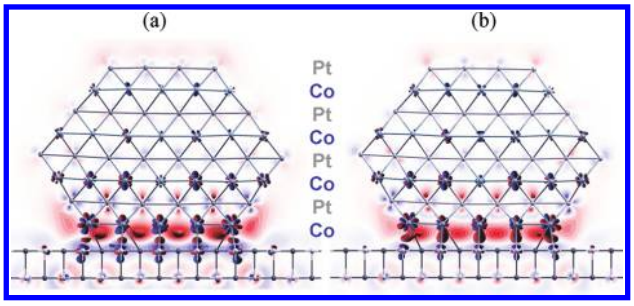

Figure 2. Isocontours of differential electronic density $\Delta\rho = \rho(\text{CoPt/MgO}) - \rho(\text{CoPt}) - \rho(\text{MgO})$, obtained by subtracting the electron density of the MgO(surface) and CoPt(wire) from the total electron density of the $W_S(8,3,4)$ wire. The total density (a) or the minority spin density (b) are shown. The view is taken along the main axis of the wire. Positive values of $\Delta\rho$ (corresponding to an increase in density) are in red. Contour value = 0.004 e/Å^3. Planes of cobalt atoms are displayed in blue, platinum atoms are displayed in dark gray.

1.76 meV per Co atom, that is, it is substantially overestimated. However, we underline that our focus here is on the qualitative trends and features of the effects of the metal/oxide interface on the magnetism of supported nanostructures, which should be correctly singled out by our first-principles approach.

In Table 2, the values of the magnetic moments and the MAE of selected suspended and supported CoPt nanowires are shown. Three main conclusions can be drawn from an analysis of this table. (i) Both free and deposited systems present large magnetic moments; their average values on the Co atoms range around $m_S = 1.9/2.0\ \mu_B$, and are roughly comparable with the bulk value of $m_S = 1.96\ \mu_B$. However, the values for the deposited systems are somewhat smaller than the gas phase, and this decrease is essentially due to the Co atoms at the interface with the MgO-(100) surface which present average m_S values around 1.78/1.80 μ_B. This is already an indication that the particle/oxide interface do play a significant role. (ii) The most stable orientation of the easy-axis of magnetization turns out to be perpendicular to the surface, thus satisfying one of the two main requests for nanospintronics. Note that we did not include in our analysis dipolar interactions among the particles that could also stabilize this magnetization orientation.[21] The second most stable orientation is invariably the one orthogonal to the wire and parallel to the surface. (iii) While the MAE of the free nanowires approaches the DF-predicted bulk value (1.76 meV/Co-atom) with increasing size, the deposited nanowires converge in this size interval to a value which is roughly one-half of the bulk one. This is not a peculiarity of our 1D modeling. The comparison of the MAE of 1D and 0D systems in fact turns out to be reasonable; for example, a $W_S(5, 2, 3)$ nanowire has a MAE per Co atom of 2.4 meV to be compared with 1.4 meV for the corresponding 62 atom $Co_{32}Pt_{30}$ cluster (see the top of Figure 1). The agreement between the two systems is thus already fair for small systems and is expected to become more and more accurate with increasing size (also the geometrical parameters of the interlayer distances and interfacial deformation, not shown, compare favorably). Moreover, this prediction is in tune with available experimental data.[22] The metal/oxide interface is therefore crucial in determining the magnetism of supported CoPt nanostructures and their possible use in applications.

Let us rationalize these findings. In Figure 2, plots of differential electron density due to the adsorption of a CoPt wire onto the MgO(100) support are shown. As clearly evidenced from

dx.doi.org/10.1021/nl203449y |Nano Lett. 2011, 11, 5542–5547

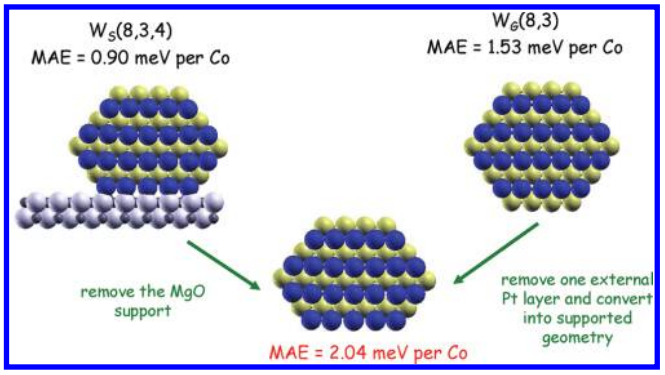

Figure 3. Interface effects on the MAE of CoPt nanostructures.

these plots, a charge transfer from the MgO surface to the CoPt clusters occurs. This is consistent with analogous charge transfer effects that have been described, for example, when MgO slabs are deposited on Ag(100), causing a substantial decrease of the system work function.[23] In the present context, the transferred electrons populate the partially vacant d-orbitals of the Co atoms, in particular the minority spin orbitals, as apparent from a comparison of Figure 2 panel a and panel b, thus explaining the decrease of their magnetic moments in Table 1. In view of tuning interface effects, it should be noted that other oxides with different work function can behave differently, and possibly produce inverse charge transfer effects (a possibility currently under study in our group). The analysis of the MAE is more subtle. First, we checked that the charge transfer from the MgO surface to the CoPt cluster is of similar entity for both directions of the magnetization axis, so that it cannot account for the reduction in the MAE. Second, this reduction is neither due to a geometric (structural reconstruction) effect. On the opposite, the structural relaxation especially of the interface Co layer with the development of interfacial dislocations is beneficial to increase the MAE of the system. In Figure 3, we indeed show that by removing the MgO surface keeping the CoPt configuration frozen and evaluating the MAE of such a hypothetical gas-phase system one find a large increase in the value of the MAE, which turns out to be even larger than that of the corresponding optimal CoPt nanowire. The MAE reduction thus has a different origin. In Figure 4, plots of differential electron density $\Delta\rho$ due to the switching of the magnetization axis from parallel to perpendicular to the surface are shown for both suspended and supported nanowires. A critical inspection of these plots shows first of all that this switching induces a charge flow into the Co and Pt(100) planes (positive value of $\Delta\rho$). For the unsupported wire this charge flow occurs especially in the external or contour atoms while it is much reduced in the interior of the wire. Deposition onto the surface appreciably increases this charge flow as demonstrated by the increase of the regions where $\Delta\rho$ is large. This behavior can be rationalized. We recall that the energetics of magnetization essentially depend on the residual orbital momentum as the spin momentum "follows" the orbital one for energetic reasons due to the LS spin−orbit term in the Hamiltonian. The inspection of Figure 4 crucially shows that switching the magnetization axis leads to occupying states that are extended in the (100) planes of the wire. The value of the MAE mainly depends on which type of d-states are available at the Fermi energy. The substantial increase of the regions where $\Delta\rho$ is large in Figure 4b with respect to Figure 4a indicates that in

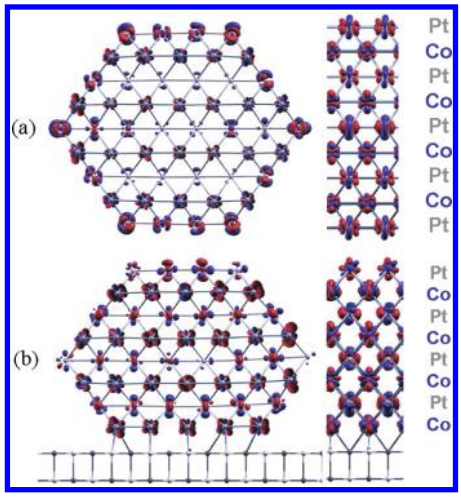

Figure 4. Isocontours of differential electronic density $\Delta\rho = \rho(M_z) - \rho(M_y)$, obtained by subtracting the total electron density of the state in which the magnetization axis is parallel to the surface and perpendicular to the wire main axis (M_y) from the state in which the magnetization axis is perpendicular to the surface (M_z), for the suspended $W_G(8,3)$ (a) or supported $W_S(8,3,4)$ (b) wires. In the larger images on the left, the view is taken along the main axis of the wire; on the right side view of the wire is also shown. Contour value = 0.004 e/Å^3. Color coding as in Figure 2.

the supported system both in- and out-of-plane d-states are available at the Fermi energy. This availability results in a reduction of the energy cost associated with magnetization switching and thus a reduction of the MAE. Note that it is not possible to associate this reduction with selective spin−orbit induced splittings at the Fermi surface as hypothesized for other systems.[24]

From the previous analysis we can then summarize the three main factors which determine the magnetism of supported nanoparticles: (a) chemical ordering: preferential metal/substrate interactions can lead to interfacial enrichment of one element; (b) epitaxy: the need to accommodate to the substrate can induce structural relaxations (prodromes of dislocations); (c) electronic structure: the mixing of the particle and support electronic states, with a possible charge transfer from/to the support and more subtle effects connected with spin−orbit coupling.

In the case of CoPt nanoparticles on MgO(100), point (a) leads to a major feature, that is, one-layer segregation of the magnetic element (Co) at the interface, due to many-body effects in the metal/surface interaction. As cubic structures are favored on checkerboard/square-symmetry surface for sufficiently large sizes, this also implies (point b) a stabilization of the $L1_0$ arrangement with respect to noncrystalline motifs, a magnetization easy axis perpendicular to the surface (thus satisfying one of the two main requirements of nanospintronics) and an interfacial deformation due to epitaxial effects that is beneficial to increase the MAE. This last effect is however overwhelmed by the mixing of particle and oxide electronic wave functions at the interface (point c) that dominates and results in a decrease of the magnetic moments at the interface and eventually to a reduction of the MAE by a factor ~1/2. For medium-sized particles of interest for nanospintronics, interface effects thus play a crucial role not only on the magnitude and orientation of the particle magnetic moments, but especially on their MAE. Apart from rationalizing the observed behavior in a specific case, a full understanding of these factors can be helpful in the design and fine-tuning of the magnetism of supported nanoparticles. By modulating the

dx.doi.org/10.1021/nl203449y |*Nano Lett.* 2011, 11, 5542–5547

mixing of electronic states at the interface via a change in the oxide support it may be possible to increase the MAE and achieve systems of use in room-temperature magnetic recording.

Methods. Total energy calculations within a DF approach are performed using periodic boundary conditions,[25] a gradient-corrected[26] XC-functional, and ultrasoft pseudopotentials.[27] In the modeling of 1D periodic systems, orthorhombic unit cells are employed, extending 2.9755 Å (corresponding to the distance between first-neighbor oxygen atoms on the MgO(100) surface) along the periodicity (x) direction and extending in the other two directions (y and z) in such a way that the distance between atoms belonging to replicated cells is at least 8−10 Å in order to reduce spurious interactions. The MgO(100) oxide surface is modeled by a three-layer slab with the first two layers free to relax and the bottom one frozen at the experimental lattice parameter, having verified that this model is converged with respect to the number of layers. In particular, calculations with five MgO layers (the first three frozen) on the $W_S(8, 3, 4)$ wire produced results essentially identical to those obtained using only three layers. In the optimization of the wires structure, we use numerical parameters similar to those employed in ref 12: 30 Ryd for the energy cutoff for the selection of the plane wave basis set for describing the wave function and 150 Ry for describing the electronic density (1 Ryd = 13.606 eV). The sampling of the first Brillouin zone is performed using a (4,1,1) mesh of k points, where the denser sampling corresponds to the wires periodicity direction. All the calculations are performed spin unrestricted. Relativistic contributions are evaluated by adding a noncollinear spin−orbit term to the scalar-relativistic approximation within a local density approximation framework, as this choice of the XC-functional does not seem to worsen the estimation of the MAE with respect to an estimation using a generalized gradient approximation approach (computationally more demanding).[28] A Lowdin projection analysis of the wave function furnishes the contribution of individual atoms to the magnetic moment of the system, while the magneto-crystalline contribution to the MAE is calculated by subtracting total energies between configurations with different orientation of the magnetization axis. In the evaluation of the MAE, we increase the numerical accuracy of the DF calculations by performing single-point DF energy evaluations by choosing 40 and 400 Ry as the energy cutoffs for the wave functions and the electronic density, respectively.

The search for the lowest-energy structures of CoPt supported nanoparticles follows the lines of our previous work.[12] In a first step, a many-body empirical potential for the metal−metal interactions and a surface energy empirical potential fitted to DF calculations for the metal-oxide ones[12] is used to perform a systematic sampling. Candidate structures for DF optimization are then taken as the low-energy configurations of each structural motif from this search at 50−50% composition but also translating those obtained at different compositions by optimizing the chemical ordering via an exchange-only approach, or as configurations built via the Wulff-Kaishev construction[6] with $L1_0$ chemical ordering. System comparison techniques are so utilized to maximize structural diversity and the thoroughness of the search. The final structures on which the MAE is calculated are thus grounded on a first-principles basis.

AUTHOR INFORMATION

Corresponding Author

*E-mail: alessandro.fortunelli@cnr.it.

ACKNOWLEDGMENT

A.F. is grateful to Paola Luches and Sergio Valeri for enlightening discussions, Livia Giordano for useful validation tests, Alberto Coduti for technical assistance, and gratefully acknowledges financial support from the SEPON project within the Advanced Grants of the European Research Council. The DF calculations have been performed at the Cineca Supercomputing Center (Bologna, Italy) within an agreement with Italian CNR. Networking via the MP0903 COST Action is also acknowledged.

REFERENCES

(1) Bernand-Mantel, A.; Seneor, P.; Bouzehouane, K.; Fusil, S.; Deranlot, C.; Petroff, F.; Fert, A. *Nat. Phys,* **2009**, *5*, 920–924.
(2) Weller, D.; Moser, A. *IEEE Trans. Magn.* **1999**, *35*, 4423–4439.
(3) Chappert, C.; Fert, A.; Nguyen Van Dau, F. *Nat. Mater.* **2007**, *6*, 813.
(4) Bansmann, J.; Baker, S. H.; Binns, C.; Blackman, J. A.; Bucher, J.-P.; Dorantes-Dávila, J.; Dupuis, V.; Favre, L.; Kechrakos, D.; Kleibert, A.; Meiwes-Broer, K.-H.; Pastor, G. M.; Perez, A.; Toulemonde, O.; Trohidou, K. N.; Tuaillon, J.; Xie, Y. *Surf. Sci. Rep.* **2005**, *56*, 189–275.
(5) Lehnert, A.; Dennler, S.; Blonski, P.; Rusponi, S.; Etzkorn, M.; Moulas, G.; Bencok, P.; Gambardella, P.; Brune, H.; Hafner, J. *Phys. Rev. B* **2010**, *82*, 094409.
(6) Henry, C. R. *Prog. Surf. Sci.* **2005**, *80*, 92–116.
(7) Favre, L.; Dupuis, V.; Bernstein, E.; Melinon, P.; Perez, A.; Stanescu, S.; Simon, J. P.; Babonneau, D.; Tonnerre, J. M.; Hodeau, J. L. *Phys. Rev. B* **2006**, *74*, 014439.
(8) Gauthier, Y.; Schmid, M.; Padovani, S.; Lundgren, E.; Bus, V.; Kresse, G.; Redinger, J.; Varga, P. *Phys. Rev. Lett.* **2001**, *87*, 036103.
(9) Ferrando, R.; Rossi, G.; Nita, F.; Barcaro, G.; Fortunelli, A. *ACS Nano* **2008**, *2*, 1849–1856.
(10) Penuelas, J.; Andreazza, P.; Andreazza-Vignolle, C.; Tolentino, H. C. N.; De Santis, M.; Mottet, C. *Phys. Rev. Lett.* **2008**, *100*, 115502.
(11) Rollmann, G.; Gruner, M. E.; Hucht, A.; Meyer, R.; Entel, P.; Tiago, M. L.; Chelikowsky, J. R. *Phys. Rev. Lett.* **2007**, *99*, 083402.
(12) Barcaro, G.; Ferrando, R.; Fortunelli, A.; Rossi, G. *J. Phys. Chem. Lett.* **2010**, *1*, 111–115.
(13) Sato, K. *Nat. Mat* **2009**, *8*, 924.
(14) Alloyeau, D.; Ricolleau, C.; Mottet, C.; Oikawa, T.; Langlois, C.; Le Bouar, Y.; Braidy, N.; Loiseau, A. *Nat. Mat.* **2009**, *8*, 940.
(15) Molina, L. M.; Hammer, B. *Phys. Rev. B* **2004**, *69*, 155424.
(16) Tommei, G. E.; Baletto, F.; Ferrando, R.; Spadacini, R.; Danani, A. *Phys. Rev. B* **2004**, *69*, 115426.
(17) Shapiro, A. I.; Rooney, P. W.; Tran, M. Q.; Hellman, F.; Ring, K. M.; Kavanagh, K. L.; Rellinghauss, B.; Weller, D. *Phys. Rev. B* **1999**, *60*, 12826.
(18) Dannenberg, A.; Gruner, M. E.; Hucht, A.; Entel, P. *Phys. Rev. B* **2009**, *80*, 245438.
(19) Freund, L. B.; Suresh, S. *Thin Film Materials: stress, defect formation surface evolution*; Cambridge University Press: Cambridge, 2003.
(20) Hultgren, R.; Desai, P. D.; Hawkins, D. T.; Gleiser, M.; Kelley, K. K. *Values of the thermodynamic properties of binary alloys*; American Society for Metals; Jossey-Bass Publishers: Materials Park, Ohio, United States, 1981.
(21) Chantrell, R. W.; Walmsley, N.; Gore, J.; Maylin, M. *Phys. Rev. B* **2000**, *63*, 024410.
(22) Ersen, O.; Parasote, V.; Pierron-Bohnes, V.; Cadeville, M. C.; Ulhaq-Bouillet, C. *J. Appl. Phys.* **2003**, *93*, 2987.
(23) Prada, S.; Martinez, U.; Pacchioni, G. *Phys. Rev. B* **2008**, *78*, 235423.
(24) Sipr, O.; Bornemann, S.; Minár, J.; Ebert, H. *Phys. Rev. B* **2010**, *82*, 174414.
(25) Giannozzi, P.; Baroni, S.; Bonini, N.; Calandra, M.; Car, R.; Cavazzoni, C.; Ceresoli, D.; Chiarotti, G. L.; Cococcioni, M.; Dabo, I.; Dal Corso, A.; de Gironcoli, S.; Fabris, S.; Gebauer, R.; Gerstmann, U.; Fratesi, G.; Gougoussis, C.; Kokalj, A.; Lazzeri, M.; Martin-Samos, L.; Marzari, N.; Mauri, F.; Mazzarello, R.; Paolini, S.; Pasquarello, A.;

Paulatto, L.; Sbraccia, C.; Scandolo, S.; Sclauzero, G.; Seitsonen, A. P.; Smogunov, A.; Umari, P.; Wentzcovitch, R. M. *J. Phys.: Condens. Matter* **2009**, *21*, 395502.
(26) Perdew, J. P.; Burke, K.; Ernzerhof, M. *Phys. Rev. Lett.* **1996**, *77*, 3865–3868.
(27) Vanderbilt, D. *Phys. Rev. B* **1990**, *41*, 7892–7895.
(28) Baroni, S.; Mosca Conte, A.; Fabris, S. *Phys. Rev. B* **2008**, *78*, 014416.

Nanoscale

Dynamic Article Links

NegreirosNS2012

Cite this: *Nanoscale*, 2012, **4**, 1208

www.rsc.org/nanoscale

PAPER

A first-principles theoretical approach to heterogeneous nanocatalysis

Fabio R. Negreiros,[a] Edoardo Aprà,[b] Giovanni Barcaro,[a] Luca Sementa,[a] Stefan Vajda[cd] and Alessandro Fortunelli*[a]

Received 9th August 2011, Accepted 30th September 2011
DOI: 10.1039/c1nr11051a

A theoretical approach to heterogeneous catalysis by sub-nanometre supported metal clusters and alloys is presented and discussed. Its goal is to perform a computational sampling of the reaction paths in nanocatalysis *via* a global search in the phase space of structures and stoichiometry combined with filtering which takes into account the given experimental conditions (catalytically relevant temperature and reactant pressure), and corresponds to an incremental exploration of the disconnectivity diagram of the system. The approach is implemented and applied to the study of propylene partial oxidation by Ag_3 supported on MgO(100). First-principles density-functional theory calculations coupled with a Reactive Global Optimization algorithm are performed, finding that: (1) the presence of an oxide support drastically changes the potential energy landscape of the system with respect to the gas phase, favoring configurations which interact positively with the electrostatic field generated by the surface; (2) the reaction energy barriers for the various mechanisms are crucial in the competition between thermodynamically and kinetically favored reaction products; (3) a topological database of structures and saddle points is produced which has general validity and can serve for future studies or for deriving general trends; (4) the MgO(100) surface captures some major features of the effect of an oxide support and appears to be a good model of a simple oxide substrate; (5) strong cooperative effects are found in the co-adsorption of O_2 and other ligands on small metal clusters. The proposed approach appears as a viable route to advance the role of predictive computational science in the field of heterogeneous nanocatalysis.

1. Introduction

Understanding, controlling, and ultimately designing catalytic systems with the desired activity and selectivity is a major challenge of contemporary chemistry.[1] The scope of this challenge is extremely wide, being relevant to battery technology, ultracapacitors, fuel cells, environmental chemistry, and catalytic processes for sustainable energy production, with heterogeneous catalysis by metal nanoclusters, *i.e.*, metallic particles in the 1–100 nm diameter range, representing one of the major avenues.[2] Improved catalysts can increase efficiency leading to reduced energy requirements, while increasing product selectivity and concomitantly decreasing wastes and emissions. Theory and simulations are expected to play an important role in this challenge. If a molecular-level understanding of the detailed steps of chemical reaction mechanisms is to be achieved, in fact, and despite the limitations of current approaches, the often sufficiently accurate prediction of the topology of local minima and saddle points in the energy hyper-surface renders theoretical simulations an invaluable tool. In addition, the possibility of performing computational 'gedanken experiment' and thus to disentangle, *via* in-depth analyses, the origin of the basic interactions in complex multifunctional systems such as those involved in catalytic chemistry is also unique to the theoretical level.

In recent years a particularly intriguing research field in heterogeneous nanocatalysis has been offered by the discovery of the importance of sub-nanometre metal clusters, *i.e.*, the experimental proof that extremely small (1–20 atoms) metal nanoparticles (pure or alloyed) are in many cases the true actors of catalysis or at least actors with rather different and sometimes more interesting behavior with respect to larger nanoparticles.[3–7] From sophisticated surface science experiments it has first been shown that size-selected clusters deposited on model surfaces in UHV exhibit peculiar adsorption and chemical properties.[3] The same has then been proven true on realistic surfaces and under non-UHV conditions, *e.g.*, in the oxidation of CO[4] or the partial oxidation of propylene by Ag_3.[7] Actually, even in real-world catalysis indications of the relevance of sub-nanometre species in specific catalytic reactions had already been drawn from *in situ* synchrotron X-ray measurements.[8] In the size range from a few

[a]*CNR-IPCF, Istituto per i Processi Chimico-Fisici del Consiglio Nazionale delle Ricerche, Pisa, 56124, Italy. E-mail: alessandro.fortunelli@cnr.it*
[b]*Computer Science and Mathematics Division, Oak Ridge National Laboratory, TN, 37831, USA*
[c]*Materials Science Division, Center for Nanoscale Materials, Argonne National Laboratory, Argonne, IL, 60439, USA*
[d]*Department of Chemical and Environmental Engineering, Yale University, New Haven, CT, 06520, USA*

to few tens of atoms metal clusters exhibit a molecule-like character, the metallic bond is only partially developed, and finite-size effects are in the extremely non-scalable regime in which adding or removing a single atom from the cluster may lead to dramatic changes in catalytic performance. This represents a complication but also a great opportunity for predictive computational science. By a noteworthy coincidence, in fact, the evolving picture of catalysis by sub-nanometre clusters at the experimental level perfectly matches recent developments in theoretical tools, in which both software and hardware advances make that systematic searches on very small nanometric particles are now accessible to first-principles computational protocols.

In the present article we follow this line of research by presenting and discussing a rigorous computational approach to heterogeneous nanocatalysis by subnanometre metal clusters (pure and alloyed). The approach is based on a systematic search in the phase space of structures and stoichiometry in which—at variance with global optimization algorithms[9]—reaction rates are evaluated in real time and are used to orient the system evolution according to the given experimental conditions (temperature and reactant pressure), thus realistically mimicking the reaction paths occurring at a specific site during the catalytic process. The approach is thus named Reactive Global Optimization (RGO). Moreover, we test the approach in the specific case of oxidation reactions catalyzed by Ag_3 supported on a model oxide substrate, the MgO(100) surface, *via* first-principles density-functional theory (DFT) calculations, focusing in particular on propylene partial oxidation and CO oxidation. Recent experiments show that supported Ag_3 clusters can act as effective oxidation catalysts, for example in the partial oxidation of propylene to propylene epoxide and acrolein.[7] In these experiments Ag_3 was deposited on an amorphous alumina support. Such a complex substrate however introduces too many degrees of freedom which make it not ideal to validate a novel methodology. We thus resorted to MgO(100) as a model substrate which has been widely investigated in the last 10–15 years and on which a wealth of information is available,[10,11] and which will allow us to single out the effects of a bare, undefected oxide surface on the catalytic activity of Ag clusters. Mixed Ag–Au trimers will also be considered. From this study several conclusions of general significance are derived: the crucial effect of the ionic substrate on the catalytic activity of small metal clusters, the role of reaction energy barriers in the interplay between thermodynamics and kinetics in the outcome of the catalytic process, the possibility of defining topological classes of local minima and saddle points as a reference for future studies, and the analogy between the present results and those obtained for amorphous alumina in the literature pointing to the MgO (100) surface as a good model of a simple ionic substrate. It will be shown that the cumulative and non-overlapping character of the knowledge generated by the RGO algorithm is advantageous with respect to standard global optimization methods, is ideally adapted to massive parallelism, and produces results which can be analyzed to derive general trends.

The article is organized as follows. The general ideas on which the approach is based are presented and discussed in Section 2. As these ideas can be implemented in several alternative ways, Section 3 describes the algorithm that we have actually used in the present implementation and the related computational details. The results obtained for oxidation reactions by MgO (100)-supported pure and mixed Ag–Au trimers are reported in Section 4. Conclusions and perspectives are summarized in Section 5.

2. The approach

Two main issues are faced when investigating at the theoretical level heterogeneous catalysis by sub-nanometre metal clusters. First, with respect to catalysis on extended metal surfaces there is no bulk system to constrain the catalytic component into a limited number of competing configurations. This entails a great structural freedom and a fluxional character of the composite metal-nanocluster-plus-ligands system, whence the need of efficient computational algorithms for structural exploration and sampling. A second issue lies in the fact that at this size range empirical potentials for the metal–metal and metal–ligand interactions are often not accurate enough to produce reliable results, also because of the strong many-body (cooperative) effects taking place in these systems. First-principles calculations must therefore be used, which are computationally much more demanding. We thus assume that any realistic simulation of heterogeneous nanocatalysis should be based on some kind of systematic search employing first-principles calculations.

Kinetics *vs.* thermodynamics

In a simplistic way, a theoretical/computational approach to nanocatalysis can be envisaged consisting of the following steps:[12,60] (1) exploring the potential energy surface (PES) of the combined substrate/metal-cluster/adsorbents system and deriving the set of local minima *via* first-principles global optimization calculations; (2) determining the energy barriers and the Arrhenius prefactors for transformation among these local minima; (3) simulating the catalytic dynamics at a finite temperature *via e.g.* kinetic Monte Carlo simulations.[13] After all, first-principles global optimization techniques are well established in the computational context,[14] and in recent years a density-functional/basin-hopping (DF–BH) approach has actually been applied to metal clusters both in the gas-phase[15] and supported on an oxide surface,[12,16,17] including oxygen ligands.[17,60] Moreover, dynamical processes such as the growth of supported metal clusters have been successfully simulated using an approach similar in spirit to that suggested above.[18,19] We indeed tested this approach in the present context but found it unsatisfactory. There are two main drawbacks. The first one is connected with the fact that catalysis is often a kinetics-driven rather than thermodynamics-driven process. For example, in the partial oxidation of propylene the desired products are propylene oxide or acrolein, not CO_2 and H_2O. The attraction basin in the phase space associated with partial oxidation is much thinner than that related to full combustion. Unless one devises ad-hoc tricks and constraints of limited validity, a global optimization search will thus spend most of the time sampling the basin of the undesired thermodynamically favored products. The reason why these products are not achieved is of course connected with energy barriers: those leading to CO_2 and H_2O are larger than those for partial oxidation, and it is sensible to use this

information in the global search. The second drawback is that the number of local minima generated by the global optimization search, even in such a simple system as $Ag_3O_2C_3H_6$/MgO(100) and limiting the energy interval to—say—2 eV from the global minimum, is of the order of a few hundreds. The number of pairs of local minima for which a kinetic constant should in principle be calculated is therefore of the order of several tens of thousands, somewhat impractical with the present computational resources and certainly very inefficient as the vast majority of these energy barriers are multiple-step and/or larger than 2 eV. One can select *a posteriori* a subset of the local minima or reaction mechanisms on the basis of ad-hoc criteria, but again this procedure lacks generality and is liable to overlooking important reaction pathways.

The alternative approach we propose here relies on the idea that the preferred reaction path should be automatically selected on the basis of energy barriers (or, better, kinetic constants), and consists of the following steps. Starting from a random structure and stoichiometry, (i) structural move: one searches for all possible neighboring local minima *via e.g.* an Intrinsic Reaction Coordinate (IRC) algorithm[20] (this thus differs from the shake move of a BH algorithm); (ii) pruning: those local minima connected to the starting one by energy differences or energy barriers larger than a given threshold (which depends on the temperature) are discarded altogether, *i.e.*, they are simply stored as pruned or dead branches of the catalytic tree; (iii) switching configuration and advancing clock: the set of the remaining reaction rates is evaluated using harmonic transition state theory as a product of Arrhenius prefactor times exponential terms, the next configuration or local minimum is selected on the basis of a kinetic Monte Carlo procedure, and the clock is advanced according to standard rules (Poisson distribution);[13] (iv) stoichiometry move: species from the gas-phase reaction mixture are added to and change the stoichiometry of the catalytic site according to a probability which depends on the pressure of these species (the collision frequency with the catalytic site) and the clock-time of the previous step; (v) cycling: starting with the new configuration or local minimum so derived, step (i) is retrieved and the process is iterated again. As the proposed search protocol is essentially based on reaction rates we call it Reactive Global Optimization (RGO). This protocol lends itself to being operated in a two-fold fashion. The process can in fact be completed until exhaustion, *i.e.*, until all the local minima and their neighbors have been explored and tested or declared as dead branches. Alternatively, it can be operated in a dynamic way, in which each virtual process represents a catalytic actor (a catalytic site) and proceeds by adding and processing incoming/outgoing species according to the structural and stoichiometry moves detailed above. Two technical points should be noted. First, the algorithm to explore the phase space neighborhood of a given configuration or local minimum in the structural move (i) should be as efficient and as thorough as possible.[21] Second, the addition of incoming species in the stoichiometry move (iv) should in principle be realized *via* scattering calculations by evaluating sticking probabilities. Given present computational resources, this in practice turns out to be too costly. One can therefore resort to a simplified approach in which the incoming species are simply adsorbed in the energetically most favorable configuration *via* a short BH search and the addition is accepted or not according to a standard Metropolis criterion. This corresponds to simulating a Langmuir–Hinshelwood mechanism. Alternatively, an Eley–Rideal mechanism can be simulated by assuming a starting configuration in which the incoming species is not physi- or chemi-sorbed but simply put next to the reacting complex. This implies solvable technical issues in the reaction path search starting from a configuration which is not a local minimum.

Exploring the disconnectivity tree

The proposed computational algorithm corresponds to exploring the disconnectivity tree (or graph) of the system.[22] Starting from any node in the tree, the algorithm explores its immediate neighborhood and proceeds from one vertex to the next according to simple rules based on the set of reaction rates. In this sense the algorithm is fully realistic, as it mimics the way a real system actually behaves, following low-energy-barrier (high-reaction-rate) paths and pruning high-energy-barrier branches. The algorithm is ideally adapted to massively parallel computers, as exploring a graph is a disconnected sequential task. In this regard, it is important to underline that the proposed protocol can efficiently exploit the cumulative character of the knowledge so generated. This is achieved by simply requiring that all the virtual actors running in parallel store their results into a common area so that unexplored branches can be picked up by a parallel process and unnecessary duplications can be avoided (which represent a great burden for global optimization algorithms). Finally, as an interesting development one can elaborate upon this protocol by combining it with previous proposals, *e.g.* one can bias the structural moves of a single actor: (1) by using an order parameter[23] or a metadynamics routine;[24] (2) on the basis of global (rather than local) information on the parallel actors (or "walkers").[25]

Structure recognition algorithm

In order to efficiently store the generated information and avoid waste of cpu time by repeating over and over the same job, it is crucial to identify homologous structures, *i.e.*, local minima which coincide up to minor differences in the coordinates or symmetry-operations (*e.g.*, due to incomplete geometry optimization, translation and/or rotation of the reference system, *etc.*). To this purpose, we have implemented a structure recognition algorithm based on a recursive comparison of the distance matrix within sets of atoms of the same chemical elements, from which corresponding pairs of atoms are identified. In the gas phase, the two configurations are centered in the center of mass and oriented along the axes of inertia before comparison. On a support, structure recognition is also connected with the issue of cluster diffusion (see the next subsection). Two configurations converted into one another by an operation of the symmetry group of the system, such as a translation of the reference system, are identified as homologous by our structure recognition algorithm. However, this can also be seen as a diffusion of the composite metal + ligand system and represents a real transformation mechanism. In the preliminary study reported in Section 4 we have not performed macro-simulations (see the next subsection) so that configurations coincident modulo a translation or a rotation have been assumed to be rigorously identical.

It can finally be added that an important option in the structure recognition algorithm is the one spotting when the system is composed of separate parts or fragments, *i.e.*, such that atoms belonging to one fragment are farther than bonding distance from those belonging to another one. In such a case, the number of possible configurations (isomers) of the total composite system is the product of the number of isomers of each fragment.

Diffusion and dis/ag-gregation: from micro- to macro-simulations

Among the neighboring local minima singled out by the search algorithm, some correspond to moves of a different kind, namely: diffusion or disgregation. In other words, the composite metal + ligand system can diffuse on the surface or break up into smaller separated pieces.

Diffusion is a phenomenon likely to occur on regular surfaces such as MgO(100). From the physics of bare metal clusters it is known that not only adatoms but also aggregates are very mobile on this substrate, and this has profound consequences on their growth.[18,19,26,27] Metal + ligand complexes make no exception to this rule. For example, we found energy barriers for diffusion typically of the order of 0.2–0.4 eV for a $Ag_3O_2C_3H_6$ complex on MgO(100). Defects such as Fs-centers or double vacancies[28,29] are needed to trap the cluster to a fixed site on the surface and avoid diffusion leading to sintering. We recall that the MgO(100) surface was selected as a model substrate to study the general effects of an oxide support on catalysis. Such a choice is justified by the analogy we found between catalytic processes occurring on MgO(100) and on other supports such as amorphous alumina (see Section 4) or the same surface containing point defects (unpublished work) but of course diffusion is one process that is quantitatively very different on regular and defected supports and for which regular MgO(100) is not a good model. Simulations on defected and thus fully realistic MgO(100) surfaces will be reported in the next future.

A related type of moves is that leading to disgregation of the complex into separate fragments. From studies of bare supported metal clusters fragmentation is a possible path: Ag clusters on a Fs-defected MgO(100) surface can fragment into dimers plus a remainder, with dissociation energies of at least ~0.7 eV also for the smallest species.[12] The presence of adsorbed ligands often weakens metal–metal bonds, thus lowering fragmentation energy barriers and greatly enhancing this possibility. Oxygen chemisorption has been suggested to increase cluster mobility, but especially CO is known to disrupt metal–metal bonding.[30–32] From the results reported in Section 4 it appears that co-adsorption of O_2 and CO further enhances cluster breaking into pieces in agreement with experimental observation that Au cluster sintering accelerates when both O_2 and CO are present in the reaction mixture.[33]

All this is connected to the phenomenon of Ostwald ripening, by which small nanoparticles dissolve into larger ones.[11] This phenomenon is accessible to simulations, but a change of perspective is needed: from micro- to macro-simulations.[34] In the macro-perspective, each actor of the catalytic process is seen as a component of a larger system, a piece of the substrate surface on which a number of similar actors are distributed according to a certain density and pattern corresponding to the given experimental conditions. Diffusion is tantamount to a change in position over the surface. When the distance between two such actors becomes small, *i.e.*, when two metal + ligand complexes get close to each other, the two virtual processes simulating each of them should give rise to a single one describing the resulting global system. Physically, this can lead to merging of the two complexes into a larger unit, but this is not necessarily the case, as the individual complexes can repel each other due *e.g.* to electrostatic interactions. *Vice versa*, upon fragmentation the virtual process simulating the dissociating complex should bifurcate giving rise to two different ones, which then follow the fate of the separated units undergoing further catalytic processes or diffusion and sintering. When studying Ostwald ripening the role played by "magic" clusters should not be underestimated. These are clusters that present electronic or structural shell closure, so that they can be particularly stable, corresponding to a spike in the plot of formation energy as a function of size, and thus act as attractors or end-points of the sintering process. For bare supported metal clusters, surface magic clusters have been shown to exist.[16,17] The same is expected for complexes formed by metal clusters and adsorbed species on a substrate. In addition to thermodynamic, kinetic magic complexes could also exist. In the simplest instance these are complexes that are stable against aggregation because they repel incoming species by presenting substantial energy barriers to further coalescence. In such a complex panorama, the end-point of Ostwald ripening can be also a function of the experimental conditions: depending on both thermodynamic and kinetic factors, a complex equilibrium can be attained among diffusion, fragmentation, aggregation and catalysis such that the system is statistically centered around a given size. The prediction of this equilibrium is in principle amenable to the combination of micro- and macro-simulations described above. Whatever the reason, it is an experimental observation that the end point of Ag_3/α-Al_2O_3 in the partial oxidation of propylene are medium-sized nanoparticles ~3.5 nm in diameter, not large aggregates,[7] and similar observations have been made on other systems.[30,35]

Topological databases of structures and saddle points

The cumulative character of the knowledge generated by the RGO algorithm has already been pointed out. The fact that the virtual actors of the computational search store the results of their explorations into a common area represents a definite advantage with respect to competing approaches. This can be exploited also in other ways to achieve a great saving in computational effort. A database of structures (local minima in the PES) can in fact be produced which furnishes a set of initial configurations to be used in future searches.[22] To make an example, this database can be used to study the same catalyst but with different reactants (*e.g.*, oxidation of a different species) or the same reactants but on a different catalyst (system comparison or composition comparison[23]). The case of nanoalloys, *i.e.*, multi-component metal nanoclusters, is well suited to exemplify this procedure. For a nanoalloy catalyst, a thorough structural search should take into account all the possible 'homotops', *i.e.*, isomers sharing the same skeletal structure and composition but differing in the mixing pattern.[36] While the number of homotops can be huge for a large alloy particle, for very small clusters local

geometry optimizations of the configurations obtained from the RGO approach as applied to pure clusters will likely be less computationally demanding than performing a complete RGO search for each alloy composition. At least, these biased searches can be used as a starting point for further sampling. In addition, it should be underlined that in our experience we found unexpected similarities (in the sense of topologically similar structures and saddle points) between rather diverse systems, such as Ag_3 and Ni_3 clusters, of course with a different energetics. This is due to some intrinsic common topological features, and it is thus important both in view of computational saving and of deeper understanding (deriving general trends) to define classes of topologically similar configurations, see *e.g.* the sets of upright *vs.* flat configurations of metal-trimers + ligand on MgO(100) discussed in Section 4. It should be noted in this connection that a database can be created not only of local minima, but also of saddle points. In our experience this proved to be very useful as a starting point of IRC searches, greatly accelerating and strengthening their convergence properties.

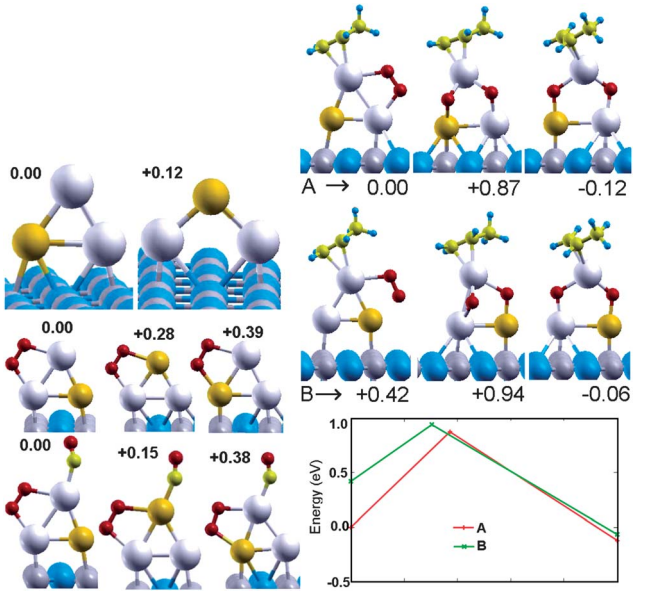

Fig. 1 Rhs: relative energy differences for the homotops of Ag_2Au, Ag_2AuO_2 and Ag_2AuO_2CO supported on MgO(100). Lhs: mechanisms for breaking of the adsorbed O_2 species for a homotop in which the Au atom is on the opposite side (A, top panel) or on the same side (B, middle panel), and the corresponding schematic energy plots (bottom panel). All the energies are in eV.

Need of a thorough sampling

Theoretical nanocatalysis has traditionally been based not on thorough search protocols such as the one here proposed, but rather on testing biased or inspired guesses of reaction mechanisms derived from experimental information or chemical intuition. While this can be a successful and very cost-effective approach (the computational effort is decreased by orders of magnitude even for the simple systems considered in Section 4), it is also prone to erroneous or at least inconsistent predictions. To make a very simple example of the issues one might run into, let us consider, the energy barrier for O_2 dissociation on a complex formed by adsorption of oxygen and propylene not on Ag_3 but on a mixed Ag_2Au trimer.[37,38] Alloying Ag_3 with a Au atom introduces us into the field of alloyed nanoclusters—or nanoalloys. From the point of view of the structural search the difference with respect to pure clusters is that one has to deal with many more configurational degrees of freedom as one has to consider all the different homotops. In the present case *e.g.* one has three homotops for the starting configuration (see Fig. 1—lhs, and paths A and B on the rhs): the Au atom can be in contact with the MgO(100) surface, with the additional option of being on the side of the oxygen molecule or on the opposite side, or can be on the apex of the triangle formed by the metal atoms. The most stable configuration according to our DFT results is the one with the Au atom in contact with the MgO(100) surface on the opposite side of the oxygen molecule, while putting the Au atom next to the oxygen molecule costs 0.42 eV. In the former configuration the energy barrier for O_2 dissociation is 0.87 eV, in the latter 0.52 eV, respectively. If one limits oneself to the latter configuration, one erroneously predicts that the effect of alloying is a substantial acceleration in the reaction rate. Assuming however that the initial configurations are equilibrated, the correct energy barrier for a path passing through higher-energy local minima is the *sum* of the energy barrier *plus* the energy difference with respect to the global minimum, thus obtaining in the present case a minor acceleration due to alloying (the energy barrier is 0.95 eV for Ag_3). Clearly, by employing the present RGO protocol one can think of a kinetics-driven process in which for some reasons the system is initially formed in a configuration that is not the global minimum and reacts before having the time of rearranging into the thermodynamically stable configuration. This is not true in the present case: the energy ordering among the three homotops is similar before adsorbing propylene or CO molecules (see Fig. 1), and the energy barriers for homotop interconversion are lower than the reaction energy barriers, so there are no reasons why the system should be frozen in the configuration with the Au atom on the same side as the oxygen molecule. Other systems may be more complicated. Indeed one can expect in some cases that deactivation of an initially more active alloyed catalyst is precisely due to the fact that the system, prepared in a higher-energy local minimum presenting lower reaction energy barriers, gradually rearranges into lower-energy structures presenting larger reaction barriers. This obviously does not mean that only the global minimum structure should be taken into account: in some cases the system finds it convenient to first transform into a low-lying active isomer before undergoing a reactive step, but as observed above in this case the correct apparent energy barrier will be the sum of the actual energy barrier plus the energy difference between the low-lying active isomer and the global minimum. Of course, a different possibility is that the energy ordering of the initial configurations predicted at the first-principles level is in error, and that the true lowest-energy state is the one presenting lower energy barrier, so that considering the latter one obtains a better agreement with experiment. If there are experimental indications that this is the case, the inconsistency between a biased or inspired guess and a fully first-principles theoretical approach (*i.e.*, one not relying on external information) should always be pointed out, at least with the goal of improving the accuracy of theoretical methods.

3. Computational details

DFT calculations were performed using two approaches: a periodic one with a basis set of plane waves *via* the Quantum Espresso package version 4.1.2,[39] and a cluster model with a localized basis set of Gaussian functions *via* the NWChem package version 5.1.1.[40] The cluster model approach had been validated in the study of bare metal clusters.[41,12] All the calculations were carried out with the PBE xc-functional[42] in the spin-unrestricted formalism. The calculations used the Gaussian-smearing technique[43,44] with a smearing parameter of 0.002 a.u. for the fractional occupation of the one-electron energy levels.

For the periodic model, ultrasoft pseudopotentials (USPP)[45] and values of 40 Ry and 320 Ry were chosen as the energy cutoff for the selection of the plane waves for the description of the wave function and the electronic density, respectively. 3×4 and 4×4 cells with 2 MgO layers (kept frozen during structural optimizations) were used in order to guarantee a sufficient distance among atoms belonging to replicated images. The vacuum region separating neighbor slabs was always at least 8 Å. Calculations were performed at the Γ point. For the cluster model, calculations were carried out using Gaussian-type orbital basis sets of triple-ζ quality for all elements and 19-valence electron effective core potential for Ag and Au.[46] The MgO cluster was embedded in an array of ± 2 a.u. point charges[12] (about 1500) extending for four layers in the direction perpendicular to the surface and up to $\sim$10 Å from the borders of the cluster in the (100) surface plane. The atoms of the central cluster and the point charges around it were located at the lattice positions of the MgO rock-salt bulk structure at the experimental lattice constant of 4.208 Å.

The efficiency of the RGO approach crucially depends on the algorithm for the exploration of the PES neighborhood of a given local minimum, which should be at the same time as fast and as thorough as possible. Many possibilities in principle exist.[21] The present implementation is based on an eigenvector-following IRC method[57] ad-hoc coded within the cluster approach. In detail, successive steps are taken in the direction of each eigenvector of the dynamical matrix. The size of the first step ranges in the interval 0.3–0.6 as the factor multiplying a normalized eigenvector, with the precise value within the interval depending on the value of the associated frequency, while the size of the second and successive steps is half of the first one. Each step was followed or not by a constrained geometry optimization minimizing the coordinates orthogonal to the given eigenvector using rough values of the convergence thresholds, then refining the given eigenvector with a local evaluation of the dynamical matrix and projection of the corresponding eigenvectors onto the given one. With the goal of performing simulations at room temperature, a threshold of 1.2 eV is used to prune not only energy barriers but also (what is crucial to speed up the approach) the local energy value during the IRC search. After a saddle point is overcome, an unconstrained geometry optimization is used to generate the configuration of a local minimum nearest-neighbor of the initial one. Once this local minimum configuration is singled out, a Nudged Elastic Band (NEB)[59] calculation using the periodic package and an IRC algorithm using the cluster approach were performed to refine the associated energy barrier.

All the local minima were cross-checked using both the cluster and the periodic approach. The search of the transition states connecting two given local minimum configurations was performed in two steps. First, the NEB tool of the periodic package was used in order to determine a path for the selected move. In this step, 3–7 intermediate images were considered, the Broyden optimization scheme was used without the climbing image option, and the intermediate images were optimized until forces were lower than 0.05 eV Å^{-1}. In a second step, the image highest in energy found in the previous step was re-optimized with the IRC algorithm using the cluster approach.[20] For the sake of clarity, the energy values reported in Sections 2 and 4 were always obtained using the cluster-model approach. The frequencies at the saddle points were usually checked and found to generally present a single non-trivial negative value (*i.e.*, modulo rotation of the methyl group and similar non-reactive paths). Sometimes other negative frequencies were found with extremely low values due to numerical inaccuracies: these were simply ignored.

In general, we note that for an efficient implementation of the RGO approach the key issues are the convergence properties and robustness of both the geometry optimisation and saddle point search algorithm. In particular, the NEB method is known to be numerically not very robust and has actually slowed down our search in several cases. It could probably be replaced by improved algorithms.[58] A more complete analysis of the PES around the saddle point taking into account the possible existence of multiple negative frequencies should also be implemented to improve the thoroughness of our exploration and sampling algorithm. Work is in progress in our lab along these lines.

The whole study was done by using several concurrent DFT calculations ("replicas"); therefore a bundle of several jobs of moderate size (some thousand cores) are typically run in a single script. Each virtual actor or replica is completely independent from all the others. Starting from a given optimized structure, the neighborhood in the phase space of structures is explored *via* the eigenvector-following search for neighboring local minima, the significant energy barriers are computed *via* a NEB and IRC procedure, high-energy or high-energy-barrier minima are pruned, the possibility of a stoichiometry move is considered and—if the case—operated, the full information so obtained is stored in a common repository, and the new structure is then taken as the starting one.

4. Propylene partial oxidation by Ag_3 and $(Ag–Au)_3$ clusters supported on the MgO(100) surface

As a test and a proof-of-principle of the protocol described in Section 2, the partial oxidation of propylene *via* Ag_3 clusters deposited on MgO(100) is investigated. This system is a subject of our interest since a few years[12,16,17] and a case study for pioneering DF–BH simulations on supported metal clusters including oxygen ligands.[17] Moreover, as mentioned in the Introduction, recent results[7] prove that Ag_3 clusters supported on an amorphous alumina can act as effective oxidation catalysts, for example in the partial oxidation of propylene to propylene epoxide and acrolein, thus providing us with

a reference system which we can compare to and use to validate our approach:

$$CH_3CH{=}CH_2 + nO_2 \rightarrow CH_3CH(O)CH_2;\ CH_2{=}CH{-}CH{=}O\ [\ldots;\ CO_2\ \&\ H_2O]$$

Already with such a simple reaction the number of investigated local minima configurations is huge: for any given stoichiometry, the RGO algorithm produced hundreds of structures and transition states.[47] Only micro-simulations were performed. We will not report all the results of the RGO approach as applied in full detail, as this would go outside the scope of this article, but rather provide the reader with the main general outcome of the present work, referring to a future publication for a full report.

Gas-phase *vs.* supported clusters

The first finding that needs to be stressed is the great difference in the PES of free and supported clusters. This is not so evident when considering adsorption of pure metal clusters: it is known that the interaction of Ag_3 with a regular, un-defected oxide surface is rather weak, of the order of few tens of an eV, and no substantial distortion of the Ag trimer occurs upon deposition.[26,48] The Ag_3 trimer is preferentially adsorbed in an upright configuration which is more stable than a flat pseudo-epitaxial one because of the so-called "metal-on-top" effect.[48] The situation however changes radically when an oxygen molecule is added. In Fig. 2 and 3 the structure and energetics of the main isomers of Ag_3O_2 are shown for free and supported cases, respectively. The main results are that O_2 adsorbs as an integer molecule (with an adsorption energy of 1.20 eV) on free Ag_3, whereas O_2 dissociation and adsorption of two oxygen atoms on bridge sites of the triangle formed by the Ag trimer become strongly favored when the system is supported even on a simple ionic substrate such as MgO(100). This prediction is in tune with experimental results showing that Ag_3 does not break the O–O bond in the gas-phase,[49] whereas it acts as an oxidation catalyst when adsorbed on an ionic substrate[7] or in the presence of a negative charge.[50] The presence of an oxide support is thus crucial for transforming Ag_3 into an oxidation catalyst. The

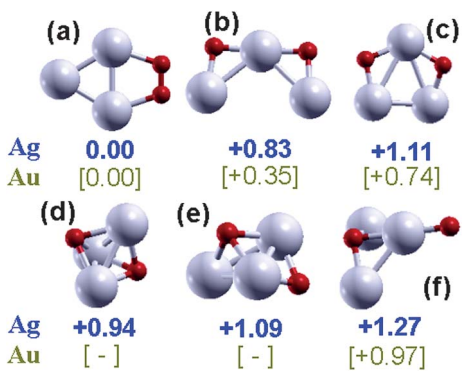

Fig. 2 Relative energetics of gas-phase Ag_3O_2. In brackets the same values for gas-phase Au_3O_2. The adsorption energy of an undissociated O_2 molecule on gas-phase metal trimers is 1.2 and 0.9 eV for Ag and Au, respectively. All the energies are in eV.

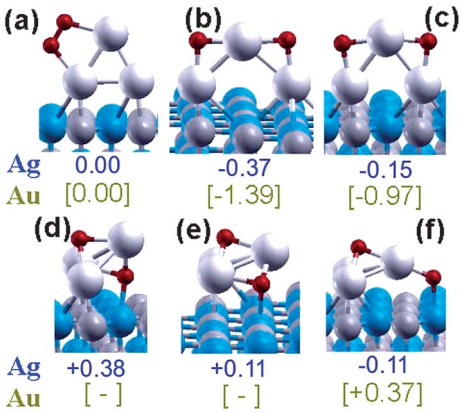

Fig. 3 Relative energetics of Ag_3O_2/MgO(100). In brackets the same values for Au_3O_2/MgO(100). The adsorption energy of an undissociated O_2 molecule on supported metal trimers is 0.9 and 1.1 eV for Ag and Au, respectively. All the energies are in eV.

reasons for this substantial change in the system energetics are of electrostatic origin: the O_2-dissociated configurations have a much larger dipole moment which can favorably interact with the electrostatic field generated by the ionic, charge-separated oxide surface. It can be underlined in passing that a qualitatively similar behavior is found not only for Ag_3 but also for Au_3: the corresponding values are also reported in Fig. 2 and 3. This means that oxide-supported Au_3 can in principle act as an oxidation catalyst in the *absence* of hydrogen (in the form of hydrogen molecule or hydroxyl functionality) contrary to what sometimes assumed.[51]

Another point worthwhile noting is that the configurations of the free Ag_3O_2 system can be classified as adsorption of molecular oxygen (Fig. 2a) or dissociated structures (Fig. 2b–f), further distinguishable according to the adsorption sites of the two oxygen atoms into: bridge–bridge (Fig. 2b and c), bridge–hollow (Fig. 2e), hollow–hollow (Fig. 2d), and bridge–tip (Fig. 2f). The configurations of the supported Ag_3O_2 system are in one-to-one correspondence with the free ones, so that they can be classified again according to whether the O_2 molecule is dissociated (Fig. 3b–f) or not (Fig. 3a) and—if dissociated—according to the adsorption sites of the two oxygen atoms. They can be further grouped into topology or universality classes or structural motifs[52] according to their relation to the surface as upright (Fig. 3a–c) or flat (Fig. 3d–f). These topological distinctions provide a great help in analyzing and rationalizing the results of the simulations. In particular, we will see below that upright and flat configurations present a partly different catalytic behavior, as it is to be expected because of the different relative stabilization of dipolar *vs.* neutral structures.

When a propylene molecule is further added to the system, another big change in the relative energy ordering among the structural motifs occurs: in particular in the absence of a donating (Lewis base) ligand such as propylene the upright configurations are lower in energy with respect to flat ones (see Fig. 3), whereas the reverse is true when propylene is co-adsorbed, as shown by the energetics reported in Fig. 4, in which one can observe the one-to-one correspondence of $Ag_3O_2C_3H_6$ configurations with those of Ag_3O_2 from Fig. 3. This does not occur with all ligands. For example, co-adsorption of a CO

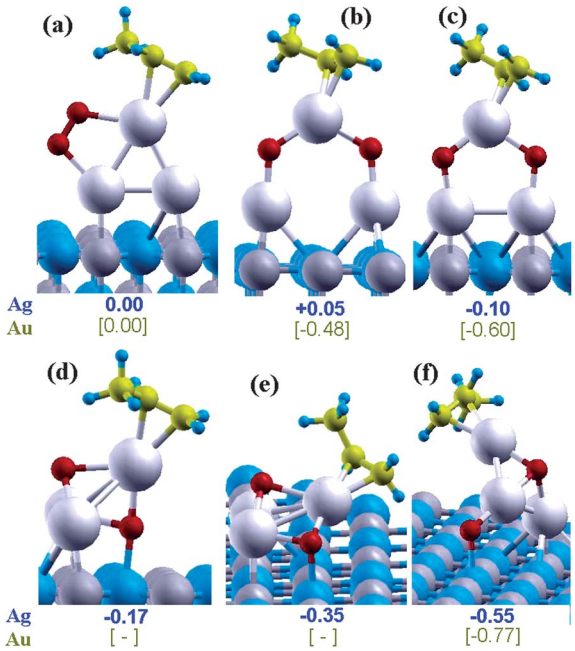

Fig. 4 Relative energetics of $Ag_3O_2C_3H_6$/MgO(100). In brackets the same values for $Au_3O_2C_3H_6$/MgO(100). The adsorption energies of a C_3H_6 molecule on the supported metal-trimers-plus-oxygen-molecule complex is 0.3 and 0.7 eV for Ag and Au, respectively. All the energies are in eV.

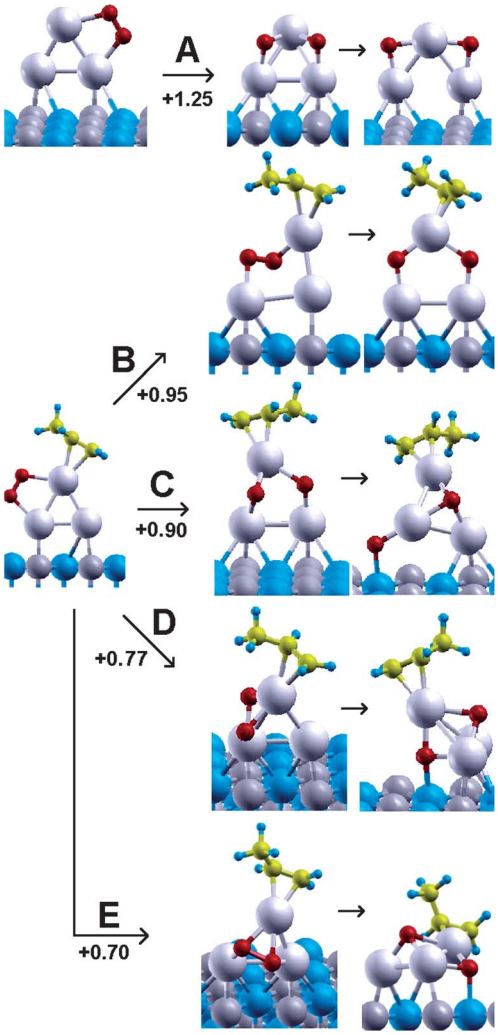

Fig. 5 Mechanisms and energy barriers of O_2 breaking in supported Ag_3O_2 (A) and $Ag_3O_2C_3H_6$ (B–E). When C_3H_6 is present, the various mechanisms give rise to the topologically different structures described in the text. All the energies are in eV.

molecule on Ag_3O_2 produces results similar to that of propylene but this is not true for gold: CO co-adsorption on Au_3O_2 supported on MgO(100) does not favor flat configurations, and upright ones still remain the lowest-energy arrangements, at variance with propylene adsorption which instead produces results analogous to those for silver. Note that in the case of CO oxidation by Ag_3/MgO(100) we did not perform the full RGO approach but we used the structural database already obtained in the study of propylene partial oxidation and performed local geometry optimizations and IRC searches to single out the local minima and the transition states resembling those of the previous (and more complex) system. This is reasonable as CO oxidation presents less degrees of freedom with respect to propylene partial oxidation and additionally selective trials did not produce any indications of further reaction paths. This is a practical example of the use of topological databases of local minima and saddle points discussed in Section 2.

Energy barriers for O_2 dissociation: cooperative effects

The fact that O_2 breaking is thermodynamically favored over supported Ag trimers does not automatically assure that dissociation will actually occur, as this will depend on the energy barriers of the process. Here another important conclusion can be drawn from an inspection of Fig. 5, in which the starting and final structures and the transition states for O_2 dissociation for supported Ag_3O_2 and $Ag_3O_2C_3H_6$ are shown. It is interesting to observe that the preferred configuration in the absence of any ligand is the upright one and that the energy barrier for O_2 dissociation for this configuration is 1.25 eV, a value large enough to hinder the catalytic activity of Ag_3 at or around room temperature. The situation changes when propylene is co-adsorbed on Ag_3O_2. To be more precise, the energy barrier for O_2 dissociation in the upright configuration is still appreciable (of the order of 1 eV), but what is different is the fact that now flat configurations are more stable and the energy barrier for O_2 dissociation in these configurations is substantially reduced and is of the order of 0.7–0.8 eV. Strong non-linear or cooperative or many-body effects are thus present in the interaction of small metal clusters with ligands.[53] It can also be noted that on the MgO(100) surface the hollow–bridge arrangement is competitive from a thermodynamic point of view, but disfavored from a kinetic point of view as it is less easily accessible and presents higher energy barriers for further conversion. This finding is at variance with the simulations on Ag_3 deposited on amorphous alumina reported in ref. 7, in which the hollow–bridge configuration seems to play a crucial role, see the pictorial comparison between the two systems in Fig. 6. We can conclude that the MgO(100) surface is indeed a good model of an ionic substrate and that the general feature of the system PES landscape (such as

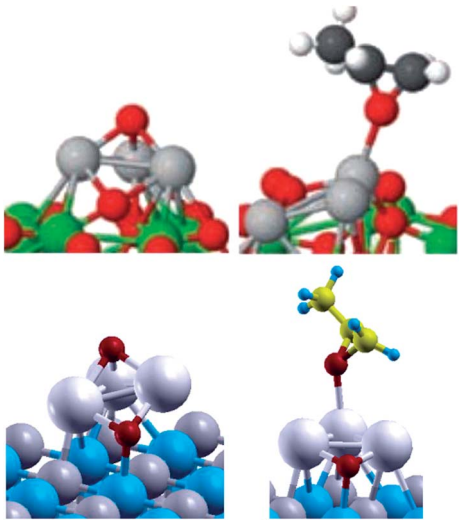

Fig. 6 Comparison of intermediates active in the oxidation for Ag_3 clusters supported on MgO(100) (left) and amorphous alumina (right, taken from ref. 7).

the preference for flat configurations only after co-adsorption of propylene) is correctly predicted, with the proviso that fine details of the energetics among flat arrangements can obviously differ and depend on the specific support under consideration. The advantage of studying a model surface such as MgO(100) is that the sources of various effects can be clearly and unambiguously identified.

Post-dissociation mechanisms

In our simulations, O_2 dissociation was often the first step of the reaction. Further steps led to epoxide or acrolein formation or full combustion. To offer a minimal sample of the mechanisms singled out by the RGO approach, we show in Fig. 7 four paths with the corresponding energy barriers. In the first one (Fig. 7a), an upright configuration with a dissociated bridge–bridge O_2 leads to propylene epoxidation *via* an oxametallacycle intermediate. This path is rather easy once the system is prepared in this configuration as the Ag–propylene bond is very weakly directional and propylene can librate around the tip Ag atom with a small energy penalty. Interestingly, we did not find a path for acrolein formation passing exclusively through upright configurations. It thus seems that upright configurations favor epoxide formation. The second path goes through a hydrogen-abstraction intermediate (Fig. 7c). This intermediate is interesting because the direct interaction of propylene with an undissociated O_2 molecule is one of the possible paths leading to CO_2 and H_2O formation. It should be noted that the energy barrier for producing this intermediate is 1.0/0.9 eV, *i.e.*, larger than that leading to epoxide (Fig. 7a) or acrolein formation (Fig. 7d) (also the energy barriers for the successive steps leading to combustion of this intermediate are lower than this). At low temperature, the catalytic process will be kinetics-driven rather than thermodynamics-driven, and the kinetic products of propylene partial oxidation (epoxide and acrolein) will be obtained. In contrast, at higher temperature the difference in the energy barriers between partial and full oxidation will be relatively less important, and CO_2 will start to be produced, in agreement with experiment.[7] In the third and fourth paths, propylene epoxide or acrolein is formed from flat configurations, namely, the hollow–bridge and hollow–hollow ones (Fig. 7b and d), in analogy with what proposed in ref. 7, thus confirming the MgO(100) surface as a good model of a simple ionic substrate.

Fragmentation

The energy differences for representative fragmentation mechanisms are reported in Fig. 8. The most significant result here is that the energy differences for fragmentation of Ag_3 are often larger than those of Au_3. Ag_3 is thus a more robust oxidation catalyst than Au_3, in tune with the experimental finding that sub-nanometre Au clusters (slightly larger: Au_{6-10}) supported on amorphous alumina in similar experimental conditions need a post-deposition treatment with further atomic deposition to stabilize the clusters against aggregation,[6] whereas this is not necessary for Ag_3/MgO(100) for which only at temperatures above 100 °C sintering is actually observed.[7] Another important observation that can be derived from Fig. 8 is that CO adsorption but especially co-adsorption of O_2 and CO promotes Au_3 cluster disgregation. In other words energy differences for Au_3 disgregation are lower when *both* O_2 and CO are adsorbed with respect to the case when only one ligand (O_2 or CO) is present: the energy difference for disgregation is only 0.17 eV. This is in nice agreement with GISAXS experiments in which sintering of Au nanoparticles is observed to be greatly enhanced when the full reaction mixture (*i.e.*, CO and O_2) is introduced into the reaction chamber.[33] Strangely enough, adsorption of only O_2 even increases the disgregation energy differences, so that one might think that for such small clusters O_2 acts as stabilizers against sintering, or at least points to strong non-linear or cooperative or many-body effects in the interaction of small metal clusters with ligands.[53]

5. Conclusions and perspectives

A first-principles computational approach to heterogeneous catalysis by metal clusters in the sub-nanometre regime is presented here. This approach is based on a thorough but efficient exploration of the potential energy landscape of the composite metal-cluster/reactant supported system to single out the relevant local minima and transition states in the energy hyper-surface. Starting from a random configuration the neighbourhood in the phase space of structures and stoichiometry is incrementally explored and the disconnectivity graph of the system is sampled *via* moves oriented by the experimental conditions (temperature and reactant pressure). Reaction energy barriers play a fundamental role in the approach, which is thus named Reactive Global Optimisation (RGO). As the approach mimics the behaviour of a real system it is claimed to be more efficient than global optimisation methods, especially in cases in which kinetic rather than thermodynamic products are sought for. The disconnected character of the algorithm is also ideally suited to massive parallelism. Finally, a database of structures and saddle points (*i.e.*, a complete set of local minima and transition states for a given catalytic system) are generated as a by-product of the structural search, which can be used for other homologous

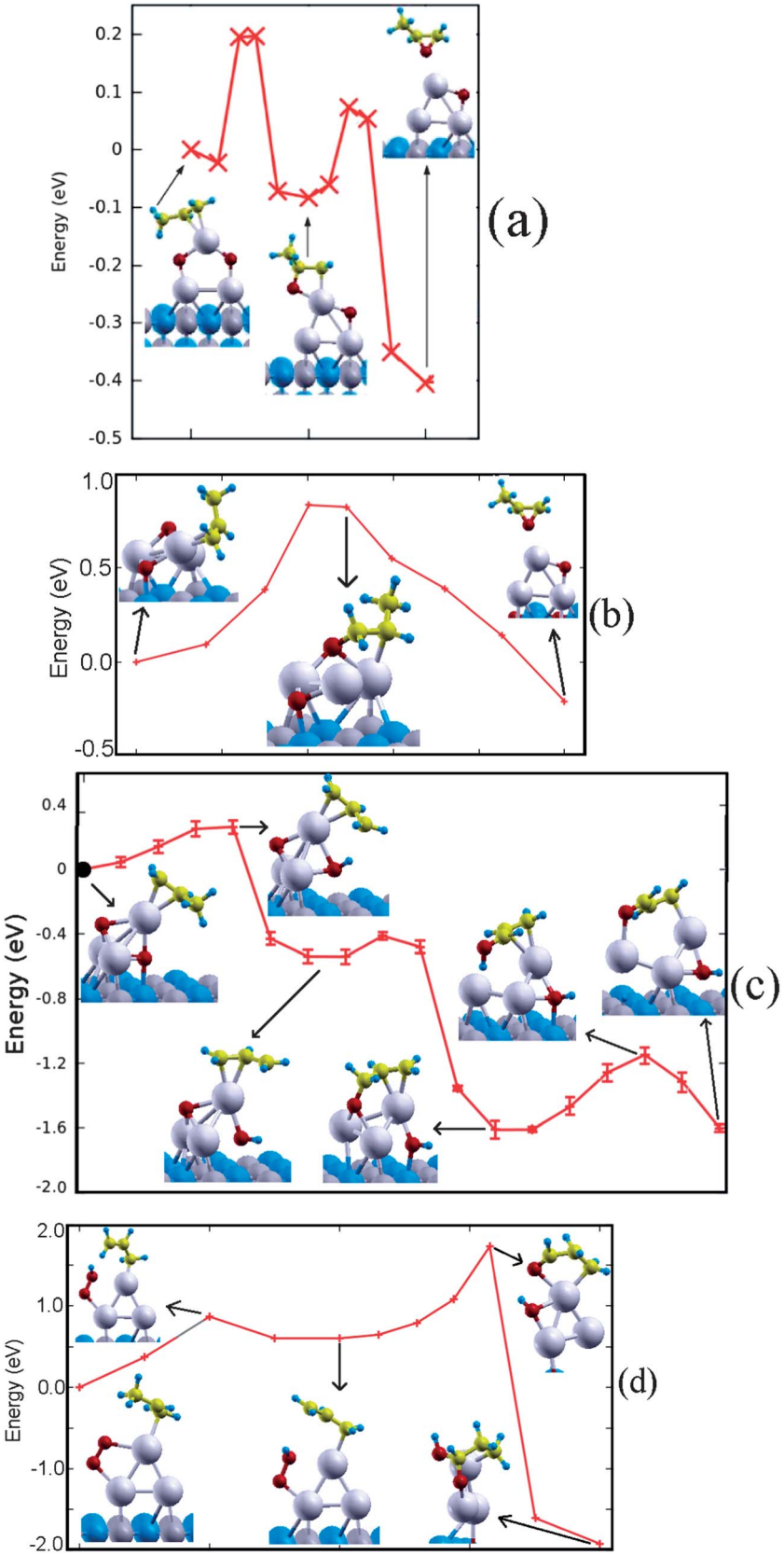

Fig. 7 Examples of post-dissociation reaction mechanisms and energy barriers for $Ag_3O_2C_3H_6$. All the energies are in eV.

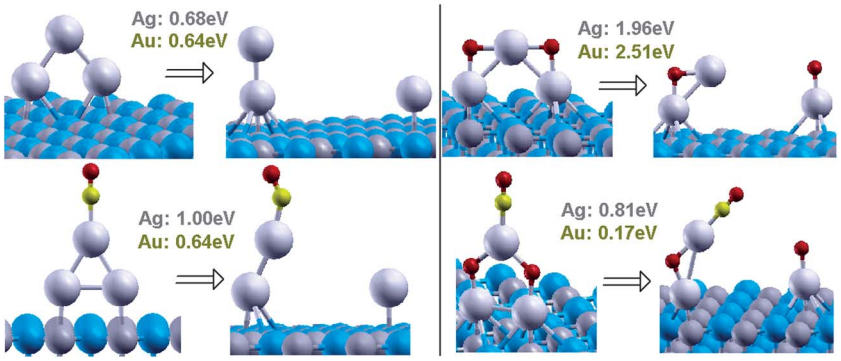

Fig. 8 Energy differences for fragmentation of Ag_3, Ag_3O_2, Ag_3CO, and Ag_3O_2CO supported on MgO(100). The values of the same quantities for Au species are reported in the underlying rows. All the energies are in eV.

systems to accelerate the search and avoid repeating the same calculations (system or composition comparison) and within which one can define topological universality classes, *i.e.*, sets of topologically equivalent configurations, which help one to rationalize the observed behavior and find general trends and concepts in the catalytic mechanisms.

The approach is exemplified in a study of propylene partial oxidation by Ag_3 supported on MgO(100) *via* first-principles (DFT) calculations, from which study several findings of general significance are derived. First, the effect of the support is crucial in favoring configurations (such as those with a dissociated O_2 molecule) with a dipole moment perpendicular to the surface and thus stabilized by its electrostatic field. Second, O_2 dissociation is often the first step of the catalytic oxidation reaction, and the associated energy barrier can be lowered by the co-adsorption of donating ligands pointing to strong non-linear or cooperative or many-body effects in the interaction of small metal clusters with ligands.[53] Third, the structural database can be divided into two topological sets comprising upright or flat configurations of Ag_3. Interestingly, upright configurations are found to favor epoxidation of propylene *vs.* acrolein formation. Fourth, the difference in reaction energy barriers for the various mechanisms distinguishes kinetically favored reaction products of partial oxidation *vs.* thermodynamically favored products of full combustion. Fifth, the MgO(100) surface captures some major features of the effect of an oxide support and appears to be a good model of a simple ionic substrate. Lastly, fragmentation can be a mechanism of disruption of the metal + ligand complex possibly leading to Ostwald ripening, especially for small Au rather than Ag clusters and when both O_2 and a donating ligand are co-adsorbed on the metal cluster.[35]

Future developments concern the role of the support. In the present exploratory work, the regular surface of a simple oxide was considered as a substrate: MgO(100). This allowed us to focus on a widely studied support[10,11] and on the general features of the effect of a charge-separated, ionic substrate on the catalytic activity, with the very interesting finding that many analogies do indeed exist between this model support and more complex ones such as amorphous alumina. As an obvious extension of this work defected surfaces could easily be considered[12] or surfaces containing hydroxyl groups,[6] which are known to be present on oxide surfaces under certain experimental conditions. In a more complicated development, the combined metal-cluster/ligand system could be enlarged to include the substrate itself, *i.e.*, part of the substrate could actively participate in the reaction by providing oxygen species or stabilizing reaction intermediates, *etc.* This possibility is not relevant in the example here considered as the MgO(100) surface is a hard, not flexible support, but it can obviously become crucial on softer, reducible oxides. It should finally be noted that the present approach has been implemented but is not limited to heterogeneous catalysis. Photo-[54] or electro-catalysis[55] and homogeneous catalysis by solvated metal complexes[56] can be dealt with using the same theoretical/computational machinery presented in this article, and will be the subject of future work.

Acknowledgements

Financial support from the SEPON project within the Advanced Grants of the European Research Council is gratefully acknowledged. Part of the calculations were performed on the CASPUR supercomputing center (Italy) within the TheoNano-Cat project. This research used resources of the Oak Ridge Leadership Computing Facility, located in the National Center for Computational Sciences at Oak Ridge National Laboratory, which is supported by the Office of Science of the Department of Energy under Contract DE-AC05-00OR22725. S.V. thanks for the support of his effort the US Department of Energy, BES-Materials Sciences, under Contract DE-AC-02-06CH11357 with UChicago Argonne, LLC, operator of Argonne National Laboratory. Networking from the MP0903 COST action is also acknowledged.

References

1 L. N. Lewis, *Chem. Rev.*, 1993, **93**, 2693.
2 *Handbook of Heterogeneous Catalysis*, ed. G. Ertl, H. Knotziger, F. Schuth and J. Weitkamp, Wiley, NY, 2nd edn, 2008.
3 A. S. Worz, K. Judai, S. Abbet and U. Heiz, *J. Am. Chem. Soc.*, 2003, **125**, 7964.
4 A. A. Herzing, C. J. Kiely, A. F. Carley, P. Landon and G. J. Hutchings, *Science*, 2008, **321**, 1331.
5 S. Vajda, M. J. Pellin, J. P. Greeley, C. L. Marshall, L. A. Curtiss, G. A. Ballentine, J. W. Elam, S. Catillon-Mucherie, P. C. Redfern, F. Mehmood and P. Zapol, *Nat. Mater.*, 2009, **8**, 213.
6 S. Lee, L. M. Molina, M. J. Lopez, J. A. Alonso, B. Hammer, B. Lee, S. Seifert, R. E. Winans, J. W. Elam, M. J. Pellin and S. Vajda, *Angew. Chem., Int. Ed.*, 2009, **48**, 1467.

7 Y. Lei, F. Mehmood, S. Lee, J. P. Greeley, B. Lee, S. Seifert, R. E. Winans, J. W. Elam, R. J. Meyer, P. C. Redfern, D. Teschner, R. Schlögl, M. J. Pellin, L. A. Curtiss and S. Vajda, *Science*, 2010, **328**, 224.
8 D. Bazin, C. Mottet and G. Treglia, *Appl. Catal., A*, 2000, **200**, 47.
9 D. J. Wales and H. A. Scheraga, *Science*, 1999, **285**, 1368.
10 O. Robach, G. Renaud and A. Barbier, *Surf. Sci.*, 1998, **401**, 227.
11 C. R. Henry, *Prog. Surf. Sci.*, 2005, **80**, 92.
12 G. Barcaro and A. Fortunelli, *Chem.–Eur. J.*, 2007, **13**, 6408.
13 K. Reuter and M. Scheffler, *Phys. Rev. B: Condens. Matter Mater. Phys.*, 2006, **73**, 045433.
14 K.-M. Ho, A. A. Shvartsburg, B. Pan, Z.-Y. Lu, C.-Z. Wang, J. G. Wacker, J. L. Fye and M. F. Jarrold, *Nature*, 1998, **392**, 582.
15 E. Aprà, R. Ferrando and A. Fortunelli, *Phys. Rev. B: Condens. Matter Mater. Phys.*, 2006, **73**, 205414.
16 G. Barcaro and A. Fortunelli, *J. Phys. Chem. C*, 2007, **111**, 11384.
17 G. Barcaro and A. Fortunelli, *Phys. Rev. B: Condens. Matter Mater. Phys.*, 2007, **76**, 165412.
18 L. J. Xu, G. Henkelman, C. T. Campbell and H. Jonsson, *Phys. Rev. Lett.*, 2005, **95**, 146103.
19 G. Barcaro, A. Fortunelli, G. Rossi, F. Nita and R. Ferrando Phys, *Phys. Rev. Lett.*, 2005, **95**, 246103.
20 C. Gonzalez and H. B. Schlegel, *J. Chem. Phys.*, 1989, **90**, 2154.
21 R. A. Olsen, G. J. Kroes, G. Henkelman, A. Arnaldsson and H. Jónsson, *J. Chem. Phys.*, 2004, **121**, 9776.
22 D. J. Wales, *Energy Landscapes: Applications to Clusters, Biomolecules and Glasses*, Cambridge University Press, 2004.
23 R. Ferrando, A. Fortunelli and R. L. Johnston, *Phys. Chem. Chem. Phys.*, 2008, **10**, 640.
24 M. Iannuzzi, A. Laio and M. Parrinello, *Phys. Rev. Lett.*, 2003, **90**, 238302.
25 G. Rossi and R. Ferrando, *Chem. Phys. Lett.*, 2006, **423**, 17.
26 G. Barcaro and A. Fortunelli, *New J. Phys.*, 2007, **9**, 22.
27 R. Ferrando and A. Fortunelli, *J. Phys.: Condens. Matter*, 2009, **21**, 264001.
28 M. Sterrer, E. Fischbach, T. Risse and J. J. Freund, *Phys. Rev. Lett.*, 2005, **94**, 186101.
29 C. Barth and C. R. Henry, *Phys. Rev. Lett.*, 2003, **91**, 196102.
30 A. J. Dent, J. Evans, S. G. Fiddy, B. Jyoti, M. A. Newton and M. Tromp, *Faraday Discuss.*, 2008, **138**, 287.
31 L. O. Paz-Borbon, R. L. Johnston, G. Barcaro and A. Fortunelli, *Eur. Phys. J. D*, 2009, **52**, 131.
32 S. Vajda, S. Wolf, T. Leisner, U. Busolt, L. Wöste and D. J. Wales, *J. Chem. Phys.*, 1997, **107**, 3492.
33 M. C. Saint-Lager, I. Laoufi, O. Robach, S. Garaudée and P. Dolle, *Faraday Discuss.*, 2011, **152**, 253.
34 J. A. Venables, L. Giordano and J. H. Harding, *J. Phys.: Condens. Matter*, 2006, **18**, S411.
35 S. Vajda, R. E. Winans, J. W. Elam, B. Lee, M. J. Pellin, S. Seifert, G. Y. Tikhonov and N. A. Tomczyk, *Top. Catal.*, 2006, **39**, 161.
36 J. Jellinek and E. B. Krissinel, *Chem. Phys. Lett.*, 1996, **258**, 283.
37 S. Chretien, M. S. Gordon and H. Metiu, *J. Chem. Phys.*, 2004, **121**, 9931.
38 D. M. Popolan, M. Nössler, R. Mitric, T. M. Bernhardt and V. Bonacic-Koutecky, *J. Phys. Chem. A*, 2011, **115**, 951.
39 P. Giannozzi, S. Baroni, N. Bonini, M. Calandra, R. Car, C. Cavazzoni, D. Ceresoli, G. Chiarotti, M. Cococcioni, I. Dabo, A. Dal Corso, S. De Gironcoli, S. Fabris, G. Fratesi, R. Gebauer, U. Gerstmann, C. Gougoussis, A. Kokalj, M. Lazzeri, L. Martin-Samos, N. Marzari, F. Mauri, R. Mazzarello, S. Paolini, A. Pasquarello, L. Paulatto, C. Sbraccia, S. Scandolo, G. Sclauzero, A. P. Seitsonen, A. Smogunov, P. Umari and R. M. Wentzcovitch, *J. Phys.: Condens. Matter*, 2009, **21**, 395502.
40 R. A. Kendall, E. Aprà, D. E. Bernholdt, E. J. Bylaska, M. Dupuis, G. I. Fann, R. J. Harrison, J. Ju, J. A. Nichols, J. Nieplocha, T. P. Straatsma, T. L. Windus and A. T. Wong, *Comput. Phys. Commun.*, 2000, **128**, 260.
41 K. M. Neyman, C. Inntam, A. V. Matveev, V. A. Nasluzov and N. Rösch, *J. Am. Chem. Soc.*, 2005, **127**, 11652.
42 J. P. Perdew, K. Burke and M. Ernzerhof, *Phys.Rev. Lett.*, 1996, **77**, 3865.
43 C. Elsasser, M. Fahnle, C. T. Chan and K. M. Ho, *Phys. Rev. B: Condens. Matter*, 1994, **49**, 13975.
44 R. W. Warren and B. I. Dunlap, *Chem. Phys. Lett.*, 1996, **262**, 384.
45 D. Vanderbilt, *Phys. Rev. B: Condens. Matter*, 1990, **41**, 7892.
46 D. Andrae, U. Haeussermann, M. Dolg, H. Stoll and H. Preuss, *Theor. Chim. Acta*, 1990, **77**, 123.
47 The coordinates with the structures and saddle points for the C_3H_6–O_2–Ag_3/MgO(100) systems are available upon request.
48 G. Barcaro and A. Fortunelli, *J. Chem. Theory Comput.*, 2005, **1**, 972.
49 D. M. Popolan and T. M. Bernhard, *J. Chem. Phys.*, 2011, **134**, 091102.
50 L. D. Socaciu, J. Hagen, J. Le Roux, D. Popolan, T. M. Bernhardt, L. Wöste and S. Vajda, *J. Chem. Phys.*, 2004, **120**, 2078.
51 Gold, *Faraday Discuss.*, 2011, entire volume **152**.
52 L. D. Marks, *Philos. Mag. A*, 1984, **49**, 81.
53 J. Hagen, L. D. Socaciu, J. Le Roux, D. Popolan, T. M. Bernhardt, L. Wöste, R. Mitric, H. Noack and V. Bonacic-Koutecky, *J. Am. Chem. Soc.*, 2004, **126**, 3442.
54 R. Asahi, T. Morikawa, T. Ohwaki, K. Aoki and Y. Taga, *Science*, 2001, **293**, 269.
55 V. R. Stamenkovic, B. S. Mun, M. Arenz, K. J. J. Mayrhofer, C. A. Lucas, G. F. Wang, P. N. Ross and N. M. Markovic, *Nat. Mater.*, 2007, **6**, 241.
56 D. Astruc, F. Lu and J. R. Aranzaes, *Angew. Chem., Int. Ed.*, 2005, **44**, 7852.
57 S. R. Billeter, A. Curioni and W. Andreoni, *Comput. Mater. Sci.*, 2003, **27**, 437.
58 J. M. del Campo and A. M. Köster, *J. Chem. Phys.*, 2008, **129**, 024107.
59 G. Mills and H. Jonsson, *Phys. Rev. Lett.*, 1994, **72**, 1124.
60 E. C. Beret, L. M. Ghirindelli and M. Scheffler, *Faraday Discuss.*, 2011, **152**, 153.